



PROCEEDINGS FROM THE
IX LATIN AMERICAN ROCK MECHANICS SYMPOSIUM

*Challenges in rock mechanics:
Towards a sustainable development of infrastructure*

Asunción, Paraguay, October 16-19, 2022

EDITOR

José Félix Pavón

AN OFFICIAL
INTERNATIONAL SOCIETY FOR ROCK MECHANICS
SYMPOSIUM

PROCEEDINGS FROM THE IX LATIN AMERICAN ROCK MECHANICS SYMPOSIUM

*Challenges in rock mechanics:
Towards a sustainable development of infrastructure
Asunción, Paraguay, October 16-19, 2022*



EDITOR

José Félix Pavón

Conference Chair

Universidad Católica de Asunción, Paraguay

AN OFFICIAL
INTERNATIONAL SOCIETY FOR ROCK MECHANICS
SYMPOSIUM



EDITOR
José Félix Pavón

COMPILER
Juan Nicolás Zabrodiec

GRAPHIC DESIGN
Juan Nicolás Zabrodiec

COVER PHOTO CREDITS
José Félix Pavón

This book of proceedings contains articles and information from authors all over the world. Many efforts have been made in order to check the format and contents of the articles, mainly concerning reliable data, but the editor and publisher cannot assume responsibility for the validity of all materials and the consequences of their use. All authors of the papers have expressed publication consent when submitting an article to the symposium. If any copyright material has not been acknowledged please contact the editor so it can be rectified.

INTERNATIONAL STANDARD BOOK NUMBER (ISBN): 978-99925-3-874-6 (eBook-PDF)

© 2022, José Félix Pavón
Sociedad Paraguaya de Geotecnia
Avda. España 959, Asunción, Paraguay

ALL RIGHTS BELONG TO THE:
INTERNATIONAL SOCIETY FOR ROCK MECHANICS (ISRM)
Av. do Brasil, 101, 1700-066 Lisbon, Portugal

ISBN: 978-99925-3-874-6



9 789992 538746

IX LATIN AMERICAN ROCK MECHANICS SYMPOSIUM (LARMS 2022)

ORGANIZING COMMITTEE

<i>Conference Chair</i>	José Félix Pavón (ISRM Vice-President for Latin America)
<i>Honorary Chair</i>	Eda Quadros (ISRM Past-President)
<i>Local Chair</i>	Roberto Andrada (Sociedad Paraguaya de Geotecnia President)
<i>Executive Secretary</i>	Juan Nicolás Zabrodiec
<i>Treasurer</i>	Tatiana Stanichevsky
<i>Scientific Committee Chair</i>	Miguel Pando
<i>Technical Program Chair</i>	Alejandro Quiñonez

ADVISORY COMMITTEE FOR ISRM

<i>ISRM President</i>	Resat Ulusay (TURKEY)
<i>Vice President for Africa</i>	Michael du Plessis (SOUTH AFRICA)
<i>Vice President for Asia</i>	Suseno Kramadibrata (INDONESIA)
<i>Vice President for Australasia</i>	Sevda Dekhoda (AUSTRALIA)
<i>Vice President for Europe</i>	Leandro Alejano (SPAIN)
<i>Vice President for North America</i>	Laura Pyrak Nolte (USA)
<i>Vice President for Latin America</i>	José Pavon (PARAGUAY)
<i>Vice President at Large</i>	Ömer Aydan (JAPAN)
<i>Vice President at Large</i>	Yang Qiang (CHINA)
<i>Vice President at Large</i>	Vojkan Jovicic (SLOVENIA)
<i>Secretary General</i>	Luis Lamas (PORTUGAL)

TABLE OF CONTENTS

KEYNOTE LECTURES

Monitoring ground surface displacements using satellite technology (GPS/GNSS and SAR) <i>Shimizu Norikazu</i>	10
Rock Mechanics for Deep Engineering <i>X.-T. Feng</i>	35
Frictional Discontinuities: the mechanics and imaging of slips <i>Antonio Bobet</i>	38
Continuum or Discontinuum - that is the question <i>Nick Barton</i>	49
Progress toward understanding complex rock slope failure mechanisms <i>D. Stead and D. Donati</i>	75
Time to failure of pillars - a limited equilibrium analysis <i>Ismet Canbulat</i>	96

TECHNICAL PAPERS

ADVANCES IN TESTING AND MONITORING IN ROCK MECHANICS

An integrated approach for monitoring movements and stability of slopes <i>Naohiko Tokashiki, Ömer Aydan and Takashi Ito</i>	105
A new approach for obtaining the shear modulus ratio during a slope failure process from instrumentation's data <i>Eduardo Medina and Luis Tejada</i>	115
Small-scale assessment of rockfall coefficients of restitution <i>Bruma Souza, Jean Benoît, Marion Bost, Philippe Reiffsteck and Noah MacAdam</i>	124
Landslide monitoring using SBAS-DInSAR along the northern Bulgarian Black Sea coast near Topola village <i>Marina Yamaguchi</i>	133
Cracking behavior of an inclined open crack in a transparent 3D printed rock-like specimen <i>Donggil Lee</i>	143
The electrical resistivity method and geological mapping for characterization of materials in linear excavation works <i>Julian Buritica Garcia</i>	149
Application of the SfM technique for geomechanical analysis according to SMR and Qslope <i>Cesar Borja and Luis Jordá</i>	159

CASE STUDIES IN ROCK MECHANICS

Sinkhole Issues in Mars <i>Ömer Aydan</i>	169
Limestone Rock in Road Projects: Case Study in the Rural Area of Vallemí – Concepción <i>Juan Carlos Berniè and Miguel Stanichevsky</i>	179
Tunnel portal instability adjoining landslide area and remedial measures: A case study of Sivoke-Rangpo railway tunnel T-7 <i>Manoj Kumar, Deepali Saxena and Armando Capellan</i>	185
Soil-structure interaction influence on shallow foundations design on rocky mass in a reinforced concrete building <i>Yago Santos, Bruno Rocha, Mayara Almeida, Paula Nascimento and Mirelly Meneses</i>	199
Numerical analysis stability of a geothermal plateau in the field “Los Azufres” Mexico <i>Ulises Talonia-Vargas</i>	209
Slope stability studies of dumps & stacks at Noamundi-Katamati iron ore mines, India—a case study <i>Manoj Tiwari</i>	219
Geological and Geotechnical 3D soil modeling of ultra deep waters oil field in the Eastern Brazilian Margin <i>Sergio Fontoura</i>	227
Evaluation of tip bearing capacity of bored piles embedded in the Vallemí-Cambajhopó limestone formation <i>Juan Nicolas Zabrodiec</i>	239
Rock slope stability issues in Afghanistan <i>Abdul Bali Jahed, Takashi Ito and Ömer Aydan</i>	247
Geotechnical design of temporary support for a drinking water transfer tunnel <i>Roy Gerardo Ruiz Vásquez</i>	257

MINING ENGINEERING

Analysing the reasons behind a large wedge failure in a room-and-pillar roofing slate mine <i>Leandro R. Alejano, Ignacio Pérez-Rey, Jing-Yun Gui and Hossein Masoumi</i>	267
Developing a Severity Index to account for seismic induced damage in a deep level mine <i>Jean-Pierre Gouvea and Michael du Plessis</i>	277
Rock fracture stimulation using slow energy releasing fracturing compounds <i>Radhika De Silva and Ranjith Pathegama Gamage</i>	289
Web-Pillar Design for Highwall Coal Mining – A case study <i>Surajit Sarkar, Manoj Kumar Tiwary, Indranil Saha, Piyush Srivastava and D.B. Sundara Ramam</i>	299
Estimation of the probability of rock fall occurrence in underground Mines <i>Fernando Fernandez and Miguel Angel Rodriguez</i>	306
Geotechnical Design Strategies in Open Pit Mine with the Presence of Old Underground Excavations <i>Victor Vergara, Victor Góngora Pérez and Oscar Cabello Robles</i>	317
Machine Learning in Mining: Uses and Techniques applied in geomechanics <i>María Elena Valencia Vera</i>	327

NUMERICAL METHODS AND MODELLING

- Behavior of Shales from Experiment to Modeling 336
Marte Gutierrez
- Modeling of the Brazilian Tensile Test on Transversely Anisotropic Rocks Using PDEM 352
Marte Gutierrez and Guowen Xu
- A trap-door experimental study on dynamic loads on the support of underground openings due to earthquake shaking 362
Michio Tamashiro, Ömer Aydan, Takashi Ito and Neamatullah Malistani
- Numerical modeling of the roughness formation of tensile fractures: is grain size heterogeneity an influential factor? 370
Jineon Kim and Jae-Joon Song
- Numerical Simulation on the Rock-Crushing Mechanism with Combined Cutter Bits under Percussive Load 379
Jiansheng Liu, Hualin Liao, Mingzhe Chao and Jun Wei
- DEM simulation on the effect of meso properties of conglomerate on its mechanical properties and failure mechanism 391
Jun Wei, Hualin Liao and Bin Huang
- Modeling of the rock fracture mechanism caused by explosives using the Discrete Element Method 401
Hazel Fernando González, Jesús Sánchez and Gabriel Auvinet

PETROLEUM AND GEOTHERMAL ENGINEERING

- Mechanical Characterization of Synthetic Carbonate Rocks for Application in Oil Reservoir Analysis 412
Yago R. P. Santos, Analice F. L. Amorim and Igor F. Gomes
- Comprehensive in-situ stress estimation for a fractured geothermal reservoir from drilling, hydraulic stimulations, and induced seismicity 421
Sehyeok Park, Kwang-Il Kim, Hwajung Yoo, Juhyi Yim and Ki-Bok Min
- CO₂ geological storage: evaluation of lightweight cement for injection well 429
Christian Martin, Jean Michel Pereira, Diego Manzanal, Siavash Ghabezloo and Teresa Piqué
- Geomechanical and Petrophysical characterization of Bajo Barreal Formation in GSJB 439
Pablo Vidal, Diego Manzanal, José Allard and Cecilia Laskowski
- Evaluation of physio-mechanical properties of Gyeongju bentonite using X-ray CT 449
Melvin Diaz, Sang Seob Kim, Gyung Won Lee, Seohyeon Yun, Kwang Yeom Kim, Changsoo Lee, Jin-Seop Kim and Minseop Kim
- Fuzzy expert system for preliminary qualification of Carbon Capture and Storage projects 456
Henrique Martínez M.
- Mechanical and microstructural behavior of cement-rock interface for CO₂ geological storage 466
Juan Barria, Diego Manzanal, Jean-Michel Pereira and Siavash Ghabezloo
- Wellbore closure in salt section with consideration of primary creep 476
Daniel Melo and Sergio Fontoura

ROCK MASS CHARACTERIZATION AND TESTING

- Laboratory 3D rock joint roughness evaluation with basic, uncomplicated close-range photogrammetry 483
José Muralha, André Paixão, Ricardo Resende and Eduardo Fortunato
- Toward a new definition of terms in the rock geomechanical classification and its relation to the numerical analysis of tunnels 493
Wagdi Naime and Roque García
- Effect of artificial joints on the mechanical response of a granitic rock 503
Javier Arzua, Loreto J. Cuevas-Ugalde, Héctor B. Ledesma-Osorio, Manuel Cánovas and Mohammad A. Maleki
- Assessment of effect of anisotropy on failure mode and shear parameters of Chamoli rock using triaxial system 511
Manish Shah and Dinesh Jaganiya
- Investigation of desiccation strains and cracks induced by heating of clay-rock by Heaviside-based digital image correlation 521
Sadek Tormos, Stephen Hedan, Richard Giot and Philippe Cosenza
- Characterization potentially expansive layer of “Chenque” and “Sarmiento” geological formation 528
Sandra Orlandi, Cecilia Laskowski and Diego Manzanal
- Estimation of Geological Strength Index in stratified rock mass based on fractal theory 538
Eduard Palmezano Pinto and Johnatan Ramos Rivera
- Use of statistical techniques for improving rock mass characterization 548
Kimie Suzuki
- Geomechanical characterization of the rock mass in Tunnels 556
Julio Cesar Chable Moreno and Jorge Antonio López Molina

SOFT ROCKS

- Effect of water content on the physico-mechanical properties of mudstone of Shimajiri formation and its water absorption and desorption characteristics 566
Takashi Ito, Ömer Aydan and Naohiko Tokashiki
- Shales and Slates of El Sillar, Bolivia: Description of degradation processes 576
Vladimir Ugarte Ontiveros and Danny Rodriguez Sandoval

TUNNELING AND DEEP EXCAVATIONS IN ROCK

Rock Load Estimation for Underground Structures <i>Charles A. Stone</i>	586
Analysis of the monitored behaviour of a hydraulic tunnel using a structural and a statistical model <i>Renato Pereira, Margarida Espada, Luís Lamas and Nuno Reis</i>	596
Influence of geotechnical parameters, in-situ stresses, and tunnel advance rate on rockburst's strain energy <i>Cristian Segura, Adeline Delonca and Yann Gunzburger</i>	606
Possible causes of unexpected cracks in a large-span railway tunnel after ring closure <i>Servet Karahan, Ozgur Yilmaz and Candan Gokceoglu</i>	616
Technical Aspects of Tunnel Construction in Anhydrite Containing Rocks <i>Vojkan Jovičić, Belmir Hekić, Muris Mujkić and Alaga Husić</i>	624
Modeling of the damage in the contour of tunnels caused by the use of blasting using the DEM <i>Hazel Fernando González, Jesús Sánchez and Gabriel Auvinet</i>	634

KEYNOTE LECTURES

Monitoring ground surface displacements using satellite technology (GPS/GNSS and SAR)

N. Shimizu

Kansai University and Yamaguchi University, Japan

ABSTRACT:

Monitoring is essential for assessing the stability of natural rocks and rock structures, confirming the validity of the design, predicting risks, managing safe operations, and reducing project costs. The monitoring system used in Rock and Geotechnical Engineering is ideally required to be able to monitor the behavior of rocks and soils in local to extensive areas, continuously and automatically, with high accuracy and at a low cost. Satellite technology (GPS/GNSS and SAR) will support the realization of such monitoring. This paper firstly outlines GPS/GNSS and SAR as tools for displacement monitoring and then describes the concept of “spatio-temporal continuous displacement monitoring” in Rock and Geotechnical Engineering. A practical application is demonstrated by means of the combination of GPS/GNSS and SAR for monitoring a slope. Then, case studies of monitoring land subsidence due to the extraction of brine from an underground salt mine and landslides in an extensive valley and along a coast, conducted as international collaborative research, are introduced.

1 INTRODUCTION

Monitoring is essential for assessing the stability of natural rocks and rock structures and for confirming the validity of the design of infrastructures and countermeasures during the construction and operation. Monitoring is also vital for predicting risks, managing safe operations, and reducing project costs. The ideal monitoring system for projects in Rock and Geotechnical Engineering should be able to monitor the behavior of rocks and soils in local to extensive areas continuously and automatically, with high accuracy. In addition, the costs should be low, and the system should be reliable and easy to handle.

There are various types of instruments for taking displacement measurements in Rock and Geotechnical Engineering, such as extensometers, inclinometers, etc. They are useful and frequently employed in various situations. However, these instruments may not be adequate for monitoring large slopes or extensive areas because generally they can only be applied to limited areas that are dozens of meters or, at most, around 100 m in size.

Satellite technology, GPS /GNSS (Global Positioning System/Global Navigation Satellite System) and SAR (Synthetic Aperture Radar), is capable of overcoming the above problems since it can be applied to monitor the displacements of the ground and structures over extensive areas. This paper firstly outlines GPS/GNSS and SAR as tools for displacement monitoring. Then, the concept of “spatio-temporal continuous displacement monitoring”, which uses satellite technology and geotechnical instruments together, is described. A practical application is demonstrated by means of the combination of GPS/GNSS and SAR for monitoring a slope. Then, case studies of monitoring land subsidence due to the extraction of brine from an underground salt mine in Bosnia and Herzegovina, and landslides in the Vipava River Valley in Slovenia and along the Black Sea coast in Bulgaria, which were conducted as international collaborative research, are discussed.

2 SATELLITE TECHNOLOGY FOR DISPLACEMENT MONITORING

2.1 *Displacement monitoring by GPS/GNSS and SAR*

GPS is a satellite-based positioning system that was developed in the USA. It was established as

a method for navigation and long baseline surveys (Hoffmann-Wellenhof et al. 2001; Misra and Enge 2006). The advantage of GPS is that it can easily provide three-dimensional displacements with mm accuracy over extensive areas. Recently, other satellite navigation systems, GLONASS, Galileo, BeiDou, QZSS, etc., have been developed; they are generally termed GNSS (Global Navigation Satellite System).

A GPS displacement monitoring system using the L1 signal was developed by the author and his colleagues (Iwasaki et al. 2003; Masunari et al. 2003; Shimizu and Matsuda 2002). It was then upgraded to a wireless data transfer system, as illustrated in Figure 1. In this system, sensors are set on monitoring points and a reference point, respectively. The data from the satellites are received at each sensor and then transferred to a control box set at the monitoring site. A computer, data memory, and network device are installed in the control box. The server computer, located in an office away from the monitoring area, automatically controls the entire system to acquire and analyze the data. Then, three-dimensional displacements are obtained for all the monitoring points and are provided to users through the Internet in real time. Users only need to access the website to see the monitoring results.

The most important issue in the practical use of GPS/GNSS is how to improve the measurement accuracy. The author and his colleagues have proposed methods for removing and/or reducing errors and for estimating the real values of the measurements. Those methods have succeeded in providing measurement results that are a few times higher (i.e., mm) in accuracy than the standard GPS/GNSS (Shimizu et al. 2011; Shimizu and Nakashima 2017). The procedure has been approved as “the ISRM suggested method for monitoring rock displacements using the Global Positioning System” (Shimizu et al. 2014).

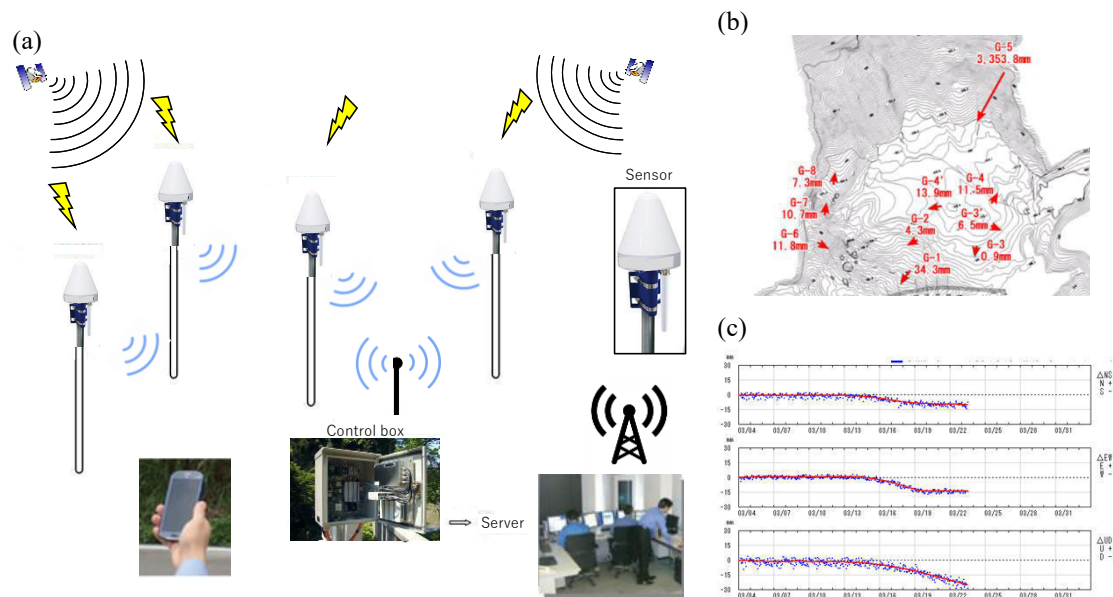
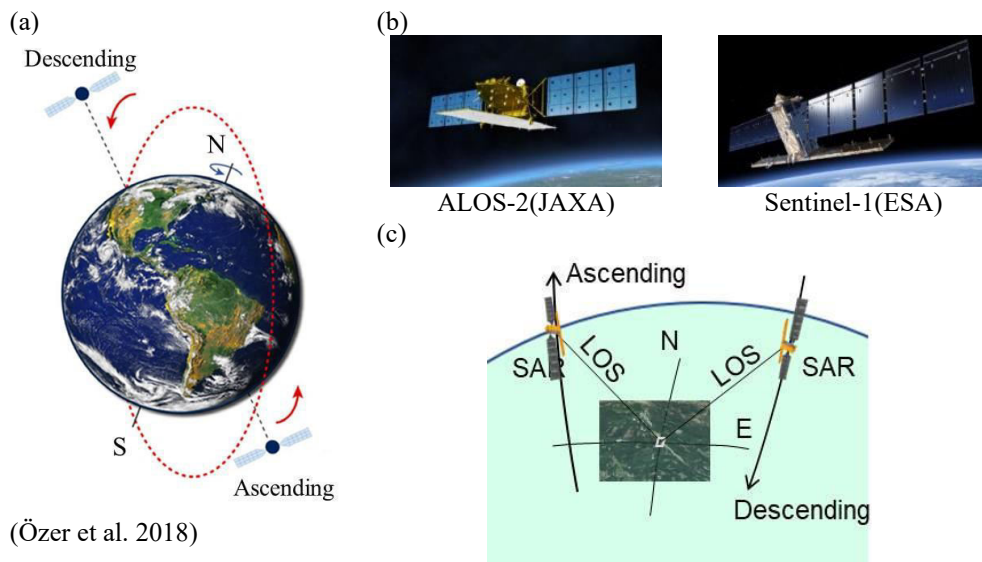


Figure 1. GPS fully automatic continuous displacement monitoring system. (a) sensors and system, (b) displacement vectors (Sato et al. 2014), and (c) transition of three-dimensional displacements.

SAR is a radar device mounted on an aircraft or artificial satellite. It is one type of active remote sensing that uses microwave radiation, enabling observations 24 hours a day under all weather conditions (Hanssen 2002). Nowadays, there are several SAR satellites orbiting the Earth, i.e., COSMO-SkyMed (ASI: Italian Space Agency), TerraSAR-X (DLR: German Aerospace Center), RADARSAT-2 (CSA: Canadian Space Agency), Sentinel-1 (ESA: European Space Agency), ALOS-2 (JAXA: Japan Aerospace Exploration Agency), etc. (Figure 2).

Interferometric SAR (InSAR) is a method for taking the signal phase difference (interference) from two SAR data images which are observed in the same area at different periods by the same SAR satellite in the same orbit.

Differential Interferometric SAR (DInSAR) is the term for the method of producing ground surface displacements by taking interferograms from which the influence of topography and the baseline length of the satellite positions has been removed (Ferretti et al. 2007). The advantage of DInSAR is that it can provide the displacement distribution of the ground surface over a vast area without the use of any sensors on the ground (Ferretti 2014). The observed displacement is one-dimensional along the Line of Sight (LOS), which is the direction from the satellite to the observed Earth's surface (Figure 2(c) and Figure 3(b)). The accuracy is around cm level. When temporal continuous displacement monitoring is conducted by DInSAR, SBAS (Small Baseline Subset) DInSAR (Berardino et al. 2002) and PS (Permanent Scatter) InSAR (Ferretti et al. 2001) are often used.



(Özer et al. 2018)

Figure 2. SAR satellites, their orbits and LOS: (a) ascending and descending orbits, (b) SAR satellites, and (c) LOS direction.

2.2 Spatio-temporal continuous displacement monitoring

The features of GPS/GNSS and DInSAR are compared in Table 1 and Figure 3. GPS/GNSS can continuously monitor three-dimensional displacements at certain points 24 hours a day with mm accuracy, whereas DInSAR can take one-dimensional displacement measurements of much greater areas usually once every several days/a few weeks with cm accuracy in spatial resolution of 3 to 30 m on the ground surface. DInSAR does not require any sensors on the ground, while GPS/GNSS requires a sensor at each monitoring point. Therefore, GPS/GNSS and DInSAR make up for each other's shortcomings.

Table 1. Features of GPS/GNSS and DInSAR (Boldface: advantages)

	GPS/GNSS	DInSAR
Required devices for user	Receivers	Not necessary
Observable displacements	Point(s)	Entire area (3-30 m spatial resolution)
Continuous monitoring	Every hour or shorter periods (available 24 hours a day)	Periodic: a week ~ several months
Dimension of measurements	3-dimensional	1-dimensional
Accuracy	mm level	cm level

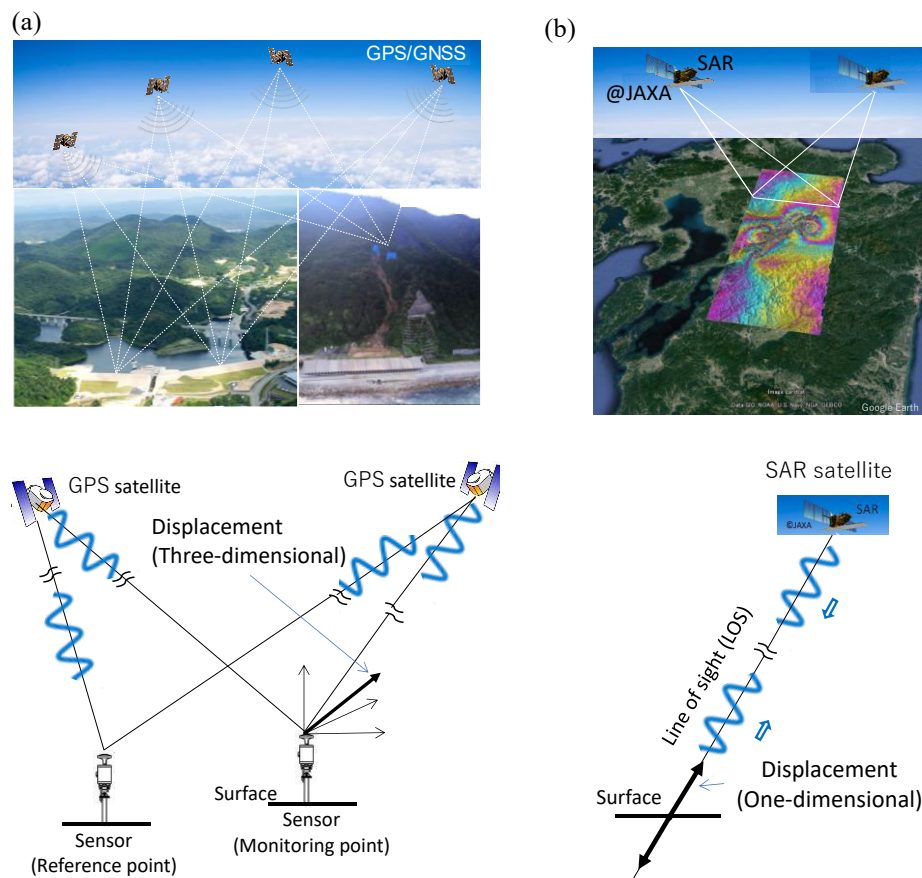


Figure 3. GPS/GNSS and DInSAR, and their monitored displacements: (a) GPS/GNSS and (b) DInSAR (photos: Google Earth).

Figure 4(a) shows a schematic diagram of the relationship between the measurement accuracy and the size of a monitoring area expressed by the baseline length. The applicable ranges of the geotechnical instruments and conventional surveying methods are illustrated in this figure. A gap in accuracy between the two methods can be seen. GPS/GNSS can cover this gap. In addition, DInSAR is able to expand the validity of the displacement monitoring to large areas.

Looking at the relative accuracies of these methods, they are almost the same, in the order of about 10^{-6} , i.e., 0.1 mm (accuracy)/100 m (baseline length) for geotechnical instruments, 1 mm/1 km for GPS/GNSS, and 10 mm/10 km for DInSAR. This means that displacements could be measured with almost the same accuracy as 10^{-6} over small to very extensive areas by applying both geotechnical instruments and satellite technology (GPS/GNSS and DInSAR). Spatially continuous (spatio-continuous) monitoring can be thus realized.

On the other hand, Figure 4(b) shows a diagram of the relationship between the measurement interval (period) and the size of a monitoring area. Geotechnical instruments can measure displacements at any interval. In the case of GPS/GNSS, the interval of the measurements is usually an hour when the baseline length is within 1 km. Recently, however, the measurement interval can be a second or less (e.g., 20 Hz) if accuracy of a few cm is acceptable.

In the case of DInSAR, the interval of the measurements depends on the satellite regression cycle. It is usually several days or a few weeks or more. Although there may be a limitation in the measurement interval for monitoring extensive areas at present, there are plans to launch numerous SAR satellites which will improve this issue. Therefore, temporal continuous monitoring can be done. Consequently, spatio-temporal continuous displacement monitoring can be realized by combining the two types of satellite technology with geotechnical instruments.

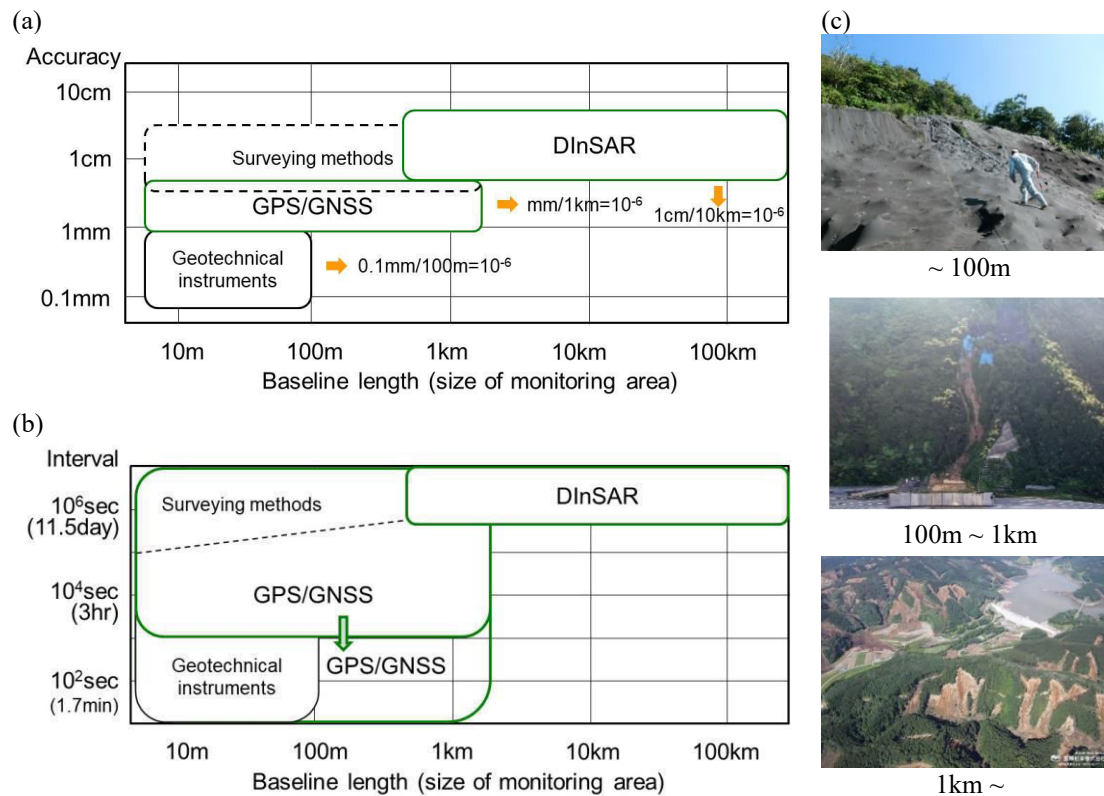


Figure 4. Spatio-temporal continuous displacement monitoring using geotechnical instruments and satellite technology: (a) measurement accuracy and baseline length, (b) measurement interval and baseline length, and (c) examples of size of monitoring area.

2.3 Coupling GPS/GNSS and SAR for monitoring a slope

A case study on the coupling application of GPS/GNSS and SAR for monitoring a slope is introduced in this section as an example of “spatio-temporal continuous displacement monitoring”.

The monitoring site is a steep slope, with a height of about 100 m, along a national road in Japan (see Figure 5). The slope is primarily composed of rhyolite and granite which formed in the Cretaceous period of the Mesozoic era, and its surface is partially covered with a colluvial deposit. Vegetation extends over the slope and creates an obstruction above the antennas of the GPS sensors.

In July 1972, the slope collapsed in large areas and deposits flowed, causing damage to a railway and a national road. The railway track was later replaced by a new route with a tunnel running through the mountain. A check dam was then constructed to collect deposits from the upper part of the slope, and a rock shed was built above the road to protect passing vehicles and people. Since then, large failures, small surface collapses, and runoffs have occasionally occurred due to heavy rainfall events from the 1990s to the early 2010s.

The slope behavior continued to be monitored by conventional geotechnical instruments, i.e., surface extensometers, borehole inclinometers etc. However, most of them have become unavailable and/or have broken due to the occurrence of large displacements. In addition, those instruments were available only in limited areas, and it was difficult to monitor the entire slope.

Therefore, GPS sensors were set in large areas of the slope: i.e., firstly at monitoring points G1 and G2 in 2012 (Furuyama et al. 2014), then at G3 and G4 in 2014 (Kien et al 2017; Sato et al. 2021), and finally at G5 and G6 in 2018 (Figure 5(b)). K1 is the reference point. G1 was removed in 2014 after a surface collapse occurred around this point. All the sensors were firmly fixed at

the monitoring points on the ground surface by a tripod with anchors (Figure 6). The height differences between monitoring points G2 to G6 and reference point K1 were from 70 to 110 m. The upper row in Figure 6 shows photographs of sky views above the sensors. It was found that the vegetation and the slope surface behind the sensors partially cover the sky area from the northeast to the southwest. The GPS monitoring system (Figure 1) has automatically monitored the three-dimensional displacement every hour at each point and provided the results on a website through the Internet.

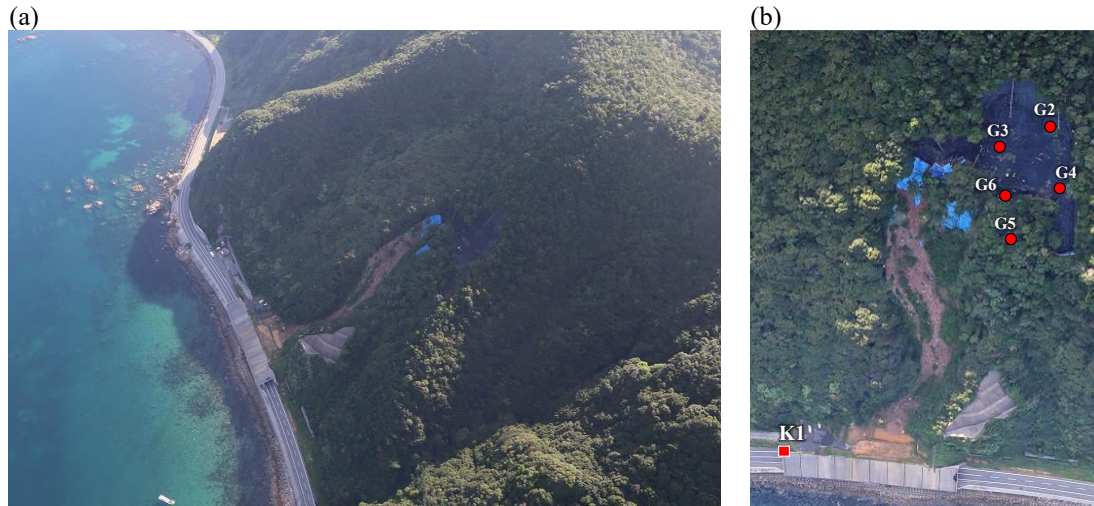


Figure 5. Monitoring site and locations of GPS sensors: (a) target slope and (b) GPS monitoring points.

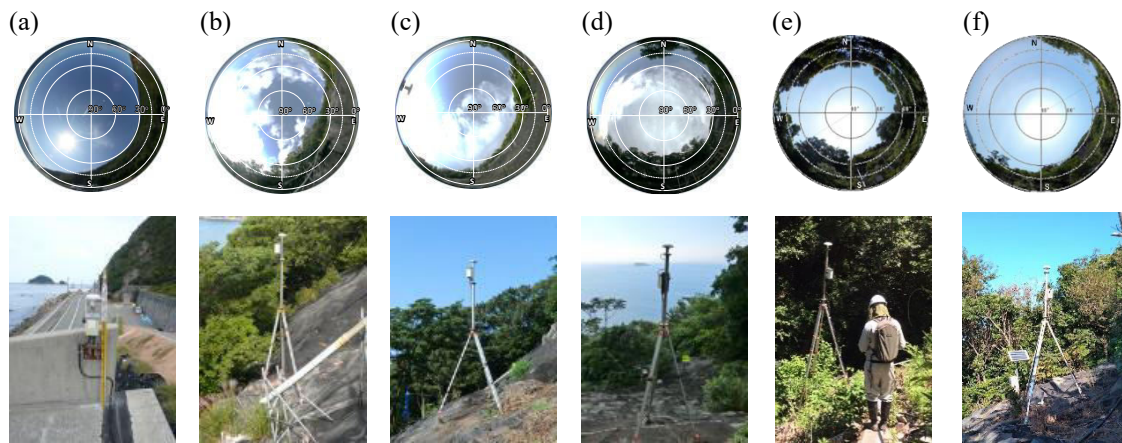


Figure 6. GPS sensors with sky view photos above sensors: (a) reference point K1, (b) monitoring points G2, (c) G3, (d) G4, (e) G5 and (f) G6.

In order to perform precise monitoring, signal disturbances due to obstructions above the antennas were reduced by the mask procedure, and errors due to tropospheric delays were corrected by a tropospheric model using meteorological data. These procedures are based on the ISRM suggested method, which the author proposed (Shimizu et al. 2014). After removing such errors, the “trend model” was applied to estimate the exact displacement (Shimizu et al. 2014).

Figure 7 shows the monitoring displacements at G2, G3, and G4 from 12 August 2014 to 1 May 2021 and at G5 and G6 from 25 December 2018 to 1 May 2021 together with the amounts of rainfall (mm/day) expressed by the bar graph. The standard deviations of the measured displacements in the horizontal directions (latitude and longitude) and in height are 1 to 2 mm and 3 to 4 mm, respectively, for all the monitoring points. Continuous three-dimensional displacement

monitoring was performed for almost seven years without missing any data, except during the maintenance period.

Table 2 shows the annual average displacement at all the monitoring points, G2 to G6. The value is seen to gradually decrease within several mm per year, although there have been heavy rainfall events with more than 100 mm/day several times since 2014. The decrease in slope displacements might have been caused by the effect of the horizontal drainage holes, drilled in 2014 as a countermeasure to the landslide, in the upper area around G4.

Figure 8 shows the transition of the displacement vectors in the plan view and in the vertical sections of the slope from August 2014 to December 2018. During this period, the displacement at G3 headed to the northeast, which is the direction of the collapsed portion, up to 9 May 2016, after which it turned to the northwest (downward movement). The displacement at G4 constantly increased in the inclination direction of the slope, while the displacement at G2 subsided. Therefore, this portion, including monitoring points G2, G3, and G4, seems to show a rotational slide.

On the other hand, the slope behavior has changed since January 2019, as shown in Figure 9. The displacements at all the points, G2 to G6, have been heading in almost the same direction as that at G3 since 9 May 2016, in both the plan view and the vertical section, as seen in the comparison in Figure 8(a) and Figure 9(a), and Figure 8(c) and Figures 9 (b) and (c). Therefore, this area seems to show translational movement along the boundary between the rhyolite (surface rock) and the granite (bedrock).

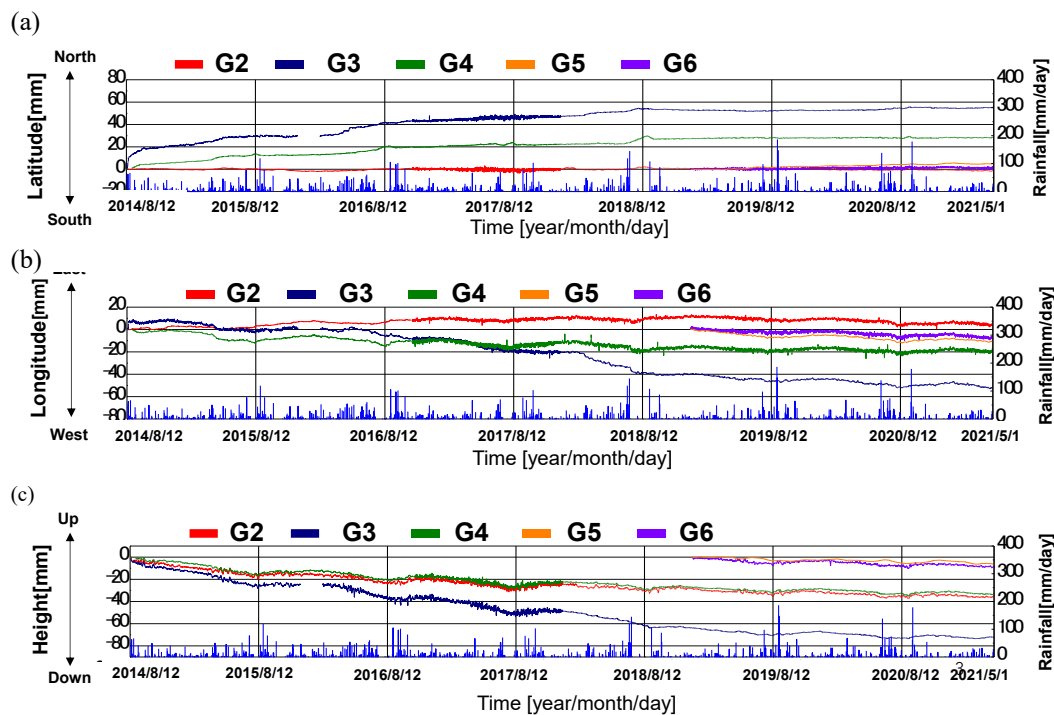


Figure 7. Temporal transition of three-dimensional displacements: (a) latitude, (b) longitude, and (c) height.

Table 2. Annual rate of displacement at monitoring points (mm/year).

No./Year	2014	2015	2016	2017	2018	2019	2020
G2	19	7	6	3	5	4	6
G3	40	18	18	24	12	6	5
G4	24	9	6	7	3	2	6
G5	-	-	-	-	13	6	3
G6	-	-	-	-	12	5	4

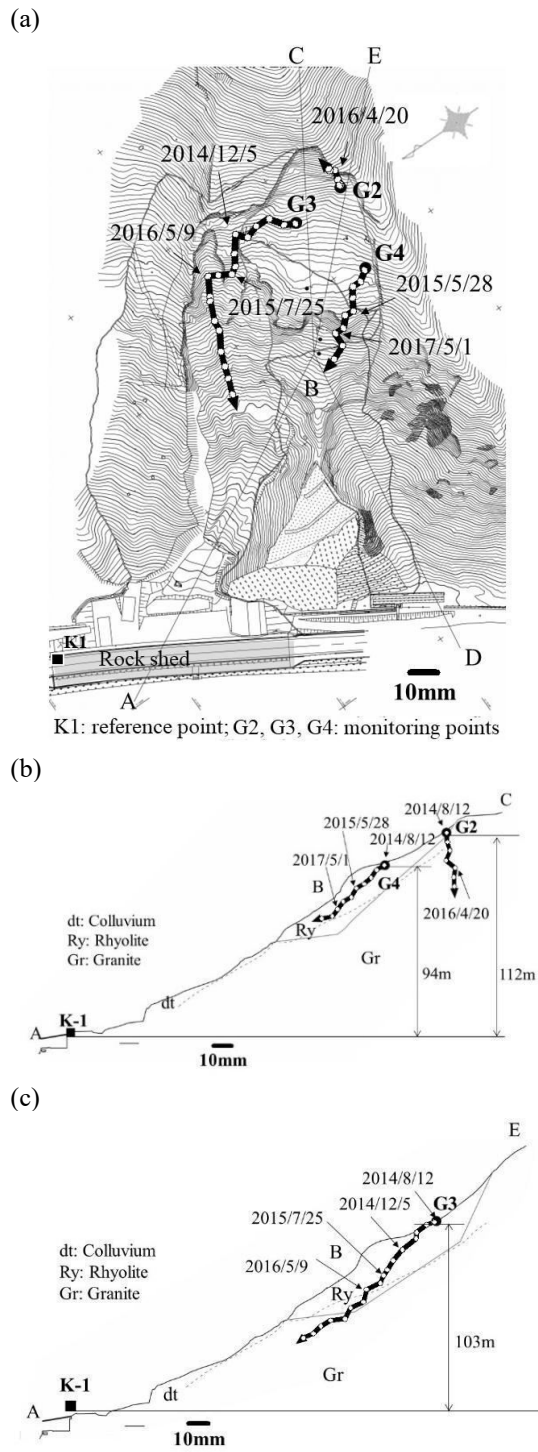


Figure 8. Transition of displacement vectors from August 2014 to December 2018: (a) plan view, (b) vertical section (B-B'), and (c) vertical section (C-C').

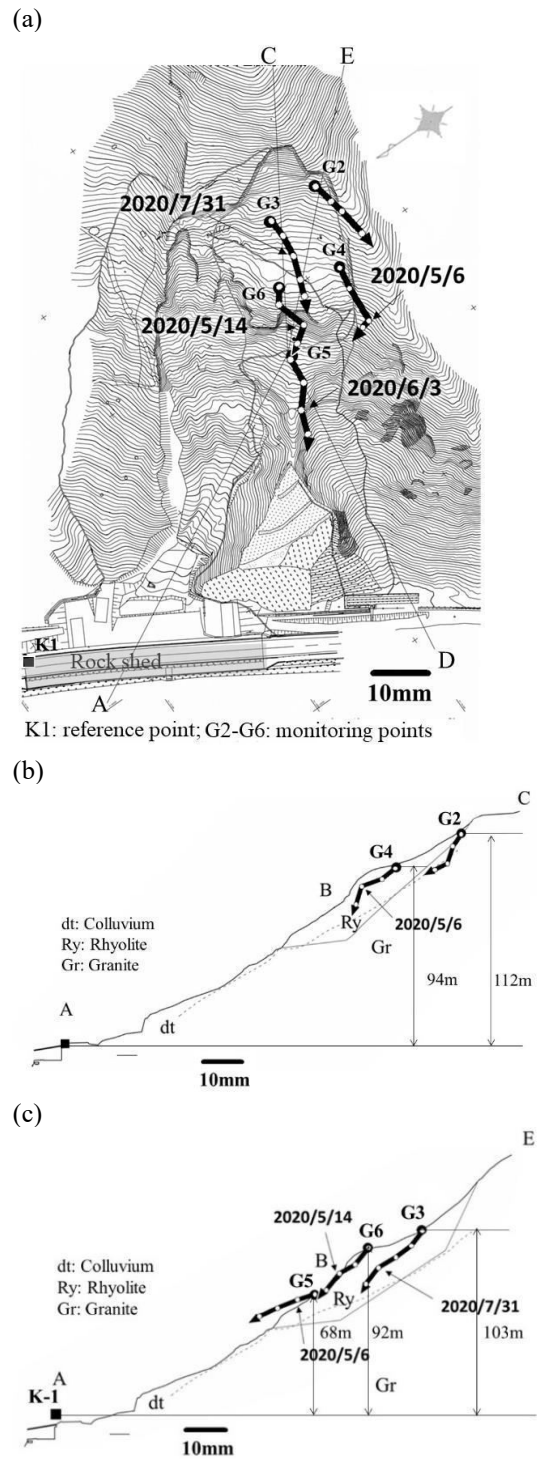


Figure 9. Transition of displacement vectors from January 2019 to May 2021: (a) plan view, (b) vertical section (B-B'), and (c) vertical section (C-C').

As seen above, GPS displacement monitoring is effective for detecting the detailed three-dimensional displacements of a slope. This is one of the great advantages of GPS monitoring. However, the slope behavior can be found only at the monitoring points set at a GPS sensor. On the other hand, SAR has the potential to find the displacement distribution of the entire area.

SBAS-DInSAR was applied to this slope for finding the transition of the displacement distribution (Nagasaki et al. 2021). L-band ALOS-2 data were employed in this analysis because the target slope is located in an area of deep vegetation. All the SAR data processing in this paper was conducted with Envi-SARscape 5.5.3.

Figures 10 and 11 show the temporal transition of the spatial distributions of the LOS displacement around the target slope obtained by SBAS-DInSAR, using ascending and descending data, respectively, for about 5 years from 2014/15 to 2021 (16 ascending and 26 descending images), respectively. The final accumulated LOS displacement distributions for the slope are shown with the horizontal displacement vectors by GPS during similar periods in Figures 12(a) and (b).

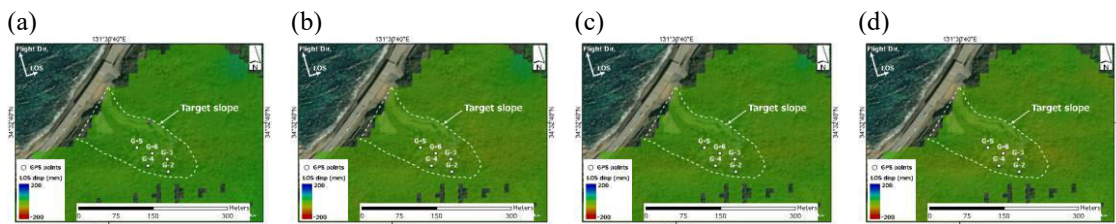


Figure 10. LOS displacement distribution by ascending data from 6 Nov. 2014: (a) 8 Apr. 2018, (b) 7 Mar. 2019, (c) 5 Mar. 2020, and (d) 4 Mar. 2021.

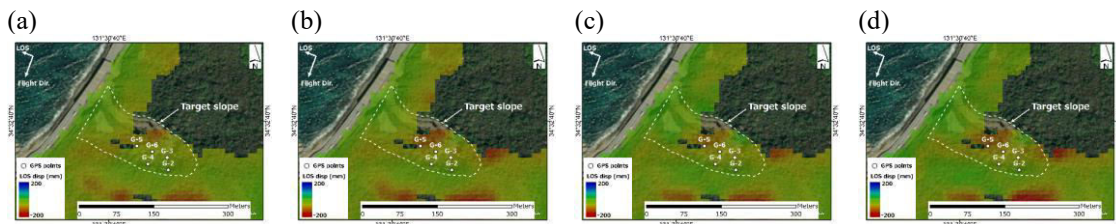


Figure 11. LOS displacement distribution by descending data from 9 Feb. 2015: (a) 5 Mar. 2018, (b) 4 Mar. 2019, (c) 2 Mar. 2020, and (d) 1 Mar. 2021.

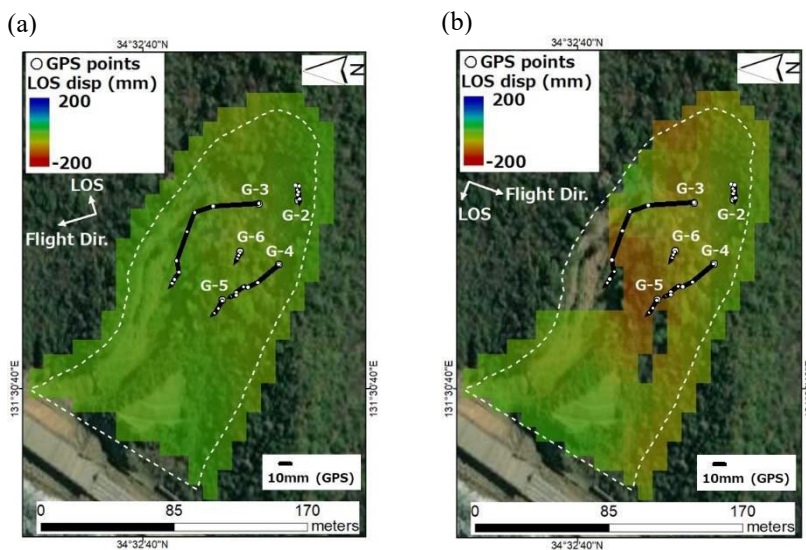


Figure 12. LOS displacement distribution by DInSAR and displacement vectors by GPS (G2 to G4: 12 Aug. 2014 to 31 May 2021; G5 and G6: 1 Jan. 2019 to 31 May 2021): (a) ascending results (6 Nov. 2014 to 4 Mar. 2021) and (b) descending results (9 Feb. 2015 to 1 Mar. 2021).

The resolution of the ground surface (unit of pixels) is 10 m x 10 m. The LOS displacements are represented by the range in color from red to blue denoting mm units from -200 mm to 200 mm. The red and blue mean negative (extension) and positive (compression) LOS displacements (Figure 3(b)), respectively.

In the area with low coherence, below the threshold value (0.3 is employed in this study), the results of the LOS displacement have been removed from the map. Coherence is an index, taken as 0 to 1, to represent whether a good interferogram has been produced. A higher value indicates a better condition for obtaining reliable results. Results are not shown in some of the vegetation area due to low coherence in the descending results (Figure 12(b)).

In order to investigate the validity of the results of DInSAR, the LOS displacements are compared with ones measured by the GPS displacement monitoring system. Since the GPS monitoring system provides three-dimensional displacements, they must be converted to the LOS direction by the following equations:

$$d_{LOS(A)} = [D_{E-W} \quad D_{N-S} \quad D_{U-D}] \begin{bmatrix} -\sin\theta_a \cos\beta_a \\ -\sin\theta_a \sin\beta_a \\ \cos\theta_a \end{bmatrix} \quad (1)$$

$$d_{LOS(D)} = [D_{E-W} \quad D_{N-S} \quad D_{U-D}] \begin{bmatrix} \sin\theta_d \cos\beta_d \\ -\sin\theta_d \sin\beta_d \\ \cos\theta_d \end{bmatrix} \quad (2)$$

where $d_{LOS(A)}$ and $d_{LOS(D)}$ are the ascending and descending LOS displacements, respectively, θ_a and θ_d are the incidence angles of the microwaves transmitted from the satellite on the ascending and descending orbits, respectively, and β_a and β_d are the angles of the ascending and descending satellite flight directions, respectively, as shown in Figure 13. D_{E-W} , D_{N-S} , and D_{U-D} are the displacement components of the longitude, latitude, and height direction, respectively.

Figures 14 and 15 present comparisons between the displacements obtained by DInSAR and GPS at G2 to G6 in the ascending and descending LOS directions, respectively. The discrepancies between the two sets of displacements are within 10 mm and 20 mm for the ascending and descending results, respectively. Figure 16 shows the correlation between DInSAR and GPS at all the GPS monitoring points, namely, G2 to G6. It is found that the DInSAR results agree well with the GPS results. This means that DInSAR can be applied for monitoring displacements with cm accuracy, even those of steep slopes in areas with dense vegetation.

As seen in Figures 7 to 12, the combination of SAR and GPS could be one desirable method for monitoring the behavior of a slope; it brings about the realization of “spatio-temporal continuous displacement monitoring”.

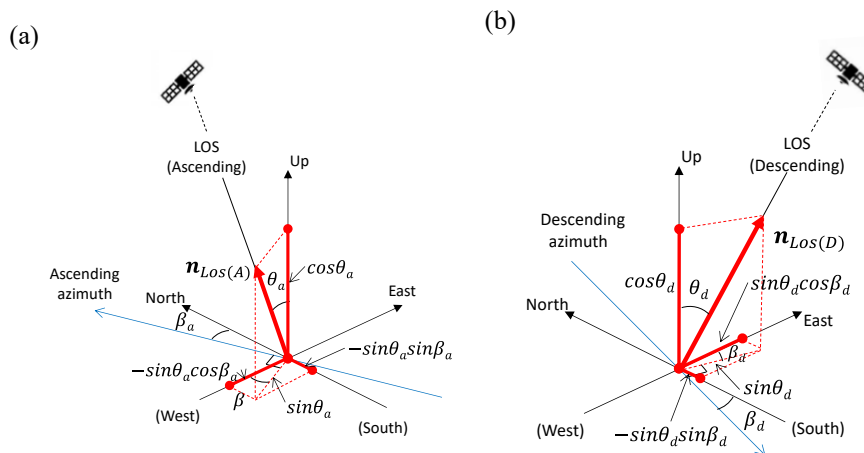


Figure 13. Geometry of three-dimensional displacements projected into LOS displacements in ascending and descending right-looking directions: (a) ascending case and (b) descending case.

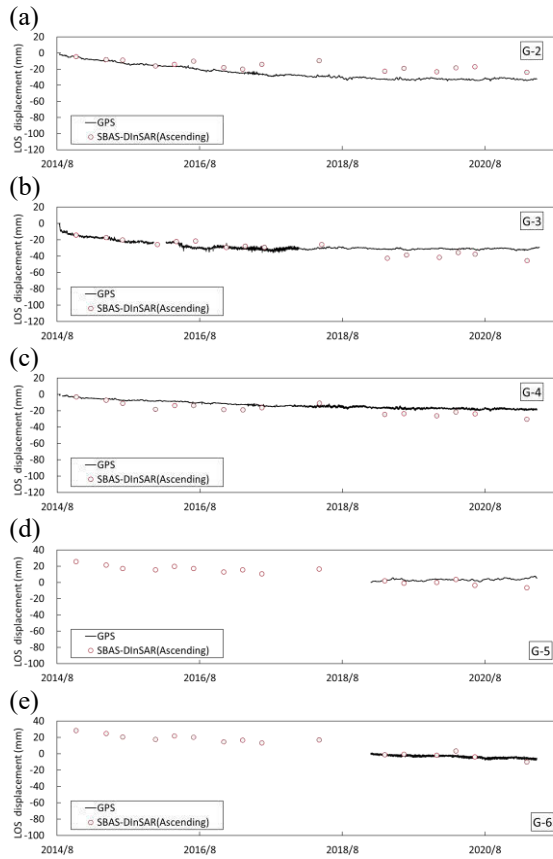


Figure 14. Temporal transition of LOS displacements by SBAS-DInSAR (ascending) and GPS: (a) G2, (b) G3, (c) G4, (d) G5, and (e) G6.

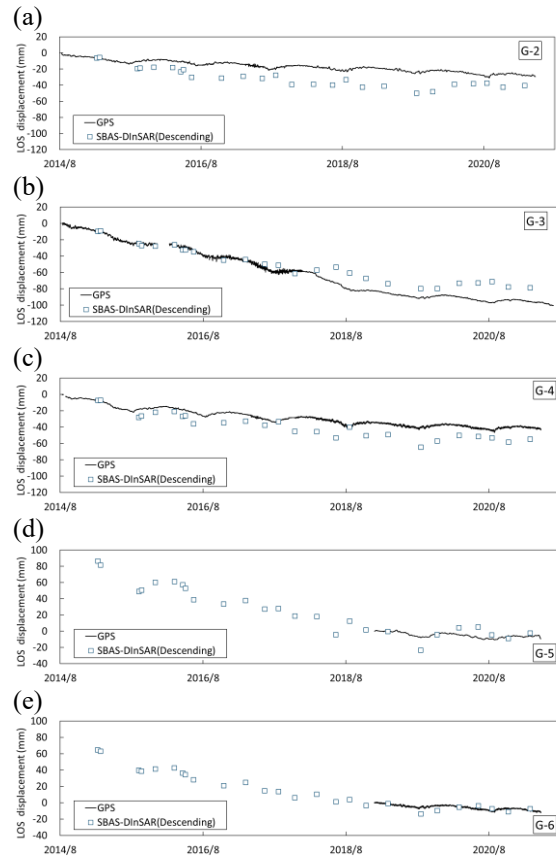


Figure 15. Temporal transition of LOS displacements by SBAS-DInSAR (descending) and GPS: (a) G2., (b) G3, (c) G4, (d) G5, and (e) G6.

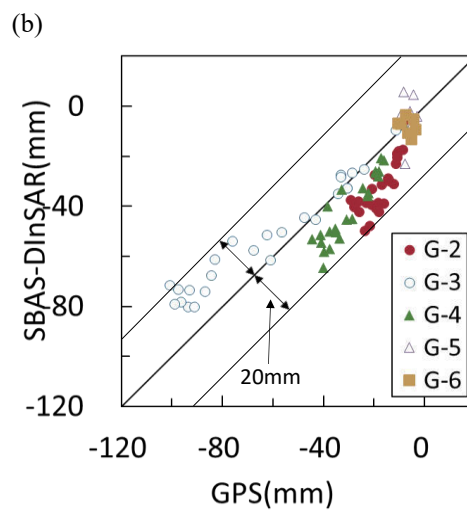
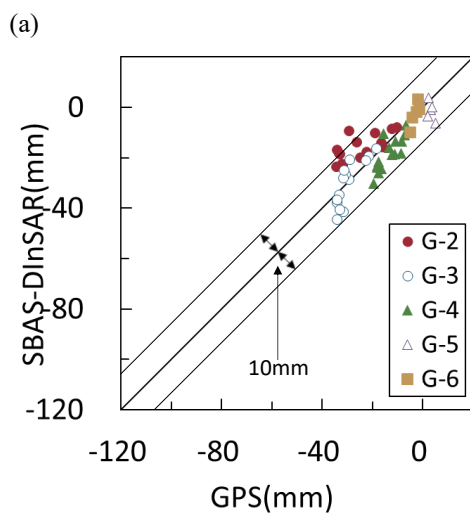


Figure 16. Correlation of LOS displacements obtained by DInSAR and GPS: (a) ascending and (b) descending.

3 CASE STUDIES

3.1 Subsidence induced by underground salt mining in Tuzla, Bosnia and Herzegovina

The subsidence in Tuzla, Bosnia and Herzegovina, has been creating a large hazard for a long period of time, mainly since the 1950s. It was reported that the main factor in this subsidence is the underground salt mining activities (Mancini et al. 2009a).

The Tuzla salt deposit is located beneath Tuzla City in an area of approximately 2 km² (Figure 17(a)). It consists of five separate salt series embedded in syncline with one of the wings close to the surface of the city's center. The maximum thickness of the salt formation is 600 meters (Figure 17(b)). The lithological composition is halite, gypsum, anhydrite, laminated and thin-layered marls, tuff, poriferous limestone, etc.

The subsidence was measured by traditional topographic surveys from 1956 to 2003. The GPS surveys produced subsidence information in three periods, namely, 2004 to 2005, 2005 to 2006, and 2006 to 2007 (Mancini et al. 2009b). From 2008, other GNSS and geodetic surveys have been conducted (Čeliković et al. 2014; Čeliković and Imamović 2016). However, a more efficient, effective, and economical monitoring method is desired in addition to the conventional method. SBAS-DInSAR was applied to update the subsidence situation by the author and his colleagues (Parwata et al. 2020; Grujić et al. 2022).

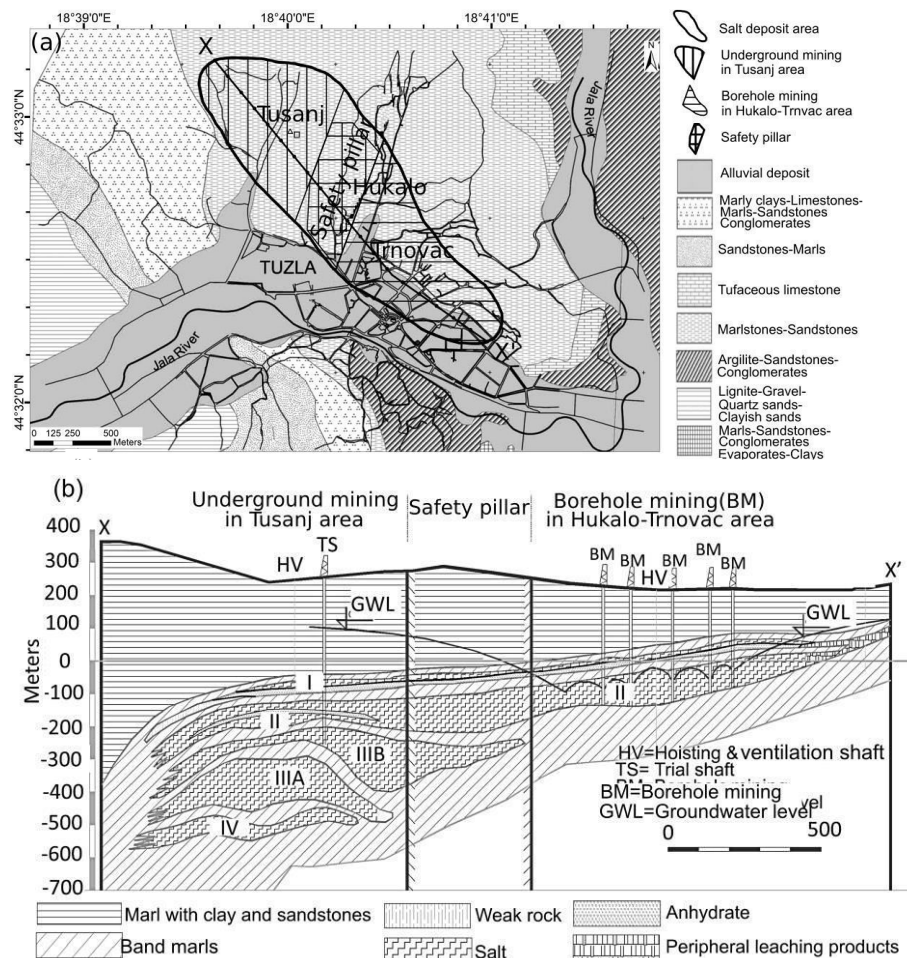


Figure 17 Geological condition of Tuzla: (a) plan view (modified from Mancini et al. (2009a)) and (b) vertical X-X' cross section (Parwata et al. 2020).

Figure 18(a) shows the contour lines for the subsidence from 1956 to 2003 (Mancini et al. 2009a; 2009b). The figure reveals that the maximum subsidence reached about -12 m. It was found that subsidence of more than 1m extended to an area of about 2 km² in the city, including a residential area, and was shaped like a trough. Figures 18(b), (c), and (d) show the subsidence distributions measured at four different times by static GPS surveys, namely, in 2004, 2005, 2006, and 2007 (Mancini et al. 2009a; Stecchi 2008). The survey network was composed of six reference points and 60 densification measurement points (Mancini et al. 2009a).

The GPS results for 2004 to 2005 show that the subsidence continued at a rate of -12 to -22 cm/year in the north part of Pannonica Lakes (Figure 18(b)), although the rate had largely decreased compared to that of the previous period (1956 to 2003). A considerable area in the north-east part of the city was subjected to subsidence rates of -2 to -5 cm/year. In the period of 2005 to 2006, the subsidence rate decreased to -8 to -22 cm/year around Pannonica Lakes (Figure 18(c)). Mancini et al. (2009a) and Stecchi (2008) stated that the GPS results from 2006 to 2007 showed that the subsidence was heading to the end almost everywhere, except for the area near Pannonica Lakes where the subsidence rate was still about -10 cm/year (Mancini et al. 2009a; Stecchi 2008) (Figure 18(d)).

The official date of termination of the salt deposit exploitation was in May 2007. GNSS and geodetic surveys were continued after the suspension of the operation of the salt wells, as the number of observed points was changing.

Figure 18(e) shows the spatial distribution of the subsidence measured by GNSS and geodetic surveys from 2008 to 2012 (Čeliković et al. 2014). The distribution of subsidence is similar to that obtained by GNSS from 2004 to 2007. Large subsidence was found around the most eastern part of the salt deposit. The subsidence became small toward the northwest parts of the salt deposit. The maximum subsidence of -53.2 cm was found at a point in a hilly area located in the southeast part of the salt deposit.

A SBAS-DInSAR analysis was applied to find the recent subsidence distribution by using 145 Sentinel-1 SAR descending Sentinel-1 data observed from October 2014 to May 2019. Figure 18(f) shows the spatial distribution of the subsidence obtained by SBAS-DInSAR. This spatial distribution is similar to those by GPS surveys from 2004 to 2007 and by GNSS and geodetic surveys from 2008 to 2012. This means that the subsidence still continued in a similar manner even after the extraction of salt water had been terminated in 2007. However, the absolute value of the subsidence has been decreasing.

From Figures 18(a) to (f), the location of the large subsidence area is seen to have moved to the southeast border of the salt mine deposit (northeast of Pannonica Lakes), while it was located in the center of the salt mine region in the previous period (1956 to 2003). It should be noted that the complex hydrodynamic groundwater system for the city of Tuzla plays a major role in the creation and speed of the settlement. In the northeast hilly area of Pannonica Lakes, large horizontal displacements were detected (Čeliković et al. 2014; Čeliković and Imamović 2016) and complex behavior comprising a combination of landslides and subsidence has appeared.

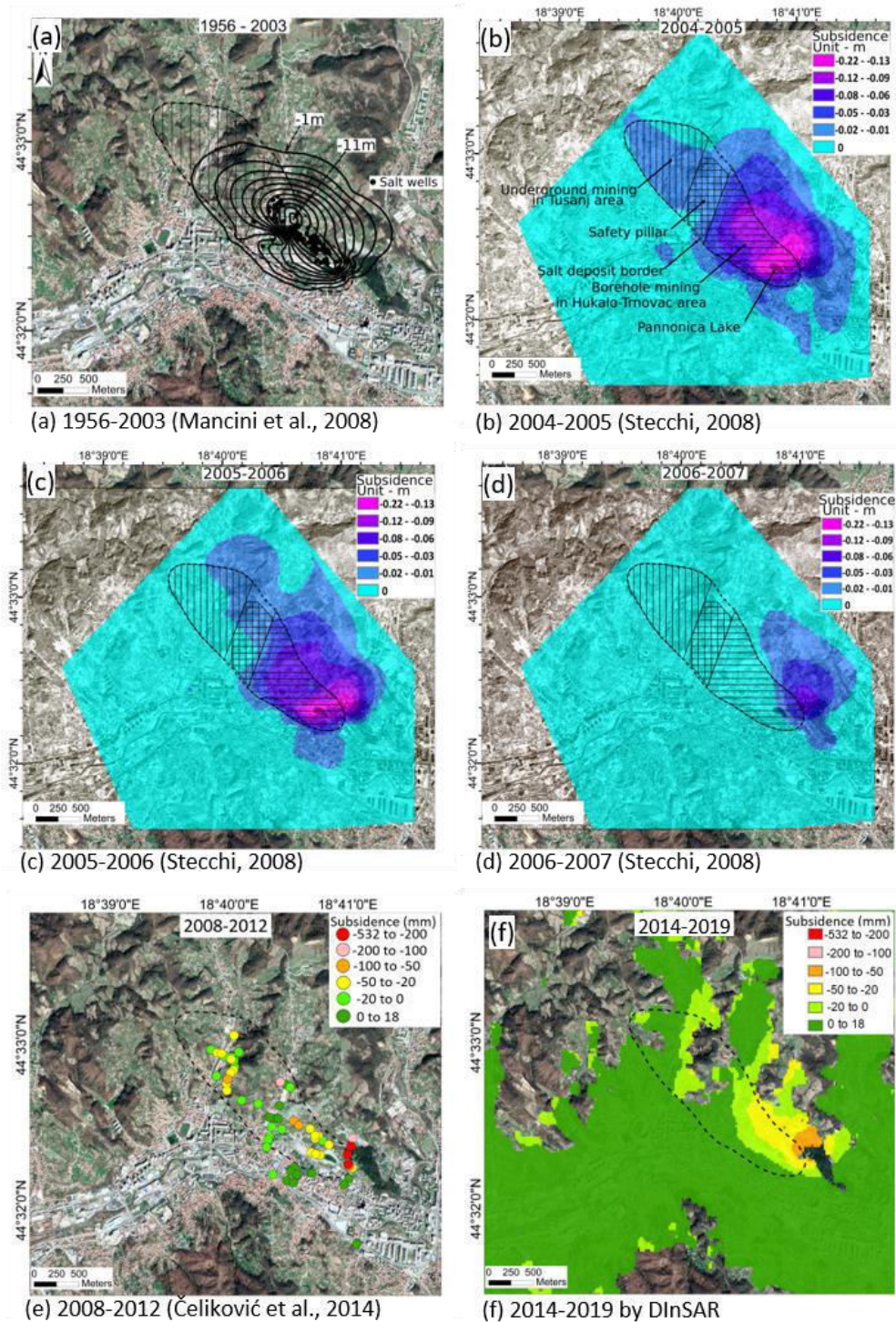


Figure 18. Temporal transition of spatial distribution of subsidence in Tuzla from 1956: (a) traditional topographic surveys presented by contour lines (1956 to 2003) (Mancini et al. 2009a) (dashed line indicates salt deposit border), (b) GPS surveys (2004 to 2005), (c) GPS surveys (2005 to 2006), (d) GPS surveys (2006 to 2007) ((b)-(d): modified from Stecchi (2008)), (e) GNSS and geodetic methods (2008 to 2012) (Čeliković et al. 2014), and (f) SBAS-DInSAR (2014 to 2019) (Grujić et al. 2022).

Figure 19 shows the accumulated subsidence distribution obtained by DInSAR and the locations of the measurement points for all the GNSS surveys. From all those points, four points are selected for a discussion on the transition of the subsidence from 2004 to 2019. Figure 20 shows the temporal transition of the subsidence obtained by GPS (2004 to 2007), GPS (2007 to 2012), GNSS (2013 to 2018), and DInSAR (2014 to 2019) at four selected points, namely, Nos. 7, 16, 34, and 37 (white numbers and filled circles in Figure 19).

No. 7 is located in the southern part of the salt deposit near Panonnica Lakes (Figure 3). From Figure 20(a), it is found that large subsidence with a value of -40 mm/year was still occurring in the period of 2004 to 2007. However, it gradually decreased in the period of 2007 to 2012 and decreased to -10 mm/year from 2013 to 2019. It should be noted that a good agreement was found between the GNSS (2013 to 2018) and the DInSAR (2014 to 2019) monitoring results.

No. 16 is located outside of the salt deposit (Figure 19). It is in the zone with the highest subsidence, as shown in Figures 18(e) and (f) (2008 to 2019). From 2004 to 2007, the rate of subsidence was about -100 mm/year (Figure 20(b)). Although it decreased to -30 mm/year from 2008 to 2012, the rate increased again to -70 mm/year from 2013 to 2019 based on the measurement results by both of GNSS and DInSAR.

No. 34 lies outside the salt deposit (around the south end of downtown). It has been stable for the last 15 to 20 years, although small subsidence appeared from 2008 to 2012 (Figure 20(c)).

No. 37 is located near the salt deposit border (dotted line in Figure 19). It has also been stable, while the subsidence tended to be -2.5 mm/year in the past (2004 to 2006) (Figure 20(d)).

It is important to note the good agreement between the monitoring results by GNSS (2013 to 2018) and DInSAR (2014 to 2019) at all the monitoring points.

Based on the continuous monitoring of the temporal transition and special distribution of the subsidence, it is found that there is an area where the yearly subsidence rate is still -10 to -40 mm/year in the hilly area around Nos. 15 and 16, and that the rate decreased to smaller than minus a few mm/year in the downtown area, including Nos. 22-24, 34-36, and 39-44 (Figure 19). In the north-west and the southeast areas of the salt deposit, the results show that the subsidence still continues at the rate of approximately -3 to -10mm/year. The combination of SBAS-DInSAR, GNSS, and geodetic surveys is effective for monitoring the displacement behavior in the entire city.

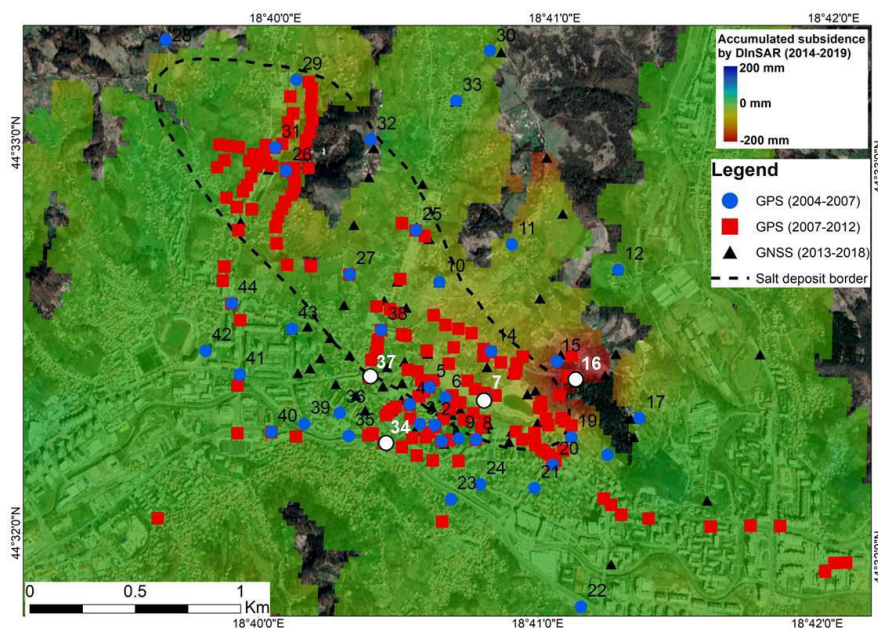


Figure 19. Accumulated subsidence distribution obtained by DInSAR (2014 to 2019) and locations of GPS and GNSS survey points (2004 to 2018) (Grujić et al. 2022).

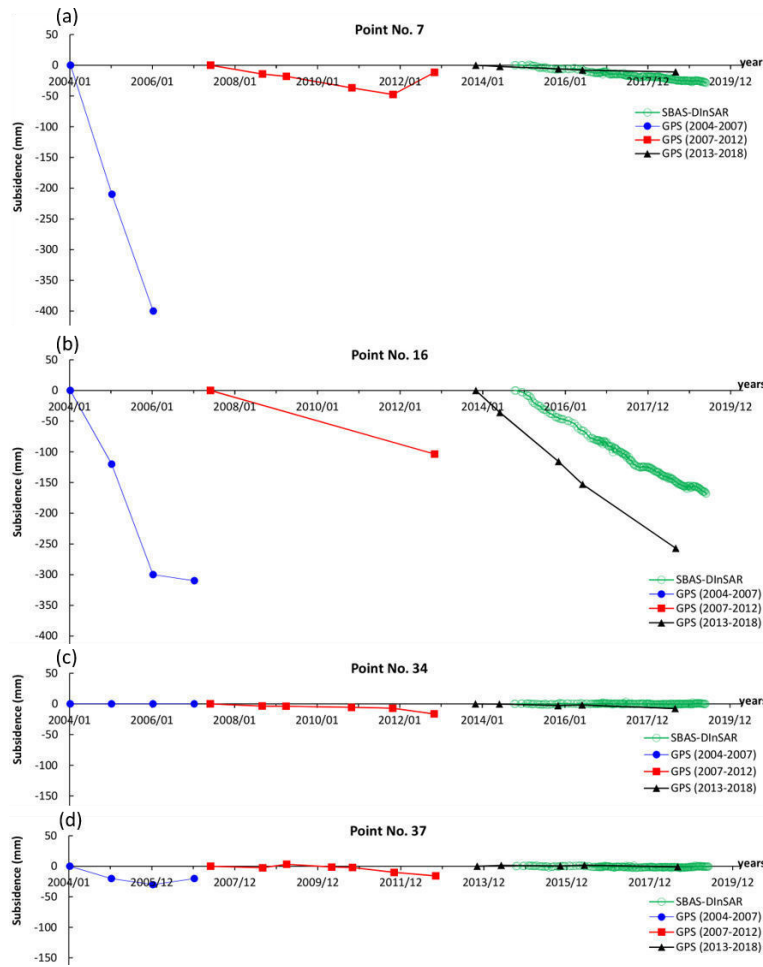


Figure 20. Temporal transition of subsidence obtained by GPS (2004 to 2007) (Stecchi, 2008), GPS (2007 to 2012) (Čeliković et al. 2014), GPS (2013 to 2018) (Čeliković and Imamović 2016), and DInSAR results (2014 to 2019) (Grujić et al. 2022): (a) No. 7, (b) No. 16, (c) No. 34, and (d) No. 37.

3.2 Landslides in Vipava River Valley, Slovenia

The Vipava River Valley, located in the southwest part of Slovenia, is well known as a landslide-prone area (see Figure 21). There are four remarkable landslides in this area (Bizjak and Zupančič 2009; Jemec Auflič et al. 2017; Verbovšek et al. 2018), namely, Rebrnice, Stogovce, Slano blato, and Selo. The area extends 40 km in length and several km in width. The landslides are characterized by the various volumes and velocities of their movement. The occurrence of debris flows and landslides sometimes causes damage to residences, infrastructures, farmland, etc.

It is vital that the current situation of these landslides be known and that better mitigation plans be designed by monitoring the landslide behavior and conducting geological and geotechnical studies. An effective monitoring method that is capable of covering extensive areas is needed. SBAS-DInSAR has been applied to this area (Yastika et al. 2019b).

Complex landslides, which have been occurring from the Pleistocene to recent times, are related to the geological structure. Mesozoic carbonates have been thrust over folded and tectonically fractured Tertiary siliciclastic flysch (Jemec Auflič et al. 2017). Such overthrusting has caused steep slopes and the fracturing of rocks, producing intensely weathered carbonates and large amounts of carbonate scree deposits.

The differences in elevation here are significant and range from 100 m at the valley bottom to over 1200 m on the high karstic plateau. The combination of unfavorable geological conditions and periods of intense short or prolonged rainfall has led to the formation of different types of complex landslides. The blue polygon in Figure 21(a) shows the study area.

This study used 134 and 139 Sentinel-1 SAR images in the ascending and descending passes, respectively, observed from September 2016 to January 2019 by Sentinel-1 satellites. Figures 22(a) and (b) show the LOS displacement distributions in the ascending and descending passes, respectively. The magenta color on the maps represents areas of geometrical distortion in the SAR data, such as radar layover or shadowing. Some areas had no results (no color) due to low coherence.

The “Slano blato landslide area” is taken to see the detailed transition of the LOS displacements from Figure 22. Figures 23(a) and (b) present ascending and descending LOS displacement distribution maps and the temporal transition at three points in the Slano blato landslide area, respectively. The spatial distribution of the surface displacements is clearly visible. Several deep wells were constructed at the top of the slope as a countermeasure to the landslide (Figure 23(c)).

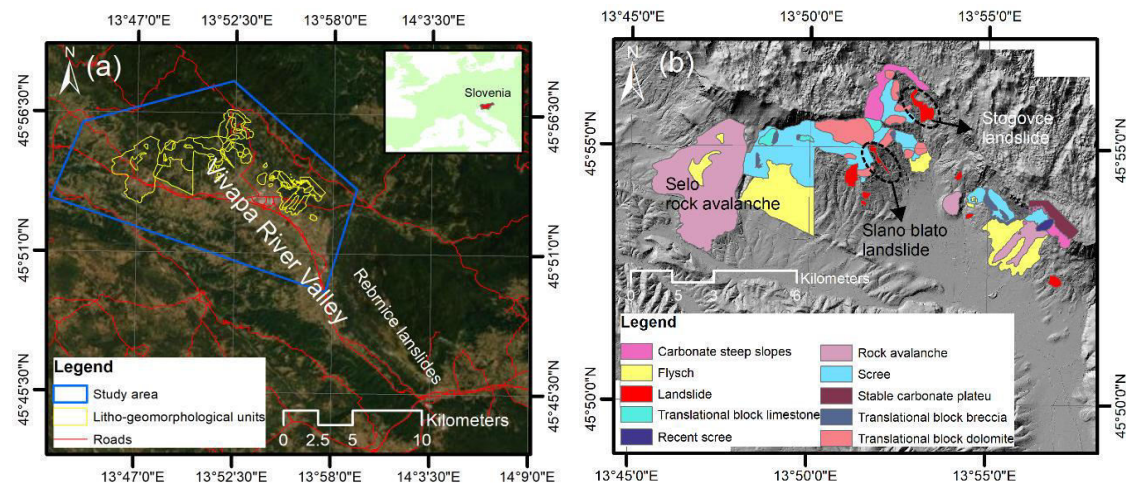


Figure 21. Vipava River Valley and surrounding area: (a) study area and (b) geomorphological map of study area (Yastika et al. 2019b).

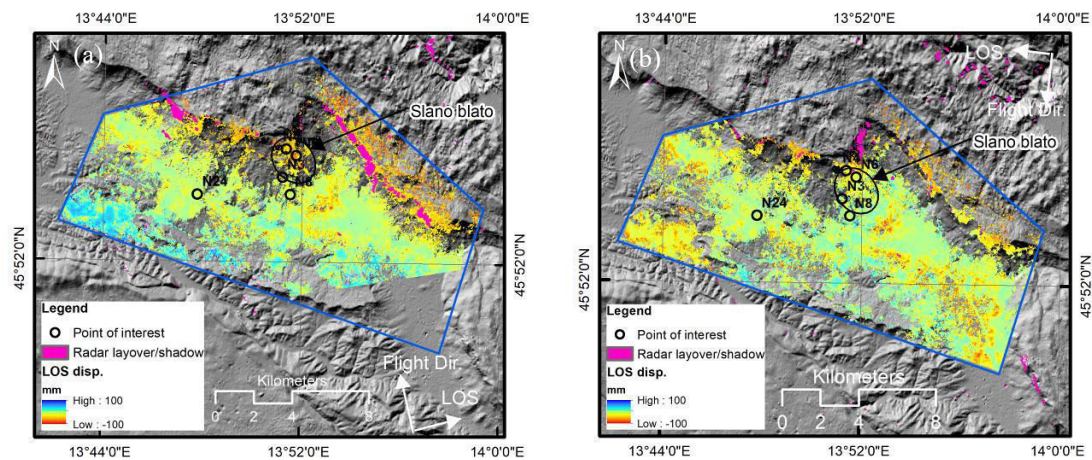


Figure 22. LOS displacement distribution maps of Vipava River Valley from 2016 to 2019: (a) results in ascending pass and (b) results in descending pass (Yastika et al. 2019b).

In Figures 23(a) and (b), the temporal transitions of the LOS displacements at W6, N20, and UD2 were taken from the upper, middle, and lower portions of the slope, respectively. Figure 24 illustrates the geometrical relationship between the actual three-dimensional displacement vector and the LOS (ascending and descending) displacements.

The results in Figure 23 indicate that the displacement of the Slano blato landslide area seems to still be moving downward at the head and the toe, and the middle portion is moving slightly toward the front of the slope at a rate of at least 50 mm/year.

DInSAR will be possible to reveal complex landslide behavior over the extensive area and to achieve a better understanding of the spatio-temporal ground surface movement.

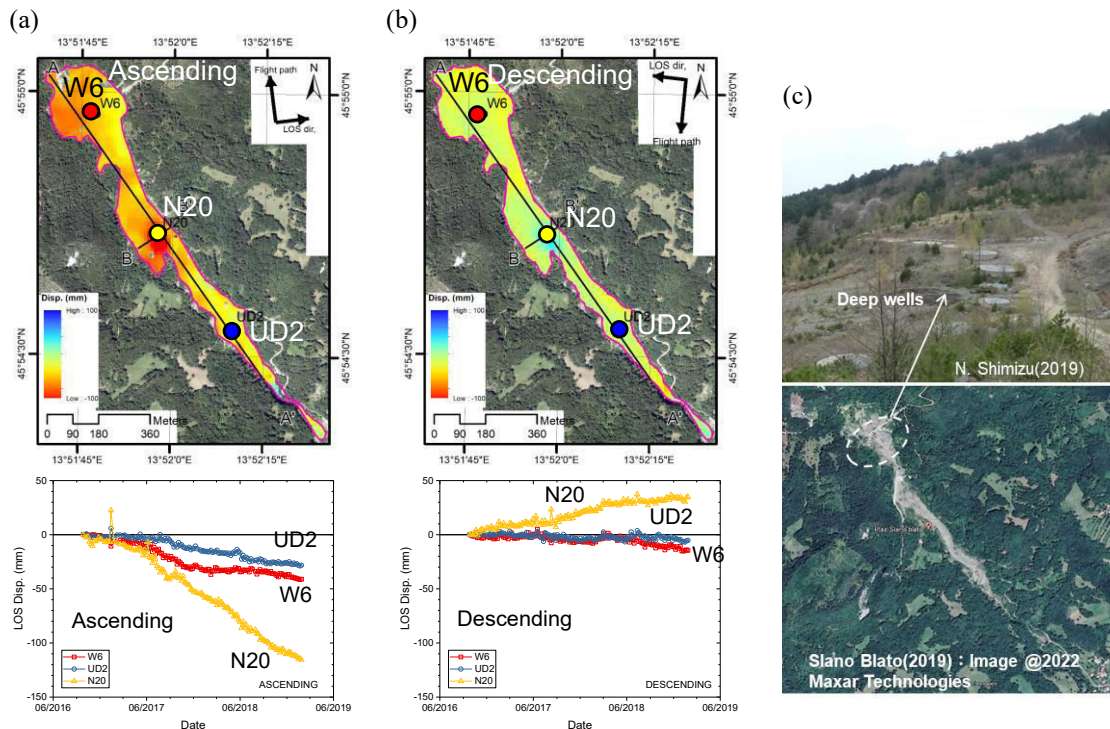


Figure 23. LOS displacement distribution maps and temporal transition at selected points in Slano blato landslide area: (a) displacements in ascending pass, (b) displacements in descending pass (Yastika et al. 2019b), and (c) deep wells constructed at the head of slope.

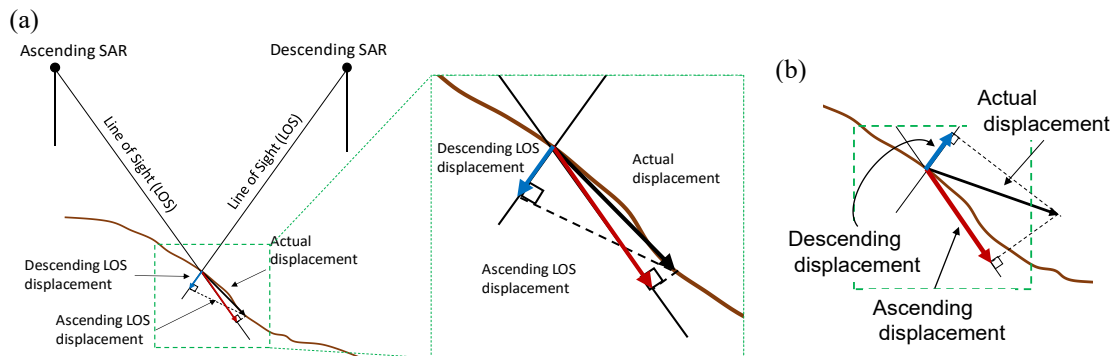


Figure 24 Schematic diagram of geometrical relationship between actual displacement vector and LOS (ascending and descending) displacements: (a) W6 and UD2, and (b) N20.

3.3 Landslides in northern Black Sea coast of Bulgaria

The Black Sea coast of Bulgaria is well known as an active landslide area across which various landslides extend (Bruchev et al. 2007). A lot of research has been done, from both geological and engineering perspectives, and countermeasures have been partially performed for stabilizing the landslide activity. On the other hand, monitoring the real behavior of landslides has not often been conducted due to technical difficulties and cost issues, although it is essential to reveal the mechanism of these landslides and to solve the problems they cause. Since SBAS-DInSAR could be an effective method for monitoring the landslide behavior in such extensive areas, it was applied to the area along the northern Black Sea coast (Yamaguchi et al. 2021, 2022).

Figure 25(a) shows the distribution of the landslide locations at Balchik and Kavarna municipality along the Black Sea coast in northern Bulgaria (Министерство на регионалното развитие и благоустройството 2021). In this region, there are four landslide hotspots, namely, Topola village, Alley Echo (EXO), Svilozha, and Fish-Fish, which are represented by the squared regions in Figure 25(a).

Figure 25(b) is a geological map with the landslides in this area (Evstatiev et al. 2013). The regions denoted by “V” and “IV” along the coast represent the target areas including the four landslide hotspots shown in Figure 25(a). These regions are composed of limestone (kvN1s), aragonite clay with limestone interaction (toN1s), and diatomaceous clay (evN1kg-s). The northern part from the crown line of the main scarp comprises limestone of the Kavarna Formation (kvN1s), and the more northern area comprises loess (yellow soil) complex (eoIQp). North of the crown line is a limestone plateau called the Lower Romanian Level (LRL).

The Sentinel-1 data are applied to create the interferogram for the SBAS-DInSAR analysis. Two datasets, namely, 273 images on the descending pass observed from 8 October 2014 to 9 May 2020, and 196 images on the ascending pass observed from 9 October 2014 to 7 September 2020, are used.

Figure 26 shows the LOS displacement distributions of the target area of Balchik and Kavarna (Figure 25(a)) from 2014 to 2020 for the descending and ascending passes. The LOS displacements are represented by the range in color from red (negative: extension) to blue (positive: compression) denoting mm units from -200 mm to 200 mm. Larger displacements are found in both eastern and western end areas of Topola village and the Fish-Fish district, respectively, in Figure 26.

To evaluate the results of SBAS-DInSAR and to discuss its applicability for monitoring the landslide behavior, the DInSAR results are compared with the actual behavior observed by field investigations (Министерство на регионалното развитие и благоустройството 2017, 2018, 2019). Topola village is taken as an example in this section for comparison.

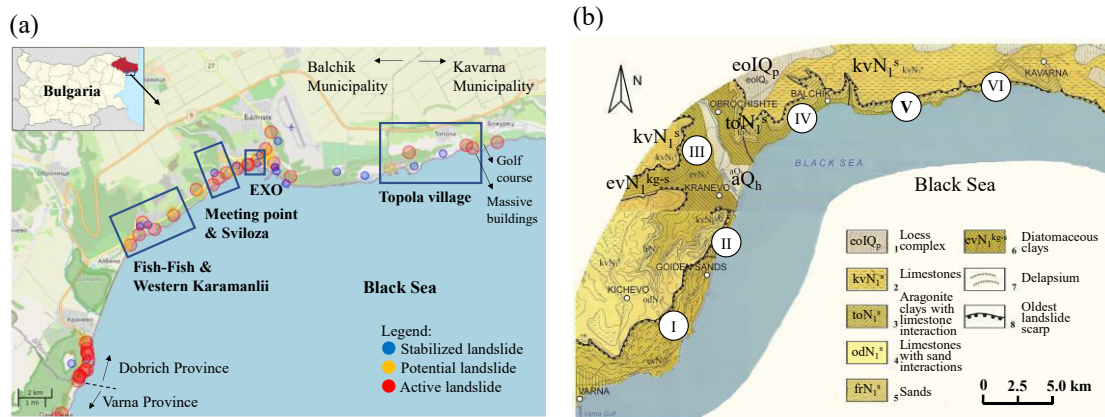


Figure 25. Study area along the northern Black Sea coast of Bulgaria: (a) map of landslides (Министерство на регионалното развитие и благоустройството 2021) and (b) geological map (Evstatiev et al. 2013).

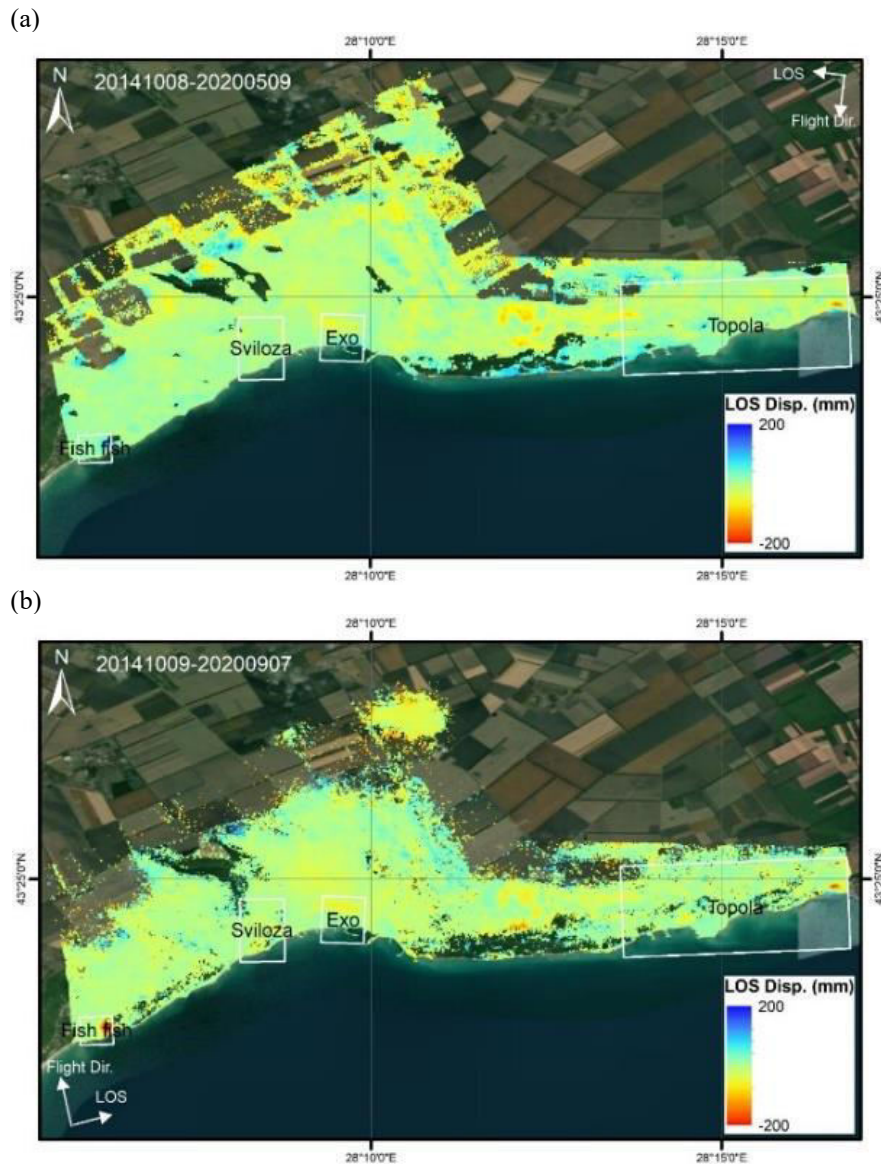


Figure 26. LOS displacement distributions in Balchik and Kavarna area by SBAS-DInSAR: (a) descending pass (8 Oct 2014 to 5 May 2020) and (b) ascending pass (9 Oct 2014 to 7 Sept 2020) (Yamaguchi et al. 2021).

Figure 27 is an enlarged view showing the LOS displacement distribution in the descending and ascending cases at the eastern end of Topola village. According to the annual reports (Министерство на регионалното развитие и благоустройството 2017, 2018, 2019), a landslide developed in the coastal area near a golf course around the eastern end of Topola village.

Large deformation has been seen among the massive buildings located inside of the landslide area (Figure 28(a)). For example, one building is inclined backward and the front of it is visibly raised, while others have moved forward and are twisted (Figure 28(b)). The landslide body has cut off the road to the golf course, and transverse ridges have appeared, as shown in Figure 28(c). There are terraces and cliffs at the landslide toe up to a height of about 3 to 4 m along the coastline.

The border of the landslide area, shown in Figure 28(a), is drawn on the displacement map in Figure 27. The area with the large displacement observed by SBAS-DInSAR coincides with the actual landslide area (Figures 27 and 28).

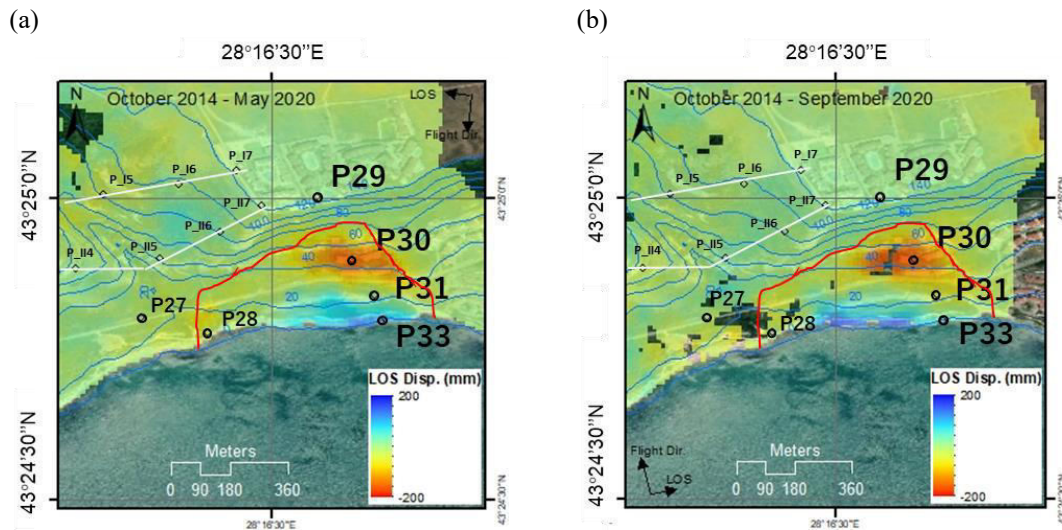


Figure 27. LOS displacement distribution maps around eastern end of Topola village: (a) descending pass and (b) ascending pass (Yamaguchi et al. 2021).



Figure 28. Landslide around eastern end of Topola village: (a) boundary of landslide body, (b) damaged buildings, and (c) transverse ridges (red line) (Министерство на регионалното развитие и благоустройството 2017, 2018, 2019).

Figure 29 shows the temporal transition of the LOS displacements in both ascending and descending cases at four points (pixels) in this area, namely, P29, P30, P31, and P33, as shown in Figure 27.

P29, on the plateau above the slope, is stable because almost no displacement appears, as shown in Figure 29(a).

At P30, located in the area of massive buildings (Figure 28(b)), both descending and ascending LOS displacements have significantly increased toward the negative side (extension) over time (Figure 29(b)). Considering the geometrical relationship between the actual three-dimensional displacement vector and the LOS (ascending and descending) displacements, shown in Figure 24, such behavior indicates that the actual displacements are dominantly subsidence. The eastern component of the displacement is estimated to be small. Since the slope faces south and the massive buildings sit on the middle terrace of the slope, the displacement is supposed to move in a southern and downward direction.

At P31, in the middle of the slope, the descending LOS displacement is almost zero or slightly positive, while the ascending one is negative (Figure 29(c)). This indicates that the actual displacement dominantly moves to the east and downward.

At P33, near the coastal area, both descending and ascending LOS displacements are compression, and the descending one is larger than the ascending one (Figure 29(d)). Therefore, the actual displacement seems to move upward and slightly to the east at the landslide toe.

From the above discussions, it is found that this area shows typical landslide behavior as shown in Figure 30. The results of SBAS-DInSAR correspond to the actual behavior described in the official reports (Министерство на регионалното развитие и благоустройството 2017, 2018, 2019), and they verify the applicability of DInSAR for monitoring landslides in extensive areas along the northern Black Sea coast.

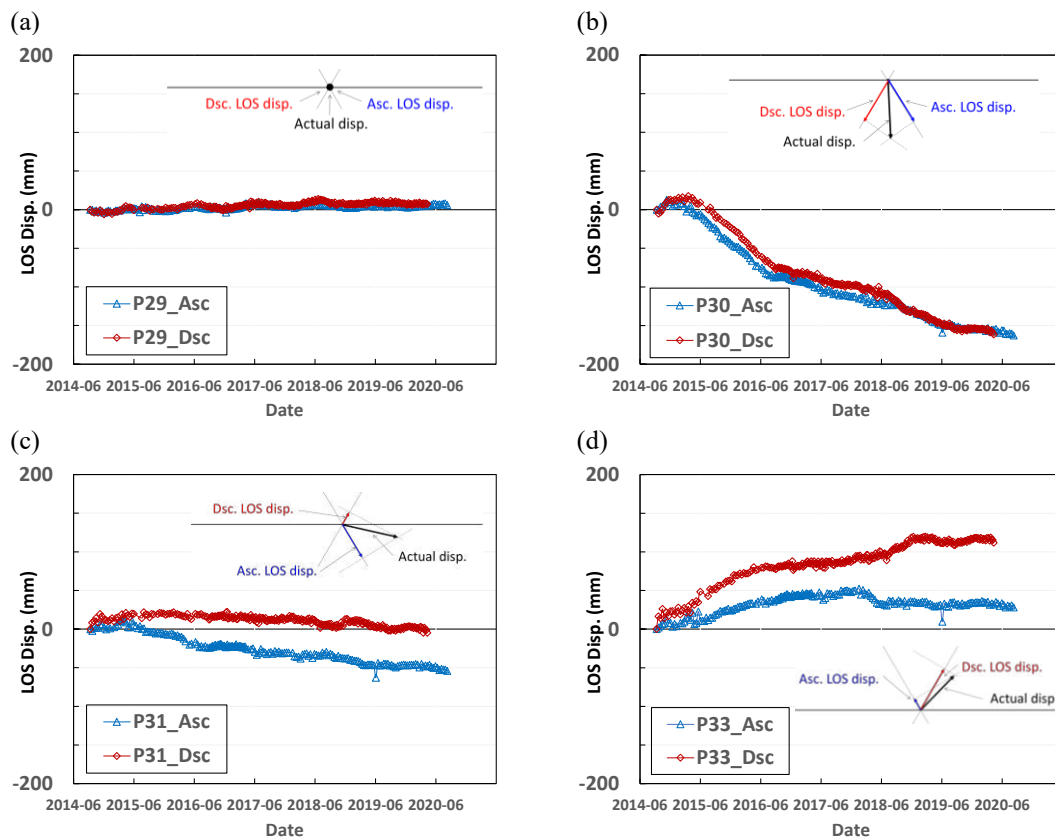


Figure 29 Temporal transition of LOS displacements by ascending and descending data around eastern end of Topola village: (a) P29, (b) P30, (c) P31, and (d) P33 (Yamaguchi et al. 2021).



Figure 24. Schematic illustration of estimated displacement directions at selected points.

4 CONCLUSIONS

Satellite technology, namely, GPS/GNSS and SAR, have become important tools for monitoring ground displacements in Rock and Geotechnical Engineering. The concluding remarks are as follows:

- Displacement monitoring using GPS/GNSS can provide the three-dimensional displacements of the ground automatically and continuously with mm accuracy.
- The International Society for Rock Mechanics and Rock Engineering approved “the ISRM suggested method for monitoring rock displacements using the Global Positioning System”. GPS/GNSS has become a standard tool for displacement monitoring.
- DInSAR analysis using SAR data can provide the displacement distribution of the ground surface in extensive areas without the necessity for any devices on the ground. The time transition of the displacement at points of interest can also be found.
- Numerous case studies of applications of GPS/GNSS and DInSAR have been accumulated by many researchers and engineers. Both methods will be very effective for realizing spatio-temporal continuous displacement monitoring in Rock and Geotechnical Engineering practice.

Satellite technology can make invisible ground behavior, which could not be detected up to now, visible. Its contribution to finding the mechanism of the ground behavior, assessing the stability, predicting risks, and preventing and mitigating disasters is highly anticipated.

ACKNOWLEDGEMENTS

This research was partially supported by JSPS KAKENHI (Grant-in-Aid for Scientific Research by the Japan Society for the Promotion of Science) Grant Number 16H03153.

The author wishes to express his sincere appreciation to Prof. Ivan Vrkljan (University of Rijeka, Croatia), Prof. Sabid Zekan and Prof. Ruža. Čeliković (University of Tuzla, Bosnia and Herzegovina), Mr. Edis Imamović (Municipality of Tuzla, Bosnia and Herzegovina), Prof. Bojana Grujić (University of Banja Luka, Bosnia and Herzegovina), Prof. Timotej Verbovšek (University of Ljubljana, Slovenia), Prof. Nikolay Milev (University of Architecture, Civil Engineering and Geodesy, Bulgaria), Dr. I Nyoman Sudi Parwata (Udayana University, Indonesia) and Dr. Putu

Edi Yastika (Mahasaraswati Denpasar University, Indonesia) for their cooperation in realizing these studies as international collaborative research.

He extends his special thanks to Prof. Shinichiro Nakashima (Yamaguchi University, Japan) and former/present students at Yamaguchi University, Ms. Marina Yamaguchi (Nippon Koei Co., Ltd., Japan), Mr. Kanta Nagasaki, Mr. Takeshi Sato and Mr. Shotaro Kubo for their effort and work on this research.

The author also expresses his gratitude to the European Space Agency (ESA) and the Japan Aerospace Exploration Agency (JAXA) for providing the Sentinel-1A/B and ALOS-2 SAR data used in these studies, respectively.

He thanks Ms. Heather Griswold for proofreading the manuscript of this paper.

REFERENCES

- Berardino P., Fornaro G., Lanari R. and Sansosti E. 2002. A new algorithm for surface deformation monitoring based on small baseline differential SAR interferograms. *IEEE Trans Geosci Remote Sens* 40, 2375–2383.
- Bruchev I, Dobrev N, Frangov G, Ivanov P, Varbanov R, Berov B, Nankin R and Krastanov M 2007. The landslides in Bulgaria – factors and distribution. *Geologica Balcanica* 36(3-4), 3–12.
- Bizjak K. F. and Zupančič A. 2009. Site and laboratory investigation of the Slano blato landslide. *Eng. Geology* 105, 171-185.
- Evstatiev D. and Evlogiev Y. 2013. Landslides along the northern Black Sea coast between Varna city and Kavarna town (Bulgaria). *Geo-Eco-Marina* 19, 39–57.
- Čeliković, R., Imamović, E., Salihović, R., Sušić, A., 2014. Prostorno vremenska analiza vertikalnih pomjeranja terena u Tuzli za period 2008-2012. *Proceedings of GEO-EXPO*, 38-44.
- Čeliković, R., Imamović, E., 2016. Continuous GNSS movement monitoring in the zone of influence of Tuzla salt deposit. *International Symposium on Engineering Geodesy*, 489–498.
- Ferretti A. 2014. *Satellite InSAR data: reservoir monitoring from space*. EAGE Publication, The Netherlands.
- Ferretti A., Monti-Guarnieri A., Prati C. and Rocca F. 2007. *InSAR Principles: Guidelines for SAR interferometry processing and interpretation*. ESA Publications, The Netherlands.
- Ferretti A., Prati C., Rocca F. 2001. Permanent scatterers in SAR interferometry. *IEEE Trans. Geosci. Remote Sens.* 39, 8–20.
- Furuyama Y., Nakashima S. and Shimizu N. 2014. Displacement monitoring using GPS for assessing stability of unstable steep slope by means of ISRM suggested method. *Proceedings of the ISRM International Symposium - 8th Asian Rock Mechanics Symposium (ARMS8)*, Sapporo, 1897-1904.
- Grujić B., Parwata I N. S., Shimizu, N., Čeliković R., Imamović E., Zekan S. and Vrkljan I. 2022. Monitoring subsidence in Tuzla (BiH) by DInSAR and GNSS from 2004-2019, *proceedings of 5th Symposium of the Macedonian Association for Geotechnics, ISRM Specialized Conference, Ohrid*, 521-529.
- Hanssen R. F. 2002. *Radar Interferometry*. New York: Kluwer Academic Publisher.
- Hoffmann-Wellenhof B., Lichtegger H. and Collins J. 2001. *GPS – Theory and Practice*. 5th revised edition, Springer.
- Iwasaki T., Takechi K., Takeishi A., Masunari T., Takechi Y. and Shimizu N. 2003. Web-based displacement monitoring system using GPS for the maintenance of roadside slopes. *Proceedings of 6th International Symposium on Field Measurements in Geomechanics, Oslo*, 137-143.
- Jemec Aulflić M., Jež J., Popit T., Košir A., Maček M., Logar J., Petkovšek A., Mikoš M., Calligaris C., Boccali C., Zini L., Reitner J. and Verbovšek T. 2017. The variety of landslide forms in Slovenia and its immediate NW surroundings. *Landslides* 14(4), 1537-1546.
- Kien, N. T., Hayashi Y., Nakashima S. and Shimizu N. 2017. Long-term displacement monitoring using GPS for assessing the stability of a steep slope. *Proceedings of ISRM Young Scholars' Symposium on Rock Mechanics & International Conference on New Development in Rock Mechanics and Geotechnical Engineering, Jeju*, 165-168.
- Mancini F., Stecchi F., and Gabbianelli G. 2009a. GIS-based assessment of risk due to salt mining activities at Tuzla (Bosnia and Herzegovina). *Engineering Geology* 109, 170–182.
- Mancini F., Stecchi F., Zanni M. and Gabbianelli G. 2009b. Monitoring ground subsidence induced by salt mining in the city of Tuzla (Bosnia and Herzegovina). *Environmental Geology* 58, 381–389.
- Masunari T., Tanaka K., Okubo N., Oikawa H., Takechi K., Iwasaki T., and Shimizu N. 2003. GPS-based

- continuous displacement monitoring system. Proceedings of 6th International Symposium on Field Measurements in Geomechanics, Oslo, 537-543.
- Misra P. and Enge P. 2006. Global Positioning System - signals, measurements, and performance. 2nd Ed. Ganga-Jamuna Press.
- Министерство на регионалното развитие и благоустройството (Ministry of Regional Development and Public Works). 2017. 2018. 2019. ГОДИШЕН ДОКЛАД (Annual Report). No.РД-02-29-23/27.02.2017 г. И; No.РД-02-29-329/10.11.2018 г.; No.РД-02-29-114/02.07.2019 г. (in Bulgarian).
- Министерство на регионалното развитие и благоустройството (Ministry of Regional Development and Public Works). Регистър на свлачищата (Landslide register). <http://gz-varna.mrrb.government.bg/map/>. Accessed on 31 December 2021 (in Bulgarian).
- Nagasaki K., Kameyama M., Yoshimoto M., Nakashima S. and Shimizu N. 2021. Applicability of SBAS-DInSAR for Monitoring Displacements of a Local Steep Slope. Proceedings of 5th International Workshop on Rock Mechanics and Engineering Geology in Volcanic Fields (RMEGV2021), ISRM Specialized Conference, OS6-4.
- Özer I. E., Leijen F. J., Jonkman N. and Hanssen R.F. 2019. Applicability of satellite radar imaging to monitor the conditions of levees, J. Flood Risk Management, 12(suppl. 2): e12509, 1-16.
- Parwata I N. S., Shimizu N., Grujić B., Zekan S., Čeliković R. and Vrkljan I. 2020. Monitoring the Subsidence Induced by Salt Mining in Tuzla, Bosnia and Herzegovina by SBAS-DInSAR Method. Rock Mechanics and Rock Engineering 53(11), 5155–5175.
- Sato, T., Kien, N. T., Nakashima, S. and Shimizu, N. 2021. Monitoring the three-dimensional displacement by GPS - a case study in a large steep slope, Proceedings of 5th International Workshop on Rock Mechanics and Engineering Geology in Volcanic Fields (RMEGV2021), ISRM Specialized Conference, Paper No. OS6-5.
- Satoh W., Iwasaki T., Sakurai W., Fujii A. and Shimizu N. 2014. Monitoring the stability of a large-scale colluvium deposited by slope failures due to heavy rainfall using a GPS automatic monitoring system. Proceedings of the ISRM International Symposium - 8th Asian Rock Mechanics Symposium (ARMS8), Sapporo, 1778-1783.
- Shimizu N., Masunari T. and Iwasaki T. 2011. GPS displacement monitoring system for the precise measuring of rock movements. Proceedings of 12th International Congress on Rock Mechanics, Beijing, 1117-1120.
- Shimizu N. and Matsuda H. 2002. Practical applications of the Global Positioning System for the assessment of slope stability based on the Displacement Monitoring Approach. Proceedings of the 3rd Korea-Japan Joint Symposium on Rock Engineering, ISRM Regional Symposium, Seoul, 57-70.
- Shimizu N. and Nakashima S. 2017. Review of GPS displacement monitoring in rock engineering. Rock Mechanics and Engineering. Volume 4, CRC Press, Chapter 19, 593-626.
- Shimizu N. Nakashima S. and Masunari T. 2014. ISRM suggested method for monitoring rock displacements using the Global Positioning System. Rock Mech and Rock Engineering 47, 313-328.
- Stecchi F. 2008. Tuzla City (BIH): An example of geohazard induced by salt extraction. Dissertation, University of Bologna.
- Verbovšek T. and Popit T. 2018. GIS-assisted classification of litho-geomorphological units using Maximum Likelihood Classification, Vipava Valley, SW Slovenia. Landslides 15(7), 1415-1424.
- Yamaguchi M., Yastika P. E. Shimizu N., Milev N., and Vrkljan I. 2021. Application of SBAS-DInSAR to monitoring landslides along the northern Black Sea coast in Bulgaria, Proceedings of EUROCK-Torino 2021, IOP Conf. Series: Earth and Environmental Science 833, Mechanics and Rock Engineering, from Theory to Practice, Turin, Paper No. 012151. doi:10.1088/1755-1315/833/1/012151
- Yamaguchi M., Yastika P. E., Shimizu N., Milev N. and Vrkljan I. 2022. Landslide monitoring using SBAS-DInSAR along the northern Bulgarian Black Sea coast near Topola village, IX Latin American Rock Mechanics Symposium, Asunción (in press).
- Yastika P. E., Shimizu N. and Verbovšek T. 2019b A case study on landslide displacement monitoring by SBAS-DInSAR in the Vipava River Valley, Slovenia. Proceedings of ISRM Specialized Conference on 5th ISRM Young Scholars' Symposium on Rock Mechanics and International Symposium on Rock Engineering for Innovative Future, 406-411.

Rock Mechanics for Deep Engineering

X.-T. Feng

Institute for Deep Engineering and Intelligent Technology, Northeastern University, Shenyang, China

EXTENDED ABSTRACT

In recent decades, there have been more and more deep hard rock projects (rock projects with buried depth exceeding 1000m or in-situ stress dominated by horizontal tectonic stress and maximum principal stress greater than 20MPa, rock uniaxial saturated compressive strength greater than 60MPa) in the fields of mining, traffic tunnel, underground powerhouse and diversion tunnel of water conservancy and hydropower, energy development such as shale oil and gas and geothermal, underground space utilization and underground physics laboratory. Most of these projects occur in extremely complex engineering geological environments such as high ground stress and strong tectonic activities, and the engineering disturbances are often very violent (large section, large volume, drilling and blasting method, TBM excavation, etc.). Geological disasters such as hard rock fracturing (deep cracking, time-dependent fracturing), rock spalling, large deformation, large-scale collapse, rockburst and so on caused by engineering excavation occur frequently, causing serious casualties, equipment damage and construction period delay. Its failure characteristics are obviously different from those of shallow engineering, which are dominated by surface deformation and structural failure of surrounding rock, mainly manifested as internal fracturing and energy releasing of surrounding rock, which pose a great challenge to the research of rock mechanical characteristics and catastrophe mechanism cognition, prediction and analysis theory, rock engineering design and disaster prevention and control.

Based on the cognition of deep engineering geological features, deep engineering excavation effects and the development process of those deep engineering disasters, a deep engineering hard rock mechanical system has been established and well applied, taking the internal fracturing process of deep engineering hard rock induced by excavation under high stress as the core. The main issues are as follows.

The rock mass structural characteristics under deep high stress environment and strong tectonic activity, including the lithology, geological structure, typical rock mass structural types and physical and mechanical characteristics are summarized from different deep rock engineering. The distribution characteristics of high in-situ stress level, large stress difference and complex spatial relationship of stress field in deep engineering are expounded. The variation characteristics of stress field in deep engineering during different excavation processes are studied, including the working face effect, layered and divisional excavation effect, the rule of stress concentration area transferring from excavation surface to inside rock, the gradual increase of stress difference, the change of stress direction and the change rule of stress path. The characteristics of rock mass structure change induced by excavation unloading of deep hard rock are studied, and the evaluation method of deep engineering hard rock integrity and excavation evolution is established. It reveals the characteristics of different types of disasters (deep cracking, zonal fracturing, time-dependent fracturing, rock spalling, collapse, large deformation and rockburst) induced by different excavation methods (drilling and blasting method and TBM).

Aiming at the characteristics of deep engineering geology and the characteristics of 3-dimensional in-situ stress and its change induced by deep engineering excavation, a series of high-pressure hard rock true triaxial test devices has been developed, as well as the test methods for studying the fracturing process of deep hard rock, including the method and apparatus for testing the mechanical properties of hard rocks under high true triaxial stress paths, testing the rheological properties of hard rocks under true triaxial compression, testing the shear behavior of hard rocks under true triaxial compression and for testing the dynamic behaviors of hard rocks under true triaxial compression. They can be used to test the mechanical characteristics, deformation and fracturing mechanism, energy evolution characteristics, etc. of deep hard rock, hard rock with

bedding plane and hard structural plane under the coupling action of true triaxial high stress loading and unloading, path change, shear, rheology and dynamic disturbance. And the in-situ comprehensive observation technology with preset series of boreholes for studying internal fracturing, deformation, stress concentration and transfer, energy accumulation and releasing of surrounding rock in deep hard rock engineering has also been developed.

Through systematic tests, the characteristics, mechanisms and laws of brittle and ductile mechanical properties, three-dimensional failure strength, anisotropic fracturing and deformation of deep hard rock induced by true three-dimensional high stress and stress path and direction changes caused by excavation are revealed, with special attention to the failure, deformation and energy accumulation and releasing process corresponding to the post peak stress-strain curve. The effects of time dependent, stress path, bedding plane and hard structural plane and dynamic disturbance have been revealed, and thereby the mechanical characteristics of deep engineering surrounding rock with the excavation disturbance under true three-dimensional high stress, including the characteristics of stress-induced brittleness and ductility, deformation and fracturing, energy releasing, excavation damage, blasting vibration, etc., focusing on the control effect of internal fracturing of surrounding rock and energy accumulation process on disasters.

In order to fully reflect the anisotropic failure, deformation and energy-release process of deep hard rock induced by high 3-dimensional stress and stress path change during deep engineering excavation, the failure mechanics theory of deep engineering hard rock is established by comprehensively considering the properties of deep hard rock mechanics, deep hard structural plane mechanics, and deep hard rock rheology mechanics. It includes three-dimensional failure criteria of deep engineering hard rock, stress-induced anisotropic failure mechanical model based on tensile fracturing, stress-induced anisotropic time-dependent failure mechanical model based on tensile fracturing, evaluation indices of rock-fracturing and energy-releasing, three-dimensional numerical analysis method of deep engineering hard rock fracturing process and three-dimensional intelligent back analysis method of rock mass mechanical parameters.

The in-situ comprehensive intelligent observation and monitoring technology and methods have been implemented in typical deep engineering, and the systematic in-situ comprehensive observation and monitoring of the internal fracturing, deformation and energy-releasing of deep surrounding hard rock have been carried out. Combined with numerical simulation deep engineering excavation induced rock fracturing process, the key information (evolution of the internal fracturing, energy and deformation of surrounding rock) and its characteristics, mechanisms and laws of the whole process of deep engineering disasters induced by the true three-dimensional high stress and the stress concentration and path change induced by excavation have been systematically recognized, and thereby the mechanism of the development process of those deep engineering disasters have been revealed, and then the intelligent assessment, prediction and early-warning methods of disaster types, grades and locations based on these key information have been proposed.

Based on the idea of reversing the development process of stress-induced disasters in deep hard rock engineering, the active and targeted control principles and methods for internal rock-fracturing and energy-releasing processes in the surrounding rock are established, including the crack-restraint methods for controlling stress-induced disasters such as rock spalling, deep cracking, zonal disintegration, large deformation and massive collapse and energy-control methods for controlling different kinds of rockbursts, as well as the deep hard rock engineering design method with the primary goal of controlling the internal fracturing and energy accumulation and release of surrounding rock. Active control technology based on optimization of excavation section and rate, stress-releasing and energy-absorbing and wave-absorbing support, and construction methods and technologies being adaptive to geological conditions and disaster risk control are developed, to suppress or reduce the internal stress concentration level, the intensity of stress adjustment, the depth and degree of surrounding rock fracture and the degree of energy release of surrounding rock in deep engineering, so as to avoid or reduce the occurrence of those deep engineering disasters.

The above proposed methods, theories, technologies and devices have been successively applied to solve the mechanical problems of different types of deep hard rock engineering with different geological conditions. These engineering cases include deep buried traffic tunnels, deep mine roadways, deep buried hydropower tunnels, underground power houses with high stress and deep underground physics laboratory projects, covering different lithology (marble, sandstone, siltstone, granite, gneiss, etc.), different tectonic stress levels and burial depths (more than 700m and even 2400m), different rock mass structures (intact rock mass, hard structural planes, faults, dikes, soft-hard interbeds, etc.), different sizes of deep underground projects (section span of 7 ~ 34m, single tunnel and multiple cavern groups) and different construction methods (drilling and blasting method, TBM) with different induced hard rock disasters (deep cracking, time-dependent cracking, rock spalling, collapse, large deformation, rock burst).

ACKNOWLEDGMENTS

The works are financed by the National Natural Science Foundation of China (Grant Nos. 51839003 and 41827806) and Liao Ning Revitalization Talents Program (Grant No. XLYCYSZX1902).

REFERENCES

- Feng, X.T. 2000. *Introduction to Intelligent Rock Mechanics*, Beijing: Science Press
- Feng, X.T., Hudson, J.A. 2011. *Rock Engineering Design*. CRC Press.
- Feng, X.T., Zhang, C., Li, S., et al. 2013. *Dynamic Design Method for Deep Tunnels in Hard Rock*, Beijing: Science Press.
- Feng, X.T., Chen, B., Zhang, C., et al. 2013. *Mechanism, Warning and Dynamic Control of Rockburst Development Processes*, Beijing: Science Press.
- Hudson, J. A., Feng, X.T. 2015. *Rock Engineering Risk*, CRC Press.
- Feng, X.T., 2016. *Rockburst: Mechanisms, monitoring, warning, and mitigation*. Butterworth-Heinemann.
- Feng, X.T., Yang, C.X., et al. *Hard Rock Mechanics in Deep Engineering*, Beijing: Science Press. (in press)
- Feng, X.T., Jiang, Q., et al. *Design Method for Large Underground Cavern Group under High Stresses*, Beijing: Science Press. (in press)
- Feng, X.T., Zhang, X.W., Kong, R., et al. 2016. A novel Mogi type true triaxial testing apparatus and its use to obtain complete stress–strain curves of hard rocks. *Rock Mech. Rock Eng.* 49(5): 1649-1662.
- Feng, X.T., Zhao, J., Zhang, X.W. et al. 2018. A novel true triaxial apparatus for studying the time-dependent behaviour of hard rocks under high stress. *Rock Mech. Rock Eng.* 51(9): 2653-2667.
- Feng, X.T., Wang, G., Zhang, X.W., et al. 2021. Experimental method for direct shear tests of hard rock under both normal stress and lateral stress. *Int. J. Geomech.* 21(3): 04021013.
- Xiao, Y.X., Feng, X.T., Hudson J.A., et al. 2016. ISRM suggested method for in situ microseismic monitoring of the fracturing process in rock masses. *Rock Mech. Rock Eng.* 49(1): 343369.
- Feng, X.T., Haimson, B., Li, X.C., et al. 2019. ISRM suggested method: Determining deformation and failure characteristics of rocks subjected to true triaxial compression. *Rock Mech. Rock Eng.* 52(6): 2011-2020.
- Feng, X.T., Young, R.P., Reyes Montes J.M., et al. 2019. ISRM suggested method for in situ acoustic emission monitoring of the fracturing process in rock masses. *Rock Mech. Rock Eng.* 52(5): 1395-1414.
- Feng, X.T., Kong, R., Yang, C.X., et al. 2019. A three-dimensional failure criterion for hard rocks under true triaxial compression. *Rock Mech. Rock Eng.* 53(1): 103-111.
- Feng, X.T., Wang, Z.F., Zhou, Y.Y., et al. 2021. Modelling three-dimensional stress-dependent failure of hard rocks. *Acta Geotech.* 16(6): 1647-1677.

Keynote Lecture: Frictional Discontinuities: The Mechanics and Imaging of Slip

A.B. Bobet

Purdue University, West Lafayette, IN, USA

ABSTRACT:

The mechanical and hydraulic properties of rocks are strongly influenced by the presence and properties of discontinuities, or fractures. The ability to locate and characterize natural as well as induced discontinuities in rock is of paramount importance to many engineering problems such as slope stability, rock bridge integrity, hydraulic fracturing, geothermal energy and CO₂ sequestration, to name a few. Although fracturing in rock has been much studied, the current state of knowledge, both theoretical and empirical, is largely based on observations on the surface of the specimens where direct inspection of the existing or induced fractures can be made. The fundamental reason for this is the limitations of our techniques to illuminate damage in the interior of rock. Experiments on rock and rock-model materials show that active seismic monitoring can be used to detect the onset of slip along a frictional discontinuity, as well as the initiation of damage inside rock in the form of tensile or shear cracks. Precursors to failure along a frictional discontinuity undergoing shear were identified as the maximum in transmitted wave amplitude across the discontinuity or the minimum in the amplitude of the wave reflected from the discontinuity. Ultrasonic precursors were observed well before slip or failure occurred along the discontinuity and were attributed to a reduction in the discontinuity local shear stiffness. In rock specimens subjected to uniaxial compression, tensile and shear crack initiation were identified as a distinct decrease in the amplitude of transmitted waves, which occurred prior to the detection of the crack on the specimen surface. In contrast, the amplitude of the transmitted waves did not change during shear crack initiation. However, seismic wave conversions (P-to-S or S-to-P wave) were found to be effective in identifying the initiation of shear cracks in rock.

1 INTRODUCTION

The mechanical and hydraulic properties of a rock are strongly influenced by the presence and properties of discontinuities, or fractures (e.g. Goodman, 1980; Jaeger et al., 2007). For the prediction of rock mass behavior, it is important to understand the initiation and propagation of new and pre-existing cracks, and how the cracks connect with each other or coalesce to form a continuous fracture surface. The ability to locate and characterize natural discontinuities in rock as well as induced discontinuities is of paramount importance to many engineering problems such as slope stability, rock bridge integrity, hydraulic fracturing, geothermal energy, CO₂ sequestration, etc. In addition, prediction of impending slip of frictional discontinuities would contribute to prevent failures and associated human and economic losses.

Fracture mechanics provides the framework to represent discontinuities in a rock as features that evolve with stresses and/or time. A basic theoretical framework is available within the field, with an increasing body of experimental and numerical research on crack initiation and propagation from pre-cracked brittle materials loaded in compression. Experimental studies have been conducted on crack initiation, propagation, and coalescence in pre-cracked brittle materials. In most of these studies, the pre-existing crack (flaw) has been subjected to either mode I or mixed mode I-II loading (Reyes and Einstein, 1991; Chen et al., 1993; Germanovich et al., 1994; Shen, 1995; Bobet, 1997; Bobet and Einstein, 1998; Wong and Chau, 1998; Wong et al., 2001; Sagong and Bobet, 2002; Li et al., 2005; Wong and Einstein, 2006; Park and Bobet, 2009; Yang and Jing, 2010; Camones et al. 2013; Zou et al. 2012, Zou and Wong 2014; Zou et al. 2016). Two most

common types of macroscopic cracks have been observed to be initiated from the tips of pre-existing flaws, when loaded in compression: tensile (wing or primary) and shear (secondary) cracks. Tensile cracks initiate at or near the tip of the flaw. They propagate towards the direction of maximum compression and are stable (i.e., further propagation of these cracks requires application of additional load). Shear cracks initiate from the tips of the flaws and are initially stable, but may become unstable as crack coalescence or specimen failure occurs. In some experiments, a white patch or zone consisting of microcracks was observed on the surfaces of marble (Wong and Einstein, 2009a, b; Wong et al., 2013) and granite (Morgan et al., 2013), prior to the formation of a crack. Coalescence is the linkage of the pre-existing flaws through tensile and/or shear cracks, and may lead to rock failure. Coalescence between flaws in specimens under compression has been studied in different rock materials. Chen et al. (1993), Li et al. (2005), and Wong and Einstein (2009a, b) studied the cracking process and coalescence in marble; Reyes and Einstein (1991), Shen (1995), Bobet and Einstein (1998), Sagong and Bobet (2002), Ko et al. (2006), Wong and Einstein (2009a, b) and De Melo Moura and Bobet (2019) in gypsum; Wong and Chau (1998) and Wong et al. (2001) in a composite material simulating sandstone; and Modiriasari et al., (2020) in Indiana limestone.

Observations of slip and damage in the laboratory have relied on direct measurements and visual inspection using optical magnification and high-speed cameras. Digital image correlation (DIC) is an advanced experimental technique that has been used to observe the fracturing process on the surface of specimens, by measuring full-field displacements, and also for kinematic measurements along discontinuities and fractures undergoing shear (Sutton et al., 2008; Lin and Labuz, 2013; Hedayat et al., 2012, 2014b). The DIC method is gaining attention in fracture mechanics because of its simple preparation process and system set-up (Lin et al., 2014). Acoustic Emission (AE) has proven an invaluable tool for locating and to some degree determining the intensity of damage. It has been successfully used to investigate damage processes in brittle materials (Anastassopoulos and Philippidis, 1995; Shiotani et al., 2003; Bentahar and Gouerjuma 2009). For example, Hu et al., (2013) employed AE to explore the fracture process in concrete through three-point bending beam tests. They concluded that AE could locate the internal cracks in the specimen and detect crack propagation until structural failure. In addition, AE can provide information about the nature of the cracks, as both tensile and shear cracks produce different signals (Carvalho and Labuz 2002; Fakhimi et al., 2002; Young and Thompson, 2007; Moradian and Einstein 2014). An alternative or complementary technique to passive AE methods is active seismic or elastic wave monitoring. The technique has been used to observe and quantify local changes in the physical properties of rocks and their discontinuities (Pyrak-Nolte et al., 1990a, b; Chen et al., 1993; Hildyard et al., 2005; Leucci and De Giorgi, 2006; Kahraman, 2002). For instance, Hedayat et al. (2014a) showed that compressional, P, and shear, S, wave propagation could be used to monitor slip initiation and propagation processes along frictional interfaces and Modiriasari et al. (2017, 2018, 2020) found that tensile cracks could be detected by monitoring changes in amplitude of transmitted or reflected waves through the specimen, while shear cracks were detected with converted waves (those are waves converted from P- to S-waves or from S- to P-waves as the waves impinge on a closed/shear fracture; for in-depth theoretical analyses of converted waves, see Nakagawa et al., 2000).

The paper provides experimental evidence that shows how slip initiates and propagates along a frictional discontinuity and how active seismic monitoring can be used to detect the onset of slip and slip failure on discontinuities undergoing shear, and to identify damage inside rock in the form of tensile and shear cracks.

2 THE IMAGING OF SLIP

Direct shear experiments on two rock blocks were conducted using a biaxial compression apparatus (Figure 1), that consisted of a horizontal loading frame to apply a normal stress on the

contact surface and a loading machine to apply a shear stress. The horizontal loading frame was composed of a flatjack, loading platens that encased the specimen and sensors, steel rods, rollers, and plates. The flatjack was positioned behind the steel plate to apply a normal stress to the loading plates and the specimen. A series of rollers were located between the loading platen and the steel plate to minimize vertical friction and to ensure that the vertical load was resisted solely by the contact surface between the blocks. The direct shear experiments were conducted under applied normal stress (1-4 MPa) and with a shearing rate of $8 \mu\text{m}/\text{sec}$. Two LVDTs placed on top of the specimen recorded the average vertical displacement of the specimen while the load cell in the loading machine recorded the applied shear load. An electronic feedback loop was used to control the flatjack pressure to maintain a constant horizontal stress, as Poisson effects could induce horizontal expansion of the specimen during shearing. Compressional and shear wave ultrasonic pulses were transmitted through and reflected off the discontinuity during the direct shear experiments. An ultrasonic wave measurement system was employed to continuously monitor a discontinuity during the shear experiments. Two arrays, each with 13 embedded seismic (ultrasonic) transducers, were contained in the loading platens of the horizontal loading frame (Figure 1). A fast LabView-controlled data acquisition system with a sampling rate of 20 million samples/s (or $0.05 \mu\text{s}$ per point) recorded full waveforms in real time.

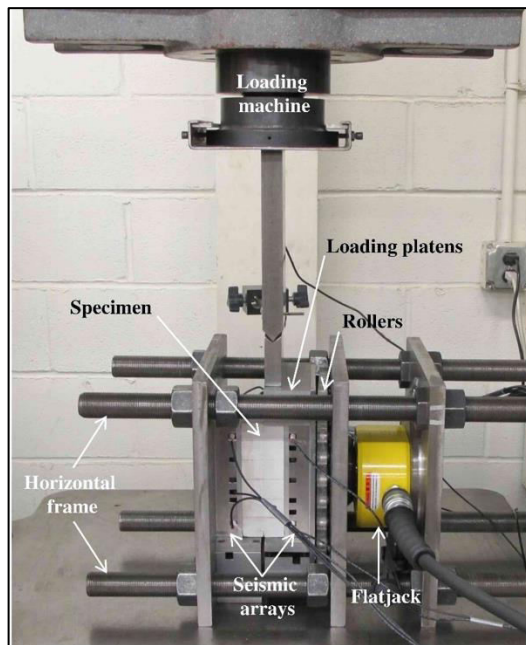


Figure 1. Experimental apparatus.

The experiments were conducted on gypsum, as a rock model material (Einstein and Hirschfeld, 1973; Shen et al., 1995; Bobet and Einstein, 1998), and on Indiana limestone specimens. The gypsum specimens were composed of two blocks with perfectly mated contact surfaces. Two types of contact surfaces were tested: homogeneous and non-homogeneous. The homogeneous contact surfaces had uniform frictional resistance (friction angle of 30°) along the discontinuity while the non-homogeneous contact surfaces consisted of an area with low frictional strength on one half and high frictional strength (frictional angle 45°) on the other half. The normalized peak-to-peak amplitude of transmitted and reflected shear waves, as a function of shear displacement, is shown in Figure 2 for a non-homogeneous rock discontinuity that was sheared in the biaxial compression apparatus. In the figure, the peak-to-peak signal amplitude is normalized with respect to its initial value prior to shear and the displacements are measured with respect to the displacement required to reach the peak shear strength. As shown in Figure 2a, after the initial

seating deformation of the specimen, the shear stress increased rapidly with shear displacement until it reached the peak shear strength of the discontinuity. The amplitude of the transmitted shear waves increased as the shear load was transferred to the specimen (Figure 2a). A distinct maxima in the normalized transmitted shear wave amplitude occurred prior to the peak shear strength. A maximum in transmitted amplitude was observed in the signals from all of the transducers and was identified as a seismic precursor that indicated impending shear failure of the discontinuity. The maximum in amplitude was followed by a decrease as additional shear displacement occurred along the discontinuity. The decrease in the amplitude was greater for the smooth surface (upper half of the discontinuity) than for the rough surface (lower half of the discontinuity). Figure 2b shows the amplitude of the reflected shear waves. The amplitude of the reflected signals decreased upon application of the shear load and attained a minimum prior to reaching the peak shear strength. The minima in the amplitude of the reflected wave corresponded to the maxima of the amplitude of the transmitted waves. After reaching the minimum, the amplitude of the reflected waves increased due to the reduction of the discontinuity's shear specific stiffness.

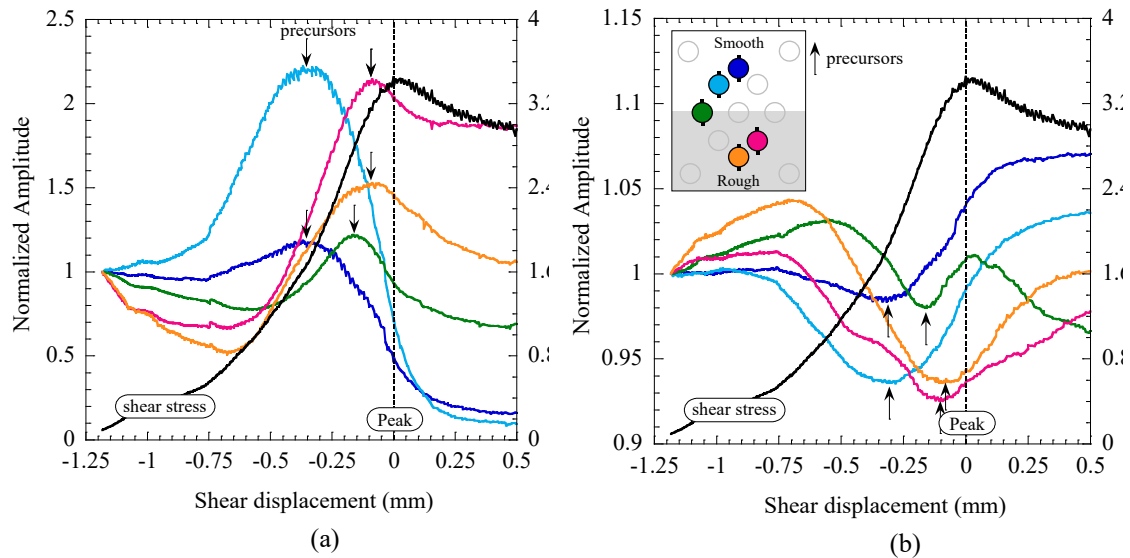


Figure 2. Seismic precursors to the failure of a non-homogeneous discontinuity subjected to a normal stress of 3 MPa: (a) Transmitted shear wave amplitude; (b) Reflected shear wave amplitude. The insets show the location of the shear wave transducers. All transducers had polarization parallel to the direction of shear loading.

The data shown in Figure 2 are representative of an extensive experimental study where over one-hundred direct shear experiments were performed on discontinuities in gypsum (those included different confinement stresses, surface roughness, repeatability and verification tests). The main implication of the data is the identification of seismic precursors as significant changes in the transmitted and reflected shear wave amplitudes that occurred prior to peak shear strength. The precursors were evaluated as a function of the distance (in terms of shear displacement) between their appearance and the peak shear strength. The discussion here is based on shear displacement rather than on time to eliminate the effect of loading rate. For a better interpretation of the precursors, negative values are used to denote the magnitude of the shear displacement that remains before reaching the peak shear stress. Thus, the more negative the value, the “earlier” the precursor. The precursors to peak shear strength were observed between -0.2 mm to 0 mm for homogeneous smooth discontinuities (Figure 3a); between -0.36 mm to -0.1 mm for homogeneous rough discontinuities (Figure 3b); and between -0.48 mm to -0.2 mm for the non-homogeneous discontinuities (Figure 3c). Although the magnitude of the displacement may seem small in terms of its

absolute value, it is an important fraction of the peak displacement. In fact, precursors appear within the range of 50% to 80% of the peak displacement. The precursors were detected closer to the macroscopic peak shear strength of the homogeneous smooth discontinuity (Figure 3a) than to the macroscopic shear strength of the homogeneous rough discontinuity (Figure 3b). For specimens with a non-homogeneous discontinuity, it was observed that the precursors occurred first on the smooth surface and later on the rough surface or almost simultaneously along the entire discontinuity. Given that the shear displacement between precursors and failure should be much smaller for a smooth surface (Figure 3a) than for a rough surface (Figure 3b), the data in Figure 3c, from nonhomogeneous discontinuities, suggest that slip occurred first along the smooth surface and later along the rough surface. This observation is in agreement with previous findings (Martel and Pollard, 1989; Bürgmann et al., 1994; Bruhn and Schultz, 1996; Mutlu and Bobet, 2006), demonstrating that slip along a discontinuity does not occur simultaneously. It starts first along a weak patch and then propagates through the discontinuity. As observed in the experiments, the sequence of the precursors prior to failure indicates the non-uniform distribution of micro-slip events along the discontinuity. Thus, failure along a frictional discontinuity is a progressive process, where micro-patches of the discontinuity fail first and slip propagates along the discontinuity until the entire surface fails, at peak strength.

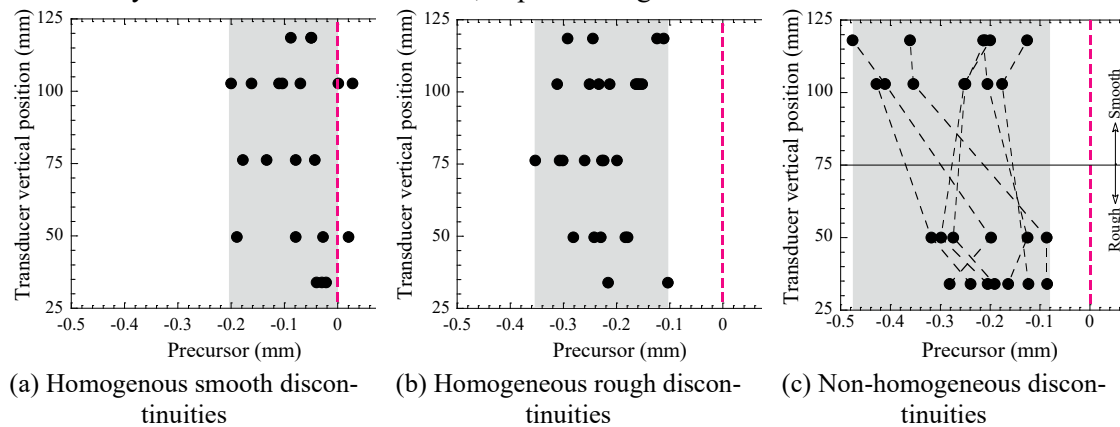


Figure 3. Seismic precursors prior to failure of gypsum discontinuities (normal stress 1-4 MPa).

We also used a Digital Image Correlation (DIC) technique to measure shear displacements along the discontinuity. Slip, defined as the relative shear displacement across the discontinuity, was calculated from the surface displacement data separately for the smooth and rough portions of the discontinuity. A comparison of the transducer measurements with slip in the experiments is made in Figure 4. A significant increase in the rate of shear displacement was observed first for the smooth surface, which was “predicted” by the precursor from the seismic transducers located on the smooth surface. The rough surface also showed a significant increase in the rate of shear, but it occurred closer to failure than with the smooth surface. The increase in the rate of shear displacement was somewhat concurrent with the corresponding seismic precursor. It is clear from the results that the precursor events were associated with the onset of slip along the discontinuity.

In another set of tests, direct shear experiments were conducted on limestone rock specimens obtained in Bedford, Indiana (the discontinuities were obtained by the splitting of a single limestone block). Similar to the observations made on the gypsum specimens, the amplitude of the transmitted shear waves across the discontinuity increased upon the application of shear load and reached a peak prior to the peak shear strength of the discontinuity. The precursors were identified as a maximum in the amplitude of the transmitted shear waves that occurred prior to the peak shear strength of the discontinuity, which were observed between -0.2 mm to -0.02 mm with respect to the macroscopic failure of the discontinuity and appeared within the range of 60% to

95% of the peak displacement. We interpret the results on limestone as a confirmation of the observations in gypsum, i.e. the findings are not specific to a given rock-model material such as gypsum, but also apply to natural rocks.

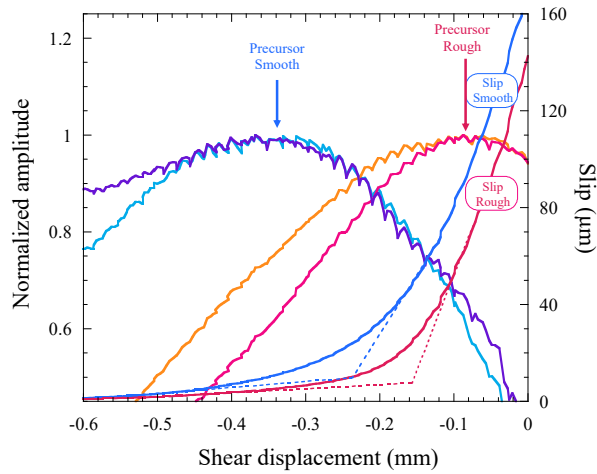


Figure 4. Normalized shear wave amplitudes showing precursors and slip along the smooth and rough surfaces obtained from DIC.

3 THE IMAGING OF FRACTURING

Uniaxial compression tests on prismatic limestone specimens, 203.2x101.6x38.1 mm, with one or two flaws with length of 19.05 mm through the thickness of the specimens were performed while P- and S-waves were transmitted through the rock. Figure 5 shows one of the specimens tested, with two parallel non-overlapping coplanar flaws.

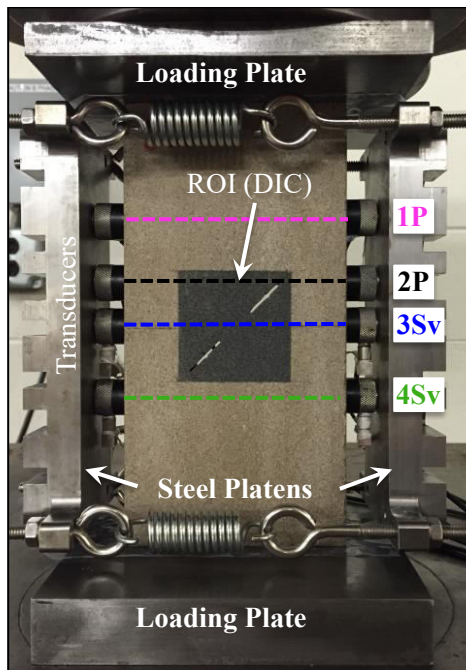


Figure 5. Experimental setup for monitoring crack initiation and coalescence in limestone specimens with two parallel coplanar flaws.

An array of emitter P-wave transducers (1P and 2P in the figure) and S-wave transducers (3Sv and 4Sv) was placed on the right hand-side of the specimens, and an analogous array of receivers on the left (Figure 5).

In the experiments, the wave signals were monitored during loading and the surface of the specimen was inspected using DIC (Digital Image Correlation), to detect new cracks. It was consistently found, through a large number of tests with different flaw geometries, that the onset of a tensile crack was unequivocally associated with a change in amplitude of transmitted P- and S-waves. Damage in tension is associated with the appearance of microcracks, which in turn induces a reduction of stiffness of the material, which is then detected by changes in amplitude of the transmitted (and reflected) waves. The damage occurs before micro-crack nucleation in the form of a tensile crack, and thus the damage is detected by the seismic waves as a precursor of tensile crack initiation. In shear, the damage is not large enough to change sufficiently the stiffness of the material and thus it does not induce observable changes in amplitude. It is hypothesized that damage in shear is associated with the creation of an array of oriented microcracks. Such an array would induce converted waves (from P- to S-waves or from S- to P-waves, as discussed by Nakagawa et al., 2000). This hypothesis was confirmed by the results shown in Figure 6, that plots the normalized amplitude of the transmitted and reflected waves from transducer 3S_v, up to failure. The figure also shows that the amplitude of transmitted waves (in blue in the figure) was not sensitive to the appearance of shear cracks (detected with DIC at 94.4 kN). However, the presence of a reflected wave (in green in the figure) and, most importantly, the appearance of converted waves worked as precursors to the onset of the shear crack (as it will be discussed, reflected waves do not always detect shear cracks, while converted waves always do). The reflected and converted waves appeared before the crack was detected with DIC. The figure also shows how the normalized amplitude of the converted waves increased with the load, an indication of the growth of the shear crack. Coalescence was observed, through DIC, at 105.6 kN.

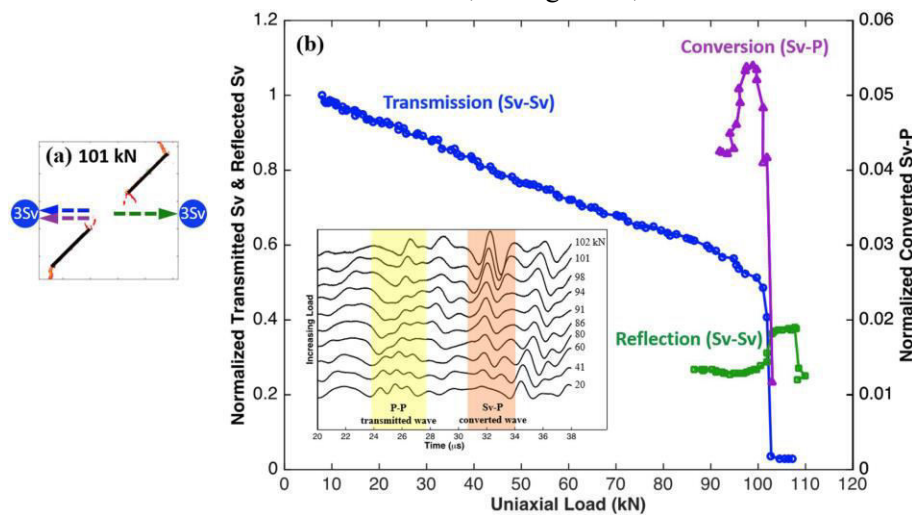


Figure 6. (a) Path of shear crack formation from DIC results, with the path of the transmitted, reflected, and converted signals (blue, green, and purple dashed lines, respectively) from transducer 3S_v; (b) normalized amplitude of wave transmission (blue circles), reflection (green squares), and conversion (purple triangles) from transducer 3S_v; the inset displays a 18- μ s window of received P-, and converted S- to P-wave waveforms from transducer 3S_v. After Modiriasari et al. (2020).

Figures 7 and 8 summarize the results from monitoring changes in amplitude of transmitted, reflected and converted waves (Modiriasari et al. 2020). Figure 7 is a graph of the ratio, in percentage, of the load of tensile/wing crack initiation obtained from changes of amplitude of transmitted or reflected waves and the load when a tensile crack was observed with the DIC. The figure shows that changes of amplitude of both transmitted and reflected waves are precursors to tensile crack

initiation (note that data plots below the 100% ratio), with transmitted waves providing the information earlier than reflected waves. Figure 8 is an analogous plot, but for the detection of shear cracks. It includes data from transmitted, reflected and converted waves. As one can see, changes in amplitude of transmitted waves appeared after the shear crack was formed, thus indicating that significant crack growth or damage was needed for the shear crack to be detected with transmitted waves. The figure also shows that reflected waves may also detect the onset of shear cracks, but not in all cases, which brings into question the effectiveness of monitoring reflected waves. Converted waves, however, systematically showed as precursors to shear crack initiation, irrespective of the orientation of the shear crack with the direction of the incident wave (either with normal or oblique incidence).

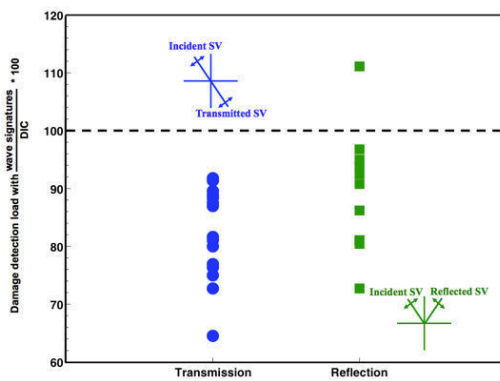


Figure 7. Detection of tensile crack initiation with seismic waves and DIC.

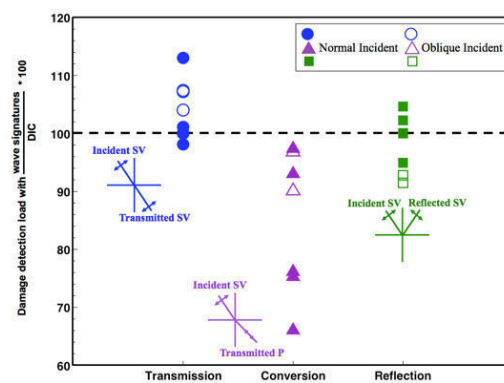


Figure 8. Detection of shear crack initiation with seismic waves and DIC.

4 CONCLUSIONS

The most important outcome of the study is the discovery of seismic precursors prior to the shear failure of frictional discontinuities in both gypsum, a rock-model material, and Indiana limestone, a natural rock. Precursors were identified as the maximum in transmitted wave amplitude or the minimum in the reflected wave amplitude. Seismic precursors were consistently observed well before slip or failure occurred along the discontinuity. Precursors are associated with the onset of slip along a patch and are attributable to a reduction in the discontinuity local shear stiffness.

In addition, active seismic monitoring, in particular compressional and shear wave propagation, were used to detect and locate damage inside rock, in the form of tensile or shear cracks (faults). The seismic monitoring method included an array of piezoelectric transducers that transmitted elastic waves in the form of ultrasonic pulses through the rock to an array of receivers. The seismic monitoring method provided a continuous and non-destructive way to probe the internal structure of the rock. Extensive experimental work determined that: (1) Changes in transmitted and reflected wave amplitudes can detect damage inside the rock; (2) Wave transmission and reflection from P- and S-wave transducers can be used to locate tensile cracks and crack coalescence, but cannot detect faults; (3) P- and S-waves that cross a fault generate S- and P-waves (converted waves) and can be used to detect the location of faults, as well as the growth of faults, because the amplitude of the converted waves increases with fault propagation; (4) Theoretical considerations suggest that shear cracks (faults) start inside the rock as an array of oriented microcracks, which, with further loading, link with each other forming a macroscopic fault; and (5) Active seismic wave monitoring is an effective tool to detect tensile and shear crack initiation, propagation and coalescence inside rock, as well as to determine the location of new cracks.

5 ACKNOWLEDGMENTS

The research discussed in this paper is the result of close collaboration with a number of students and colleagues. Dr. Ahmad Hedayat and Dr. Anahita Modiriasari conducted all the experiments. Dr. Pyrak-Nolte's expertise in geophysics and wave propagation in fractured media was crucial to interpret the results. Funding for the work was provided by the National Science Foundation with grants CMS-0856296 and CMMI-1162082.

6 REFERENCES

- Anastassopoulos, A.A. & Philippidis, T.P. 1995. Clustering methodology for evaluation of acoustic emission from composites. *Journal of Acoustic Emission*, 13(1/2):11–22.
- Bentahar, M. & Guerjouma, R. El. 2009. Monitoring progressive damage in polymer- based composite using nonlinear dynamics and and acoustic emission. *The Journal of the Acoustical Society of America*, 125(EL39), doi: 10.1121/1.2993755
- Bobet, A. 1997. *Fracture coalescence in rock materials experimental observations and numerical predictions*. Doctoral Dissretation, Massachussets Institute of Technology, Cambridge, MA.
- Bobet, A. & Einstein, H.H. 1998. Fracture coalescence in rock-type materials under uniaxial and biaxial compression. *International Journal of Rock Mechanics and Mining Sciences*, 35:863–888. doi: 10.1016/S0148-9062(98)00005-9
- Bruhn, R. L. & Schultz, R. A. 1996. Geometry and slip distribution in normal fault systems: Implications for mechanics and fault-related hazards. *Journal of Geophysical Research*, 101:3401-3412.
- Burgmann, R., Pollard, D. D. & Martel, S. J. 1994. Slip distributions on faults: Effects of stress gradients, inelastic deformation, heterogeneous host-rock stiffness, and fault interaction. *Journal of Structural Geology*, 16:1675-1690.
- Camones, L.A.M., Vargas, E. do A., de Figueiredo, R.P. & Velloso, R.Q. 2013. Application of the discrete element method for modeling of rock crack propagation and coalescence in the step-path failure mechanism. *Engineering Geology*, 153:80–94. doi: 10.1016/j.enggeo.2012.11.013
- Carvalho, F.C.S. & Labuz, J.F. (2002). Moment tensors of acoustic emissions in shear faulting under plane-strain compression. *Tectonophysics*, 356:199–211. doi: 10.1016/S0040-1951(02)00385-2
- Chen, G., Kemeny, J. & Harpalani, S. 1993. Fracture propagation and coalescence in marble plates with pre-cut notches under compression. *International Journal of Rock Mechanics, Mining Sciences and Geomechanics Abstracts*, 30(5):279.
- Chen, W.-Y., Lovell, C.W., Haley, G.M. & Pyrak-Nolte, L.J. 1993. Variation of shear-wave amplitude during frictional sliding. *International Journal of Rock Mechanics, Mining Sciences & Geomechanics Abstracts*, 30:779–784. doi: 10.1016/0148-9062(93)90022-6
- De Melo Moura, D. & Bobet, A. 2019. Cracking across a Smooth Interface in a Rock-Model Material. *ISRM 14th International Congress of Rock Mechanics*, Iguassu Falls, Brazil, September 13-18, 2019.
- Einstein, H. H. & Hirschfeld, R. C. 1973. Model studies on mechanics of jointed rocks. *ASCE Journal of the Geotechnical Division*, 99:229-248.
- Fakhimi, A., Carvalho, F., Ishida, T. & Labuz, J.F. 2002. Simulation of failure around a circular opening in rock. *International Journal of Rock Mechanics and Mining Sciences*, 39:507–515. doi:10.1016/S1365-1609(02)00041-2
- Germanovich, L.N., Salganik, R.L., Dyskin, A.V. & Lee, K.K. 1994. Mechanisms of brittle fracture of rock with pre-existing cracks in compression. *Pure and Applied Geophysics PAGEOPH*, 143:117–149. doi: 10.1007/BF00874326
- Goodman, R. E. 1980. *Introduction to Rock Mechanics*. John Wiley & Sons, USA.
- Hedayat, A., Bobet A. & Pyrak-Nolte L. J. 2012. Monitoring Slip Initiation And Propagation Along Frictional Interfaces With Seismic Wave Transmission. *Proceeding of the 46th U.S. Rock Mechanics/Geomechanics Symposium*, Chicago, 24-27 June 2012.
- Hedayat, A., Pyrak-Nolte, L.J. & Bobet, A. 2014a. Precursors to the shear failure of rock discontinuities. *Geophysical Research Letters*, 41:5467–5475. doi: 10.1002/2014GL060848

- Hedayat, A., Pyrak-Nolte, L. & Bobet, A. 2014b. Multi-modal monitoring of slip along frictional discontinuities. *Rock Mechanics and Rock Engineering*, 47(5):1575-1587.
- Hildyard, M.W., Young, R.P., Collins, D.S. & Pettitt, W. 2005. Seismic wave propagation to diagnose the state of fracturing. *The Journal of The South African Institute of Mining and Metallurgy*, 105:437-446.
- Hu, S., Lu, J. & Xiao, F. 2013. Evaluation of concrete fracture procedure based on acoustic emission parameters. *Construction and Building Materials*, 47:1249-1256. doi: 10.1016/j.conbuildmat.2013.06.034
- Jaeger, J.C., Cook, N.G.W. & Zimmerman, R.W. 2007. *Fundamentals of Rock Mechanics*. Blackwell Publishing, UK.
- Kahraman, S. 2002. The effects of fracture roughness on P-wave velocity. *Engineering Geology*, 63: 347-350. doi: 10.1016/S0013-7952(01)00089-8
- Ko, T.Y., Einstein, H.H. & Kemeny, J.M. 2006. Crack coalescence in brittle material under cyclic loading. *Proceeding of the 41st U.S. Rock Mechanics Symposium*, June 17-21, Golden, CO.
- Leucci, G. & De Giorgi, L. 2006. Experimental studies on the effects of fracture on the P and S wave velocity propagation in sedimentary rock ("Calcarene del Salento"). *Engineering Geology*, 84:130-142. doi: 10.1016/j.enggeo.2005.12.004
- Li, Y.-P., Chen, L.-Z. & Wang, Y.-H. 2005. Experimental research on pre-cracked marble under compression. *International Journal of Solids and Structures*, 42:2505-2516. doi: 10.1016/j.ijsolstr.2004.09.033
- Lin, Q. & Labuz, J.F. 2013. Fracture of sandstone characterized by digital image correlation. *International Journal of Rock Mechanics and Mining Sciences*, 60:235-245. doi: 10.1016/j.ijrmms.2012.12.043
- Lin, Q., Yuan, H., Biolzi, L. & Labuz, J.F. 2014. Opening and mixed mode fracture processes in a quasi-brittle material via digital imaging. *Engineering Fracture Mechanics*, 131:176-193. doi: 10.1016/j.engfracmech.2014.07.028
- Martel, S. J., & Pollard, D. D. 1989. Mechanics of slip and fracture along small faults and simple strike-slip fault zones in granitic rock. *Journal of Geophysical Research*, 94:9417-9428.
- Modiriasari, A., Bobet, A. & Pyrak-Nolte, L.J. 2017. Active Seismic Monitoring of Crack Initiation, Propagation, and Coalescence in Rock. *Rock Mechanics and Rock Engineering*, 50(9):2311-2325, <https://doi.org/10.1007/s00603-017-1235-x>
- Modiriasari, A., Pyrak-Nolte, L.J. & Bobet, A. 2018. Emergent Wave Conversion as a Precursor to Shear Crack Initiation. *Geophysical Research Letters*, 45:9516-9522. DOI: 10.1029/2018GL078622.
- Modiriasari, A., Bobet, A. & Pyrak-Nolte, L.J. 2020. Seismic Wave Conversion Caused by Shear Crack Initiation and Growth. *Rock Mechanics and Rock Engineering*, 53:2805-2818. <https://doi.org/10.1007/s00603-020-02079-2>
- Moradian, Z. & Einstein H.H. 2014. Monitoring Cracking Process of Gypsum by Means of Acoustic Emission and High Speed Camera Imaging. Proceedings of the 48th U.S. Rock Mechanics/Geomechanics Symposium, June 1-4, 2014. Paper Number: ARMA-2014-7528
- Morgan, S., Johnson, C. & Einstein, H.H. 2013. Cracking processes in Barre granite: fracturing process zones and crack coalescence. *International Journal of Fracture*, 180:177-204.
- Mutlu, O. & Bobet, A. 2006. Slip propagation along frictional discontinuities. *International Journal of Rock Mechanics and Mining Sciences*, 43:860-876.
- Nakagawa, S., Nihei, K.T.T. & Myer, L.R.R. 2000. Shear-induced conversion of seismic waves across single fractures. *International Journal of Rock Mechanics and Mining Sciences*, 37:203-218. doi: 10.1016/S1365-1609(99)00101-X
- Park, C.H. & Bobet, A. 2009. Crack coalescence in specimens with open and closed flaws: A comparison. *International Journal of Rock Mechanics and Mining Sciences*, 46:819-829. doi: 10.1016/j.ijrmms.2009.02.006
- Pyrak-Nolte, L.J., Myer L.R. & Cook, N.G.W. 1990a. Anisotropy in seismic velocities and amplitudes from multiple parallel fractures. *International Journal of Rock Mechanics, Mining Sciences and Geomechanics Abstracts*, 28(2-3):A154.
- Pyrak-Nolte, L.J., Myer L.R. & Cook, N.G.W. 1990b. Transmission of seismic waves across single natural fractures. *Journal of Geophysical Research*, 95(B6):8617-8638. doi: 10.1029/JB095iB06p08617

- Reyes, O. & Einstein H. H. 1991. Failure mechanisms of fractured rock: A fracture coalescence model. *Proceedings of the 7th International Congress on Rock Mechanics*, 1:333–340.
- Sagong M. & Bobet, A. 2002. Coalescence of multiple flaws in a rock-model material in uniaxial compression. *International Journal of Rock Mechanics and Mining Sciences*, 39:229–241. doi: 10.1016/S1365-1609(02)00027-8
- Shen, B. 1995. The mechanism of fracture coalescence in compression—experimental study and numerical simulation. *Engineering Fracture Mechanics*, 51:73–85. doi: 10.1016/0013-7944(94)00201-R
- Shen, B., Stephansson, O., Einstein, H.H., & Ghahreman, B. 1995. Coalescence of fractures under shear stress experiments. *Journal of Geophysical Research*, 100:5975–5990.
- Shiotani, T., Bisschop, J. & Van Mier, J.G.M. 2003. Temporal and spatial development of drying shrinkage cracking in cement-based materials. *Engineering Fracture Mechanics*, 70(12):1509–1525. doi: 10.1016/S0013-7944(02)00150-9
- Sutton, M. A., Yan, J. H., Tiwari, V., Schreier, H. W. & Ortu J.J. 2008. The effect of out-of-plane motion on 2D and 3D digital image correlation measurements. *Optics and Lasers in Engineering*, 46(10):746–757.
- Wong, L. & Einstein, H.H. 2006. Fracturing Behavior of Prismatic Specimens Containing Single Flaws. In *Proceedings of the 41th U.S. Symposium on Rock Mechanics*, Colorado, 17-21 June 2006.
- Wong, R.H.C. & Chau, K.T. 1998. Crack coalescence in a rock-like material containing two cracks. *International Journal of Rock Mechanics and Mining Sciences*, 35:147–164. doi: 10.1016/S0148-9062(97)00303-3
- Wong, R.H., Chau, K., Tang, C. & Lin, P. 2001. Analysis of crack coalescence in rock-like materials containing three flaws—Part I: experimental approach. *International Journal of Rock Mechanics and Mining Sciences*, 38:909–924. doi: 10.1016/S1365-1609(01)00064-8
- Wong, L.N.Y. & Einstein, H.H. 2009a. Crack coalescence in molded gypsum and carrara marble: Part 1. macroscopic observations and interpretation. *Rock Mechanics and Rock Engineering*, 42:475–511. doi: 10.1007/s00603-008-0002-4
- Wong, L.N.Y. & Einstein, H.H. 2009b. Systematic evaluation of cracking behavior in specimens containing single flaws under uniaxial compression. *Rock Mechanics and Rock Engineering*, 46:239–249.
- Wong, L.N.Y., Zou, C. & Cheng, Y. 2013. Fracturing and failure behavior of Carrara marble in quasistatic and dynamic Brazilian dist tests. *Rock Mechanics and Rock Engineering*, 47(4):1–17. doi: 10.1007/s00603-013-0465-9
- Yang, S.-Q. & Jing, H.-W. 2010. Strength failure and crack coalescence behavior of brittle sandstone samples containing a single fissure under uniaxial compression. *International Journal of Fracture*, 168:227–250. doi: 10.1007/s10704-010-9576-4
- Young, R.P. & Thompson, B.D. 2007. Imaging dynamic rock fracture with acoustic emission and x-ray tomography. *Proceedings of the 11th Congress of International Society for Rock Mechanics*, Lisbon, July 9-13, Specialty Session.
- Zou, C., Wong, L.N.Y. & Cheng, Y. 2012. The strength and crack behavior of the rock-like gypsum under high strain rate. *ARMA, 46th US Rock Mechanics/Geomechanics Symposium* Chicago, IL, USA
- Zou, C. & Wong, L.N.Y. 2014. Experimental studies on cracking processes and failure in marble under dynamic loading. *Engineering Geology*, 173:19–31.
- Zou, C., Wong, L.N.Y., Loo, J.J. & Gan, B.S. 2016. Different mechanical and cracking behaviors of single-flawed brittle gypsum specimens under dynamic and quasi-static loadings. *Engineering Geology*, 201:71–84. doi: 10.1016/j.enggeo.2015.12.014

Keynote Lecture: Continuum or Discontinuum – That is the Question

N.R. Barton

Nick Barton and Associates, Oslo, Norway

ABSTRACT:

Several decades ago there was a strong focus on the need for discontinuum modelling to improve upon the empirically based analysis of excavations in jointed rock. The remarkable codes developed by Peter Cundall: UDEC and 3DEC were put to full use in the nineteen eighties and nineties. For example, Q-system based cavern support could be verified or improved with such analyses. Of course, these codes preferably require knowledge of rock mechanics and rock joint behaviour, and perhaps familiarity with non-linear constitutive models as in UDEC-BB. Regrettably the classic textbooks of Hoek and Bray and Hoek and Brown in this period were subsequently followed by the suggestions for continuum modelling using a still not finalized GSI – there are many attempts at improved quantification. JRC now reaching 50 years is also the subject of improved quantification, but it is not followed by the extraordinary page-wide equations for ‘c’ and ‘ ϕ ’ so no software is needed. The incorrect addition of these components of shear strength (as indeed in Mohr-Coulomb) in commercial continuum codes is the final source of error of so many analyses. So-called plastic zones are exaggerated around tunnels, and rock slopes are given seldom observed deep spoon-shaped failure predictions, ignoring the frequent influence of major discontinuities, and the usual failures within the slope faces. Of course, lake-bed open-pit slope deposits or extremely weathered rock will give spoon-shaped failures as for rock-fill and soil, but competent jointed rock will not fail like this: major discontinuities will usually be involved, and wedge or planar failures will be the usual reality.

1 INTRODUCTION

We were advised more than 50 years ago by Brace and Müller that cohesion is broken before friction is fully mobilized. Gross errors are caused by adding these components of shear strength when estimating the maximum height of cliffs and mountain walls. Since ‘c’ is not the lowest component of strength, artificially lowered estimates are needed, or tensile strength and Poisson’s ratio are used (Barton and Shen, 2017). There is precious little empirical basis for the Hoek-Brown equations for rock mass strength, but an excellent experimental basis of course for the earlier intact rock H-B criterion. We may ask if it is logical to downgrade the strength of intact rock to model rock masses (using opaque equations with joint roughness and number of joint sets ignored) or better to apply the equations for the shear strength of joints and fractures and estimate the initial cohesive contribution of intact bridges between the kinematically capable joint sets? In this lecture the author will be showing studies with UDEC, 3DEC, FLAC and FLAC3D and FRACOD, and will be illustrating both discontinuum and continuum analyses for tunnels, caverns and open-pit slopes. An earlier than UDEC phase, with fractured (2D) models of underground excavations, will also be shown as an introduction.

2 PHYSICAL MODELS WITH FRACTURES PRE UDEC

The author was a student colleague of Cundall while he started to develop his first remarkable computer code with blocks. However, we may start with what could be achieved with physical

models of fractured media *before Cundall's codes became available*, both pre-1970 and from just prior to the Cundall/Itasca UDEC release in 1980. He was inspired to do better, as in Fig. 1.

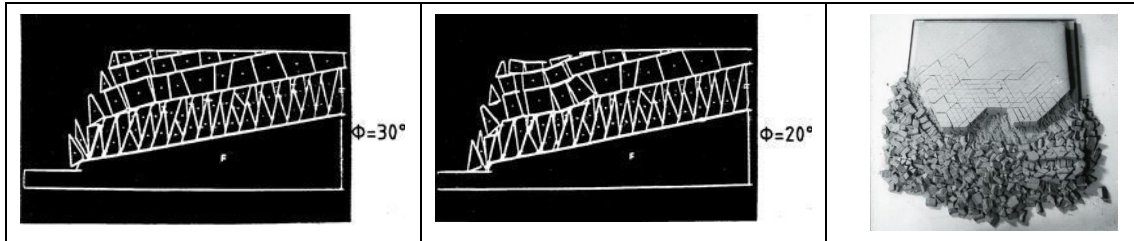


Figure 1. The contrasting flexibility of Cundall's intelligent computer code μ DEC: two of four results of varying angle ϕ from Cundall et al. (1975). A big contrast to the 'fixed-fracture-sets' fractured 2D models developed some years earlier by the author in 1968. These physical models were utilized on two occasions before UDEC was released. Several 2D 'slab models' with carefully loaded and excavated slope models of 40,000 blocks were followed some years later with underground opening models with 20,000 blocks (Figs 2, 3 & 4). Individual slab models also allowed investigation of the relative effects of 4,000, 1,000 and 250 blocks in biaxial loading, which assisted in block-size scale effect understanding. The smallest block sizes gave unexpected 'linear' stress-strain behaviour and some kink-band modes.

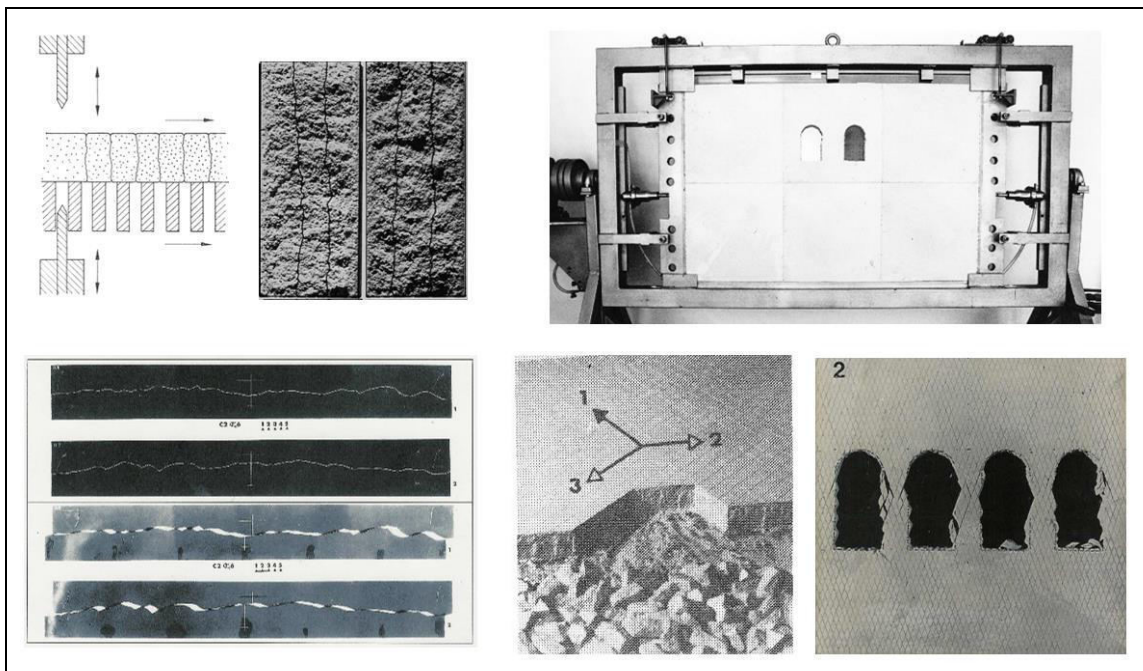


Figure 2. The principal mechanism of tension-fracture development and their roughness are illustrated top left. A subsequent physical model series reported by Barton & Hansteen (1979) is shown on the right. (My NGI colleague provided the continuum model comparisons). One year after publication of these UNPP (underground nuclear power plant) studies, UDEC became commercially available. No regrets.

Some of these early pre-UDEC physical fracture models are reproduced in this lecture as they still appear not to have been repeated by others and represent a 'physical reality' even though not a 'geological reality'. They may serve as 2D code verification objects. In the end the early UNPP studies in Norway including site characterization, came to nothing, and Sweden (who had part-funded these physical model studies through BeFo) built surface nuclear plants, while Norway continued with more extensive underground hydroelectric power developments.

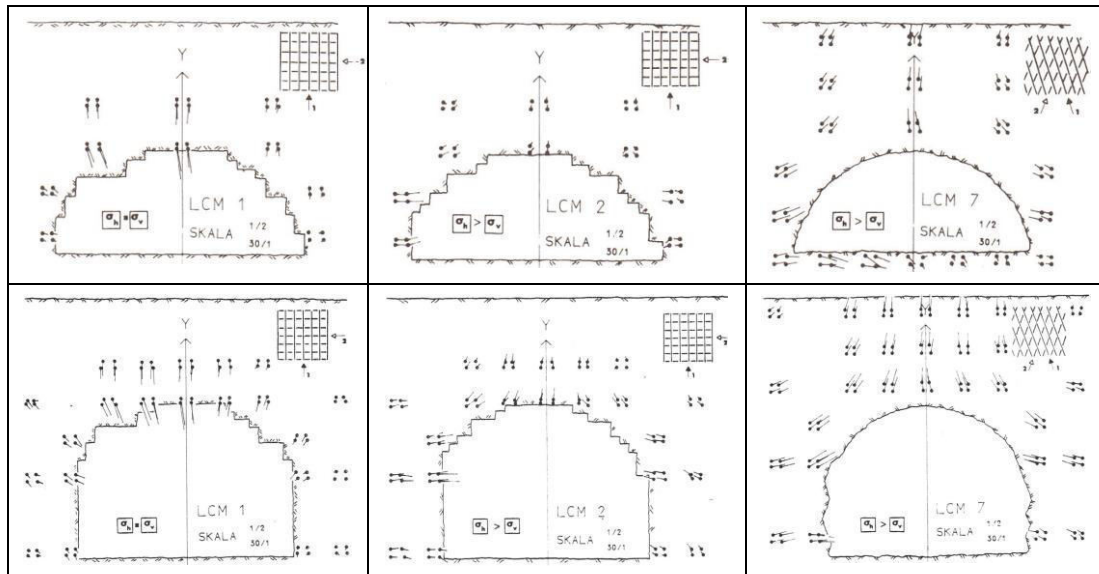


Figure 3. A selection of the cavern models which were studied in the pre-UDEC period, in order to evaluate the feasibility of underground nuclear power plant (UNPP) spans of 50m. The deformation vectors show the importance of horizontal stress and demonstrate the inevitable inadequacy of isotropic continuum modelling. The inset joint (fracture) structures are at correct scale and show primary and secondary fracture sets. All models had 20,000 blocks, meaning distant boundaries. Barton & Hansteen (1979).

3 SOME FUNDAMENTALS OF JOINT BEHAVIOUR

The physical fracture models suggested significant differences to continuum modelling, with joint orientations being particularly important. In Figure 4 we can also see a more fundamental feature of joint behavior. The four caverns were excavated one after the other in a high horizontal stress situation, as in four of the cases in Figure 3. Of particular note is the hysteresis or ‘deformation set’ seen in the narrow pillars. The photogrammetry-determined deformations did not reverse noticeably, when a new cavern was excavated, as would have happened in an elastic continuum model.

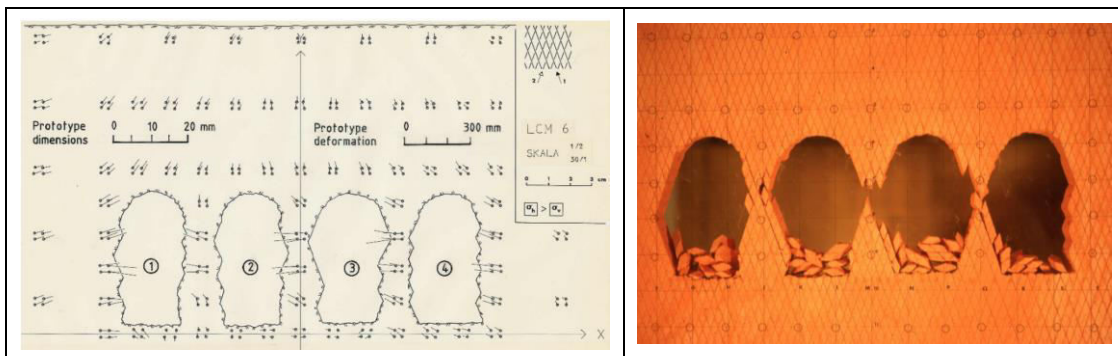


Figure 4. A multi-cavern experiment with ultra-narrow pillars, prior to model earthquake loading monitored with an accelerometer (giving a scaled 0.1 to 0.7g). Note the hysteresis in the cavern pillars. No reversal of deformations with successive cavern excavation. Fracture roughness and dilation explain the apparent tensile strength. Note that primary (continuous) fracture set #1 dips to the right, and has no

cohesive strength, just very high dilation and total friction angles at low normal stress. (Barton, 1973). Figure 2, bottom right, shows the cavern degradation progress during the model ‘earthquake’. In the next figure we see that three basic styles of rock mass deformation may occur with jointed rock masses, and each have been recorded by large scale *in situ* loading tests. They are clearly absent from conventional continuum modelling.

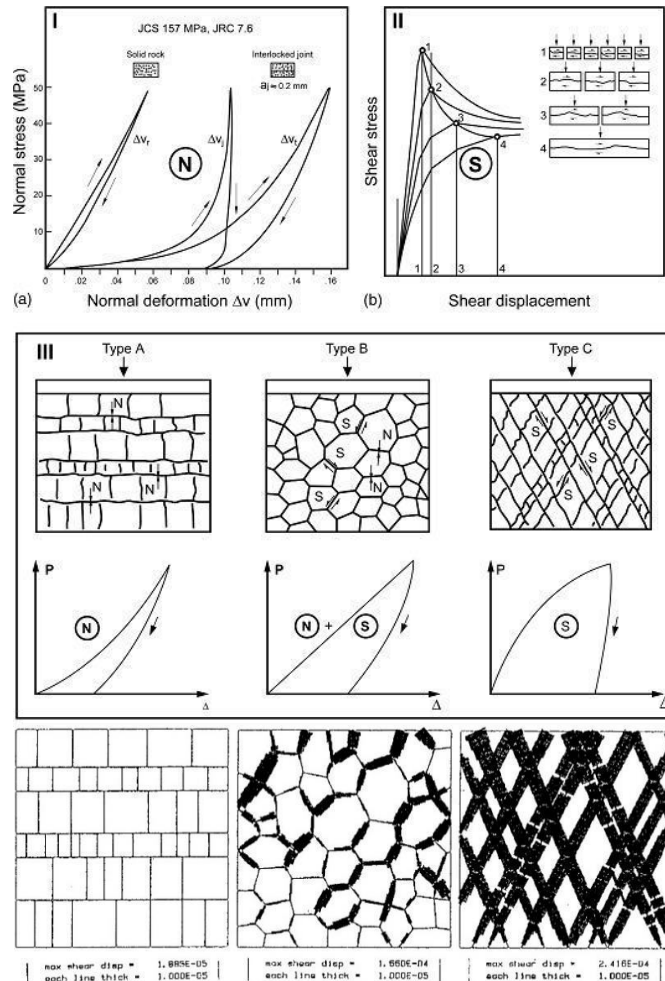


Figure 5. The N (normal) Type A concave deformation and the S (shear) Type C convex deformation, with the combined mode Type B as seen in loading tests across columnar basalt. Chryssanthakis et al. (1991) matched these three styles of deformation using UDEC-BB after this code became available in 1985. Note the normal stress-closure curves from Bandis et al. (1983) and the shear stress-displacement curves (with scale effects) from Bandis et al. (1981). The N and S and N+S load-deformation trends and the three rock mass assemblies are from Barton (1986).

To state the obvious there are no continuum model or GSI-based Hoek-Brown equations to match the essentially discontinuous behaviour shown in any of the previous figures, nor the shear strength details seen in Figure 6. GSI users can perhaps be happy that their ‘rock engineering’ activities are significantly easier thanks to RocScience software. But was the practice of rock mechanics for rock engineering supposed to be so easy? In the opinion of the author the use of GSI and continuum models has taken the realism out of the subject, which was not the original intention of Hoek and Bray and Hoek and Brown. These were classically helpful textbooks that also addressed discontinuum behaviour, the first one especially so.

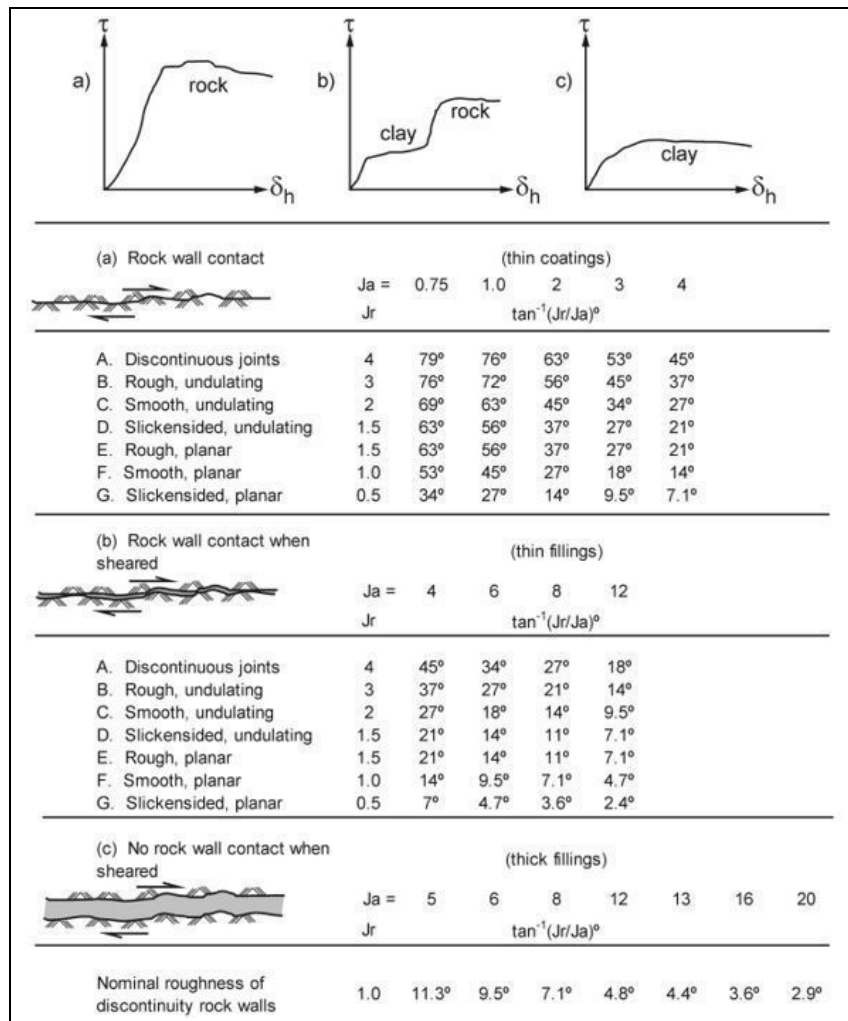


Figure 6. Variations in the shear strength of unfilled, clay-coated, and clay-filled discontinuities as illustrated here from the two Q-system parameters Jr/Ja cannot be included in GSI in a ‘free manner’ independent of joint roughness, because the GSI use of Bieniawski’s joint condition factor (along the x-axis) does not make such differentiation possible. The Bieniawski (1989) ‘joint condition’ moves in one direction, so rougher joints cannot have clay coatings or fillings, and even more remarkably: slickensides must be weathered. Figure from Barton (2002).

4 SOME EXAMPLES OF UDEC-BB MODELS SHOWING GEOLOGICAL DETAIL

In the following rather concentrated selection of discontinuum models the author will show features of potential behaviour that can hardly be matched by continuum modelling. The exception – to a degree – is the redistribution of stress, from principle far-field stresses to tangential and radial stresses. The rotation of the small ‘crosses’ are of course seen clearly in continuum models, but the loading of bolts where they cross and support wedges, and the unstressed unstable wedges are not seen in continuum models. The discontinuum model teaches us to look out for important behaviour that is absent from continuum modelling. In UDEC-BB we see the distribution of joint shearing and also the stress- or depth-dependent physical apertures, and JRC-estimated hydraulic apertures, for coupled H-M modelling. An introductory set of results with input is shown in Fig. 7.

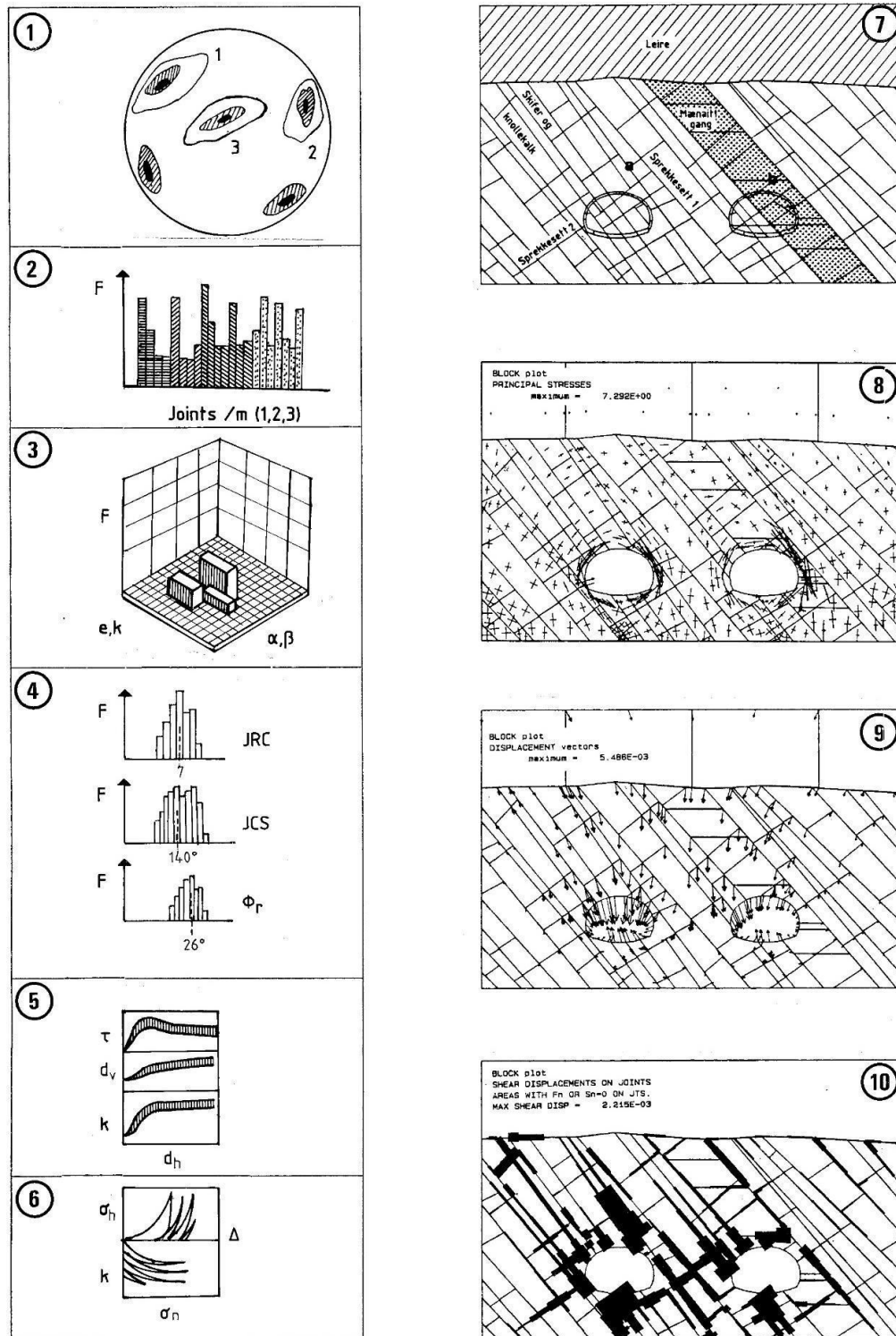


Figure 7. A glimpse of the principles of discontinuum modelling input data operations as applying to UDEC-BB. On the left: joint orientations and frequencies, permeability and aperture estimation (but this will be estimated by UDEC-BB) and joint index test results for JRC, JCS and ϕ_r . Boxes 5 and 6 symbolize the shear stress-displacement-dilation-permeability and normal stress-closure operations of the Barton-Bandis model. (See Barton et al., 1985, Barton, 1993 and Barton and Bandis, 2017 for examples).

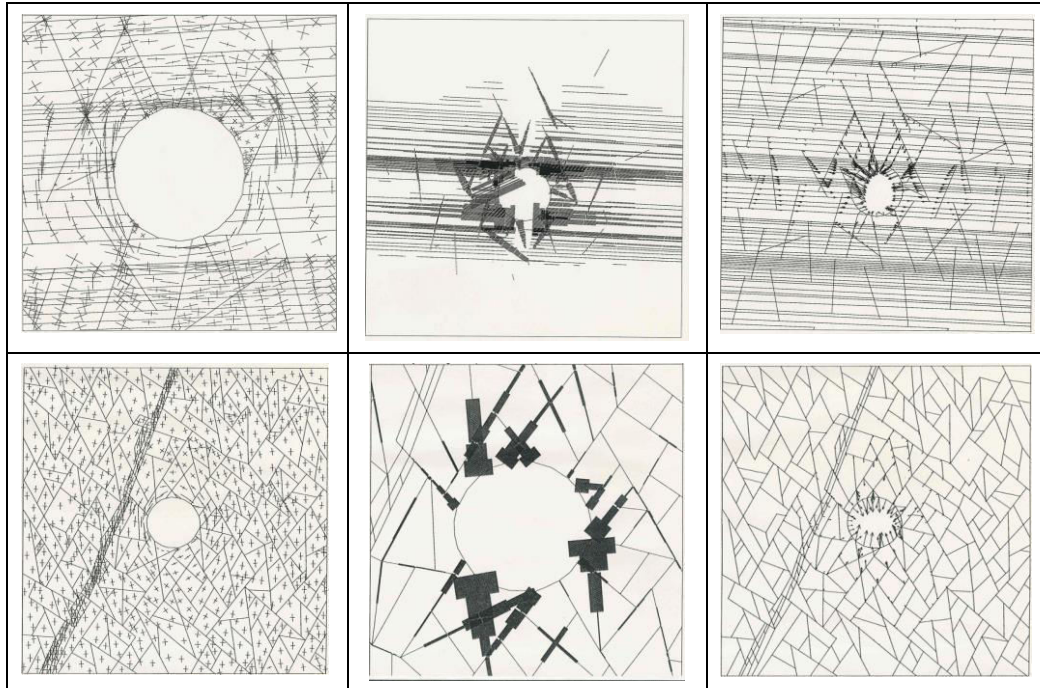


Figure 8. Selected UDEC-BB studies of a 250m deep section and a 700m deep section of a planned TBM spiral access tunnel through the interbedded St Bees sandstones and siltstones (top) and through the Borrowdale welded tuffs-ignimbrites (bottom) at the planned Sellafield LLW/ILW nuclear waste repository, from 1992. Thanks are due to NGI's numerical modelling team, during our 6 years geotechnical consultancy for UK Nirex, 1990-1996 which the author had the privilege to project-manage. All names later.



Figure 9. The discontinuum-modelling advantages of representing adversely steeply-dipping bedding. This late 1980's UDEC-BB model of a tunnel in Japan showed distinct signs of over-loading of the bolting. The bonding failure of the modelled S(fr) is also shown, bottom left.

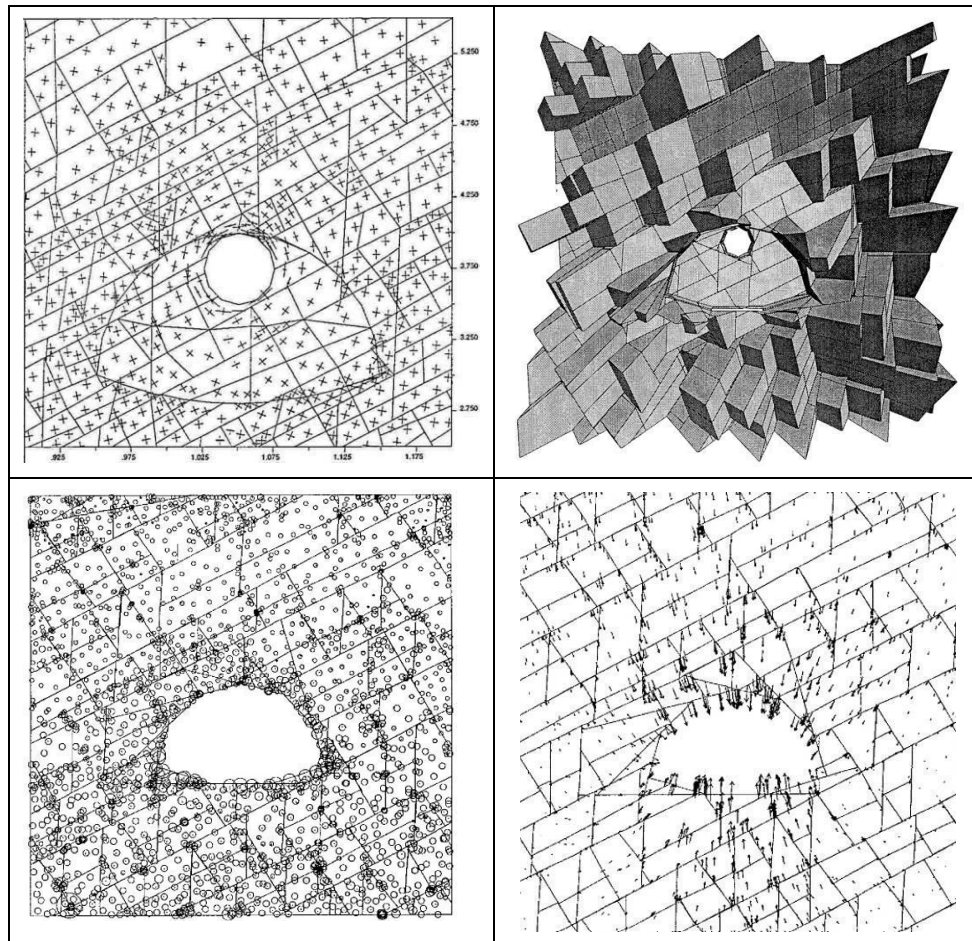


Figure 10. Top left: UDEC-BB to check TBM pilot tunnel break-out to full section. The 3DEC sections show a maximum tangential stress of 7.9 MPa and a maximum displacement of 8.0mm. This motorway project study is illustrated further in the next figure.



Figure 11. The unusual motorway pilot-TBM for the Tokyo-Osaka Tomei 2 Shimizu 3 motorway project. The specially designed TBM could turn so as to provide a pilot bore for the parallel tube. It proved important to ‘turn’ prior to reaching highly weathered rock. Dr Juhn Itoh of the Fuji Research Institute was responsible for this interesting NGI contract from Japan. NGI UDEC-BB and 3DEC modellers from the late 1980’s and early 1990’s included Dr Mark Christianson (Itasca/NGI) who was responsible for putting BB and UDEC ‘together’ in 1985 (with strong pleading to NGI’s director Kaare Høeg from Barton and Bandis), Dr Axel Makurat (later Shell), Linda Hårvik, Dr Marte Gutierrez (later distinguished US professor), Dr Karstein Monsen (later Geoscan), Panos Chryssenthakakis (later COWI), Dr Harald Hansteen, Dr Baotang Shen (later CSIRO in Australia), Lise Bacher, Dr Rajinder Bhasin – and since then several more.

A particularly notable discontinuum modelling contract for NGI was the design check for the designers of the 62m span Gjøvik Olympic cavern. This was done on behalf of owner Fortifikasjon, whose director Jan Rygh had drawn the ‘classic serviette sketch’ for the town’s chief planning engineer some years earlier, before the winter games were finally awarded to nearby Lillehammer, and ice hockey was played in this unique cavern. Modelled UDEC-BB deformation 7 to 9mm, MPBX recorded deformation a constant 7 to 8mm after 5 years of monitoring.

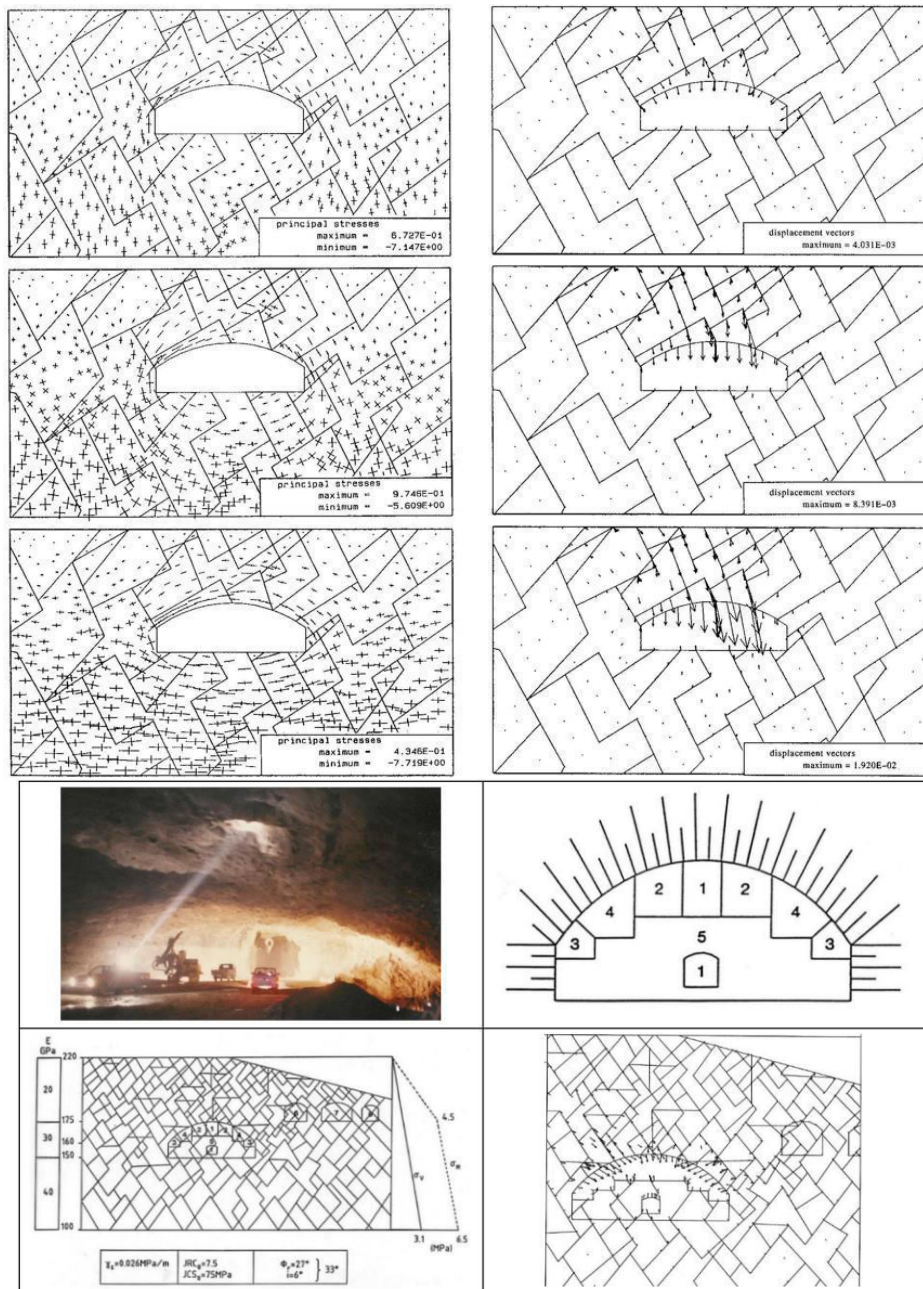


Figure 12. Top: Horizontal stress sensitivity studies conducted by Lloyd Tunbridge, and bottom: subsequently more detailed UDEC-BB modelling by Chryssanthakis, for the 62m span Gjøvik cavern. Note multi-author reference due also to Q-logging, cross-hole seismic tomography and rock stress measurement by the NGI team. Barton, Chryssanthakis, Tunbridge, Kristiansen, Løset, Bhasin, Westerdahl, Vik (1994).

4 OVERBREAK AND TUNNEL AND STOPE STABILITY

A feature of excavation effects in rock masses that particularly marks the stark difference between continuum and discontinuum modelling is *overbreak*. In Barton (2007) it was suggested that this could be quantified by the Q-parameter ratio J_n/J_r . Figure 13 (top photos and roughness sketches) shows how this works. The red-coloured ratios show $J_n/J_r < 6$ (no overbreak expected) while the blue-coloured ratios show $J_n/J_r \geq 6$ which is the suggested criterion. Extreme-value Q-parameter statistics at the LKAB mine explain the overbreak experienced in drilling drifts. Elevated values of J_a (clay coatings) obviously add to the likelihood of overbreak.

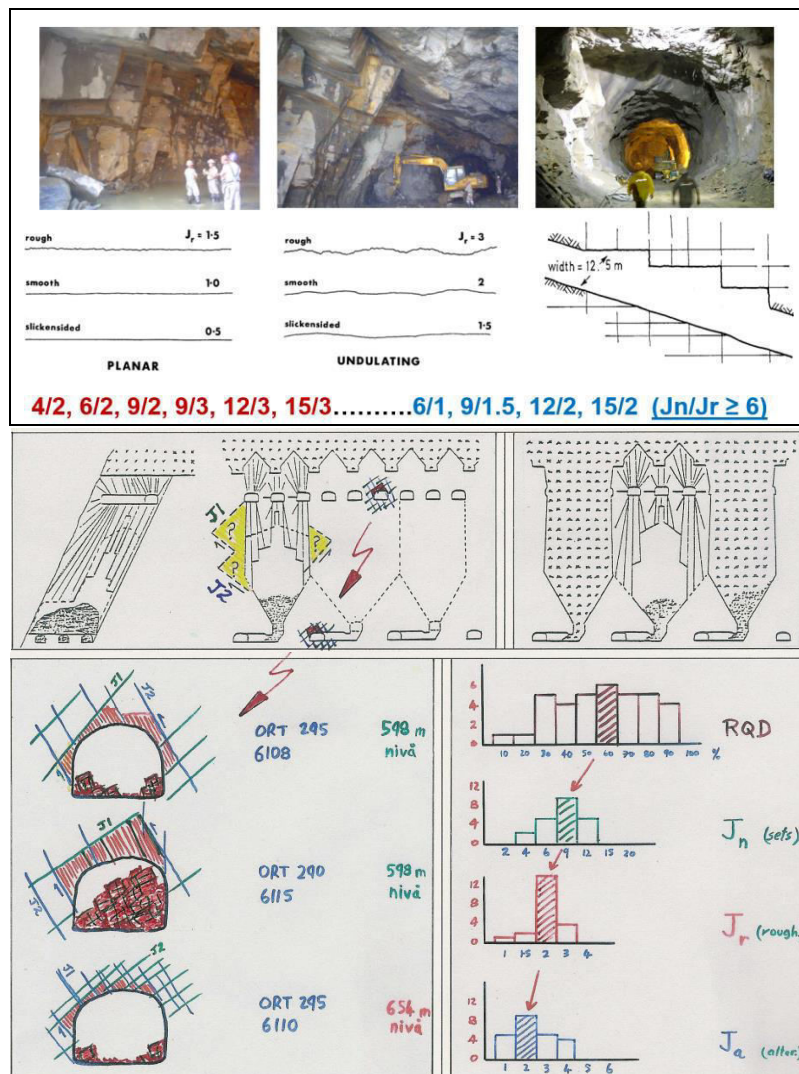


Figure 13. Top: the Q-parameter ratio $J_n/J_r \geq 6$ suggests almost unavoidable overbreak if there are sufficient degrees of freedom for block fall-out (higher J_n) and if joint roughness is low enough (low J_r). Bottom: observations performed by the writer in 1988 in LKAB's 'Oscar' long-hole drilling stope-development project in Kiruna in northern Sweden. Explanations for the excessive overbreak were sought. This was the first time that *Q-parameter histograms* were used by the author, and soon this became a systematic way of logging individual Q parameters. Note the potentially serious large-scale J_1/J_2 deformation mechanism in the future stopes (shown in yellow). Problematic details for continuum modelers, or an interesting expansion of their possibilities to influence design decisions – in many areas.

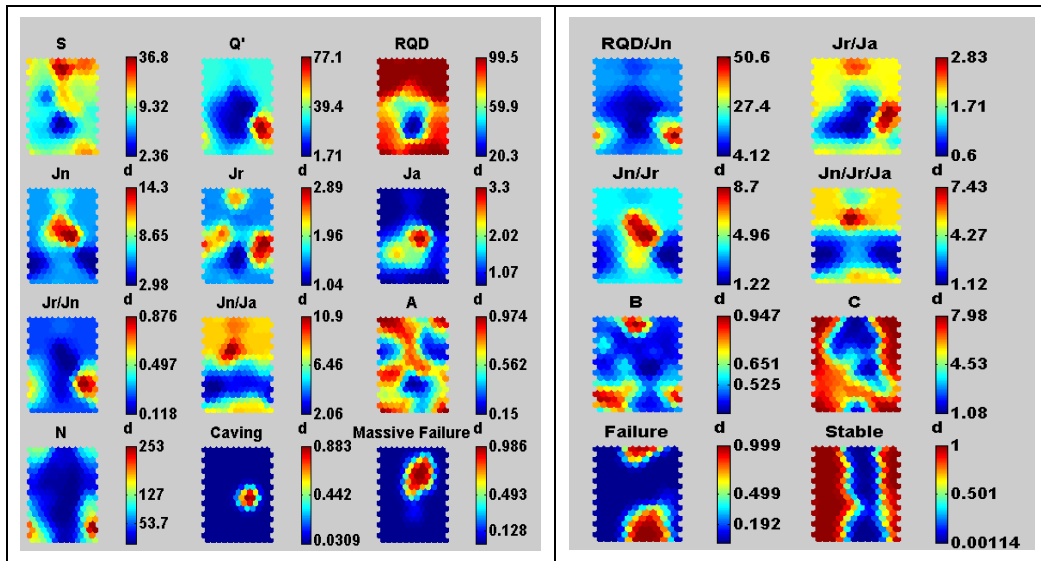


Figure 14. This ‘graphical matrix’ scheme developed by Dr Fraser of CSIRO, was shown to the writer during a two-days rock engineering course given in Melbourne in 2005. The subject matter is stoping for mineral extraction, and stable, caving, failure, and massive failure are the operative terms. The relative influence of various separate and combined Q-parameters are taken from the Potvin scheme of utilizing $Q' = RQD/J_n \times J_r/J_a$ in mine-stope dimensioning. ‘Caving’ is seen bottom-left. J_n and J_a alone, and J_n/J_r are seen to be important. They are absent in continuum modelling schemes.

5 INPUT DATA NEEDS FOR DISCONTINUUM MODELS ARE MORE THAN GSI

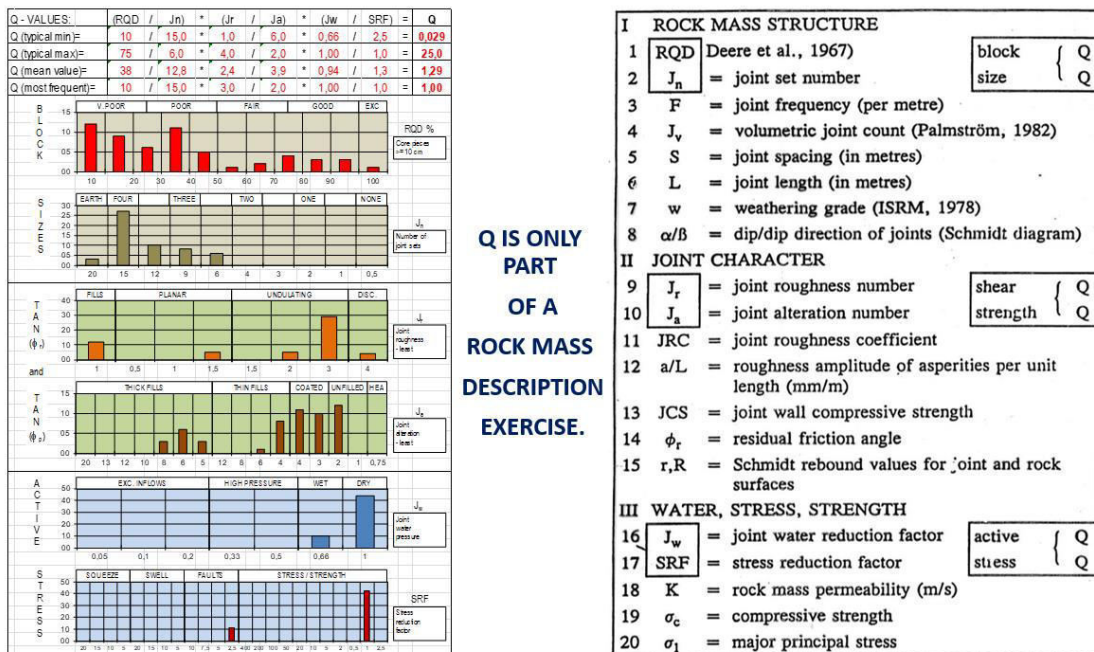


Figure 15. The six Q-parameters (seen as histograms on the left) that are used in characterizing rock masses and tunnelling conditions more fully are obviously just part of the comprehensive data needed for a thorough engineering geological description. Serious consultants do not / should not put a ‘blob’ on a GSI chart and be satisfied that it will give the required input data for their (‘black-box’) modelling.

Three of the most commonly used shear strength criteria for rock joints are illustrated in Figure 16. The classic Mohr-Coulomb involving a cohesion intercept 'c' and a stress-independent friction angle 'φ' was not developed from testing rock joints, which actually do not display actual cohesion intercepts unless very steep (60-90°) steps are present in the joint plane, due for instance to cross-joint influence. An improvement for lower stress was suggested by Patton, 1966 with his well-known 'i-values' where 'φ + i' will be the lower-stress estimate. The problem of course is which combination of 'i-values' one should use. This was the impetus for a new student in 1966, and the resulting parameters described below took some years to materialize.

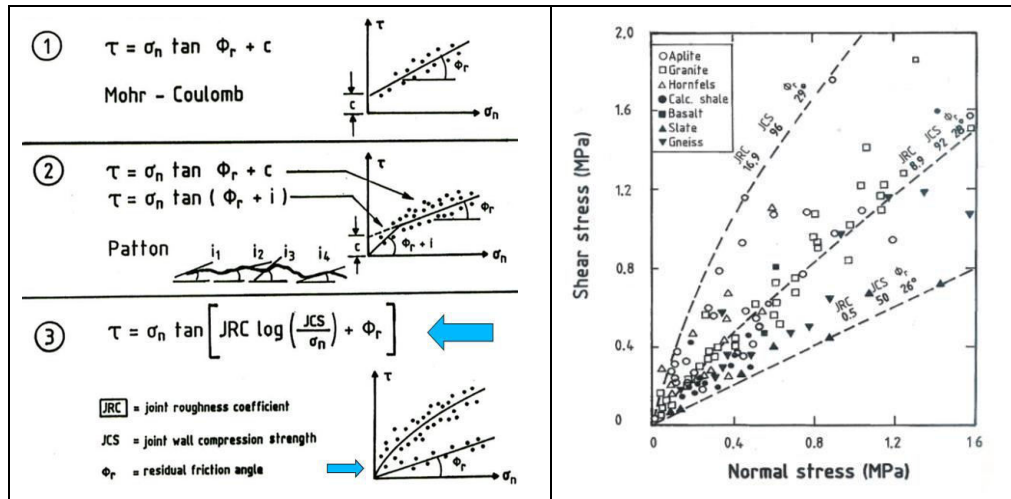


Figure 16. Mohr-Coulomb, Patton (1966) and Barton (1973) shear strength criteria for rock joints. The first version of the JRC, JCS, φ_r criterion (in 1967) was developed from DST tests on 200 tension fractures. One is shown in Figure 2: with respective values of 20, UCS (since no weathering) and 30°.

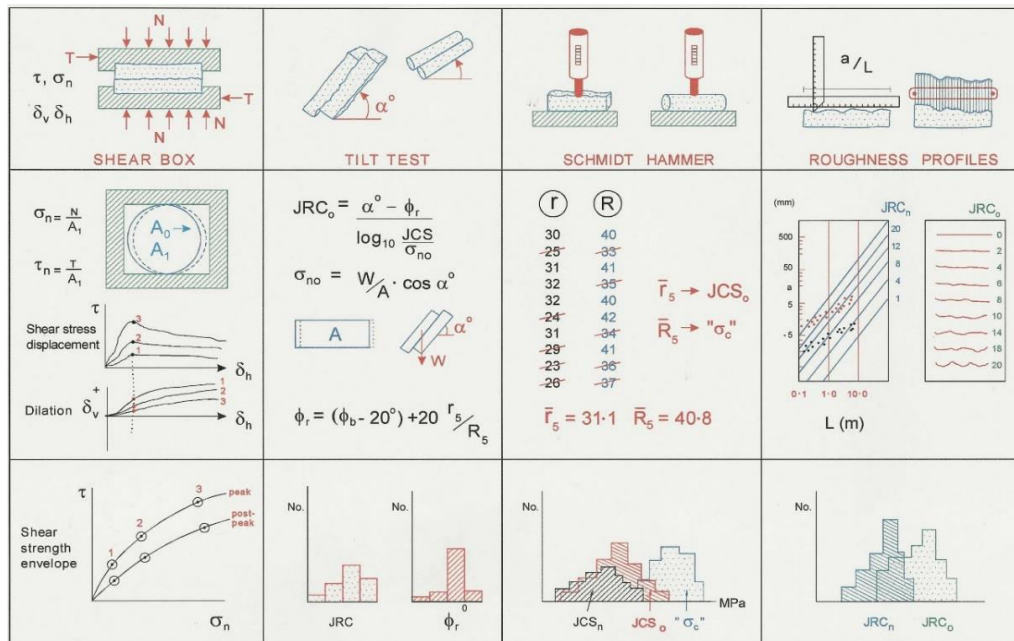


Figure 17. Shear box, tilt test, Schmidt hammer and roughness profiling methods (including a/L) used for evaluating the JRC, JCS and φ_r data for UDEC-BB and other discontinuum modelling projects.

In the case of NGI's Sellafield project for UK Nirex (1990-1996) some 10 kilometers of core were logged and numerous joint samples representing each joint set were prepared. Besides tunnel models (Figure 8) a large number of deep cavern models in welded tuff (ignimbrite) were also performed using UDEC-BB to check on self-supporting abilities and EDZ depths. Note that multi-stage shear testing of the same joint sample at increasing normal stress causes rotation of the shear strength envelope. (Barton, 2013). This gives artificial 'life support' for 'c' and also gives reduced ' ϕ '. (Increased open pit costs if 'c' is ignored and set to 'zero' with ' ϕ ' too low).

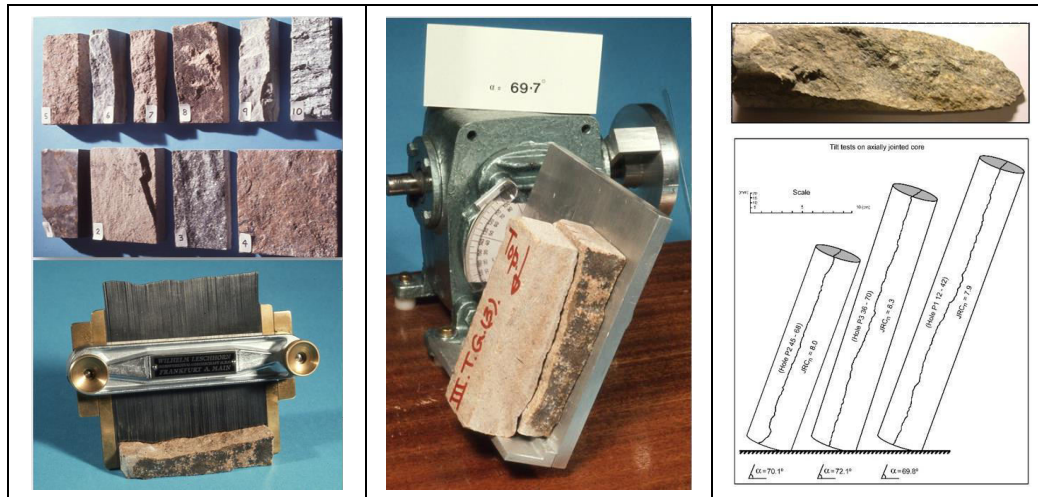


Figure 18. Left: examples of joint profiling and tilt tests. From Barton and Choubey (1977). Note that the profile gage had four 'shims' per millimeter. There were no steps as some critics have assumed. Right: tilt-tested joint samples (at correct angles) from TerraTek's heated block test in Colorado. Barton, 1982.

6 WHEN CONTINUUM MODELLING CAN BE THE ONLY CHOICE

A suggested scheme for choosing *which type* of computer modelling is appropriate for *which type* of rock mass, is shown in Figure 19. In the earlier examples of UDEC-BB given in this paper, we were well within the suggested Q-range of 0.1 (very poor) to 100 (very good). It was possible for engineering geologists (in the case of the UK Nirex project it was often Fredrik Løset) to suggest a realistic and representative joint pattern, which was digitized so that it could be reproduced as perhaps one of several UDEC model geometries. One can 'move models around' in a big jointing 'template' and include faults in some models.

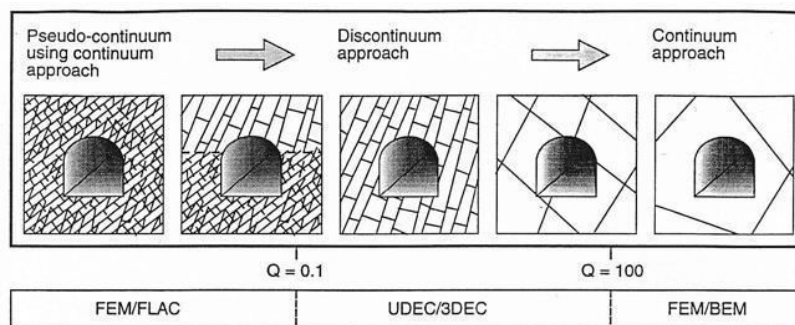


Figure 19. A scheme for helping in the selection of appropriate computer models, based on a 'degree-of-fracturing' scheme with suggested Q-value scale for UDEC and 3DEC. Continuum at either end implied.

If the rock mass is highly fractured as symbolized in the left side of Figure 19, then a continuum approach may be needed. Logic would suggest that Q is stretched to 0.01 or worse to the left side, and to an almost unjointed $Q = 500$ to 1000 on the right side. However, care is needed in assuming that GSI and Hoek-Brown equations of assumed rock mass behaviour will give relevant results. There is unfortunately evidence of grossly exaggerated ‘plastic zone’ prediction, as revealed in an international court case some years ago. This can hardly be due to the commercial FEM method used at that time though it might be partly due to *adding* the strength components related with ‘ c ’ and ‘ φ ’. ($c + \sigma_n \tan \varphi$).

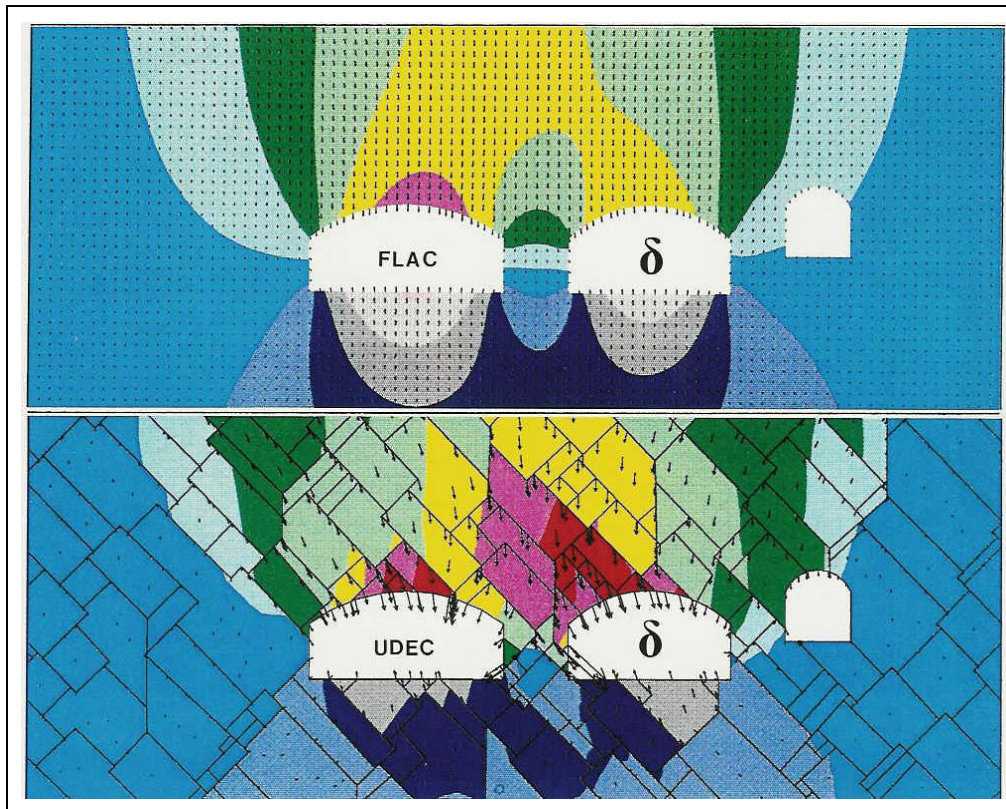


Figure 20. Comparison of FLAC and UDEC-BB by a former NGI colleague Lise Backer (now BaneNor). The same triple-tunnel motorway is modelled using the same boundary stresses and the same intact-block moduli. The jointing makes the UDEC-BB model significantly more relevant than the continuum model. Anisotropy and pillar distress is also seen.

In Figure 20 a continuum model using FLAC is compared with a UDEC-BB model. In this particular case low Q -values are not being modelled, so the deformation is small in both cases, but the UDEC-BB model teaches us much more than the continuum FLAC model.

In the next figure we see something that was a great surprise to the present author when first seen in an SKB document with Prof Derek Martin as lead author. The date was 2002 or 2003. Figure 21 shows part of the PhD study by an Iranian author: Dr. HajiabdoImajid. In his 2000 publication he is supported by his presumed internal and external supervisors Prof Derek Martin and Dr Peter Kaiser, both well known specialists in rock engineering and mining engineering. The results they present, reproduced in Figures 21 and 22 were very important, but a huge majority of people working in rock mechanics have ignored the message and continue with GSI, Hoek-Brown equations and FEM continuum software with ‘ $c + \sigma_n \tan \varphi$ ’.

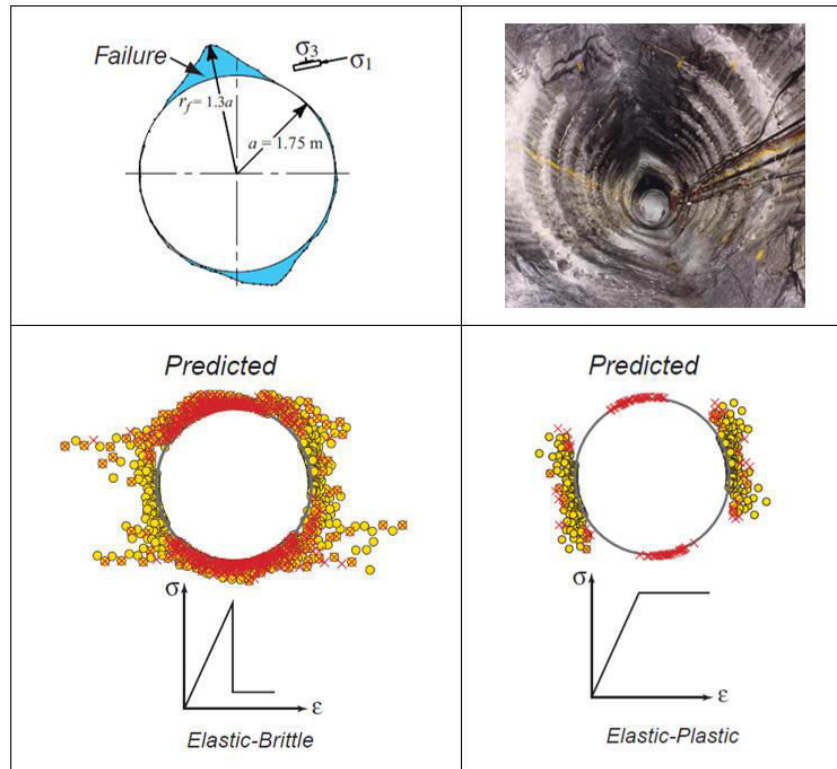


Figure 21. Mohr-Coulomb tri- and bi-linear elastic-brittle and elastic-plastic models of the well-known URL (Manitoba) line-drilled mine-by tunnel. Magnitudes of the input parameters came from GSI and H-B estimation. The objective of the modelling was to show the great improvement that results if the cohesion is degraded while friction is mobilized, shown in Figure 22. The Mohr-Coulomb results are surprisingly unrealistic, yet the criterion is so widely used. It is remarkable that so much incorrect modelling is performed. The three authors are listed here Hajiabdolmajid, Martin and Kaiser (2000).

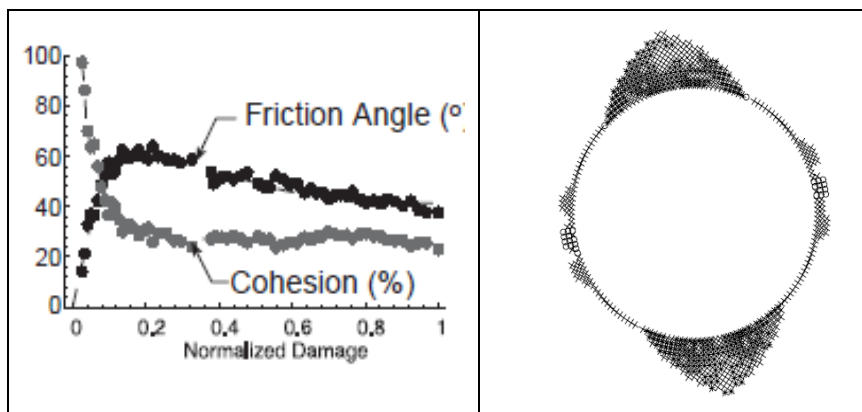


Figure 22. A greatly improved result using a CWFH (cohesion weakening friction hardening) approach. Hajiabdolmajid et al. (2000). The over-stressed volumes do not fall out as the analysis is still a continuum solution, but the reality of location is convincing. The author and a colleague (Barton and Pandey, 2011) also used this CWFH approach in mine stope modelling using Q-based input data CC and FC (see Barton, 2002) in FLAC3D models of pre-instrumented stope areas.

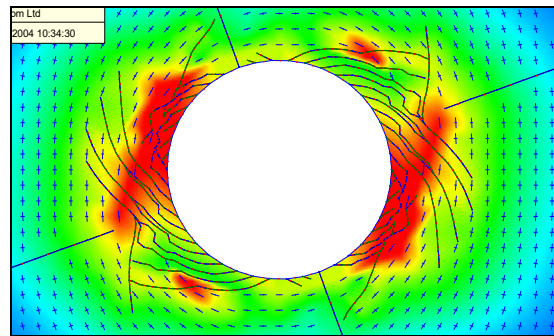


Figure 23. The BEM fracture mechanics code FRACOD developed by Shen et al. (2013). This shows a realistic development of log-spiral failure surfaces when jointing is sparse (the right-hand side of Figure 19). Red represents low, and green represents high factor of safety against further fracturing. In situ stress levels were > 40% of UCS. These were scoping studies for the sub-Andean Olmos tunnel where there were rock-burst challenges, since a ‘stress-raising’ TBM had to be used in the new contract. Shen 2004.

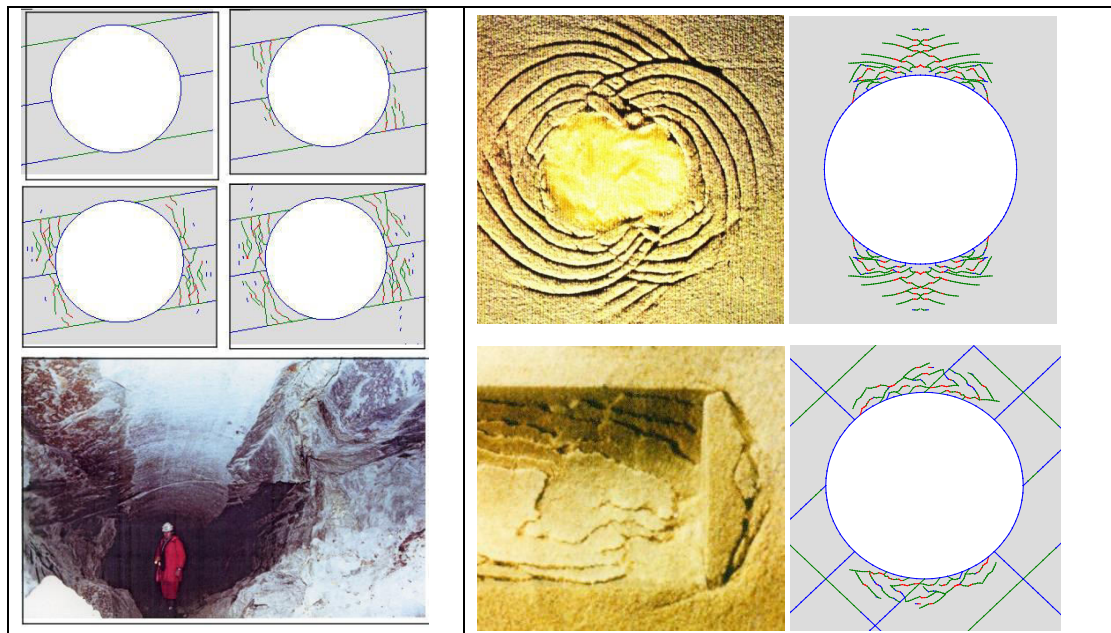


Figure 24. Left: FRACOD BEM fracture mechanics model of failure in a TBM tunnel (the English/Old Beaumont tunnel). Centre: physical model of a bored tunnel (or well) in a 3D loaded block showing intersecting log-spiral shear surfaces due to inclined boring. Right: FRACOD models of 1,000m deep TBM tunnel in massive or jointed rock. Shen and Barton, 2018. This ‘starting as a continuum’ model (FRACOD) is of course in an elevated category in relation to the usual ‘continuously’ continuum models.

7 A CRITIQUE OF GSI, HOEK-BROWN EQUATIONS, AND THEREFORE CONTINUUM ANALYSES THAT DEPEND ON THEM

In the opinion of the author it is rather remarkable and somewhat discouraging for the past and future of our subject ‘rock engineering’, that so many young (and not so young) people have adopted the RocScience-promoted and of course Hoek-promoted GSI, with the associated Hoek-Brown equations. The following three pages (by others) came as a shock to this author.

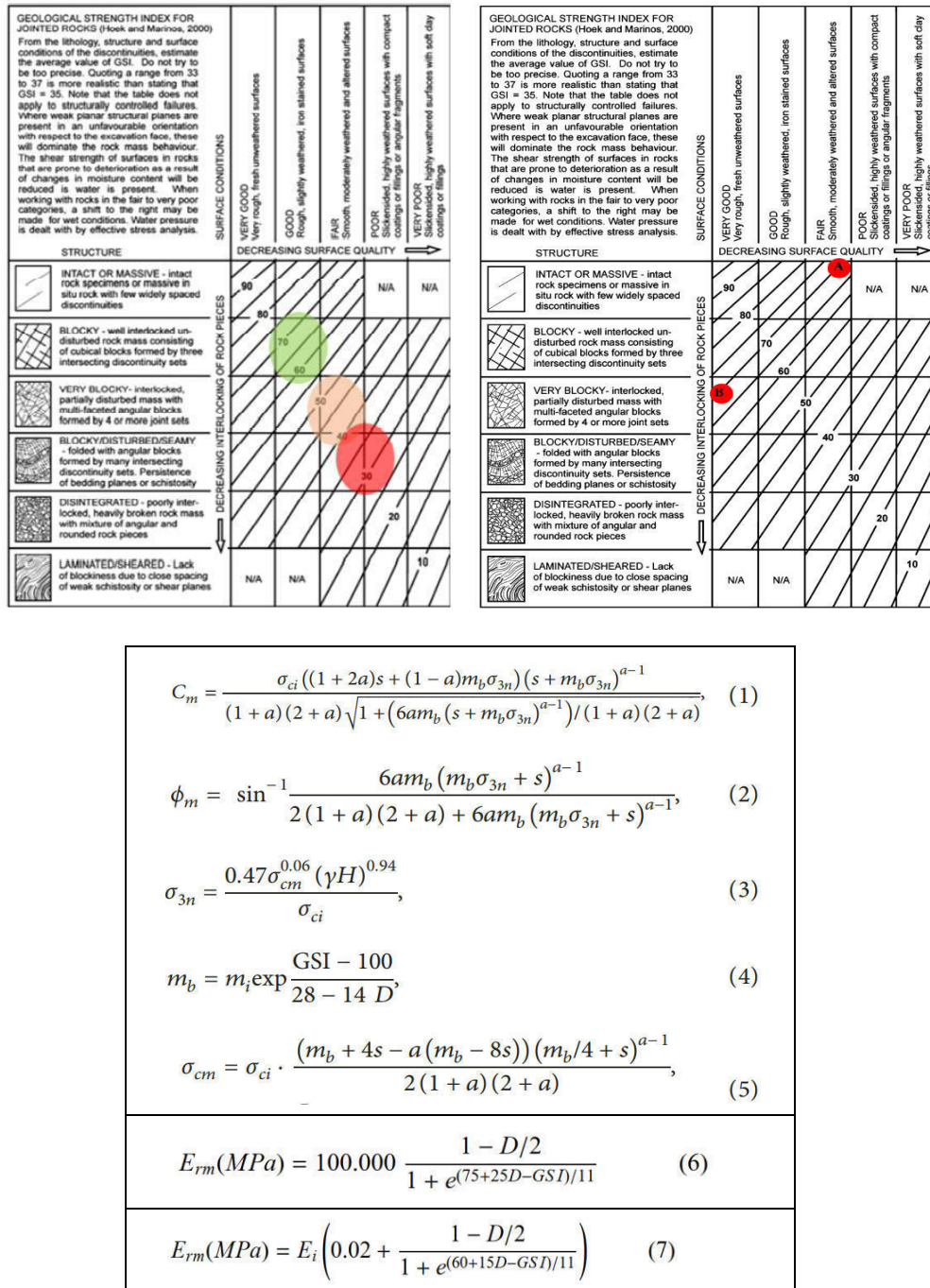


Figure 25. The GSI-rating selection scheme based on a brief encounter with ‘geology’ (the sketches) is followed by what could truly be called black-box modelling. Where does the number of joint sets actually appear? Why does slickensiding have to be ‘highly weathered? Why cannot rougher joints have clay filling and be weathered? GSI is actually the least logical and least ‘geological’ method in use in rock engineering, and the sequence of Hoek-Brown equations are much more a priori than a posteriori (Barton, 2011). Yet one researcher recently expressed the opinion that finally one has a ‘geological’ classification method. The reality is that any chance of ‘geology’ is immediately smoothed in a ‘continuum blender’ giving different viscosities i.e. shear strength. The result is not a geological representation of rock masses. (Hoek et al. 2002, Renani & Cai, 2021).

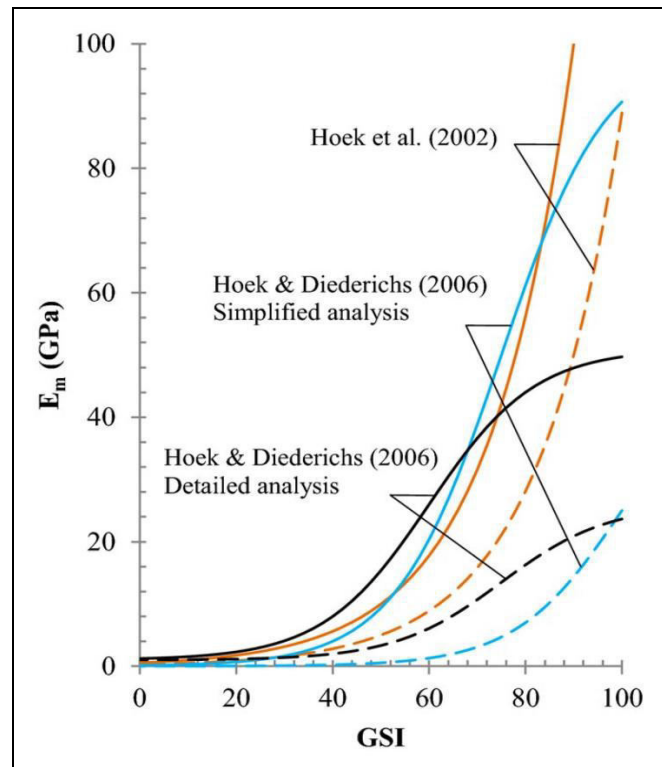


Figure 26. The widely varying deformation modulus estimates connected with GSI. From: Renani & Cai (2021): Forty-Year Review of the Hoek–Brown Failure Criterion for Jointed Rock Masses. One may seriously ask how continuum modellers are choosing deformation modulus. Perhaps by waiting for the results of the modelling and adjusting the disturbance factor *D*? Several private communications have stated such, and if this is so it seems hardly defensible for presenting to a client.

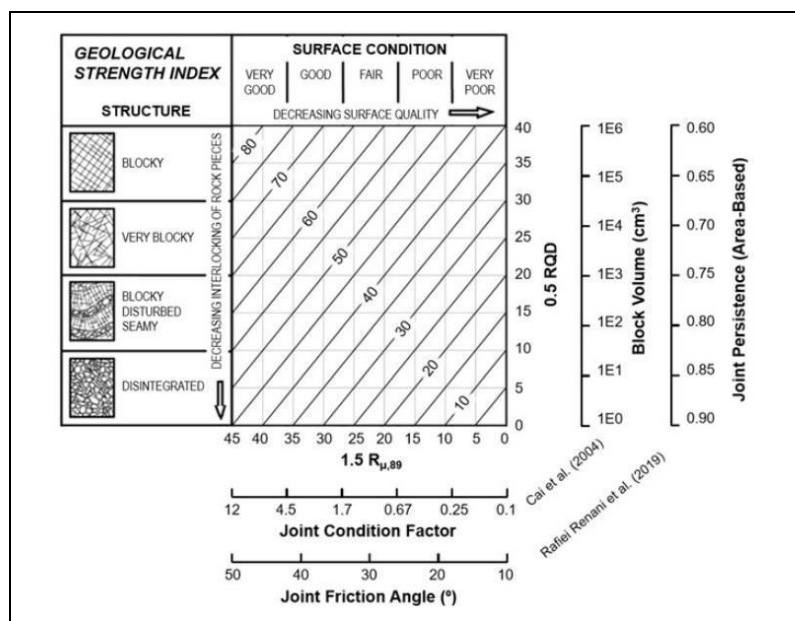


Figure 27. Surprisingly creative additions for ‘better’ quantifying GSI. Renani and Cai, 2021. The better-known methods are listed in Table 1. It is a somewhat surprising list. With all the proposed improvements what happens to the predicted H-B shear strength results? Is this a form of empiricism or just guessing?

Table 1. A selection of some equations used to improve the quantification of GSI. Why a published and widely used method should require so much improvement, or indeed be used by so many with such apparent confidence, is not clear. Ván & Vásárhelyi (2014).

$GSI_1 = RMR - 5 = R1+R2+R3+R4+R5(=15) - 5$	(1)
$GSI_2 = 1.5 R4 + 0.5 RQD$	(2)
$GSI_3 = 15 \log \left(\frac{RQD}{J_n} \frac{J_r}{J_a} \right) + 50$	(3)
$GSI_4 = 9 \ln \left(\frac{RQD}{J_n} \frac{J_r}{J_a} \right) + 44$	(4)
$GSI_5 = \frac{52J_r/J_a}{(1 + J_r/J_a)} + 0,5RQD$	(5)
$GSI_6 = \frac{26,5 + 8,79 \ln J_c + 0,9 \ln V_b}{1 + 0,0151 \ln J_c - 0,0253 \ln V_b}$	(6)
$GSI_7 = 153 - \frac{165}{\left[1 + \left(\frac{J_p}{0,19} \right)^{0,44} \right]}$	(7)

8 EXAMPLES OF ROCK SLOPES: REAL, DISCONTINUUM, CONTINUUM

With the exception of highly trafficked road-cuttings and railway-cuttings, and steep urban slopes above busy pavements, there will generally not be much enthusiasm for bolting or cable anchors for ensuring rock slope stability in general. This is because there are millions and millions of rock cuttings and they cover a huge area all around the world. Of course, this support reluctance will not apply to some critical high-dam valley slopes as especially seen in deep and already naturally over-steepened valleys in China,

Temporary and more permanent open-pit mine slopes suffer the same no-bolting fate for obvious economic reasons. Since there may be no rock bolts, the alternative selection of *stable slope angles* will usually have to depend on the shear strength properties of the local rock joints, and especially joint orientations. This is the philosophy behind Q_{slope} . The first client wanted a 20km dam access road in a steep valley without bolts. (Barton and Bar, 2015). Some five hundred design-chart case records mostly collected by Bar are shown later. (Bar and Barton, 2017).

Of more concern in this final section is the misinformation promoted by commercial software companies, who hold courses showing the popular but hardly existing curved ('spoon-shaped') potential failure surfaces that are relevant for soil slopes and rockfill, *but not for slopes in jointed rock* unless this is extremely weak. (In fact, in about 1968 the author had sketched a curved failure surface for completely disintegrated slates in an open pit, but such weakness is the exception as most of our civil and mining slopes are in jointed rock with enough strength to cause deformation along discontinuities as opposed to ignoring their existence.) It seems that the assumed 'rock mechanics' modelling performed by hundreds or perhaps thousands of young engineers has actually been based on old-fashioned soil mechanics continuum principles, and such is regrettably the case when adding c and $\sigma_n \tan \phi$ as in misleading Mohr-Coulomb and Hoek-Brown methods. Figure 28 shows some alternatives that address discontinuities, whether joints or filled discontinuities or fault planes., from Hoek and Bray (1974) and Barton (1971).

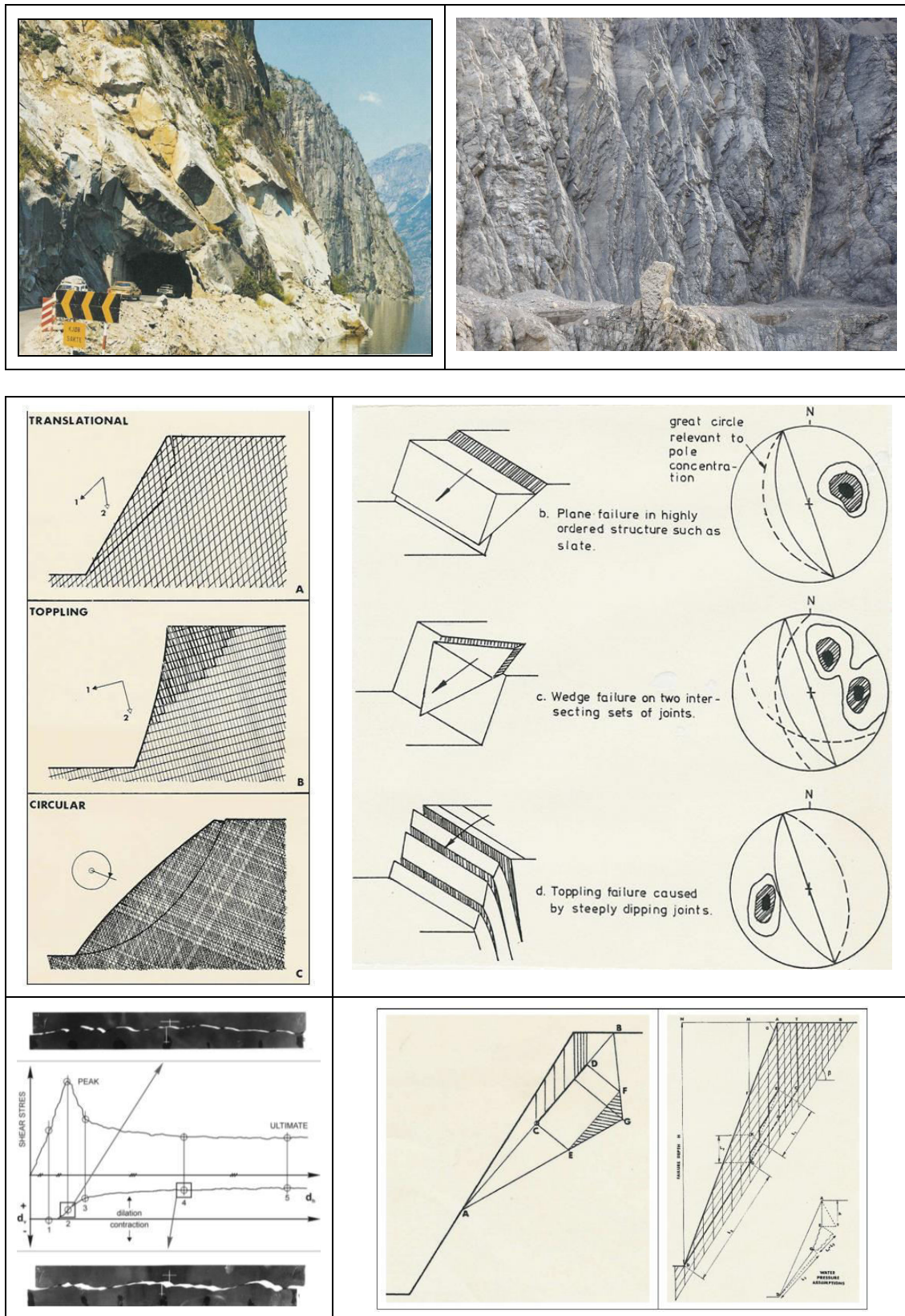


Figure 28. Reality and representation – as discontinua. Central right diagram: Hoek and Bray.

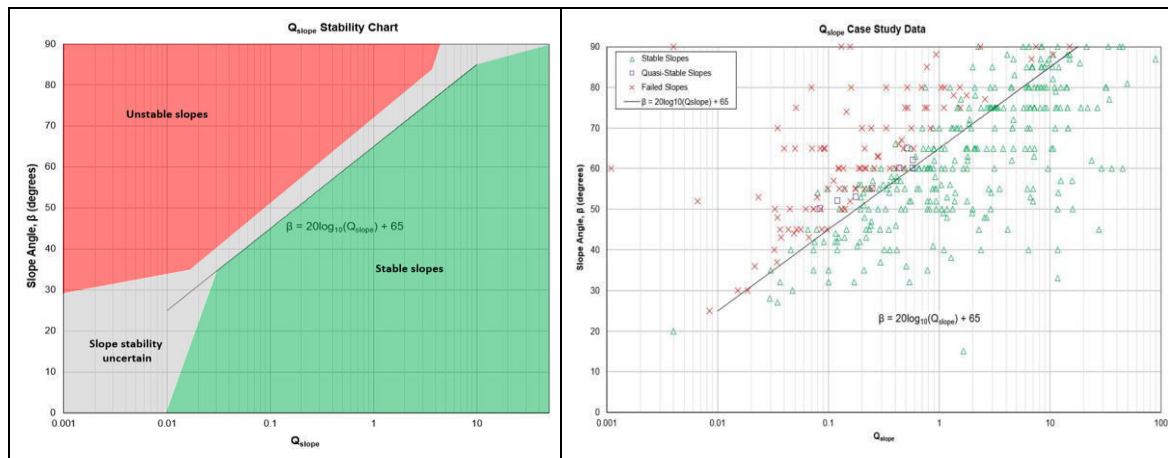


Figure 29. The Q_{slope} method is based on Q parameters with almost unchanged RQD, J_n , J_r and J_a . However wedge stability is considered so pairs of J_r/J_a apply to different sides of potential wedges, with relevant orientation weightings. Since slopes are under lower stress than many tunnels, SRF has three appropriate categories, and J_w is now called J_{wice} . The relative effects of tropical rain and ice-wedging can be roughly assessed. Co-author Neil Bar has been a very active collector of case records. Barton & Bar (2015), Bar & Barton (2017). Q_{slope} : 0.01, 0.1, 1, 10, 100. Critical slopes: 25°, 45°, 65°, 85°, ‘half tunnels’ meaning over-hang is possible. Not advised but likely to be possible due to cohesive strength.

Returning to continuum models, according to Styles & Vakili (2020), the recently developed *Improved Unified Constitutive Model* (IUCM) ‘takes the best parts of Mohr-Coulomb and Hoek-Brown, with integrated confinement-controlled softening/hardening of cohesion and friction, confinement-controlled changes in the dilation angle, and porosity-controlled modulus softening’. However, the slope failure predictions shown in Figure 30 represent something usually only seen in rockfill or hard soil. The ‘spoon’ mode shown apparently has a limited actual relation to geology or jointed/faulted rock. Open pit slopes fortunately seldom if ever fail like this.

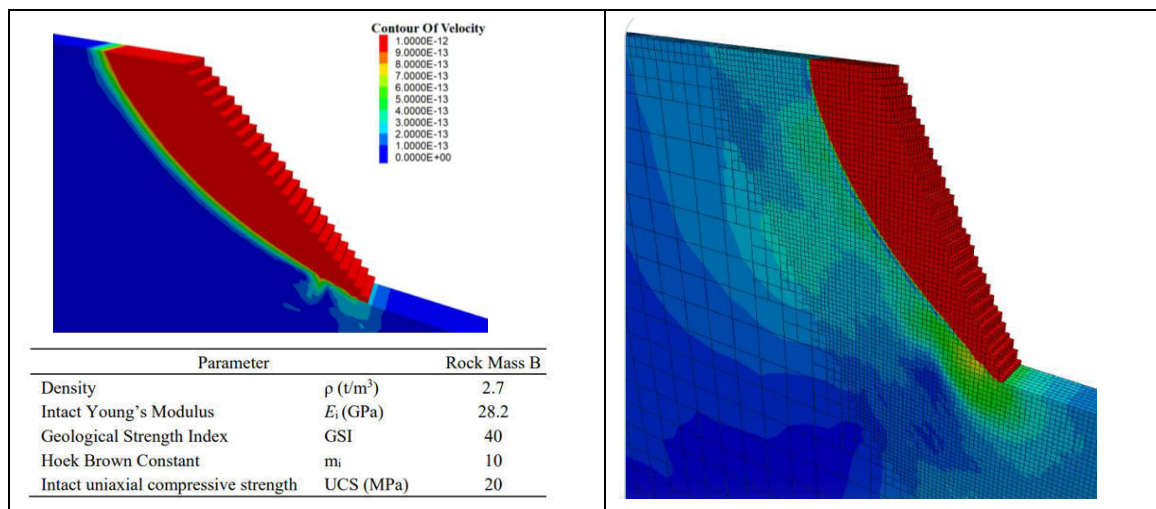


Figure 30. 3DEC slice of a 200m high open-pit slope, using the IUCM constitutive model. Such spoon-shaped failure is possible in rockfill and in hard soil, but the writer does not believe it has been seen in competent jointed and sometimes faulted rock. Perhaps with this relatively low UCS = 20MPa input, such an unusual (for rock) failure mode is possible. Styles & Vakili (2020).

The circular failure beliefs of Mohr-Coulomb and Hoek-Brown modelers, with Carranza-Torres (2021) a presumed chief contributor and probably largely responsible for the smooth curves of the H-B rockmass criterion of Hoek et al. (2002) and the associated most complex equations, has given a very detailed recent treatise concerning ‘rock slope’ stability. Figure 31 is his clear but apparently misleading introduction, as it does not and cannot correspond to slope failure in competent, jointed, and perhaps faulted rock because the UCS and actual cohesion are too high in relation to the artificial ‘lowering’ in the H-B shear strength beliefs.

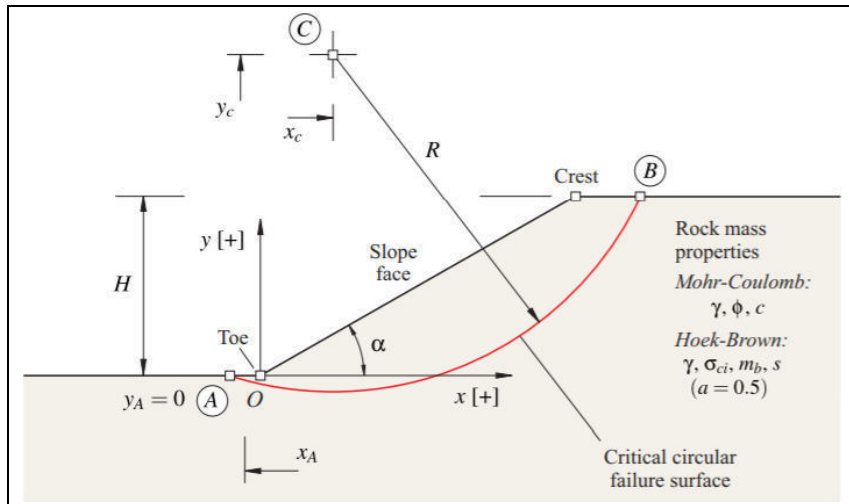


Figure 31 According to Carranza-Torres, 2021 this figure represents ‘a section of a rock slope in a rock mass that obeys the Mohr-Coulomb or Hoek-Brown failure criteria’. Slopes in competent jointed rock cannot actually fail as in this figure. A continuum myth is presented, only valid for very weak saprolite or soil-like material.

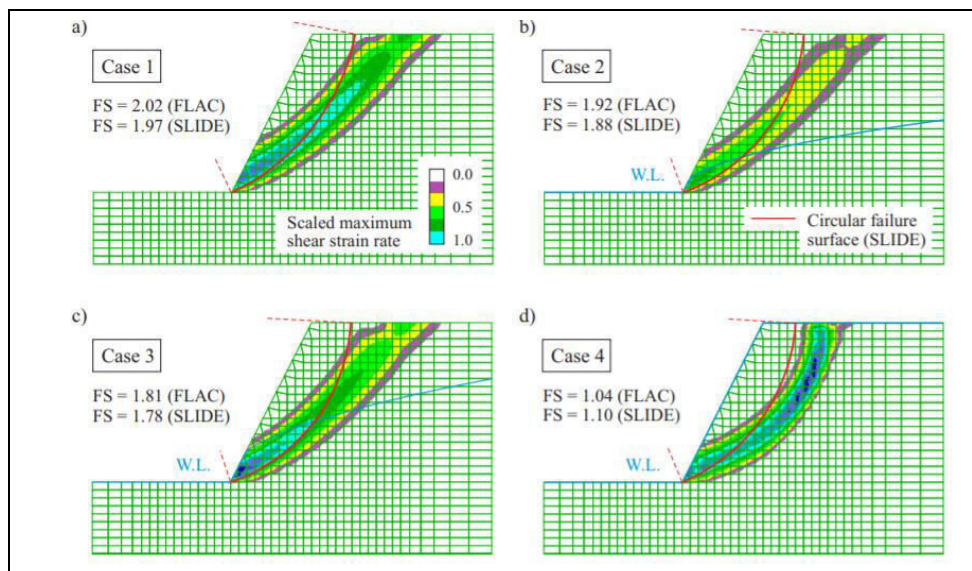


Figure 32. Further ‘circular’ failure analyses using both FLAC and SLIDE computer modelling, apparently with input of c and ϕ derived from combined GSI and Hoek-Brown. Carranza-Torres (2021). These are basically resembling failure in hard soil, perhaps also very weak rock like saprolite, and rockfill.

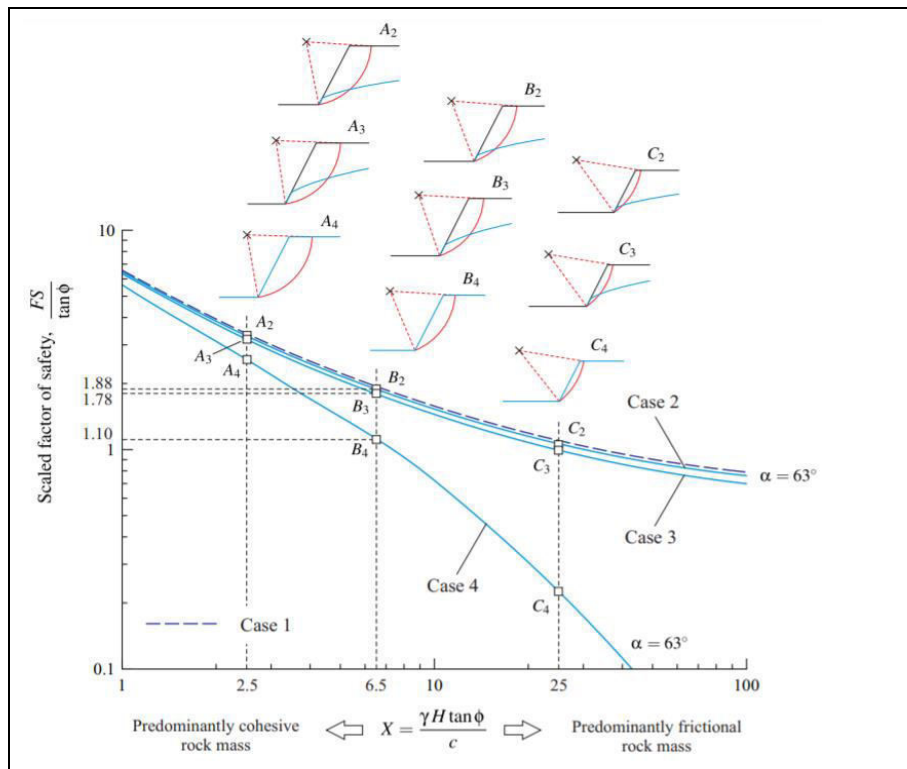


Figure 33 The ‘elegance’ of the relative ‘c’ or ‘φ’ dominance given by Carranza-Torres (2021) in his many impressive ‘design charts’ cannot be denied. The relative depths of the various spoon-shaped predicted failures are interesting. But they do not apply to competent jointed rock. Joints sets, intact bridges, and possible faults are each going to bring back reality.



Figure 34. Four major open-pit failures reproduced by Carranza-Torres (2021).

The four major open-pit failures shown in Figure 34 were reproduced again by the present author, but for different reasons compared to Carranza-Torres. Cases a) and b) are strictly ‘internal’ failures that hardly extend to the crest of the slopes. Only case b) looks like jointed rock. Case c) is lake-bed sediments and saprolite, so not jointed rock. Case d) which certainly extends beyond the pit crest is actually an example of a wedge failure (Lorig et al. 2009), as was also the case for the record Bingham Canyon mine failure shown in Figure 35.

Case d) was a major slope failure in northern Chile. Looking closer to the source, Chapter 10 of the invaluable ‘Guidelines for Open Pit Slope Design edited and partly written by John Read and Peter Stacey, we can see reference to the failure as a ‘wedge failure’ example (Lorig, Stacey and Read, Chapter 10: their Figure 10.12 caption reads: ‘Wedge failure disrupting the entire slope’. So it is not an example of ‘circular’ (or ‘spoon-shaped’) failure. An even larger (and world-record) failure involving a major planar discontinuity is shown in Figure 35.

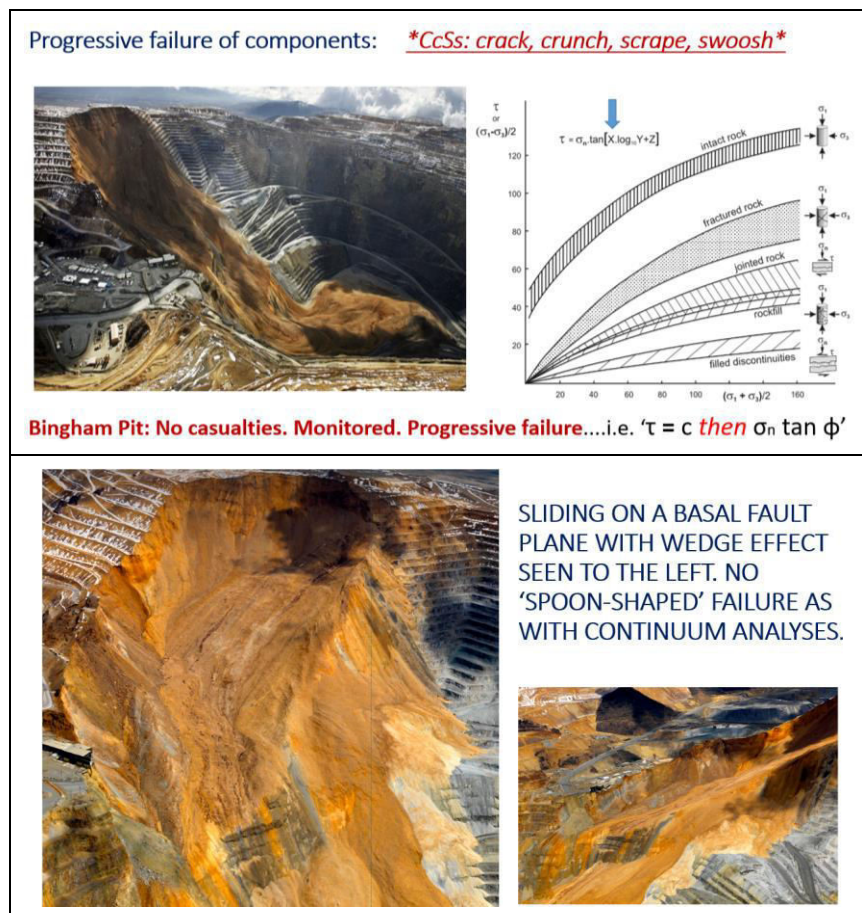


Figure 35 Bingham Canyon mine with its 70,000,000 m³ failure. From top-to-toe the slide measured a surprising 3km, and the debris looks like a frozen ‘liquid’. The adverse (tangential stress eliminating) ‘nose’ and a major discontinuity (a fault?) of many 100’s of meters length seem to be the main culprits.

9 CONCLUSIONS

1. In this lecture the writer has suggested ‘putting back jointing and geology’ into the practice of rock mechanics modelling and understanding. Following the limitations but useful lessons from physical fracture models, a number of UDEC-BB models were re-

- produced to emphasize the possibility of representing some details of ‘geology and structure’ at least in 2D and occasionally in the more demanding 3DEC.
2. GSI with the ‘G’ in its initials has actually removed the geology from our subject, once users leave the six ‘sketches’ and progress to the Hoek-Brown equations and commercial software with the impressive but misleading curves of shear strength. Regrettably the uniquely opaque ‘black-box’ analyses effectively become homogenized as in a food blender, but with variable viscosities. Continuum behaviour is clearly misleading many and, in the opinion of this author, is hardly to be considered as rock engineering or rock mechanics since missing engineering geology input. Looking at sketches and guessing a representative ‘joint condition’ (and modulus) is not defensible.
 3. We have been warned for more than 5 decades – historians in our subject would claim even longer – that we should not add ‘c’ and the frictional component of strength based on ‘ ϕ ’ ($\sigma_n \tan \phi$). At the very least it should be ‘*c then sigma n tan phi*’. This separation in time and deformation is logical and urgently needed.
 4. A newer proposal for a more comprehensive (progressive) failure criterion is the CcSs ‘*crack*’ ‘*crunch*’ ‘*scrape*’ ‘*swoosh*’ concept applied in Barton (2021). This has the ability to add the progressive contributions of the broken cohesion of rock bridges, the resulting rough, fresh fracture surfaces, the joints (if one or more sets are suitably oriented), and finally the lower resistance of faults or clay-filled discontinuities.

10 REFERENCES

- Bandis, S. C., Lumsden, A. & Barton, N. 1981. Experimental studies of scale effects on the shear behaviour of rock joints. *Int. J. of Rock Mech. Min. Sci. and Geomech. Abstr.* 18, 1-21.
- Bandis, S. C., Lumsden, A.C. & Barton, N. 1983. Fundamentals of rock joint deformation. *Int. J. Rock Mech. Min. Sci. and Geomech. Abstr.* Vol. 20: 6: 249-268.
- Bar, N. and N. Barton, 2017. The Q-slope method for rock slope engineering. *Rock Mechanics and Rock Engineering. Springer (2017)* 50: 3307-3322.
- Barton, N. 1971. *A model study of the behaviour of steep excavated rock slopes. Ph.D. Thesis*, Univ. of London.
- Barton, N. 1971. Progressive failure of excavated rock slopes. *13th US Symp. of Rock Mech. Stability of rock slopes, Illinois*, 139-170.
- Barton, N. 1973. Review of a new shear strength criterion for rock joints, *Engineering Geology, Elsevier, Amsterdam*, Vol. 7, 287-332.
- Barton, N. & Hansteen, H. 1979. Very large span openings at shallow depth: Deformation magnitudes from jointed models and F.E. analysis. *4th RETC; Atlanta Georgia*, Vol. 2: 1131-1353. Eds Maeviss and Hustrulid. *Am. Inst. of Min. & Metall., and Petr. Engrs, Inc. New York*.
- Barton, N. 1982. Modelling rock joint behaviour from in situ block tests: Implications for nuclear waste repository design. *Office of Nuclear Waste Isolation, Columbus, OH*, 96 p., ONWI-308, September 1982.
- Barton, N., Bandis, S. & Bakhtar, K. 1985. Strength, deformation and conductivity coupling of rock joints. *Int. J. Rock Mech. & Min. Sci. & Geomech. Abstr.* 22: 3: 121-140.
- Barton, N. 1986. Deformation phenomena in jointed rock. 8th Laurits Bjerrum Memorial Lecture, Oslo. *Geotechnique*, Vol. 36: 2: 147-167.
- Barton, N. 1993. Physical and discrete element models of excavation and failure in jointed rock. Key-note lecture, *ISRM Int. Symp. on Assessment and Prevention of Failure Phenomena in Rock Engineering*, 5-7 April, Istanbul, Turkey.
- Barton, N., By, T.L., Chryssanthakis, P., Tunbridge, L., Kristiansen, J., Løset, F., Bhasin, R.K., Westerdahl, H. & Vik, G. 1994. Predicted and measured performance of the 62m span Norwegian Olympic Ice Hockey Cavern at Gjøvik. *Int. J. Rock Mech, Min. Sci. & Geomech. Abstr.* 31:6: 617-641.

- Barton, N. 1999. General report concerning some 20th Century lessons and 21st Century challenges in applied rock mechanics, safety and control of the environment. *Proc. of 9th ISRM Congress, Paris*, 3: 1659-1679, Balkema, Netherlands.
- Barton, N. 2002. Some new Q-value correlations to assist in site characterization and tunnel design. *Int. J. Rock Mech. & Min. Sci.* Vol. 39/2:185-216.
- Barton, N. 2007. Near-surface gradients of rock quality, deformation modulus, Vp and Qp to 1km depth. *First Break, EAGE*, October, 2007, Vol. 25, 53-60.
- Barton N. 2011. From empiricism, through theory, to problem solving in rock engineering. *ISRM Cong., Beijing. 6th Müller Lecture. Proceedings. Harmonising Rock Engineering and the Environment*, (Qian & Zhou ed), Beijing Taylor & Francis, (1):3-14.
- Barton, N. and S.K. Pandey, 2011. Numerical modelling of two stoping methods in two Indian mines using degradation of c and mobilization of ϕ based on Q-parameters. *Int. J. Rock Mech. & Min. Sci.*, 48,7: 1095-1112.
- Barton, N. 2013. Shear strength criteria for rock, rock joints, rockfill and rock masses: problems and some solutions. *J. of Rock Mech. & Geotech. Engr.*, Wuhan, Elsevier 5(2013) 249-261.
- Barton N and N. Bar. 2015. Introducing the Q-slope method and its intended use within civil and mining engineering projects. In Schubert & Kluckner (ed.), *Future Development of Rock Mechanics; Proc. ISRM symp. Eurock 2015 & 64th Geomechanics Colloquium*, Salzburg: 157-162.
- Barton, N.R. and S.C. Bandis, 2017. Characterization and modelling of the shear strength, stiffness and hydraulic behaviour of rock joints for engineering purposes. *Rock Mechanics and Engineering*, Ed. Xia-Ting Feng, Vol. 1, Principles. Ch. 1, 3-40. Taylor & Francis.
- Barton, N. and Shen, B. 2017. Extension failure mechanisms explain failure initiation in deep tunnels and critical heights of cliff faces and near-vertical mountain walls. *US Rock Mech. Symp. San Francisco*, ARMA17-686, 20p.
- Barton, N. 2021. New ideas about failure modes in rock masses – from tunnels to Prekestolen to El Capitan to Everest. *Bergmekanikkdag*, Oslo. 33.1-33.20.
- Bieniawski Z.T. 1989. *Engineering Rock Mass Classifications: A Complete Manual for Engineers and Geologists in Mining, Civil, and Petroleum Engineering*, New York, Wiley, 272p.
- Carranza-Torres, C. 2021. Computational tools for the analysis of circular failure of rock slopes. Key-note Lecture. In *Proceedings of EUROCK 2021. Mechanics and Rock Engineering from theory to practice*. Turin. Italy.
- Chryssanthakis, P., Monsen, K. & Barton, N. 1991. Tunnelling in jointed rock simulated in a computer. (In Norwegian). *Tunneller og Undergrunnsplanlegg*, 1989-1991, NTNf, Oslo, pp. 23-28.
- Hajjibdolmaji, V., C. D. Martin and P. K. Kaiser, 2000. Modelling brittle failure. *Proc. 4th North American Rock Mechanics Symposium, NARMS 2000* Seattle, J. Girard, M. Liebman, C. Breeds and T. Doe (Eds), 991-998. Balkema.
- Hoek, E. and J. Bray, 1974. *Rock slope engineering*. Institute of Mining.
- Hoek, E, C. Carranza-Torres & B. Corkum, 2002. Hoek-Brown failure criterion – 2002 Edition. *Proc. NARMS-TAC Conference*, Toronto, 2002, 1, 267-273.
- Lorig, L., P. Stacey and J. Read 2009. Slope design methods, *Ch 10 in Guidelines for Open Pit Slope Design*, Eds. Read and Stacey, CSIRO Publishing.
- Martin, C. D. and P. F. Stacey, 2013. Pit slopes in weathered and weak rocks. *Slope Stability 2013*. Brisbane. P. M. Dight (ed), Australian Centre for Geomechanics, Perth, 29p.
- Patton, F. D. 1966. Multiple modes of shear failure in rock. *Proc. 1st Cong. of Int. Soc. Rock Mech. Lisbon*. Vol. 1, 509-513.
- Potvin, Y. 1988. *Empirical open slope design in Canada*, Ph.D. thesis. Univ. of British Columbia, Canada, 350p.
- Renani, H.R. and M. Cai, 2021. Forty-Year Review of the Hoek–Brown Failure Criterion for Jointed Rock Masses. *Rock Mechanics and Rock Engineering* 55(4):1-23.
- Shen, B., O. Stephansson, and M. Rinnie, 2013. *Modelling Rock fracturing Processes – A Fracture Mechanics Approach Using FRACOD*. Springer, 173p.
- Styles, T.D. & A. Vakili, 2020. Slope Angle Versus Slope Height - The Basis of an Empirical Tool for Slope Design Within Fractured Rock Masses using IUCM. *EUROCK 2020*, Trondheim
- Ván, P. and B. Vásárhelyi, 2014. Sensitivity analysis of GSI based mechanical parameters of the rock mass. *Periodica Polytechnica, Civil Engineering*. 58/4 (2014) 379–386.

Progress toward understanding complex rock slope failure mechanisms

D. Stead

Simon Fraser University, Vancouver, B.C., Canada

D. Donati

University of Bologna, Bologna, Italy

ABSTRACT:

With increased application of remote sensing techniques and three-dimensional numerical models the complexity of large landslides and rock slopes has become evident. The morphology of the landslide ground surface can now be investigated in detail even in heavily vegetated slope and used to constrain damage and numerical models. In this paper we show the importance of characterising sliding, lateral and rear release surfaces and realistically importing these surfaces into 3D numerical models. The contribution of brittle fracture of intact rock bridges and step-path lateral and sliding surfaces to rock slope failure mechanisms is illustrated. Past rock slope/landslide models have considered failure growth through retrogression into the slopes, in itself a challenging process to model. We show how it is necessary to consider the growth of landslides both into and along the slope to capture the true progressive three-dimensional slope failure mechanism. We illustrate the importance of considering the detachment surface of rockfalls and the propagation of extensile and shear dominated rockfall mechanisms. The need to consider landform evolution and changing slope kinematics is demonstrated and potential methods discussed. for optimizing the use of rock slope/landslide “bigdata” sets reducing uncertainty

1 INTRODUCTION

1.1 *Background*

Early rock slope engineers performed elegant vector algebra recognizing the complex block shapes involved in rock slope failures and considering both sliding and rotational forces/moments (Londe 1965, 1973, Londe et al 1969 and Wittke 1965). The major impetus in rock slope engineering came from the publication of “Rock Slope Engineering” by Hoek and Bray (1974) and the CANMET Pit Slope manuals (1977). At this time highly practical stereographic techniques were developed to consider the three most simple failure mechanisms (i.e., planar, wedge, and toppling). Limit equilibrium techniques developed rapidly following the Aberfan disaster with the use of block analyses and methods of slices. Small scale bench/multi-bench analyses using planar/wedge and toppling analysis necessitated simplifying assumptions regarding daylighting of failure surfaces, rigid impermeable blocks (no fracture/yield), and, of particular importance to slope kinematics, the presence of lateral and rear release surfaces offering no resistance to movement (Figure 1, Table 1). Although toppling analyses considered 2D-rotational moments, the assumption of simple planar surfaces made limit equilibrium analyses easy to undertake by graphical methods or hand calculators. The methods of slices were adopted from soil mechanics for large scale rock slope failures, but generally assumed simplified 2D sections and plane strain. Although limit equilibrium analyses of wedges using vector algebra allowed the rotation of blocks to be considered, these have not been routinely adopted in current commercial codes. Subsequent development of methods based on columns has allowed three-dimensional limit equilibrium analysis of rock slopes and landslides, but these methods still retain assumptions, such as rigid impermeable blocks with no brittle fracture and shear dominated failure criteria, that may in some cases, limit their applicability

In this paper the authors summarize important research over the last two decades using both remote sensing and numerical modelling observations that have provided considerable insight into the complexity of landslide and rock slope failure mechanisms.

1.2 Rock slope/landslide failure mechanisms.

There has been extensive discussion on landslide failure mechanisms since the early landslide classifications of Varnes (1978) with the latest modification being Hungr et al. (2014). Important work was also published by Glastonbury and Fell (2010) and Varga and Gorbushina (1996). The latter, although never widely recognized, contained insightful recognition of the importance of geology and tectonic structures. The common factor in all these classifications is the consideration of landslides to a large degree as 2D phenomena; this is increasingly problematic given recent research using remote sensing techniques to characterize and monitor landslides.

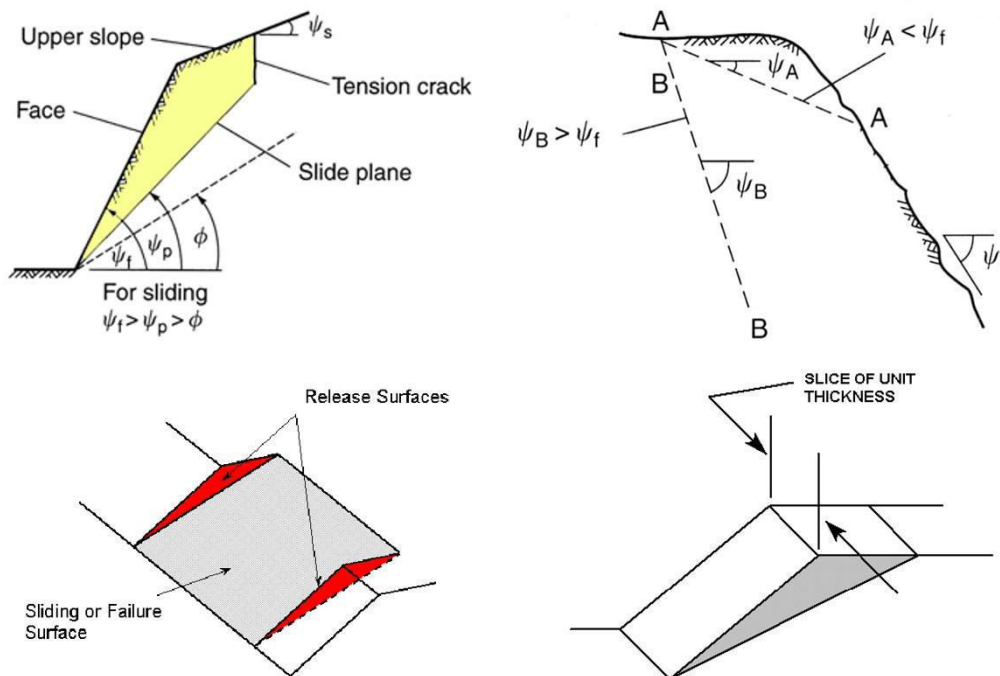


Figure 1. Kinematics of planar rockslides a. Daylighting and sliding criteria, after Wyllie and Mah (2004, 2018), b. Lateral release assumptions, (after Hoek and Bray 1974).

THE ANATOMY OF LANDSLIDES AND ROCK SLOPE FAILURES

1.3 Background

The body of a landslide/rock slope failure can be considered as comprising five main types of surface viz. the ground surface, the sliding or basal surface, the lateral and rear release surfaces and the rockfall detachment (separation) surface.

1.4 The ground surface

Originally the surface of rock slopes and landslides were characterized mainly using field surveys. In areas where rock outcrops and are devoid of vegetation, high quality engineering geology and geomorphology mapping is possible. In areas that are forested and/or difficult to access, terrain mapping can be severely limited. The availability of airborne and ground-based multi-sensor remote sensing techniques has made it possible to map the ground surface morphology in great

detail even in forested terrain. The structures controlling rock slope and landslide stability can be mapped remotely (including through automated mapping methods) with the exception of joint surface characteristics (e.g., compressive strength, alteration, infill) which generally still require field mapping. As a pre-requisite for rock slope/landslide investigations, the authors strongly recommend field mapping wherever possible, in addition to historic air photointerpretation.

Table 1. Assumptions made, and their implications and validity in complex landslide/rock slope analysis

Assumptions	Implications	Validity
Rigid block	Weight acting through centroid, No intact rock fracture or yield	Large landslides/open pit slopes commonly involve both brittle fracture and yield which may change kinematics
Plane/wedge joint intersection daylights	Dip/plunge of intersection < dip of slope	Does not consider basal wedges, active passive failure and non-daylighting wedges
Lateral and rear release surfaces present	No resistance on release surfaces	Often considerable roughness/rock bridges on lateral and rear release surfaces – complex 3D geology mobilizes resistance
Strike of plane	+/- 20 degrees to strike of slope	Can have important implications for kinematic confinement and depth of support installation
Impermeable block	Pore water pressures act on sliding and rear release surfaces	Often highly fractured rock masses requiring more sophisticated groundwater analysis in large/ high risk slopes. Compartmentalization of groundwater tables may be present in faulted terrain.

Important factors, when interpreting the data from ground surface remote sensing include, but are not limited to, slope (dip), aspect (dip direction), deformation (qualitative and quantitative evidence), morphology, surface drainage, seepage, erosional/depositional features, evidence of instability (cracking, lineaments, failure blocks, intact rock fracture), structures and changes in remote sensing imagery texture and colour. Remote sensing of landslides has shown that the surface features such as lineaments, depression, cracks, etc. contain important information on the underlying failure surface mechanism. The remote sensing imagery can also allow recognition of multiple blocks within landslides exhibiting changes in surface morphology/texture and displacement, possibly reflecting changes in the dip/dip direction of the failure surface. The Downie Slide, BC (Canada) is a $1 \times 10^9 \text{ m}^3$ volume post-glacial landslide, which is currently sliding at rates of 3-5 mm/yr Figure 2a shows the heavily vegetated nature of the Downie Slide and is an excellent example of how airborne LiDAR (Figure 2b, 2c) can be used to further our understanding of the 3D complexity of the landslide ground surface morphology (Donati et al. 2020, 2021a; Westin 2017). The central part of the Downie Slide LiDAR shows smooth texture with little evidence of surface deformation corresponding to uniform translational sliding along the sliding surface. Other areas show highly disturbed topography where there is a change in the dip of the sliding surface and an active-passive block deformation. Lineaments on the Downie Slide ground surface trend in varied directions (Figure 2b), reflecting changes in the dip direction (aspect) of the sliding surface and zones of compression and extension. The direction of the recorded slope displacements also reflects 3D changes in the failure surface orientation (Figure 2d). Varied failure mechanisms occur across the Downie Slide, with hummocky ground morphology in the upper slope, associated with secondary slumping failures within damaged rock, contrasting with uniform translational sliding and active passive ground surface morphologies in the central and lower slope.

Figure 2e shows a preliminary interpretation of a structure through the Downie slide resulting in the changes in orientation of the failure surface and post failure retrogression along a possible linear structural damage zone. As a recommended practice, ground surface features such as scarps/lineaments recognized on remote sensing imagery should be investigated using 2D sections to determine the relief and inclination, and then imported into slope analysis models as constraints (if a 2D mechanism is appropriate). However, it is now relatively easy to import the 3D ground surface into limit equilibrium, continuum, discontinuum and hybrid numerical models (Figure 3). Block boundaries and lineaments can often form important constraints for 3D slope modeling. Figure 3a shows the block boundaries interpreted at the Downie Slide and imported into the three-dimensional distinct element code 3DEC, and Figure 3b displays the results of simulation using a strain softening constitutive criterion; close agreement is obtained between the observed surface lineaments in the airborne LiDAR and the damage simulated in the numerical model. Figure 3c shows a current view of the 1965 Hope Slide and Figure 3d a Structure-from-Motion (SfM) photogrammetry model constructed from pre-failure historic air photographs. The old air photographs were used along with recent field mapping and multi-sensor remote sensing to interpret the multi-block three dimensional structures at the slide. Figure 3e shows the results of a 3DEC analysis with the model simulation proceeding from left to right from 65000 to 72000, 77000, and 95000 calculation steps. It is observed, agreeing with earthquake records, that the failure occurred in two stages involving failure of block 4 and block 5, which formed the upper part of the slope. A prehistoric landslide slide was determined to be a keyblock which provided the kinematic release for the eventual 1965 failure. The complex 3D multi-block structure and its control on rock slope failure is clear.

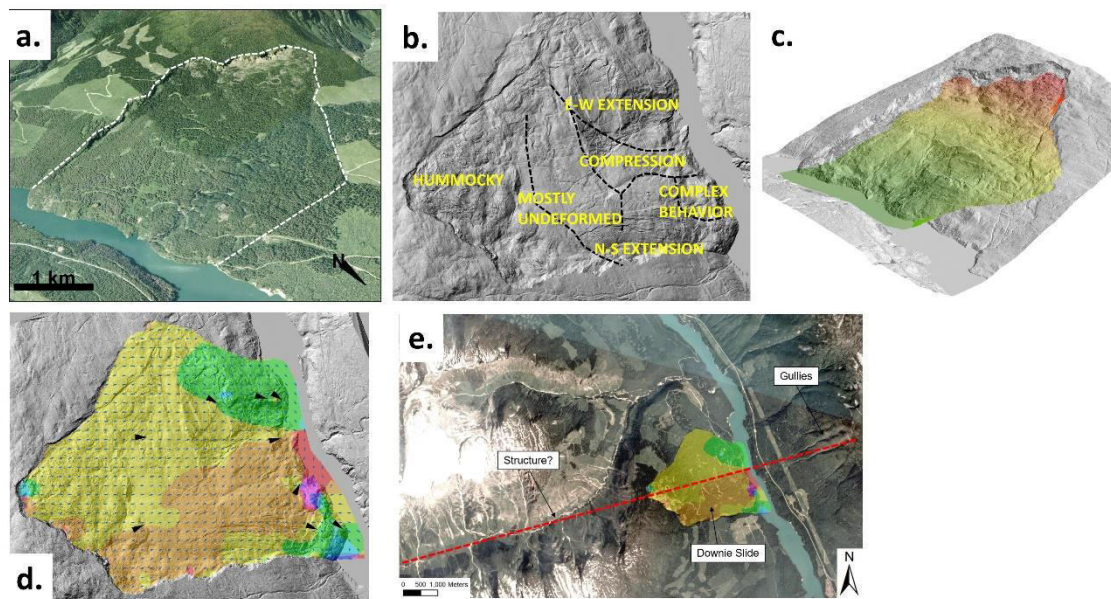


Figure 2. a. Heavily vegetated Downie Slide, British Columbia (Canada), b. Airborne LiDAR imagery showing lineaments and zones of surface damage, c. Shear zone reconstruction overlain on LiDAR, d. Variation in dip direction of failure surface, e. Preliminary interpretation of structural damage zone, showing the alignment between the valley behind the landslide crest, and the intersection of the planes forming the shear zone.

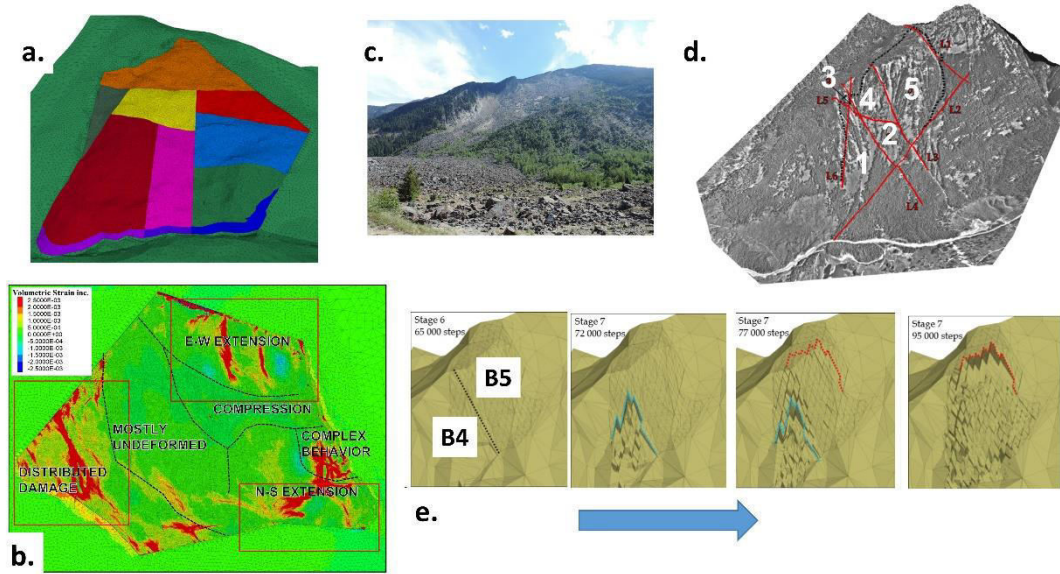


Figure 3. a. Multiblock 3DEC model geometry based on Airborne LiDAR and GIS failure surface reconstruction b. Results of strain softening 3DEC simulation show good agreement between observed ground damage in airborne LiDAR imagery and simulated model damage. c. Photograph of Hope Slide, British Columbia (Canada), d. Multiblock geometry of the Hope Slide based on SfM model from pre-failure air photographs and recent field and remote sensing mapping, e. Results of 3DEC simulation based on remote sensing and field mapping showing two-stage failure involving blocks 4 (B4) and 5 (B5) with initial failure outline in blue and final failure outline in red; blue arrow indicates model simulation from 65000 to 95000 calculation steps.

1.5 The sliding surface

Landslide sliding surfaces may be considered in terms of their genesis, the number of surfaces involved, orientation, planarity or curvilinear nature, roughness/morphology, continuity/connectivity, and shear zone thickness. In landslides in rock the sliding surface is usually sedimentologically or structurally-controlled, ranging from simple bedding plane sliding to failures controlled by complex faulting, folding and metamorphic structures. It is common to recognize instability along single, multiple-planar or folded curved surfaces in 2D, but in reality, the failure may be complex, involving 3D surfaces with varying dip and dip direction potentially leading to segmentation and multi-block failures as shown in Figures 2 and 3. The 3D morphology of the sliding surface may be influenced by undulating metamorphic foliations as at the Downie Slide (Figure 4a), Aknes slide (Norway, Figure 4b) and Fels slide (Alaska, Figure 4c), or complex multi-stage folding and fold interference patterns, as at the Vajont Slide (Italy, Figure 4d).

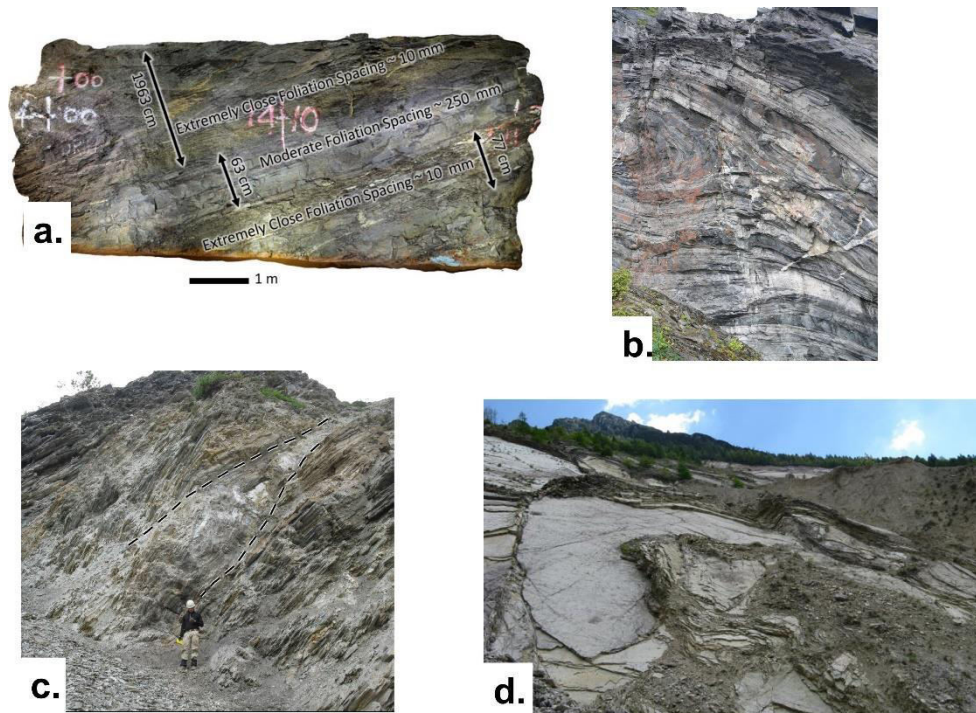


Figure 4. Foliated rock masses influencing the three-dimensional complexity of rock slope failures at a. the Downie Slide, BC. b. Aknes, Norway and c. Fels, Alaska, d. Complex folding, and interference structures observed along the exposed failure surface at the Vajont Slide (Italy).

Whereas small rock slopes may occur within with one structural/geotechnical domain with rock-fall/rock slope failures from single or multiple planes, large open pit slopes and landslides commonly involve multiple domains. Wolter (2014) recognized the distinct variations in failure mechanisms of the two blocks, separated by the Massallezza gully, forming the Vajont Slide whereas Donati (2019) proposed the division of the Downie slide into damage domains. We suggest that landslides, as is common in open mining practice, should be sub-divided into landslide domains that display variations in structure, geotechnical characteristics and failure surface/mechanism and observed displacement magnitudes/direction. This activity was shown to be beneficial in supporting the interpretation of failure mechanism and style of deformation, particularly at sites with limited (or no) availability of subsurface data.

The roughness of a sliding surface may thus be considered at varying scales from the small scale as measured using shear box tests/JRC field charts to large scale morphologic changes. At the small-scale, 3D roughness may be influenced by sedimentological features such as turbidite structures or tectonic structures such as fold/fault slickensides. Movement along a fault may result in meter-scale features which can be along dip, strike or oblique depending on fault block movement. The reader is referred to Stead and Wolter (2015) who provide a detailed discussion on the influence of structural geology on rock slope stability. The persistence or continuity of structures is a critical factor in rock slopes and landslide instability. As suggested by Sturzenegger (2010) the ISRM's "Suggested methods for discontinuity characterization" (1978) is not amenable to the description of extremely persistence structures such as faults and bedding plane which may lead to single sliding surfaces of 10's to 100's m and mountain slope/pit slope scale instability. In practice it is important to consider 3D persistence along both strike and dip. The persistence or continuity of a sliding surface is usually considered only in 2D along the dip direction where it may comprise multiple discontinuities linked together by inclined or orthogonal joints and/or intact rock bridges that require to be fractured to allow displacement. The percentage of rock bridges may be estimated using discrete fracture network (DFN) modelling based on field mapping, but this is an extremely challenging task. In reality, the persistence of discontinuities in 3D must have

an important effect. Jennings (1970) recognized 3D dimensional step-paths and Sturzenegger and Stead (2012) show a range of types of step-paths at varying scales observed at the Palliser landslide in Alberta (Canada, Figure 5). Tuckey and Stead (2016) and Elmo et al. (2018) describe the complexity in characterizing the influence of rock bridges on rock slopes stability.

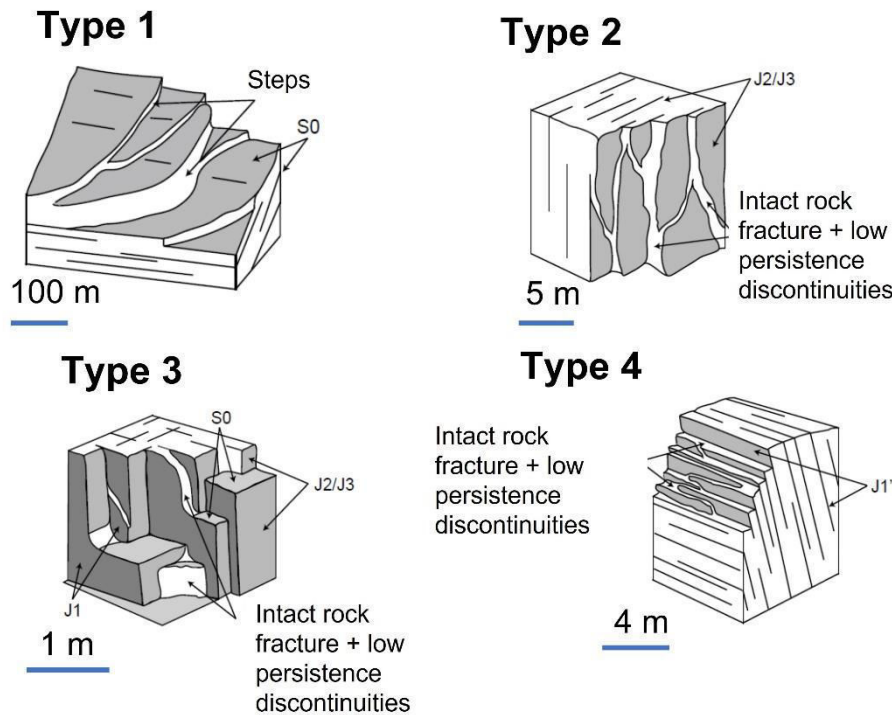


Figure 5. Step-path types recognized at the Palliser Landslide, Alberta (Canada), modified after Sturzenegger and Stead (2012). Note the extreme variation in scale of the step-paths from 1 – 10's m.

An example of a complex undulating step-path surface in a rock slope near Canmore (Alberta) is shown in Figure 6. In rock masses with multiple deformation episodes and complex jointing such as porphyry copper deposits complex, 3D step-paths may develop. The importance of considering connectivity in rock mass instability has been shown by Alghalandis et al. (2014), Elmo et al. (2022) and Karami-Shariff et al (2022). When considering the failure mechanism in landslides and rock slopes it is suggested that 3D connectivity should be investigated, as it may play a crucial role in the slope evolution and the associated hazard.

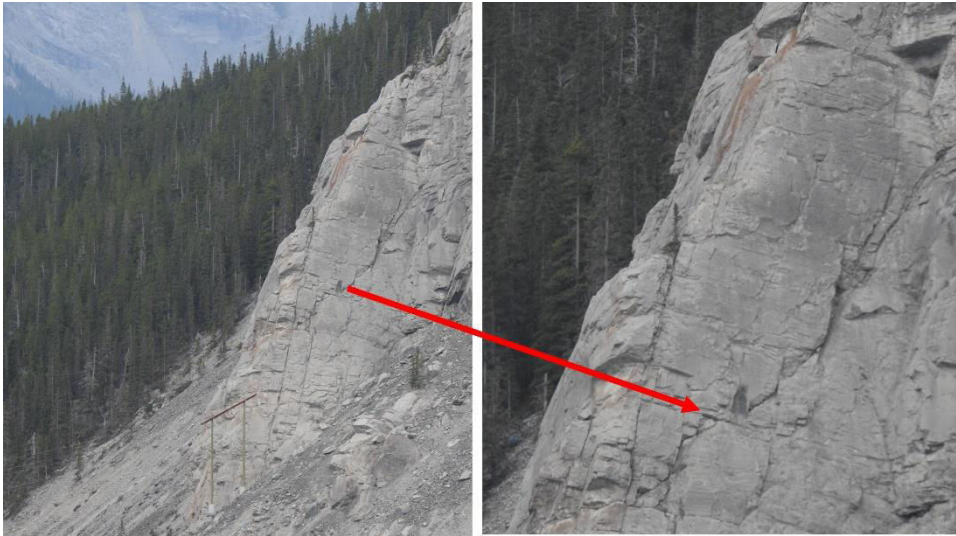


Figure 6. Complex undulating step path formed by a combination of discontinuity sets and intact rock fracture, Canmore, Alberta (Canada).

The greater the connectivity of the fracture network in a slope, the less intact rock (rock bridge) fracture/damage required for a slope failure. Conversely, the lower the rock mass connectivity, the more stable the rock slope should be. It is important, however, to consider connectivity in terms of both adversely oriented discrete structures, as well as the rock mass slope network (i.e., a through-going highly connected fault/fault zone may exist within a massive low-connectivity rock mass). The degree of brittle fracture and damage involved in landslides and rock slope failures has been the subject of considerable research by Havaej (2015) and Donati (2019). Failure along a single through-going sliding surface may involve brittle fracture and failure of along plane (dip and strike) rock bridges as well as failure of small-scale rock asperities that occur along the sliding surface. An active-passive or biplanar failure may involve considerable yield and brittle fracture at the interface between the upper active block and the lower passive block, commonly referred to as transition zone or Prandtl prism (Figure 7a,b). Variations in strike of the transition zone failure may also occur, resulting in an inherently 3D failure mechanism (Figures 7 d,e). Non-daylighting structures may form wedges plunging steeper than the slope surface, which may fail by brittle breakout mechanisms (Figure 7c). Brittle failure may also lead to the development of a “root sliding surface” at the limit of flexure of toppling columns in rock slopes with the potential for sudden global slope translational/rotational failure (Figure 7f). Brittle fracture is also a key component of buckling failures in footwall open pit slope slopes and bedding parallel mountain slopes.

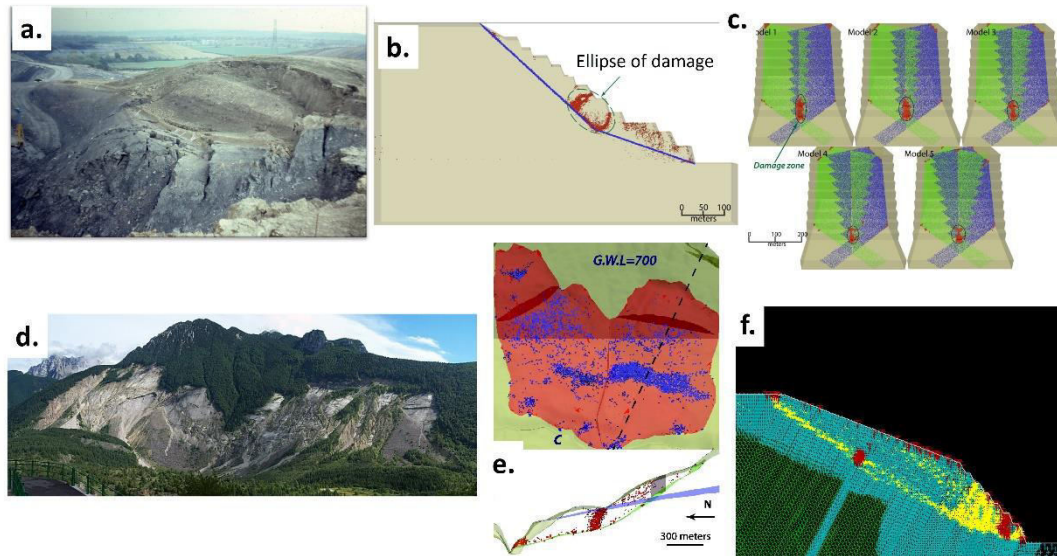


Figure 7. a. Brittle fracture and graben features associated with active-passive slope failure in faulted Coal Measures., b. Brittle fracture model of active-passive slope failure, after Havaej, 2015, Havaej and Stead, 2016, c. 3D brittle fracture model of non-daylighting wedges, d. Vajont Side, Italy, e. 3D brittle fracture model of Vajont Slide showing brittle fracture at active-passive block transition, f. UDEC model of toppling failure showing development of tension red and root zone (yellow)

1.6 Rear and lateral release surfaces

Rear and lateral release surfaces have been the subject of limited research, yet are often a critical element in landslides and rock slope failures. Release surface may vary in scale from joint-controlled rock fall, where the lateral boundaries and ends of the block form the release surfaces, to mountain/pit slope scale features. There is a wide range of release surface geometries dependent on the interaction between the structural geological features and geomorphic processes/landforms.

1.6.1 Rear release surfaces

Rear release surfaces were originally treated in limit equilibrium analyses as having critical locations and depths dependent on the relationship between the tensile strength of the rock, the failure surface orientation, and the slope geometry. In most rock masses, the location of the rear release surface will be dependent upon the presence of appropriately oriented planes of weakness, such as faults or joints. Where through-going persistent faults or bedding planes extend to and intersect the slope surface at the back of the landslide, no rear release surface may be present, apart from tensile cracks through the soil cover. The scale of rear release surfaces (depth, length, and width) has yet to be rigorously investigated. In small scale rock slopes, rear release surfaces may be formed by usually subvertical metre-scale joint planes. However, at mountain scale, rear release surfaces may be formed by extremely persistent joints and faults (Figure 8a), or combined bedding-cleavage-jointing step-paths within fold hinges (Figure 8b)

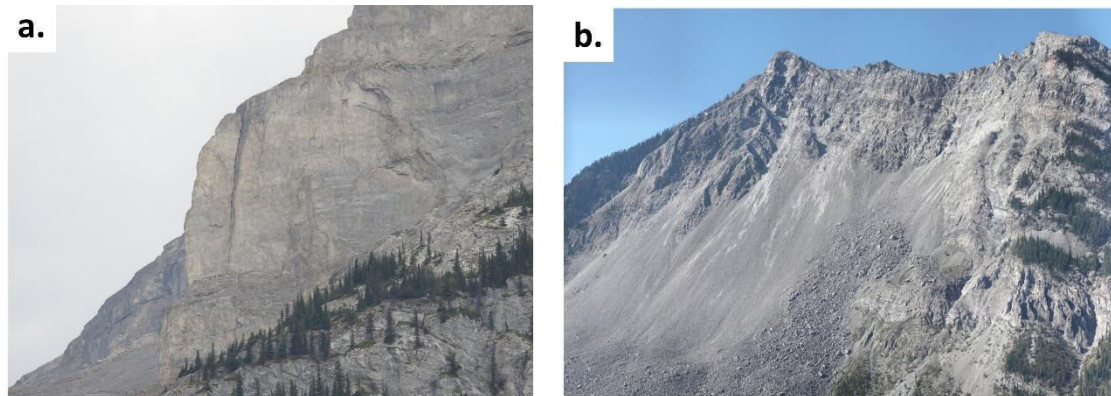


Figure 8. Examples of mountain scale rear release structures, a. Active-passive failure with dilation along high angle rear release surface and failure involving combined jointing – intact rock fracture at the toe (Mt Kidd, Alberta, Canada), b. Rear release of the 1903 Frank Slide, Alberta (Canada) involving combined brittle fracture and jointing within the hinge of a major fold.

The spacing of the structures may play an important role in step-path rear release. The length and orientation of rear release surfaces determines the volume of the slope failure. Rear release surfaces may strike in a direction oblique to the strike of the slope face, with important implications for both the three-dimensionality of the failure mechanisms and for support design. In large open pit slopes and landslides, rear release surfaces tend to be more complex, and may involve multiple structures with the global release surfaces branching across different structural and geotechnical domains. Release surfaces may also be stepped in plan or encompass zones of localised wedge/toppling instability as observed at the Downie Slide, BC. Variations in the rock mass quality may see more retrogression in the weaker more weathered rock mass. In such cases, it is important to consider different generations of releases surfaces with primary release surfacers for the main failure and secondary release surfaces corresponding to post-main failure instability (Figure 3b). The existence of multiple rear release surfaces is evident in long-term failures which retrogress into and extend in length over time along the slope as the failure grows and/or local failures coalesce into larger global slope failures, as noted at the Alexandria slope failure, BC (Canada, Figure 9a) and at the Fels slide (Alaska, Figure 9b). Geoscientists and engineers should also consider that in a retrogressing failure the main failure process may involve multiple “internal” rear release surfaces with sometimes evidence only of the final rear release surface at the headscarp of the landslide. In-slope rear release “surfaces” may also form at fault zones within a tectonically damaged rock mass with expression in the topography as depressions, grabens or sacking features.

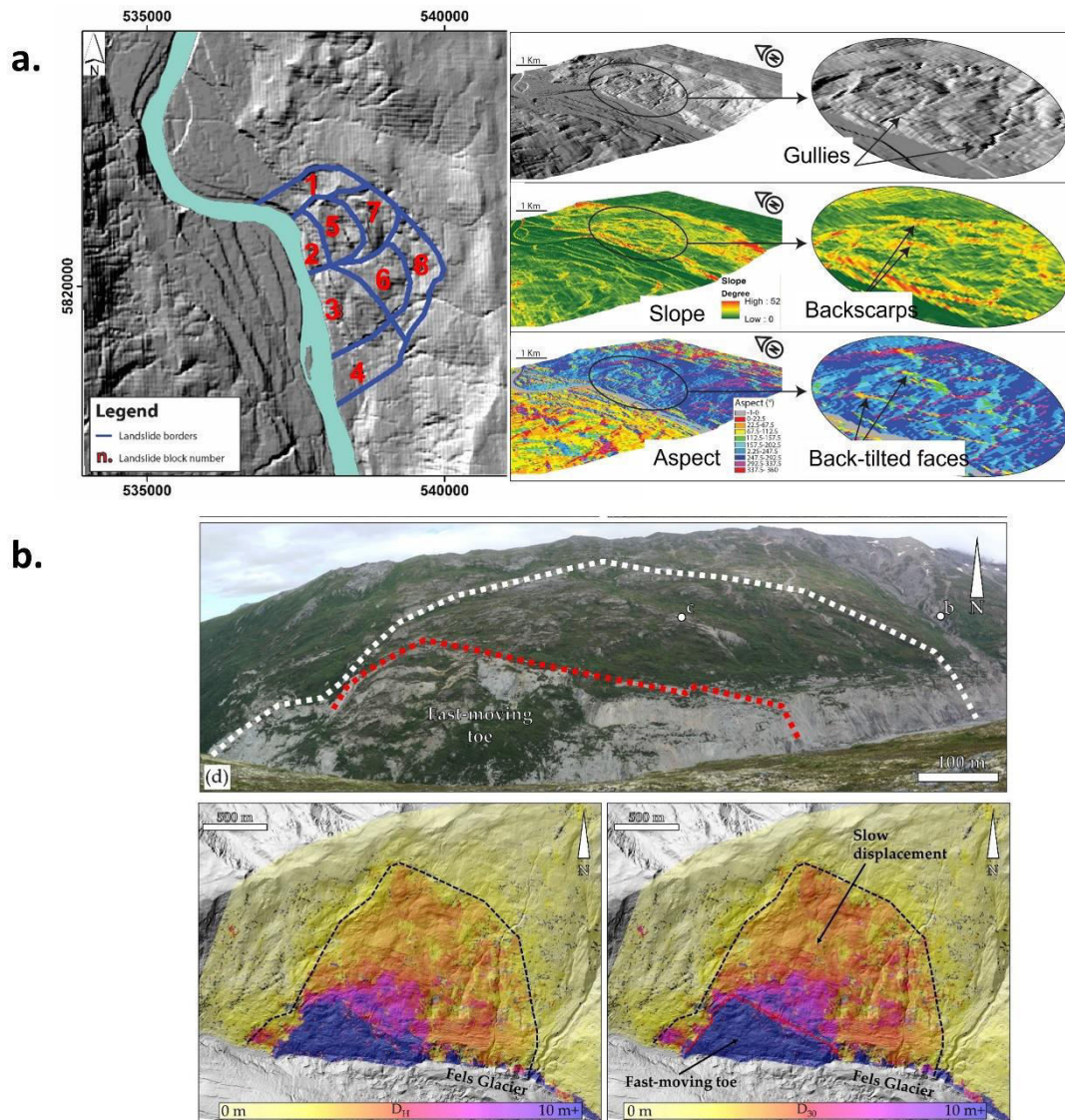


Figure 9. Retgression and lateral growth of landslides, a. Multiblock failure of the Alexandria landslide with eight blocks defined based on GIS, geomorphic mapping and InSAR displacements (after Francioni et al 2021), b. Progressive growth of the Fels Landslide along and into the slope with retreat of the Fels glacier based on SAR-speckle tracking and GIS interpretation, after Donati et al. (2021c)

1.6.2 Lateral release surfaces

Lateral releases surfaces have often been considered (or assumed) as sub-vertical surfaces orthogonal to the strike of the slope and sliding surface, thus providing no restraint to the landslide movement or rock slope failure. Lateral kinematic release may be provided by topography, for instance through gully incision on one or both sides of a landslide. Where two gullies exist or where there is a change in slope strike such as at a promontory, then lateral release structures may not be required (e.g., Randa rockslides, Leith 2012). Where a gully exists on one side only, then a structure is required on the other side. Where no gullies are present then structural surface for lateral release, or a combination of structures and intact rock fracture may be required. (Brideau 2010). Figure 10 shows lateral and rear release characteristics for several major landslides.

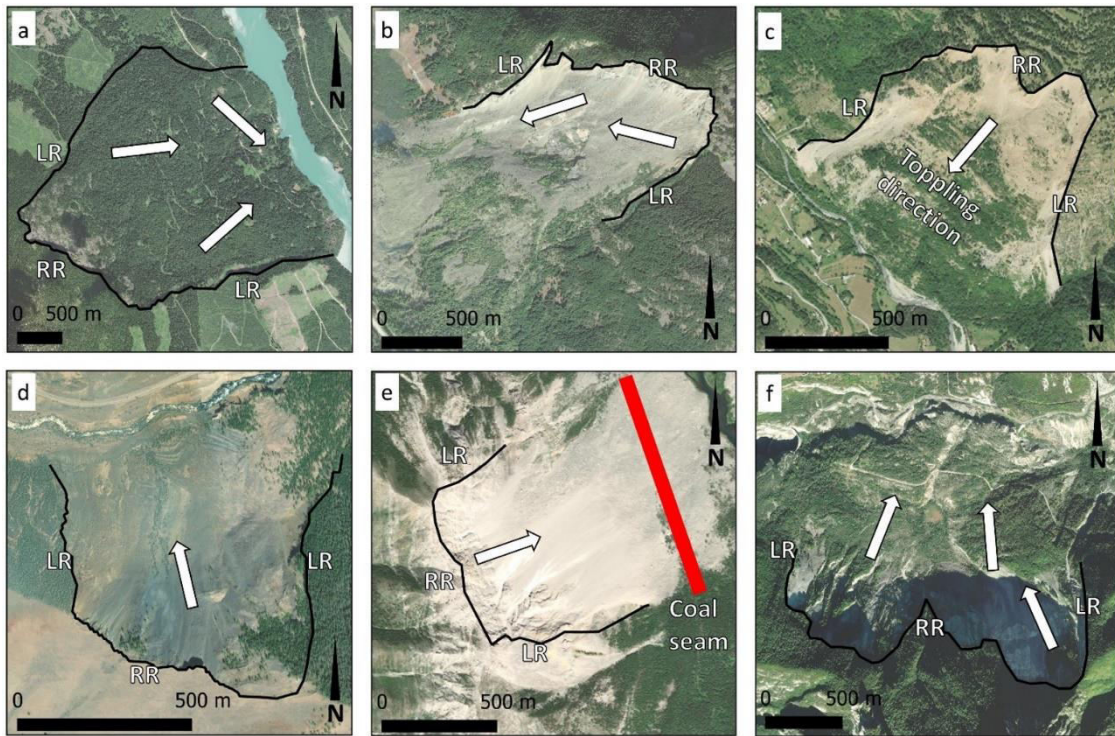


Figure 10. Selected major landslides showing complex landslide boundaries and lateral and rear release surfaces, a. Downie Slide, British Columbia (Canada), b. Hope Slide, British Columbia (Canada), c. La Clapiere (France), d. Madison Canyon (US), e., Frank Slide, Alberta (Canada), f. Vajont Slide (Italy)

Remote sensing has shown that the morphology of lateral release surfaces, as with the sliding and rear release surfaces, may be complex with significant surface roughness necessitating significant dilation, and even intact rock fracture for a slope block to move. The combined roughness of the lateral release surface and the failure block geometry (shape) may lead to complex translation and rotational block movements. Figure 11 and 12 shows the use of LiDAR combined with GIS and amplitude profiles to characterize the morphology of the lateral and sliding release surfaces at the Palliser Landslide in Alberta.

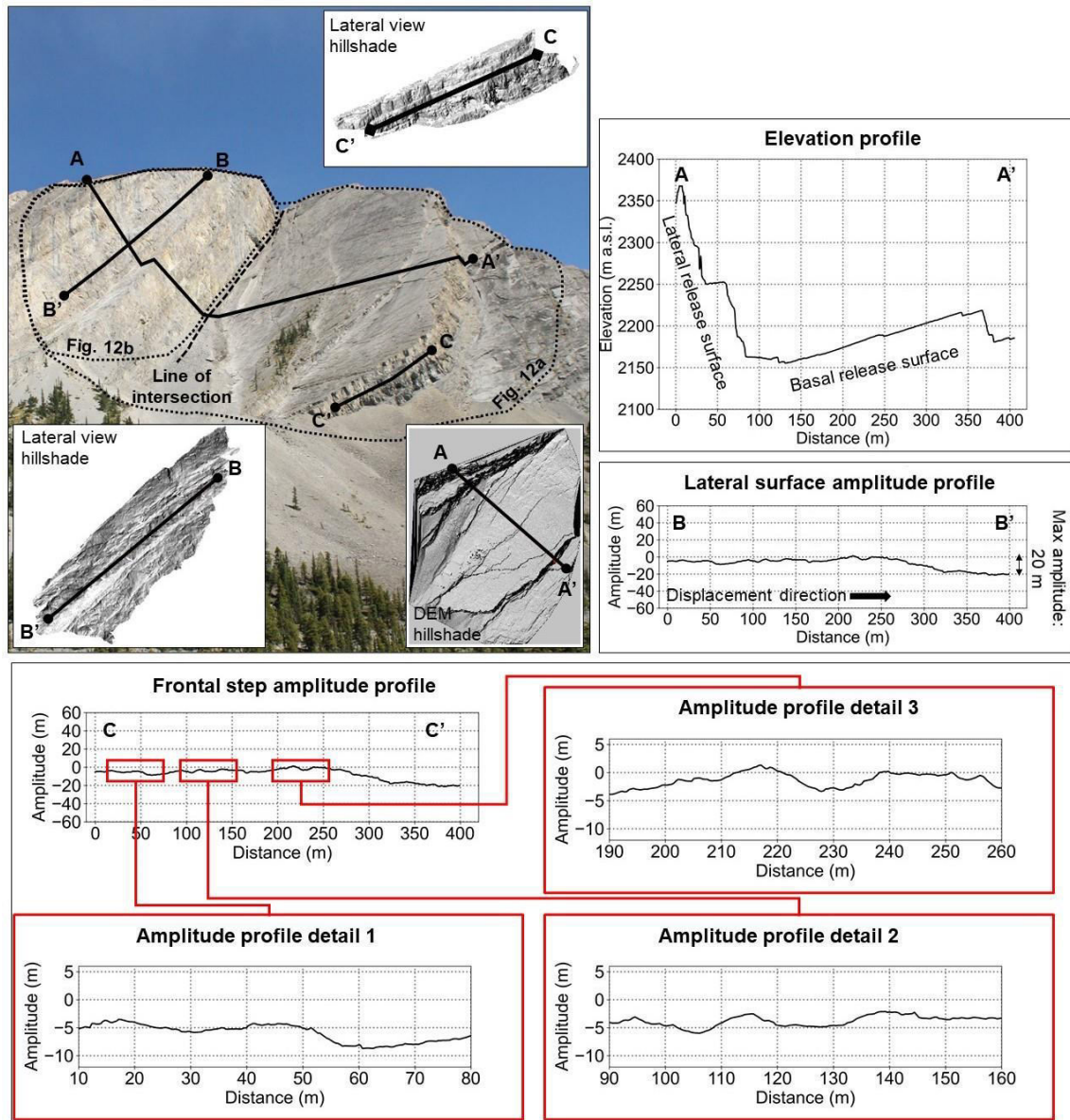


Figure 11. Morphology of the Palliser landslide, Alberta (Canada), lateral and sliding surfaces. Sections through the ground-based LIDAR show large variations in the amplitude of roughness which would have provided significant resistance to sliding.

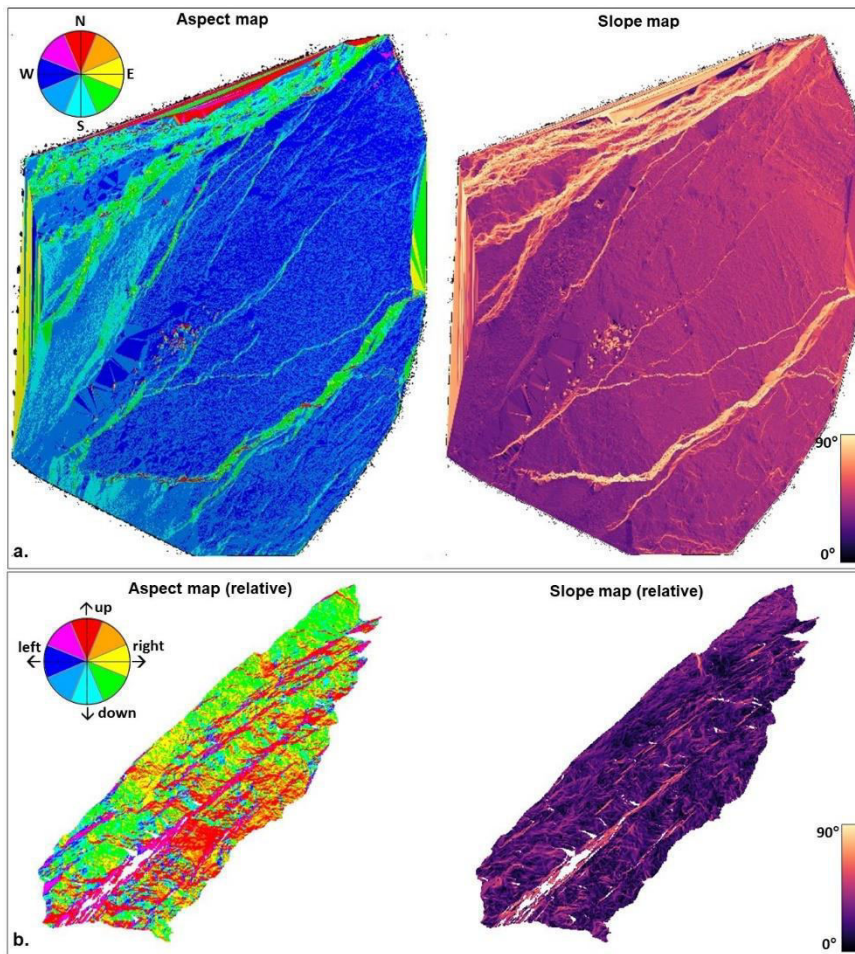


Figure 12. Aspect and slope maps of the basal (a) and lateral (b) surfaces of Palliser landslide, Alberta (Canada), highlighting the roughness and undulations. See fig. 11 for location. Note that the aspect and slope maps of the lateral surface (b) were created after registering the surface on a horizontal plane. Therefore, the orientation of the surfaces is relative.

As with rear release surfaces, multiple lateral release surfaces, reflecting a complex structural geological setting, may allow over time, the lateral growth of multi-block, 3D landslides. As previously discussed, extensive research conducted at the Hope Slide, BC (Brideau et al., 2005, Donati et al. 2021b) has shown that multiple internal lateral release surfaces were present as shear zones within the rock mass and were an important control on the kinematics of the failure. Engineers and geoscientists should consider not only the dip and dip direction of the lateral and rear release surfaces, but also the plunge of the mutual intersections between the sliding, lateral and rear release surfaces forming the landslide block geometry. It is recommended that the plunge and trend of all such major structure intersections be systematically compared to three-dimensional monitoring data from remote sensing (e.g., InSAR, LiDAR) and geodetic monitoring methods (e.g., GNSS) to investigate the structural controls on the failure mechanism. An example is presented by Donati et al (2021c) who were able to estimate the shape of the failure surface beneath the Fels slide (Alaska) using SAR speckle tracking data and the calculated plunge and trend of the displacement vectors.

1.6.3 Understanding the importance of tectonic control on release surfaces

As evident from previous discussions and work by the authors tectonic structures have an overriding effect on rock slope failures and landslides. All too often, however, particularly with the advent of remote sensing and autorecognition of joints and joint sets, there is arguably a lack of

critical analysis as to which structures are important in a slope. The authors recommended tectonic structures be treated in a hierarchical 1st, 2nd, 3rd, 4th order manner as is done in groundwater studies in large open pits, Beale and Read (2014). 1st order faults, shears and major joints spanning the entire slope clearly have the potential to form release surface for major failures as observed in the Vajont Slide (Italy, Figure 13a), translational failure along Maligne Canyon (Figure 13b), Goldau Slide in Switzerland (Figure 13c), the Hope Slide, BC (Figure 3) or to form damage zones, such as at the Downie Slide, BC (Figure 2).

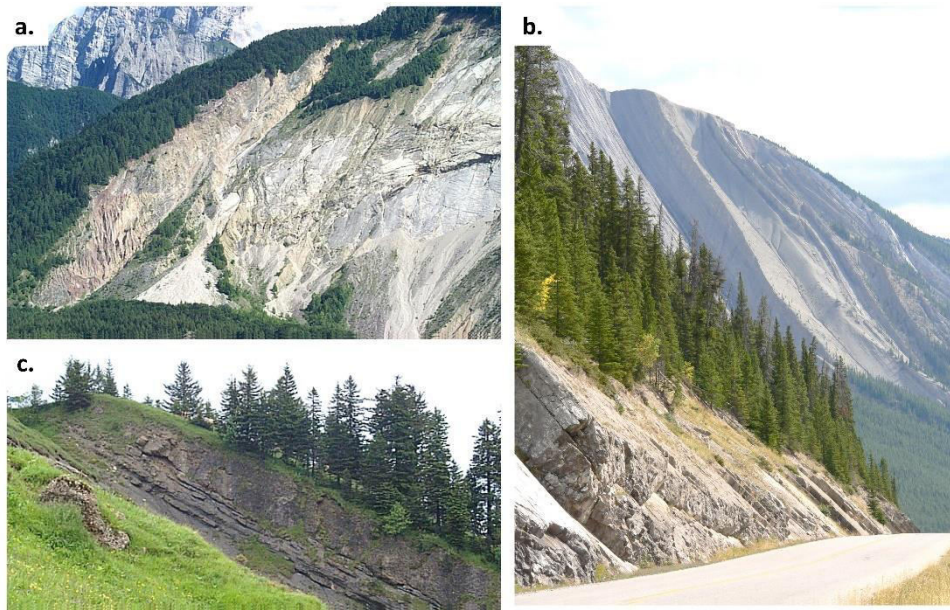


Figure 13. Major 1st order structures forming the lateral release surfaces at a. The Vajont Slide, Italy, b. Maligne Canyon, Alberta, Canada and c. Goldau Slide, Switzerland.

In contrast, minor, 4th order lower persistence joint sets are more liable to provide release for rockfall/bench scale instabilities. Where major fault zones exist along a valley, the possibility of tectonic damage at the toe and associated fault structures/splays forming release surfaces should be considered (Kremsater 2021). The observed progressive failure of post-glacial slopes and deep-seated gravitational displacements may involve on-going fracture of the rock mass until lateral or rear release is through-going and the slope is brought to a state of failure.

1.4 *The detachment surface*

Conventional kinematic analyses using stereographic procedures consider sliding failures (planar and wedge) and rotational/toppling failures; these modes of failure are dominated by shear failure. In rockfalls on high rock slopes the engineer must consider the above modes but should also consider extensile gravity failure of rock blocks from undercut sub-horizontal detachment surfaces. Such failures are similar to underground gravity wedges and hence can easily be incorporated into slope stereographic kinematic analysis. These sub-vertical blocks detach over time through a combination of tensile fracture and separation on joints. They clearly provide evidence of the importance of rock bridges in rock slope stability as tensile strength dominates over mobilised shear strength in these environments. Extensile dominated rockfall may involve free fall or cantilevering of beams away from the overlying detachment surface. In shear-dominated rockfalls, the rockfall separates away from the detachment surface, which is orthogonal to the sliding surface. Rockfall on steep rock slopes has been investigated in detail by many researchers using change detection laser scanning methods. Real time laser scanning monitoring by Williams (2017) showed how rockfalls are more frequent and of lower magnitude than indicated by monitoring

over longer time intervals. Small scale release surfaces and block failures (generally referred to as precursor rockfalls) may provide the kinematic conditions (removal of toe and/or lateral confinement) for larger scale failures that mobilize larger slope scale release surfaces. Kromer et al. (2015) present an interesting case study demonstrating the importance of rock slope precursor activity using change detection ground-based LIDAR; this is an important area for future research. Failure sources areas may grow and coalesce both retrogressively into the slope and along slope in an inherently three-dimensional process. The authors have investigated the lateral and rear release and detachments surfaces of rockfalls at numerous high rock slopes in Western Canada and Europe. Figure 14 shows examples of upslope rockfall migration with evidence of shear and extensile beam modes of failure. Shear dominated rockfalls typically occur as sliding and wedge failures, whereas extensile failures show clear brittle fracture in the subvertical source zones. Shear dominated rockfall source zones may be bounded by step-path lateral release surfaces on one side and brittle fracture on the other (Figure 15b). The step-path lateral boundary reflects the upward propagation and growth of the source zone over time. Subvertical rockfall may culminate in a circular step-path detachment surface or involve multiple lateral release surfaces forming blocks that progressively detach along the length of the slope. In more massive rock slopes cantilevering of joint-bounded blocks may occur with cracking and rockfall due to beam failure (Figure 14b). Rockfall may also involve plan rotation movements (Figure 16a, b). In such cases, it important to consider not only the dip of the folded sliding surface but the plunge of the fold which can exacerbate oblique rockfall displacements.

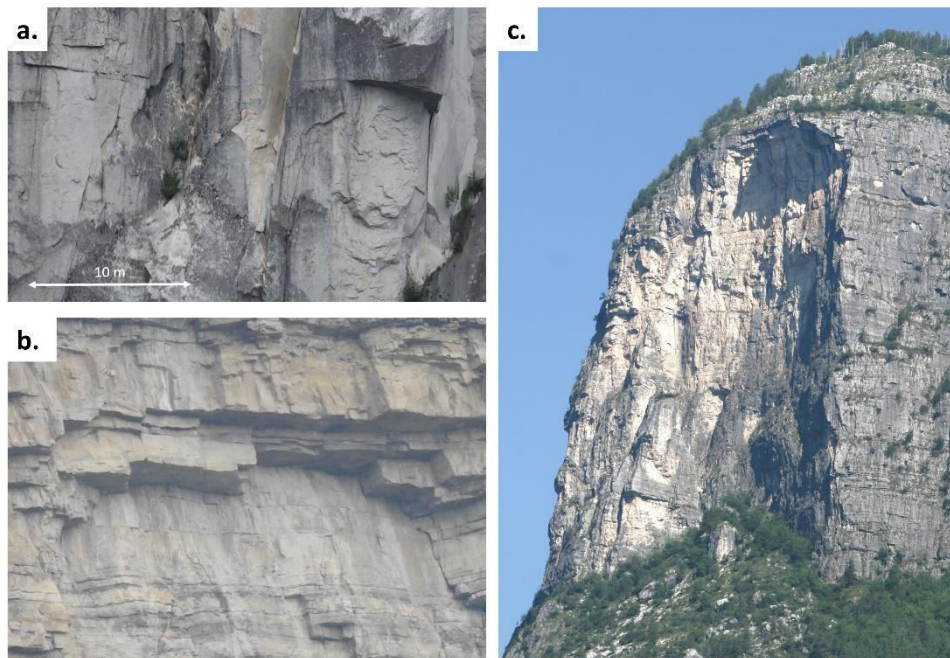


Figure 14. Extensile dominated rockfall with a sub-horizontal detachment. a. Detachment of block involving intact rock fracture along sub-vertical jointing, Squamish Chief, BC (Canada). B. Extensile detachment of blocks involving cantilevering beam pinned at one end with rotating out of slope c. Curvilinear detachment roof rockfall, Lago di Pontesi (Italy).

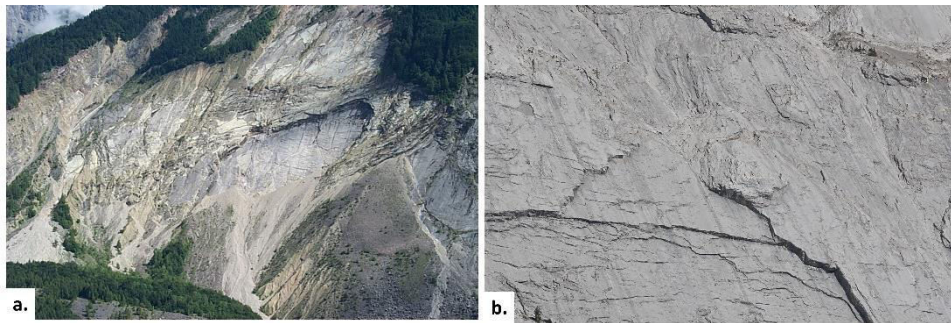


Figure 15. Shear dominated rockfall with detachment progressing upslope. a. Detachment from joints orthogonal to bedding with V-shaped upward migration, Vajont slide, b. Upslope migration of rockfall involving step-path detachment surface on one side and brittle fracture on upper right, Maligne Canyon, Alberta (Canada).

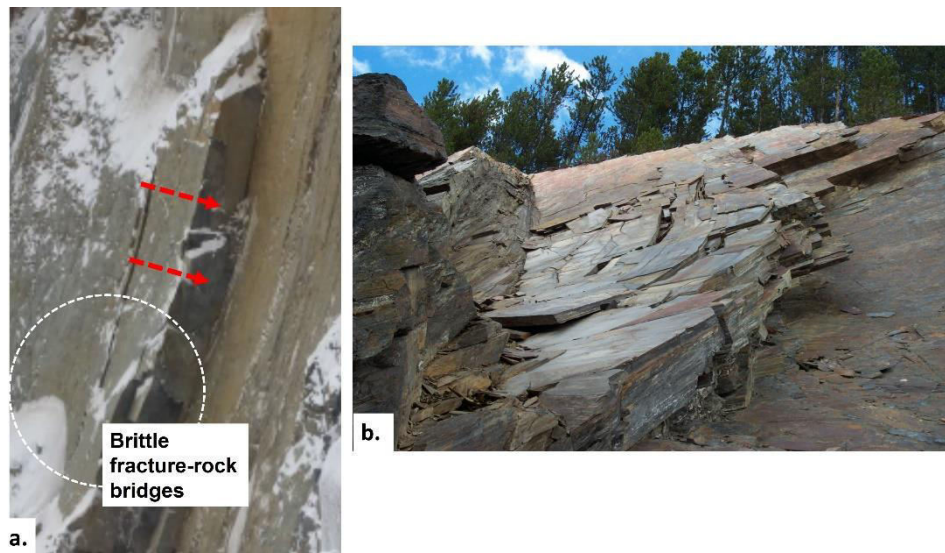


Figure 16. Plan rotational rock slope displacements a. Block rotation along strike resulting in dilation of step path jointing and brittle fracture at the toe of the column, Joffre, BC (Canada). b. Plan rotation of foliated rock mass along a plunging fold limb, Lake Louise, roadcut, Alberta (Canada).

2 SLOPE KINEMATICS AND LANDFORM EVOLUTION

Remote sensing (characterization and monitoring) and numerical modeling of landslides over recent years have clearly shown the importance of considering landslides as 3D block movements as opposed to the 2D blocks adopted in conventional 2D analyses. Investigations on the Downie Slide, the Hope Slide, and Elliot Slide, BC (Canada), the Aknes slide (Norway), Fels slide (Alaska), and Vajont Slide (Italy) have all indicated that slope failures comprise multiple blocks that move often at different rates and different directions. The size and shape of the blocks involved is important as keyblocks may be present as at the Hope and Elliot Slide removal of which by ancient landslides predetermine eventual failure. Changes in the landslide release surfaces with respect to landform evolution, slope damage and the importance of kinematic confinement both in-slope and along slope should always be considered. Keyblocks at the slope toe may be removed by undercutting (glaciation/river/coastal erosion) and result in the generation of new release surfaces that bound landslide blocks that were previously non-removable. Loss of confinement may occur within a slope when a block fails allowing lateral progression of instability. The interaction between geomorphic process such as glacial retreat, river and coastal erosion can be controversial,

e.g. it the removal of the support of the ice or the changing kinematics that is important.? Notwithstanding, the observed slope toe that follows glacier retreat is both damaged by glacial processes and steeper due to glacier erosion; this can facilitate either daylighting of incipient basal release/failure surfaces, rock mass failure, or both, Figure 17 In foliated metamorphic rocks of low rock mass strength failure may occur concurrent with glacier retreat with the failure developing laterally and in-slope instantaneously. In stronger, brittle rocks the undercut toe may fail long after the glacier has disappeared sometimes in a violent, energetic manner. It is important to also consider the effect of marine erosion removing weak rock/faulted rock masses to form lateral or rear release to major coastal landslide blocks or rivers/gullies incising into mountain slope to form lateral release surfaces. Geomorphic processes include the removal of toe/lateral keyblocks, the effects of stress-relief, and weathering. The kinematics of a rock slope may change with block removal as observed at the Joffre Slide, BC, where the translational failure of one block allowed an adjacent block to fail along slope by toppling/rotation of rock columns (Fullin, 2020). Failure of a surface layer of a steep rock slope may occur within a stress-relief loosened “damage skin” that moves into the slope with time through continuing rockfall at multiple scales. Such a migration of the damage skin may lead to larger scale landslides where the necessary large scale release surfaces are present. In 2D simple failure mechanism are assumed to involve one block (planar/wedge), two-three blocks (active passive +/- Prandtl deformation zone). When a slope is considered in three dimension it is common to see multiple blocks along slope in addition to in-slope. The blocks interact along internal lateral and rear release surface often with varying dip/sip direction basal sliding surface. The rock block shape is critical in three-dimensional stability and requires a 3D-distinct element keyblock approach. Constraining rock slope modelling using combined remote sensing (characterization-monitoring) and boreholes is essential.

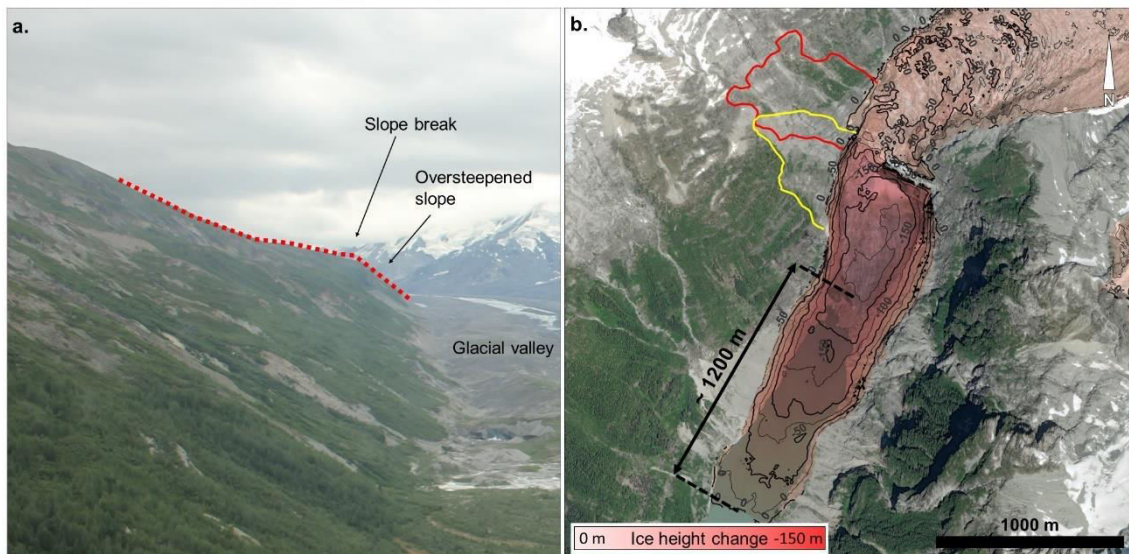


Figure 17. Examples of slope instabilities driven by glacial retreat: a. view of the oversteepened slope left by the retreat of the Fels glacier, which initiated the movement of the Fels slide (Figure 9b); c. results from a change detection analysis, showing the retreat of the West Grenville Glacier between 1965 and 2021, which promoted the detachment of the 2021 Elliot Creek slide, British Columbia (Canada), outlined in red. The yellow line shows the boundaries of an older landslide scar, which also enhanced the kinematic freedom of the 2021 landslide.

3 CONCLUSIONS AND FUTURE CHALLENGES IN UNDERSTANDING COMPLEX ROCK SLOPE FAILURE MECHANISMS

Remote sensing has clearly shown the variations in slope displacements in 3D and allowed correlations between the failure surface morphology and slope deformations. To improve our understanding of rock slope failure mechanisms we must fully utilize the enormous amounts of data that are being collected Figure 18a.

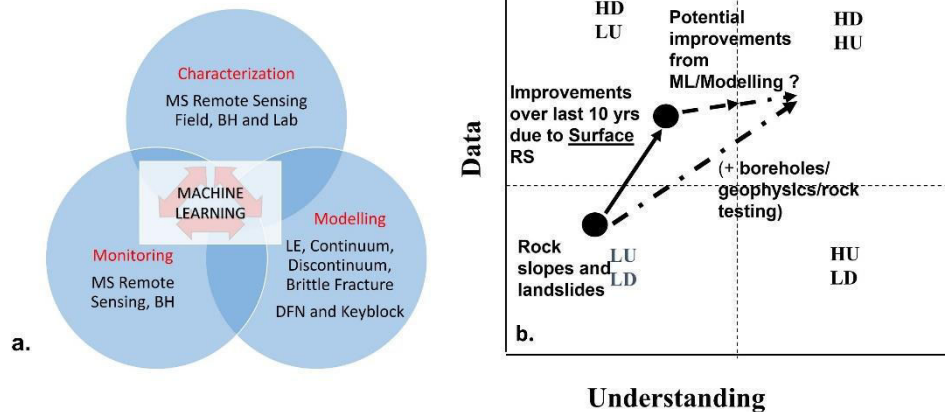


Figure 18 a. “Bigdata” sets being collected on rock slope characterisation, monitoring and modelling, b. Conceptual uncertainty in rock slopes and landslides and potential improvements through combined machine learning (ML), modelling and site investigation methods.

This data also needs to be used in constraining numerical models. The problem of analyzing “bigdata” sets in a timely fashion is a major challenge to rock engineers and requires the use of improved methods of data analysis and visualization. Collecting remote sensing data, in itself, does not improve our understanding of slope failure mechanism unless the right data is being collected and the relationships between data can be identified. The authors suggest that a machine-learning approach is essential to allow the enormous data sets to be fully utilized in constraining numerical models, reducing uncertainty, improving our understanding and reducing risk, Figure 18b. Further research is required to characterize sliding, lateral, rear and detachment surfaces in detail using remote sensing, geophysics, borehole methods and numerical modelling. The mechanical properties assumed for numerical modelling of large-scale release surfaces also requires further investigation and constraint through combined remote sensing and numerical modelling of rock slopes and landslides at varying engineering scales. It is essential that 3D models that realistically simulate observed slope behavior be adopted more widely. These models should be able to simulate multi-block landslides involving brittle fracture but should not be oversimplified to do this. The role of groundwater pressures on release surfaces in three-dimensional rock slope/landslides models has been the subject of limited research. The water pressures along the base of landslide blocks have been considered in 3D distinct element models and similarly the influence of rear release (tension crack) water pressures has received considerable emphasis in rock slope stability. The role of water pressures on lateral release surfaces however requires further investigation. It is known that the same structures that may function as lateral release surfaces in landslides can also result in compartmentalization of groundwater pressures. It is thus highly likely that different blocks within landslides may be influenced to very degrees by groundwater. The role of pre-failure landslide fracturing, and structures have been suggested to result in amplification of earthquake waves; releases surfaces both internal and bounding may interact with seismicity in a complex manner. The time dependency of displacements in slopes and their relationship to lateral release surfaces (block shape) is an area for future research using InSAR/GPS combined with 3D numerical modelling. Remote sensing should be used to characterize

lineaments related to release surfaces and the three-dimensional plunge/trend of slope displacement vectors over time compared with the plunge/trend of release structures. Emphasis should be given to constraining and differentiating time dependent movements related to release surfaces and to the rock mass.

Considerable potential now exists for using remote sensing and numerical models to improve our understanding of the three-dimensional nature of landslides and simplification of landslides/rock slope failures to 2D entities should only be done after careful and rigorous justification.

REFERENCES

- Alghalandis, Y.F., Dowd, P.A. & Xu, C., 2014. Connectivity field: a measure for characterising fracture networks. *Math. Geosci.*, 47:1:63-83
- Beale, G. & Read, J. 2014. Guidelines for evaluating water in pit slope stability, CSIRO, Australia.
- Brideau, M-A., Stead, D., Kinakin, D. & Fekova, K. 2005. Influence of tectonic structures on the Hope Slide, British Columbia, Canada, *Engineering Geology*, 80:242-259
- CANMET (1977). Pit Slope Manual. Canadian Centre for Mineral and Energy Technology, 10 Volumes with Supplements, Ottawa.
- Dershowitz, W., Finnilla, A., Rogers, S., Hamdi, P. & Moffit, K., Step path rock bridge percentage for analysis of slope stability, *ARMA* 17-1045.
- Donati, D. 2019. The characterization of slope damage using an integrated remote sensing-numerical modelling approach, PhD Thesis, Simon Fraser University, BC., Canada.
- Donati, D., Stead, D., Stewart, T., Marsh, J. 2020. Numerical modelling of slope damage in large, slowly moving rockslides: Insights from the Downie Slide, British Columbia, Canada. *Engineering Geology* 273
- Donati, D., Westin, A., Stead, D., Clague, J.J., Stewart, T., Lawrence, M., Marsh, J. 2021a. A reinterpretation of the Downie Slide (British Columbia, Canada) based on slope damage characterization and subsurface data interpretation. *Landslides* 18,5,1561-1583.
- Donati, D., Stead, D., Brideau, M.A., & Ghirotti, M. 2021b. Using pre-failure and post-failure remote sensing data to constrain the three-dimensional numerical model of a large rock slope failure. *Landslides* 18,3,827-847
- Donati, D., Rabus, B., Engelbrecht, J., Stead, D., Clague, J.J., Francioni, M. 2021c. A robust SAR speckle tracking workflow for measuring and interpreting the 3d surface displacement of landslides. *Remote Sensing* 13,15, 3048.
- Elmo, D., Donati, D. & Stead, D. 2018, Challenges in the characterisation of intact rock bridges in rock slopes, *Engineering Geology*, 245:81-96.
- Francioni, M., Stead, D., Sharma, J., Clague, J.J. & Brideau, M-A. 2021. An integrated InSAR-borehole inclinometer-numerical modeling approach to the assessment of a slow-moving landslide, *Environmental and Engineering Geoscience* 27:3: 287-305
- Fullin, N. 2020. Characterising the kinematics of the Joffre Peak landslides using a combined numerical modeling -remote sensing approach. M.Sc. Thesis. University of Ferrara, Ferrara, Italy.
- Glastonbury, J. & Fell, R. 2010. Geotechnical characteristics of large rapid rock slides, *Canadian Geotechnical Journal*, 47:116-13
- Havaej, M. 2015. Characterisation of high rock slopes using an integrated numerical modelling - remote sensing approach, PhD Thesis, Simon Fraser University, BC, Canada.
- Havaej M. & Stead, D. Investigating the role of kinematics and damage in the failure of rock slopes, *Computers and Geotechnics* 78, 181-193
- Hoek, E. & Bray, J.W. 1974. *Rock Slope Engineering*, 3rd edition. London: Institute of Mining & Metallurgy, 1st Edition
- Hungr, O., Leroueil, S. & Picarelli, L. 2014. The Varnes classification of landslide types, an update, *Landslides*, 11:167-194
- Jennings, J., 1970. A mathematical theory for the calculation of the stability of slopes in open cast mines, *Proc. Open Pit Mining Symposium, Planning Open Pit Mines*, South Africa.
- Karami-Shariff, L., Elmo, D. & Stead, D. 2022. New approaches to quantify progressive damage and associated dynamic rock mass blockiness. *Journal of Rock Mechanics and Geotechnical Engineering* (in press).

- Kremsater, R. 2021. Investigating the potential hazard, mechanisms of failure and evolution of the Cascade Bay Landslide, BC., MSc Thesis, Simon Fraser University, Canada.
- Kromer, R., Hutchinson, J., Lato, M., Gauthier, D., Edwards, T. 2015. Identifying rock slope failure precursors using LiDAR for transportation corridor hazard management. *Engineering Geology* 195, 93-103.
- Leith, K. (2012) Stress development and geomechanical controls on the geomorphic evolution of alpine valleys, P.h.D Thesis, ETH, Switzerland.
- Londe, P. 1965. Une méthode d'analyse à trois dimensions de la stabilité d'une rive rocheuse. *Annales des Ponts et Chaussées* 135 (1), 37-60.
- Londe, P., Vigier, G. and Vormeringer, R. 1969. The stability of rock slopes, a three-dimensional study. *J. Soil Mech. Foundns Div., ASCE* 95 (SM 1), 235-262.
- Londe, P. 1973. The role of rock mechanics in the reconnaissance of rock foundations, *QJEG*, 6:57-74.
- Stead, D. & Wolter, A. 2015. A critical review of rock slope failure mechanisms: The importance of structural geology, *J. Structural Geology*, 74:1-23.
- Sturzenegger, M., Multi-scale characterization of rock mass discontinuities and rock slope geometry using terrestrial remote sensing techniques, PhD Thesis, Simon Fraser University, BC., Canada.
- Sturzenegger, M. & Stead, D. 2012. The Palliser Rockslide, Canadian Rocky Mountains: Characterization and modeling of a stepped failure surface, *Geomorphology*, 138:1:145-61
- Tuckey, Z. & Stead, D. 2016. Improvements to field and remote sensing methods for mapping discontinuity persistence and intact rock bridges in rock slopes, *Engineering Geology*, 208:136-153
- Varga, A. & Gorbushina, V. 1996. Geostructural classification of unstable rock masses, Proc 8th IAEG Congress, Balkema, Rotterdam, ISBN 90 5410 990 4
- Varnes, D.J. 1978. Slope movement types and processes. In: Schuster RL, Krizek RJ (eds) *Landslides, analysis and control*, special report 176: Transportation research board, National Academy of Sciences, Washington, DC., pp. 11-33
- Westin, A.M. 2017. Downie Slide: An integrated remote sensing approach to characterization of a very slow-moving landslide, MSc. Thesis, Simon Fraser University, BC., Canada.
- Williams, J.G. 2017. Insights into rockfall from constant \$D\$ monitoring, PhD Thesis, Durham University.
- Wittke, W.W. 1965. Method to analyse the stability of rock slopes with and without additional loading. (in German) *Felsmechanik und Ingerieurgeologie*, Supp. 11, 30, 52-79. English translation in Imperial College Rock Mechanics Research Report.
- Wolter, W.E. 2014. Characterisation of large catastrophic landslides using an integrated field, remote sensing and numerical modelling approach, PhD Thesis, Simon Fraser University, BC., Canada.
- Wyllie, D. & Mah, 2004, *Rock Slope Engineering*. CRC Press.

Investigation into long-term coal pillar stability

I. Canbulat, J. Watson & C. Wei

School of Minerals and Energy Resources Engineering, University of New South Wales, Sydney NSW 2052, Australia

ABSTRACT:

Although the basic mechanisms of coal pillars are well understood, gaps exist in some critical areas, particularly in relation to long-term stability. This study investigates the long-term stability of coal pillars by considering three-pillar system failure modes: (i) pillar failures due to pillar spalling (i.e., reduced pillar width), (ii) pillar failures due to continuous roof failures (i.e., increased mining height), and (iii) pillar failures due to weakened floor. The mechanisms of pillar failure caused by the three failure modes are discussed. The concept of ‘geometrical limits’ is implemented to calculate the critical spalling depth for pillar failure caused by rib spalling, and the critical mining height for pillar failure due to roof falling in long-term. In addition, an analytical technique has been developed to quantitatively assess the bearing capacity of soft floor. This analytical model shows that the bearing capacity decreases linearly with decreasing cohesion of the floor. The assessment approach proposed in this study can help to quantify the long-term stability of coal pillars.

1 INTRODUCTION

Despite coal pillars being one of the most researched aspects of underground coal mining, their behaviour, interaction with surrounding rock masses and strength remain a subject of research due to the inherent complexity and variability of rock masses. Although the basic mechanisms of pillars are well understood, gaps exist in some critical areas, particularly in relation to long-term stability.

Pillar stability is an important consideration during mining and following mining. During mining, pillars provide a safe working environment for underground workers. In the long-term, after mining has ceased, in many cases, the pillars are required to stay stable for subsidence control purposes.

The design of long-term stability of coal pillars in Australia is currently based on a factor of safety of 2.11 using the well-known UNSW pillar design formulae (Salamon et al, 1996), which corresponds to a probability of failure of 1 in a million. However, an important limitation of the UNSW formulae in its derivation was that it could not define the annualised probability of failure; that is, the effect of time was not quantified.

A pillar system comprises the coal pillar, roof, and floor. The strength of pillars can reduce over time due to two distinct spalling processes that (i) start at pillar edges and work their way towards the pillar core, and (ii) start in the roof and continues until it reaches equilibrium. The long-term pillar system failures can also be caused by the progressive weakening of the floor.

This study aims to examine the long-term stability of coal pillars by considering the three pillar system failure modes: (i) pillar failures due to pillar spalling (ii) pillar failures due to continuous roof failures, and (iii) pillar failures due to weakened floor. The concept of ‘geometrical limits’ is implemented to assess the pillar failure caused by rib spalling and roof failure with time. Furthermore, an analytical technique is developed to investigate the pillar failure due to softened floor in the long-term.

2 ANALYSIS OF FAILURE MODE OF LONG-TERM STABILITY OF COAL PILLARS

2.1 Australian coal pillar design methodology

The methodology used in the studies of Salamon and Munro (1967) in South Africa and Salamon et al (1996) in Australia are identical. In both studies, it was postulated that (i) the strength of a pillar can be expressed as a function of the linear dimensions of the pillar, (ii) the mean stress acting on a pillar is the tributary area load, and (iii) failure occurs when the true load exceeds the actual strength, which can be expressed in terms of the conventional factor of safety (SF):

$$FoS = \frac{\text{Strength}}{\text{Load}} \quad (1)$$

The general ‘power’ formula for strength (σ_p) was defined by Salamon et al (1996) as:

$$\sigma_p = K \frac{(w\Theta)^\alpha}{h^\beta} \quad (2)$$

where K , α and β were determined by a statistical analysis of collapsed and uncollapsed pillar geometries, w and h are pillar width and mining height, in metres. Θ is a dimensionless ‘aspect ratio’ factor to account for pillar length. Salamon et al (1996) determined the values for K , α and β to be 8.6 MPa, 0.51 and -0.84 respectively.

The dimensionless aspect ratio is a modification of hydraulic radius concept (effective pillar width) of Wagner (1980) and is as follows:

When pillar width to height (w/h) ratio <3 :

$$\Theta = 1 \quad (3)$$

When $3 \leq w/h \leq 6$:

$$\Theta = \left[\frac{2l}{w+l} \right]^{\frac{(w/h)-3}{3}} \quad (4)$$

where l is pillar length in metres.

When $w/h >6$:

$$\Theta = \left[\frac{2l}{w+l} \right] \quad (5)$$

Salamon (1982) proposed an extension to his original pillar strength formula to account for the increased strength of “squat” pillars with large width-to-height (w/h) ratios (Madden and York, 1998). Salamon et al (1996) proposed the following squat pillar formula in Australia:

$$\sigma_s = \frac{27.63 \Theta^{0.51}}{w^{0.22} h^{0.11}} \left\{ 0.29 \left[\left(\frac{w}{5h} \right)^{2.5} - 1 \right] + 1 \right\} \quad (6)$$

Where σ_s is the strength of a squat pillar.

In the analyses, the load acting on pillars was calculated using the Tributary Area Theory (TAT), which assumes that each pillar carries a proportionate share of the full overburden load. Assuming H is depth to the seam floor (m), b is roadway width (m), w is pillar width (m), C is centre distance (m), then for a square pillar layout the pillar load (q_m) can be estimated in MPa units as:

$$q_m = \frac{\gamma HC^2}{w^2} \quad (7)$$

where $C = w + b$ and γ is the average specific weight of the overburden rocks.

2.2 Conventional modes of pillar failure

The exact mode of failure of coal pillars is not known with any certainty, particularly in old, sealed panels. The majority of cases in the failed databases collated around the world were gathered using the observed surface subsidence and, where possible, mining experiences in neighbouring panels of the failed panels. Nevertheless, many authors discussed the possible pillar failure modes and found that there are four conventional long-term failure modes of a pillar system (excluding; (i) sudden, violent failure due to instantaneous release of strain energy and (ii) flooded workings that may completely disintegrate the coal pillar). These modes are:

- (a) Progressive pillar spalling (i.e., pillar is the weakest element in the system).
- (b) Progressive roof spalling (i.e., the roof is the weakest element in the system).
- (c) Pillar foundation (i.e., floor) failure, which, in turn, pulls the pillars apart and fails it (i.e., floor is the weakest element in the system)
- (d) Any combination of the above.

3 ASSESSMENT OF LONG-TERM STABILITY OF COAL PILLARS

3.1 Pillar failure caused by rib spalling

3.1.1 Progressive pillar spalling mechanism

It is well-known that the strength of pillars may reduce over time by a spalling process that starts at pillar edges and works its way into the pillar core (van der Merwe, 1993; van der Merwe, 2003; Salamon et al, 2006; Canbulat, 2010). In this failure mode, it is assumed that the weakest element of the pillar system is the pillar, whilst the roof and floor are stable. As the pillar ribs weaken, spalling occurs, and the effective size of the pillar decreases. Eventually, it reaches the stage where the loss of strength is sufficient to result in failure of the pillar (van der Merwe, 1993). This failure mechanism is entirely controlled by the volume of space available underground to allow sufficient spalling for failure, which also implies a maximum depth of spalling. This limitation is referred to as “Geometrical Limits”. This concept of spalling was first suggested by Salamon et al (1998).

A further study conducted by Canbulat and Ryder (2002) simplified the model for the South African strength formulae. In their study, Canbulat and Ryder (2002) assumed that a spalling pillar, of original width (w) and height (h), continues to scale until a width (w_1) is reached at which the ‘apron’ of scaled material forms a fully confining rim of height h and width c , this is given by:

$$c = h \cot \phi \quad (8)$$

where ϕ = angle of repose.

A field observation of pillar rib spalling is shown in Figure 1, illustrating the geometry involved. It may be that the total width of the spalled apron $w_1 + 2c$ exceeds the centre spacing “ C ” of the pillars, and overlap occurs with the aprons around the neighbouring pillars.

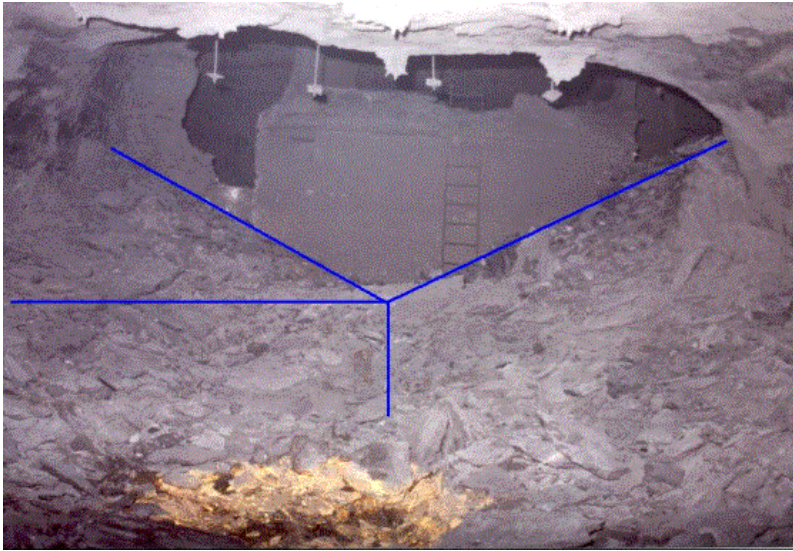


Figure 1. A scaled pillar indicating the angle of repose and the height of the rubble, after Canbulat and Ryder (2002)

3.1.2 Spalling of pillar at failure

In order to determine the required spalling distance to reduce the factor of safety to the critical factor of safety (i.e., $S_c=1$), the approach developed by (van der Merwe, 1993) can be used. In this approach, it is assumed that the original pillar width spalls by an amount, d_c , then the effective pillar width at critical factor of safety is $w - 2d_c$. The critical spalling depth at failure can be solved in Equations (1), (2), (6) and (7) by assuming that the pillar centre distance is constant; that is:

$$d_c(S_c) = \frac{1}{2} \left[w - \left(\frac{\gamma H S_c h^\beta C^2}{K \Theta^\alpha} \right)^{\frac{1}{2+\alpha}} \right] \quad (9)$$

$$d_c(S_c) = \frac{1}{2} \left[w - \left(\frac{\gamma H S_c h^{0.11} C^2}{27.63 \Theta^\alpha \left\{ 0.29 \left[\left(\frac{w - d_{\max}}{5h} \right)^{2.5} - 1 \right] + 1 \right\}} \right)^{\frac{1}{0.78}} \right] \quad (10)$$

where d_{\max} is maximum possible spalling.

Once the critical spalling depth is known, and the rate of spalling is known, the time elapsed to failure may then be calculated using the following formula:

$$t_c(S_c) = \frac{d_c(S_c)}{r} \quad (11)$$

where r is the rate of rib spalling in m/year.

3.2 Pillar failure caused by roof failure

3.2.1 Progressive failure of roof

Previously a number of authors have stated that pillars may also fail through progressive roof failure, which, in turn, increases the effective mining height and reduces pillar strength and stiffness of the pillar, as stated by Salamon and Wagner (1985). In this mode of failure, it is as-

sumed that the weakest element in the pillar system is the roof, i.e., the immediate strength of the roof is less or equal to coal.

In this case, the failure is driven by increased roof height through progressive failure of immediate roof. In theory, as the roof fails, due to bulking factor, the failed material will chock up at some distance into the roof and will reach the maximum height possible, provided that the pillars are not at shallow depth and the failure does not reach the surface (i.e., bulking controlled failure). However, the bulking controlled failure rarely fully develops due to the fact that as the roof failure occurs, the top of the failure will reach a certain width and the failure will be arrested. It is postulated in this analysis that the failure of the roof increases the pillar height. The final shape of the roof is not known with any certainty; it may be parabolic, ellipse or square.

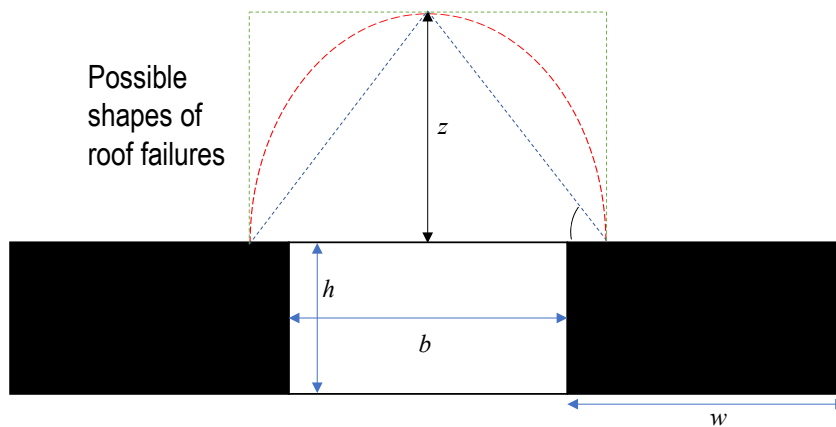


Figure 2. Section view of progressive roof failure

3.2.2 Critical mining height in case of roof failures

Similar to the above pillar spalling calculations, the critical mining height (z_c) at failure can be solved in Equations (1), (2), (6) and (7):

$$z_c(S_c) = \left[\frac{8.6(w\Theta)^{2.51}}{\gamma HC^2 S_c} \right]^{1/0.84} \quad (12)$$

where $z_c(S_c) = z + h$, and z is the roof falling height at pillar failure. It is of note that in the case of roof spalling, only slender pillar formula is utilised. This is because of the fact that for all practical purposes increased mining height due to roof spalling will result in pillars with $w/h < 5$.

Once the critical mining height (z_c) is known, the time elapsed to failure can then be estimated using the following formula:

$$t_c(S_c) = \frac{z_c(S_c) - h}{r_r} \quad (13)$$

where r_r is the rate of roof failure in m/year.

3.3 Pillar failure caused by floor failure

Three different types of floor failures were identified in the past, namely, bearing capacity failure, swelling failure and buckling failure. Buckling failures are observed only where the immediate floor strata are relatively strong, whereas weak floor strata have been associated with both bearing capacity failure and swelling mechanisms (Mo, 2019).

The bearing capacity failure can occur during mining and many years after mining due to environmental factors. In this failure mode, the floor is (or become over a period of time) the weakest element in the pillar system. Many attempts have been made to adjust the bearing capacity theory from civil engineering to coal mining environment. However, the calculation of ultimate bearing capacity developed by Terzaghi and others may not be applicable to the case of a mine roadway (Galvin, 2016). It is because the calculated bearing capacity is based upon a failure mechanism in which the floor material would move upwards beneath pillars adjacent to that below which the bearing failure occurs. Furthermore, the slip circle method fails if the angle of friction of the floor is not zero. Therefore, a novel analytical model is developed. In the mechanism considered here, a mass A of the floor material rotates as in Bishop's slip circle method and a mass B slides up into the roadway, to each side of the roadway centreline, as shown in Figure 3.

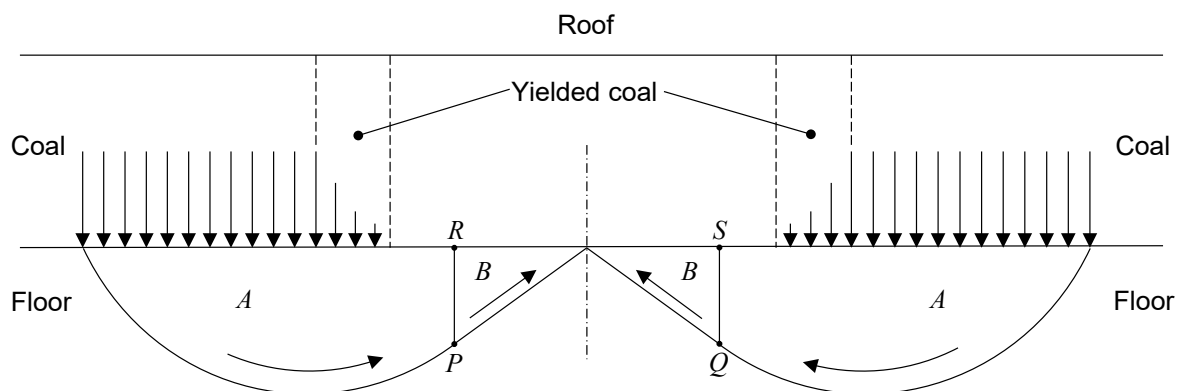


Figure 3 A limiting equilibrium model for assessing the bearing capacity of soft floor

As shown above, the vertical stress is taken to be uniform in the elastic cores of the adjacent pillars, and to vary parabolically within yielded coal as indicated a numerical analysis conducted by the authors (Wei et al, 2022). Input data to the analysis comprises the cohesion, angle of friction and unit weight of each floor layer, roadway width, and depth of yielding into a pillar.

For example, for a 12m wide pillar (with a factor of safety of 2.16) at 100m depth of mining, the figure below shows the bearing capacity of floor in relation to its cohesion and the maximum allowable average pillar stress. The other input parameters are: 6m roadway width, 1.5m depth of yielding into the pillar in long-term, 25 degrees of angle of friction, and 25kN/m³ of rock unit weight.

As evident in Figure 4, the floor bearing capacity increases linearly with increasing cohesion. For a pillar with 12m pillar width at 100m depth of mining, the tributary load is approximately 5.6MPa according to Equation (7). The maximum allowable average pillar stress is approximately 5.6MPa when the cohesion is lower than 0.31MPa. Thus, for this pillar scenario, a bearing capacity failure would occur if the cohesion of floor deteriorates to a value that is lower than 0.31MPa in the long-term.

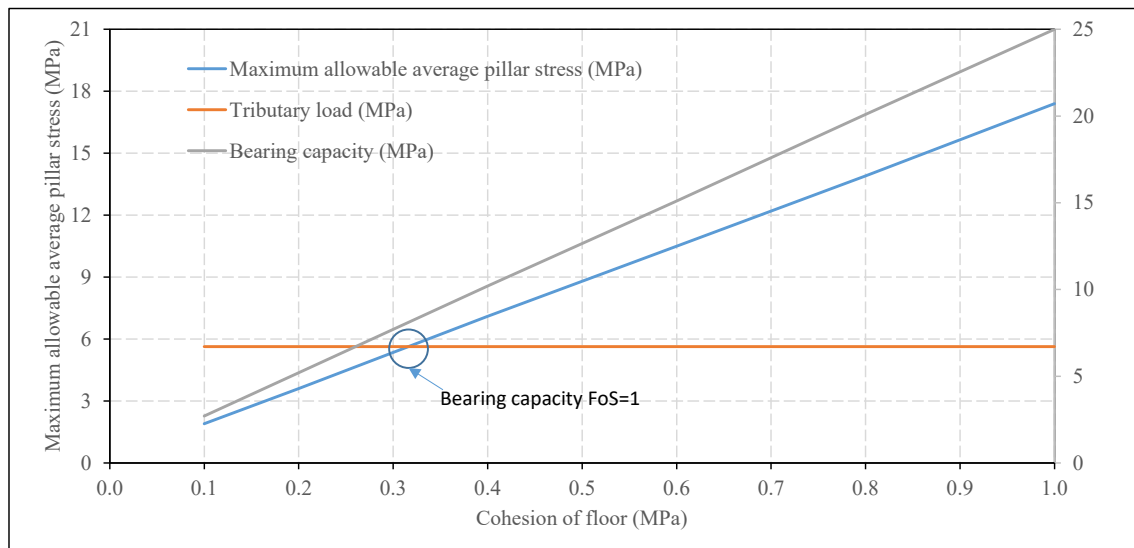


Figure 4 An example of the bearing capacity of soft floor in relation to its cohesion

4 CONCLUSIONS

This study investigates the long-term stability of coal pillars by considering the three pillar system failure modes: (i) pillar failures due to pillar spalling (i.e., reduced pillar width), (ii) pillar failures due to continuous roof failures (i.e., increased mining height), and (iii) pillar failures due to weakened floor.

The concept of 'geometrical limits' was implemented to estimate the critical spalling depth for pillar failure caused by rib spalling, and the critical mining height for pillar failure due to roof falling in long-term. A limiting equilibrium model has been developed to quantitatively assess the bearing capacity of soft floor, hence the pillar failure caused by deterioration of floor in the long-term. The assessment approach proposed in this study can help to quantify the long-term stability of coal pillars.

5 REFERENCE

- Canbulat, I, 2010. Life of Coal Pillars and Design Considerations, *Second Australian Ground Control in Mining Conference*. Sydney, Australia.
- Canbulat, I and Ryder, J, 2002. Prediction of surface subsidence and sinkholes, in *Proceedings of SANIRE 2002 Symposium: Redefining the Boundaries*, Vereeniging, South Africa.
- Galvin, J M, 2016. *Ground engineering principles and practices for underground coal mining*, (Springer).
- Madden, B, Canbulat, I. and York, G, 1998. Current South African coal pillar research, *Journal of the Southern African Institute of Mining and Metallurgy*, 98(1), 7-10.
- Mo, S, 2019. Floor heave mechanisms in underground coal mine roadways, PhD Thesis, University of New South Wales, Sydney, Australia.
- Salamon, M, Canbulat, I and Ryder, J, 2006. Development of seam-specific strength formulae for South African collieries.
- Salamon, M, Galvin, J, Hocking, G and Anderson, I, 1996. Coal pillar strength from back-calculation. University of New South Wales, Sydney.
- Salamon, M and Munro, A, 1967. A study of the strength of coal pillars, *Journal of the Southern African Institute of Mining and Metallurgy*, 68(2), 55-67.

- Salamon, M, Ozbay, M and Madden, B, 1998. Life and design of bord-and-pillar workings affected by pillar scaling, *Journal of the Southern African Institute of Mining and Metallurgy*, 98(3), 135-145.
- Salamon, M and Wagner, H, 1985. Practical experiences in the design of coal pillars, in *Proceedings Proceedings of the 21st International Conference of Safety in Mines Research Institutes*, pp 3-9 (CRC Press Sydney).
- van der Merwe, J, 1993. Revised strength factor for coal in the Vaal Basin, *Journal of the Southern African Institute of Mining and Metallurgy*, 93(3), 71-77.
- van der Merwe, J, 2003. New pillar strength formula for South African coal, *Journal of the Southern African Institute of Mining and Metallurgy*, 103(5), 281-292.
- Wagner, H, 1980. Pillar design in coal mines, *Journal of the Southern African Institute of Mining and Metallurgy*, 80(1), 37-45.
- Wei, C, Watson, J and Canbulat, I, 2022. Numerical analysis of long-term stability of coal pillar caused by rib spalling, in *Proceedings IX Latin American Rock Mechanics Symposium*, Asuncion, Paraguay (Under review).

TECHNICAL PAPERS

An integrated approach for monitoring movements and stability of slopes

N. Tokashiki, T. Ito and Ö. Aydan
University of the Ryukyus, Okinawa, Japan

N. Shimizu
Yamaguchi University, Ube, Japan

N. Iwata, K. Kanose, Y. Saruwatari
Chuden Engineering Consultants, Hiroshima, Japan

H. Takamura, T. Kuroda
Nishimatsu Construction Co. Ltd., Tokyo, Japan

K. Suzuki, T. Miyagi, N. Okabe
Green Earth NPO, Okinawa, Japan

Y. Shuri
Asahi Consultants Co., Urasoe, Okinawa, Japan

S. Nakamine
Chubu Civil Engineering Section of Okinawa Prefectural Gov., Okinawa, Japan

ABSTRACT:

In this study, the authors describe an integrated approach for monitoring movements and assessing the stability of slopes utilizing, satellite based remote sensing techniques, laser scanning and contact type monitoring schemes. Satellite based remote sensing techniques utilizes SAR and its derivatives while laser technology is based on UAV and/or ground-based laser techniques. Upon identifying one or several critical locations, the contact type multi-parameter monitoring techniques are implemented for higher accuracy and prompt actions. The principles of this integrated approach and its applications to several rock engineering sites are briefly explained. It is shown that this new technology could be a very powerful tool for monitoring and assessing rock engineering structures.

1 INTRODUCTION

Slope failures may be caused as a result of various triggering factors; such as geological conditions, topography, time-dependent variation of physical and mechanical properties of discontinuities, geomechanical characteristics of geo-materials constituting the slope, groundwater, dynamic forces from natural and artificial sources and surface loading. Therefore, the short-term and long-term monitoring of man-made as well as natural structures are essential for assessing their stability and the integrated utilization of satellite, laser and contact monitoring technologies may be quite suitable for this purpose. Remote sensing monitoring technologies such as SAR or its derivatives are desirable in monitoring structures at a large scale and it can be utilized to identify areas with large movements and the laser scanners, which can be ground-based or air-borne, can be utilized to monitor in localized manner at a smaller scale. As the laser scanners are somewhat heavy, unmanned aerial vehicles (UAV) should be capable of lifting off and scanning under stable conditions. These days, unmanned helicopters can be used for this purpose as present drones cannot handle the heavy laser scanning equipments. Once the specific areas are identified, contact type monitoring systems consisting of relative displacement, groundwater fluctuations, gravitational tilting, in-situ acoustic emissions and climatic conditions can be

utilized for checking remote sensing monitoring systems as well as introducing some criteria for different warning levels for the stability. The authors explain briefly the principles of this integrated approach and present several applications in rock engineering. It is shown that this new technology could be a very powerful tool in rock engineering.

2 ELEMENTS OF INTEGRATED APPROACH

As slopes involve large areas, it is essential to evaluate their state and time response in a global scale through satellite or airborne remote sensing techniques. Once critical area/s or location/s are identified in local scale, laser-scanning techniques can be utilized for better accuracy and denser coverage of the identified critical areas or locations. Due to issues associated with accuracy and prompt time-response, the spot-like multi-parameters monitoring techniques have to be implemented. Within this frame-work, all these techniques should be utilized in a harmonious manner. In this section, the essential components of an integrated approach for monitoring movements and assessing the stability of slopes, which fundamentally consists of three major components, namely, satellite based remote sensing techniques, laser scanning and contact type monitoring schemes, are explained.

2.1 Satellite-based Remote Sensing

Synthetic-aperture radar (SAR) is an imaging radar mounted on an airborne or spaceborne moving platform (Figure 1(a)). It transmits electromagnetic waves (EMs) sequentially and the echoes are collected and digitized and stored for processing. As transmission and reception of EMs occur at different times, they are mapped to different positions. The well-ordered combination of the received signals results in a virtual aperture. It is therefore called "synthetic aperture" of imaging radar. The range direction is parallel to the flight track and perpendicular to the azimuth direction. SAR utilizes the amplitude and the absolute phase of the backscattered radar signal. The wavelength of EMs ranges from a few millimeters to tens of centimeters. The amplitude image records include information on the terrain slope and surface roughness, while the phase image records are the information on the distance between the satellite and the Earth's surface. As the reflected signals of electromagnetic waves affected by the topography and objects on the ground surface, foreshortening and shadow occurs in reflected signals (Figure 1(b)). **Layover** occurs when the radar beam reaches the top of a tall feature before it reaches the base. **Layover effects** on a radar image is very similar to the effects resulting from foreshortening.

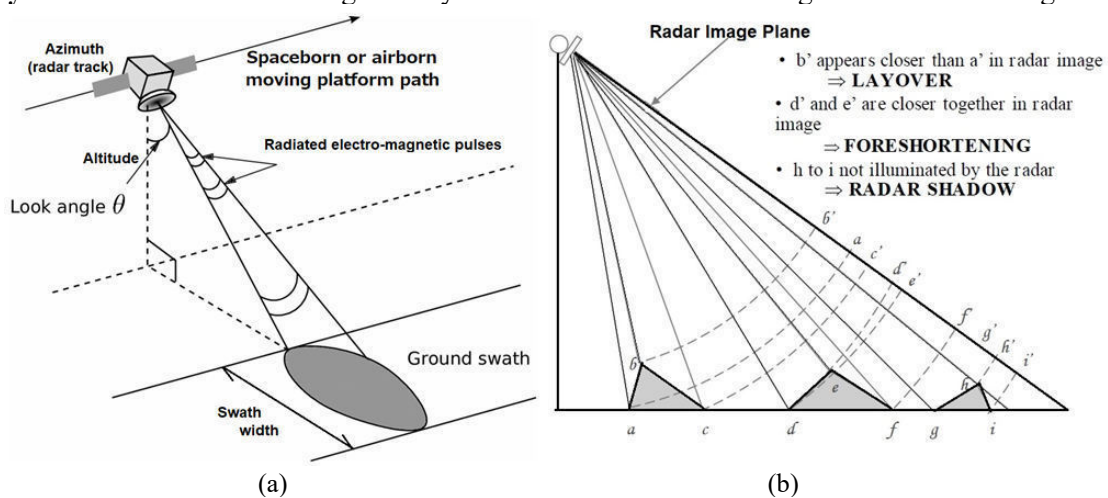


Figure 1. (a) Main concept of the moving platform radar (from Laukness, 2010), and (b) Geometric distortions in radar imaging (from Zyl and Kim, 2011).

Interferometry Synthetic-Aperture Radar (InSAR) utilizes the differential phase of two or more SAR images obtained at different times along the same trajectory. Differential Interferometry SAR (DInSAR) is used to identify surface movements through time (e.g., Ferretti 2014) and it is a radar technique for geodesy and remote sensing. The technique can measure centimetre-scale changes in deformation over spans of days to years. It has been applied for monitoring of natural hazards, such as earthquakes, volcanoes and landslides, and in structural engineering, in particular monitoring of subsidence and structural stability. InSAR has the potential to detect ground surface motion phenomena with the accuracy of a small fraction of the radar wavelength, usually from 3 (X-band) to 24 cm (L-band) on large areas.

In general, detection accuracy is estimated to be 1/10 to 1/15 of the wavelength. There are some limitations, such as the size and geometry of the monitoring area and the vegetation that covers the site. The ascending and descending tracks observe a slope movement that is not facing N or S. The vegetation causes temporal decorrelation and thus inability to distinguish between a local slope movement and a vegetation movement. Low frequency SAR systems (e.g. L-band SAR satellites such as Japanese ALOS-2) can reduce this limitation to some extent by its penetration capacity. However, observations by ALOS-2 in the same mode are performed usually about several times a year, and acquisition data is charged. Satellites with shorter wavelengths (e.g. C-band SAR satellites such as Sentinel-1A/B (S-1A/B)) can reduce the decorrelation due to vegetation growth by a frequent revisit time. S-1A/B revisits a track every 12 days and offers a good opportunity for monitoring ground surface displacements as S-1A provides the data by free of charge.

Small Baseline Subset (SBAS) technique (Berardino et al. 2002) is one of the techniques to reduce the decorrelation effect caused by the noises and errors from many interferograms. SBAS method is employed in this study along with the quadratic model (Berardino et. al. 2002), which is implemented using the software ENVI SARscape 5.5.1 (Sarmap 2020).

2.2 *Ground or UAV-based Laser Scanning*

Laser scanning technology has become quite advanced and it has been now extensively used for assessing the geometry of structures as well as the monitoring of engineering structures. The recent applications involve three-dimensional scanning of existing or newly constructed structures. They provide digital data on the structure, which can be used for different purposes such as checking the construction geometry with designed geometry, for carrying out numerical computations for the performance under static and dynamic conditions.

The basic principle is based on the emission of a light signal (Laser) by a transmitter and receiving the return signal by a receiver. The scanner uses different techniques for distance calculation that distinguish the type of instrument in the receiving phase. The distance is computed from the time elapsed between the emission of the laser and the reception of the return signal or phase shift based when the computation is carried out by comparing the phases of the output and return signals. The laser scanner devices operate by rotating a pulsed laser light at high speed and measuring reflected pulses with a sensor (Figure 2). The scanner automatically rotates around its vertical axis and an oscillating mirror moves the beam up and down. The scanner calculates the distance of a measured point together with its angular parameters. The measured points constitute a set of points called cloud points, which are used to quantify the geometry of the structure or surface in 3D. Laser scanners can be ground-based or air-borne. As they are somewhat heavy, unmanned aerial vehicles (UAV) should be capable of lifting off and scanning under stable conditions. These days, unmanned helicopters are used for this purpose as present drones cannot handle the heavy laser scanning equipment (Figure 3).



Figure 2: Views of the utilization of laser scanners in Ryukyu Archipelago

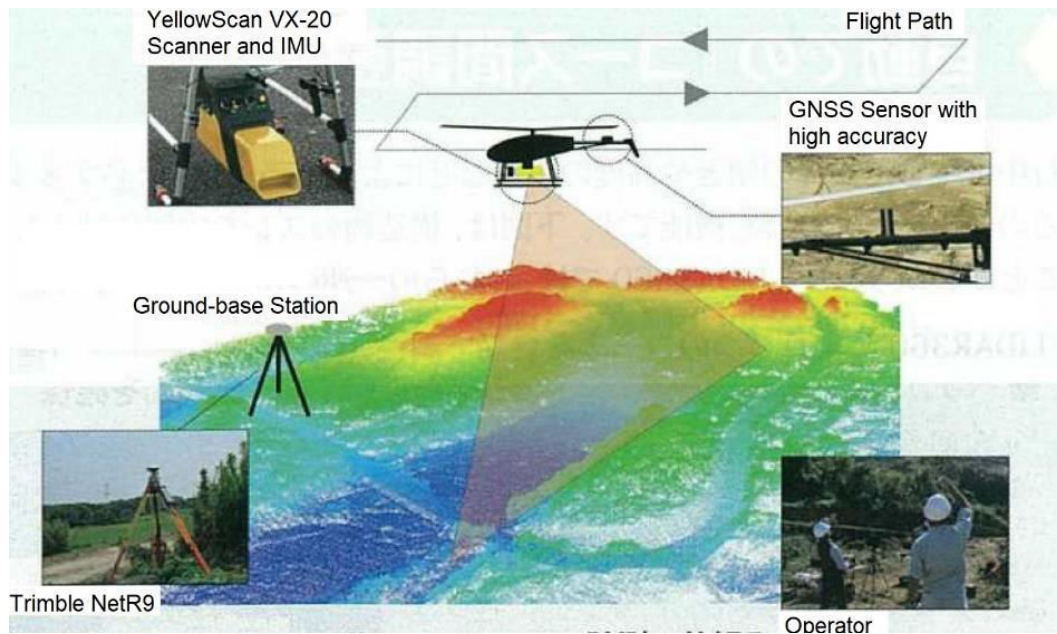


Figure 3. Principles and system of UAV-based laser scanning.

2.3 Sensor-based Multi-parameter Monitoring

As for sensor-based monitoring within the frame-work of the integrated approach, a multi-parameter monitoring concept can be utilized at a given site/s at higher level of accuracy for monitoring crack movements and making prompt decisions for assessing the stability. This concept was used by the authors in several projects in the past and it was implemented at Nakagusuku Castle first time in Okinawa Prefecture, Japan (Aydan et al. 2005; Tokashiki and Aydan 2019; Aydan 2020). On the bases of evaluations at global and local scales through the utilization of satellite-based remote sensing and laser-based scanning as well as the risk of cliff collapse on the nearby settlement area and structures, a site shown in Figure 4 was selected for installing multi-parameter monitoring system for sensor-based monitoring along the major cliff in Miyagi Island. At the selected site, there are separation cracks along the cliff and their widths are generally more than 1000 mm. A multi-parameter system consisting of gap sensors, inclinometers, climatic sensors, an accelerometer was installed on October 3, 2021 as shown in Figure 4(a). Besides the inclinometer (G-Sensor), two OKIPPA devices were installed. The OKIPPA device can also be used like an extensometer to measure the crack separation movements. At this site, we utilize OKIPPA system for both measuring inclinations and crack separation as shown in Figure 4(b).

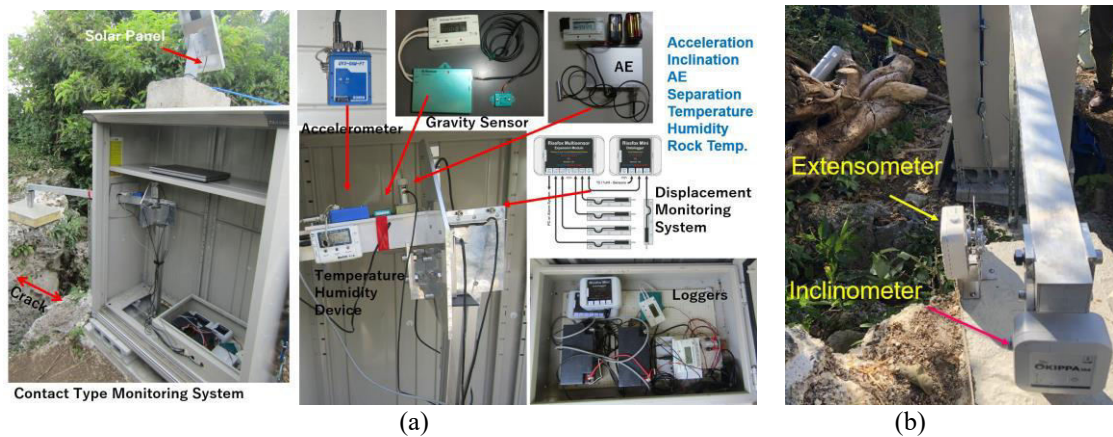


Figure 4. Views of sensor-based multi-parameter monitoring system

3 APPLICATIONS

On the bases of satellite based remote-sensing as well as past studies, movements of slopes constituting the eastern side of Okinawa Main Island are noted and their stability was of great concern for the authorities and local people. Among all areas where large slope movements have been occurring, the cliff site at Miyagi Island and Toma landslide in Okinawa Main Island have been selected for more detailed monitoring movements and assessing their stability as applications of the integrated approach described in the previous section.

3.1 Application to Miyagi Island Cliff Monitoring and Stability Assessment

Miyagi Island is located at east of Okinawa Main Island and connected through bridges to the main island. The geology consists of Ryukyu limestone on top and intercalated sedimentary rocks such as sandstone, mudstone beneath. The mudstone and sandstone layers are particularly prone to weathering. As a result, there are many overhanging Ryukyu limestone cliffs due to differential weathering of mudstone and sandstone layers beneath as seen in Figure 5(b). There are also huge boulders with a diameter up to 20 m in the settlement area (Figure 5(a)). Furthermore, Miyagi Island is affected by normal faults and it has a triangular shape in plane.

DInSAR analyses clearly showed that some movements along the cliff have been taking place as seen in Figure 5(c). During site investigations, it was noted that there are open cracks at the crest of the cliff. The estimated thickness of the Ryukyu limestone formation is about 18-22 m at the site. Cracks have been mapped (Figure 18b) using a portable GPS (Global Positioning System) device with the support of a RTK (Real-time Kinematic) station on the grounds of the University of the Ryukyus (Figure 18a). It was decided to carry out some detailed investigations and analyses. For increasing the accuracy of SAR images at the cliff site, a marker station was established as seen in Figure 18(d).

A portable laser-scanning device was utilized to evaluate the condition and the geometry of the cliff (Figure 18c). The cliff has been recently re-scanned using the system shown in Figure 3. Figure 7 show an image of the cliff scanned by the portable system. Despite very undesirable conditions, the geometry of the cliff was clearly obtained. However, areas appearing as dark areas could not be scanned. Some of these dark areas are cavities in the Ryukyu limestone formation. The height of the cliff was about 18 m high, which roughly corresponds to the thickness of the limestone formation. Furthermore, the erosion depth was up to 4 m.

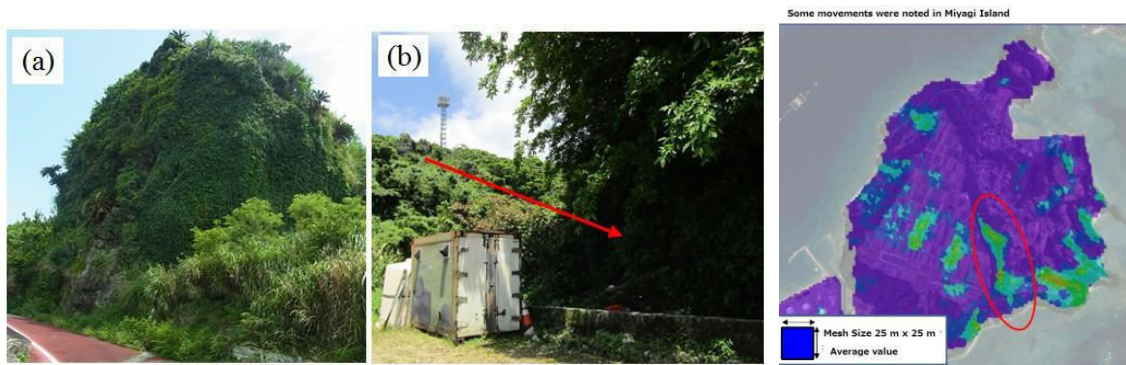
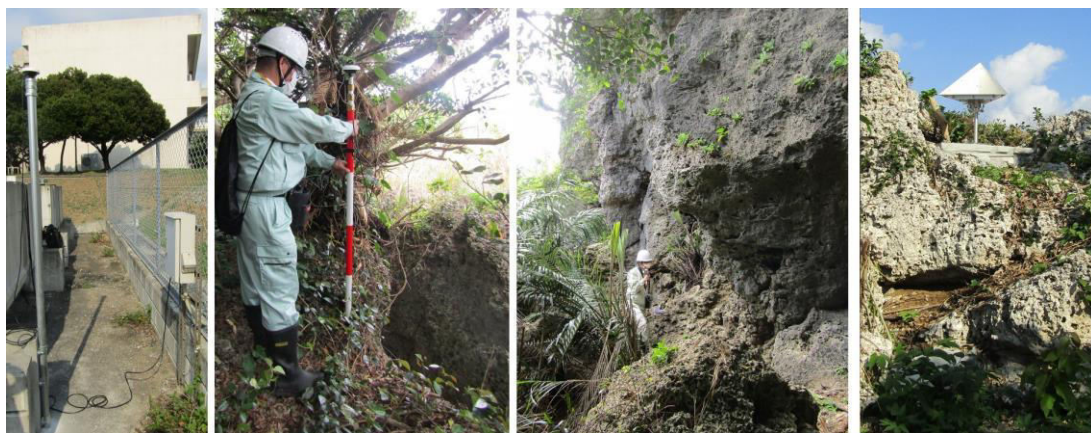


Figure 5. (a,b) Views of boulders in the Miyagijima Village (c) DInSAR analysis.



(a) RTK (b) Crack mapping (c) Laser Scanning of the cliff (d) Marker
 Figure 6. Views of RTK, crack mapping, laser scanning of the cliff and Marker for SAR.

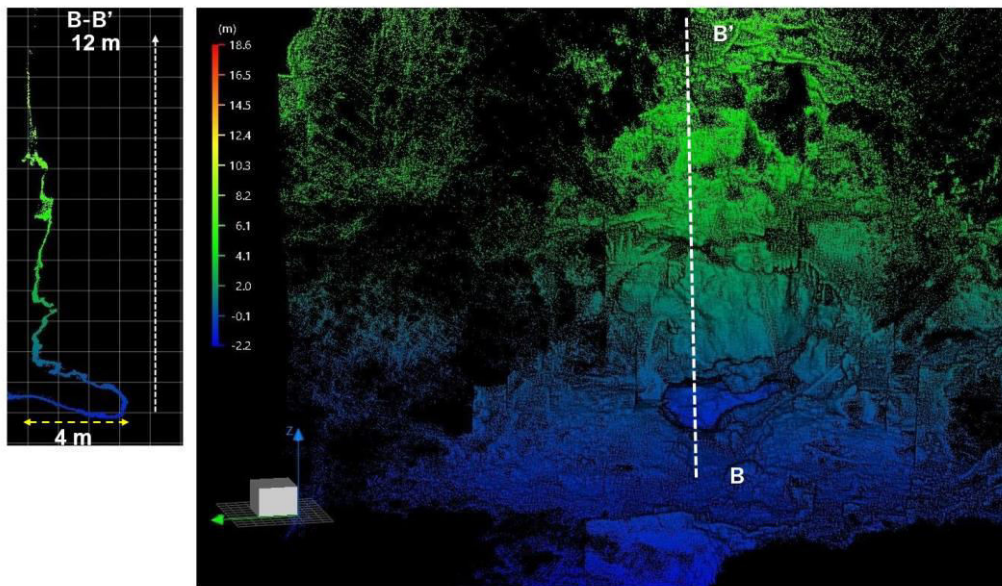


Figure 7. Scanned image of the cliff with an underground opening at the toe region.

Figure 8 shows a 3D and cross section of the same site scanned using an UAV-based scanner where the enlargement of roadway is planned. As can be seen from this figure, the cliff and the profile are accurately obtained and these data could be used for the stability assessments of the potentially unstable cliff.

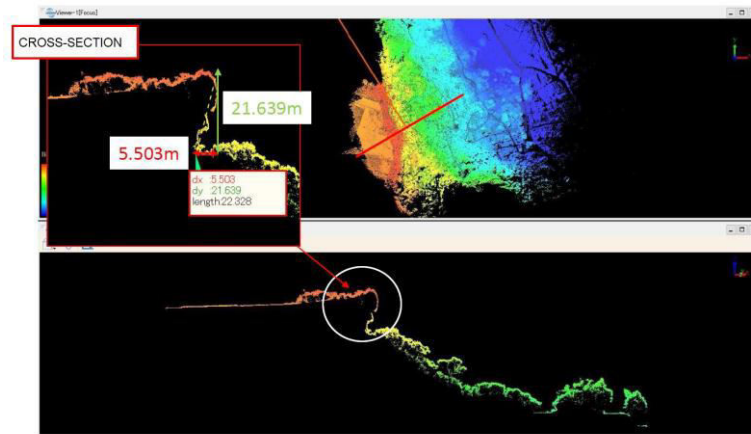


Figure 8. Images of the cliff by UAV-based scanning device and its cross-section.

As mentioned previously, the sensor-based multi-parameter monitoring system involves the measurement of 3D displacement response of open crack (width is about 1000 mm) and OKIP-PA extensometer, climatic conditions (temperature (rock and air), humidity), inclination (G-Sensor and OKIPPA). Figure 9 shows an example of crack response and temperature during the period of 2021 Oct.4 and 2022 Feb. 13. As noted from the figure, crack tends to widen and the potentially unstable rock block tends to tilt towards the cliff. However, the cliff opening is limited to 0.6 mm for the period. If the potentially unstable block is assumed to be 18 m high, this will cause 0.0019 degree rigid body rotation. Therefore, we could not notice any major change in OKIPPA inclinometer.

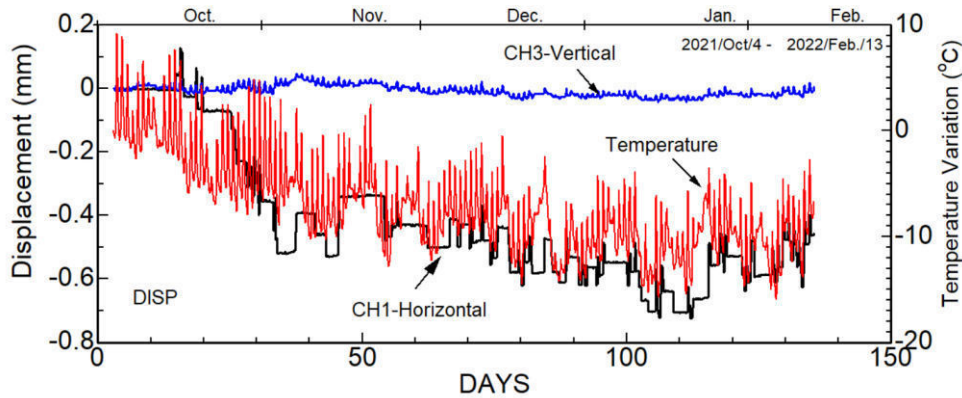


Figure 9. Displacement response of crack measured by the multi-parameter system.

3.2 Application to Toma Landslide Monitoring

Toma landslide is located in the eastern side of Okinawa Main Island. The geology consists of intercalated sedimentary rocks such as sandstone, mudstone, belonging to Shimajiri formation. The mudstone and sandstone layers are particularly prone to weathering. Furthermore, there are many normal faults and there was a large-scale landslide at Kita-Uebaru district in 2010, which was about 2 km south of Toma landslide (Tokashiki and Aydan, 2010).

As a preliminary evaluation of satellite remote sensing techniques, 22 Ascending images (September 26, 2014-June 12, 2020) taken by ALOS-2 from the west (behind the slope) and 24 Descending images (February 28, 2015 ~to November 13, 2021) were used to perform time series interferometric SAR using the SBAS method. Figure 10 shows the LOS (line-of-sight) displacement distribution evaluated from these images and the time series of monitoring points in the Ascending direction; negative LOS displacements indicate the direction away from the satellite direction or the subsidence direction. LOS displacements at the slope ridge near moni-

toring points A to E are -80 to -200 mm in the Ascending direction and -20 to -60 mm in the Descending direction, both negative, and the Ascending direction is predominant. This indicates that eastward slip occurs along the slope. The LOS displacement at monitoring point F at the top of the slope is almost negligible, indicating that this is a surface landslide. The absolute value of displacement varies from place to place, but it is clear that there is an annual LOS displacement of 10 to 30 mm/year. The site-observations indicate some separation movements of cracks in some simple structures in the landslide area and they are consistent with inferred displacement values. Furthermore, the maximum displacement rate measured previously by extensometers was about 30 mm/year, which is consistent with the SBAS results.

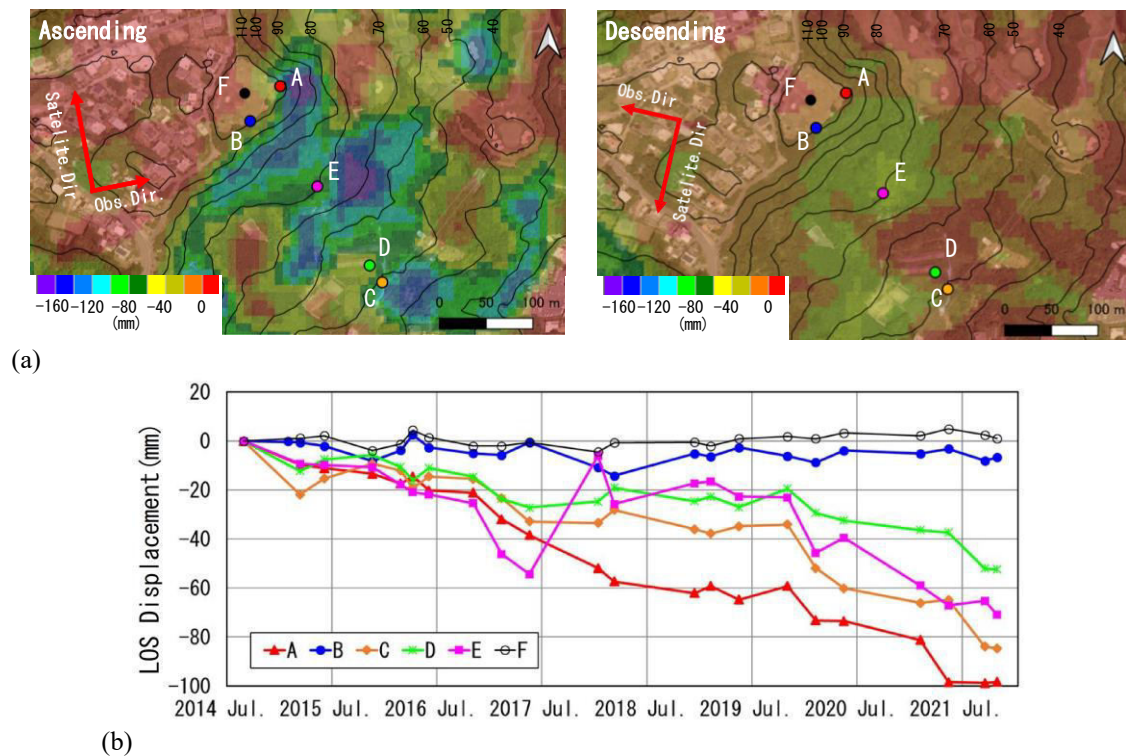


Figure 10. (a) Areal LOS displacement distribution and (b) the time series of monitoring points in the Ascending direction.

In the Toma landslide area, we have installed 4 OKIPPA inclinometers and one GNSS station for GPS monitoring as seen in Figure 11. The base GNSS Station was installed in the ground of the University of the Ryukyus. The monitoring was initiated in October 21, 2021 and results for OKIPPA inclinometers are shown in Figure 12 together with rainfall data. The variations are within 0.05 and 0.4 degrees. As noted from the plotted data, the rainfall has great influence on the movements as expected. Despite some technical problems during the initial period of installation, the overall trends of inclinometers indicate that movements associated with landslide despite some counter-measures have been continuing. The main issue with inclinometers is that the displacement value could not be evaluated directly. However, if the inclinometer at the surface of landslide body moves in the direction of sliding and tilted, the displacement computed from the multiplication of tilt angle multiplied by the depth of the landslide may correspond to movements of landslide body. On the bases of boring data of the investigations previously, the movements are limited to 4-5 m from the surface of the landslide body. If the procedure suggested is adopted, the expected movements would be within 5-35 mm for the measurement period, which are consistent with data from satellite-based remote sensing SBAS evaluations.

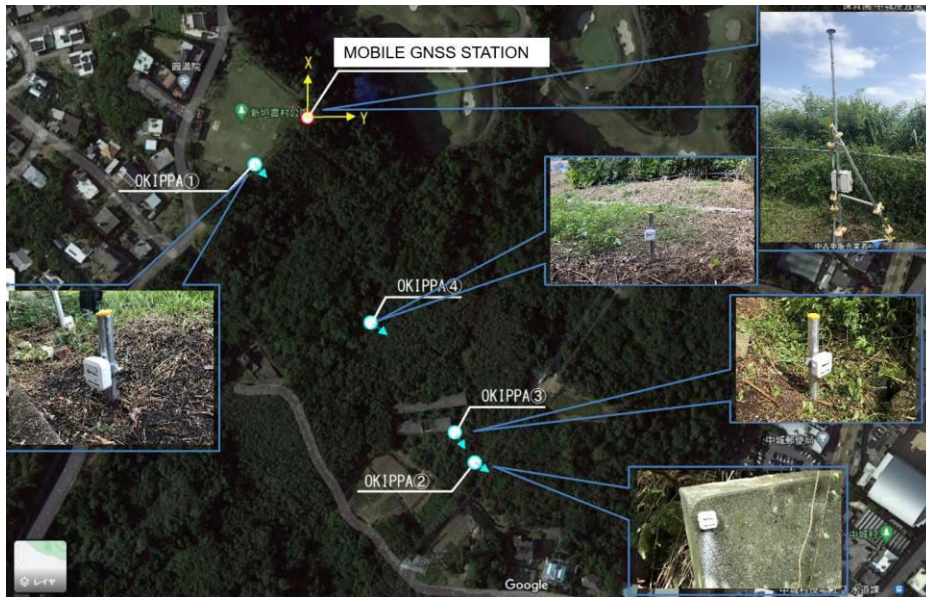


Figure 11. Locations of OKIPPA inclinometers and GNSS monitoring point in the Toma landslide area.

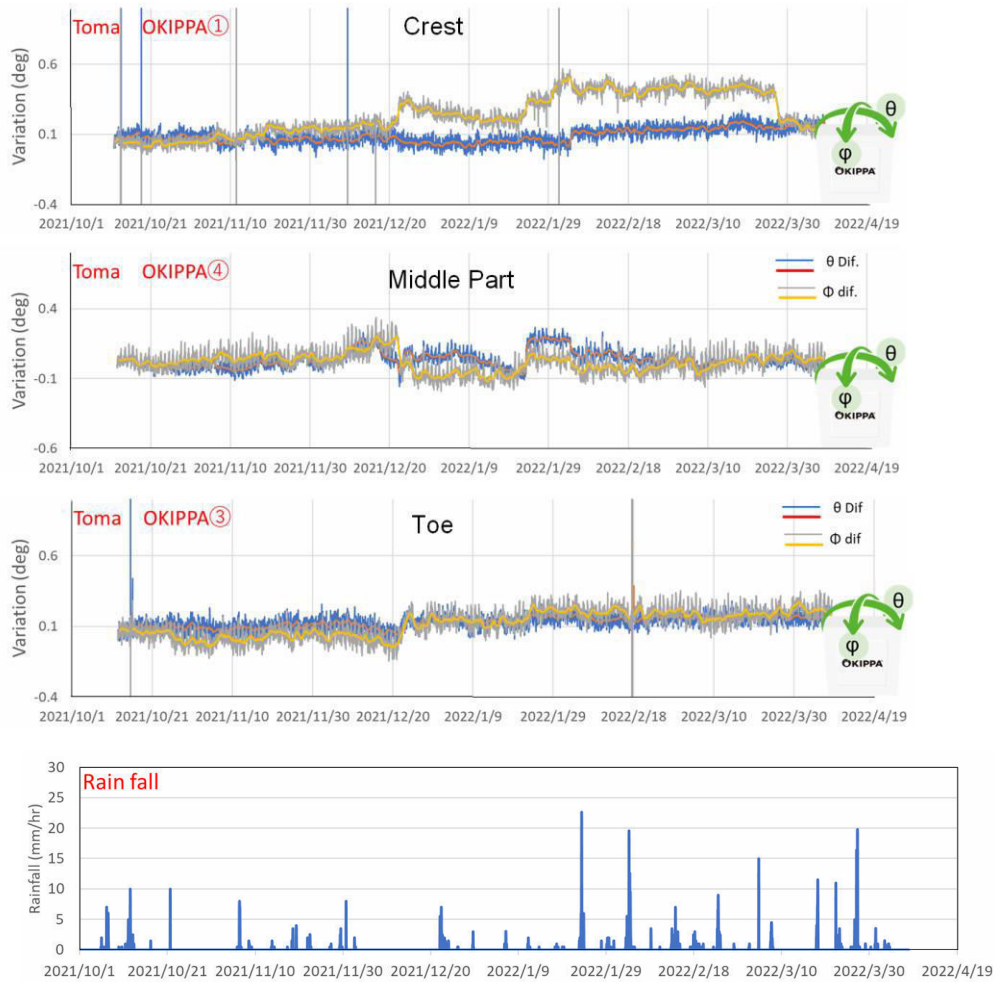


Figure 12. Inclination measurements in relation to rainfall for Toma landslide area.

4 CONCLUSIONS

Although it is still at the preliminary stage yet, some of the conclusions from this integrated approach utilizing satellite-based remote sensing techniques, UAV/ground-based laser technologies and sensor-based multi-parameter system for monitoring movements and stability of slopes are as follow:

- 1) Long-term monitoring of structures is possible, and they provide better assessment and evaluation of deformation response of structures as compared with point-like measurements, only.
- 2) These technologies can be easily used in any place, where the human-based measurements may be unsafe.
- 3) The stability assessment also requires some analyses of slopes using the possible appropriate methods. The results from such analyses would be quite useful for interpretation and the assessment of the stability of slopes.

ACKNOWLEDGEMENTS

Some part of this study was financially supported by Shimatate Kyokai, Okinawa and it is gratefully acknowledged. The authors also acknowledge JAXA for ALOS-2 data used in this study.

REFERENCES

- Aydan, Ö. 2018. Some Thoughts on the Risk of Natural Disasters in Ryukyu Archipelago. *International Journal of Environmental Science and Development*, 9(10), 282-289.
- Aydan, Ö. 2020. *Rock Mechanics and Rock Engineering: Volume 2: Applications*. CRC Press, Taylor and Francis Group, 383p.
- Aydan, Ö., Tokashiki, N. 2019. Tsunami Boulders and Their Implications on the Mega Earthquake Potential along Ryukyu Archipelago, Japan. *Bull. of Eng. Geol. and Env.*, 78, 3917–3925.
- Aydan, Ö., Daido, M., Tano, H., Tokashiki, N., Ohkubo, K. 2005. *A real-time multi-parameter monitoring system for assessing the stability of tunnels during excavation*. ITA Conference, Istanbul, 1253-1259.
- Curlander, John C., McDonough, Robert N., 1992. *Synthetic Aperture Radar: Systems and Signal Processing*. Remote Sensing and Image Processing. Wiley.
- Ferretti A. 2014. Satellite InSAR data: reservoir monitoring from space. *EAGE Pub.*, The Netherlands.
- Ito, T., Aydan, Ö. Tokashiki N. 2022. DInSAR Technique and Laser Scanning Technology and Their Utilizations in Rock Engineering and Natural Disaster Management and Prevention. *Journal of Research Institute for Islands and Sustainability (RIIS)* (in Press).
- Laukness, T.R. 2010. Rockslide Mapping in Norway by Means of Interferometric SAR Time Series Analysis. *Doctorate Thesis*, University of Tromso, 112p.
- Özcan, Tunar, N., Aydan, Ö., Murayama, Y., Horiuchi, K., Ulusay, R. 2021. A study on model experiments and numerical simulations on rockfalls and its utilization to assess the rockfall hazards in Miyagi Island (Japan) and Cappadocia (Turkey). *IACMAG*, Torino, 482-490.
- Berardino P, Fornaro G, Lanari R, Sansosti E. 2002. A new algorithm for surface deformation monitoring based on small baseline differential SAR interferograms. *IEEE Transactions on Geoscience and Remote Sensing*, 40(11), 2375–2383.
- Raucoules D, Colesanti C, Carnec, C. 2007. Use of SAR interferometry for detecting and assessing ground subsidence”. *Comptes Rendus Geoscience*, 339(5), 289-302.
- Sarmap. “Getting started with SARscape for Windows”. <http://www.sarmap.ch/> (10.03.2020)
- Tokashiki, N. Aydan, Ö. 2010. The stability assessment of overhanging Ryukyu limestone cliffs with an emphasis on the evaluation of tensile strength of Rock Mass. *J. of Geotech. Eng., JSCE*, 66(2), 397-406.
- Tokashiki, N. Aydan, Ö. N. 2019. Some examples of damage to rock masonry structures caused by recent earthquakes. *Proceedings of 2019 Rock Dynamics Summit in Okinawa*, 7-11, May, 2019, Okinawa, Japan, ISRM (Editors: Aydan, Ö., Ito, T., Seiki T., Kamemura, K., Iwata, N.), 561-566.
- Zyl, J.V. and Kim, 2011. *Synthetic Aperture Radar Polarimetry*. John Wiley & Sons, 287p.

A new approach for obtaining the shear modulus ratio during a slope failure process from instrumentation's data

E. Medina

Geomechanics and Environment S.A.C., Peru

L. Tejada

Vale S.A., Brazil

ABSTRACT:

During the slope instability process the level of deformations within the rock mass increases over time as the competency of the rock degrades and relevant parameters such as the Shear Modulus G^* diminish. Similarly, to the curve obtained in a laboratory testing for the intact rock but at much greater scale for the rock mass there will be three different stages; linear, non-linear with small deformations and non-linear with large deformations being the start of the last stage the onset of the progressive stage and the imminence of slope failure. At the open pit scale, it means that in the 1st stage cracks may be non-noticeable yet in the field while during the 2nd stage cracks will be visible during field inspections due to a progressive lack of confinement and during the 3rd stage large deformations will develop progressively until the onset of failure has been reached with the total collapse of the slope.

It has been investigated that during the slope instability process deformations will change its behavior over time from linear to non-linear ranging varying from 0.01% to 0.1% of deformation for deformable to very deformable rock mass types respectively. For purposes of simplicity in this paper it has been considered that weak/deformable rock masses will have a transition limit from linear to non-linear behavior at 0.1% of deformation. These changes affect important parameters of the rock mass such as the shear modulus that must be quantified for small to large deformations because they can be relevant to predicting the time of collapse for different rock mass qualities. For simplification some assumptions were made for the analysis method and are based on field observations of several slope instabilities, they mainly considered that; approximately at 0.1% of deformation the rock mass start to become plastic at a low rate, and the loose of confinement in the rock mass gradually increase between 0.25% - 0.7% of deformation where the failure process initiate. With these considerations, the analysis method has been used to match existing real historical data of deformations taken within a few areas of instability to understand at which average percentage of deformation it was triggered the failure mechanism as to calibrate the design/assumed elastic parameters such as E_m . The correlation obtained from the second objective will help out to verifying the above-mentioned indicators. This information will be used to set up empirically the basic indicators of collapse and be used to infer the preliminary threshold alerts for similar rock mass types used in previous research.

Finally, conclusions on the results obtained from the empirical model probed with two historical instabilities occurred in a mine located in the north of Peru and recommendations for performance monitoring will be provided. At the same time, it will be established the basis for future research on the influence of the shear modulus in the velocity and deformation of the failure mass for prediction of the time of collapse.

Keywords: shear modulus, real-time monitoring, weak/deformable rock masses, time of failure

*Shear modulus $G = E_m / 2 * (1 + \gamma)$

1 INTRODUCTION

Based on careful data processing from geotechnical instrumentation and field observations throughout the years is possible to state that a slope failure process depends on several factors, in addition to the basics identified: the material characteristics and the geology and hydrogeology conditions of the site. The slope failure process as observed in an open pit mine differs to the behavior under loading of an intact rock sample in the laboratory testing. In the reality, for weak/deformable rock masses which are the objective of this paper, the movements are visible in the field as a series of cracks once the failure mechanism has already started even though the stage of movements may be considered incipient the velocities could be around 10 mm/day or even much higher. On the other, hand brittle rock masses could exhibit cracks below 5 mm/day of measured velocity. Finally, measured velocities between 1 – 2 mm/day can be considered as noise or response to mining activities that are close to the instrumentation.

2 OBJECTIVES

- 2.1 The primary objective is to propose an analysis method that allows quantifying the variation of the shear modulus from real-time monitoring data during the failure process
- 2.2 Secondly, to investigate on the influence of the shear modulus in the rate of movement of the unstable rock mass and from these correlations to estimate critical alert levels for purposes of a safe operation
- 2.3 Lastly, and based on the previous achievements to establish the basis for future research works that determine relevant indicators from the curve of the shear modulus vs deformation (G vs ϵ) and providing with an empirical method for a reliably prediction of the time of collapse

3 METHODOLOGY

3.1 *Background*

From geotechnical instrumentation data it can be observed that during the failure process of an open pit slope of weak/deformable rock mass the level of deformations will increase over time, and similarly to what can be observed in the laboratory testing for intact rock samples the curve of deformation over time for the rock mass during an open pit slope failure present three well defined stages but at a much bigger scale where changes in the in-situ rock mass affect important parameters including the shear modulus G . These three stages include linear behavior up to deformations $\Delta < 0.1\%$, non-linear behavior with small deformations between $0.1\% < \Delta < 1\%$ that include the origin and development of the plastic zone, and non-linear behavior in a progressive stage to failure with large deformations $\Delta > 1\%$, where a critical plastic limit ($> 70\%$) for the rock mass can be reached for the area of instability (E. Medina, 1995). This last stage is of high relevancy to predicting the time of failure for different conditions of weak rock masses.

3.2 *Procedure*

Firstly, an empirical model will be used to determine deformations from measured displacements to validate/calibrate the strength parameters that were assumed. For this it was constructed the original slope geometry at the time of failure for the two historical cases of slope instability in open pit mines. Next, using a stress-strain numerical analysis software and using different strength values there were matched calculated displacement from the software with real displacements from monitoring data. Once the geotechnical model has been calibrated, the shear modulus will be determined for a deformation of 0.1% where it is expected the shear modulus will change from linear to non-linear for weak/deformable rocks. In this way, during the failure

process the shear modulus curve can be constructed by direct measure of displacements in real-time from instrumentation data as a continuous and interactive process. Thus, the shear modulus will be determined over time for the non-linear stage with small deformations during the failure process ($0.1\% < \Delta < 1\%$). Preliminary threshold alerts are proposed to be used as a first approach to estimate the onset of failure and will be adjusted in real time for the specific site conditions that exist at the failure time.

Finally, conclusions on results from the empirical model will be presented for determining the curve G vs ϵ in a more realistic way. In addition, it will be established the basis for future research on the influence of the shear modulus in the velocity of the failure and for a better prediction of the time of collapse.

4 DATA

It is important to note the instrumentation used to collect data for the historical instabilities presented herein was a Leica total station 2000 series that at the time were not considered instruments for real-time measurement. It is the intention of this work that real-time monitoring devices such as robotic total stations (RTS) should be used for a continuous data collection process when using this methodology for future performance monitoring projects being that the shear modulus curve can be constructed faster and efficiently for purposes of setting the initial threshold limits in a more realistic way.

RTS can provide vectors of movement within the area of instability, vectors are not possible to produce using radars which should be used as a complimentary monitoring tool because radars have only good accuracy in the line-of sight. Both RTS and radars are considered real-time monitoring systems. At the same time the curve of shear modulus vs deformation (G vs ϵ) will be plotted out during the failure process.

4.1 Historical Case 1

It has been utilized curves of displacement vs time for open pit slope under a failure process in low strength - weak/deformable rock masses (a typical graphic is shown in Figure 1 for a representative prism). Using the measured displacements, it was back-calculated the material's strength (m, s, a) with the Hoek & Brown criterion (Hoek, E. and Brown E.T. 1980) by creating a 2D geotechnical model with the slope geometry at the failure's time (e.g. $H = 120\text{m}$, slope angle = 35°) in the geotechnical software Phase 2.

The materials strength used in the original design was obtained from laboratory testing and geotechnical core logging and using the Mohr-Coulomb criterion ($C = 150\text{ KPa}$, $\Phi = 22^\circ$). In the numerical analysis sets of parameters were obtained by using the Hoek indexes; geological strength index GSI (see E. Hoek, P. Marinos, M. Benissi 1998) and the stress relaxation D (Hoek, E & Karzulovic, A 2000) for quality and disturbance of the rock mass respectively (graphics of these calculations can be seen in Figures 2 and 3). The analysis was made for different deformation levels (%) to obtain the shear modulus in addition to the quality index for the rock mass.

In the numerical analysis a unique deformation modulus (E_m) was used during the linear behavior of the rock mass (elastic stage). On the other hand, different deformation modulus were obtained for different percentage values of deformation for a numerical analysis in a plastic mode; 0.1, 0.15, 0.25, 0.5, 0.75, 1, 2, 3, 4 y 4.5% (see Figure 4). Moreover, as shown in Figure 5 the GSI index and stress relaxation coefficient D were determined to match deformation levels. Once these values are obtained the modulus G can be related to the degree of deformation of the rock mass.

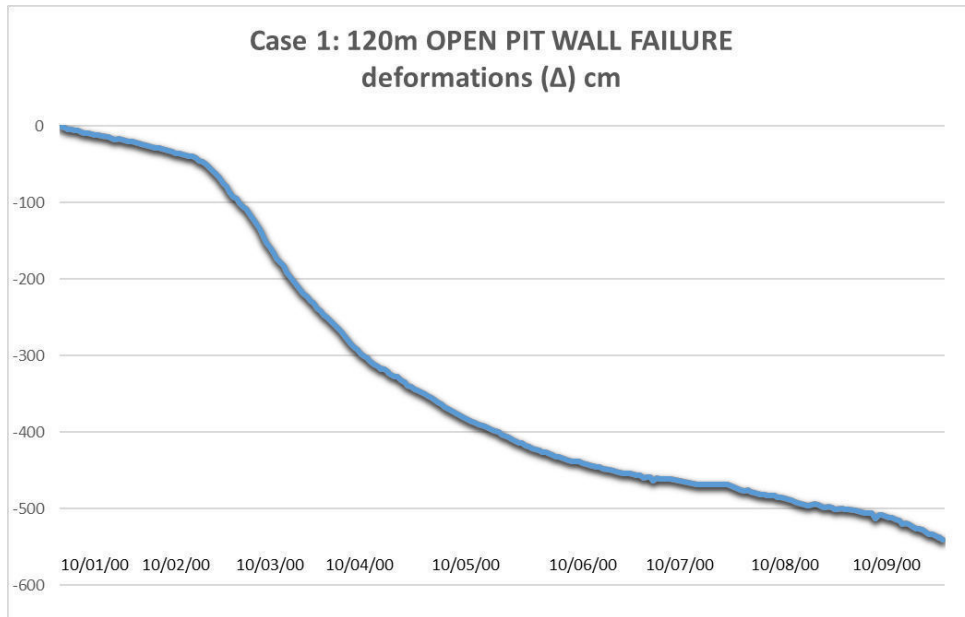


Figure 1. Case 1, Measured deformations during the slope failure process.

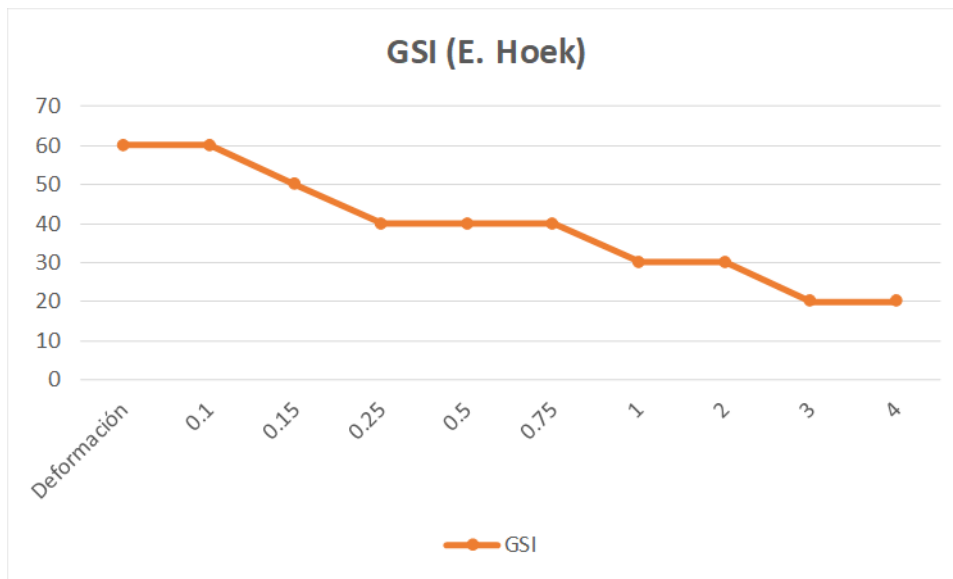


Figure 2. Case 1, Variation of the GSI with rock mass deformations.

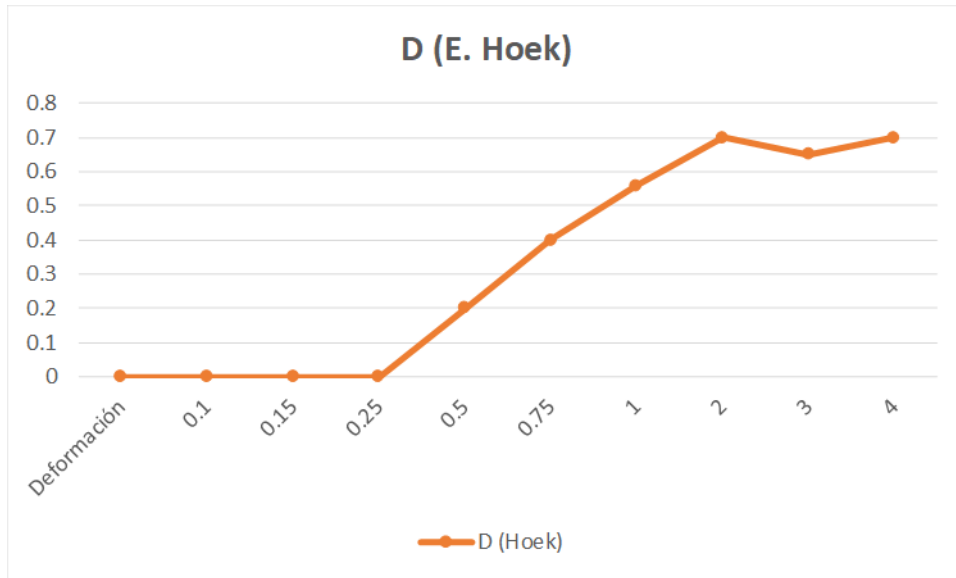


Figure 3. Case 1, Relationship between stress relaxation (D) and deformations (ϵ).

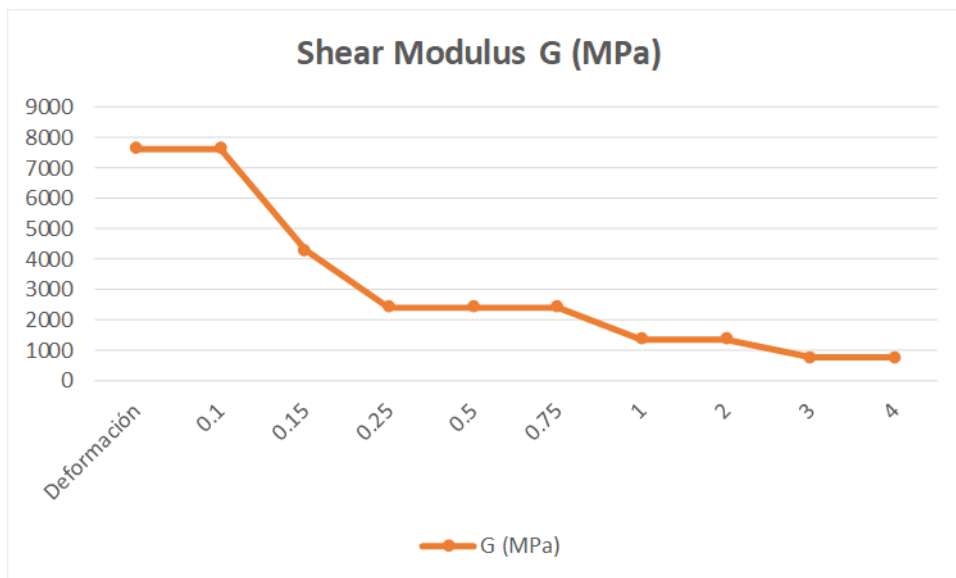


Figure 4. Case 1, Variation of the shear modulus with deformation of the rock mass.

Deformación	G (MPa)	D (Hoek)	GSI
0.1	7638.845	0	60
0.15	7638.8455	0	60
0.25	4295.6375	0	50
0.5	2415.6165	0	40
0.75	2415.6165	0.2	40
1	2415.6165	0.4	40
2	1357.9665	0.56	30
3	1357.9665	0.7	30
4	763.88	0.65	20
4.5	763.88	0.7	20

Figure 5. Case 1.- Influence of the stress relaxation factor D in the GSI and in the shear modulus G.

4.2 Historical Case 2

Like Case 1 it was utilized curves of displacement vs time for open pit slope under a failure process in low strength - weak/deformable rock masses (a typical graphic is shown in Figure 6 for a representative prism). Using the measured displacements, it was back-calculated the material's strength by creating a 2D geotechnical model with the slope geometry at the failure's time (e.g. H = 100m, slope angle = 37°) in the geotechnical software Phase 2. In the numerical analysis sets of parameters were obtained by using the Hoek indexes GSI and D for quality and stress relaxation of the rock mass respectively. The analysis was made for different deformation levels (%) to obtain the shear modulus in addition to the quality index for the rock mass.

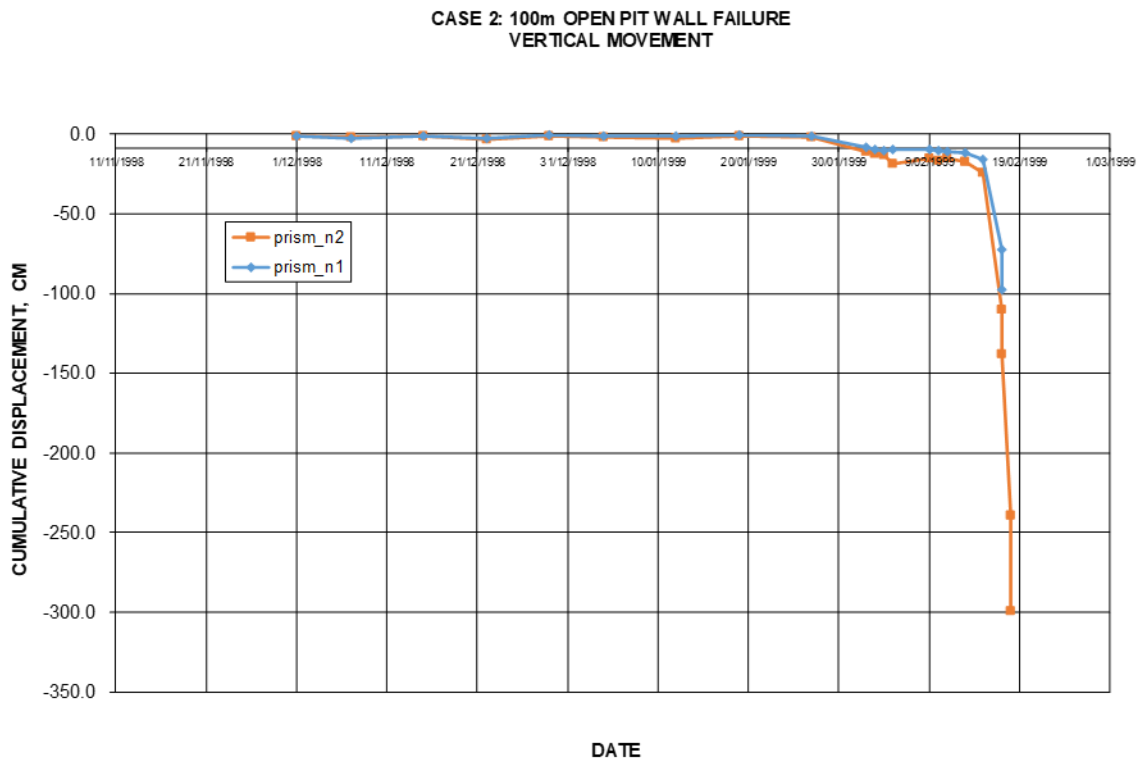


Figure 6.- Case 2, Measured deformation during the slope failure process

In the numerical analysis a unique deformation modulus (E_m) was used during the linear behavior of the rock mass (elastic stage). On the other hand, different deformation modulus were obtained for different percentage values of deformation (see Figure 6).

The values of the corresponding shear modulus of the rock mass (E_m) have been utilized to estimate the shear modulus G (see Figure 7) by using the relationship:

$$G = E_m / 2 * (1 + \gamma)$$

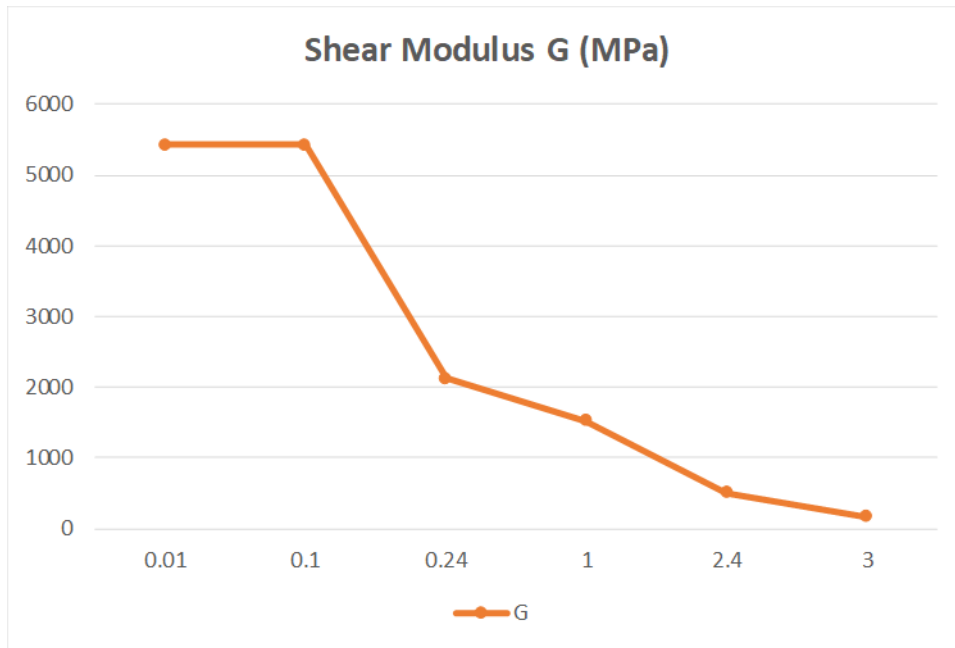


Figure 7.- Case 2, Variation of the shear modulus with deformation of the rock mass

5 RESULTS

Based on field observations and monitoring data from geotechnical instrumentation it is possible to make an interpretation of the slope performance during a failure process in an open pit mine. From detailed field inspections and a careful review of the movement vectors from monitoring data it can be obtained that the rock mass performance under a failure process is not uniform in the whole unstable mass and that local failures are being developed within the global instability mass with different velocities and accelerations and that secondary local instabilities break apart prior to the main event occurring at a global scale with the loss of integrity of the slope. In addition, it can be obtained there are important differences in the rock mass behavior at different deformation levels (%) for each sector of movement. However, it is required to select the most representative vectors of movement of the instability mass. This will allow defining the different levels of deformation of the rock mass that better represent the following stages: linear, non-linear with small deformations and non-linear with large deformations. This is also relevant to define more realistic alert thresholds that can avoid an operational impact due to a failure in the alert system. A preliminary alert threshold level is proposed for consideration as shown in Figure 8.

Alert Threshold	TARP Level	strain (%)	Shear modulus G reduction (%)	Operational action taken
Green	TARP 1	0.01 - 0.1	0	No action
Yellow	TARP 2	0.1 - 0.25	40 - 60	Field inspection and cross-check with data, install barricades
Orange	TARP 3	0.25 - 1.0	> 60	Field inspection and notify QP/geotechnical manager/Mine chief
Red	TARP 4	> 1.0		Evacuate and notify, activate ERAP

Figure 8.- Proposed alert threshold levels based on variation of the shear modulus during failure

6 CONCLUSIONS

The behavior of the rock mass shear modulus differs from the intact rock shear modulus that is measured in the laboratory testing. The rock mass shear modulus at real scale can be only measured from geotechnical instrumentation data;

It can be observed that for weak/deformable rock masses the rock mass behavior during a failure condition is linear up to an approximate strain value of 0.1% where this condition changes to non-linear up to a strain of 1% is being reached with a gradual reduction in the GSI's values. From this value a new stage with large deformations and loss of confinement is started until the total loss of integrity of the rock mass occur;

The primary instrumentation system that must be utilized to measure real-time deformations of the rock mass is a robotic total station (RTS) with a net of prisms, it allows obtaining information on the movement vectors (3D) throughout the time;

It is possible identifying the three deformation stages of the rock mass (linear, non-linear with small deformations and non-linear with large deformations) from graphics made from the geotechnical instrumentation data. This, allows using numerical analysis to develop deformation curves that matches to the real behavior of the rock mass under failure;

The present research work was obtained based on interpretation from data collected prior and during slope failures of open pit mines in weak/deformable rock masses. It cannot be generalized to all rock mass types;

Having a real-time monitoring information available it will be possible to define threshold alerts in a more realistic way based on accurate predictions of the variation of the shear modulus during the failure process for a more efficient emergency response plan;

Future research can be made for a better estimation of the failure time based on a continuous calibration process of the shear modulus with numerical analysis from geotechnical instrumentation data in real-time (integrated monitoring platform);

The geotechnical instrumentation must be highly reliable and installed prior to mining excavation activities to obtain historical data that allows the geotechnical responsible person to identifying failure mechanisms from incipient stages to taking opportune contingencies and designing effective emergency response plans;

ACKNOWLEDGEMENT

We would like to acknowledge Mr. Robert Sharon for having reviewed the abstract and providing with valuable comments to develop this paper.

REFERENCES

- Medina, E 1995, 'Estabilidade de taludes de grande altura em minas a céu aberto', Master's thesis, pp. 53–75.
- Hoek, E. and Brown E.T. 1980, 'Empirical strength criterion for rock masses', J. Geotech. Engng Div., ASCE 106 (GT9), 1013-1035.
- Hoek, E, Marinos, P, Benissi, M 1998, 'Applicability of the geological strength index (GSI) classification for very weak and sheared rock masses. The case of the Athens Schist Formation'.
- Hoek, E & Karzulovic, A 2000, 'Rock mass properties for surface mines', Society for mining, metallurgical and exploration (SME), Colorado, pp. 59–70.

Small-scale assessment of rockfall coefficients of restitution

B. Souza

University of New Hampshire, Department of Civil and Environmental Engineering, Durham, NH, USA
Université Gustave Eiffel, GERS-RRO, Bron, France

J. Benoît

University of New Hampshire, Department of Civil and Environmental Engineering, Durham, NH, USA

M. Bost

Université Gustave Eiffel, GERS-RRO, Bron, France

P. Reiffsteck

Université Gustave Eiffel, GERS-SRO, Champs sur Marne, France

N. MacAdam

University of New Hampshire, Technical Service Center, Durham, NH, USA

ABSTRACT:

Rockfall events attract significant attention and adverse reaction from the public, especially near highways and residential areas. Reliable hazard mapping and management require reliable predictions of rockfall kinematics and trajectories. However, the uncertainty related to rockfall behavior and model input parameters turns this task significantly difficult. Research conducted at the University of New Hampshire (USA) over the last decade developed Smart Rock (SR) sensors capable of instrumenting rockfall experiments while embedded in test blocks (natural rocks or fabricated concrete blocks). The latest SRs are small capsules 58.0 mm in length and 25.4 mm in diameter, equipped with a ± 400 g and a ± 16 g 3-axis accelerometer, a ± 4000 dps high-rate gyroscope, and an altimeter. This paper summarizes the results of small-scale tests to determine coefficients of restitution of a granite block lying at angles ranging between 0° and 45° . One-kilogram concrete blocks reinforced with steel fibers were released under controlled conditions, and video and SR data were used to calculate coefficients of restitution from block translation and rotation. This research aims to enhance input parameters in rockfall modeling, which often disregards the contribution of block rotation in energy estimates. It was demonstrated that different surface inclinations produce distinct energy restitution responses. For surfaces inclined at 0° and 45° , the results show that block rotational kinetic energy increases from 0% to up to 40% of the translational energy after impact.

1 INTRODUCTION

Rockfall events are an increasing hazard concern, especially near highways, railways, and residential areas. Rockfalls are associated with natural phenomena such as weathering, rainfall, freeze-thaw cycles, vegetation growth, and activities by animals and the public (Dochez et al., 2012; Bost and Pouya, 2016). These processes disrupt portions of slopes, which lead to falling rocks and pose a safety hazard to motorists, infrastructure, and buildings nearby—the risk of irreversible damage increases in areas with significant population density, such as near the French-Swiss Alps and in roads near rock cuts across the United States.

Falling blocks can experience one or more modes of travel, including free-fall, bouncing, rolling, and sliding. Rock bouncing motion occurs when falling blocks impact the rock slope or other surfaces (sand, grass, gravel, asphalt, etc.). Although discussions regarding rock bouncing behavior have dominated research in recent years, this phenomenon is still not fully understood. Several studies identified that the bouncing of blocks depends on several factors that include

both impact surfaces and block characteristics, as well as the consequent kinematics produced from such interactions (Ritchie, 1963; Peng, 2000; Heidenreich, 2004; Labiouse and Heidenreich, 2009; Turner and Duffy, 2012; Wyllie, 2015).

The present-day mitigation and protective design are based on velocity and kinetic energy estimates in 2D and 3D modeling softwares. Rockfall bouncing behaviors and their resultant trajectories are governed in modeling software by one or two values, designated coefficients of restitution (COR), defined for each impacted surface in both normal (COR_N) and tangential (COR_T) directions. However, there are currently multiple definitions and interpretations in the literature for these coefficients. The lack of consensus illustrates the existing gap in understanding rockfall impacts against typical surfaces (Heidenreich, 2004; Turner and Duffy, 2012).

In addition to generally conservative simulation models, current rockfall analysis methods typically include field/laboratory measurements, video recording systems, and back-analyses. Several authors conducted experimental studies to determine the coefficient of restitution values for typical surfaces present near rock cuts with the aid of video recording systems (Wu, 1985; Peng, 2000; Chau et al., 2002; Giani et al., 2004; Heidenreich, 2004; Asteriou et al., 2012; Giacomini et al., 2012; Saeidi et al., 2014; Ansari et al., 2015; Asteriou and Tsiambaos, 2016; Wang et al., 2018). However, the lack of standardized methods to evaluate these coefficients highlight the uncertainty associated with rockfall model input parameters, which often disregard or inaccurately predict inherent and essential aspects of rockfall modeling, such as rotational energy and rock rebound.

Lastly observational techniques used in rockfall assessments often do not provide detailed information about rock-surface interaction and translational and rotational rock kinematics (Caviezel and Gerber, 2018). Therefore, researchers have started to instrument test rocks with high-rate sampling acceleration and rotational velocity sensors in field and laboratory rockfall experiments to address these limitations (Caviezel et al., 2018; Disenhof, 2018; Souza, 2021; Caviezel et al., 2021; Disenhof et al., 2021; Benoît et al., 2022; Souza and Benoît, 2022; Souza et al., 2022).

This paper presents the preliminary results of a small-scale experimental campaign designed to better understand the contribution of block rotation in energy restitution after impact with the aid of Smart Rock sensors. These autonomous devices can instrument field and laboratory experiments from the perspective of the falling rock.

2 SMART ROCK SENSORS

In response to the lack of accurate measurements of kinematics and rock rebound behavior during rockfalls, a sensor was developed at the University of New Hampshire to make realistic evaluations of these events from the perspective of the falling rock. These sensors, called Smart Rocks (SRs), are small and fully autonomous and can be used in various applications such as landslides, debris flow, and rockfalls (Harding, 2011; Gullison, 2013; Harding et al., 2014; Apostolov, 2016; Apostolov and Benoît, 2017; Disenhof, 2018; Souza, 2021). The latest Smart Rocks consist of 3D printed capsules 58.0 mm in length and 25.4 mm in diameter (Figure 1), equipped with two three-axis accelerometers (± 400 g and ± 16 g), a ± 4000 dps high-rate gyroscope, and an altimeter. The data is automatically saved to a micro-SD card as a .csv file.

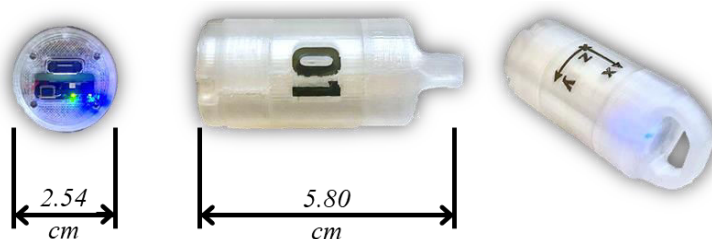


Figure 1. Fifth-generation Smart Rock sensor.

Preliminary field experiments recently conducted in New Hampshire (USA) have provided SR data on blocks as they fall (Souza, 2021). Approximately 80 experimental rockfalls with rocks of different shapes and sizes were performed and analyzed, where SRs were embedded at the center of gravity of over 50 field-collected rocks. These measurements, along with video recordings, have formed the basis for a new methodology to improve inputs for rockfall models. This preliminary work concluded that acceleration and rotational velocity data from the rock perspective present a high potential to enhance rockfall understanding and modeling.

3 TEST METHODOLOGY

Energy restitution experiments were carried out to determine the coefficients of restitution of a natural granite block. One-kilogram concrete test blocks were fabricated in a rhombicuboctahedron shape, used in the European standard ETAG 027 to certify falling rock protection kits. The test blocks were reinforced with steel fibers and presented an average compressive strength of 45 MPa after 15 days. Each block contained an orifice for the Smart Rock sensor to be confined with a 3D printed cap. The tests were instrumented at a sampling frequency of 500 Hz, and the altimeter was disabled due to its significant data noise at high sampling frequencies.

The test block was consistently dropped from 1 and 2 meters onto the rough granite block using a drop device with a trap door mechanism. This mechanism was designed to drop the test block vertically, and avoid rotation during the fall. The granite block was positioned at 0° , 15° , 30° , and 45° angles (β), and three drop tests were performed for each test configuration. Figure 2 presents the experimental setup and test block schematic.

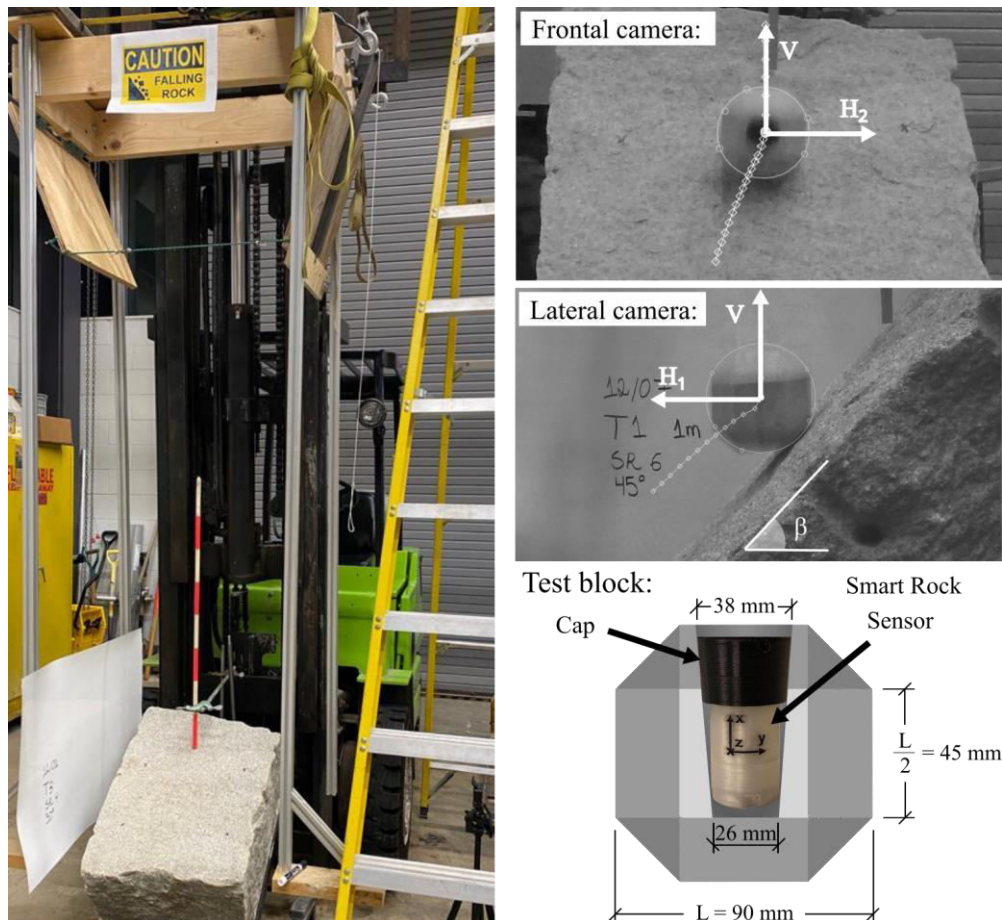


Figure 2. Experimental setup, video tracking, and test block schematic.

Each experiment was recorded with frontal and side cameras at 240 fps. The application Tracker 5.1.5 by Physlets was used to track the falling block in each video frame. Each camera perspective provided displacement information in three directions (Vertical, V – captured with both cameras; Horizontal 1, H1 – captured with the side camera; Horizontal 2, H2 – captured with the front camera). These reference axes allowed to obtain the velocity components normal and tangential to each impact surface inclination. These measurements were used to calculate the angle of block deviation and the surface inclination corresponding to the projected trajectory, used to estimate the normal and translational velocities after impact.

Normal (COR_N) and tangential (COR_T) coefficients of restitution for a rough rock were calculated through ratios of velocities immediately after and immediately before the impact (Equations 1 and 2). This definition is extensively used in rockfall models and does not account for the contribution of block rotation.

$$COR_N = V_{RN} / V_{IN} \quad (1)$$

$$COR_T = V_{RT} / V_{IT} \quad (2)$$

where COR_N = normal COR; COR_T = tangential COR;

V_{RN} = normal translational velocity immediately after impact (m/s);

V_{IN} = normal translational velocity immediately before impact (m/s);

V_{RT} = tangential translational velocity immediately after impact (m/s);

V_{IT} = tangential translational velocity immediately before impact (m/s).

In addition to rockfall model input parameters, the results of these tests were also used to calculate the kinetic energy (KE) developed by the falling blocks before and after impact. The total kinetic energy (KE) is described by the sum of translational (KE_{TRANS} , Equation 3) and rotational (KE_{ROT} , Equation 4) energies (Equation 5). Since the Smart Rock sensor provides triaxial rotation data, the resultant rotational velocity is calculated to estimate KE_{ROT} accurately.

$$KE_{TRANS} = 0.5 mV^2 \quad (3)$$

$$KE_{ROT} = 0.5 I\omega^2 \quad (4)$$

$$KE = KE_{TRANS} + KE_{ROT} \quad (5)$$

where KE_{TRANS} = translational KE (J); KE_{ROT} = rotational KE (J); KE = total KE (J);

V = block translational velocity (m/s); m = block mass (kg);

ω = block rotational resultant velocity (rad/s);

I = block moment of inertia (0.0008 kg.m²).

The theoretical scalar velocity of free-falling blocks can be estimated through Equation 6 and used to calculate the expected kinetic energy before impact at each experimental trial (Equations 3, 4, and 5). The rotational velocity can be disregarded until immediately before impact, as the block does not develop initial rotation, and no external forces act on it during the fall.

$$V = (2 g h)^{0.5} \quad (6)$$

where V = block translational velocity (m/s); g = acceleration of gravity (9.81 m/s²);

h = drop height (m).

Therefore, for a 1 m drop height, the 1-kg test block is expected to develop a peak velocity of 4.5 m/s, and 10 J of total kinetic energy immediately before impact. For a 2 m drop height, the expected impact velocity and total KE increase to 6.3 m/s and 20 J, respectively.

4 RESULTS AND DISCUSSION

The video recordings and measured block velocities were used to calculate the normal and tangential coefficients of restitution of the natural granite block, as shown in Figure 3 as individual data points representing the average results of each test series. Tangential coefficients of restitution cannot be calculated for 90° drops onto flat surfaces (0°) since the tangential velocity before impact is equal to zero under this impact condition.

An initial comparison between COR values demonstrated that the coefficients of restitution do not significantly differ between 1- and 2-meter drop heights. However, different surface inclinations produced distinct responses in terms of rebound. Higher surface inclinations led to an increase in COR_N , and a decrease in COR_T . This behavior was observed in other published assessments on rock, such as by Asteriou et al. (2012), Saeidi et al. (2014), and Wang et al. (2018), whose results are included in the grey-shaded areas presented in Figure 3. In addition, both normal and tangential coefficients converged to an average value of 0.52 at 45° for both drop heights in these preliminary tests.

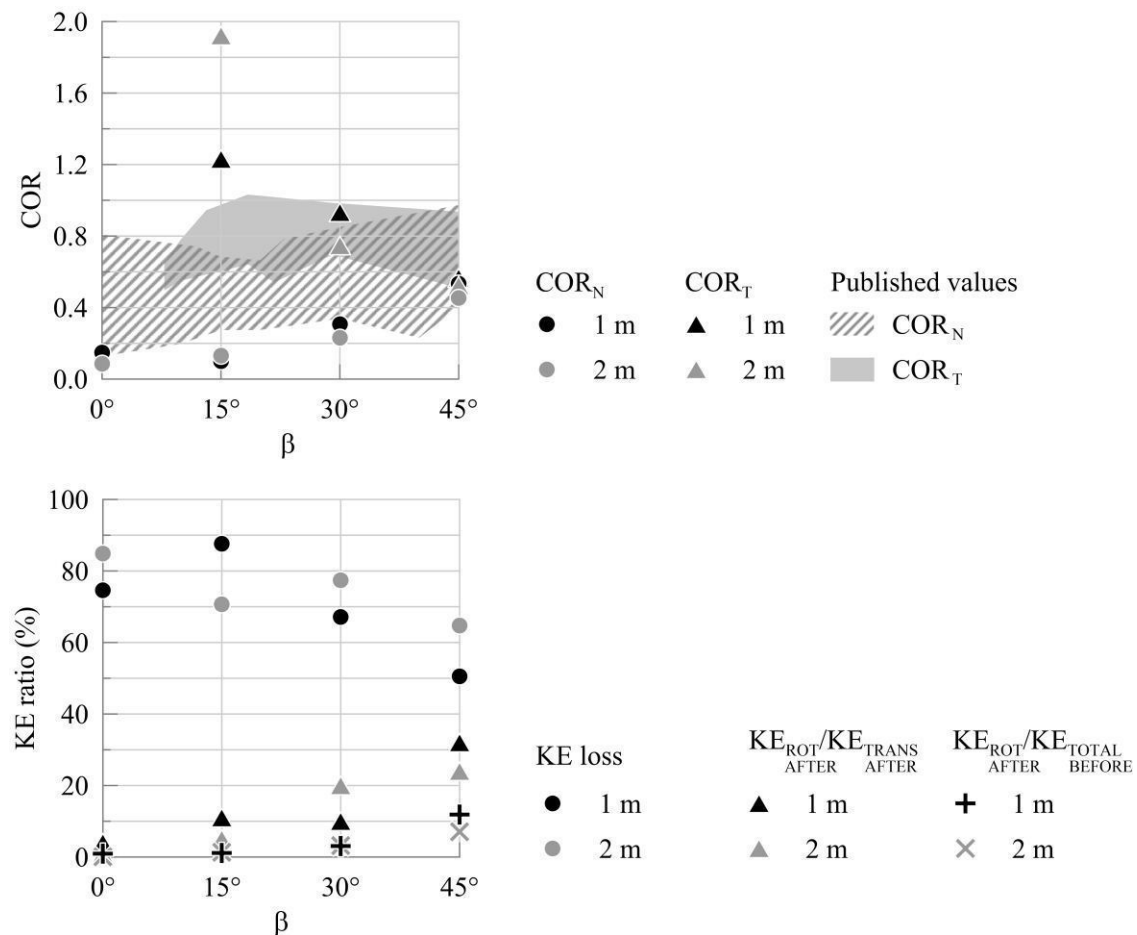


Figure 3. Coefficients of restitution (COR) and relevant kinetic energy ratios (KE) upon different impact conditions on a natural granite block.

The gray-shaded areas in the first graph represent ranges of values for normal drop tests onto rock published in the literature (Peng, 2000; Asteriou et al., 2012; Saeidi et al., 2014; Ansari et al., 2015; Wang et al., 2018). Except for the tangential restitution at 15°, it was shown that the results are primarily near the lower limits of the literature range. Such behavior can be attributed

to factors such as surface roughness, block size, and block shape/angularity. According to Heidenreich (2004), these factors can significantly affect the behavior of bouncing blocks. For example, Ghana et al. (2019) observed lower energy restitution values on rough surfaces upon comparing drop tests on natural and polished limestone blocks.

From the kinetic energy measurements, Figure 3 also displays the percentages of total kinetic energy lost after impact, a ratio between the rotational KE and translational KE, ($KE_{ROT\ AFTER} / KE_{TRANS\ AFTER}$) as well as the percentage of the rotational KE after the impact and total KE before the impact ($KE_{ROT\ AFTER} / KE_{TOT\ BEFORE}$). The $KE_{ROT\ AFTER} / KE_{TOT\ BEFORE}$ ratio allows for a normalized visualization of the contribution of block rotation as the surface angle is increased since the total KE before impact is constant for all drops performed from a same drop height. In addition, the $KE_{ROT\ AFTER} / KE_{TRANS\ AFTER}$ ratio has been used by Chau et al. (2002) to represent the contribution of block rotation without considering pre-impact conditions.

Table 1 summarizes the mean and standard deviation values for each test condition. It was observed that the 2-meter tests typically presented higher standard deviations compared to the 1-meter tests. Therefore, while different drop heights do not seem to significantly influence average results up to 2 meters, it can be suggested that higher drops might increase data dispersion. Aspects related to surface roughness, block surface contact area, and additional test conditions, including block sizes and impact surfaces, need to be further addressed to confirm or reject this hypothesis for this experimental setup.

Table 1. COR and KE result summary (mean \pm standard deviation) for both 1 m and 2 m drop heights. Before impact, the measured kinetic energies were equal to approximately 10 and 20 J, respectively.

Parameter	1 m drop height				2 m drop height			
	0°	15°	30°	45°	0°	15°	30°	45°
COR _N	0.15 \pm 0.08	0.10 \pm 0.04	0.31 \pm 0.01	0.53 \pm 0.02	0.09 \pm 0.07	0.13 \pm 0.02	0.23 \pm 0.08	0.45 \pm 0.05
COR _T	-	1.23 \pm 0.08	0.93 \pm 0.06	0.57 \pm 0.01	-	1.92 \pm 0.12	0.75 \pm 0.19	0.52 \pm 0.07
KE _{TRANS AFTER} (J)	2.54 \pm 0.48	1.20 \pm 0.13	3.30 \pm 0.42	4.13 \pm 0.15	3.51 \pm 1.88	6.20 \pm 0.12	4.14 \pm 2.32	6.32 \pm 1.35
KE _{ROT AFTER} (J)	0.10 \pm 0.11	0.12 \pm 0.06	0.34 \pm 0.33	1.32 \pm 0.16	0.02 \pm 0.00	0.30 \pm 0.11	0.69 \pm 0.20	1.59 \pm 1.04
KE loss	75% \pm 5%	88% \pm 1%	67% \pm 5%	51% \pm 3%	85% \pm 8%	71% \pm 1%	77% \pm 11%	65% \pm 11%
$\frac{KE_{ROT\ AFTER}}{KE_{TOT\ BEFORE}}$	1.0% \pm 1.1%	1.2% \pm 0.6%	3% \pm 3%	11% \pm 2%	0.1% \pm 0.02%	1.3% \pm 0.5%	3% \pm 0.8%	8% \pm 5%
$\frac{KE_{ROT\ AFTER}}{KE_{TRANS\ AFTER}}$	4% \pm 4%	11% \pm 6%	10% \pm 9%	32% \pm 5%	1% \pm 1%	5% \pm 2%	20% \pm 10%	24% \pm 13%

The increase in surface inclination also increases block rotation. The increasing contributions of block rotation for impact on steeper surfaces also led to lower kinetic energy losses. The maximum contribution of the rotational kinetic energy in a single test is equivalent to 37% of the translational kinetic energy after impact. Chau et al. (2002) also identified that rotational velocity strongly depends on the impact angles. For the same slope inclination, the ratios between measured translational and rotational velocity obtained by Chau et al. (2002) were roughly constant, regardless of the mass of the block or energy levels achieved. Observations from their video frames demonstrated that the rotational kinetic energy represented up to 40% of the translational kinetic energy. Therefore, rockfall rotational motion cannot be disregarded during trajectory and energy estimates. Rotational velocities are critical during oblique impacts, and it is vital to assess how motion characteristics change during rockfall impacts.

The uncertainty related to rockfall assessments can also be associated with the different parameters and methodologies to evaluate energy restitution (which typically do not quantify block rotation), with no agreement on what approaches are more accurate and/or better repro-

duce reality (Asteriou et al., 2012). There exists a significant variety of experimental strategies to address rockfall mechanics. Although assumptions concerning the Newtonian physics of falling blocks are identical, it has been demonstrated that different test conditions will provide different restitution parameter values, even if the assessed materials are similar. Besides significant differences between test setups, aspects inherent to the test blocks (material composition, mass, shape) and impact surfaces (material composition, size, presence of irregularities) will affect COR in modeled trajectories (Turner and Duffy, 2012a; Saeidi et al., 2014; Ghana et al., 2019). The variation between test conditions often results in COR values from experimental studies significantly different from default published values, which typically provide a broad description of the impact materials and generally do not describe their characteristics (Heidenreich, 2004; Asteriou et al., 2012). For example, laboratory tests conducted by Peng (2000) evaluated COR_N values obtained on marl at different slope angles. Their results ranged between 0.25 at 0° and 0.88 for the same material at a 45° slope (Peng, 2000). The default COR_N used in two-dimensional modeling is equal to 0.35 for rock (Rocscience, 2017).

5 CONCLUSIONS AND PERSPECTIVES

Accurate rockfall hazard assessments demand realistic estimates of potential falling block trajectories. The literature widely discusses how several parameters, including the released block, the impact surface, and the fall kinematics, affect the energy restitution at a given site. Furthermore, the lack of a standardized methodology among published studies to evaluate CORs reinforces the difficulty of selecting representative model input parameters. Rockfall models currently assume material-constant COR values for each impact surface type (e.g., bedrock, sand...) regardless of site-specific characteristics, including different slopes. In addition, over-conservative rockfall model predictions can be associated with the lack of measured rotation data and its difficulty in being obtained through traditional camera approaches. The Smart Rock sensor can be considered a promising tool for accurate energy assessments and consequent hazard mitigation.

This research aims to enhance input parameters in rockfall modeling, which often disregards the contribution of block rotation in energy estimates. The first test results suggest that increasing inclinations of the impact surface exerts a higher effect on energy restitution and block rotation than increasing drop heights. It was demonstrated that, for a block released vertically with no initial rotation, different surface inclinations produce distinct energy restitution responses, as block rotational kinetic energy increases from 0% to up to 40% of the translational energy after impact, comparing tests at 0° and 45° . Additional tests will complete this ongoing preliminary assessment on typical impact surfaces (e.g., rock, sand, gravel) and create a database on instrumented small- and large-scale COR tests, coupled with impact surface characterization.

6 REFERENCES

- Ansari, M. K., Ahmad, M., Singh, R., and Singh, T. N. 2015. Correlation between Schmidt hardness and coefficient of restitution of rocks. *Journal of African Earth Sciences*, 104, 1- 5.
- Apostolov, A. 2016. Development and testing of motion tracking "Smart Rock" devices for geotechnical applications. (Master's thesis). University of New Hampshire, Durham, NH.
- Apostolov, A. and Benoit, J. 2017. Motion Tracking "Smart Rock" Device for the Study of Landslide and Debris Flow Mechanisms. *North American Symposium on Landslides*. Roanoke, VA, June 4-8.
- Asteriou, P., Saroglou, H., and Tsiambaos, G. 2012. Geotechnical and kinematic parameters affecting the coefficients of restitution for rock fall analysis. *International Journal of Rock Mechanics and Mining Sciences*, 54, 103-113.
- Asteriou, P., and Tsiambaos, G. 2016. Empirical model for predicting rockfall trajectory direction. *Rock Mechanics and Rock Engineering*, 49(3), 927-941.
- Benoit, J., Souza, B. and Pelham, K. In situ instrumented rockfall testing with Smart Rock sensors. In 7th

- Interdisciplinary Workshop on Rockfall Protection, Sapporo, Japan.
- Bost, M. and Pouya, A. 2016. Stress generated by the freeze-thaw process in open cracks of rock walls: empirical model for tight limestone, *Bulletin of Engineering Geology and the Environment*, 76(4), 1491-1505.
- Caviezel, A., and Gerber, W. 2018. Brief Communication: Measuring rock decelerations and rotation changes during short-duration ground impacts. *Natural Hazards and Earth System Sciences*, 18(11), 3145-3151.
- Caviezel, A., Schaffner, M., Cavigelli, L., Niklaus, P., Bühler, Y., Bartelt, P., and Magno, M. 2018. Design and evaluation of a low-power sensor device for induced rockfall experiments. *ISEE Transactions on Instrumentation and Measurement*. 67(4), 767-779.
- Caviezel, A., Ringenbach, A., Demmel, S.E. et al. The relevance of rock shape over mass—implications for rockfall hazard assessments. *Nature Communications* 12, 5546 (2021).
- Chau, K. T., Wong, R. H. C., and Wu, J. J. 2002. Coefficient of restitution and rotational motions of rockfall impacts. *International Journal of Rock Mechanics and Mining Sciences*, 39(1), 69-77.
- Chau, K. T., Wong, R. H. C., Liu, J., and Lee, C. F. 2003. Rockfall hazard analysis for Hong Kong based on rockfall inventory. *Rock Mechanics and Rock Engineering*, 36(5), 383-408
- Descocedres, F. 1997. Aspects géomécaniques des instabilités de falaises rocheuses et des chutes de blocs. *Publications de la société suisse de mécanique des sols et des roches*, 135, 3-11. In French.
- Disenhof, C. R. 2018. Investigation of Surface Models and the Use of a Smart Rock for Rockfall Modeling. (Master's thesis). University of New Hampshire, Durham, NH.
- Disenhof, C., Benoît, J., Apostolov, A., Pelham, K., and Olson, N. 2021. Comparison of rockfall models using photogrammetry to data from an experimental Smart Rock. In 6th International Conference on Geotechnical and Geophysical Site Characterisation, Budapest, Hungary.
- Dochez S., Laouafa F., Franck C., Guedon S., Martineau F., and Bost M. 2012. Waterweathering in rocks discontinuities. 12. *International Congress on the Deterioration and Conservation of Stone*, New York, United States.
- Ghana, M. F. A., Simon, N., and Lai, G. T. 2019. Coefficient of restitution of limestone determined from normal drop laboratory test. In *AIP Conference Proceedings* (Vol. 2111, No. 1, p. 060014). AIP Publishing LLC.
- Giacomini, A., Thoeni, K., Lambert, C., Booth, S., and Sloan, S. W. 2012. Experimental study on rockfall drapery systems for open pit highwalls. *International Journal of Rock Mechanics and Mining Sciences*, 56, 171-181.
- Giani, G. P., Giacomini, A., Migliazza, M., and Segalini, A. 2004. Experimental and theoretical studies to improve rock fall analysis and protection work design. *Rock Mechanics and Rock Engineering*, 37(5), 369-389.
- Gullison, M. 2013. Analysis of Smart Rock data from debris flow experimentation. (Master's thesis). University of New Hampshire, Durham, NH.
- Harding, M. 2011. Design and development of a debris flow tracking "Smart Rock". (Master's thesis). University of New Hampshire, Durham, NH.
- Harding, M. J., Fussell, B. K., Gullison, M. A., Benoît, J., and de Alba, P. A. 2014. Design and testing of a debris flow 'smart rock'. *Geotechnical Testing Journal*, 37(5), 769-785
- Heidenreich, B. 2004. Small- and Half- Scale Experimental Studies of Rockfall Impacts on Sandy Slopes. (Doctoral thesis). École Polytechnique Fédérale de Lausanne, Lausanne, Switzerland.
- Heidenreich, B., and Labiouse, V. 2009. Small-scale experimental studies of rockfall impacts on granular slopes. *Rivista Italiana di Geotecnica*, 38(2), 80-91
- Peng, B. 2000. Rockfall Trajectory Analysis – Parameter Determination and Application (Master's thesis). University of Canterbury, Christchurch, New Zealand
- Pierson, L.A., and Van Vickle, R. 1993. Rockfall Hazard Rating System – Participants' Manual. FHWA-SA-93-057, U.S. Department of Transportation
- Reiffsteck, P., Benoît, J., Bourdeau, C., and Desanexaux, G. 2018. Enhancing geotechnical investigations using drilling parameters. *Journal of Geotechnical and Geoenvironmental Engineering*, 144(3), 04018006.
- Ritchie, A. 1963. Evaluation of Rockfall and its Control. Highway Research Board, N.17, 13-28
- Saeidi, S., Gratchev, I., Kim, D. H., and Chung, M. (2014). Evaluation of restitution coefficients concerning surface roughness. In 23rd Australasian Conference on the Mechanics of Structures and Materials (ACMSM23) Byron Bay, Australia (pp. 1-6).
- Souza, B. 2021. Use of Smart Rocks to improve rock slope design. (Master's thesis). University of New Hampshire, Durham, NH.

- Souza, B. and Benoît, J. 2022. Use of Smart Rocks to improve rock slope design. Highway Geology Symposium, Asheville, North Carolina, USA.
- Souza, B. Miller, H. Benoît, J. and MacAdam, N. 2022a. Evaluation of coefficients of restitution for rockfall modeling. In 20th International Conference on Soil Mechanics and Geotechnical Engineering, Sydney, Australia.
- Turner, A.K., and Duffy, J.D. 2012. "Evaluation of Rockfall Mechanics." In Turner, A.K. and Schuster, R.L. (Eds). Rockfall Characterization and Control (pp. 285-333). Washington, D.C.: Transportation Research Board.
- Turner, A.K., and Jayaprakash, G. P. 2012. "Introduction." In Turner, A.K. and Schuster, R.L. (Eds). Rockfall Characterization and Control (pp. 3-20). Washington, D.C.: Transportation Research Board.
- Wang, Y., Jiang, W., Cheng, S., Song, P., and Mao, C. 2018. Effects of the impact angle on the coefficient of restitution in rockfall analysis based on a medium-scale laboratory test. *Natural Hazards and Earth System Sciences*, 18(11), 3045-3061.
- Wu, S. S. 1985. Rockfall evaluation by computer simulation. Transportation research record, 1031, Transportation research Board, National Research Council, Washington, D.C., 1-5.
- Wyllie, D.C. 2015. Rock Fall Engineering. New York, NY: CRC Press, Taylor & Francis Group.

Landslide monitoring using SBAS-DInSAR along the northern Bulgarian Black Sea coast near Topola village

M. Yamaguchi

Nippon Koei Co., Ltd, Tokyo, Japan

P.E. Yastika

Universitas Mahasaraswati Denpasar, Indonesia

N. Shimizu

Kansai University & Yamaguchi University, Japan

N. Milev

University of Architecture, Civil Engineering and Geodesy, Sofia, Bulgaria

I. Vrkljan

University of Rijeka, Croatia

ABSTRACT:

DInSAR is used to monitor the landslide behavior along the northern Black Sea coast of Bulgaria, and its applicability is investigated. The distribution maps and time transitions of the displacements were obtained over the period from 2014 to 2020. The results and applicability of this method are discussed by a comparison with the actual behavior described in the official reports of the Bulgarian Ministry of Regional Development and Public Works. This study suggests that DInSAR will be a useful tool for long-term continuous landslide monitoring over extensive areas, such as along the northern Black Sea coast.

1 INTRODUCTION

The Black Sea coast in Bulgaria is well known as an active landslide area in Eastern Europe, with various landslides extending across it (Bruchev et al. 2007). A lot of research has been done, from both geological and engineering perspectives, and countermeasures have been partially performed for stabilizing the landslide activity and protecting people's lives and properties. On the other hand, monitoring the real behavior of landslides has not often been conducted due to technical difficulties and cost issues, although it is essential to reveal the mechanism of these landslides and to solve the problems they cause.

Differential Interferometric Synthetic Aperture Radar (DInSAR) (Ferretti 2014) has the potential to be an efficient, effective, and economical method for monitoring the landslide behavior of extensive areas. With this method, expansive areas can be monitored without the use of any sensors on the ground surface, and ground surface displacements can be measured with centimeter-level accuracy.

The authors applied DInSAR to monitor the behavior of the northern Bulgarian Black Sea coast (Yamaguchi et al. 2021) and the results were confirmed by comparing them with the actual behavior of landslides described in Bulgarian official annual reports (MPPB 2017, 2018, 2019). Previous DInSAR studies of this area are also found (Nikolov & Atanasova 2016, Atanasova et al. 2020).

This paper describes the results of the application of DInSAR to monitor landslide displacements, focusing on an area near Topola village in the northern Bulgarian Black Sea coast. The Sentinel-1A/B SAR data provided by the European Space Agency (ESA) are used. The distribution of displacements was obtained about every 10 days from 2014 to 2020, and the temporal transitions of the displacements at selected points along a section of the landslide slope, marine

terraces, gullies, and coast with a beach area were also computed. The results are compared with the actual behavior described in Bulgarian official annual reports (MPPB 2017, 2018, 2019), and the applicability of DInSAR is discussed.

2 OUTLINE OF SBAS-DINSAR

Synthetic Aperture Radar (SAR) is a high-resolution radar device that is mounted on an aircraft or artificial satellite. It can be used efficiently even at night and under any weather conditions (Hanssen 2002). The SAR satellite travels on ascending (northward) and descending (southward) orbits (Figure 1). It transmits microwave signals in the direction of the radar beam's line, i.e., Line of Sight (LOS), and observes the amplitude and phase of the reflected waves from the Earth's surface (Figure 2).

Interferometric SAR (InSAR) is a method for taking the signal phase difference from two scenes of SAR data observed in the same area at different times. Differential Interferometric SAR (DInSAR) is a method for finding the displacements of the Earth's surface over vast areas using two scenes of SAR data (Ferretti 2014). The displacement obtained by DInSAR is one-dimensional along the LOS, i.e., extension and compression (Figure 3).

When continuous displacement monitoring is conducted by DInSAR, a time-series analysis is applied to many pairs of SAR data. The Small Baseline Subset (SBAS) method (Berardino et al. 2002) is one such temporal DInSAR analysis. It enables the reduction of phase noises and errors from many interferograms and is capable of isolating only the phases that were caused by the deformation. In this paper, SBAS-DInSAR is employed to conduct a temporal DInSAR analysis.

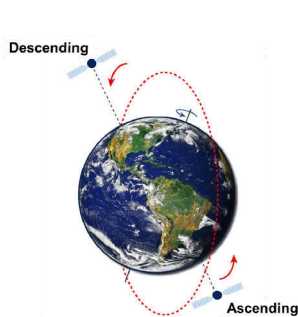


Figure 1. SAR satellite orbits (Özer et al. 2018)

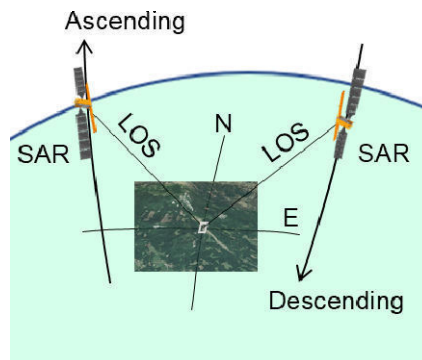


Figure 2. Image acquisition from ascending and descending orbits

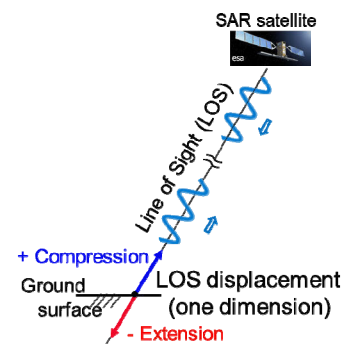


Figure 3. Line of Sight (LOS) and LOS displacement

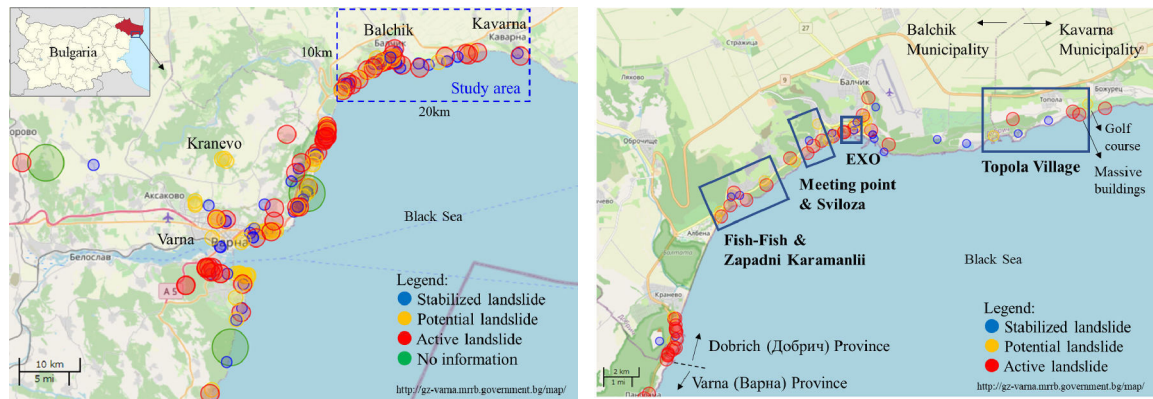
3 STUDY AREA AND SBAS-DINSAR PROCESSING

3.1 Study area

Figure 4 shows the distributions of landslide locations at Balchik and Kavarna Municipalities along the Black Sea coast in northern Bulgaria (MPPB 2022). In this region, there are four landslide hotspots, namely, Topola village, Alley Echo (EXO), Sviloza, and Fish-Fish, which are represented by the squared regions in Figure 4b. Focus is placed on an area near Topola village located in the western part of Kavarna Municipality.

Figure 5 is a geomorphological map of the Topola village area; it divides the landslide area into five sections, i.e., Topola 1 to Topola 5 (Evstatiev & Evlogiev 2013). Along the coastline, a steep slope of diatomaceous clays of the Euxinograd Formation (evN1kg-s) has formed. The geological composition is as follows: south of the crown line of the sliding cliff comprises arag-

onite clays with limestone intercalations, Topola Formation (toN1s), north of the crown line of the sliding cliff is limestone of the Kavarna Formation (kvN1s), and north of that is a loess (yellow soil) complex (eoIQp). North of the crown line of the sliding cliff is a limestone plateau called the Lower Romanian Level (LRL).



a. Kavarna, Balchik, Kranevo, and Varna b. Topola village and other areas
 Figure 4. Maps of landslides along coastal area in northern Black Sea, Bulgaria (MPPБ 2022)

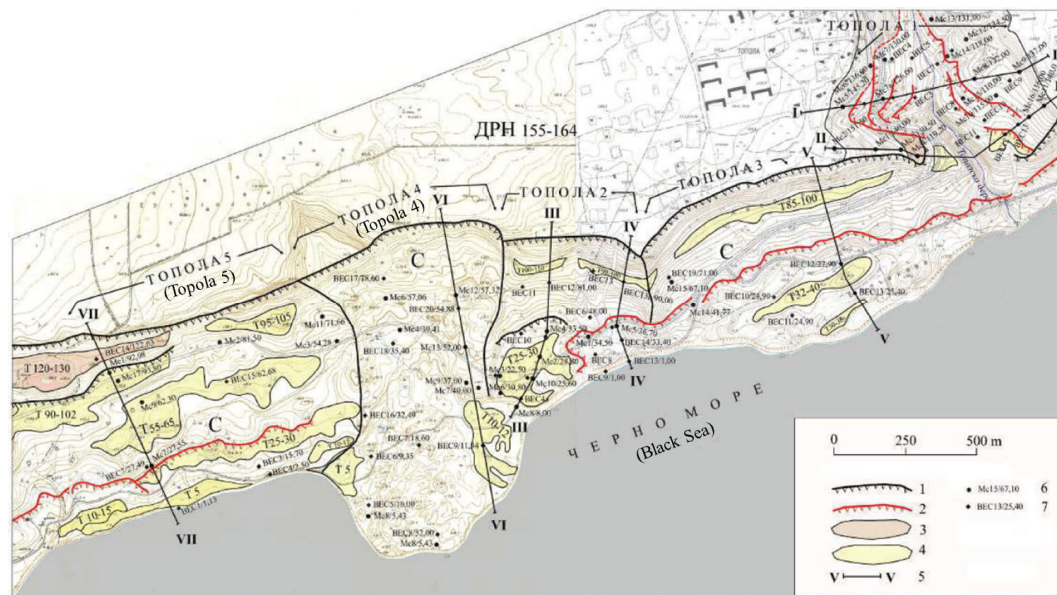


Figure 5. Geomorphological map of landslides in Topola village area (see Figure 4b) (Evstatiev & Evlogiev 2013)

3.2 SBAS-DInSAR processing

In this study, the Sentinel-1A/B data are applied to create the interferogram for the DInSAR analysis. Two datasets, namely, 273 scenes on the descending pass observed from 8 October 2014 to 9 May 2020, and 196 scenes on the ascending pass observed from 9 October 2014 to 7 September 2020, are used. The number of orbit paths for the descending data is 36, while that for the ascending data is 58. All scenes are right-looking observation data. All the Sentinel data were provided free of charge by the European Space Agency (ESA).

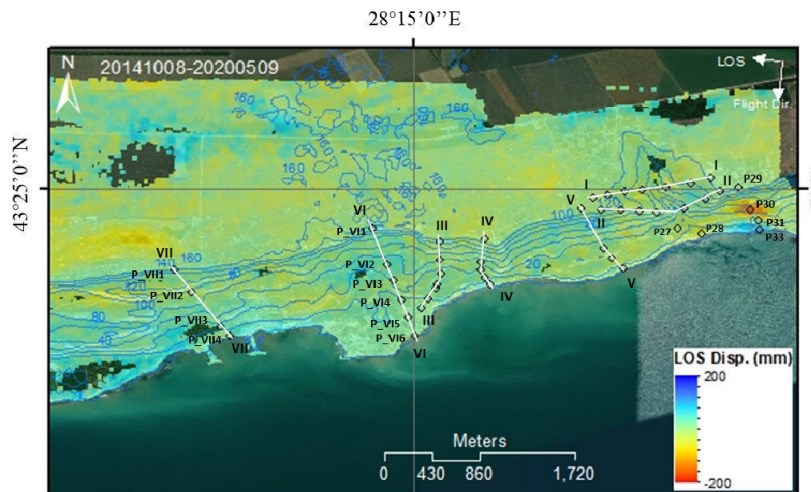
The SBAS-DInSAR processing for the descending and ascending data was conducted separately. The thresholds of the temporal and perpendicular baselines are set at 36 days and 2% of

the critical baseline length, respectively, for selecting the pairs of SAR data to obtain the interferograms. The total numbers of pairs of descending and ascending data are 1228 and 746, respectively. All the SAR data processing was conducted using Envi-SARscape 5.5.3. (Harris Geospatial Solutions, Inc.).

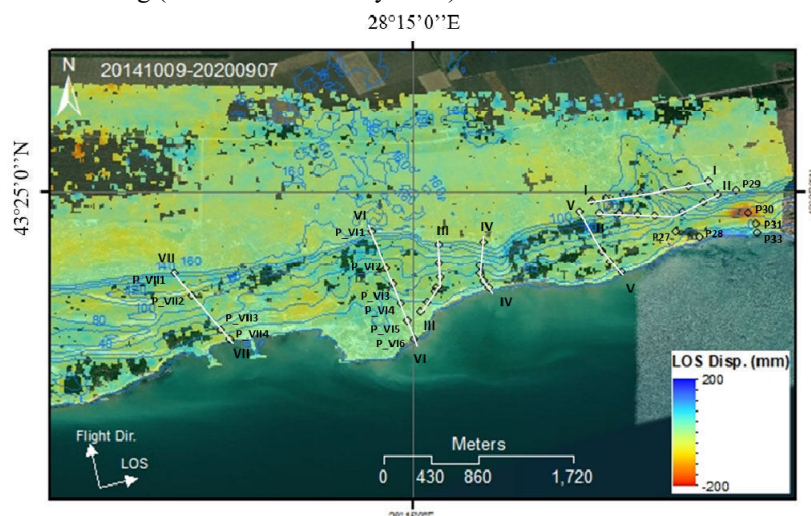
4 RESULTS AND DISCUSSION

4.1 Spatial distribution of LOS displacements

Figure 6 shows the LOS displacement distributions of the target area, Topola village, which includes vertical sections I-I to VII-VII, as shown in Figure 5, from October 2014 to May 2020 for the descending and ascending passes obtained by the SBAS-DInSAR analysis. The displacements are represented by the range in colors from red to blue denoting mm units from -200 mm to 200 mm. The red and blue colors mean negative (extension) and positive (compression) LOS displacements, respectively. In the area of low coherence, below the threshold value (0.2), the results of the LOS displacements have been removed from the map.



a. Descending (8 Oct 2014 to 5 May 2020)



b. Ascending (9 Oct 2014 to 7 Sept 2020)

Figure 6. LOS displacement distributions in Topola village by SBAS-DInSAR

4.2 Time transitions of displacements and landslide behavior

To evaluate the results of SBAS-DInSAR and to discuss its applicability for monitoring the landslide behavior in the area of Topola village, the displacements in Topola 4, Topola 5, and the eastern end area (Figures 5 and 6) are taken for a comparison with the field observation results.

4.2.1 Topola 4 (section VI-VI)

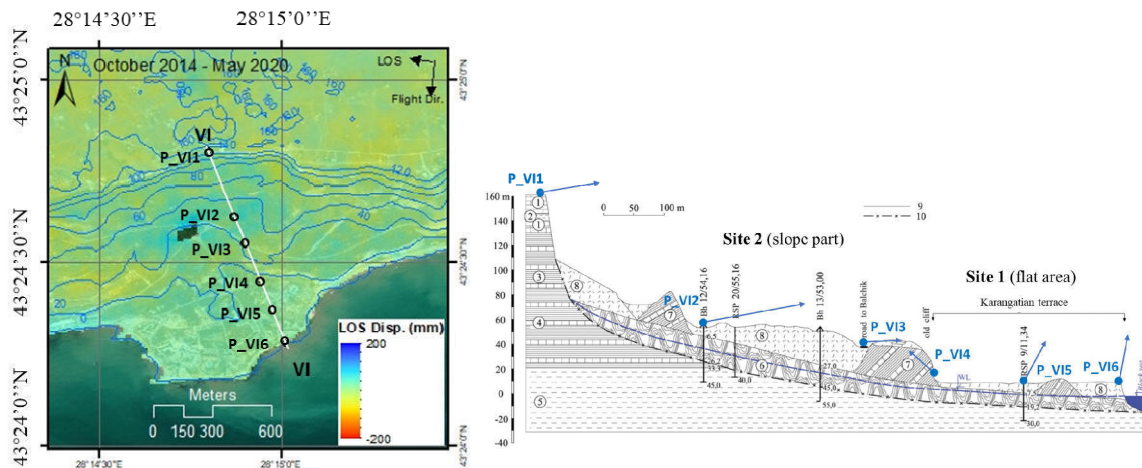
The area around section VI-VI in Topola 4 is known as the “Ikantalaka” landslide, and it is considered to be provisionally stabilized for now. Figure 7 shows the LOS displacement distribution of the descending case and the geological features of section VI-VI. The section is divided into two areas: a slope part and a coastal flat area. The coastal flat area offers better conditions, and numerous hotels and other resort facilities have been built there. In the slope part, the sliding zone comprises clay with an undulated structure (Evstatiev & Evlogiev 2013).

The time transitions of the LOS displacements at the points of interest (POI: P_VI1, 2, 5, and 6), selected from vertical section VI-VI, are shown in Figure 8.

P_VI1 is located on the Lower Romanian Level (LRL) plateau above the main scarp, denoted by Site 2 in Figure 7b. As seen in Figure 8a, the descending and ascending displacements are negative and positive, respectively. Therefore, the displacement direction can be estimated to be horizontal and slightly upward (Figure 7b). The displacement at P_VI2 in the flat area of Site 2 (slope part) is larger than the one at P_VI1, and the direction is similar to the one at P_VI1 (Figures 7b and 8b). Displacements at both P_VI3 and P_VI4 are smaller than the ones at other points (those results are omitted here due to the space limitation of the paper).

The descending and ascending displacements at P_VI5 and P_VI6 in Site 1 (flat area) are continuously increasing to the positive side (Figures 8c and 8d). From these results, the displacements at both points are moving upward and slightly to the east.

Consequently, it is assessed from the SBAS-DInSAR analysis that this area does not show any landslide activity and is stable at present. On the other hand, the displacements in the upper part are larger than those in the lower flat area. Therefore, monitoring should be carefully continued.



a. LOS displacement distribution (descending) from Oct. 2014 to May 2020
 b. Vertical section VI-VI (Evstatiev & Evlogiev 2013) and estimated displacement directions

Figure 7. SBAS-DInSAR results and geological features in Topola 4

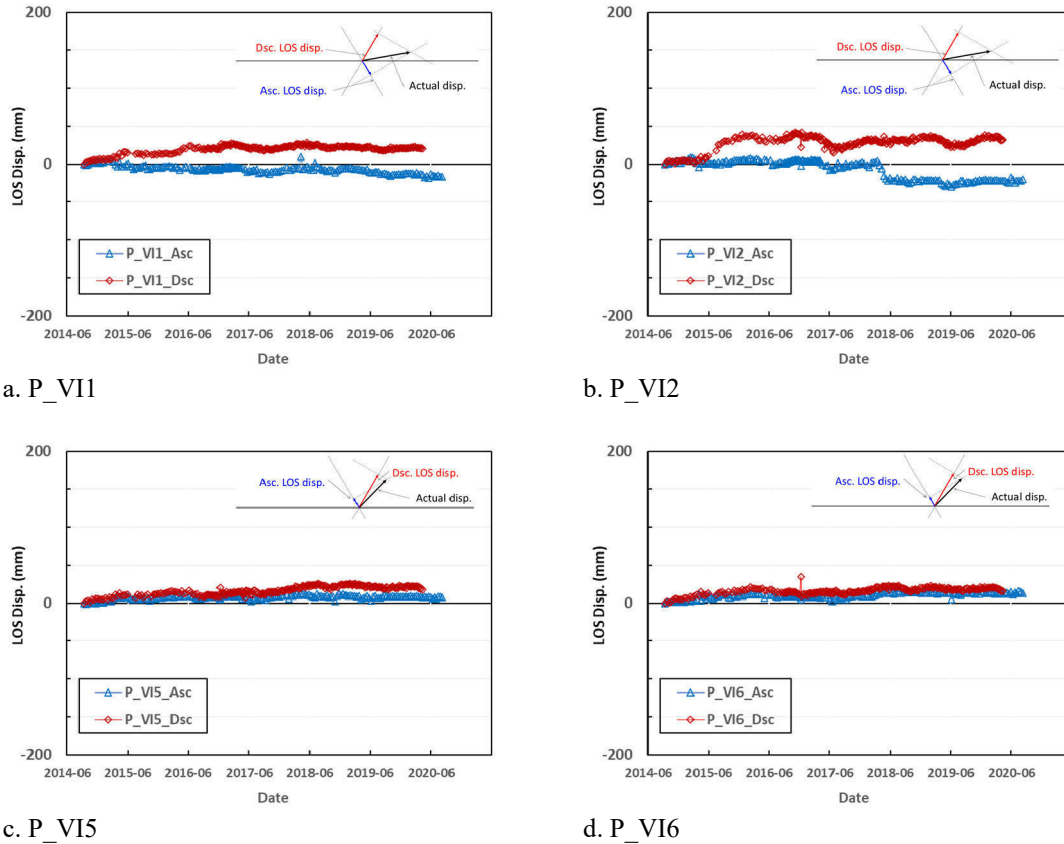


Figure 8. Transitions of descending and ascending LOS displacements along VI-VI line

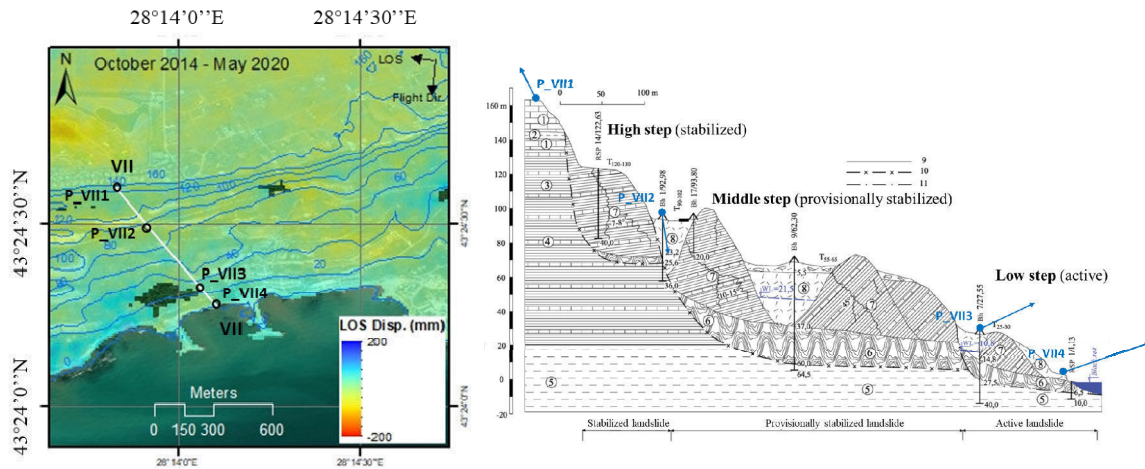
4.2.2 Topola 5 (section VII-VII)

Figure 9a shows the LOS displacement distribution in the descending case. The geological and geomorphological structure of the western half of the terrain is rather different from the eastern one in Topola 5 (Figure 5). In the vertical section of VII-VII, the landslide has three-stories (high, middle, and low steps in Figure 9b). The high step is considered to be relatively stable. The sliding surface of the high step crosses the Topola Formation (toN1s). The middle step occupies the largest Euxinograd Formation (evN1kg-s). These upper two landslide blocks (high and middle steps) are provisionally stable for now. Contemporary movements have been appearing in the low step, where the equilibrium was disturbed by active marine abrasion (Evstatiev & Evlogiev 2013).

The time transitions of the LOS displacements at the points of interest (POI: P_VII1 to P_VII4), selected from reference vertical section VII-VII (Figure 9), are shown in Figure 10.

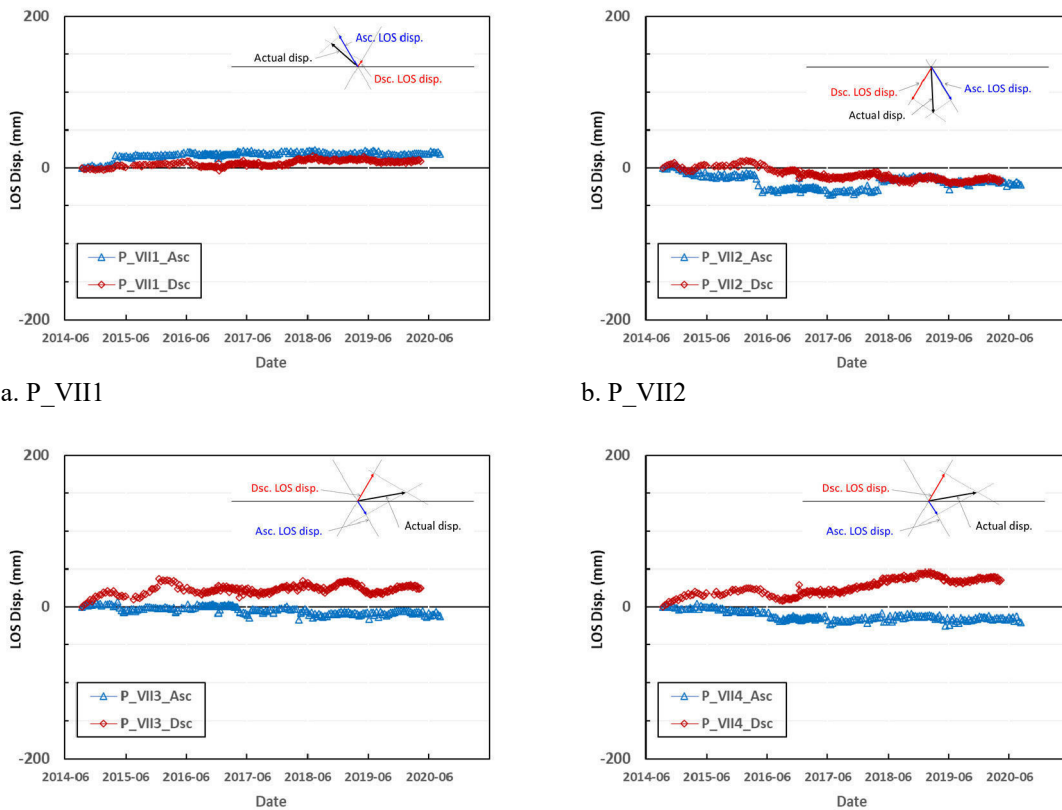
The displacements at P_VII1 (Figure 7a), on the LRL plateau, are seen to move slightly upward (Figure 9a). The displacement at P_VII2, on the second terrace from the main scarp, slightly subsides (Figure 9b). Around the coastal area affected by active marine erosion, the displacements at P_VII3 and P_VII4 exhibit a slight uplift (Figures 9c and 9d) and move to the east.

Consequently, as SBAS-DInSAR detected active displacements at the low step, Topola 5 was determined to be an active landslide area even now.



a. LOS displacement distribution (descending) from Oct. 2014 to May 2020
 b. Vertical section VII-VII (Evstatiev & Evlogiev 2013) and estimated displacement directions

Figure 9. SBAS-DInSAR results and geological features in Topola 5



a. P_VII1

b. P_VII2

c. P_VII3

d. P_VII4

Figure 10. Transitions of descending and ascending LOS displacements along VII-VII line

4.2.3 Eastern end of Topola village

SBAS-DInSAR detected large displacements in the eastern portion of Topola village which are denoted in red, orange, and blue in Figure 6. According to the official reports (MPPB 2017, 2018, 2019), a landslide area is clearly found in the coastal area, and large deformation has been

seen among the massive buildings located inside of the landslide area (Figure 11). One building is inclined backward and the front of it is visibly raised, while others have moved forward and are twisted. The landslide has cut off the road, and transverse ridges have appeared, as shown in Figure 11. It was registered in 2014 as No. DOB 17.05009-01-03 (MPPB 2022). There are terraces and cliffs at the landslide toe up to a height of about 3.0 to 4.0 m along the coastline. On the western side, near the coastal cliff, a scarp with preserved sediments and a sloping formation is visible. The scarp may have been affected by sea erosion (MPPB 2017, 2018, 2019).

LOS displacement distribution maps for the descending and ascending data around the eastern end of Topola village are given in Figure 12. Figure 13 shows the time transitions of the LOS displacements at four points (pixels) of interest (P29, P30, P31, and P33) in this area.

P29, on the plateau above the slope, is stable because almost no displacement appears (Figure 13a). At P30, located in the area of massive buildings (Figure 11b), both descending and ascending LOS displacements have significantly increased toward the negative side (extension) with time (Figure 13b). Such behavior indicates that the actual displacements are dominantly subsidence. The eastern component of the displacement is estimated to be small. Since the slope faces south and the massive buildings sit on the middle terrace of the slope, the displacement is supposed to move in a southern and downward direction. At P31, in the middle of the slope, the descending LOS displacement is almost zero or slightly positive, while the ascending one is negative (Figure 13c). This indicates that the actual displacement dominantly moves to the east and downward. At P33, near the coastal area, both descending and ascending LOS displacements are compression, and the descending one is larger than the ascending one (Figure 13d). Therefore, the actual displacement seems to move upward and slightly to the east at the landslide toe.

From the above results, it is found that this area shows typical landslide behavior along the vertical sections of P29, P30, P31, and P33. The SBAS-DInSAR results correspond to the actual behavior described in the official reports (MPPB 2017, 2018, 2019).



a. Aerial photo and landslide boundary



b. Buildings in landslide area

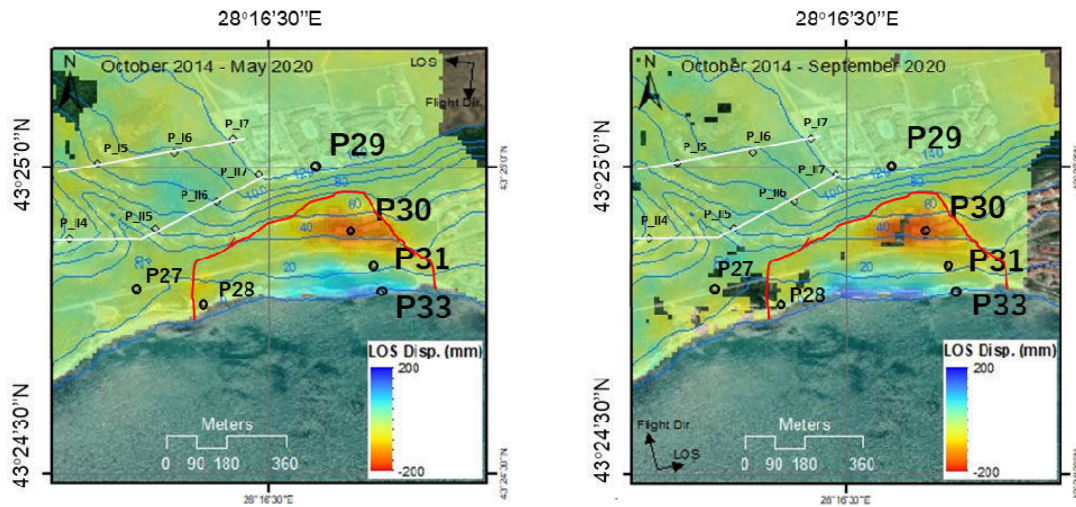


c. Transverse ridge of landslide boundary



d. Landslide area shot from the west

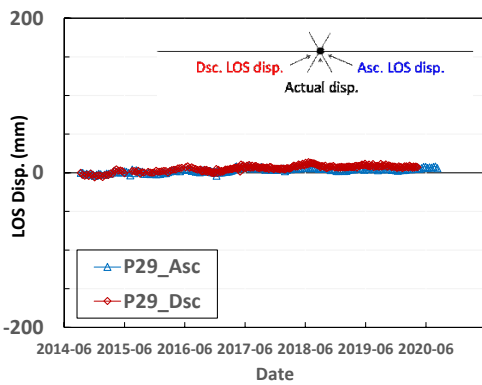
Figure 11 Landslide around eastern end of Topola village



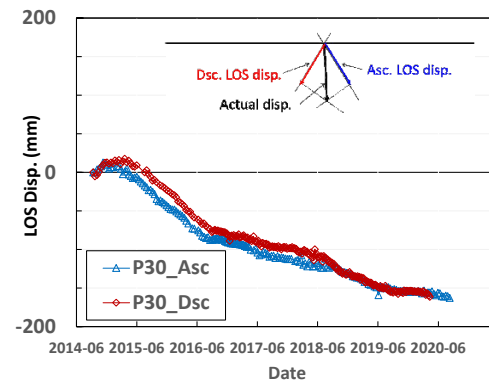
a. Descending

b. Ascending

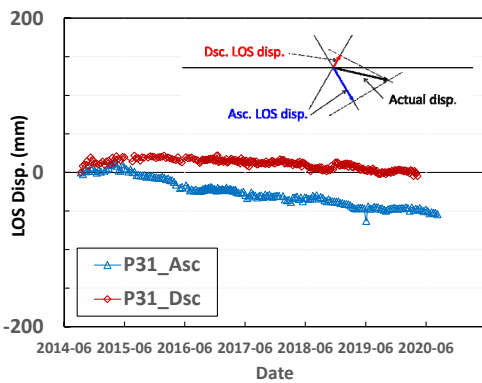
Figure 12. LOS displacement distributions around eastern end of Topola village



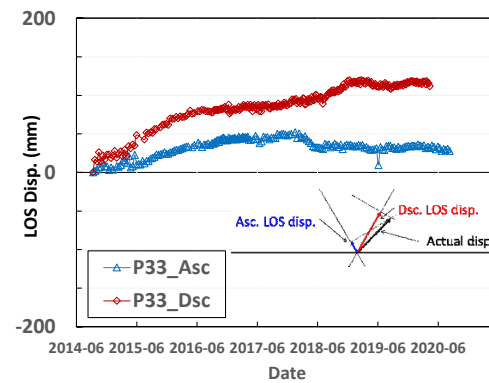
a. P29



b. P30



c. P31



d. P33

Figure 13. Transitions of LOS displacements by ascending and descending data around eastern end of Topola village

5 CONCLUSIONS

In this study, SBAS-DInSAR was employed to monitor the landslide behavior in Topola village along the northern Black Sea coast of Bulgaria, and its applicability was investigated by a comparison with the actual behavior described in site observation reports.

The distribution maps and time transitions of the LOS displacements were obtained over a period of six years starting in 2014. SBAS-DInSAR was able to detect small displacements in old landslide areas and active landslide behavior at the eastern end of Topola village area, which corresponded to the actual behavior described in the official reports of landslides published by the Bulgarian Ministry of Regional Development and Public Works.

This study has suggested that DInSAR will be a useful tool for long-term continuous landslide monitoring along the northern Black Sea coast.

ACKNOWLEDGEMENTS

This research was partially supported by JSPS KAKENHI (Grant-in-Aid for Scientific Research, Japan Society for the Promotion of Science) Grant Number 16H03153. The authors express their gratitude to the European Space Agency (ESA) for providing the Sentinel-1 SAR data. They also extend their appreciation to Ms. H. Griswold for proofreading the manuscript.

REFERENCES

- Atanasova, M., Nikolov, H., Vassileva, K., Nankin, R., Ivanov, P. & Dimitrov, N. 2020. Study of the contemporary state of the landslides in the northern Bulgarian Black Sea coast. *Proceedings of SPIE Vol. 11524, Eighth International Conference on Remote Sensing and Geoinformation of the Environment (RSCy2020)* 115241C:1-15. doi: 10.1117/12.2570678
- Berardino, P., Fornaro, G., Lanari, R., & Sansosti, E. 2002. A new algorithm for surface deformation monitoring based on small baseline differential SAR interferograms. *IEEE Trans. Geosci. Remote Sens* 40:2375–2383. doi.org/10.1109/TGRS.2002.803792
- Bruchev, I., Dobrev, N., Frangov, G., Ivanov, P., Varbanov, R., Berov, B., Nankin, R. & Krastanov, M. 2007. The landslides in Bulgaria – factors and distribution. *Geologica Balcanica* 36(3-4): 3–12
- Evstatiev, D. & Evlogiev, Y. 2013. Landslides along the northern Black Sea coast between Varna city and Kavarna town (Bulgaria). *Geo-Eco-Marina* 19: 39–57
- Ferretti, A. 2014. *Satellite InSAR data: reservoir monitoring from space*. The Netherlands: EAGE Publication.
- Hanssen, R.F. 2001. *Radar interferometry: data interpretation and error analysis*. Dordrecht, Kluwer Academic Publishers.
- МРРБ (Министерство на регионалното развитие и благоустройството: Ministry of Regional Development and Public Works). 2017, 2018, 2019. ГОДИШЕН ДОКЛАД (Annual Report), No. РД-02-29-23/27.02.2017 г. И, No. РД-02-29-198/02.05.2018 г., No. РД-02-29-114/02.07.2019 г. (in Bulgarian).
- МРРБ (Министерство на регионалното развитие и благоустройството: Ministry of Regional Development and Public Works). 2022. Регистър на свлачищата (Landslide register). <http://gz-varna.mrrb.government.bg/map/>. Accessed on 9 June 2022 (in Bulgarian).
- Nikolov, H. & Atanasova, M. 2016. Landslides monitoring near Kranevo by means of InSAR. *Third European SCGIS Conference on Geoinformation Technologies for Natural and Cultural Heritage Conservation*: 54–63
- Özer, I.E., Leijen, F.J., Jonkman, S.N. & Hanssen, R.F. 2018. Applicability of satellite radar imaging to monitor the conditions of levees. *J Flood Risk Management*. 2018; e12509. doi:10.1111/jfr3.12509
- Yamaguchi, M., Yastika, P.E., Shimizu, N., Milev, N. & Vrkljan, I. 2021. Application of SBAS-DInSAR to monitoring landslides along the northern Black Sea coast in Bulgaria, *Proceedings of EUROCK-Torino 2021*, IOP Conf. Series: Earth and Environmental Science 833, 012151. doi:10.1088/1755-1315/833/1/012151

Cracking behavior of an inclined open crack in transparent 3D printed rock-like specimen

W. Lee, D. Lee, S. Jeon
Seoul National University, Seoul, South Korea

ABSTRACT:

To observe the aspect of crack growth in rock is the main purpose of this study. Due to the geological nature of rock, rock specimens present scattered testing results. On the while, artificial rock-like specimens, for instance mortar specimens or 3D printed specimens, have advantages that allow reproduction with the identical and/or desired properties at high accuracy and resolution. The Objet30 Pro 3D printer from Stratasys was used in this study along with VeroClear, a transparent PMMA printing material. Transparent 3D printed specimen was expected to allow visual examination of crack behavior inside the specimen as it is affected under compressive loading. When PMMA 3D printed specimen is tested under compressive loading in frozen condition, it is known to show more of brittle behavior than in room temperature. Therefore, in this study, specimens containing single open crack with 30, 45 and 60 degrees in inclination angle were tested under frozen condition. The crack tip shape was either square or sharp with the tip angle of 20°, 45°, and 90°. Specimens under uniaxial compression test were filmed by a high-speed camera with the resolution of 640×352 and the frame speed of 30,000 f/s to observe the cracking behavior. Through compressive loading test, strength of the specimens with higher tip angles and 45° inclination angle was found to be the weakest. It was also observed that the decrease in inclination angle or the increase in tip angle resulted in higher wing crack angle development.

1 INTRODUCTION

Cracking behavior of rock is difficult to be fully understood especially for inclusion cracks in three-dimensional space because rock is opaque and the cracking speed is very fast. On the while, artificial specimens are known to be advantageous in which its reproducibility and characteristics outstands the needs in certain tests where natural rock specimens are limited to be. The main applications of 3DP technology in the current field of rock mechanics are making rock-like specimens including cracks or joints, reproducing physical modeling, reconstructing complex rock structures, and linking actual experiments with numerical simulation results. On the other hand, the main limitations are the issues in printing materials, accuracy, and function. None of the materials currently available for 3D printing satisfies all of the rock-like properties of high strength, stiffness, and brittleness. Also, printing capability for extended duration and precision to produce large-scale printouts are still lacking (Gao et al. 2021). Ma et al. (2018) found out that the tensile wing crack propagation is the main form of failure of the antisymmetric kinked fissures, but the inclination of the branch fissures also played a key role on the location of initial fracture, through the uniaxial compression tests using 3D printed specimens having various types of kinked fissures. Zhou et al. (2019) conducted static uniaxial compression tests on resin-based artificial 3DP rocks containing single flaw and double pre-existing penny-shaped 3D internal flaws to investigate the influence of flaw number, flaw angle and ligament angle on the volumetric fracturing behaviors. Ge and Xu (2019) developed a kind of transparent hard rock material that can replace existing materials to solve the problem of not being able to directly observe cracks in models made of cement mortar, helping experimental studies of blasting crack propagation in deep rock mass.

2 EXPERIMENTAL WORK

2.1 *Testing specimen*

Precise production and duplication of intended specimen was done by a 3D printer with high resolution. In this study, a polyjet type 3D printer, Objet30 Pro of Stratasys, was used using an ink material, Veroclear, which is transparent PMMA (Polymerization of Methyl MethAcrylate, synthetic resin). Specimens were cuboid in shape, which enabled easy visual observation of inside of the specimen through planar surface, and 25×25×60 mm in size. Each specimen had a penny-shaped open crack of 15 mm in length and 1 mm in thickness at the center as shown in Figure 1. The crack had three different inclination angles of 30°, 45° and 60° and four different tip angles of 20°, 45°, 90° and square tip as shown in Figure 2. For each case, three specimens were prepared and tested. Thus, a total number of specimens were thirty-six while twenty-four among them were filmed with high speed camera. The specimen was not brittle enough at room temperature to present stress drop at failure under uniaxial load. But the specimen presented brittle failure behavior at freezing temperature (Zhou and Zhu, 2018). Therefore, in this study, the specimen and the platens were put in the cold chamber at -50°C for at least 24 hours before testing was carried out. An anti-freezing substance was sprayed on the surface of the specimen before testing to prevent frosting which can hinder clear visual observation. The specimen at the freezing temperature showed the stress-strain curve as presented in Figure 3. The strength was about 140 MPa while the strain at failure was about 0.055.

2.2 *Loading rate and high-speed camera*

In the uniaxial compression test, MTS 816 testing system was used to apply a quasi-static load to the specimen at 0.4 mm/s of constant displacement rate which is equivalent to strain rate of $6.7 \times 10^{-3} \text{ s}^{-1}$. The cracking behavior was observed and recorded using a high-speed camera, Phantom T1340, at the resolution of 640×352 pixels and the frame speed of 30,000 fps.

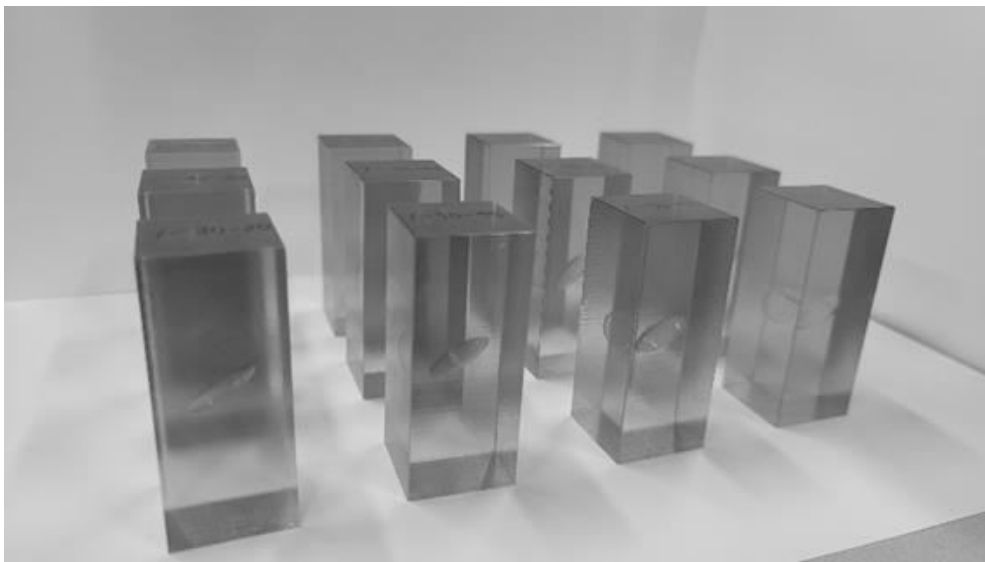


Figure 1. Cuboid specimens with a penny-shaped crack in it

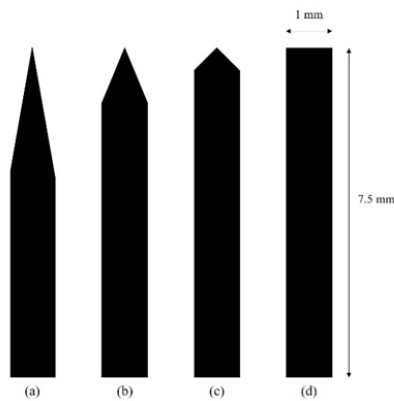


Figure 2. Crack tip angle of (a) 20°, (b) 45°, (c) 90°, and (d) square tip (shown in a half crack length)

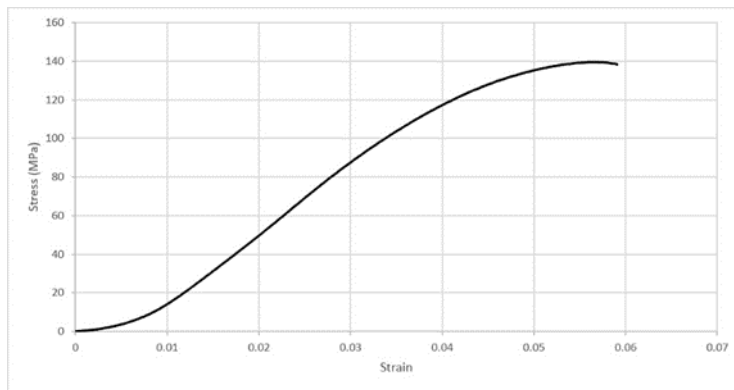


Figure 3. Result of uniaxial compression test of a solid Veroclear specimen at -50°C

3 RESULTS AND DISCUSSION

In this study, both wing crack growth and secondary crack growth were observed depending on crack inclination (θ) and tip angle, where the wing crack angle (α) and secondary crack angle (β) were measured from the crack surface orientation as shown in Figure 4. But, wing crack growth was dominant than secondary crack growth in most cases.

Figure 5 presents the variation of wing crack angle at different tip and inclination angles. Wing crack angle increased as the tip angle increased, while it decreased as the inclination angle increased. A few specimens showed secondary cracks before wing cracks grew, which was observed mostly for the specimens with a crack at low inclination angle of 30°.

Because wing crack does not grow straight, combination of Mode I and Mode II crack behavior is involved resulting in the final crack orientation parallel to the maximum principal stress. Thus, the summation of inclination angle and wing crack angle, which is named 'constant angle' in this study, was examined. Figure 6(a) shows that the constant angle increased as the tip angle increased while it is roughly 105° on average as shown in Figure 6(b). Comparing Figure 5(b) and 6(b), it could be confirmed that wing crack angle is mostly affected by inclination angle.

Figure 7(a) shows that the peak strength was higher for the specimens with smaller tip angles. This is contradictory because a sharp crack is easier to grow related to higher stress concentration. But, in this study, the crack tip had polygonal shape of which the corners, rather than the tip, could be the crack initiation point when it is located in a preferable position. Figure 7(b) shows that the peak strength was smallest when the inclination angle was 45°. Strength anisot-

ropy due to a single discontinuity can be presented as shown in Figure 8. Assuming that the friction angle of an open crack surface is zero, the minimum strength can be obtained at the inclination angle of 45°.

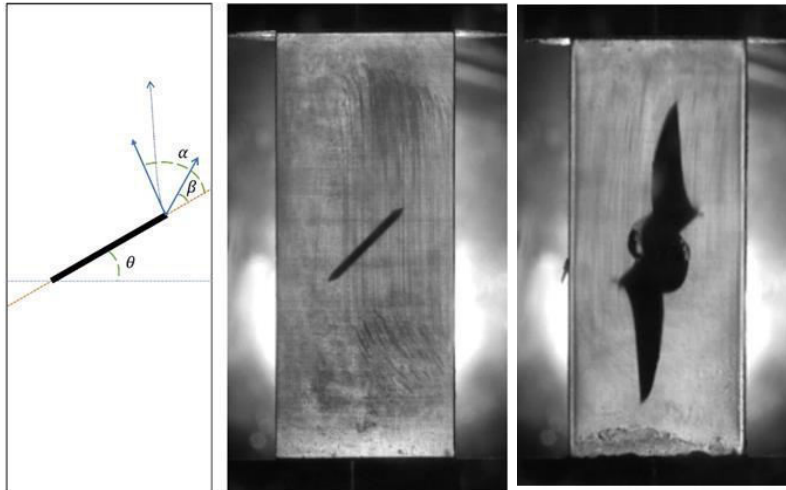


Figure 4. Configuration of crack angle: crack inclination angle θ , wing crack angle α , and secondary crack angle β

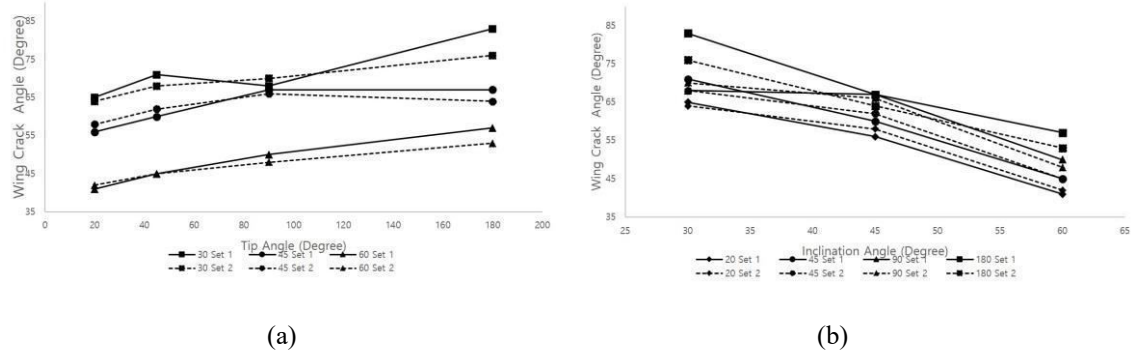


Figure 5. Observed wing crack angle at various tip angle (a) and inclination angle (b).

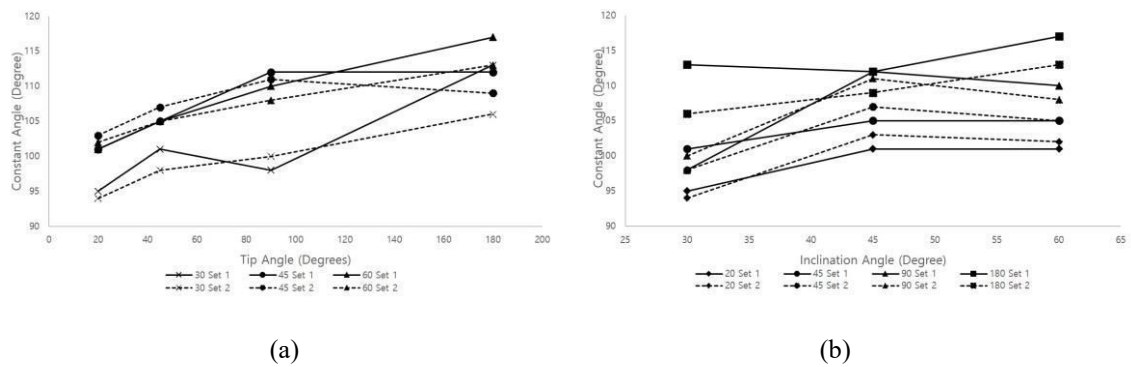


Figure 6. Constant angle at various tip angle (a) and inclination angle (b).

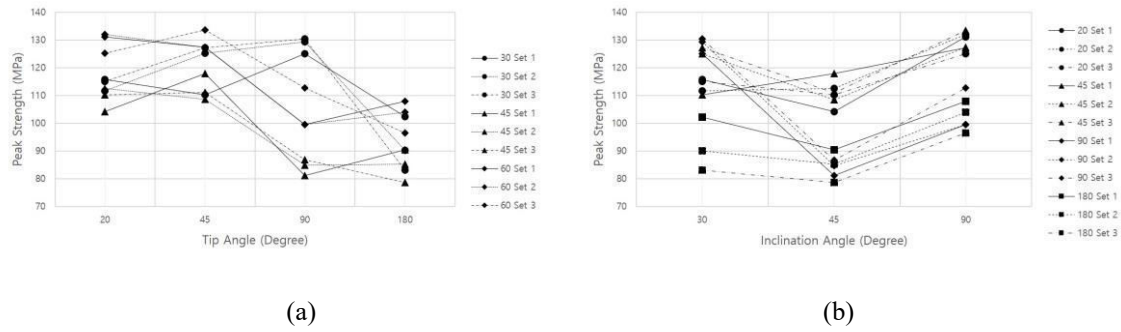


Figure 7. Peak stress at various tip angle (a) and inclination angle (b)

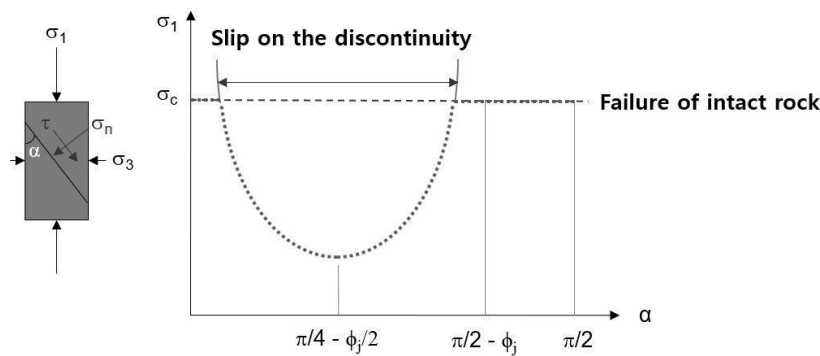


Figure 8. Strength anisotropy due to a single discontinuity, where ϕ_j is the friction angle of discontinuity surface

4 CONCLUSION

The use of 3D printed transparent specimens has advantages in being able to visualize the growth of cracks inside the specimen under loading conditions. In this study, with the use of highspeed cameras, growth of wing cracks and its angles could be visualized and observed along with the strength of specimens having various single open crack conditions. Wing crack angle increased as the tip angle increased while it decreased in larger inclination angle. It was observed that the ‘constant angle’ was around 105° on average when inclination angle was matched with wing crack angle. Except the outlier at a certain condition, i.e. 30° of inclination angle and 90° of tip angle, strength presented a uniform trend. Despite the lack of variety of samples, this study could observe characteristics of cracking behavior at different inclination angle-tip angle combinations.

5 ACKNOWLEDGEMENTS

This work was supported by the Institute for Korea Spent Nuclear Fuel (iKSNF) and National Research Foundation of Korea(NRF) grant funded by the Korea government(Ministry of Science and ICT, MSIT)(2021M2E1A1085196).

This work was supported by Energy & Mineral Resources Development Association of Korea (EMRD) grant funded by the Korean government (MOTIE) (0456-20220020, Training Program for Specialists in Smart Mining).

6 REFERENCES

- [1] Xia, Y., Meng, Q., Zhang, C., Liu, N., Zhao, Z., Chen, J., and Yang, G., 2021, Application of 3D printing technology in the mechanical testing of complex structural rock masses, *Geofluids*, Article 7278131.
- [2] Gao, Y.T., Wu, T., and Zhou, Y., 2021, Application and prospective of 3D printing in rock mechanics: A review, *International Journal of Minerals, Metallurgy and Materials*, 28(1), 1-17.
- [3] Ma, G., Dong, Q., and Wang, L., 2018, Experimental investigation on the cracking behavior of 3D printed kinked fissure, *Science China Technological Sciences*, 61, 1872-1881.
- [4] Zhou, T., Zhu, J.B., Ju, Y., and Xie, H.P., 2019, Volumetric fracturing behavior of 3D printed artificial rocks containing single and double 3D internal flaws under static uniaxial compression, *Engineering Fracture Mechanics*, 205, 190-204.
- [5] Ge, J., and Xu, Y., 2019, A method for making transparent hard rock-like material and its application, *Advances in Materials Science and Engineering*, Article 1274171.
- [6] Zhou, T., and Zhu, J.B., 2018, Identification of a suitable 3D printing material for mimicking brittle and hard rocks and its brittleness enhancements, *Rock Mechanics and Rock Engineering*, 51, 765-777.
- [7] Zhang, Q.B., and Zhao, J., 2014, A review of dynamic experimental techniques and mechanical behavior of rock materials, *Rock Mechanics and Rock Engineering*, 47, 1411-1478.

The electrical resistivity method and geological mapping for characterization of materials in linear excavation works

J.A.B. Garcia

Universidade Federal de Santa Catarina UFSC, Joinville, Brazil

A.F.B Cordeiro

Dinamiza, Consultoria e Engenharia, Brasília, Brazil

R. P. Cunha

Universidade de Brasília UnB, Brasília, Brazil

L. S. Cunha

Universidade de Brasília UnB, Brasília, Brazil

ABSTRACT:

The characterization, rock excavatability and volume calculation of excavations carried out during infrastructure works are extremely important given the large amount of ground movement that takes place in this type of construction. The poor characterization of materials can bring to almost any field work significant changes in the initial budget due to the high cost of excavation of rock materials as compared with the conventional soil excavation. On many occasions, a limited geological information, together with a reduced number or low quality of the specified (direct) site investigations, turns more feasible the usage of indirect methods to determine the characteristics of the materials to excavate. Given the heterogeneous characteristics of the soil layers, and the high changes of rock lithology and fracturing state, it becomes very difficult to distinguish the transition zones based solely on few punctual surveys. For this reason, indirect methods of investigation shall be specified together with the direct ones to allow a better and continuous assessment of the subsoil, possibly at a lower cost and with a nondestructively manner. With this set of field information, it is undoubtedly easier to interpret and identify the linear stratigraphy of the construction site, hence performing a tailored budget based on more realistic cut and excavation sections of soil, rock and saprolite slopes. Therefore, this paper presents a real case history where the rock excavatability and the classification methodology of 1st, 2nd and 3rd category material in a non-continuous linear (25 km) cut was interpreted through the use of an electrical resistivity survey, complemented with direct in situ investigations (SPT, rock coring and topography) and geological mapping in the same region. The cuttings were specified as part of a large railroad project design in the state of Bahia – Brazil, where great part of the construction budget was involved with the excavation phase. As it will be demonstrated, satisfactory interpretation results were found by adopting the advocated methodology, as they yielded more realistic excavation volumes than those initially forecasted solely with SPT or rock drilling soundings.

Keywords

Geophysics, rock excavatability, electrical resistivity, in situ testing, excavation, infrastructure works

1 INTRODUCTION

The characterization and volume calculation of the excavation material are of paramount importance in infrastructure projects, especially railroad projects due to the large movement of earth during the implementation of this type of work. Poor characterization can bring significant changes to a project due to the great difference in prices between excavation of rock and earthy

materials. The cost of excavating rock is high and will depend directly on material properties such as the degree of fracturing, coherence, alteration, and mineralogy.

Due to the extent of linear works, geotechnical geological information is generally scarce. Large projects often have few and poor-quality direct borings such as SPT and rotary drilling, which makes it difficult to classify the materials as to their excavatability. To execute a good classification job, the professional must have a good amount of direct drilling, must perform continuous indirect drilling such as geophysical prospection, must perform adequate fieldwork allied to common sense, and have plenty of experience in similar projects in the region of the work's implantation, because, in a certain way, the classification criteria have subjective components.

Furthermore, given the great variation of soil characteristics and the high alteration and fracturing of the rock, it becomes very difficult to distinguish the transition of the layers with punctual drilling, often of poor quality, with inadequate diameters, and with a low percentage of the recovery.

Thus, the objective of this research was to propose a methodology for the classification of excavation materials (soils and rocks) from the information available in the early stages of large infrastructure projects such as direct drilling (SPT and rotary), geophysical surveys, and structural field surveys by geology teams. In addition, a case study was evaluated, where a comparison was made between the initial classification prepared with only one direct bore for each proposed cut, a classification performed later with some complementary boreholes and electrical resistivity surveys, and a verification classification performed with field mapping to evaluate the rippability and excavatability.

The research was carried out in five sections The West-East Integration Railway, FIOL (EF-334), a railway project currently being executed in the state of Bahia and Tocantins, Brazil, in a very complex and heterogeneous region from the geological point of view.

The significant differences in the excavatability of the materials have an impact on the final construction budget due to the significant increase in excavation volumes and on the definition of the project slope gradient and definition of containment structures on unstable slopes.

2 CLASSIFICATION OF EXCAVATION MATERIALS

The purpose of classification is to predict the excavation volumes of each type of material for planning and budgeting the work and consequent measurements and payments to contractors hired for a particular task. It is clear that the cost of excavating rock is much higher than the cost of excavating soil because it consumes many more resources, such as the use of explosives and special blasting equipment.

The concept of excavatability adopted by VALEC makes reference to DNIT STANDARD 106/2009-ES: Earthwork-Cuts-Service Specifications, where the cutting material is divided into three categories as follows:

1st category material: comprises soils in general, residual or sedimentary, pebbles rolled or not, with a maximum diameter of less than 0.15m, whatever the moisture content presented. The extraction process is compatible with the use of a "dozer" or "scraper" towed or motorized.

The 2nd category of material - comprises the soils with resistance to mechanical disassembly lower than that of unaltered rock, whose extraction is processed by a combination of methods that require the use of the largest ripper equipment contractually required; the extraction may eventually involve the use of explosives or an adequate manual process, including in this classification the rock blocks with a volume lower than 2 m³ and the crags or stones of an average diameter between 0.15m and 1.00m.

Third category materials include those with resistance to mechanical disassembly equivalent to unaltered rock and blocks of rock with an average diameter exceeding 1.00m or with a volume equal to or greater than 2m³, whose extraction and reduction, in order to make loading possible, are processed with the continuous use of explosives.

The problem with classifying the materials adopting the three categories mentioned is that, besides being subjective criteria, these categories of excitability were developed for the use of

motor scrapers and crawler tractors, equipment that was used a few years ago; however, currently, the use of excavators has replaced this equipment, in search of greater productivity. Track-type tractors cannot work in specific situations and need the support of other equipment or even their replacement by hydraulic excavators.

There is, therefore, a big difference in the assignment of excavation categories: 1st Category and 2nd Category; and what conditions are needed to start excavating with the use of explosives, 3rd Category.

2.1 Rock mass excavatability classification

Rippability can be evaluated by means of the rock mass characteristics in terms of their degree of alteration, spacing of discontinuities and consequent size of individual pre-existing blocks in the rock, their intermingling and block shape, characteristics of joints and fractures, and their persistence, which may be associated, as a whole, with the velocity of propagation of P-type seismic waves. In the international technical environment, there are several publications on developments in excavation methods and equipment. Initially, Frankine et al. (1971) proposed a method based on the point load strength of intact rock, I_{s50} , and the fracture index.

Pettifer and Fookes (1994) stated that the excavatability of rocks depends on their individual properties, on the excavation equipment, and on the method of working. They also stated that, apart from the strength of rock expressed by point load index or rock strength criteria indicated by ISRM (International Society for Rock Mechanics), the discontinuity characteristics define the individual size of rock blocks, which constitutes one of the most important parameters for rock rippability. They presented a detailed chart (Figure 1), which is similar to that proposed by Franklin et al. (1971).

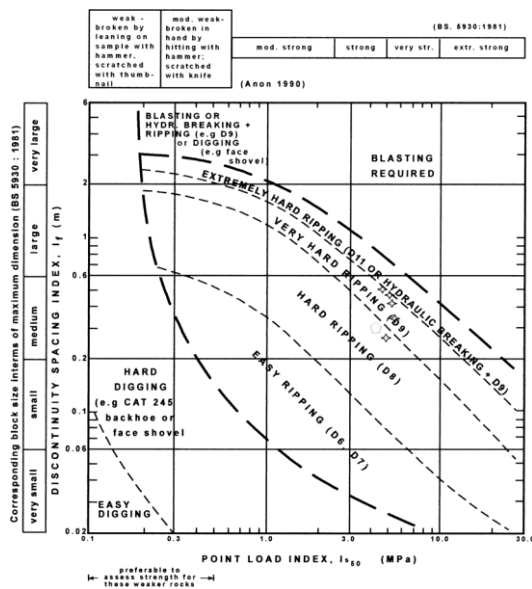


Figure 1. Assessment of rock masses with reference to excavatability classification system recommended by Pettifer and Fookes (1994)

Other methodologies for evaluating excavatability have used rock mass grading, such as the method proposed by Weaver (1975), based on the RMR system. This method was later perfected by Smith (1986) using grades given within a system very similar to RMR, not taking into account the seismic velocity but the simple compressive strength (UCS) of the rock. With the sum of these scores, he assigned the rock masses a RR (Rippability Rating).

current faults, following the same preferential direction.

Locally, the project is inserted into different geomorphological compartments, marked by many mountain ranges with an approximately north-south direction at the beginning of the route, passing into the dissected valleys of the Contas River.

The thickness of the residual soil layer varies along the route, with a generally high rocky top described, as well as the presence of boulders. Rock fragments of varying dimensions, as can be seen in Figure 6, which represents typical situations encountered after the opening of the project's mandatory cuts.



Figure 6. Presence of rocks in the crest of the excavation slopes: (a) ES 1264+040 - Cut 14; (b) ES 1268 + 640 - Cut 21; (c) ES 1271+880 - Cut 25; (d) ES 1275+540 - Cut 36

Boreholes executed in the region indicate a layer of topsoil, mostly residual, whose thickness varies between 1m and 4.5m, with local alteration zones reaching a depth of 14m. rock blocks appear scattered in the middle of this soil layer.

The rock mass beneath the soil layer varies from very altered to altered and fractured to very fractured, with oxidized discontinuity surfaces. The degree of alteration is related to the geological structures.

The rocks that constitute the massif are mostly described as foliated granites or gneisses, with other lithologies occurring with less representativeness, such as quartzites and schists.

Such structural complexity is evidenced by distinct metamorphic foliations and fracture systems, locally, reflected in different problems related to the classification of excavation materials and problems in the execution of the cuts.

4 METHODOLOGIES FOR CLASSIFYING MATERIALS

In order to classify the materials for excavation, the use of three methodologies is recommended. The first is the classification by means of SPT and rotary surveys. It is indicated to have at least two surveys for each cut. The second methodology is the use of electrical resistivity geophysical soundings or seismic geophysical soundings. The interpretation should be accompanied by direct soundings for adjustments. The third methodology is an adjustment methodology based on the geological mapping of the first cuts performed.

4.1 Characterization based on site investigation

It is the most limited methodology, depending on the number of boreholes in the cut. In the case study, the first material classification was initially performed using a single SPT probe for each cut, and then a new adjusted classification was performed by means of some complementary rotary probes. For all cuts, the differences in material volumes are very considerable. The classification done with SPT and rotary drilling is presented in Figure 7.

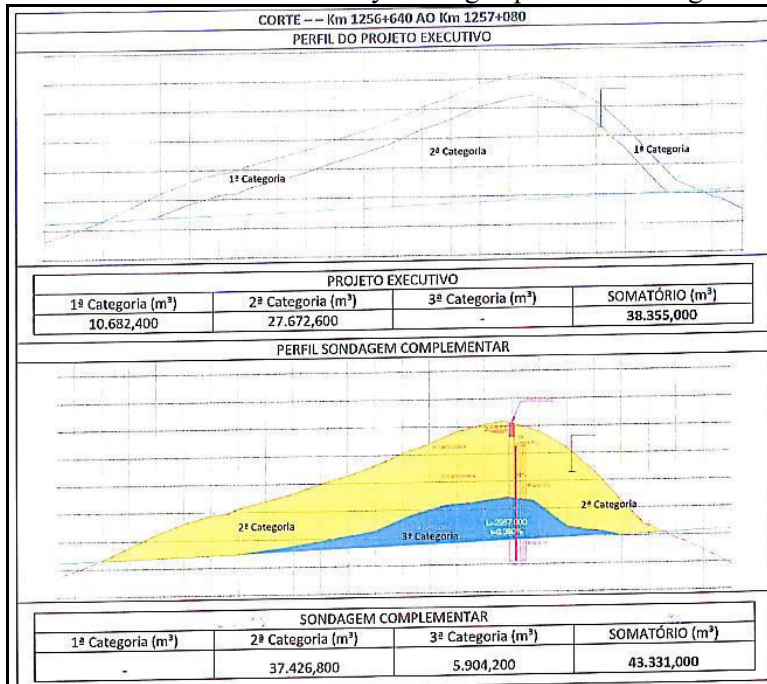


Figure 7. Classification of materials with SPT and rotary drilling.

In these Figures, the location of the boreholes is observed within the geophysical prospection carried out in each cut. It can be concluded that because the cut is very heterogeneous, the borehole is not representative of the materials found along the axis of the project, which makes any correlation obtained through this incoherent when replicating the entire cut.

4.2 Electrical resistivity for the characterization of materials

The influence of complex geology on the project was apparently not taken into consideration in the characterization and prediction of excavation quantities during the preparation of the executive project. For this reason, complementary geophysical investigations were carried out using the electrical resistivity method.

Although the refraction seismic method may present more advantages for establishing correlations with types of materials and the difficulty of ripping rock, the electrical resistivity geophysical prospection can also help to establish correlations between electrical resistivity and the type of materials present. The geophysical study serves to get a clear idea of the variability of the materials in this section and can be adjusted by means of good quality direct soundings. The main advantages of geophysical methods are the speed of execution and low cost compared to mechanical surveys.

In addition to the variations in depth clearly observed in the geophysical survey, the section will also have variations in materials in the transverse direction because the study was performed on the axis of the railroad. These changes could be observed in a 3D electrical resistivity geophysical representation.

As part of the benchmarking stage of the executive project, a geophysical campaign was carried out where 86 geoelectric profiles (SEVME) of the cuts were made using the electrical walk

technique (EC). The SEVME multi-electrode vertical electric sounding was performed using SAS 4000 equipment from ABEM manufacturer and the data processing was performed using the Res2DInv program.

The acquisition of geophysical data in this case is limited to a maximum depth of 30 m. It is important to point out that the same lithological type can present a wide range of variation in resistivity values because there are many factors that interfere in the resistivity value of a material, mainly depending on the minerals present, liquids and gases filling the voids, humidity of the materials, porosity, texture, and pore distribution, among others.

The results were classified into three distinct zones, lithotypes framed as high apparent resistivity zone (HAZ), low apparent resistivity zone (LARZ) and intermediate resistivity zone (IRZ). As an example, Figure 8.

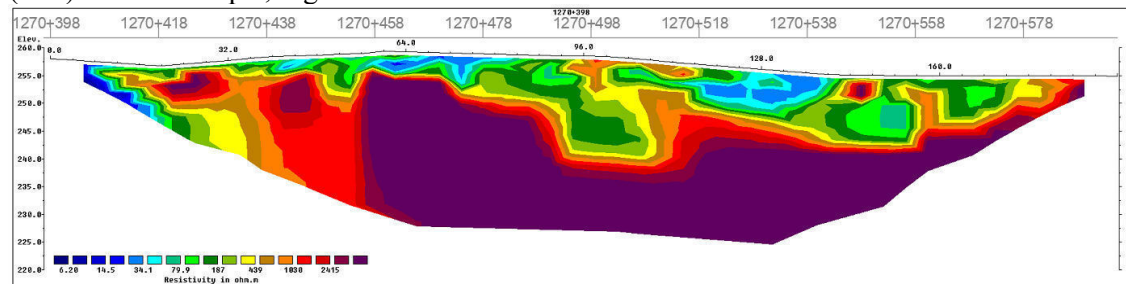


Figure 8. An example of a geophysical survey conducted on the project

High apparent resistivity values were associated with more compact and/or poorly fractured rocks or rock blocks, as well as with more compact, dry soil with pores filled by air. The low apparent resistivity values were related to more fractured rocks with the presence of water filling pores or rock fractures. It can also indicate the presence of clay material accumulated by the weathering process of the rocks. Intermediate apparent resistivity can indicate more fractured rocks.

From the geophysical soundings bulletins and the complementary direct sounding reports, it was observed that the easily excavated material (1st category material) was almost non-existent in the analyzed sections. The geophysical interpretation was performed with the help of the borehole reports. An example of the classification based on the geophysical surveys is presented in Figure 9. In this classification, 1a: 1st category material, cover material; 3ax: 3rd category material with high fracture index and low cohesion; 3a: 3rd category material with low fracture index, sound rock.

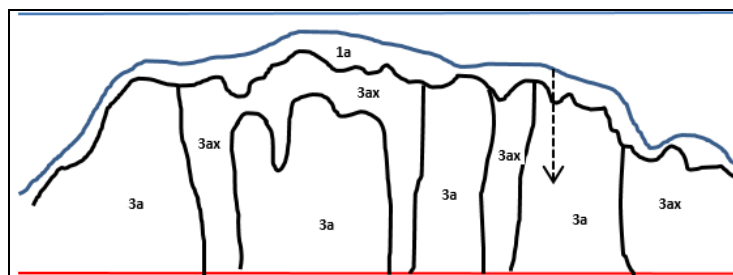


Figure 9. An example of material characterization with geophysical

4.3 Classification verification by mapping and field inspection of excavations performed

An inspection was conducted in some of the project's sections in order to validate the excavation conditions of the rock sections. The field procedure consisted of taking georeferenced photos of each slope. The geological, lithological, structural, and geomechanical aspects of each excavated slope were marked on these images.

The rock mass fracture classification is presented as volumetric joint count, J_v , described by

With field data that can be verified by inspection at any time, it is possible to classify the excavated rock masses as to whether they are easy or not to excavate mechanically with a D8 tractor, or whether they need to be excavated with explosives.

5 CONCLUSIONS

At the start of the execution of the services, the considerable difference in the volumes of excavation materials was immediately noticeable, because the quantification of the service had been carried out using only one SPT borehole for each cut. In the complex geological context where the project is located, the difference is very significant.

Due to the heterogeneity of the materials found in all cuts, it can be concluded that there is no correlation between the boreholes (reduced quantity and low quality) and the characterization profile of the materials found in situ, which justifies the great variability of the excavation volumes,

In most cases, the inclination of the slopes was different from the initial design to guarantee their stability.

The electrical resistivity geophysical investigation in conjunction with conventional geotechnical investigation and geological mapping is an important tool to characterize and classify excavation materials and serves to predict some problems related to slope inclination and the eventual need to implement containment solutions.

The case presented in this paper explores the feasibility of using geophysics to quantify excavation materials. It was possible to observe that the volume calculated by geophysics, in conjunction with direct drilling and geological mapping, was similar to the volume measured in the execution of the services of cutting and transportation of excavated material.

REFERENCES

- Deere DU (1964). Technical description of rock cores for engineering purposes. *Rock Mech. Rock Eng.*, 1: 17-22.
- Deere DU, Miller RP (1966). Engineering classification and index properties for intact rock. Air Force Weapons Laboratory Technical Report, AFWL-TR, Kirtland Base, New Mexico, pp. 65-116.
- DNIT 106/2009 – ES: Terraplanagem – Cortes – Especificações de serviço
- Franklin JA, Broch E, Walton G (1971). Logging the mechanical character of rock. *Transactions of the Institut. Min. Metallurgy.* 80: A1-9.
- Palmström A (1982): The volumetric joint count - a useful and simple measure of the degree of jointing. *Proc. int. Congr. IAEG, New Delhi, 1982*, pp. V.221 - V.228.
- Palmström A. (1995): RMI - a rock mass characterization system for rock engineering purposes. Ph.D thesis, University of Oslo, Norway, 409 p.
- Palmström A (1982). The volumetric joint count- A useful and simple measure of the degree of jointing. *4th Int. Congress Int. Assoc. Eng. Geol. New Delhi.*, pp. 221-228.
- Pettifer GS, Fookes PG (1994). A revision of the graphical method for assessing the excavatability of rock. *Quart. J. Eng. Geol.*, 27: 145-164
- Tsiambaos G, Saroglou H (2009). Excavatability assessment of rock masses using the Geological Strength Index (GSI). *Bullet. Eng. Geol. Environ.*, 69(1): 13-27

Application of the SfM technique for geomechanical analysis according to SMR and Qslope

C. P. Borja-Bernal

ETSI Minas y Energía. Universidad Politécnica de Madrid. Calle de Ríos Rosas, 21, 28003 Madrid, Spain

Universidad de Guayaquil, Facultad de Ciencias Naturales, Av. Raúl Gómez Lince s/n y Av. Juan Tanca Marengo, Guayaquil, Ecuador.

L. Jordá-Bordehore

Departamento de Ingeniería del Terreno. Escuela Técnica Superior de Ingenieros de Caminos, Canales y Puertos. Universidad Politécnica de Madrid. Campus Ciudad Universitaria, Calle del Prof. Aranguren, 3, 28040 Madrid, Spain

ABSTRACT:

The stability of a rock mass is influenced by the multiple interactions between the rock matrix, planes of weakness, the surrounding environment and the human processes that shaped the actual slope. The objective of this paper is to apply the Structure from Motion (SfM) photogrammetric survey technique to obtain reliable data that can be used to determine the relative stability of a slope. Data extracted from the 3D model were processed with kinematic analysis and subsequently applied to the SMR and Qslope geomechanics classification systems. The case study is in an almost stable state according to SMR and unstable for Qslope, clarifying that in the latter classification system the value is located very close to the zone called "uncertain slope stability", results that coincide with the physical evidence of instability found at the time of the field survey. It can be concluded that the SfM technique is applicable for the calculation of slope stability through empirical methods in tropical environments of the Andean countries.

Keywords: Smartphone, 3D model, Structure from motion, Qslope, Slope Mass Rating.

1 INTRODUCTION

When we talk about Rock Mechanics, the mind of the researcher is transported to an idealized world in which the problem to be addressed is simplified to two fundamental actors, rock matrix and discontinuities, which when combined allow the movement of rock masses of different sizes (Ramirez & Alejano, 2008). These rock masses are influenced by environmental and anthropic processes that facilitate or not the displacement of rock bodies in search of a position of equilibrium of forces and moments. Geomechanics classifications for tunnels and subway mining have been around since 1946 when Terzagui presented his version called Rock Load. It was not until 1973 when Bieniawski modified his RMR and applied it to slopes (Hernan & Andrade, 2007), this milestone gave way for Romana to propose his method known as SMR Slope Mass Rating in 1985 (Romana, 1985) and in 2015 Barton presented the most recent method of geomechanics classifications for slopes known as Qslope (Barton & Bar, 2015). The technician or researcher when performing a geomechanical survey, i.e. structural survey of existing weakness planes in logically unstable conditions for data collection and sampling, is subject to constant danger due to the hazardous working environment surrounding the slope as well as the scale of the work and the limited access to the unstable cut faces (Adrián Riquelme et al., 2020).

Photogrammetry is a common practice nowadays, although photogrammetric monitoring is the most economical alternative (Roberto Tomás et al., 2016) compared to other surface survey methods, it is still less accurate compared to models obtained with terrestrial laser scanner (Jordá et al., 2016; Roberto Tomás et al., 2016), this alleged lack of accuracy is compensated by the versatility of photogrammetry which allows the collection of information and the acquisition of photographs by means of ordinary equipment such as smartphones. The goodness of the SfM technique and the use of cell phones for taking photographs has been widely studied in the laboratory and in the field, comparing its results with other more precise techniques but also more complicated from the point of view of logistics and processing (An et al., 2021; A. Riquelme et al., 2021). Two main techniques are currently recognized for rock slope modeling in three dimensions, the first is the terrestrial laser scanner (TLS) and the second is the Structure from Motion (SfM) (A. Riquelme et al., 2021), 2021) which for the practical case deliver the same information that can be obtained in the field and used to determine the stability of a slope by empirical methods, we must remember that in direct survey with the use of compasses it is considered that the data are acceptable, only if it is under a certain value of acceptable deviation (Jordá Bordehore et al., 2017), value that can be extrapolated to the SfM technique, evidencing that the final result obtained for the geomechanics classification does not change significantly.

2 METHODOLOGY

In this study, we considered three fundamental stages (Figure 1); the first one is related to the field data collection, the second stage in which the 3D model is generated to obtain semi-automatic structural data and the last stage in which the 3D model data is used to calculate slope stability by using current geomechanics classification methods.

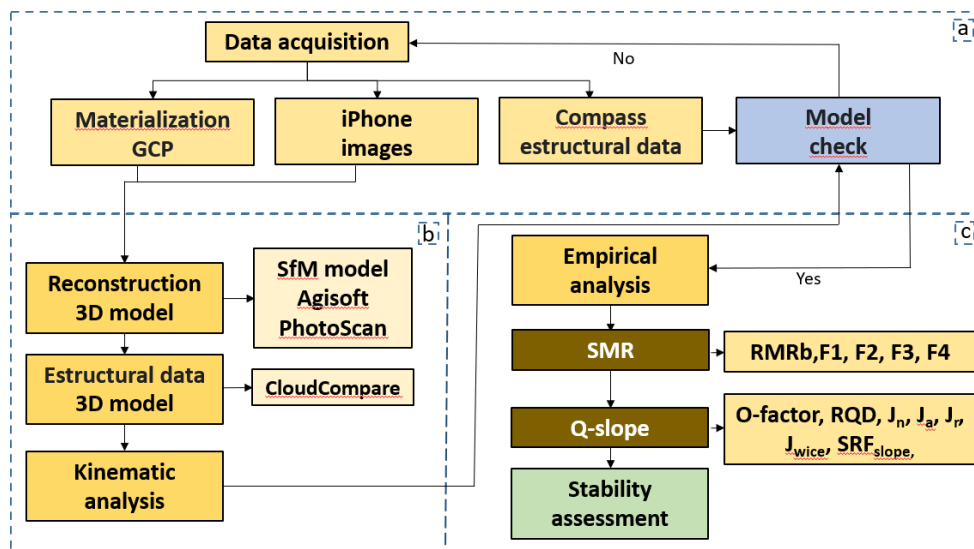


Figure 1. Process diagram: a) information gathering in the field, b) 3D modeling to obtain structural data in the office, and c) geomechanical analysis to determine slope stability.

2.1 Data collection

To collect the information in the field, an ordinary smartphone, a conventional compass and a tape measure were used. First, the control points were materialized on the slope to later measure structural and metric data on the alignments formed between them. With the materialization of the Ground Control Points (GCP), we proceeded to define bases for taking photographs from

which we were able to cover the entire slope under analysis. It should be clarified that depending on the geomechanical classification method to be used, the photographs taken in this step become a support point when choosing the values to be considered in the empirical calculation, which is why it is important to carry out a good photographic survey of the slope under study.

2.2 3D modeling and obtaining structural data.

The first objective of the information processing is to create the point cloud that allows using specialized programs to obtain structural data of the 3D model. For the processing of field photographs, the Photo shop program was used, which with a standardized workflow allows obtaining a point cloud of the studied object, which is spatially positioned by means of the GCPs. This dense point cloud is taken to the Discontinuity Set Extractor or Cloud Compare programs to obtain semi-automatically the structural data (Nagendran et al., 2019; A. J. Riquelme et al., 2014), which will later be used for the geomechanical processing see Figure 2.

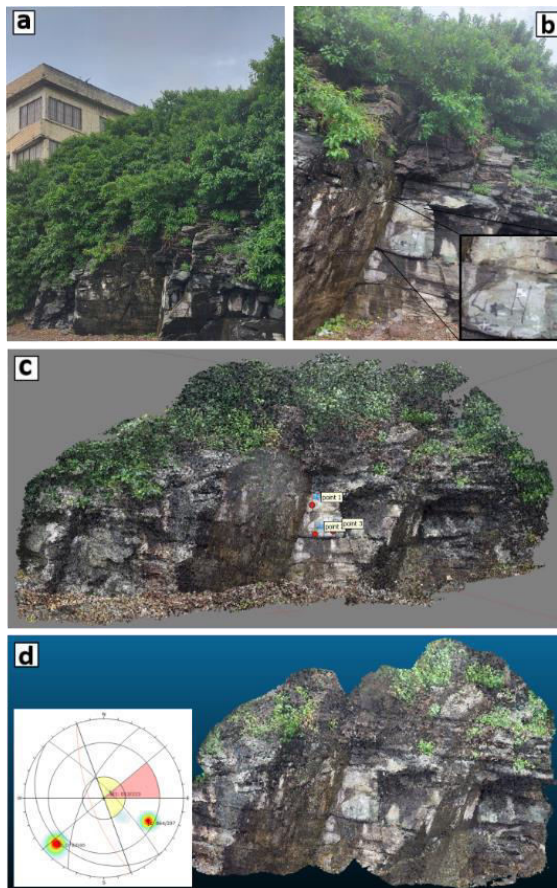


Figure 2. a) Panoramic view of the study slope, b) Materialization of GCP, conventional geomechanics survey and location of stations for photographic survey, c) dense cloud of points, d) obtaining structural data (Dip/Dip dir) of families of joints identified in the photogrammetric process.

2.3 Shear strength of discontinuities

It is a necessary parameter for kinematic analysis because in all of them (wedge, planar, overturning) we trace the so-called "friction circle". The use of a peak or residual value will depend on whether or not the rock mass has undergone significant mobilization or stress relaxation. The

"usual" values of joint friction range between 20 and 40 degrees, although there are lithologies and discontinuities with very low values such as fault zones, coal, serpentines and talc; and abnormally high values in discontinuities with high roughness, voids and dissolution zones (hydrothermal karst). According to the formulation of Barton and Choubey (1977) the peak shear strength of discontinuities is defined by the equation 1:

$$\tau = \sigma n \tan \left\{ \varphi r + JRC \log_{10} \left(\frac{L_0}{L_n} \right) \right\} \quad \text{Eq. 1}$$

Being:

JRC The roughness coefficient scaled to the length of the test joint
 JCS the compressive strength of the lips of the gaskets
 σn is the normal stress at the center point of the joint.

For simplicity we will consider a value common to all joints which will be the lithostatic load at the bottom of the slope $\sigma n \sim \gamma z$ where z is the height of the slope and γ the specific weight of the material.

The part of the equation that corresponds to peak friction will be, equation 2:

$$\varphi p = \varphi r + JRC n \log_{10} \left(\frac{L_0}{L_n} \right) \quad \text{Eq. 2}$$

The residual friction of the joints φr is given by the expression, equation 3:

$$\varphi r = (\varphi b - 20) + 20 \left(\frac{L}{n} \right) \quad \text{Eq. 3}$$

Where: φb is the basic friction of the material, which can be obtained from the tilt test, but which is often found in the bibliographic references of each material (Ramirez and Alejano, 2004). r and R values are the sclerometer rebounds in wet and altered and sound joints, respectively. Regarding the values of r and R in Jordá et al (2021), the criterion of Barton is considered in which the bounces have a bimodal distribution. Twenty sclerometer measurements are made in the joints and the 10 high and 10 low values are grouped taking the average of the five highest of each group, the group of high values will be R and that of the low ones will be r ; from the first one we determine UCS and from the second one JCS0.

For this purpose, the scale effect is applied according to the Barton - Bandis (1990) relationships, equation 4 and 5.

$$JRC n = JRC0 \left(\frac{L_0}{L_n} \right) \quad \text{Eq. 4}$$

$$JCS n = JCS0 \left(\frac{L_0}{L_n} \right) \quad \text{Eq. 5}$$

Being $L_0 = 0.1$ m and L_n the length in meters or persistence of the joint that is analyzed in the block.

2.4 Kinematic analysis

The kinematic analysis allows homogenizing the information obtained in the field and in the office by means of the 3D model and calculation of shear strength of discontinuities. This activity allows to clearly define a single structural value for the joints present in the slope under study. The values obtained in the kinematic analysis can be considered as appropriate in the em-

pirical analysis, obtaining at the same time the most probable type of rupture present in the rock mass and the joints most prone to failure. The final results of this analysis are very important at the moment of defining a technical criterion during the choice of calculation values requested in the empirical methods.

2.5 Empirical analysis

In this section we used the two most current and widespread techniques worldwide which are SMR and Qslope (Bar & McQuillan, 2021; Romana et al., 2015).

Slope Mass Rating (SMR)

The Slope Mass Rating (Romana, 1985) is based on the world famous Rock Mass Rating (RMR) for slopes proposed by Bieniawski, which presented serious problems to be applied to slopes due to the correction factors recommended by the author (Romana et al., 2015). The SMR, by considering the strengths and eliminating the weaknesses of the RMR for slopes, has become one of the most widely used geomechanical classifications in the contemporary world. The SMR is calculated by first obtaining the basic RMR to which is added the multiplication of a series of factors that depend on the relationship between the joints and the slope angle (F1, F2 and F3) and a fourth factor that depends on the excavation method used (F4) see equation 6 (R Tomás et al., 2011, 2012).

$$SMR = RMR_b + (F_1 \times F_2 \times F_3) + F_4 \quad \text{Eq. 6}$$

Q slope classification

The well-known Q-slope is a geomechanics classification method based on the Q-index initially created for tunnels and coupled for slopes (Jordá-Bordehore, 2017). The modification of the Q-index for subway works allows the researcher or field technician to determine quickly and on site the stability state of a slope and to propose constructive recommendations in the process. The Q-Slope considers in its calculation six fundamental parameters RQD, Jn, Jr, Ja, Jw and SRF (Barton & Bar, 2015), reflected in Equations 7 and 8 of this article.

$$Q_{slope} = \frac{\pi Q \nu}{\gamma} \cdot \left(\frac{J_r}{\gamma} \right) \cdot \frac{J_{wice}}{c \cdot n} \quad \text{Eq. 7}$$

The maximum slope angle can be calculated with (Eq.3).

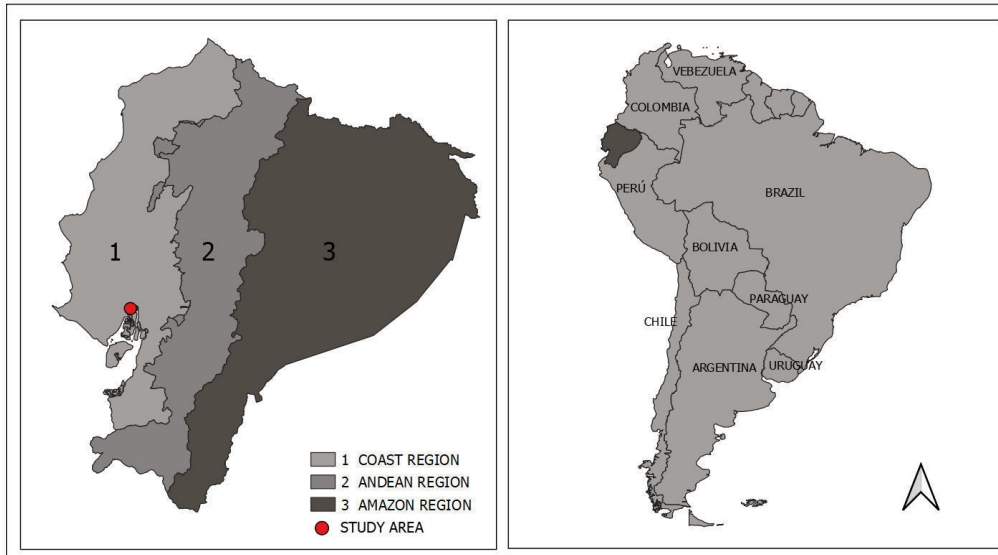
$$\beta = 20 \log_{10} Q_{slope} + 65^\circ \quad \text{Eq. 8}$$

The reader is recommended to refer to the bibliography published by the authors for details on the geomechanical methods used in this study for more information on the empirical methods.

3 CASE STUDY

Continental Ecuador is located in South America, bordered to the north by Colombia, to the south and east by Peru and to the west by the Pacific Ocean. Among its most interesting geological features are the Oriente Basin in the Amazon region, multiple fine sandy beaches in the coastal region, some volcanoes such as Chimborazo, Cotopaxi, Tungurahua that dominate the inter-Andean region (see Figure 3), and the Galapagos Islands located outside the continent, which are completely located in the Pacific Ocean.

The study area is located in the coastal region of Ecuador, which has a tropical savanna climate with high humidity throughout most of the year, this area has heavy seasonal rainfall and abundant vegetation. The slope is located on a main road in the city of Guayaquil and on it there are currently buildings that serve as housing for many families in the area.



3.1.1 Figure 3. Geographic location of the study area, INFOPLAN 2010 source and layer downloaded from <http://www.efrainmaps.es>. Carlos Efraín Porto Tapiquen. *Geography, GIS and Digital Cartography*. Valencia, Spain, 2020 elaborated in Qgis software.

4 RESULTS

This paper demonstrates the application of the SfM technique using smart phones and the use of data cleaned by kinematic analysis for slope classification using recent empirical methods in a tropical environment of continental Ecuador.

4.1 3D modeling

By applying the SfM technique, it was possible to create a 3D model which allowed, in a semi-automatic way, to obtain structural parameters that were later used for kinematic analysis and geomechanical classification. For this purpose, with a SM-A725M (5.23mm) phone with 4624x3468 resolution and pixel size of 1.63 x 1.63 μm , 65 digital images were taken, which after an analysis to determine their sharpness and preferential location were reduced to 45. After processing the cleaned images, a dense point cloud was obtained, which after eliminating 600000 points that had no direct relation with the slope, a file with 24159534 points was obtained. From the dense point cloud, 47 structural data were extracted for the two main families of joints called j1, j2 and stratification planes st1.

4.2 Kinematic analysis

Prior to the kinematic analysis, the peak and residual friction was determined for each family of joints to define the final calculation value after the analysis of the rock mass condition, Table 1.

Table 1.- Parameters and values obtained for the calculation of peak and residual friction to be used in kinematic analysis.

Parameter	Family of joints		
	J1	J2	J3
ϕ_b	27	27	27
r	47	50	41
R	59	63	55
JCS0	59	62	49
JRC0	10	10	10
Ln	2	2	3
JCSn	24.02	25.24	17.66
JRCn	5.49	5.49	5.06
σ_n	0.078	0.078	0.078
ϕ_r	23	23	22
ϕ_p	32	32	30

Due to the evidence observed in the field on the study slope, it was considered pertinent to take the value of 22 degrees of ϕ_r as calculation data and enter it in the Dips program.

The kinematic analysis made it possible to obtain from the 47 structural data taken from the 3D model the representative structural values for the joints investigated. These values were compared with control points obtained with conventional techniques, verifying that the existing differences between planes range from 1 to 3 degrees for the DIP values and from 1 to 5 degrees for the Dip/Dir values (Table 2). This difference is mainly due to the fact that the joint walls present irregularities that were probably created during the construction stage. It should also be noted that the joints are not completely smooth and flat, which could also influence the values obtained using the Cloud compare program, as well as the normal errors produced at the moment of placing the flat part of the compass on an irregular measurement surface. However, despite all the singularities of the joints, the values for empirical analysis can be considered as acceptable and of good quality. Once the kinematic analysis was completed, it was confirmed that the slope under study presents a risk of failure due to Direct Toppling.

Table 2. Comparative analysis of structural data obtained by kinematic analysis of 3D data and conventional method.

Check points	DIPS (ccp)		Compass		Difference	
	Dip	Dip Dir	Dip	Dip Dir	Dip	Dip Dir
j1	064	297	066	298	2°	1°
j2	078	046	075	041	3°	5°
st1	013	223	014	227	1°	4°

4.3 Empirical analysis

In the study slope, important structural data such as lithology, height, environmental parameters, orientation of discontinuities and slope, etc. were collected. These field data allowed to define in cabinet calculation parameters such as JCS, RMRb, F4, Jn/Ja, Ofactor, among others, which are used for the final calculation of SMR and Qslope.

The results of the two geomechanics classification methods determine that the slope studied is partially stable and unstable, which is in agreement with the evidence found on the slope at the time of the field survey. The values and characteristics of the slope are reflected in Table 3, as well as in Figure 4 of this article.

Table 3. Results of the parameters obtained and calculated for the case study.

Use	Lithology	Height, in meters	Slope angle, in degrees	Failure mode		
Byway	Shale	10	45	Direct Toppling		
Q-slope value calculation factors						
RQD	Jn	(Jr/Ja)o	Jwice	SRF _{slope}	Q _{slope} value	Stability
90	12	0,375	0,05	10	0,375	unstable
SMR value calculation factors						
RMRb	F1 x F2 x F3			F4	SMR value	Stability
58	-6			0	52	Partially stable

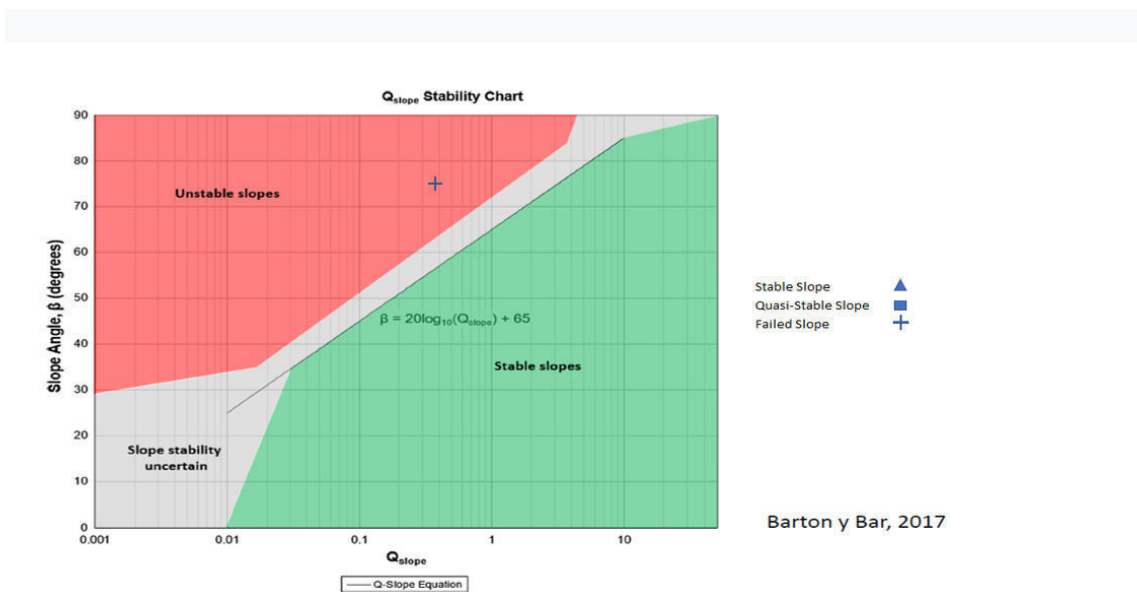


Figure 4. Criterion proposed by Barton and Bar in 2015 and 2016 to determine the stability of slopes according to their type Stable, Quasi-Stable and Failed. It is noted that the case study is located in the area for Unstable slope.

5 CONCLUSION

The objective of this study was to demonstrate the applicability of the use of the SfM technique to obtain calculation values to be used in empirical methods of slope stability in tropical

zones of continental Ecuador. The SMR and Qslope geomechanics classifications are two of the most current and widespread techniques worldwide (Tomás et al., 2017) which give good results when classifying rock slopes.

The data obtained from the 3D model of the rock mass are very similar to those obtained by conventional structural survey methods, this similarity of values allowed us to guarantee that the data for kinematic analysis are correct and that the structural values of the joints for empirical analysis are consistent with the reality of the shear.

The stability of a slope, in addition to the relationship between the joints, depends to a large extent on the environmental parameters that affect it; the combination of factors places a slope in a quasi-stable, unstable or stable state. In our study, although the Qslope method defines the slope as unstable, this value is very close to the slope stability uncertain zone, a result that is very close to that obtained by the SMR classification. These results allowed concluding that the SfM analysis for empirical geomechanical calculation is applicable in tropical zones of Andean countries.

BIBLIOGRAPHY

- An, P., Fang, K., Jiang, Q., Zhang, H., & Zhang, Y. (2021). Measurement of rock joint surfaces by using smartphone structure from motion (SfM) photogrammetry. In *Sensors (Switzerland)* (Vol. 21, Issue 3, pp. 1–22). <https://doi.org/10.3390/s21030922>
- Bar, N., & McQuillan, A. (2021). Q-slope and SSAM applied to excavated coal mine slopes. *MethodsX*, 8, 101191. <https://doi.org/10.1016/J.MEX.2020.101191>
- Barton, N., & Bar, N. (2015). Introducing the Q-slope method and its intended use within civil and mining engineering projects. *ISRM Regional Symposium, EUROCK 2015*, 157–162. https://www.researchgate.net/publication/318117219_Introducing_the_Q-slope_method_and_its_intended_use_within_civil_and_mining_engineering_projects
- Hernan, G., & Andrade, B. (2007). Ingeniería , Geotecnia y Geomecánica. *Introducción a La Ingeniería De Tuneles*, 3ra. http://www.aimecuador.org/articulos_archivos_pdf/Libro_Ing_Tuneles.pdf
- Jordá-Bordhore, L., Alejano, L., Tomás, R., Loaiza, S. C., García, M. T., Galindo, R. Á., Pérez-Rey, I., Riquelme-Guill, A., Cano, M., Borja-Bernal, C. P., & Medinaceli Torrez, R. (2021). Determination of the basic friction angle ϕ_b of joints using the field tilt test: results of various “fast” tests on outcrops. *IOP Conference Series: Earth and Environmental Science*, 833(1), 012048. <https://doi.org/10.1088/1755-1315/833/1/012048>
- Jordá-Bordhore, L. (2017). Application of Q slope to Assess the Stability of Rock Slopes in Madrid Province, Spain. *Rock Mechanics and Rock Engineering*, 50(7), 1947–1957. <https://doi.org/10.1007/s00603-017-1211-5>
- Jordá Bordhore, L., Riquelme, A., Cano, M., & Tomás, R. (2017). Comparing manual and remote sensing field discontinuity collection used in kinematic stability assessment of failed rock slopes. *International Journal of Rock Mechanics and Mining Sciences*, 97(October 2016), 24–32. <https://doi.org/10.1016/j.ijrmms.2017.06.004>
- Jorda et al. (2016). *Manual de estaciones geomecánicas* (E. técnica S. de I. de M. De (ed.); p. 208).
- Nagendran, S. K., Ismail, M. A. M., & Tung, W. Y. (2019). Photogrammetry approach on geological plane extraction using cloudcompare FACET plugin and scanline survey. *Bulletin of the Geological Society of Malaysia*, 68, 151–158. <https://doi.org/10.7186/bgsm68201916>
- Ramírez, P., & Alejano, L. (2008). Mecánica de Rocas: Fundamentos e Ingeniería de Taludes. In *Journal of Chemical Information and Modeling*. Gráficas Monterreina S.A. http://oa.upm.es/14183/1/MECANICA_DE_ROCAS_1.pdf

- Riquelme, A. J., Abellán, A., Tomás, R., & Jaboyedoff, M. (2014). A new approach for semi-automatic rock mass joints recognition from 3D point clouds. *Computers and Geosciences*, 68, 38–52. <https://doi.org/10.1016/j.cageo.2014.03.014>
- Riquelme, A., Tomás, R., Cano, M., Pastor, J. L., & Jordá-Bordehore, L. (2021). Extraction of discontinuity sets of rocky slopes using iPhone-12 derived 3DPC and comparison to TLS and SfM datasets. *IOP Conference Series: Earth and Environmental Science*, 833(1), 0–8. <https://doi.org/10.1088/1755-1315/833/1/012056>
- Riquelme, Adrián, Araújo, N., Cano, M., Pastor, J. L., Tomás, R., & Miranda, T. (2020). Identification of Persistent Discontinuities on a Granitic Rock Mass Through 3D Datasets and Traditional Fieldwork: A Comparative Analysis. *Springer Series in Geomechanics and Geoengineering*, 868–878. https://doi.org/10.1007/978-3-030-32029-4_73
- Romana, M. (1985). New Adjustment Ratings for Application of Bieniawski Classification to Slopes. In ISRM (Ed.), *Proceedings of the International Symposium on the Role of Rock Mechanics in Excavations for Mining and Civil Works* (pp. 49-53.). [https://www.scirp.org/\(S\(i43dyn45teexjx455qlt3d2q\)\)/reference/ReferencesPapers.aspx?ReferenceID=1611730](https://www.scirp.org/(S(i43dyn45teexjx455qlt3d2q))/reference/ReferencesPapers.aspx?ReferenceID=1611730)
- Romana, M., Tomás, R., & Serón, J. B. (2015). Slope Mass Rating (SMR) geomechanics classification: Thirty years review. *13th ISRM International Congress of Rock Mechanics, 2015-MAY*, 1–10.
- Tomás et al. (2017). Review of the Current Status of the Geomechanic Classification Slope Mass Rating (SMR). *Boletín de La Sociedad Española de Mecánica de Suelos e Ingeniería Geotécnica*, 190, 25–32. <http://rua.ua.es/dspace/handle/10045/70953>
- Tomás, R., Cuenca, A., & Cano, M. (2011). A graphical approach for slope mass rating (SMR). *Engineering Geology*, 124, 67–76. <https://doi.org/10.1016/j.enggeo.2011.10.004>
- Tomás, R., Vldes, A., Tenza, A., & Cano, M. (2012). New insight into the slope mass rating geomechanical classification through four-dimensional visualization. *International Journal of Rock Mechanics & Mining Sciences*, 53, 64–69. <https://doi.org/10.1016/j.ijrmms.2012.04.002>
- Tomás, Roberto, Riquelme, A., Cano, M., & Abellán, A. (2016). Structure from Motion (SfM): una técnica fotogramétrica de bajo coste para la caracterización y monitoreo de macizos rocosos. *10º Simposio Nacional de Ingeniería Geotécnica, A Coruña, España, 1(1)*, 209–216. https://www.researchgate.net/publication/309611177_Structure_from_Motion_SfM_una_tecnica_fotogrametrica_de_bajo_coste_para_la_caracterizacion_y_monitoreo_de_macizos_rocosos

Sinkhole Issues in Mars

Ö. Aydan

University of the Ryukyus, Okinawa, Japan

ABSTRACT:

The images from Mars Reconnaissance Orbiter (MRO) of NASA showed that sinkholes also formed in Mars and they are found in basaltic lava flow areas. The sinkhole issue in Mars is considered in this study with some reference to sinkholes observed on Earth such as the volcanic caves in Japan, Türkiye and Hawaii Island and Mainland of USA. The geometry and size of sinkholes of Mars are categorized and their stability is evaluated on the basis of principles of Rock Mechanics and Rock Engineering with reference to those of Earth. The author presents the outcomes of this research and discusses its implications within the Planetary Rock Mechanics.

1 INTRODUCTION

Mankind is now exploring the ways to find out the characteristics of other planets and possibility of exploiting their mineral resources. The images from recent Mars exploration rovers showed the striking similarities between rocks on Earth and those of Mars. Like on Earth, sinkholes are also observed in Mars as well as in Moon. Sinkholes may also be of great significance in other extraterrestrial objects. Although the gravitational acceleration and environmental conditions are different from those of Earth, sinkhole issues are likely to be similar to those of Earth as shown.

Sinkholes cause severe problems on Earth. This problem has been often observed in karstic terrains, evaporitic formations and volcanic regions on Earth. The preliminary observations by MRO indicated that these sinkholes have been found in basaltic lava flow areas. Some of sinkholes may also be formed by impacts of meteorites and/or rifting induced by tectonic movements. Radiation issue is a major issue for manned space explorations and sinkholes of Mars may provide as a shelter against radiation. Therefore, their stability is of great importance for the habitation and utilization of the sinkholes of Mars.

In this study, the author considers the sinkhole issue in Mars with some references to some sinkholes of Earth such as the volcanic sinkholes and caves in Japan, Türkiye and Hawaii Island and Mainland of USA. The geometry and size of sinkholes of Mars categorized and their stability is evaluated on the basis of Rock Mechanics and Rock Engineering and compared with those of Earth. The stability evaluations involve empirical rock classifications, analytical methods and numerical methods. The outcomes of this research are presented and its implications are discussed within the frame-work of explorations in other planets.

2 SINKHOLES AND CHARACTERISTICS OF VOLCANIC ROCKS IN MARS

2.1 Sinkholes

Sinkholes may form due to collapse of natural underground openings under gravity, seismic loading, groundwater seepage and degradation of rocks. This problem has been often observed in karstic terrains, evaporitic formations and volcanic regions on Earth. As reported by Cushing (2012) and Cushing et al. (2007, 2015), there are a number of sinkholes mainly in basaltic lava flow plains of Mars as seen in Figure 1. In these mages one can also notice skylights, which are use to infer the geometry of sinkholes such as depth, size and cover rock thickness. In the same figure, one can also notice the natural rock bridges, which could be interpreted as another evidence of the cause of the sinkhole formation due to the collapse of the rock cover. Undoubtedly, sinkholes may also be formed due to impacts of meteorites and/or rifting induced by tectonic

movements. Although there are presently no water-like fluid bodies, there could be solution cavities and associated sinkholes in Mars in the past.

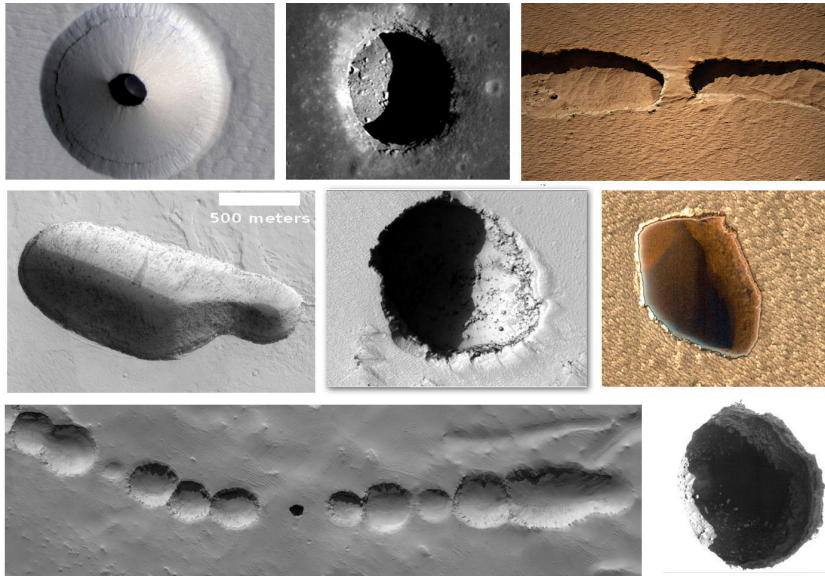


Figure 1. Images of sinkholes in Mars (compiled from the images released by NASA).

2.2 Characteristics of Volcanic Rocks in Mars

Mars explorer rovers (MER), namely, Opportunity, Spirit, Curiosity and Perseverance provided some scientific data on the composition and characteristics of rocks of in the surveyed areas of Mars. Figure 2 shows some views of basaltic rocks. As noted from the figure, basalts of Mars are quite porous, which may be called vesicular basalt. It is very likely that the porous structure may lead heavy weathering as well as a decrease of mechanical properties. As there is no experimental data on Martian basalt, the drilling and grinding operations by the rovers on rocks of Mars may be utilized to infer their mechanical properties. Figure 3 shows some views of vesicular basalt samples from different parts of Earth. Figure 4 shows the variation of uniaxial compression strength (UCS) and Brazilian tensile strength of basalt sampled from Japan and Türkiye as a function of porosity. As noted from Figure 3, the basalts of Mars resemble to those of Earth. Therefore, the mechanical properties of the vesicular basalt of Earth may be utilized to evaluate the mechanical properties of Martian vesicular basalts.

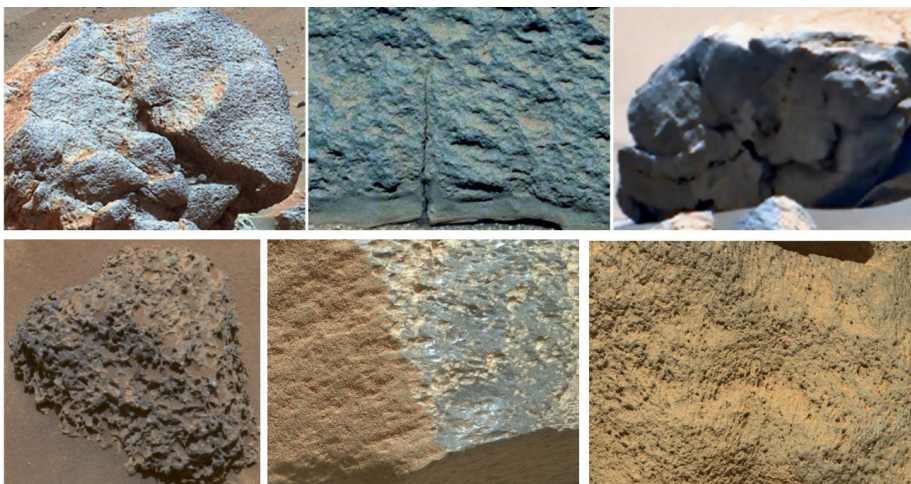


Figure 2. Views of Martian basalts.

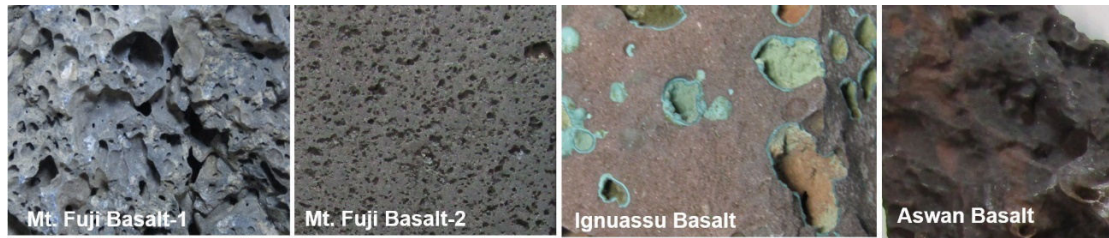


Figure 3. Views of basalts sampled from different parts of Earth.

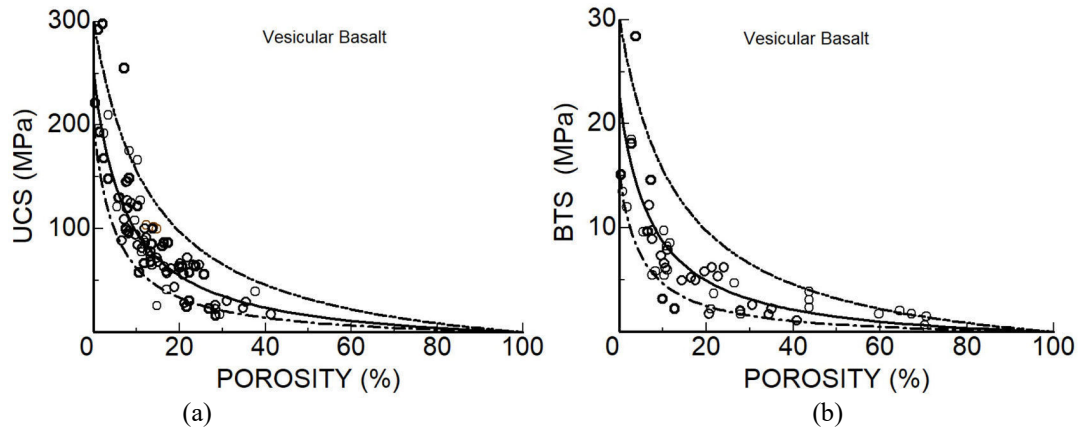


Figure 4. Variation of (a) uniaxial compressive strength and (b) Brazilian tensile strength of basalt from Türkiye and Japan with porosity.

3 ROCK MASS CONDITIONS IN MARS AND THEIR PROPERTIES

As discussed earlier by Aydan (2017, 2020, 2021a,b, 2022), rocks, discontinuities and rock masses are quite similar to those of Earth. Therefore, it is quite possible to evaluate their mechanical properties utilizing the methods developed for those of Earth. Aydan et al. (2014) recently developed a new rock classification and proposed a procedure for evaluating mechanical properties (ψ_m) of rock masses in terms of intact rock properties (ψ_i) and a state variable-like parameter for rock masses, which is called the new rock mass quality rating (RMQR) using the following formula:

$$\frac{\psi_m}{\psi_i} = \alpha_{100} - (\alpha_{100} - \alpha_0) \frac{RMQR}{RMQR + \beta(100 - RMQR)} \quad (1)$$

where α_0 and α_{100} normalized properties for the values of RMQR as 0 and 100. β is an empirical coefficient. Their values change according to the property of rock mass under consideration. On the bases of in-situ tests on rock masses, Table 1 summarizes the values of parameters for each respective property of rock masses.

Table 1. Values of α_0 , α_{100} and β for various properties of rock mass

Property (α)	α_0	α_{100}	β
Deformation modulus	0.0	1.0	6
Poisson's ratio	2.5	1.0	0.3
Uniaxial compressive strength	0.0	1.0	6
Tensile strength	0.0	1.0	6
Cohesion	0.0	1.0	6
Friction angle	0.3	1.0	1.0

Horiuchi et al. (2019) advanced Eq. (1) by taking into account the porosity of intact rock as given below:

$$\frac{\psi_m}{\psi_i} = \alpha_{100} - (\alpha_{100} - \alpha_0) \frac{RMQR}{RMQR + \beta(100 - RMQR)} \cdot \left(1 - \frac{n}{n + \theta(100 - n)} \right) \quad (2)$$

Where n and θ are porosity and empirical coefficient. The value of coefficient θ is generally 1 or greater depending upon the rock type and intact rock property.

4 STABILITY ASSESSMENT TECHNIQUES

In this section, some stability assessment techniques are presented. Specifically, empirical and analytical methods are described. In addition, numerical methods such as finite element method, discrete finite element method and other discrete numerical methods are available. However, although they are not presented herein, the interested readers can consult some publications (e.g., Kawamoto and Aydan 1999; Aydan et al. 1996; Aydan and Tokashiki 2011).

4.1 Empirical Methods based on Rock Classifications

The empirical techniques generally involve rock mass classifications. Several empirical relations between allowable span or height and rock mass quality value (Q) or rock mass rate (RMR) were proposed in literature. Barton et al. (1980) suggested an empirical line for the non-supported span (L) of the underground openings in relation to the Q-value as follows.

$$L = 2 \cdot ESR \cdot Q^{0.4} \quad (3)$$

where ESR is called Equivalent Support Ratio. When the value of ESR is 1, it corresponds to the empirical line for unsupported span limit in the original article of Q-System by Barton et al. (1974). Barton (1976) also suggested the following formula between the unsupported span (L) (unit is m) and Q-value on the basis of his observations on the Carlsbad karstic caves in USA:

$$L = 66 \log Q + 2 \quad (4)$$

Lang (1994) proposed two empirical bounding lines for the span between stable and unstable openings on the basis of observations in mines using the RMR. However, he did not provide any specific equation for his bounds. When these empirical relations are applied to natural rock underground structures, they would generally yield very conservative results. Furthermore, the physical interpretation of the empirical bounds is very difficult in practice. One may find numerous examples such that the natural rock underground structures are stable although data of caves may require some levels of rock support.

Karstic caves may present some engineering problems especially in urbanized areas along shorelines and riversides. The effect of karstic caves on the overall stability of the castle remains were investigated using empirical, analytical and static and dynamic numerical techniques by Aydan and Tokashiki (2011). In addition, some one-dimensional shaking table experiments on model caves were performed and the effect of cavity filling as a counter-measure was investigated. These investigations clearly demonstrated that the filling of cavities should be an effective measure to achieve the overall safety of superstructures.

On the basis of observations on the Karstic natural caves in Ryukyu limestone, Tokashiki (2011) and, Aydan and Tokashiki (2011) defined four different stability categories defined for natural underground openings in Ryukyu limestone utilizing RMR rock classification system (Bieniawski 1973, 1989). However, Aydan (2018) updated this system and related to the RMQR and increasing the stability category to 6 as shown in Figure 5. The limiting lines of each category are fitted to the following two formulas for the span (L) (unit is m) of natural underground openings as a function of RMQR:

Linear function formula:

$$L = aRMQR + b \quad (5)$$

Power function formula:

$$L = aRMQR^b \tag{6}$$


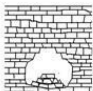
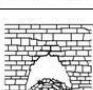
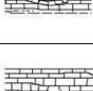
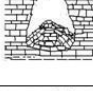

where a and b are empirical coefficients. The values of the parameters are given in Table 2 and 3 for caves in Ryukyu limestone (UCS=25 MPa) and the Alpine limestone (UCS=60 MPa).

Table 2. Values of empirical constants.

Lines	$L = aRMQR + b$		$L = aRMQR^b$	
	a	b	a	b
I-II	0.58	-50.0	0.008	1.5
II-III	0.60	-42.0	0.018	1.5
III-IV	0.62	-32.0	0.030	1.5
IV-V	0.64	-22.0	0.042	1.5
V-VI	0.66	-6.0	0.060	1.5

Table 3. Values of empirical constants in Eqs.(3) & (4)

Lines	Linear Function		Power Function	
	a	b	a	b
I-II	2.0	-120	0.007	2.0
II-III	2.4	-120	0.012	2.0
III-IV	2.8	-112	0.017	2.0
IV-V	3.2	-96	0.022	2.0
V-VI	3.6	-72	0.029	2.0

Category	State	$\frac{H_f}{H_r}$	$\frac{B_s}{B}$	Comments
I		0.0	0.0	Opening locally and globally stable
II		0.0-0.1	0.0	Some rock block falls from roof. Opening globally stable
III		0.1-0.3	0.0	Block falls from roof and sidewalls into the opening occur and the failure zone increases in size. Roof height is higher than opening width. The failure zone may increase in size with time.
IV		0.3-0.7	0.0	Considerable scale of falls and sliding of rock blocks from the roof and sidewall of openings occur and the failure zone larger in size. Roof height is much higher than opening width. The failure zone may increase reach ground surface in long-term
V		0.7-1.0	0.8-1.0	Failure zone reaches to ground surface and a small size crater develops at ground surface. The possibility of collapse zone may increase in size and shoulder may fall into opening in long-term
VI		≥ 1.0	> 1.0	Opening globally unstable. In other words, it is in a total collapse state. Deep Sinkhole appear on the ground surface.

(a)

(b)

Figure 5. (a) Categorization and (b) Comparison of empirical bounds for of state of karstic caves.

4.2 Analytical Methods

The stability assessment methods for the roof of shallow underground openings are generally based on the bending theory of beams or arching theory used in structural mechanics (Figure 6). Particularly, the arching theory has been popular in mining engineering and many formulations are developed with the consideration of various modes of failure (i.e. Aydan, 1989, 2008; Kawamoto et al. 1991; Aydan and Tokashiki 2007, 2011).

The limit of roof span (L) normalized by roof rock layer thickness (h_r) under its dead weight and topsoil with thickness of (h_s) can be obtained in the following form:

$$\frac{L}{h_r} = \sqrt{\lambda \frac{\sigma_t}{(\gamma_r h_r + \gamma_s h_s)}} \quad (7)$$

where σ_t is the tensile strength of roof layer. The value of λ would take the following values 1/3, 2/3 and 2 for cantilever, simple and built-in beams. Cantilever beam situation may arise when the roof of opening crossed by a fault, which is a common situation in karstic caves.

The arching theory for assessing the stability of roofs of the shallow underground openings is generally based on three-hinged beams. As discussed by Aydan (1989, 2008), and Aydan and Tokashiki (2011), the rotation of rock layer, in which arch is formed, should be initiated in order the arch action to take place. The failure modes of an arch are various and they are crushing at the crown and/or abutments, vertical or horizontal sliding at abutments and sliding along an existent discontinuity within the arch. The detailed derivations for each failure mode are presented in the doctorate thesis of Aydan (1989) and in the article by Kawamoto et al. (1991). The classical arching theory assumes that the failure mode of the arch takes place by crushing at the crown or abutments and the final form for the limit of roof span (L) normalized by rock roof layer thickness (h_r) under its own weight and topsoil with thickness of (h_s) as follows:

$$\frac{L}{h_r} = \sqrt{\lambda \frac{\sigma_c}{(\gamma_r h_r + \gamma_s h_s)}} \quad (8)$$

where σ_c is the compressive strength of roof layer. The value of λ would take the following values 4/3 when crack length (ℓ_c) is zero. However, the maximum resistance of the arch would be attained when the value of λ is 3/2 after some manipulations concerning the crack length in the arch. The effect of concentrated loads can be taken into account if necessary.

If Terzaghi's arching theory is adopted for cohesive (c) and frictional (ϕ) ground conditions, one can also derive the following relation Terzaghi 1943).

$$\frac{L}{h_r} = 2 \left(\frac{c}{\gamma} + K_h \tan \phi \right) \quad (9)$$

Theoretically, the lateral stress coefficient (K_h) would be equal to 1. The tensile, uniaxial compressive and cohesive strengths and friction angle of rock mass in Eqs. (5)-(7) can be obtained using the formulas suggested by Aydan et al. (2014, 2017) in terms of those of intact rock and RMQR value of rock masses. It should be noted that the bending and arching theory should not be applied when the value of RMQR is less than 30 due to poor conditions of rock masses (Aydan et al. 2017). Furthermore, the bending theory provides a theoretical basis for local stability while the arching theory theoretically establishes the limit spans for collapse of natural underground openings.

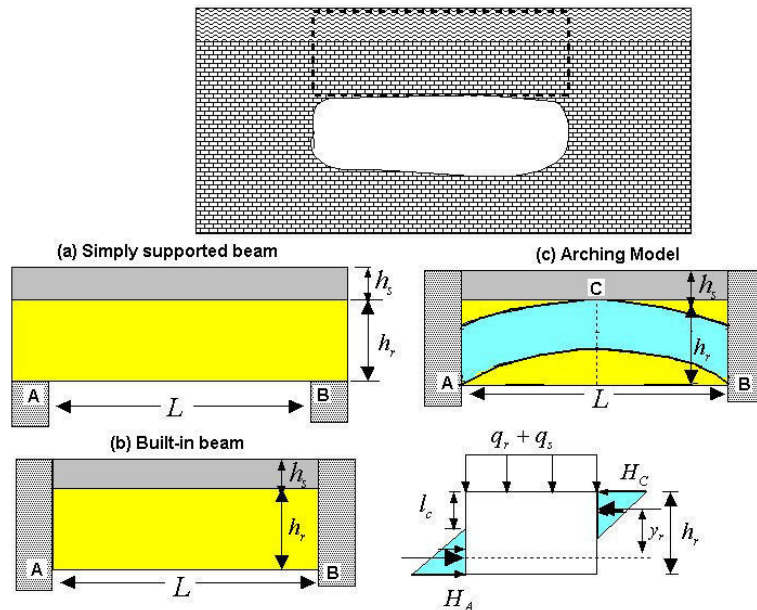


Figure 6. Illustrations of mechanical models for theories of bending and arching of beams.

5 APPLICATIONS TO SINKHOLES ON EARTH AND MARS

5.1 Survey of Sinkholes and Comparison with Empirical and Analytical Estimations for Earth

The author first surveyed the sinkhole issue in Earth. The case history data was obtained from sinkholes observed in the vicinity of Mt. Fuji in Japan, Mt. Ağrı, Karacadağ and Hatay region in Türkiye, Hawaii and Mainland USA (Figure 7). Some of sinkholes and volcanic caves in Japan, Türkiye and Hawaii were visited by the other personally. In addition, some data was gathered from Azerbaijan, Taiwan, Iceland. The geometry and size of sinkholes are evaluated and their stability is categorized according to Table 1. For sinkholes and caves on Earth, RMQR values are determined. Figure 8 compares with observational data on caves and sinkholes on Earth with empirical bounds given by Eqs. (3-4) together with constants given in Table 2. Both linear and power functions provide good estimations for observational data.

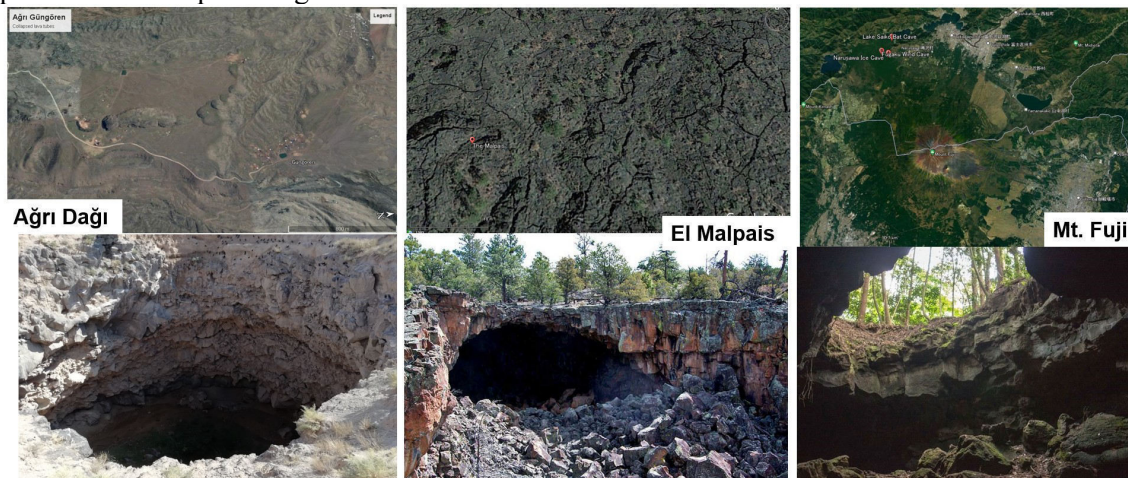
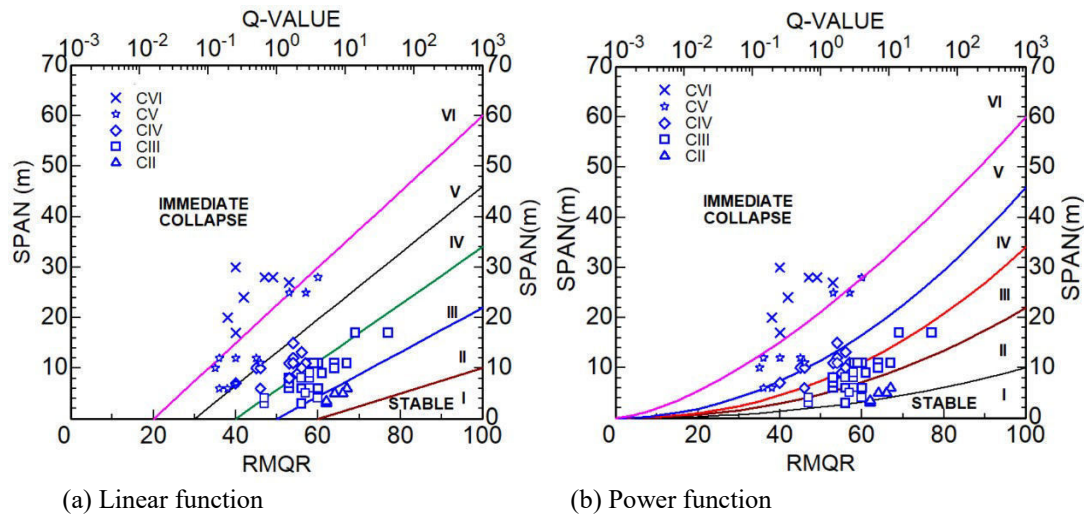


Figure 7. Locations and views of some sinkholes in the vicinity of Mt. Fuji, Japan, in the vicinity of Mt. Fuji in Japan, Mt. Ağrı, in Türkiye, and Mainland USA.



(a) Linear function (b) Power function
 Figure 8. Comparison of empirical stability charts with observation data on Earth.

The stability estimations based on analytical methods compared with observational data for sinkholes in Figure 9 for the given parameters for intact rock and rock mass. It seems that the arching theory provides an upper bound for the formation of sinkholes provided that the material properties of intact rock and rock mass are properly evaluated. Nevertheless, more detailed explorations and analyses of each site should provide better estimations.

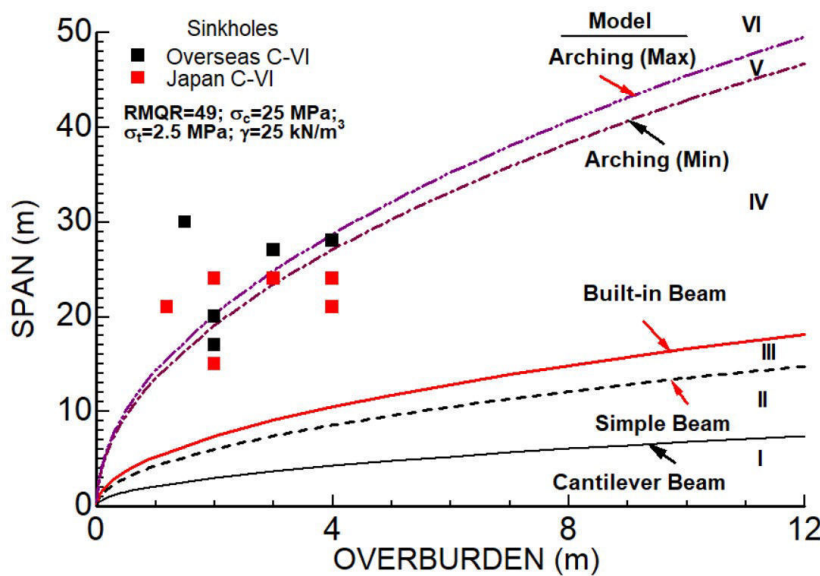


Figure 9. Comparison of analytical stability charts with observation data of sinkholes on Earth.

5.2 Survey of Sinkholes and Comparison with Empirical and Analytical Estimations for Mars

Cushing (2012) and Cushing et al. (2007, 2015) investigated the sinkholes of Mars and provided a detailed information about each sinkhole. However, some additional data are necessary for stability analyses. For such a purpose, important parameters are the thickness of the cover rock and the rock mass state variable. Some attempts have been done to evaluate these two parameters from images on the bases of knowledge available from sinkholes of Earth. Furthermore, that the strength of vesicular basalt is estimated to be about 25 MPa in view of its porosity and the experiments on Mt. Fuji basalt. As the gravity coefficient of Mars is 0.387 times that of Earth, the stress induced by the Mars gravity is assumed to be 0.387 times that on Earth. By consider-

ing these facts, the empirical and analytical methods have been used to assess the sinkholes occurrence. The estimations from empirical and analytical methods are shown and compared with observational data in Figure 10. The overall trend is quite promising despite many data are based on some inferences for similar situations on Earth. Once again it is noted that the analytical methods yield also the bounds to be on the safe side. When observational data is compared with empirical estimations, the overall trend are quite similar and the empirical estimation is on the safe side.

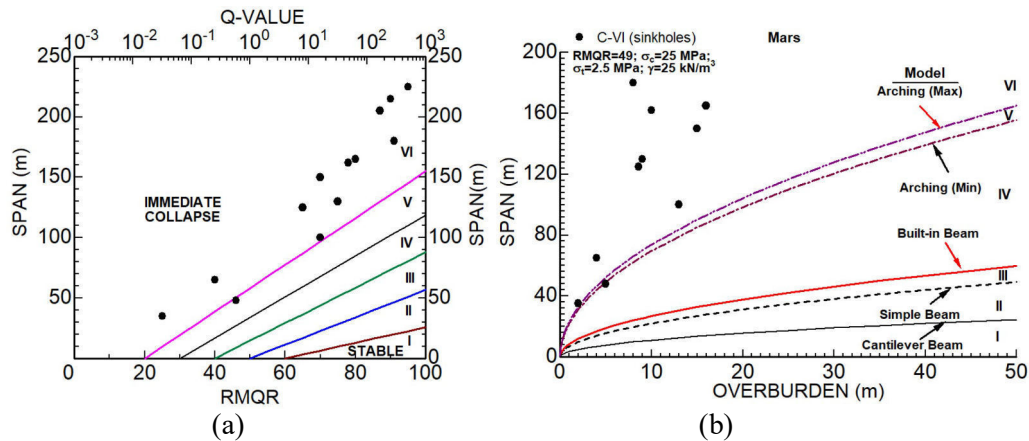


Figure 10. Comparison of (a) empirical and (b) analytical stability charts with observation data on Mars.

6 CONCLUSIONS

This study is probably one of the first attempts to evaluate the stability of natural underground structures and sinkhole formation in Mars on the bases of some information, data and inferences obtained from the natural underground structures in volcanic areas on Earth. The available techniques and mechanical data were utilized by considering the gravitational conditions in Mars. Despite some ambiguities on material properties as well as rock mass conditions in Mars, these preliminary analyses provide some insight view of sinkholes on Mars and their possible stability situations. Undoubtedly more data and more detailed analyses utilizing numerical techniques would provide better information about the stability of caves and conditions of sinkhole formation in Mars. In addition to the conditions considered in this study, the dynamic loading conditions due to marsquakes and impacts by the meteorites will be necessary in future studies.

REFERENCES

- Aydan, Ö., 1989. The Stabilisation of Rock Engineering Structures by Rockbolts. Doctorate Thesis, Nagoya University, Faculty of Engineering.
- Aydan Ö (2008) Investigation of the seismic damage to the cave of Gunung Sitoli (Tögi-Ndrawa) by the 2005 Great Nias earthquake. *Yerbilimleri*, Vol. 29, No.1, 1-16.
- Aydan Ö 2017. Some Thoughts About Rock Mechanics Aspects of Mars. *UNSW, 3rd Off Earth Mining Forum - 2017OEMF*.
- Aydan Ö (2018) Some Thoughts on the Risk of Natural Disasters in Ryukyu Archipelago. *International Journal of Environmental Science and Development*, 9(10), 282-289.
- Aydan, Ö. (2020). *Rock Mechanics and Rock Engineering: Applications*. CRC Press, Taylor and Francis Group, 410p.
- Aydan Ö 2021a. Some thoughts on Rock Mechanics in Mars. *15th Japan Domestic Rock Mechanics Symposium*, Paper No. 49, 273-278.
- Aydan Ö 2021b. A Thermo-elasto-plastic Evaluation of Stress State of Mars. *EUROCK2021, IOP Conf. Ser.: Earth Environ. Sci.* **833** 012089, 8p.

- Aydan Ö 2022. Some thoughts on rock slope stability issues in Mars. *EUROCK2022, Helsinki*, 8p.
- Aydan, Ö. and T. Kawamoto, 2000. Assessing mechanical properties of rock masses by RMR rock classification method. *GeoEngineering 2000 Symposium*, Sydney, OA0926.
- Aydan Ö, Tokashiki N (2007) Some damage observations in Ryukyu limestone caves of Ishigaki and Miyako Islands and their possible relations to the 1771 Meiwa Earthquake. *J. of The School of Marine Science and Technology, Tokai University*, 5(1), 23-39.
- Aydan, Ö. and Tokashiki, N. (2011): A comparative study on the applicability of analytical stability assessment methods with numerical methods for shallow natural underground openings. *The 13th International Conference of the International Association for Computer Methods and Advances in Geomechanics*, Melbourne, Australia, pp.964-969.
- Aydan Ö, Mamaghani, IHP, Kawamoto T (1996) Application of discrete finite element method (DFEM) to rock engineering structures. *NARMS'96*, 2039-2046.
- Aydan Ö, Ulusay R, Tokashiki N (2014) A new rock mass quality rating system: Rock Mass Quality Rating (RMQR) and its application to the estimation of geomechanical characteristics of rock masses., *Rock Mech Rock Eng.*, 47:1255–1276.
- Aydan Ö, Tokashiki N, Kumsar H, Geniş M (2017) Some empirical guidelines on the stability of karstic caves based on Rock Mass Quality Rating (RMQR) classification system, 1st Int. WS on Role of Microorganism and Thermo-Hydro-Chemico-Mechanical Process in Geoengineering and Geoscience, 20 March, 2017, Okinawa, Japan, p 43-50.
- Barton, N., 1976. Unsupported under-ground openings. In *Rock Mechanics Meeting*, Swedish Rock Mechanics research Foundation, Stockholm, 61-94.
- Barton, N.R., Lien, R. and Lunde, J. 1974. Engineering classification of rock masses for the design of tunnel support. *Rock Mech.* 6(4), 189-239.
- Barton N, Løset F, Lien R, Lunde J (1980) Application of the Q-system in design decisions. In *Subsurface space*, (ed. M. Bergman) 2, 553-561. New York: Pergamon.
- Bieniawski ZT (1973) Engineering classification of jointed rock masses. *Trans South Afr Inst Civil Eng* 15:335–344.
- Bieniawski, Z.T. 1989. *Engineering rock mass classifications*. New York: Wiley.
- Cushing, G. E. (2012). Candidate cave entrances on Mars. *Journal of Cave and Karst Studies*, 33-47.
- Cushing, G.E., Titus, T.N., Wynne, J.J., and Christensen, P.R., 2007, THEMIS observes possible cave skylights on Mars: *Geophysical Research Letters*, v. 34, L17201, 5 pages,
- Cushing, G. E., Okubo, C. H., & Titus, T. N. 2015. Atypical pit craters on Mars: New insights from THEMIS, CTX, and HiRISE observations. *Journal of Geophysical Research: Planets*, 120, 1023-1043.
- Horiuchi, K, Aydan, Ö, Tokashiki, N., Nasiry, N.Z. (2019). Some considerations on the causes of cliff failures in Ryukyu limestone formation in Ryukyu Archipelago and the analysis of a recent cliff failure. *ir analyses.*, JSCCE, Division C: Geotechnics, 75(2), 216-233.
- Kawamoto, T. and Aydan, Ö. (1999): A review of numerical analysis of tunnels in discontinuous rock masses. *Int. J. of Numerical and Analytical Methods in Geomechanics*, Vol. 23, 1377-1391
- Kawamoto, T., Ö. Aydan, and S. Tsuchiyama, 1991. A consideration on the local instability of large underground openings. *Int. Conf., GEOMECHANICS'91*, Hradec, 33-41.
- Lang, B., 1994. Span design for entry type excavations. M.Sc. Thesis, British Columbia Univ., Vancouver, BC.
- NASA 2022: Images. <https://mars.nasa.gov/mer/gallery/images.html>
- Terzaghi, K. (1943). *Theoretical Soil Mechanics*, Wiley, New York.
- Tokashiki N (2011). Study on the engineering properties of Ryukyu limestone and the evaluation of the stability of its rock mass and masonry structures. PhD thesis, Waseda University (in Japanese with English abstract)
- Tokashiki, N. and Ö. Aydan, 2010. The stability assessment of overhanging Ryukyu limestone cliffs with an emphasis on the evaluation of tensile strength of Rock Mass. *Journal of Geotechnical Engineering*, JSCE, Vol. 66, No. 2, 397-406.

Limestone rock in road projects: case study in the rural area of Vallemí - Concepción

J.C. Bernie

Ingesul Ingeniería S.R.L., Asuncion, Paraguay

M. Stanichevsky & T. Stanichevsky

Geostan S.R.L., Asuncion, Paraguay

ABSTRACT:

The Road Project between the cities of Concepción and Vallemí (169 km), located in the northern area of the Paraguayan Oriental Region, in the Concepción Department, faced some challenges regarding the road construction materials. The absence of basaltic rocks, or other igneous rocks typically used in the country, in the road's vicinity, forced the companies in charge to carry out numerous tests and trials to use the limestone rocks that were largely available in the surroundings of the project. The lack of information of the use of this rock type in regional road projects and the necessity to comply with the Paraguayan Ministry of Public Works were challenges to overcome to accept the use of this material in some of the structural pavement layers. This paper presents a description of the rock type, the locations of extraction areas and quarries, the tests carried out and the results obtained.

Keywords: limestone, road project, subbase aggregate.

1 INTRODUCTION

The technical and economical feasibility of a road project is always greatly influenced by the availability of adequate aggregate material for the execution of the road structural components. Being the nearest basaltic quarry (material mainly used in Paraguay as base and subbase aggregate) more than 650 km away from the Road Project between the cities of Concepción and Vallemí (169 km), a decision was made regarding the use of crushed local limestone as subbase aggregate material. This work summarizes the rock type, areas of extraction, considerations made by the Paraguayan ministry of public works and tests performed.

1.1 *Limestone characteristics*

The Limestone is a sedimentary rock that is composed of at least 50% calcium carbonate (CaCO₃) present as calcite. It mainly originates in shallow marine environments because of biochemical-organic processes, but it can also be formed by chemical precipitation in evaporitic continental environments.

Mineralogically, a limestone is dominated by calcite (more than 50%), aragonite, and magnesium carbonate. However, there may also be smaller amounts of quartz, clay minerals, feldspars, siderite, and some sulfide such as pyrite. Normally, calcium carbonate can be formed by the accumulation of shells and shells of living organisms or by direct chemical precipitation from aqueous solutions.

As for the chemical composition of limestones, the ratio of calcium (calcite) and magnesium (dolomite) in the rock plays a very important role. Regarding this aspect, it should be mentioned that a pure limestone would theoretically have more than 95% calcite in its composition and possibly 4% magnesium (dolomite). While if the rock has around 90% calcite and 10% dolomite, it would be called magnesian limestone. Furthermore, if calcite represents 50% to 90% of the total composition, and dolomite 10% to 50%, the rock is known as a dolomitic limestone.

Limestones found in the department of Concepción can be considered as dolomitic limestones.

To achieve a proper limestone characterization, it is necessary to observe the main rock properties such as texture, structural configuration, and the ratio of primary structural components: grains (intraclasts, granules, pelloids, wrapped grains, bioclasts and skeleton), carbonate sludge and calcite cement. Additionally, it is also necessary to evaluate the presence or absence of calcareous sludge, the relative proportion of grains and calcareous sludge, the appearance of skeletal signs of organogenic binding on its development, the in-situ lithification, and the growth position.

Limestone classification is simple and easy to perform through a field description with a geologist's magnifying glass. Limestones usually do not present a recognizable sedimentary texture.

1.2 *History of use in road projects*

Limestone is used in road projects in numerous places in the world. One example is described by (Serrano et al, 1995) that refer to limestone use in road projects in Cuba. In the mentioned work, limestone characteristics are exposed, as well as possibilities for its employment and application case studies. An economical general analysis and use recommendations are also included. They conclude the following:

- If national guidelines are complied, based on chemical composition, particle size distribution, Atterberg limits, humidity-density and CBR, a good onsite behavior is observed.
- A simplification of the construction method is achieved.
- With adequate equivalent thicknesses, the materials can be used indistinctly as an option to the traditional ones.
- Due to their sufficiently good behavior and the economical savings obtained by their use, limestone materials are an attractive alternative for road projects.

2 REGIONAL GEOLOGY

The Itapucumi (Neoproterozoic, Cambrian) formation is represented by metamorphized limestones and calcareous marble from the Upper Precambrian system, corresponding to the final part of the myosinclinal of the Botorantin formation of Brazil. Its extension in the Concepción Department can be seen in **Figure 1**.

In the set of different deposits of the Quaternary it is possible to distinguish packages consisting of colluvial-alluvial, alluvial, and ferruginous laterites, apart from those formed by unconsolidated detritus of fine to medium grains. These would be the predominant lithologies in the section considered.

It is important to highlight the presence of shallow gravel outcrops of different sizes (boulders), mainly south of the Aquidaban River, relicts of ancient meanders of rivers that derived their waters towards the Paraguay River forming gravel pits of little power and of considerable extension, generally with matrices of clay and silt that cement and lithify these deposits.

There is a great difference in texture and structure between the outcropping flows in the area, evidenced mainly in the quarries where grayish limestones are observed, while in the river there are rocks with a certain degree of metamorphism.

The different rocks are separated from each other by sediment zones that occasionally include levels of fluvial sandstones a few centimeters thick that have undergone metamorphism of thermal origin that modified them to meta quartzite.

The region is characterized by a contrast between the sediment plains of the Chaco type and the folds of limestone and sandstone that make up the elevations of the characteristic relief of the area.

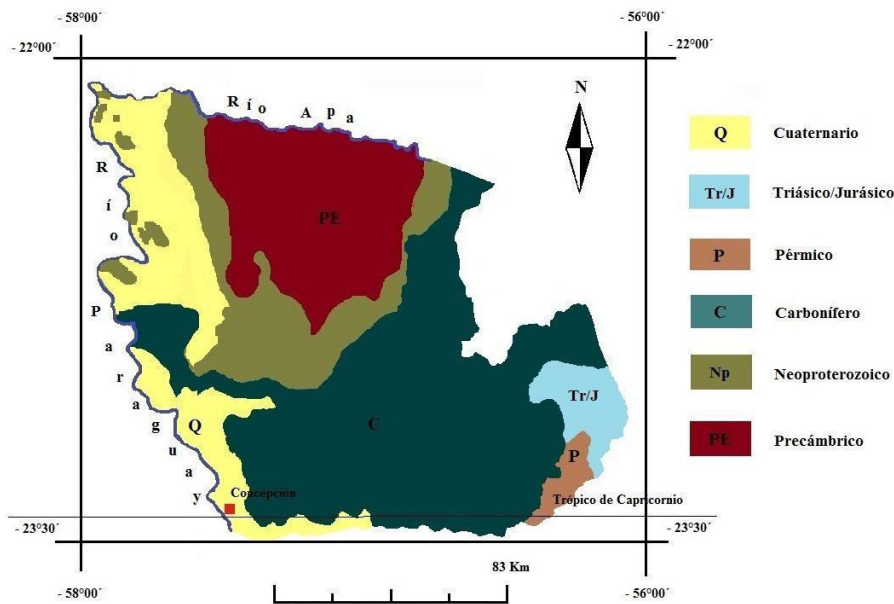


Figure 1. Geological map of the Concepción Department (Organization of American States, 1986).

3 LOCAL LIMESTONE ROCK PETROLOGY

It consists exclusively of calcite minerals (calcium carbonate: CaCO_3), of chemical origin (precipitated from an aqueous solution). The average size of the crystals varies between 0.2 mm and 0.6 mm. Calcite crystals have mainly subhedral shapes, anhedral in some cases, which are cloudy in parallel light. An obtained sample is shown in Figure 2.

Euhedral crystals of dolomite (Ca Mg CO_3) are observed in isolation, in a small proportion. The amount of dolomite present is less than 3%. Microfractures with posterior filling of calcite veins are observed. In addition, brown stylolitic structures occur, typical in calcareous rocks.



Figure 2. Local limestone obtained sample.

3.1 Microscopic description

Rock of light brown tone, holocrystalline, of porphyritic texture, with mineral phenocrystals of calcite, that appear with tabular habit of vitreous luster. Under the binocular magnifying glass, thick parallel joints and zoning are observed, characterized as calcareous minerals.

Among the mafic phenocrysts, calcite tabular crystals of light tone, somewhat altered, are observed. Biotite (Bi) of vitreous brightness and brown tone, with prismatic habit and scaly appearance, is also present. Both are smaller than calcite phenocrysts.

4 PERFORMED TESTS

To use the local limestone rocks in road projects of the area, given that there were no previous references of their use, the MOPC (Paraguayan Ministry of Public Works and Communications) requested the consulting firms who elaborated the road project to carry out tests that demonstrate the viability of its use.

The nearest basaltic quarry was more than 650 km away from the road site, approximately. Most of the tests were conducted at the INTN (Paraguayan National Institute of Technology and Standardization).

The results were extracted from the official project report (GEOCON & EIT, 2008) presented to the mentioned entity.

4.1 *Petrographic classification*

The FACEN (Faculty of Natural Sciences of the National University of Asuncion) classified rock specimens described in this work as fine grained crystalline dolomitic limestone.

4.2 *Abrasion tests*

Los angeles abrasion tests were carried out on two samples of the regional limestones. The applied method was the one described in the IRAM 1532-2000 standard (Argentine Institute for Standardization and Certification, 2000).

For the first sample values of 27.2% and 28.0% were obtained. For the second sample, the values were of 26.6% and 27.1%.

The NP 193/7-1980 standard (Paraguayan Institute of Technology, Standardization and Metrology, 1980) states that a maximum value of 50% should be obtained for the material to be used in concrete general mixes. For its use in concrete mixes performed for highways, roads, and pavements the stated allowed maximum value is of 30%.

4.3 *Other tests*

Other tests performed were:

- Sulfate resistance test. No alteration was recorded.
- Immersion tests in ethylene glycol. No alteration was recorded.
- Aggregate cubicity test. Test result of 31%.

5 QUARRY

After the execution of diverse tests on samples extracted from various locations in the vicinity of the road project, and considering the results obtained, the Roads Department of the Ministry of Public Works of Paraguay accepted the use of the local limestone under certain specific requirements.

During the execution of the road project, a permit was warranted for the opening of a quarry located 30 km north from the San Carlos City (21K, 470088.11 mE, 7539817.28 mS), given that the environmental permits were complied. A photograph showing the local limestone aggregate trituration facility is presented in Figure 3.



Figure 3. Local limestone aggregate trituration facility.

5.1 Ministry of public works requisites

The crushed local limestone obtained from the previously mentioned quarry was mainly used as subbase material. The prerequisites for its use were:

- The material should only be used as subbase material and not be exposed in any case.
- The crushed local limestone should have less than 35% wear in the Los Angeles Abrasion test.
- Constant control tests should be carried out on the used material.
- The subbase mix particle size distribution should comply with Table 1.

Table 1. Subbase mix particle size distribution requirements

Sieve dimension	%Passing
2" – 50 mm	100
1 1/2" – 38 mm	
1" – 25 mm	75 - 95
3/4" – 19 mm	
3/8" – 9.5 mm	40 - 75
No. 4 – 4.75 mm	20 - 40
No. 10 – 2.0 mm	15 - 40
No. 40 – 0.42 mm	8 - 20

6 CONCLUSIONS

This work presented a case of use of crushed local limestone as subbase material for a road project. Details of the material characterization and quarry location in the Concepción Department were exposed and remain as a reference source for future near projects. Furthermore, considerations taken by the Paraguayan ministry of public works, for a successful implementation, were also shown.

7 REFERENCES

- Serrano, L.E. 1999. utilización de calizas blandas en bases y subbases de las carreteras cubanas. *Revista Técnica de la Asociación Española de la Carretera* 101:79-84.
- Organization of American States. 1986. National Commission of Regional Development, Par/86 Project.

Geocon & EIT Partnership. 2008. Road Project Concepción Vallemi: Technical Report.
Argentine Institute for Standardization and Certification. 2000. Coarse Aggregates, Test Method of resistance to the abrasion with the “Los Angeles” machine. IRAM 1532-2000.
Paraguayan Institute of Technology, Standardization and Metrology. Coarse Aggregates, Test Method of resistance to the abrasion with the “Los Angeles” machine 1980. NP 193/7-1980

Tunnel Portal Instability Adjoining Landslide Area and Remedial Measures: A Case Study of Sivoke-Rangpo Railway Tunnel T-7

Manoj Kumar, Deepali Saxena, Armando Capellan
Amberg Engineering AG, Gurgaon, India

Corresponding Author- manojgeologist1@gmail.com

ABSTRACT: The construction of tunnel portals in hilly terrain or in slope areas often involves difficulties, which are closely related to features, such as slope topography, geology, underneath water, geotechnics, construction geometry and the tunnel excavation method. The initiation of landslides or the acceleration of these actions is one of the main challenges faced during construction of the tunnel portals. In this paper, the instability problems in Sivoke-Rangpo Railway tunnel portal T7- P1 that has been excavated with a thick slope wash material, water charged conditions and complex geological conditions (Phyllite, schist and quartzitic schist) and heavy rainfall in this region have been addressed. The geotechnical investigation carried out to ascertain the rock mass conditions and its geo-mechanical parameters. Micro-pile solutions with permanent anchors designed for slope protection at different levels and installation of deep drainage provisions considered to drain out the underneath water. This case study highlights the sufficient ground investigation, slope support design, appropriate excavation and support sequence, required slope monitoring during and after construction process.

Keywords: Slope instability, landslide, Railway Tunnel, Monitoring. Seepage, Remedial solution

1 INTRODUCTION

Ministry of Railways has decided to provide rail connectivity to Gangtok in Sikkim from North of West Bengal by constructing a railway line taking off from existing railway line of Siliguri - Alipurduar section. The line in first phase is proposed to be connected to Rangpo (in Sikkim) to be finally connected to Gangtok. IRCON INTERNATIONAL LIMITED, Government of India Undertaking, under Ministry of Railways, hereinafter referred to as IRCON, has been entrusted with the design and construction of Sivok (West Bengal) to Rangpo (Sikkim) New BG Railway Line Project connecting the state of West Bengal to Sikkim in North-East Region of India.

The proposed railway line passes through foothills of Kanchenjunga ranges of Himalayas and is running near river Teesta and National Highway NH-31A and passes through dense reserve forest of Darjeeling District of West Bengal and East Sikkim District of the State of Sikkim.

2 SALIENT FEATURES OF PROJECT

Owner:	Northeast Frontier Railway (NFR)
Client:	IRCON INTERNATIONAL LTD
Tunnel Length:	3072.54m
Cost of Project (Tunnel T-7):	428 Crores (Approx.)
Project Duration:	36 Months.

3 LOCATION PLAN & ALIGNMENT OF TUNNEL

T-7 Railway Tunnel Construction Portal locations is approximately defined by Chainage Km 19+043 for South End portal and Km 22+090 for North End portal

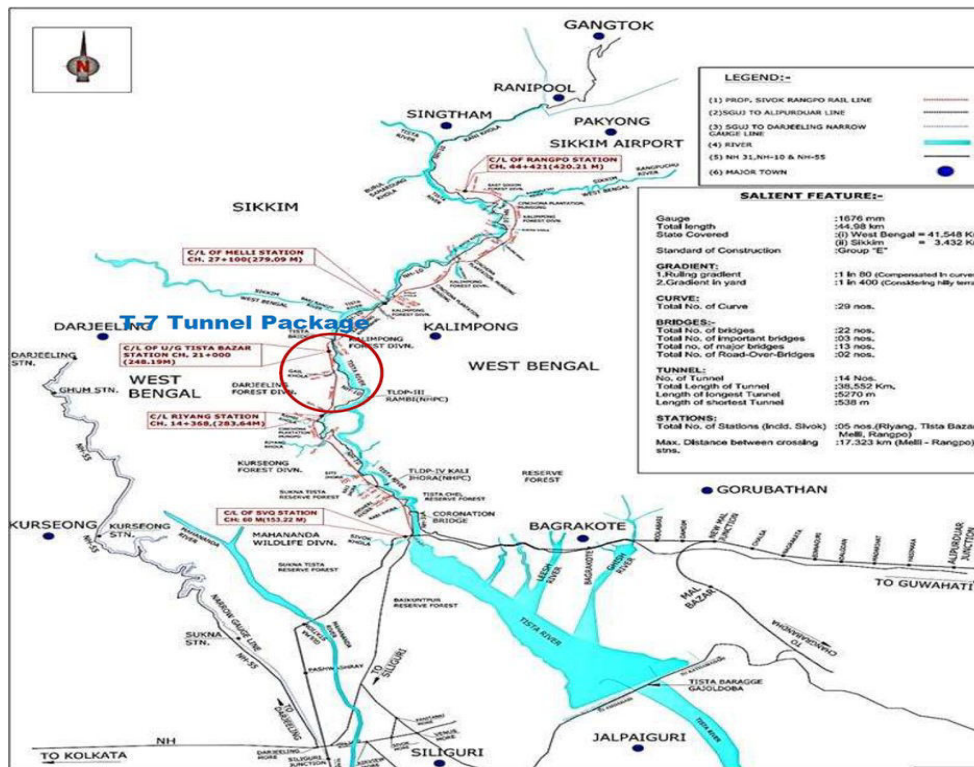
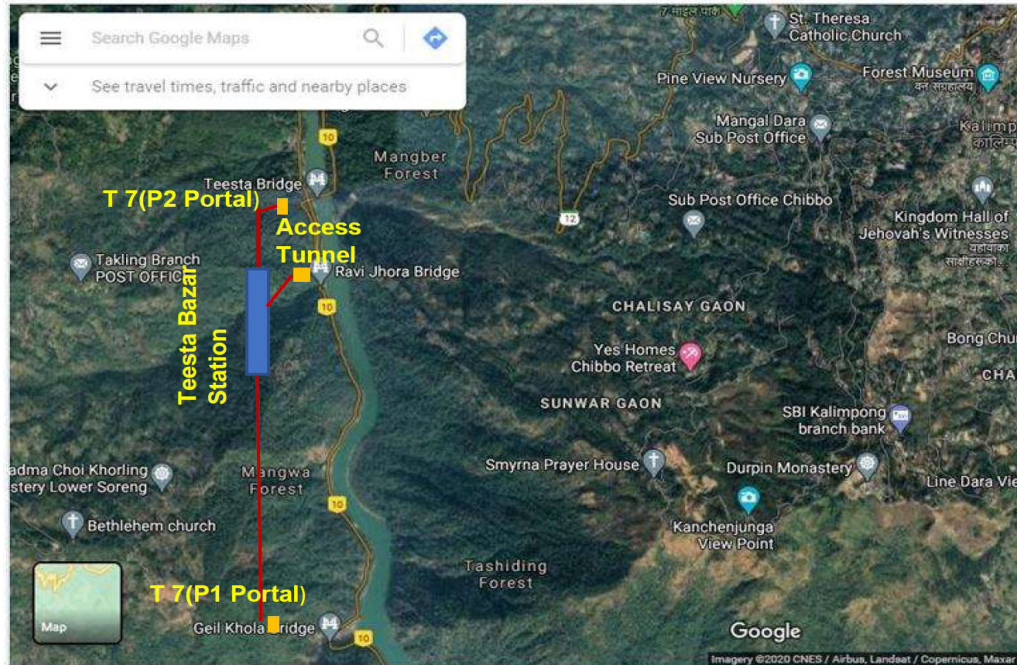


Figure 1(a) & 1 (b)- Satellite Image and Location Map of T-7 Tunnel, Sivok (West Bengal) Rangpo (Sikkim) BG Railway Line Project

4 PROJECT SITE GEOLOGY

Geologically, T-7 project area lies in the Paleoproterozoic group of Lesser Himalayan and is mainly composed of rocks belonging to Gorubanthan Formation of Daling group. The Gorubanthan Formation consist of monotonous sequence of inter banded chlorite sericite schist/phyllite, quartzite, meta greywacke, pyritiferous black slate /carbon phyllite, chlorite schist and quartz schist.

As the project falls in Zone IV as per seismic zone map of India w.r.t to IS 1893 (Part-1):2002, the area lies in zone which is moderately high seismic hazard with expected shaking intensity of VIII on MSK scale and zone factor (Z) of 0.24g as the maximum considered earthquake. For the preliminary design, the parameters recommended in zone IV utilized.

The approach road to tunnel portal and slope location consists of fractured, weathered, sheared and jointed rock mass phyllite, chlorotic schist and phyllitic quartzite are exposed at road cutting location. The extension of rock mass has been observed downward at portal location in Nallah and up to National Highway. For confirmation of rock mass at portal location, 3 numbers boreholes done namely DH-06, DH-07 & DH-08 adjacent to portal (one at centre line another two numbers upward and downward of portal location). The Rock encountered in boreholes varying from 2.0m to 5.25m depth.



Photo- 1- View of Active slide zone and weathered, sheared and jointed rock mass phyllite, chlorotic schist are exposed at road cutting location on the way to T7-P2 Portal

5 ACTIVE LANDSLIDE AND ADJACENT TUNNEL PORTAL

The area above the portal was studied including the slide zone and further geotechnical investigation such as 4 nos. boreholes carried out to establish the rock-line (Figure 2b). The surrounding area, slope to approach road was found under water charged condition.

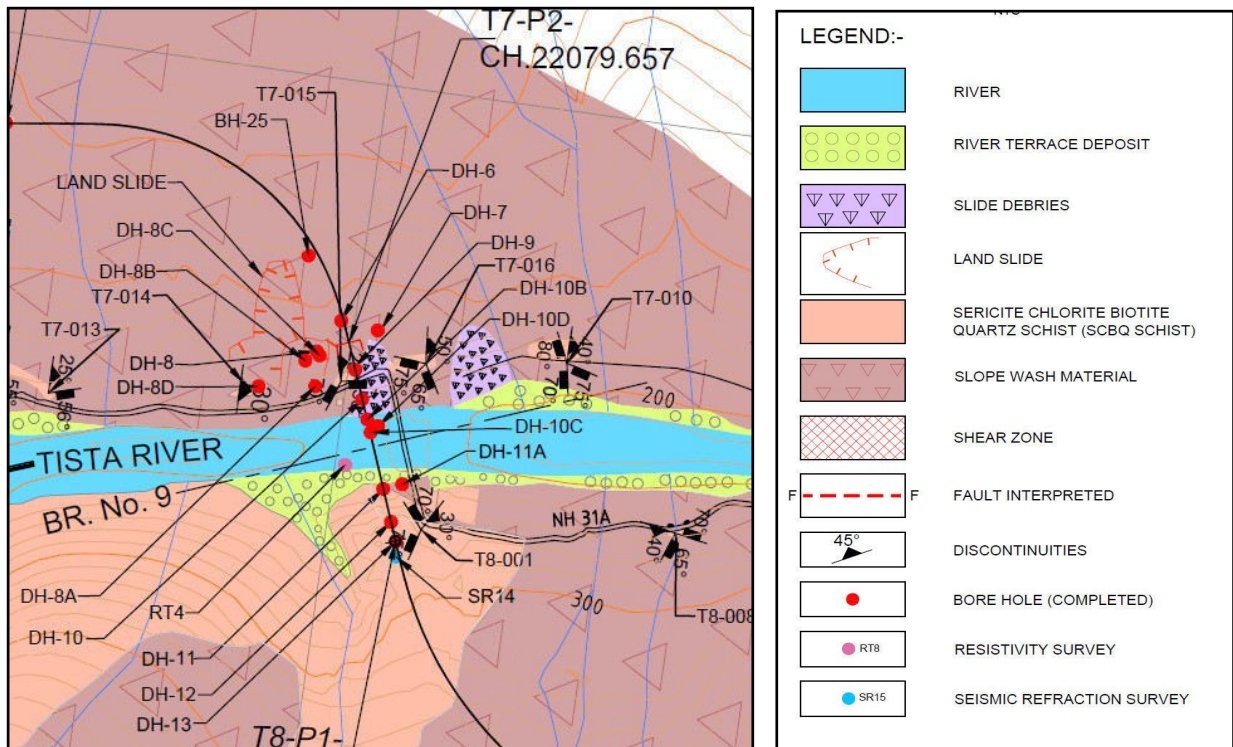


Figure 2 (a) – Geological Plan of Portal T7-P2

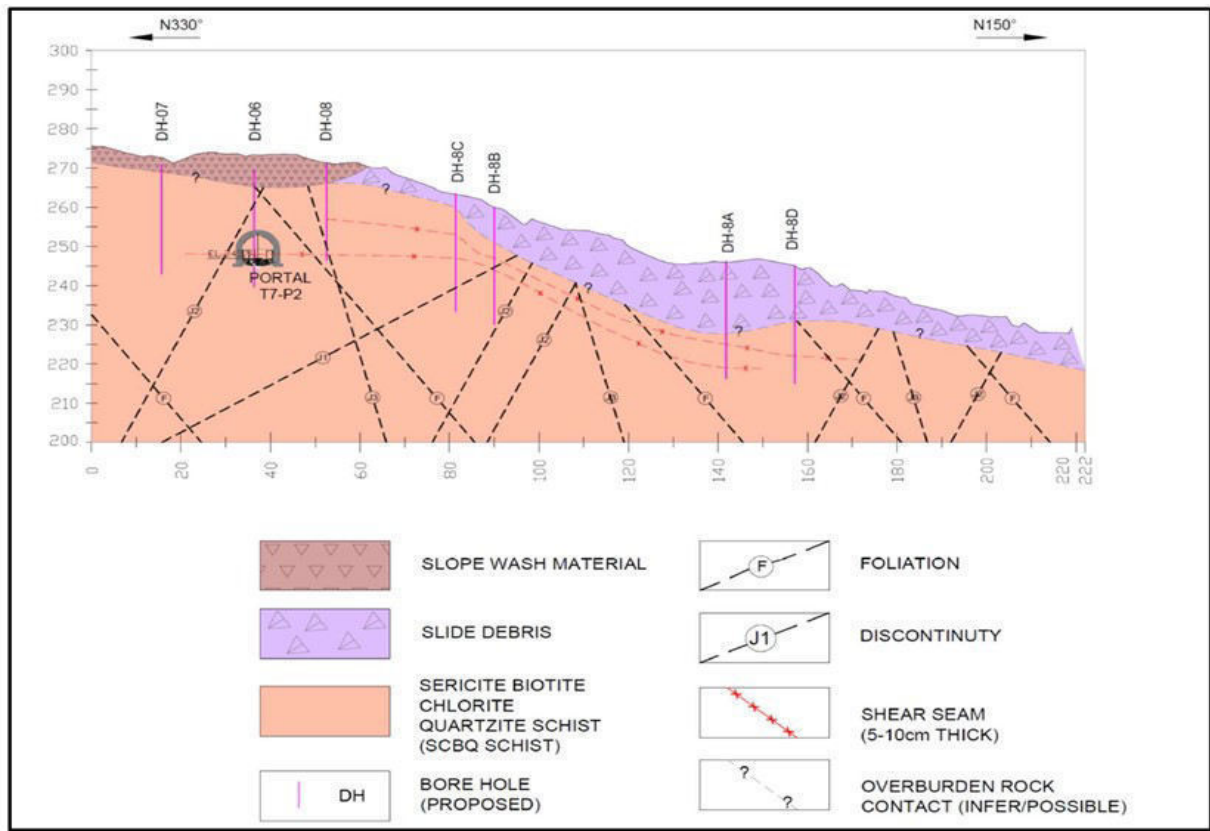


Figure 2(b) –Geological Section along slide and approach road to portal T7-P2

6 GEOTECHNICAL INVESTIGATION

To establish the rock line along approach road to portal and at location of active slide zone 4 nos. additional borehole proposed and drilled up to a maximum depth of 30m. After obtaining the factual borehole investigation data, in-situ and lab tests conducted on selected samples to derive the design parameters for slope stability analysis and support measures.



Photo- 2 (a) - Geotechnical Investigation: 04 nos. borehole along slide zone to establish the rock line for remedial measures

As per the bore holes data the rock depth varies from 3.5m to 18m along road and slide zone. The rock mass discovered in borehole at shallow depth was found to be fractured and shattered and shearing 10-15cm thick along foliation plane.

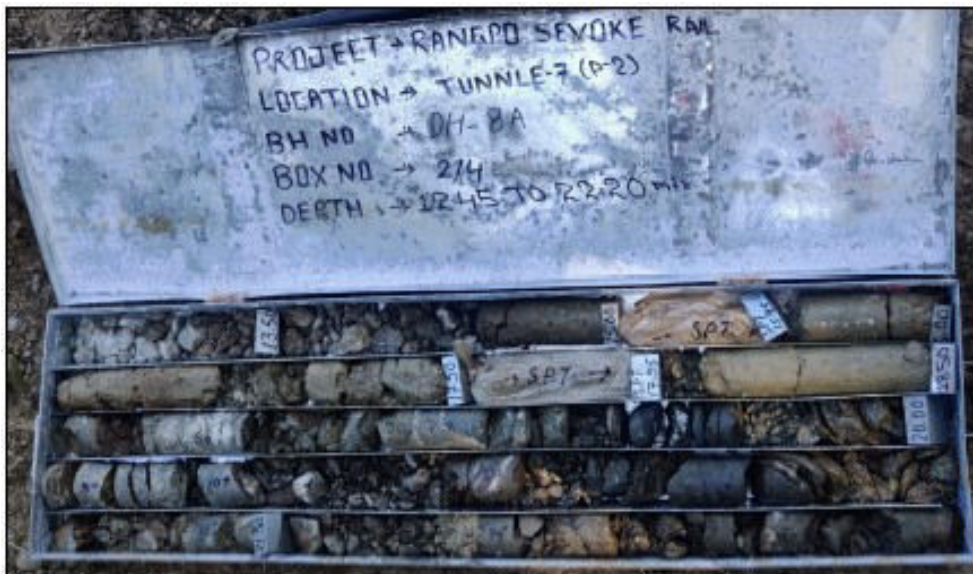


Photo- 2 (b) – Rock core details from geotechnical investigation

7 DESIGN FOR SLOPE STABILITY

- *Design principle*

Slope stability analysis has been performed using RS2 software considering Shear Strength Reduction (SSR) technique. This technique gives the overview for the stability of the system. Stress analysis has also been performed for the slopes to check the convergence of the system and horizontal movements observed during open cut excavation. Forces in micropile has been checked for the allowable stresses. In highly weathered or closely fractured rock, failure occurs along a surface that is more or less towards circular shape. The slope support system has been designed considering the failure behavior as interpreted from finite element stress analysis.

- *Methods of analysis*

Stability analysis of cut slope has been carried out based on Finite Element method. Finite Element software – RS2 has been used to check the stability of the portal cut slope.

- *Design loads and Combinations*

Following loads have been considered for the analysis:

- *Dead load*

Dead load is the weight of the slope material that is involved in the stability of the slope.

- *Water load*

Water load is the pore-pressure that gets generated due to presence of water table in the slope material

- *Seismic loading*

The design value of horizontal seismic coefficient, a_h shall be computed by the following expression given in Clause 6.4.2 of IS:1893 (Part 1): 2016.

$$a_h = \frac{ZIS_a}{2Rg}$$

where,

Seismic zone coefficient = 0.36 (Zone V) (as per Table 3 of IS 1893:2016)

Response Reduction Factor = 3 (as per Table 9 of IS 1893:2016)

Importance Factor = 1.5 (as per Table 8 of IS 1893:2016)

The factor (Sa/g) has been taken as 2.5 to be on the conservative side.

Hence, the design value of horizontal seismic coefficient as calculated is 0.23. The design value of vertical seismic co-efficient is to be adopted as (2/3) of design value of horizontal seismic coefficient as per Clause 6.4.6 of IS:1893:2016.

Extreme loading condition has been analysed in RS2 which comprises of Dead load, Water load, and Seismic Load. The combination considered is

DL + 1.0 WL + 1.0 SL.

- *Input design parameters*

Geology of cut slope consists of varying thickness of overburden material which is underlain by moderately weathered sericite chlorite biotite quartz schist rockmass. A critical section having nearly 5 m thick overburden has been analyzed in FEM to check the adequacy of proposed support system. Rock line is taken from geological section along road to portal P2 of T-7. Geotechnical design parameters considered in slope stability analysis has been summarized below:

Geotechnical Unit	Unit Weight γ	c (kPa)	Φ (Degree)	E (MPa)	ν
Overburden	18.5	30	32	17.5	0.3
Schist	27	239	25	4200	0.2

Table 1 Design Parameters for Soil & Rock

• *Results of Analysis*

Initial in-situ condition has been generated as per rock line from geological section along T7 (Figure-4). Uniform, 6 noded mesh has been used in FEM modelling. Micro-pile has been installed at first stage. Then excavation shall be carried out in stages along with installation of rock anchor. Same has been followed in the analysis model. In last stage water table has been activated in the model to account for water load on the slope and support system

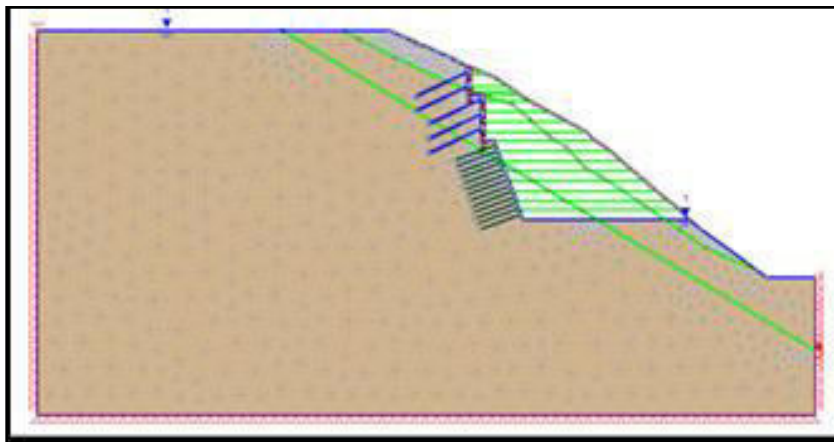


Figure 3 – Finite Element Model used for Slope Stability Analysis

Three scenarios have been analyzed for checking the adequacy of proposed support system and the corresponding FOS.

1. Stress Analysis with Water Loads
2. Strength Reduction Factor with Water Loads
3. Strength Reduction Factor with Water and Earthquake Loading (Extreme Loading)

The results of analysis have been summarized below:

Displacements, refer Figure-4, has been reported to check whether the system has limited deformation or not. In case of high movement, slope may fall. Forces generated in the micropile shall also be checked for structural capacity of micropile. Factor of Safety has been summarised to evaluate the global stability factor of safety.

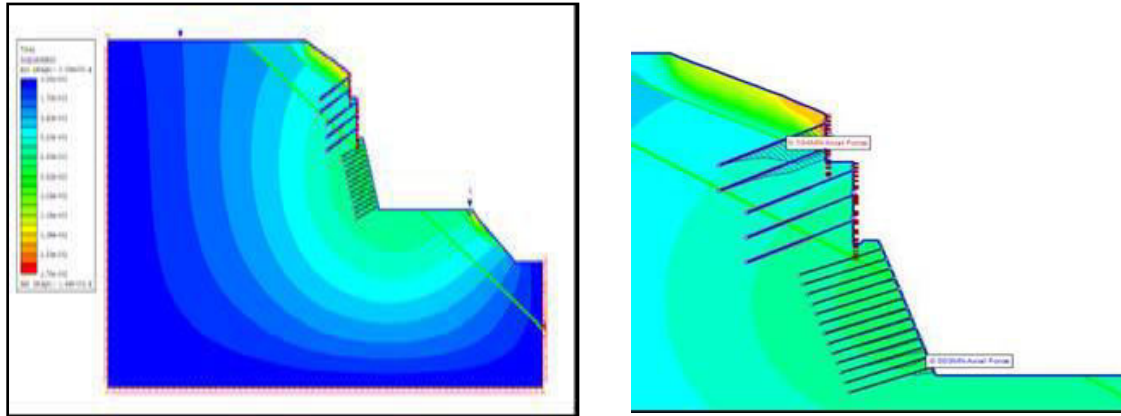


Figure 4 – Maximum displacement in the system 15 mm (red envelope) and Maximum force in anchor 104 kN

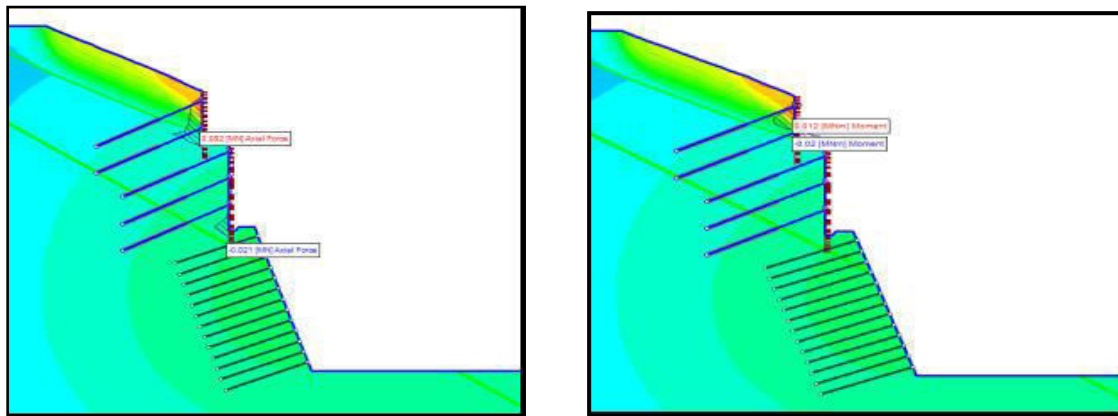


Figure 5 – Axial force in micropile 82 kN & Bending moment in micropile 6.0 kNm

- *Design conclusions*
- *Analysis performed indicates that the proposed cut slope will be safe with the recommended support system.*
- *Micropiles will be installed at spacing of 750 mm c/c. Top of all piles will be held together with capping beam.*
- *Immediately after excavation of slope 50 mm thick shotcrete layer has to be applied followed by installation of wire mesh. Finally, second layer of 100 mm thick shotcrete needs to be installed to achieve the total design thickness of 150mm*
- *After shotcrete, prestressed rock anchors of 760 kN capacity will be installed at spacing of 3.0 m (H) x 3.0 m (V).*

8 CONSTRUCTION PROCESS FOR SLOPE PROTECTION

After design analysis of slope stability, the solution for slope protection given with micro-piling, UC beam /Concrete beam, anchors, deep drains and catch water drain in sequence.

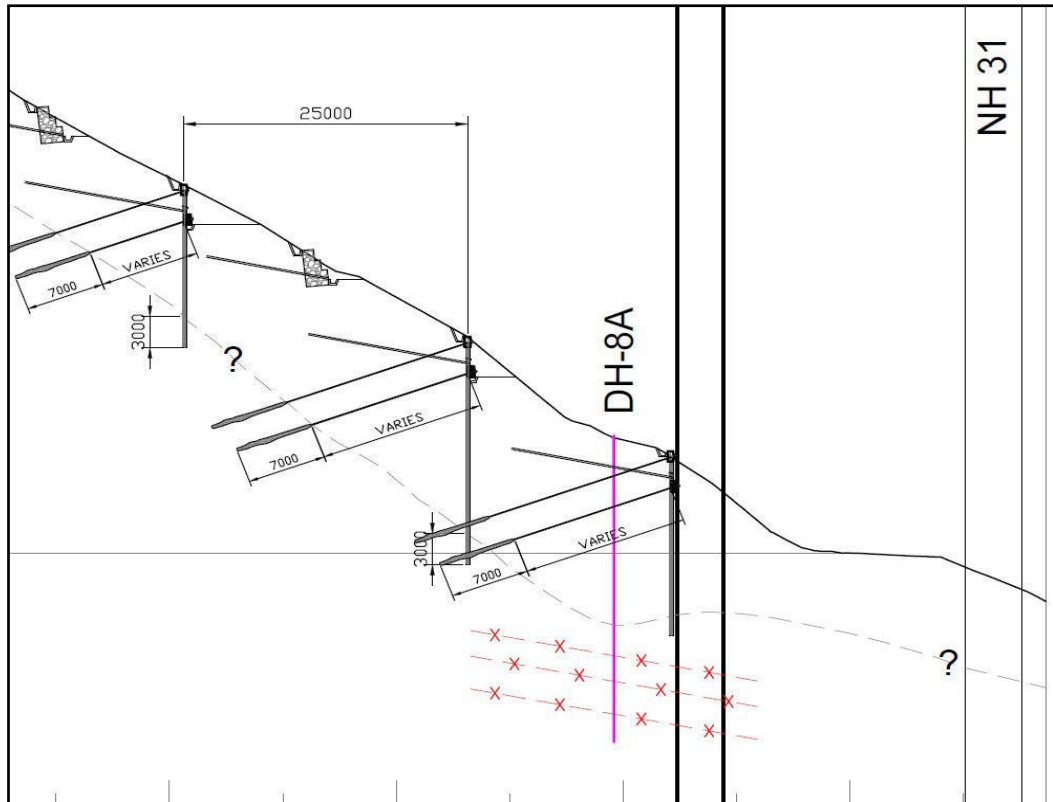


Figure 6 (a) - Longitudinal Section along slide showing rock line and plan showing active slide zone

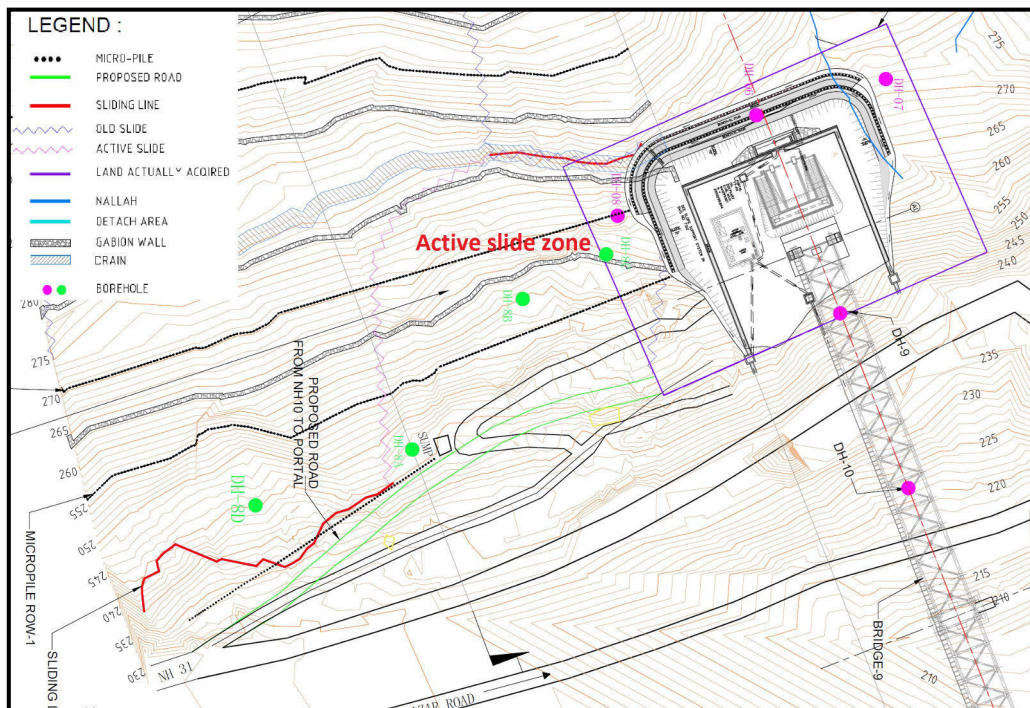


Figure 6 (b)- Location plan of active slide and Tunnel T-1 Portal with remedial measures such as Micro-pile at different levels, gabions, catch water drains

The following construction sequence followed at site during slope excavation and support measures:

- *Installation of micropile up to minimum 3.0m embedment in hard rock*
- *Grouting of Micropile pipes*
- *Casting of capping beam*
- *Excavation up to 2 to 2.5m below capping beam*
- *Support of Micro-pile wall with wire mesh and shotcrete*
- *Fixing of UC or Concrete beam*
- *Installation of Permanent pre-stressed rock anchors ensuring 6m fixed length in hard rock*
- *Grouting and stressing of anchors*
- *Installation of deep drains to release the water pressure and making catch water drain for collection of surface water.*

The above sequence followed at each level of excavation and support as designed for slope support and stability.



Photo- 3- Micro-pile installation work at top of slide zone for slope protection

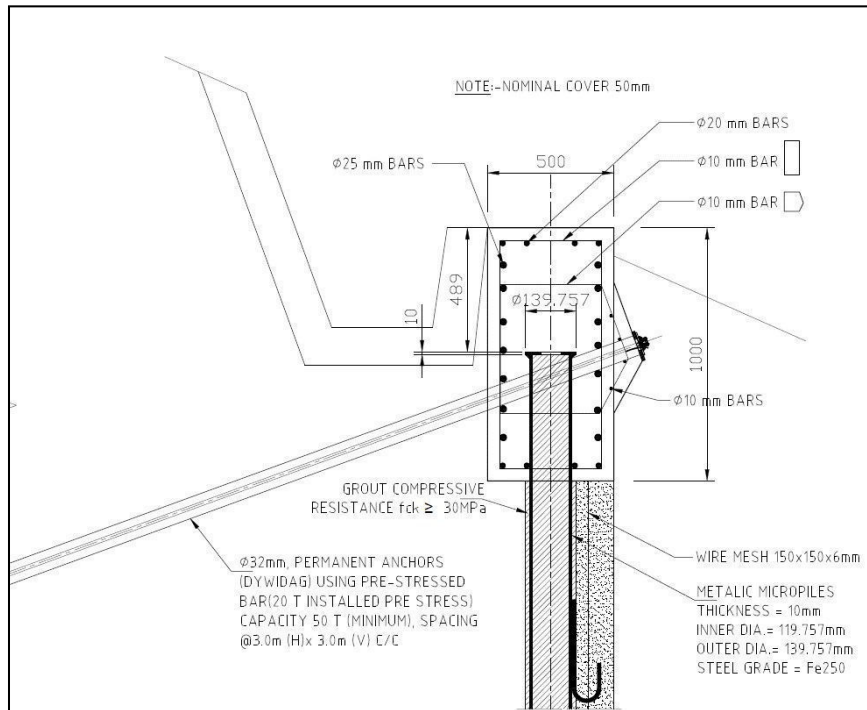


Figure 7 - Section showing arrangement of permanent anchors through beam and details of micro-pile



Photo- 4 (a) & 4 (b)- Casting of capping beam and micro-pile wall support with wiremesh and shotcrete and installation of deep drains and Installation of Permanent anchors after drilling



Photo- 5 (a) & 5 (b)- View of slide protection after several level of supports and View of active slide after slope support

9 INSTRUMENTATION AND MONITORING OF CONSTRUCTION ACTIVITY

For monitoring of construction activity at tunnel portal and slide zone, geotechnical instrumentation scheme proposed to monitor the change in water table levels, ground settlements, deformation, lateral movement or deflection and monitoring of installed anchors after stressing.

The following geotechnical instruments proposed at portal and slide zone:

- In-place Inclinometer for lateral movement of ground
- Anchor load cells for monitoring of permanent anchors
- Bi-reflex targets for slope monitoring
- Standpipe piezometer for monitoring of ground water table

Some of the instruments were installed prior to construction such as In-Place inclinometer and standpipe piezometer at top elevation of slide and Tunnel portal and others Bi-reflex targets and anchor load cell during slope support for monitoring.

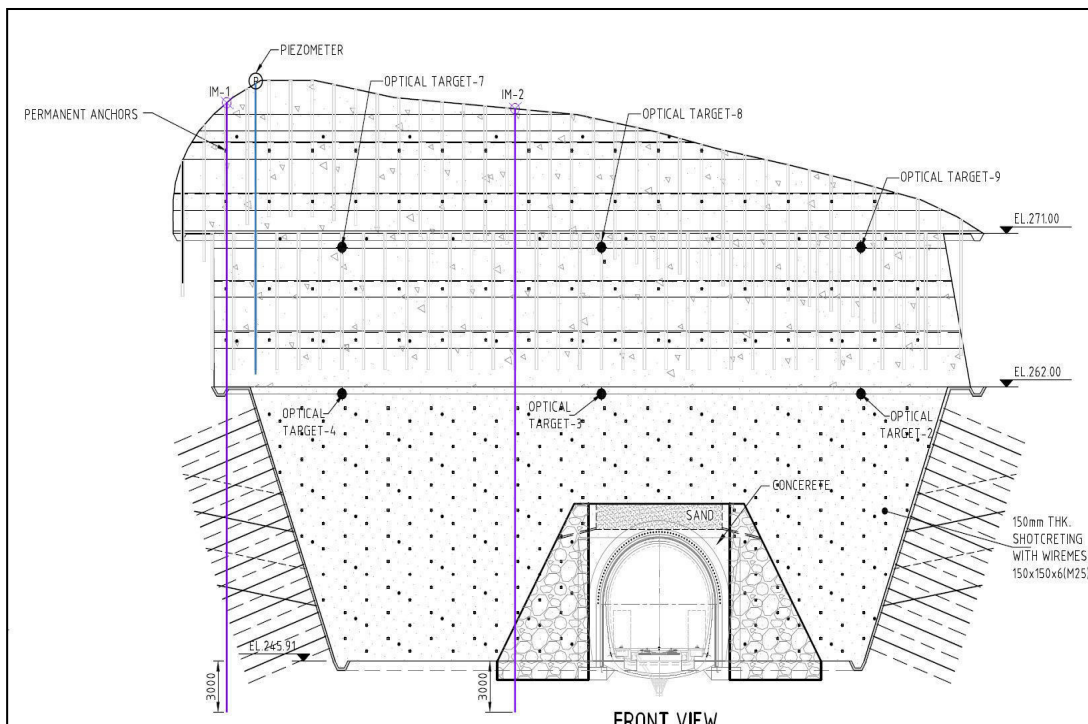


Figure 8- Section showing proposed and installed geotechnical instruments for monitoring of slide and portal constructions and supports and in-place inclinometer after installation at top of slide

10 CONCLUSION & RISK ANALYSIS

The stability and risk analysis during excavation and support for active slide and tunnel portal has been done and appropriate construction sequence followed at site to prevent any slope failure.

Heavy water ingress during excavation and drastic changes in water tables due to heavy rain fall experienced previously start of approach road protection and portal development. During geotechnical investigation slope wash materials and fractured/sheared and weathered rock mass

conditions encountered and the project location having experience of tectonic activity such as earthquake and falls in Seismic zone IV.

However, considering the above-mentioned risks appropriate Geotechnical investigation has been carried out at the concerned locations to ascertain the slope instability challenges and to adopt adequate remedial precautionary measures during construction and post construction.

During installation of Mico-piling it is ensured termination in hard rock minimum 3.0m as given in design and anchors also done 7.0m in rock (fixed length) to achieve the bond strength. After each level of stressing of anchor further below excavation done.

Construction sequence has been followed strictly and support implementation and monitoring done as per design recommendations and timely installation of adequate slope support to prevent any failure. Provision of continuous geological mapping during slope excavation and support and collecting the data i.e., weak zone, water condition, geological condition such as fractured and sheared rock mass etc.

Vibration monitoring shall be done near tunnel portal during blasting due to slide slope excavation and support simultaneously. Provision of immediate quick setting Grouting implementation after high ingress of water controlled/split blasting during excavation in rock near portal

11 REFERENCES

- *Micropile Design and Construction (Reference Manual for NHI Course 132078), FHWA NHI 05-039, December 2005, Paul J. Sabatinia P.E., Ph.D.; Burak Tanyua Ph.D.; Tom Armourb P.E.; Paul Groneckb P.E.; and James Keeleyb P.E.*
- *GEOTECHNICAL ENGINEERING CIRCULAR NO. 4 Ground Anchors and Anchored Systems, FHWA-IF-99-015, June 1999, P.J. Sabatini, D.G. Pass, R.C. Bachus*
- *Summary Report of Research on Permanent Ground Anchor . FHWA – RD – 97 – 130 “Design Guidelines for Permanent Ground Anchors” (1998)*
- *Practical Rock Engineering by Dr. Evert Hoek, 2007 ed.*
- *RS2 (Phase2 version 9.0)- Rocscience Software, Finite Element Analysis for Excavations and Slopes.*
- *RocLab (Version 1.031)- Rocscience Software, for Determining the Rock Mass Strength Parameters.*
- *International Tunnel Association (ITA): Guideline for the Design of Tunnels*
- *International Tunnel Association (ITA): Seismic Design and Analysis of Underground Structures*
- *Hoek-Brown Failure Criterion – 2002 Edition*
- *Austrian Society for Geomechanics: Guideline for the Geotechnical Design of Underground Structures with Conventional Excavation, 2010.*
- *Geological Interpretative Report (Tunnel-T7)*
- *Quantification of Geological Strength Index Chart by Hoek, E., Carter, T.G., Diederichs, M.S. 47th US Rock Mechanics/ Geomechanics Symposium, 2013. ARMA 13-672, Page 5*
- *BS 8002:1994, Code of practice for Earth retaining structures.*
- *Code of Practice for Reinforcement of Rock Slopes with Plane Wedge Failure, IS 14448: 1997 (Reaffirmed - 2012)*

Soil-structure interaction influence on shallow foundations design on rocky mass in a reinforced concrete building

Y.R.P. Santos

Federal University of Pernambuco, Recife, Pernambuco, Brazil

B.C.F. Rocha

UNINASSAU, Caruaru, Pernambuco, Brazil

M.A. Lima

UNINASSAU, Caruaru, Pernambuco, Brazil

P.D.L. Nascimento

UNINASSAU, Caruaru, Pernambuco, Brazil

M.M.M. Meneses

UNINASSAU, Caruaru, Pernambuco, Brazil

ABSTRACT:

Soil-structure interaction (SSI) has mechanisms that allow analyzing the structural performance of a building, considering its foundation, its superstructure and as singularities of the terrain on which it will be built as a single system. The present study aims to carry out the redesign foundations project of a reinforced concrete building (tower "A"), consisting of 22 pillars, with isolated and associated footings foundations on a rock mass of granitic composition and RQD predominantly higher than 75%, considering this interaction, based on the redistribution of efforts between the pillars of the structure, verifying its influence on the geometry and consumption of materials in the design of its foundation elements. After redesign, the results obtained revealed that there was no significant change in foundation geometry, as well as in the consumption of concrete comparing the projects with and without SSI. For steel consumption, the results showed an increase in the steel area of the associated footings SPA-07/13 and SPA-10/16 and the isolated footings SPA-15 and SPA-20; while the SPA-01 and SPA-21 isolated footings obtained a certain decrease in this material. It is concluded that, for this project, the soil-structure interaction did not have a significant influence on the observed points, due to the low efforts redistribution on the analyzed pillars, which was reflected in the maintenance of dimensions and quantity of materials in almost all of the foundation elements studied.

Keywords: Soil-Structure interaction, Shallow foundations, Redesign, Rocky mass foundations.

1 INTRODUCTION

Buildings can have shallow and deep foundations, and have the function of supporting all loads from the structure, safely meeting requests. Foundation system depends on the project requests and the study of the subsoil is considered fundamental, as it provides a range of information necessary to avoid failures in the design. According to Brito (1987), foundations with well-designed projects have a final cost of 3% to 10% of the total value of the building, and when poorly designed, they can cost 5 to 10 times more than what had been established.

The design of foundations of a building is usually carried out separately from the structural design, in this way it is common for the designer to analyze the behavior of the foundation considering non-displaceable supports, that is, disregarding the soil-structure interaction. The soil-structure interaction is the method that analyzes the soil mass together with the infrastructure and the superstructure as a single system, applying the analysis model proposed by Winkler (1867) that represents the foundation elements with elastic supports (springs). This mechanism

leads to a more real estimation of the structure's behavior and, therefore, the importance of considering the soil-structure interaction (SSI) is highlighted.

Studies presented by Meyerhof (1953), Morris (1966), Lee & Brown (1972), and Poulos (1975) proposed SSI analysis, verifying factors such as construction processes, floor numbers, construction sequence, building shape and other effects related to soil/rock and structure behavior. Gusmão (1990) reported that the performance of a building is managed by the conditioned rigidity of the effects of the soil-structure interaction and Colares (2006) presented in his study that considering the mechanisms of the soil-structure interaction causes a redistribution of the forces acting on the structural elements, causing the uniformity of settlements. In this way, when considering the SSI, it is possible to develop more efficient and adequate projects.

Savaris et al. (2011), Santos (2016) and Santos et al. (2021) analyzing real cases of buildings through monitored settlements, also showed that, the settlements measurement along different construction stages enables to observe loads redistribution between central and the edge reinforced concrete columns.

This study was been prepared in order to report the changes in the design of the foundations of the analyzed building considering the SSI, being carried out the redesign of the footings according to the new calculated loads and also making a comparison between the geometry and the amount of materials for the resized elements.

2 STUDY AREA PRESENTATION

The construction analyzed in this study is a multi-story residential building called tower "A", which is part of a two-tower complex located on Adjar da Silva Casé Avenue, Indianópolis, city of Caruaru-PE. The building consists of a ground floor, two mezzanines that serve as parking, 32 slabs-floor where the apartments are located, in addition to the roof and attic floors. According to Santos (2018), all structure was been designed in reinforced concrete, according NBR 6118 (2003).

The city of Caruaru-PE is located on the Borborema plateau and presents terrains with more resistant characteristics, with the presence of rocks. Eight mixed-type drilling holes were carried out, with SPT (Standard Penetration Test) and rotating drilling, in order to know the terrain of the project site, totaling 8 drilling holes that revealed a superficial layer of sandy soil with boulders, followed by from the presence of cataclasite with little altered granitic composition (Figure 1), whose RQD (rock quality designation) indicates values predominantly higher than 75%, classifying them as good to excellent, average simple compressive strength of 110.90 MPa and absence of water level up to the investigated average depth, which was around 10 meters in relation to the ground level.



Figure 1. Granitic rock sample obtained by the subsoil investigation (Santos, 2018).

As a result of the characteristics presented by the terrain after the surveys, with favorable strength properties, the project was developed using shallow foundations, consisting of 18 isolated footings and 2 associated footings, represented in the projection plan of the footings with the location of the pillars as shown in Figure 2, as well as the drilling holes carried out for the subsoil investigation. The original footing projects were designed for an allowable bearing capacity of 800 kPa, with a 30% increase in this stress (920 KPa), as defined by NBR 6122 (2019), a standard taken as a basis for the design and execution of foundations.

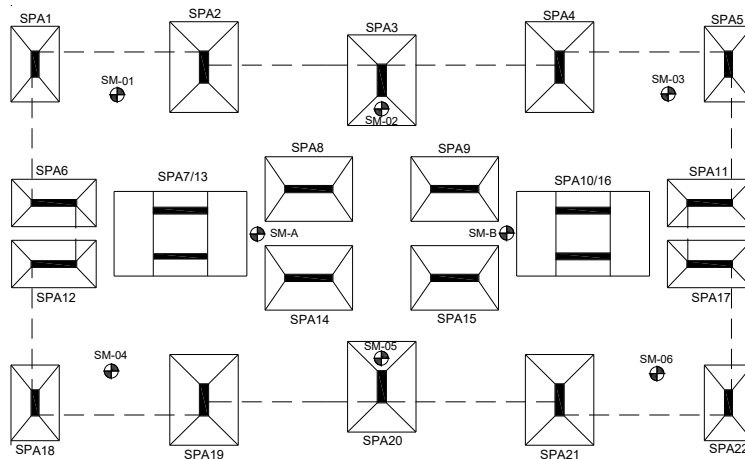


Figure 2. Projection plan and location of drill holes, original pillars and footings (Santos, 2018).

3 MATERIALS AND METHODOLOGY

3.1 Redesign of foundation system

An analysis of the structural behavior was carried out considering the mechanisms of soil-structure interaction in the analyzed building, in a study developed by Santos (2018), based on a monitoring of settlements carried out during its construction. The CAD/TQS® software was used to carry out the structural modeling of the building, considering the information about the materials used in the construction, in order to obtain a more faithful result of the entire structural part, considering two scenarios: the first, considering the non-displaceable supports, and the second, considering the building with its displaceable supports, represented by stiffness spring coefficients “K”, obtained by the ratio between the total efforts and the settlements suffered by each of the foundation elements in the final stage of the construction.

3.1.1 Determination of loads (efforts) and bending moments

The design was carried out based on the efforts acting on the 22 pillars of the “A” tower, according to Santos (2018), resulting from the design considering the real loads acting on the structure that were determined with and without soil-structure interaction effect, being analyzed only the stage end of the construction, with all loads already applied to the structure and considering bending moments acting on each foundation element. The loads on the pillars are shown in Table 1, while the bending moments acting in the x and y directions of the foundations can be seen in Table 2. For this study, an allowable bearing capacity of 920 kPa was adopted for all footings, based on the information present in the original construction project report. The safety factor adopted was $FS= 3.0$ for shallow foundations based on rock ground.

In order to compare the effects of this interaction, this redesign determined the new dimensions of the footings, considering the modeling after using the real information of the building elements with the non-displaceable supports, without SSI, and with the displaceable supports,

with SSI effects. The model used to calculate foundation elements was based on NBR 6118 (2014).

Table 1. Loads (efforts) (kN) on pillars without and with SSI.

Pillar	No SSI (kN)	With SSI (kN)	Diference (%)
P-01	6897.41	6509.92	-5.62
P-02	11,755.32	11,717.06	-0.33
P-03	12,461.64	12,409.65	-0.42
P-04	11,623.87	11,563.05	-0.52
P-05	6564.85	6458.90	-1.61
P-06	7036.71	7006.30	-0.43
P-07	10,129.81	10,077.81	0.51
P-08	12,076.11	12,012.35	-0.53
P-09	11,196.15	11,302.10	0.95
P-10	9422.51	10,096.45	7.15
P-11	7711.64	7703.79	-0.10
P-12	7293.74	7288.83	-0.07
P-13	10,695.84	10,588.91	-1.00
P-14	11,870.10	11,907.38	0.31
P-15	11,077.45	11,679.79	5.44
P-16	8619.07	7831.32	-9.14
P-17	8549.42	8527.83	-0.25
P-18	7268.23	7248.61	-0.27
P-19	12,894.26	12,879.55	-0.11
P-20	12,856.99	13,120.88	2.05
P-21	12,743.19	12,054.53	-5.40
P-22	7288.83	7603.73	4.32

Table 2. Bending Moments (kN.m) without and with SSI.

Pillar	No SSI		With SSI	
	Mx (kN.m)	My (kN.m)	Mx (kN.m)	My (kN.m)
P-01	27.09	-544.61	25.57	-514.00
P-02	-37.82	-1221.91	-37.70	-1217.87
P-03	-28.92	-1307.90	-28.80	-1302.40
P-04	40.08	-1127.86	39.87	-1121.99
P-05	-36.83	-457.38	-36.23	-450.02
P-06	-409.59	-84.47	-407.83	-84.10
P-07	-788.13	-92.44	-784.11	-91.97
P-08	-744.15	85.55	-740.21	85.09
P-09	-689.36	78.05	-695.91	78.79
P-10	-730.84	-77.25	-783.10	-82.77
P-11	-477.72	-82.53	-477.24	-82.45
P-12	-394.80	91.91	-394.53	91.84
P-13	-777.76	105.20	-769.99	104.14
P-14	-691.08	-74.49	-693.22	-74.72
P-15	-644.36	-70.12	-679.41	-73.94
P-16	-628.32	80.35	-570.89	73.01
P-17	-490.58	99.82	-489.35	99.57
P-18	-30.13	534.77	-30.05	533.32
P-19	-34.09	1266.58	-34.05	1265.19
P-20	-29.01	1263.97	-29.60	1289.88
P-21	39.84	1183.98	37.69	1120.04
P-22	21.25	479.03	22.17	499.72

3.1.2 *Steel sizing of footings*

The steel calculation was carried out according to the original project for bending efforts, which guides the use of CA-50 steel and C45 concrete in the foundation design. The sizing of the footings was prepared according to recommendations of NBR 6118 (2014), which does not define a specific minimum bending reinforcement for footings.

3.1.3 *Geometry and concrete sizing of footings*

The concrete volume of the footings, with and without SSI, was calculated through the volumes of the element geometry (base + pyramid trunk), being for the base the formula for calculating the volume of the parallelepiped according to Equation 1 (having as base the dimensions A and B (length and width of the base, respectively) and its total height (H_0), and for the pyramid trunk the formula presented in Equation 2, where H represents the total height, H_0 represents the height of the vertical face of the trunk of the pyramid, with a_p as the largest dimension of the pillar and b_p as the smallest dimension of the pillar.

$$V_b = A.B.H_0 \quad (1)$$

$$V_t = \frac{Ht - H_0}{3} \cdot [(A.B) + (a_p.b_p) + \sqrt{(A.B).(a_p.b_p)}] \quad (2)$$

3.2 *Comparative analyzes considering soil-structure interaction*

The SSI effects on the foundation elements was considered, in order to verify the changes caused in their geometries, which consists in the alteration of the dimensions of their base and their height. The consumption of materials for the realization of the project was also analyzed, focusing on the quantity of steel and concrete necessary for the execution of the elements.

4 RESULTS AND DISCUSSION

4.1 *SSI influence on footings geometry*

As a result of the new loads acting on each pillar, it was found, according to Table 3, that the changes were considerably low for each of them. When comparing the two situations, it is observed that the highest percentages of load alteration occur in pillars P-16, P-10 and P-01 respectively.

For the P-10 pillar, there was an increase of 7.15%, which was offset by the load relief that occurred in the P-16 (-9.14%), with the loads from these two pillars being unloaded under an associated footing. The third highest percentage of load change under a footing occurred in column P-01, where there was a decrease of -5.62%, followed by the P-15 pillar (increase of 5.44%). The same was observed comparing the values of bending moments acting between the elements.

The redesign was carried out in both situations to analyze the differences, resulting in the dimensions of Table 3, showing the footings dimensions without SSI and Table 4 showing the dimensions after SSI considerations.

Table 3. Footings dimensions without SSI.

Sapata	A (m)	B (m)	Asap (m ²)	H0 (m)	H1 (m)	Ht (m)
SPA-01	2.55	3.45	8.80	0.35	0.65	1.00
SPA-02	3.35	4.50	15.08	0.35	0.65	1.00
SPA-03	3.45	4.60	15.87	0.40	0.70	1.10
SPA-04	3.35	4.45	14.91	0.35	0.65	1.00
SPA-05	2.50	3.40	8.50	0.35	0.65	1.00
SPA-06	4.05	2.20	8.91	0.35	0.65	1.00
SPA-07/13	4.85	4.75	23.04	0.45	0.80	1.25
SPA-08	5.10	3.05	15.56	0.35	0.65	1.00
SPA-09	4.95	2.90	14.36	0.35	0.65	1.00
SPA-10/16	4.50	4.45	20.03	0.40	0.80	1.20
SPA-11	4.25	2.35	9.99	0.35	0.65	1.00
SPA-12	4.10	2.25	9.23	0.35	0.65	1.00
SPA-14	5.05	3.00	15.15	0.35	0.65	1.00
SPA-15	4.90	2.90	13.63	0.35	0.65	1.00
SPA-17	4.40	2.50	11.00	0.35	0.65	1.00
SPA-18	2.65	3.55	9.41	0.35	0.65	1.00
SPA-19	3.50	4.65	16.28	0.40	0.70	1.10
SPA-20	3.50	4.65	16.28	0.40	0.70	1.10
SPA-21	3.50	4.65	16.28	0.40	0.70	1.10
SPA-22	2.65	3.55	9.41	0.35	0.65	1.00

Table 4. Footings dimensions with SSI.

Sapata	A (m)	B (m)	Asap (m ²)	H0 (m)	H1 (m)	Ht (m)
SPA-01	2.55	3.45	8.80	0.35	0.65	1.00
SPA-02	3.35	4.50	15.08	0.35	0.65	1.00
SPA-03	3.45	4.60	15.87	0.40	0.70	1.10
SPA-04	3.35	4.45	14.91	0.35	0.65	1.00
SPA-05	2.50	3.40	8.50	0.35	0.65	1.00
SPA-06	4.05	2.20	8.91	0.35	0.65	1.00
SPA-07/13	4.85	4.75	23.04	0.45	0.80	1.25
SPA-08	5.10	3.05	15.56	0.35	0.65	1.00
SPA-09	4.95	2.90	14.36	0.35	0.65	1.00
SPA-10/16	4.50	4.45	20.03	0.40	0.80	1.20
SPA-11	4.25	2.35	9.99	0.35	0.65	1.00
SPA-12	4.10	2.25	9.23	0.35	0.65	1.00
SPA-14	5.05	3.00	15.15	0.35	0.65	1.00
SPA-15	5.00	3.00	15.00	0.35	0.65	1.00
SPA-17	4.40	2.50	11.00	0.35	0.65	1.00
SPA-18	2.65	3.55	9.41	0.35	0.65	1.00
SPA-19	3.50	4.65	16.28	0.40	0.70	1.10
SPA-20	3.50	4.65	16.28	0.40	0.70	1.10
SPA-21	3.50	4.65	16.28	0.40	0.70	1.10
SPA-22	2.65	3.55	9.41	0.35	0.65	1.00

It can be observed in the tables presented that there was no change in the geometry of most of the footings, with only a change in the geometry of the SPA-15, which resulted in an increase of 10 cm in the dimensions “A” and “B”. In both cases, the total footing heights (Ht) remained the same, as well as H0 and H1. The redistribution of loads observed in the pillars P-01, P-10 and P-16 did not influence on footings geometry.

Figure 3 illustrates a comparison of the geometries when overlaying the projections of the footings dimensioned with SSI, in green dashed lines and without SSI, in solid blue lines, showing the only change in relation to the size change of the shoes, seen in SPA-15, where there was an increase of 10 cm for each direction (Lx and Ly) – A and B, after SSI effects.

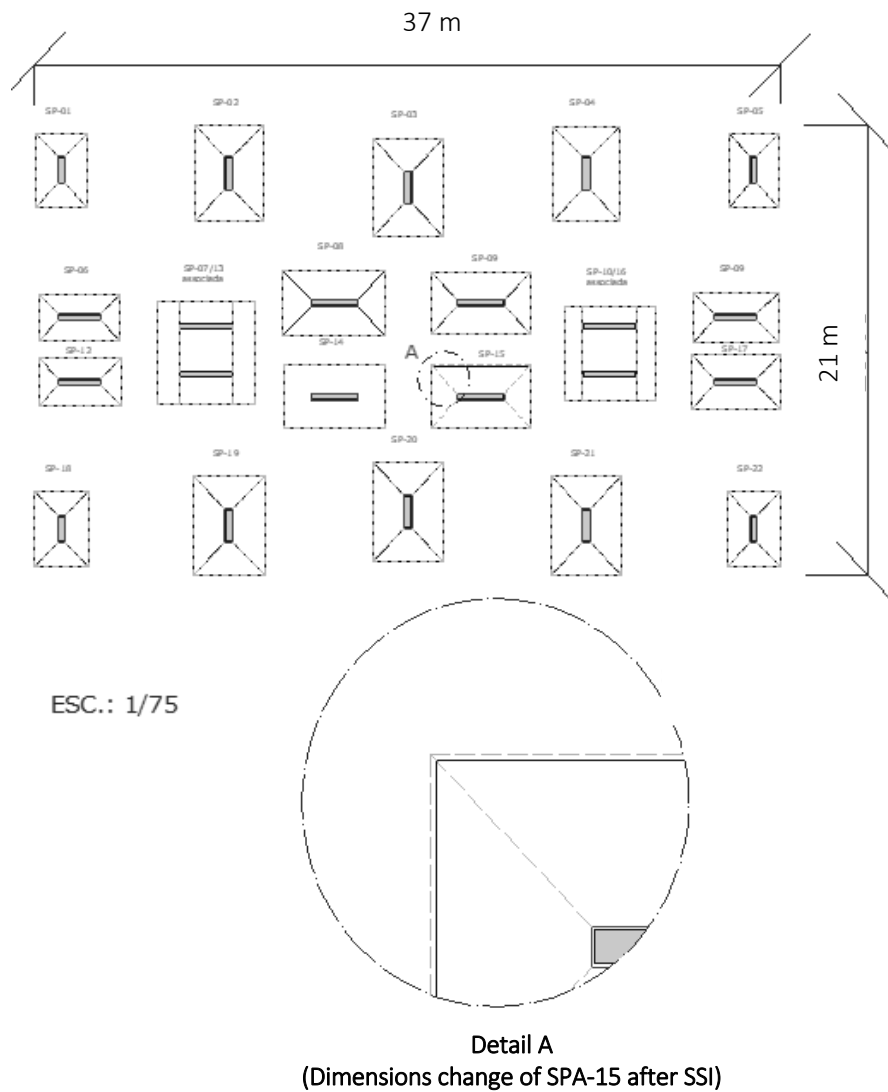


Figure 3. Overlaying the projections and detailing the change in the dimension of the SPA-15.

4.2 SSI influence of Concrete and steel consumption

4.2.1 Steel consumption

The calculation of the steel areas of the footings was based on the CEB-70 method and according to the results obtained in Table 5, which presents a comparison between the steel areas after the redesign. It can be seen from the values shown in Table 5 that some footings showed changes in the steel areas after SSI. In the SPA-01 and SPA-21, for example, there was a decrease in steel after the soil-structure interaction (350.13 cm² to 330.52 cm² for SPA-01 and

562.71 cm² to 532.30 cm² for SPA-21), because when considering the SSI, the pillars P-01 and P-21 obtained load relief, with this, there is a relief in the footing request, requiring less steel area to supply the bending forces acting on the elements.

Table 5. Resulting total steel areas in cm².

Footing	No SSI (cm ²)	With SSI (cm ²)
SPA-01	350.13	330.52
SPA-02	534.94	533.38
SPA-03	546.75	544.66
SPA-04	1026.35	1021.16
SPA-05	161.66	159.11
SPA-06	134.57	134.03
SPA-07/13	591.96	610.88
SPA-08	974.67	969.69
SPA-09	813.09	820.92
SPA-10/16	493.53	511.03
SPA-11	170.88	170.77
SPA-12	323.58	310.04
SPA-14	442.89	444.43
SPA-15	383.74	435.94
SPA-17	463.96	462.86
SPA-18	401.93	400.92
SPA-19	1153.02	1151.90
SPA-20	1149.64	1173.44
SPA-21	562.71	532.30
SPA-22	199.21	207.81

As for the SPA-15, S-20 and associated SPA-07/13 and SPA-10/16 shoes (the latter, from 493.53 cm² to 511.03 cm²), there was an increase in loads, resulting in an increase in steel areas, because, with the increase of the acting forces, a larger area of steel is necessary to support the bending forces acting on these elements. The SPA-01 was been detailed for two analyses, without SSI and with SSI, in order to illustrate the little change in steel consumption. The choice of the SPA-01 shoe was due to the fact that it had the greatest load reduction. The required anchorage length for the footings was calculated for concrete with a strength of 45 MPa (C-45). Gauges of 20 mm and 22 mm were considered for the dimensioning for the steel and hook in the reinforcements. Figure 4 represents SPA-01 without SSI and Figure 5 represents SPA-01 after SSI.

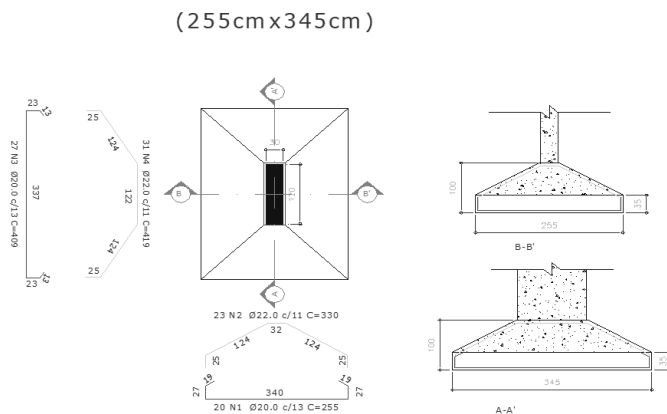


Figure 4. Steel details (cm) for SPA-01 without SSI.

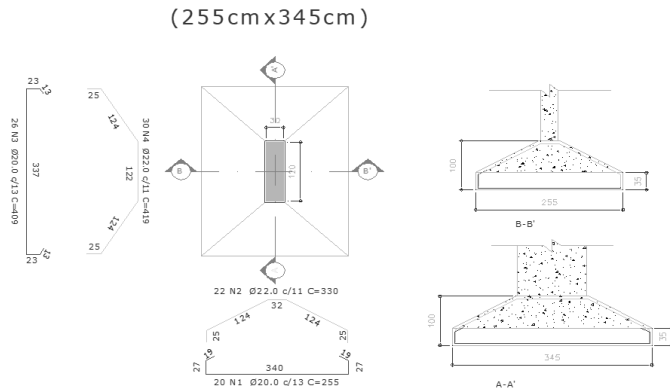


Figure 5. Steel details (cm) for SPA-01 with SSI.

4.2.2 Concrete consumption

To verify concrete consumption in each foundation elements, Table 8 shows the values obtained in m³ for a comparison of the volume of concrete of the footings for the two analyses, with and without SSI.

Table 6. Concrete volume in m³ of each footing Without and with SSI.

Footing	No SSI (cm ²)	With SSI (cm ²)
SPA-01	5.29	5.29
SPA-02	9.11	9.11
SPA-03	10.68	10.68
SPA-04	9.02	9.02
SPA-05	5.12	5.12
SPA-06	5.48	5.48
SPA-07/13	24.52	24.52
SPA-08	9.46	9.46
SPA-09	8.75	8.75
SPA-10/16	20.65	20.65
SPA-11	6.11	6.11
SPA-12	5.67	5.67
SPA-14	9.22	9.22
SPA-15	8.67	9.13
SPA-17	6.70	6.70
SPA-18	5.65	5.65
SPA-19	10.94	10.94
SPA-20	10.94	10.94
SPA-21	10.94	10.94
SPA-22	5.65	5.65

The results in Table 8 show that only the SPA-15 had an increase in material consumption (from 8.67 m³ to 9.13 m³) due to the increase in its geometry. For the other elements the consumption remained stable for the analysis without interaction and with the interaction. This continuity is justified for the two analyses, since the total heights (Ht) and also H0 and H1 of these footings did not change.

5 CONCLUSIONS

The redesign results showed that there was no significant change in the geometry of the footings, where only the SPA-15 footing showed an increase in its section (with an increase of 10

cm in the two dimensions “A” and “B”), as well as also in the consumption of concrete comparing the projects with and without considering the soil-structure interaction.

For steel consumption, the results showed that there was an increase in the steel area of the associated footings SPA-07/13 and SPA-10/16 and the isolated footings SPA-15 and SPA-20; however, SPA-01 and SPA-21 elements had a certain decrease in this material. It is concluded, for this project, that the soil-structure interaction had no significant influence on the observed points, due to the low change in the redistribution of loads acting on the analyzed pillars considering the interaction, which was been reflected in the maintenance of dimensions and volume of materials in almost all of the verified foundation elements. From the results presented, the analyzes for the building were satisfactory when considering the interaction, making it evident that the new loads do not harm the structural elements of the dimensioned project without considering the soil-structure interaction.

6 REFERENCES

- Brazilian Technical Standards Association. 2014. *NBR 6118: concrete structure design - procedure*. Rio de Janeiro, 238p.
- Brazilian Technical Standards Association. 2019. *NBR 6122: design and execution of foundations*. Rio de Janeiro, 108p.
- Brito, J. L. W. 1987. *Building Foundations*. University of São Paulo.
- Colares, G. M. 2006. *Program for analysis of soil-structure interaction in building design*. Master's dissertation. University of São Paulo.
- Gusmão, A. D. 1990. *Study of soil-structure interaction and its influence on building settlement*. Master's dissertation. Federal University of Rio de Janeiro.
- Lee, I.K., & Brown, P.T. 1972. Structure-foundation interaction analysis. *Journal of the Structural Division*, 98(11), 2413-2431.
- Meyerhof, G.G. 1953. Some recent foundation research and its application to design. *Structural Engineering*, 31, 151-167.
- Morris, D. 1966. Interaction of continuous frames and soil media. *Journal of the Structural Division*, 92(5), 13-44. <http://dx.doi.org/10.1061/JSDEAG.0001505>.
- Santos, M.J.A.P. 2016. *Soil x structure interaction: analysis of a work case with repression monitoring since the beginning of construction*. Master's dissertation. Rio de Janeiro State University (in Portuguese). Retrieved in April 20, 2021, from <http://www.bdt.uerj.br/handle/1/11641>
- Santos, Y.R.P., Bello, M.I.M.C.V., Gusmão, A.D. & Patricio, J.D. 2021. Soil-structure interaction analysis in reinforced concrete structures on footing foundation. *Soils and Rocks*, 44(2), e2021058020 (2021).
- Santos, Y. R. P. 2018. *Study of soil-structure interaction of a case of building work with foundation in rock mass*. Master's dissertation. Federal University of Pernambuco, 174p.
- Savaris, G., Hallak, P.H., & Maia, P.C.A. 2011. Understanding the mechanism of static soil-structure interaction: a case study. *Soils and Rocks*, 34(3), 195-206.
- Vesic, A. S. (ed) 1975. Bearing capacity of shallow foundations, cap.3 in: winterkorn, h. F e fang, h. Y. *Foundation engineering handbook*. New york: van nostrand reinhold.
- WINKLER, E. 1867. *Theory of elasticity and strength*. Dominicus Prague: Czechoslovakia.

Numerical analysis stability of a geothermal plateau in the field “Los Azufres” Mexico

U. Talonia-Vargas, V. Castellanos-Pedroza, G. Vargas-Benítez, J. E. Álvarez-Cornejo,
L. N. Equihua-Anguiano
GEIC-CFE, Augusto Rodin 265, 03720, Ciudad de México, Mexico

A. M. Garciadiego-Martínez
GPG-CFE, Campo Geotérmico los Azufres, Mexico

ABSTRACT:

This paper presents a study of a geothermal plateau that houses a well and a cooling stack, in which were identified slope stability problems. Zone was geologically characterized to describe lithology of the area besides, mechanical, physical and *in situ* tests were performed and from those, a geotechnical profile was proposed. Numerical analysis were carried out considering different conditions: static, pseudo-static, saturated material and degradation of the rock, for review and define the most unfavorable state. Software used in analysis was the Slide® from Rocscience in two dimensions (2D), considering the Hoek-Brown and Mohr-Coulomb failure criteria, to reproduce behavior of the materials according to its geotechnical characteristics. Results show that for current conditions and with the defined geotechnical parameters, the analyzed zone is stable for local and general failure mechanisms, being the safety factors (SF) greater than the admissible ones, according with the stability criteria taken in this study. However, for areas in which there is a mass degradation of the surface materials and, which are susceptible to the saturation, resulting safety depth is less than admissible and there is a risk of mass wasting encompassing since a few centimeters until meters of depth. Finally, some recommendations to stabilize the medium are proposed, according to the established analysis in this study.

1 INTRODUCTION

"Los Azufres" was the second geothermal field developed in Mexico, starting its exploitation activities for electrical generation in 1982 (CFE-GEIC, 2021a). Currently, due to the exploitation processes and for effects of hydrothermalism, the *in-situ* soil and rocks present a poor quality. Furthermore, deforestation and natural topography have propitiated the appearance of cracks and landslides in the surrounding zone, which constitutes a probable affectation on geothermal infrastructure.

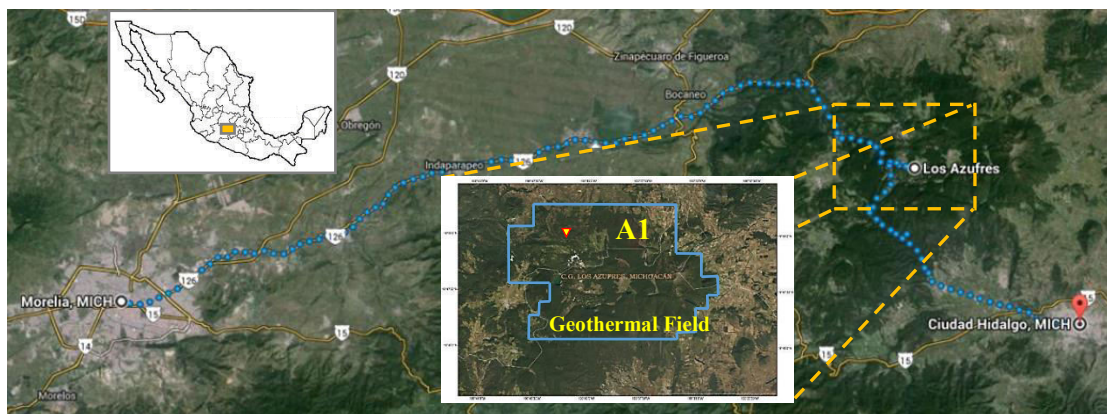


Figure 1. Location of the geothermal field “Los Azufres” Mexico. Coordinates of the plateau A1: X= 24,569,751, Y=2,193,617.937, Z = 2,758 masl.

Figures 1 and 2 shown location of the geothermal plateau, hereinafter referred as A1 and a top view of the plateau and of the geothermal cooling stack respectively.



Figure 2. Overview of the geothermal plateau A1 and of the geothermal cooling stack.

Figure 3 shows the locations of the identified profiles with greatest possibility to have instability problems around of the geothermal plateau, which are named LA-1, LA-2, LA-3 and LA-3'. In those zones the stronger movements observed are onward progressions of rock and soil as well as, discontinuities with intersections among them. These characteristics can generate local or rotational failure mechanisms of materials, since the cohesive material formed by the rock degradation is deposited in the terrain surface. This paper summarizes results corresponding to the LA-3' profile due to the unfavorable topographic conditions observed and because traverses the geothermal cooling stack, which has presented surface landslides in recent years.

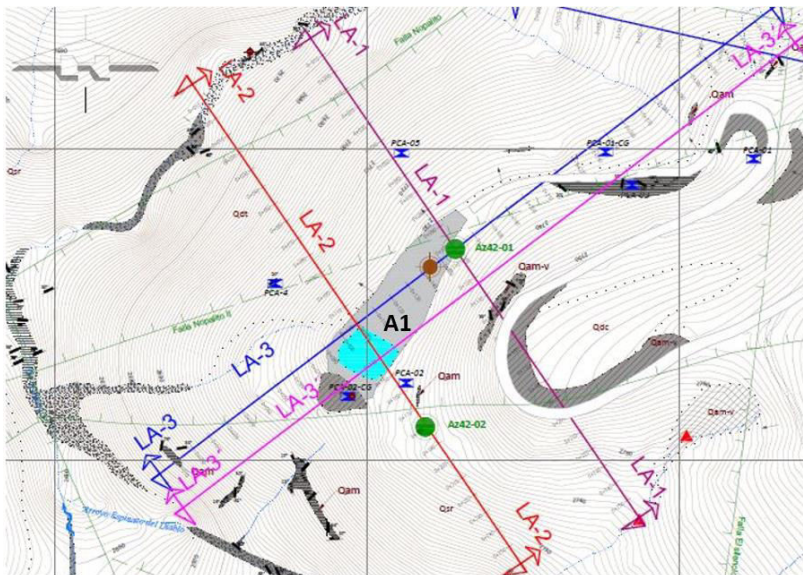


Figure 3. Location of profiles identified with greatest georisks in the zone around of the plateau A1: LA-1, LA-2, LA-3 and LA-3'.

2 GEOTECHNICAL STUDIES FOR CHARACTERIZATION

Geothermal plateau A1 is formed by series of spills of microlithic (Q_{am}) and vesicular andesites (Q_{am-v}) (CFE-GEIC, 2017b). Those materials have been affected in different degrees by hydrothermal actions, generating argilization and chloritization on the rocks. From this effect, a sub-horizontal layer was constituted throughout the zone, parallel to the ground surface with thickness that reach up to 30.0m. Geomechanical characterization of the LA-3' profile was carried out performing open pits (PCA's), boreholes (Bno's) and laboratory tests (see Figure 4). Figure 5 shown the Geological-Geophysical profile characterized from the field works and laboratory tests.



Figure 4. *In situ* boreholes (Bno's), open pits (PCA's) and laboratory tests.

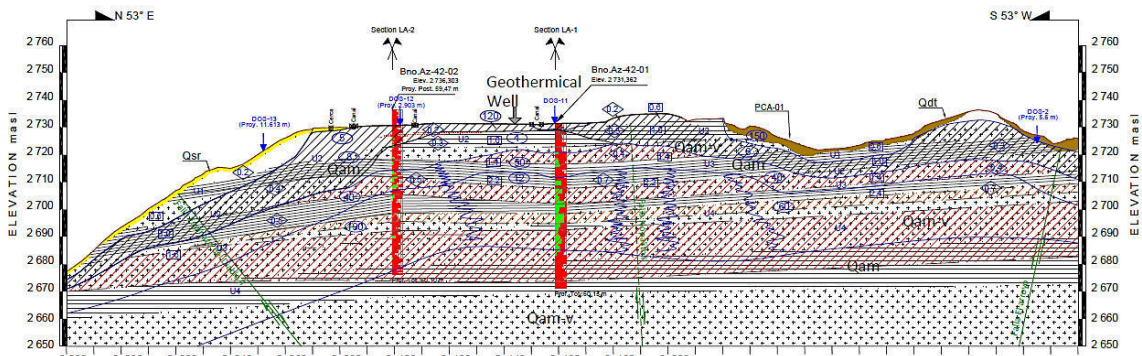


Figure 5. Geological-Geophysical profile of the LA-3' section that houses a well, the geothermal cooling stack and location of the open pits (PCA's) and boreholes (Bno's).

Lithological mass was discretized into four "Geotechnical Units - UG" as shown Figure 6. Rock mass was characterized according to the GSI criteria (Hoek et al., 2013). Descriptions of the geotechnical materials are displayed in Table 1 and Table 2 shows the summarized conditions to define the most unfavorable condition on the slope stability: static, pseudo-static, saturated material and degradation of the rocks.

Mechanical properties for each characterized unit (UG) that were used in the static, pseudo-static and saturated numerical analysis are presented in Table 3 and in Table 4 are shown the modifications to the

Regarding to the admissible SF, these were taken from Read and Stacey (2009). This criterion considers the reliability of the parameters used for the models, as well as the consequences of a possible failure of the slope based on the average annual rainfall in the area (Table 5).

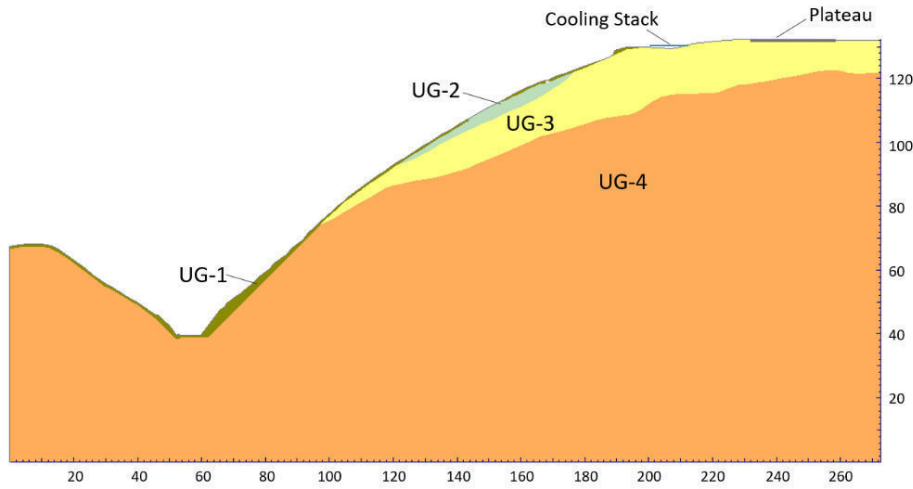


Figure 6. Geotechnical characterized geotechnical units - UG's on the LA-3' profile.

Table 1. Descriptions of materials for Geotechnical Units - UG.

Unit	Description
UG-1	Surface material by slope deposits and residual soil formed from hydrothermal action.
UG-2	Rock mass with high hydrothermal alterations, formed by intercalations of microlithic (Q_{am}) and vesicular microlithic (Q_{am-v}) andesites.
UG-3	Rock mass with low hydrothermal alterations, formed by intercalations of microlithic (Q_{am}) and vesicular microlithic (Q_{am-v}) andesites.
UG-4	Rock mass formed by intercalations of microlithic (Q_{am}) and vesicular microlithic (Q_{am-v}) andesites.

Table 2. Conditions of slope stability analyzed for the LA-3' profile.

Slope conditions	Numerical Analysis
Actual	Static condition Pseudo-static (effects of earthquake acceleration)
Another	Saturated material Degradation material (hydrothermal effects)

Table 3. Material properties used on the static, pseudo-static and saturated - numerical analyses.

Unit	Volumetric weight γ kN/m ³	Saturated vol. weight γ_{sat} kN/m ³	Hoek & Brown			Mohr-Coulomb	
			GSI	σ_{ci} Mpa	m_i	c' kPa	ϕ' °
UG-1	10.0	12.0	n/a	n/a	n/a	15	22
UG-2	13.0	18.0	39	10.0	8.0	n/a	n/a
UG-3	20.0	21.0	43	15.0	9.0	n/a	n/a
UG-4	19.0	22.0	42	33.0	15.0	n/a	n/a

n/a = not apply for the constitutive model.

Table 4. Material properties used on the degradation material - numerical analyses.

Unit	Volumetric weight γ kN/m ³	Saturated vol. weight γ_{sat} kN/m ³	Hoek & Brown			Mohr-Coulomb	
			GSI	σ_{ci} Mpa	m_i	c' kPa	ϕ' °
UG-1	10.0	12.0	n/a	n/a	n/a	4.0	25
UG-2	13.0	18.0	31	4.0	0.34	n/a	n/a

n/a = not apply for the constitutive model.

Table 5. Safety Factors, SF (Read and Stacey, 2009).

Failure Consequences	SF Static and Static with hydraulic load			SF Pseudo-static		
	Reliability					
	Low	Medium	High	Low	Medium	High
Low	1.3	1.2	1.1	1.05	1.0	1.0
Medium	1.4	1.3	1.2	1.1	1.05	1.0
High	1.5	1.4	1.3	1.15	1.1	1.05

3 NUMERICAL SIMULATIONS

Numerical simulations were carried out using Slide® software, applying the Bishop's method. Constitutive models taken correspond to the Hoek & Brown for areas characterized with rock and the Mohr-Coulomb for residual material, considering an elastoplastic perfect behavior. Criteria are shown in Figures 7a and 7b. Different conditions were revised to define the most unfavorable slope condition: static, pseudo-static, saturated and effect of the rock degradation (see Table 2).

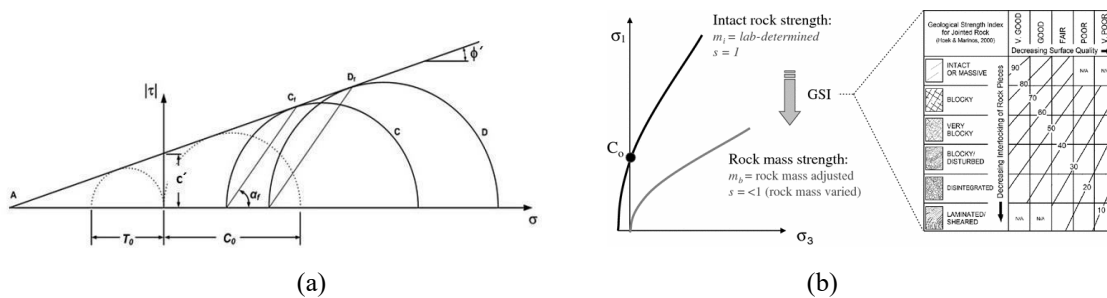


Figure 7. Criteria (a) Mohr-Coulomb (Labuz & Zang, 2012) and (b) Hoek & Brown (Hoek & Brown, 1997).

Hoek & Brown criterion determines the stress according with expressions (1), (1a), (1b) and (1c). Factor D in expressions, depends on the degree of rock disturbance due to blast damage or stress relaxation, it takes values from 0 for undisturbed to 1 for highly disturbed rock masses and GSI is the Geological Strength Index (Marinos et. al., 2007).

$$\sigma'_1 = \sigma'_3 + \sigma_{ci} \left(m_b \frac{\sigma'_3}{\sigma_{ci}} + s \right)^a \quad (1)$$

where m_b is a reduced value and is given by (1a), σ_{ci} is the uniaxial compressive strength and s and a are calculated with (1b) and (1c) respectively:

$$m_b = m_i \exp\left(\frac{GSI-100}{28-14D}\right) \quad (1a)$$

$$s = \exp\left(\frac{GSI - 100}{9 - 3D}\right) \quad (1b)$$

$$a = \frac{1}{2} + \frac{1}{6} (e^{GSI/15} - e^{-20/3}) \quad (1c)$$

Safety factor FS is obtained with expression (2) as:

$$FS = \frac{\tau_f}{\tau_d} \quad (2)$$

where τ_f represents the shear strength of material and τ_b represents the shear stress acting on failure surface.

Effects produced by earthquakes on the geothermal plateau were revised, considering a Pseudo-static analysis, using a horizontal coefficient $k_h=0.212$ that was obtained according to expression (3) (CFE, 2015).

$$k_h = \frac{a_0}{1 + 2a_0} \quad (3)$$

where a_0 is the ground acceleration coefficient, depending on the dominant period on the site.

4 NUMERICAL RESULTS

Results for the SF factors obtained from the numerical analysis are summarized in Table 6. In the same way, each one of these are described in the next incises.

Table 6. Numerical Safety Factors (SF) for the LA-3' profile.

Slope conditions		SF
Actual	Static condition	3.55
	Pseudo-static	1.06
Another	Saturated material	0.99
	Degradation material	0.75

4.1 Static Conditions

Figure 8 shows the position of the critical failure surface obtained from the numerical analysis, which occurs through the UG-3 and UG-4 geotechnical units and the possibility of the other circular failures with a minor risk are also observed in Figure. The circular failure affects the adjacent area where the geothermal cooling stack is placed. Nevertheless, a safety factor for the actual conditions of the platform under static conditions of SF=3.55 was obtained, which complies with the minimum FS of 1.3 established in Table 5, taking a high failure consequence and a high reliability. The slope complies with safety hence at this point, it is important to stabilize the zones that already show superficial movement.

4.2 Pseudo-Static Conditions

Figure 9 shows the pseudo-static analysis of the LA-3' section. The most unfavorable rotational failure occurs through geotechnical units UG-1. As a result of these analyses, a safety factor SF=1.06 was obtained, which is higher than SF=1.05, established for the pseudo-static conditions in Table 5, considering a medium failure consequences and reliability. In this case the circular failure reaches the foot of the slope, but from the numerical results and for the ground acceleration considered, possibility of occurrence is lower.

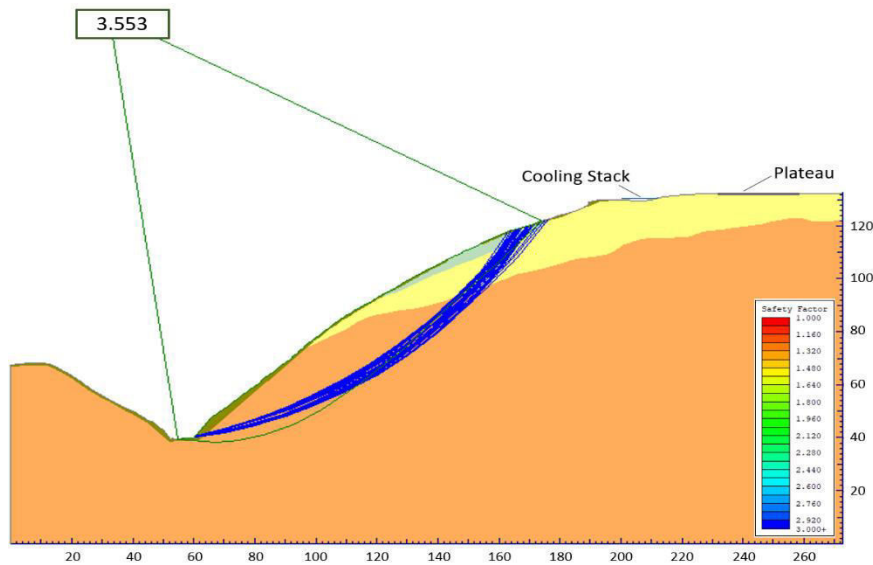


Figure 8. Critical rotational failure surface for the static conditions - profile LA-3'.

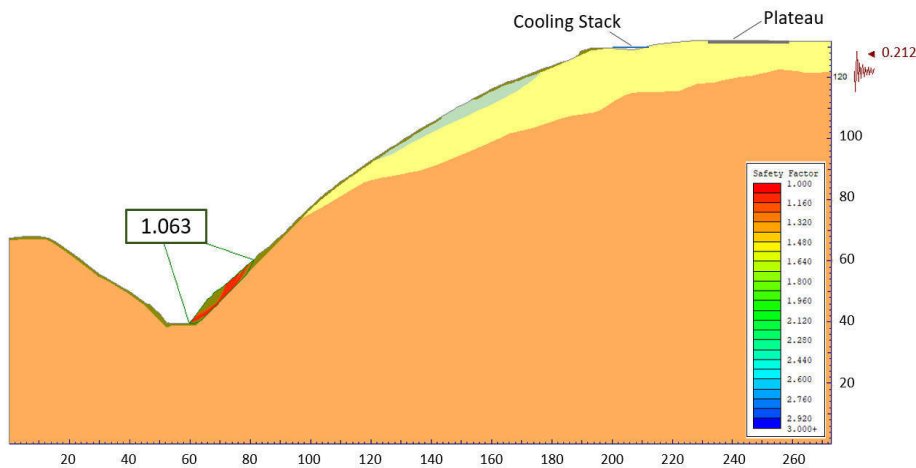


Figure 9. Critical rotational failure surface for pseudo-static conditions – $k_h=0.212$ – profile LA-3'.

4.3 Saturated Conditions

In order to consider the most unfavorable conditions on the slope, an analysis taking in account the material completely saturated was carried out. For this, the water level (NAF) was placed on the surface of the model as is showed in Figure 10. In this case the obtained SF=0.99 diminished respect to the static and pseudo-static conditions.

To this point, saturated material is the most unfavorable condition. Nevertheless, in Figure 10 a local failure is observed, hence a minor risk for the geothermal plateau respect to the previous cases analyzed is developed from the numerical analysis. Comparative SF=1.3 was considered from the Table 5 and was the same that it taken for the static conditions, so the SF=0.99 resultant is considered unstable under this condition. In this case, it is enough to improve the stability conditions of the foot of the slope as a preventive measure to avoid future stability problems, although these do not affect the infrastructure of the well.

4.4 Degradation Material

In order to simulate the effect on the safety factor of the slope, the degradation of the properties of resistance to shear stress of the geotechnical unit 2 was evaluated, since it is the one that has the greatest influence on the stability of the platform. The following figure shows this condition.

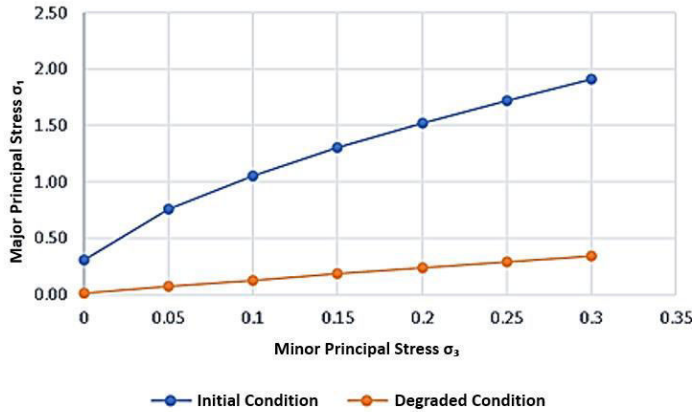


Figure 10. Comparison of resistance to shear stress in geotechnical unit 2 between initial and degraded conditions.

Numerical analysis considering degradation on properties of the surface materials were carried out to simulate the long-term conditions due to the geothermal effects. A circular failure is developed as is shown in Figure 11, but comprises a minor active zone that those generated for the static and pseudo-static conditions. It is important to mention that the failure occurs near to the plateau and can start the infrastructure failure.

Obtained numerical safety factor was $SF=0.75$ and for the cases analyzed in this paper, this condition is the most unfavorable, representing the critical condition that need to be considered in the util life of the geothermal plateau. Comparative SF value taken was $SF=1.3$ then, geothermal rock degradation is the most critical condition that need be considered a long-term. As resulting SF is less than admissible and there is a risk of mass wasting encompassing since a few centimeters until meters of depth. Furthermore, degradation in this study is considered in the surface, due to the depth of exploratory tests and the scope of this study.

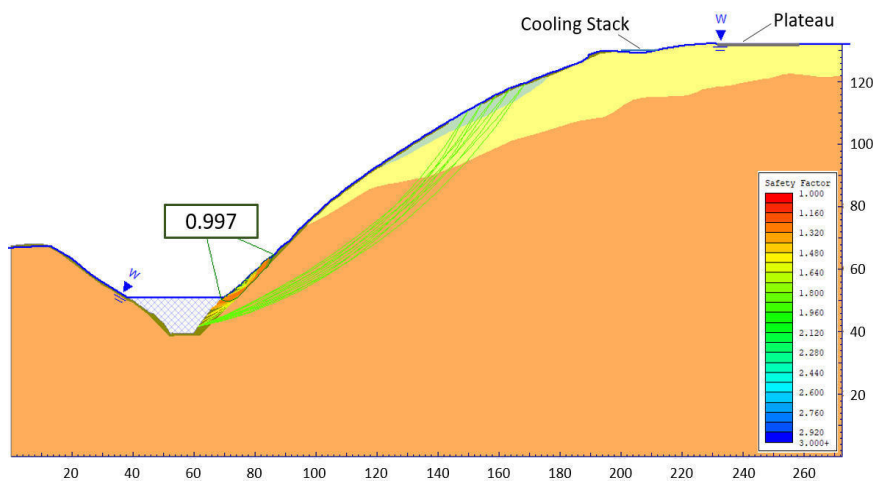


Figure 10. Critical local failure for saturated material conditions –profile LA-3’.

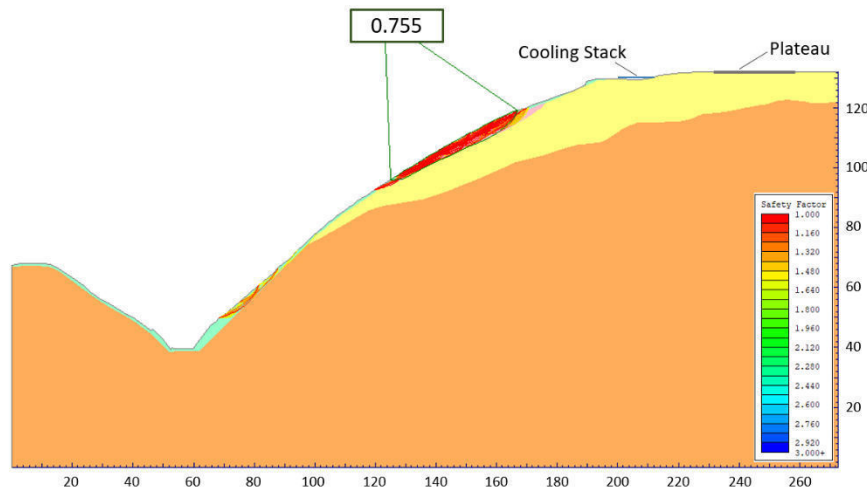


Figure 11. Critical local failure for material with degradation on properties UG-1 and UG2 and – profile LA-3’.

5 CONCLUSIONS

Geotechnical conditions of the study were defined from results of the *in situ* and from the laboratory tests. Four Geotechnical Units (UG) were defined to characterize the LA-3 profile where the A1 well and the hydrothermal cooling stack are located.

For the parameters of the materials determined for this study, under current conditions: static and the earthquake occurrence, slope LA-3’ where the platform and well are located are stable for local failure surfaces and general failure, with the safety factors being greater than those admissible.

Hydrothermal effects are a problem that need be considered a long term in geothermal fields because represent a georisk identified in the slope stability, in the other hand it is necessary to consider in a future to study the subsidence (compaction) of the geothermal field, due that this effect can be responsible for the surface movements.

From this study, the actual solutions correspond to stabilize de surface slope and avoid the deforestation process, actions that can stopped the movements observed in the geothermal plateau.

Among the principal recommendations, there are filtration control around of the plateau, as well as the reinforcement of the geothermal cooling stack or its relocation. In the same way, the reinforcement of the local zones detected with the appearance of cracks and landslides in the surrounding zone is suggested, using retaining walls or high resistance mesh systems.

In addition, it is recommended monitor using specialized instrumentation, to detect movements that can occur in the future and establish if it is an internal process due to the exploitation of the field or if it is a surface problematic.

The degradation effects of materials is a function of time, so it is necessary to implement additional studies to verify these processes and their effect on the hillside.

6 REFERENCES

- Barton, N. 2002. Some new Q-value correlations to assist in site characterisation and tunnel design. *International journal of rock mechanics and mining sciences*, 39(2), 185-216.
- Bieniawski, Z. T. 1989. Engineering rock mass classifications: a complete manual for engineers and geologists in mining, civil, and petroleum engineering. *John Wiley & Sons*.
- CFE-GEIC. 2021a. Informe del estudio geotécnico para la estabilización de zonas expuestas a riesgo geológico de deslizamiento en el sector el nopalito y espinazo del diablo (plataforma az-68d). Informe SGM-DMR-K1326-I-011/2021.
- CFE-GEIC. 2017b. Informe de peligro geológico por procesos de remoción en masa en el Campo Geotér-

- mico, los Azufres, Comisión Federal De Electricidad, Subgerencia de Estudios Geológicos. Departamento de Geología enero de 2017. I-KG3LT-GEOL-16-0816.
- CFE. 2015. Manual de Diseño de Obras Civiles, capítulo C.1.3 Diseño por Sismo, *INEEL*, Mexico 2015.
- Hoek, E. & Brown, E. T. 1997. Practical estimates of rock mass strength, *Int. J. Rock Mech. Min.*, 34, 1165–1186, [https://doi.org/10.1016/S1365-1609\(97\)80069-X](https://doi.org/10.1016/S1365-1609(97)80069-X), 1997
- Hoek, E., Carter, T. & Diederich, M. 2013. Quantification of the Geological Strength Index Chart. *Geomechanics Symposium held in San Francisco, CA, USA*.
- Labuz, J. F. & Zang, A. 2012. Mohr–Coulomb Failure Criterion. *Rock Mech Rock Eng* 45, 975–979. <https://doi.org/10.1007/s00603-012-0281-7>.
- Marinos, P. G., Marinos, V., & Hoek, E. 2007. THE GEOLOGICAL STRENGTH INDEX (GSI): A CHARACTERIZATION TOOL. In *Proceedings of the international workshop on rock mass classification in underground mining* (No. 9498, p. 87). Department of Health and Human Services, Centers for Disease Control and Prevention, National Institute for Occupational Safety and Health, Pittsburgh Research Laboratory.
- Palmström, A. 1995. RMi – a rock mass characterization system for rock engineering purposes. Ph.D. thesis, *Oslo University*, Norway, 400 p. http://www.rockmass.net/phd/contents_all_text.pdf.
- Read, J. & Stacey, P. 2009. Guidelines for open pit slope design. *Csiro Publishing*. Published in 2009 DOI: 10.1071/9780643101104.
- Slide Versión 6.020 Copyright 1998-2012 Rocscience Inc. [2D and 3D Geotechnical Software | Rocscience Inc.](#)

Slope stability studies of dumps & stacks at Noamundi-Katamati iron ore mines, India – a case study

M. Tiwari, S. Sarkar, I. Saha, P. Srivastava, A. Bhatnagar
Tata Steel Limited, Jamshedpur, Jharkhand, India

ABSTRACT:

Dump slope stability is an important aspect of open cast mining. It has a direct impact on the safety of man and machinery as well as the mine economics. Noamundi and Katamati captive iron ore mines of Tata Steel Limited, India have been supplying iron ores to its own steel works since decades. The waste and reject material generated during excavation are placed in dumps and stacks respectively at designated places within the leasehold. In this paper, the factor of safety (FoS) for all the waste dumps and reject stacks have been calculated using FLAC 3D software. The waste dump material properties like density, cohesion, internal angle of friction, optimum moisture content, natural angle of repose have been determined in the geotechnical laboratories. Empirical equations are used to calibrate the values of cohesion and angle of internal friction to represent the original dump mix responsible for stability. 3D numerical modelling was carried out by averaging the results of the samples of each dump and reject stacks. Further, a few more analyses were also carried out along selected sections with low FoS values using parameters sampled from the vicinity of those corresponding lines. Finally, a risk matrix was prepared based on the FoS values obtained through this study & monitoring strategy framework was proposed accordingly to monitor dumps and stacks in an effective and sustainable manner.

Keywords: Slope stability, cohesion, internal angle of friction, Factor of Safety.

1. INTRODUCTION

In opencast mining operation, the stability of waste dumps and reject stacks stands at high priority from the safety perspective. Poor management of dump results in the instability of slopes which may pose a risk for the mining activity. Stability of waste dump is mainly related to the design of slopes and the waste dump material properties. The factor of safety as per Verma et. al. (2017) is thus dependent on the type and nature of the waste dump material. In this paper slope stability of dumps have been carried out for Katamati iron ore deposits of Orissa, India and Noamundi iron ore deposits of Jharkhand, India. Representative loose dump material samples were collected from the site and tested to determine the physico-mechanical properties of dump material. Numerical investigations have been carried out to determine the factor of safety of Noamundi & Katamati waste dumps & reject stacks by using FLAC 3D software. Finally, for effective monitoring, a monitoring strategy framework has been proposed through this study.

2. LOCATION AND GEOLOGY

Katamati iron ore deposits lie in Champua sub-division of Keonjhar district, Odisha India bounded by latitudes $22^{\circ}06'40''$ and $22^{\circ}08'00''$ & longitudes $85^{\circ}28'14''$ and $85^{\circ}30'00''$ in Survey of India toposheet 73F/8. Similarly, Noamundi iron ore deposits lie in Chaibasa sub-division of West Singhbhum district, Jharkhand bounded by latitudes $22^{\circ}07'10''$ N & $22^{\circ}09'55''$ N and longitudes $85^{\circ}28'33''$ E & $85^{\circ}30'52''$ E in Survey of India toposheet 73F/8 & 73F/12. Noamundi and Katamati iron ore deposit belongs to Pre-Cambrian era of Dharwarian age of slightly metamorphosed sedimentary formations. The rocktypes found here are iron ores, laterites, Banded Hematite Jasper (BHJ), shales and chert. Iron ore bodies are sometimes found on the ridge and

sometimes on the hill slopes. Iron ores are generally overlain by laterites and/or soil/floats and underlain by BHI or shale. The ore body has a strike of NNE – SSW and dip varying between 20° - 40° due west.

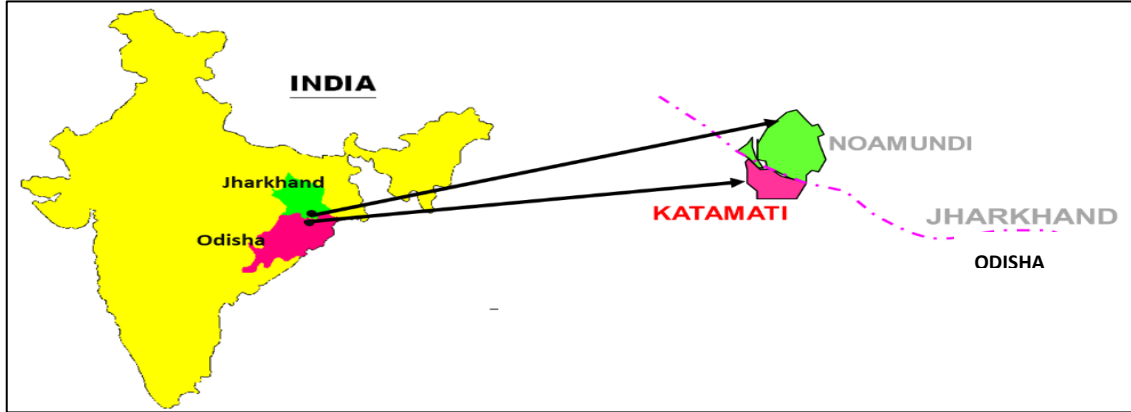


Figure 1: Location plan of mining leaseholds

3. CHARACTERISTICS OF THE DUMPS AND STACKS

The Noamundi sub grade stack is located on the eastern fringes of the leasehold area. It is partly dumped in pit on the eastern edge of the quarry and is partly dumped on the original topography of the area. Similarly, the waste dump in the central portion of the leasehold area is completely placed on the original topography. Both the waste dump and sub grade stack of Katamati area are completely stacked on the original topography of the area.

Sub-grade stack at Noamundi reaches a height of 41 m from the ground and is distributed in three to four benches with an average bench height of 8 to 15 m. The individual face angle varies from 25 - 36°. The waste dump at Noamundi reaches a height of 36 m from the ground and distributed in two to three benches with an average bench height of 10 to 12 m. The individual face angle varies from 25 - 33°. Similarly, the reject stack at Katamati is just 22 m from the ground and is distributed in two to three benches with an average bench height of 12 to 18 m. The individual face angle varies from 28 - 30°. The waste dump at Katamati is 31 m high and the entire material is distributed in two to three benches with an average height of 10 to 14m. The individual face angle varies between 23 - 33°. The layout of dumps is shown in the Figure 2 below.

Table 1: Geometry of dumps & stacks at Noamundi and Katamati

Dump/Stack	Base of the dump/stack	Elevation of the dump/stack (in m)	No of Benches	Bench Height (in m)	Bench Angle (in °)
Noamundi Reject stack	Topography + In-Pit	41	3-4	8-15	25-36
Noamundi Waste	Topography	36	2-3	10-12	25-33
Katamati Reject	Topography	22	2-3	12-18	28-30
Katamati Waste	Topography	31	2-3	10-14	23-33

The slope geometry of the dump/stack is one of the most important characteristics that control its stability. These are of moderate height and the bench angle slopes are within the stipulated guidelines of 37.5°.

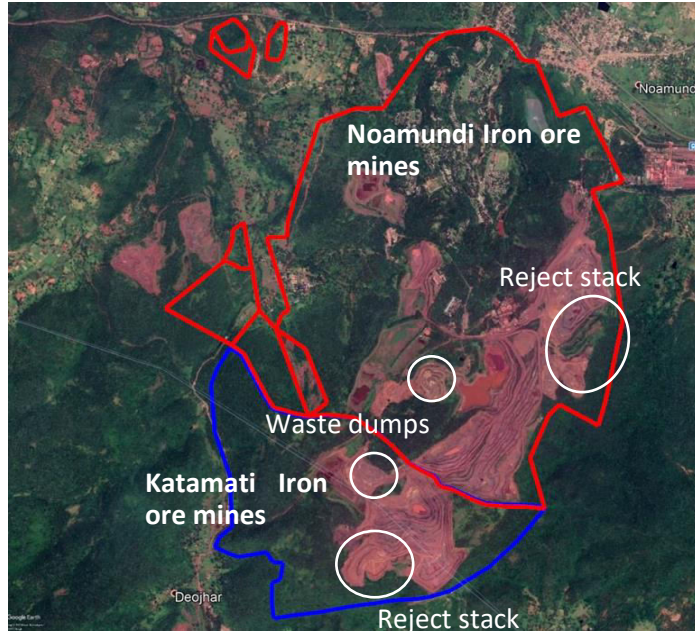


Figure 2: Location of dumps and stacks in the mining leasehold

Low grade iron ores and lateritic ores constitutes major material types which are taken to the sub grade stack. Generally, pebble sized clasts floating with finer matrix varying from sand to silt size are a common occurrence in the sub grade stacks. Fine grained ochres are also found at places with sticky limonitic material. At some places, white coloured fine-grained kaolinite is also observed. Mainly Fe shale, shale, kaolinite, weathered BHJ are transported into waste dumps. Occasionally, laterite and murrum are also dumped at places.

4. ANALYTICAL RESULTS AND DISCUSSIONS

Total of 31 samples of varied lithologies were collected across dumps/stacks for laboratory testing of important parameters. Based on the shear test results, the internal friction angle and cohesion of waste rocks in different parts of the dump/stacks were obtained. The composite results of the four different dumps/stacks are listed below in table 2.

Table 2: Shear strength of different dump samples for a size mix < 4.75 mm as obtained from laboratory

Sample rocks from	Cohesion in Kpa	Internal Angle of friction in °	Optimum Water Content (%)
Noamundi Sub Grade	11.65	32.75	16.41
Noamundi Waste	4.67	31.83	18.97
Katamati Sub grade	28.20	32.80	10.52
Katamati Waste	21.40	33.40	12.64

The shear test results of fine particles (c and ϕ) and the distribution of the particles of different areas have been obtained through laboratory tests. Through the size analysis of the samples, the proportion of fine particle and large particle waste rock can be calculated. The formula for calculating the cohesion and internal friction angle of waste rocks in the entire dump/stack as determined by Zou et. al. (2018) is shown in equations (1) and (2) and the calculation results are shown in Table 3.

$$C_{hi} = C_{Mhi} \times A_{Mhi} \quad (1)$$

$$\tan \Phi_{hi} = \tan \Phi_k - (\tan \Phi_k - \tan \Phi_{Mhi}) A_{Mhi} \quad (2)$$

where C_{Mhi} = measured cohesion; A_{Mhi} = % of fine waste rock for which “c” & “ ϕ ” was measured at lab; Φ_k = angle of repose, Φ_{Mhi} = measured angle of friction

Table 3: Calculated shear strength to represent the dump mix.

Sample rocks from	Cohesion in Kpa	Internal Angle of friction in °	% of rock < 4.75 mm in the dump	Natural Angle of Repose (°)	Cohesion in Kpa	Internal Angle of friction in °	Density in gm/cc	Optimum Water Content (%)
	Lab result of shear strength for size < 4.75mm				Derived Shear strength of the dump mix used in the model			
Noamundi Reject	11.65	32.75	84.6	28.71	9.83	32.05	2.209	16.41
Noamundi Waste	4.67	31.83	81	28.1	3.83	31.14	2.265	18.97
Katamati Reject	28.20	32.80	76.4	26.94	21.80	31.39	2.646	10.52
Katamati Waste	21.40	33.40	88.4	29.82	19.77	33.04	2.560	12.64

It is evident from the table above, that the percentage of rock which is less than 4.75 mm has a direct relation with cohesion and angle of friction values of the representative dump/stack mix. More the percentage of fines, lesser would be the variation in the shear strength of the material between the lab tested value and the calculated value. Thus, it is to be noted that the samples collection from any spot should be representative of the material mix present at that location.

5. NUMERICAL MODEL

Numerical modelling was done using software FLAC 3D. FLAC 3D software of ITASCA consulting ltd. uses continuum approach to solve the slope stability issues, Wyllie and Mah (2007). Modelling idealises or simplifies the real problem to fit the constraints imposed by factors such as available material models and computer capacity. Analyses of rock mass response involve different scales. It is impossible and undesirable to include all features, and details of rock mass response mechanisms, into one model. In addition, many of the details of rock mass behaviour are unknown and unknowable; therefore, the approach to modelling is not as straightforward. In the context of this report the vegetation cover of the Noamundi sub-grade stack in the northern fringes has not been considered in the model. However, the factor of safety increases by 17% in case the slope is covered by a young forest, Kokutse et. al. (2016). In this model simulations have been carried out at maximum dry density and optimum moisture content. A factor of safety of 1.3 & above in a dump slope indicates stability.

The typical slope stability issues in this paper are approached in a two-pronged manner. The whole of the dump or stack surface is solved for FoS at one go using the average cohesion and internal angle values of all the samples of the dump/stack. The whole dump profile is imported as an input to the software. Alternatively, in the second approach, the dump is distributed in a representative number of sections (x-z plane) and extruded in the y-axis to collectively represent the whole of the dump/stack. The samples close to the section lines are averaged out to solve the extrusion model. This method requires to import a cross-sectional plane/drawing into the software.

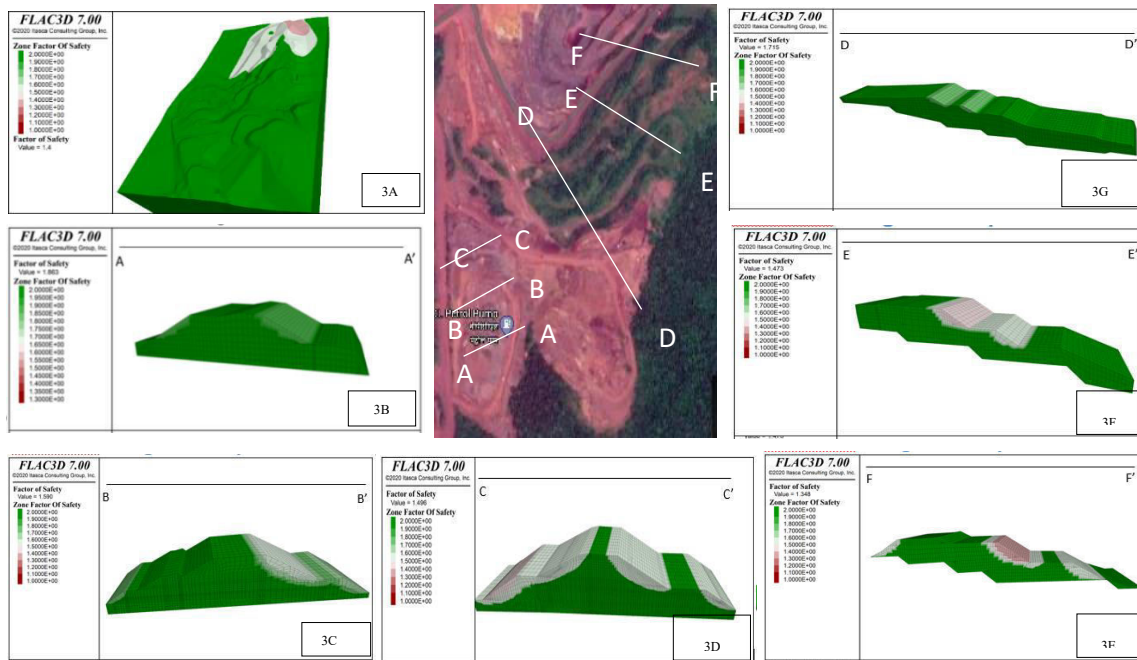


Figure 3A: 3D model of Noamundi sub-grade dump-
 Figure 3B-3G: Sectional models (Extrusions) of Noamundi sub-grade dump

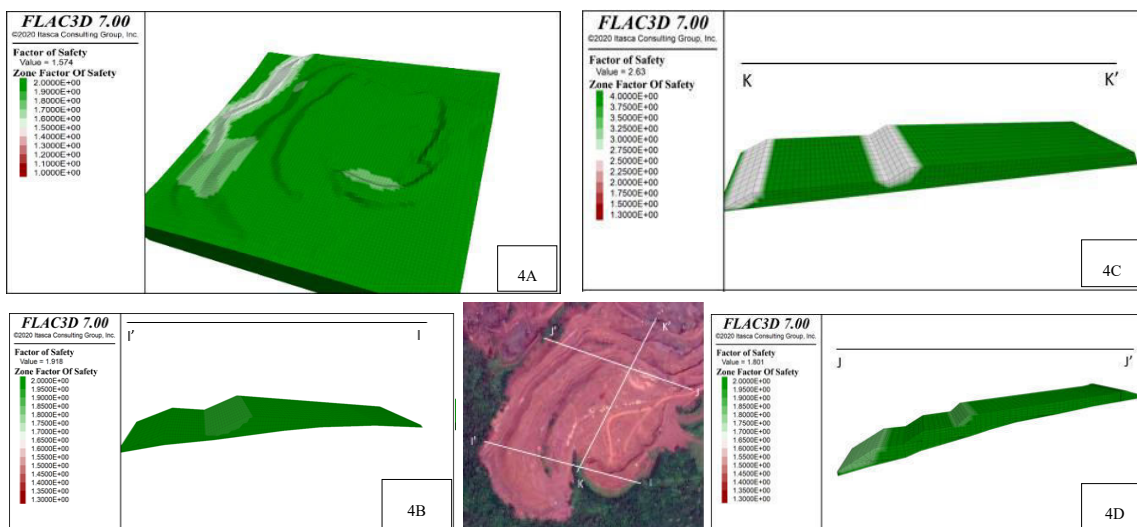


Figure 4A: 3D model of Katamati sub-grade dump
 Figure 4B-4D: Sectional models (Extrusions) of Katamati sub-grade dump

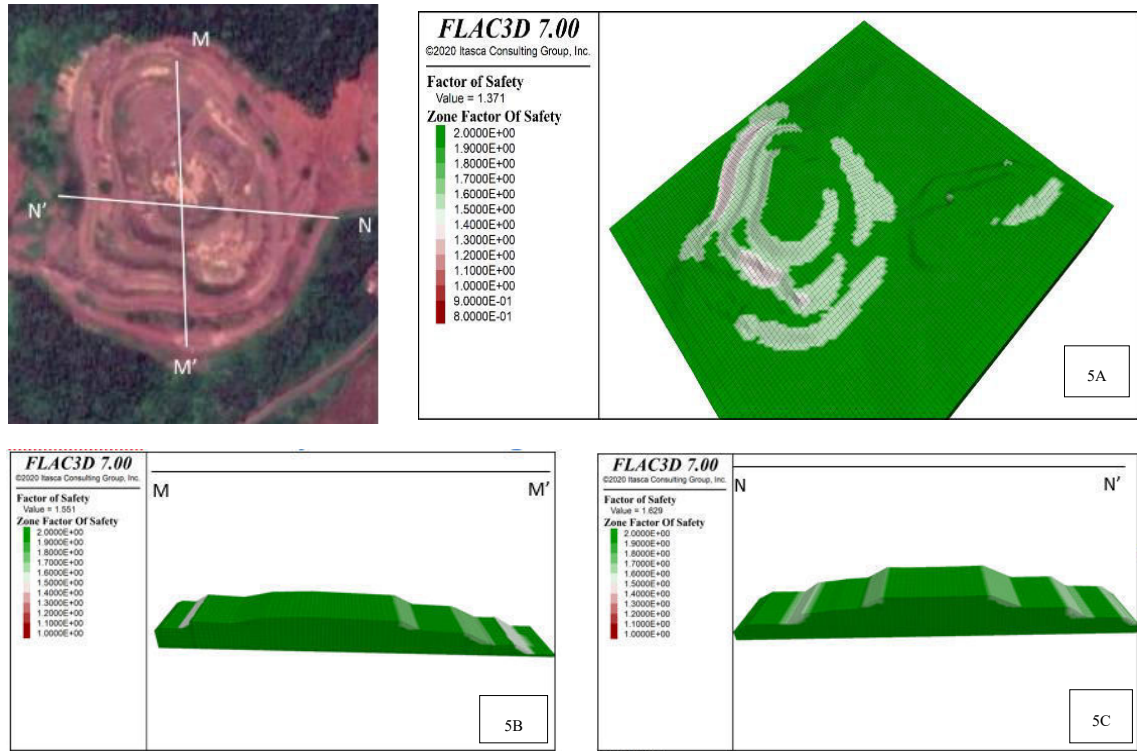


Figure 5A: 3D model of Noamundi Waste dump
 Figure 5B-5C: Sectional models (Extrusions) of Noamundi Waste dump

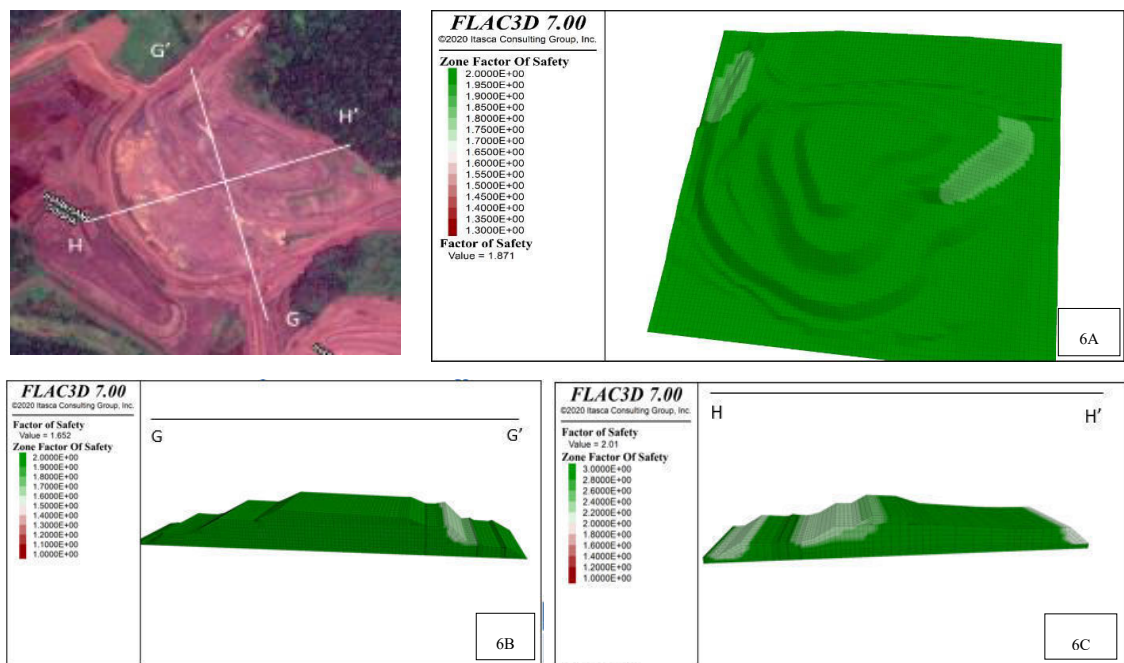


Figure 6A: 3D model of Katamati Waste dump
 Figure 6B-6C: Sectional models (Extrusions) of Katamati Waste

6. DISCUSSIONS

All the waste dumps & reject stacks of Noamundi & Katamati are mostly stable and shows higher order of FoS. Noamundi waste Dump FoS is in order of 1.4 -1.6 & reject Stack FoS is in order of 1.3 - 1.9 which indicates that these are relatively stable dumps. In section F-F' bench scale FoS is found to be 1.3 with lift face angle in the order of 36 degree. Such signatures of instability may be local & may cause shallow failures at bench scale. This type of local instability conditions may be improved by reducing the face angle. (Bench scale FoS increases to 1.5 with a reduction in lift face angle to 30 degree). The area in F-F' section has vegetation which may lead to higher FoS than the estimated value of 1.3 [Generally young forest cover increases the FoS by 17%, Kokutse et. al. (2016)]. Katamati waste dump FoS is in order of 1.7 - 2.0 & reject Stack FoS is 1.6 - 1.9 which indicates that these are stable dumps.

Table 4: The factor of safety for all the dumps/stacks of Noamundi and Katamati

Dump	Method	Section Line	FoS
Noamundi Sub-grade stack	Extrusion	A-A'	1.9
		B-B'	1.6
		C-C'	1.5
		D-D'	1.7
		E-E'	1.5
		F-F'	1.3
		Building Block	1.4
Noamundi Waste dump	Extrusion	M-M'	1.5
		N-N'	1.6
	Building Block	1.4	
Katamati Sub-grade stack	Extrusion	I-I'	1.9
		J-J'	1.8
		K-K'	2.6
	Building block	1.6	
Katamati Waste Dump	Extrusion	G-G'	1.7
		H-H'	2.0
	Building Block	1.9	

7. MONITORING STRATEGY AND CONCLUSION

Based on the Factor of Safety (FoS) value, risk matrix has been prepared where all the dumps of Noamundi & Katamati has been classified in different categories. This classification enables Tata Steel to prioritize & customize the monitoring strategy for each dump along with the focussed approach for devising the mitigation plan for dumps as per their severity. The FoS baselines have been formulated based on the British Columbia Mine Dump Committee, 1991 recommendations and has also been referred in various other reports on dump stability like Kainthola et. al (2011) and Verma et. al. (2017).

Most of the dumps of OMQ are stable but still it needs continuous monitoring & management as per the Dump slope management plan (SMP). The monitoring strategy, activity, and inspection frequency required for each activity related to slope management has been listed in the strategy plan.

Table 5: Monitoring strategy of dumps/stacks of Noamundi and Katamati

Risk Category	FoS	Monitoring techniques	Frequency	Remedies
A (HIGH)	< 1.3	Prism survey Drone survey	Fortnightly/Monthly Yearly	1. Analysis of the slope angle 2. Increase Vegetation cover 3. Analysis of tension cracks 4. Proper dredging of garland drain (Monsoon season)
B (MODERATE)	1.3 – 1.5	Prism survey Drone survey	Half yearly Yearly	1. Analysis of the slope angle 2. Increase Vegetation cover 3. Analysis of tension cracks 4. Proper dredging of garland drain (Monsoon season)
C (LOW)	1.5-2	Drone survey	Yearly	1. Analysis of the slope angle 2. Analysis of tension cracks 3. Proper dredging of garland drain (Monsoon season)
D (UNLIKELY)	> 2	Drone survey	Yearly	1. Analysis of the slope angle 2. Analysis of tension cracks

REFERENCES

- Kainthola, A., Verma, D., Gupte, S. & Singh, T. 2011. A Coal Mine Dump Stability Analysis—A Case Study. *Geomaterials* 1(1): 1-13.
- Kokutse, N., Temgoua, A.G.T., Kavazovic, Z. 2016. Slope stability and vegetation: Conceptual and numerical investigation of mechanical effects. *Ecological Engineering* 86: 146-153.
- Verma, A., Deb, D. & Mukhopadhyay, S. 2017. Stability analysis of a mine waste dump over an existing dump. *Journal of mines, metals & fuels* 65: 41-48.
- Wyllie, D.L. & Mah, C.W. 2007. In *Rock Slope Engineering, Civil and Mining* (4th Ed). *Rock slope engineering*. London & New York: Spon Press.
- Zou, P., Zhao, X., Meng, Z., Li, A., Liu, Z. & Hu, W. 2018. Sample Rocks Tests and Slope Stability Analysis of a Mine Waste Dump. *Advances in Civil Engineering*: 1-17.

Geological and Geotechnical 3D soil modeling of ultra-deep waters oil field in the Eastern Brazilian Margin

J.N. Cruz

PUC-Rio, Rio de Janeiro, Brazil

D. Pilloto, N.C Ferreira, , J.O Peixoto and S.A.B Fontoura.

PUC-Rio, Rio de Janeiro, Brazil

Dias, R. and Gonçalves, C

Petrobras, Rio de Janeiro, Brazil

ABSTRACT:

Knowledge of the properties of very shallow, unconsolidated sediments is crucial to minimize drilling problems. This work was performed in ultra deep-water at the Brazilian Eastern Margin and the results address important issues including the distribution of materials and properties throughout a given field, it is necessary to 3D model both the geology and the geotechnical properties of these shallow, unconsolidated sediments. The data set used was a 3D seismic reflection in-depth domain, the results of cone penetration tests and multi-sensor core logger data to a maximum of 20 mbsf (meters below the seafloor). To construct the 3D static models, a specific protocol was followed which included the definition of grid architecture, upscaling routine, lithological and geotechnical model, and stochastic simulation through the use of sequential indicator simulation method. Therefore, for validating the models, qualitative and quantitative criteria were used. The results provide probabilistic field scenarios to compensate the lack of direct measurement from field data, such as undrained shear strength and lithological profile

1 GENERAL INSTRUCTIONS

Oil and gas exploration in ultra-deep-water is exposed to several geomechanical risks. The foundation design of subsea structures requires knowledge about the soil proprieties. In very soft soil there are risks of low load-bearing and low holding capacity of structures, anchorages failures, and installation problems of well-head structures and conductors during the initial phase of well construction. In order to minimize the geomechanical risks, it is important to start their analysis as soon as possible, hence it is necessary for multidisciplinary professionals, such as geotechnical, geologist, and geophysicists. Several oil and gas companies have problems during the installation of subsea structures due to, for example, the inadequate characterization of the top few meters of seabed soil and the lack of geotechnical knowledge (Power 2001). To minimize drilling problems, this paper focuses on to building 3D static model soil of the first 20 meters below the seafloor (mbsf), predicting areas that show anomalies values of undrained shear strength, using the stochastic method. The region has unconsolidated sediments that represent very recent soil, probably the Quaternary geological period.

2 METHODOLOGY AND MATERIAL

This paper shows a workflow to build a 3D geological and geotechnical soil model. The methodology for 3D models followed in several steps, summarized in figure

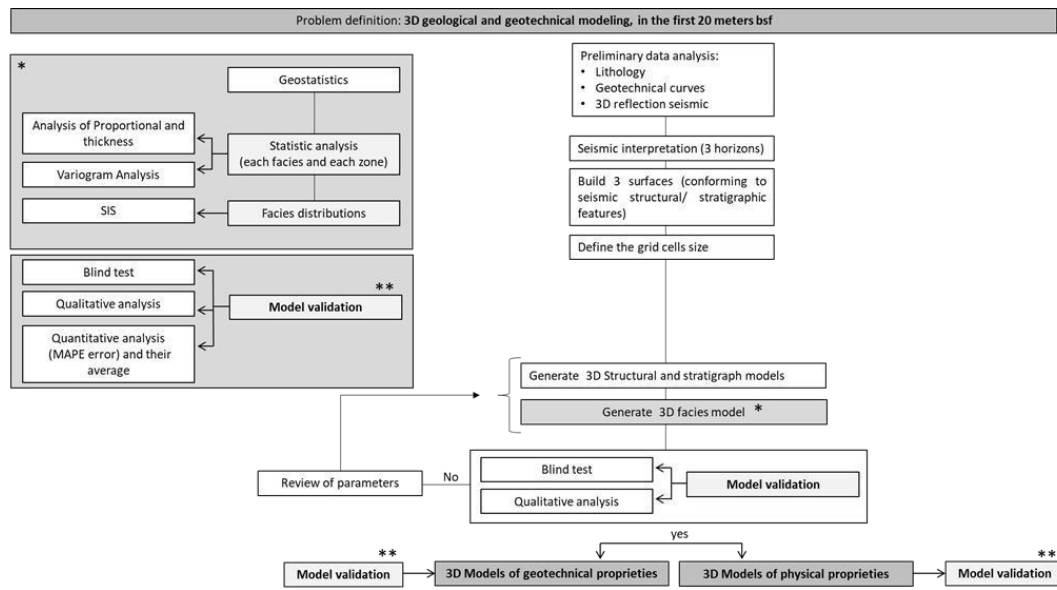


Figure 1. The workflow of 3D geological and geotechnical modelling.

The first step is to define the depth of the model and collect the available data. After that, import the data and make a preliminary analysis of the lithological profile, geotechnical curves, and interpretation of seismic horizons. To compose the 3D structural and stratigraphy model, three horizons were interpreted based on seismic stratigraphy principles (Michtum et al 1977b). After that, they were transformed into surfaces (figure 2)

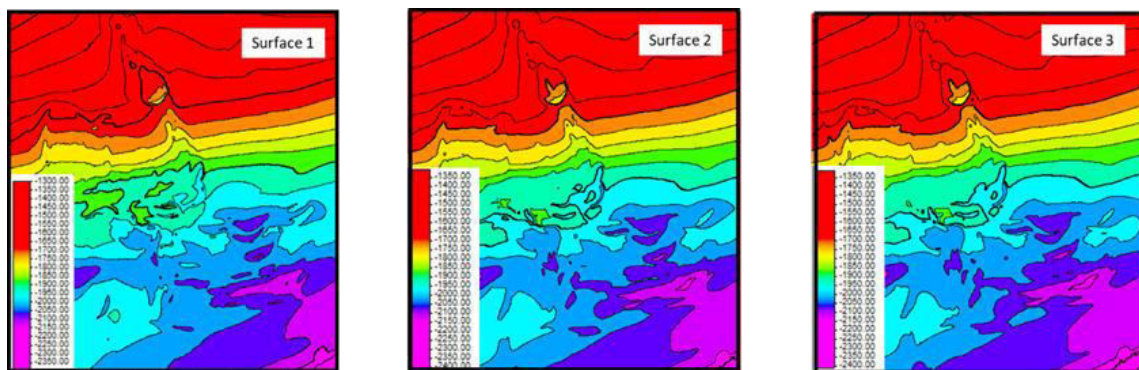


Figure 2. Surfaces are used as the limit in the grid. The scale of depth is in meters.

It is important to highlight that the 3D seismic data contains more information on inter-well distribution to help us to distribute the 3D proprieties, but the seismic interpretation is normally non-unique (here, we interpreted 3 horizons, as showed before) and the modeling depends on seismic data quality and mathematical algorithms used on distribution. Secondly, these horizons were transformed into 3 surfaces, consequently 2 zones in a grid (figure 3).

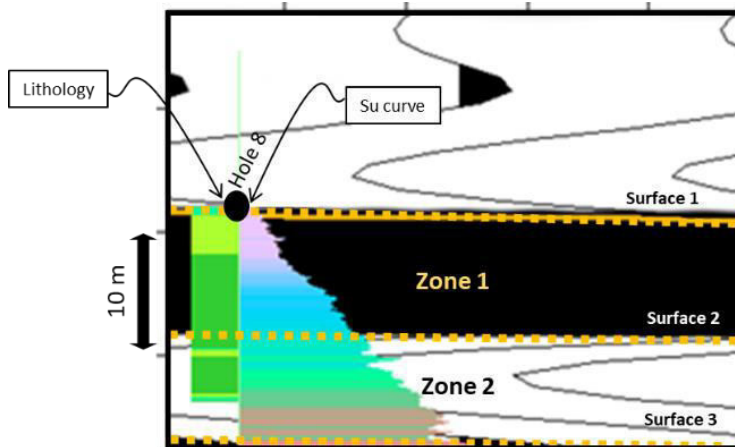


Figure 3. Sketch of limits of zones used in the soil grid.

Each zone was divided into several layers with 0.5 meters of thickness. Zone 1 has around 5 meters of thickness, with 10 layers. Zone 2 shows around 15 meters of thickness, with 35 layers (figure 4).

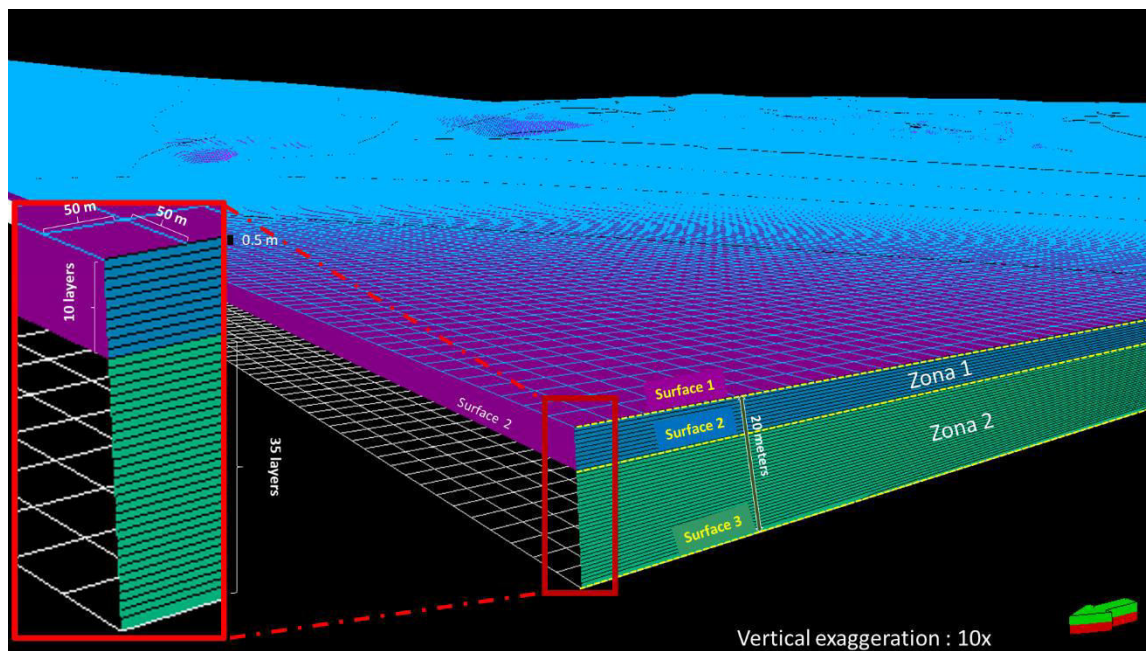


Figure 4. The structural grid of the studied soil; dimensions of blocks are 50 m * 50 m * 0.5 m along X, Y, and Z directions, respectively.

The grid dimensions were bounded by a userdefined polygon converted to a grid boundary with 1002 x 1277 x 45 (I, J, K) grid cells. Individual cells were defined as 50 m x 50 m x 0.5 m (I, J, K) as shown in table 1.

Table 1: Parameters of grid.

Statistics for 3D grid with 2 zones	
Grid cells (nI x nJ x nK)	1002 x 1277 x 45
Total number of grid cells:	57579930
Number of geological layers:	45
Total number of 2D cells:	1279554
Average Xinc (m):	50
Average Yinc (m):	50
Average Zinc (along pillar, in m)	0.54

The lithological data was transformed into indicator data and the variograms (each lithology in each zone) were calculated for both the horizontal and vertical directions based on the dataset. In this work, each lithofacies were classified according to their percentage of carbonate and sand (figure 6) and spatially distributed, for each zone (zones 1 and 2). Then, a theoretical variogram model was used to fit the calculated values (figure 5) and the model with the best fitting value was selected (tables 2 and 3).

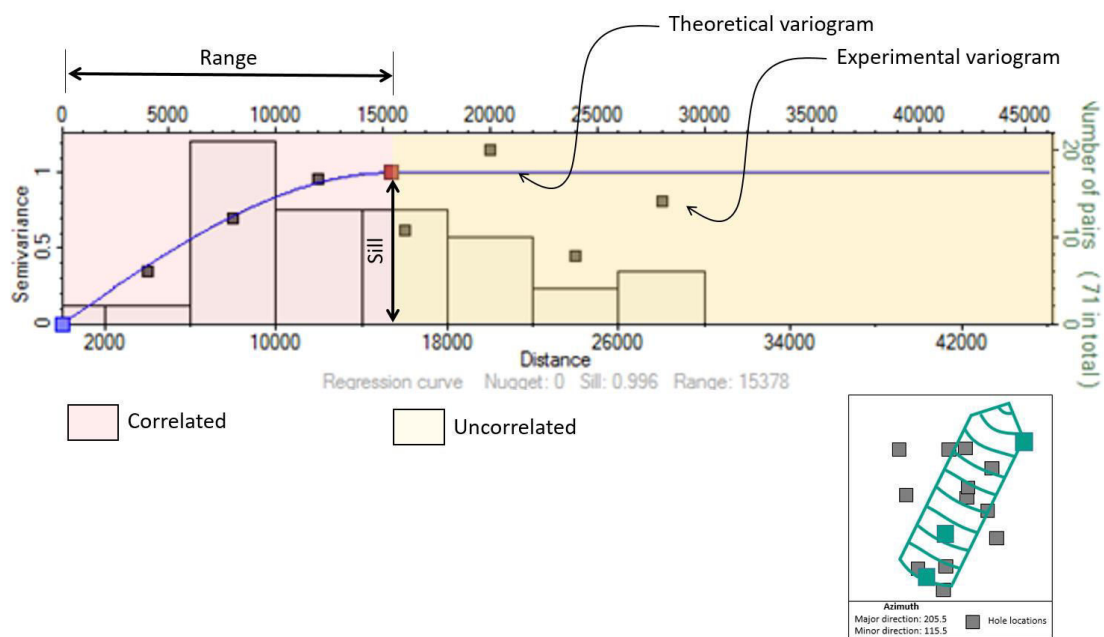


Figure 5. Example of variogram for specific lithology carbonate slightly mud, in the zone 1. Variogram type is spherical, the sill is 0.996 and the nugget is 0.

To perform the 3D facies modeling approach, it was used a stochastic simulation: the sequential indicator simulation method (Petrel software, version 2016). The 3D SIS estimations were conducted on 30 scenarios. Then, the most frequent scenario was used for the facies model. These numbers of realizations were adequate because adding another scenario to any model resulted in no significant change of the most frequent scenario. To validate the facies model, we applied qualitative analysis using histograms. After all these steps, 3D facies modeling was done. To make the 3D geotechnical modeling (Su), we calculated variograms (each zone) for both the horizontal and vertical directions based on the dataset. A theoretical variogram model

was used to fit the calculated values and the model with the best fitting value was selected. To make the 3D distribution, we used the geostatistical algorithm, SIS. To validate these models, we applied qualitative analysis, with the use of histograms. The MAPE error Eq. (1) and their average error were used for quantitative analysis.

$$MAPE (\%) = \sum \frac{Abs(Prop_{est} - Prop_{real})}{Prop_{real}} \times 100$$

Where:

Abs: absolute value

Prop real: real property (blind test)

Prop pred: predicted property (SIS)

We calculated the average from 30 scenarios (each property) and applied it to generate maps. The available data for the field in question is confidential and therefore specific details cannot be provided, but we used: • In situ CPTU penetrations (undrained strength resistance, S_u) at 22 locations to a maximum of 20 mbsf; • Lithological profile at 10 locations to a maximum of 20 mbsf, where the lithological classification considered in this study was the percentage of carbonates and sand (figure 6); • 3D conventional seismic reflection.

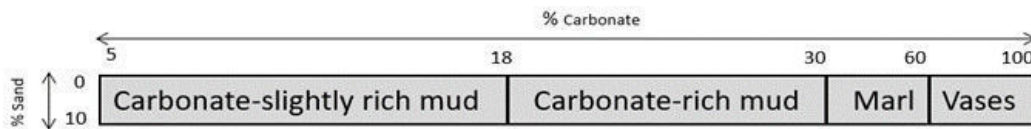


Figure 6. Lithological classification of soil.

3 RESULTS AND DISCUSSIONS

3.1 Three-dimensional Facies modeling, applying SIS.

The lithological distribution can be performed using artificial intelligence (neural networks), geostatistical algorithms, or both. Here, we used a geostatistical algorithm, SIS. To make a lithological distribution (discrete variable), we used studies of variograms (table 2), adjustment of the vertical proportion curve (figure 7), and thickness histograms analysis (figure 8).

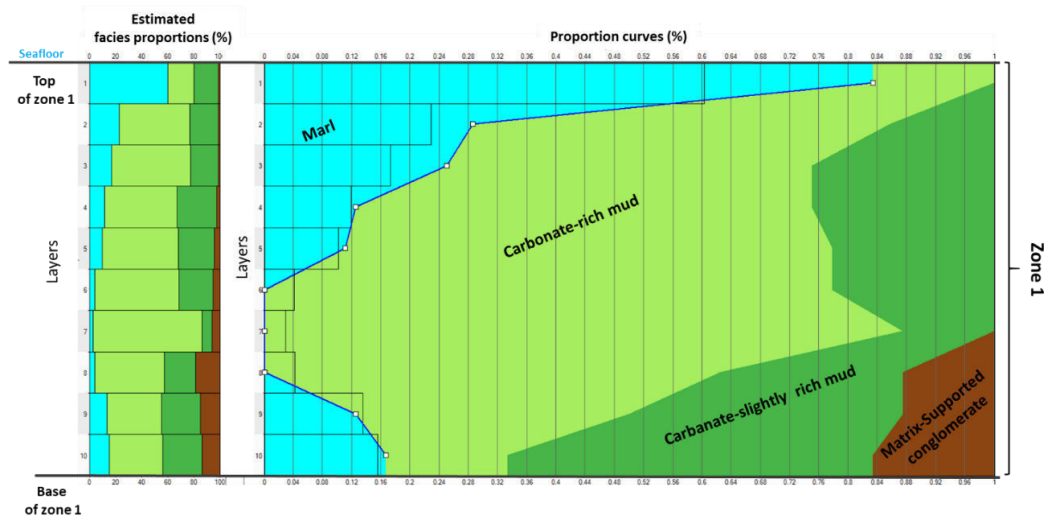


Figure 7. The Vertical proportional curve of lithology, zone 1.

The vertical proportion analysis and thickness histograms helped us to adjust theoretical models of the variograms of each lithology, summarized in the table (table 2) below. According to the vertical proportion curve, for example, 60% of lithology localized next to the top of zone 1 (layer 1) are marls. On other hand, next to the base of the same zone, we find predominately carbonate rich mud, which can represent almost 90%, on layer 7 (figure 8).

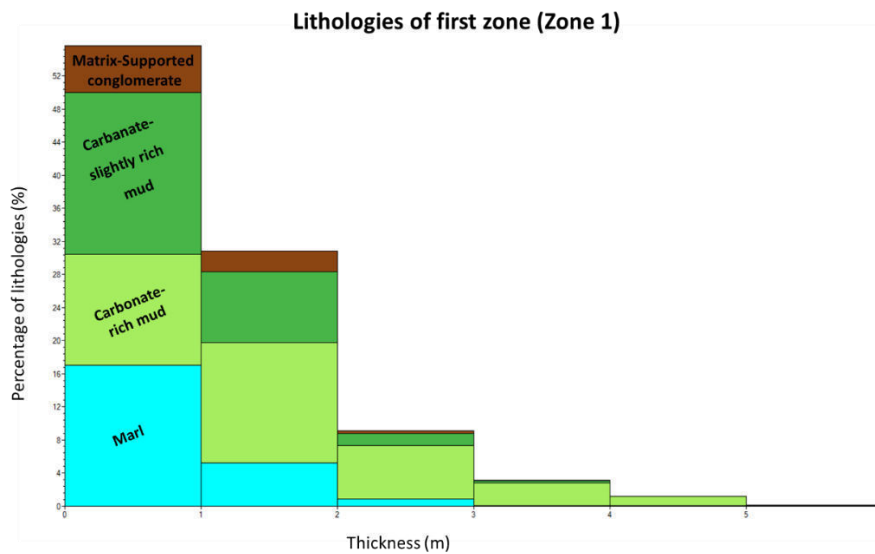


Figure 8. Thickness histogram of lithology, zone 1.

The thickness histogram of lithology shows us for example the average thickness versus their percentage, in the case of marl and their thickness can be until 3 meters, but the majority has 1 meter of thickness. We can analyse each lithology, in each zone. Table 2. Parameters of variogram models in the horizontal (major and minor, in meters) and vertical directions for both zones (in meters) delineated for each zone and each lithology separately. Theoretical variogram in all facies was exponential. Facies code: 1 marl, 2 carbonate-rich mud, 3 carbonate-slightly rich mud, 4 landslide deposit, 5 classsupported conglomerate, 6 matrix-supported conglomerate and 7 vase. Sill of all lithologies: 1. Nuggets of all lithologies: 0.

Table 2. Parameters of variogram models in the horizontal (major and minor, in meters) and vertical directions for both zones (in meters) delineated for each zone and each lithology separately. Theoretical variogram in all facies was exponential. Facies code: 1 marl, 2 carbonate-rich mud, 3 carbonate-slightly rich mud, 4 landslide deposit, 5 classsupported conglomerate, 6 matrix-supported conglomerate and 7 vase. Sill of all lithologies: 1. Nuggets of all lithologies: 0.

Zone 1

Facies	Fraction	Azimuth	Major	Minor	Vertical
1	15.61	327.4	9000	7000	3
2	53.93	146.5	7566	7566	5
3	26.73	306.8	10143	10143	3
4	x	x	x	x	x
5	x	x	x	x	x
6	3.73	294.4	1500	1500	4

Zone 2

Facies	Fraction	Azimuth	Major	Minor	Vertical
1	10.73	307.9	4500	5.307	3
2	14.66	132.6	10000	8	5
3	66.7	308.8	13806	7.998	3
4	2.27	329.6	7500	5.307	x
5	1.48	274.4	1500	3.5	x
6	2.32	225.8	1500	3.5	4
7	1.84	329.6	1500	3	

After the generation of the 30 scenarios, the most frequent (most of) scenario was applied (figure 9). The first step was to observe in different directions that each lithology was well represented geologically.

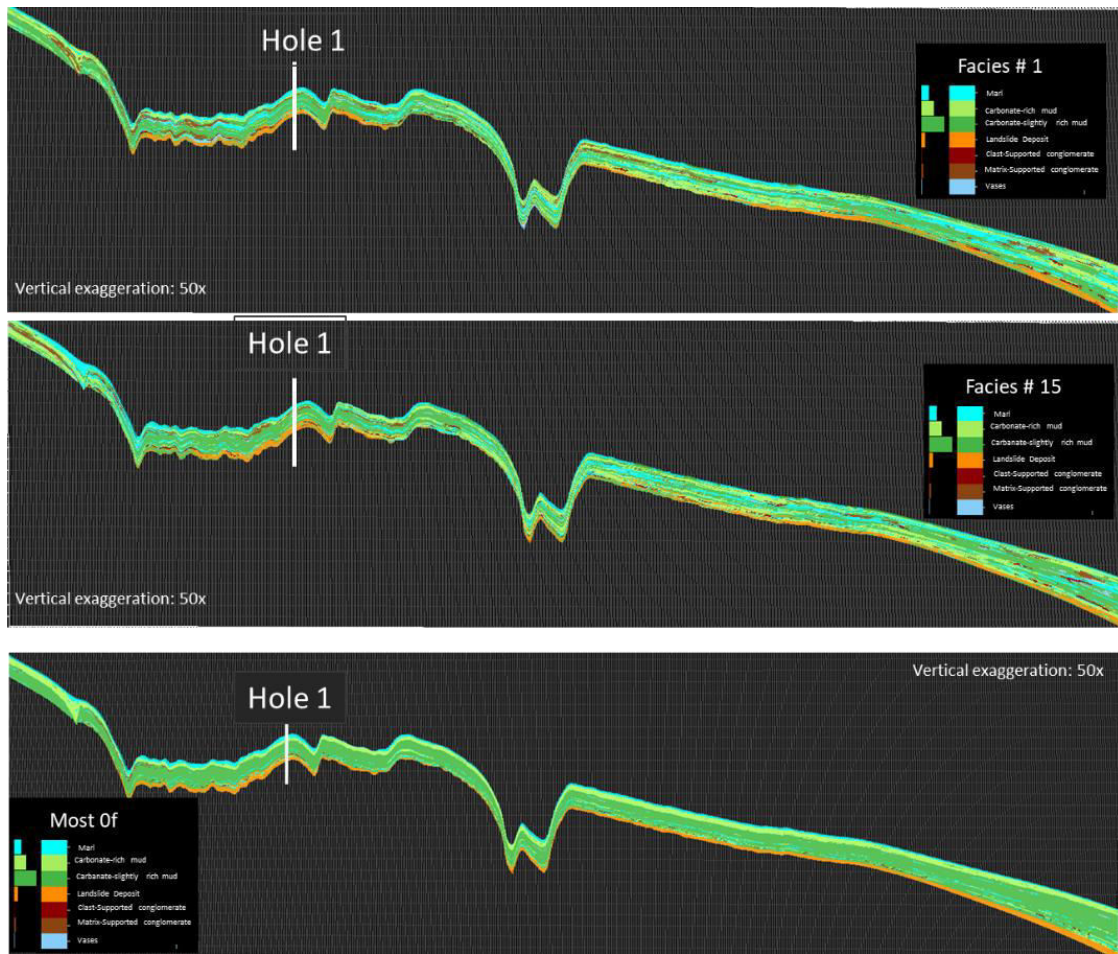


Figure 9. Cross-sections of 3 scenarios of facies distribution which is modelled using SIS algorithm. Note, align along J-Direction. Scenario#1, Scenario#15 and most frequent scenario.

The quantitative analysis took place with the use of histograms (figure 10), where the difference of lithology using SIS, real data (well logs), and upscaled data is shown.

We can note a small difference between the model (estimated) and the lithology profile (real data), less than 3% in almost all lithologies. The carbonate-slightly-rich mud was underestimated 9% and the landslide deposit was super estimated 7%, probably due to the weight in the up-scale process.

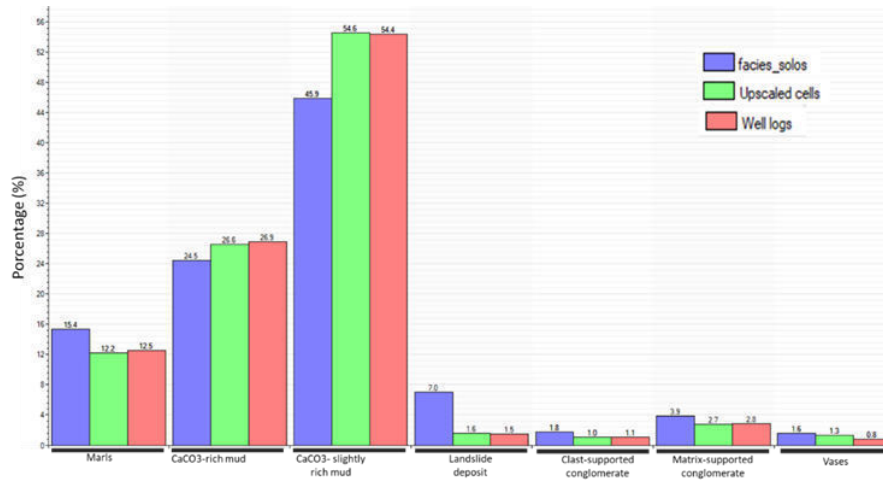


Figure 10. Histogram reproduction of the percentage distribution of lithologies by SIS (facies_solos), upscaled cells, and well logs (real data).

3.2 Three-dimensional modelling of Su, applying SIS.

The Su profiles show thin-crust near the seabed in several deep-water regions, where we found relatively unusual high strength (figure 11). Generally, the Su profile starts with the lowest values and increases linearly with depth. The same Su behavior has been found offshore of Nigeria (Ehlers et al 2005). They attributed this high Su due to bioturbations and geochemical transformations. From the CPTU results, a general deep-sea superficial crust was observed with a maximum of 14.03 kPa to 0.62 m below the seafloor.

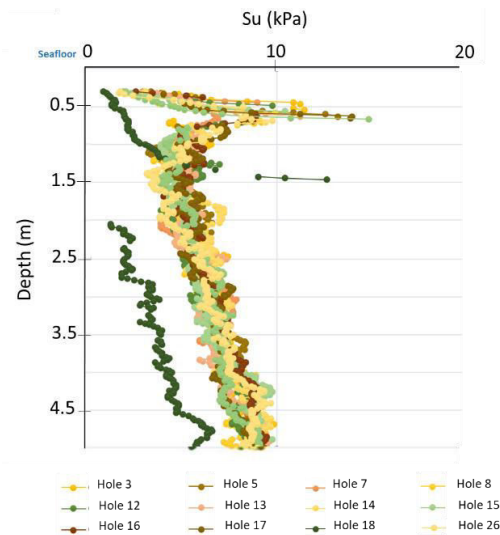


Figure 11. Su versus depth graph. All the holes show a high Su anomaly next to the seafloor, in the first meters below the seafloor

The 3D strength resistance distribution (Su), was performed using the SIS distribution method, in which variography studies were made for each zone, as showed in table 3.

Table 3. Parameters of variogram model of Su, in the horizontal (major and minor, in meters) and vertical directions for both zones (in meters)

	Su variogram				
	Azimuth	Major	Minor	Vertical	Sill
Zone 1	132.9	15000	15000	4.8	1
Zone 2	119	8500	8500	10	1

Using the same variograms, 30 scenarios were generated for each property (figure 12), then their average scenario was applied for each zone.

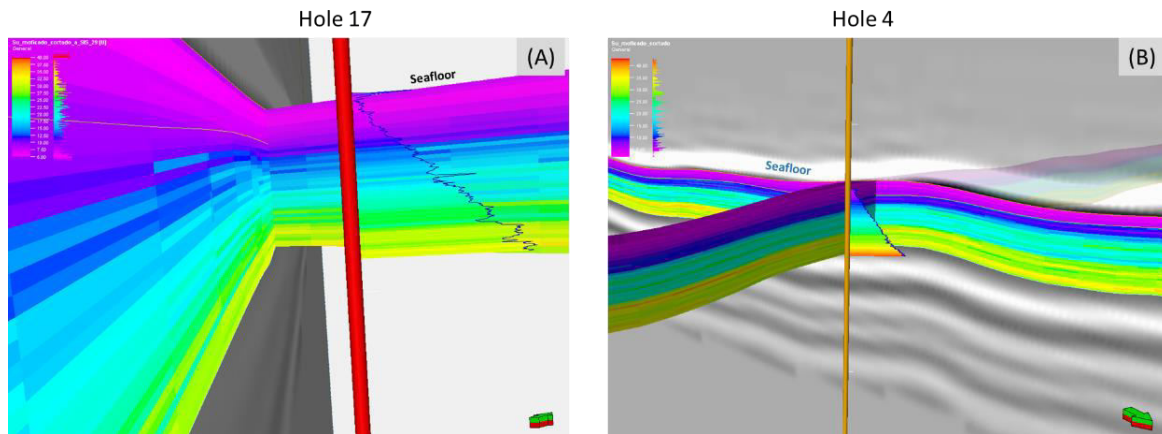


Fig.12. Example of Su scenario (a) Su model is superimposed to seismic reflection data and Su profile of Hole 17 (used on the modeling) (b) Su model is supposed to seismic data and real Su profile of Hole 4 (blind test).

To validate the Su model, a qualitative analysis was firstly performed and then a quantitative one was applied (MAPE error). The blind test was used for the Su model was Hole 4. As we can note, there is a small difference between the real data and the model (figure 13).

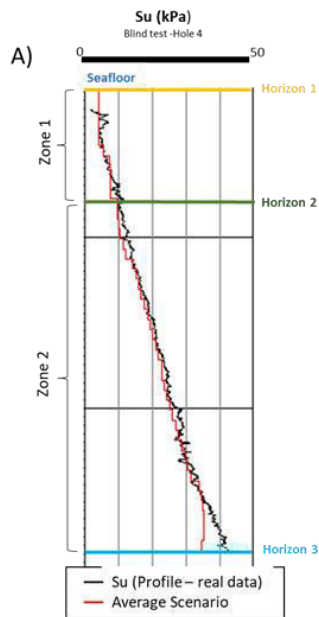


Figure 13. Validation of Su model, with the superposition of Model and Blind test.

Then, the MAPE error of S_u propriety was calculated, averaging (figure 14) values less than 8%.

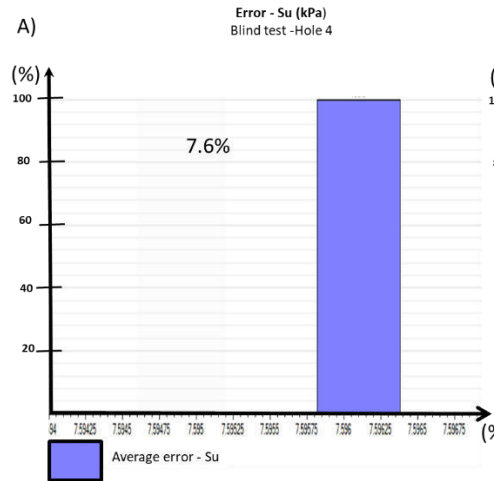


Figure 14. Calculation of the average error of S_u model

Subsequently, the arithmetic mean was calculated for each zone separately, for S_u (figure 15). High S_u anomaly values were found in the northwest region of the studied area for both zones (zone 1 and zone 2)

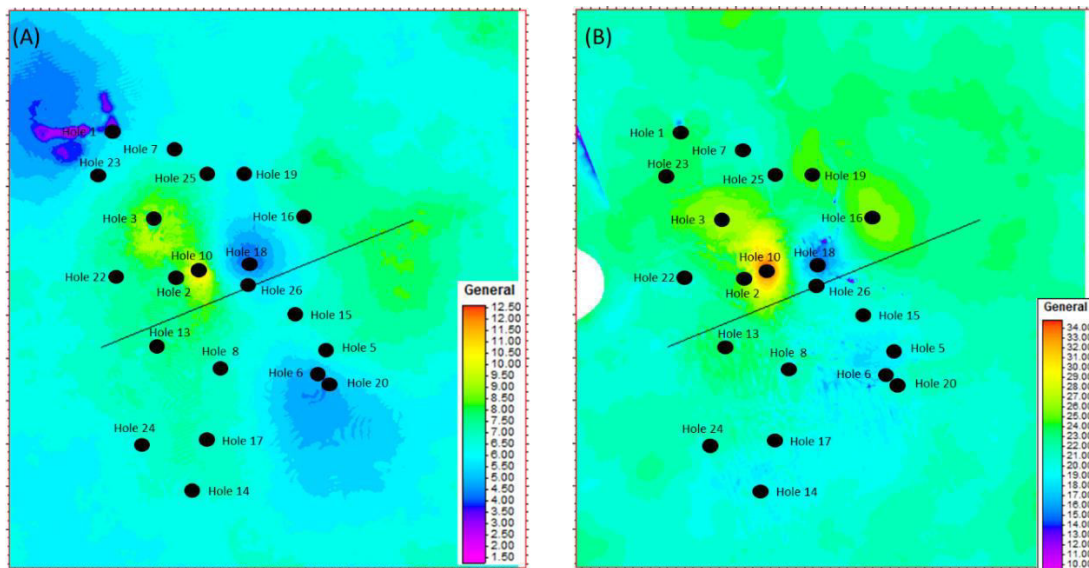


Figure 15. Plan view of average of S_u property, calculated for each zone separately. (a) Zone 1, 1.5 – 12.5 kPa (b) Zone 2, 10 – 34 kPa. Each zone has a different scale. Note, align along k-Direction

4 CONCLUSIONS

(i) There is a predominance of lithologies with a higher percentage of carbonates in the layers closer to the seafloor.

- (ii) The 3D lithological distribution by Indicative Sequential Simulation (SIS) proved to be efficient since the differences between the real data and the model were on average smaller than 3%, except carbonate lightly mud, which was underestimated by 9%, and the landslide deposit, which was overestimated by 5%. This analysis of probability distribution showed good consistency, indicating that the model has good reliability and predictability.
- (iii) Although we do not show in this work, there is a presence of low angle faults providing the appearance of landslide deposits, matrix-supported conglomerate, and clast-supported matrix.
- (iv) The workflow proposed was capable to identify zones with different anomalies and can be used in well planning.

5 PREFERENCES

- Ehlers, C.J., Chen, J., Roberts, H. H., and Lee, Y.C. 2005. The origin of near-seafloor “crust zones” in deep water. In Gourvenec S. and Cassidy M (eds) Proc. Int. Symp. On Frontiers in Offshore Geotechnics. Taylor and Francis, 927-933
- Mitchum Jr, R.M., Vail, P.R., Thompson III, S., 1977b. Seismic stratigraphy and global changes of sea level, Part 2: The depositional sequence as a basic unit for stratigraphic analysis. See Payton 1977, pp. 53-62.
- Power, P.T. "Geotechnical Sensitivities of Deep-Water subsea Structures- The results of an industry survey", 2001. Contributors Summary Report, OSIF, 26 April

Evaluation of tip bearing capacity of bored piles embedded in the Vallemí-Cambajhopo limestone formation

Juan Nicolás Zabrodiec

Tecnología Aplicada a Fundaciones SRL, Asunción, Paraguay

ABSTRACT:

The construction of a large industry in the proximity of the city of Vallemí, Concepción, North Eastern Paraguay, involved the use of thousands of bored piles embedded in rock, more specifically in the Vallemí-Cambajhopo limestone formation. Due to importance of the project, an exhaustive campaign of geotechnical characterization was conducted, alongside with detailed bearing capacity analysis and dynamic testing on piles.

This article presents the results of the theoretical bearing capacity analysis performed using several methods and international codes, and compares them with the results obtained in numerous dynamic tests performed on piles. The evaluation found that the estimation of bearing capacity using the equations of the Canadian Foundation Engineering Manual had the best results compared to the values obtained in the dynamic tests.

1 INTRODUCTION

The city of Vallemí, located in the North Eastern region of Paraguay, sits on a valley surrounded by the Paraguay river and several hills. Due to its strategic location, many industries are installed in the area, mainly related to processing lime for agricultural and construction purposes. Amongst the industries that are located in the region, one of the oldest is the Paraguayan National Industry of Cement (INC), established in 1969.

At the beginning of the year 2019, a large private investment established CECON SAE, an ambitious project of a new, state-of the art, cement and lime industry. Taking advantage of its location, this industry was established at the foot of the Cerro Morado, a large reservoir of limestone.

The foundations for most structures at the new plant were designed with piles, embedded in rock. Initial estimations evaluated over 9.000 linear meters of piles, with a volume of over 7.000 m³ of concrete. A comprehensive geotechnical analysis, characterization, and testing campaign was performed, allowing higher bearing capacities for piles. The studies performed helped to optimize the initially proposed foundations, with final quantities of approximately 10.000 linear meters of piles, but in smaller diameter, resulting in a total of approximately 3.500 m³ of concrete. This paper presents the geotechnical conditions on site, the pile testing program designed, a review of methods used for determining tip capacity, and an evaluation of the results obtained with the pile testing program performed.

2 GEOTECHNICAL CONDITIONS IN THE VALLEMÍ REGION

2.1 *Local Geology*

The geology of the department of Concepción, in North Eastern Paraguay is mainly composed of the Aquidaban (Carboniferous) and San Ramón (Precambrian) formations, taking more than 75% of the department area, as it can be seen in Figure 1 (MOPC, 2018). In this region, it is common to find sandstones, with an initial layer of boulders (“canto rodado”, as it is named in the region) on the surface. Next to the Paraguay River (West boundary of the department) quaternary sediments are found, with certain spots of Neoproterozoic formations (Itapucumí Group).

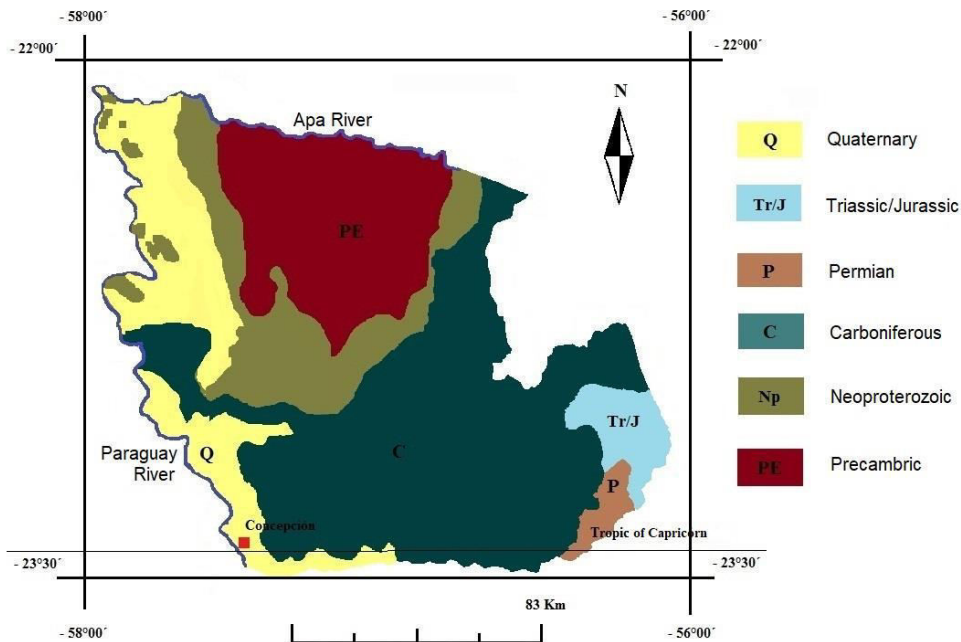


Figure 1. Geological map of Concepción (MOPC, 2018).

The influence area where the new industry is located, is dominated by the Itapucumí Group, which is divided in two geological formations. The lower sequence, called Vallemí Formation, is mainly constituted by conglomerates, archoses, sandstones, shales, marls and thin layers of limestones. On top of that, the Cambajhopo formation (Figure 2) is mainly formed by limestones, oolitic limestones, and magnesian limestones (Orué, 1996).

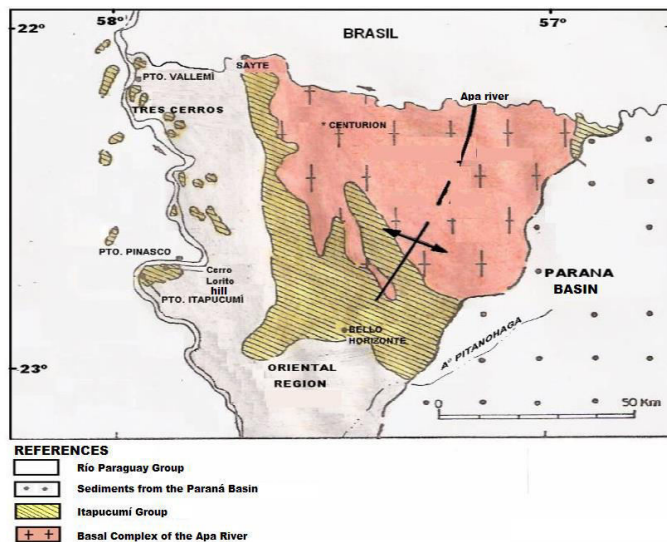


Figure 2. Geological map of the area where the CECON SAE industry is located (Orué, 1996).

All around the district of San Lazaro, where the towns of Vallemí, San Lazaro, and Tres Cerros are located, there are many limestone outcrops. The geological background of the area indicates that it is expected to find thick layers of grey limestones, massive, with parallel stratification.

2.2 Geotechnical investigation

Due to the importance of the project, many local and international geotechnical consultants and contractors were involved. The exhaustive investigation campaigns performed on site, included over 75 boreholes with rotary drilling (some of the reaching 30 m), SPT tests, CPTu tests, geophysical techniques (MASW), electrical resistivity tomography (ERT), and laboratory tests on soil and rock samples.

Summarizing the stratigraphy in the area of interest of the project, the following profile is typically found:

- An initial stratum of soft to medium silty clays, reaching depths between 6 m and 10 m.
- Underneath the initial soil stratum, the presence of a very altered limestone rock layer (thickness between 3 to 5m) is found.
- Below, the massive limestone formation is reached, extending until known depths of at least 20 m.

A typical borehole has a core logging as it can be seen in Figure 3 below.



Figure 3. Soil and rock core drilling for borehole VM-CZ (CECON SAE, 2020).

Most structures for the new plant that was built have significant foundation loads, and the stratigraphy in the area of interest of the project suggested that the most suitable foundation in most cases involved the use of piles. Since the initial stratum of clays is not very thick, the main component of the bearing capacity of the piles that were going to be used is the tip component of piles embedded in the limestone rock formation. As it was mentioned above, the representative geotechnical profile indicates the presence of an initial layer of very altered limestone, followed by sound, massive limestone. A summary of the main rock parameters considered for the estimations performed is included in Table 1 below:

Table 1. Geotechnical parameters considered

Parameter	RQD	UCS (MPa)	Density (gr/cm ³)	Dry shear wave velocity (m/s)
Layer 1:	90-100%	30-60	2,68-2,72	5400-6000

3 ESTIMATION OF PILE TIP BEARING CAPACITY BY ANALYTICAL METHODS

It is well known that the ultimate pile bearing capacity is a function of dimensions of the pile (length and diameter) as well as properties of the materials that are found on site (lateral resistance along the shaft and tip resistance of the formation where the pile is embedded). Taking this into consideration, the ultimate pile bearing capacity can be expressed by the following equation:

$$Q_u = q_t A_t + q_f A_f \quad (1)$$

where q_t = ultimate unit bearing capacity on tip; A_t = tip area; q_f = friction resistance along the shaft; A_f = lateral shaft area.

There are several methods in order to estimate the unit tip bearing capacity, starting from methods developed in the soil mechanics field, considering theoretical (c and ϕ angle) parameters. When dealing with a soil mechanics approach, the dispersion of results is important, more over, considering a rock mechanics approach, the dispersion of results can be even higher. Several authors mention that the real bearing capacity of piles in rock is very difficult to predict, due to a lack of documented cases, also the fact that the mobilized resistance in service conditions is usually lower than the available resistance. In order to simplify the bearing capacity approach, in most used formulas, the tip resistance is just directly proportional to UCS, and shear resistance is usually simplified as a fraction of tip resistance.

Looking at a Rock Mechanics approach, Serrano González et al (2010), mentioned that some of the most important factors that affect bearing capacity of piles embedded in rock include:

- Rock type
- Rock matrix and discontinuity resistance
- Quality, type and fracture of rock matrix
- Embedment length
- Relationship between deformation moduli between rock and pile

Taking into consideration all factors explained above, the ultimate tip bearing capacities were estimated for the project mentioned. The analytical estimations were performed choosing three of the most widely used approaches: Spanish Guide of Roadworks (2002); Canadian Foundation Engineering Manual (2007) and the FWHA Manual (1999). All estimations assumed 80 cm diameter piles, embedded 2 diameters (160 cm) in sound rock.

3.1 Estimation using the Spanish Guide of Roadworks (2002) guidelines

The Spanish Guide of Roadworks (Guía de Cimentaciones en Obras de Carretera) (2002) includes a very detailed method in order to estimate bearing capacity of shallow foundations in rock, and it uses the same concepts in order to define bearing capacities of piles in rock. This manual indicates that the ultimate pile tip bearing capacity can be expressed by the following equation:

$$q_t = 2 p_{vadm} d_f \quad (2)$$

where $p_{vadm} = p_0 \alpha_1 \alpha_2 \alpha_3 \sqrt{q_u/p_0}$; and the other factors are explained below:

p_0 is a reference pressure of 1MPa;

q_u is the UCS

α_1 =influence of the type of rock

α_2 =influence of the meteorization degree

α_3 =influence of the spacing between joints

d_f =embedment factor= $1+0.4 L_r/D \leq 2$ (L_r is the length embedded in rock; D is the pile diameter)

The use of parameters α_1 , α_2 and α_3 is well explained in the manual, and for this estimation, the following parameters were used:

$\alpha_1 = \sqrt{10q_t/q_u}$; where q_t is the tensile strength, therefore

$\alpha_1 = \sqrt{10(4)/40} = 1$ (which equals the recommended value for sound limestones)

$\alpha_2 = 1$ (recommended value for sound limestones)

$\alpha_3 = 1$ (recommended value for RQD=100)

Taking all these parameters into consideration, the following value was calculated for the pile tip bearing capacity using the Spanish Guide of Roadworks guideline:

$$q_t = 21.2 \text{ MPa}$$

3.2 Estimation using the Canadian Foundation Engineering Manual (2007) guidelines

The Canadian Foundation Engineering Manual also has an expression that takes many of the considerations mentioned earlier in order to estimate the pile tip bearing capacity for sound rocks.

This guideline mentions that the ultimate pile tip bearing capacity can be calculated by the following formula:

$$q_t = 3K_{sp}d_fq_u \quad (4)$$

Where K_{sp} is a factor that depends on the joint spacing, joint opening and pile diameter; d_f is an embedment and q_u is the UCS of the rock.

$$K_{sp} = \frac{3 + \frac{s}{B}}{10 \sqrt{1 + 300\frac{\alpha}{s}}} \quad (5)$$

If s is the spacing between joints = 0.5; and α = joint spacing = 0.01, then $K_{sp} = 0.13$.

Therefore, the pile tip bearing capacity is the following, considering d_f equals to 1.40:

$$q_t = 3(0.13)(1.80) (35 \text{ MPa}) = 24.5 \text{ MPa}$$

3.3 Estimation using the FWHA (1999) guidelines

The Federal Highway Administration (USA, 1999) also includes a formula for estimating the ultimate tip bearing capacity of a pile embedded in rock. This international guideline contemplates that the tip bearing capacity is mainly a function of the rock type, rock quality, embedment degree and the UCS.

If the rock underneath the pile tip is very good (sound, RQD=100%) and the pile embedment is over 1.5 times the diameter, the O'Neill & Reese criterion is recommended, limiting the bearing capacity to the following expression:

$$q_t = 2,5 q_u \quad (6)$$

If the rock is embedded in a material with poor geotechnical characteristics, the following value can be used:

$$q_t = 2,0 q_u \quad (7)$$

If the rock presents RQD values between 70 and 100, with close joints, approximately horizontal, and a q_u over 0.5 MPa, the Zhang & Einstein (1998) expression is recommended:

$$q_t = 4,83 q_c^{0,51} \quad (8)$$

In this case, if we adopt $q_u = 35$ MPa, we have the following value:

$$q_t = 4,83 (35)^{0,51} = 29,6 \text{ MPa}$$

4 DYNAMIC TESTING PROGRAM

As part of the tests performed on site, a series of dynamic tests were performed on piles, establishing test fields around the influence areas of the three most important structures on site. The dynamic tests on piles differ from the static (traditional) pile load tests mainly on the fact that the load is applied dynamically through blows of a hammer, using an adequate percussion system. These tests are based on the wave propagation method on elastic mediums. It is known that a tension wave is generated when a blow is applied in the pile top. This wave moves around the pile with a steady speed, depending only on the elastic characteristics of the material. This research, started in the 1960s by Prof. George G. Goble from Case Western University, USA, developed in what is currently known as the PDA testing method. On top of the pile, sensors measuring accelerations and settlement are installed. The signals are sent to a data control unit, where they are stored and analyzed.

Tests on site were performed by the Paraguayan firm LOGOS SRL (Figure 4), using hammer made out of a 10.400 kg concrete mass, with falling heights in between 0.50 m to 1.30 m. The interpretation of the results was performed by Mr. Jorge Bein, from JWB Consulting LLC and also by Mr. César López Bosio from LOGOS SRL.



Figure 4. Image of the tests performed on site

5 EVALUATION OF RESULTS OBTAINED

As it was previously mentioned, several tests were performed on site, establishing tests fields around the three most important structures on site. Piles on each test field had variations of embedment on sound rock between 1 and 3 diameters. In order to make an evaluation of the results obtained in the tests, all tests with rock embedment length of 2 diameters were compared. The results are included in the following table:

Table 2. Results obtained in the field dynamic tests performed

Test 1	Test 2	Test 3	Test 4	Test 5	Mean	Standard deviation
30,7 MPa	20,4 MPa	26,3 MPa	31,0 MPa	16,7 MPa	25,0 MPa	6,3

In order to make a comparison in between the results obtained in the field tests performed and the estimations from the different guidelines previously mentioned, Figure 5 summarizes all the obtained data. From this figure it can be clearly seen that the estimation calculated using the Canadian FEM (2007) almost matches the mean of the values obtained in the field tests. Also, more important, all three estimations calculated fall in the range of values obtained in the field tests, showing that all these formulas can successfully be used for estimations when they are used with good input parameters.

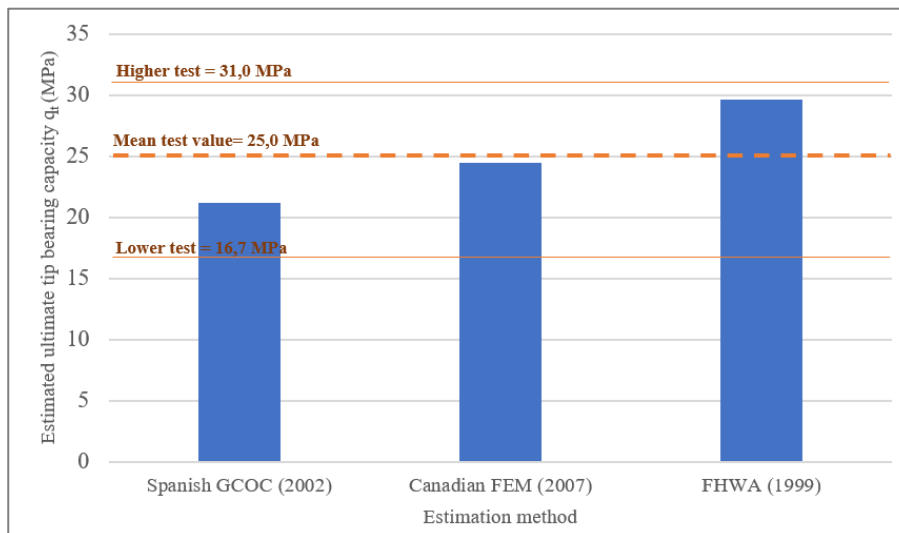


Figure 5. Evaluation of results obtained

6 CONCLUSIONS

The analysis performed shows the usual dispersion of results obtained when calculating bearing capacities for piles in rock. From the Table 2 included above, it can be seen that the mean value obtained in field dynamic tests almost matches the estimation calculated the using the Canadian Foundation Engineering Manual formula.

The extensive geotechnical characterization allowed the use of good input parameters for initial estimations that were later evidenced by a field testing program. This technical support provided strong evidence in order to have higher bearing capacities for piles. With these capacities considered, the total volume of concrete for piles decreased from approximately 7.000 m³ to 3.500 m³,

not only providing economy for the project, but also with strong theoretical and practical evidence in order to have safety for the project.

7 ACKNOWLEDGEMENTS

Special acknowledgements to all the team from AGB Constructora, the main contractor of the project, who provided support with technical documentation and visits to the project site. Also, the author of this article would like to thank Mr. Cesar López Bosio from LOGOS SRL, who provided technical information about the dynamic tests performed on site.

8 REFERENCES

- Canadian Geotechnical Society. 2007. *Canadian Foundation Engineering Manual, Canada*.
- Federal Highway Administration. 1999. *Design and Construction of Driven Pile Foundations*.
- Ministerio de Fomento. 2002. *Guía de Cimentaciones de Obras de Carretera*, España.
- Ministerio de Obras Públicas y Comunicaciones. 2018. Mapa Geológico del Paraguay.
- O'Neill, M. W., and Reese, L. C. 1999. Drilled Shafts: *Construction Procedures and Design Methods, FHWA-IF-99-025*, Department of Transportation, Federal Highway Administration, U.S.A.
- Orue, D., 1996. Síntese da geología do Paraguai Oriental con ênfase para o magnetismo alcalino asociado. Master's Thesis, Universidade de Sao Paulo.
- Zhang, L., and Einstein, H. H. 1998. "End bearing capacity of drilled shafts in rock", *Journal of Geotechnical and Geoenvironmental Engineering*, Vol.124, No.7, pp. 574-584.

Rock slope stability issues in Afghanistan

A.B. Jahed, T. Ito, Ö. Aydan
University of the Ryukyus, Okinawa, Japan

N. Z. Nasiry
Helmand Higher Education Institute, Helmand, Afghanistan

ABSTRACT:

In this study, the authors compiled some case history data and present some typical examples of rock slope stability issues in Afghanistan with a special emphasis on Kandahar region and categorize rock slope failures according to the principles of modern rock slope engineering. The slopes considered involve rock-cut, natural rock slopes mainly. The effect of structural geology and discontinuous nature of rock mass on both slope-cuts and natural rock slopes is taken into account and some preliminary assessments on the stable and unstable rock slopes are presented. Furthermore, the seismic effect on their stability is also considered. It is also pointed out that similar issues could be observed in open-pit mines, which may be exploited in years to come.

1 INTRODUCTION

Afghanistan is a land-lock country and the northern part of Afghanistan is highly mountainous and Hindu-Kush mountains shape her landscape (Figure 1a). The region along the Chaman fault constitutes a plate boundary between Indo-Australian plate and Euro-Asian plate, which is tectonically deformed so that folded sedimentary formations as well as basaltic intrusions and dykes are abundant within this tectonic boundary (Figure 1b). The southern part of Afghanistan is known as Chagai Arc and it is also highly deformed due to the subduction of Arabian plate beneath Euroasian plate along the Makran zone. The west side of Afghanistan is also highly deformed by dextral strike-slip faulting along Sistan Suture Zone. The region bounded by these tectonic features is named as Helmand Block. Kandahar is located at the north-east corner of Helmand block and it is about 100 km away from the Chaman Fault (Figure 1).

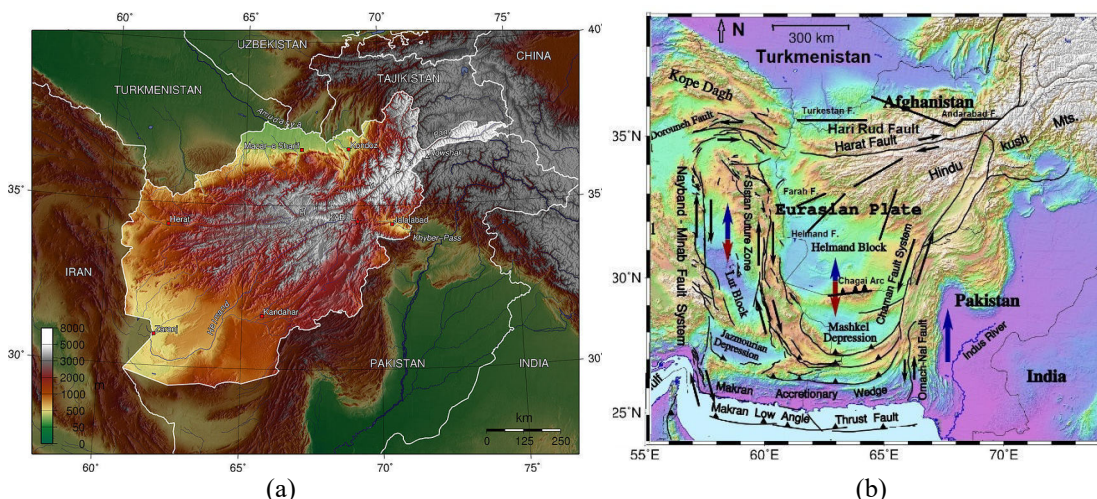


Figure 1. (a) Topography and (b) tectonics of Afghanistan and neighboring countries (modified from Nemati, 2018).

The large-scale rock slope stability issues are common in Afghanistan and there are also very large deep-seated slope failures and such an event recently occurred in Badakshan Province in 2014. However, there is almost no study on rock slope stability issues in Afghanistan. One of

reasons could be the internal instability and invasions of Afghanistan by the former Soviets Union and the United States of America, which hindered both academic studies and the education of scientists and engineers of Afghanistan. Therefore, this study undertaken by the authors could be one of the pioneering studies for Afghanistan.

The authors compiled some case history data on rock slope failures in Afghanistan with an emphasis on Kandahar Region. The rock slope failures can be broadly categorized as planar/wedge sliding, flexural/columnar toppling and deep-seated circular failures in view of modern rock slope engineering. In addition, huge boulders exist on slopes and they may topple and fall over the transportation routes as well as settlement areas. In addition, open-pit mines to be exploited in years to come may also have the rock slope stability issues. The slopes of reservoirs of existing dams and those to be built in future would present similar issues. Besides gravitational and climatic effects, the seismic effects must be also considered when rock slope stability is assessed as Afghanistan is a seismically active country.

In this study, the authors present some typical examples of rock slope stability issues in Afghanistan with an emphasis on Kandahar region and categorize rock slope failures according to the principles of modern rock slope engineering. The effect of structural geology and discontinuous nature of rock mass on both slope-cuts and natural rock slopes are taken into account and some preliminary assessments on the stable and unstable rock slopes are presented. Furthermore, the seismic effect on their stability is also discussed.

2 GEOLOGY, SEISMO-TECTONICS AND SEISMICITY

Afghanistan is underlain by Precambrian metamorphic rocks, which form high regions in the center of the country and in the Hindu Kush. The Central Afghanistan between Herat and Panjab is the northernmost structural high, encompassing metamorphic rocks. The part is connected to the Hindu Kush by Precambrian rocks in Koh-i-Baba. Precambrian rocks outcrop locally west of Jalalabad, close to Kabul and Khost, and are likely present in the Safed Koh Range. The Precambrian rocks of Afghanistan include phyllite, greenschist, garnet-mica schist and partially melted gneiss that experienced anatexis. Highly folded sedimentary formations are seen along tectonic boundaries and the South Turkestan suture zone in the northern part of Afghanistan. Figure 2 shows the geology of Afghanistan

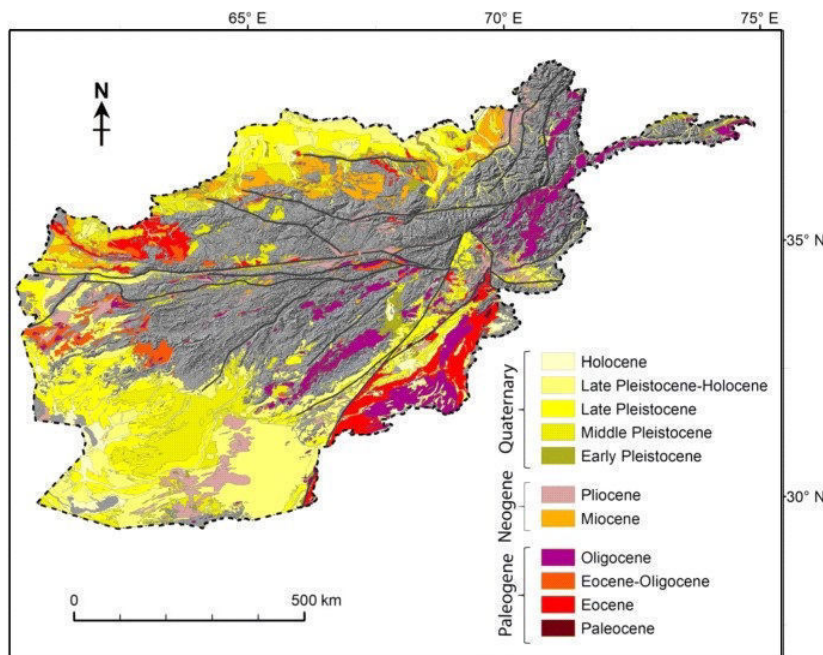


Figure 2. Geology of Afghanistan (from USGS)

Afghanistan is in Eurasian orogenic belt and one of the seismically active belts in the world. Modern fault movements, deformations, and earthquakes in Afghanistan are driven by the northward subduction of Indian and Arabian plates beneath Eurasia plate (Figure 1 & 3). The subduction of Arabian plate along Makran subduction zone and the intrusion of Indian plate into Eurasian plate resulted in some major tectonic structures in the region. The Chaman Fault System is said to be accommodating 200 km relative slip and caused some earthquakes greater than 7. The most recent event was the 1935 Quetta earthquake. The subduction Arabian plate beneath Eurasian plate causes a relative slip between the Lut block in Iran and the Helmand/Sistan block of Afghanistan, and it is called Sistan Suture zone.

The active faults within Afghanistan can be divided into 5 fault systems; namely, Chaman, Hari-rud (Herat) and Central Badakhshan fault systems and Helmand internal fault system and South Turkestan fault system (Figure 1b). In the southeastern Afghanistan and adjacent Pakistan, the Chaman fault system accommodates much of the differential movements between the Indian and Eurasian plates. The fault system has a reported slip rate of 2-20mm/year and higher where it enters western Pakistan. The Indian plate has a 20-40mm/year velocity where it comes close to a 300-400km segment of Chaman fault between (31°N-33.5°N), suggesting that $M > 7.0$ could occur at 200 years interval in this location. In central Afghanistan, the Hari Rud (Herat) fault having dextral sense extends from north of Kabul westward to Iran border with a slip rate of 2mm/year, but evidence for active faulting remain controversial. In northeast Afghanistan, Badakhshan and Dawraz-Karakul faults extends into in Pamir and Hindu Kush Mountains. Further north next to Turkmenistan and Uzbekistan, there are some faults such as Turkestan fault zone and Andarabad fault. Hindukush region of Afghanistan is seismically very active (Malistani et al. 2016; Nasiry 2020). The next seismically active regions are located along Chaman fault in east, Chagai Arc and Makran region in south and Sistan Suture Zone along Iran and Afghanistan Border in west. The north Afghanistan is also known to be very seismically active with earthquakes greater than M7.

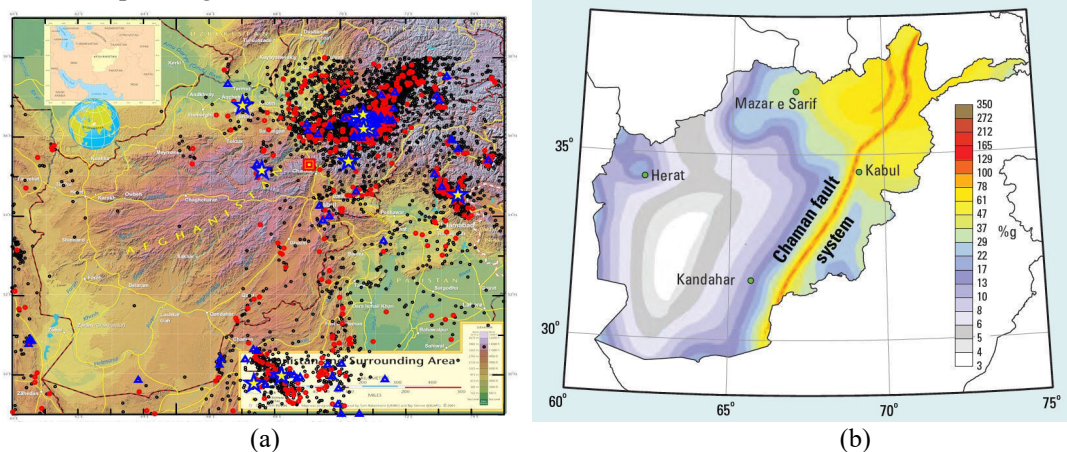


Figure 3. (a) Recent seismicity (from Malistani et al. 2016) and (b) estimated maximum ground acceleration for Afghanistan (from USGS).

3 SLOPE FAILURES AND SOME EXAMPLES FROM AFGHANISTAN

3.1 Slope Failures

The slope failures induce tremendous damage to infrastructures as well as to residential areas, and they involve not only cut slopes but also natural rock slopes. Compared to the scale of soil slope failures, the scale and the impact of rock slope failures are very large and the form of failure differs depending upon the geological structures of rock masses of slopes (Figure 4) (Aydan 1989, 2017, 2018; Aydan et al. 1989, 2011, 2012). The slope stabilities may be categorized into three classes. The first category involves the failure of intact material under shearing, tensile or compressive stresses and the failure modes are shear or bending failure. The second category

failures involve the failure of intact rock in shear or tension and slip or separation of discontinuities. The failure modes are combined shearing and sliding, buckling and flexural toppling failures. The third category is associated with the slip or separation of discontinuities and failure modes are planar or wedge sliding, toppling and/or block buckling failure. Furthermore, the failure of the rock slope failures may involve both active and passive modes under dynamic conditions such as earthquakes. However, the passive modes are generally observed when the ground shaking is quite large.

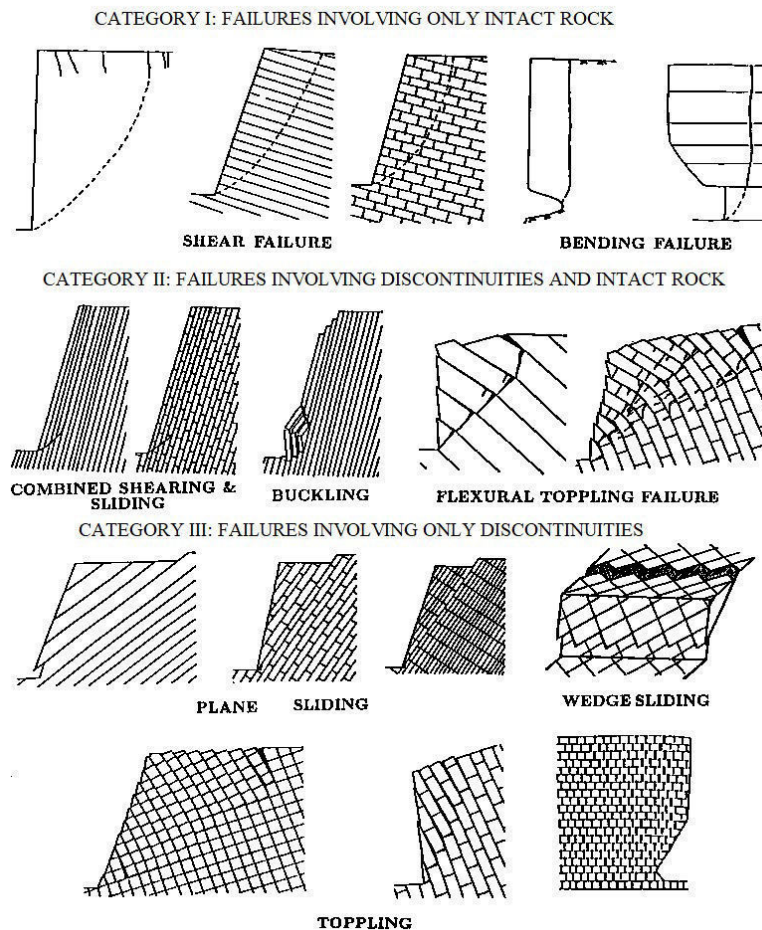


Figure 4. Active failure modes of rock slopes (modified from Aydan 1989, 2020).

3.2 Examples of Slope Failures in Afghanistan

A survey of available digital images from various parts of Afghanistan related to the issues of this study was implemented. The pictures are trimmed for the purpose of this study and rearranged. Figures 5-10 show the failures according to the classifications given in previous subsection. As noted from Figures 5 to 10, the failures of rock slopes obey to those known in Rock Slope Engineering. They clearly indicate that the slope cuts must be evaluated according to the well known principles and techniques developed and utilized in Rock Slope Engineering. The natural rock slopes are much more difficult as the information would be quite limited and it must be borne in mind that earthquakes and time-dependent weathering and degradation are another important parameters. Some guidelines would be presented for this purpose (Aydan 2017, 2020).

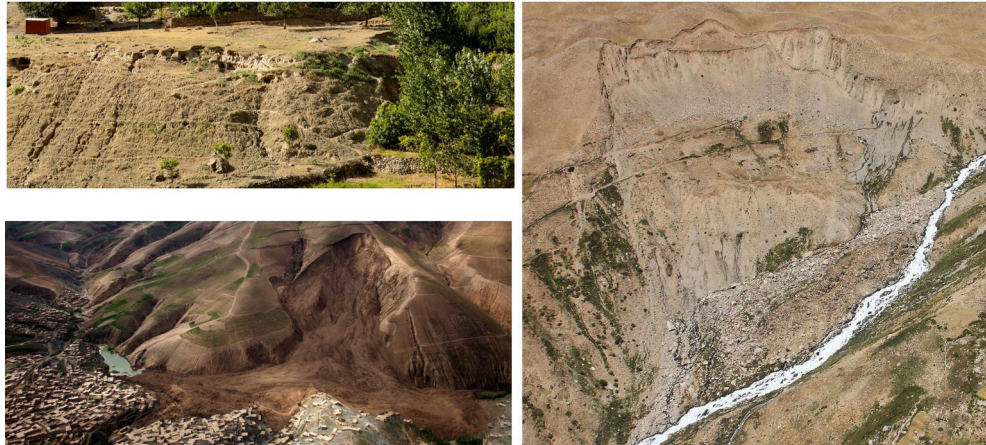


Figure 5. Slope failures belonging to Category I involving shearing.



Figure 6. Slope failures belonging to Category I involving bending due to differential weathering.



Figure 7. Slope failures belonging to Category II involving combined shearing and sliding or flexural toppling.



Figure 8. Slope failures belonging to Category III involving planar or wedge sliding



Figure 9. Slope failures belonging to Category III involving columnar toppling.



Figure 10. Slope failures belonging to Category III involving rock falls

4 STRONG-MOTION ESTIMATIONS FOR KANDAHAR

This section is based on a recent study by Nasiry (2020) and Nasiry and Aydan (2022) on the strong motion estimation for some hypothetical earthquakes along Chaman fault with an emphasis on Kandahar Region. The Chaman Faults pass Kandahar City at a distance of 100 km. An earthquake along this fault occurred in 1935 with an estimated magnitude of 7.7-7.8. The fault parameters given in Table 1 were used to estimate ground motions at the epicenter and Kandahar City for a rocky ground. Figure 11(a) shows the fault, location of Kandahar City and the asperity distribution for Green-function method. The estimated AMAX and VMAX are 77 gals and 26 kines. Figure 11(b) shows the estimated ground acceleration records at the epicenter and Kandahar City by using the Sugito's method. Figure 13 shows the AMAX and VMAX contours estimated to according to Aydan's method (Aydan 2007, 2012) and the estimated AMAX and VMAX are 77 gals and 26 kines. The estimated AMAX and VMAX at Kandahar City are 211 and 27 kines by the Sugito's method. While the estimated AMAX by the Sugito's method is much larger, the estimated VMAX values are close to each other. ground motions are somewhat closer to each other.

Table 1. Characteristics of anticipated earthquake.

Length (km)	Mw	Slip (cm)	Duration (s)
168	7.7	600	40

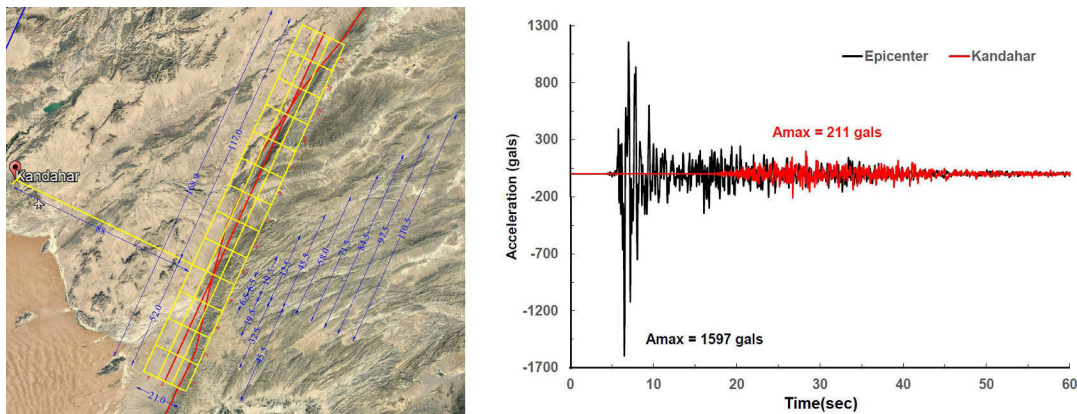


Figure 11. (a) Location of Kandahar and discretised fault into equal elements and source parameters and (b) Estimated accelerations at the epicenter & Kandahar.(from Nasiry and Aydan 2022).

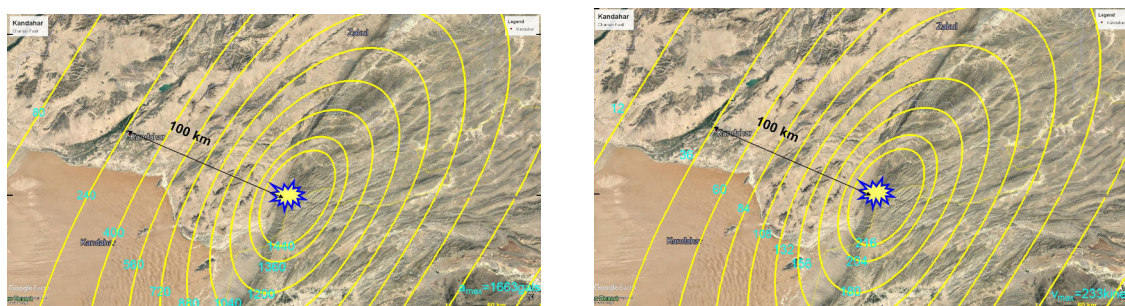


Figure 12. Estimated (a) AMAX and (b) VMAX contours for M7.7 earthquake on Chaman fault

5 GUIDELINES FOR ASSESSING THE STABILITY OF SLOPES

The stability assessment of rock slopes should consider by classifying slopes as soil slopes and rock slopes. Soil slopes can be generally analyzed using limiting equilibrium methods based on circular sliding method with several variations. Although numerical analyses based on FEM or FDM may also be used, it is not common to do so. As said before, the scale of soil slope fail-

ures is small while the scale and the impact of rock slope failures are very large and the form of failure differs depending upon the geological structures of rock mass of slopes (Figure 4) (Aydan 1989; Aydan et al. 1989, 1991, 2011). Aydan (1989, 2017, 2016, 2018, 2020) and Aydan et al. (1989, 1991) proposed an approach combining several methods based on the limiting equilibrium approach. This approach can be utilized for any slope of rock including soil slopes also. The readers are recommended to refer quoted references to determine the limiting stable slope angle under the given seismic, geometrical and physical conditions.

Figure 13 shows a plot of the slope angle of various rock slopes versus the inclination of the thoroughgoing discontinuity set, whose strike is parallel or nearly parallel to the axis of the slope. The plotted data include the data on stable and unstable natural rock slopes as well as manmade stable and man-made unstable rock slopes. Plotted data cover Afghanistan. In the plots, the stability charts of a slope with a ratio of $t/H:1/75$ for cross continuous and intermittent patterns ($\xi=26.5^\circ$) for $\eta=0.0$ are also included to have a qualitative insight rather than a quantitative comparison. The chosen value of t/H is arbitrary and may not correspond to the ratios of slopes plotted in the figure. It is also interesting to note there is almost no failed slopes when the slope angle is less than $25-30^\circ$ and most of the failed slopes have a slope angle greater than $25-30^\circ$. This is in accordance with the conclusion of Keefer (1984). Nevertheless, it is also noted that there are a great number of stable slopes having slope angle greater than $25-30^\circ$. This implies that the angle and the height of slopes cannot be only parameters determining the overall stability of natural rock slopes. Therefore, their geometrical orientations of discontinuities with respect to slope geometry and their mechanical properties and loading conditions must also play a great role in determining the stable angles of natural rock slopes. The results shown in Figure 13 may serve as guidelines for a quick assessment of the stability of natural rock slopes and how to select the slope-cutting angle in actual constructions involving rock slopes.

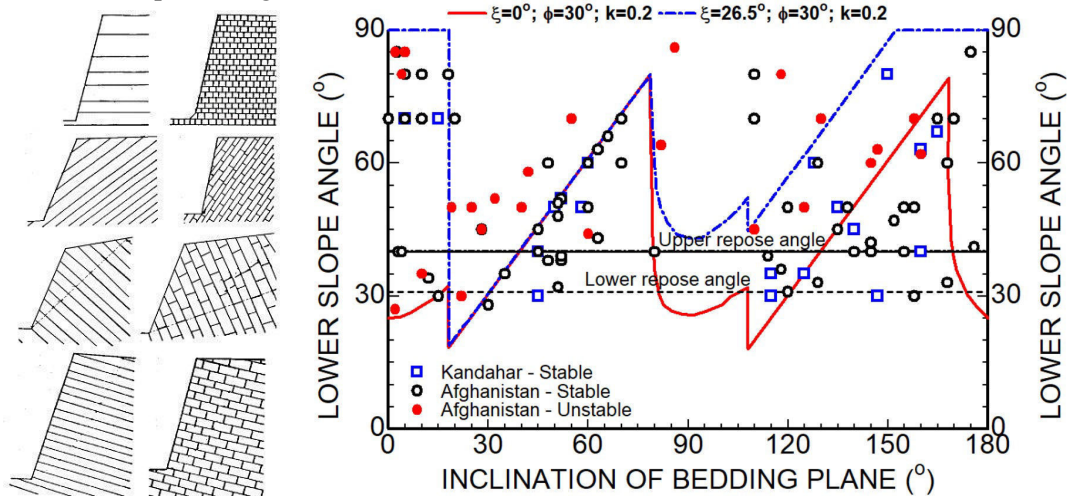


Figure 13. The relation between slope angle and bedding plane angle for stable and failed case histories in Afghanistan.

For practical purpose to assess the stability of slopes, Keefer (1984) studied slope failures induced by earthquakes and he proposed some empirical bounds for slope failures, which are classified as disrupted or coherent. However, the empirical bounds of Keefer are not specifically given as formula. Aydan et al. (2009, 2012) and Aydan (2007, 2017) also compiled slope failures caused by recent worldwide earthquakes according to Keefer's classifications and proposed an empirical equation for the maximum hypocentral distance of disrupted and coherent slope failures as a function of earthquake magnitude and fault orientation as shown in Figure 14. This approach can also be used for practical purposes to assess the stability of rock slopes subjected to earthquakes in the region.

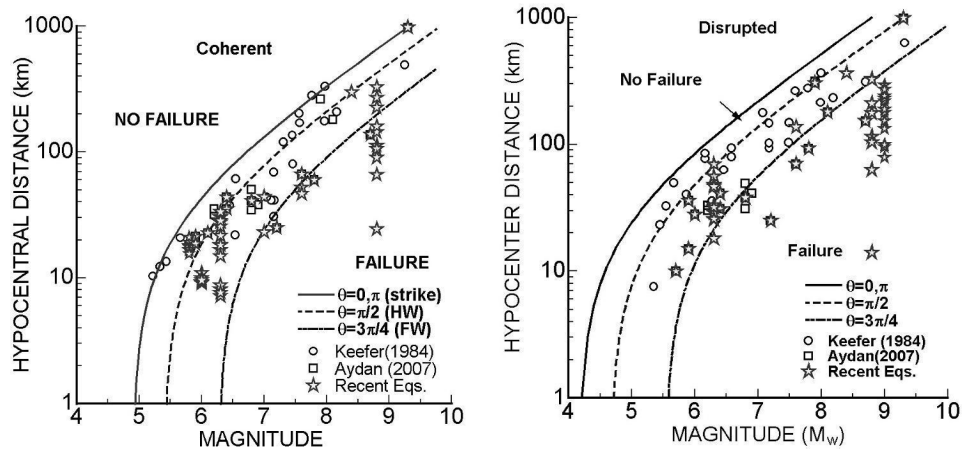


Figure 14: Comparison of empirical relations with observations.



Figure 15. Views of natural slopes in the close vicinity of Kandahar.

6 SUGGESTIONS FOR SLOPE STABILITY ISSUES IN KANDAHAR REGION

As explained in previous sections, the slope stability assessment should be carried out according to the principles of modern principles of rock slope engineering and some possible approaches are briefly explained in the previous section. The volcanic rocks and folded sedimentary units exist in the vicinity of Kandahar region. Furthermore, the south of Kandahar is covered sand dunes and called Registan Desert (Figure 15). Some possible rock slope stability issues considered on the bases of the geographical and physical conditions and available photos with the knowledge of Rock Mechanics and Rock Engineering as well as modern rock slope engineering. The structural geology of the slopes of the region implies that planar sliding or wedge sliding and columnar toppling are possible. Furthermore, the faults may facilitate more complex failure modes. In addition, some failures are possible due to degradation and differential weathering of rock masses. The simplest yet economical solution would be providing some safety zones between slopes and settlements as recommended by Aydan et al. (2009) for Kashmir, if necessary. In addition, some rock anchoring, dewatering and prevention of rock degradation, which may not be very economical, could be implemented.

7 CONCLUSIONS

Some possible rock slope stability issues in Afghanistan with a special emphasis on Kandahar region have been considered in this study based on information gathered from available sources of documents and photos in the lights of principles of Rock Mechanics and Rock Engineering, Engineering Geology, and modern Rock Slope Engineering. It is clarified that the slope failures observed in Afghanistan are quite similar to those observed in other regions of the world. Therefore, when the slopes are to be cut in relation to new construction, the well-known principles of modern Rock Slope Engineering. Furthermore, the stability of natural rock slopes would be necessary and their stability condition must be evaluated by considering likely earthquake motions as well as rock mass conditions. There may be some rock slope stability issues during the construction of new transportation structures, existing and planned dams and open-pit mines and the current static and seismic design of slopes can be adopted.

REFERENCES

- Aydan, Ö. 1989. The stabilization of rock engineering structures by rockbolts. *Doctorate Thesis*, Nagoya University, 204 pages.
- Aydan, Ö. 2007. The inference of seismic and strong motion characteristics of earthquakes from faults with a particular emphasis on Turkish earthquakes. *The 6th Nat. Earthquake Eng. Conf. of Turkey*, 563-574.
- Aydan, Ö. 2012. "Ground motions and deformations associated with earthquake faulting and their effects on the safety of engineering structures." *Encyclopedia of Sustainability Science and Technology*, Springer, R. Meyers (Ed.) 3233-3253.
- Aydan, Ö. (2017). *Rock Dynamics*. CRC Press, ISRM Book Series No.3, 462p.
- Aydan, Ö. (2020). *Rock Mechanics and Rock Engineering: Volume 2: Applications*. CRC Press, Taylor and Francis Group, 383p.
- Aydan, Ö., Shimizu, Y., Ichikawa, Y. 1989. The Effective Failure Modes and Stability of Slopes in Rock Mass with Two Discontinuity Sets. *Rock Mechanics and Rock Engineering*, **22**(3), 163-188.
- Aydan, Ö., Y. Ichikawa, Y. Shimizu, and K. Murata (1991). An integrated system for the stability of rock slopes. *The 5th Int. Conf. on Computer Methods and Advances in Geomechanics*, Cairns, **1**, 469-465.
- Aydan, Ö., Ohta, S., Hamada, M. 2009. Geotechnical evaluation of slope and ground failures during the 8 October 2005 Muzaffarabad Earthquake, Pakistan. *Journal of Seismology*, **13**(3), 399-413.
- Aydan, Ö., Ohta, Y., Daido, M., Kumsar, H. Genis, M., Tokashiki, N., Ito, T., Amini, M. 2011. Chapter 15: Earthquakes as a rock dynamic problem and their effects on rock engineering structures. *Advances in Rock Dynamics and Applications*, CRC Press, Taylor and Francis Group, 341-422.
- Aydan, Ö., Ulusay, R., Hamada, M. and Beetham, D. 2012. Geotechnical aspects of the 2010 Darfield and 2011 Christchurch earthquakes of New Zealand and geotechnical damage to structures and lifelines. *Bulletin of Engineering Geology and Environment*, **71**(4), 637-662.
- Keefer, D.K. 1984. Slope failures caused by earthquakes. *Geological Society of American Bulletin*, **95**, 406-421
- Malistani, N., Ö. Aydan, J. Tomiyama (2016). Preliminary Rock Engineering Assessment of Salang Tunnels (Afghanistan). *EUROCK2016, Ürgüp*, 763-769.
- Nasiry, N.Z. (2020). A fundamental study on the seismic risk and seismic vulnerability of common buildings in Afghanistan. Doctoral Thesis of Engineering, University of the Ryukyus Graduate School of Science and Engineering, 154p.
- Nasiry, N.Z. and Aydan, Ö. (2022). Estimation of ground motions due to potential earthquakes along Chaman Fault with particular emphases on Kabul and Kandahar Cities in Afghanistan. *RocDyn4, Xuzhou* (in press).
- Nemati, M. (2018). Seismotectonic and seismicity of Makran, a bimodal subduction zone, SE Iran. *Journal of Asian Earth Sciences* **169**, 139-161.
- Sugito, M., Furumoto, Y. & Sugiyama, T 2000. Strong Motion Prediction on Rock Surface by Superposed Evolutionary Spectra, 12th World Conference on Earthquake Engineering, 2111/4/A, CD-ROM.

Geotechnical design of temporary support for a drinking water transfer tunnel

R.G. Ruiz

Universidad de Costa Rica, San José, Costa Rica

ABSTRACT:

The geotechnical design of the tunnel consists of adequately establishing the geotechnical model, with a characterization of both the parameters of the intact rock and the rock mass, which allows the application of different geomechanical classification methodologies, as well as the establishment of the main parameters of deformability and shear strength for the different materials, which can then be used in the geotechnical design of the temporary support. The geotechnical design of the tunnel is focused on establishing the necessary temporary support to guarantee the adequate convergence of the materials that make up the different geotechnical units identified along the entire route of the tunnel, which will later allow the conceptualization and design of the final lining.

1. INTRODUCTION

The geotechnical design of this tunnel is part of a set of works that make up a project to supply water to the Central Region of Costa Rica, which aims to provide a flow of about 2,5 m³/s in addition to the 2,1 m³/s already being extracted.

The development of this project is intended to mitigate the consequences of the lack of drinking water that is experienced year after year by a large part of the population of the cantons of San José, Costa Rica, during the months of the country's dry season.

1.1. Problem statement

The geotechnical design of a tunnel involves an important study of the materials it passes through along the proposed alignment, evaluating outcrops and carrying out a strong surface geology work. The methods of investigation must be in accordance with the geological setting, the objectives and the scope of the investigation that must be outlined from the previous stages of the project.

A series of aspects must be evaluated, among which stand out the evaluation of potential geological-geotechnical problems, the geomechanical characteristics of the materials, the presence of complex geological structures such as faults or discontinuities along the tunnel route, evaluate the terrain conditions, mainly in mountainous areas, as well as consider control measures for instabilities, filtrations and treatments of the materials to be excavated.

The work is located in a mountainous context, which makes it difficult in many cases that the research is carried out from the surface, mainly due to issues associated with access for the entry of drilling equipment, having to resort to indirect research methods, such as geophysical techniques of seismic refraction and electrical resistivity.

It is required to establish a proposal of temporary support for the construction of a tunnel, which presents a length equal to 4600 m and an equivalent diameter of 4,30 m, located in a varied geological context and in a condition of varied lithological cover above the tunnel, without forgetting that the entire route of the tunnel is subjected to a significant hydrostatic load.

Different temporary support alternatives should be evaluated, such as friction bolts, shotcrete in different thicknesses, steel arches in different profiles, and in those sectors with high stress concentration and low geomechanical quality of the materials, the excavation of a lower arch ("invert") should be considered. It is not excluded that injections at the excavation face should be recommended to consolidate and improve the medium to be excavated.

Figure 1 shows the location of the topographic environment where it is intended to design and build the tunnel for the transfer of drinking water.



Figure 1. Drinking water conduction tunnel route.

Source: Google Earth, 2021

1.2. Scope

The characterization of the materials present along the route of the tunnel is carried out, using the results obtained from the execution of tests by indirect methods, such as seismic refraction, as well as electrical resistivity. In addition, a set of perforations were made from the surface, which allowed obtaining samples of intact rock, for the execution of tests in the laboratory, which allowed characterizing the materials and thus obtaining the properties of the intact rock for each of the geotechnical units identified.

The characterization of the rock mass was carried out thanks to the estimation of the intact rock properties, as well as the use of Rocscience's RocData 3.0 software, using the Hoek-Brown and Mohr-Coulomb criteria.

A preliminary establishment of the type of temporary support will be carried out according to empirical methods valid for tunnels excavated according to the conventional method. Subsequently, two-dimensional finite element models will be used to evaluate the most suitable type of temporary support, according to the shear strength and deformability properties of the different geotechnical units identified along the entire alignment of the subway work. For this purpose, the Rocscience RS2 program will be used.

Alternatives will be sought to stabilize the materials that make up the rock massif, using steel profiles to form arches, excavation of the lower arch of the tunnel, shotcrete in different thicknesses, friction bolts, as well as proposing techniques to stabilize the excavation face, if necessary, given the characteristics of the materials to be expected.

1.3. Methodology

The details of the methodology to be carried out are described below:

It begins with obtaining the geological-geotechnical investigation that has been carried out along the entire route of the subway work on the same materials identified in situ, considering those investigations in other works near the route of the conduction tunnel for drinking water.

As part of the design work, a review of the geological environment is carried out, to consider the factors that could intervene in the geotechnical design of the work, such as the consideration of lithostatic and hydrostatic loads, the existence of geological faults along the entire route of the tunnel, lithological changes along the entire alignment, among the main aspects.

Subsequently, all available information is analyzed to establish a geotechnical model along the entire route of the subterranean work, which allows defining the properties for each of the different geotechnical units that are identified.

Once the pressures that intervene on the excavation have been determined, in this case the lithostatic pressure, as well as the hydrostatic pressure, we proceed to make a support proposal based on empirical methods used in the design of tunnels, allowing in this way to establish a first theoretical support proposal, which serves as reference to the analysis of stresses and deformations from which the definitive alternatives of the temporary support will be obtained.

The stress and deformation analysis is performed for each section of the tunnel that presents some special condition, with issues associated with coverings, presence of geological faults, hydrostatic pressures on the crown of the tunnel, as well as with the geomechanical properties of the different geotechnical units along the tunnel route. This analysis is performed by means of Rocscience RS2 software.

Once the definitive temporary support has been established, the main geotechnical risks that could occur at the time of excavation of the subway work are to be identified for each excavation section.

2. GEOLOGY

2.1. Regional geology

Sedimentary rocks from the Tertiary Period are identified in the project area, as well as the presence of more recent intrusive and extrusive igneous rocks. This area has very strong active tectonics, as it is surrounded by faults considered geologically active, such as the Navarro fault and the Agua Caliente fault.

The following figure shows an adaptation of the regional geology, highlighting the area where the zone of interest is located.

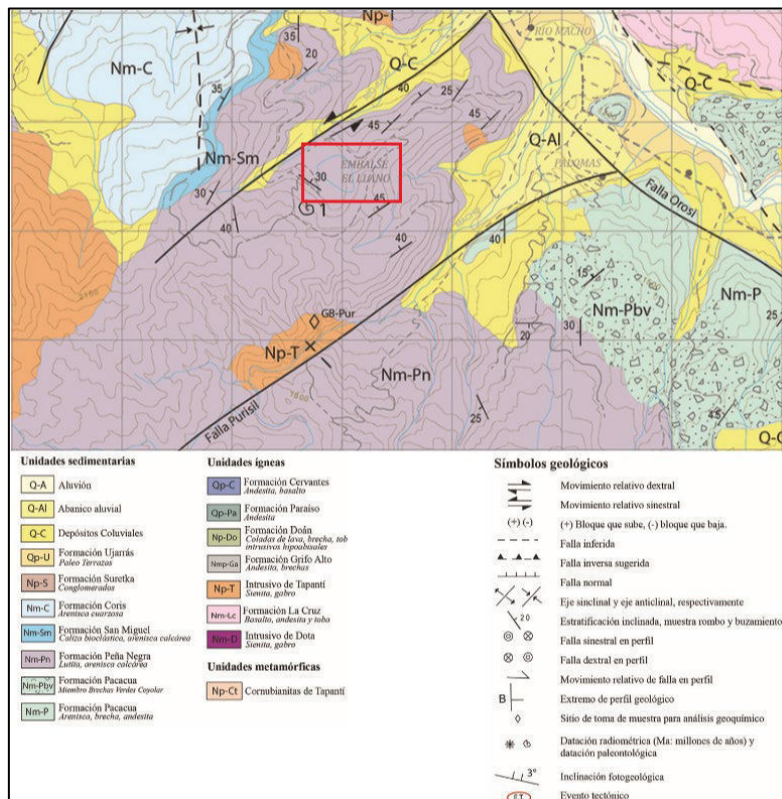


Figure 2. Regional geological map.

Source: Sojo et al., 2017

2.2. Local geology

The geological formations along the entire tunnel route comprise several lithologies, which are detailed below:

2.2.1. Regolith soils

According to Espinoza (2020), which correspond to soils composed of weathered blocks of adjacent rock, sandy silt matrix, in contact with the blocky structure of the rock, the sills generate a structure of arenitization around the fractures and weathering of the rock.

2.2.2. Andesitic sills

According to Espinoza (2020), which correspond to healthy rock, hard, slightly to moderately weathered, fractured rock, with at least 3 families of joints, with decimetric to metric separation, fractures little altered. This unit is stratified with sandstones and breccias of the underlying formations, they are quite thick in the area, so there are sections of up to 80 m thick intercalated with the breccia, shales, and sandstone units.

2.2.3. Silicified sandstones

Espinoza (2020) points out that these are rocks that are silicified due to the hydrothermalization of fluids with silica as the main cementation, they are composed of sandstones, they present fossil fragments, they are hard, healthy rocks, they are altered to an orange color due to alteration by fault zones.

2.2.4. Breccias and sandstones

According to Espinoza (2020) it corresponds to healthy rock, silicified, hard, brecciated texture, moderately fractured, fractures of three main families, transitional contact with sills.

2.2.5. Shales

According to Espinoza (2020), it corresponds to hard, healthy rock with presence of shell fossils, highly fractured, affected by andesitic sills, which generate alterations in its structure, when weathered it is friable and of very low rock quality. In the surrounding area it appears as a healthy rock, little altered.

Finally, the detail of the geological model of the materials identified along the tunnel route is shown in Figure 3.

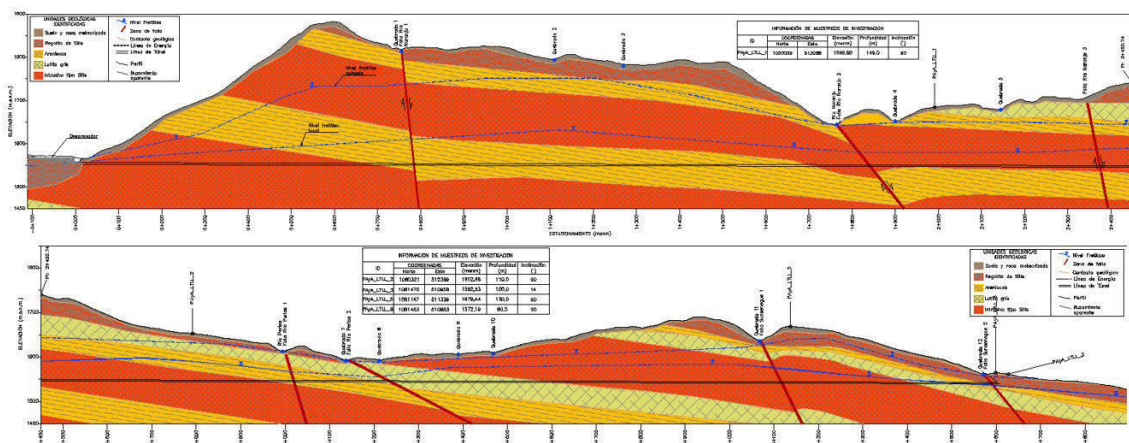


Figure 3. Geological model defined along the entire tunnel route.
 Source: Espinoza, 2020

3. CHARACTERIZATION OF MATERIAL AND GEOTECHNICAL MODEL

3.1. Determination of material properties

Laboratory tests were carried out by obtaining intact rock samples from five boreholes along the entire tunnel route. In addition, indirect information was obtained from seismic refraction profiles, as well as electrical resistivity profiles that were carried out along the entire surface of the tunnel.

Through the realization of continuous seismic refraction and electrical resistivity profiles, with a length of 4600 m, both carried out from the surface of the tunnel route, it was possible to carry out an indirect characterization of the materials along the entire tunnel alignment.

It was then possible to obtain the compressional wave velocity v_p , as well as to obtain the electrical resistivity values for each of the lithologies identified along the entire tunnel alignment.

A total of 41 samples of intact rock and regolith soils were obtained from the 5 boreholes drilled along the tunnel route, which were divided into 20 intrusive samples, 11 sandstone samples and 10 regolith soil samples.

From the set of samples obtained, it was possible to obtain the following laboratory parameters for the intact rock:

- Porosity (n).
- Specific gravity (G_s).
- Specific gravity saturated dry surface (G_{SSS}).
- Absorption (Abs).
- Specific dry weight (γ_s).
- Simple compressive strength (σ_c).
- Tensile strength (σ_t).
- Ultrasonic pulse velocity (v_p).
- Triaxial strength.

For the case of the samples obtained for the regolith soil, it was possible to obtain the following laboratory parameters:

- Specific gravity (G_s).
- Specific dry weight (γ_s).
- Simple compressive strength (σ_c).
- Undrained shear strength (s_u).

As a result of the characterization carried out for the intact rock, we proceeded to characterize the rock mass for each of the geotechnical units that were defined, using Rocscience's RocData 3.0 software, which allows an analysis of the rock mass, based on the estimation of parameters of the intact rock.

Therefore, using the data obtained from the triaxial tests carried out for both intrusives and sandstones, it was possible to estimate the input parameters for the application of the Hoek and Brown classification, in this case, the simple compressive strength and the m_i parameter, which depends on the origin and texture of the rock.

By establishing the remaining two parameters of the classification, such as the GSI and the disturbance factor D , it was possible to establish the nonlinear failure criterion of Hoek and Brown.

The software allows establishing the resistance parameters of the Mohr - Coulomb criterion, equivalent to the nonlinear failure criterion of Hoek and Brown. In this case, the failure envelope range for tunnels was used, which considers two aspects: the tunnel coverage and the unit weight of the materials.

3.2. Geotechnical model

A total of four main geotechnical units were established with their respective subdivisions, which are described below:

3.2.1. Geotechnical Unit UG1 - Sills intrusive

Within this unit are considered intrusive bodies of the sills type, which correspond to laminar intrusions of sub horizontal disposition that have been deposited under the same dip of the sedimentary units that outcrop at the site.

3.2.2. Geotechnical Unit UG2 - Sandstones with shale intercalations

Within this unit, sedimentary lithologies are considered, in this case silicified sandstones and gray shales, both improved in their mineralogical composition as a consequence of the increase in temperature that these materials underwent in the presence of the intrusive deposited in the form of sills. They are categorized in two sub-units to differentiate between sandstones and shales.

Geotechnical Unit 2a: Corresponds to the materials identified as sandstones.

Geotechnical Unit 2b: Corresponds to the materials identified as gray shales.

3.2.3. Geotechnical Unit UG3 - Sills regoliths

Within this unit are considered the altered deposits of the sills type intrusive. They correspond to regolith soil deposits, unconsolidated, altered materials, which may present rock fragments, wrapped in a generally clayey matrix.

3.2.4. Geotechnical Unit UG4 - Materials affected by the presence of faults

Within this unit are considered all the materials that are affected by the presence of a geological fault. In total, six sectors have been identified with the presence of faults, which cut the route of the tunnel, mainly affecting the geotechnical units 1 and 2, which correspond to the sills and sandstones with shales.

In this particular case, geotechnical unit 4 is subdivided into a total of 3 sub-units, which allows classifying the fault zones according to the lithology in which they occur.

Geotechnical Unit 4a: Corresponds to the materials affected by the presence of a geological fault in the sandstone lithology.

Geotechnical Unit 4b: Corresponds to the materials affected by the presence of a geological fault in the intrusive lithology.

Geotechnical Unit 4c: Corresponds to the materials affected by the presence of a geological fault in the lithology of shales.

A guitar table has been generated where all the necessary information of the geotechnical model is included. The detail of the information included in the following table, along the entire tunnel route, is presented below:

- Geological lithology.
- Geotechnical unit.
- Vertical cover of the tunnel.
- Hydrostatic load considered.
- Characterization by indirect methods (seismic refraction and electrical resistivity).
- Geotechnical characterization of intact rock.
- Geomechanical classifications.
- Modulus of elasticity of the rock mass, E_{mr} .
- Shear strength of the rock mass.

The guitar table condenses all the characterization information of the different geotechnical units identified along the tunnel route. However, due to its size it is not possible to present it in this document, since it is not compatible with the format to be respected for this article.

Figure 4 shows the identification of the different geotechnical units along the entire tunnel route, based on the geological model.

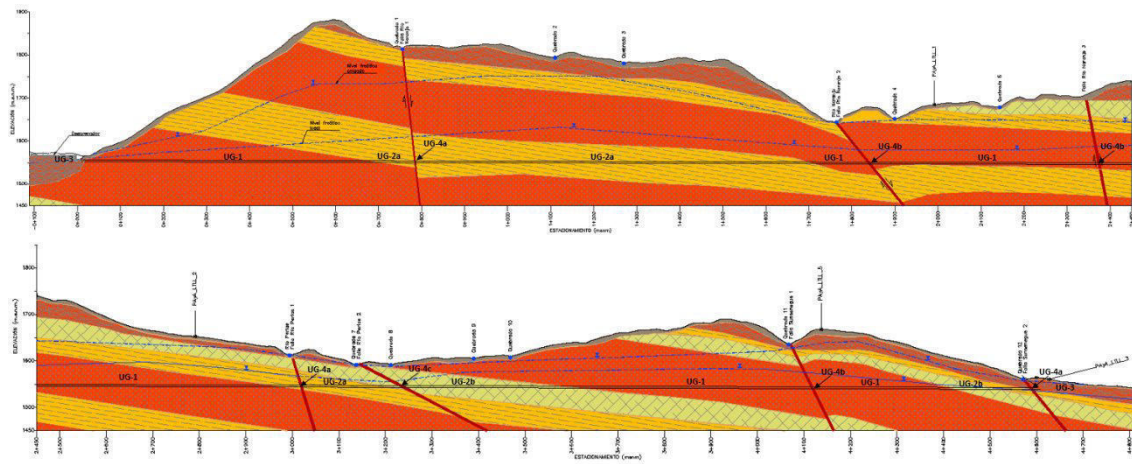


Figure 4. Geological model defined along the entire tunnel route.
 Source: Espinoza, 2020

4. ESTABLISHMENT OF TEMPORARY SUPPORT

4.1. Temporary support by empirical methods

It is possible to establish the characteristics of the temporary support of a tunnel by means of empirical methods. In our case, we used the method proposed by Gianfranco Perri in 2006 for tunnels excavated by the conventional method.

For each of the geotechnical units that were established, the excavation competence index (IC) was estimated for the minimum and maximum coverages along the tunnel route for each geotechnical unit identified, as summarized in Table 1 below.

Table 1. Definition of the parameters for the type of competence according to Perri.

UG	σ_{cm} (MPa)	GSI	H_{min} (m)	H_{max} (m)	IC_{max}	IC_{min}	RMR	H_i (m)	H_s (m)
UG-1	31.23	74	30.0	327.6	2.17	23.66	63-80	2.9	63.6
UG-2a	24.62	65	44.9	283.7	1.97	12.46	53	3.3	55.9
UG-2b	22.07	60	24.6	90.7	5.53	20.39	54	3.6	51.6
UG-3	0.01	20	11.8	24.6	0.01	0.02	< 20	10.8	17.2
UG-4a	1.42	35	261.9	265.6	0.12	0.12	< 30	6.1	30.1
UG-4b	0.36	20	65.0	155.5	0.05	0.13	< 20	10.8	17.2
UG-4c	0.31	20	44.9	58.6	0.12	0.16	< 20	10.8	17.2

According to the above, it was possible to delimit for each geotechnical unit the type of excavation behavior referred to the criteria of Perri (2006), as well as to associate it to a type of minimum necessary temporary support, according to the same criteria.

Table 2. Definition of the type of excavation behavior according to Perri (2006).

UG	H (m)	Behavior Type	Type of Coverage	Type of Support Estimated
UG-1	30.0 - 327.6	A / B	Intermediate/High	SP-A / SP-B
UG-2a	44.9 - 283.7	A / B	Intermediate/High	SP-A / SP-B
UG-2b	24.6 - 90.7	B	Intermediate/High	SP-B
UG-3	11.8 - 30.0	C	Intermediate	SP-E
UG-4a	261.9 - 265.6	E	High	SP-E
UG-4b	65.0 - 155.5	E	High	SP-E
UG-4c	44.9 - 58.6	E	High	SP-E

4.2. Identification of the main geotechnical hazards during excavation

The multiple graph proposed by Russo (2014) is used to identify those potential geotechnical hazards for each geotechnical unit, along the tunnel excavation route.

Despite the preliminary character of the prediction, which involves some simplifying assumptions e.g. circular tunnel in homogeneous rock mass, isotropic, equivalent continuous modeling, $k = 1$, the described method can be a useful tool, either in the early design phases, for a quick identification of potential critical scenarios and in the construction phase, for the selection of the appropriate type of support section at the tunnel face based on the predefined design criteria.

In the following, each of the geotechnical units defined for the case of the tunnel route are identified within the multiple chart established and updated by Russo (2014).

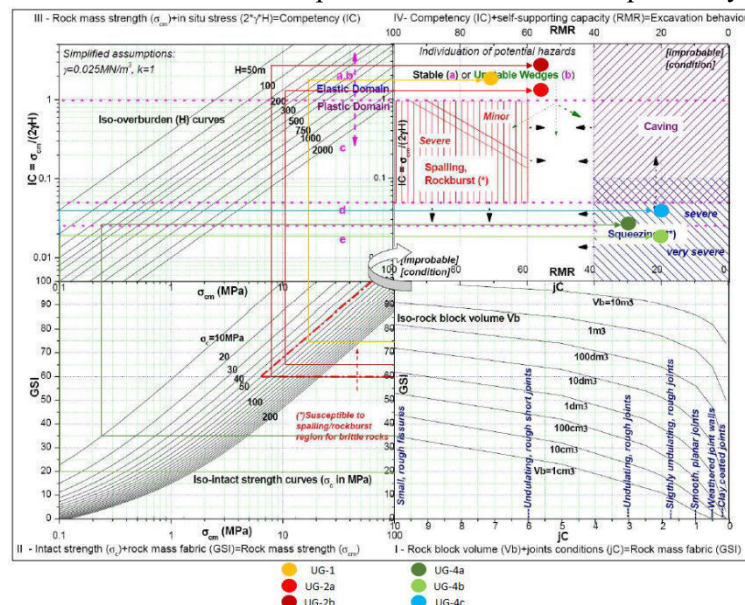


Figure 5. Identification of potential geotechnical hazards employing Russo's (2014) multiplot for each of the geotechnical units along the tunnel route.

Source: Adapted from Russo, 2014

4.3. Stress and strain analysis by finite methods

A total of 14 cross sections were analyzed along the entire length of the tunnel, considered as critical analysis sections, by means of which the type of temporary support for the entire tunnel was established.

For each critical cross-section, a total of 3 different types of temporary support were analyzed, where the characteristics of each were evaluated by comparing the following variables:

- Radius of the plasticized zone.
- Ratio between the plastic radius and the radius of the tunnel section.
- Maximum displacement recorded.
- Percentage of convergence obtained, with respect to the tunnel diameter.

The results obtained for one of the 14 cross sections analyzed are presented below, as an example of the stress and deformation analysis carried out along the tunnel.

The analyzed section is located on the parking 3+237 m, within the geotechnical unit UG-4b, integrated in this case by fault materials within the gray shales.

The influence of temporary support on one of the sectors affected by the presence of a geological fault is analyzed in this section of the analysis.

A total of 3 types of temporary supports were analyzed. The first one corresponded to the inclusion of steel arches, considering a W8X31 profile, spaced every 1.0 m and accompanied by shotcrete, at a constant thickness of 0.10 m.

The second alternative is the same as the previous one, in terms of the inclusion of arches and shotcrete, only that it considers an increase in the thickness of the concrete, in this case to 0.15 m.

Finally, the third option consisted of increasing again the shotcrete to a constant thickness of 0.20 m, accompanying the arches made considering a W8X31 profile and under a reduction in the spacing defined in this case at 0.75 m.

The results obtained for each of the three types of temporary support analyzed in this case are shown in Table 3.

Table 3. Results obtained in the analysis of section 3+237 m for UG-4c materials.

Support Element		Type 1	Type 2	Type 3
Arches W8X31 and Shotcrete		Spacing: 1,0 m Thickness: 0,10 m	-	-
Arches W8X31 and Shotcrete		-	Spacing: 1,0 m Thickness: 0,15 m	-
Arches W8X31 and Shotcrete		-	-	Spacing: 1,0 m Thickness: 0,20 m
Plastic Zone Radio (m)	No Support (m)		11,538	
	With Support (m)	11,537	11,537	8,589
Rp / Ro	No Support		5,367	
	With Support	5,366	5,366	3,995
Maximum displacement (m)	No Support (m)		0,056	
	With Support (m)	0,053	0,051	0,021
Convergence (%)	No Support (%)		1,295	
	With Support (%)	1,233	1,184	0,477

Figure 6 shows the detail of the maximum displacements obtained in the contour of the excavation, for the type of support established. It can be seen that the maximum displacements recorded occur in the lateral part of the section, with a maximum value of 20,5 mm.

Similarly, the capacity graph of the type of support established for the UG-4c materials is shown, evaluating the condition of the shotcrete, as well as the W8X31 steel arches, both in shear and moment, under the consideration of 3 different values of the safety factor: 1.0, 1.2 and 1.4, respectively.

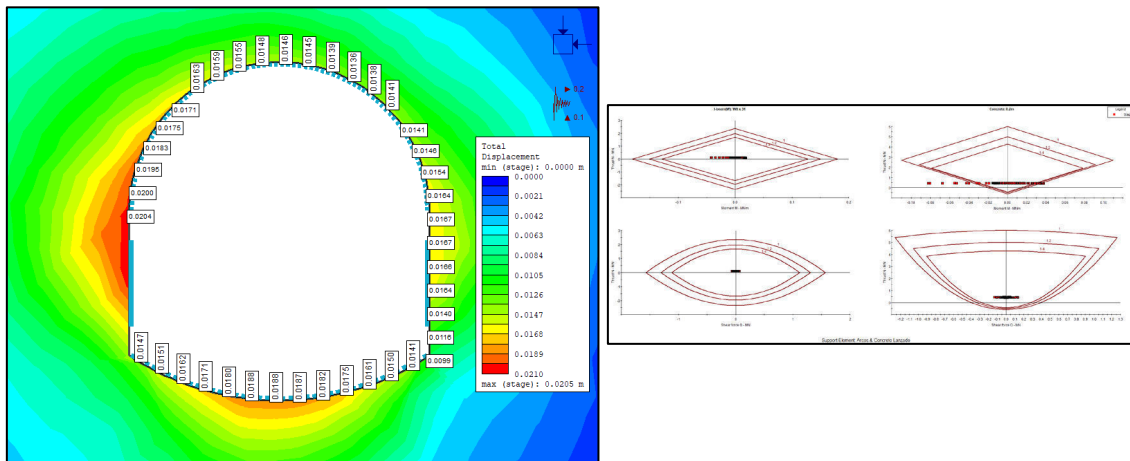


Figure 6. Detail of the vertical displacements in the contour of the excavation with the inclusion of the analyzed temporary support type 3 and the support capacity graph.
Source: RS2 2019 software output.

5. CONCLUSIONS

- The empirical method proposed by Perri (2006) was used for the design of the temporary support of the tunnel, which allowed to have a first approximation of the characteristics of the primary support, necessary to guarantee the stability of the subterranean work.
- The multiple graph established by Russo (2014) was used, which allows, according to the characteristics of the materials present at the site and that have been studied, to establish the main geotechnical risks that may be present in a subterranean excavation.
- A stress and deformation analysis was performed using the finite element technique by means of RS2 2019 software, which allowed the analysis of a total of 14 cross sections along the entire length of the tunnel, considered as critical sections, which allowed establishing the characteristics of the temporary support that was proposed along the entire route of the tunnel.

6. REFERENCES

- Espinoza , J. (2020). Informe de diseño: Ingeniería geológica y características geológicas Parte 2. Sabana, San José, Costa Rica.
- Perri, G. (2006). Clases de comportamiento y cargas de diseño para túneles excavados convencionalmente. Clases de comportamiento y cargas de diseño para túneles excavados convencionalmente (págs. 411-421). Cartagena, Colombia: Sociedad Colombiana de Geotecnia.
- Russo, G. (2014). An Update of the “Multiple Geaph” Approach for the Preliminary Assessment of the Excavation Behaviour in Rock Tunnelling. *Tunnelling and Underground Space Technology*, 74-81.
- Sojo, D., Denyer, P., Gazel , P., & Alvarado, G. (2017). Geología del Cuadrante Tapanti (1:50000). *Revista Geológica de América Central*, 83-116.

Analyzing the reasons behind a large wedge failure in a room-and-pillar roofing slate mine

L.R. Alejano

GESSMin, CINTECX, Dept. of Natural Resources and Environmental Eng., University of Vigo, Spain

I. Pérez-Rey

Laboratorio de Geotecnia, CEDEX, Madrid, Spain

J.-Y. Gui

College of Geol. Eng. & Surveying and Mapping, Chang'An University, Xi'an, Shaanxi, P. R. China
GESSMin, CINTECX, Dept. of Natural Resources and Environmental Eng., University of Vigo, Spain

H. Masoumi

Department of Civil Engineering, Monash University, Melbourne, VIC 3800, Australia

ABSTRACT:

Roofing slate was traditionally quarried in Spain for roofing purposes since the Middle Ages. 40 years ago, and due to an increasing market demand from European countries, convenient prices and depletion of old quarries, producers envisaged the underground exploitation of these deposits. Nowadays, there are some underground room and pillar roofing slate mines operating in NW-Spain, and some projects under assessment. In this study, we analyze, from a geomechanical point of view, a wedge failure in a large 50-m high and 30-m wide room in one of these mines. Most of these rooms were observed to be stable in the mines, but for a particular case of a not so deep room, a relevant structural wedge instability problem took place. It was the case of a shallow room with its longitudinal axis normal to a river valley. The geomechanical features of slate rock mass and their discontinuities are briefly presented to explain the reasons behind this failure in relation to previous rock mechanics studies. With the idea of learning from errors, some considerations are finally discussed regarding rock mass characterization and design decisions for this type of applications.

1 INTRODUCTION

1.1 Roofing slate

Slate is a finely grained, foliated, homogeneous metamorphic rock derived from an original shale sedimentary rock composed of clay through low-grade regional metamorphism (García Guinea et al., 1997). It is typically composed of white micas, chlorite, quartz and minor quantities of other minerals. The grain size is typically under 75 μm . Slate is the finest grained foliated metamorphic rock and its foliation or slate cleavage does not usually correspond to the original sedimentary bedding; it is oriented though in planes perpendicular to the direction of the largest metamorphic compression stress suffered along its geological history (Marshak & Repcheck, 2009).

As other metamorphic rocks, and particularly the fine-grained ones, slates show a significant degree of anisotropy due to the processes of rock formation (Fig. 1). Slate is formed by recrystallization of the composing minerals under oriented high stress levels, which produces highly continuous and narrowly spaced weakness planes, the so-called cleavage. This cleavage controls the behavior and fracturing of these materials (Debecker & Vervoort, 2009; Alejano et al., 2021). Slates show a large degree of fissility, an ability to split along cleavage planes, which make them suitable for producing slim tiles with thicknesses in the range of 3 to 10 mm used to build roofs, which is why they are usually known as roofing-slates.



Figure 1. Slate cylindrical specimens cut with different angles in relation to cleavage, showing varied fracturing patterns after compression tests at different confinement levels. Tested at the laboratory of the University of Vigo according to Alejano et al. (2021).

1.2 Roofing slate mining

In recent decades, the stringent environmental standards in Europe, good prices of some ornamental rocks (marble and roofing slate) and depletion of old quarries has led quarrying companies to envisage the underground mining of these rocks. Obviously, the mining costs tended to increase in relation to quarrying. However, economic underground mining approaches, such as the room and pillar mining method, can attain reasonably low mining costs (20-40 €/t) in such a way that mining of these resources can be still a profitable business (Alejano et al., 2012). The high economic investment needed to launch a roofing slate underground mining project is probably the main drawback and the main reason why only a few underground slate mines currently exist, even if this solves the continuation of the extraction work of the present quarries.

Still mined in many quarries (Fig. 2a), there are now some operating slate underground room and pillar mines. One of the key issues of this mining approach to keep such low costs is the generation of wide rooms (Fig. 2b). In this large rooms, underground mining can proceed in a similar way to quarrying, that is, extracting large blocks of rock properly oriented and cut by means of diamond thread, so they are properly benefit in the tiling producing plant.



Figure 2. a) Roofing slate quarry and b) Roofing slate underground mine: 25-m wide and 50-m high room.

It is also relevant to note that in roofing slate mines, the high quantity of waste generated for producing marketable tiles, in the range of 75 to 90 % of extracted material, is used to fill the excavated rooms. This helps overall mine stability and facilitates ventilation. Moreover, this has contributed to mitigate the present environmental problems (landscape visual impact, river blocking...) caused by the large waste dumps generated in traditional slate quarries (Fig. 3).

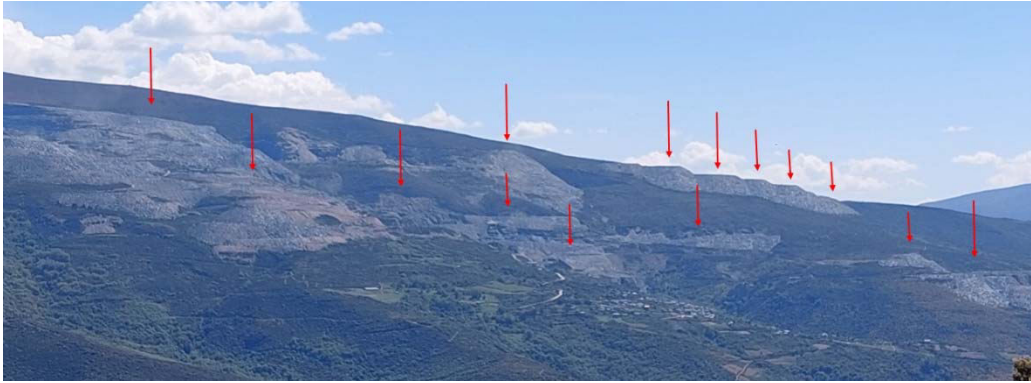


Figure 3. a) Mountain slope in NW-Spain, a landscape with scattered waste dumps of slate exploitations.

Authors of this paper and other colleagues have been involved in the design, redesign and instability analysis of some of these roofing slate underground mines for the last years (Alejano et al., 1998). Based on their experience, it is possible to conclude that currently, we have available a number of sufficiently developed rock mechanics tools in order to reasonably design room and pillar mines in shallow ornamental rock deposits (Iglesias Comesaña et al., 2017).

A proper rock mechanics approach should start with careful field data recovery, a proper understanding of the geology at stake including relevant structures (faults, folds...) and painstaking laboratory testing. Design techniques include the selection of empirical or analytical simple methods for initial design, and the application of advanced analytical and numerical techniques to simulate in an adequate form the proposed design models. The combination of empirical, analytical and numerical techniques provides more confident results for these design processes, since when one single method is applied, some topics may be overlooked (Alejano et al., 2008).

These techniques can foresee a number of instability mechanisms, which may occur in this type of exploitations. In practice, even for good designs, a number of local instability phenomena may arise. They should be controlled and monitored by means of observational techniques, but a few cases are reported where serious stability problems have largely affected these mines.

2 GEOLOGY

2.1 Basic geology of roofing slate deposits

Mineable roofing slate deposits usually occur in asymmetric anticlinal folded structures, sometimes showing a thick limb (Fig. 4). These folds formed during the Variscan orogeny, when a more or less continuous sequence of deformation phases was accompanied by regional metamorphism. This orogeny gave rise to the formation of folds, thrusts, kink-bands and crenulation schistosity. Linear relevant orientations are produced by the intersection of two or more surfaces in space. The intersection between the original bedding (S_0) and the main foliation or cleavage (S_1) is known as the “strand” of the slate. The strand is the direction normal to the plane of representation in Figure 4, and it marks the easiest direction of mining rooms to produce large blocks easy to be cut. S_1 marks the fissile or weakness plane used to process the roofing slate tiles.

The geological factors affecting the quality of a slate deposit are of three types: stratigraphic, structural and metamorphic. For a mass of slate rock to be considered a slate deposit, it must show a series of properties that should be accounted for when assessing its mining potential (Taboada

et al., 1997). They can be divided into two large groups: rock characteristics and deposit characteristics. The first would be the mineralogical composition, grain size, homogeneity, microstructure and long grain; the second would be the strength of the layer, the structural position, the contact metamorphism, the state of fracturing and its morphology.



Figure 4. Typical asymmetric fold, whose inverse limb can make out a good roofing slate deposit.

The macroscopic geological aspects of the massif are also essential to determine whether a particular area constitutes a slate deposit, or not. The thickness of the layer is the first factor to consider, where values greater than 15 m could be mined. The position of the deposit is also relevant. The slate layers are very folded in asymmetrical folds, the limbs are more productive than the hinges, since in the former the bedding and foliation form a smaller angle than in the hinges, so the slate tend to be more homogeneous (Fig. 4). Another factor that has a negative influence is the existence of contact metamorphism after very low-grade regional metamorphism, characteristic of slates, since the metamorphic recrystallization produced by it "welds" the cleavage planes and prevents good exfoliation.

But the most relevant limiting factor in the exploitability of a slate massif is its fracturing level. In this context, we understand by fractures not only joints and faults, but also quartz dikes, kink-bands and other discontinuities, different from bedding and cleavage. The state of fracturing determines the size of the extractable block, which is sent to the plant for sawing, saw-cutting into smaller slab-like blocks and to produce tiles. This block size decisively influences the extraction methods and the mine economics. The presence of pyrite more or less rusted and the so-called carbonate moons (white stains) also tends to decrease the value of the mineral.

2.2 Rock mass characterization with particular emphasis on discontinuities

Rock masses characterization is typically performed following standard techniques (ISRM, 2007). Slate rock masses tend to present good to average quality in terms of RMR (Bieniawski, 1979) within the range of 55 to 70. The stability graph method (Potvin, 1988) could also be an acceptable starting point for a preliminary room size estimate, but underground wedge stability must be checked in a detailed manner afterwards.

Slate is a hard rock with uniaxial compressive strength values typically well over 100 MPa when tested parallel or normal to foliation. More detailed characterizations, attending to anisotropy, can be found elsewhere (Alejano et al., 2021). With these typical rather high values of strength, massive rock failure or even pillar failure have never been observed in underground mines. Problems have typically been associated to structurally controlled instability phenomena.

We present here the joint characterization carried out in a quarry, located in the vicinity of the underground mine where the large wedge failure under analysis took place. More than 200 discontinuities were measured in an outcrop of a slate rock mass according to ISRM suggested methods (ISRM, 2007). Based on field observations and joint representation in stereographic projection (Fig. 5), four discontinuity sets were identified. This includes S_1 , the cleavage or schistosity, J_2 called vein (sub-vertical and normal to cleavage), J_3 called grain (more or less normal to both S_1 and J_2) and F_4 , a set of faults, some of which present relevant gouge contain.

Table 1 presents the main geotechnical features of the joint sets identified, including either mean values and standard deviations of numerically measured parameters (dip, dip direction, JRC, JCS...) and ranges of values for parameters associated to group values (spacing, continuity, water...). As it can be observed, both joint sets S_1 and F_4 are highly continuous, and well over the typical threshold of 20 m recommended as a limit according to ISRM SMs (ISRM, 2007). Figure 6 illustrates the aspect of a local area in the outcrop where representatives of all joint sets can be readily identified.

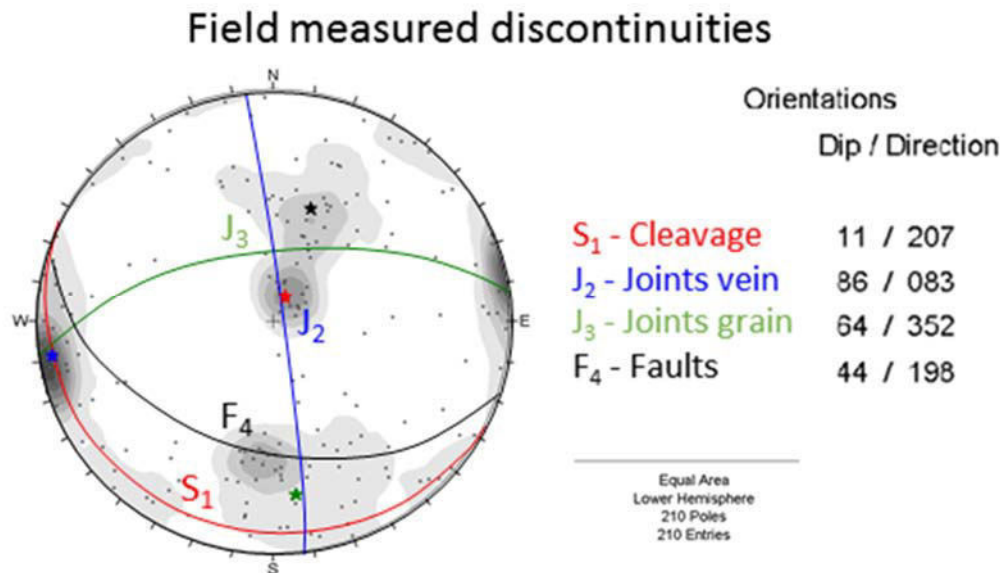


Figure 5. Meridional equal-area stereographic representation of the poles and mean great circles of the four sets of discontinuities identified from field data, with the help of DIPS (Rocscience, 2002a).

Table 1. Table abstracting joint set relevant geomechanical parameters*.

Parameter	Units	Joint set			
		S_1	J_2	J_3	Faults F_4
Dip direction	°	207 (21)	83 (11)	352 (15)	198 (19)
Dip	°	11 (6)	86 (8)	64 (14)	44 (10)
Persistence (strike)	m	> 20	10-20	3-10 to 10-20	> 20
Persistence (dip direction)	m	> 20	10-20	3-10 to 10-20	> 20
Spacing	m	0,54 (0,2-1)	1,8 (0,5-3)	1,8 (0,6-2,5)	> 2
JRC		4 (1)	12 (7)	12 (5)	
JCS	MPa	100 (45)	76 (41)	60 (35)	
Fill width or aperture		---	0,1-1 mm	0,1-1 mm	5-10 cm
Fill material		---	Oxides	Oxides	Gouge
Weathering	Degree	I	II	II	III
Water presence		Dry	Lightly wet	Lightly wet	Wet

* For each parameter the average value is presented together with the standard deviation in brackets when available.

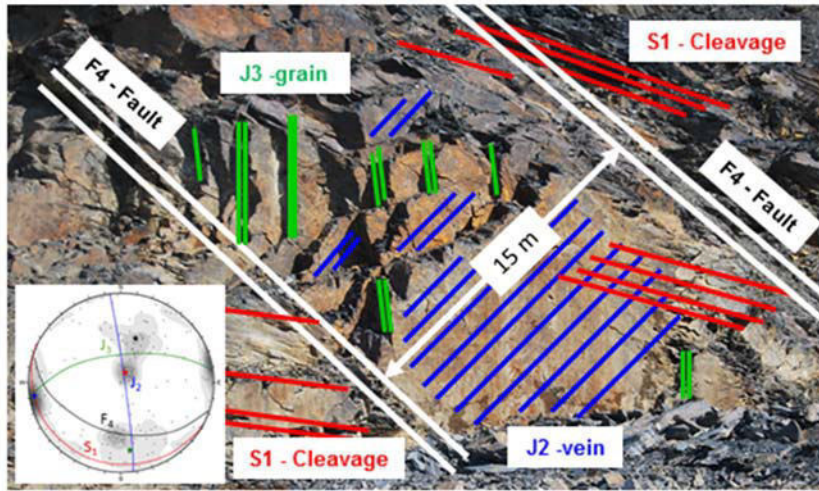


Figure 6. Picture of an outcrop area where joints corresponding to the four discontinuity sets are identified.

3 DESCRIPTION OF A WEDGE FAILURE

3.1 Basic information

In this section, we report a wedge failure occurred in a 50-m high and 30-m wide room of one of these roofing slate mines. We will intend to look for the ultimate reasons that made this accident happened, more than to report accurately the parameter associated to the phenomenon. Similar large rooms were observed to be stable in the same mine, but for this particular case of a roughly 70-m-deep room with its longitudinal axis perpendicular to a river valley, a relevant instability problem took place.

Before mining started, a good number of geological, mining and geotechnical studies were carried out, including the continuous numerical modelling of the rooms. In a first mining phase, four rooms of the mentioned dimensions were excavated, mined and filled, with no geotechnical problems being detected, disregarding mining minor incidents. The experience was positive.

In a new stage of exploitation, new rooms were designed following the local strand (cleavage strike) of the slate (N-104) and began to be exploited, based on geotechnical studies of these new areas. One of these new rooms happened to be below a river at a depth of about 70 m. On a winter Saturday some years ago, and after a day of heavy rains, a significant part of a 50-m high, 30-m wide and 180-m long room collapsed (Fig. 7).

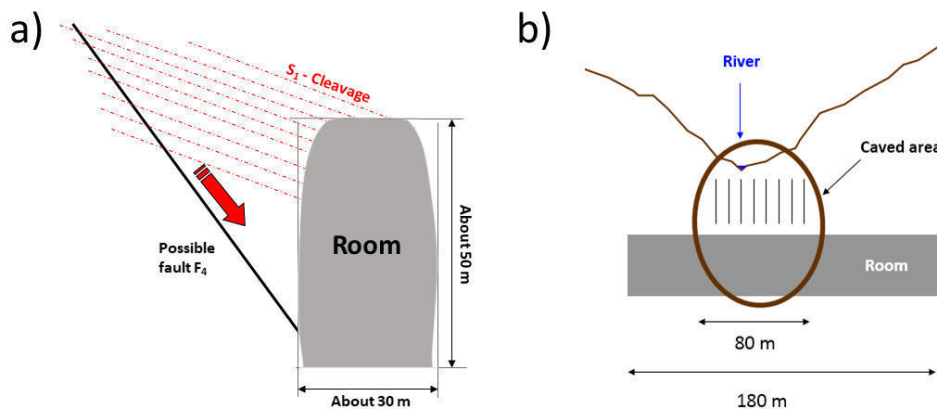


Figure 7. a) Section of the caved room with the orientation of cleavage and a possible failure plane (F_4). b) Location of the room with direction normal to a river valley and indicative extent of the caved area.

Meteorological records during this time indicated large rainfalls around 100 l/m^2 the week before the collapse took place. Some small machines were buried, but there were no injuries. Extensometers in the wall were measured a month before with total displacements around 10 mm, which were not considered worrying. Since the river was passing over the room, after some new evolved collapse, the mine was flooded by the river. Above the collapsed area of the mine, a crater took place where water of the river was embanked (Fig. 8). The joint sets measured and contemplated in the geotechnical study followed the same patterns as those measured by the authors nearby (Table 1), even if the average dip and dip direction values differed slightly. These dip directions and dips reflected in the geotechnical study were S_1 (186/22), J_2 (092/73), J_3 (013/79) and F_4 (173/44).

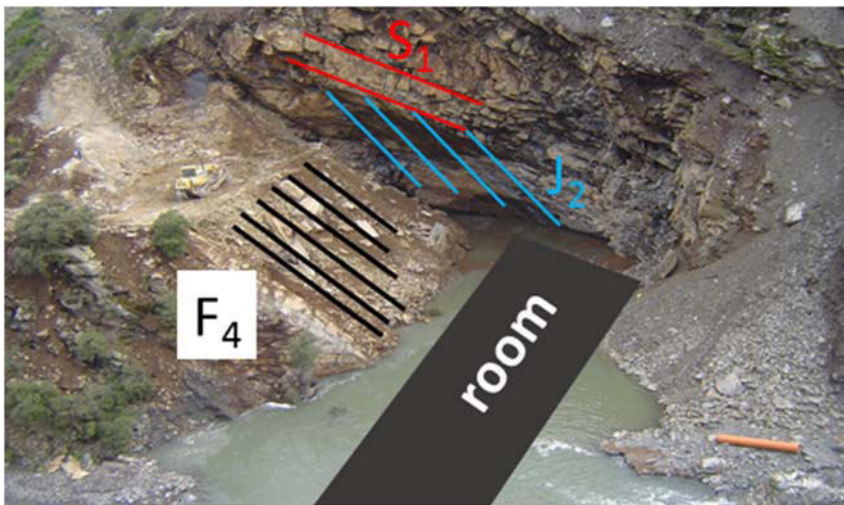


Figure 8. General aspect of the caved zone in surface with indication of potential discontinuities involved.

3.2 Understanding wedge failure

The authors have carried out an analysis of underground wedge stability based on the orientation and size of the room and in more or less conservative strength parameters based on Barton and co-workers' approaches (Barton & Choubey, 1977; Barton & Bandis, 1990). It turns out that indeed, a large wedge failure was predicted to occur in the northern side of the room. This was a very large 500,000 t wedge and for the parameters provided it was unstable, with a safety factor (SF) of 0.89 for the unsupported cavity and 0.94 for the supported case (Fig. 9). The recommended support included 50-t 12-m long cables with spacing $2 \text{ m} \times 2 \text{ m}$, 25 mm threaded bar 4-m long rock-bolts with spacing $2 \text{ m} \times 2 \text{ m}$ (in-between cables), mesh and at least a 10-cm thick layer of reinforced shotcrete.

In the previous original rock engineering reports, this wedge was observed, but failure was considered highly unlikely because of the large continuity of joints needed to attain very large wedge volumes. In fact, it was mentioned that in reality, persistence over 50 m was highly unlikely for J_2 and F_4 , and uncommon for S_1 . For this reason, they considered the probability of large wedge occurrence (for continuities over 50 m) very low. Therefore, and since all wedges with traces less than 50 m were stable, with safety factors greater than 1.5, it was concluded that with the above-mentioned designed support, all the actual potential wedges would be stable.

However, the study recommended to increase the support density, in case that during the execution of the room it was observed that possible S_1 - J_2 - F_4 wedges on the left wall presented joint continuities over 50 m. This is very difficult to see, mostly when shotcrete is used. No clear indications were provided by the extensometers. Tentative studies suggest that even for the large wedge actually formed and slid, an increase in support density would not have helped too much.

Geotechnical control and extensometers were also recommended. Unfortunately, the measurements were not conclusive.

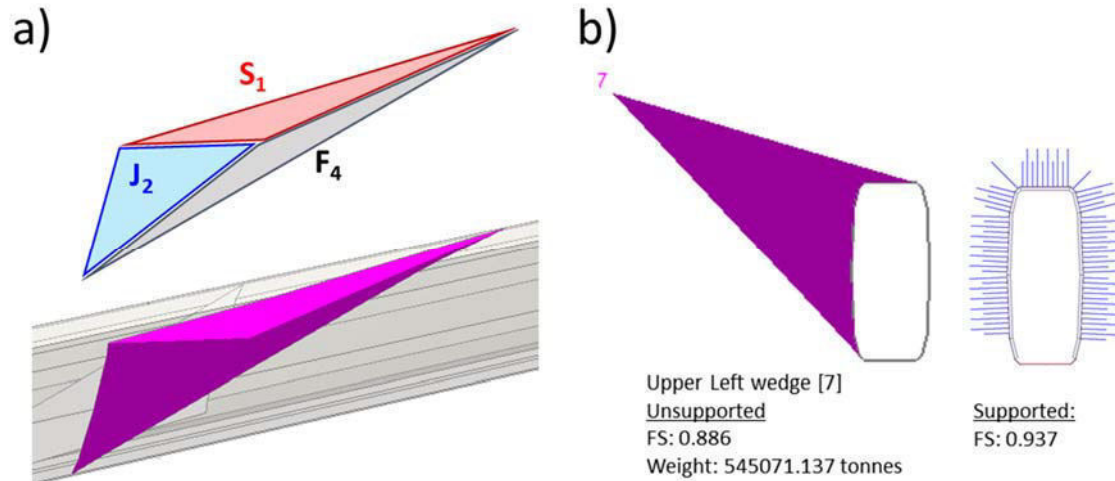


Figure 9. Main results of the underground wedge stability analysis, with code UNWEDGE (Rocscience, 2020b): a) View of the large wedge formed and representation with the corresponding joint sets. B) Section of the room and wedge, normal to room direction, and sketch of support used for computations.

In reality and to the best knowledge of the authors, a large wedge was formed. Probably, this wedge was somewhat smaller than the largest one proposed by the computation program UNWEDGE (Rocscience, 2020b). But it was still rather large and well over the size produced when limiting continuity to 50 m. To tentatively explain what actually happened, it seems that during the first developments of the room, this wedge could have been stable helped also by the effect of stresses (Brady & Brown, 2006) and even if the room was shallow. Water flow from the river, after some relevant rainfall, probably induced joint opening, increased water pressure in some joints and ultimately triggered the failure. The main drive of failure was though the wedge enormous weight.

4 DISCUSSION

When any new development associated to rock engineering starts, the first approaches to the problem and the first undertakings tend to be conservative so everything is under control. If things start to work well, people tend to be optimistic and proceed towards more economic-risky approaches, until eventually a limit is found. This was probably the case of roofing slate mines in Spain. After the initial success, a first relevant problem occurred 20 years after starting mining in the form of the described wedge failure. Fortunately, there were no injuries and only acceptable losses. This was a warning, and it will be wise to learn from errors made.

Among the problems detected, a not so detailed geotechnical characterization of the rock mass, including discontinuity data collection, was carried out, in such a way that joint set J_4 was not clearly identified as embedding a group of faults. Some of these discontinuities were not faults, but the most relevant ones were.

Additionally, when characterizing discontinuities, the persistence or continuity of joints tends to be measured as suggested by ISRM (2007), with the larger group classified as larger than 20 m (>20 m). This approach was not conclusive in this case. Even if discontinuities with persistence over 20 m were identified, it was unclear if this continuity was smaller than 50 m (in which case, no wedge would have occurred), between 50 and 100 m or larger up to some hundreds of meters, which seems to be the case based on the size of the estimated wedge failure. It is recommended

to estimate continuity in a more accurate manner, so far as large underground excavations are concerned. Future versions of suggested methods on rock mass characterization may at least comment on the potential limitations of characterization approaches for the case of highly continuous rock discontinuities.

Water, in this case, as in many other rock mechanics case studies, was also at the root of the problem. It is still difficult how to characterize water occurrence, flow, presence and originated pressure in this case.

Starting from these observations and when carrying out new geotechnical studies and mine designs, the authors have followed new guidelines. For the wedge stability calculations, they have considered infinitely continuous joints. Joint and fault strength parameters have been computed in a moderately conservative way according to the available techniques. In this way, and when focusing a new mine design for a deposit located not far from the mine where the instability took place, underground wedge stability analyses indicated the potential instability of very large wedges, similar to the one reported above. Based on that, different potential orientations of the rooms were analyzed, and the one providing the safest results was eventually selected. This corresponds to a direction oblique in relation to the strand. This design decision was made, even at the cost of producing a not so comfortable mine approach. A general view of the access drifts and four rooms designed in this new mine is illustrated in Figure 10.

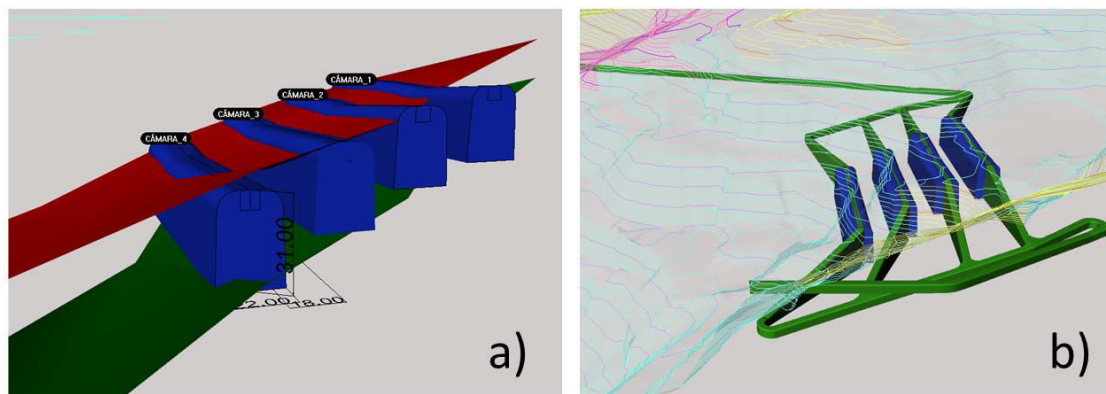


Figure 10. Roofing slate mine rooms designed following a direction oblique to the strand a) Detail of room locations between mineral limits. b) Mine layout including entrance, ramp, rooms and access drifts.

Other design trends include the consideration of somewhat smaller rooms with the idea of generating not so large walls, which can ultimately control the potential size of sliding wedges, something that can be quantified by means of underground wedge stability analyses (Rocscience, 2020b) or by means of the *stability graph* approach (Potvin, 1988).

The authors expect that this incident, associated studies, and future understanding of all the relevant issues at stake, can ultimately contribute to produce safer designs for underground roofing slate mines.

5 CONCLUSIONS

In light of the in-situ observations, the information collected and the geotechnical study, the observed collapse was due to the sliding of a large rock wedge that made ultimately caving a mining room. This wedge was formed by discontinuity planes S_1 (cleavage), J_2 and F_4 (a fault along which sliding took place). The instability was catalyzed by the flow of water from the river through open discontinuities, which led to a safety factor below 1. This resulted in the wedge detachment and its breaking into multiple blocks of rock as it slid towards the room, destabilizing it and producing a progressive collapse that ended up generating the crater shown in Figure 8.

This structurally controlled instability is a well-known mechanism that was identified as a potential problem in previous studies, but discarded based on the large persistence of discontinuities necessary to actually produce a failure. Indeed, the persistence of the F_4 discontinuity was unusual, but a more conservative approach would have been convenient. Even so it was recommended to control and follow-up of the possibility that this phenomenon occurs, by means of extensometer measurements and observations of traces of joints in the walls of the room. This follow-up was partially carried out, but the extensometer measurements were inconclusive as indicators of final displacements.

Finally, the fact that the shallow room was located under the river, and the verification that the first relevant movement of the wedge occurred after some days of heavy rain, are indicators that the water could cause pressure in some joints that finally triggered the instability.

This failure has helped us to understand better rock engineering issues applied to roofing slate underground mines, and to identify critical aspects of their geotechnical design. The presented results aim at contributing to have clearer characterization guidelines and ultimately generating safer designs.

REFERENCES

- Alejano L.R., Taboada, J., Alonso, E. & Varas F. 1998. Modelling & design of an underground room & pillar mine. *In: Proc. Geomechanics/Ground Control in Mining and Underground Construction. Wollongong, NSW, Australia, July 1998.* pp. 349-358. University of Wollongong.
- Alejano, L.R., García-Bastante, F., Taboada, J. & Migliazza, R. 2012. Design of room & pillar exploitations of non-expensive minerals and ornamental rocks in Spain.(2012) *Harmonising Rock Engineering and the Environment - Proceedings of the 12th ISRM Int. Cong. on Rock Mech., Beijing 2011.* pp. 1453-1456. Rotterdam: Balkema.
- Alejano, L.R., González-Fernández, M.A., Estévez-Ventosa, X., Song, F., Delgado, J., Muñoz-Ibáñez, A., González-Molano, N. & Alvarellós, J. 2021. Anisotropic deformability and strength of slate from NW-Spain. *International Journal of Rock Mechanics and Mining Sciences* 148, art. no. 104923.
- Alejano, L.R., Taboada, J., García-Bastante, F. & Rodríguez, P. 2008. Multi-approach back-analysis of a roof bed collapse in a mining room excavated in stratified rock. *International Journal of Rock Mechanics and Mining Sciences* 45(6): 899-913.
- Barton, N. & Bandis, S. 1990. Review of predictive capabilities of JRC-JCS model in engineering practice. *Proc. ISRM Symp. on Rock Joints. Loen, Norway. Pp. 603-610.* Rotterdam: Balkema.
- Barton, N. & Choubey, V. 1977. The shear strength of rock joints in theory and practice. *Rock Mechanics* 10, 1-54.
- Bieniawski, Z.T. 1979. The geomechanics classifications in rock engineering application. *Proceedings 4th International Congress on Rock Mechanics, Montreux, 2-8 September 1979, Vol. 2, 41-48.*
- Brady, B.H.G. & Brown, E.T. 2006. *Rock mechanics for underground mining.* 3rd ed. Wien: Springer.
- Debecker, B. & Vervoort, A. 2009. Experimental observation of fracture patterns in layered slate. *International Journal of Fracture.* 159(1):51-62.
- García-Guinea, J., Lombardero, M., Roberts, B. & Taboada, J. 1997. Spanish roofing slate deposits. *Transaction of the Institution of Mining & Metallurgy: Sect B Appl Earth Sci.* 106: B205-B214.
- Iglesias Comesaña, C., Taboada Castro, J., Arzúa Touriño, J., Giráldez Pérez, E. & Martín Suárez, J.E. 2017. Geotechnical design of underground slate mines. *Boletín Geológico y Minero* 128 (2): 405-420.
- ISRM (2007). *The complete ISRM suggested methods for rock characterization, testing and monitoring: 1974–2006.* Ulusay, R. & Hudson, J.A. (eds.) Suggested Methods prepared by the Commission on Testing Methods, ISRM. Compilation arranged by ISRM Turkish NG, Kozan Ofset, Ankara, Turkey.
- Marshak, S. & Repcheck, J. 2009. *Essentials of Geology.* New York: WW Norton.
- Menéndez-Díaz, A., Argüelles, R., Ordóñez, C. & Bouza, J.B. 2016. Room design for underground slate workings: analysis of safety factors for keyblocks. *Rock Mechanics & Rock Engineering*, 49: 1107-13.
- Potvin, Y. 1988. *Empirical open stope design in Canada.* PhD. Thesis, Dept. Mining and Mineral Processing, University of British Columbia.
- Rocscience (2020a). DIPS. Graphical and Statistical Analysis of Orientation Data, Toronto, Canada.
- Rocscience (2020b). UNWEDGE. Underground Wedge Stability Analysis. Toronto, Canada.
- Taboada, J., Vaamonde, A., Saavedra, A. & Alejano, L. 1997. Application of geostatistical techniques to exploitation planning in slate quarries. *Engineering Geology* 47(3): 269-277.

Developing a Severity Index to account for seismic induced damage in a deep level mine

J.P. Gouvea
Goldfields, South Africa

M. du Plessis
Goldfields, South Africa

ABSTRACT:

Most traditionally used rockburst damage scales were developed from Kaiser's procedure to assess rockburst damage. Kaiser's damage scales were applied at a South African deep level mine in an attempt to benchmark the severity of rockbursts experienced to other international operations. The inability of the Kaiser damage scales, including other modified and simplified versions, to properly classify the severity of rockbursts experienced at the mine, necessitated the development of a more suitable and alternative severity index. The paper describes the methodology applied to develop a more suitable Severity Index and demonstrates the benefits of the application.

1 BACKGROUND

A deep level South African mine implemented the Kaiser rockburst damage assessment procedure to classify the severity of seismic related damage and to benchmark it against other international operations. The Kaiser damage scales (Table 1 and Table 2) were initially derived from rockburst case studies investigated in Canadian mines between 1985 and 1991. The methodology followed (Kaiser et al, 1992) attempted to quantify both the rockmass and support damage experienced from rockburst incidents. The damage classes, however, poorly reflect the degree of damage sustained at the South African mine where the classification was being applied. This necessitated the development of a more suitable and alternative Severity Index (SI). The SI considered approaches followed by Heal (2010) and Duan et al. (2015) to modify and simplify the original Kaiser indices.

Table 1. Rockmass damage scale (RDS) after Kaiser et al. (1992).

Damage Level	General Description	Rockmass / Excavation Description
R0	Conditions unchanged	No damage
R1	Undamaged	Fresh but minor fractures ('loose')
R2	Slight damage	Less than 1 t displaced
R3	Minor damage	1 – 10 t displaced
R4	Moderate to considerable damage	10 – 100 t displaced
R5	Serious or severe damage	>100 t displaced

Table 2. Support damage scale (SDS) after Kaiser et al. (1992).

Damage Level	General Description	Support Damage
S0	Conditions unchanged	No damage or signs of loading on support system
S1	Undamaged	First signs of minor loading on support system, no damage to support components
S2	Slight damage	Clear signs of loading on support system, failed mesh wires, face plates deformed
S3	Minor damage	Significant loading on support system, bagging mesh, rock bolts pulling into support holes
S4	Moderate to considerable damage	Major damage to support system, failed rock bolts, torn mesh.
S5	Serious or severe damage	Complete failure of support system.

1.1 Description of the mine and evolution of the high stress “destressing” mining method

The mine is situated along the West Rand Goldfield on the north-western rim of the Witwatersrand Basin of South Africa, mining the Upper Elsburg Reef conglomerate package at approximately 2700 m below surface. The orebody varies between 20 m – 120 m in thickness and dips at approximately 13 degrees towards the South. The mineralised zone consist of various strategic horizons of Quartz-pebble conglomerates (reefs) which are sporadically located between finer grained quartzitic units. The conglomerate units are strong brittle rocks with an average rock strength of approximately 200 MPa.

The mine has undergone several mining method transformations over the past 25 years. This has been key in managing the high stress at depth through a destressing slot, enabling follow behind extraction of the wide reef in a low stress environment through massive mining methods. Seismicity at the mine is strongly related to the destress production output. Significant delays are therefore often caused by rockbursts resulting from seismic events. As the majority of production is generated from long hole stoping, significant delays to the high stressed development “destressing” cut enabling long hole stoping, are intolerable.

The destress mining method evolved from an initial conventional method using backfill (James et al, 1998) to a low-profile mechanised apparent dip destressing method applying backfill. The apparent dip layout was replaced with a horizontal low-profile layout using originally backfill (Joughin et al, 2011) and subsequently crush pillars (Watson et al, 2014). The destress layout eventually transformed to a high-profile method using crush pillars in 2016 (Andrews et al, 2019).

The high-profile layout consists of a modified bord and pillar mining method where 5.5 m high and 6.0 m wide arched drives are developed horizontally through the wide reef orebody to create the destressed environment. Traditionally, the mine attempted to remedy seismic induced damage through support design, however, the extent of these dynamic failures rendered most support systems ineffective (Gouvea and du Plessis, 2022).

In 2020, the high-profile destressing layout was adjusted to mitigate instances of extensive sidewall and pillar burst incidents. Changes were made to the destress layout to mitigate the mechanisms driving failure, limit reoccurrences, manage the stress ahead of the advancing destress front and reduce the exposure to people and equipment (Fig. 1).

Changes were made to the mining direction (from E-W to N-S) orientating the long axis of the pillars in the direction of the major principal stress and negotiating potential bedding plane ride. The dimensions of the crush pillars were reduced from 8 m x 20 m to 7 m x 20 m to ensure that the pillars crush at the face whilst being formed (du Plessis and Malan, 2022). Additionally, the overall face shape of advancing destress fronts were flattened by ensuring leads and lags be-

tween excavations are maintained at 0 – 6 m (previous 6 - 12 m) to manage the stress ahead of the advancing destress mining front and to mitigate instances of sidewall bursts along the leading ends. This also assisted in ensuring that the high stress is predominantly concentrated ahead of the mining faces where it could be controlled by applying other additional strategies (also referred to as critical controls).

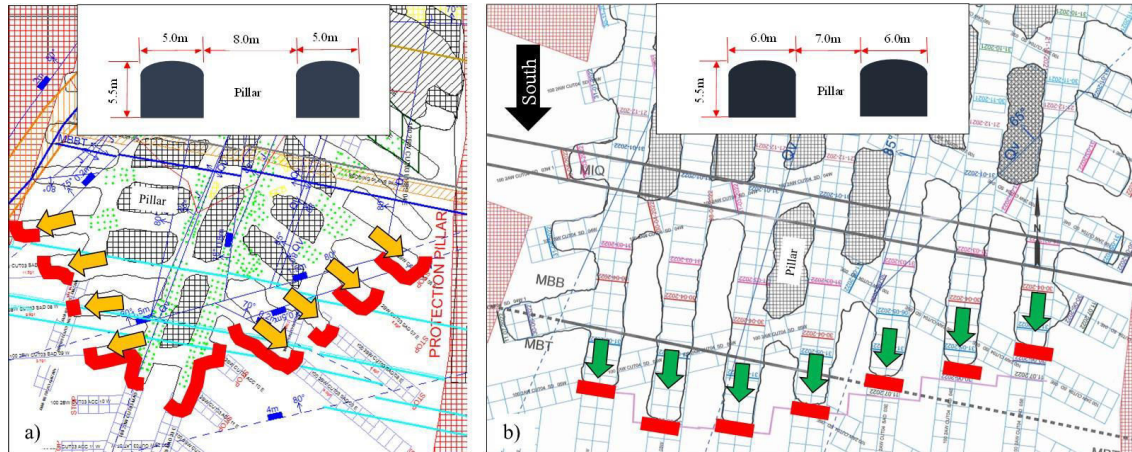


Figure 1. High profile modified bord and pillar destress layout; (a) E-W layout versus (b) N-S layout. Areas indicated in red are prone to seismic induced damage. Note that the diagrams are not to the same scale but reflect the same regional span.

1.2 Seismicity overview

Figure 2 shows that transitioning from low profile destress to high profile destress has, in general, not increased the energy output of seismicity at the mine. Joughin (2010) and Watson et al. (2014) stated that an increase in excavation height would result in an increased tendency for buckling and violent failure of the excavations, which showed to be incorrect. Significantly less closure was measured in the high profile destress sections compared to low profile destress sections. This was mostly attributed to poor support strategies applied at the time, not being able to confine the fractured pillar material. Repetitive mucking of the fractured pillar material rendered most pillars ineffective and induced closure. This directly impacted on seismicity.

Studies conducted at the mine have indicated that the advancing high stress ‘destressing’ fronts experience the most seismicity compared to any other area on the mine (structurally or stress related). Consequently, the destress excavations suffer the most instances of seismic induced damage. Seismicity at these advancing destress fronts are strongly associated with production rates and predominantly burst-type events (dominant ISO component). Slip-type events (dominant DC component) are generally limited to mining abutments. These events are infrequent with relatively long reoccurrence intervals (≈ 14 months).

The seismic overview focusses on the seismic data from 2018 to June 2022. Pre 2018, changes were made to regional corridor mining spans (2016) and crush pillar dimensions (2017). The impact of these changes is only seen once the corridors have matured under these layouts. Hence, the data considered consist of data sets which are comparable.

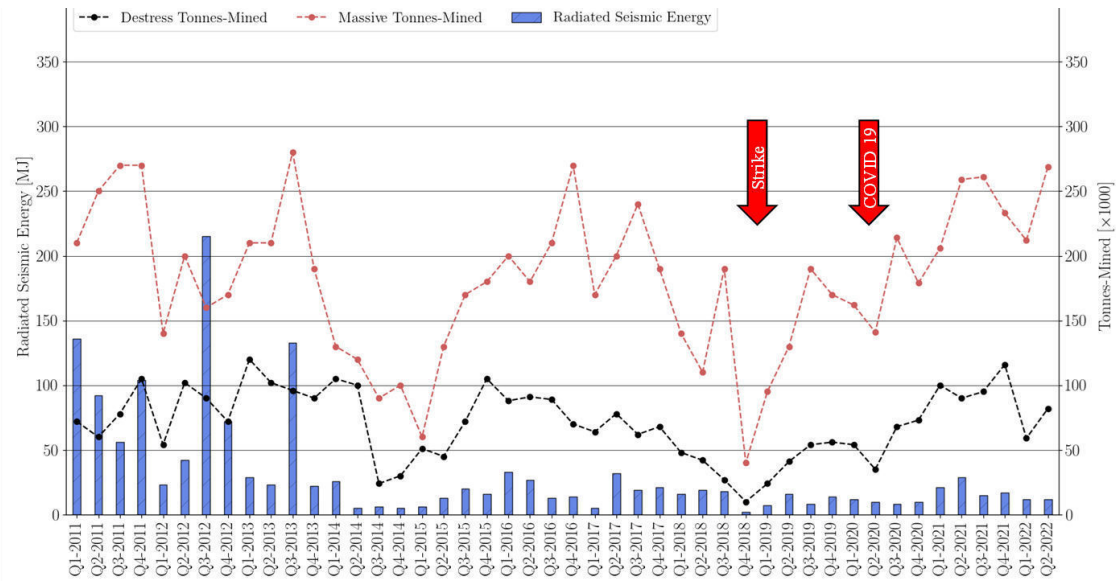


Figure 2. Radiated seismic energy versus production for various mining methods. The radiated seismic energy shown relates to destress mining. The impact of distant abutment related events are not included.

Figure 3 shows that the majority of seismic events resulting in damage have relatively small magnitudes (greater than M_L 0.0). Small magnitude seismic events locate close to advancing destress fronts and are mostly triggered during blasting times. The number of damaging seismic events have steadily increased year on year (excluding 2020 where production was interrupted by the COVID-19 pandemic). The trend should be viewed against numerous other factors to holistically quantify the significance (e.g. production rates, area being mined, total number of events within the specific magnitude range, severity of rockbursts etc.).

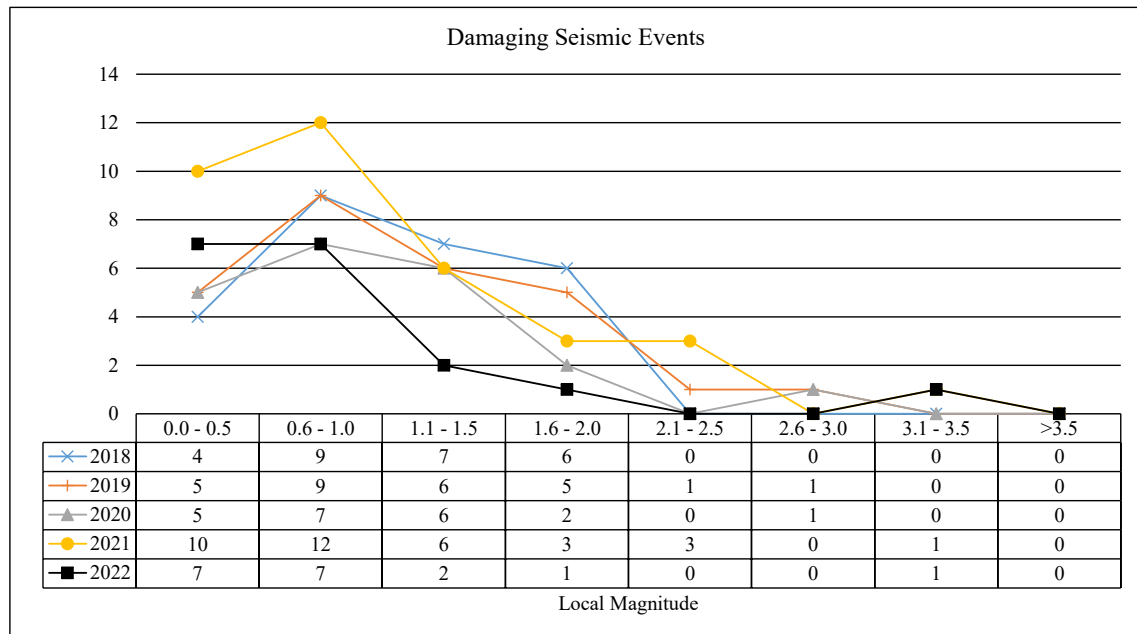


Figure 3. Number of damaging seismic events per year for a range of magnitudes (January 2018 – June 2022).

Historical seismic data indicates that the potential reoccurrence magnitude at advancing destress fronts are generally less than M_L 1.5. Event magnitudes greater than M_L 1.5 are usually associated with violent pillar failures (pillar bursts) and abutment zones. The average distance between the location of the seismic events and the areas that got damaged is fairly consistent for magnitudes between 0.0 and 1.5 (Fig. 4).

The probability of seismic damage per magnitude range is shown in Table 3. The table compares seismic events which caused damage versus the total number of seismic events within the particular magnitude range. Table 4 shows the same data grouped per year. It illustrates how the mining layout changes implemented in 2020 has significantly reduced the probability of damage year on year for the destress areas (excluding large distant events $M_L > 2.0$).

Table 3. Probability of damage per magnitude range.

Magnitude range (M_L)	0.0 - 0.5	0.6 - 1.0	1.1 - 1.5	1.6 - 2.0	2.1 - 2.5	2.6 - 3.0	3.1 - 3.5
Probability of damage	2%	5%	15%	23%	33%	50%	67%

Table 4. Probability of damage per magnitude range per year.

Magnitude range (M_L)	0.0 - 0.5	0.6 - 1.0	1.1 - 1.5	1.6 - 2.0	2.1 - 2.5	2.6 - 3.0	3.1 - 3.5
Probability of damage (per year)	2018	1%	7%	21%	46%	0%	0%
	2019	1%	6%	23%	29%	50%	0%
	2020	1%	5%	14%	20%	0%	100%
	2021	2%	5%	12%	17%	75%	0%
	2022	2%	5%	8%	6%	0%	0%

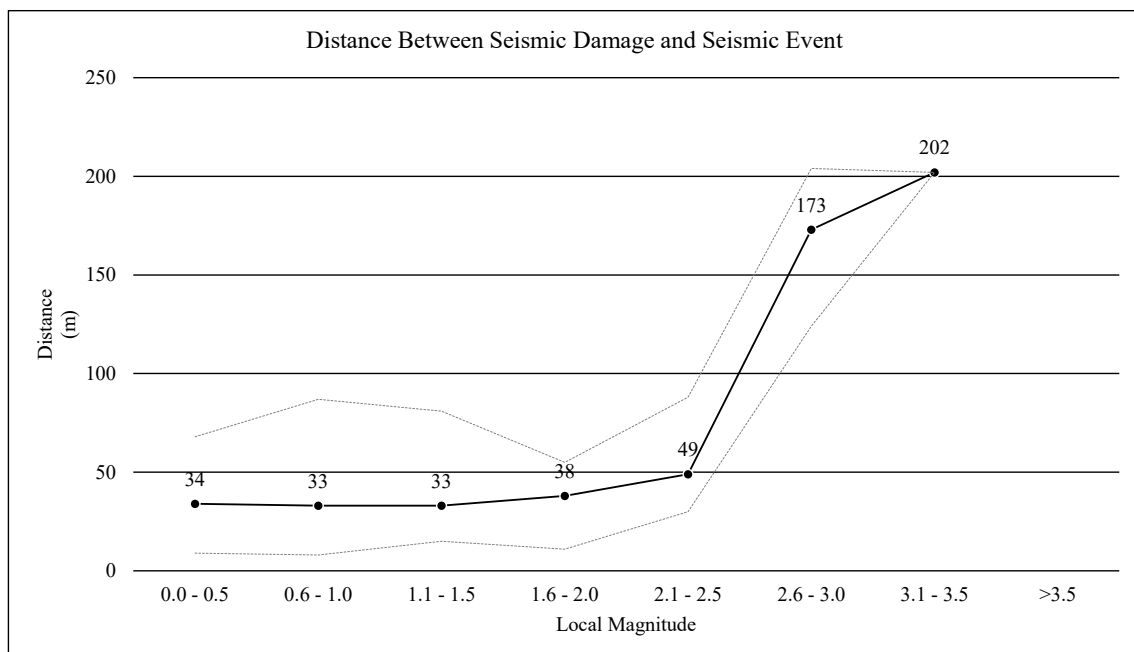


Figure 4. Average distance between the rockburst damage location and seismic event location for a range of event magnitudes. The lines above and below are minimum and maximum distances recorded for the specific magnitude ranges.

2 SEVERITY INDEX (SI)

The Severity Index (SI) considered data from January 2018 to June 2022 applicable to the high-profile destressing mining method. More than 170 rockburst damage locations were considered. Various contributors and data sources were reviewed, which included lithology, presence of bedding planes, stress state data, rockmass and support behaviour (both measured and observed), back analyses of burst incidents, seismic source parameters and moment tensor inversions.

Owing to the unique destressing layout of the mine, two damage classes were defined namely; (i) Face Burst Index (FBI) and (ii) Perimeter Burst Index (PBI). The face burst index considers any seismic damage at / on the mining face whilst the perimeter burst index considers any seismic damage from the excavation perimeter (hangingwall, footwall and sidewalls).

Excavation peripheries are supported with sheets of 5.6 mm welded mesh pinned with 2.4 m long high dynamic capable rock bolts (229 kN ultimate tensile strength, 53 kJ energy absorption capability and 230 mm yield capacity). The entire excavation is supported to a height of 0.5 m from the footwall. A layer of 50 mm thick 40 MPa fibre reinforced shotcrete (200 J capacity) is applied over the mesh along the excavation sidewalls as a secondary application. The shotcrete was initially applied to contain fractured pillar material behind the mesh. However the application also improved the ability of the support system to contain seismic damage along the sidewalls and therefore it was extended to cover the entire sidewall (to hangingwall).

Face support and preconditioning is applied to reduce the severity of face burst incidents. The excavation faces are supported with sheets of 5.6 mm welded mesh pinned with 2.4 m long Splitsets (\approx 30 cm protrusion) covering approximately 65% of the total face area. A 1.5 m gap is left to the footwall of the face area to accommodate loading activities. Five preconditioning holes are drilled into a distress face. These holes are 1.8m longer than production drill holes. The front 1.0 m of a preconditioning hole is charged with emulsion and timed to detonate before production holes.

Figure 5 indicates the number of damaging seismic events, distinguishing between face and perimeter damage locations for a range of seismic event magnitudes. For seismic event magnitudes greater than 1.5, there is a clear increase in excavation perimeter damage compared to face damage. The severity of the events relating to these two classes vary considerably, and hence it needs to be evaluated separated.

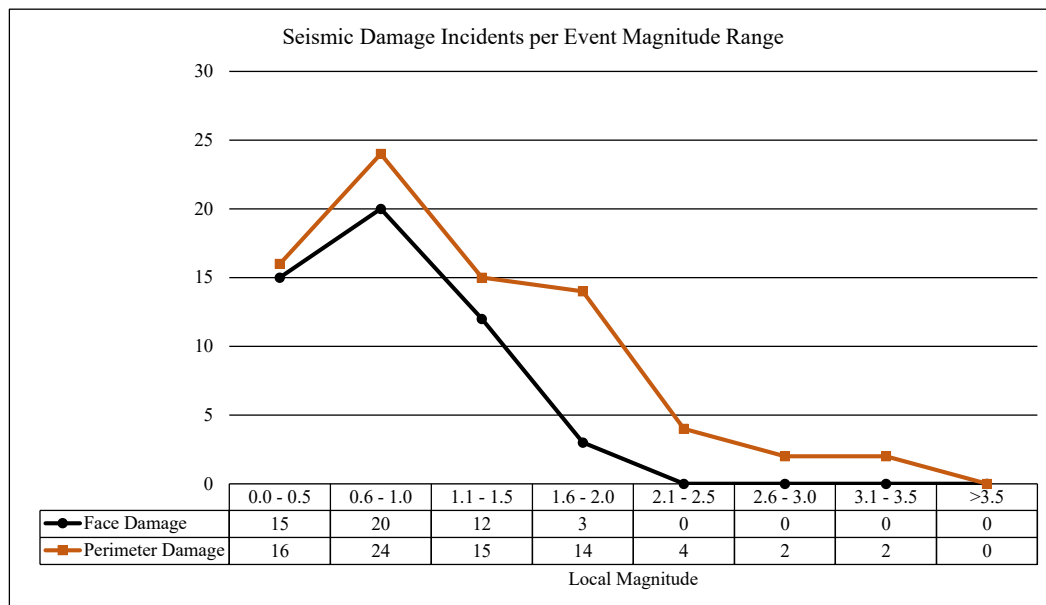


Figure 5. Number of damaging seismic events resulting in face damage and damage to excavation peripheries for a range of event magnitudes.

2.1 Face Burst Index (FBI)

Distinctive signatures could be observed from underground assessments where seismic damage took place. These signatures are summarized in Table 5 and Figure 6 illustrates an example of each face burst damage classification. The classification considers seismic damage with no support failure (1) versus the support system being completely ineffective (4).

It should be noted that the Face Burst Index data only considered supported face areas. Face bursts are recorded at unsupported face areas, however these are considered no entry zones on the mine.

Table 5. Face Burst Index.

Damage Rating			
1	2	3	4
Damage Depth < Support Length			Damage Depth > Support Length
No Failures	Bolts Intact Mesh Failed	Bolts Failed Mesh Failed	Support Ineffective

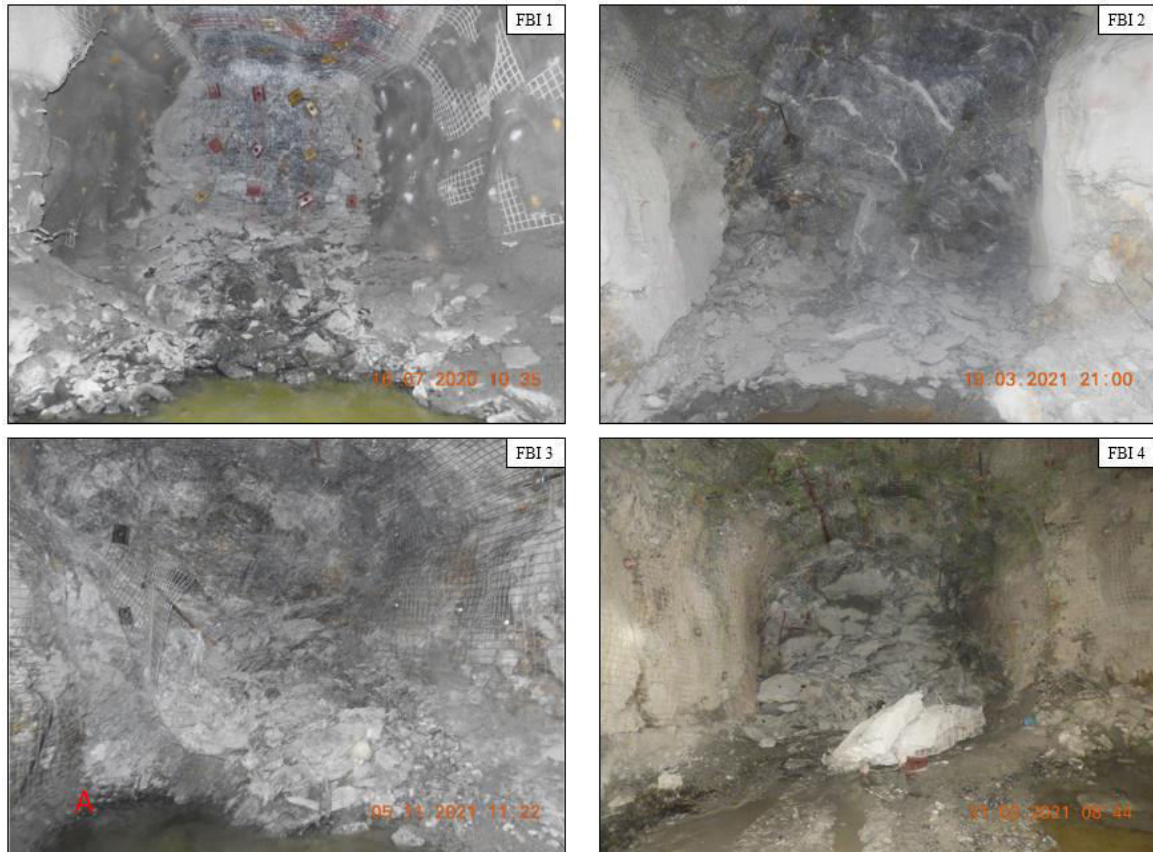


Figure 6. Examples of different Face Burst Index damage classifications.

Figure 7 summarises the categorised face bursts occurrences. Damage classification relating to FBI 1 is generally under recorded as mining crews tend to report seismic events that resulted in more significant damage (e.g. FBI 2 – FBI 4) which may potentially impact the mining cycle.

On average, higher tonnages (t) of rock is displaced for higher severity face bursts. The average tonnes displaced for FBI 1, FBI 2, FBI 3 and FBI 4 are 9 t, 14 t, 45 t and 187 t respectively. Of interest was the numerous severe face bursts recorded for relatively low tonnages displaced,

especially where critical controls (face support and preconditioning) were absent. The distribution of displaced tonnes further indicate the inaptness of the Kaiser rockmass damage scales. The vast majority of face burst instances would mistakenly be deemed too severe and intolerable based on this sole metric (Table 1).

The number of face burst incidents significantly increased since 2021. This is mainly attributed to the mining orientation and the implementation of a flatter face shape for advancing destress fronts. The severity of these events is controlled by applying additional strategies (critical controls) which include preconditioning, face meshing and distancing people from the face.

Face support is responsible for retaining ejected rocks from destress faces. The effectiveness of face support is significantly impacted by different size distributions of ejected rock. Larger rock sizes result in more severe face bursts. This is directly related to preconditioning practices. Preconditioning induces fracturing ahead of the advancing destress front. Based on data collected from rockburst instances, preconditioning effectively reduced the size distribution of ejected rocks, and didn't necessarily reduce the number of face burst instances. The average dimensions of rocks ejected during a face burst (no preconditioning) measured 0.4 m x 0.5 m x 0.2 m, compared to 0.3 m x 0.2 m x 0.1 m (85% reduction) when a face was preconditioned beforehand. This suggests that the effectiveness of face support is directly related to the application of preconditioning (FBI 1 vs. FBI 4).

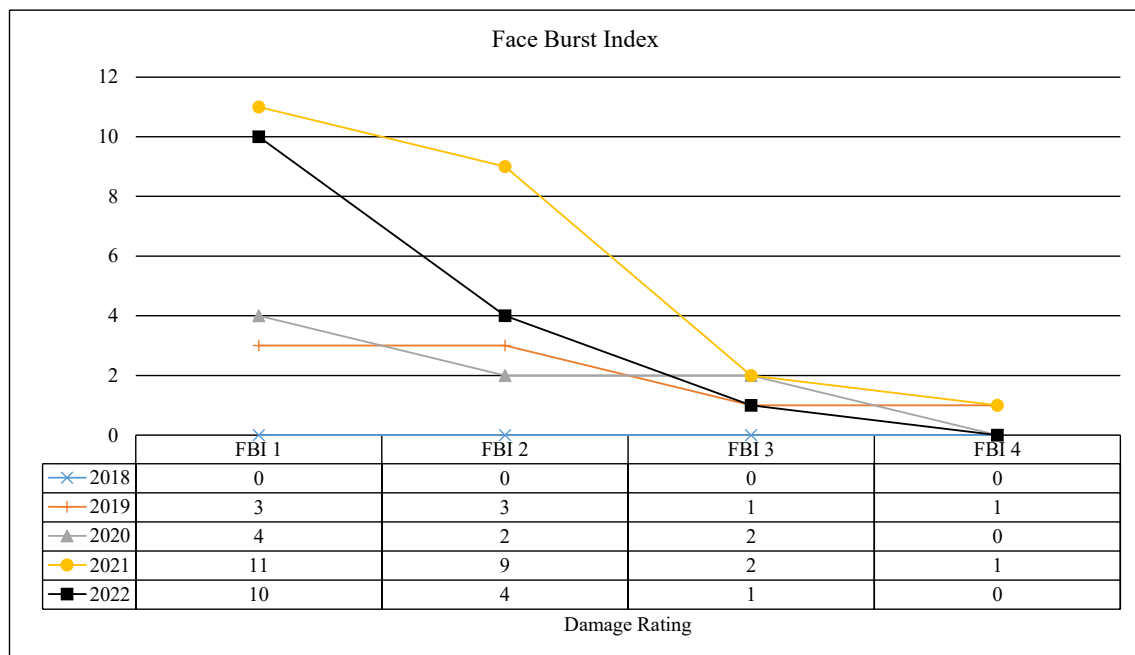


Figure 7. Face Burst Index damage classification between January 2018 and June 2022.

2.2 Perimeter Burst Index (PBI)

Similarly to the FBI, distinctive signatures could be observed from underground assessments where seismic damage took place resulting in perimeter damage. These signatures are summarized in Table 6 and Figure 8 illustrate an example of each perimeter burst damage classification.

Table 6. Perimeter Burst Index.

Damage Rating			
1	2	3	4
Damage Depth < Support Length			Damage Depth > Support Length
No Failures	Bolts Intact Mesh Failed	Bolts Failed Mesh Failed	Support Ineffective



Figure 8. Examples of different Perimeter Burst Index damage classifications.

Figure 9 summarises the categorised perimeter burst occurrences. PBI 1 is generally under recorded as it does not necessarily impact the mining cycle.

On average, higher tonnes (t) of rock is displaced for higher severity perimeter bursts. The average tonnes displaced for PBI 1, PBI 2, PBI 3 and PBI 4 are 28 t, 29 t, 132 t and 329 t respectively. The unsuitability of traditional Kaiser rockmass damage scales are again observed as most of the perimeter bursts would be deemed too severe and intolerable.

The number of perimeter burst incidents per category has decreased year on year. The impact of reducing/ eliminating perimeter bursts and subsequent severity thereof, is a major safety improvement for the operation.

The mining layout changes introduced in 2020 were aimed at decreasing perimeter damage events which presented both high exposure and severity. Pillar burst incidents result in severe sidewall ejections (PBI4) which render most support systems ineffective. Similarly, long exposed abutments (Fig. 1) cause substantial sidewall damage. The reduction in pillar dimensions ensured that pillars crush whilst being formed at the advancing destress face. It was also observed that, although seismicity was still occurring, it moved further ahead of the mining front, reducing instances of associated stress related bursting at the mining face.

Limiting lead and lag distances between destress ends to a maximum of 6 m significantly reduced the exposure to and potential for perimeter bursting (sidewalls) along the leading ends. The majority of PBI 2 and PBI 3 failures were situated along the sidewalls of excavations leading adjacent ends by more than 6 m. The benefits associated with remote mechanised mining is therefore achievable.

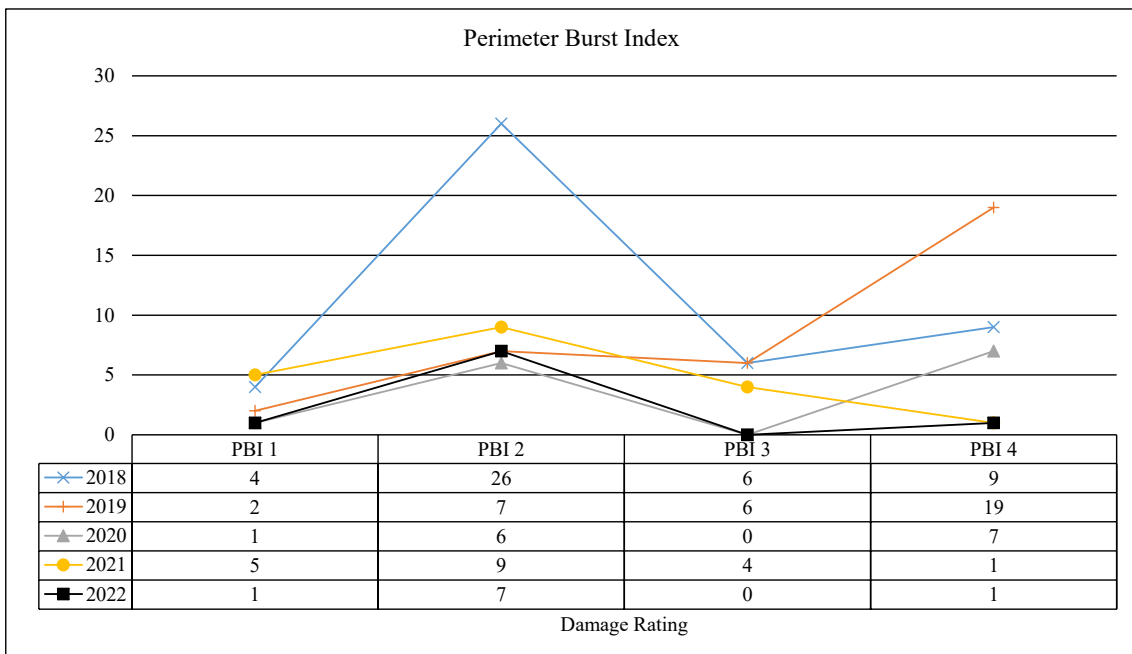


Figure 9. Perimeter Burst Index damage classification between 2018 and June 2022.

2.3 Overview of Severity Index (SI) results

The alternative Severity Index is able to evaluate and quantify the damage classes experienced at the mine. Figure 10 shows that the layout improvements introduced in 2020, coupled with the application of critical controls, have reduced both the linear meters of damage and severity of seismic damage experienced for a higher number of potentially damaging seismic events ($M_L \geq 0.0$). Even with the mine producing higher volumes of destress (Fig. 2), the impact of the associated seismicity is mitigated. The results support the notion that there shouldn't be a geotechnical restriction placed on productivity (mining rate or volume) where the seismic hazard can be managed effectively.

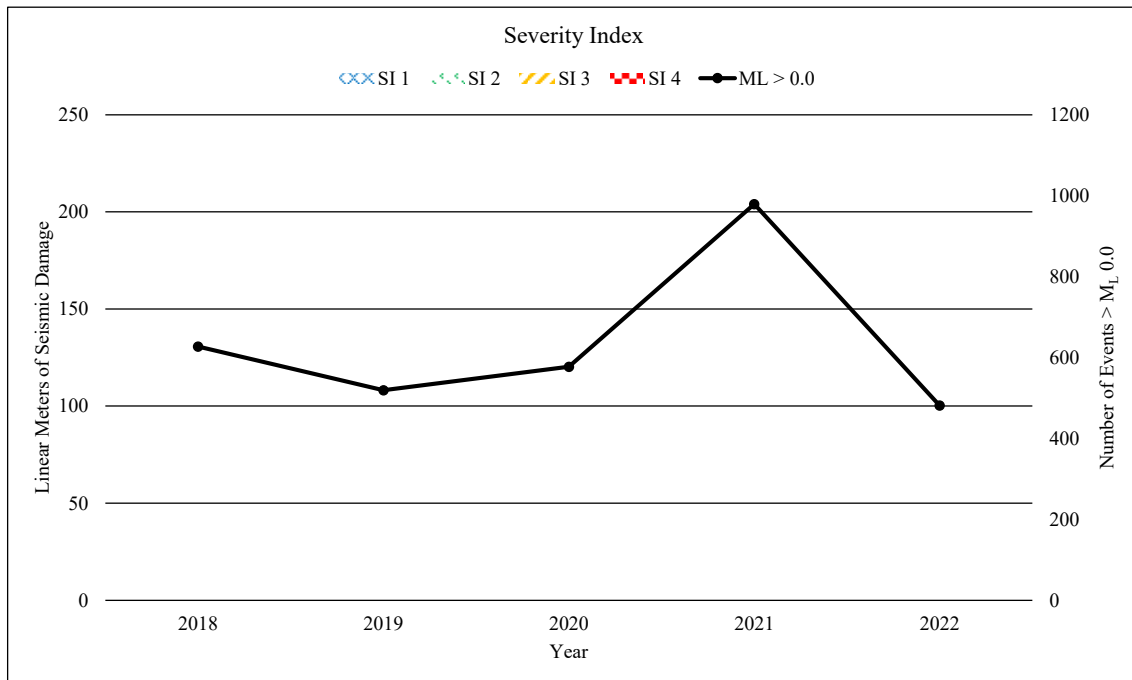


Figure 10. Linear meters of rockburst damage relative to the number of potentially damaging seismic events between January 2018 and June 2022.

3 CONCLUSIONS

The lack of quality data relating to severity adversely impacts on the reliability and interpretation of traditional rockburst damage scales. Traditional classifications were based on the resulting displaced volume (tonnes), which does not necessarily provide a good indication of severity.

The paper describes how the mine developed a Severity Index based on more than 170 rockburst incidents. The distinction between face and perimeter seismic damage was a vital and significant improvement from the limits set by traditional rockburst damage scales as the associated severity differ considerably between the two classes.

The Severity Index was used to compare instances and severity of associated rockbursts. It demonstrated the benefits of the optimized classification system to both quantify and evaluate damage sustained from rockburst incidents. It is also a useful tool to assess and validate layout or support improvements over time.

REFERENCES

- Andrews, P.G., Butcher, R.J. and Ekkerd, J. (2019). The geotechnical evolution of deep level mechanised destress mining at South Deep. *Proceedings of the Ninth International Conference on Deep and High Stress Mining*, The Southern African Institute of Mining and Metallurgy, Johannesburg, pp. 15-28
- Duan, W., Wesseloo, J. and Potvin, Y. (2015). Evaluation of the adjusted rockburst damage potential method for dynamic ground support selection in extreme rockburst conditions. *Proceedings of the International Seminar on Design Methods in Underground Mining*, pp 399–418 (Australian Centre for Geomechanics).
- Du Plessis, M and Malan, D.F. (2022). Improved destress mining at Goldfield’s South Deep mine to effectively manage seismic induced instabilities. *Journal of the Southern African Institute of Mining and Metallurgy*. In prep.
- Gouvea, J.P. and du Plessis, M. (2022). Establishing a testing criteria to relate the in-situ performance of static and dynamic capable mesh. *Proc. RaSim 2022*, Tuscon, USA.
- Heal, D.P. (2010). Observations and Analysis of Incidences of Rockburst Damages in Underground Mines. *PhD thesis*, The University of Western Australia.
- James, J.V., MacDonald, A.J. and Raffield, M.P. (1998). The backfilling philosophy for massive mining at depth in the South Deep Section, Western Areas Gold Mine. *Proceedings of the Sixth International*

- Symposium on Mining with Backfill*. Bloss, M.L. (editor) Australasian Institute of Mining and Metallurgy.
- Joughin, W.C. (2010). Comparative rockburst risk for 3.0 m and 2.2 m high stoping height mechanised de-stressing with bolting crews and mechanical bolters, *Internal Document*, 396956/L7, April 2010.
- Joughin, W.C, Bester, W.M, and Du Plooy, M. (2011). Mining methods and backfill at South Deep Gold Mine. Minefill 2011, *International Conference on Mining with Backfill*, The Southern African Institute of Mining and Metallurgy, 2011.
- Kaiser, P.K., Tannant, D.D., McCreath, D.R. & Jesenak, P. (1992). Rockburst damage assessment procedure, *Rock Support in Mining and Underground Construction*, eds. Kaiser & McCreath, Balkema, Rotterdam, pp. 639-647.
- Watson, B.P., Pretorius, W., Mpunzi, P., Du Plooy, M., Matthysen, K., and Kuijpers, J.S. (2014). Design and positive financial impact of crush pillars on mechanised deep-level mining at South Deep Gold Mine. *Journal of the Southern African Institute of Mining and Metallurgy*, volume 114, n 10, Johannesburg October 2014.

Rock fracture stimulation using slow energy releasing fracturing compounds.

V.R.S. De Silva

Geotechnical Institute, TU Bergakademie Freiberg, Germany

P.G. Ranjith

Department of Civil Engineering, Monash University, Australia

ABSTRACT:

Conventional mining methods are becoming increasingly uneconomical with declining ore grades. In-Situ Leaching (ISL) of minerals is one alternative technology that can be adapted to extract minerals from low-grade permeable mineral deposits. The susceptibility to ISL is dependent on the permeability of the host-rock formation. Although prevailing methods such as hydraulic fracturing and explosive blasting are used for host-rock preconditioning, these methods have limitations such as excessive formation damage around well fields and uncontrolled fracture propagation. Therefore, an alternative method is proposed to initiate fractures around an injection well using a patented hydrophobic, injectable, Soundless Cracking Demolition Agent (SCDA). The fracture performance of the compound was investigated by numerically simulating the fracture initiation and propagation using the Discrete Element Method. It was also tested in the laboratory to fracture multiple low permeability sandstone specimens under hydrostatic stresses up to 20MPa. Due to the fracturing nature of the agent, the fracture density can be significantly improved (by 116%) with increasing confining pressure (from 70kPa to 20MPa). Furthermore, the rock is subjected to a gradual fracturing process (10–25 hrs) facilitating safer, controlled fracture propagation, around the borehole. Afterwards, the fracture permeability of the specimen was calculated. Compared to the very low intact sandstone permeability ($7.6 \times 10^{-20} \text{ m}^2$) an improved permeability of $9.79 \times 10^{-13} \text{ m}^2$ at a confining pressure of 30 MPa was observed following pre-conditioning. The radial fracturing observed using this method indicates that non-explosive rock fragmentation is a potential catalyst to improve the permeability of host-rock formations for ISL among other applications.

1 INTRODUCTION

1.1 *Mining: a global outlook and an alternative approach*

The ongoing global decline in ore grades has led to increased energy consumption in mineral liberation using conventional mining methods. Conventional mining accounts for over 6% of world energy consumption (Holmberg et al. 2017) and ore grades are further expected to decline in the future (Rötzer & Schmidt 2018). Despite this trend, mineral extraction is further expected to rise with the transition to renewable energy and electric vehicles (Watari et al. 2022). The increasing waste rock volume in the mineral extraction process is the main contributor to the elevated energy expenditure in mining. The impact of increased energy expenditure with declining ore grades can be explained considering the global trends of copper as illustrated in Figure 1. In conventional mining operations, as the host rock volume increases the subsequent processes of haulage and grinding operations (Fig. 1b) result in a drastic increase in the energy consumption.

The target to limit the global temperature rise to 1.5°C by 2050 calls for alternate mining technologies that can eliminate the current practices of energy-intensive mining operations. Furthermore, these technologies must enable the economic recovery of minerals from deposits that are below the cutoff grade for conventional mining. In-situ recovery (ISR) is an alternative, nonintrusive mining technology that may be adopted for low-grade mineral extraction. However, ISR is limited to permeable host-rock formations where a leaching solution is circulated through an ore body to dissolve target minerals. This is done by injecting a lixiviant (typically a weak acid) through a well field drilled into the target ore deposit. The mineral-rich solution is then extracted from the orebody using recovery wells. Typical recovery rates of minerals

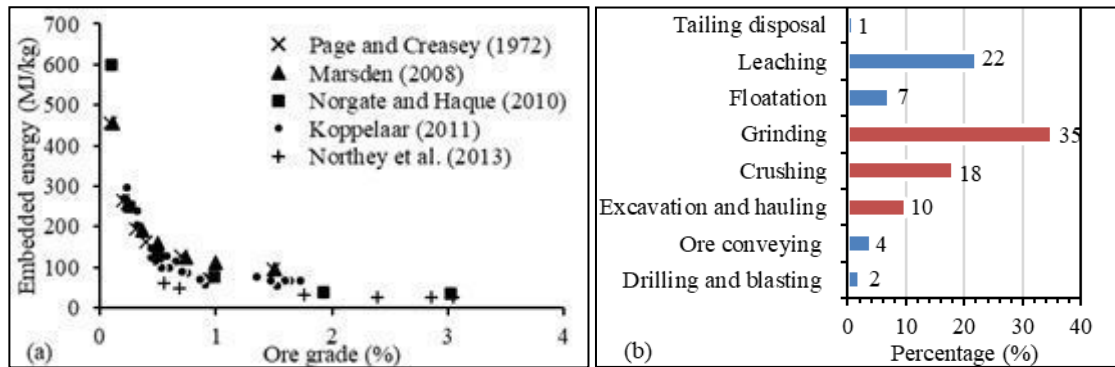


Figure 1: Energy consumption in conventional mining (a) with declining ore grade, (b) proportion of energy usage in operations (Stadler, A. & Boucaut, S. 2015)

for ISR could range between 60- 90% (Northey et al. 2013) depending on the host-rock formation and mineralogy. Compared to conventional methods of mining, ISR is less intrusive and requires only the injection and extraction wells to be formed on-site leading to a lower operation footprint. Thus, ISR could eliminate excavating, hauling, crushing and grinding operations that account for over 60 % of the total energy expenditure of conventional mining (Fig. 1b).

However, the efficiency of ISR is reliant on the permeability of the host rock and at present ISR is limited to previous ore bodies. Application of ISR in impervious host rocks requires permeability enhancement by artificial fracture stimulation. Current practices for fracture stimulation include blasting (McCarter 1996) and hydraulic fracturing (He et al. 2016). However, both these methods have characteristics, which are detrimental to the ISR process. Blasting produces localized fractures that are difficult to control with large variability of fragment size (Saharan et al. 2006). On the other hand, hydraulic fracturing mainly generates a single uncontrolled fracture, the direction of which is dictated by the in-situ stress anisotropy. This is suboptimal for ISR as the risk of groundwater contamination from the leaching solution increases if the preconditioning is uncontrolled. From an environmental point of view, hydraulic fracturing requires a large amount of fracturing fluid, which could potentially leak off to surrounding aquifers from uncontrolled fracture initiation. Therefore, any artificial fracture stimulation method for enhanced ISR must be able to initiate a controllable and localized fracture network in the host rock.

1.2 Rock fragmentation using Soundless Cracking Demolition Agents

SCDA also known as soundless cracking agents, expansive demolition agents, and non-explosive demolition agents, are rock fragmentation agents. The material used in the soundless cracking is a cementitious powdery substance predominantly consisting of Calcium oxide and other cementing materials. When hydrated, SCDA solidifies and expands volumetrically through the formation of Calcium Hydroxide (Eq. 1) and Ettringite (Eq. 2). When this crystal growth is restrained inside a borehole it exerts an outward thrusting pressure known as crystal growth pressure ΔP , given by $\Delta P = RT/V_m \cdot \ln(a_s/a_o)$, where V_m is the molar volume of the Ca(OH)_2 crystal, R is the gas constant, T is the absolute temperature, a_s and a_o are the mean activity of the supersaturated and saturated solutions in the aqueous slurry respectively. This expansion is explained by the Spherical expansion model for Ca(OH)_2 , where an expansive pressure is exerted in the surrounding body when the volumetric expansion of Ca(OH)_2 is restrained (Ish-Shalom & Bentur, 1975).



During the fracturing process, SCDA is mixed with water (30 % by weight of SCDA) to form a slurry and injected into the pre-drilled holes in the rock. The subsequent exothermic reaction allows the material to volumetrically expand over several hours. Under the confinement in a borehole, the volumetric expansion generates an expansive pressure and initiates fractures around the vicinity of the borehole when it exceeds the tensile strength of the rock (Laefer et al. 2010) (Fig. 4a). Initiation of a fracture indicates a release of confinement of the rock and a resulting drop in expansive pressure can be observed. The idealized pressure plot in Figure. 4b shows that the expansive pressure P_0 exceeds the tensile strength of the rock at t_0 which initiates the first crack caused by SCDA expansion. The fracture is only propagated when the tensile stress is further increased by SCDA expansion. The slow energy releasing mechanism and the corresponding controlled fracture initiation and growth mean that stable and quasi-static crack growth can be maintained during the fracturing process.

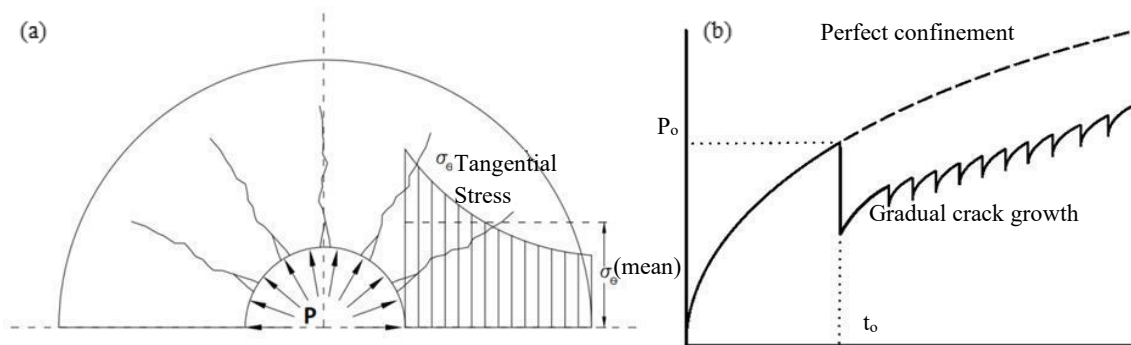


Figure 2: SCDA charged crack propagation (a) crack propagation from the borehole, (b) Expansive pressure development in the borehole during crack growth

The application of SCDA in underground conditions has been widely avoided due to the inability of SCDA to fracture rock in underwater conditions and its slower expansive pressure generation. In this paper, we present a modified Patented SCDA that can be used for subsurface rock pre-conditioning applications under submerged conditions. Next, the fracturing potential of the modified SCDA is investigated both experimentally and numerically. Finally, the fracturing potential and the resultant permeability improvement of SCDA are compared against hydraulic fracturing in laboratory conditions.

2 A MODIFIED SCDA FOR ROCK PRECONDITIONING

Considering the existing limitations of SCDA in subsurface applications, the formula was modified to incorporate hydrophobicity and fluidity in SCDA. This was achieved by a three-step process involving the precise inclusion of three additives to SCDA. 1) A viscosifier (VEA- Viscosity enhancing agent) in the form of welan gum, an anionic exopolysaccharide to introduce hydrophobic properties to SCDA. 2) A high-range water reducer (HRWR) in the form of Sodium naphthalene formaldehyde sulphonate to increase the fluidity of SCDA without increasing the water content. 3) A chemical accelerator in the form of anhydrous calcium chloride (CaCl_2) to alter/increase the reaction rate of SCDA.

Welan gum is a long-chained biopolymer produced by a controlled submerged fermentation using *Alcaligenes* ATCC 31555 microorganism species (Kaur et al., 2014). It adheres to water molecules in the slurry and intertwines with adjacent molecules (Fig. 3a) at sufficiently high concentrations. Adding 0.15% (w/w) welan gum to the mixing water was sufficient to decrease the washout mass loss of SCDA from 36% to 2% (improve hydrophobicity). However, the adsorption of carboxyl (-COOH) and hydroxyl (-OH) groups in welan gum (Fig.3a) to SCDA particles decelerate the onset of expansive pressure by 400 % (Fig.3b) and the intertwining of molecules reduces the fluidity of SCDA by 60 % (Fig.3c). The fluidity degradation of SCDA

was mitigated with the addition of HRWR (by 1 % to 2 %). The electrostatic repulsion forces created by the HRWR maintain fluidity in the SCDA slurry. The retardation caused by welan gum was adjusted by adding anhydrous calcium chloride (by 1 % - 2 %), which increased the reaction rate of SCDA without altering the hydration products. The Cl^- ions introduced by CaCl_2 accelerate the reaction rate by creating voids in the Calcium Silicate Hydrate (CSH) gel diffusion barrier providing access for water molecules to unhydrated SCDA particles in the system (Fig.10d). Consequently, this reaction produces smaller clusters of hydrated products (Fig.10e) allowing more free water to permeate into unhydrated SCDA particles.

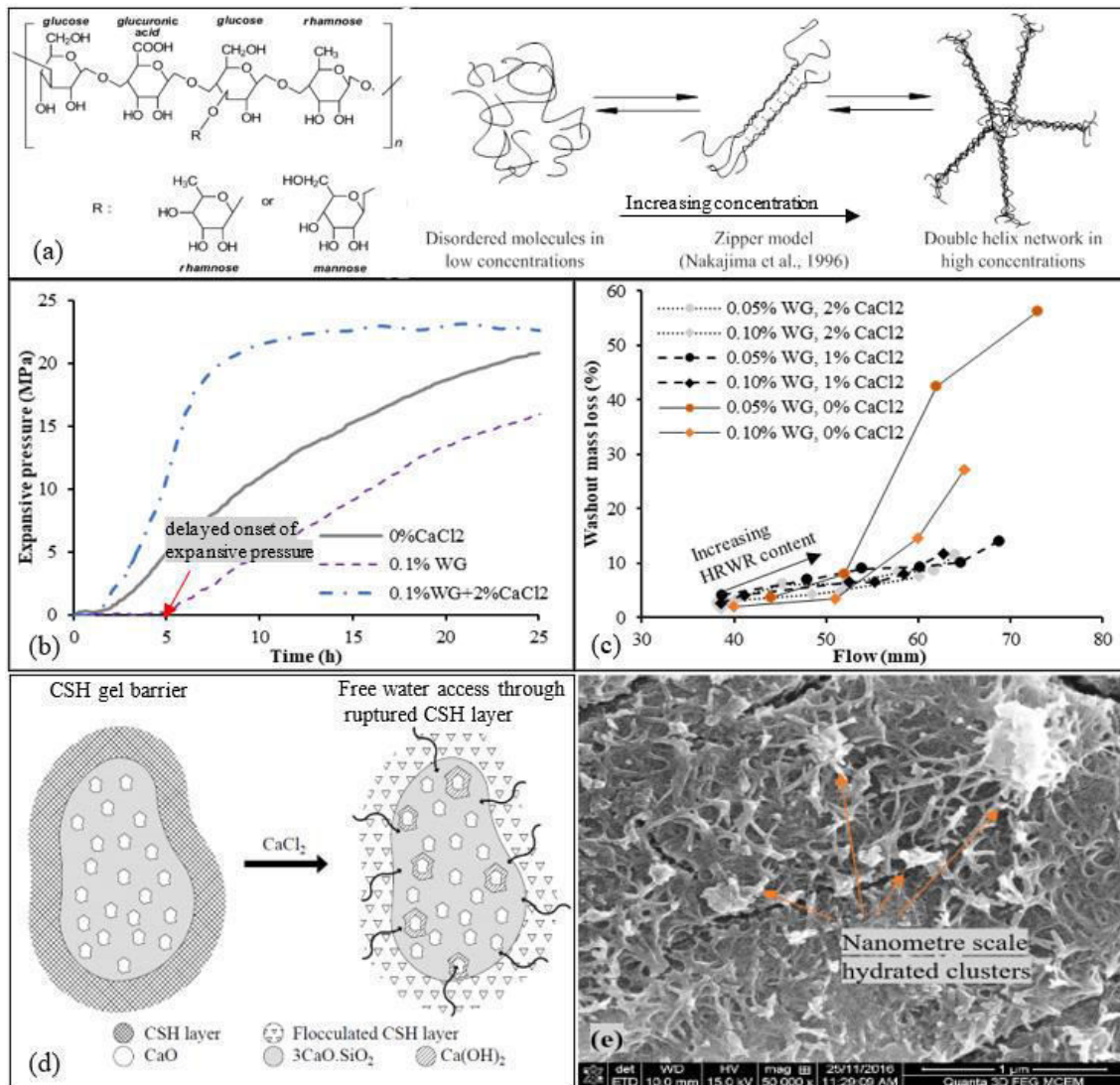


Figure 3: Modification of SCDA (a) welan gum molecular structure and intertwinement, (b) SCDA expansive pressure comparison, (c) SCDA fluidity/flow (mini-slump cone spread) and hydrophobicity (washout mass loss) comparison, (d) effects of CaCl_2 in SCDA hydration, and (e) SEM micrograph of CaCl_2 induced nano-scale hydration clusters, WG – welan gum (De Silva et al., 2019)

The final composition of 2% CaCl_2 , 0.1% VEA, and 2.5% of HRWR with 30% of water by weight of SCDA was found to produce a superior SCDA having a 79% improvement in washout resistance and a 44% improvement in the expansive pressure generation rate compared to the base SCDA. This new fracturing compound shows the potential to be used in the subsurface, and submerged conditions for rock fracture stimulation in various engineering applications including permeability-enhanced ISL.

3 NUMERICAL SIMULATION OF SCDA CHARGED FRACTURE PROPAGATION

After modifying SCDA for host rock preconditioning deep saturated host-rock formations, its fracturing performance was evaluated using the Discrete Element Method. The numerical simulations were performed using the general-purpose discrete element modelling software, particle flow code 3D (PFC3D 5.0 by ITASCA). The numerical tool was developed to predict and accurately capture the fracturing process during SCDA charging.

3.1 The numerical grain assembly

The laboratory fracturing tests were performed on homogenous coarse-grained silicate cemented Hawkesbury sandstone, obtained from the Sydney basin in Australia. Prior to SCDA charged fracture simulations, a numerical rock mass was assembled in PFC3D using the flat-jointed contact model (Itasca, 2014). The numerical rock mass was assembled by packing spherical particles in a vessel to a predetermined porosity and a density using the grain scaling method under zero friction, which iteratively scales the grain size to allow dense packing of particles in a vessel. Once the desired porosity of the numerical rock mass is achieved, the intergranular contact properties were assigned to particles in the assembly. The flat-jointed model was used to create the inter-particle bonds of the model. Multiple interface elements in the flat jointed model allow partial damage to the bond and are capable of resisting moments at the bond contact. The bonded assembly was then calibrated using laboratory test results for Uniaxial Compressive Strength (UCS). Afterwards, the model was validated against Brazilian disk Tensile Strength tests (BTS). A comparison between the experimental results and the numerical simulations for the mechanical strength tests of the specimens and the calibration parameters of the flat jointed model are shown in Table 1.

Table 1. Comparison of experimental and numerical strength results.

Micromechanical properties		Calibration results			
Parameters	Value	Parameter	Experiment	Numerical	Error %
Bonded contact E. modulus, \bar{E} (GPa)	5.9	UCS (MPa)	61.97	63.80	2.95
Bonded contact k-ratio (\bar{k}_n / \bar{k}_s)	0.86	E mod. (GPa)	7.77	7.85	1.03
Bonded contact Tensile strength (MPa)	5.0	Strain at failure	0.0084	0.0086	2.38
Bonded contact cohesion, C (MPa)	21.0	BTS (MPa)	3.94	3.89	1.27
Bonded contact friction angle, φ (°)	40				
Interface elements, on contact	3				
Unbonded contact E. modulus (GPa)	1.5				
Unbonded contact k-ratio (k_n/k_s)	3.0				
Unbonded contact friction coefficient, μ	0.1				

3.2 SCDA charged fracture simulation

Following the micro-mechanical damage simulation in the numerical rock mass assembly, the model was used to simulate SCDA charging. A cylindrical numerical rock assembly with 18064 bonded spherical particles (2.5mm - 3.0mm dia.) was produced by packing in a vessel (54 mm diameter and 108 mm height). A 5mm diameter injection well was simulated in the centre of the cylinder and the particles around the injection well were scaled by a factor of 0.6 to minimize the size effect on fracture initiation. The expansion caused by SCDA in the injection well was simulated using a servo-controlled rigid cylinder where the wall diameter of the cylinder was set to increase radially. The expansive pressure generated within the borehole was measured by dividing the sum of contact forces acting on the inner wall by the contact area of the borehole. The top and bottom flat plates, and the outer walls of the vessel were also servo controlled where wall velocities were controlled to apply a constant stress acting on the particle assembly. This method of simulation allowed the expansive pressure developed within an injection hole to be monitored with fracture propagation as shown in Figure 4. Experimentally observed fracture

propagation obtained from intermittently scanning the specimen during the fracturing process using X-Ray computed tomography (X-Ray CT) at the Australian Synchrotron imaging and medical beamline is also shown in Figure 4 for comparison.

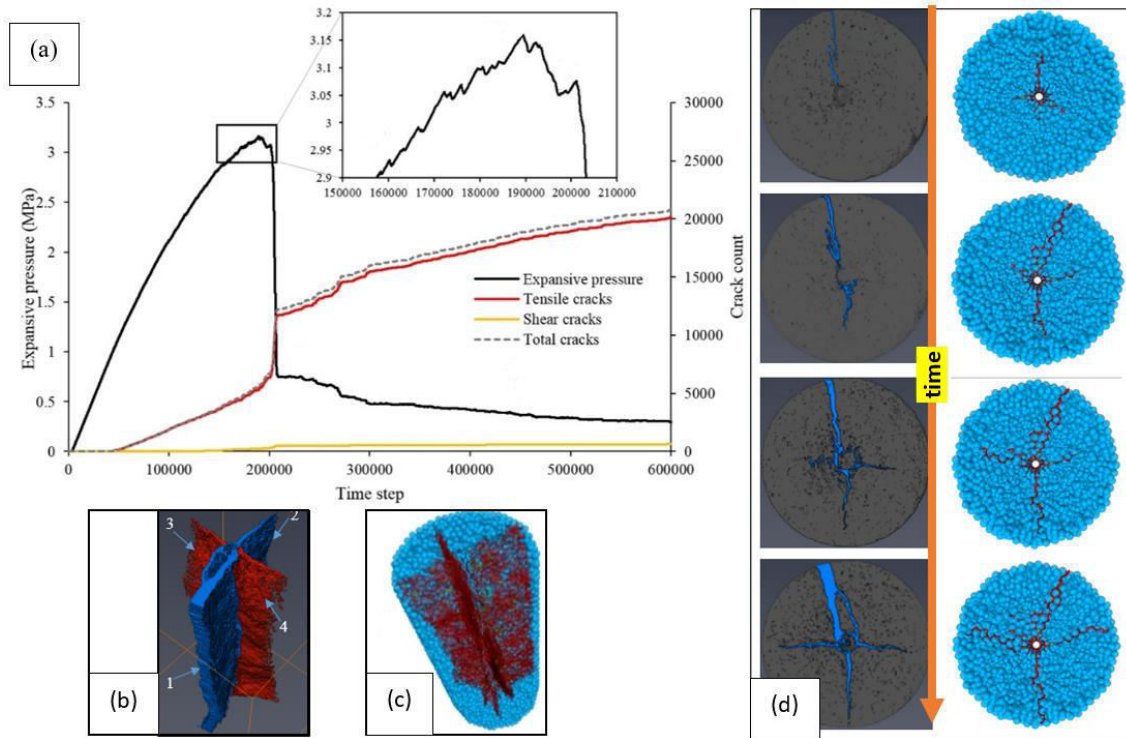


Figure 4: (a) Expansive pressure development in the injection well with fracture propagation, final fracture pattern of the rock specimen (b) CT reconstruction, (c) numerical simulation, and (d) fracture evolution during SCDA charging, experimental (left) and numerical (right).

The expansive pressure variation within the borehole under zero confinement is shown in Figure 4a. The expansive pressure development within the borehole could be idealized as a staggered pattern (minor pressure drops) due to the stress release during fracture propagation around the pressurized borehole (Dowding and Labuz, 1983) (Fig.3b), which was accurately captured in the model at peak expansive pressure (Fig. 4a). As the expansive pressure increased, the tensile stress in the vicinity of the borehole increased and resulted in radial fracture propagation. Consequently, the fractures under zero confinement are predominantly tensile as shown in Fig.4a. As shown in Figure 4d, the fractures propagate to the edge of the specimen leading to an abrupt drop in the expansive pressure causing the specimen to split.

4 SCDA CHARGING UNDER ISOTROPIC CONFINEMENT

4.1 The effect of confining pressure

Following the preconditioning numerical simulations using SCDA, fracturing experiments were performed to assess the effects of lateral confinement on the fracture performance. The lateral restraint against crack growth provided by large confining pressures results in the development of higher peak expansive pressures with increasing confinement. Furthermore, with increasing confining pressure, the failure mode of the specimen transitions from a tensile to a mixed tensile and shear failure (De Silva et al. 2018). This is due to the confining pressure increase around the

borehole; the stress state changes from pure tensile to a mixed tensile and compressive stress state. The tensile stresses are caused by the expansive pressure generated within the borehole, and the compressive stresses are applied by the confining pressure in the current model. The greater resistance for crack growth with increasing confinement tends to initiate additional fractures around the borehole during SCDA charging as opposed to crack growth. This phenomenon is particularly useful in deep host-rock formations, where fracture density around the injection well takes precedence over the extent of a single fracture.

The fracture patterns observed for specimens fractured under different confining pressures are shown in Figure 5a. As discussed, the experimental fracture observations indicate an increase in the fracture density and decrease in the fracture tortuosity around the injection well with increasing confining pressure (Figs. 5b and c).

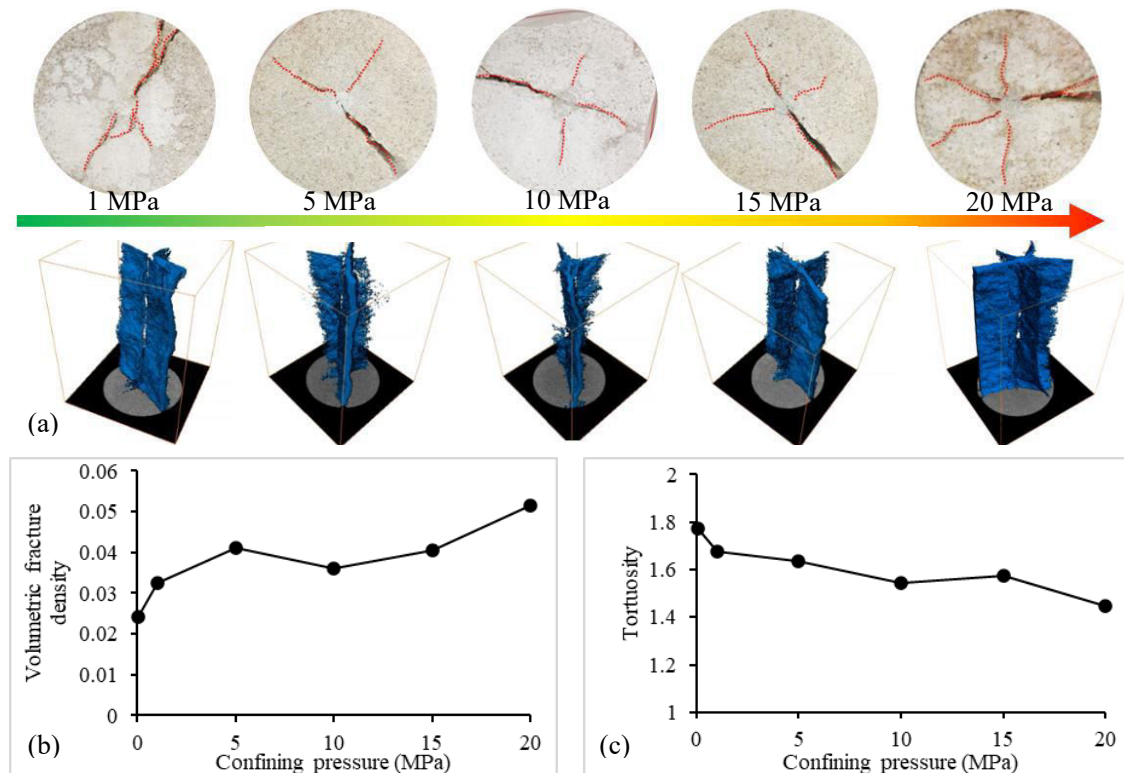


Figure 5: SCDA charged fracturing (a) with increasing confining pressure, (b) fracture density and (c) tortuosity

4.2 A comparison of hydraulic fracturing and SCDA charging

The fracturing performance of SCDA was evaluated against hydraulic fracturing in the laboratory by considering the number of fractures initiated around an injection well. Two identical specimens (54 mm dia. And 108 mm height) were fractured in the laboratory using hydraulic fracturing and SCDA charging. The isolated fracture network details of each of the specimens obtained by CT scanning are shown in Figure 6 and Table 2. The fracture growth direction in hydraulic fracturing is dictated by the rock mass heterogeneity and stress anisotropy. This was evident in the experimental observations. First, the fracture initiated parallel to the injection well (in the direction of the major principal stress) and then branched out perpendicular to the initial direction in a plane parallel to the bedding layers of the specimen (Fig. 6a). Consequently, a continuous fracture spanning across the entire length of the specimen was not attainable. Fracture propagation in toughness dominant hydraulic fracturing results when the fluid pressure at the crack tip exceeds the toughness of the rock. When a weaker plane such as bedding layers ex-

ists in the fracture path, the fractures tend to propagate in the direction of the weaker plane and result in fluid leak off preventing further crack propagation. Although horizontal fracture propagation is unlikely due to the stress conditions in this experiment, the presence of faults or weaker planes (bedding in this case) altered the direction of fracturing (Hossain et al. 2000).

On the other hand, SCDA charging introduces multiple radial fractures initiating from the borehole, irrespective of material heterogeneity due to the nature of pressure exertion described in section 1.2. Four major fractures were identified in the SCDA charged specimen. Out of the four fractures in the SCDA charged specimen, fracture 1 and 2 are continuous fractures and fracture 3 and 4 are connected fractures spanning the entire length of the specimen.

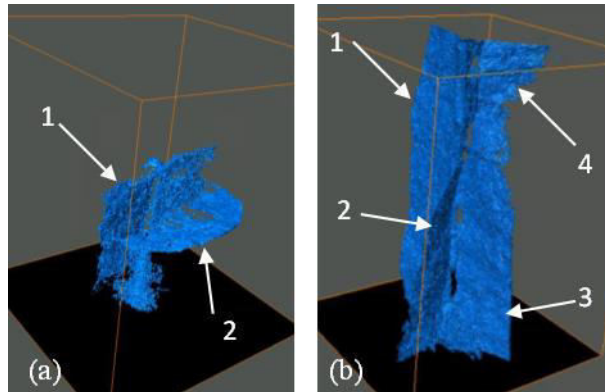


Figure 6: fracture networks (a) hydraulic fracturing, and (b) SCDA charging

Table 2. fracture details

	HF	SCDA
Fracture volume fraction	0.006	0.061
Tortuosity	5.83	1.26
Avg. fracture length (mm)	1	30.6
	2	23.73
	3	-
	4	-
		78.67
		29.33

5 FRACTURE PERMEABILITY

Due to the nature of the hydraulic fracture in the experiment (Fig. 6), the specimen permeability was dictated by the rock matrix permeability of $7.6 \times 10^{-20} \text{ m}^2$ (a flow rate of $3.2 \times 10^{-4} \text{ ml/s}$) for water at the confinement of 30 MPa and an injection pressure of 6 MPa. Figure 7 shows the flow rate variation with injection pressure at different confining pressures for the SCDA charged specimen. At high confining pressures (20 – 30 MPa), a linear correlation was observed in the fracture flow and the cubic law was used to calculate an average hydraulic aperture for the fracture flow in SCDA charged specimen. Figure 7b shows the variation of the pressure gradient across the SCDA charged specimen with flow velocity, which is represented by a second-order polynomial. Therefore, Forchheimer's equation was used to calculate the Darcian and the non-Darcian permeability components of the fluid flow in the SCDA charged fracture.

$$(P_i - P_o) / L = \mu/k_1 \cdot v_s + \rho/k_2 \cdot v_s^2 \quad (3)$$

In Equation 3, P_i and P_o are the inlet and outlet pressures of the specimen, L is the fracture length, v_s is the fluid velocity, μ is the fluid viscosity, and ρ is the fluid density. k_1 and k_2 are termed as Darcian and non-Darcian permeabilities of the material. Here, the $\mu/k_1 \cdot v_s$ component represents the frictional flow resistance between fluid layers and the $\rho/k_2 \cdot v_s^2$ component represents the inertial and turbulence contributions (Innocentini et al., 1999). The experimental results indicate, that SCDA charging improves the specimen permeability from $7.6 \times 10^{-20} \text{ m}^2$ ($7.7\text{e-}5 \text{ mD}$) intact rock matrix permeability to a fracture flow permeability of $9.79 \times 10^{-13} \text{ m}^2$ (992 mD) at 30 MPa confining pressure.

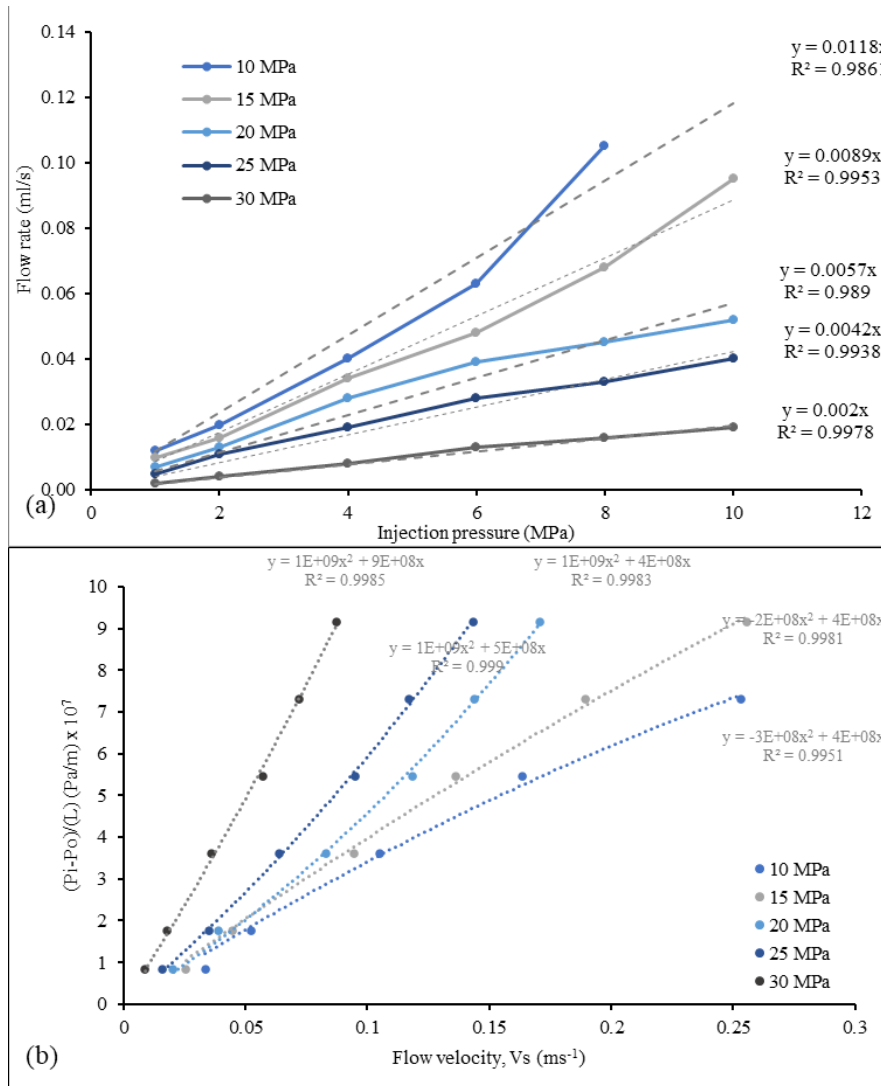


Figure 7: Fracture flow permeability in SCDA charged specimen. (a) flow rate variation with injection pressure and (b) pressure gradient with flow velocity

6 CONCLUSIONS

This paper presents a new technology for host-rock preconditioning in In-Situ Leaching mining applications using Soundless Cracking Demolition Agents (SCDAs). First, the study involves the development of a patented (US Patent No. 10836955) hydrophobic slow energy releasing SCDA compound which can be used for deep rock fracture initiation applications under submerged conditions. Next, a DEM-based numerical tool is presented to simulate the slow energy releasing fracturing process of SCDA that was used to understand the underlying mechanics of SCDA charged charging. Following the numerical model development, a series of laboratory experiments were carried out to investigate the fracturing performance of SCDA under different confining pressures. Finally, the fracturing performance near the injection well and the resultant permeability improvement following SCDA charging was investigated and compared against the existing method of hydraulic fracturing in a series of laboratory experiments. Based on the results of this study the following key conclusions can be drawn.

- The patented SCDA improves hydrophobicity by 79 % compared to generic SCDAs and the onset of expansive pressure development is improved by 52 %. The expansive pressure de-

velopment rate is further improved by 45 %. This allows SCDA to be pumped into deep geological formations and initiate controlled fractures.

- The DEM-based numerical model successfully simulates the expansive pressure development inside an SCDA injected borehole and the subsequent radial fracture propagation, which were validated by experimental studies.
- Increasing the confining pressure of the surrounding rock causes the SCDA fracturing mode to transition from a tensile to a shear dominant mixed tensile-shear failure. Laboratory experiments conducted on specimens under large confining pressures (up to 20 MPa) indicate SCDA chagrining produces multiple radial fractures around an injection well.
- Compared to fracture stimulation using pure hydrofracking at the near vicinity of the injection well, SCDA charging creates multi-directional fractures around an injection well independent of rock mass heterogeneity.

REFERENCES

- Dowding, C.H. & Labuz, J.F., 1983. Closure to “fracturing of rock with expansive cement” by Charles H. Dowding and Joseph F. Labuz (October, 1982). *Journal of Geotechnical Engineering*, 109(9), pp.1208-1209.
- De Silva, V.R.S., Ranjith, P.G., Perera, M.S.A., Wu, B. & Wanniarachchi, W.A.M., 2018. A low energy rock fragmentation technique for in-situ leaching. *Journal of Cleaner Production*, 204, pp.586-606.
- He, Q., Suorineni, F.T. & Oh, J., 2016. Review of hydraulic fracturing for preconditioning in cave mining. *Rock Mechanics and Rock Engineering*, 49(12), pp.4893-4910.
- Holmberg, K., Kivikytö-Reponen, P., Härkisaari, P., Valtonen, K. & Erdemir, A., 2017. Global energy consumption due to friction and wear in the mining industry. *Tribology International*, 115, pp.116-139.
- Innocentini, M.D., Salvini, V.R., Pandolfelli, V.C. and Coury, J.R., 1999. Assessment of Forchheimer's equation to predict the permeability of ceramic foams. *Journal of the American Ceramic Society*, 82(7), pp.1945-1948.
- Ish-Shalom, M. & Bentur, A., 1975. Properties of type K expansive cement of pure components III. Hydration of pure expansive component under varying restraining conditions. *Cement and Concrete Research*, 5(2), pp.139-152.
- Itasca (2014) PFC 5.0 Documentation. Itasca Consulting Group Inc. Minneapolis, MN, USA.
- Kaur, V., Bera, M.B., Panesar, P.S., Kumar, H. & Kennedy, J., 2014. Welan gum: microbial production, characterization, and applications. *International journal of biological macromolecules*, 65, 454-461.
- Laefer, D.F., Ambrozovitch-Cooper, N., Huynh, M.P., Midgette, J., Ceribasi, S. & Wortman, J., 2010. Expansive fracture agent behaviour for concrete cracking. *Magazine of concrete research*, 62(6), pp.443-452.
- McCarter, M.K., 1996. Effect of blast preconditioning on comminution for selected rock types (No. CONF-960234-). International Society of Explosives Engineers, Cleveland, OH (United States).
- Hossain, M.M., Rahman, M.K. & Rahman, S.S., 2000. Hydraulic fracture initiation and propagation: roles of wellbore trajectory, perforation and stress regimes. *Journal of petroleum science and engineering*, 27(3-4), pp.129-149.
- Saharan, M.R., Mitri, H.S., & Jethwa, J.L., 2006. Rock fracturing by explosive energy: review of state-of-the-art. *Fragblast*, vol. 10, pp. 61-81
- Northey, S., Haque, N. & Mudd, G., 2013. Using sustainability reporting to assess the environmental footprint of copper mining. *Journal of Cleaner Production*, 40, pp.118-128.
- Rötzer, N. & Schmidt, M., 2018. Decreasing metal ore grades—is the fear of resource depletion justified? *Resources*, 7(4), p.88.
- Stadler, A. & Boucaut, S., 2015. Unlocking the energy productivity value proposition. *AusIMM Bulletin*, (Aug 2015), pp.52-55.
- Watari, T., Northey, S., Giurco, D., Hata, S., Yokoi, R., Nansai, K. & Nakajima, K., 2022. Global copper cycles and greenhouse gas emissions in a 1.5° C world. *Resources, Conservation and Recycling*, 179, p.106118.

Web-pillar design for highwall coal mining – a case study

S. Sarkar, M. Tiwari, I. Saha, P. Srivastava & D. B. Sundara Ramam
Tata Steel Limited, Jamshedpur, Jharkhand, India

ABSTRACT:

Highwall mining is a mechanized and effective way to recover coal which is locked-up in the barrier of open cast mines. In a multi-seam environment, the design of the highwall ribs or web-pillars pose a great challenge as most of the areas either have human population or have rural/industrial infrastructure. West Bokaro open cast coal project is one of the captive mines of Tata Steel Limited, India. Here, high wall mining is now a well-established process and is being operated since last six years. All the seams are gently dipping, with 3°-6° inclination and occur at a depth of 75 – 110 m within the proposed highwall site. In this paper, design of the web pillars is done through numerical modelling using FLAC 3D even for thick seams considering multi-pass extraction condition. The paper explains the procedure adopted to design web pillars based on the depth of penetration of galleries, gallery width, height of extraction, deviation of the highwall miner and the physico-mechanical properties of rocks/coal in PCP3 area (Primary Crushing Plant 3) of Quarry AB in West Bokaro open cast coal project. Simulation through numerical modelling is done by two methods viz. long pillars and equivalent square pillars and the results are compared. The coal seams designed for extraction through highwall mining in this PCP3 area are seams V, VI & VII. The width of web pillar is designed to optimize the extraction percentage of coal without compromising the risk of subsidence by maintaining a Factor of Safety (FoS) more than 2.0.

Keywords: Highwall mining, web-pillar, numerical modelling, Factor of Safety.

1. INTRODUCTION

Highwall mining is a method of surface mining that produces locked-up coal from the base of highwalls, Shen and Duncan (2001). In this method, a series of parallel entries are driven through the coal seams from the final highwall portions of the mine beyond which normal drilling and blasting techniques cannot be implemented due to various technical and statutory constraints. Continuous highwall miners (CHMs) are deployed to drive the entries into the coal seams. According to Verma et. al (2014) the mined-out gallery or drivage is referred as “web cut” while the left-out coal in the pillars between two parallel galleries is called “web pillar”. The web cuts are not supported or ventilated in general.

Highwall mining in West Bokaro division of Tata Steel Limited has now been a well-established process in the last few years. There are two operative quarries in West Bokaro division namely quarry AB and quarry South Eastern Block (SEB). Panels A, B and C in quarry SEB and panels in Banji area of quarry AB had been operative since the last six years. In this paper, the coal seams considered feasible for extraction from the highwall panel is the PCP3 area of quarry AB as shown in fig 1. PCP3 area has coal seams V, VI and VII, occurring in ascending order. All the seams are gently dipping, with 3°-7° inclination and occur at a depth of 75 – 110 m within the proposed highwall site as shown in fig 2.

In the current study, feasibility of extraction of coal from the above targeted seams at specific locations in quarry AB is analysed and web pillar width for such extraction have been designed for individual seams. The main consideration is to maximise coal recovery with adequate safety factors and to protect surface and sub-surface property from subsidence.

2. LOCATION AND GEOLOGY

West Bokaro Leasehold is in the central portion of West Bokaro coalfield Administratively, it falls in Kedla block of Ramgarh district, Jharkhand. The block is bounded by latitudes $23^{\circ}48'16''$ to $23^{\circ}48'57''$ & longitudes $85^{\circ}33'07''$ to $85^{\circ}34'34''$ and falls in Survey of India toposheet no. 73E/5. The district capital Ramgarh is about 30 kms from the block. The West Bokaro Coalfield is a broad half basin, with its closure on the West. The other half of the basin is represented by East Bokaro Coalfield. The Pre-Cambrian-Gondwana boundary in the north is marked by an east-west trending set fault. Most of the coal seams are confined to the upper and middle sections of the Barakar formation. Igneous intrusives are sometimes outcropped in quarries and intersected in a few boreholes. There are fourteen major coal seams within the leasehold area (Seam XIV to seam I). The coal seams have a strike of E – W and dip varying between 3° - 7° due south.

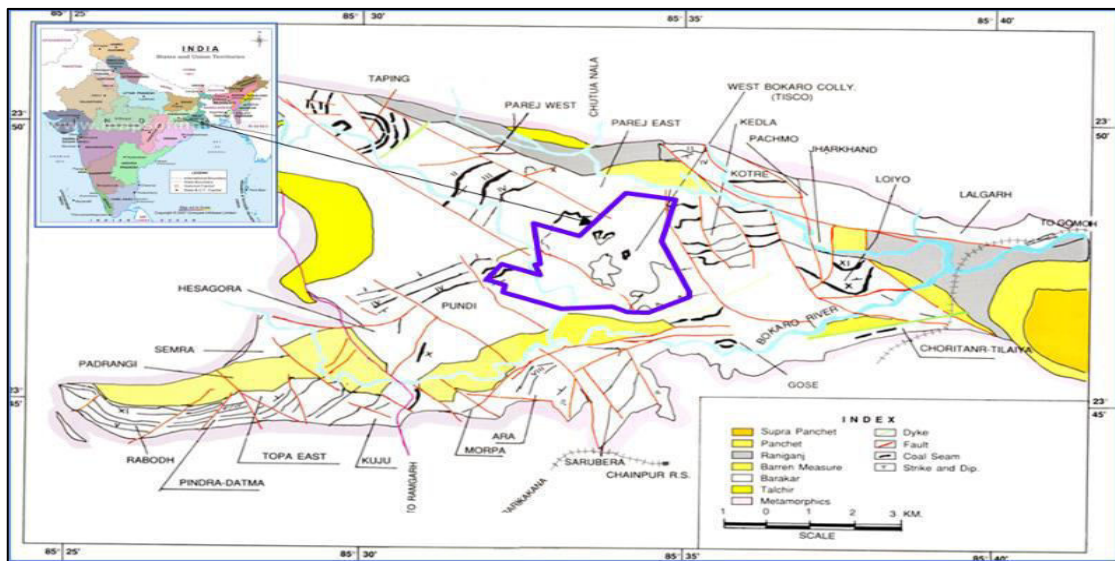


Figure 1. Location plan of West Bokaro Colliery in West Bokaro Coalfield.

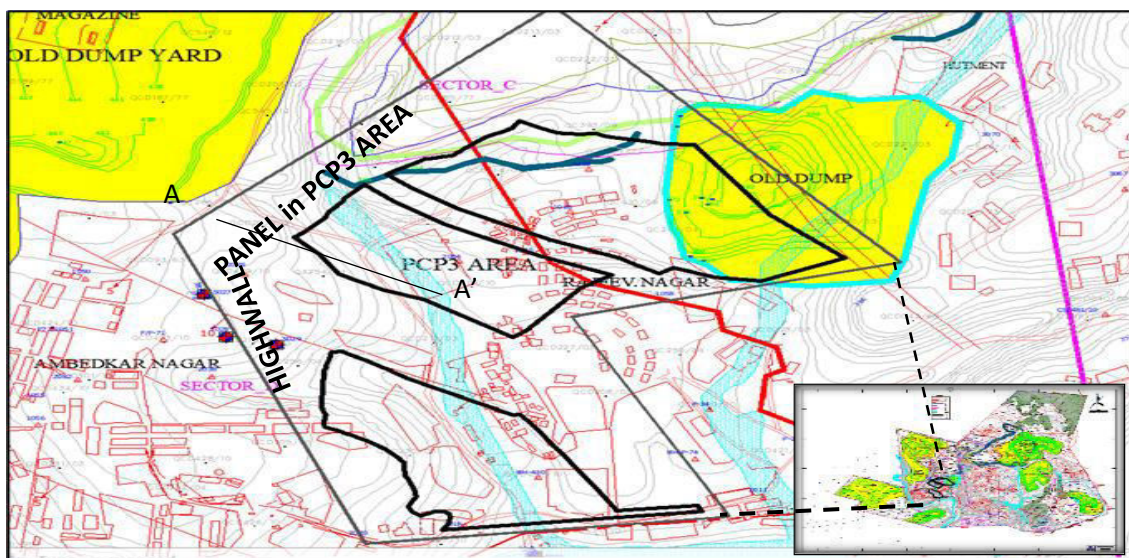


Figure 2. Highwall panels marked in the PCP3 area of QAB, West Bokaro Colliery (inset)

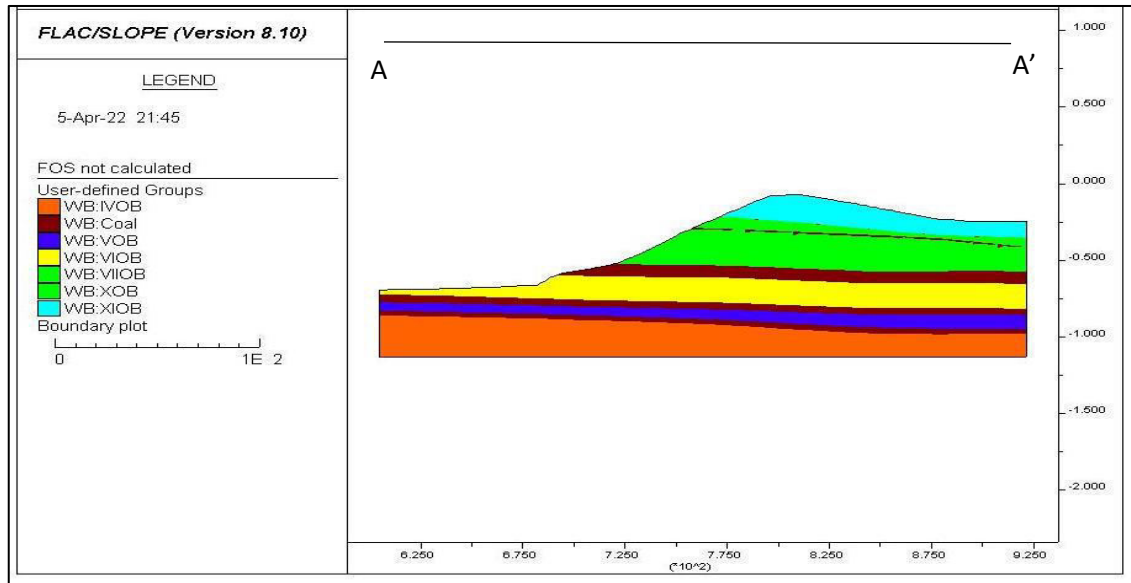


Figure 3. Cross-section along A-A' showing several seams and highwall faces

3. GEOTECHNICAL DETAILS

The topmost target seam below PCP3 is VII seam, which occurs at about 75 m (max) below depth of cover. Seams occurring above seam VII at PCP3 are IX and X which are partially developed by board and pillar method. The workable seams by highwall method in Quarry AB below PCP3 area are given in the table 1. Rock and rock mass properties used for numerical modelling studies is given below in the table 2 are referred from CIMFR technical report (2013).

Table 1: Seam details in PCP3 area

Sl. No.	Seam	Depth (m)	Avg. thickness (m)	Parting (m)
1	VII	75	8	22-47
2	VI	90	4.5	15-16
3	V	110	3.5	9-11

Table 2: Rock and Rockmass properties used for numerical modelling studies.

Strata	Compressive strength (MPa)	Young's modulus (GPa)	Poisson's ratio	Density (kg/m ³)	Rock Mass Rating (RMR)
VIII Roof	39.5	10	0.25	2500	55
VIII Seam	20	2	0.25	1500	55
VIII – VII parting	35	10	0.25	2500	55
VII Seam	20	2	0.25	1500	55
VII – VI Parting	31	10	0.25	2500	55
VI Seam	20	2	0.25	1500	55
VI – V Parting	30.7	10	0.25	2500	60
V Seam	20	2	0.25	1500	55

4. NUMERICAL MODELLING INPUTS

FLAC3D software provides for elasto-plastic analysis of rock excavations with strain-softening material model using the linear Mohr-Coulomb failure criterion (Itasca Manuals, FLAC 3D). The strength and elastic constants necessary for numerical modelling using FLAC3D in the strain-softening models are:

- Elastic constants (Young’s modulus and poisson ratio)
- Peak and residual shear strength and its variation with shear strain
- Peak and residual angle of internal friction and its variation with shear strain
- Angle of dilation

All these properties are specified for the coal seams and the respective roof and floor rocks. The input parameters used for the strain-softening models are given in the table 3.

Table 3: Physico-mechanical properties of coal and roof/floor lithologies

Shear Strain	Cohesion (Mpa)	Friction angle (°)
0	C	Φ
0.005	$C / 5$	$\Phi - 2.5$
0.010	0	$\Phi - 5$
0.050	0	$\Phi - 5$

The variations of cohesion and friction angle with respect to shear strain are given below in the table 4.

Rock	Cohesion (Mpa) – (C)	Friction angle (°) – Φ	Tensile strength (Mpa)	Youngs modulus (Gpa)	Poisson’s ratio	Density (kg/m3)	Dilation angle
Coal	1.6	29	0.63	3.33	0.25	1500	0
Roof/floor rocks	3.2	34	1.3	10.0	0.25	2500	0

Table 4: Variation of cohesion and friction angle w.r.t strain

5. NUMERICAL MODELLING APPROACH

The numerical models were done using two techniques. The first technique was a simulation of infinitely long pillars where two vertical planes of symmetry are taken, one passing through the centre of the roadway and the other through the centre of the long pillar. The second technique involved a square pillar, where pillar width considered is twice the value of the long pillar scenario. The model is simulated by taking only a quarter portion of the pillar, bound by four vertical planes of symmetry, two passing through the centre of the pillar and the other two passing through the centre of the roadways. The results of all the seams have been reported from the square pillar simulation and a reduction of 20% peak load is considered for pillars whose width and height ratio is less than 1.0 as mentioned in CIMFR technical report, 2013 and Louis et. al. (2011).

Figure 4: Schematic diagrams showing model areas for long pillars and square pillars

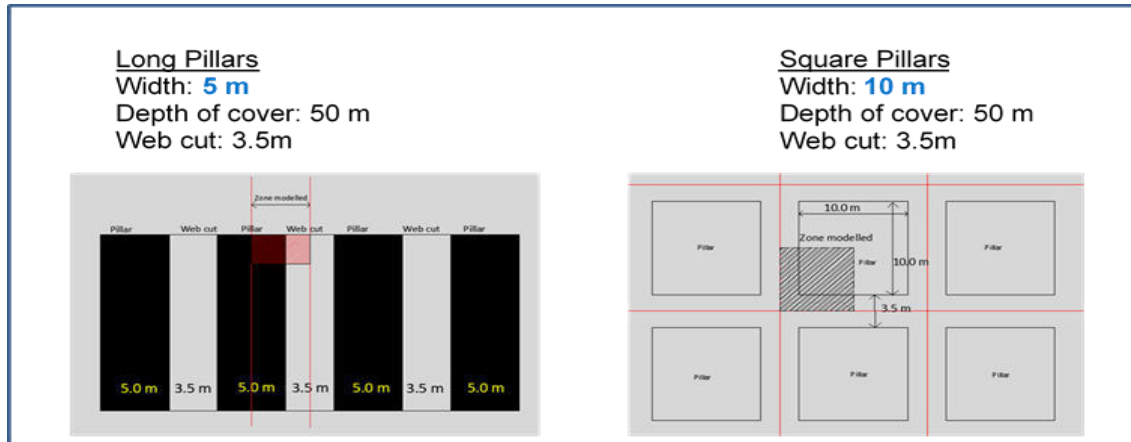


Figure 4. Schematic diagrams showing model areas for long pillars and square pillars

6. RESULTS AND DISCUSSION

It is observed in Indian coalfields that a pillar with safety factor of more than 2.0 is stable over a long period of time, i.e., for many decades. A safety factor between 1.5 and 2.0 is stable for a few years and may be taken as medium-term stable. Finally, as mentioned by Louis et. al. (2013) a safety factor of the pillar 1.0 may be treated as short-term stable, with a stand-up time of a few weeks or a month. The strength-stress ratio plots of seams VII, VI and V of the long pillar simulation and their corresponding square pillars are shown in figs 5A to 7B. The x-axis in all the figures 5-7 represents the vertical strain while the y-axis represents the vertical stress. The curve shows the peak load carrying capacity plotted for all the seams in both the techniques adopted. The Factor of Safety calculated using both the techniques is shown in table 5 and 6.

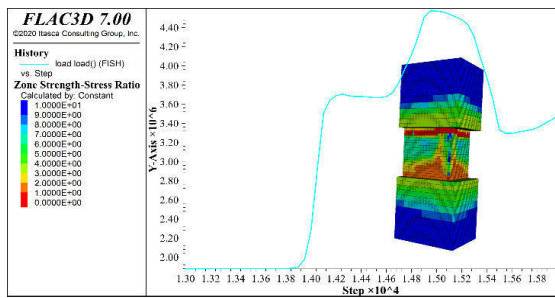


Figure 5A. Stress and strain curves for seam VII sq pillar

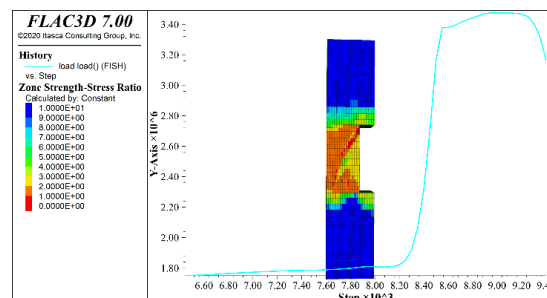


Figure 5B. Stress and strain curves for seam VII long pillar

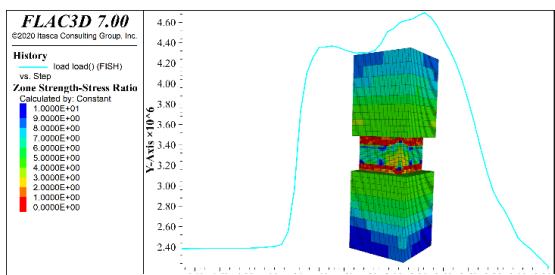


Figure 6A. Stress and strain curves for seam VI sq pillar

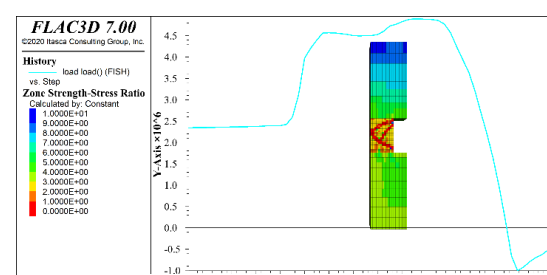


Figure 6B. Stress and strain curves for seam VI long pillar

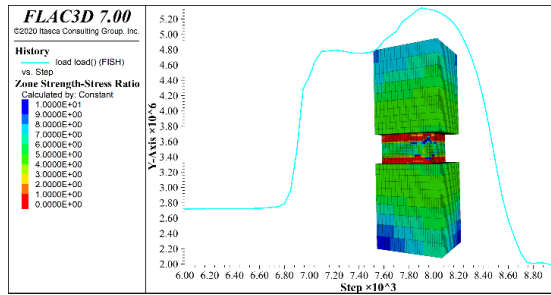


Figure 7A. Stress and strain curves for seam V sq pillar

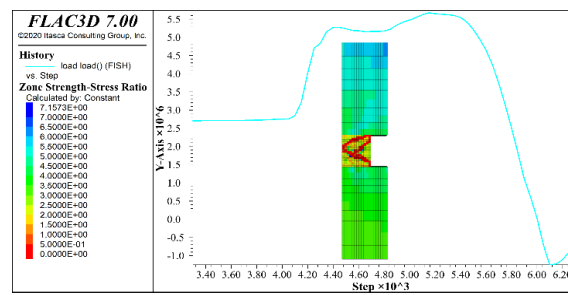


Figure 7B. Stress and strain curves for seam V long pillar

Table 5: Minimum and maximum load as per long pillar simulation

Seam	Pillar width (m)	Initial Load on the base (Mpa)	Peak Load on the base (Mpa)	Initial Load on the pillar (Mpa)	Peak Load on the pillar (Mpa)	FoS
VII	9.00 (w/o dev)	1.87	4.94	2.60	6.86	2.64
	7.75 (with dev)	1.75	3.46	2.54	5.02	1.98
VI	7.25 (w/o dev)	2.35	5.40	3.48	8.01	2.30
	6.0 (with dev)	2.34	4.89	3.71	7.74	2.09
V	7.25 (w/o dev)	2.70	5.75	4.00	8.53	2.13
	6.0 (with dev)	2.75	5.66	4.35	8.96	2.06

Table 6: Minimum and maximum load as per square pillar simulation

Seam	Pillar width (m)	Initial Load on the base (Mpa)	Peak Load on the base (Mpa)	Initial Load on the pillar (Mpa)	Peak Load on the pillar (Mpa)	FoS
VII	9.00 (w/o dev)	1.88	4.96	2.68	7.08	2.64
	7.75 (with dev)	1.87	4.60*0.8=3.68*	2.81	5.53	1.97
VI	7.25 (w/o dev)	2.38	5.40	3.67	8.32	2.27
	6.0 (with dev)	2.38	4.70	3.97	7.84	1.97
V	7.25 (w/o dev)	2.72	6.08	4.19	9.37	2.24
	6.0 (with dev)	2.71	5.34	4.52	8.91	1.97

*since w/h ratio is less than 1, peak load is reduced by 20%.

The comparison of FoS values for each seam based on the square pillar simulation and its equivalent long pillar simulation is shown in table 7. The percentage extraction of each seam has been worked out based on the width of the predicted web pillar. Seam VII having a pillar width of 9.0 m has an extraction percentage of 28% while seam VI and seam V have a pillar width of 7.25 m and the extraction percentage stands at 33% for each of them.

Table 7: Factor of Safety and predicted web pillar width

Seam	Extraction height (m)	Max length of extraction (m)	Max width deviation (\pm 0.4%); m	Web Pillar Width (m)	Max and Min FoS (Sq. Pillar)	Max and Min FoS (long pillar)	% extraction
VII	8.0	300	1.25	9.00	2.64 & 1.97	2.64 & 1.98	28
VI	4.5	300	1.25	7.25	2.27 & 1.97	2.30 & 2.09	33
V	3.5	300	1.25	7.25	2.24 & 1.97	2.13 & 2.06	33

7. CONCLUSIONS

The Optimal size of web pillars was worked by maintaining minimum FoS for each seam around 2.0. The pillar width of seam VII may be kept as 9.0 m followed by 7.25 m for seam VI and seam V, respectively. As per the pillar width the extraction percentage of seam VII is 28% while it is 33% each for seam VI and seam V. Analysis using long pillars and their equivalent square pillars have similar kind of results with a maximum difference of 0.12 observed in case of seam VI.

8. ACKNOWLEDGEMENTS

The authors express sincere gratitude to the management of Tata Steel, India especially Vice President Raw Materials; General Manager, West Bokaro Division; Chief Natural Resources Division (NRD) & Chief Mine Planning, NRD for providing all the support & necessary guidance. The views expressed in the paper are those of the authors and not of the organization.

REFERENCES

- CIMFR Technical Report: “Feasibility study for Highwall Mining at Quarry SEB (and Quarry AB), West Bokaro Division of M/s Tata Steel Limited”, No. GC/MT/174/2008-2009, March 2013.
- FLAC 3D. 1997. Itasca Manuals, Itasca Consulting Group, Inc, USA
- Loui, J. P., Palroy, P. & Sinha, A. 2011. Design of Highwall Mining at West Bokaro Division of Tata Steel Limited, India. *Journal of Institution of Engineers India* 92: 1-7.
- Loui, J.P., Verma, C.P., Palroy, P. & Sinha, A. 2013. Design and development norms for Highwall Mining in India, *Procs. 25th National Convention of Mining Engineers and the National Seminar on Policies, Statutes and Legislation in Mines - Recent Reforms and their Impacts on Indian Mining Industry, India, POSTALE 2013*. India
- Shen, B. & Fama, M.E.D. 2001. Review of highwall mining experience in Australia and a case study. *Aust Geomech* 36(2): 25–32.
- Verma, C.P., Porathur, J.L. & Thote, N.R. 2014. Empirical Approaches for Design of Web Pillars in Highwall Mining: Review and Analysis. *Geotech Geol Eng* 32: 587–599.

Estimation of the Probability of Rock fall Occurrence in Underground Mines

F. Fernandez, FF GeoMechanics (Chile)
FF GeoMechanics, Valparaiso, Chile

M.A. Rodriguez (Spain)
University of Oviedo, Oviedo, Spain

ABSTRACT:

During the last twenty years' significant changes of the mining paradigm has been observed mainly related to the transformation of mine methods that have evolved from massive open pit extractions to deep underground mining with reduced ore grades and highly complex geotechnical environments which have posed increasing restrictions on this type of operation.

Despite the vertiginous advance of technology that has helped to overcome many limitations, in addition to the development and improvements of mine methods and risk management, the rock fall events still cause an important number of accidents to workers and/or damage to facilities and equipment in underground mines. This problem emphasizes the relevance of a better comprehension and quantification of the probability of fall of ground occurrence in underground mines by considering information that may be captured at the early stages of a project.

1 INTRODUCTION

A “state of the art” related to the methodologies for the estimation of the underground mine risk reflects that research developed during the last ten years come from China, Australia and North America (Canada and the USA) and has focused mainly on environment, general issues and machines (Tubis et al., 2020).

According to Tubis et al (2020), most publications were found by typing the keywords “risk assessment”, which together accounted for almost 80% of all the analyzed texts.

Publications related to geotechnical risk and/or hazard occurrence are scarce and has been oriented to the construction of “matrix type” and semi-quantitative assessments. It is worth note the work developed by the Australian Centre for Geomechanics (ACG) for example: Hadjigeorgiou (2019), Wesseloo et al (2020), Joughin et al (2020) and previous research developed by Owen and Potvin (2003).

2 OBJECTIVES

The main objective of this research is focused on the construction of a probabilistic model for the estimation of rock fall occurrence in underground mines that can be supported on basic geotechnical data to be obtained during the early stages of a mining project.

On this regard, the specific objectives are oriented to propose a probabilistic methodology to quantifying the rock fall occurrence based on the GSI Index (Marinos & Hoek, 2000, Cai et al, 2004), and the “unit cell method” for key-block occurrence (Kuszmaul, 1999).

In other words, the methodology will deliver the first part of the risk estimation which is related to the probability of hazard occurrence.

3 OVERVIEW OF GEOTECHNICAL RISK

According to Cole (1993) and Stacey (2001), an acceptable life-time probability of loss of life in respect of voluntary employment in underground mines would be 0.7% or 0.007 (or 7 in 100 million hours).

Lilly (2004) suggests that acceptable levels for probabilities of failure for which designs may be prepared should be significantly smaller than the actual probabilities of failure observed for similar situations. This is required to account for the following aspects:

- 1) Natural aversion to involuntary total loss
- 2) Variations in perceptions
- 3) Non-representativeness of actual comparative probabilities of failure
- 4) Variations in parameter values and biases in calculation procedures
- 5) Deficiencies in design data

Ground conditions are known to carry potentially high risks and uncertainty. According to Sowers (1993) a study of 500 geotechnical failures revealed that 88% of the failures were produced by human shortcomings and that 75% of the failures originated in the design process. These problems are directly and largely attributable to deficiencies in the site investigations undertaken for design purposes.

As part of this research a detailed review of underground mine fatalities was developed by considering on-line information published from government agencies in Chile, Peru, USA and Western Australia.

Records of mine accidents and fatalities were analyzed and integrated with the purpose of obtaining graphical representations for benchmarking purposes as it shown in Figures 1 and 2.

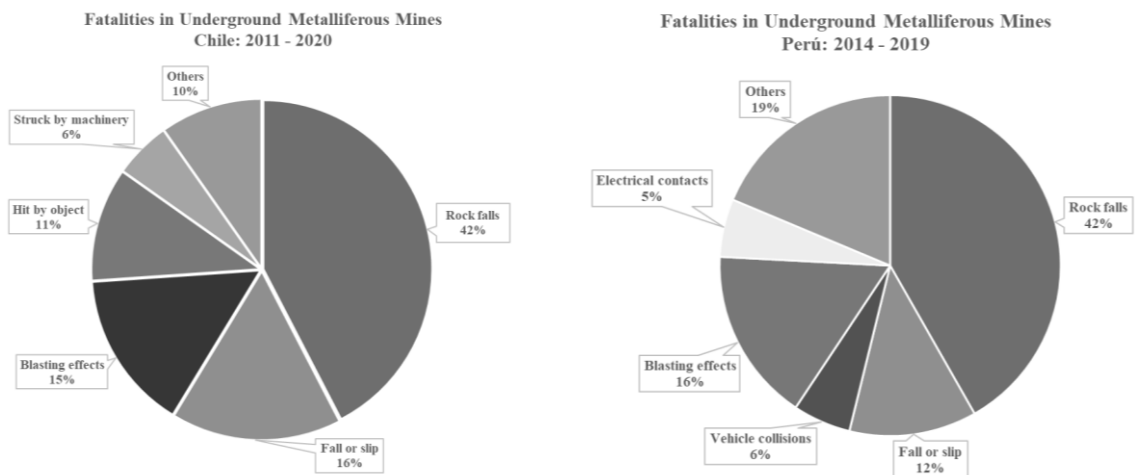


Figure 1. Fatalities recorded by different causes in underground metalliferous mines. Records for Chile (on the left, between years 2011 and 2020) and Peru (on the right, between years 2014 and 2019).

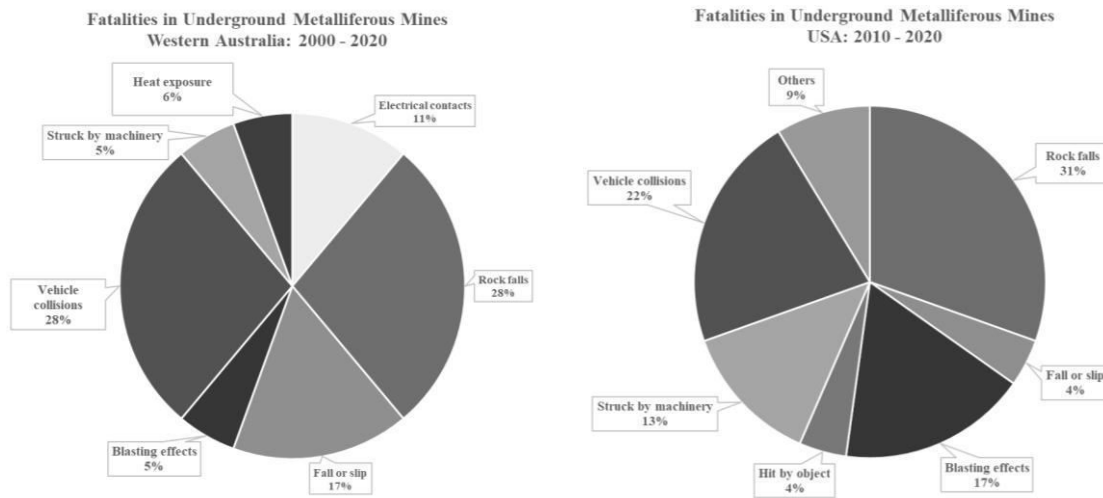


Figure 2. Fatalities recorded by different causes in underground metalliferous mines. Records for Western Australia (on the left, for years 2000 to 2020) and the USA (on the right, between years 2010 and 2020).

The interpretation of the graphs reflects that during the last ten years, rock falls represent the main cause of accidents in underground mines accounting for 40% of the fatalities in both Chile and Peru. The percentage of accidents caused by rock falls it is lower in WA and USA, with 28% and 31% respectively.

As part of this research the statistical information of accidents was integrated to work force data in order to obtain the values of risk of death due to geotechnical (rock fall) causes to be benchmarked against the risks of other activities and the acceptability threshold for underground metalliferous mines. In addition, the values of risk for supported and unsupported conditions extracted from the work of Fernandez (2011) are listed in Table 1.

Table 1. Rock fall risk in an underground metalliferous mine benchmarked against other activities.

Activity	Risk of death x 10 ⁻⁸ hours (FAR)
Rock fall (unsupported excavation) - UG Mine	542.00
Helicopter travel	500.00
Motorcycle travel	300.00
Rock fall (incomplete support) - UG Mine	116.00
High rise construction erection	70.00
Smoking	40.00
Walking beside a road	20.00
Rock fall (Peruvian UG Mines)	18.90
Air travel	15.00
Car travel	15.00
Coal Mining (UK)	8.00
Rock fall (Chilean UG Mines)	7.10
Acceptability for UG metalliferous Mines	7.00
Train travel	5.00
Construction (average)	5.00
Metal manufacturing	4.00
Rock fall (USA UG Mines)	2.43
Rock fall (fully supported) UG Mine	1.94
Rock fall (WA UG Mines)	1.12
Bus travel	1.00
Terrorist bomb in London street	0.10

It is possible to note a series of conclusions from Table 1:

- The rock fall risk in underground mines in Peru is higher than the threshold value.
- The rock fall risk in underground mines in Chile is slightly higher than the acceptable value.
- Statistical rock fall risks in WA and USA are lower than the threshold value.

4 CONSTRUCTION OF A ROCK FALL PROBABILISTIC MODEL

Failure mechanisms within the rock mass related to the “In-Situ” stresses and/or structural conditions related to the fabric of rock in addition to major structures may determine the occurrence of rock falls in an underground environment.

The model proposed in this paper utilizes the outcomes obtained from the research of Kuszmaul (1999) for the estimation of rock blocks occurrence possible to form around the perimeter of an underground excavation. This approach is known as the “unit cell method”. The volumes of rock blocks that may fail (or “key-blocks”) required by the Kuszmaul (1999) “unit cell method” are obtained by the work developed by Cai et al (2004) which is sustained on the GSI (Marinos & Hoek, 2000) Index.

Discrete fracture network (DFN) models may be used for the probabilistic determination of rock blocks stability by using specialized software packages. However, it is worth noting that for preliminary geotechnical investigations a simplified analytical model based on the estimation of GSI, it is proposed in this paper over the use of complex approaches.

The stages for the construction of the rock fall probabilistic model are defined in the diagram of Figure 3.

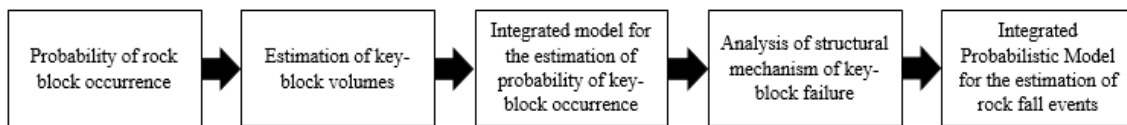


Figure 3. Schematic representation of stages for the construction of a model of rock fall estimation.

The first stage of the model implies the estimation of probability of key-block occurrence based on the “unit cell method”. This approach developed by Kuszmaul (1999) provides a method of taking account of the spacing of discontinuities and the dimensions of the opening to estimate both the expected probability of a key-block forming within a randomly selected excavation cross-section.

For the construction of the proposed model, the key-block volumes required as input parameters in the “unit cell method” are provided by the GSI approach developed by Cai et al. (2004) which employs the block volume and a joint condition factor as quantitative characterization parameters, to utilize the GSI system.

Figure 4 presents the quantified GSI system chart (Cai et al., 2004).

For a rhombohedral block, the block volume is usually larger than that of cubic blocks with the same joint spacing. However, compared to the variation in joint spacing, the effect of the intersection angle between joint sets is relatively small. Hence, for practical purpose, the block volume can be approximated as:

$$Vb = s_1 \times s_2 \times s_3 \tag{1}$$

where s_i are the joint spacing.

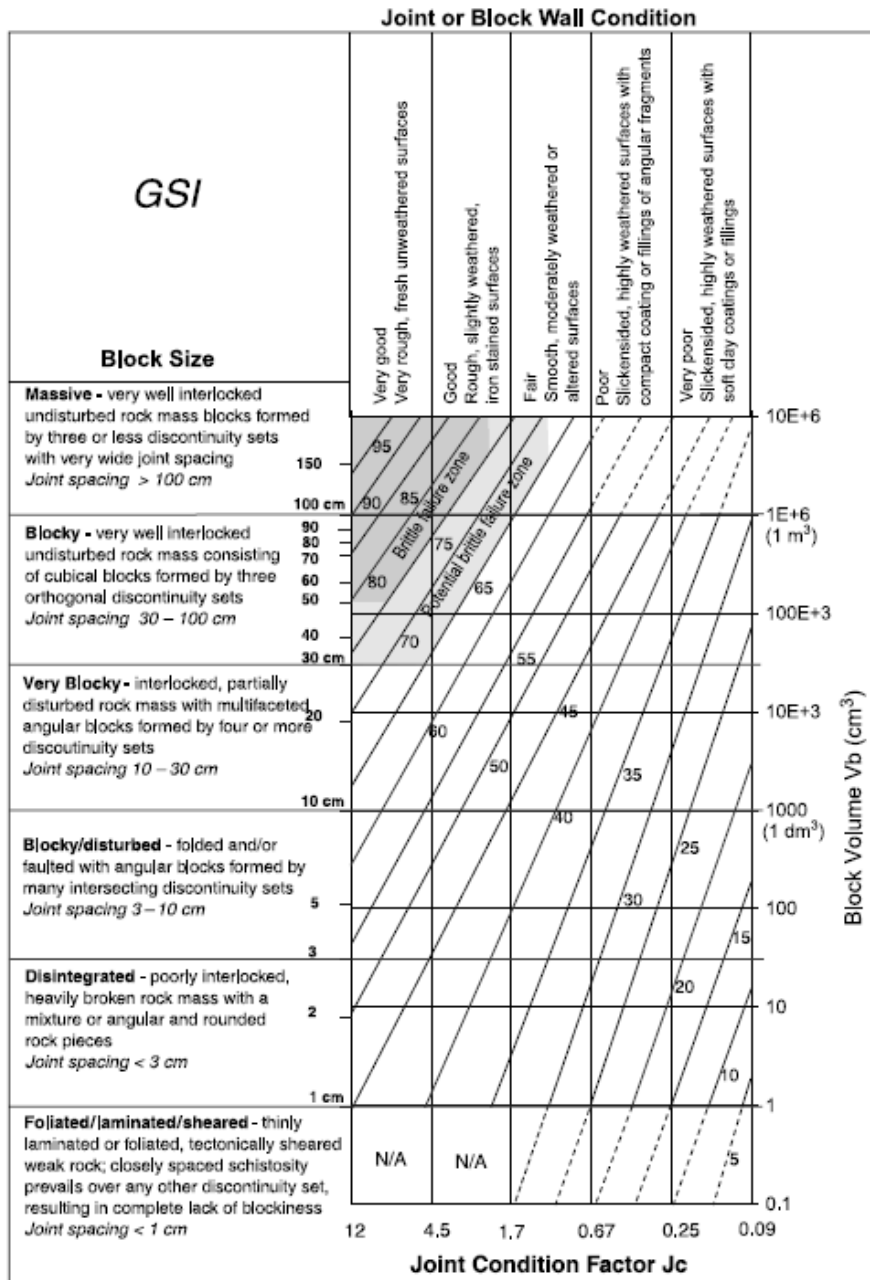


Figure 4. Quantification of GSI chart (Cai et al., 2004).

Based upon the “unit cell method” introduced by Kuszmaul (1999), related to the probability of key-block occurrence in addition to the estimation of rock blocks volumes in relation to GSI according to Cai et al (2004), a methodology for the estimation of rock fall occurrence it is introduced by considering the following assumptions:

- Minimum and maximum joint spacing are derived from the GSI chart (Cai et al, 2004).
- According to the “unit cell method” (Kuszmaul, 1999), failure is defined by the formation of a key-block of any size within the particular cross section of interest. A basic parameter in the analysis is the factor x , the key block size fraction of interest in the assessment of excavation stability. It is defined by:

$$x = \text{minimum key block volume of interest} / \text{volume of maximum key block} \quad (2)$$

- The unconditional probability of key-block occurrence, defined as the probability that a key-block larger than size x will intersect a randomly selected tunnel cross section, is shown to be given by:

$$P_o = C (1 - 3x^{2/3} + 2x) \quad (3)$$

- To assess key block sizes, the cumulative distribution function (cdf) $FX(x)$ is obtained from:

$$FX(x) = 1 - P_o \quad (4)$$

- For the model purpose the “unit cell constant”, C , is derived from the distributions of joint spacing for different GSI values extracted from the Cai et al (2004) chart. In these particular cases the intercept for $x = 0$ of the cumulative block or spacing distributions represents the value $1-C$ according to the Kuszmaul (1999) approach.
- For practical estimations the $1-C$ values are calculated for each distribution of joint spacing according to different GSI, by considering a fixed joint spacing of 0.1 m (or 10 cm). It is important to note that the selection of this particular spacing is not arbitrary. In fact, the 10 cm value corresponds to the threshold size defined by numerous authors such as Deere (1963, 1967), and Hudson & Harrison (1997). In addition, the 10 cm value is equivalent to the opening of the traditional metallic mesh usually installed around the underground excavations for rock support purposes.
- In addition, a minimum joint spacing of 0.1 m determines a small block of 2 to 3 kg of weight which can induce an impact energy of 50 J, equivalent to the maximum strength that can withstand a hard hat (Owen and Potvin, 2003).

The $1-C$ parameters are derived from Figure 5 as follows.

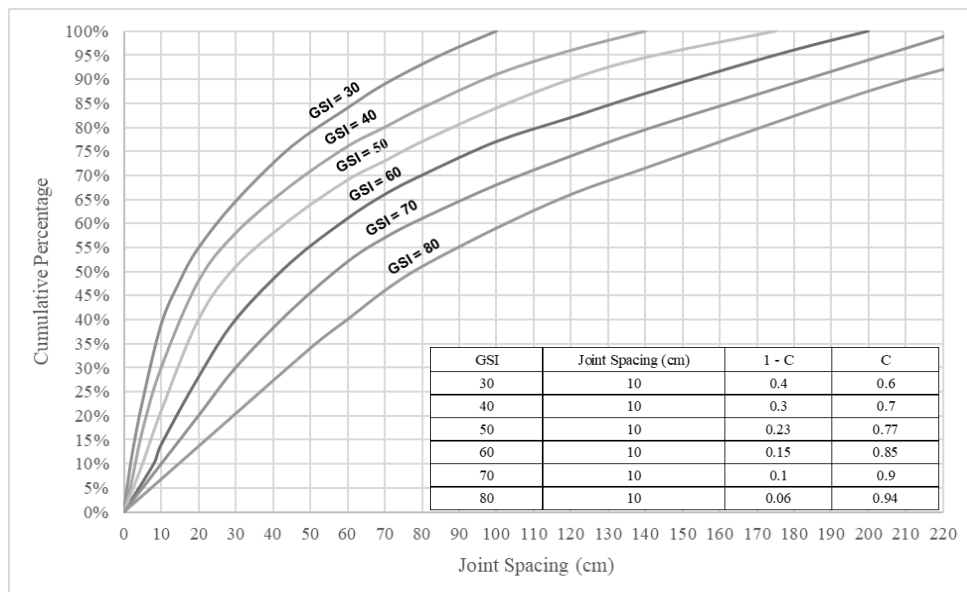


Figure 5. Cumulative distribution of joint spacing according to different values of GSI.

By considering the previous assumptions, it is possible to obtain a graphical representation of the cumulative distributions of key-blocks occurrence according to different values of GSI as shown in Figure 6.

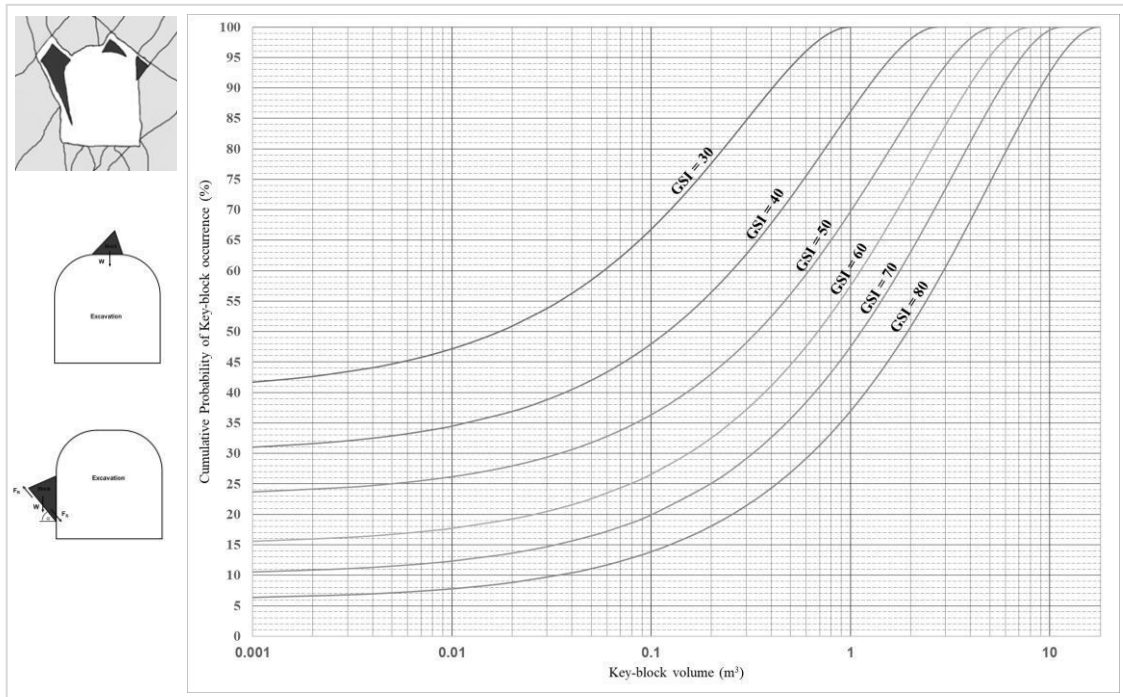


Figure 6. Cumulative probability of key-block occurrence according to different values of GSI.

According to Potvin & Hadjigeorgiou (2020), in a jointed rock mass the reduction of stress may induce geotechnical instabilities. In fact, reducing the normal stress may reduce the shear strength along discontinuities inducing the relaxation of blocks and trigger sliding or gravity falls. An example of stress relaxation in a jointed rock mass causing gravity failure of rock blocks is shown in Figure 7.



Figure 7. Stress relaxation in a jointed rock mass causing gravity failure of rock blocks from the back of the intersection of drifts (courtesy FF GeoMechanics, 2021).

Intuitively, from the stress relaxation approach affecting a rock mass it is possible to deduce that the probability of rock falls from the back of an excavation caused by a gravity failure mechanism is higher in relation to the probability of block sliding from the walls, for the same excavation. In fact, if a key-block is formed in the back of an excavation emplaced in a jointed rock mass affected by stress relaxation, the probability of falling for this particular block may be 100% or close to this value. This situation confirms the main assumption of the “unitary cell method” proposed by Kuzmaul (1999) which establishes that when a key-block forms in a roof of an excavation, this will fail.

At a first glance this approach sounds to be conservative however the stress relaxation condition is not uncommon in underground environments especially when excavations are affected by vibrations induced by blasting, intersection of drifts and widening of excavations, among other factors that may trigger this type of failure mechanism.

Key-blocks located at the walls of excavations usually fails under sliding mechanisms through a particular joint plane or intersection of planes for particular values of dips. With the aim of analyzing this type of blocks a stability chart is constructed based on the Mohr-Coulomb failure criterion.

The main assumptions for these calculations are the following:

- Dip of slide failures between 20° and 70° are considered on this assessment.
- Characteristic friction angles of joints ranges between 20° and 40° are used.
- Different values of residual cohesions are utilized for each GSI, as described in Table 2:

Table 2. Residual cohesion for GSI ranges used on stability assessment for sliding key-blocks.

GSI	Cohesion (kPa)
80 - 100	2.0
60 - 80	1.0
40 - 60	0.5
20 - 40	0.1

- Key-blocks volumes are estimated by using the Cai et al (2004) approach.
- The density of blocks used on the stability chart for sliding failure is 3 (t/m³).

The stability chart for sliding key-blocks is shown in Figure 8.

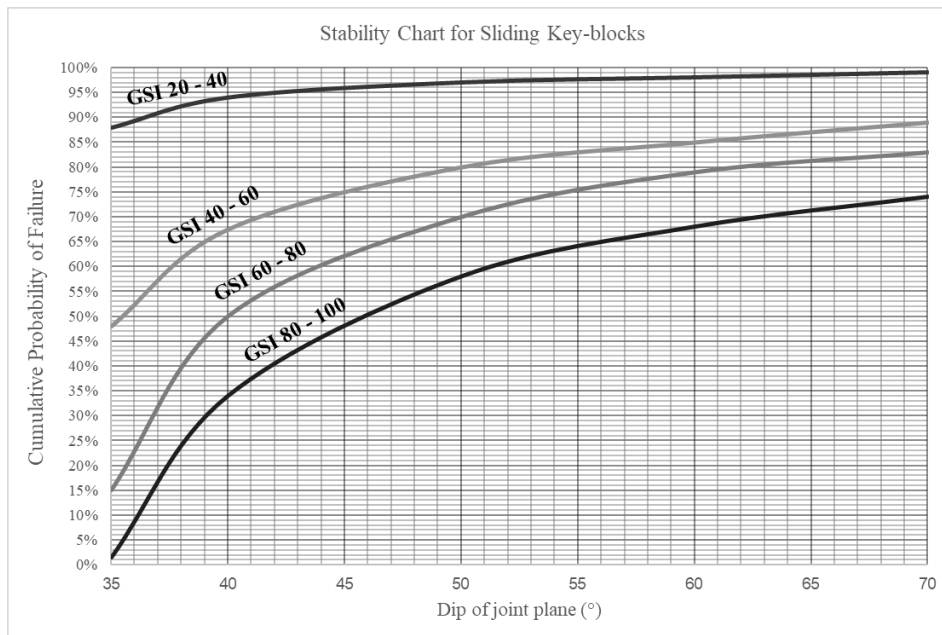


Figure 8. Cumulative probability of failure for sliding key-blocks for different GSI values.

4.1 Probabilistic Approach

By considering the previous assessment, it is possible to establish an integrated probabilistic model for the estimation of rock fall by accounting the key-block occurrence around underground excavations.

The main assumptions for the proposed probabilistic approach are the following:

- The space around the excavation is divided on to three (3) areas: roof (R), left wall (WL) and right wall (WR).
- Probabilistic events are independent between each other.
- For estimation purposes a series of equations based upon conditional probabilities are used.

The equations used on the model for the estimation of overall probabilities of rock block failures ($P(F/B)$), possible to occur from the excavation perimeter, are depicted in Figure 9.

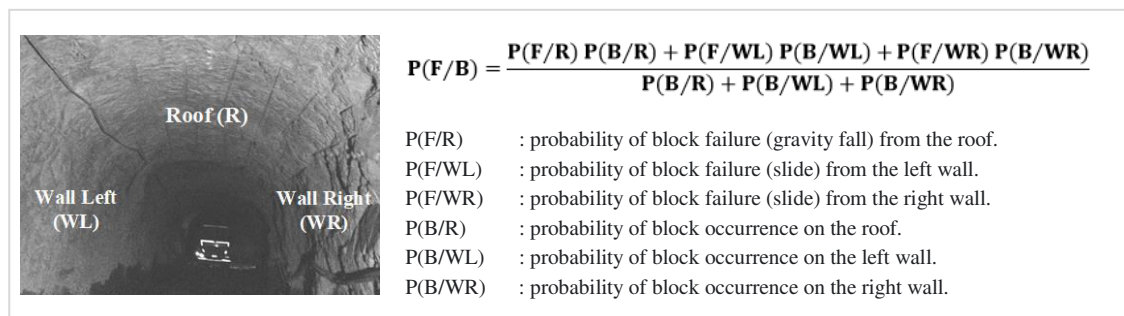


Figure 9. Schematic representation and equations used on the model for the estimation of overall probabilities of rock block failure ($P(F/B)$) from the perimeter of underground excavations.

Probabilities of block occurrence (for roof and walls) can be calculated by using the chart of Figure 6. As was previously mentioned the probability of block failure (gravity fall) from the roof considered in this model is 100%. The probability of failure from the walls depends on the sliding conditions and can be calculated by using the stability chart of Figure 8. Each compound on the numerator of the equation depicted in Figure 9 must be multiplied by a factor corresponding to the roof or wall's width divided by the perimeter of the excavation.

4.2 Example of Application

The geotechnical conditions around an underground excavation of 5 m wide by 4 m high determine a GSI index between 40 and 60 on the roof and a GSI value of 60 to 80 at both walls. Fracture spacing obtained from geotechnical mapping define block volumes between 0.01 m³ to 1.0 m³ and 0.1 m³ to 1.0 m³ for the roof and walls, respectively. Dip of joints planes varies between 40° and 60°. With this data it is possible to estimate the probability of block failures from the excavation as follows:

- Probabilities of block occurrence are estimated for the excavation's roof and walls by using the chart of Figure 6. The input parameters are the GSI and block size intervals that define the following results (Table 3):

Table 3. Estimation of Block Occurrence.

GSI	P(B) min	P(B) max	P(B)
40 - 60 (Roof)	26%	70%	$P(B/R) = 44\%$
60 - 80 (Wall Left)	20%	47%	$P(B/WL) = 27\%$
60 - 80 (Wall Right)	20%	47%	$P(B/WR) = 27\%$

- Probabilities of block failure are estimated for the excavation's walls by using the chart of Figure 8. The input parameters are the GSI and joint dips that define the following results (Table 4):

Table 4. Estimation of failure for sliding blocks (located at the walls)

GSI	P(F) min	P(F) max	P(F)
60 - 80 (Wall Left)	50%	70%	P(F/WL) = 20%
60 - 80 (Wall Right)	50%	70%	P(F/WR) = 20%

By replacing the values of Tables 3 and 4 on the equation depicted in Figure 9, it is possible to obtain an overall probability of failure of rock blocks of 20% for the excavation described previously. This probability is higher than the acceptability risk threshold for underground mines (0.7% of loss of life). This result determines the installation of rock support in order to reduce the overall geotechnical probability/risk to acceptable values.

5 CONCLUSIONS

Fatalities recorded by different causes in underground metalliferous mines around the world reflects that during the last ten years, rock falls represent the main cause of fatal accidents.

The statistical information of accidents was integrated to work force data in order to obtain the values of risk of death due to geotechnical (rock fall) causes to be benchmarked against the risks of other activities and the acceptability threshold for underground metalliferous mines. The results of this assessment indicate that rock fall risk overcome the threshold acceptable value in several countries.

In this paper, a graphical methodology to quantifying rock block failures based on the GSI Index, and the “unit cell method” for key-block occurrence was introduced. By considering this approach, it was possible to establishing an integrated probabilistic model for the estimation of rock fall by accounting the key-block occurrence around underground excavations that may be sustained on the collection of basic information at the early stages of a project. In addition, the results of application may assist on the decision making process for rock support installation in any particular case.

REFERENCES

- Australian Centre for Geomechanics, ACG. (2003). “*Management of Rockfall Risk in Underground Metalliferous Mines*”. Minerals Council of Australia.
- Cai, M., Kaiser, P., Uno, H., Tasaka, Y., & Minami, M. (2004). “*Estimation of rock mass deformation modulus and strength of jointed hard rock masses using the GSI system*”. International Journal of Rock Mechanics and Mining Sciences, vol 41, N°1, pp. 3-19.
- Cole, K. (1993). “*Building over abandoned shallowed mines*”. Paper 1: considerations of risk and reliability. Ground Engineering, pp. 35-37.
- Fernandez, F. (2011). “*Determination of Geotechnical Vulnerabilities in Argyle Diamonds Block Cave Project*”. Thesis presented for the degree of Master of Eng. Science of Mining Geomechanics, Curtin University (Western Australia School of Mines).
- Fernandez, F., Evans, P., & Gelson, R. (2010). “*Design and implementation of a damage assessment system at Argyle Diamond's block cave project*”, in Y. Potvin (ed.), Proceeding of the 2nd International Symposium on Block and Sublevel Caving, Australian Centre for Geomechanics, Perth, pp. 65-81.
- Fernandez, F., Watt, G., & Ooi, J. (2011). “*Strategic management for squeezing ground conditions at the Argyle Diamonds block cave project*”, in Y. Potvin (ed.), Proceedings of the Fourth International Seminar on Strategic versus Tactical Approaches in Mining, Australian Centre for Geomechanics, Perth, pp. 55-72.
- Government of Western Australia. (2021). Minerals Safety Statistics. Department of Mines, Industry Regulation and Safety: <https://www.dmp.wa.gov.au/Safety/Safety-statistics-16198.aspx>
- Hadjigeorgiou, J. (2019). “*Understanding, managing and communicating geomechanical mining risk*”. In J. Wesseloo (ed.), Proceedings of the First International Conference on Mining Geomechanics Risk, Australian Centre for Geomechanics, Perth, pp. 3-20.
- Hudson, J. A., & Harrison, J. P. (1997). “*Engineering Rock Mechanics, An Introduction to the Principles*”. UK: Imperial College of Science, Technology and Medicine University of London.

- Joughin, W.C., Wesseloo, J., Mbenza, J., Sewnun, D. (2020). "A risk-based approach to ground support design". Chapter 16: Ground Support for Underground Mines, Y. Potvin and Hadjigeorgiou (ed.). Australian Centre for Geomechanics, Perth, pp. 397-433.
- Kuszmaul, J. (1999). "Estimating keyblock sizes in underground excavations: accounting for joint set spacing". International Journal of Rock Mechanics and Mining Sciences N°36, pp. 217-232. Pergamon Ed.
- Lilly, P.A.. (2004). "Geotechnical risk considerations in mine planning". Proceedings of the International Conference on Ore Body Modelling and Strategic Mine Planning, Perth, pp. 253-256.
- Marinos, P., Hoek, E. (2000). "GSI - a geologically friendly tool for rock mass strength estimation". Proceedings of the International Conference on Geotechnical and Geological Engineering (GeoEng 2000), Tecnonomic Publishers, Lancaster, pp. 1422-1446.
- Mine Safety and Health Administration. (2021). MSHA (U.S.A), Fatality Reports: <https://www.msha.gov/data-reports/fatality-reports/search>
- Osinermin. (2019). Publicaciones de Compendios ilustrativos de Accidentes en el Sector de Mediana Minería y Gran Minería en Perú. Obtenido de Organismo Supervisor de la Inversión en Energía y Minería : <https://www.osinermin.gob.pe/empresas/mineria/publicaciones>
- Owen, M., & Potvin, Y. (2003). "Exposure of Underground Mine Personnel and Equipment to Geotechnical Hazards". In M. D. Kuruppu and P. A. Lilly (ed.), Proceedings of the Twelfth International Symposium on Mine Planning and Equipment Selection, Kalgoorlie, p.p. 543-551.
- Potvin, Y., & Hadjigeorgiou, J. (2020). "Ground Support for Underground Mines". Chapter 2: Rock mass behaviour and failure mechanisms, Y. Potvin and Hadjigeorgiou (ed.). Australian Centre for Geomechanics, Perth, pp. 13-24.
- Sernageomin. (2021). Estadísticas de Accidentabilidad Industria Extractiva Minera en Chile. Obtenido de Servicio Nacional de Geología y Minería: <https://www.sernageomin.cl/accidentabilidad-minera>.
- Sowers, G. F (1993). "Human Factors in Civil and Geotechnical Engineering Failures". J. Geotech. Engrg., ASCE, pp. 119-238.
- Stacey, T.R. (2001). "Best Practice Rock Engineering Handbook for Other Mines". Safety in Mines Research Advisory Committee (SIMRAC), Final Report. SRK Consulting, South Africa, pp. 188.
- Tubis, A., Werbinka-Wojciechowska, S., Wroblenski, A. (2020). "Risk Assessment Methods in Mining Industry - A Systematic Review". Applied Sciences, pp. 1-34.
- Wesseloo, J., Joughin, W.C. (2020). "Probability, risk and design". Chapter 15: Ground Support for Underground Mines, Y. Potvin and Hadjigeorgiou (ed.). Australian Centre for Geomechanics, Perth, pp. 375-396.

Geotechnical Design Strategies in Open Pit Mine with the Presence of Old Underground Excavations

V.M. Vergara

Assistant Research in Mining Engineering, Pontificia Universidad Católica del Perú

V. Góngora

Professional Mining Engineering, SRK Consulting (Peru)

O. Cabello

Professional Mining Engineering, Professor at Pontificia Universidad Católica del Perú

ABSTRACT:

The realities of different open mines that are characterized by carrying out and extracting large amounts of ore, as well as generating large economic investments, allow for a geotechnical design that is sustainable and allows maximum profitability in the project; therefore, in the geotechnical design stage and the consideration in the analysis of the optimal bench and berm, as well as the optimization for the design of the global slope angles and inter-ramp slope. However, there may be excavated areas due to old mines that have already been mined and that have not identified voids that at the time of mining lead to instability at the time of deepening. For this, this publication presents the methodology of design in an open pit considering geotechnical domains and recommended design suitable for the different geological domains presented, as well as the mining strategy for the optimization of the appropriate critical width for the crown pillar at the time of the interaction.

KEYWORDS: Open pit, slope stability, numerical modelling

1 LOCATION

The area of influence for the mining project is in an area 3.5 km long from E-W and 2.5 km from N-S. Likewise, the mine has a projected production of 3,300 tons with Zn grades of 1.5% and Pb of 1.2%.



Figure 1. Location of the open pit mine project

2 GEOTECHNICAL INFORMATION

Within the project area, a total of 7,257 m of geotechnical logging (field logging and digital logging) and seventy-five geomechanics stations have been carried out (2016 and 2018). Likewise, it was considered to carry out a campaign of laboratory tests that are detailed below:

- 3 Uniaxial compression tests
- 2 Triaxial tests
- 2 Direct shear tests
- 2 Physical property tests
- 5 Indirect tensile tests
- 8 Point load tests

3 GEOTECHNICAL MODEL

3.1 Geology

The geology that occurs in the study area is made up of limestone, breccias and marble (35%); the intrusive zone runs from Northwest to Southeast which encompasses a total of 20% of the study area; Lastly, the Sandstone zone is presented, which is found in the North zone of the open pit project.

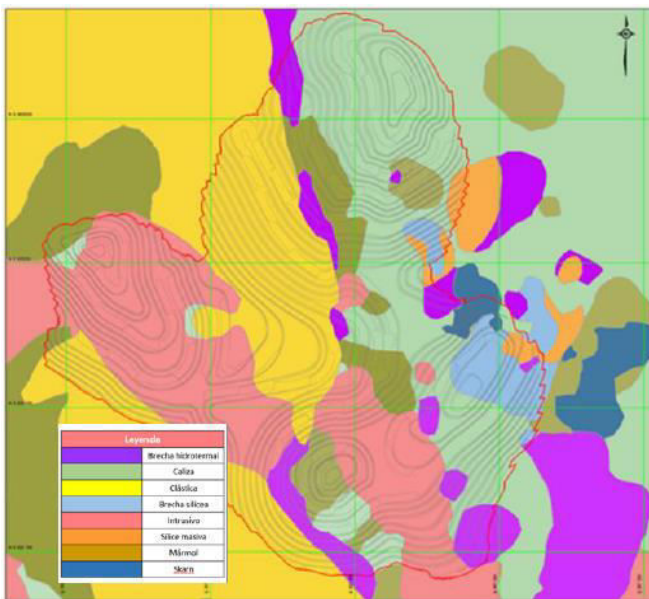


Figure 2. Plan View of the Geological Model

3.2 Structural Geology

Concerning the structural geology of the project zone in the open pit, five main fault zones are presented that divide the geological zone between sandstone, intrusive and limestone. The main faults in the area are named below:

- Main Fault
- Fault 13
- East-West Fault
- NW-SE Fault System
- NE-SW Fault System

Once the main fault system was defined and by collecting geotechnical mapping, structural domains were defined for each of the geological zones detailed below:

Table 1. Structural domains defined for the project zone

Domain	Set	Dip (°)	Dip direction (°)
Structural Domain 01	1	72	239
	2	58	73
	3	81	327
	4	87	153
	5	29	132
Structural Domain 02	1	64	218
	2	61	97
	3	37	157
	4	75	182
Structural Domain 03	1	61	247
	2	74	16
	3	49	157

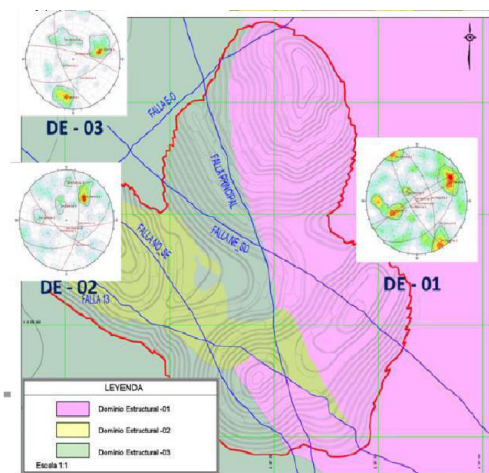


Figure 3. Structural domains defined for the project zone

3.3 Hydrogeological model

On-site investigations and rainfall characteristics in the study area have determined the presence of water on the walls of the current pit. In this sense, for the design stage, a saturated state has been considered for the design in the stability runs as a critical case to determine the minimum Safety Factor.

3.4 Rock Mass model

From the geotechnical tests, the intact rock properties were determined for each of the geological domains within the open pit zone.

Table 2. Intact Rock Properties

Lithological Unit	Density (kN/m ³)	UCS (MPa)	mi
Limestone, breccia, marble	26.1	67	12
Intrusive	26.6	77	12
Sandstone	24.5	53	10

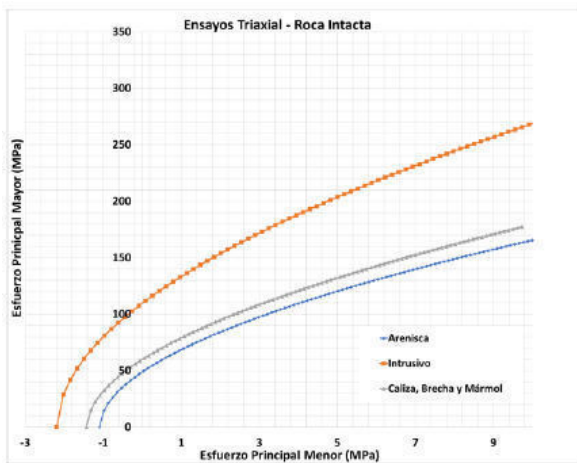


Figure 4. Intact rock properties for each of the geotechnical units present in the open pit zone

4 GEOTECHNICAL DOMAINS

From the geotechnical characterization of each of the geological units, a statistical analysis will be established that allows encompassing the rock mass characteristics present in the open pit area. For this, the geotechnical domains were determined and included based on the characteristics of RQD, RMR and Simple Compression Strength (UCS) that resulted from the laboratory tests. Table 3 presents each of the geotechnical domains.

Table 3. Characteristics for each geotechnical domain

Geotechnical Domain	Lithology	RMR ₇₆	RMR ₈₉	RQD (%)	UCS
DG-I	Limestone, breccia, marble	45-60	50-65	55-80	70-80
DG-II	Intrusive	50-65	55-70	65-85	80-120
DG-III	Sandstone	40-50	45-55	45-60	40-70

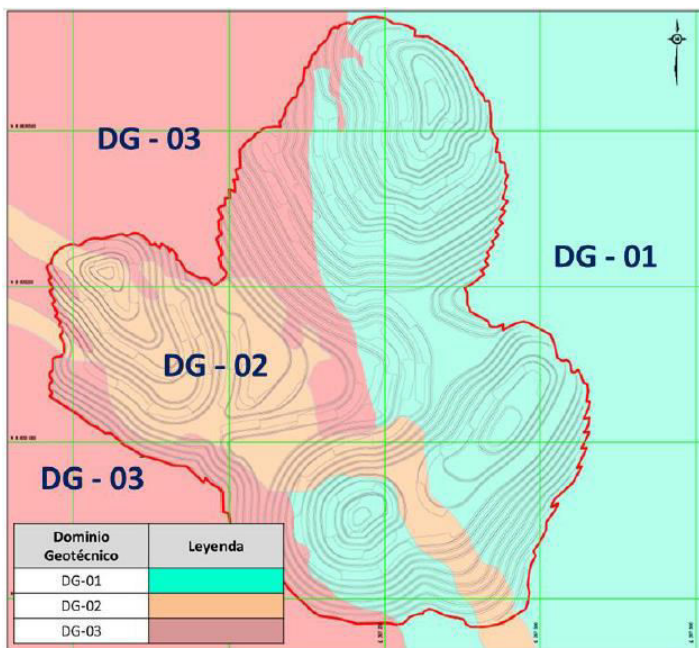


Figure 5. Geotechnical domains in the open pit zone

5 SLOPE STABILITY DESIGN AND ANALYSIS

For the calculation of the global and inter-ramp angle, it was carried out following the stability criteria detailed by Read & Stacey (2009) for the design at the bench, inter-ramp and global scale.

Table 4. Acceptability criteria for slope design

Scale	Consequence of failure	Factor of Safety		Probability of failure
		Static	Dynamic	
Bench	Low-High	1.1	N/A	25-50%
	Low	1.15-1.2	1.0	25%
Inter-ramp	Moderate	1.2	1.0	20%
	High	1.2-1.3	1.1	10%
	Low	1.2-1.3	1.0	15-20%
Global	Moderate	1.3	1.1	5-10%
	High	1.3-1.5	1.1	<5%

This methodology consists of limit equilibrium analysis by varying the orientation (Dip Direction) of each of the sectors from an angle of 30° with the aim of determining the slope angle for each sector. In addition, the variation of the inclination of the slope angle (Dip) and slope height was carried out, in such a way that the safety factor is obtained for each combination, generating design curves based on the safety factor.

In the Geotechnical Domain - I, an analysis was carried out for a global slope of 250 m height, as well as an analysis for an inter-ramp angle of 50 and 100 m height. Likewise, the orientations established for the DG-I result from 0 – 360° for each 30° orientation.

For the Geotechnical Domain – II, a global slope analysis was carried out at a height of 200 m and an inter-ramp level analysis for heights of 50 and 100 m. Likewise, it is highlighted that for the anisotropic analysis only the orientations where the DG-II was found were considered.

In the case of the Geotechnical Domain - III, an analysis was carried out only for the 50 m inter-ramp because in the limit equilibrium analysis for heights greater than this value, the FS is below 1.1 and does not comply with the limits established according to the Open Pit Guidelines.

Table 5. Dimensioning in order to determine the global slope angle based on its maximum depths

Geotechnical Domain	Orientation	IRA Max	RMR ₈₉	Overall Max	
		H=50 m	H=100 m	Angle	Max Height
DG-I	0-30	41	50	39	250
	30-60	44	45	41	250
	60-90	42	42	35	250
	90-120	<55	<50	48	250
	120-150	<55	<50	32	250
	150-180	<55	<50	47	250
	180-210	<55	<50	49	250
	210-240	<55	<50	48	250
	240-270	<55	<50	45	250
	270-300	<55	<50	48	250
	300-330	<55	<50	49	250

6 BENCH AND BERM DESIGN

The objective of carrying out the bench reconciliation is to use the current topography of the current pit, which is to observe if the effective berm widths comply with the initial berm width design, which is 3.2 m. Statistical results showed that 73% accumulate an effective berm width below 3.2 m, which does not meet the established design conditions according to Ritchie's formula (1963). Figure 6 shows the sections that were created every 5 m, in such a way as to be able to record the width of the berm for the current topography of the DG-I.

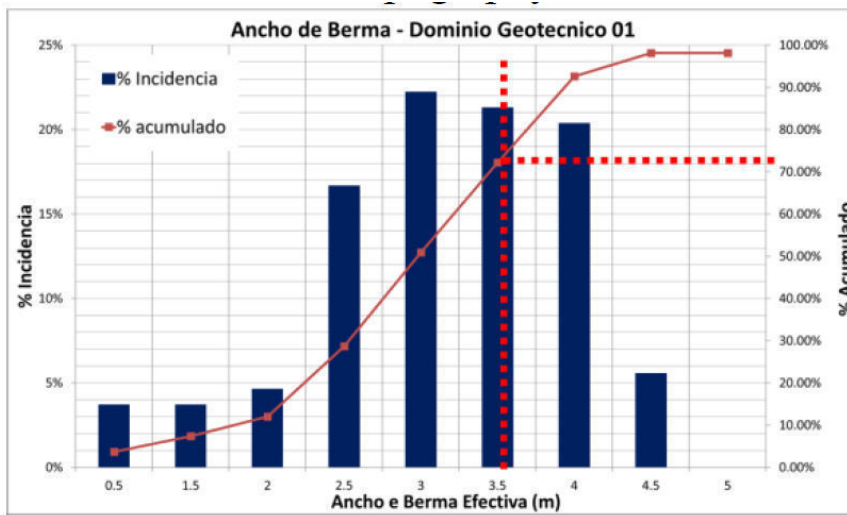


Figure 6. Compliance diagram for berm width in the DG-I

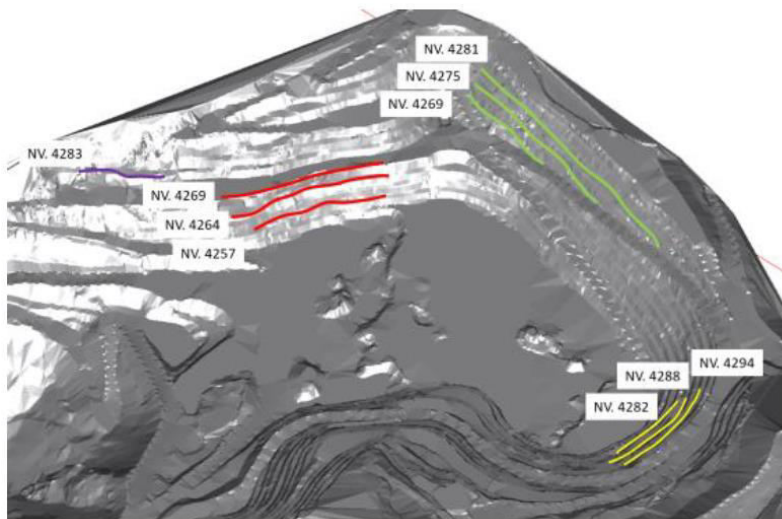


Figure 7. Zones in the current pit to determine berm width compliance

6.1 Berm Width Optimization

The berm design aims to retain the blocks that break off from upper benches; For this, the berm design factors must have a retention capacity between 75 to 80% of the volume of blocks with potential for failure.

In order to comply with the established criteria, the Sblockv2022 software (Esterhuizen, 2004) was used, which adopts the Goodman & Shi (1985) block theory criterion, in such a way as to estimate the optimal berm widths for each of the geotechnical domains.

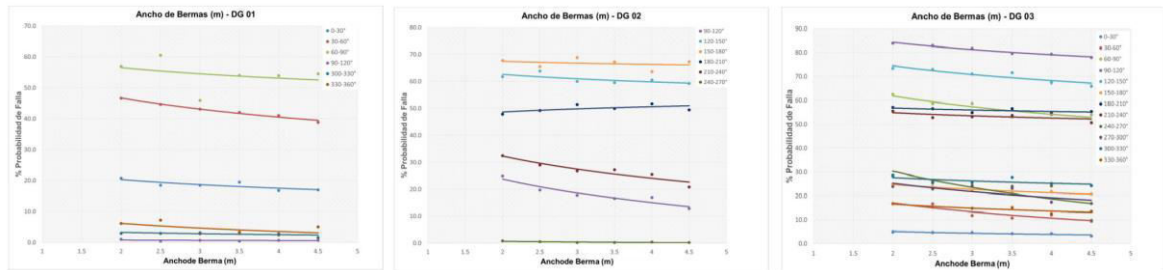


Figure 8. The curves of % Probability of failure are observed through a probabilistic analysis for the optimization of the berm width for each of the Geotechnical Domains based on the orientations of each sector of the open pit

7 OPEN PIT FINAL DESIGN SECTORS

From the geotechnical information, the orientation of the slope angles and the continuity of the geotechnical domains have been determined. Table 7 shows the summary of the twenty-one design sectors showing the bench, inter-ramp and global angles, as well as the shoulder width for each of the recommended design sectors.

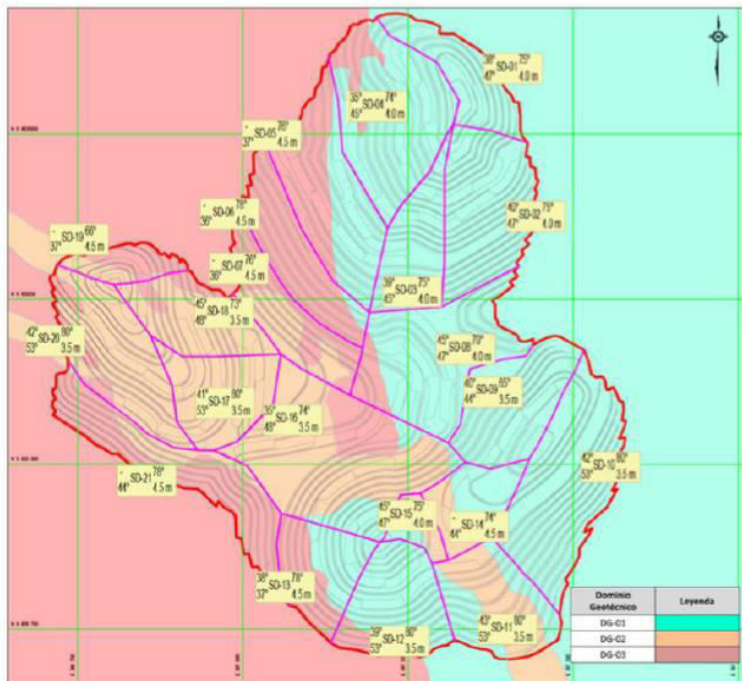


Figure 9. Design sectors defined for the open pit

Geotechnical Domain	Slope Dip Direction (°)	Bench design				Evaluation criteria	
		H _b (m)	α _b (°)	B (m)	α _{IR} (°)	Prob. Failure(%)	Effective Width (m)
DG-01	00-30	6	75	4.00	47	16.80	3.33
	30-60	6	74	4.50	44	38.80	2.75
	60-90	6	70	4.50	42	54.50	2.05
	90-120	6	73	4.00	46	0.90	3.96
	120-150	6	75	4.00	47	0.00	4.00
	150-180	6	75	4.00	47	0.00	4.00
	150-210	6	75	4.00	47	0.00	4.00
	210-240	6	75	4.00	47	0.00	4.00
	240-270	6	75	4.00	47	0.00	4.00
	270-300	6	76	4.00	48	0.50	3.98
	300-330	6	75	4.00	47	2.80	3.89
	330-360	6	75	4.00	47	2.40	3.90
DG-02	00-30	6	75	3.50	50	0.00	3.50
	30-60	6	80	3.50	53	0.00	3.50
	90-120	6	74	4.00	46	16.90	3.32
	120-150	6	70	4.50	42	59.20	1.84
	150-180	6	65	3.50	44	67.20	1.15
	240-270	6	74	3.50	49	0.20	3.49
	270-300	6	73	3.50	48	0.00	3.50
	300-330	6	80	3.50	53	0.00	3.50
	330-360	6	80	3.50	53	0.00	3.50
	00-30	6	78	4.50	46	3.20	4.36
	30-60	6	76	4.50	44	9.40	4.08
	60-90	6	78	4.50	37	53.90	2.07
90-120	6	78	4.50	46	77.90	0.99	
120-150	6	71	4.50	42	66.00	1.53	
150-180	6	66	4.50	38	20.80	3.56	
210-240	6	80	4.50	37	51.00	2.21	
330-360	6	80	4.50	47	13.50	3.89	

H_b: bench height
 α_b: bench angle
 B: bench angle
 α_{IR}: Inter-ramp Angle

Figure 10. Values for dimensioning BFA, inter-ramp and bench width

Design Sector	Geotechnical Domain	Orientation (°)	Slope Design			Bench slope design		
			Maximum Inter-ramp Angle (°)	Maximum Inter-ramp Angle (°)	Overall slope angle (°)	bench height (m)	bench angle (°)	Berm Width (m)
			50 (m)	100 (m)				
SD-01	DG-01	210-270	47	-	38	6	75	4.0
SD-02	DG-01	330-360	55	47	40	6	75	4.0
SD-03	DG-01	30-60	44	45	39	6	75	4.0
SD-04	DG-01	30-60	44	45	35	6	74	4.0
SD-05	DG-03	30-60	37	-	-	6	76	4.5
SD-06	DG-03	30-60	36	-	-	6	78	4.5
SD-07	DG-03	30-60	36	-	-	6	76	4.5
SD-08	DG-01	240-270	60	47	45	6	70	4.0
SD-09	DG-01	150-180	55	44	40	6	65	3.5
SD-10	DG-01	300-330	60	53	42	6	80	3.5
SD-11	DG-02	330-360	65	53	43	6	80	3.5
SD-12	DG-01	330-360	60	53	39	6	80	3.5
SD-13	DG-01	30-60	44	37	38	6	78	4.5
SD-14	DG-02	60-90	44	-	-	6	74	4.5
SD-15	DG-01	210-240	47	-	45	6	75	4.5
SD-16	DG-02	150-180	65	48	35	6	74	4.0
SD-17	DG-02	300-330	65	53	41	6	80	3.5
SD-18	DG-02	240-270	65	48	45	6	73	3.5
SD-19	DG-03	240-270	37	-	-	6	66	3.5
SD-20	DG-02	30-60	65	53	42	6	80	3.5
SD-21	DG-03	30-60	44	-	-	6	78	3.5

Figure 11. Recommendations of Design Sectors depending on the orientation of the slope face

8 NUMERICAL MODELING BETWEEN THE OPEN PIT AND ANCIENT UNDERGROUND EXCAVATIONS

Once the design sectors for the open pit were considered, the analysis of existing voids due to old underground excavations that would cause instability when deepening the pit was considered.

For this, it was carried out from a numerical model to determine the influence and variation of the efforts in the crown pillar at the moment of interaction, in such a way as to guarantee the stability of the walls of the open pit and avoid the presence of operational risks such as are:

- Sudden and unexpected collapse of the floor and/or walls of the open pit.
- Loss of people and/or equipment that are in the pit, due to different Tajeos that are not completed.
- Subsidence in certain areas of the open pit that cause instability in the lower part of the pit.

For the stress behavior variation analysis, the Map 3D Fault-Slip Version 64 software was used. For this, the direction of the main stress (σ_1) was considered to have a direction of 135° SE. Likewise, the 3D geometry of the exploited underground excavations was replicated, which will be found on the walls of the pit from Nv. 4294 up to Lv. 4162 from the open pit.

Once the mining sequencing has been completed at the time of deepening, it is necessary to set the in-situ stress parameters with which we are going to perform the simulation. For this, values of Kmax of 1.50 and Kmin of 1.30 have been considered, as well as the direction of maximum main stresses. Likewise, the stress parameters are placed in situ considering the 4294 level with the value equal to 0 as surface level and observing the stress distribution as a function of depth.

At the time of the analysis to determine the minimum thickness of mining in such a way that there is no deconfinement between the surface mining and the old excavations, the analysis was carried out using the Hoek & Brown failure envelope in order to observe the rupture behavior of the rock mass by the crown pillar, where it turned out that for Step 6 of the numerical model, the pillar will present a deconfinement behavior at a pit depth of 70 m, reaching a minimum thickness of 17 m that guarantees the mining of the open pit and there are no subsidence problems.

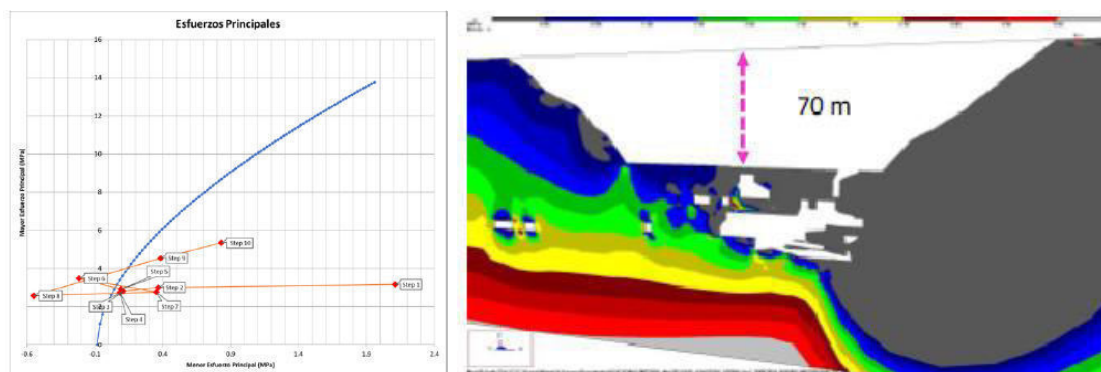


Figure 12. Failure envelope analysis for crown pillar analysis at the time of mining

9 CONCLUSIONS AND RECOMMENDATIONS

Regarding the open pit geotechnical design, the design curves were made with the objective of guaranteeing the global slope angle and inter-ramp in such a way that they comply with the safety factors in Static and Pseudo-Static conditions. Likewise, the bench reconciliation analysis was carried out in such a way as to optimize the bench angle for each of the geotechnical domains, as well as to obtain the appropriate berm widths that allow containing the material that comes from higher levels.

From the numerical evaluation, it has been determined that the crown pillar obtained during surface mining and underground excavations show an increase in compressive stresses (σ_1) and a decrease in confining stresses (σ_3). Therefore, it has been determined that the minimum thickness of the stable crown pillar at the moment of the interaction must be 17 m. Likewise, it is recommended that during open pit mining with depths greater than 70 m, a set of procedures be implemented in such a way as to guarantee safety and productivity in the operation, such as directed test drills that allow observing the real shape of the excavation, geophysical methods that

include tests to observe unidentified voids, use of real-time radars in order to observe deformations in the terrain and in areas that present subsidence due to interaction with old underground excavations and electronic topographic measurement methods (EDM).) with total stations and the use of prisms that allow observing the total displacement that exists on the ground.

10 REFERENCES

- Deere et. (1963,1967). Rock Quality Designation.
- Barton, N. (1976). *The Shear Strength of Rock and Joints*.
- Barton, N. (2007). *Rock quality, seismic velocity, attenuation, and anisotropy*. London: Taylor & Francis e- Library.
- Bieniawski, Z. (1989). *Engineering Rock Mass Classifications*. J. Willey & Sons.
- Call, R. a. (1991). *Open Pit Rock Mechanics*. SME Mine.
- Castagna, J.P., M.L. Batzle, and R.L. Eastwood. (1985). *Relationship between compressional wave and shear wave velocities in clastic silicate rocks*. Geophysics, 50, 571-581.
- Estherhuizen, G. (2004). *SBlock v2.01, User Guide and Reference Manual*.
- Goodman, R. &. (1985). *Block Theory and Its Application to Rock Engineering*. Prentice Hall: Englewood Cliffs, NJ.
- Goodman, R. E. (1989). *Introduction to Rock Mechanics*. New York: Willey.
- Hoek and Bray. (1981). *Rock Slope Engineering*. 3rd Edition.
- Hoek, E., Carranza, C & Corkum B. (2002). (2002). *Hoek-Brown Failure Criterion 2002 Edition*. Toronto: 5th North American Rock Mechanics Symposium & 17th Tunneling Association of Canada Conference.
- Hoek, E. (s.f.). *Strength of Rock and Rock Masses*. ISRM News J., 2(2):4-16.
- Hormazabal, E. (2013). *Bench Berm design using Probabilistic Keyblock Analysis*. Brisbane: Australian Centre for Geomechanics, pp:227-236.
- Kennedy, B. (1989). *Surface Mining*. Colorado: SME.
- Priest, S.D. & Hudson, J.A. (1976). *Discontinuity spacings in rocks*. Int J Rock Mech Min Sci & Geomech Abstr, 13(5): 135 - 148.
- Read, J. & Stacey, P. (2009). *Guidelines for Open Pit Slope Design*. CRC Press, 1st Ed. USA.
- Subterránea, F. C. (2009). *Hidrogeología Conceptos básicos de hidrología subterránea*. Barcelona: Comisión Docente Curso Interancional de Hidrología Subterránea.
- W. Hustrulid, M. K. (2013). *Open Pit Mine Planing & Design*. CRC Press.
- W. Hustrulid, M. McCarer, & Van Zyl, D. (2001). *Slope Stability in Surface Mining*

Machine Learning in Mining: Uses and Techniques applied in geomechanics

M.E. Valencia

Itasca Chile SpA, Santiago, Chile

ABSTRACT:

While machine learning methods learn from data to make predictions or decisions without being explicitly programmed, geomechanics involves theoretical and applied sciences to understand rock and soil in response to its physical environment. Conventional rock/soil engineering faces challenges with empirical and numerical modeling solutions. However, both practices require experience and knowledge in practice. This paper aims to connect both fields; machine learning and geomechanics. It reviews standard machine learning methods to understand how they could be used to understand rock and soil mechanics. Present three examples of predictive models applied in geomechanics as well. Furthermore, it proposes de discussion about the uses of machine learning tools in the field.

1 INTRODUCTION

Machine learning tools are meant to understand and build methods that learn from data to make predictions or decisions without being explicitly programmed to do so (Koza et al., 1996). In the last 20 years, machine learning has been present in different fields and industries. Some reasons for its popularity are related to better computational processing and the increased storage capacity for data (physical devices and the cloud). Moreover, the leading cause of why machine learning is so popular these days is the easy access to tools that can build a model in a matter of minutes.

On the other hand, geomechanics involves theoretical and applied sciences of the mechanical behavior of rock and soil in response to its physical environment. It has been considered a formal field of study since the '60s (Hoek, 1966). Design in rock deals with difficulties due to the variability of natural materials involved in a project. Today, conventional geomechanics faces challenges with empirical and numerical modeling solutions. However, both practices require experience and knowledge in practice. Furthermore, both methods are essential to understanding rock mass behavior and predicting the design response in different scenarios.

This paper aims to connect both fields; machine learning and geomechanics. The work reviews some of the most common machine learning methods to understand them and discover how they could be used to understand rock and soil mechanics. Also, it is essential to conduct a critical analysis of the boundaries of the presented machine learning methods and if they are possible to execute in geomechanics.

2 THE METHODOLOGY OF BUILDING A PREDICTIVE MODEL

According to Müller and Guido (2016), machine learning is about extracting knowledge from data to predict something. Building a robust predictive model requires large volumes of data from different sources. Sources that could not have a direct and intuitive connection between them. For example, data could not be balanced in time scales or periodicity. What about missing values inside the databases? There are several issues and questions before building an accurate predictive model. To solve the problems and understand the machine learning model's requirements, it is required to follow a methodology.

2.1 Data Collection

In the path of classical machine learning methods, it is necessary to answer two questions. The first is: What to predict? The second question is: What factors influence the mentioned *something* to predict? Both answers should provide how to characterize and measure the said *something* and the factors that help to predict it. Table 1 presents a straightforward example of the mentioned questions and answers. These answers provide the sources to populate a database.

Table 1. Data collection: Simple example of how to define the sources of the predictive model

Question	Answer	Methods to characterize or measure
What to predict?	Rain	Precipitation
Factors influencing the prediction	Water in environment Climatic condition	Humidity, Temperature, atmospheric pressure, etc.

Data collection should always be based on conducted research or experience in the field to predict. Associate causes and consequences without sustained knowledge could lead to incorrect findings.

2.2 Analysis and Cleaning

The first step provides the data to build the model. A database could have different sources to characterize a phenomenon that is expected to predict. The second step is to create a consolidated database based on the provided data from the previous phase.

A consolidated database to be used in a machine learning method should homogeneously extract data from each source of information. For example, if data is collected temporally, it should be by a defined period (daily, weekly, monthly, etc.). Alternatively, if it is measured in length intervals, it should be defined for each meter, kilometer, etc.

Decisions about homogenization should always be justified and based on knowledge and experience criteria (for example: should the variable be repeated, divided, added, or selected the max/min or trend). In addition, determining how to homogenize the database (how frequently it is characterized) should align with the objectives of the prediction in terms of expected accuracy.

Understanding the behavior of each variable in the consolidated database is expected to be analyzed in this step to detect possible errors. Under the same process, it is necessary to deal with missing values. The instance should be filled or eliminated.

This step also considers the first exploratory analysis of the variables, intending to understand and find the first patterns and relationships between variables. This process helps to gain knowledge about the database and allows to make funded decisions about selecting the machine learning method to predict the expected value.

Analysis and cleaning are the more time-consuming step to building a predictive model. It is expected to cover more than 70% of the entire process. Nevertheless, these decisions are the fabric to build the expected predictive model.

2.3 Machine learning method selection

The next step is to define which machine learning method is better for predicting the expected value. The decision relies on three factors: How the database is populated (size and level of redundancy), the objectives of the prediction to model, and the level of accuracy and precision reached. The first two instances are discussed in the following section (3) because there are more related to the machine learning method's applicability.

To build a robust prediction model is recommended to split the consolidated database and use only one portion to train the machine learning model (Picard & Kenneth, 1990). The remaining database is used to assess the quality of predictions. The split is generally conducted by 75% / 25% fractions to train and test the model, respectively.

Accuracy and precision are related to the success of predicting the model. While accuracy refers to how close the prediction is to the actual value, precision refers to how close the different predictions of the same item are to each other. Both values are independent of each other. Moreover, the decision between both types of assessment relies on the scope of the prediction.

Finally, it is essential to perform cross-validation to check that the prediction model is independent of the database selection to train the model (Ojala & Garriga, 2010).

3 A QUICK REVIEW OF MACHINE LEARNING METHODS

In general terms, machine learning methods classify into two big groups depending on the approach and the expected purpose of the database: Supervised and unsupervised.

In supervised learning, the inputs and outputs of the model are known. The user knows what to predict (output) and what variables influence the phenomenon (inputs or features). On the other hand, unsupervised learning describes how data is organized or clustered and only features observation without measuring an outcome (Hastie et al., 2009). The focus of this paper is on supervised learning.

Today there are many machine learning methods, even algorithms that mix the simpler ones, and each differs in the internal algorithm and its mathematics. Nevertheless, methods can be classified in terms of practical concepts like the type of expected outputs or the condition of the inputs.

The first categorization of methods is in terms of the objective of the prediction, the type of expected value, regression, or classification. Classification methods aim to predict a class, and this class is a possible alternative in a predefined list. On the other hand, in regression methods, the task goal is to predict a continuous number. A way to tell between classification and regression is to ask if there is continuity in the input (Müller & Guido, 2016).

The mathematical formulation of a machine learning method defines if the constitution of the database is enough to generate an acceptable model. While some methods require considerable data, other algorithms need redundancy. Redundancy refers to how many samples of a particular phenomenon are required to predict it reliably (Morgenroth et al., 2019).

All the methods have internal parameters that control the learning process and the estimator's ability to provide accurate predictions on unseen data (generalization). These parameters are often called hyper-parameters and can be tuned.

Methods are presented in order of complexity.

3.1 *k*-Nearest Neighbors

The k-NN algorithm is the simplest machine-learning classification method. The model entails only storing the training dataset. The algorithm finds the closest data points in the training dataset to predict a new data point.

The hyperparameters of this method manage:

- How to measure the distance between points
- The number of “neighbors” required to point out a prediction.

Figure 1 shows the prediction of a value in simple terms. In this case, the number of neighbors required to point out the prediction is three. The nearest three points to the point to predict (in purple color) belongs to class A and B, one and two points, respectively. Hence, the prediction is class B.

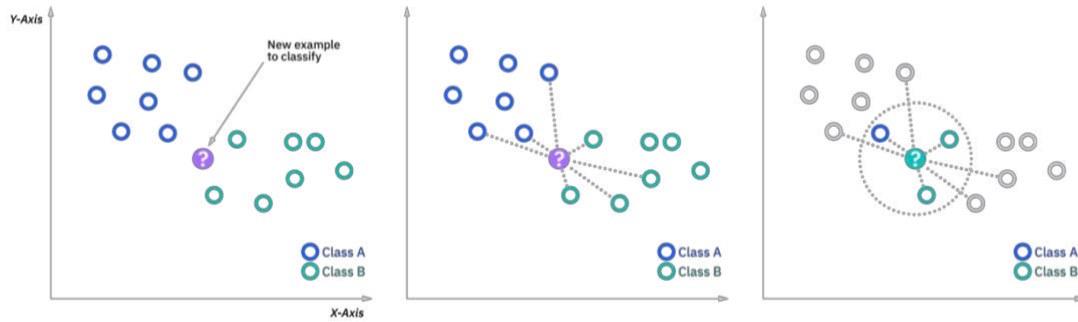


Figure 1. k-NN methodology (IBM, 2022a)

This method is an excellent baseline for exploring the database and is easy to implement. However, the prediction can be slow when the number of features in the training dataset is large (+100).

The k-NN method requires a medium volume of data and a medium level of redundancy.

3.2 Linear regression models

Linear regression models are regression methods that use a linear function of the input features to predict a value. Several types of linear machine learning methods depend on the process to minimize the error and the level of restrictions applied to the model. The selection of the type of linear model relies on things like the number of expected inputs and the amount of sparse data (null values). Hyperparameters, in this case, define the complexity of the regression mode, for example, in terms of the degrees of the equation defined to predict the value.

Linear regression models are fast to train and predict. Moreover, these models are easy to understand because there is an explicit formula to make a prediction. Most of the time, the feature coefficients can be interpreted as the weight of the feature in the equation. In general, a linear model looks as follows:

$$\hat{y} = w[0] \cdot x[0] + w[1] \cdot x[1] + \dots + w[p] \cdot x[p] + b \quad (1)$$

Where $x[0]$ to $x[p]$ denote the features of a single data point, w and b are parameters of the model that are learned; and \hat{y} is the prediction that the model makes.

The method does not demand high levels of volume data and redundancy.

3.3 Logistic regression

Linear models also are used for classification, changing equation (1) as follows:

$$\hat{y} = w[0] \cdot x[0] + w[1] \cdot x[1] + \dots + w[p] \cdot x[p] + b > 0 \quad (2)$$

The line becomes a threshold separating the space into two categories, called the decision boundary.

Logistic regression is a typical linear classification used to estimate the probability that an instance belongs to a particular class (Géron, 2017). In its simplest form is a binary classifier. In logistic regression, a logit transformation is applied to the odds (probability of success divided by the probability of failure) (IBM, 2022b). The logistic regression function is often presented as follows in equation (3):

$$p(x) = \frac{1}{1 + e^{-(w[0] \cdot x[0] + w[1] \cdot x[1] + \dots + w[p] \cdot x[p] + b)}} \quad (3)$$

Where p is the value of probability.

As linear models, logistic regression is fast to train and predict. It also is possible to represent the model clearly by a formula. The coefficients are commonly interpreted as weights in the predicted phenomena.

Another benefit of logistic regression is that the method does not require large databases to train the model. Redundancy is welcomed, but there are cases where logistic regression can predict rare events (phenomena than occurs less than 1% in the database) (King & Zeng, 2001).

Hyperparameters for this method are similar to linear regression models.

3.4 Decision trees and random forests

Decision trees are a non-parametric learning method used for classification. The goal is to create a model that predicts the value of a target variable by learning simple decision rules inferred from data features (Scikit-learn, 2022). Essentially the modern learn a hierarchy of if/else questions, leading to a decision.

Decision trees are simple to understand and interpret. In more straightforward cases, the trees can be visualized, as shown in Figure 2.

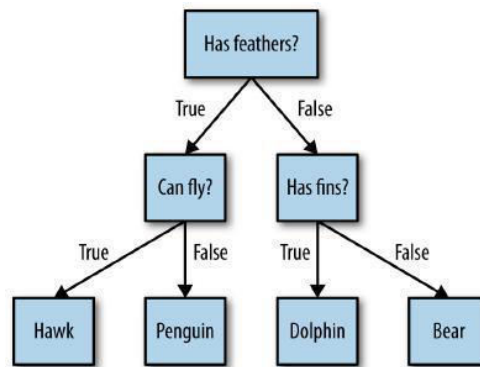


Figure 2. Example of a decision tree model visualization (Müller & Guido, 2016)

Hyperparameters for this method control the complexity of the tree to avoid overfitting the prediction model by conducting a process called pre-pruning. These parameters generally define the tree's depth, referring to how many levels or questions the model has. It also considers the max number of leaf nodes, referring to the number of possible answers. Finally, the database's minimum of samples per answer is also controlled (a good model has high redundancy).

Random forests are one of the most widely used machine learning methods, an ensemble of different decision trees. A random forest is a collection of decision trees, where each tree is slightly different from the others. The idea of random forests is that each tree might do a relatively good job predicting but will be overfitting differently. The overfitting can be reducing averaging the results.

3.5 Artificial Neural networks (deep learning)

Artificial neural networks (ANN) are the heart of deep learning algorithms. ANN structure and name are inspired by the human brain, mimicking how neurons signal to one another (IBM, 2022c). Multilayer perceptrons are a simple method to start analyzing deep learning.

Multilayer perceptrons (MLPs) are a generalization of linear models that perform multiple stages of processing a decision. If the predicted value is a sum of the weighted features in linear regression, in MLPs, this process is conducted multiple times in hidden units, as is shown in Figure 3. These hidden units (nodes) are combined using a weighted sum to define the final prediction. Depending on the requirements' complexity, it is possible to add extra hidden layers.

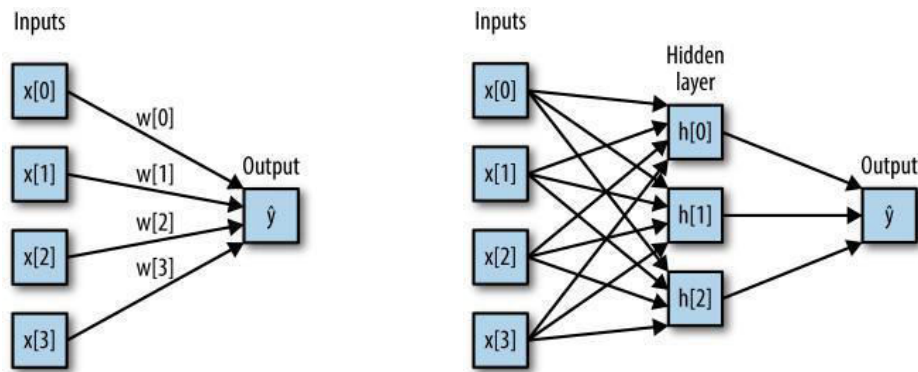


Figure 3. Comparison between the linear model and MLP process for ANN left and right, respectively (Müller & Guido, 2016)

To manage the complexity of an ANN prediction, the number of hidden layers, nodes per layer, and regularization (how generalizable the prediction is) operate as hyperparameters.

Artificial neural networks can capture information in large amounts of data and build complex models. However, the counterbalance requires a large volume of heavily preprocessed data (uniform and scaled). Moreover, its complexity and amount of data require time to process, much more than previously presented methods.

4 MACHINE LEARNING OPPORTUNITIES IN GEOMECHANICS

The previous section shows how machine learning methods can be applied from several approaches and adapted according to the presented requirements. Implementing machine learning methods in geomechanics is not so different from generating an empirical or numerical model. All three cases involve data, and the difference is the amount required. Moreover, it is always present that collecting data in quality and quantity is not always feasible due to time and budget constraints. Hence is necessary to find the most suitable way to apply machine learning models in rock and soil engineering predictions.

Bellow, there are three examples of machine learning applications in geomechanics with different strategies for making predictions.

4.1 *A logistic regression tool: Calculating the risk of operational interference*

Events involving a risk for people and infrastructure in mining operations are not always regular. Moreover, even in some cases is not clear what are the causes or mechanisms involved in the phenomena.

A case in point is mudrushes in block caving mining. A mudrush is a sudden and violent inflow of a mixture of water and fines to mine openings (Valencia et al., 2014). Mudrushes can damage equipment, cause operating losses, and even cause fatalities (Butcher et al., 2005). Furthermore, the problem involves geomechanics and mining fields, like mine planning, considering extraction sequence, and gravity flow hypothesis.

While there is a fair amount of data involving rock characterization and extraction information, mudrushes events represent less than 1% of the database (Navia et al., 2014). In this case, rare-case logistic regression determines the probability of mud entry in drawpoints, taking advantage of the method's convenience. While it is not a direct prediction of mud rushes, mud entry is critical for this operation. According to the mine protocols, the mud appearance is sufficient to close the drawpoint and lose the resources.

In logistic regression, there are no heavy demands on the input variables for the model in terms of uniformity, type, and sparsity. The authors got to generate a model that incorporated draw rate

(ton/m² day), fine material content (%), draw height (m), and season as variables to predict the mud appearance probability for each drawpoint. Moreover, an explicit equation indicates the weights for each variable; these coefficients sort the importance of each variable in the mud entry. This effort was step one to predicting mudrushes considering the decisions conducted in mine, getting a precision of 74%. Figure 4 presents the real data and predictions conducted on Diablo Regimiento Mine in detail for each drawpoint, where W represents wet points (with mud), and D are dry drawpoints.

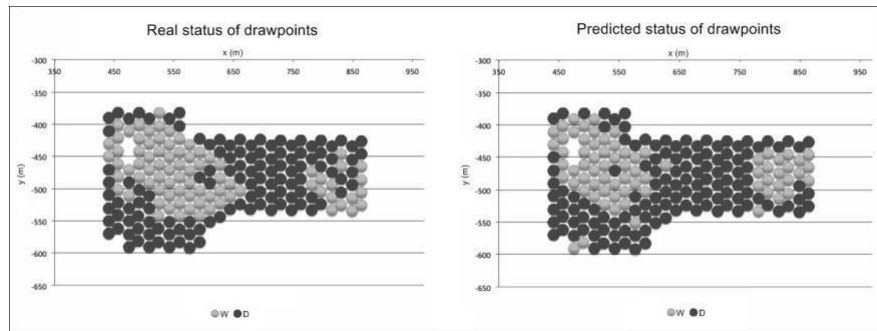


Figure 4. Comparison between real data (left) and predicted data (right) for mud appearance in drawpoints (Navia et al. 2014)

4.2 A classification tool: Estimation of geotechnical parameters

The understanding of spatial variation in intact and defective rock is critical to mine design. Testing is commonly used to measure the strength of intact rock and individual defects (like veins) along boreholes. According to Thielsen et al. (2022), Newcrest Cadia East mine point load testing (PLT) only covers 1.3% of the 590 km of boreholes logged at the mine.

The authors used a procedure to homogenize the available geotechnical and geological logging data, infill missing values, and encode raw data into engineered features for a machine learning model. A random forest classifier was applied to constructed to predict the point load index (Is50) from core logging data where tests were not performed. The random forest model predicted the rolling average Is50 value within 1 MPa 48% of the time. Figure shows an example of two predicted holes compared to its actual PLT measurements.

Additionally, the model gives insights into which core logging quantities have the most robust controls on rock strength, and the confidence level for each prediction is calculated.

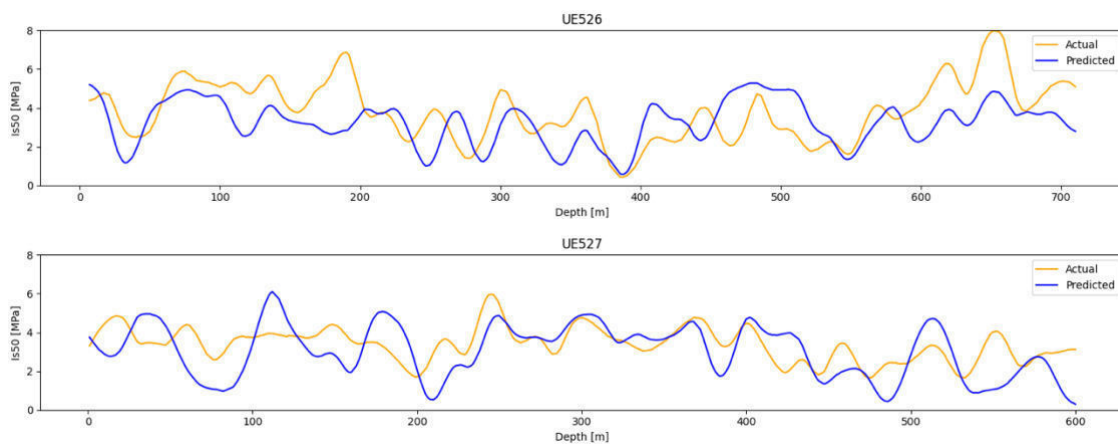


Figure 5. Plots depicting actual and predicted Is50 rolling mean curves for five of the training holes (Thielsen et al., 2022)

4.3 Using synthetic data: Reliability analysis of soil slopes using metamodels

When the assessment of the reliability of a system is complex, the uncertainties of the characterization are high, or there is no data about failures, surrogate models arise as a possible solution. Built a surrogate model in simple terms is to create synthetic data via numerical models to generate each scenario based on the uncertainties of each input value. However, if this is not done correctly, it can be time-consuming or impossible to conduct, considering time constraints in mine design projects. To solve the issue, interpolation methods like kriging can predict intermediate values without extensive data and estimate the prediction's local variance.

Arévalo (2022) proposed an iterative approach based on Monte Carlo Simulation (MCS) and adaptive kriging metamodel efficiently assess soil slope reliability. The proposed adaptive kriging model was used as a surrogate for the system response of the soil slope. It was established by a sequential design of experiments, which updates the Kriging model at each iteration by adding new support points according to some selection rule. Finally, MCS was applied using the adaptive kriging metamodel to evaluate the system failure probability of the slope.

The method was applied in an illustrative 2-dimensional example using two different factors of safety, 1.0 and 1.4. Results indicate that the new approach provides an accurate estimation of failure with a significantly reduced number of deterministic stability analyses compared with direct MCS, making the proposed methodology attractive from a computational perspective.

4.4 Discussion and final comments

The present paper aims to connect machine learning and geomechanics. The most standard predictive models were analyzed to establish their applicability in rock and soil mechanics. Furthermore, each method has constraints in terms of data structure and size.

While the artificial neural networks is the prediction model with the significant capacity to add complexity, it is unlikely to apply due to its requirements in data volume. On the other hand, interpretable and explicit models with fewer input restrictions allow connecting the results of the predictive models with the known mechanism in rock and soil engineering.

The last sentence acquires importance because these days are too easy to build a predictive model that, without the proper knowledge, it can lead to erroneous conclusions.

The review of the examples showed how more straightforward methods predict behaviors and parameters that can be applied directly in the mining business delivering value in the process. The first two examples reduced the uncertainties in the mine planning and mine design process, respectively. The third example presented the potential of surrogate models in extreme cases where the data is too uncertain, or there is no data. However, this requires complete knowledge of the prevailing mechanisms that need to be reproducible in the numerical model that will populate the database along with the interpolation model.

Machine learning methods are an excellent tool to predict or estimate behaviors that are not described in empirical models or take too much time to run in a numerical model.

5 REFERENCES

- Butcher, R., Stacey, TR & Joughin, WC. 2005. Mud rushes and methods of combating them. *Journal of the Southern African Institute of Mining and Metallurgy* 105.11: 817-824.
- Géron, A. 2017. *Hands-On Machine Learning with Scikit-Learn and TensorFlow: Concepts, Tools, and Techniques to Build Intelligent Systems* O'Reilly Media.
- Hastie, T., Tibshirani R. & Friedman J. 2009. *The elements of statistical learning: data mining, inference, and prediction*. Vol. 2. New York: Springer.
- Hoek, E. 1966. Rock Mechanics-an Introduction for the Practical Engineer. *Mining Magazine*. 1–67.
- IBM. 2022a. K-Nearest Neighbors Algorithm. <https://www.ibm.com/topics/knn>
- IBM. 2022b. What is Logistic Regression. <https://www.ibm.com/topics/logistic-regression>
- IBM. 2022c. Neural Networks. <https://www.ibm.com/cloud/learn/neural-networks>
- King, G., and Zeng L. 2001. Logistic regression in rare events data. *Political analysis* 9.2: 137-163.

- Koza, J. R., et al. 1996. Automated design of both the topology and sizing of analog electrical circuits using genetic programming. *Artificial intelligence in design '96*. Springer, Dordrecht. 151-170.
- Morgenroth, J., Usman T. K., and Matthew A. P. 2019. An overview of opportunities for machine learning methods in underground rock engineering design. *Geosciences* 9.12: 504.
- Müller, A. C., and Guido S. 2016. Introduction to machine learning with Python: a guide for data scientists. O'Reilly Media, Inc.
- Navia, I., Castro, R. & Valencia, M.E., 2014. Statistical analyses of mud entry at Diablo Regimiento sector – El Teniente's Mine. *3rd International Symposium on Block and Sublevel Caving*. Santiago, Chile, pp. 363-371.
- Ojala, M. and Garriga, G. 2010. Permutation Tests for Studying Classifier Performance. *Journal of Machine Learning Research* 11:1833-1863.
- Picard, R. R., and Kenneth N. B. 1990. Data splitting. *The American Statistician* 44.2: 140-147.
- Scikit-learn. 2022. Decision Trees. <https://scikit-learn.org/stable/modules/tree.html>
- Thielsen C., Furtney, J.K., Valencia M. E., Pierce M., Orrego P., Stonestreet P., Tennant D. 2022. Application of Machine Learning to the Estimation of Intact Rock Strength from Core Logging Data: A Case Study at the Newcrest Cadia East Mine. *In 56th US Rock Mechanics/Geomechanics Symposium 2022*. 26-29, Santa Fe, New Mexico, USA.
- Valencia, M.E., Basaure, K., Castro, R. and, Vallejos J., 2014. Towards an understanding of mud rush behavior in block-panel caving mines. *3rd International Symposium on Block and Sublevel Caving*. Santiago, Chile, pp. 363-371.

Behavior of Shales from Experiment to Modeling

Marte Gutierrez

Civil and Environmental Engineering, Colorado School of Mines, Golden, CO 80401, USA

ABSTRACT:

Shale is the most ubiquitous material on the earth's surface and plays important roles in underground excavations and in geo-energy and geo-environmental applications. At the same time, shale is a very complicated material because of its mineralogical composition, heterogeneity, extremely low porosity and permeability, loading-rate dependency, anisotropy, and interactions with the pore fluid. Tight shale oil gas is becoming a valuable source of energy that produces less climate-changing CO₂ compared to other fossil fuels. Due to their very low permeability, economic shale gas/oil production is only possible by enhancing shale permeability through hydraulic fracturing techniques. Also, due to their low permeability, shales are a common cap rock layers for carbon dioxide (CO₂) sequestration in geological reservoirs such as deep saline aquifers. The caprock layers are expected to physically trap the CO₂ plume in the reservoir for an extended period. The fracturing of caprock shales would allow the sequestered CO₂ to escape to drinking water aquifers or the atmosphere, thereby reducing the effectiveness of geological sequestration. Shales are also the main cap rock in trapping of hydrocarbons in reservoirs. In oil and gas extraction in shale reservoirs, hydraulic fracturing is the most common form of reservoir stimulation by increasing the pore pressure until it exceeds the combined minimum effective principal stress and the rock's tensile strength. Similarly, hydraulic or shear fracturing of shales can be one cause of leakage in CO₂ storage caprocks. This paper presents experimental data on different aspects of shale behavior including its compaction characteristics, poroelasticity, shear stress-strain relation, brittle-to-ductile transition, time-dependent stress-strain response, shear failure and strain softening, fracturing and damage, and eventual strain softening, and anisotropy. Using the experimental results, models to account for the multi-faceted shales behavior are presented.

1. SHALE COMPACTION AND PERMEABILITY BEHAVIOR

Shales typically have very low porosity and permeability ranging in the order of pico- to nano-Darcy (Brace 1984; Dewhurst 1989; and Neuzil 1994) due to their very tight matrices mainly composed of kerogen, other organic matters, clay minerals, and silica. The behavior of argillaceous materials during sedimentation, burial and uplift has been extensively studied and presented in the literature. For instance, Athy's (1930) model relates sediment porosity, $\varphi = V_v/V$ =volume of voids/total volume, with burial depth z according to the relation:

$$\varphi = \varphi_i \exp(c \cdot z) \quad (1)$$

The mechanical compaction of shale under high effective stresses can also be adequately represented as function of the effective vertical σ'_v applied to compact the shale (Fig. 1). One commonly used model is the empirical relationship between void ratio $e = \varphi/(1 - \varphi)$ =volume of voids/volume of solids, and effective vertical stress σ'_v from soil mechanics (e.g., Lambe & Whitman 1979):

$$e = e_o - C_c \log \left(\frac{\sigma'_v}{\sigma'_{v0}} \right) \quad (2)$$

where C_c is the called the compression index and e_o is the void ratio at the reference effective vertical stress σ'_{v0} . The motivation for the use of Eq. (2) is that mechanical compaction of sediments is governed by effective stresses in a sedimentary column. The effective vertical stress σ'_v is equal to the difference between the total vertical stress σ_v and the pore pressure u according to Terzaghi's (1925) effective stress principle:

$$\sigma'_v = \sigma_v - u \quad (3)$$

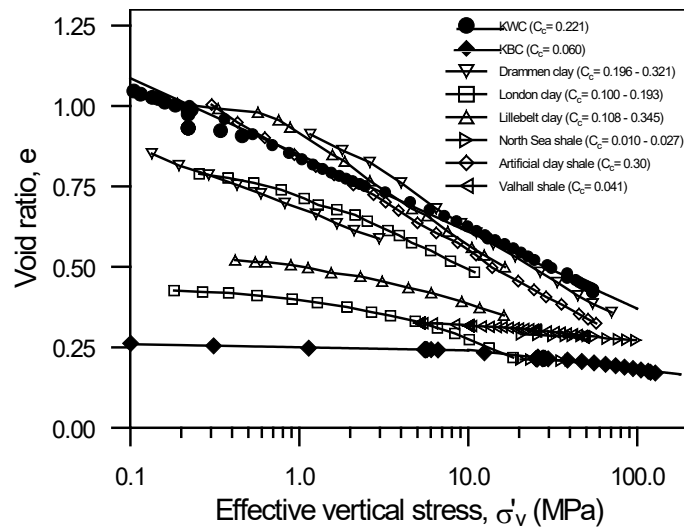


Figure 1. Comparison of compaction curves for different clays and shales (Nygaard et al. 2003).

Often, a bi-linear relationship between void ratio e and the logarithm of the effective vertical stress $\log(\sigma'_v)$ is needed due to the change in compaction behavior from “normally consolidated” to “over-consolidated” behavior. Fig. 2 shows an example of this bi-linear compaction response for Kimmeridge Bay shale with a stiff e vs. $\log(\sigma'_v)$ response for stresses below the apparent pre-consolidation stress of σ'_{vmax} of 22 MPa. For stresses above this value, the shale is more compressible and exhibit “normally consolidated” behavior.

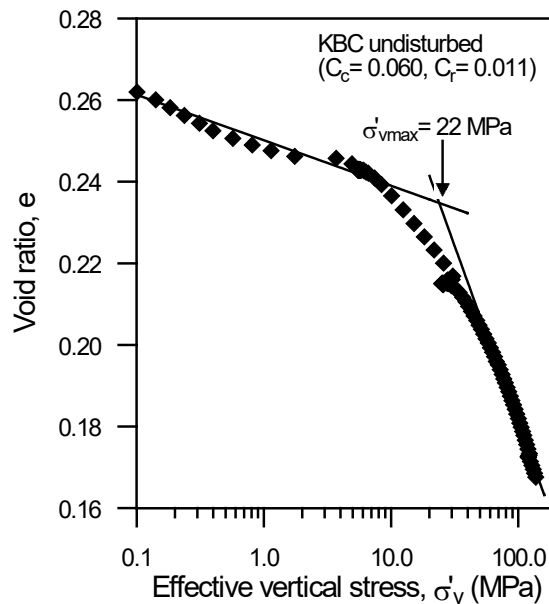


Figure 2. Bi-linear compaction behavior of Kimmeridge Bay shale showing apparent pre consolidation at 22 MPa (Nygaard et al. 2003).

Permeability decreases considerably as shale is compacted and its porosity or void ratio is reduced. The logarithm of permeability $\log(k)$ of shale is shown to varies linearly with void ratio e for different types of shales and clays. (Fig. 3) This relationship is very similar to the well-

known Carman-Kozeny (Carman 1937; Kozeny 1917) relationship between permeability and porosity.

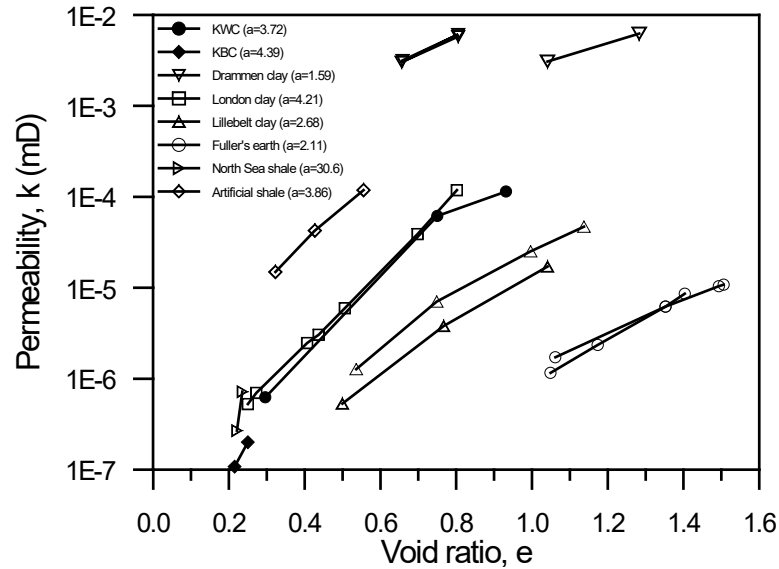


Figure 3. Bi-linear compaction behavior of Kimmeridge Bay shale showing apparent pre consolidation at 22 MPa (Nygaard et al. 2003).

During oedometric loading where lateral strain is prevented, cemented shales show lower K_o -values than uncemented sediments such as clays (Fig. 4). The K_o -value is constant for normally consolidated uncemented clays. On the other hand, the K_o -value seems to decrease with overconsolidation for cemented shales before the apparent pre-consolidation of 22 MPa is reached. Above the apparent pre-consolidation, the K_o -value increases and become comparable to the uncemented clay.

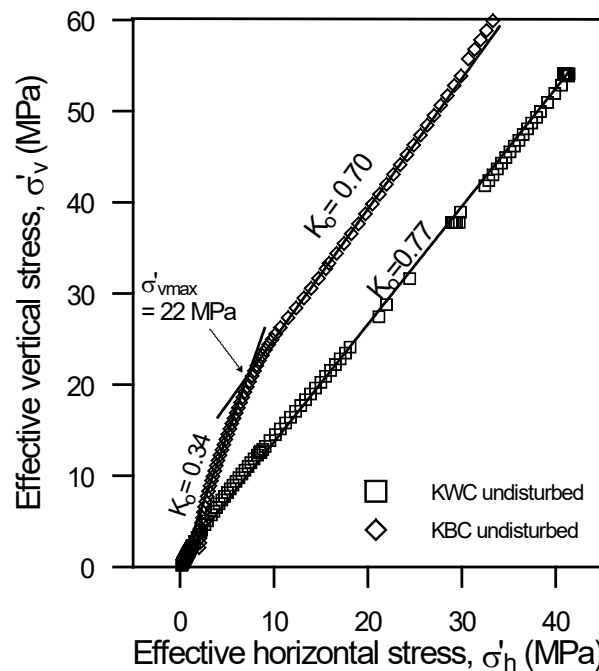


Figure 4. Differences in effective stress paths and K_o -values for clay (KWC) and shale (KBC) (Nygaard et al. 2003).

Mechanical compaction alone cannot explain the much lower porosity, permeability and compressibility, and the increased shear strength of lithified shale compared to young deposits of clay. The very low porosity of shale is not only due to mechanical compaction but also chemical diagenesis. The reduction in porosity and lower compressibility of shale from chemical diagenesis compared to mechanically compacted clays is most due to the precipitation of minerals in the pores of the sediment and cementation of the grains. Chemical diagenesis can also increase the apparent pre-consolidation stress and decreases the K_o -value of shales. Once sediments have undergone chemical diagenesis, they become more difficult to compact mechanically, and mechanical compaction becomes less important. Also, due to chemical diagenesis, the permeability of undisturbed shales can be several orders of magnitude smaller than clays for the same void ratio. The reduction in permeability is partly due to the reduction in pore throat sizes from mineral precipitation. Chemical diagenesis can also increase the anisotropy in the arrangement of clay particles in shales.

2. SHALE POROELASTIC BEHAVIOR

Shales are highly poroelastic materials because of their tight microstructure and very stiff skeletal response with skeletal stiffness comparable to the stiffness of its solid mineral grains. As a result, the Biot-Willis (1957) effective stress law given below applies instead of Terzaghi's (1925) effective stress law (Eq. 3):

$$\sigma' = \sigma - \alpha \cdot u \quad (4)$$

where σ' is the effective stress, σ is the total stress, and u is the pore pressure. The Biot-Willis poroelastic coefficient α is defined as:

$$\alpha = 1 - \frac{K}{K_s} = 1 - \frac{\Delta V_s}{\Delta V} = 1 - \frac{\Delta V_{pore}}{\Delta V} \quad (5)$$

where K is the drained bulk modulus of porous medium, K_s is the bulk modulus of solid grains of porous medium, and ΔV_s is the bulk volume change of solid grains. ΔV_{pore} is given as the change of pore fluid volume produced from a saturated sample during compaction. For soft sediments $\alpha=1.0$ and Terzaghi's effective stress law applies. Using a Constant Rate of Strain (CRS) consolidation testing, previously used only for clays, experimental results show that the poroelastic coefficient α for shale, similar to permeability and compressibility, is not constant but stress dependent (Gutierrez et al. 2015). A typical variation of α with compressive effective confining stress for Mancos shale is shown in Fig. 5.

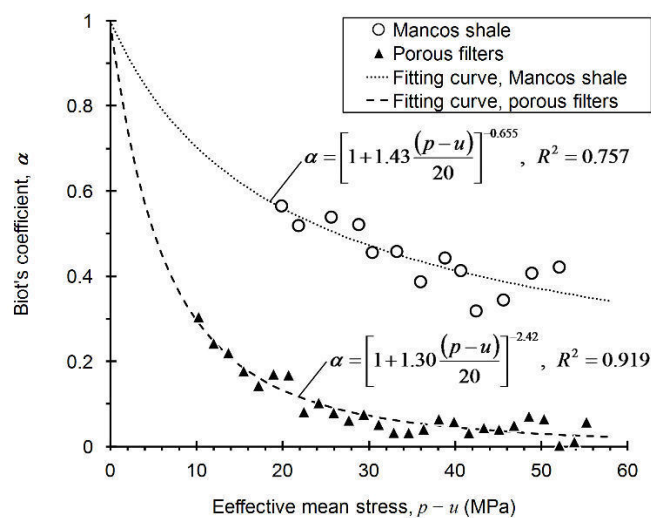


Figure 5. Stress dependency of the Biot-Willis poroelastic coefficient α of Mancos shale and porous metal filters. Dotted curves are respective best-fitting results of the proposed model of Biot-Willis coefficient for Mancos shale and porous metal filters (Gutierrez et al. 2015).

3. SHALE SHEAR STRESS-STRAIN BEHAVIOR AND BRITTLE TO DUCTILE TRANSITION

Because of their very low permeability, triaxial shearing of shales can only be done under undrained conditions. Drained tests are nearly impossible because drainage will take an inordinately long time. In undrained shear tests, the effective stress behavior can be determined by measuring the pore pressure in the sample. Undrained tests can still take time to allow for the pore pressure to equilibrate within the sample but is much faster than drained test. Fig. 6a and b show typical shear stress-strain and effective stress path behavior of a Kimmeridge Bay shale during consolidated undrained (CU) triaxial tests at different effective confining pressures.

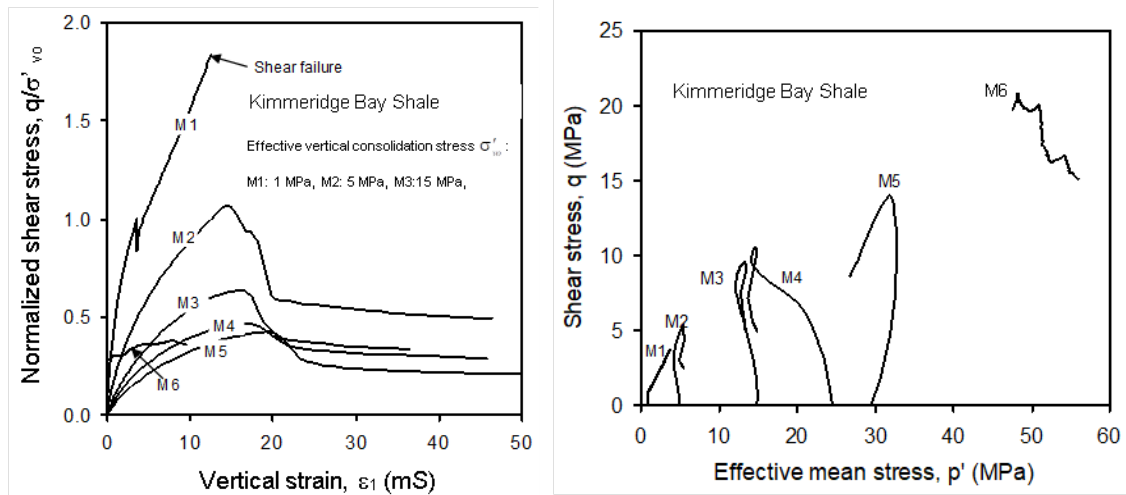


Figure 6. Normalized shear stress vs. axial strain and effective stress path response of Kimmeridge Bay shale during CU triaxial compression test at different effective confining pressure (Nygaard et al. 2005).

As can be seen, the undrained shear response of Kimmeridge Bay shale is very much dependent on the effective confining pressure. In general, the slope of the stress-strain curve is steeper signifying higher elastic modulus for low confining stress than at high confining pressure. The normalized undrained shear strength corresponding to the peak of the stress-strain curve also increases with confining pressure $\sigma'_3 = p$. Sample M1, which was consolidated at $\sigma'_3 = 1$ MPa, shows a very brittle behavior with very violent failure after which the vertical loading frame was unable to follow the stress-strain curve. Samples M2 and M3, which were consolidated at $\sigma'_3 = 5$ and 15 MPa, respectively, also each exhibit very brittle behavior with strain hardening and distinct peak followed by pronounced strain softening to residual shear stress. The brittle behavior of samples M2 and M3 is also observed in the effective stress paths characterized by dilatant behavior resulting in effective stress paths that bend to the right. Samples M5 and M6 (which was consolidated anisotropically) showed ductile response with less pronounced peak and strain softening. The effective stress paths show contractive behavior with the curves bending to the left. Sample M4 appear to show transitional brittle-to-ductile response with initially contractive then dilatative stress path.

As shown above, shales can behave in ductile or brittle manner with significant consequences on the stress-strain curve and effective stress path response. To summarize, brittle shale shows distinct peak shear stress and strain softening and dilatative response while ductile shale exhibits less distinct peak shear stress and strain softening and contractive response. Ductility and brittleness also play an important role in how shales fail under shear loading. Fig. 7 shows pictures of Samples M1 and M5 after they have been loaded to failure and post-failure. As can be seen, sample M1 (Fig. 7a) showed the development of a distinct shear plane, consistent with a brittle material, while sample M5 (Fig. 7b) showed ductility by bulging laterally and shortening vertically without the development of shear planes

There have been many methods to characterize the ductility/brittleness of shales. Some methods are based on the mineral composition of the shale. For example, shales with high quartz content are deemed brittle because quartz is inherently brittle. Other methods are based on the shape of the stress-strain curve and the energy stored then dissipated by the shale sample during shearing. The results presented above show that the shape of the stress-strain curve, the effective stress path and the mode of failure must be all taken into consideration when determining if a shale sample is ductile or brittle. The mode of failure is important. Brittle samples that fracture with distinct fracture plane(s) at failure will allow fluid to flow in shales with otherwise very low permeability. Ductile samples, on the other hand, will show very little permeability change or reduced permeability after failure.

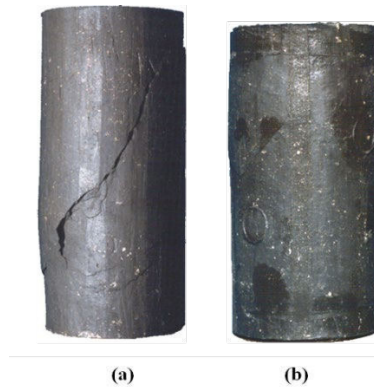


Figure 7. Pictures of Kimmeridge Bay shale after loading and failure. (a) Sample M1 consolidated at 1 MPa, and (b) Sample M5 consolidated at 30 MPa.

Very importantly, ductility and brittleness are not intrinsic properties but are dependent on the stress level. As shown above, shales at low effective confining stress are generally brittle while shales at high effective confining stress are generally ductile. Fig. 8 summarizes the effects of confining stress on the mode of failure of shales under triaxial loading showing behavior from brittle to transitional and ductile response. Under tensile load (e.g., during hydraulic fracturing) a vertical extensional fracture will form. At low confining stress, a combined tensile and shear fracture, or a distinct fracture will form. With increasing confining pressure, the shear plane becomes thicker or more diffused, or the sample will not exhibit a failure plane and will just bulge laterally and shorten vertically.

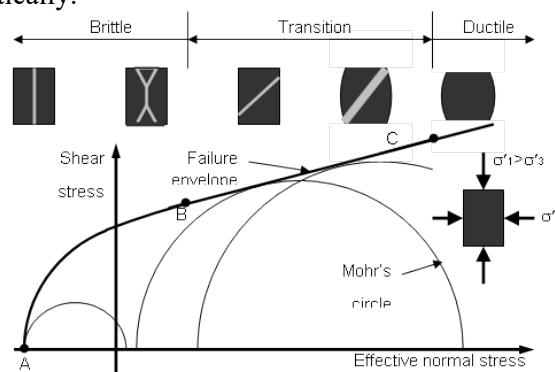


Figure 8. Mohr-Coulomb diagram showing possible modes of failure and fracturing of shale as function of effective confining stress (Nygaard et al. 2005).

Nygaard et al. (2005) modified a parameter widely used in soil mechanics to quantify the ductility or brittleness of clays, namely the over-consolidation ratio (*OCR*). For soils, *OCR* is defined as the ratio between the maximum effective vertical stress σ'_{vmax} the clay has been subjected to in its geologic history, and the present effective vertical stress σ'_v . The maximum

effective vertical stress σ'_{vmax} is called the pre-consolidation stress. Nygaard et al. (2006) showed that OCR could be expressed in terms of isotropic mean stress or anisotropic (vertical) stress conditions, provided the same state of stress is used to define the pre-consolidation stress and the current stress.

For clays, σ'_{vmax} is only due to the maximum mechanical compaction stress that it has been subjected. The difference with shales is that shales undergo not only mechanical compaction/compression but also other diagenetic processes such as aging, cementation, mineral transformation, and long-term secondary compression or creep. The increase in over-consolidation due to non-mechanical processes was called “pseudo-over-consolidation” by Bjerrum and Wu (1967) and Burland (1990). Nygaard et al. (2005) argued that the transition from stiff to more compressible response under compression (isotropic or uniaxial strain) can be used as an “apparent pre-consolidation stress stress” σ'_{pc} that accounts for all the diagenetic changes in the shale. They then introduced an “apparent over-consolidation ratio” $AOCR$ defined as:

$$AOCR = \frac{\sigma'_{pc}}{p'} \quad (6)$$

where p' is the current effective mean stress applied on the shale. Note that $AOCR$ can never be less than one because if p' exceeds σ'_{pc} then the apparent pre-consolidation is erased and $\sigma'_{pc} = p'$. For clays, $AOCR=1.0$ corresponds to normal consolidation and ductile response. Shales with $AOCR>1.0$ are over-consolidated and exhibit brittle behavior. The higher the $AOCR$, the more brittle the shale is. For shales, Nygaard et al. (2005) showed that ductile-to-brittle transition can occur at a much higher $AOCR$ of 1.0 to 2.5. For an $AOCR>1.0$ to 2.5, shales behave as a brittle material. For $AOCR<1.0$ to 2.5 the effects of the mechanical pre-consolidation and cementation are removed, and the shale can become a more compressible, ductile or “normally consolidated”. For $AOCR$ between 1.0 and 2.5 the shale is in brittle-to-ductile transition.

The determination of “apparent pre-consolidation stress stress” σ'_{pc} for shale is the same as in soil mechanics. An oedometric or isotropic compression/compaction loading test of a shale sample is performed, and the result of the test is plotted in the $\log(p')$ (or σ'_v for oedometric test) vs. void ratio e plot as shown in Fig. 9. For isotropic loading $p' = (\sigma'_1 + 2\sigma'_3)/3$ is the mean stress (σ'_1 and σ'_3 , are the major and minor effective principal stresses, respectively). As can be seen from Fig. (9), the compression/compaction curve for Mancos shale can be approximated by two straight lines intersecting at $\sigma'_{pc} = p' = 15$ MPa, which is deemed as the “apparent pre-consolidation stress” because it marks a distinct change in the compression behavior of the shale. For $p'<15$ MPa, there is very little void ratio change, indicating a very stiff and less compressible “overconsolidated” response. Once the compressive stress exceeds $\sigma'_{pc}=15$ MPa, the pre-consolidation is erased, and the shale becomes “normally consolidated” and more compressible.

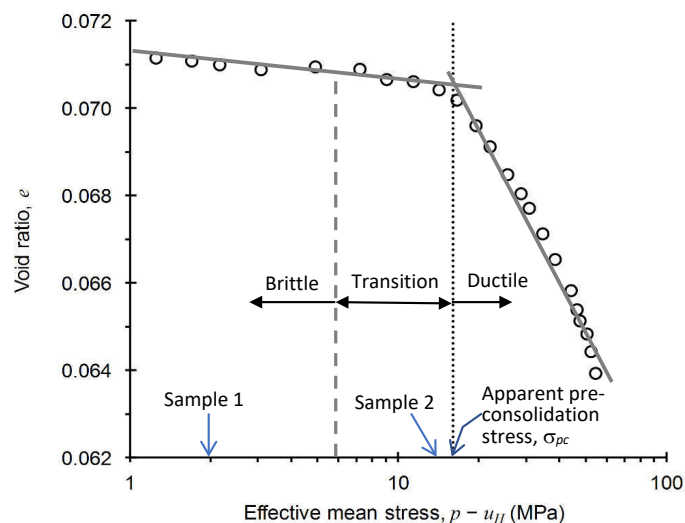


Figure 9. Compression curve of Mancos shale from the drained isotropic compression test showing apparent pre-consolidation at 15 MPa.

For Kimmeridge Bay shale, the apparent pre-consolidation stress was found to be $\sigma'_{pc}=22$ MPa (Fig. 2). Thus, Sample M1 has an $AOCR < 22$ and this very high value befits a very brittle response as verified in Fig. 7. For Sample M5, $AOCR=1$ or “normally consolidated” with characteristic that yields a ductile response as verified in Fig. 7.

Apparent or “mechanical-only” over-consolidation can also be used as a quick index to determine the normalized undrained shear strength of shales and mudrocks (shales exhibit fissility but not mudrocks) as shown by Nygaard et al. (2005). Fig. 10 shows the undrained shear strength normalized with respect to the consolidation stress of 40 different types of mudrocks and shales as function of OCR (or $AOCR$ for lithified mudrocks and shales).

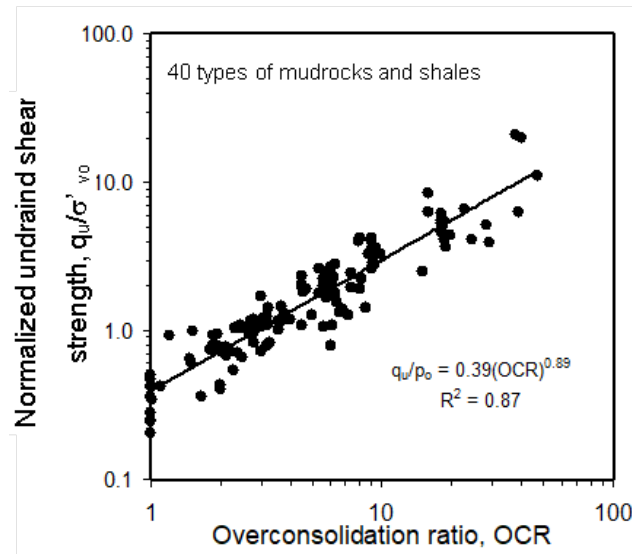


Figure 10. Compression curve of Mancos shale from the drained isotropic compression test showing apparent pre-consolidation at 15 MPa (Nygaard et al. 2005).

The plot shown in Fig. 10 is similar to SHANSEP (Stress History and Normalized Soil Engineering Properties), which is a widely used procedure developed by Ladd and Foott (1977) to predict the undrained shear strength of clays. According to this procedure, the normalized undrained shear strength q_u/σ'_{v0} of normally consolidated (NC) clays is unique, while the normalized undrained shear strength of over-consolidated clays can be represented by the relation:

$$\frac{q_u}{\sigma'_{v0}} = a(OCR)^b \quad (7)$$

where b is an empirical constant, and $a=(q_u/\sigma'_{v0})_{NC}$ is the normalized undrained shear strength of an NC clay, i.e., the value of q_u/σ'_{v0} for $OCR=1$. The results from 40 different clays and shale show a linear relationship between the logarithms of q_u/σ'_{v0} and OCR , which agrees with the power function given in Eq. (7). The reasonably good correlation between q_u/σ'_{v0} and OCR for 40 types of shales and mudrocks is promising. OCR or $AOCR$ provides a good index of the increase in shear strength and brittleness of the shales and mudrocks. The average values of a and b for the different the 40 different shales and mudrocks are equal to 0.39 and 0.89, respectively. The normalized undrained shear strength $a=(q_u/\sigma'_{v0})_{NC}=0.39$ appears to be a reasonable average value for shales and mudrocks under NC conditions. In comparison, for several clays, Ladd and Foott (1977) obtained values of $a=0.20$ and $b=0.77$.

4. VISCOELASTIC DAMAGE MODEL FOR STRAIN-RATE DEPENDENT SHALE RESPONSE UP TO THE STRAIN SOFTENING REGIME

Another challenging and interesting aspect of shales is the strain-rate dependency of its shear stress-strain response. Fig. 11 shows the shear (or deviatoric) stress ($\sigma_1 - \sigma_3$) vs. axial strain ϵ_1 curves for Longmaxi shale obtained from consolidated undrained (CU) triaxial compression tests

at different axial strain rates $\dot{\epsilon}_1$ and constant confining pressure of $\sigma_3=50$ MPa. Pore pressure was not measured but the shear/deviatoric stress is independent of the pore pressure.

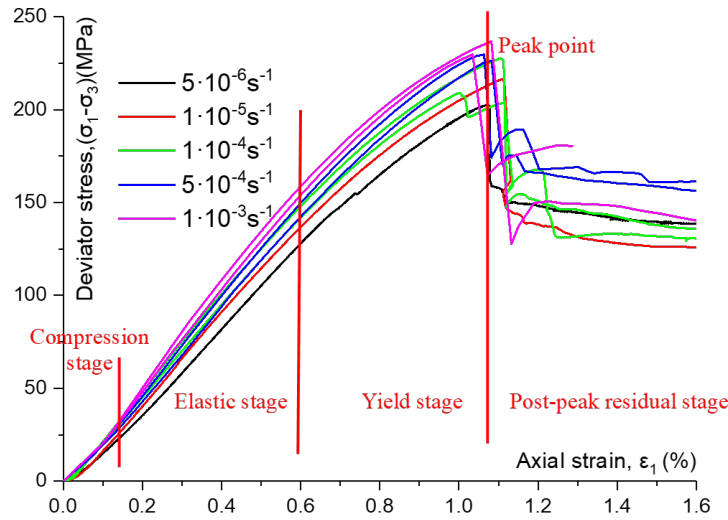


Figure 11. Shear stress vs. axial strain curves for different axial strain rates for Longmaxi shale from consolidated undrained (CU) triaxial test at consolidation pressure of $\sigma_3=50$ MPa (Hou et al. 2019).

As can be seen in Fig. 11, the elastic Young's modulus E corresponding to the linear part of the stress-strain curve and the peak strength $(\sigma_1 - \sigma_3)_{max}$ increase with the axial strain rate $\dot{\epsilon}_1$. The axial strain rates used in the tests are 5×10^{-6} , 1×10^{-5} , 1×10^{-4} , 5×10^{-4} and $1 \times 10^{-3} \text{ s}^{-1}$. The strain-rate dependencies of the Young's modulus E and the peak strength $(\sigma_1 - \sigma_3)_{max}$ are shown in Fig. 12 as function of $\log(\dot{\epsilon}_1)$. For each strain rate, two to three tests were performed. The average values of E and $(\sigma_1 - \sigma_3)_{max}$ for each strain rate are used to determine the strain-rate dependencies. The mean values of E (in GPa) for each strain rate have an exponential function relationship with $\dot{\epsilon}_1$, as represented by the correlation:

$$E = 31.12(\dot{\epsilon}_1)^{0.024} ; R^2 = 0.94 \quad (8)$$

Similar to the elastic modulus, an exponential function relationship exists between the mean values of $(\sigma_1 - \sigma_3)_{max}$ (in MPa) for each test and $\dot{\epsilon}_1$:

$$(\sigma_1 - \sigma_3)_{max} = 264.91(\dot{\epsilon}_1)^{0.02} ; R^2 = 0.98 \quad (9)$$

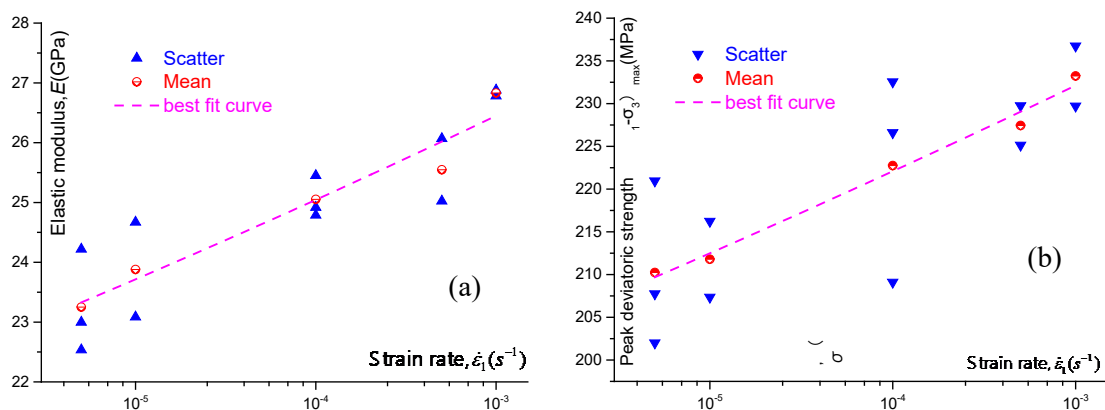


Figure 12. (a) Young's modulus E and (b) peak strength $(\sigma_1 - \sigma_3)_{max}$ of Longmaxi shale as function of axial strain rate $\dot{\epsilon}_1$ (Hou et al. 2019).

The failure patterns of the test specimens at failure different strain rates are shown in Fig.13 and clearly indicate brittle behavior for all samples. The figures clearly show that the samples

developed distinct fractures following post-peak loading. For $\dot{\epsilon}_1 \leq 1 \cdot 10^{-5} s^{-1}$ a pronounced single shear failure is formed, and the shear plane runs through the entire sample with some visible shear displacement. The angle between the failure surface and horizontal axis ranges from 66 to 74°. For $\dot{\epsilon}_1 \geq 1 \cdot 10^{-4} s^{-1}$, the fracture morphology of shale is more complex. The number of shear fracture planes increases significantly with axial strain rate $\dot{\epsilon}_1$. There are many small vertical cracks between the shear fracture surfaces. Under high strain rates, the fracture morphology shows simultaneous development of multiple microcracks, resulting in the destabilization of shale and increased damage, eventually forming a complex crisscrossing fracture network.

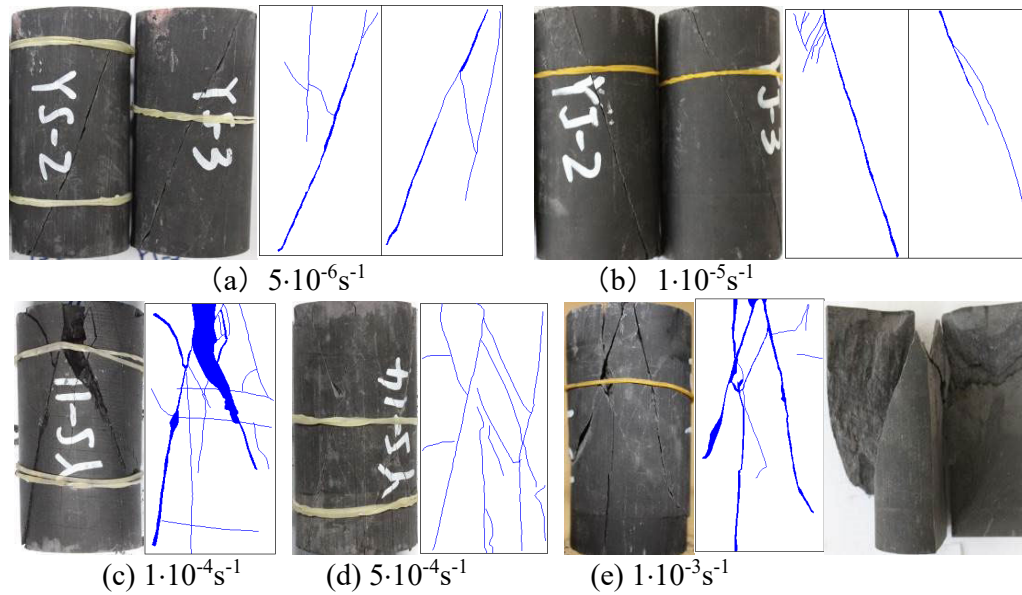


Figure 13. Samples of Longmaxi shale after failure and fracture geometries under different axial strain rates from CU triaxial shear tests (Hou et al. 2019).

The strain-rate dependency of Young's modulus has been shown in Fig. 12a and Eq. (8). Generalizing Eq. (8), the strain rate dependency of Young's modulus of shale can be written as:

$$E = E_v (\dot{\epsilon}_1)^n \quad (10)$$

where n is the exponent for the rate-dependent Young's modulus and E_v is the reference Young's modulus at a strain rate of 1 unit of length per time. The Young's modulus of shale is expected to be insensitive to the strain rate at very low strain rates and become constant at very low strain rates. In other words, the elastic response is rate-independent at very low strain rates, and rate-dependent high strain rates. Based on this observation, the model for the linear stress-strain response for shale is assumed to consist of a static spring E_s and a strain rate-dependent viscous spring E_v given in Eq. (10) connected in parallel as shown schematically in Fig. 14a. Because of the parallel connection, the static or rate-independent modulus E_s can be simply added to the rate-dependent one given in Eq. (10) to give a viscoelastic Young's modulus:

$$E = E_s + E_v (\dot{\epsilon}_1)^n \quad (11)$$

In Fig. 14b, Eq. (11) is curve-fitted through the data of Young's modulus against the logarithm of $\dot{\epsilon}_1$ for Longmaxi shale. As can be seen, Eq. (11) can represent the experimental data satisfactorily with $E_s = 5$ GPa, $E_v = 25$ GPa, and $n = 0.024$. The R^2 -value of 0.92 in Fig. 9 is comparable to that of $R^2 = 0.94$ in Fig. 1 where there is no static Young's modulus.

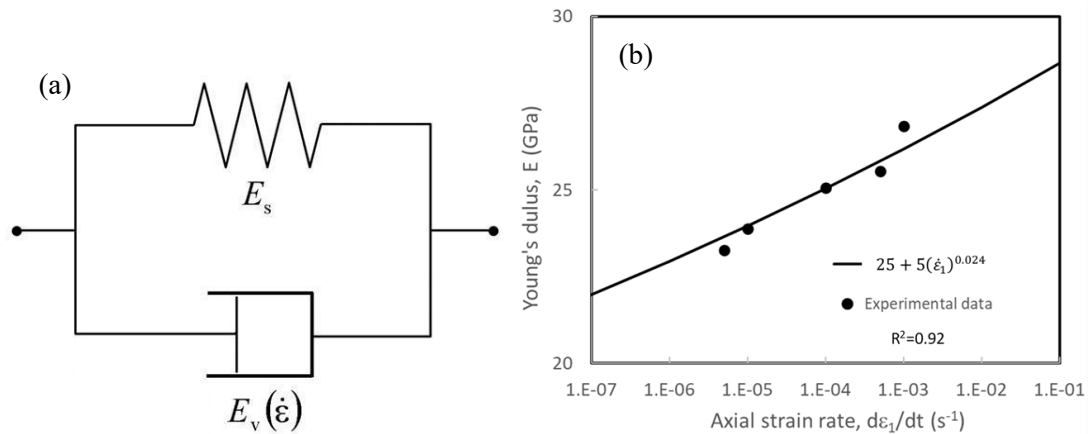


Figure 14. (a) Visco-elastic model consisting of a dashpot, representing the viscous rate dependent Young's modulus $E_v(\dot{\epsilon})$, and a spring, representing the rate-independent static Young's modulus E_s . The spring and dashpot are arranged in parallel. (b) Comparison of the Young's modulus E from the visco-elastic model (Eq. 11) with $E_s=5$ GPa and $E_v=25$ GPa) and experimental data.

It can be seen in Fig. 11 that the shear stress ($\sigma_1 - \sigma_3$) vs. axial strain ϵ_1 curves at different axial strain rates $\dot{\epsilon}_1$ can be divided into different stages. These stages are the initial compression (due to sample disturbance and eventually neglected), linear elastic, yield, strain-hardening to peak point, and post-peak strain-softening. Each stress-strain curve becomes nonlinear and before reaching the peak point following the initial linear response. Then the stress-strain curves drop rapidly, resulting in pronounced strain-softening to residual shear stress. Overall, the greater the strain rate $\dot{\epsilon}_1$ the larger the elastic modulus, peak strength, and residual strength. On the other hand, despite the change in the strain rates of more than three orders of magnitude, the axial strain values at the peak shear points are observed to occur in a narrow range from 1% to 1.15%. Also, the stress-strain curves appear to deviate from linearity at an axial strain ϵ_1 of about 0.5 to 0.6% for all strain rates. From the post-peak slopes and rapid decline of the stress-strain curves of all shale samples (Fig. 11), all shale samples show brittle characteristics from the shape of the stress-strain curves and the shear fracturing shown in Fig. 13.

It is important to model the complete stress-strain response of shales from initial linear elastic to the non-linear strain hardening to the peak, to the post-peak strain softening and to residual strength. Constitutive models can be non-linear elastic or elasto-plastic, however, neither of these formulations can be used to model strain softening behavior without violating thermodynamical principles. Given that the non-linearity, shear failure, strain softening and residual shear strength lead to or are due to shear fracturing of shale sample as shown Fig. 13, it is realistic to model the different aspects of shale stress-strain response using damage mechanics.

The concept of damage is based on the relative volumes of the damaged and undamaged (or intact) parts of a materials (Fig. 15).

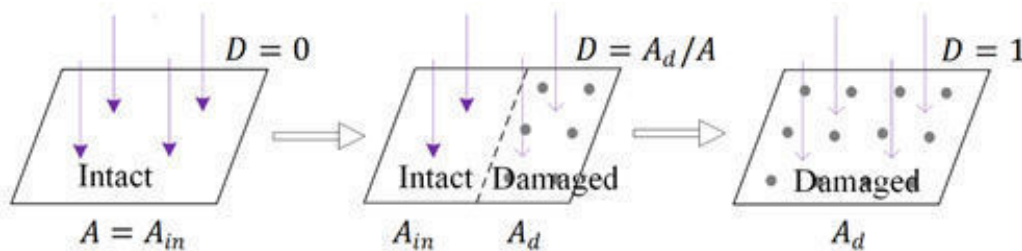


Figure 15. Schematic diagram of the damage evolution process. Dots represent damage in a material, which in the case of shales are fractures.

The total force applied to the geomaterial can be decomposed into the force carried by the intact part and the force by the damaged part. From equilibrium

$$\sigma A = \sigma' A_{in} \quad (12)$$

where $A = A_{in} + A_d$ is the total area on which the total force σA is acting on; σ is the nominal stress; σ' is the "effective stress" acting on the undamaged or intact area A_{in} of the material, and A_d is the area of the damaged portion of the material. A scalar isotropic damage variable D is defined to indicate the amount of damage a material has with regards to its total volume to quantify the change in the microstructure of a material:

$$D = \frac{A_d}{A} \quad (13)$$

where D is in the range of $0 \leq D \leq 1$. For $D=0$, the material contains no damage, and for $D=1$ the material has undergone complete damage and can no longer carry any load. The damage variable must approach but be always less than 1.0 to ensure that the material has a non-zero residual shear strength. From the definition of D , the intact or undamaged area of the material A_{in} can be obtained as:

$$A_{in} = A - A_d \quad ; \quad A_{in} = A - DA = A(1 - D) \quad (14)$$

Substituting the above equation in Eq. (3) gives:

$$\sigma A = (1 - D)A\sigma' \quad ; \quad \sigma = (1 - D)\sigma' \quad (15)$$

It is reasonable to assume that the number and length of fractures increase with increasing axial strain. It can also be rationally assumed that damage is related to fracture initiation and growth. The locations and eventually the propagation of fractures is affected by the distribution of initial microfractures and rock heterogeneities, which are random and statistical in nature. As such, it may be assumed that damage is random and can be represented by a probability distribution as function of axial strain ε_1 . A possible distribution to represent the statistical damage of shale is the Weibull (1951) probability distribution function (PDF):

$$D = \frac{A_d(\varepsilon_1)}{A} = \left\{ 1 - \exp \left[- \left(\frac{\varepsilon_1}{\varepsilon_o} \right)^m \right] \right\} \quad (16)$$

where ε_o is the reference axial strain, and m is the Weibull modulus which reflects the brittleness of shale. Using an initially linear elastic relation $\sigma'_1 = E \cdot \varepsilon'_1$, invoking Lemaitre (1984) equivalence of nominal and effective strain $\varepsilon'_1 = \varepsilon_1$, using the viscoelastic Young's modulus in Eq. (11), and substituting in Eq. (15) together with the Weibull PDF (Eq. 16) yields a very simple viscoelastic damage model is obtained. Before the yield strain is reached, damage $D=0$ and the stress-strain relation is linear viscoelastic given as:

$$q = [E_s + E_{vo}(\dot{\varepsilon}_1)^n] \varepsilon_1 \quad ; \quad \text{for } \varepsilon_1 < \varepsilon_{1y} \quad (17)$$

Once the axial strain reaches and exceeds the axial yield strain ε_{1y} , damage occurs, and the stress-strain relation becomes nonlinear viscoelastic:

$$q = q_y + [E_s + E_v(\dot{\varepsilon}_1)^n] \left(\exp \left[- \left(\frac{\varepsilon_1 - \varepsilon_{1y}}{\varepsilon_o} \right)^m \right] \right) (\varepsilon_1 - \varepsilon_{1y}) \quad ; \quad \text{for } \varepsilon_1 \geq \varepsilon_{1y} \quad (18)$$

where $q = (\sigma_1 - \sigma_3)$ is the shear or deviatoric stress, $q_y = [E_s + E_v(\dot{\varepsilon}_1)^n] \varepsilon_{1y}$ is the rate-dependent shear yield stress where the stress-strain curve starts to become non-linear. The model requires only six parameters, and their values for Longmaxi shale are: $E_s = 5$ MPa, $E_v = 25$ MPa, $n = 0.024$, $\varepsilon_{1y} = 0.5$, $\varepsilon_o = 0.65$ and $m = 5$.

Fig. 16a shows the predicted stress-strain response of Longmaxi shale under the same loading conditions shown in Fig. 11 for different strain rates. By comparing Figs. 11 and 16a, it can be seen than the model is able to satisfactorily predict the strain-rate dependent stress-strain response of shale from pre-peak, peak to post-peak regimes.

Note that the model does not require a failure criterion to be prescribed a-priori. Instead, shear failure, like deviation from linear elastic response, and strain softening and residual shear strength, are all outcomes of damage. It can be shown that maximum value of shear stress q_{max} that can be obtained from Eq. (18) can be expressed as function of the axial strain rate $\dot{\varepsilon}_1$:

$$q_{max} = C [E_s + E_v(\dot{\varepsilon}_1)^n] \quad ; \quad C = \left[\varepsilon_o \exp \left(- \frac{1}{m} \right)^{-\frac{1}{m}} \right] + \varepsilon_{1y} \quad (19)$$

This equation also predicts that the axial strain-rate dependent shear strength of shales q_{max} is a function of the elastic moduli E_s and E_v and the model parameters ε_{1y} , ε_0 , m and n . It can also be shown that the model predicts that for failure $m=n$, whose values 0.019 and 0.024, respectively, are very close to each other. Substituting the model parameters used to generate the predicted stress-strain curves in Fig. 16a gives the following axial-strain rate $\dot{\varepsilon}_1$ dependent shear strength for Longmaxi shale:

$$q_{max} = 44.3 + 221.4(\dot{\varepsilon}_1)^{0.024} \quad (20)$$

The above equation is compared with the experimental peak shear strength (average for each strain rate) as a function of the strain rate $\dot{\varepsilon}_1$ in Fig. 16b. The model prediction from the above equation fits with the experimental data accurately with $R^2 = 0.99$, which is even slightly better than $R^2 = 0.98$ in Eq. (9). The result shown in Fig. 16b shows the ability of the model to predict (in the strictest definition of “prediction”) of the strain-rate dependent shear failure of shale.

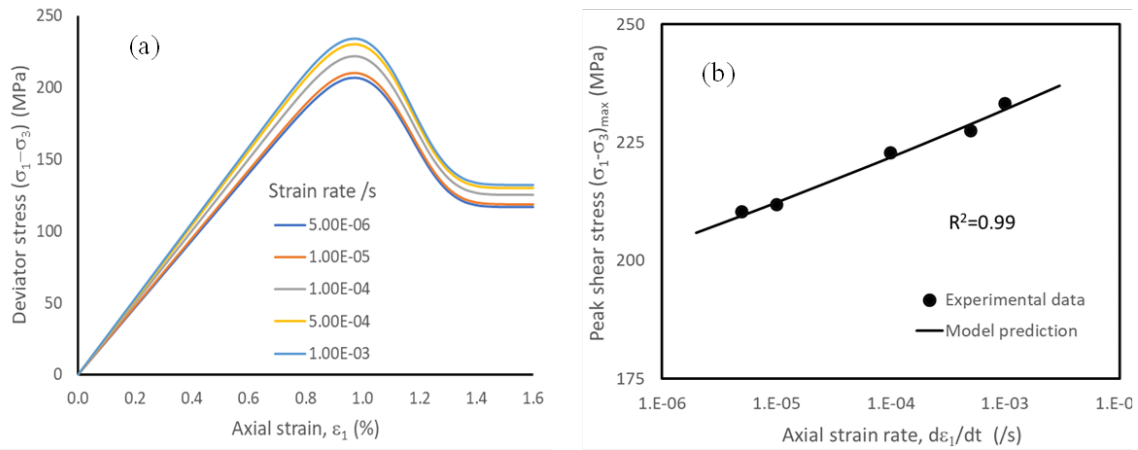


Figure 16. (a) Predicted shear stress-strain curves for different axial strain rates for Longmaxi shale (these curves should be compared to the experimental curves in Fig. 11). (b) Experimental (from Fig. 12b) and predicted (in Eq. 18) axial-strain rate $\dot{\varepsilon}_1$ dependent shear strength of Longmaxi shale.

5. CREEP BEHAVIOR OF SHALES

Given the rate-dependency of the stress-strain response of shale, it can be expected that shale can also experience creep or continued deformation under constant load with time. The model presented above for the axial-strain rate dependent response of shales should be able to predict such creep behavior. Eq. (18) can also be inverted to yield an equation for the axial strain rate:

$$\frac{d\varepsilon}{dt} = \left\{ 1 - \left(\frac{q}{E_{vr}\varepsilon} \right) \exp \left[\left(\frac{\varepsilon}{\varepsilon_0} \right)^m \right] - \frac{E_s}{E_{vr}} \right\}^{1/r} \quad (21)$$

This equation can be numerically integrated with respect to time to simulate the deformation of shale during creep under constant stress levels shear stress q . To verify the validity of such creep model, its predictions are compared to experimental creep behavior of sandstone by Heap et al. (2009) (similar behavior should be observed for shale) in Fig. 17 for two constant stress levels shear stress levels of 141 and 125 MPa. As can be seen, there is good agreement between experimental results and model predictions. It is remarkable that the model can predict the three stages of creep response of soft rocks, namely, 1) Primary, 2) Secondary, and 3) Tertiary. The creep strain rate during the primary creep stage decays gradually with time. During secondary creep, the strain rate remains nearly constant. The strain rate during tertiary creep increases exponentially before rupture.

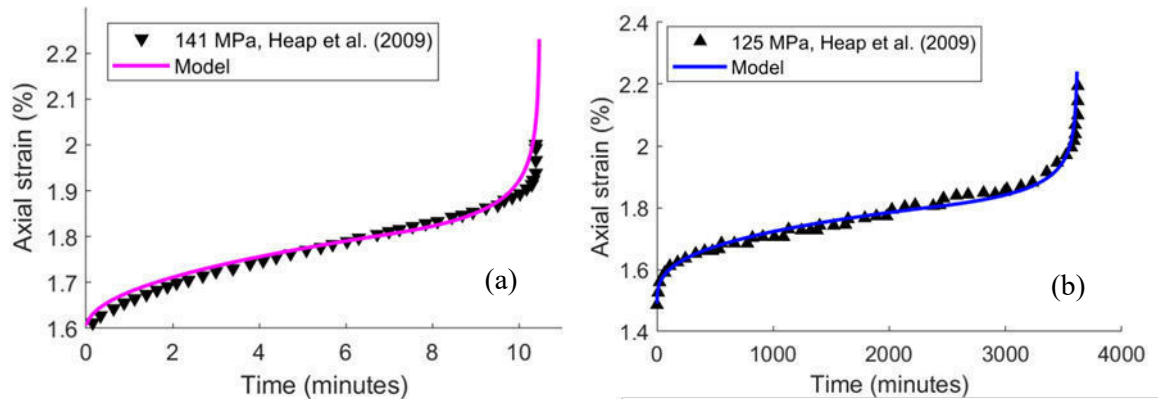


Figure 17. Strain-time curves of sandstone subjected to creep loading constant shear stresses of (a) 141 MPa and (b) 125 MPa. Similar response should be obtained for shale (Ma and Gutierrez 2020).

6. ANISOTROPIC BEHAVIOR OF SHALES

Shales have naturally inherent anisotropic structure due their depositional history resulting in layered structures. The bedding planes created during deposition and compaction are typically weaker than the host rock and is the source of shale fissility. One simple and effective way to model the anisotropic effects is to directly add a loading-direction dependent parameter in the failure envelope. To account for anisotropy in shear strength, an “anisotropic function” $f(\theta)$ is incorporated in the failure envelope. The angle θ is measured from the major principal stress σ_1 to the bedding plane as illustrated in Fig. 18. The function $f(\theta)$, which represents the effect of strength anisotropy, depends on the angle between the σ_1 loading direction and the bedding planes. The anisotropic function $f(\theta)$ is proposed to have the following form:

$$f(\theta) = \frac{kc}{(1+k)+(1-k)\cos(3\theta+d)} \quad (22)$$

where k , d , and c are anisotropy related parameters. Note that different sets of parameters are used for $\theta < \theta_{min}$ and for $\theta \geq \theta_{min}$ where for θ_{min} is the orientation that gives the minimum shear strength.

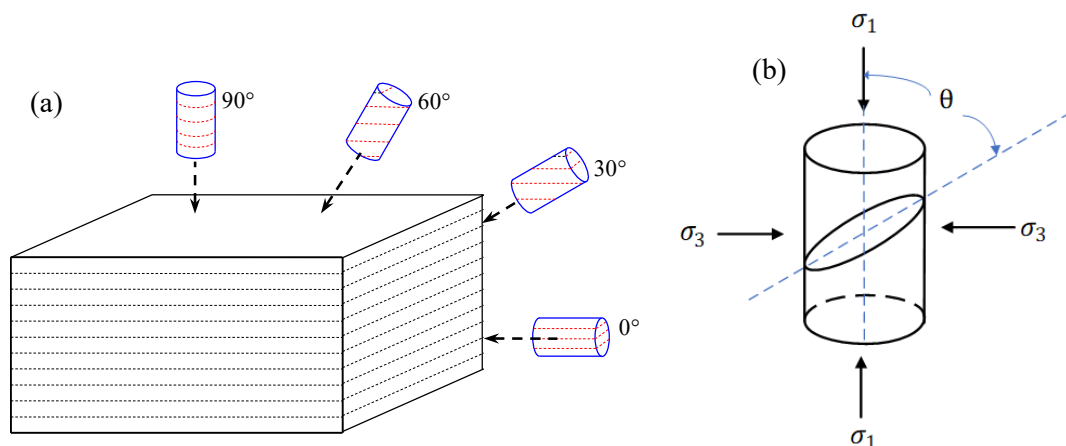


Figure 18. (a) Core samples drilled at different directions with respect to the bedding planes. (b) The angle θ is measured between the major principal stress σ_1 and the bedding plane.

The proposed anisotropic function in Eq. (22) is validated against test data. CU triaxial tests were performed on Longmaxi shale that were drilled at different orientations θ with respect the bedding plane (Fig. 18). CU triaxial shear tests on these samples under shear stresses of $\sigma_3 = 20$

and 30 MPa were carried out and the peak shear stresses were recorded (Fig. 19). The samples with $\theta = 0^\circ$ have the highest peak shear stresses and the lowest peak stresses appears at about $\theta = 30^\circ$. Hence, $\theta_{min} = 30^\circ$ for the triaxial tests. The predicted curves from the function $f^\theta(\theta)$ are also shown in Fig. 19. The proposed anisotropic function can match well with the experimentally obtained anisotropic peak shear stresses.

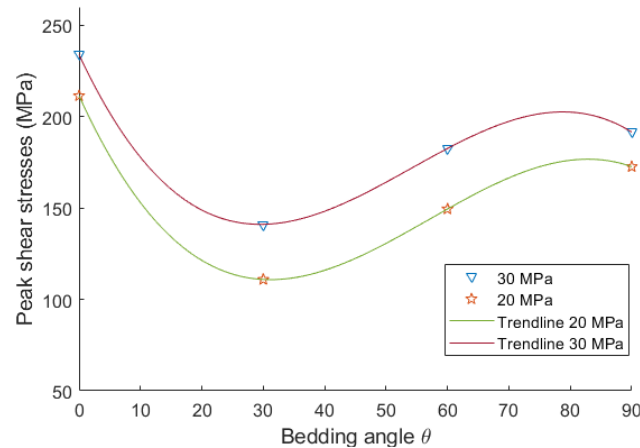


Figure 19. Peak shear stresses vs. θ at confining stresses of $\sigma_3=20$ and 30 MPa for Longmaxi shale.

7. SUMMARY AND CONCLUSIONS

Different aspects of the hydro-mechanical behavior of shales were investigated experimentally and the experimental results were used in the development of constitutive models for shale. The following conclusions were obtained from this study:

- 1) It was shown that the compaction behavior of shale can be modeled using Lambe and Whitman's (1979) soil compression model relating void ratio to effective vertical stress (or effective confining stress). Similar to clays, shales exhibit bi-linear compression curves which transition at the "apparent effective pre-consolidation stress." For shales the "apparent pre-consolidation stress" is due not only from mechanical compaction (as in clays) but also due to chemical diagenesis which cements and stiffens the grains of shale and reduces the shale porosity. For effective confining stresses below the apparent pre-consolidation, shale is "over-consolidated" with brittle behavior and lower compressibility. Once the compressive stress exceeds the effective pre-consolidation stress, the shale becomes "normally-preconsolidated," ductile and more compressible than over-consolidate shale.
- 2) Over-consolidated shales show lower K_o -value while normally consolidated shales show higher K_o -value comparable to that of young sediments and clays.
- 3) The permeability of shale, which are very small in the pico- to nano-Darcy range, becomes even lower as the shale is compacted mechanically and chemically. A power relationship can be used between permeability and void ratio, similar to the Carman-Kozeny equation.
- 4) The shear behavior of shales can be ductile or brittle depending on the "apparent over-consolidation ratio, $AOCR$ " which is the ratio of the apparent pre-consolidation stress and the current effective confining. Shales with an $AOCR < 1.0$ to 2.5 are ductile showing less pronounced peak shear stress and strain softening, contractive response and no signs of shear fracturing. Shales with an $AOCR > 1.0$ to 2.5 are brittle showing distinct peak shear stress and strain softening, dilative response and clear shear fracturing. Shales with $AOCR$ between 1.0 and 2.5 show transitional brittle-to-ductile shear behavior. Shear fracturing due to brittle behavior can enhance the permeability and leakage and flow potential of shales.
- 5) Shale elastic stress-strain behavior is dependent on axial strain rate and can be adequately represented by a viscoelastic model. Damage due to fracturing can account for the non-linearity in the shear stress-strain curve, peak or failure shear stress, and strain softening. A viscoelastic

damage model was found to adequately predict the stress-strain response as well as the strain-rate dependent peak shear strength of shale. A shale failure criterion need not be prescribed a-priori and failure simply emanates from the damage model.

- 6) The viscoelastic damage model can adequately predict the creep behavior of sandstone which is expected to be like shale.
- 7) A loading-direction dependent failure criterion can adequately predict the anisotropy in the shear strength of shale.

8. REFERENCES

- Athy, L.F. 1930. Density, porosity and compaction of sedimentary rocks. *AAPG Bulletin*, 14(1): 1-24.
- Biot M.A. & Willis, D.G. 1957. The elastic coefficients of the theory of consolidation. *J. Applied Mech.* 24: 594-601.
- Bjerrum, L. & Wu, T.H. 1967. Fundamental shear strength properties of the Lilla Edet clay. *Géotechnique*, 10(3): 101-109.
- Brace, W.F. 1980. Permeability of crystalline and argillaceous rocks. *Int. J. Rock Mech. Min. Sci. Geomech. Abs.* 17(5): 241-251.
- Carman, P. (1937). Fluid flow through granular beds. *Transactions, Institution of Chemical Engineers, London*, 15: 150-166.
- Dewhurst, D.N. & Siggins, A.F. 2006. Impact of fabric, microcracks and stress field on shale anisotropy. *Geophys. J. Int.* 65: 135-148.
- Dewhurst, D.N., Yang, Y. & Aplin, A. 1999. Permeability and fluid flow in natural mudstones. In Aplin, A, Fleet, AJ & Macquaker JHS (eds.) *Muds and Mudstones. Physical and Fluid Flow Properties*, (23-43). Geol. Soc., London, Special Publication, No 158.
- Heap, M.J., Baud, P., Meredith, P.G., Bell, A.F. & Main, I.G. 2009. Time-dependent brittle creep in Darley Dale sandstone. *J. Geophys. Res.: Solid Earth* 114.
- Hou, Z., Gutierrez, M., Ma, S., Almrabat, A. & Yang, C. 2019. Mechanical behavior of shale at different strain rates. *Rock Mech. Rock Eng.* 52: 3531–3544.
- Gutierrez, M., Katsuki, D. & Tutuncu, A. 2015. Determination of the continuous stress-dependent permeability, compressibility and poroelasticity of shale. *Mar. Petrol. Geol.*, 68,(A): 614–628.
- Kozeny, J. (1927) Ueber kapillare Leitung des Wassers im Boden. *Sitzungsber Akad. Wiss.*, Wien, 136(2a): 271-306, 1927.
- Ladd, C.C. & Foott, R. 1977. New design procedure for stability of soft clays. *J. Geotech. Eng. Div., ASCE*, 100(4), 763-779.
- Lambe, T.W. & Whitman, R.V. 1979. *Soil Mechanics S.I. version*, 2nd ed. New York, J. Wiley and Sons, Inc.
- Lemaitre, J. 1984. How to use damage mechanics. *Nuclear Eng. Design.* 80(2): 233-245.
- Ma, S. & Gutierrez, M. 2020. A time-dependent creep model for rock based on damage mechanics. *Environmental Earth Sciences*, 79: 466
- Neuzil, C.E. 1994. How permeable are clays and shales? *Water Resour. Res.*, 30(2): 145-140.
- Nygaard, R., Gutierrez, M., Brattli, R.K. & Høeg, K. 2005. “Brittle-ductile transition, shear failure and leakage in mudrocks from the North Sea and adjacent areas,” *Mar. Petrol. Geol.*, 23: 201-212.
- Nygaard, R., Gutierrez, M., Gautam, R. & Høeg, K. 2003. “Compaction behaviour of argillaceous sediments as function of diagenesis. *Mar. Petrol. Geol.*, 21(3): 349-362.
- Terzaghi, K. 1925. *Erbbaumechanik auf bodenphysikalischer Grundlage*. Leipzig: Deuticke.
- Weibull, G.W. 1951. A statistical distribution function of wide applicability. *Appl. Mech.* 18:293–297.

Modeling of the Brazilian Tensile Test on Transversely Anisotropic Rocks using PDEM

Marte Gutierrez

Civil and Environmental Engineering, Colorado School of Mines, Golden, CO 80401, USA

Guowen Xu

Southwest Jiaotong University, Chengdu 610031, Sichuan, China

ABSTRACT:

A new numerical approach based on the particle discrete element method (PDEM) is put forward to investigate the mechanical behavior of transversely isotropic rocks with non-continuous planar fabrics. In this numerical model, the rock matrix and fabric are represented as flat joint contacts and smooth joint contacts, respectively. The following are studied using the numerical model: (1) the effects of the micro-structure of the rock matrix and the fabric micro-parameters on the shear strength and the fracture patterns of rocks under Brazilian tests, and (2) the model calibration process for determining the micro-parameters and the failure process of borehole stability in layered rock. The results show that: (1) Based on the Brazilian test results of 20 kinds of transversely isotropic rocks with non-continuous planar fabrics, six patterns regarding the relationship between the normalized failure strength (NFS) and fabric-loading angles are obtained; (2) The patterns of NFS curves are slightly affected by the coordination numbers of particle in rock matrix, while greatly affected by the amount of pre-existing micro-cracks in rock matrix, and the stiffness, strength and distributed region of the fabrics; (3) The calibrated results of six typical rocks with different patterns agreed well with the experimental results in regard to failure strength and fracture patterns; (4) The fracture of layered surrounding rock after borehole excavation is concentrated in two zones with the line connecting the center of the two zones is normal to the plane of non-continuous fabrics for isotropic geo-stress field, while the connecting line is deflected to the direction of minor principal stress to a certain extent for non-isotropic geo-stress field.

1 INTRODUCTION

The physical and mechanical behavior (e.g., deformability, strength, elastic wave velocity, and thermal and hydraulic conductivity) of transversely isotropic rocks show evident directional anisotropy due to layered structures such as bedding planes, foliations, stratifications, fissurings, and jointing (Dewhurst and Siggins 1985). Rock anisotropy strongly affects civil, mining, geological and petroleum engineering applications in many aspects, such as, the initiation and propagation of the damage zone (EDZ) in surrounding rock during tunnel excavation, hydraulic fracturing, in-situ stress measurement, and TBM tunneling. Thus, a thorough understanding of the tensile behavior of transversely isotropic rocks is important for rock engineering.

Xu et al. (2020) found that the micro-structure of transversely isotropic rocks can be divided into two types: (1) type I where the fabrics (fabric is used to describe any weak planar feature in rock matrix) is straight and continuous from micro- to macro-scale, and (2) type II where the distribution of fabrics is not straight or continuous. Numerical simulation, including equivalent continuum methods (ECM), discrete element methods (DEM) and combined finite-discrete element method (FDEM) have been adopted to systematically investigate the mechanical behavior of type I rocks, and the influence of fabrics on the stability of underground structures.

The results obtained from investigations reveal that the failure strength and fracture patterns of type II rocks are mainly controlled by the micro-structure of rock matrix and micro-parameters of fabrics. However, it is difficult to quantify the impacts of these factors through laboratory tests.

Thus, in this article, a numerical approach based on the Particle-DEM (PDEM) is proposed to represent the transversely isotropic rocks with non-continuous planar fabrics. Firstly, the patterns regarding the relationship between the failure strength and the fabric-loading angles are classified based on the numerical Brazilian test results in existing literature. Then, the effect of micro-structure of rock matrix and micro-parameters of fabrics on the mechanical behavior of rocks under Brazilian test are systematically investigated. Then, the method for determining the micro-parameters is proposed, and the PDEM model is validated by reproducing the behavior of rocks with different curved failure patterns. Finally, the numerical approach is applied to study the failure process of layered rocks under Brazilian test.

2 NUMERICAL APPROACH

The Particle-DEM (PDEM) is widely used to study the crack initiation, propagation, and coalescence of rocks (Duan et al. 2008). In this article, a new numerical approach based on PFC2D (Particle Flow Code 2D) developed by Itasca (20087) is put forward to study the mechanical behavior of transversely isotropic rocks with non-continuous fabrics under Brazilian tests. In this PDEM model, the flat joint contact (FJC) model is used to represent rock matrix and the smooth joint contact (SJC) model is used to represent rock fabrics.

2.1 Flat joint contact (FJC) model

Prior to the development of FJC, parallel-bond contact (BPC)⁶² has been widely adopted to investigate the mechanical behavior of rocks (Potyondy and Cundall 2008). However, the BPC cannot provide adequate rotational resistance between particles and the circular particles cannot reproduce reasonable grain interlocking, which leads to three inherent defects in simulating rocks⁶³: (1) the ratio of uniaxial compressive strength to tensile strength is low; (2) the internal friction angle is low; and (3) the shear strength envelop is linear. To overcome these shortcomings in BPC, the FJC model was proposed by Potyondy (2012) and it has succeeded in describing the behavior of granite, marble, limestone, and sandstone. Three types of contacted state may exist between particles connected by FJC (Fig. 1). That is, type B is the bonded contact, type S is the unbonded contact, and type G represents the uncontacted state with a gap greater than zero. Therefore, type S and type G can denote pre-existing cracks and open pores in rock matrix, respectively.

In FJC, the g_{ratio} (installation gap ratio) and φ_s (the slit element fraction) are the micro-parameters which have great influence on the micro-structure of rock matrix. The type B contacts are installed between adjacent particles if their gaps between the notional surfaces are equal or less than the specified installation gap, and the contacted interface is segmented with several bonded segments:

$$g = g_{ratio} \times \min(R_1, R_2) \quad (1)$$

where g is the installation gap, and R_1, R_2 are the radii of two adjacent particles.

Type B contacts obey the Mohr-coulomb shear strength ($\bar{\tau}_c$, line BD in Fig. 1b) criterion with tension cutoff (line AB in Fig. 1b):

$$\bar{\tau}_c = \bar{c}_b - \bar{\sigma}_c \tan \bar{\varphi}_b \quad (2)$$

where $\bar{\varphi}_b, \bar{c}_b$ are the friction angle and cohesive strength of contact, respectively, $\bar{\sigma}_c$ is the normal stress acting on contact. If the normal stress $|\bar{\sigma}_c| > \bar{\sigma}_b$ ($\bar{\sigma}_b$ is tensile strength of contact), the contact undergoes tensile failure. If the contact breaks in shear, its strength envelope changes from line CD'D to line CD'E'E with residual strength $\bar{\tau}_r$ is:

$$\bar{\tau}_r = -\bar{\sigma}_c \tan \bar{\varphi}_r \quad (3)$$

where $\bar{\varphi}_r$ is the residual friction angle.

When the bonded segments break, the behavior of contacted interface evolves from a fully bonded state to a fully unbonded and frictional state, that is, the contacted state changes from type B to type G or type S (their strength envelop is shown in Fig. 1b). Because the flat joint contact is not removed, even a fully broken interface can resist relative rotation between particles.

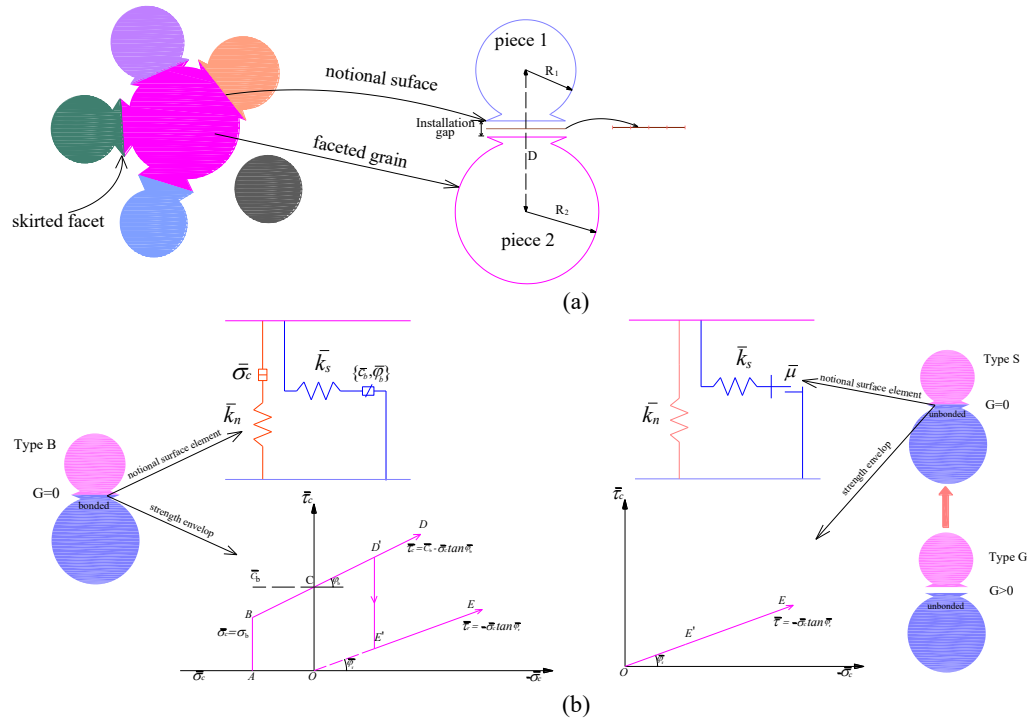


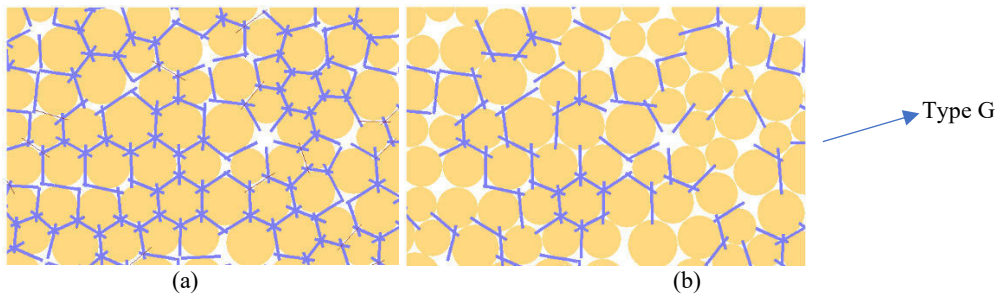
Figure 1. Flat joint contact (FJC) model: a) schematic diagram; b) strength envelope.

In addition, as it can be seen in Figs. 2a-b, the amount of type B contacts increases with the increase of g_{ratio} , which mainly strengthens the grain interlocking of particles, other than increases the coordination number of particles. The slit element fraction ϕ_s is used to determine the proportion of type S contact as follows:

$$\phi_s = 1 - \phi_b \tag{4}$$

where ϕ_b is bonded element fraction.

As shown in Figs. 2c-d, a higher ϕ_s can make more type S contacts be installed between adjacent particles in rock matrix for the same value of g_{ratio} . It can be concluded that a larger g_{ratio} means the integrity of rock matrix is higher, and a larger ϕ_s means a looser rock matrix.



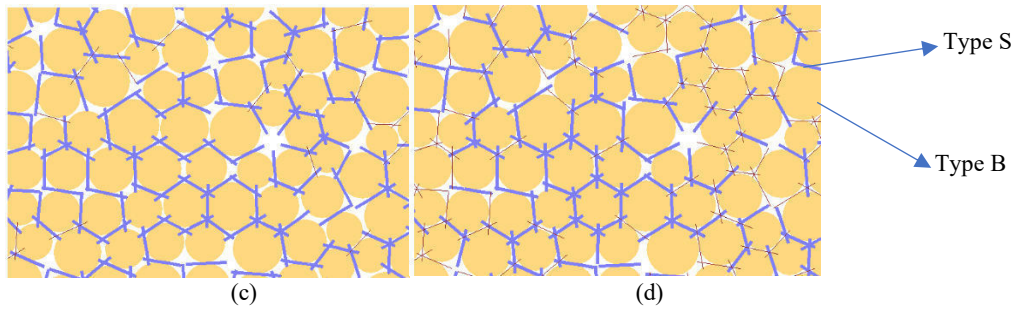


Figure 2. Effects of g_{ratio} and φ_s on the micro-structure of rock matrix: a) $g_{ratio}=0.5$, $\varphi_s=0$; b) $g_{ratio}=0$, $\varphi_s=0$; c) $g_{ratio}=0.3$, $\varphi_s=0.1$; d) $g_{ratio}=0.3$, $\varphi_s=0.5$. (from Xu et al. 2018)

2.2 Smooth joint contact (SJC) model

It can be seen from Fig. 3a that particles connected by SJC can slide along the joint surface rather than move around the contacted interface. Thus, it is commonly adopted to represent the frictional or bonded joint in rocks (Mehranpour & Kulatilake 2017). The figure below shows the main elements of the SJC model.

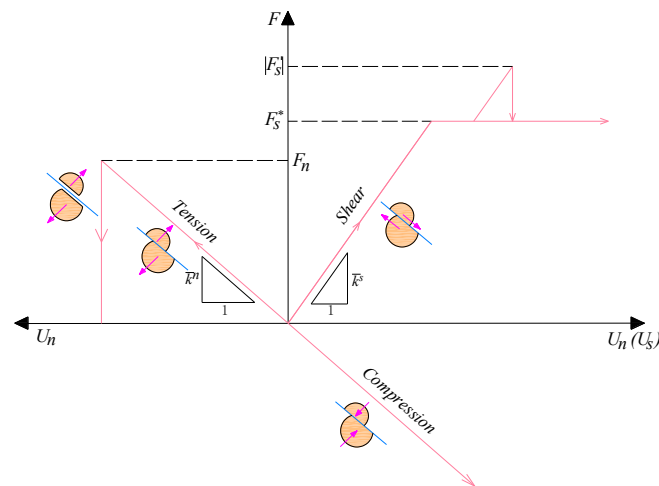
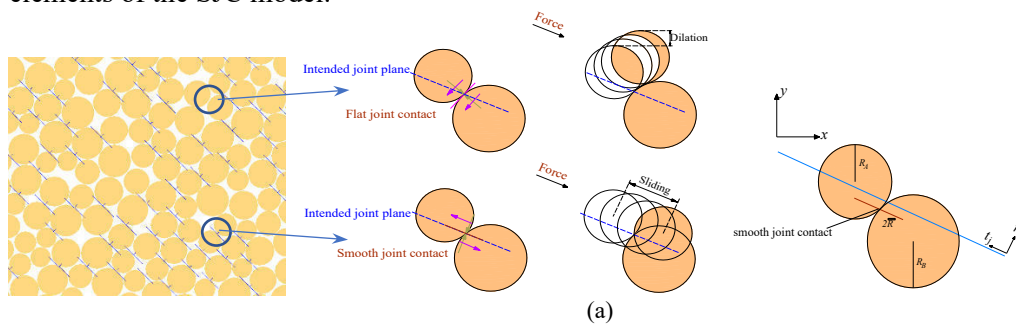


Figure 3. Smooth joint contact (SJC) model: a) Installation of SJC; b) force–displacement relationship at SJC.

The contact forces and displacements expressed in the joint plane are:

$$F = F_n \hat{n}_j + F_s \quad ; \quad U = U_n \hat{n}_j + U_s \quad (5)$$

where F , F_n and F_s are the resultant, normal and tangential forces at the contact; and U , U_n and U_s are resultant, normal and tangential displacements at the contact. The kinetic mechanisms of smooth joint contact are shown in Fig. 3b. For an unbonded joint, if $|F_s'| \leq F_s^* = \mu F_n$, then $|F_s| = |F_s'|$. Otherwise, sliding occurs, and shear displacement during sliding results in an increase in normal force:

$$|F_s| = |F_s^*| \quad ; \quad F_n = F_n + \left(\frac{|F_s'| - F_s^*}{\bar{k}^s} \right) \bar{k}^n \tan \psi \quad (11)$$

where μ is the friction coefficient, and ψ is the dilation angle, and \bar{k}^n and \bar{k}^s are, respectively, the normal and shear stiffnesses of the contact. For bonded joint, if $F_n \leq -\sigma_c A$ (σ_c is the tensile strength of contact and A is the contacted area), the bond breaks in tension. If $|F_s'| \geq \tau_c A$ (τ_c is the shear strength of contact and F_s' is shear force acting on contact), the bond breaks in shear and $|F_s| = |F_s^*|$. Otherwise, the bond remains intact and $|F_s| = |F_s'|$.

2.3 Generation of specimens

Fig. 4 illustrates the steps used to generate a transversely isotropic specimen with non-continuous fabrics.

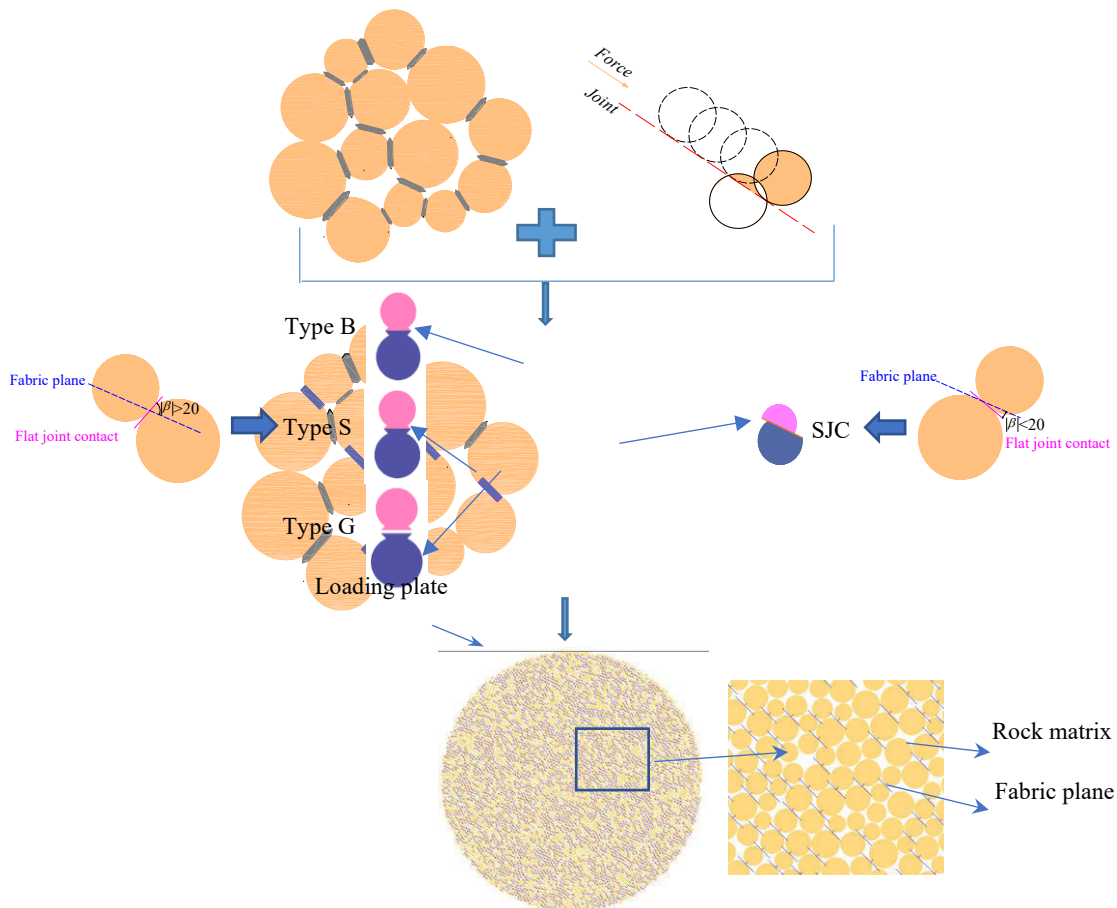


Figure 4. Generation of specimens.

- 1) A circular isotropic specimen is generated. The three types of flat joint contacts are installed between particles according to the certain proportion determined by g_{ratio} and ϕ_s . The diameter of particles and its distribution, and the porosity of the rock has evident influence on the mechanical behavior of rocks. Research by Koyama & Jing (2007) showed that the micro-

mechanical properties of rocks remain nearly constant when $L/r_{min} > 85$, where L is the length of the square specimen and r_{min} is the minimum radius of particles. Li et al. (2018) investigated the effect of particle size distribution on the Brazilian tensile strength (BTS) of Lac du Bonnet granite. They showed that the rock BTS undergoes a rapid decrease when $D/r < 70$, where D is the diameter of specimen and r is the average radius of particles), while it remains nearly constant with the further increase in D/r . Thus, in our simulations, the following values are adopted: $r_{min} = 0.2$ mm, $r_{max}/r_{min} = 1.5$, where r_{max} is the maximum radius of particles, and $D = 50$ mm, giving $D/r_{min} = 250$ and $D/r_{max} = 166.7$. In addition, the radius of particles follows the Gaussian distribution and the total number of particles is 8325. The response depends crucially on the sample porosity. In this article, the rock is more densely compacted than the sand. In this article, the porosity was set as 0.16 based on the research of Potyondy & Cundall (2004).

- 2) Smooth joint contacts are applied into the isotropic specimen. Any FJC contacts (those dipping angle within $\theta - \beta \sim \theta + \beta$, β is the angle range) are removed and replaced by smooth joint contacts. In this way, a transversely isotropic specimen with non-continuous planar fabrics with certain angle θ will be built.
- 3) Two wall elements were assigned as the loading plates at the upper and lower boundary of specimen. The loading speed is 1×10^{-6} m/step, and the loading process stops when the residual stress equals to eighty percentage of the peak strength at the post-peak stage.

The procedure to calibrate the model and determine the required model parameters to obtain a good fit between model predictions and experimental results are discussed in Xu et al. (2020). The calibrated micro-parameters used in the PDEM modeling are provided in Table 1.

Table 1. Parameters of the flat joint contacts.

Particle	Value	Bond	Value
E_c (GPa)	30	\bar{E}_c (GPa)	30
k^n/k^s	2.5	\bar{k}_n/\bar{k}_s	2.5
μ	0.5	$\bar{\sigma}_b$ (MPa)	40±7
r_{max}/r_{min}	1.5	\bar{c}_b (MPa)	40±7
r_{min} (mm)	0.2	$\bar{\varphi}_b$ (°)	10
ρ (kg·m ⁻³)	2800	φ_r (°)	5
		g_{ratio}	0.3
		φ_s (°)	0.1

3. MODELING RESULTS AND DISCUSSIONS

Using the PDEM with FJC and SJC contact models, the above methods to generate numerical test models and procedures to calibrate parameters described in Xu et al. (2020), modeling of the BTS testing of rocks with different micro structural pattern were conducted. Rocks that were simulated and compared with published BTS experimental results included saturated schist 1A and Lyons sandstone. As shown in Figs. 5 to 7, good agreements between numerical simulation and experiment results were found in terms of: 1) the relationship between the tensile failure strength and the fabric-loading angle θ , which is the angle between the plane of fabric and loading direction, 2) the stress-strain curves, and 3) the microscopic failure patterns of the tested specimens. It can be concluded from the fracture patterns that, even through the fabrics may change the propagated path of macro-cracks, for transversely isotropic rocks with non-continuous fabrics, the major fractured plane is roughly parallel to the loading direction and concentrated in the middle part of specimen in most cases.

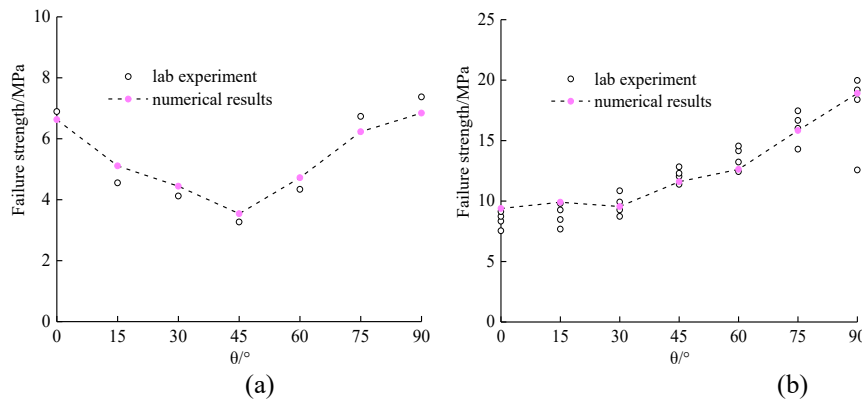


Figure 5. Comparisons of the numerical and experimental tensile failure strength as function of angle θ between the plane of fabric and loading direction for a) saturated schist and b) Leubsdorfer gneiss.

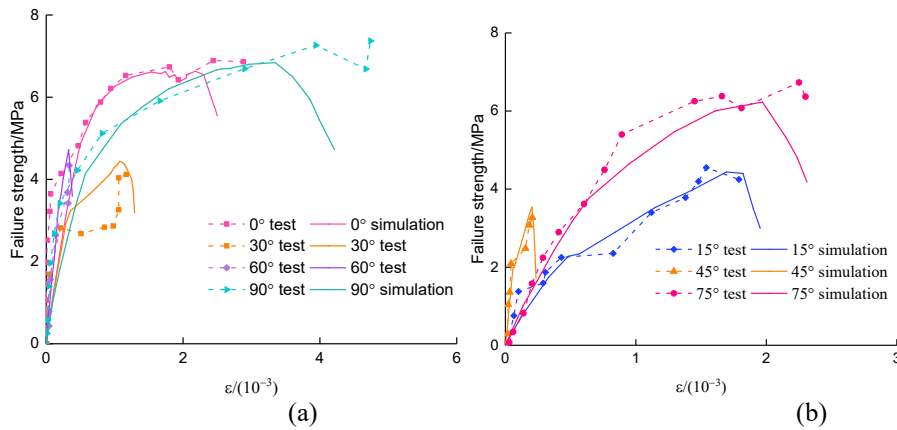


Figure 6. Comparison of the numerical and experimental stress-strain curves for angle θ between the plane of fabric and loading direction for a) saturated schist 1A and b) saturated schist 2A.

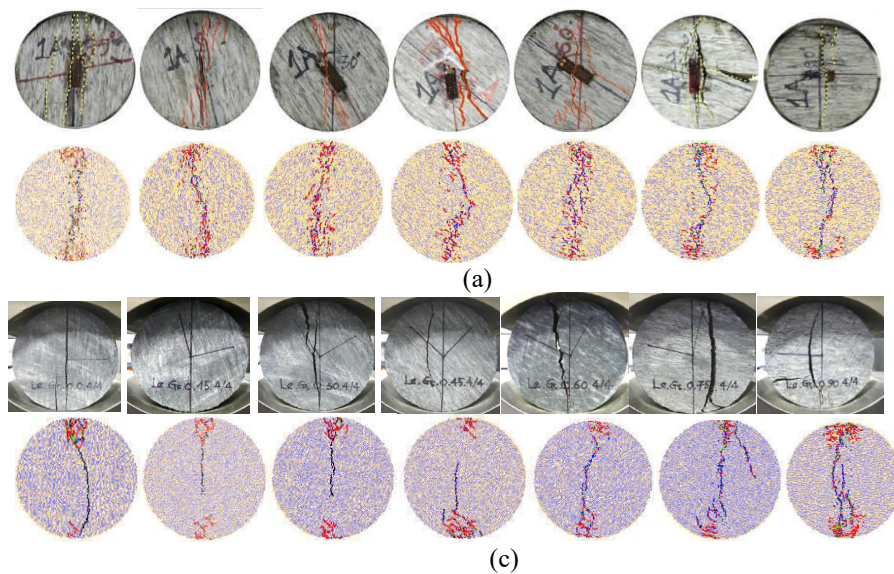


Figure 7. Comparison of the numerical microstructural and experimental fracture patterns for a) saturated schist 1A and b) Leubsdorfer gneiss. The images of experimental results are from Dan et al. (2014) and Kundu et al. (2018).

To better understand the influence of micro-structure of the rock matrix and the distribution of fabrics to the failure process of rocks, the relationship between stress and strain in Brazilian tests and the evolution of micro-cracks and contact forces for Lyons sandstone with $\theta=0^\circ$ and 45° are shown in Figs. 8 and 9.

For Lyons sandstone with $\theta=0^\circ$ (Fig. 8), few micro-cracks are scattered in the middle part of disc at loading point a, with the compressive and tensile stress evenly distributed in the middle part of the specimen. When the specimen was loaded to point b, more micro-cracks formed and scattered in the middle part of disc with the compressive and tensile stress attenuated in the cracking region. With the further increase of axial loading from point b to point c, cracks concentrated and coalesced in the middle part of disc with the tensile stress concentrated in the boundary of disc specimen until its failure. During the whole loading process, tensile cracks on fabrics are dominant.

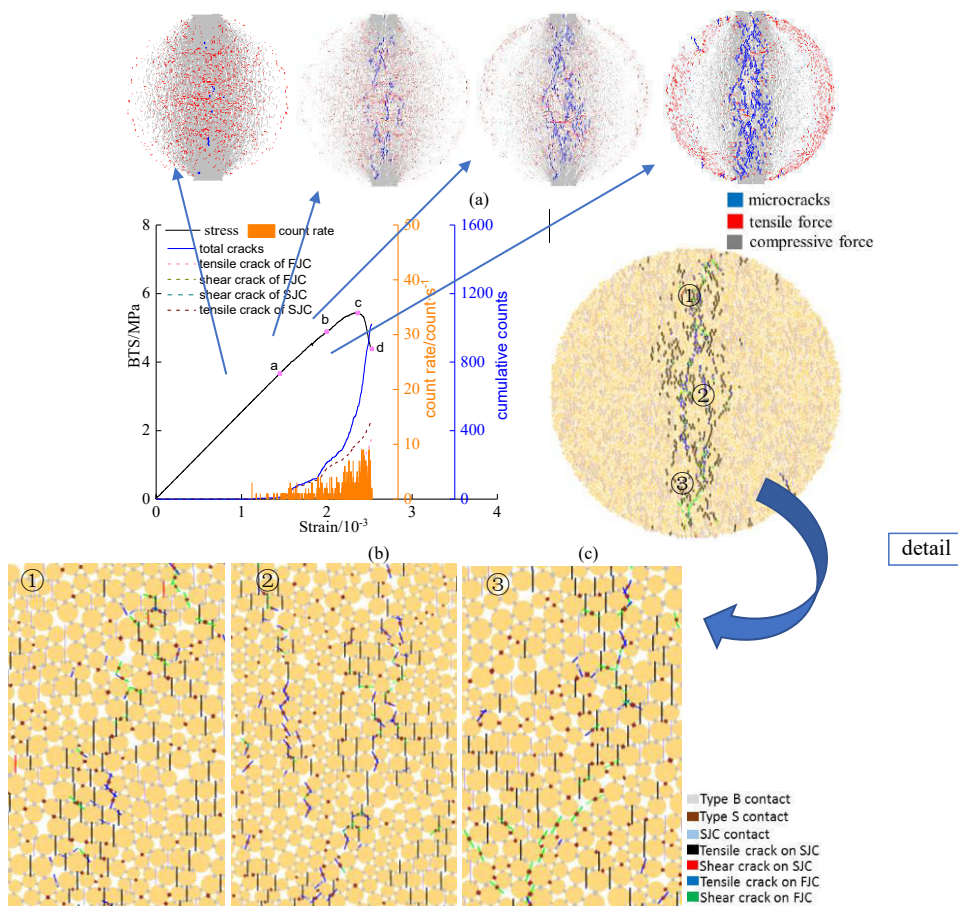


Figure 8. Failure process of Lyons sandstone with $\theta=0^\circ$: a) contact force between particles; b) failure strength versus strain and number of micro-cracks; and c) detailed failure pattern.

For Lyons sandstone with $\theta=45^\circ$ (Fig. 9), few micro-cracks scattered in the compressive stress concentrated region at loading point a. When the specimen was loaded from point a to point b, the initiated path of micro-cracks was firstly determined by the distribution of pre-existing cracks (forming crack ① in this stage, tensile and shear cracks on type S contacts were dominant and only a few cracks on SJC occurred), then the initiated path reversed due to the influence of fabrics (forming crack ② in this stage, tensile and shear cracks on fabrics are dominant). From point b to point c, crack ② propagated a little forward and then stopped. Crack ① propagated downward parallel to the loading direction as the result of tensile cracks on pre-existing cracks

until the failure of rock. In the rock failure stage, tensile stress concentrated in the boundary of disc specimen and compressive stress concentrated in the middle part of disc specimen.

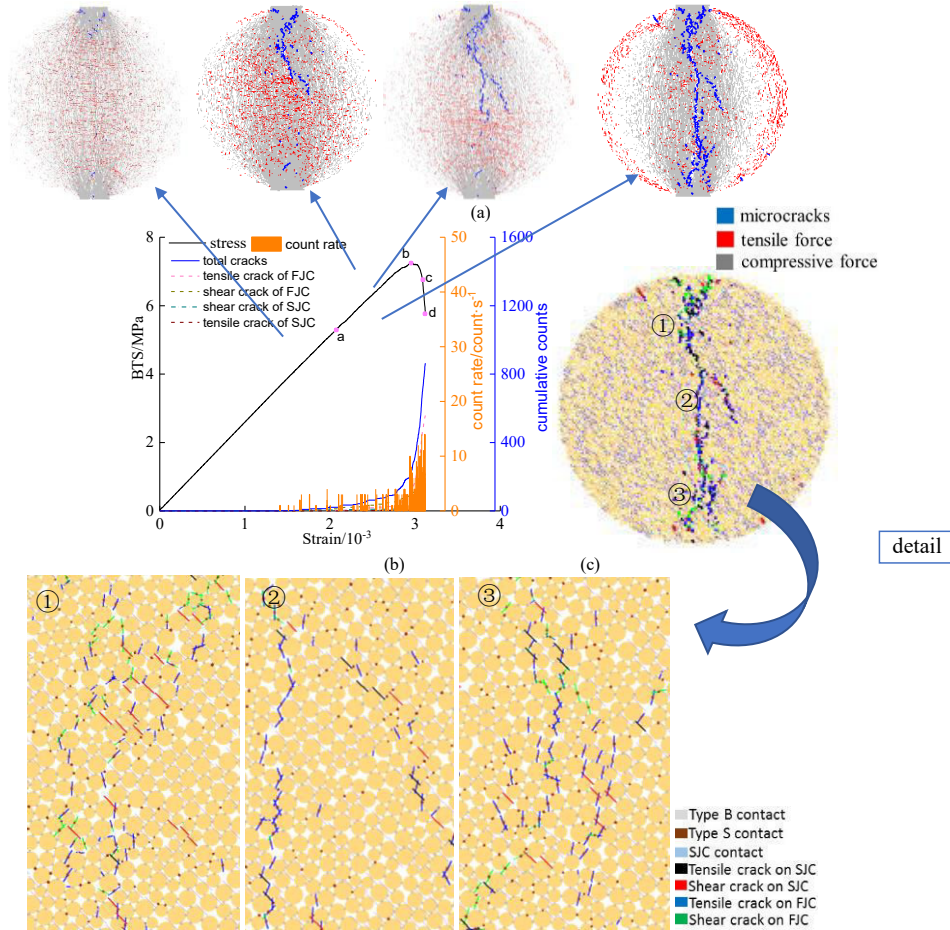


Figure 9. Failure process of Lyons sandstone with $\theta=45^\circ$: a) contact force between particles; b) failure strength versus strain and number of micro-cracks; and c) detailed failure pattern.

4. SUMMARY AND CONCLUSIONS

A new numerical approach based on the particle discrete element method is proposed to represent transversely isotropic rocks with non-continuous planar fabrics. The effect of micro-structure of rock matrix and micro-parameters of the fabrics on the failure strength and fracture patterns of rocks under Brazilian tests, the calibration process for determining the micro-parameters and the failure process of rocks are studied by adopting this numerical approach. The main conclusions of this study are as summarized as follows:

- 1) Based on the Brazilian test results of different kinds of transversely isotropic rocks with non-continuous planar fabrics, six patterns regarding the relationship between the normalized failure strength (NFS) and fabric-loading angles are obtained.
- 2) The patterns of NFS curves are slightly affected by the coordination numbers of particle in rock matrix, while greatly affected by the amount of pre-existing micro-cracks in rock matrix, and the stiffness, strength and distributed region of the fabrics.
- 3) The calibrated results of six typical rocks with different patterns agreed well with the

experimental results regarding failure strength and fracture patterns.

- 4) During the fracturing process, micro-cracks in the rock matrix are mainly formed as tensile and shear breakages of pre-existing cracks, and micro-cracks on fabrics appeared mostly at the aggregated region of pre-existing cracks.

5. REFERENCES

- Dan, D.Q. & Konietzky, H. 2014. Numerical simulations and interpretations of Brazilian tensile tests on transversely isotropic rocks. *Int J Rock Mech Min Sci.* 71: 53–63.
- Dewhurst, D.N. & Siggins, A.F. 2006. Impact of fabric, microcracks and stress field on shale anisotropy. *Geophys J Int.* 65: 135-148.
- Duan, K. Kwok, C. Wu, W. & Lu, J. 2018. DEM modeling of hydraulic fracturing in permeable rock: influence of viscosity, injection rate and in situ states. *Acta Geotechnica.* 13:1187–1202
- Itasca Consulting Group Inc. 2008 Particle flow code in two dimensions: User's guide. Minneapolis, Minnesota.
- Koyama, T. & Jin, L.R. 2007. Effects of model scale and particle size on micro-mechanical properties and failure processes of rocks: A particle-mechanics approach. *Eng Anal Bound Elem.*; 31(5):458-472.
- Kundu, J., Mahanta, B., Sarkar, K. et al. 2018. The effect of lineation on anisotropy in dry and saturated Himalayan schistose rock under Brazilian test conditions. *Rock Mech Rock Eng.* 2018; 51: 5-21
- Li, K.H., Cheng, Y.M. & Fan, X. 2018. Roles of model size and particle size distribution on macro-mechanical properties of Lac du Bonnet granite using flat-joint model. *Comput Geotech*; 103: 43-60.
- Mehranpour, M.H. & Kulatilake, P.H.S.W. 2017. Improvements for the smooth joint contact model of the particle flow code and its applications. *Comput Geotech*; 87: 163-177.
- Potyondy, D.O. & Cundall, P. 2004. A bonded-particle model for rock. *Int J Rock Mech Min Sci.* 41(8):1329–1364.
- Potyondy, D.O. 2012. PFC 2D flat joint contact model. Itasca Consulting Group Inc, Minneapolis.
- Xu, G., Gutierrez, M., He, C. & Wang, S. 2020. Modeling of the effects of weakness planes in rock masses on the stability of tunnels using an equivalent continuum and damage model, *Acta Geotechnica.* 5: 2277–2304.
- Xu, G., He, C., Chen, Z. & Wu, D. 2018. Effects of the micro-structure and micro-parameters on the mechanical behavior of transversely isotropic rock in Brazilian tests, *Acta Geotechnica.* 13: 887-910.

Acknowledgements

This research presented in this paper was supported by the U.S. Department of Transportation (DOT) under Grant No. 69A3551747118. The opinions expressed in this paper are those of the Authors and not of the DOT.

A Trap-door experimental study on dynamic loads on the support of underground openings due to earthquake shaking

M. Tamashiro

University of the Ryukyus, Graduate School of Engineering and Science, Japan

Ö. Aydan

University of Ryukyus, Department of Civil Engineering, Japan

T. Ito

University of Ryukyus, Department of Civil Engineering, Japan

N. Malistani

Kabul polytechnic University, Afghanistan

ABSTRACT:

Rock load concept was first proposed by Terzaghi in 1946 and it served as an essential item for designing underground structures and many modern rock classifications utilize this concept. Terzaghi's trap-door experiments and following experimental studies have been carried out under static conditions. Therefore, it is important to check this commonly used concept and re-evaluate the present design philosophies for dynamic conditions. In this study the authors performed trap-door experiments including both static and dynamic aspects by considering various discontinuity patterns including the original model tests of Terzaghi. The experiments showed that the discontinuity pattern has great influence on possible rock loads, and it may be increased by earthquake shaking. The authors describe experiments and present experimental results and discuss their implications in practice.

1 INTRODUCTION

There is a great interest on the stability and response of underground openings during earthquakes as well as man-made induced vibrations. Terzaghi proposed the rock load concept in 1946 on the basis of his findings from trap-door experiments in which granular soils were used. This concept was utilized in his qualitative rock classifications and it served as an essential item for designing underground structures and many modern rock classifications. However, trap-door experiments by Terzaghi and following experimental studies were carried out under static conditions (e.g., Ladanyi and Hoyaux, 1969; Adachi et al. 2003). Aydan (2018) performed some preliminary trap-door experiments under both static and dynamic conditions and showed loads could not remain the same and it may be increased during and after the earthquakes. Therefore, it is important to check this commonly used concept of Terzaghi and to re-evaluate the validity of present design philosophies. Although the original concept of Terzaghi was proposed for loads on roof support, it was also extended to side-wall loads on supports. Aydan (2019) also checked the validity of this concept for load to be carried out by Rockbolts/rockanchors under both static and dynamic conditions. The main conclusion was the load increases following shaking and the load acting in rockbolts/rock anchors continues to increase after each major shaking.

In this study, the authors performed some trap-door experiments with different model materials and discontinuity pattern under static and dynamic conditions. Furthermore, experiments involve crushed and granular materials. The authors report these experiments and the experimental findings and discuss the validity of rock load concept under both static and dynamic conditions. The findings can be valid for various rock mass conditions as well as tunnels in crushed or granular ground.

2 ARCH ACTION CONCEPT

Terzaghi (1943) proposed his arching theory concept and it was extended to tunnels as illustrated in Figure 1. This figure shows the concept of the load acting on the tunnel support. The roof and side walls of the tunnel are required to react by the support required to balance the load equivalent to the height D , and the rock width B_1 and they are related to the tunnel dimensions, namely, height H_t and width B . When this concept is utilized in rock engineering a loosening zone is assumed to form around the underground opening and it is visualized that the zone is separated from the true in-situ stress field and its load is purely gravitational (e.g. Evans 1960; Széchy, 1973). In other words, the zone designated ground arch acts against the true stress field following the stress re-distribution. However, the ground arch and loosening zone concept are wrongly interpreted by many tunneling engineers (e.g., Rabcewicz 1955, 1964, 1969). Aydan (1989, 2016, 2018) corrected this concept and proposed a procedure how to evaluate loosening zone in relation to the true in-situ stress field and the geometry of opening including the effect of discontinuity patterns. It should be noted that rock arch can also be formed within the loosening zone if reinforcement system consisting of rockbolts/rock anchors can induce such action as illustrated in Figure 2. The support systems for underground openings can resist to rock loads associated with the dead weight of rock mass and the additional loading resulting from the yielding of rock mass due to true in-situ stress field. It should be noted that the rock load concept of Terzaghi and his followers is based fundamentally to the dead load resulting from the loosening zone. The arch action appears in any rock mass irrespective of overburden depth while it may not be possible for tunnels in soils at shallow depths. As noted from this discussion in this section, the rock load concept is based on the static conditions and it is necessary to check if the arch action is still valid under dynamic conditions. Therefore, the trap-door experiments under dynamic conditions are necessary and such experiments are presented in the next sections.

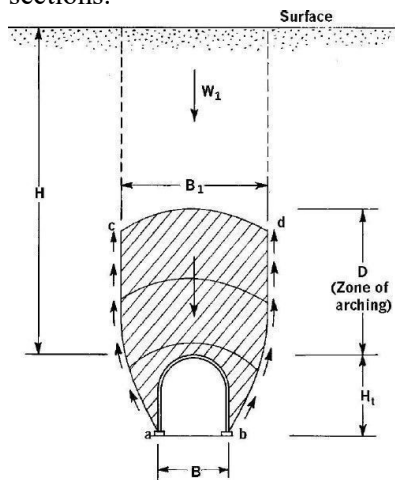


Figure 1. Arching theory of Terzaghi

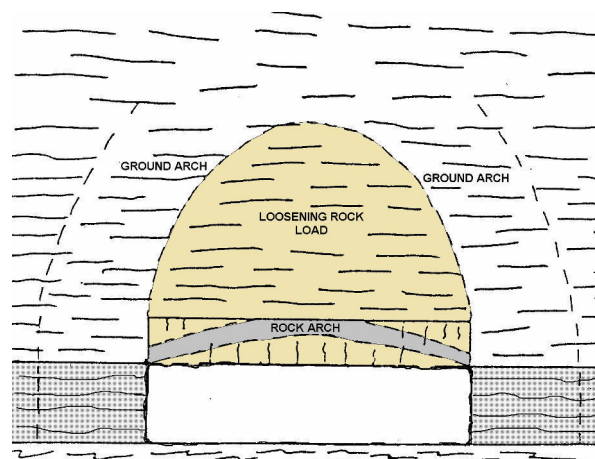


Figure 2. Grand arch and loosening load concept

3 STATIC AND DYNAMIC TRAP-DOOR EXPERIMENTS

3.1 Model materials

The model materials used in trap-door experiments in the experiments are rectangular parallelepiped aluminum blocks, crushed Ryukyu limestone, river gravel, and glass beads with a diameter of 8 mm while many previous trap-door experiments utilize generally granular soils. There are some experiments on crushed rock in relation to cave mining studies as well as silos (e.g., Butterfield 1969; Harris 1974). If granular model material with a particle size less than the gap width is used the utmost care should be taken to prevent the grains entering the gap between stationary base and movable trap-door. Specifically, we have used 4 different model materials, rec-

tangular parallelepiped aluminum blocks, crushed Ryukyu limestone, river gravel, and glass beads with a diameter of 8 mm. Table 1 shows the frictional properties of interfaces of rectangular parallelepiped aluminum and frictional properties of other model materials. Rectangular parallelepiped aluminum blocks were classified as a 1:1 model (width 10 mm, height 10 mm, depth 50 mm) and a 1:2 model (width 20 mm, height 10 mm, depth 50 mm). Figures 3 and 4 illustrate the discontinuity pattern created using rectangular parallelepiped aluminum blocks. Patterns were horizontal (HIP), vertical intermittent (VIP) patterns and cross-continuous (CCP) pattern. In order to observe the movements of blocks, circular blue markers were attached to side of the blocks and a transparent acrylic plate attached to both sides of the model in order to prevent out-of-plane movements.

Tables 1. Material characteristics of rectangular parallelepiped aluminum

Model Material	Size (mm)	Static friction angle	Kinetic friction angle
Aluminum	10:10 & 10:20	18.4-24.5	17.7-22.3
Crushed limestone	1.6-10.0(3.4)	58.8-67.0-	52.7-59.0
River gravel	5.1-15.6(10.3)	42.0-55.7(45.2)	27.0-33.7-
Glass beads	8	20.0-21.68	8.7-11.3-

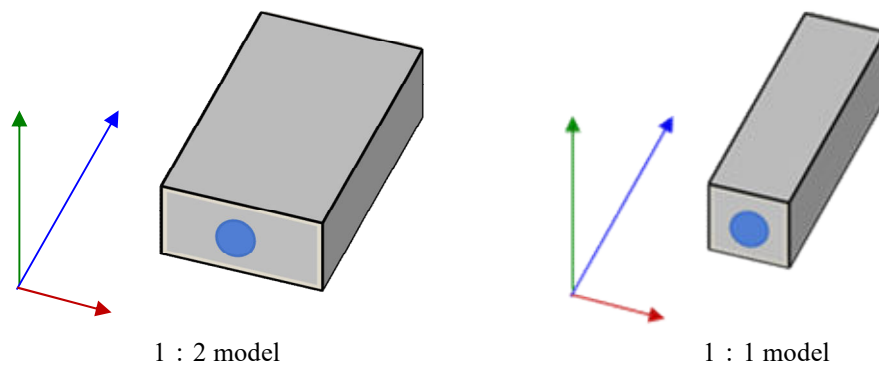


Figure 3. The shape of rectangular parallelepiped aluminum blocks

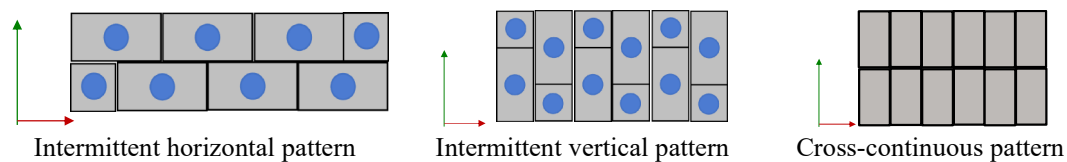


Figure 4. Shape of rectangular parallelepiped aluminum block and direction of discontinuity

3.2 Experimental method

Figure 5 shows the test equipment used in the trap-door test and the dynamic model experiment. This device was fixed to the shaking table device. In this experiment, the trap-door (50x50 mm) was first lowered and then horizontal vibration was applied to the trap-door model to measure the variation of μ in relation to overburden height ratio H/B . The lowering of the trap-door was repeated in some tests. During the experiment, the acceleration of the shaking table, the load and displacement of the trap-door were recorded simultaneously. The acceleration of the shaking table was measured using an accelerometer and the load cell was installed between the trap-door and the screw-type support. The load was initialized so that the load shown in respective figures correspond to changes related to lowering the trap-door. An additional laser displacement meter was used for the purpose of examining the displacement during lowering of the trap-door. The vibration having the frequency of 3 Hz was gradually increased from 50 gal to about 300 gal for duration of 45 seconds. Front and rear acrylic plates were fixed without any contact to model blocks. However, these plates provide lateral confinement for granular models.

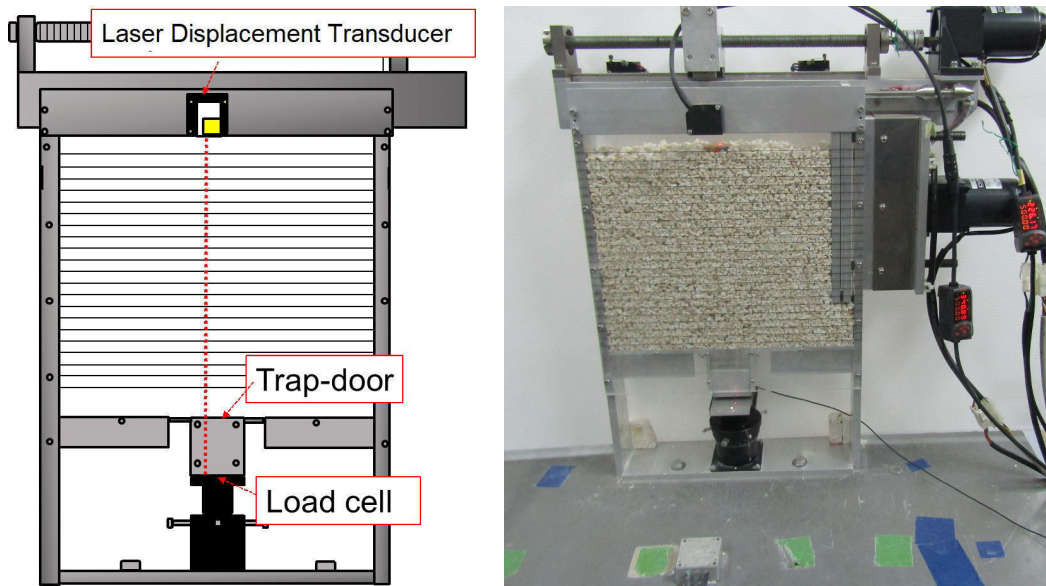


Figure 5. An illustration and a view of a trap-door test device.

4 EXPERIMENTS

4.1 Experiments on Aluminum 1:2 and 1:1 blocks

The experimental results of the trap-door and dynamic test considering the intermittent (IP) and cross-continuous (CCP) pattern are shown in Figures 6 to 7. Figure 8 shows the state of blocks above the trap-door following the experiments. As noted from these views, the blocks above the trap-door forms an unstable region of a triangular shape while the whole blocks above the trap-door are mobilized during the lowering process. Therefore, the load on the trap-door remained same irrespective of overburden depth and shaking level. On the other hand, the load tended to increase during shaking for both the vertical intermittent pattern (V-IP) and horizontal/vertical cross-continuous pattern. Although the other inclinations were not tested, it is very likely that the load will increase during shaking when thoroughgoing discontinuity present in rock mass, which was previously reported by Aydan et al. (1994).

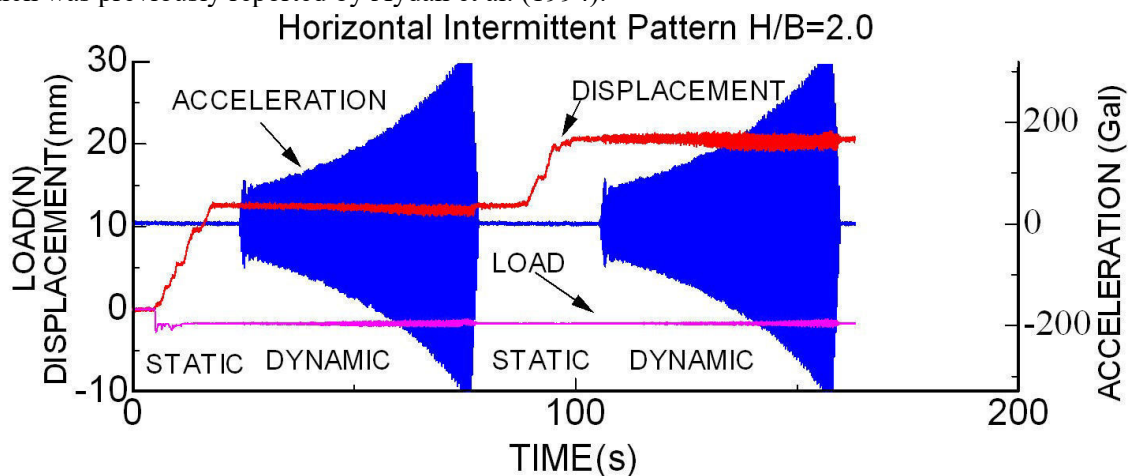


Figure 6. Measured load and displacement responses during tests for horizontal intermittent pattern (H/B = 2.0)

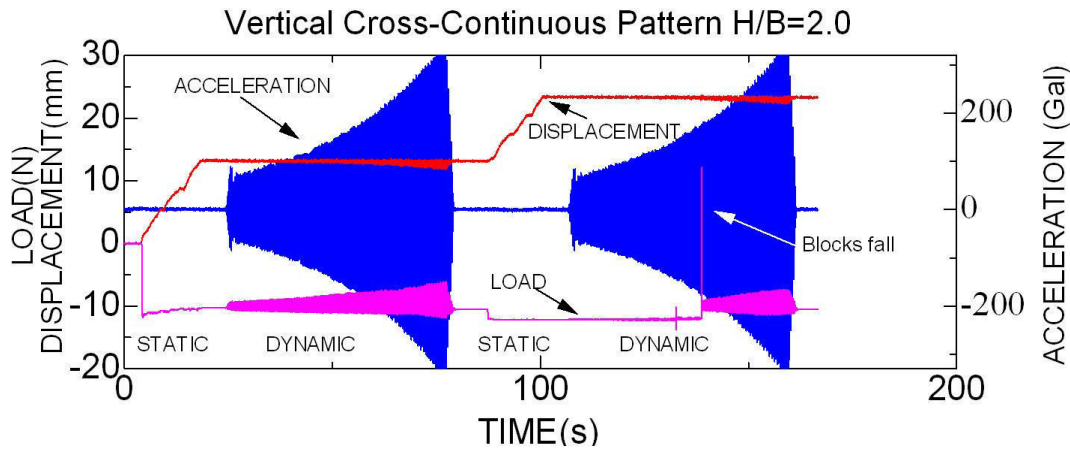


Figure 7. Measured load and displacement responses during tests for vertical cross-continuous pattern (H/B = 2.0)

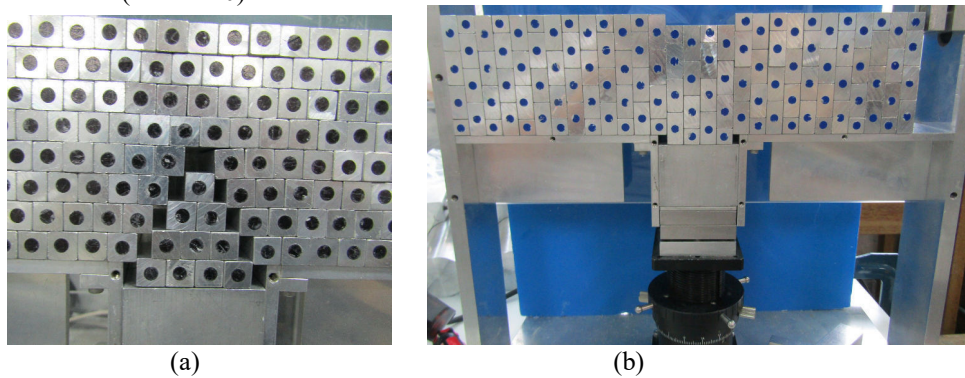


Figure 8. Views of blocks above the trap-door.

4.2 Crushed Ryukyu limestone.

As the most-disturbed state of rock mass, some trap-door experiments were carried out and results are shown in Figure 9. Figure 10 shows the variation of load as a function of overburden ratio for static and dynamic conditions. As noted from figures the load fluctuates during shaking and the final level of load is increased irrespective of overburden depth. However, load level variations are much larger when overburden ratio is smaller.

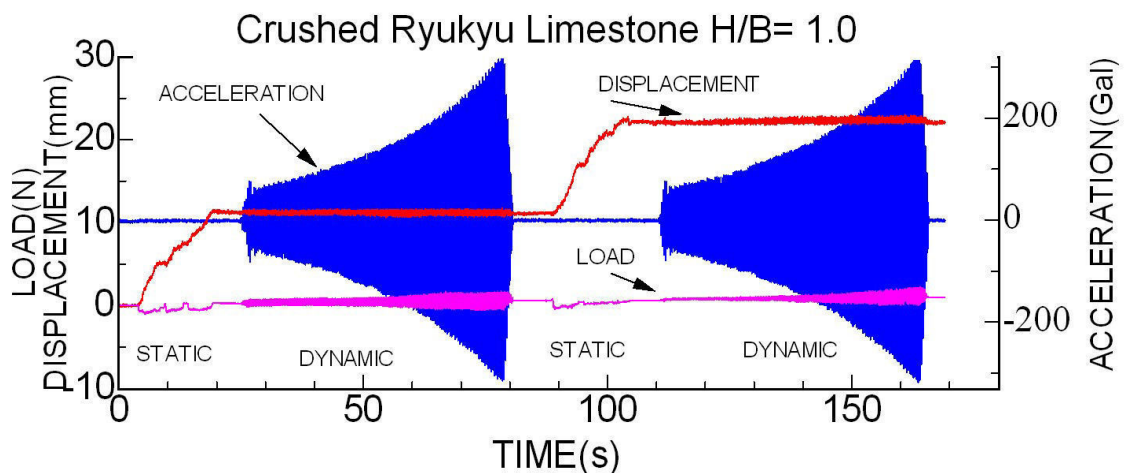


Figure 9. Measured load and displacement responses during tests on crushed Ryukyu limestone (H/B = 1.0)

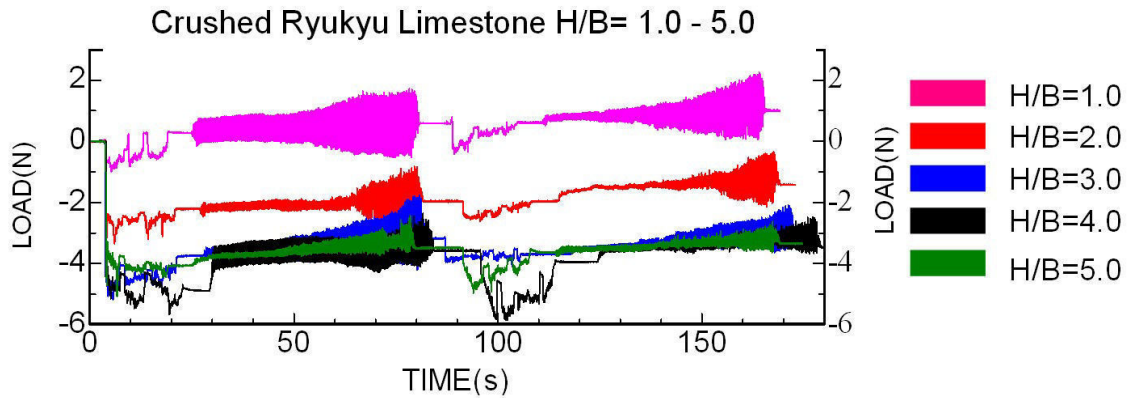


Figure 10. Relationship between overburden ratio and load (crushed Ryukyu limestone)

4.3 River Gravel

As noted from Table 1, the ratio of trap-door width to average gravel size is about 10. The experiments on rounded gravels may simulate the condition of ground consisting of large rock boulders in nature, which may be resulted from the pyroclastic flows. Figure 11 shows some of the experimental results for river gravels while Figure 12 shows the variation of the load on the trap-door as a function of overburden ratio. As noted from figures, the load increases due to shaking and its level increases as the overburden increases.

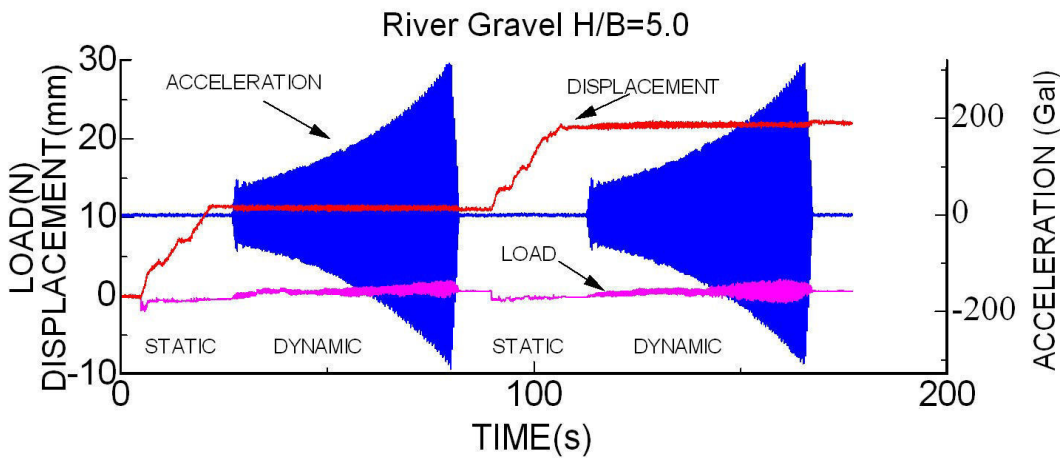


Figure 11. Measured load and displacement responses during tests utilizing river gravel ($H/B = 5.0$).

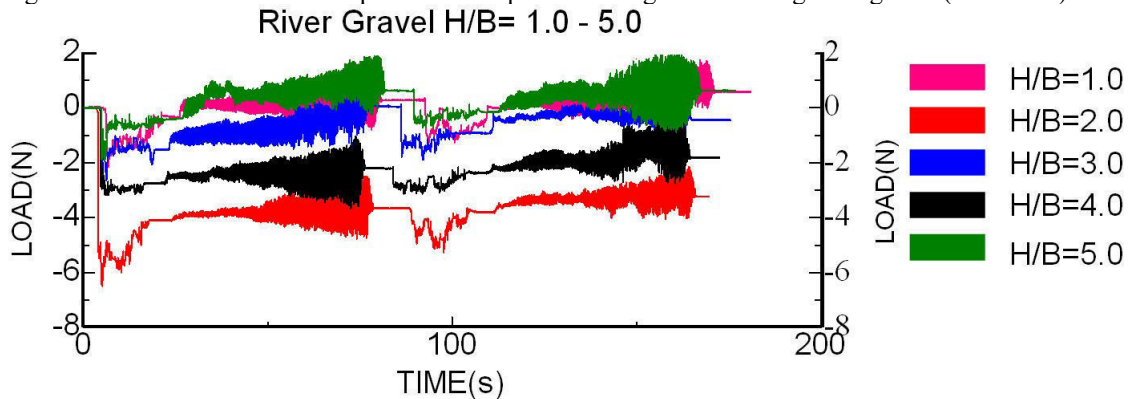


Figure 12. Relationship between overburden ratio and load (River gravel).

4.4 Glass Beads

The utilization of glass beads provides the most extreme case in terms of the load condition to be encountered in nature. Figure 13 shows some of the experimental results for glass beads while Figure 14 shows the variation of the load on the trap-door as a function of overburden ratio. As noted from figures, the load increases due to shaking and its level increases as the overburden increases.

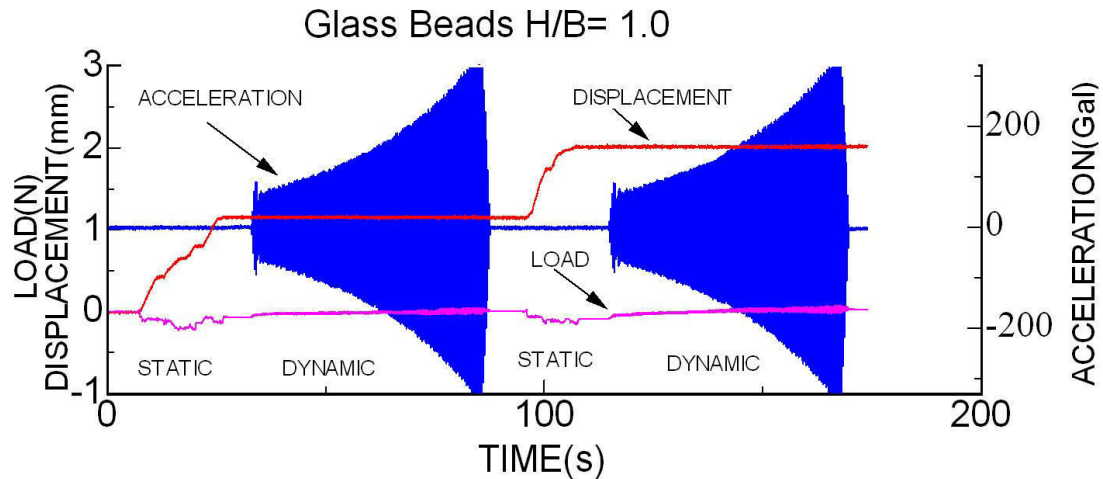


Figure 13. Measured load and displacement responses during tests for glass beads ($H/B = 1.0$).

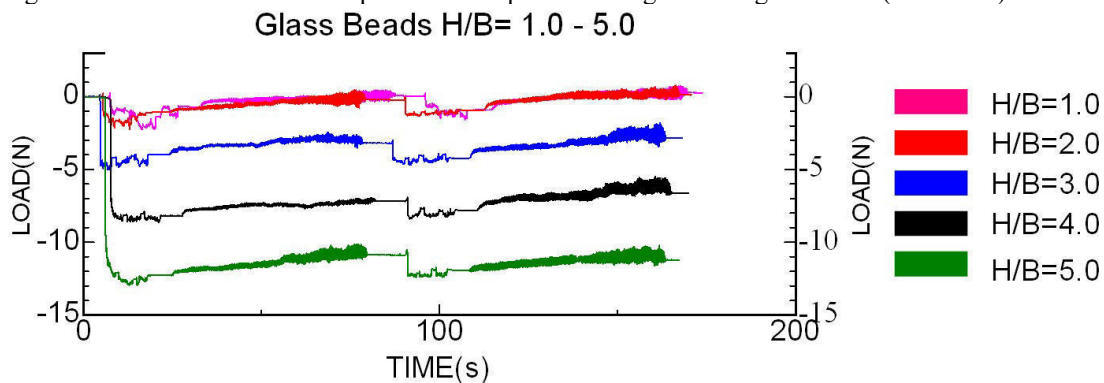


Figure 14. Relationship between overburden ratio and load (glass beads)

5 CONSIDERATION AND FUTURE ISSUES

It is shown that the load acting on trap-doors increased during vibration and its level never returns its original level despite shaking disappears. There is no doubt that the arch action continues and rock load level may depend upon the discontinuity pattern and their frictional characteristics, opening geometry and overburden ratio. However, the value of lateral pressure coefficient utilized in theoretical formulation in the arching theory may decrease during shaking. Such a concept was introduced for assessing the stability of layered roofs of abandoned lignite mines. As noted from these experiments on intermittent and cross-continuous pattern, the blocks above the trap-door forms an unstable region of a triangular shape for horizontal intermittent pattern while the whole blocks above the trap-door are mobilized in the vertical intermittent and cross-continuous pattern during the lowering process. It is inferred that lateral stress coefficient could be also an important factor for rock loads acting on trap-doors. Although these experiments provided very important information about the rock loads due to ground shaking, further studies are necessary on the effect of lateral stress coefficient and the inclination of thoroughgoing discontinuity set.

6 CONCLUSIONS

In this study, trap-door experiments carried out under static and dynamic conditions are presented in order to clarify whether the rock loads acting on the support system of shallow underground openings in discontinuous/crushed rock mass conditions and granular ground remains the same or not. The conclusions and findings from this experimental study are as follows.

- 1) The trap-door experiments, which are of its new kind, clearly showed the rock load increases during ground shaking and may not return to its initial value. This experimental fact clearly indicates that the present seismic design of support system based on rock load concept must be re-evaluated.
- 2) As a simple implication of the previous conclusion, the rock loads suggested in present rock classifications must be revised.
- 3) Depending on the discontinuity pattern, spacing and overburden ratio, the rock load would increase under dynamic conditions.
- 4) If the overburden is shallow, the ground arch may be lost due to the action of seismic forces.

REFERENCES

- Adachi, T., Kimura, M. and Kishida, K. (2003). Experimental study on the distribution of earth pressure and surface settlement through three-dimensional trapdoor tests. *Tunnelling and Underground Space Technology* 18, 171–183.
- Aydan Ö. (1989). Reinforcement of rock engineering structures. PhD Thesis. Nagoya University.
- Aydan, Ö. (2016): The state of art on large cavern design for underground powerhouses and some long-term issues. In *Lehr/Wiley Encyclopedia Energy: Science, Technology and Applications*, John Wiley and Sons, Chp45; 465-487.
- Aydan Ö. 2018. Rock reinforcement and rock support. ISRM Book Series. CRC Press.
- Aydan Ö. (2019). Dynamic response of support systems during excavation of underground openings. *Journal of Rock Mechanics and Geotechnical Engineering* 11, 954-964.
- Aydan, Ö., Y. Shimizu, M. Karaca (1994). The dynamic and static stability of shallow underground openings in jointed rock masses. *The 3rd Int. Symp. on Mine Planning and Equipment Selection*, Istanbul, October, 851-858.
- Aydan, Ö., Daido, M., Ito, T., Tano, H. and Kawamoto, T. (2006): Instability of abandoned lignite mines and the assessment of their stability in long term and during earthquakes. 4th Asian Rock Mechanics Symposium, Singapore, Paper No. A0355 (on CD).
- Butterfield, R. (1969) "A Theoretical Study of the Pressures Developed in a Silo Containing Single-Sized Particles in a Regular Packing", *International Journal of Rock Mechanics and Mining Sciences*, Pergamon Press, Vol. 6, pp. 227-247.
- Evans, W.H. (1960). Roof bolting and the stabilisation of natural arches on roadways. *Colliery Engineering*, 293-296.
- Harris, G.W. (1974) 191 "A Sandbox Model Used to Examine the Stress Distribution Around a Simulated Longwall Coal-Face", *International Journal of Rock Mechanics, Mining Sciences and Geomechanical Abstracts*, Pergamon Press, Vol. 11, pp. 325-335.
- Ladanyi, B., and Hoyaux, B. (1969). A study of the trap-door problem in a granular mass. *Can. Geotech. J.*, 6(1), 1–14
- Rabcewicz, L. (1955). Bolted support for tunnels. *Mine and Quarry Engineering*, 153–159.
- Rabcewicz, L. (1964). New Austrian Tunnelling Method. *Water Power*, 453–457 (Nov. 1964), 511–515 (Dec. 1964) and 19–24 (Jan. 1965).
- Rabcewicz, L. (1969). Stability of tunnels under rock load. *Water Power*, 225–229 (June), 266–273 (July) and 297–302 (Aug.).
- Széchy, K. (1973). *The Art of Tunnelling, Akadémia Kiads*, Budapest.
- Terzaghi K. (1943). *Theoretical Soil Mechanics*, Wiley, New York.
- Terzaghi, K. (1946). *Rock Tunnelling with Steel Supports*, Youngstown, Ohio, Commercial Shearing and Stamping Co..

Numerical modeling of the roughness formation of tensile fractures: is grain size heterogeneity an influential factor?

J. Kim

Seoul National University, Seoul, Korea

J.-J. Song

Research Institute of Energy and Resources, Seoul National University, Seoul, Korea

ABSTRACT:

The influence of grain size heterogeneity on tensile fracture roughness was investigated by numerical simulations using PFC2D. Models with different ball size ratios were constructed, and for each model, the tensile fracture roughness was quantified and compared. The numerical simulation results revealed that ball size heterogeneity has little effect on the roughness of tensile fractures. The insensitivity of fracture roughness with respect to ball size heterogeneity was further analyzed based on ball contact geometry. The geometric analysis showed that the preferential route of tensile fracture propagation is barely influenced by ball size heterogeneity.

1 INTRODUCTION

Empirical relations show that various fracture mechanical properties such as shear strength, peak shear displacement and normal stiffness, and also hydraulic properties such as fracture hydraulic conductivity and hydraulic aperture, are strongly affected by fracture roughness (Barton and Choubey, 1977; Bandis et al., 1983; Barton et al., 1985). Fracture roughness is as an important geometric parameter that characterizes fracture properties and, therefore, should be carefully investigated throughout rock engineering applications.

Considering the importance of fracture roughness, it is consequently important to understand the formation of fracture roughness with respect to its host rock properties. Although the effect of fracture roughness to the mechanical and hydraulic properties of a fracture has been intensively examined and investigated through various studies (Barton and Choubey, 1977; Bandis et al., 1983; Barton et al., 1985), not as much has been investigated on how fracture roughness is determined with respect to the host rock conditions. An experimental study by Dam and Pater (1999) showed that the surface roughness of hydraulically-induced fractures is affected by the type of host rock and the in-situ stress conditions. A more recent study by Diaz et al. (2016) show that the roughness of tensile fractures correlates with the host rock's mineral composition in terms of mineral strength and grain size. These lab observations provide evidence that fracture roughness is affected by its host rock properties, but more investigation is still required to understand the mechanism of fracture roughness formation.

This study expands our understanding by investigating the influence of grain size heterogeneity on the roughness formation of tensile fractures. Grain size heterogeneity is known to affect various rock properties such as uniaxial compression strength (UCS), microcracking behavior (Lan et al., 2010) and rock response to hydraulic fracturing (Han et al., 2018). Its influence on (hydraulic) fracture roughness has been mentioned by Han et al. (2018), but is only based on visual observation. In this study, the effect of grain size heterogeneity was investigated thoroughly and quantitatively based on a series of discrete element method (DEM) numerical simulations. The fracturing process of brittle rock was simulated by a commercial DEM code, PFC2D, by which direct tensile tests were numerically conducted upon models of different ball size heterogeneity. The surfaces of the generated tensile fractures were extracted to quantify their roughness for detailed comparison. The trend between ball size heterogeneity and fracture roughness is presented with further discussion based on a geometric analysis of ball contact geometry.

2 DEM MODELING OF TENSILE FRACTURES

2.1 Model descriptions

PFC2D, a 2D DEM code developed by ITASCA, is used to numerically simulate the propagation of a tensile fracture. The host rock is modelled through the parallel-bond model which mimics the grain cementation of rock formation. Grains are represented as circular balls attached together by bonds that transmit both force and moment. The bond is removed when the force applied on the bond exceeds a specific limit and, instead, a linear contact model is applied between the balls. The parallel-bond model has been effectively used in various studies to simulate brittle rock behavior (Potyondy and Cundall, 2004; Zhou et al., 2016), and, accordingly, it is adapted in this study to simulate the roughness formation of tensile fractures.

The model used in this study, shown in Figure 1, is 100mm in width and 100mm in height. To simulate the propagation of a tensile fracture, tensile displacement is applied to the model by controlling the upper wall and lower wall with constant velocity. In addition, a fracture (or notch) is initially inserted into the model to orient the fracture propagation along the horizontal axis. The length of the initial fracture is 1/10 the model size, 10mm. The microparameters of the PFC2D model were set as shown in Table 1. The UCS and direct tensile strength were 136MPa and 31MPa for the model with uniform ball size distribution between 0.376-0.624mm

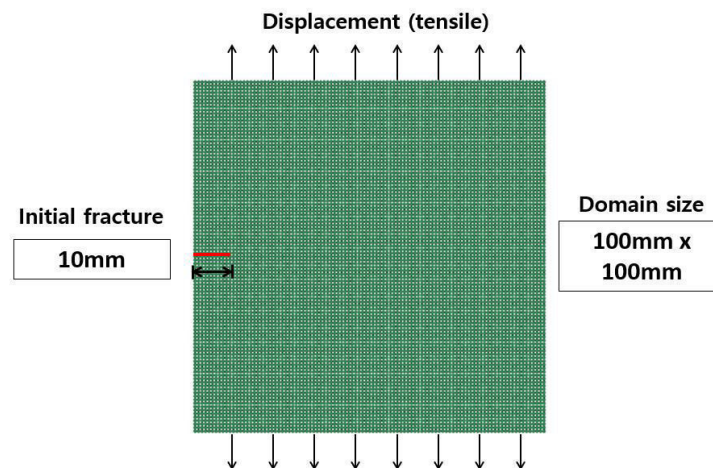


Figure 1. Numerical model to simulate growth of tensile fractures. Constant displacement is applied to the upper and lower walls to generate tensile stress, while the side walls are enabled to move freely (red indicates the initial fracture to orient fracture growth)

Table 1. Microparameters of PFC2D tensile fracturing model

	Microparameters	Values
Particle	Density (kg/m^3)	2650
	Contact modulus (GPa)	38
	Ratio of normal to shear stiffness	3.5
	Friction coefficient	0.577
Parallel bond	Tensile strength (MPa)	60
	Cohesion (MPa)	50
	Ratio of normal to shear stiffness	3.5
	Bond modulus (GPa)	38

2.2 Model verification

To verify the model, the numerically simulated tensile force was inspected at the vicinity of the initial fracture tip and compared with the analytical values derived from linear elastic fracture mechanics (LEFM). This verification approach refers to the reproduction of fracture mechanics behavior using the parallel-bond model in Potyondy and Cundall (2004).

The concentrated forces near the fracture tip can be explained by LEFM using the stress intensity factor. For a through-thickness fracture of length a in a semi-infinitely wide plate of isotropic linear elastic material subjected to a remote tensile stress (σ_t), the induced stress (σ_n) acting on the fracture plane near the tip can be expressed as (Anderson, 2017):

$$\sigma_n = 1.12\sigma_t\sqrt{\frac{a}{2r}} \quad (1)$$

where r is the distance from the tip.

The force acting on a line segment equal to a ball diameter ($2R$) at a mean distance of $r = (2m - 1)R$ can be derived as:

$$F = \int_{r-R}^{r+R} \sigma_n t dr = 1.12\sigma_t \sqrt{\frac{a}{2}} \int_{r-R}^{r+R} r^{-1/2} dr = 2.24\sigma_t t \sqrt{aR} (\sqrt{m} - \sqrt{m-1}) \quad (2)$$

where m is a positive integer indicating the ball sequence number.

To compare the tensile forces of the model with those of LEFM, the LEFM tensile force is normalized and compared in the form of:

$$\tilde{F} = \frac{F}{2.24\sigma_t t \sqrt{aR}} = \sqrt{m} - \sqrt{m-1} \quad (3)$$

The model's normalized tensile force is plotted with those of LEFM in Figure 2. The plot illustrates the match between the model and analytical values of concentrated forces near the fracture tip. This indicates that the model is capable of simulating tensile fracture propagation since the stress concentration near the fracture tip drives fracture propagation.

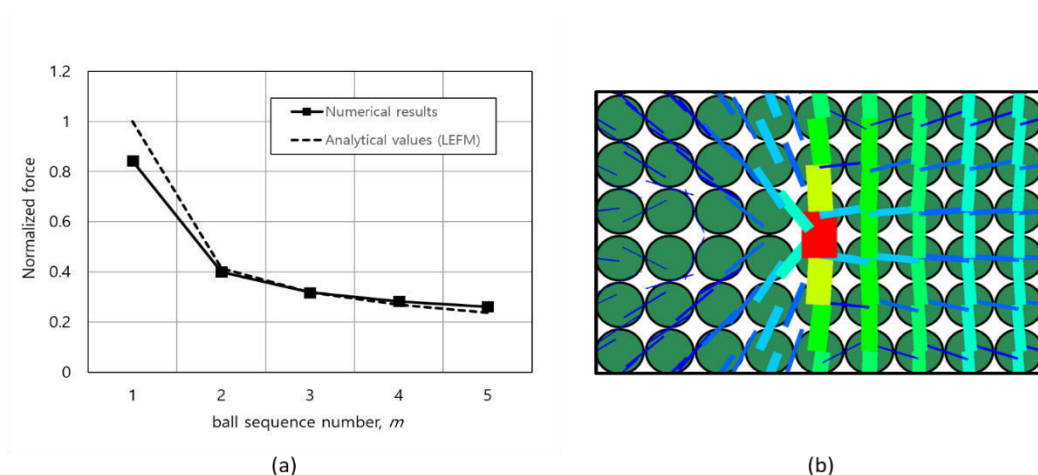


Figure 2. (a) Normalized tensile force of numerical results and analytical values (LEFM) at the contacts ahead of fracture tip and (b) force distribution near the fracture tip with magnitude indicated as line thickness

2.3 Modeling schemes

Models with five different ball size ratios (R_{max}/R_{min}), 1.2, 1.5, 2, 2.5 and 3.0 were simulated to investigate the influence of grain size heterogeneity on the roughness of tensile fractures. The maximum and minimum ball radius for each ball size ratio are tabulated in Table 2. The average ball size is fixed as 0.5mm to exclude any systematic effect of average ball size. Close-up views of models with different ball size ratios are shown in Figure 3.

Table 2. Ball size heterogeneity and corresponding maximum and minimum ball radius

Case	R_{max}/R_{min}	R_{max} (mm)	R_{min} (mm)
1	1.2	0.546	0.455
2	1.5	0.6	0.4
3	2	0.666	0.333
4	2.5	0.715	0.286
5	3	0.75	0.25

The roughness of the simulated tensile fractures was profiled by extracting the positions of the broken bonds between balls assuming that they indicate the fracture asperity. Then, as depicted in Figure 4, the roughness profile was derived by fitting a smoothing-spline curve to the broken bond positions.

The roughness of the profiles was quantified by deriving the root mean square of the first deviation of the profile (Z_2) and the ultimate slope of the profile (λ), considering that these parameters have strong correlation with JRC (Li and Zhang, 2015). Each parameter is derived by the following equations:

$$Z_2 = \left[\frac{1}{L} \int_{x=0}^{x=L} \left(\frac{dy}{dx} \right)^2 dx \right]^{1/2} = \left[\frac{1}{N(\Delta x)^2} \sum_{i=1}^N (y_{i+1} - y_i)^2 \right]^{1/2} \quad (3)$$

$$\lambda = R_z/L \quad (4)$$

where L is the length of the profile, Δx is the sampling interval set as 0.4mm, N is the number of sampling points, and R_z is the maximum amplitude of the profile.

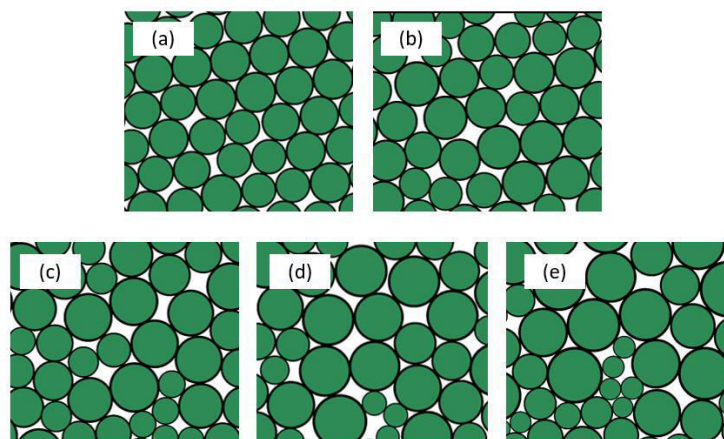


Figure 3. Close-up view of models with different ball size ratios (a) $R_{max}/R_{min} = 1.2$; (b) $R_{max}/R_{min} = 1.5$; (c) $R_{max}/R_{min} = 2.0$; (d) $R_{max}/R_{min} = 2.5$; (e) $R_{max}/R_{min} = 3.0$

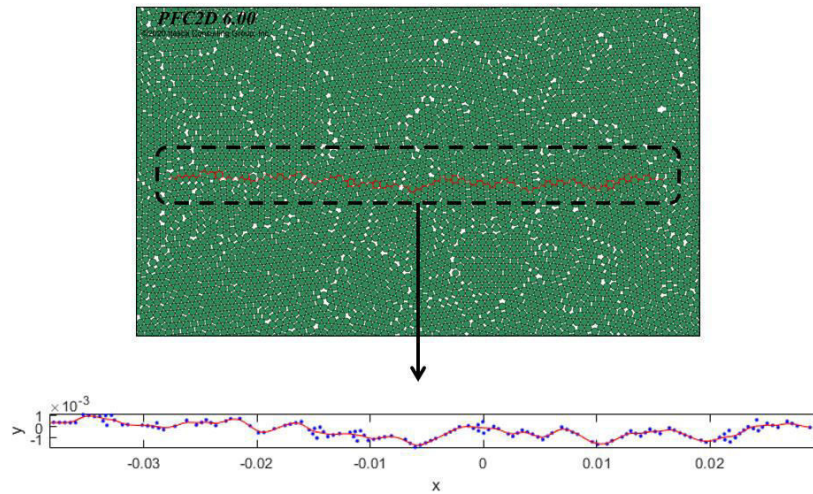


Figure 4. Extraction of roughness profile based on position of broken bonds in PFC2D simulation

3 RESULTS

For each case of different ball size heterogeneity, five simulations were repeatedly conducted to account for the randomness of ball geometry configuration, and, for each simulation, the fracture profiles were extracted and quantified.

The numerical simulation results tabulated in Table 3 show that ball size heterogeneity has no systematic effect on Z_2 and λ of fractures profiles. Figure 5 compares the roughness profiles of models of ball size heterogeneity of $R_{max}/R_{min}=1.2$ and $R_{max}/R_{min}=3$. The tensile fractures have similar roughness profiles even though the two cases have large difference in the degree of ball size heterogeneity. The insensitivity of fracture roughness with respect to ball size heterogeneity is further discussed in the next section through geometric analysis of ball contact configuration.

Table 3. Roughness parameters of tensile fractures of DEM models with different ball size heterogeneity

Size heterogeneity (R_{max}/R_{min})	Z_2		λ	
	Mean	Standard deviation	Mean	Standard deviation
1.2	0.307	0.03	0.074	0.012
1.5	0.276	0.02	0.065	0.014
2	0.301	0.02	0.057	0.014
2.5	0.296	0.03	0.078	0.026
3	0.321	0.03	0.063	0.015

4 DISCUSSION

The numerical simulation results indicate that grain size heterogeneity is not an influential factor to fracture roughness. An analytical explanation can be given by analyzing the geometry of ball contact configurations of ball-based DEM models. As depicted in Figure 6, which are close-up views of the cases in Figure 5, the propagation route of tensile fractures can be analyzed by assessing the three-ball contact geometry which are indicated as white triangles in the figure.

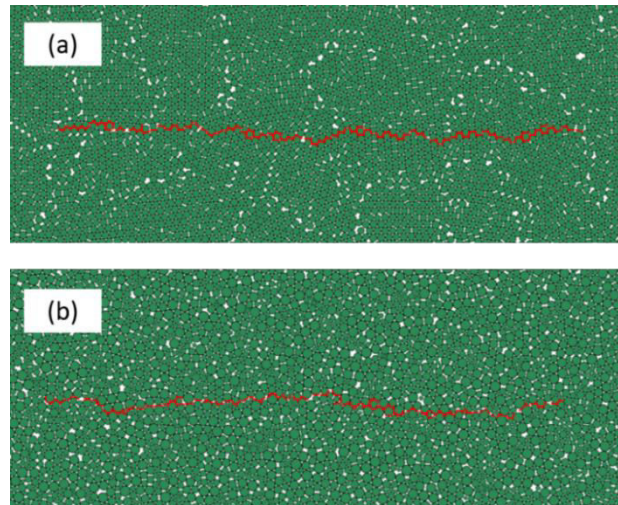


Figure 5. Tensile fractures indicated in red for (a) $R_{max}/R_{min} = 1.2$ and (b) $R_{max}/R_{min} = 3$

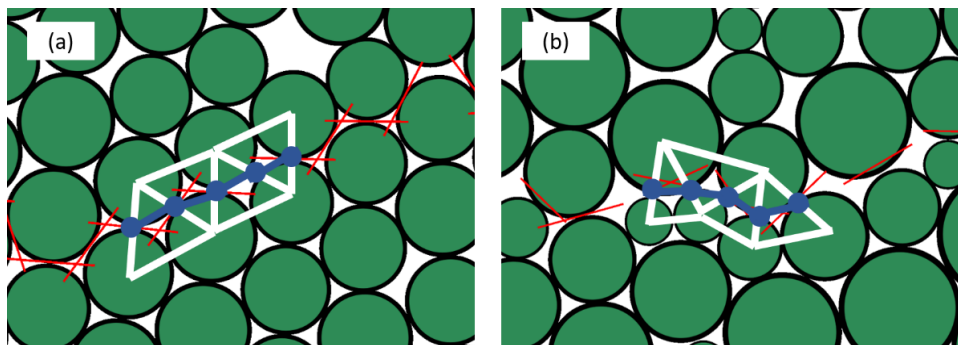


Figure 6. The propagation route of tensile fractures determined by three-ball contact geometry. The white triangles indicate three-ball contact geometry and the blue lines indicate the fracture propagation route. Close-up view for (a) $R_{max}/R_{min} = 1.2$ and (b) $R_{max}/R_{min} = 3$

The triangular geometry of three-ball contact is configured by the radius of the three balls as shown in Figure 7. Assuming that the contact between ball 1 and ball 2 is the tip of the tensile fracture, the next propagation route will be either along the contact between ball 1 and ball 3 or the contact between ball 2 and ball 3. The route is determined by comparing θ_1 and θ_2 which are the angles between the direction perpendicular to the tensile stress and the ball contacts. The bond with the smaller angle is preferably oriented to the far-field tensile stress for failure and, consequently, becomes the route of fracture propagation. With the new fracture tip, the propagation route is again determined by the newly encountered three-ball contact geometry. The fracture will propagate along a series of three-ball contact geometries which macroscopically results in the formation of a roughness profile.

Assuming that tensile fractures propagate along the simplified geometry of three-ball contact, a computer algorithm was constructed based on the aforementioned mechanism. For each case of ball size heterogeneity, 100 realizations were generated based on the three-ball contact geometry analysis. The corresponding roughness parameters of the obtained profiles are presented in Table 4.

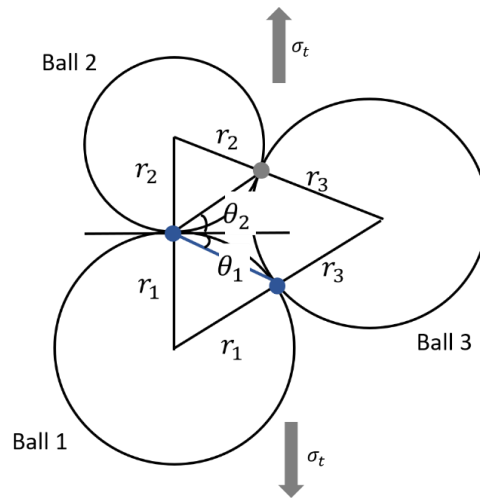


Figure 7. Three-ball contact geometry and determination of tensile fracture propagation. The blue line indicates the next propagation route.

Table 4. Roughness parameters of tensile fractures derived from the analysis of three-ball contact geometry

Size heterogeneity (R_{max}/R_{min})	Z_2		λ	
	Mean	Standard deviation	Mean	Standard deviation
1.2	0.306	0.057	0.148	0.059
1.5	0.3	0.028	0.088	0.028
2	0.305	0.019	0.065	0.021
2.5	0.317	0.023	0.069	0.02
3	0.325	0.024	0.067	0.021

The results of the geometric analysis of ball contacts support that of the numerical simulations; the roughness obtained by the geometric analysis shows no systematic relation with ball size heterogeneity. The results illustrate that the preferred geometric orientation of tensile fracture propagation and fracture roughness is barely influenced by ball size heterogeneity. Meanwhile, the ultimate slope (λ) of the profile of the geometric analysis is relatively large especially for cases of homogeneous size distribution. This is due to the fact that the three-ball contact geometry analysis assumes that all balls are in contact, whereas in numerical simulations, and also in natural rock, there are microcracks which distort the three-ball contact geometry. Without microcracks, the fractures modeled by the geometric analysis tend to propagate in oblique orientations for longer and continuous distances when ball size heterogeneity is small, eventually resulting in larger λ . It should be noted that the geometric analysis also neglects ball displacement and local stress deviations which may occur during fracture propagation.

The numerical and geometric analysis show that ball size heterogeneity is not an influential factor regarding tensile fracture roughness. Although the analysis is limited to ball-shaped grains, the contact geometry between non-circular grains can be simplified by a similar approach in which the number of potential propagation routes is larger than that of ball-shaped grains. The roughness profiles of non-circular grains will likely be smoother since the fracture propagates at the fracture tip along a larger set of potential propagation routes. Nevertheless, further investigation with non-circular grains will be required to confirm that ‘grain’ size heterogeneity is not influential factor regarding fracture roughness.

5 CONCLUSIONS

The influence of grain size heterogeneity on tensile fracture roughness was investigated through numerical simulations using PFC2D. Numerical models with different ball size ratios were constructed, and for each model, tensile fractures were generated by conducting direct tensile tests. The roughness of the generated tensile fractures was quantified by extracting the roughness profiles with respect to the broken bonds of the PFC2D models.

The numerical simulation results and their corresponding roughness parameters revealed that ball size heterogeneity has little effect on the roughness of tensile fractures. The insensitivity of fracture roughness with respect to ball size heterogeneity was further investigated by analyzing the geometry of ball contact configurations. Based on the geometry of three-ball contact, a fracture propagation model was devised to examine the formation of fracture roughness. The roughness parameters derived by the geometric analysis supported the results of the numerical simulations by illustrating that ball size heterogeneity barely affects the route of tensile fracture propagation.

Although this study was focused on ball-shaped grains, the geometric analysis implies that tensile fracture roughness is not influenced by grain size heterogeneity in general. Nevertheless, further investigation with non-circular grains will be required. Regarding that the correlation between fracture roughness and host rock can play important roles in rock engineering applications, more investigations are required to identify host rock properties that are influential to the formation of fracture roughness.

ACKNOWLEDGEMENT

This work was supported by a grant from the Human Resources Development program of the Korea Institute of Energy Technology Evaluation and Planning (KETEP) (No.20204010600250) and by the National Foundation of Korea (NRF) (No. 2022R1F1A1076409) grant funded by both the Ministry of Trade, Industry, and Energy of the Korean Government (MSIT)

REFERENCES

- Anderson, T.L. 2017. *Fracture Mechanics: Fundamentals and Applications*. Boca Raton: CRC Press
- Barton, N. & Choubey, V. 1997. The shear strength of rock joints in theory and practice. *Rock Mech. Felsmechanik Mécanique des Roches*, 10:1–54
- Bandis, S.C., Lumsden, A.C. & Barton, N. 1983. Fundamentals of rock joint deformation. *Int. J. Rock Mech. Min. Sci.* 20(6):249–268
- Barton, N., Bandis, S.C. & Bakhtar, K. 1985. Strength, deformation and conductivity coupling of rock joints. *Int. J. Rock Mech. Min. Sci.* 22(3):121–140
- van Dam, D.B. & de Pater, C.J. 1999. Roughness of hydraulic fractures: Importance of in-situ stress and tip processes. *SPE Annual Technical Conference and Exhibition, Houston, Texas, October 1999*
- Diaz, M.B., Jung, S.G., Zhuang, L., Kim, K.Y., Jung, J.H. & Shin, H.S. 2016. Tensile strength anisotropy of Pocheon granite and roughness evaluation of its failure planes. *ISRM Int. Symp. - EUROCK 2016, Ürgüp, Turkey*
- Li, Y. & Zhang, Y. 2015. Quantitative estimation of joint roughness coefficient using statistical parameters. *Int. J. Rock Mech. Min. Sci.* 77:27-35

Lan, H., Martin, C.D. & Hu, B. 2010. Effect of heterogeneity of brittle rock on micromechanical extensile behavior during compression loading *J. Geophys. Res.*, 115(B1)

Han, Z., Zhou, J. & Zhang, L. 2018. Influence of grain size heterogeneity and in-situ stress on the hydraulic fracturing process by PFC2D Modeling *Energies* 11(6):1413

Potyondy, D.O. & Cundall, P.A. 2004. A bonded-particle model for rock *Int. J. Rock Mech. Min. Sci.*, 41(8): 1329–1364

Zhou, J., Zhang, L., Pan, Z. & Han, Z. 2016. Numerical investigation of fluid-driven near-borehole fracture propagation in laminated reservoir rock using PFC2D *J. Nat. Gas Sci. Eng.* 36:719–733

Numerical simulation on the rock-breaking mechanism with combined cutters under percussive load

Jiansheng Liu, Hualin Liao, Jun Wei

China University of Petroleum (East China), Qingdao, China

Mingzhe Chao

China Petroleum Offshore Engineering Limited Company, Beijing, China

ABSTRACT:

The percussive-rotary drilling technique using drill bits with combined cutter types has been widely used for accelerating the drilling of deep wells through hard strata. However, the combination of different cutting cutters and its effect on rock-crushing remain unclear. Thus, there is a lack of reference for selecting proper cutter configurations in actual drilling. To this end, the ABAQUS software was employed to develop a three-dimensional numerical model of the percussive-rotary drilling of the dolomite stratum of the Cambrian Lower Qiulitage Formation with three different cutter combinations: conical cutter & flat cutter, conical cutter & axe-shaped cutter, and flat cutter & axe-shaped cutter. The model was used to investigate the stress distribution and specific energy under axial impact load during the dual-cutter rock-crushing process. The results indicate that the stress waves generated by the different cutting cutters are superimposed on each other; thus, tensile and compressive stresses appear alternately inside the rock along the axial direction in this study. Moreover, the rock-crushing efficiency of the "conical cutter & axe cutter" combination is higher than that of the "conical cutter & flat cutter" combination. Therefore, it is more conducive to the propagation of stress waves inside the rock. Micro-cracks are produced in the rock during the first cutting cycle, reducing the cutting resistance and crushing specific energy when the same position is cut again. This study can provide a theoretical basis for the optimal design on drill bit cutter placement.

1 INTRODUCTION

Percussive-rotary drilling using drill bits with combined cutters has been widely used in deep wells with hard formations to enhance the rock-crushing efficiency (Xiong et al. 2020, Chen et al. 2021, Cheng et al. 2019, Zhang et al. 2012). Many researchers have used the finite element method to analyze the rock-crushing process in percussive-rotary drilling with polycrystalline diamond compact (PDC) cutters, and reported that, while percussive-rotary drilling had a significant speed-up effect on hard and brittle formations, it exhibited a worse speed-up effect on plastic formations (Hareland et al. 2009, Mensa-Wilmot et al. 2003, Pessier et al. 2011, Rahmani et al. 2020, Amar et al. 2019). Rocks with different strength have different response characteristics to impact load. The changes in the mechanical properties of rock caused by impact cracks around the borehole are more obvious for compact rocks (Shamea et al. 2020, Sheikhrzaei et al. 2019), while bedding rock formations are more prone to volume fracture during cutting using PDC cutters. The rock-crushing efficiency of PDC cutters differs significantly under longitudinal and torsional impact loads with different amplitudes and frequencies (Tulu & Heasley 2009). At present, the cooperation mechanism between different types of cutting cutters is not clear, and the formations to which each cutting cutter under vibration load is applicable are different (Wang et al. 2020, Deng et al. 2011). Therefore, when targeting at crushing hard rocks, it is of particular importance to conduct research on the speed-up mechanisms of percussive-rotary drilling with combined cutter configurations. Based on oil field data, this paper employed the ABAQUS finite element software to develop a three-dimensional finite element sim-

ulation model for cutting rock with combined cutters. The stress distribution and crushing specific energy during the cutting process by combined cutters under axial impact load were investigated, and the effects of cutter profile combinations on stress distribution was analyzed, providing a theoretical basis for the optimal design on bit cutter placement.

2 NUMERICAL MODEL AND BASIC PARAMETERS

2.1 Numerical model on percussive-rotary drilling of combined cutters

In this paper, a numerical simulation study on the dual-cutter percussive-rotary drilling of hard formations was performed using flat, conical, and axe-shaped cutters. The diameter of all three cutter profiles was 14.5 mm and the height from cutter bottom to top was 16 mm. The specific shapes are demonstrated in Figure 2. The above three cutting cutters form three different combinations: "conical cutter & flat cutter"; "conical cutter & axe-shaped cutter"; and "flat cutter & axe-shaped cutter". These three combinations provide a relatively high crushing efficiency for hard rock formations with a compressive strength greater than 70 MPa, and have been widely used in deep drilling. The model was meshed with hexahedral elements. The total number of elements was 75600, which is sufficient to obtain accurate results. The numerical model of the rock was 60 mm long, 60 mm wide, and 25 mm high. The back rake angle of the axe-shaped and flat cutters was 15° , and that of the conical cutter was 0° . The double cutters were arranged in a staggered manner, and they were set as rigid body. The pitch of the rotary track on the cutter top surface was 7.25 mm. The exposed height of the front row cutters was 2 mm higher than that of the rear row ones (as shown in Figure 3). Consequently, the front cutter would touch the rock first at the beginning of the simulation. In actual drilling, the drill bit rotary speed may fluctuate over time, exerting torsional impact on the rock. In order to eliminate the effect of such torsional impact, the parameters of this model were set as follows: the rotary angle speed of the double cutters was a constant value of 4π rad/s; the double cutters moved synchronously in a circular motion around the axis of the rock upper surface center point; the simulation time was 1 s; and two cycles of dual-cutter percussive-rotary system impact and cutting were simulated.

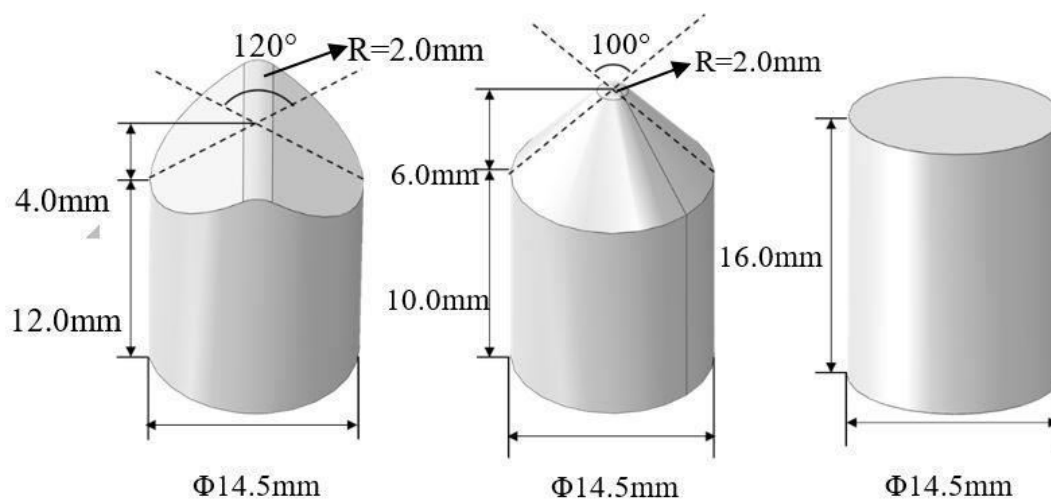


Figure 1 The shapes of axe-shaped, conical, and flat cutters

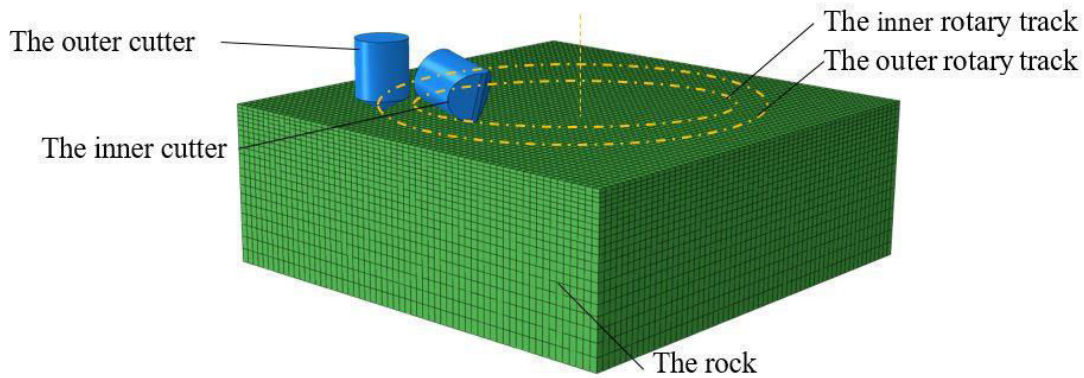


Figure 2 The positions of the cutters and rock

2.2 Numerical simulation parameter settings

There were 23 cutting cutters bearing the pressure exerted on the bit; thus, the average force on each cutter was about 5 kN. In the numerical simulation, a vertical force was applied separately to each cutting cutter and the bit pressure was regarded as the superposition of static load and dynamic load. The static load and the dynamic load amplitude of a single cutter were 4 kN and 0~2 kN, respectively. The total bit pressure fluctuated linearly between 4~6 kN and the impact frequency of the axial load was fixed at 16 Hz.

In this paper, a deep hard rock (dolomite of the Lower Cambrian Qiulitage Formation) was taken as the research object, and the physical parameters of the rock are given in Table 1.

Table 1 Physical and mechanical properties of dolomite of the Lower Cambrian Qiulitage Formation

Overburden pressure /MPa	Maximum horizontal stress /MPa	Minimum horizontal stress /MPa	Uniaxial compressive strength /MPa	Young's modulus /GPa	Poisson ratio	Internal friction angle /°	Cohesive strength /MPa
120	127	90	73.91	48.72	0.29	55.21°	10.94

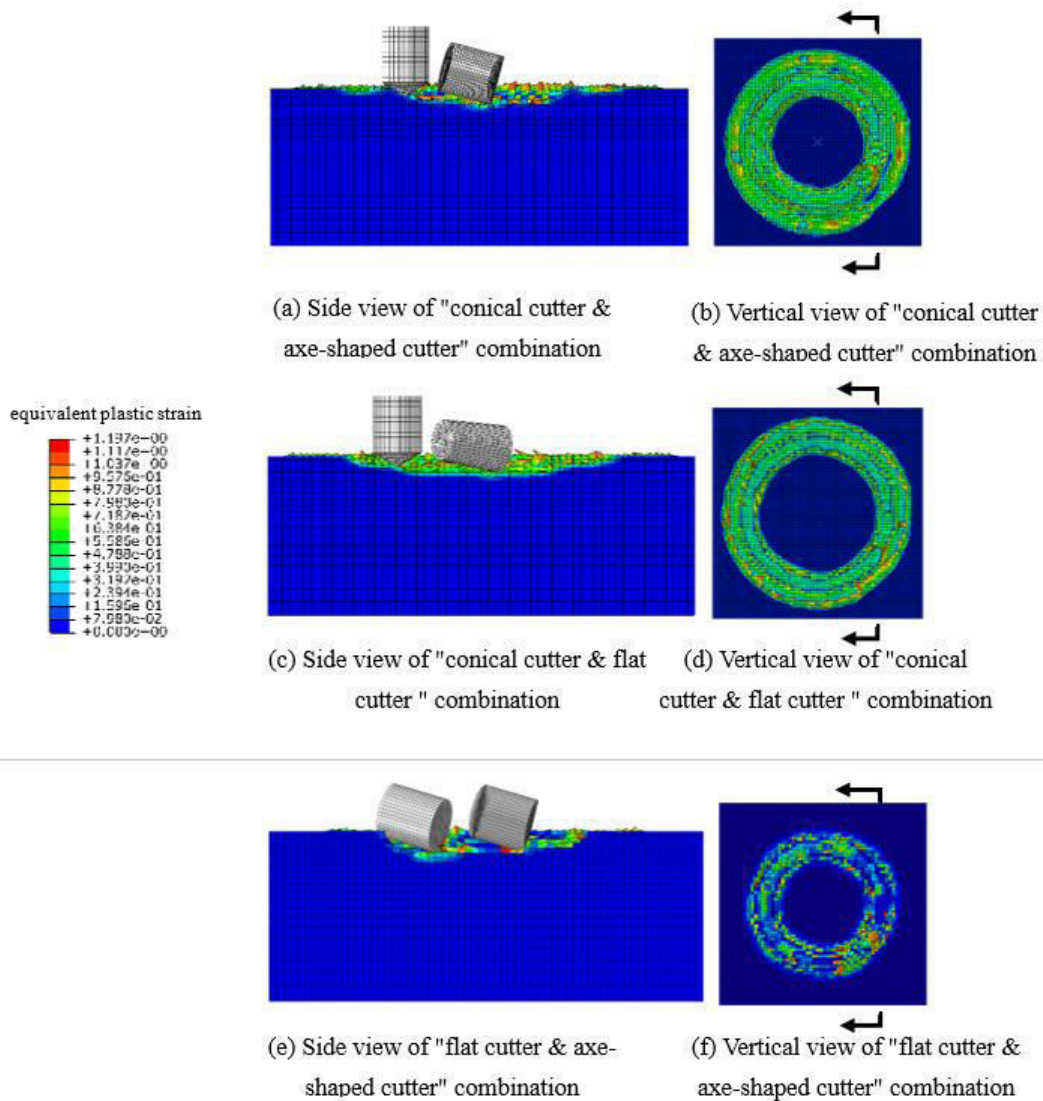


Figure 3 Cloud chart of equivalent plastic strain of rock cut by different cutter combinations

3 EFFECTS OF DIFFERENT CUTTER COMBINATIONS ON ROCK-BREAKING PARAMETERS

3.1 Equivalent plastic strain of rock

The point at the middle of the cutting process (simulation time $t=0.5$ s) was selected to analyze the top view of the rock and the side view of the rock section, where the axis of the front row of cutting cutters was located. On this point of view, the cutters rotated one revolution. The numerical simulation results of the three cutter-combinations under axial impact load are shown in Figure 4. The blue region in Figure 4 indicates that there was no plastic deformation, while the other colors indicate different degrees of plastic deformation. In addition, it can be seen that under the action of axial impact load, the "conical cutter & axe-shaped cutter" and "flat cutter & axe-shaped cutter" configurations caused mainly brittle fracture on the rock, and the equivalent plastic strain was not uniformly distributed when the rock was crushed. There were elements with zero strain on the rock fracture surface, and the deformation of the elements was small. The "conical cutter & flat cutter" combination induced mainly plastic fracture on the rock, and the

equivalent plastic strain distribution when the rock was crushed was relatively uniform. The elements in the rock fracture area mainly underwent a plastic deformation with large strain magnitudes.

3.2 *Stress distribution of rock*

The maximum principal stress distributions developed under the three cutter combinations are shown in **错误!未找到引用源。**. When the maximum principal stress was lower than 0, it indicated the presence of compressive stress, which was mainly distributed in the blue area. When the maximum principal stress was larger than 0, it indicated the presence of tensile stress, which was mainly distributed in the red and green areas. Under the loading conditions of this paper, it can be observed that the absolute value of the maximum principal stress was higher when the "conical cutter & axe-shaped cutter" combination was used to crush the rock. High stress concentration was mainly observed in the region where the cutting cutters contacted the rock. Taking the direction of the cutter horizontal movement as the forward direction, the cutting cutter generated a compressive stress concentration in front of the contact point with the rock, resulting in shear failure of the rock. However, stress concentration occurred also behind the cutter, which was favorable for the formation and expansion of tensile cracks inside the rock. The absolute value of the maximum principal stress generated during the rock-crushing process with the "conical cutter & flat cutter" combination was relatively small. The tensile stresses were concentrated inside the rock at a depth of about 3 mm behind the contact point between cutting cutter and rock, and the rock surface elements at the contact point were mainly subjected to compressive stress.

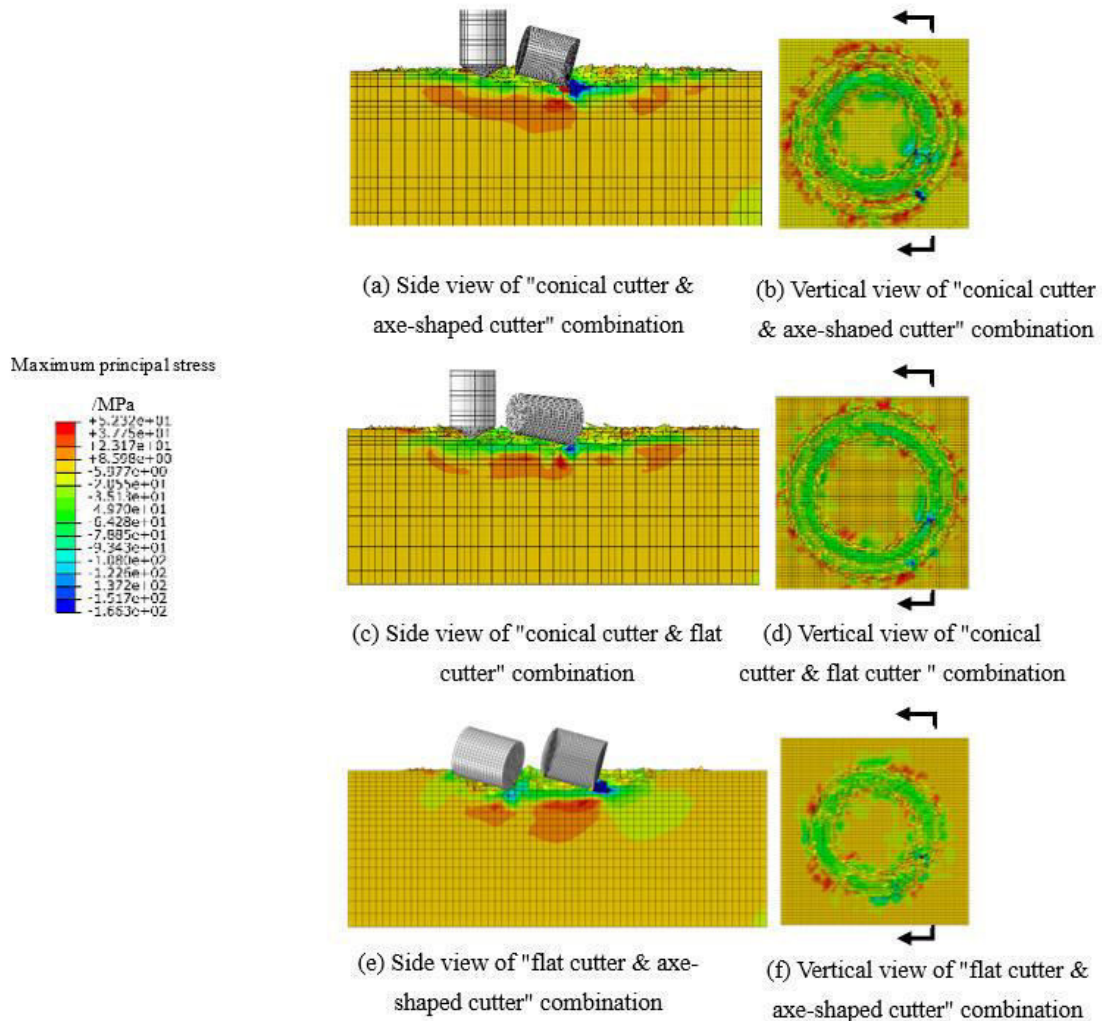


Figure 5 Cloud chart of maximum principal stress of rock cut by different cutter combinations

Under the action of axial impact load, the von Mises stress distributions developed during rock-crushing using the three cutter combinations are shown in Figure 4. By comparison, it was found that the "conical cutter & axe-shaped cutter" and "flat cutter & axe-shaped cutter" combinations induced higher von Mises stresses on the rock. In the area near the contact point between cutting cutter and rock, the gradient of stress change was larger with an apparent stress concentration, which facilitated the fracture of the rock.

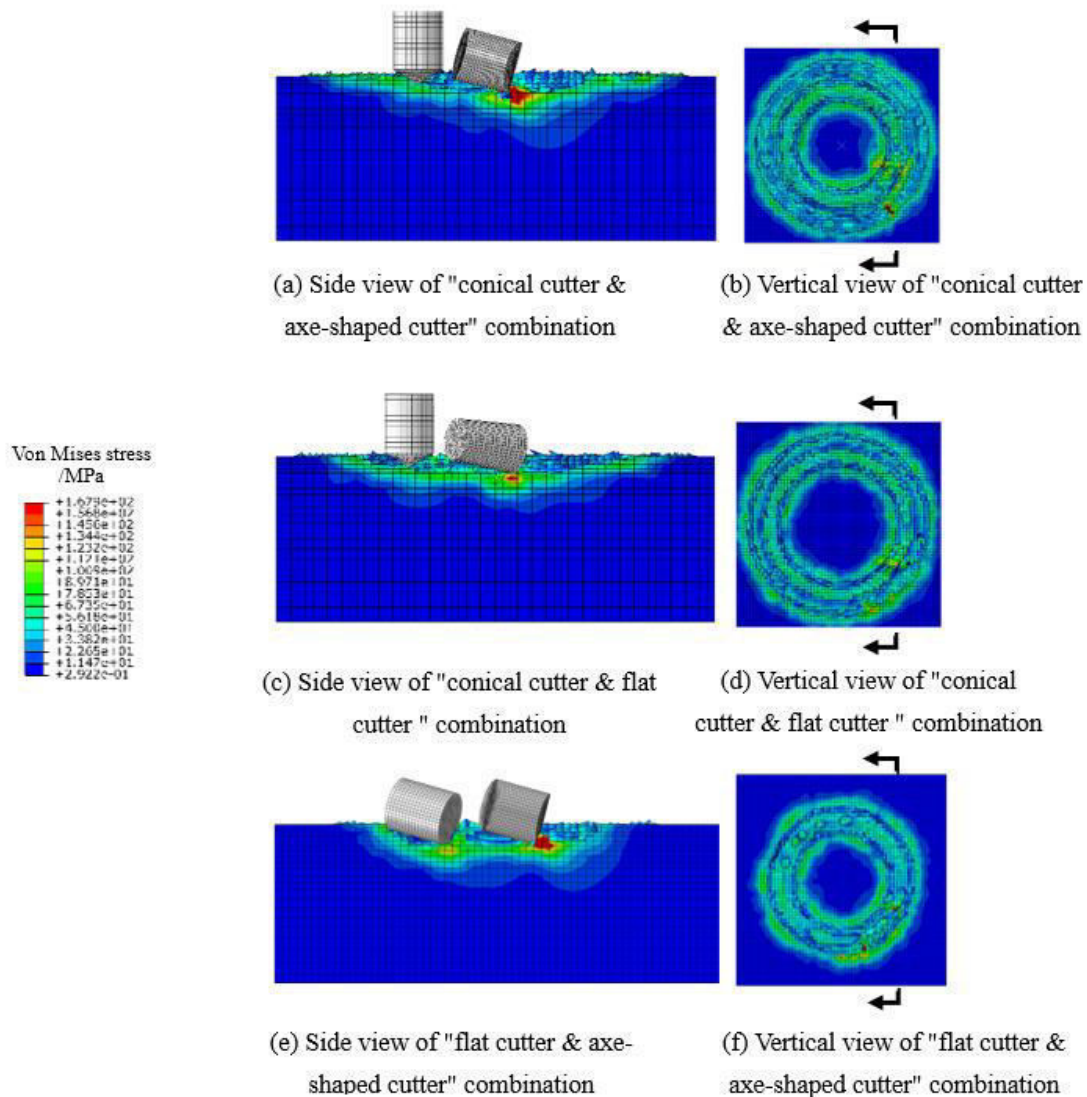


Figure 4 Cloud chart of von Mises stress of rock cut by different cutter combinations

3.3 Cutting force and rock-crushing efficiency

The change of the circumferential cutting force with time during the two cycles of percussive-rotary cutting with different cutter combinations is presented in Figure 5. The circumferential cutting force fluctuated continuously within a certain range. When the cutting cutter penetrated into the rock, the circumferential cutting force increased, and the rock absorbed the cutting energy; thus, the mechanical energy was transformed into internal energy of the rock. When the circumferential cutting force reached its peak value, chips were formed and separated from the rock body. Immediately, the circumferential cutting force was decreased to its minimum value and the cutting cutter continued to penetrate into the rock, beginning a new round of cutting. It can be observed in Figure 5 that, under the same axial impact load, the "conical cutter & axe-shaped cutter" combination had larger fluctuation amplitude and average circumferential cutting force than the other two combinations. This indicates that the "conical cutter & axe-shaped cutter" combination can penetrate deeper into the stratum, enabling more effective rock crushing. During the second cutting cycle using the three combinations, the circumferential cutting force

was reduced to varying degrees, indicating that, during the first cutting cycle, an irreversible damage was caused to the inside of the rock. While this damage is not adequate to form chips, it can reduce the strength of the rock and decrease the difficulty in crushing the rock during subsequent cutting cycles.

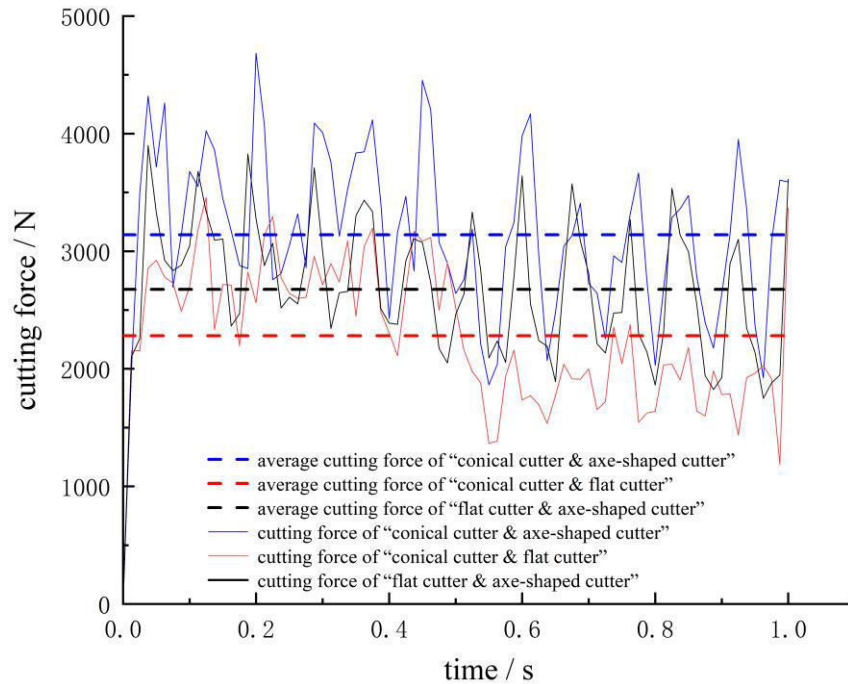


Figure 5 The circumferential cutting force of different cutter combinations

The cumulative volume change curve of the crushed rock for two cycles under the different cutter profile combinations is demonstrated in

Figure 6. The slope of the curve represents the rock-crushing speed. The curve of the mechanical specific energy change with time is displayed in Figure 7. In the first cutting cycle, the volume changes of the rock crushed by the three cutter combinations increased linearly with time. The crushing specific energy in the first cycle using the "flat cutter & axe-shaped cutter" combination was the highest, followed by that using the "conical cutter & axe-shaped cutter" combination, while that using the "conical cutter & flat cutter" combination was the lowest. In the second cutting cycle, the rock-crushing speed of the "conical cutter & axe-shaped cutter" combination increased compared to that in the first cycle, and the average rock-crushing specific energy decreased by about 18%. On the other hand, the rock crushing speeds and crushing specific energy of the other two combinations decreased by less than 5% compared to those in the first cycle. This phenomenon is mainly attributed to that during the first cutting cycle, the local stress generated by the "conical cutter & axe-shaped cutter" combination was higher, introducing a more significant stress concentration on the rock, generating a tensile stress area with higher magnitude and larger range inside the rock, and thus, promoting the formation and propagation of micro-cracks in the rock. Since, during the first cutting cycle, these micro-cracks could not break the rock and generate chips, the difference in the crushing efficiencies of the cutter combinations was slight. In the second cutting cycle, the pre-existing micro-cracks were further expanded and merged, making the rock more prone to fracture. Local fracture pits were also formed on the rock under the action of axial impact, which accelerated the generation of chips. Therefore, the "conical cutter & axe-shaped cutter" combination consumes less mechanical en-

ergy for crushing a unit volume of rock, exhibiting a lower crushing specific energy and a higher cumulative rock-crushing volume.

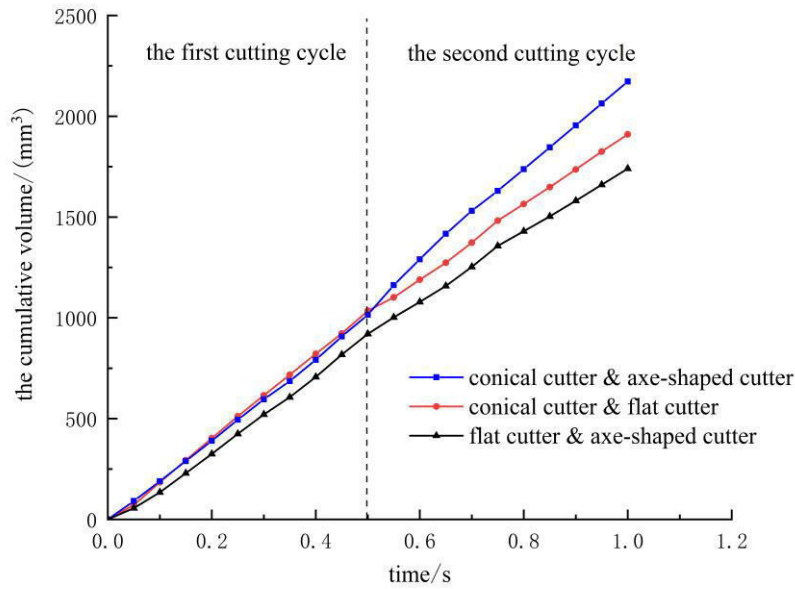


Figure 6 The cumulative volume of the crushed rock under different cutter combinations

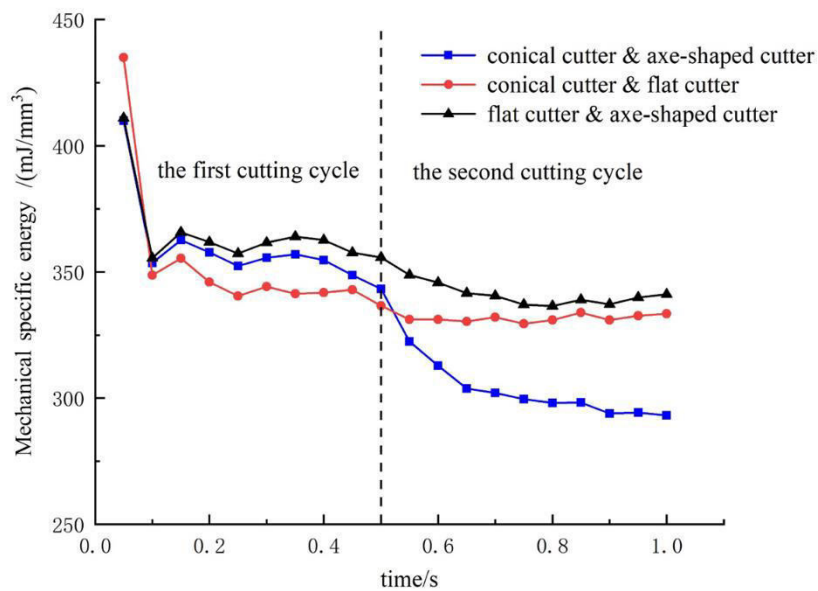


Figure 7 The rock-crushing specific energy under different cutter combinations

4 ANALYSIS ON THE PROPAGATION OF DUAL-CUTTER ROCK-CRUSHING STRESS WAVE

Under the action of axial impact load, the force exerted by the double cutters on the rock changes significantly in a very short time, and the effective rock-crushing energy expands outward from the impacting point in the form of stress waves. Since there are interfaces inside the rock, such as fault planes and joint planes, the stress waves are transmitted and reflected on the interface. The superposition of the incident and reflected waves induce the development of tensile or compressive stresses in different areas.

The three cutter combinations investigated in this paper exhibited approximately the same patterns; however, the "conical cutter & axe-shaped cutter" combination produced higher stress and larger stress response area. Therefore, the "conical cutter & axe-shaped cutter" combination was taken as an example to illustrate the propagation characteristics of stress waves in hard rock. Figure 8 shows the tensile and compressive stress distribution inside the rock, induced by the "conical cutter & axe-shaped cutter" combination during percussive-rotary drilling. The axe-shaped cutter first contacted and penetrated the rock under the action of impact load and rotary torque. Meanwhile, the stress below the impact point appeared alternately as "tensile stress - compressive stress - tensile stress" in the tangential direction. After the axe-shaped cutter penetrated the rock to a certain depth, a stress concentration area was formed within a small region below the contact point. The area was divided into two parts: compressive stress was developed in the area in front of the cutting direction of the axe-shaped cutter, while tensile stress was developed in the rear area. Under the combined action of the two types of stresses, the rock was subject to multiple actions, including pressing, shearing, and ploughing. When the conical cutter contacted the rock, local crushing pits were generated at the impact point, mitigating the impact. Under the action of compressive stress, energy is accumulated at the pits to form a compact core, which causes the generation of tensile cracks in the rock, and may even lead to brittle fracture. The stress waves generated by these cutter profiles are easy to propagate inside hard and brittle rocks, forming a stress diffusion zone with a large range and small absolute value. While the stresses in this area are not adequate to crush the rock, they can promote the propagation of micro-cracks inside the rock, thus causing damage to the rock body and decreasing the difficulty in rock crushing during subsequent cutting cycles.

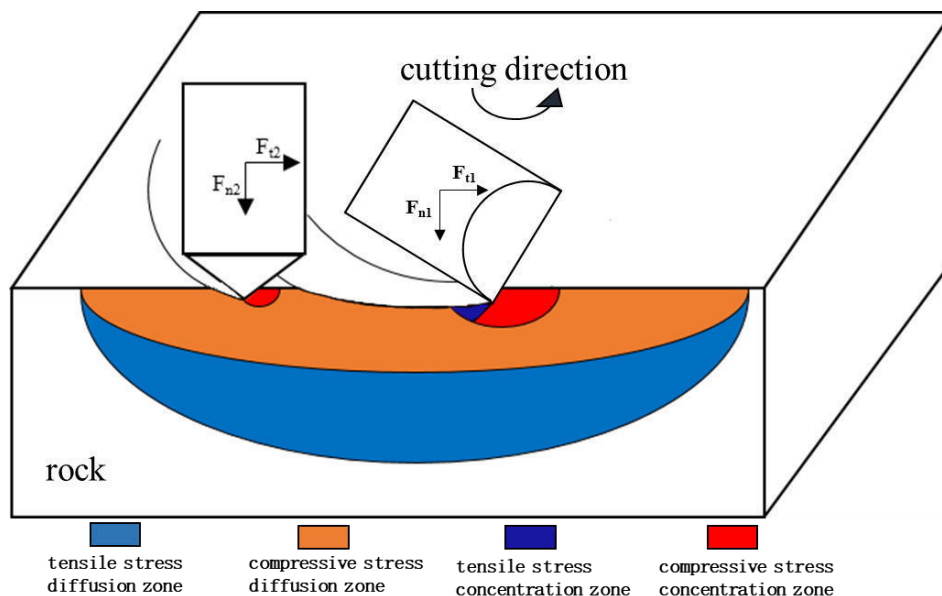


Figure 8 Diagram of the stress distribution inside the rock

5 CONCLUSIONS

(1) In percussive-rotary drilling for hard formations, the “conical cutter & axe-shaped cutter” combination can impose high stresses on the rock and generate tensile stress, which easily reaches or exceeds the strength limit of the rock, causing fracture of the rock and the formation of apparent fracture pits. Compared to the previous combination, the “conical cutter-flat cutter” combination can generate lower stress, which mainly introduces compressive stress to the rock. Its failure mode is mainly shear failure, which causes plastic fracture and partial brittle fracture to the rock; thus, large broken pits cannot be easily formed.

(2) The ability of the axe-shaped cutter to penetrate into the formation is stronger than that of the flat cutter. Under axial impact force, the “conical cutter & axe-shaped cutter” combination penetrates the rock to larger depth and the cutting force fluctuates significantly. Consequently, the average cutting force is higher and the generated stress wave has a larger propagation range. The axial impact force can be extended from the rock surface to deeper areas, and damage cracks develop from the deeper position to the free surface, which is easier to form large rock chips.

(3) The impact load promotes the formation and propagation of micro-cracks. When the cutting cutter cuts the same position again, both the cutting resistance and crushing specific energy decrease. The “conical cutter-flat cutter” combination imposes less stress on the rock and generates fewer micro-cracks, which only reduce the cutting resistance. However, the “conical cutter & axe-shaped cutter” combination has a stronger ability to promote the formation and expansion of micro-cracks. In addition to reducing the cutting resistance, the volume of crushed rock increases as well, resulting in a lower mechanical specific energy.

(4) In percussive-rotary drilling, the stress waves generated by the different cutting cutters are superimposed on each other. Consequently, tensile or compressive stresses are generated in different areas, and the corresponding two stress areas appear alternately. In the same-track arrangement, when the rear cutter contacts the rock, the propagation direction of the stress wave generated by the front cutter changes. The change in direction expands the areas inside the rock that bear tensile and compressive stresses and further extends the micro-cracks generated by the impact of the front cutter, which is conducive to rock crushing.

REFERENCES

- Chao Xiong, Zhongwei Huang, Ruiyue Yang, Mao Sheng, Huaizhong Shi, Xianwei Dai, Xiaoguang Wu, and Shikun Zhang. 2020. Comparative analysis cutting characteristics of stinger PDC cutter and conventional PDC cutter. *Journal of Petroleum Science and Engineering* 189.
- Pengju Chen, Stefan Miska, Mengjiao Yu, and Evren Ozbayoglu. 2021. Modeling of Cutting Rock: From PDC Cutter to PDC Bit—Modeling of PDC Cutter. *SPE Journal*, 1–21.
- Zhen Cheng, Gensheng Li, Zhongwei Huang, Mao Sheng, Xiaoguang Wu, and Jiawei Yang. 2019. Analytical modelling of rock cutting force and failure surface in linear cutting test by single PDC cutter. *Journal of Petroleum Science and Engineering* 177, 306–316.
- De Rong Zhang, Amy Chang, Chun Yan Kong, and Xiao Fei Zhang. 2012. The Structure Design of Special-Shaped PDC Reinforced-Cutter and its Finite Element Method Analysis. *Applied Mechanics and Materials* 2023.
- G. Hareland, R. Nygaard, W. Yan, and J. L. Wise. 2009. Cutting Efficiency of a Single PDC Cutter on Hard Rock. *Journal of Canadian Petroleum Technology* 48, 06, 60–65.

- Graham Mensa-Wilmot, Robert Soza, and Kyle Hudson. 2003. Advanced Cutting Structure Improves PDC Bit Performance in Hard Rock Drilling Environments. SPE-84354-MS.
- Pessier, Rudolf, Damschen, and Michael. 2011. Hybrid Bits Offer Distinct Advantages in Selected Roller-Cone and PDC-Bit Applications. *SPE Drilling & Completion* 26, 01.
- Reza Rahmani, Paul Pastusek, Geng Yun, and Tom Roberts. 2020. Investigation of PDC Cutter Structural Integrity in Hard Rocks. *SPE Drilling & Completion*.
- Muhammad Shafiq Shahrul Amar, Beng Chai Seow, Muhammad afiq Za'ba, M. Khairol A Razak, and W. Nor W Aziz. 2019. Revolutionary PDC Cutter Design Help Improve Bit Performance in Malay Basin. D021S022R004.
- Nooh Shamea, Ahmed Suleiman, Michael James Bailey, Richard Rivera, and Ahmed A. Thallab. 2020. Demonstrating Reliability, Improved Efficiency And Robustness Whilst Deploying Novel Shaped PDC Cutter Geometries. D041S113R001.
- K. Sheikhezai and B. Akbari. 2019. An Experimental Study on the Impacts of Different PDC Cutters Arrangements on a Bit on Rock Cutting Process. ARMA-2019-0368.
- I. B. Tulu and K. A. Heasley. 2009. Calibration of 3D Cutter-Rock Model With Single Cutter Tests. ARMA-09-160.
- Bin Wang, Jun Li, and Deyong Zou. 2020. Application of a PDC Hybrid Drill Bit with Impregnated—Diamond Cutter (IDC) for the Hard and Strong Abrasive Formations. ARMA-2020-1606.
- Zhao Hui Deng, Zhan Pan, Qiao Ping Wu, G. F. Zhang, and B. Zhang. 2011. Research on Finite Element Simulation and Experiment of Temperature Field in Surface Cutting Used a New PDC Cutter. *Key Engineering Materials* 1371.

DEM simulation on the effect of meso properties of conglomerate on its mechanical properties and failure mechanism

Jun Wei, Hualin Liao*, Bin Huang, Huajian Wang

School of Petroleum Engineering, China University of Petroleum (East China), Qingdao, China

Ning Li, Hongjun Liang, Erbiao Lou, Hui Feng, Yutian Han, Hui Yan

Oil and Gas Engineering Research Institute, CNPC Tarim Oilfield Company, Korla, China

ABSTRACT:

Conglomerate is a kind of terrigenous sedimentary rock, which is the main component of gravel layer, its mechanical properties and failure mechanism are the basis of efficient rock breaking method developing while drilling in gravel layer, where lots of high-quality oil and natural gas resources had been discovered. The gravel content of the specimen was obtained by CT scanning and the mechanical properties of conglomerate were tested. A kind of simulating method for analyzing the mechanical properties of conglomerate and studying its influencing factor was proposed base on discrete element method, and the meso-mechanical parameters were calibrated by trial and error. According to the established DEM model, the mechanical properties of conglomerate under different meso parameters are studied, the results show that the crack propagation and stress-strain curves of numerical and physical test are in a good agreement. The number of meso particles and the loading rate of axial stress do a great to the computing time, but show a little influence on the elastic modulus of conglomerate. With the increase of meso particles, the UCS increase linearly first and then the growth rate decrease, while the UCS increase linearly continuously with loading rate of axial stress. There are different failure patterns such as cementation failure, matrix failure and gravel failure under a series of cementation strength ratio between the matrix and gravel particles. This research is of great significance to the exploration of the physical and mechanical properties of the bottom rock in gravel layer.

1 INTRODUCTION

Conglomerate is a kind of terrigenous sedimentary rock, which is the main component of gravel layer (Schmidt, 2004; Rogers, 2007; Shafiei, 2008). More and more attention had been paid on the oil and natural gas resources covered by gravel layer. The exploration results show that the reserves in Kuqa Depression in Tarim Basin, northwest China (Zheng, 2016; Teng, 2016) are more than 1 trillion cubic meters gas and 50 million tons high-quality oil. This block is the main block for increasing conventional oil and gas production in China in the future (Zhang, 2020; Neng, 2013). However, the drilling well in this block is usually more than 7000 meters (Zheng, 2016; Tian, 2019), and there is a huge thick gravel layer developed in the formation of 500 m ~ 6500 m (with an average thickness of 5300 m) (Tian, 2019; Teng, 2021; Wang, 2012). So that, the gravel layer must be broken first to reach to the target reservoir.

The characteristics of high strength, poor cementation and strong heterogeneity in gravel layer lead to the severe vibration of drill string, serious wear of drill bit and low rate of penetration (ROP) (Li, 2017; Galarraga, 2016; Rodriguez, 2015). All of this seriously restricts the drilling development process (Teng, 2016; Zhang, 2020; Neng, 2013). The mechanical properties and failure mechanism of conglomerate are the basis of efficient rock breaking method developing while drilling in gravel layer. The author (Jun, 2022)⁰ has studied the dynamic and static tensile strength and failure characteristics of conglomerate based on Brazilian disc tests, the results indicate that because of the energy absorbed increased exponentially under impact loads, volume crushing failure mainly produced in the dynamic test, while brittle splitting failure formed mainly in the static. Luo (Luo, 2021), Liu (Liu, 2018) and Akram (Akram, 2010) characterized the heterogeneity and studied the effect of content and distribution of gravels on the strength of

$$\Delta F_i^s = -k_s A \Delta \delta_i^s \quad (3)$$

Where \vec{F} is vector of the contact force of any two particles, \vec{F}_n and \vec{F}_s are the vectors of contact force in normal and shear directions respectively, ΔF^n is the incremental normal contact force, ΔF^s is the incremental shear force, k_n is the normal stiffness, k_s is the shear stiffness, $\Delta \delta^n$ and $\Delta \delta^s$ are the incremental normal and shear displacement, A is the area of contact surface.

The slip model describes a kind of frictional behavior between contact entities and the relative sliding particles is allowed by limiting the shear force. The friction coefficient μ is used to define the shear force at the contact. While the total shear contact force exceeds the allowable, a slip condition is satisfied and then slip occurred.

$$F_{\max}^s = \mu \cdot F_i^n \quad (4)$$

The parallel bond model is used to define the normal and shear contact bond strength. And the relative motion between particles formed by the slip could cause force and moment at the parallel bond positions, which can be considered as a set of springs that are parallel to the contact surface so that to establish an elastic interaction between particles. This kind of force is related to the normal and shear stresses acting on the bond can be shown in Eq(5). A bond is broken while either of these two stresses exceed the total bond strength.

$$\begin{cases} \bar{\sigma} = \frac{F_i^n}{A} + \bar{\beta} \cdot \frac{M}{I} \\ \bar{\tau} = \frac{F_i^s}{A} \end{cases} \quad (5)$$

Where M is the parallel bond moment, $I=2\bar{R}/3$ is the inertia moment on the bond cross-section, \bar{R} is the bond radius of particles, $\bar{\beta}$ is the moment-contribution factor, ranging from 0 to 1.

The bond broken can be divided into shear failure and tensile failure. The shear stress of the DEM specimen can be calculated as $\bar{\tau}=c+\sigma \tan \varphi$, the average normal stress is described as $\sigma=F^n/A$. When the maximum normal stress between particles is greater than the tensile strength, tensile failure occurred. While the maximum shear stress between particles is greater than the shear strength, shear failure occurs.

In addition, A time-stepping algorithm is used to solve the equations of motion as following Eqs.

$$F_i = m \cdot (\ddot{\delta}_i - g_i) \quad (5)$$

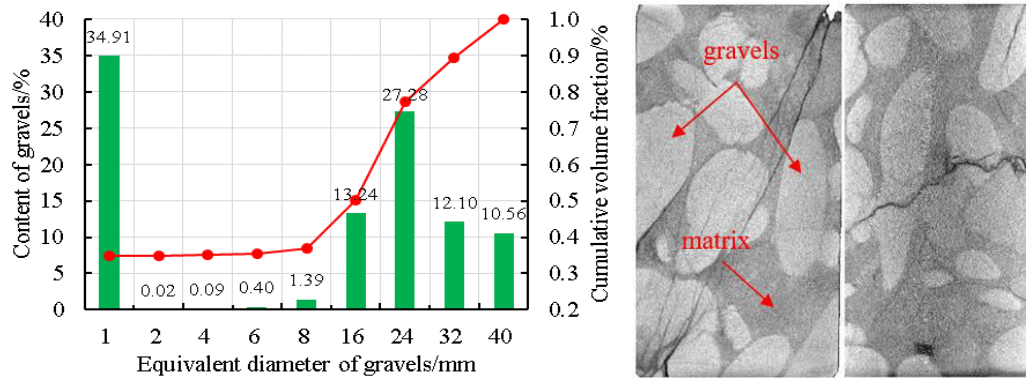
$$M_i = I \dot{\omega}_i \quad (6)$$

Where, m is the mass, $\ddot{\delta}_i$ is the acceleration, and g_i is the body force acceleration, $\dot{\omega}_i$ is the angular acceleration about the principal axis.

The laws of motion are applied to each particle to have its velocity and position updated based on the force and moment acting on the particle. The movement and interactions of all the particles represent the dynamic process of the particle assembly.

2.2 Content of gravel particles

As for conglomerate, there is such of complex component in gravel particle size, shape, type and property of contacts, amount and type of cementation and matrix (Zorlu, 2008), all of which causing a strong heterogeneity. In this paper, the conglomerate outcrops were used to study the failure characteristics under axial compressive loadings, and then the effect of gravel distribution and content characteristics on its UCS was analyzed. To figure out the content of gravel particles in the outcrop, the CT scanner was adopted, the results can be shown in.



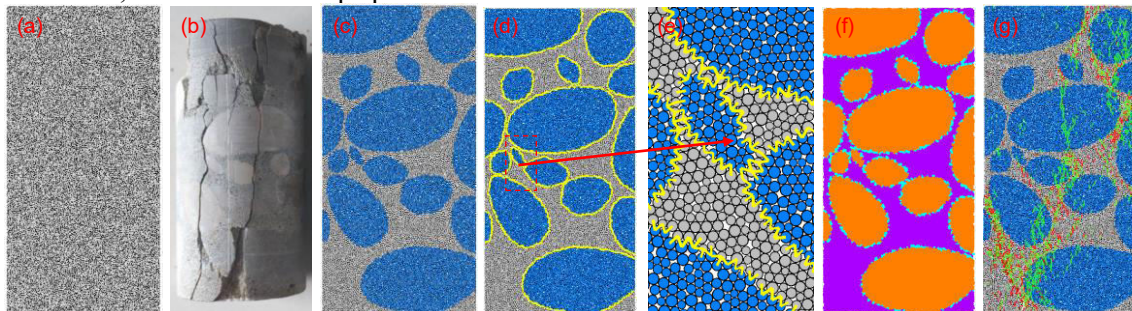
(a) the content of gravel particles (b) the distribution of gravel particles (destroyed)

Fig.2 CT scan results of conglomerate outcrop

The CT scanning results in Fig.2 indicate that the conglomerate outcrops tested in this study is characterized by strongly heterogeneity in the content, size, shape and distribution of gravel particles. According to the definition of conglomerate, the particles with a size greater than 2 mm are defined as gravel. From Fig.2(a) we can know that the conglomerate outcrop contains a large amount of gravels which differ greatly in size and shape, and the content of particles whose size is less than 2 mm is about 34.93%, which indicates that the gravel content is 65.07% approximately. Besides, the size and position of gravel particles have strongly randomness. Therefore, the size, shape, content and distribution characteristics of gravel shall be fully considered.

2.3 DEM model construction

The PFC2D platform was adopted, and the cylindrical specimen was constructed as a rectangle. According to the physical specimen used in the uniaxial test, the original compact rectangular DEM model with the height H and width W of 100 mm and 50 mm respectively were generated, shown in Fig.3. It is worth mentioning that the radius of the meso particles in the DEM model was set to be 0.25 to 0.4 mm, and the initial porosity was set to be 16%. And, there was a total of 12417 particles generated. Assuming that both the gravel particles and the matrix are a single substance, the UC-01 outcrop specimen was taken as a reference to construct the DEM model.



(a)The original DEM model (b)Physical specimen (c)classified meso particles (d)DEM model (e)Cementing state (f)Parameters assigned (g)Crack propagation

Fig.3 construction of the DEM model of conglomerate

Significantly, by the operation of installing the isotropic stress, the porosity of the DEM model changed to be 7.39%. Because there is cementation failure and gravel particles failure in the physical test seen in Fig.2, the gravel particles in the DEM model were simulated by a group of flexible clusters bonded together. When the model was solved to equilibrium, the gravel content was counted to be 64.78%, which was in accordance with the CT results.

2.4 Meso parameters calibration

As it is known that conglomerate is composed of three parts, gravel, matrix and cement, the average strength ranked could be gravel > matrix > cement. In the DEM model, the cementing situa-

tion and contact properties were set to be a different group of values. Followed as the experimental conditions, the special DEM model was established and simulated through the uniaxial compressive test for several times. The micro-mechanical parameters of gravel and matrix were assigned to be a certain group of values, and then the micro-mechanical parameters of cementation were set according to a certain proportion of gravel, the proportion was gone by the name of cementation strength ratio (CSR), ranging from 0.1 ~ 1.

Table 1 The meso-mechanical parameters of each components of conglomerate

Description	Parameters	Matrix	Gravel	cement
Ball density / $\text{kg}\cdot\text{m}^{-3}$	ρ	2500	2875	/
Ball-ball contact modulus / GPa	E_c	11.4	25.2	12.6
Ball stiffness ratio	k_n / k_s	2.21	1.52	0.76
Parallel-bond Young's modulus / GPa	\bar{E}_c	11.4	25.2	12.6
particle contact normal to shear stiffness ratio	\bar{k}_n / \bar{k}_s	2.21	1.52	0.76
Parallel bond normal strength / MPa	$\bar{\sigma}_c$	31.1	45.4	22.7
parallel bond cohesion / MPa	\bar{c}	31.1	45.4	22.7
parallel bond frictional angle / °	$\bar{\varphi}$	38	49	24.5
Ball friction coefficient	μ	0.31	0.24	0.12

There is no direct correspondence between the micro- and macro- parameters in the DEM model and the physical specimen respectively. it is necessary to carry out a trial calculation and then adjust the preset parameters according to the physical test. Through repeated trial and error, the meso-mechanical parameters of each components of the special DEM model were obtained and listed in Table 1, where the CSR was equal to 0.5. The stress-strain curves of the three physical test and the special DEM model are presented in Fig.4. Obviously, there are brittleness characteristics for the specimens, the cracks produced vertically and expanded rapidly along the radial direction. The crack propagation and the stress-strain curves of numerical and experimental test are in a good agreement with each other. Therefore, the selected micro-mechanical parameters of the special DEM model are considered to be reasonable.

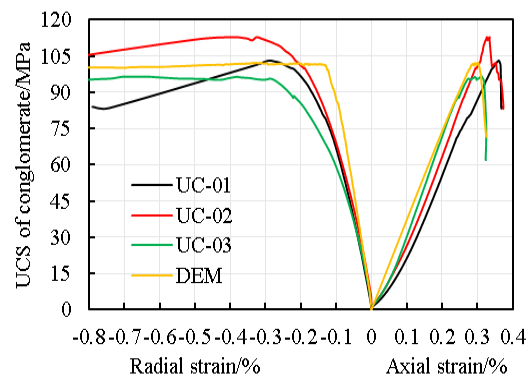


Fig.4 Experimental and numerical stress-strain curves of conglomerate specimen

3 RESULTS AND DISCUSSION

3.1 Effect of the number of meso particles

Generally, the more particles in the PFC model, the more accurate the simulation results. However, in the same conditions, too many particles in the DEM model will greatly consume computer resources, occupying a lot of computing time and reduce the efficiency. If the calculation results of the DEM model reach to a certain accuracy, the number of the meso particles should be reduced as much as possible to realize rapid calculation. By setting the initial porosity and particle radius, a certain number of particles can be generated within the preset range. A series of DEM model was established with different number of particles. Based on the meso paramete-

ters determined in the above section, the porosity of each DEM model was set to be 16%, and then the number of particles was controlled by controlling the radius range of particles.

The effect of the number of meso particle on the DEM results of conglomerate is shown in Fig.5 and Fig.6, from which we can know that the number of meso particles has little effect on the elastic modulus and Poisson's ratio of conglomerate, but show a great difference in its failure pattern and the compressive strength.

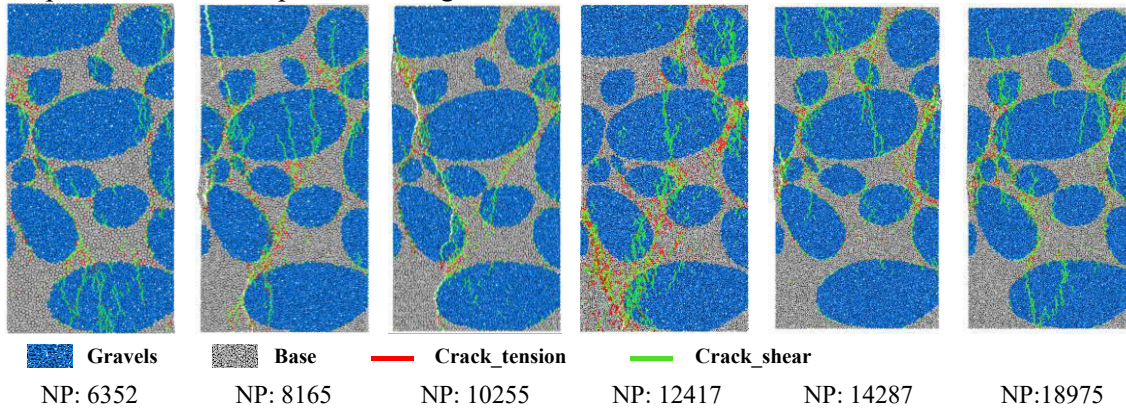


Fig.5 Failure characteristics of conglomerate under different number of meso particle

There are a lot of through crack bundles produced in the failure process under the action of uniaxial compressive loadings. The porosity between particles is large with small particles, which makes it easier to produce shear failure and forms large fragments. With the increase of the number of particles, the porosity decreases, and the contact area between particles increase, leading to increased adhesion in the same meso parameters. It can be found by comparing the simulation results and the physical experimental results that while the number of particles is 12417, the simulated cracks are more similar to the physical specimen.

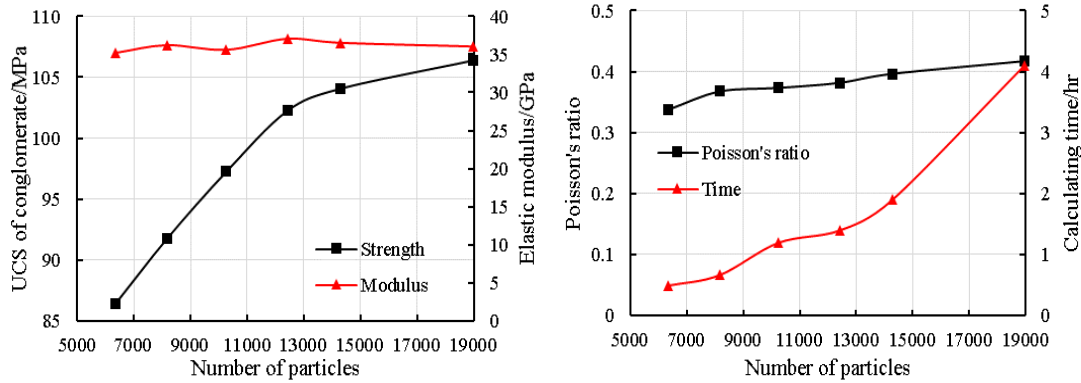


Fig.6 Effect of number of particles on the macro-mechanical parameters of conglomerate

Fig.6 indicates that if the number is lower than 12417, the strength of conglomerate increases linearly with the number of meso particles, and then it slows down after exceeding that value. When the number of meso particles increases from 12417 to 14287 and 18975, the UCS increases by 1.78% and 4.05% from 102.26 MPa respectively, while the calculating time increases by 35.72% and 192.86% respectively from 1.4 h. The reason for this phenomenon is that the more the number of meso particles in the DEM model, the slower the progress of the force and displacement to be transmitted while calculating. However, when the number increased to a certain extent, the simulation results are close to the physical test, so that it plays a less important role to further increase the number of meso particles.

Therefore, in order to improve the computational efficiency, the number should be appropriately reduced while the simulation results reach to a certain accuracy. According to the above analysis, the DEM model with 12417 particles whose size ranging from 0.25 ~ 0.4 mm represents high calculation efficiency, and it gives accurate results.

3.2 Effect of the loading rate

As we know, in the uniaxial test of rock-like material, the loading rate (LR) represents the loading velocity of the axial stress applied on the specimen, it has a significant impact on the testing results. Generally, according to the recommendation of ISRM (ISRM, 1978), when the specimen is subjected to different loadings, the failure process can be divided into five levels, namely creep, static compression, quasi dynamic compression, dynamic compression and super dynamic compression. The lower the LR, the slower the deformation process of the specimen, the longer the calculation time and the lower the calculating efficiency. Therefore, it is of great significance to analyze the influence of LR in the DEM model on the simulation results.

The DEM simulating results of failure pattern (partly) and mechanical parameters of conglomerate under different LR can be found in Fig.7 and Fig.8, which shows that LR has an important effect on the number of cracks generated and the failure types obviously, and the higher the LR, the more crack bundles produced. When LR was small, there are mainly local failure formed in the specimen, while LR exceeds 0.2 m/s, the cracks generated gradually develops into a through type, resulting in the formation of large debris.

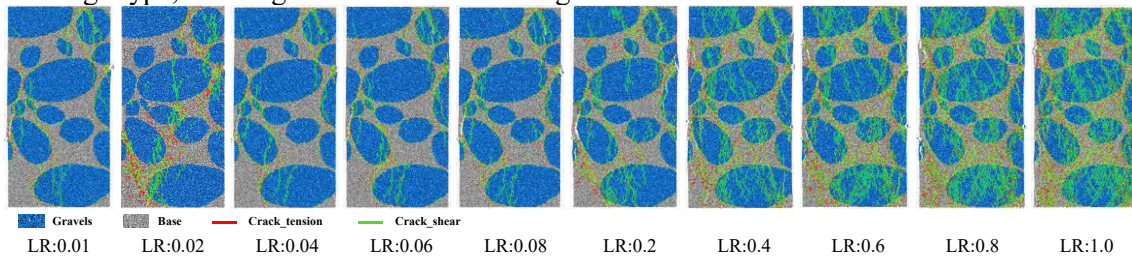


Fig.7 Failure characteristics of conglomerate under different loading rate

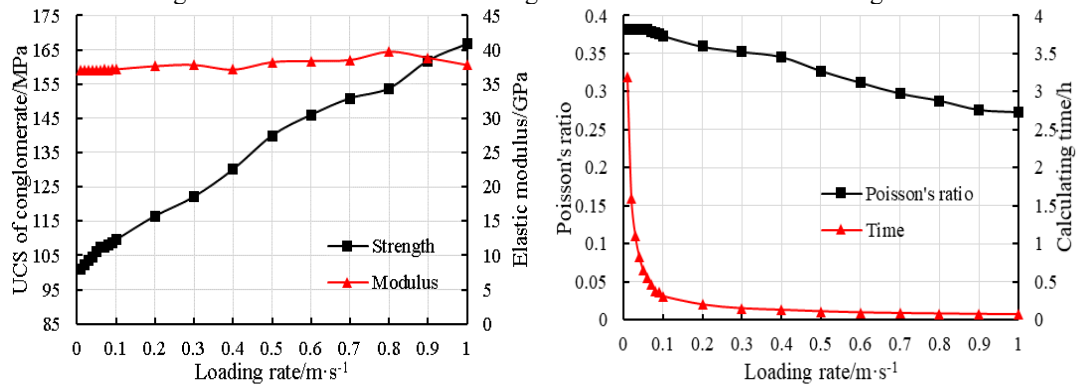


Fig.8 Effect of loading rate on the macro-mechanical parameters of conglomerate

In general, the higher the LR, the higher the UCS of conglomerate, and it shows a linear tendency, while there is a little effect on the simulated elastic modulus. As for the Poisson's ratio of conglomerate in the DEM model, when LR is lower than 0.06 m/s, it remains unchanged nearly. And then, with the increase of LR, the simulated Poisson's ratio shows a downward tendency linearly. Under the same simulation conditions, the smaller the LR of axial loads, the longer the failure process of simulation, the smaller the deformation rate of the specimen, the more sufficient the transfer of force and displacement between particles in the DEM model. The results (Fig.8) of the DEM model under different LR indicates that when the loading rate increases from 0.01 m/s, the calculating time decreases sharply from 3.17 hours, and when it exceeds 0.3 m/s, the calculating time decreases to several minutes and the UCS increased to a higher level. On the other hand, during increasing LR from 0.01 m/s to 0.05 m/s, the calculating time was reduced from 190 minutes by 93 minutes, 124 minutes, 140.2 minutes and 150.5 minutes to 39.5 minutes respectively, and the maximum decrease is 79.2%, while the simulated elastic modulus and Poisson's ratio of conglomerate remain unchanged barely, and the UCS increases by 1.483 MPa, 2.648 MPa, 3.637 MPa and 5.076 MPa respectively with the growth rates of 1.29%, 2.62%, 3.60% and 5.03% correspondingly.

Consequently, to improve the simulation efficiency and ensure the accuracy, the optimal loading rate was set to be 0.02 m/s in the subsequent simulations. And it is worth mentioning that the UCS, elastic modulus and Poisson's ratio of conglomerate while simulating with the optimal LR are 102.26 MPa, 37.09 GPa and 0.3817 respectively.

3.3 Effect of the cementation properties

The cementation properties of conglomerate are characterized by the cementation strength ratio (CSR), the values of which in the DEM models were set to be a certain proportion of the meso parameters of gravel particles. In this study, to figure out the effect of the cementation properties on the failure and strength characteristics, the value of CSR in each DEM model was defined to be 0.1 ~ 1 respectively, the simulated results are illustrated in Fig.9 and Fig.10.

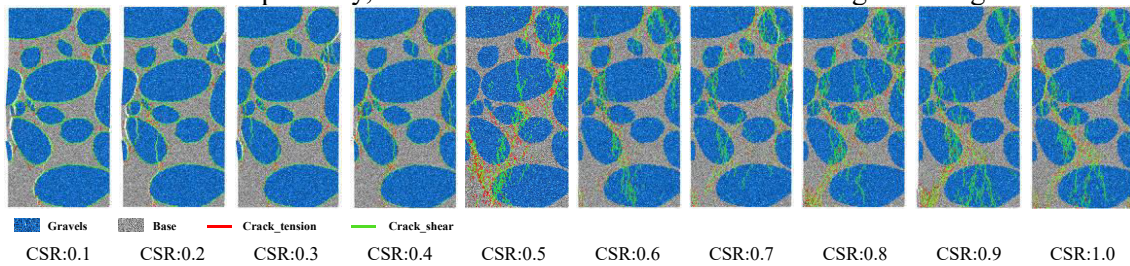


Fig.9 Failure characteristics of conglomerate under different cementation properties

Fig.9 shows that the cementation properties between gravel particles and the matrix in conglomerate have an important effect on the crack development trend and failure types under the action of external loadings. Overall, the higher the CSR, the more crack bundles produced. In addition, there are the phenomenon of surrounding and penetrating gravel accompanied by the collapse of large debris in the crack propagation process. The cemented surfaces broken quickly leads to the crack mainly develops around gravel particles, and there are a lower compressive strength and a larger displacement of gravel particles, which further resulting in a larger peak strain (shown in Fig.10) and the collapse of gravel particles. While CSR is equal to 0.4, it is still dominated by cementation failure, but there are lots of local crack bundles formed in the matrix, and the compressive strength and the ability to resist failure (also named elastic modulus) improved, whereas the peak strain reduced. With the increase of CSR, the cracks generated gradually develop into through type, and there are the situations of cementation failure, damage of matrix and splitting of gravel particles.

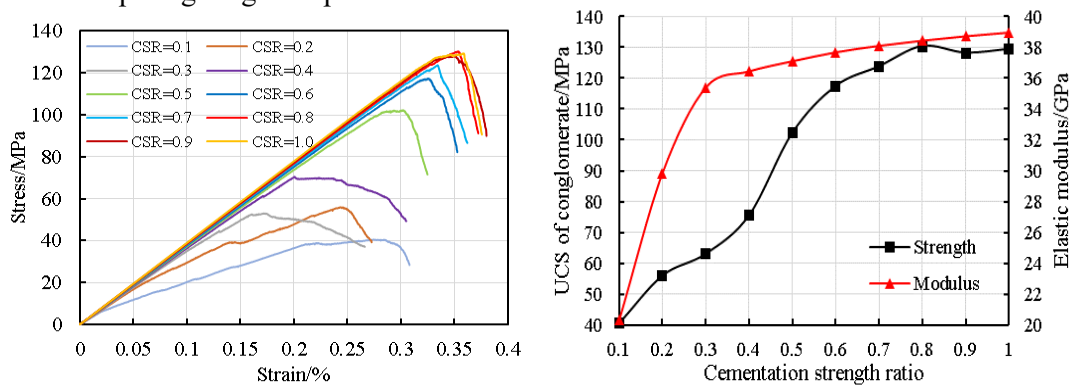


Fig.10 Effect of cementation properties on the macro-mechanical parameters of conglomerate

According to Fig.10 we can know that the cementation properties of conglomerate have a significant influence on its failure strength and elastic modulus. The compressive strength of conglomerate increase linearly with the increase of CSR while it is less than 0.8. When the CSR reaches to 0.8, the strength property of cement is higher than that of matrix and lower than that of gravel particles, which makes it more difficult to be damaged for the specimen resulting in the splitting failure of gravel particles and matrix. At the same time, the compressive strength of the specimen remains unchanged almost. On the other hand, with the increase of CSR, the elas-

tic modulus of conglomerate increases significantly. Especially, when CSR exceeds 0.3, the growth tendency of the modulus slows down, but changes linearly.

4 CONCLUSIONS

(1) The properties of conglomerate are the basis of efficient rock breaking method developing while drilling in gravel layer. According to the physical test, the mechanical properties such as the UCS, elastic modulus and the Poisson's ratio of conglomerate were obtained, and the content of gravel particles in the outcrop was obtained by CT scanning. A kind of simulating method was constructed base on discrete element method in this paper, and the effect of the meso properties of the DEM model of conglomerate on its mechanical properties were analyzed.

(2) The CT scanning results indicate that conglomerate is characterized by strongly heterogeneity, and the gravel content is about 65.07%. According to the profile of the physical specimen, a special DEM model of conglomerate was constructed with 64.78% of gravel content. Through repeated trial and error, the meso-mechanical parameters were calibrated and the crack propagation and stress-strain curves of numerical and physical test are in a good agreement.

(3) The number of meso particles, the loading rate and the cementation properties in the DEM model may lead to the difference of the simulation results and the computational efficiency. The former two do a great to the computing time, but show a little influence on the elastic modulus of conglomerate. With the increase of meso particles, the UCS increase linearly first and then the growth rate decrease, while the UCS increase linearly continuously with loading rate of axial stress. Due to the different failure patterns such as cementation failure, matrix failure and gravel failure, the UCS of conglomerate changes a lot with the increase of cementation strength ratio. While the CSR is lower than 0.4, cementation failure occurred mainly. And then, both the matrix and gravel particles broken may occurred.

(4) A kind of simulating method for analyzing the mechanical properties of conglomerate and studying its influencing factor is proposed in this paper, the components and cementation properties of conglomerate can be considered, it is of great significance to the exploration of the physical and mechanical properties of the bottom rock in gravel layer.

REFERENCES

- Schmidt G. A, Pemberton S. G. 2004 Stratigraphy and paleogeography of a conglomeratic shoreline: the Notikewin Member of the Spirit River Formation in the Wapiti Area of westcentral Alberta. *Bull. Can. Petrol. Geol.* 52, 57–76.
- Rogers J. P. 2007 New reservoir model from an old oil field: Garfield conglomerate pool, Pawnee County, Kansas. *AAPG Bull.* 91, 1349–1365.
- Shafiei, A. and Dusseault, M. B. 2008. Geomechanical properties of a conglomerate from Iran. The 42nd US Rock Mechanics Symposium and 2nd U.S.-Canada Rock Mechanics Symposium, San Francisco, ARMA 08-053, 2008.
- Zheng Z. D. ROP. 2016. enhancement techniques in ultradeep exploratory wells in the piedmont area of Tarim Basin. Daqing: Northeast Petroleum University.
- Teng X. Q, Chen M, Yang P, et al. 2016. Whole well ROP enhancement technology for super-deep wells in Kuqa foreland basin. *China Petroleum Exploration*, 21(1): 76-88.
- Zhang D. R, Wen T., Lei P.U, et al. 2020. Pilot test on the ROP-improvement BHA of vertical drilling tool & screw rod with equal wall thickness: A case study on Well Keshen A in the high-steep structure of Kuqa piedmont area[J]. *Oil Drilling & Production Technology*, 42(06):684-690.
- Neng Y., Xie H. W., Sun T. R, Lei G. L, et al. 2013. Structural characteristics of Keshen segmentation in Kelasu structural belt and its petroleum significance. *China Petroleum Exploration*, 18(2):1-6.
- Tian J, Liu H. T, Teng X. Q, et al. 2019. Geology-engineering integration practices throughout well lifecycle in ultra-deep complex gas reservoirs of Kelasu tectonic belt, Tarim Basin. *China Petroleum Exploration*, 24(02):165-173.
- Teng X. Q, Liu H. T, Li N, et al. 2021. Technology Difficulties and Countermeasures of Automatic Vertical Drilling for Ultra-Deep Wells in Bozi Block of Tarim Basin[J]. *Petroleum Drilling Techniques*, 49(01): 11-15. (in Chinese))

- Wang Y. M, Liang H. J, Li G., et al. 2012. Characteristics of gravel layer in DB block Tarim and it's affection of fasten drilling. *Xinjiang Geology*, 30(1):113-115.
- Li N., Zhang S. C., Ma X. F., et al. 2017. Experimental study on the propagation mechanism of hydraulic fracture in glutenite formations. *Chinese Journal of Rock Mechanics and Engineering*, 36(10):2383-2392.
- Galarraga, C., Fierro, J. C., Al Riyami, I., et al. 2016. An Unconventional Fixed Cutter Cutting Structure Layout to Drill Through Hard, Abrasive Conglomerates in Deep Wells -A Case Study[C]// Abu Dhabi International Petroleum Exhibition & Conference.
- Rodriguez, R., Laguna, A., Caselles, M. G., et al. 2015. Durable Yet Aggressive Conical Diamond Element Bit Increases ROP by 34% Drilling Difficult Lower Chert/Conglomerate Section, Ecuador. *Society of Petroleum Engineers*.
- Jun W., Hualin L., Huajian W., et al. 2022. Experimental investigation on the dynamic tensile characteristics of conglomerate based on 3D SHPB system. *Journal of Petroleum Science and Engineering*, 213, 110350.
- Luo S. L, Ge H. K, Wang J. B, et al. 2021. Numerical simulation study on the crack propagation of conglomerate. *Royal Society*.
- Liu G, Cai M, Huang M. 2018. Mechanical properties of brittle rock governed by micro-geometric heterogeneity[J]. *Computers & Geotechnics*, 104(DEC.): 358-372.
- Akram M S. 2010. *Physical and Numerical Investigation of Conglomeratic Rocks*. New South Wales Australia Sydney: University of New South Wales.
- Satoru K, Hiroshi I, Kazuhiro K. 2010. Evaluation on Scale Effect of Conglomerate Core Sample and Disturbance by Core Sampling. *Journal of the Japan Society of Engineering Geology*, 39(4):391-400.
- Bing H., Chao Z., Dong C., et al. 2016. Prediction of Wellbore Stability in Conglomerate Formation Using Discrete Element Method. *Arabian Journal for Science and Engineering*, 42(4), 1609-1619.
- P.A. Cundall, O.D.L. 2019. Strack. A discrete numerical model for granular assemblies. *Geotechnique*, 29, 47-65.
- Potyondy, D.O., 2015. The bonded-particle model as a tool for rock mechanics research and application: current trends and future directions. *Geosystem Engineering* 18 (1), 1-28.
- Lei S. T, Kaitkay P. 2003. Distinct Element Modeling of Rock Cutting under Hydrostatic Pressure[J]. *Key Engineering Materials*, 250:110-117.
- Itasca Consulting Group, Inc, 2016. PFC (Particle Flow code in 2 and 3 Dimensions), version 5.0 [User's manual]. ICG, Minneapolis, MN.
- Zorlu K., Gokceoglu C., Ocakoglu F., et al. 2008. Prediction of uniaxial compressive strength of sandstones using petrography-based models. *Eng Geol* 96:141-158.
- International Society for Rock Mechanics (ISRM). 1978. Suggested methods for determining tensile strength of rock materials. *International Journal of Rock Mechanics and Mining Sciences and Geomechanics Abstracts*, 15(1): 99-103.

Modeling of the rock fracture mechanism caused by explosives using the Discrete Element Method.

H. F. González

Instituto de Ingeniería-UNAM, Ciudad de México, México

J. Sánchez

FES-Aragón-UNAM, Estado de México, México

G. Auvinet

Instituto de Ingeniería-UNAM, Ciudad de México, México

ABSTRACT:

Blasting used for rock excavations induces damage in two stages. First, they generate compression and tension waves, which cause the medium to break. Next, a large volume of gases expands, amplifying the fragmentation of the material and displacing the rock. To estimate the fracturing and the fragmented zone, an analysis based on the discrete element method (DEM) is presented. The rocky medium is represented by a set of circular particles joined together by a bonded contact model. The blasting is simulated with a particle expansion algorithm.

Through simulations, it is concluded that the results of the DEM are comparable with those of analytical criteria of rock damage and the models can reproduce the different behavior of the detonation when the pressure-time curve of the explosive changes. In addition, it is observed that the efficiency of the explosive is affected by the rock confinement, the distance between blastholes, and the detonation sequence in a drilling pattern.

1 INTRODUCTION

1.1 Introduction

In rock engineering, the energy of explosives is used to carry out excavations. During the explosion shock waves are created and a large volume of high-pressure gases are released in a very short period (thousandths of a second). The pressure generates compression strains (which fragment the rock) and stress fractures that propagate through the medium (Fakhimi & Lanri, 2013).

Improper blast design can cause unwanted damage to the excavation perimeter and jeopardize the stability of the excavation. Therefore, it is important to assess the damage that blasting causes to the rock mass. The fracturing mechanisms are not well understood; therefore, the methods of rupture analysis and damage location are mostly empirical (Bernaola *et al.*, 2013).

To estimate the blast damage in rock, commonly three zones that are generated by the explosion are considered: In the first (R_{crush}), the compressive stresses pulverize the rock around the blasthole, in a space approximately 3 to 7 times the radius of the blasthole; In the second (R_{crack}), the wave generates tangential tension stresses, creating radial fractures. These ruptures will continue to propagate if the stress exceeds the resistance of the rock, approximately 7 to 12 times the radius of the blasthole; In the third, the pressure wave energy decays due to the distance from detonation point (Oyanguren and Monge, 2004; Hoek and Brown, 1986).

To simulate the fracture mechanism and blast damage in the rock caused by the use of explosives, computational models have been used, most of them are continuous descriptions of the phenomenon, based on generalized laws of elasticity together with constitutive equations of the material. The results of these models are estimates of the damage resulting from the shock wave but cannot calculate the movement and separation of rock fragments (Potyondy & Cundall, 1996).

This article describes a methodology to simulate the fracturing of rocks, due to the detonation of explosives. In addition, the area of influence that the blast has in a rocky medium. Two-dimensional models are used with the Discrete Element Method (DEM), using a set of circular particles joined together. Blasting and the rocks damage due to propagation of stress waves are analyzed using the theory of continuum mechanics.

The analysis of rock damage caused by explosives focuses on the evolution of fractures and the estimation of the fragmented and fractured zone of the rock, according to the processes that occur in microseconds during the detonation of a blast. Likewise, the damage is evaluated by quantifying

the length of the fractures from the contour of a blasthole or the excavation section (area of influence of the blast), in addition to the persistence and density of the cracks.

2 SIMULATION OF THE INTACT ROCK AND PROPAGATION OF WAVES IN THE MEDIUM.

In the DEM, the models are made up of individual bodies, which can be rigid or deformable, these interact with each other in contact zones, which allows discontinuous phenomena such as cracking, large displacements and separation from the medium to be represented (Cundall and Hart, 1992; Potyondy and Cundall, 2004). Rock mass is a discrete material, and rock damage from blasting is a problem of displacement of all material. Therefore, the DEM can effectively simulate rock blasting.

2.1 *Intact rock modeling using DEM*

The Flat-Joint or FJ Contact Model assumes that the rock behaves as a bonded granular material, in which the bond is deformable and can break (completely or partially). It provides an interface between two theoretical flat cemented surfaces, which are rigidly connected to a portion of the particles that are in contact.

The behavior of an element bonded by FJ is linear elastic, it also assumes resistance to shear and tension, when these are exceeded, the element passes to a linear elastic and frictional behavior (non-bonded). Each contact admits a force and a moment. The entire interface of the FJ contact has a force-displacement response that arises from the union of all its bonded elements and their evolution to the non-bonded state.

This behavior model can reproduce friction angles in the material greater than 30° , ratios between compressive and tensile strength greater than 6, represent partial damage in the material (contacts may be partially broken) and increase in the material resistance with the increase in confinement (Potyondy, 2015; Castro-Figueira *et al.*, 2017). Due to this the FJ represents a tool for rock engineering and in this work, it was implemented.

In continuum models, the input properties can be taken directly from measurements made in the laboratory. On the other hand, for the Flat-Joint contact model in DEM, the behavior of the rock is represented from the interactions of the micro-components (grains and cement), whose micro-properties are not commonly known. The relationship between the parameters of the model and those of the material is found from an iterative calibration process where the micro-properties are adjusted to reproduce the relevant properties of the target material, measured in laboratory tests (Potyondy, 2017). In this paper, the properties of the FJ contact model (micro-properties) were calibrated from compression and Brazilian tests, provided by the Rock Mechanics Laboratory of the Federal Electricity Commission.

The two-dimensional models used for simulating simple and triaxial compression tests (Figure 1 a and b) are rectangular $0.06 \text{ m} \times 0.14 \text{ m}$, contain 6598 particles. On the other hand, the models used in the simulations of the Brazilian tests (Figure 1 c) are circular with a diameter of 0.06 m and contain 2309 particles. In all the models, the size of the grains obeys a uniform distribution of radii between 7.6×10^{-4} and 4.58×10^{-4} m.

After the iterative procedure calibration, in which comparison between the responses of simulation tests and laboratory test, the micro-parameter values calibrate were:

- Particle/ Linear contact: grain density = $2,340 \text{ kg/m}^3$; effective modulus = 20.5 GPa; friction coefficient = 0.4; and stiffness ratio = 2.3.
- Cement/ Flat-Joint contact: bond effective modulus = 20.5 GPa; bond stiffness ratio = 2.3; bond tensile strength = 8.8 MPa; bond cohesion = 59.98 MPa; and bond friction angle = 40° .

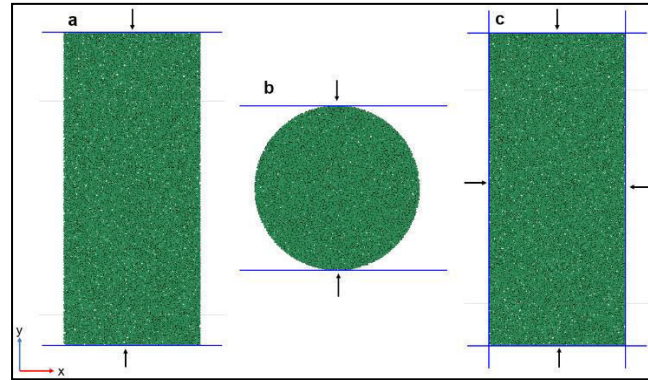


Figure 1. Numerical simulation tests: UCS test; b) Brazilian test; c) triaxial compression test

Table 1 compares the average resistance parameters of the rock obtained in the simulations and in the laboratory, with a relative error (E_r) in the range of 0 to 4% in all the results, with this an adequate adjustment is considered. Likewise, Figure 2 compares the adjustments to the Hoek-Brown criterion of the results of the compression tests (simulated and laboratory). From the curves it can be concluded that the Flat-Joint contact model accurately represents the resistant behavior of the rock tested at different confinements.

Table 1. Intact rock strength parameters obtained by laboratory and simulations.

Parameter	Laboratory	Simulation	E_r (%)
E	18.7 x109 [Pa]	18.5 x109 [Pa]	1.08
ν	0.24	0.24	0
σ_{ucs}	87.6x106 [Pa]	84.3 x106 [Pa]	3.91
σ_t	6.7x106 [Pa]	6.69x106 [Pa]	0.15

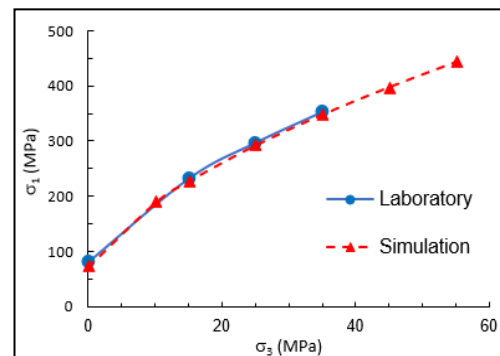


Figure 2. Adjustment of the Hoek-Brown criterion of the compression tests results

2.2 Simulation of wave propagation in DEM

To verify that the calibrated model will perform an adequate representation of wave propagation. In the models of the compression test specimens, a sinusoidal impulse was applied at one end and at the other the propagation velocity of the longitudinal wave was interpreted, whose value was also obtained theoretically. These were compared with that measured in the laboratory (sonic test). The relative error of the P-wave velocity between the value of the simulation and the laboratory value was 3.1% and between the theoretical value and the laboratory value was 22.1%.

Due to the discontinuous character in the DEM, the phenomenon of wave reflection can be represented. In this work, viscous boundary conditions are used that reduce or eliminate the influence of reflected waves on the model contour (Lysmer and Kuhlemeyer, 1969). The condition is applied as a force in the center of the particles that are part of the border by taking care that the number of selected grains is large enough to not have spaces without viscous condition in the boundary (equation 1).

Let F_{vis} the viscous force, C the wave velocity, ρ_r the density of the rock, v_n the n -particle velocity, r_n the n -particle radius, L the length of the boundary of the model y N_n the number of particles of the boundary.

$$F_{vis} = -\rho_r C v_n \left(\frac{L r_n}{\sum_i N_n r_i} \right) \quad (1)$$

In the largest model used in this work (12 m × 12 m), wave propagation simulations were carried out to verify that the use of boundary conditions was adequate and to analyze the behavior of wave

propagation in the different parts of the model, as well as possible changes in the speed of the P-wave, since the wave passes through more empty spaces that decrease its speed. The model consists in 263,578 particles, two types of simulations were carried out, in both a sinusoidal impulse was applied on the left side, while on the right side in one type of simulation the viscous boundary condition was imposed and in the other it was not. In addition, 9 wave velocity monitoring points were placed, three at the beginning, three in the middle and three at the end, with three different depths in the model (Figure 3).

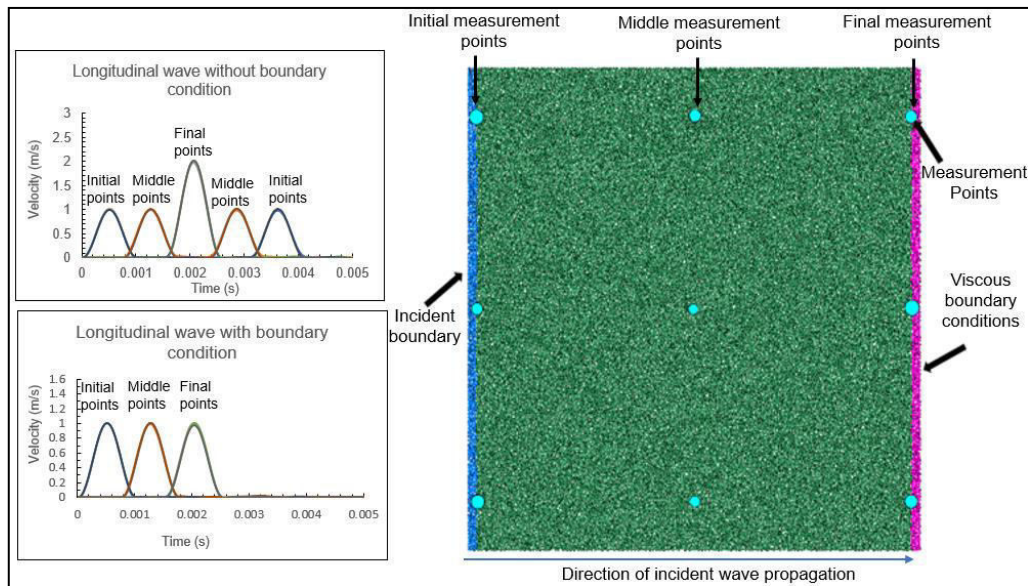


Figure 3. Wave propagation test

The wave propagation velocity in the model was 3,210 m/s at all depths, which is reasonable considering that the simulated material has the same physical and mechanical conditions in all directions. Comparing the value of the wave velocity of the complete medium with the theoretical and the laboratory values, it can be concluded that the model is reliable and has a reasonable representativeness of the medium.

The upper graph shows the results of wave velocity when there is no boundary condition, it is observed that the model adequately simulates the phenomenon of wave reflection, since after recording the velocity at the final point, velocity is recorded at the final point. medium. In the case of the lower graph, the results are shown when viscous boundary conditions are imposed, it is observed that it practically eliminates the wave reflection in the contour of the model, apart from that, the amplitude of this point is equal to that of the others, as if it would react with more medium, therefore, the boundary condition works properly, representing an infinite medium.

3 APPLICATION OF THE EXPLOSIVE LOAD.

3.1 Simulation of the explosive load

According to blasting theory, rock damage occurs in two stages. First, immediately after the detonation, the shock wave causes intense fracturing in the surroundings of the explosion point with minimal fragmentation in the contour of the blasthole, then a large volume of gases expands through the existing cracks, amplifying the fragmentation of the hole. material and displacing rock. The simulation of the explosion effect in models of bonded particles can be represented by two techniques. In the first, the shock energy and the gas energy are simulated separately. Shock pressure is applied indirectly to the particles in the blasthole boundary by an initial velocity, which is calculated using the law of conservation of momentum. Then, in the broken links (fractures) that have contact with the blasthole, either directly or because they form a network of cracks, where some are in contact with the blasthole, forces perpendicular and opposite to the fracture direction are applied, which are equivalent to gas pressure (Yang *et al*, 2019).

In the second simulation method, a particle expansion algorithm is used, in which an explosive particle is generated at the detonation point, it expands its diameter instantly. After expansion, an overlap is created between the explosive particle and the surrounding particles. As the particles and contacts are considered rigid, forces or moments will be generated, which push the surrounding particles in the opposite direction to the point of explosion (Zehua *et al.*, 2020; Xue *et al.*, 2022). Compared to the first, this simulation method requires less computing capacity, which significantly reduces simulation times, this allows representative analyzes to be carried out in models of more than one blasthole, including drilling patterns, for these reasons, in this work the particle expansion algorithm was used.

The forces generated by the expansion and superposition of the explosive particle must be equivalent to the pressure produced by the blasting in the blasthole contour. Equation 2 calculates the explosion pressure on the blasthole walls (P_b), considering the adiabatic expansion state theory of the explosives and the change in pressure due to uncoupled charges.

Let R_b and R_c be the radius of the hole and of the charge, respectively (mm), r the exponent of adiabatic expansion of the explosive (on average it is 1.5), v_d the detonation velocity and ρ_e the explosive density.

$$P_b = (((\rho_e)(v_d^2))/8) \left(\frac{R_c}{R_b}\right)^{2(r)} \quad (2)$$

To calculate the particle expansion (Figure 4), it assumes a particle with an initial radius (r_0), which will expand until it reaches the walls of the blasthole, this will cause pressure on the particles that the contour of the blasthole (P_b). The equation 3 and equation 4 determine the stiffness (k_{ne}) of the explosive particle (Zehua *et al.*, 2020). The density of the explosive used is 1,250 kg/m³ and the detonation velocity is 5,200 m/s, these values are kept constants for all simulations.

Let r_{max} and r_{min} be the maximum and minimum radius that the particle will have

$$d_r = \frac{P_b * 2 * r_0 * \pi}{k_n} \text{ and } k_{ne} = \frac{2 * P_b * (r_{max} + r_{min}) * \pi}{(r_{max} - r_{min})} \quad (3 \text{ and } 4)$$

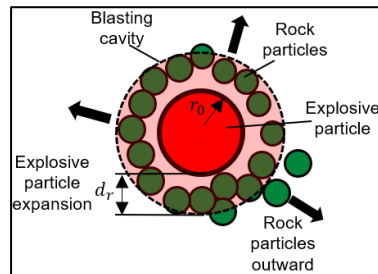


Figure 4. Schematic diagram of the charge explosion (modified from Zehua *et al.*, 2020)

The behavior of the explosion pressure is a function of time; therefore, the detonation could be ideal or non-ideal. The ideal detonation corresponds to explosives that mostly generate shock energy (high explosive), where the time of rising of the maximum detonation pressure (t_r) is very short and the pressure drop is very fast. Non-ideal detonation corresponds to explosives that produce higher gas energy, where the rise time to maximum detonation pressure is longer and the pressure drop is slow (compared to ideal detonation). In this work the t_r is represented with an exponential function as a function of time, a t_r of 2 ms was used (Yilmaz & Unlu, 2013).

3.2 Verification of the explosive model

In the detonation of a blasthole in a medium without discontinuities, the wave expands in a spherical way and as it moves away from the point of explosion it gradually weakens. In the case of having a free face, a crater is formed with an opening to the free zone and the expansion of the material will be in this direction (Saharan *et al.*, 2006).

Figure 5-a shows the force on the contacts after detonation in a blasthole in the center of a model without free surfaces. It is observed that stress waves are formed. As time passes, the wave is transmitted radially and attenuates as it recedes from the detonation point. Figure 5-b shows the velocity of the particles after the detonation of a blasthole, located 0.5 m from a free face. It is ob-

served that the material moves towards the free face, forming a crater with an opening towards it. These described behaviors are consistent with the physical phenomenon of a blast.

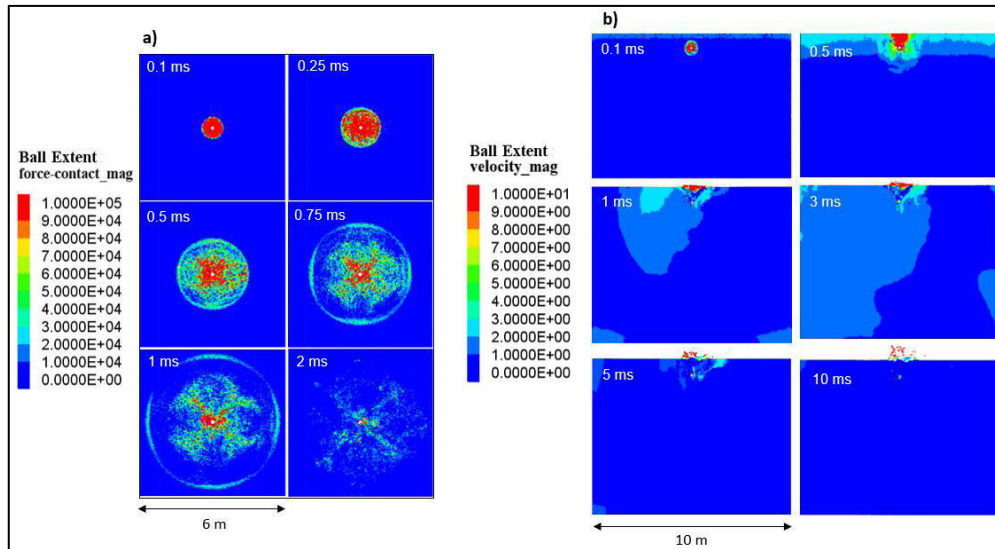


Figure 5. a) Blasting action, isotropic stress wave propagation; b) Blasting action, release of the material to the free face.

Compared to other simulation methods, the particle expansion algorithm has the advantage that the forces caused by blasting are distributed spherically. However, the effect of the shock wave and detonation gas cannot be reflected separately. To verify the reliability of the method, a detonation was simulated at a point in a 5 m × 10 m model, monitoring points for radial stress were placed at every 0.5 m in the longitudinal direction from the point of explosion (Figure 6). To obtain the shock wave attenuation curve, which was compared with the one obtained by the shock wave effort attenuation rule (equation 5).

Sea σ_r , the peak radial stress, R the radius of blasthole, d the distance away from the borehole and α coefficient of pressure attenuation.

$$\sigma_r = P_b \left(\frac{R}{d}\right)^{(-\alpha)} \tag{5}$$

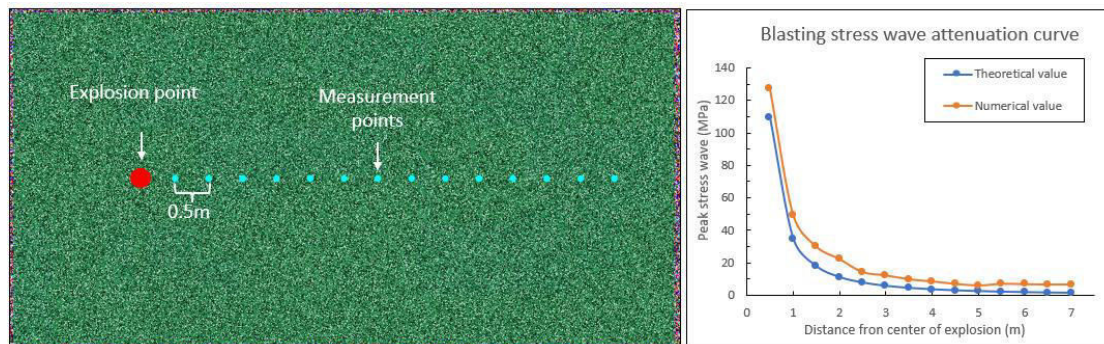


Figure 6. Blasting stress wave attenuation curve

Figure 6 shows that the numeric values of peak stresses were relatively close to the theoretical values, which proves the feasibility of simulating rock blasting through particle expansion algorithm.

4 RESULTS OF THE SIMULATIONS

The methodology to apply the explosive load was applied in different types of blasting simulations (in a blasthole and drilling patterns). Analyzed: the influence of the state of stress in the mate-

rial, the time of rising to the maximum detonation pressure, the damage in the rock (quantified by the R_{crush} and the R_{crack}), the influence of the separation between blastholes and the response of the rock to different detonation sequences.

In all the models, the red lines represent fractures (completely or partially broken contacts) and the white spaces represent areas void or cavities caused by blasting (areas without particles or with particles detached from the bonded set).

4.1 Influence of the rising time to maximum detonation pressure (t_r).

The detonation of a blasthole was simulated in a 3 m × 3 m model with 6 different rising times, it is worth mentioning that it was the only parameter that was varied. The graph in Figure 7 shows different Pressure-Time curves for different t_r . The graphs show that even though it is the same explosive and is simulated in the same way, the maximum detonation pressure decreases, and the pressure drop time is shorter as the t_r increases.

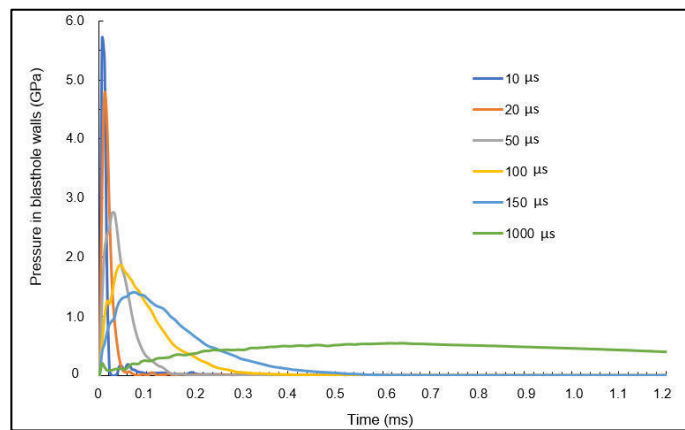


Figure 7. Rise time to maximum pressure in different types of explosions

Figure 8-a shows the change in the R_{crack} with the different t_r . As the t_r increases, R_{crack} is greater, therefore, the number of damaged contacts also increases. On the other hand, in Figure 8-b the R_{crush} decreases as the t_r increases. This shows that when t_r is higher, there is a change from a detonation that uses mostly the shock energy (causing large cavities and open fractures) to a detonation that uses mostly gas energy (generating large areas of fissures).

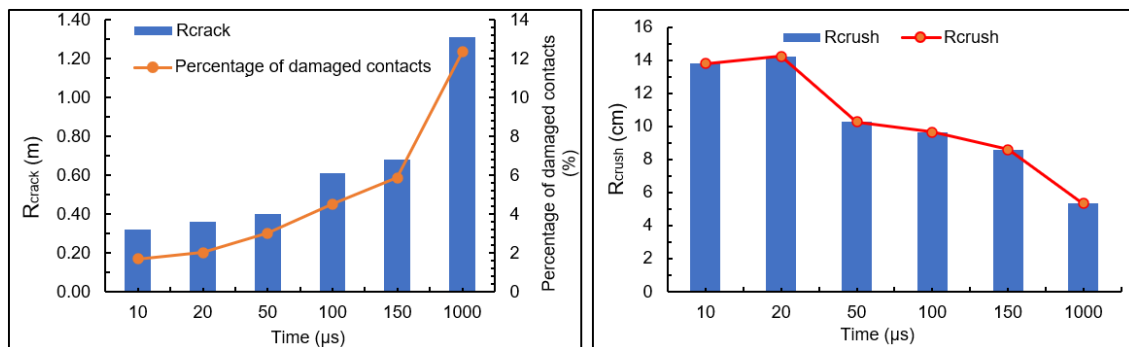


Figure 8. a) R_{crack} for different t_r ; b) R_{crush} for different t_r

4.2 Damage in a blasthole and comparison with traditional methods of blasting damage analysis.

The detonation of a blasthole is simulated in a 3 m × 3 m model with different states of isotropic stress and the damage in the blasthole contour is compared with the criteria of Dai (2002), Kumar (2016) and Austin-USA (2012), the last three are criteria to estimate the peak particle velocity (v_{pp}) at different distances from the detonation point, in them only the R_{crack} was calculated by means of the estimation of the critical v_{pp} .

The graphs in Figure 9-a show that the presence of confinement significantly influences the ex-

tension of the fractures. Since, these increase by 25% from when the model has 10 MPa of confinement to when there is not confinement. On the other hand, the explosive efficiency is lower as the stress state increases, since the fragmentation zone, the extension of the fractures, and the percentage of damaged contacts decrease as the confinement increases.

Comparing the R_{crack} and R_{crush} zones (Figure 9 a and b) estimated by DEM and by traditional methods, the fractured zone of the traditional methods gives values above a when there is a confinement of 10 MPa, however, they do not exceed the extension of fractures when there is not stress condition. In the case of R_{crush} , the value obtained by the Dai (2002) criterion is found at a midpoint between the fragmented zones of the models with confinements of 10 and 20 MPa.

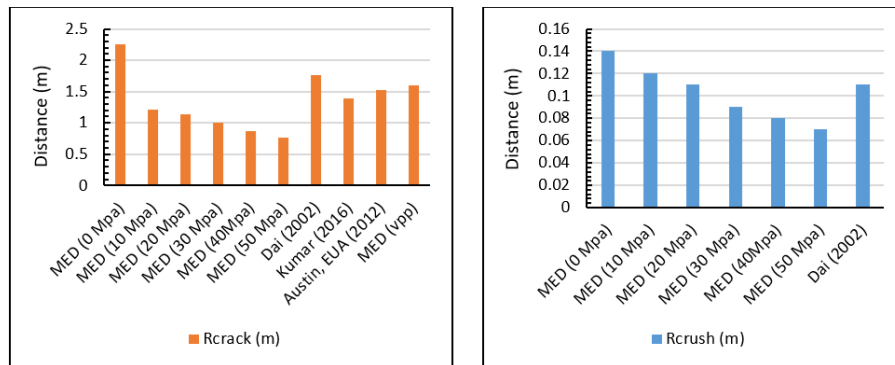


Figure 9. a) R_{crack} for different blasting damage analysis; b) R_{crush} for different blasting damage analysis

4.3 Influence of the separation between blastholes and sensitivity to delay between detonations.

Were simulated 11 models with two blastholes, in 5 models the distance between blastholes was varied (0.15 m, 0.25 m, 0.5 m, 0.75 m and 1 m) and in 6 the delay between detonations (0 ms, 5 ms, 10 ms, 15 ms, 20 ms, and 25 ms). The model used measures 8 m × 5 m and has 130,000 particles

From the simulations with different distances between blastholes, it was observed that as they are closer, the fractures are concentrated at the center of the distance between them, otherwise, the fractures of each blasthole extend in the opposite direction to the other blasthole. In agreement, with the explosive used in the models of this article, from a distance between blastholes of 0.75 m, no opening is formed between the two detonations (Figure 10-b, 0 ms).

Figure 10 shows the models with different detonation times, the distance between blastholes of 0.75 m was chosen, since, from this, there is not an opening between the two detonations. Figure 10-a shows that when there is a delay between detonations, the fractures are concentrated in the center of the blastholes. On the other hand, in Figure 10-b, there is an opening between the blastholes when there is a delay of 5 ms, even when there is a delay of 25 ms there is still an opening between the blastholes, unlike when the two detonate at the same time.

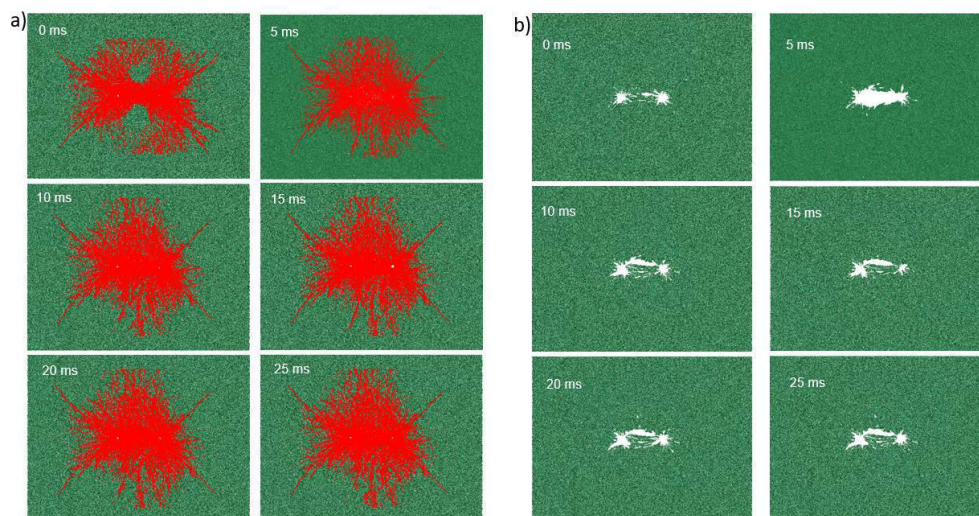


Figure 10. a) Fractures by different delays between detonations; b) Opening by different delays between detonations

4.4 Influence of the detonation sequence in drilling patterns

Four simulations were carried out with different detonation sequences in a drilling pattern, the model measures 12 m x 12 m and has 263,578 particles, a vertical stress of 10 MPa and horizontal stress of 15 MPa were imposed (Figure 11-a). The delays between sequences were 25 ms, because, in the analysis of delays between detonation, there was opening between blastholes with this delay and commercially there are delays of 25 ms.

The first simulation detonated all the blastholes at the same time, in the second the blastholes were detonated according to the numbering indicated in Figure 11-b (post-cutting). The third simulation was done with the same sequence as the second, with the difference that the contour blastholes were fired first (pre-cutting). The fourth simulation used the sequence indicated by the numbering in Figure 11-c (post-cutting).

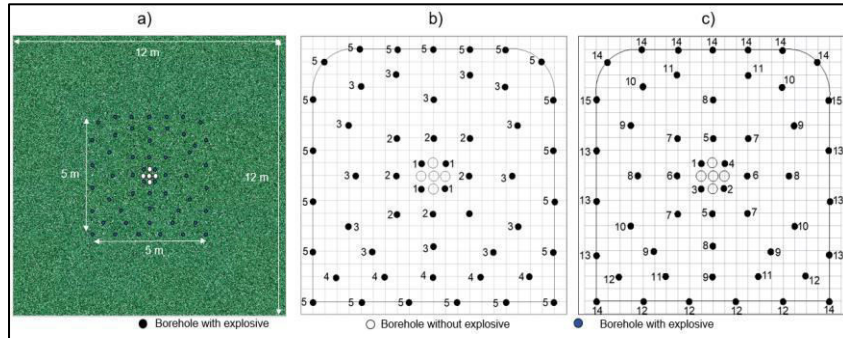


Figure 11. Drill pattern model with different detonation sequences.

Figure 12-a shows the simulation after detonating all the blastholes at the same time, it shows that the blasting did not achieve the excavation of the section, it had a lower number of broken contacts (fractures) compared to the other simulations.

Figure 12-b shows the excavation generated by the second simulation, it shows an outline with large blocks and areas that were not completely excavated. In the case of the fractures, these extended approximately up to 0.63 m from the designed contour of the excavation.

In the third simulation (Figure 12-c), a poor excavation was obtained, since the lower zone of the section was not completely fragmented. The fractures extended on average up to 0.83 m in the horizontal direction and 0.56 m in the vertical direction, from the designed contour of the excavation.

In the fourth simulation (Figure 12-d) a complete excavation of the section was obtained; however, the contour of the excavation was uneven, mainly in the gables and the floor. The generated fractures extended approximately 0.48 m from the designed perimeter of the excavation.

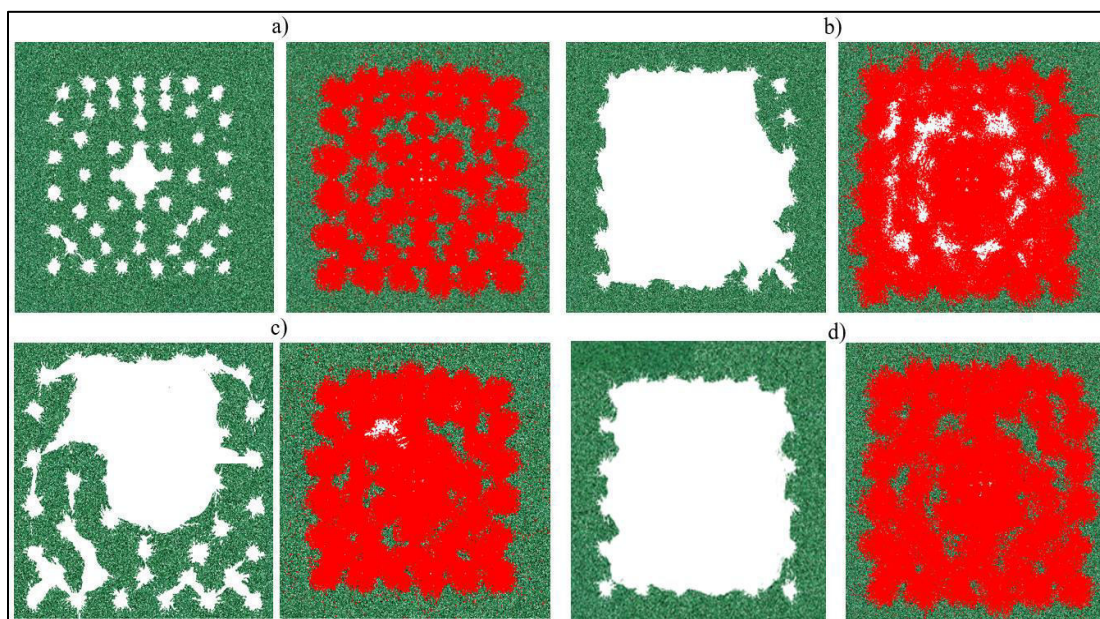


Figure 12. Models after blasting with different detonation sequences.

5 CONCLUSIONS

- The Discrete Element Method can simulate materials that presenting fractures, large displacements, relations between the compressive and tensile strengths greater than 6, an increase in resistance with increasing confinement and residual resistance, therefore, it is considered a tool for rock engineering.
- In this work, the models were calibrated with data from laboratory compression and tension tests.
- The simulations carried out to analyze the response of a medium formed by DEM to controlled impulses, allowed us to observe that these models can represent wave propagation, wave energy attenuation and reproducing the wave reflection phenomenon.
- Based on the relative error obtained from the comparison between the laboratory wave propagation velocity measurements with those of DEM and, those calculated with the continuous theory, it is concluded that the discontinuous models represent a better approximation than the theories that assume the medium as continuous.
- Comparing the results of monitoring the stress wave velocity in the blasting simulation, with values obtained through the stress wave attenuation law, it is concluded that the detonation phenomenon in the medium can be represented by particle expansion.
- Blast simulations through DEM can analyze rock damage with different rise time at maximum explosive pressure, confinement, distance between blastholes and different detonation sequences.
- The increase in rise time at maximum explosive pressure has directly influences changing an ideal detonation into a non-ideal one, so the damage to the material will be different, even when explosives with the same physical properties are simulated, therefore, to obtain correct results, it is important to know the t_r of the explosive. As the rise time increases, the fracture zone increases, and the fragmentation zone decreases.
- Through blasting simulations with different stress states, it was observed that the confinement to which the rock is subjected has an influence on the efficiency of the explosive. Well, the greater the confinement, the smaller the fracturing and fragmentation zones caused by the blasting.
- By blasting simulations with two holes, where different detonation times and distances between drilling were used. Was observed, that the smaller the distance between blastholes the fractures will be concentrated mostly in the center of them and the delay time between detonations increases the efficiency of the explosives.
- According the simulations with drilling patterns, underground blasting with pre-cutting techniques has greater fracturing in the direction of the major principal stress. On the other hand, blasting with post-cutting technique are more efficient, because theoretically having an empty space in the center, the minor principal stress is radial, and the major principal stress is tangential to the excavation. Fractures open easily in a direction perpendicular to the minor principal stress, therefore, cracking is mostly concentrated between the contour boreholes.
- With the results of the drilling patterns with different detonation times, it is concluded that through the DEM it is possible to analyze drilling patterns with different detonation sequences.
- Through simulations with different detonation sequences, it was shown that these influence the quality of the excavation. Since, the simulations where the detonation was allowed to detonate piecemeal from the center of the tunnel to the edge, had a better-excavated section.
- In other investigations, the changes in the excavations with different geometric arrangements of blastholes should be analyzed, in addition, to extend the analyzes presented in this article to three dimensions

6 REFERENCIAS

- Bernalao, J., Castilla, J., & Herrera, J. (2009). *Perforación y voladura de rocas en minería*. Madrid, España: Universidad Politécnica de Madrid.
- Castro-Filgueira, U., Alejano, L., J.Arzuá, & Mas-Ivars, D. (2017). Sensitivity Analysis of the Micro-Parameters Used in a PFC Analysis Towards the Mechanical Properties of Rocks . *Procedia Engineering*, 191, 488-495.

- Cundall, P., & Hart, R. (1992). Numerical modelling of discontinua. *Engineering Computations*, Vol. 9, 101-113.
- Dai, J. (2002). *Rock Dynamics and blasting theory*. China: Metallurgical Industry Press.
- Fakhimi, A., & Lanari, M. (2013). *DEM-SPH simulation of rock blasting*. London, United Kingdom: Mc Graw Hill.
- Hoek, E., & Brown, E. (1985). *Underground excavations in rock*. London, United Kingdom: Mc Graw Hill.
- Konya. (1990). *Manual de Voladuras*. EUA: ESING.
- Kumar, H., Kumar, N., Singh, M., & Venkat, V. (2014). Blast induced damage to surrounding rock mass underground excavation. *Journal of Geological Resource and Engineering*, 13-19.
- Lysmer, J., & Kuhlemeyer, R. (1969). Finite dynamic model for infinite media. *Journal of engineering mechanics, ASCE -95*, 859-877.
- Oyanguren, P. R., & Monge, L. A. (2004). *Mecánica de Rocas: Fundamentos e Ingeniería de Taludes*. Madrid, España: Universidad Politécnica de Madrid.
- Potyondy, D. (2015). The bonded-particle model as a tool for rock mechanics research and application: current trends and future directions. *Geosystem Engineering*, EUA.
- Potyondy, D., & Cundall, P. (1996). *Modeling of shock and gas driven fractures induced by a blast using bonded assemblies of spherical particles*. Minneapolis, EUA: Itasca consulting group.
- Potyondy, D., & Cundall, P. (2004). A bonded-particle model for rock. *International Journal of Rock Mechanics and Mining Sciences*, 1329-1364.
- Saharan, M., Mitri, H., & Jethwa, J. (2006). Rock fracturing by explosive energy: review of state-of-the-art. *Fragblast: International Journal for Blasting and Fragmentation Vol. 10*, 61-81.
- Sun, C. (2013). *Damage zone prediction for rock*. Utah, EUA: Universidad de Utah.
- Xue, Y., Jiang, X., Kong, F., Li, Z., Gong, H., Yang, F., & Chen, H. (2022). Rupture of rock with discontinuities under blasting disturbance: Insights from discrete element method modeling. *Simulation Modelling Practice and Theory* 116.
- Yang, J., Shi, C., Yang, W., Chen, X., & Zhang, Y. (2019). Numerical simulation of column charge explosive in rock masses with particle flow code. *Granular Matter*.
- Yilmaz, O., & Unlu, T. (2013). Three dimensional numerical rock damage analysis under blasting load. *Tunnelling and Underground Space Technology, Vol. 38*, 266-278.
- Zehua, Z., Wenle, G., Kunpeng, L., & Baojie, L. (2020). Numerical simulation of rock mass blasting using particle flow code and particle expansion loading algorithm. *Simulation modelling practice and theory*, 102-119.

Mechanical characterization of synthetic carbonate rocks for application in oil reservoir analysis

Y.R.P. Santos

Federal University of Pernambuco, Recife, Brazil

A.F.L. Amorim

Federal University of Pernambuco, Recife, Brazil

I.F. Gomes

Federal University of Pernambuco, Recife, Brazil

ABSTRACT:

This research aims to present the preparation and mechanical characterization of a synthetic carbonate porous medium for application in oil reservoir Analysis. Eight samples of synthetic carbonate rock were prepared with dimensions of 8 x 4 cm (height x diameter), using a proportion of 85% limestone powder and 15% epoxy resin, consolidated through the compaction process at 20 MPa and oven dried at 60°C for 24 hours. Then, rocks produced were been instrumented and submitted to Unconfined Compressive Strength tests (UCS), where the stress-strain behavior, Young's Modulus (E) and Poisson's coefficient were determined. Among the results obtained, the synthetic rock presented maximum compressive strength of 86.92 MPa, with an average UCS of 80.20 MPa, in addition to average values of Young's Modulus and Poisson's ratio of 7.28 GPa and 0.34, respectively. It is observed through the values presented, that these do not present great variations if compared with data extracted from analyzes of natural rocks, indicating a greater homogeneity and meeting one of the objectives of the preparation of synthetic porous media, which aims at a repeatability for a better understanding of rock-fluid interactions, which can be applied in analyzes that simulate processes involving oil wells.

KEYWORDS: Synthetic rocks. Unconfined Compressive Strength test. Young's Modulus. Poisson's ratio.

1 INTRODUCTION

The oil industry aims a large part of its resources to the exploration and production of hydrocarbons (oil and natural gas), stored in reservoir rocks (such as sandstones and carbonates), in order to guarantee and meet the growing world energy demand.

Although there is interest in knowing the behavior and properties of reservoir rocks to explore new areas and increase the extraction/production of hydrocarbons, analyzes on natural rocks are complex, due to the high cost of their extraction, as well as because of the present high heterogeneity in their characteristics, making it difficult to analyze their behavior; for this, studies advance in the design of synthetic porous media that aim to represent, in an analogous way, the structure and characteristics of these natural specimens, using different methodologies of preparation and consolidation for their synthesis.

The combination of analogous materials and cementing/binding agents are usually studied for the representation of rock matrices. Among them, the use of sand (Wang et al., 2008; Tillotson et al., 2012; Melo, 2012; Guo et al., 2016; Oliveira, 2016; Ding et al., 2017; Yu et al., 2020) and rock powder (Wang et al., 2015; Wang et al., 2017) as analogous solid materials; Portland cement (Santos et al., 2017; Fedrizzi et al., 2018; Shakiba et al., 2020; Galindo et al., 2021) and epoxy resin (Wang et al., 2015; Guo et al., 2016; Wang et al., 2017; Mohammed & Schmitt, 2020; Yu et al., 2020) are commonly used as binding materials.

As for the methodologies used for the preparation and consolidation of the synthetic samples, consolidation using a compressive stress is the most used, followed by heat treatment in an oven

or muffle, according to the material adopted. Hussein & Vanorio (2015), Wang et al. (2015), Guo et al. (2016), Santos et al. (2017), Wang, et al. (2017), Fedrizzi et al. (2018), Mohammed & Schmitt (2020), Yu et al. (2020), Galindo et al. (2021) use a compressive stress to consolidation in molds of different geometries, and then submit the samples to heat treatment in an oven for periods ranging from 12 to 24 hours with temperatures between 65°C (Mohammed & Schmitt, 2020) and 100°C with increments of 25°C until reaching 300°C (Fedrizzi et al., 2018).

Studies are been focused on establishing information about petrophysical properties, such as porosity and permeability (Santos et al., 2017; Fedrizzi et al., 2018; Shakiba et al., 2020); electrical conductivity (Mohammed & Schmitt, 2020), dielectric anisotropy (Ding et al., 2017), mechanical properties after chemical dissolution effects (Shakiba et al., 2020; Galindo et al., 2021) changes in wettability (Yu et al., 2020) of these rocks; Shakiba et al. (2020) also state that the production of synthetic samples allows controlling properties such as porosity, permeability and compressive strength, in order to help petroleum engineering in understanding the interrelationships between the physical and geomechanical parameters of reservoir rocks under different conditions and for different hydrocarbon production processes.

Due to the importance of theme, this study presents the development of carbonate synthetic rocks produced from rock powder from analogous reservoirs and epoxy resin and, its subsequent mechanical characterization, for expansion on studies related to the oil reservoir, in order to contribute to applications in analyzes involving oil wells.

2 EXPERIMENTAL PROCEDURE

2.1 *Materials*

The production of synthetic carbonate rocks used as materials a mixture of epoxy resin as a cementing/binding agent and carbonate rock powder from an analogous outcrop (solid matrix).

As cementing/binding material, epoxy resin was chosen, used in the literature (Wang et al., 2015; Guo et al., 2016; Wang et al., 2017; Mohammed & Schmitt, 2020; Yu et al., 2020) for presenting satisfactory results in the agglutination of the particles used and in the ease of application.

Low viscosity transparent epoxy resin 2004 with hardener 3154 from Redelease® was used, with use in a 2:1 ratio (resin:hardener). According to producer, the product has high chemical and mechanical resistance, low contraction, good adhesion, stability to thermal cycles and impacts, good fluidity and does not release by-products in its use.

The rock powder comes from laminated limestone outcrops (carbonate deposits) located on the northern edge of the Araripe Basin, between the cities of Santana do Cariri and Nova Olin-da, in the state of Ceará, and are exposed on pavements and vertical surfaces, with 25 meters high and hundreds of meters of side exposure. These deposits can be considered as rocks analogous to the carbonate interval of the pre-salt reservoir of the marginal basins of southeastern Brazil, in petrophysical, depositional and geochronological terms (Santos et al., 2015).

Carbonate outcrops were collected in small blocks (Figure 1(a)), and taken to be fragmented into smaller pieces through a jaw crusher. Then, the material was pulverized with the disc mill in successive portions for 40 seconds, until reaching the desired granulometry for this step. Finally, the collected material that turned into powder was sieved, selecting all the analogous carbonate powder passing through the sieve with a 425 µm (Figure 1(b)) for synthetic rocks production.

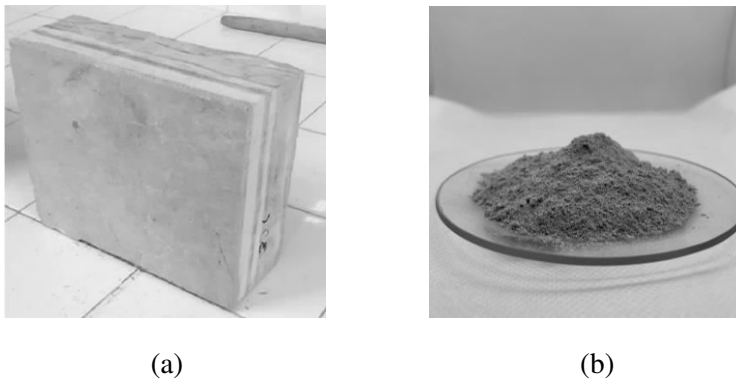


Figure 1. (a) Limestone rock block and; (b) powdered limestone rock ($< 425 \mu\text{m}$).

2.2 Sample Production

The synthetic rock samples were been prepared through the compaction process, a procedure used in the production of synthetic porous media described by Hussein & Vanorio (2015), Wang et al. (2015), Guo et al. (2016), Ding et al. (2017), Santos et al. (2017), Wang et al. (2017), Fedrizzi et al. (2018), Mohammed and Schmitt (2020), Yu et al. (2020) and Galindo et al. (2021), which consists of applying a load to the prepared material that is placed inside a metal mold until it is consolidated.

The amounts of epoxy resin used for preparation indicated in the literature vary – 20% used in Wang et al. (2015) and Wang et al. (2017), 15% used in Guo et al. (2016), 10% used in Yu et al. (2020), for example; a proportion of 85%:15% (solid matrix:binder) was been chosen, 85% of analogous carbonate powder and 15% of epoxy resin for samples with 8 cm in height, 4 cm in diameter and volume of 100.53 cm^3 , dimensions of the cylindrical mold used to consolidate the samples, establishing different quantities of materials, in order to adjust and establish a specific weight value that would make it possible to prepare samples with initial height and appearance consolidated, without superficial voids and irregularities along its extension.

The resin and hardener were previously mixed according to the recommendations, and then mixed with the analog powder, until the mixture becomes homogeneous, not allowing long periods of mixing, due to the rapid hardening reaction of the epoxy. The mixture was then sieved through a sieve to break up the larger lumps of remaining material, leaving the preparation uniform. The synthetic rocks were molded in a metallic cylindrical mold, consisting of a base, body and extender.

The preparation was placed in the cylindrical mold, which is internally coated with a thin layer of release agent (solid Vaseline) to facilitate sample extraction. The collar (extender), on the other hand, ensures that the material is placed in a single layer in the mold which, as it is still in the loose state, occupies a volume greater than sample volume. The mixture was compacted in a single layer, using a compression press with a capacity of 50 kN at 20 MPa, until the sample reached the pre-established height, leaving the compaction stress applied for 10 minutes. Filter paper discs were placed at the base and top so that a possible material portion does not adhere to the mold during compaction.

The sample was removed from the mold and taken to the oven at a temperature of 60°C (recommended by the resin manufacturer) for a period of 24 hours, to complete its consolidation.

2.3 Mechanical characterization tests

Eight synthetic samples were been tested for their mechanical properties through the protocols established by the UCS (Unconfined Compressive Strength) tests, which consists of applying a uniaxial compressive load on longitudinal direction until sample rupture, followed the procedures described by ASTM D2938-95 (2002). Cylindrical samples were molded respecting the recom-

mended minimum height: diameter ratio of 2:1 (8:4 cm) and tested using a servo-controlled hydraulic compression press with 1000 kN of capacity, with a constant speed of 0.122 mm/min.

The measurements of axial and radial displacements of the samples were recorded through instrumentation, using extensometers installed in appropriate positions for such readings, to determine the axial and radial deformations, in addition to evaluating the stress behavior versus axial deformation presented by the sample during execution.

With the applied load, and the section area, it is possible to determine its Unconfined Compressive Strength (UCS), through Equation 01:

$$UCS = \frac{F}{A} \quad (1)$$

where UCS (MPa) = Unconfined Compressive Strength; F (kN) = applied load and; A (cm²) = section area.

Correlating the dimensions of the sample with its axial and radial deformation, Poisson's ratio (ν) of the rock is determined, through Equation 02:

$$\nu = -\frac{\Delta e / e_0}{\Delta l / l_0} \quad (2)$$

where ν = Poisson's Ratio; Δe (mm) = radial displacement; e_0 (mm) = initial diameter; Δl (mm) = longitudinal displacement; l_0 (mm) = initial height.

From the stress versus strain behavior curves, it is possible to determine the average Young's Modulus (E), corresponding to the elastic stretch of the curve (equal to the slope of the secant line between the origin and the rupture point), according to Equation 03:

$$E = \frac{\sigma}{\varepsilon} \quad (3)$$

where E (Pa) = Young's Modulus; σ (Pa) = axial stress; ε = axial strain.

The mechanical characterization was based on the analysis of the stress x strain curves of the samples, as well as the mechanical parameters obtained through equations 01, 02 and 03, correlating such information.

3 RESULTS AND DISCUSSION

To define the quantities necessary for the production of an artificial carbonate rock, a mixture of analogous rock powder:resin in the proportion 85%:15% with a total mass of 191g (162.35g of rock powder and 28.65 g of resin), quantity necessary to occupy the mold to be used for preparation, obtaining a specific weight of 19 kN/m³; however, it was noticed that, for the used compaction energy of 20 MPa, the samples presented height less than 8 cm (height of the mold) and irregularities in their surface, being necessary to add material so that they reach the specifications of reference (samples with a height:diameter ratio equal to 2), meeting the requirement of sample dimensions for UCS tests.

After material increments, samples with mass proportions equal to 196.54 g of analogous carbonate powder and 34.68 g of epoxy resin mixture 2:1 (23.12 g of g of resin and 11.56 g of hardener) were defined as the synthetic porous medium for this research and in a percentage of 85%:15%, guaranteeing the reference specifications established at the beginning of the research, obtaining, at the end, a specific weight between 22 and 23 kN/m³. Figure 2 shows the synthetic rock produced.

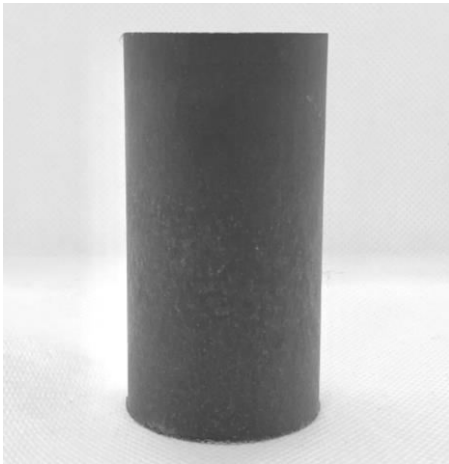


Figure 2. Synthetic carbonate rock sample with 8:4 cm (height:diameter 2:1).

These quantities were been adopted for preparation of eight samples to be submitted to UCS tests to obtain mechanical parameters. Table 1 presents the identification of the prepared samples, with their dimensions (cm) and specific weight (kN/m³).

Table 1. Dimensions and specific weight of samples.

Sample	height:diameter (cm)	γ_s (kN/m ³)
AM-01	8:4	22.39
AM-02	8:4	22.41
AM-03	8:4	22.34
AM-04	8:4	22.56
AM-05	8:4	22.52
AM-06	8:4	22.63
AM-07	8:4	22.79
AM-08	8:4	22.48

During preparation, it was noticed that a small portion of material was lost during the mixing of materials, being retained in the containers used for preparation; as a result, there is a variation in specific weight of the specimens, ranging between 22.34 and 22.79 kN/m³.

3.1 Mechanical characterization of artificial carbonate rocks

The strength of the synthetic samples was been analyzed using the unconfined compressive strength test (UCS), in order to evaluate mechanical parameters for its characterization. For this, eight samples were prepared following the previously mentioned experimental procedure and subjected to UCS test conditions until rupture. During the test, for each predefined axial displacement of 0.1 mm measured by means of an extensometer, the corresponding load was recorded; in addition, its radial displacement corresponding to the center of the samples was collected using extensometers, also at each corresponding load at the time of the axial displacement readings.

Table 2 presents Maximum strength (UCS_{max} - MPa), corresponding to rupture, Young's Modulus E (GPa) and Poisson's Ratio (ν) of sample tested. Figure 3 shows the behavior of the samples during the UCS test, relating the applied stress (MPa) versus the specific axial strain (%) to which they were subjected.

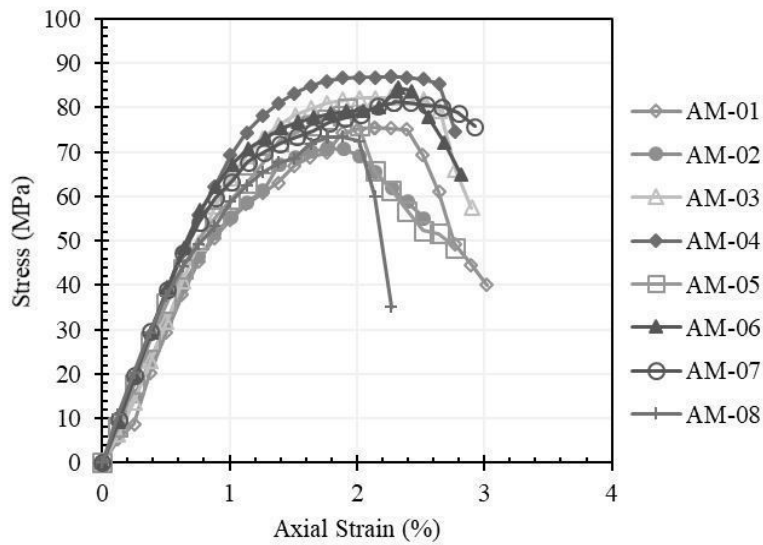


Figure 3. Stress versus axial strain (%) of samples during UCS tests.

Table 2. Maximum Strength, Young's Modulus and Poisson's ratio of samples.

Sample	UCS _{max} (MPa)	E (GPa)	ν
AM-01	75.56	6.62	0.32
AM-02	71.00	6.66	0.28
AM-03	82.41	7.19	0.34
AM-04	86.52	7.84	0.29
AM-05	79.75	7.24	0.34
AM-06	84.46	7.79	0.35
AM-07	81.25	7.54	0.42
AM-08	73.40	7.34	0.37
AVERAGE	80.20	7.28	0.34

Maximum strength values of 86.92 MPa are observed among the samples, with an average UCS equal to 80.20 MPa, being classified, according to the ISRM (1981), as a hard rock, as they present values of compressive strength between 50 and 100 MPa. It was observed that the samples had a defined rupture plane in their central portion, as shown in Figure 4.



Figure 4. Rock after UCS test, with defined rupture plane.

It is noted that the UCS values found for the synthetic rocks produced are high, if compared with the values obtained by Melo (2012), Oliveira (2016), Shakiba et al. (2020) and Galindo et al. (2021) for artificial carbonate rocks; with this, the porous medium produced can represent, from a mechanical point of view, reservoir rocks that present high mechanical strength.

Young's Modulus (E) varied between 6.62 GPa and 7.84 GPa, with an average value of 7.28 GPa; Poisson's ratio (ν) varied between 0.28 and 0.42, with an average value of 0.34, expected values for porous media.

As for the stress versus axial strain behavior presented by the curves, an elastoplastic behavior is observed (beginning of the curve with linear tendency - elastic - followed by a yield level with permanent strain - plastic), with maintenance of behavior in elastic region of the curves with similar slopes, which is reflected in Young's Modulus values (E), whose calculation criterion took into account the average slope of the linear portion of this region, generating similar values for this property .

It is observed that the materials and the methodology used for rock preparation provided high strength in maximum and average terms, due to the compaction energy used and the binding/cementing properties of the epoxy, promoting a high cohesion between the particles, in addition to E and ν values close to those observed for natural carbonate rocks, indicating a satisfactory representativity, from a mechanical point of view.

It is noteworthy that, given the values presented, these do not present great variations if compared with data extracted from analyzes of natural rocks, indicating a greater homogeneity and meeting one of the objectives of the preparation of synthetic porous media, which aims at repeatability for a better understanding of rock-fluid interactions in oil reservoirs.

4 CONCLUSIONS

The methodology used for synthetic rocks preparation is shown to be adequate, evidenced by the consolidation of the produced samples, without surface irregularities, maintenance in their dimensions and by the achieved repeatability having been satisfactory, desirable when developing means synthetic porous materials for understanding the phenomena of rock-fluid interaction and corroborated by the similarity in the behavior of the stress versus axial strain curves) and by the proximity between the values of simple compressive strength (UCS) obtained by tests.

The proportions adopted between the analogous rock powder and the epoxy as a binding material for preparation proved to be favorable for the mechanical strength, representing a hard rock when reaching values in the range between 80 - 90 MPa (in proportion 85%:15%), this strength are superior to the values commonly found in the literature for synthetic carbonate rocks.

Such characteristics confirm that the combination of the preparation methodology and the materials used can be adopted for synthetic rocks production for purposes of analysis involving oil reservoir rocks, being able to evaluate, for example, their interaction with heterogeneities present in these porous media and their interaction with fluids used during hydrocarbons production.

5 REFERENCES

ASTM D2938-95. 2002. *Standard Test Method for Unconfined Compressive Strength of Intact Rock Core Specimens* (Withdrawn 2005), ASTM International, West Conshohocken, PA.

- Ding, P.; Di, B.; Wang, D. Wei, J.; Li, X. 2017. Measurements of Seismic Anisotropy in Synthetic Rocks with Controlled Crack Geometry and Different Crack Densities. *Pure Appl. Geophys.* 174, 1907–1922. <https://doi.org/10.1007/s00024-017-1520-3>
- Fedrizzi, R.M.; Ceia, M. A.R.; Misságia, R.M.; Santos, V.H.; Lima Neto, I. 2018. Artificial carbonate rocks: Synthesis and petrophysical characterization, *Journal of Petroleum Science and Engineering*, Volume 163, Pages 303-310, ISSN 0920-4105, <https://doi.org/10.1016/j.petrol.2017.12.089>.
- Husseiny, A.E. & Vanorio, T. 2015. The effect of micrite content on the acoustic velocity of carbonate rocks, *Geophysics*, Volume 80, ISSN 1942-2156, <https://doi.org/10.1190/geo2014-0599.1>.
- Galindo, K.; Guimarães, L.; Lins, C.; Lima, A.; Santos, Y.; Gomes, I. 2021. Minerals Dissolution Effect on the Mechanical Properties of Synthetic Carbonatic Rocks under a Reactive Fluid Injection, *ASRJETS Journal*, ISSN 2313-4402.
- Guo, Y.; Hu, J.; Zhang, X.; Feng, R.; Huabing L. 2016. Flow Behavior Through Porous Media and Microdisplacement Performances of Hydrophobically Modified Partially Hydrolyzed Polyacrylamide. *SPE Journal*, Volume 21: 688–705. doi: <https://doi.org/10.2118/178921-PA>.
- International Society for Rock Mechanics. 1981. *Rock characterization, testing & monitoring: ISRM suggested methods*. Oxford: Published for the Commission on Testing Methods, International Society for Rock Mechanics, editor Brown, E. T. & by Pergamon Press.
- Melo, L.M.P. 2012. *Numerical-experimental analysis of synthetic carbonate rocks subjected to the injection of a reactive fluid*. Dissertation (Master in civil engineer) – Federal University of Pernambuco, Recife.
- Mohammed, T.E. & Schmitt, D.R. 2020. Preliminary experiments towards understanding the influence of fractures on the anisotropy of electrical conductivity, *Journal of Applied Geophysics*, Volume 182, 104197, ISSN 0926-9851, <https://doi.org/10.1016/j.jappgeo.2020.104197>.
- Oliveira, A.D. 2016. *Analysis of physicochemical changes resulting from dissolution tests in synthetic carbonate rocks*. Dissertation (Master in civil engineer) – Federal University of Pernambuco, Recife.
- Santos, L.K.; Figueiredo, J.J.S.; Macedo, D.L.; Melo, A.L.; Silva, C.B. 2017. A new way to construct synthetic porous fractured medium, *Journal of Petroleum Science and Engineering*, Volume 156, Pages 763-768, ISSN 0920-4105, <https://doi.org/10.1016/j.petrol.2017.06.044>.
- Santos, R.F.V.C; Miranda, T.S.; Barbosa, J.A.; Gomes I.F.; Gabriel, G.C.; Gale, J.F.W.; Neumann, V.H.L.M.; Guimarães, L.J.N. 2015. Characterization of natural fracture systems: Analysis of uncertainty effects in linear scanline results, *AAPG Bulletin*, v. 99, n. 12, p. 2203–2219.
- Shakiba, M.; Khamehchi, E.; Fahimifar, B.; Dabir, B. 2020. An experimental investigation of the proportion of mortar components on physical and geomechanical characteristics of unconsolidated artificial reservoir sandstones, *Journal of Petroleum Science and Engineering*, Volume 189, 107022, ISSN 0920-4105, <https://doi.org/10.1016/j.petrol.2020.107022>.

- Tillotson, P.; Sothcott, J; Best, A.I.; Chapman, M. & Li, X-Y. 2012. Experimental verification of the fracture density and shear-wave splitting relationship using synthetic silica cemented sandstones with a controlled fracture geometry. *Geophysical Prospecting*, 60: 516-525. <https://doi.org/10.1111/j.1365-2478.2011.01021.x>.
- Yu, H.; Gong, L.; Qu, Z.; Hao, P.; Liu, J.; Fu, L. 2020. Wettability enhancement of hydrophobic artificial sandstones by using the pulsed microwave plasma jet, *Colloid and Interface Science Communications*, Volume 36, 100266, ISSN 2215-0382, <https://doi.org/10.1016/j.colcom.2020.100266>.
- Wang, R.; Chen, Z.; Jishun, Q.; Zhao, M. 2008. Performance of Drainage Experiments With Orinoco Belt Heavy Oil in a Long Laboratory Core in Simulated Reservoir Conditions. *SPE Journal*, 13: 474–479. doi: <https://doi.org/10.2118/104377-PA>.
- Wang, Z.; Wang, R.; Li, T.; Zhao, M. 2017. The combined effects of pore structure and pore fluid on the acoustic properties of cracked and vuggy synthetic rocks, *Journal of Petroleum Science and Engineering*, Volume 156, Pages 202-211, ISSN 0920-4105, <https://doi.org/10.1016/j.petrol.2017.05.023>.
- Wang, Z.; Wang, R.; Wang, F.; Qiu, H.; Li, T. 2015. Experiment study of pore structure effects on velocities in synthetic carbonate rocks, *Geophysics*, Volume 80, ISSN 1942-2156, <https://doi.org/10.1190/geo2014-0366.1>.

Comprehensive in-situ stress estimation for a fractured geothermal reservoir from drilling, hydraulic stimulations, and induced seismicity

S. Park

Korea Institute of Geoscience and Mineral Resources, Daejeon, Republic of Korea

K. I. Kim

Korea Atomic Energy Research Institute, Daejeon, Republic of Korea

H. Yoo, J. Yim, K. B. Min*

Seoul National University, Seoul, Republic of Korea

*Corresponding author (e-mail: kbmin@snu.ac.kr)

ABSTRACT:

In November 2017, a M_w 5.5 earthquake occurred in vicinity of the geothermal development site in Pohang, South Korea. The Korean government-appointed investigation commission concluded that the earthquake was affected by a series of hydraulic stimulations conducted at the geothermal development site. In spite of its critical importance, the previously suggested stress models for the Pohang geothermal site had large discrepancies, based on limited number and types of stress-indicating data and each different stress estimation approach. In this study, a comprehensive in-situ stress estimation was conducted for the target depth of the enhanced geothermal system development site in Pohang, South Korea, based on variety of direct and indirect in-situ stress indicators collected from drilling, logging, hydraulic stimulations, and induced seismicity data. The stress magnitudes and orientations are suggested as well as the possible range of friction coefficient of the dominant fault structures at the site. The stress model of this study well explains the characteristics of the Pohang earthquake in terms of the slip direction and the slip tendency of the mainshock fault, and can be used for various studies clarifying the causal mechanism of the Pohang earthquake, thus providing an insight for fault stability analysis and geo-energy development applications in the southeastern part of the Korean Peninsula.

1 INTRODUCTION

An enhanced geothermal system (EGS) is a system that makes geothermal heat production possible in a non-volcanic region. The core part of EGS development is hydraulic stimulation, which is a technique to enhance the permeability of the rock mass by injecting water and creating or opening the fractures which act as the fluid pathways. Permeability enhancement by hydraulic stimulation is achieved in three conceptual mechanisms at large: 1) hydraulic fracturing, or creating new fractures in tensile mode (Hubbert and Willis, 1957), 2) hydraulic jacking, or reopening preexisting fractures in tensile mode (Rutqvist and Stephansson, 1996), and 3) hydraulic shearing, or inducing slip and dilation of natural fractures in shear mode (Cladouhos et al., 2009; McClure and Horne, 2014). Depending on geological conditions and operational parameters, in-situ stimulation may involve multiple mechanisms (McClure and Horne, 2014; Norbeck et al., 2018). Including several cases of hydraulic stimulation for EGS development, many field applications of large-scale fluid injection into underground rock mass accompany induced or triggered seismic events.

In Korea, an EGS project was carried out at the Pohang city located in the southeastern region of the country. Two wells at the site, PX-1 and PX-2, were drilled deeper than 4 km for geothermal development. Starting from the first stimulation in PX-2, total five hydraulic stimulations were conducted in the two wells in alternating order between January 2016 and September 2017. A series of seismic events with the maximum magnitudes over M_L 2~3 occurred during

the five stimulations, and an M_L 5.4 earthquake occurred two months after the last stimulation. An investigation and research commission were appointed by the Korean government to search for the causality of the M_L 5.4 Pohang earthquake, and after a year-long study, the commission suggested that the M_L 5.4 earthquake had been triggered by hydraulic stimulation operations (Lee, 2019; Lee et al., 2019).

Similar to any other geomechanical behaviors, permeability enhancement and occurrence of induced seismic events by hydraulic stimulation are highly affected by the in-situ stress state of the targeted rock mass. The stress state at/near the Pohang EGS project site was suggested by several studies (Chang et al., 2016; Kim et al., 2017; Kim, 2017; Lee, 2019); however, the suggested stress models disagree in terms of both stress magnitude and orientation, requiring further detailed and comprehensive study. In this circumstance, this study focusses on delivering a stress model which best represent and explain the stress state of the rock volume encompassing the time and space of five stimulations and the M_L 5.4 earthquake. A new in-situ stress model is estimated from detailed and comprehensive approach based on variety of field observations, such as drilling records, well logs, lab test data of cores, hydraulic stimulation data, and induced seismic events.

2 COLLECTING STRESS INDICATORS FROM THE FIELD DATA

There were a few field tests designed for in-situ stress measurement conducted at relatively shallow depths (< 1 km) in the wells near the Pohang EGS project site, but no such dedicated test was conducted at the target depth of EGS development (> 4 km) in the wells drilled at the project site. In this regard, the in-situ stress estimation approach of the current study starts from collecting various direct and indirect stress indicators from field observations; this section conveys a brief of the collected stress indicators.

2.1 *Fluid pressure to shear a fault intersecting 3.8 km depth of PX-2*

Lost circulations occurred while drilling both the PX-2 and PX-1 wells at the Pohang EGS site. High-density drilling fluid was used in PX-2 to control rock caving, and the corresponding flowing bottomhole pressure of drilling mud was approximately 26–29 MPa above the hydrostatic water pressure. A considerable amount of drilling fluid was lost below 3.8 km depth of PX-2, which later appeared to be intersected by the fault on which the M_w 5.5 earthquake occurred (Lee, 2019). A series of microseismic events with maximum M_L 0.8 occurred after the mud loss at 3.8 km depth and continued for approximately one month, supporting the argument that the fault was sheared by the lost circulation (Lee, 2019). In comparison, there is a closed vertical downhole section of PX-1, so called as PX-1V, drilled prior to PX-2; no lost circulation occurred during drilling the same 3.8 km depth of PX-1V using a drilling fluid with lower density than that of PX-2. From these observations, the corresponding pressure window bounded by the flowing bottomhole pressures applied to the same 3.8 km depth while drilling PX-1V and PX-2 is selected as the pressure range enclosing a critical pressure for shearing the fault intersecting 3.8 km depth of PX-2. If the orientation of the sheared fault is estimated or assumed, the critical fluid pressure for shearing can be converted to a stress magnitude constraint with given stress orientation scenario.

2.2 *Fluid pressure to shear fracture/fault at the openhole section of PX-1*

While drilling the inclined downhole section of PX-1 after the first stimulation in PX-2, the mud density was maintained in a low-to-moderate range based on the experience in PX-2 drilling. Lost circulations occurred while drilling the final openhole section of the well, and the mud overpressure was approximately 14.5 MPa. Interestingly, pressure signals were observed at similar pressure range during the stimulation in PX-1 (Fig.1). During the second stimulation at the Pohang EGS site, conducted in December 2016 at PX-1, clear pressure peaks in 15 to 17 MPa

(wellhead pressure) and subsequent pressure declines were observed, indicating abrupt fracture volume (and/or permeability) increase by the injected fluid (Park et al., 2020). From the similarity between the pressures for lost circulation during drilling and permeability enhancement during hydraulic stimulation, the corresponding pressure range is selected as indicating a critical pressure for shearing fracture or fault intersecting the openhole (uncased) section of PX-1. If the orientation of the sheared fracture/fault is estimated or assumed, the critical fluid pressure for shearing can be converted to a stress magnitude constraint with given stress orientation scenario.

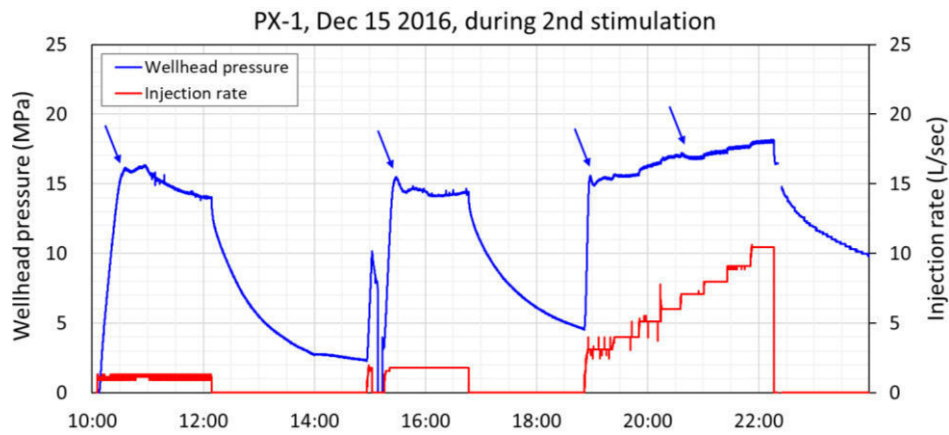


Figure 1. Pressure peaks and declines during the second stimulation (modified from Park et al., 2020).

2.3 Stress magnitude constraint from borehole washout

In PX-2, a caliper logging was performed in the temporary uncased section below 2.4 km depth, before running the innermost casings. The caliper log result showed that borehole washouts as well as breakouts were found at various depths. The equation on the maximum horizontal stress to cause a borehole breakout is expressed as Equation 1 (Barton et al., 1988; Zoback et al., 2003):

$$S_{Hmax} = \frac{UCS + 2P_p + \Delta P + \sigma^{\Delta T} - S_{hmin}(1 + 2\cos 2\theta_b)}{1 - 2\cos 2\theta_b} \quad (1)$$

Where S_{Hmax} and S_{hmin} are the maximum and minimum horizontal stresses, respectively, UCS is the uniaxial compressive strength, P_p is the pore pressure, ΔP is the inner-well fluid pressure minus P_p , $\sigma^{\Delta T}$ is the thermal stress.

There is no direct measure of the breakout widths at the Pohang site. However, it is empirically known that a borehole breakout with w_{BO} initially wider than 90° pervasively grows to borehole washout (Zoback, 2010). Considering that the breakouts and washouts as well as intact circular sections were all found in PX-2, the stress level is expected to be in a range covering the critical level to potentially cause borehole washout. In this regard, for the angle between S_{Hmax} and the breakout tip θ_b , $40^\circ \leq \theta_b \leq 50^\circ$ was assumed to constrain S_{Hmax} in a range explaining both stable breakout and potential pervasive washout.

2.4 Fracture closure pressure during shut-in

During the stimulations in PX-2, the fracture closure pressures (FCP) were observed as obvious ‘kinks’ recognizable on the pressure-time curves (Fig. 2), and also on the pressure-(time)^{1/2} curves as suggested by Zoback (2010). FCP is regarded as a lower bound of the initial normal stress acting on the fracture (Zang and Stephansson, 2009), and various fractures are expected to intersect the 140-m-long openhole section of PX-2; thus, the fracture requiring the lowest pres-

sure for opening could have been predominantly responded to the stimulations. In such a case, the lowermost FCP can be assumed as a reasonable estimate of the minimum principal stress. The 60 MPa FCP consistent after 14 months supports its reliability.

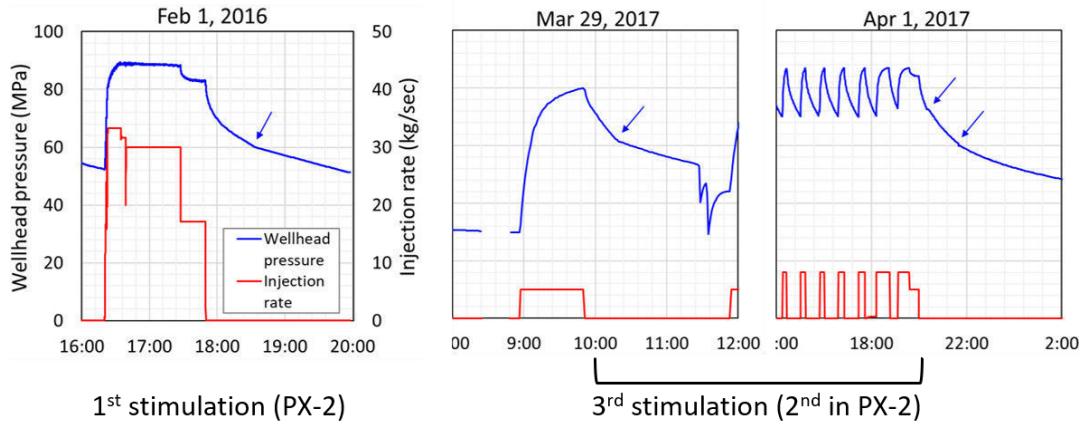


Figure 2. Fracture closure pressures in PX-2, consistent in the first and third stimulations at the site.

2.5 Stress inversion of seismicity focal mechanisms

There have been several stress inversion results suggested for the Pohang EGS site, using focal mechanisms of the earthquakes before and after the M_w 5.5 earthquake and the seismic events induced by the five hydraulic stimulations (Table 1). One can find that the strike-slip faulting regime is dominant in general, and the inversion results by Lee (2019) and Ree et al. (2019) all provide high stress ratios of $R=0.87-0.89$. From its consistency across different stress inversion results, the stress ratio range is selected as a stress constraint for the relation between the maximum and minimum principal stresses.

Table 1. Focal mechanism stress inversion results suggested for the Pohang EGS site

Type / number of focal mechanisms	Period	Distance from the site (km)	Depth (km)	S_{Hmax} azimuth ($^{\circ}$)	$R=(S1-S2)/(S1-S3)$	Stress regime	Reference
Natural earthquake before stimulations / 21	1997-2016	< 70	7.7-17.9	74	0.88	SSF	Lee, 2019
Induced seismicity & foreshocks of M_w 5.5 / 53	Feb 2016-Nov 2017	< 1.1	3.7-4.4	96	-	SSF	Lee, 2019
Aftershocks of M_w 5.5 / 202	-	-	3.0-7.0	86	0.87	SSF	Lee, 2019
Foreshocks, M_w 5.5 mainshock, aftershocks / -	Nov 2017-Oct 2018	-	2.5-7.0	109	0.89	RF	Ree et al., 2019

3 COMPREHENSIVE IN-SITU STRESS ESTIMATION

3.1 Graphical expression and integration of stress constraints

Stress polygon is a useful tool to graphically suggest every possible combinations of maximum and minimum horizontal stress for three different stress regimes (normal, strike-slip, reverse), and compare various stress constraints under a given vertical stress. However, stress constraints

are usually obtained from each different depth in the region of interest, and it is also the case for the current study. In this regard, conventional stress polygon for a single, fixed vertical stress (i.e., fixed depth) is hardly applicable for a situation comparing stress constraints from different depths. To avoid this issue, a concept of normalized, dimensionless stress polygon is employed in the current study; the maximum and minimum horizontal stresses are replaced by their ratio over vertical stress, thus the hydrostatic point (S_v, S_v) is then changed to (1, 1).

Stress constraints addressed in section 2 are graphically expressed and integrated on a single normalized stress polygon. Among five stress constraints (sections 2.1 ~ 2.5), the constraints related with fracture or fault shearing (sections 2.1, 2.2) vary depending on the stress orientation and friction coefficient, whereas the constraints from the borehole breakout in PX-2, the fracture closure pressure in PX-2, and the stress inversion of focal mechanisms (sections 2.3~2.5) are independent. As no decisive information on the friction coefficient and stress orientation is available for targeted rock mass, the agreement / disagreement of stress constraints is examined by changing friction coefficient from 0.35 to 0.6 and SHmax azimuth from 80° to 120° . Figure 3 is an example case at friction coefficient of 0.45 and SHmax azimuth of 93° , showing that all five stress constraints overlap in a same area on a normalized stress polygon; the SHmax/ S_v and Shmin/ S_v ranges indicated by blue solid lines on a zoomed-in subfigure are the stress ranges resulting from this example case.

From the integrated stress estimation, the strike-slip faulting regime is confirmed for the Pohang EGS site. The stress ratios of $S_v:S_{hmin}:S_{hmax}$ is deduced as 1:0.92-0.94:1.42-1.66. The stress magnitudes at a reference depth of 4.2 km are suggested as: $S_v=108$ MPa, $S_{hmin}=100$ MPa, and $S_{hmax}=154-180$ MPa. The friction coefficients that fulfill all stress constraints were found in 0.35-0.50 range for the Pohang EGS site.

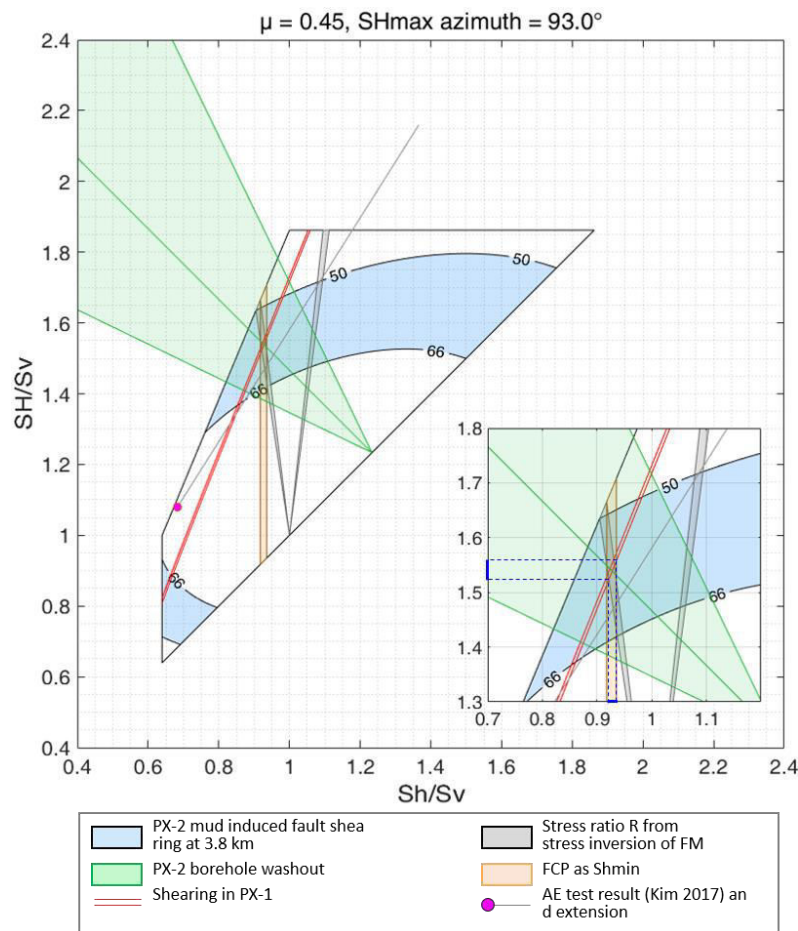


Figure 3. Example case of integrated stress estimation fulfilling all stress constraints

3.2 Slip tendency of the fault at the Pohang EGS site

The slip tendency T_s is defined as $T_s = \tau/\sigma_n$, where τ is the resolved shear stress and σ_n is the resolved effective normal stress on a given fault or fracture plane (Morris et al., 1996). Slip tendency is lower than the friction coefficient μ when the stress state is stable for frictional failure, and when the slip tendency reaches the friction coefficient, the stress state becomes critical for slip.

The slip tendency of the fault which hosted the Pohang earthquake was assessed using the stress model of this study. As shown in Figure 4 (a), only one out of six candidate orientations of the fault have a low slip tendency of 0.28, and the rest five result in the relatively high slip tendencies in 0.32-0.34 range. When assuming $\mu = 0.35$ for the Pohang mainshock fault, the slip tendencies of the fault orientations are assessed as 92-96% of the critically stressed state except the orientation of lowest slip tendency. It implies that the stress model and possible friction coefficient range suggested in this study can explain that the mainshock fault of the Pohang earthquake was in sub-critically stressed condition.

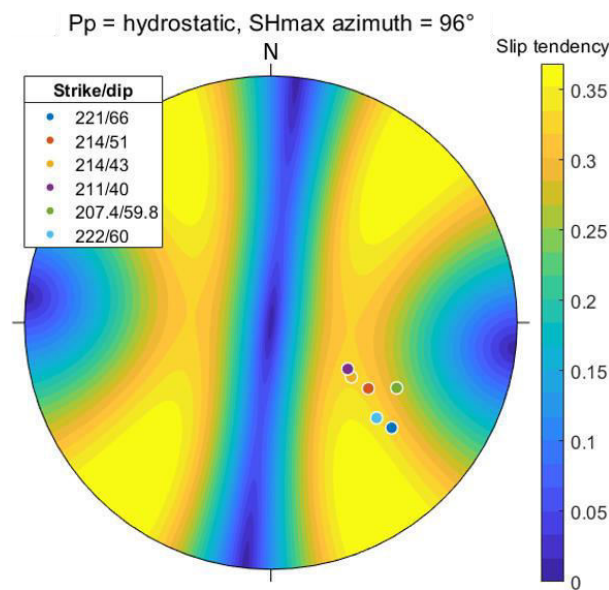


Figure 4. Stereographic projection of slip tendency contours; lower hemisphere, equal angle projection

4 CONCLUSION

In the current study, a comprehensive estimation of in-situ stress model in the reservoir depth at the Pohang enhanced geothermal system development site was conducted. Stress indicators were collected from field observations of drilling, logging, hydraulic stimulations, and seismicity occurrence, and the in-situ stress model was suggested by integrating the stress constraints.

Based on the understandings on the reservoir responses observed during hydraulic stimulations and various stress indicators, the in-situ stress state of the reservoir volume at the Pohang EGS site was re-assessed by virtue of integrated stress estimation. The fault shearing induced by the mud loss in PX-2 3.8 km depth and the hydraulic shearing within the PX-1 openhole were used, and contributed as the stress constraints varying with the friction coefficient and stress orientation. The condition to enable both borehole breakout and washout in PX-2 was used considering realistic field operational parameters such as flowing bottomhole mud pressure and the cooling of the well during drilling. The observed fracture closure pressure, the previously reported focal mechanism stress inversion data, and the acoustic emission test data were also included as the stress constraints. The resulting stress model suggests the possible stress ratio for

the reservoir depth at the Pohang EGS site as $S_v:Sh_{min}:SH_{max} = 1:0.92-0.94:1.42-1.66$, based on the compilation of direct and indirect stress indicators. The result also suggests the possible range of friction coefficient as 0.35-0.50, which can best explain the involved stress constraints.

Comprehensive in-situ stress estimation suggested in this study demonstrates that the appropriate integration of direct and indirect stress indicators from various field records can improve the credibility of the in-situ stress model at a fractured reservoir. The resulting stress model is coherent with the field observations during the geothermal development activities such as drilling, logging, hydraulic stimulation, and induced seismicity, and also can explain the characteristics of the Pohang earthquake. The stress model suggested in this study can be used for clarifying the causal mechanism of the Pohang earthquake. Furthermore, the stress model from this study can provide an insight for fault stability analysis or possible geo-energy application, such as CO₂ geo-sequestration, in the southeastern part of the Korean Peninsula.

ACKNOWLEDGEMENT

This study is based on the first author's doctoral dissertation (Park, 2021) in Seoul National University. The Pohang EGS development project was funded by the Korea Institute of Energy Technology Evaluation and Planning (KETEP) granted financial resources from the Ministry of Trade, Industry & Energy, Republic of Korea (No. 20123010110010). NexGeo, Inc. provided additional financial support for the Pohang EGS development project as a leading organization. This work was partially supported by the Korea-EU Joint Research Support Program of the National Research Foundation of Korea (NRF) through a grant funded by the Korean Government's Ministry of Science and ICT (No. NRF-2015K1A3A7A03074226) as part of the EU DESTRESS project, which has received funding from the European Union's Horizon 2020 research and innovation programme under grant agreement No. 691728. The preparation of this manuscript was also supported by a grant from the Innovative Technology Development Program for High-level waste management of the National Research Foundation of Korea (NRF) funded by the Korea government (Ministry of Science and ICT, MSIT) (Grant No. 2021M2E3A2044264).

REFERENCES

- Barton, C.A., Zoback, M.D., & Burns, K.L. (1988). In-situ stress orientation and magnitude at the Fenton Geothermal Site, New Mexico, determined from wellbore breakouts. *Geophysical Research Letters* 15(5), 467-470.
- Chang, C., Jo, Y., Quach, N., Shinn, Y. J., Song, I., & Kwon, Y.K. (2016, June). Geomechanical characterization for the CO₂ injection test site, offshore Pohang Basin, SE Korea. In *50th US Rock Mechanics/Geomechanics Symposium*. Houston, Texas, USA, Paper No.: 541.
- Cladouhos, T., Petty, S., Larson, B., Iovenitti, J., Livesay, B., & Baria, R. (2009). Toward more efficient heat mining: a planned enhanced geothermal system demonstration project. *GRC Transactions* 33, 165-170.
- Hubbert, M.K., & Willis, D.G. (1957). Mechanics of hydraulic fracturing. *Transactions of the AIME* 210(01), 153-168.
- Kim, H. (2017). Integrated Estimation of In-Situ Rock Stress at Pohang Geothermal Reservoir in Korea (Doctoral dissertation). Seoul National University, Seoul, Republic of Korea.
- Kim, H., Xie, L., Min, K.B., Bae, S., & Stephansson, O. (2017). Integrated in situ stress estimation by hydraulic fracturing, borehole observations and numerical analysis at the EXP-1 borehole in Pohang, Korea. *Rock Mechanics and Rock Engineering* 50(12), 3141-3155.
- Lee, K.K. (2019). Final Report of the Korean Government Commission on Relations between the 2017 Pohang Earthquake and EGS Project. The Geological Society of Korea. <https://doi.org/10.22719/KETEP-2019043001>.
- Lee, K.K., Ellsworth, W.L., Giardini, D., Townend, J., Ge, S., Shimamoto, T., ... & Langenbruch, C. (2019). Managing injection-induced seismic risks. *Science* 364(6442), 730-732.

- McClure, M.W., & Horne, R.N. (2014). An investigation of stimulation mechanisms in Enhanced Geothermal Systems. *International Journal of Rock Mechanics and Mining Sciences* 72, 242-260.
- Morris, A., Ferrill, D.A., & Henderson, D.B. (1996). Slip-tendency analysis and fault reactivation. *Geology* 24(3), 275-278.
- Norbeck, J.H., McClure, M.W., & Horne, R.N. (2018). Field observations at the Fenton Hill enhanced geothermal system test site support mixed-mechanism stimulation. *Geothermics* 74, 135-149.
- Park, S. (2021). Comprehensive In-Situ Stress Estimation in a Fractured Geothermal Reservoir from Drilling, Hydraulic Stimulations, and Induced Seismicity (Doctoral dissertation). Seoul National University, Seoul, Republic of Korea.
- Park, S., Kim, K.I., Xie, L., Yoo, H., Min, K.B., Kim, M., ... & Meier, P. (2020). Observations and analyses of the first two hydraulic stimulations in the Pohang geothermal development site, South Korea. *Geothermics* 88, 101905.
- Ree, J. H., Kim, K. H., Kim, S., et al. (2019). Fluid-driven reactivation of unfavorably oriented faults for the 2017 Pohang earthquake sequence. In *EGU General Assembly 2019*, Vienna, Austria. Paper No: 5043.
- Rutqvist, J., & Stephansson, O. (1996). A cyclic hydraulic jacking test to determine the in situ stress normal to a fracture. *International Journal of Rock Mechanics and Mining Sciences & Geomechanics Abstracts* 33(7), 695-711.
- Zang, A., & Stephansson, O. (2009). *Stress field of the Earth's crust*. Springer Science & Business Media.
- Zoback, M.D., Barton, C.A., Brudy, M., Castillo, D.A., Finkbeiner, T., Grollmund, B.R., ... & Wiprut, D.J. (2003). Determination of stress orientation and magnitude in deep wells. *International Journal of Rock Mechanics and Mining Sciences* 40(7-8), 1049-1076.
- Zoback, M. D. (2010). *Reservoir geomechanics*. Cambridge University Press.

CO₂ geological storage: evaluation of lightweight cement for injection well

C. M. Martín^{1,2,6}, J.M. Pereira¹, D. Manzanal^{3*}, S. Ghabezloo¹, T. Piqué^{4,5}

¹*École des Ponts ParisTech, Paris, France*

²*Universidad Nacional de la Patagonia San Juan Bosco, Comodoro Rivadavia, Argentina*

³*Universidad Politécnica de Madrid, Madrid, España*

⁴*YPF Tecnología S.A., Buenos Aires, Argentina*

⁵*CONICET, Buenos Aires, Argentina*

⁶*Universidad de Buenos Aires, Argentina*

*corresponding author: d.manzanal@upm.es

ABSTRACT:

Carbon dioxide capture and geological storage (CCS) is a climate change mitigation measure that seeks to reduce the greenhouse gases emitted to the atmosphere by injecting carbon dioxide in a supercritical state (scCO₂) into deep reservoirs. The injection wells are a source of weakness in the "rock-cement-casing" system. Cement fills the annular space between the casing and the rock borehole. Once the scCO₂ is stored, the rock-casing-cement system must ensure that the scCO₂ does not migrate through the different possible paths. These paths can be the seal rock containing the reservoir, the cement-rock interface, the cement itself, and the cement-casing interface. This work focuses on studying cement as a possible migration pathway for scCO₂. It will mainly focus on lightweight cement pastes, which will be achieved by replacing cement with hollow glass microspheres (HGMS). The stability of wells cemented with lightweight cement pastes under CCS injection wells conditions is studied. Cement pastes were subjected to carbon dioxide geological storage conditions for 60 days. The evolution of the cement pastes' physical and mechanical properties was measured before and after this procedure. By analyzing the data obtained from the laboratory tests, the presence of HGMS influence the performance of cement pastes subjected to CCS conditions. HGMS provide the cement matrix with a high amount of unconnected porosity, which lightens it without affecting its mechanical properties. Nevertheless, under CCS conditions, this porous structure could modify the carbonation mechanisms and the advancement of carbonation in the cement sheath.

KEYWORDS: CO₂ geological storage, wellbore integrity, lightweight cement paste, hollow glass microspheres.

1 INTRODUCTION

Storing CO₂ in deep underground reservoirs is key to decreasing greenhouse gas emissions and standing against climate change. One of the critical storage factors in assessing the sustainability and safety of the geological site is the sealing capacity of the wellbore system (Barria et al., 2018, 2019). The hardened cement paste aims at maintaining the integrity of the casing-cement-wellbore system by filling the gaps between the casing and the geological formations. The cement sheath must assure zonal isolation to prevent fluid migration (Barria et al., 2022). Geochemical studies of cement paste show that the diffusion of carbonic acid through cement paste principally produces the dissolution of portlandite CH and C-S-H (calcium silicate hydrate) and the precipitation of calcium carbonate. These chemical reactions will induce changes in porosity and the mineral composition of the solid phase

affecting its microstructure and mechanical properties. Both properties are related to the durability of the cement paste and its ability to avoid scCO₂ migration paths (Duguid et al., 2011, Carey, 2013).

The modification of cement to improve some properties is a subject of interest in the cement wellbore industry. Recently, new additives have focused on improving the cement, making it lighter while maintaining high strength and low permeability properties (Barria et al., 2020, Martín et al., 2021). This paper focuses on the design of lightweight cement paste with the addition of hollow glass microspheres (HGMS). The evolution of modified cement paste's porosity and mechanical properties, when subjected to a scCO₂ environment, will be evaluated through laboratory tests. Mercury intrusion porosimetry (MIP) tests were performed to study the interconnected porosity while these results correlated to the pastes' uniaxial compressive strength.

2 MATERIALS AND METHODS

2.1 Materials

Class G portland cement provided by Petroquímica Comodoro Rivadavia (Argentina), HGMS (3M), deionized water and polycarbonate-based superplasticizer (ADVA 570, GCP Applied Technologies) were used for the cement pastes. Class G cement has a density of 3.18 g/cm³. Two types of HGMS were used in this research, HGMS27 and HGMS41. HGMS27 have a density of 0.28 g/cm³, a mean particle size (D₅₀) of 30 μm and a crushing strength of 27 MPa. HGMS41 are more resistant, bigger and of a higher density. They have a density of 0.46 g/cm³, a mean particle size (D₅₀) of 40 μm and crushing strength of 41 MPa.

For the dosing of the pastes, a water-to-solid ratio (w/s) of 0.44 was used following the specifications given by the American Petroleum Institute for the design of class G oil well cement pastes (American Petroleum Institute 2013). Table 1 shows the names and proportions of the pastes used in this research. Figure 1 shows the particle size curves of class G cement and both HGMS.

Table 1. Cement pastes classification and dosages.

Slurry	Cement [kg/m ³]	HGMS27 [kg/m ³]	HGMS41 [kg/m ³]	Water [kg/m ³]	Superplasticizer [kg/m ³]
CS00	1320.2	-	-	580.9	-
CS27	829.0	92.1	-	405.3	2.8
CS41	952.5	-	105.8	465.6	2.1

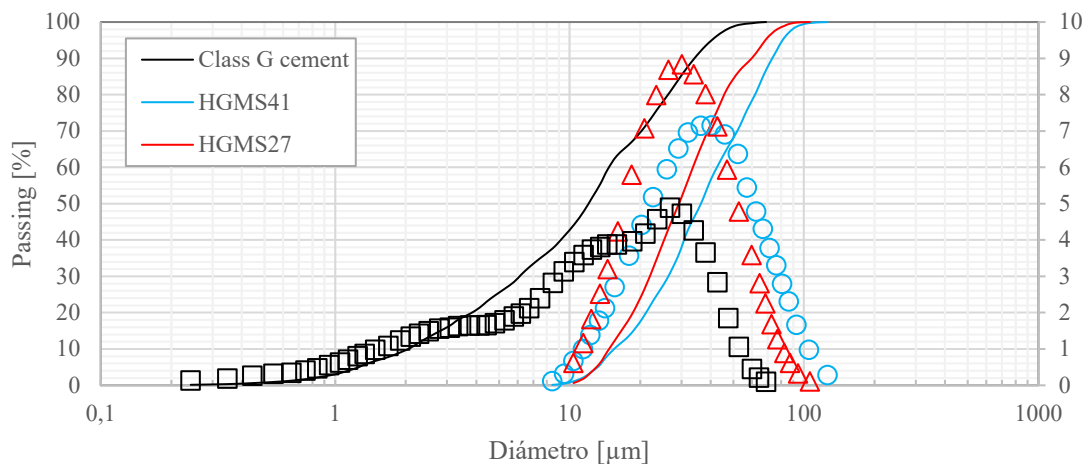


Figure 1. Particle size distribution of class G cement, HGMS27 and HGMS41 (Martín et al. 2021).

2.2 Experimental methods

Carbonation is a chemical process in which the CO_2 , present due to its geological storage, reacts with the alkaline components of cement, i.e., calcium hydroxide (CH) and calcium silicate hydrate (CSH). During this process, the CH is initially consumed, generating a decrease in the paste's pH, favouring the attack's advance towards the hydrated calcium silicate, thus generating a progressive deterioration of the pastes (Barría et al., 2019, 2021).

In order to achieve an environment comparable to that reached in CO_2 geological storage wells, a cell capable of withstanding high pressure and temperature conditions is used, as shown in Figure 2. In this cell, the samples are subjected to a pressure of 20 MPa and 90°C in a CO_2 -saturated atmosphere with the presence of water for 60 days (Barría et al., 2022).



Figure 2: Cell used for subjecting cement samples to CCS conditions

Since the cement paste aims to isolate the stored CO_2 to avoid fluid migrations, its permeability is a fundamental factor in its performance (Bai, Zhang, and Fu, 2016). Thus, measuring the porosity of each of the proposed pastes is necessary. The mercury intrusion porosimetry (MIP) test evaluated the microstructure-modified cement pastes. This test implies placing a small sample of about 1 cm^3 in a penetrometer (a small recipient capable of supporting internal pressures of up to 220 MPa), which will be filled with mercury. Then, the mercury will gradually increase its pressure in steps, and the apparatus quantifies the amount of mercury that was necessary to be injected to reach it.

The physics behind this test is related to the surface tension and contact angle between mercury and cement (Scrivener, Snellings, and Lothenbach 2016). Surface tension is a force per unit length associated with the mercury's cohesion, which generates the lowest potential energy. This variable depends on three factors: the nature of the liquid (cohesion), the surrounding medium and the temperature at which it is found. The contact angle of a given liquid is the angle between the liquid-air and liquid-solid surfaces. This parameter determines the ability of the liquid to wet the solid with which it is in contact. It is closely related to surface tension, particularly the cohesion of the liquid and the adhesion between the liquid and the solid. Usual values of surface tension and contact angle for mercury in contact with hydrated cement paste are 0.480 to 0.485 N/m and 130° to 140° , respectively.

It shall be mentioned that the value obtained from MIP tests is not the actual porosity but the intruded mercury volume for each pressure step. Each of these pressure steps was performed with an

equilibrating time of 120 seconds to ensure that all the related entry pore size pores were filled. From the intruded mercury volume, the actual porosity of the sample could be obtained, as shown in Equation 1.

$$\Phi_{Hg} = \frac{V_{intrusion}}{V_{sample}} = \frac{\gamma_{dry} V_{intrusion}}{M_{sample}} \quad (1)$$

Where Φ_{Hg} : MIP porosity; $V_{intrusion}$: mercury intruded volume; V_{sample} : sample volume; γ_{dry} : dry specific weight of the sample; and M_{sample} : sample mass.

Finally, uniaxial compressive strength tests were performed to assess the relationship between the mechanical properties, the presence of HGMS of different classes and the effect of carbonation. This test was done on three samples for each dosage to obtain their uniaxial compressive strength before and after carbonation. It consists of subjecting cylindrical specimens of 1.5 inches diameter and 3 inches height to compressive stress until failure is reached.

3 RESULTS AND DISCUSSION

3.1 Mercury intrusion porosimetry

Figure 3 presents the results of MIP porosity obtained for each of the slurries studied in this research. It shall be noted that there are six classes of samples, the three classes specified in Table 1 before and after carbonation. These are classified as "C00" and "C60" for 0 days of carbonation and 60 days of carbonation, respectively.

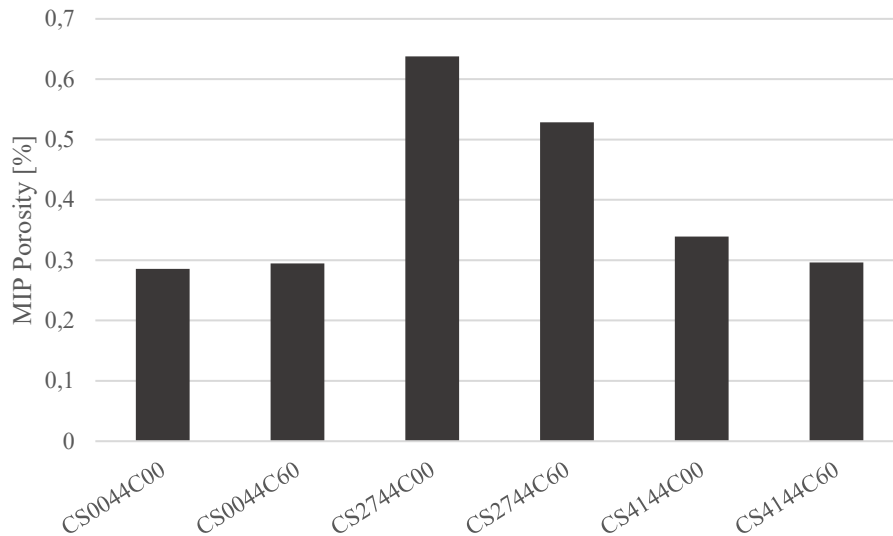


Figure 3: MIP porosity results

It is worth noting that MIP's lowest porosity is reached for cement paste CS00, followed by CS41 and CS27. Besides, after carbonation, the porosity appears to increase slightly for CS00, while for CS27 and CS41 it decreases between 5% and 10%.

One matter of main importance for properly analyzing these results is related to how the pore size diameter is measured within this test. The MIP mainly measures the volume of mercury needed to be injected to reach some pressure. Also, given that each pressure is related to an entry pore size

according to Equation 2 (Hall and Hodd 2009), the entry pore size distribution will be obtained. This is different from the actual pore size distribution since it could happen that a pore presents an entry diameter which could be smaller than its diameter somewhere beyond the entry, as shown in Figure 4. As some larger pores (ink-bottle pores) are only accessible for the mercury through smaller ones, this technique leads to overestimating small pores and underestimating larger pores (Ahmed 2022; Scrivener, Snellings, and Lothenbach 2016). The central fact for evidencing this phenomenon is that during the extrusion cycle, not all the mercury intruded into the sample during the intrusion cycle will leave the pores, as shown in Figure 5 for one of the cement samples modified with HGMS tested in this research.

$$D = -\frac{4\gamma\cos(\theta)}{P} \quad (2)$$

Where D: entry pore size diameter; γ : surface tension; θ : contact angle between mercury and cement; and P: pressure applied.

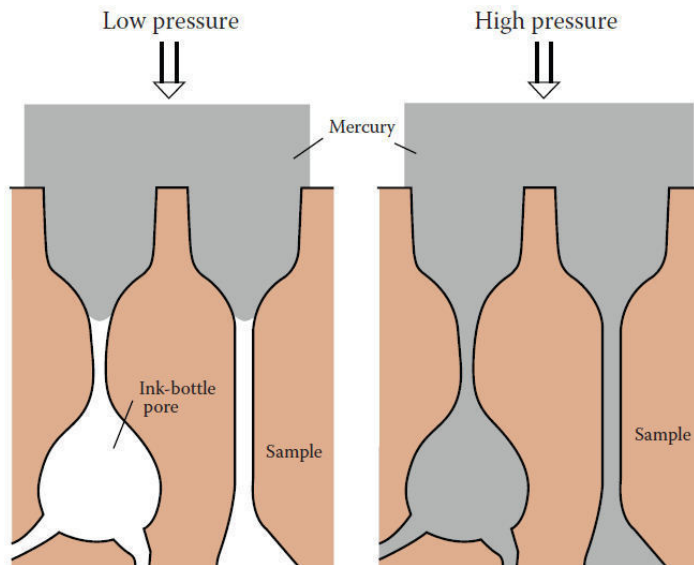


Figure 4: Ink-bottle pore (image obtained from (Scrivener, Snellings, and Lothenbach 2016))

The importance of this effect in the samples of this research relies on the presence of HGMS. This material consists of hollow spheres with crushing strengths that are overpassed throughout the MIP test and could break throughout the test as suggested by Krakowiak et al. (Krakowiak et al. 2020). In addition, this material was also proven in previous research (Martín et al., 2021) to present chemical interaction with cement hydration products, which affects the outer shell and could also lead to mercury intruding into them. This would lead to a potential ink-bottle effect since the pore size of cement is generally much smaller than the size of both HGMS27 and HGMS41 (Fig. 6). Therefore, samples with no ink-bottle pores, intrusion and extrusion curves are coincident. Nevertheless, for our samples, as exemplified in Figure 5, there is an important difference between these two curves.

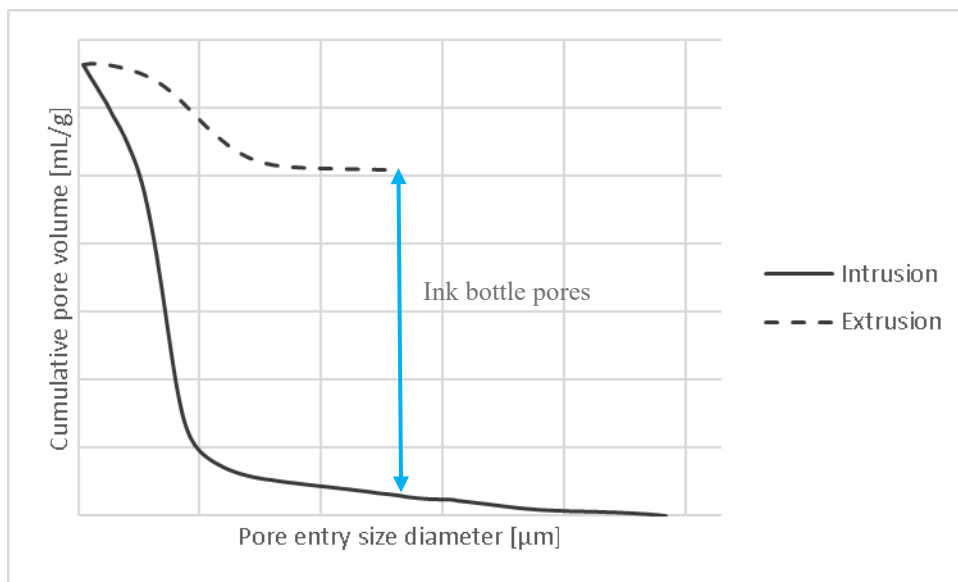


Figure 5: Intrusion and extrusion curves for modified cement sample

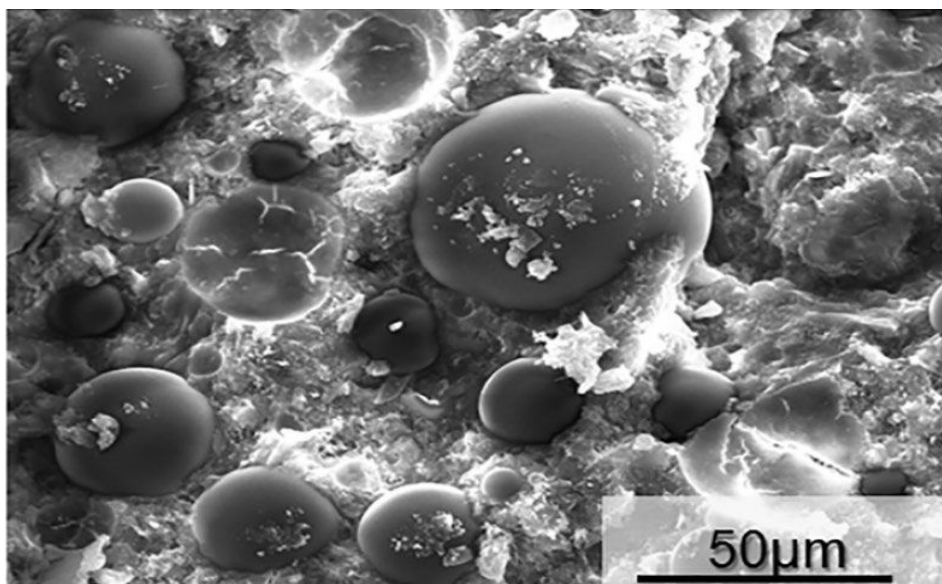


Figure 6: SEM image of HGMS in cement paste

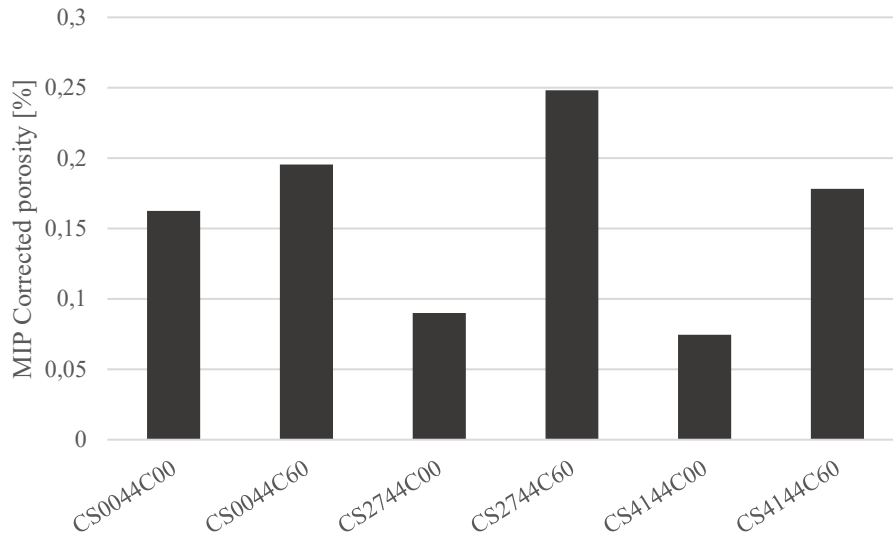


Figure 7: MIP corrected porosity results

The porosity of the cement matrix could then be calculated, as explained in the research of Ahmed (Ahmed 2022), by subtracting the difference between intrusion and extrusion as indicated in Figure 5. It should be noted that this correction was performed because it was considered that the MIP porosity result might be overestimating the interconnected porosity of cement samples CS27 and CS41 both before and after carbonation.

With this correction, the results of the cement matrix porosity are presented in Figure 7. Remarkably, the porosities of CS27C00 and CS41C00 decreased from more than 0.6 and 0.3, respectively, to less than 0.1. The low density of both HGMS results in a high volume fraction when they are added to the cement at 10% by weight of cement. This explains the important variation in the results with and without correction. Besides, in some previous research, it was verified that HGMS act as nucleation agents for cement hydration products, which densifies cement matrix (Martín et al. 2021). This could also be related to the decrease in MIP corrected porosity from CS0044C00 to CS2744C00 and CS4144C00.

Corrected MIP porosity results after carbonation for samples CS27C60 and CS41C60 showed a decrease of around 25% and 12%, respectively. Both differences are lower than those obtained for CS27C00 and CS41C00, respectively. This could be related to the cement matrix reacting with scCO_2 leading to a broader entry pore size distribution in the cement matrix. After that, the ink-bottle effect might no longer be appreciated for some HGMS since the pore size of the cement matrix could be the same as the diameter of the HGMS. In addition, HGMS turned out to be more accessible for scCO_2 after the carbonation of the cement matrix. Possibly HGMS could react with scCO_2 , and it would no longer be correct to make any correction on the MIP porosity. Nevertheless, some research has been done on the interaction of scCO_2 and borosilicate glass or SiO_2 , indicating no chemical interaction between these two materials (Barrow et al., 2020; Caserini et al., 2017).

3.2 Uniaxial compressive strength

Figure 8 shows the uniaxial compressive strength results obtained for each studied sample. It can be seen that from all the non-carbonated samples, CS0044C00 yields the highest compressive strength, followed by CS4144C00 and CS2744C00. This could be explained by the MIP porosity results, for

which a good correlation between porosity and compressive strength exists. The higher the porosity, the lower the strength.

Nevertheless, considering the MIP corrected porosity results, this correlation appears invalid. For non-carbonated samples, the highest MIP corrected porosity corresponds to CS0044, followed by CS2744 and CS4144. Therefore, the sample with the highest MIP corrected porosity also yields the highest compressive strength. However, by analyzing CS2744C00 and CS4144C00, the higher the corrected porosity, the lower the strength. It could be stated that the porosity correction is valid for modified cement samples. However, it is challenging to analyze cross-data between plain and modified cement samples.

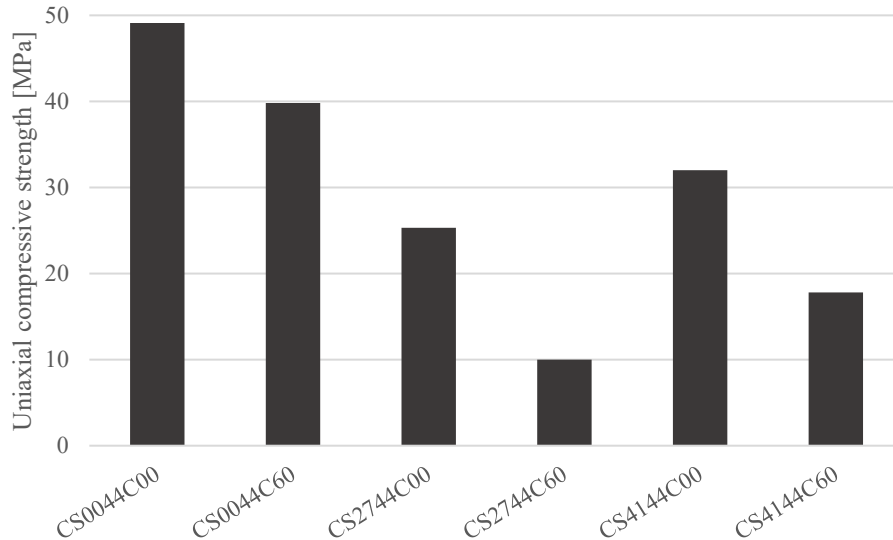


Figure 8: Uniaxial compressive strength results

Previous research shows that carbonation affects hardened cement's mechanical properties (Barriá et al., 2019). The carbonated samples show a decrease in compressive strength after carbonation for every cement sample. This is related to the degradation of the cement matrix as cement hydration products react with scCO_2 to form carbonates (Kuo, Wang, and Hsiang, 2017).

To find a correlation between strength and MIP porosity for carbonated samples, it is worth noting that CS0044C00 presents a lower MIP porosity than CS0044C60 and, as expected, the first presents a higher compressive strength. However, this tendency is not as expected for cement samples modified with HGMS. CS2744C00 presents a higher MIP porosity and a higher compressive strength than CS2744C60. The same happens between CS4144C00 and CS4144C60.

When analyzing the MIP corrected porosity results, the tendency agrees with what is expected. After carbonation, the porosity increases for all cement samples, which is correlated with a significant decrease in compressive strength for all of them.

There might be many reasons to explain the behaviour of the samples studied. Previous research reports a relation between compressive strength and HGMS crushing strength (Martín et al., 2021). The higher the crushing strength of HGMS, the higher the compressive strength. Moreover, the more volume fraction of HGMS, the lower the compressive strength. This is interesting for understanding the different results obtained for CS2744C00 and CS4144C00. HGMS27 presents a lower crushing strength and density than HGMS41, which means that in addition to being weaker, they were added in a higher volume fraction (since the cement pastes were designed for having the same amount by weight of cement of HGMS).

Moreover, the chemical interaction between HGMS and cement hydration products was confirmed (Martín et al., 2021). This implies that the outer shell of HGMS is being partially consumed by cement, which could affect the actual crushing strength of HGMS within the cement samples.

As regards the compressive strength results obtained for carbonated samples and their correlation with MIP-corrected porosity, it could be argued that there is an important increase in the entry pore size, which results in a reduction in the ink-bottle pores. Furthermore, the HGMS status before and after carbonation is not yet well defined. It could have been severely affected by their chemical interaction with cement hydration products and exposure to scCO_2 .

4 CONCLUSIONS

This research analyzed the microstructure and strength of both plain and modified cement pastes intended to be used for scCO_2 injection wells. For this purpose, mercury intrusion porosimetry and uniaxial compressive strength tests were performed. Samples were subjected to well conditions, and their properties were assessed before and after carbonation.

MIP and corrected porosities were obtained for all the cement samples analyzed in this research. A significant decrease in cement modified with HGMS before carbonation could be measured between the porosity and the corrected porosity results. This is related to the presence of HGMS that generate ink-bottle pores and possibly to the higher compacity of modified cement pastes due to the nucleation effect of HGMS for cement hydration products.

A good correlation was obtained between either porosity or corrected porosity and compressive strength results. Since many factors affect the compressive strength of modified cement samples, further research needs to be done to thoroughly understand the behavior of modified cement samples before and after carbonation.

5 ACKNOWLEDGEMENTS

The authors acknowledged the financial support of the European Union's Horizon 2020 research and innovation program under Grant Agreement No 101007851 (H2020 MSCA-RISE 2020 Project DISCO2-STORE), the Universidad Nacional de la Patagonia San Juan Bosco -Project UNPSJB PI1614 80020190200006 IP, Res. R/9N°207-2020 CRD1365 FI004/ 17-, the Agency of Scientific and Technological Promotion from the Argentine Republic. (Projects PICT 2016–4543, PICT 2020-SERIEA 02088), and the PIP project N° 11220200103043CO (CONICET). The authors also thank the technical staff of Petroquímica Comodoro Rivadavia and Laboratoire Navier for helping with the tests performed.

4 REFERENCES

- Ahmed, Hady Sadok. 2022. "New Approach of Mercury Intrusion Porosimetry to Evaluate the Microstructure of Cement-Bases Matrixes : Application on Slag Cement Mortars." *Materials Today: Proceedings* (xxxx). <https://doi.org/10.1016/j.matpr.2022.02.233>.
- American Petroleum Institute. 2013. "API 10B-2: Recommended Practice for Testing Well Cements, Second Edition."
- Bagheri, M., S. M. Shariatipour, and E. Ganjian. 2018. "A Review of Oil Well Cement Alteration in CO₂-Rich Environments." *Construction and Building Materials* 186: 946–68. <https://doi.org/10.1016/j.conbuildmat.2018.07.250>.
- Bai, Mingxing, Zhichao Zhang, and Xiaofei Fu. 2016. "A Review on Well Integrity Issues for CO₂ Geological Storage and Enhanced Gas Recovery." *Renewable and Sustainable Energy Reviews* 59: 920–26. <http://dx.doi.org/10.1016/j.rser.2016.01.043>.

- Barría, Juan Cruz et al. 2019. "Analysis of Modified Cement Paste in the Context of CO₂ Geological Storage : Analysis of Modified Cement Paste in the Context of CO₂ Geological Storage." In International Symposium on Energy Geotechnics. http://dx.doi.org/10.1007/978-3-319-99670-7_50
- Barría, J.C., Vázquez, A., Pereira, J.M., Manzanal, D., 2021b. Effect of bacterial nanocellulose on the fresh and hardened states of oil well cement. *J. Pet. Sci. Eng.* 199. <https://doi.org/10.1016/j.petrol.2020.108259>
- Barría, J.C., Manzanal, D., Cerrutti, P., Pereira, J.M., 2021a Cement with bacterial nanocellulose cured at high temperature: mechanical performance in the context of CO₂ geological storage. *Geomechanics for Energy and the Environment*. Doi: <https://doi.org/10.1016/j.gete.2021.100267>
- Barría, JC; Manzanal, D; Pereira, JM; Ghabezloo, 2020. CO₂ Geological storage: Microstructure and mechanical behaviour of cement modified with biopolymers after carbonation. *E3S Web Conf.* Vol. 205, 2020. 2nd International Conference on Energy Geotechnics (ICEGT 2020), section: CO₂ Sequestration and Deep Geothermal Energy 18 November 2020 <https://doi.org/10.1051/e3sconf/202020502007>
- Barría, J.C., Manzanal, D. Pereira, J.M., 2022. Effect of supercritical carbonation on porous structure and mechanical strength of cementitious materials modified with bacterial nanocellulose. *Mater. and Struct.* (under review)
- Barría, J.C., Bagheri, M., Manzanal, D., Shariatipour, S.M., Pereira, J.M., 2022. Poromechanical analysis of oil well cement in CO₂-rich environments. *International Journal of Greenhouse Gas Control*. Vol. 119, <https://doi.org/10.1016/j.ijggc.2022.103734>
- Barrow, Nathan et al. 2020. "MAS-NMR Studies of Carbonate Retention in a Very Wide Range of Na₂O-SiO₂ Glasses." *Journal of Non-Crystalline Solids* 534(November 2019).
- Carey, J. W. 2013. "Geochemistry of Wellbore Integrity in CO₂ Sequestration: Portland Cement-Steel-Brine-CO₂ Interactions." *Reviews in Mineralogy and Geochemistry* 77(1): 505–39.
- Caserini, Stefano et al. 2017. "Evaluation of a New Technology for Carbon Dioxide Submarine Storage in Glass Capsules." *International Journal of Greenhouse Gas Control* 60: 140–55. <http://dx.doi.org/10.1016/j.ijggc.2017.03.007>.
- Duguid, A., M. Radonjic, and G. W. Scherer. 2011. "Degradation of Cement at the Reservoir/Cement Interface from Exposure to Carbonated Brine." *International Journal of Greenhouse Gas Control* 5(6): 1413–28.
- Hall, Christopher, and William D. Hodd. 2009. *Water Transport in Brick, Stone and Concrete*. Florida: CRC Press.
- Krakowiak, Konrad J et al. 2020. "Engineering of High Specific Strength and Low Thermal Conductivity Cementitious Composites with Hollow Glass Microspheres for High-Temperature High-Pressure Applications." *Cement and Concrete Composites* 108(May 2019): 103514. <https://doi.org/10.1016/j.cemconcomp.2020.103514>.
- Kuo, Chun-Chin, Chein-Lee Wang, and Hsing-I Hsiang. 2017. "Mechanical and Microscopic Properties of API G Cement after Exposure to Supercritical CO₂." *Terrestrial, Atmospheric and Oceanic Sciences* 28(3): 209–16.
- Martín, Christian M. et al. 2021. "Pozzolanic Activity Quantification of Hollow Glass Microspheres." *Cement and Concrete Composites journal* 118, 103981. <https://doi.org/10.1016/j.cemconcomp.2021.103981>.
- Scrivener, Karen, Ruben Snellings, and Barbara Lothenbach. 2016. *A Practical Guide to Microstructural Analysis of Cementitious Materials*.

Geomechanical and Petrophysical characterization of Bajo Barreal Formation in GSJB

P.A. Vidal^{1,2}, D.G. Manzanal³, J.O. Allard², & C.B. Laskowsky^{1,2,3}

¹*Conicet, Chubut, Argentina.*

²*Universidad Nacional de la Patagonia San Juan Bosco, Chubut, Argentina.*

³*Universidad Politecnica de Madrid*

ABSTRACT:

This study presents geomechanical and petrophysical characterization focused on analyzing outcrop analogue samples of clastic reservoirs and mudstones equivalent to the caprock in the Cerro Colorado de Galveniz (Chubut) and the Cerro Ballena (Santa Cruz) area, Argentina. The mean and median values of dry density measured in rocks of Cerro Ballena (CB) area are at least 0.5 g/cm³ higher than those of Cerro Colorado de Galveniz (CG) area. The CB values show a more extensive range of variation in CB than in CG. The Schmidt hammer index shows that CB locality has higher values than CG, with a difference of approximately 12R among both localities' median and mean values. The permeability was measured with a handheld portable air-permeameter, and the highest values were found in the channel lithofacies. A marked heterogeneity was seen in the permeability values depending on the direction of the measurement. It was carried out perpendicular and parallel to the stratification, being the parallel bearing which presented higher values. This study demonstrates the potential of testing with portable tools for rapid and non-destructive geomechanical and petrophysical characterization. The results contribute to the comprehensive understanding of outcrop analogues to improve subsurface interpretations associated with static and dynamic models.

1 INTRODUCTION

Geomechanical and Petrophysical characterization of stratigraphic units is a fundamental methodology for analyzing hydrocarbon-producing sedimentary basins. The Golfo San Jorge basin has accumulated more than 39,300 wells drilled since 1907 and more than 13,500 active producer wells. However, geomechanical studies are scarce. Petrophysical contributions mainly focus on subsurface data, and outcrop studies are practically nonexistent. This deficit limits the calibration of static and dynamic subsurface models and the decision-making related to the behaviour of geomechanical units. In particular, Bajo Barreal Formation is the fundamental lithostratigraphic unit of the most important petroleum system in The Golfo San Jorge Basin. This unit contains the primary levels of hydrocarbon reservoir sandstones. Its superior sequences are the caprock. The outcrops of the San Bernardo Fold Belt constitute a source of analogues for the oil system par excellence. Previous studies focus on sedimentology and fluvial architecture parameters, clays' characterization, and geochemical petrography studies without covering the geomechanical or petrophysical parameters. The geomechanical and petrophysical characterization focuses on analyzing outcrop analogue of clastic reservoirs and mudstones equivalent to the caprock. The selected areas are Cerro Colorado de Galveniz (Chubut) and Cerro Ballena (Santa Cruz) in Argentina, which are separated by 150 km, aiming to evaluate the variability among the parameters (Fig. 1).

Unconfined compressive strength (UCS) is the most direct geomechanical parameter to evaluate rock strength. Generally, the UCS of rocks can be determined by two different methods: 1) The direct methods carried out in the laboratory as Uniaxial Compressive tests, as suggested by the International Society of Rock Mechanics and American Standards for Testing Materials (ISRM, 1979; ASTM D7012, 2004). These methods are based on procedures under strict sample preparation conditions (ASTM D4543, 2019), are time-consuming, and are destructive. 2) indirect methods for estimating the UCS of rocks are widely used due to several advantages. We can mention, for example, no specimen preparation, usable when the rocks are weak or intensely fractured/weathered and unsophisticated and easily applied equipment. The Schmidt Hammer is the most widely used instrument for the indirect estimation of the UCS in rocks in the field.

Permeability is crucial to understand the petrophysical properties of reservoirs and caprock and is typically considered a critical parameter for hydrocarbon production. Permeability is generally estimated from well-log data in the hydrocarbon industry. The laboratory determinations are expensive, time-consuming, and limited in the number of measurements. Due to this, testing permeability in the field with portable equipment may be the most reliable method of obtaining representative permeability measurements.

This study aims to contribute with a set of reference values of the main hydrocarbon production unit of the Golfo San Jorge Basin. Stratigraphic sections for geomechanical and petrophysical tests were carried out in the field. A portable handheld air permeameter measured *in-situ* permeability, and the Rock Schmidt hammer measured the rebound values "R" (Type L and N). The field data were correlated with laboratory studies of core plugs' mechanical properties (UCS).

2 GEOLOGICAL SETTINGS

The Golfo San Jorge Basin (GSJB) is located in central Argentinian Patagonia (45°00' - 47°30'S latitude and 63°30' - 72°00'W longitude). GSJB corresponds to an intracratonic basin elongated in an east-west direction (Fig. 1). The North Patagonian region surrounds it in the north; the Deseado region in the south; the South Patagonian Andes in the west, and, in the east, the limit is defined by subsurface information under the South American Atlantic Margin. The Golfo San Jorge Basin is divided into five regions according to the current structural style (Fig. 1). The Western Flank and The San Bernardo Fold Belt are characterized by positive inversion characteristics. In contrast, the North Flank, the Basin Center and the South Flank are distinguished for having east-west normal faults.

The economic relevance of GSJB is because it is one of Argentina's most important hydrocarbon-producing areas. GSJB has produced up to 1500 billion m³ of oil from mainly conventional reservoirs in channel fills of Bajo Barreal Formation and its subsurface equivalents. The Bajo Barreal Formation contains the primary levels of hydrocarbon reservoir coarse-grained sandstones, and its superior sequences are the caprock of the system.

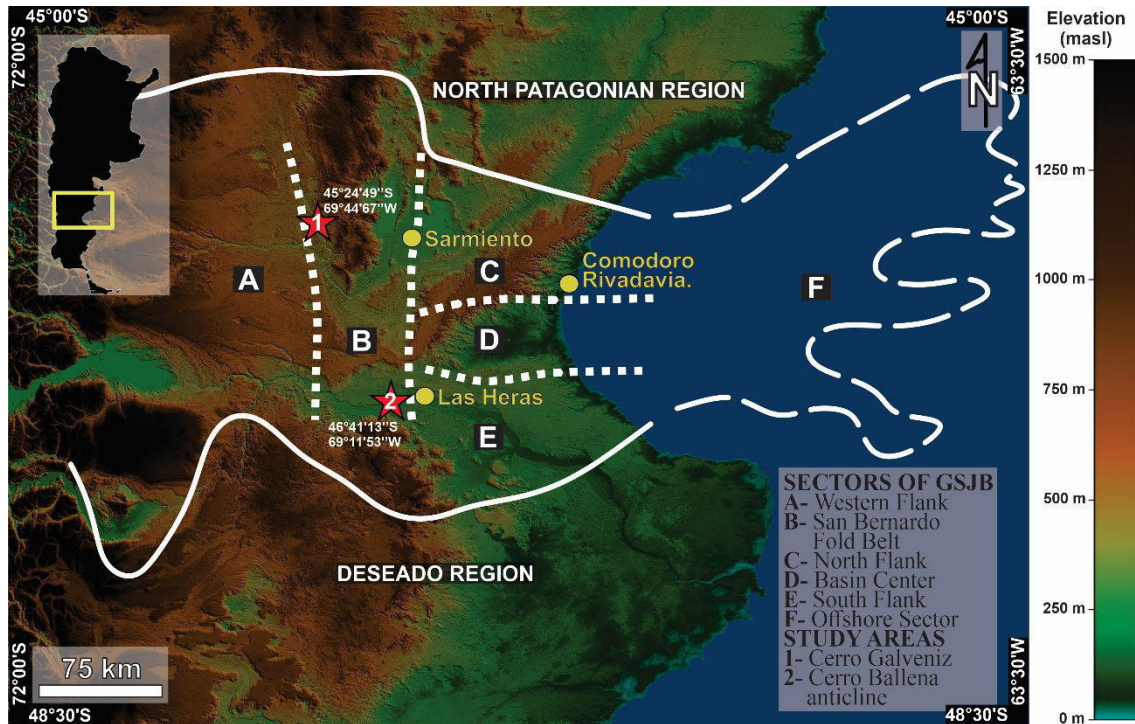


Figure 1: Digital Elevation Model showing GSJB limits and different sectors of the basin, studied areas at the San Bernardo Fold Belt are marked with red stars and urban centers in yellow.

2.1 Stratigraphy

As shown in a simplified lithostratigraphic chart (Fig. 2), the sedimentary record of the GSJB ranges from Middle Jurassic (Bahía Laura Group) to Miocene (Santa Cruz Formation). The focus of this contribution is Bajo Barreal Formation. This Formation was deposited throughout the Upper Cretaceous in an endorheic basin over an area exceeding 150,000 km² with maximum thickness up to 1,300 m due to its wide distribution. The paleoenvironment changes across the basin are represented by sandstones, conglomerates, thick intervals of mudstones, and tuffaceous mudstones. There are thin intercalations of tuffs in lacustrine fan-deltas, volcanoclastic alluvial fans, meandering and braided rivers, and ephemeral rivers. Based on the floodplain composition, the Bajo Barreal Formation is divided into two members (Lower Member and Upper Member). The Lower Member is characterized by channelized sandstones interbedded with fine-grained tuffaceous strata. In contrast, the Upper Member comprises large-scale, isolated channel sand bodies surrounded by grey siltstones and siliciclastic mudstones.

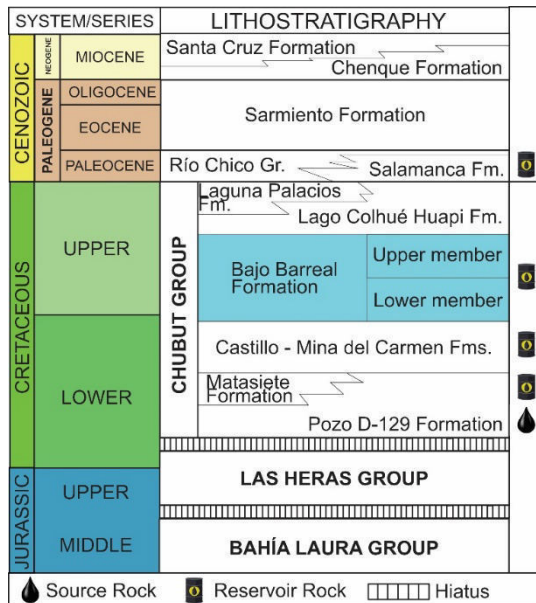


Figure 2: Simplified Chronostratigraphic Chart of the Golfo San Jorge Basin. The rocks studied in this contribution are contained within the Bajo Barreal Formation (Upper Cretaceous) highlighted in sky blue. Modified from Paredes et al. (2020)

3 METHODOLOGY

Geomechanical and Petrophysical characterization was carried out on two stratigraphic sections built up in the studied locations using the Jacob Staff. A total of 180 m and 48m thick of Bajo Barreal Formation was measured in CB (Section A) and CG, respectively. Three lithofacies associations were defined: 1) Siliciclastic Channels (sandstones), 2) Floodplains (mudstones) 3) Tuffs paleosoils (volcaniclastic rocks).

Samples were taken in rock blocks of approximately 0.03 m³ and positioned in the sedimentary logs. Dry density and Unconfined Compressive Strength tests were conducted in the laboratory. In addition, the Schmidt hammer rebound index and air permeability measurements were carried out with portable equipment.

3.1 Schmidt Hammer

The rock hardness was measured with Rock Schmidt N-type and L-type hammers, which consist of a spring-loaded piston that slides on a plunger that releases constant potential energy of N=2.207 Nm and L=0.735 Nm against a metal anvil that is in contact with the rock surface. The plunger hits the rock surface, and the rebound is measured on an arbitrary scale from 10R to 100R. It is called the rebound index, R. According to the ASTM D5873 (2014) standard, the mean values were obtained from 10 representative measurements on the specimen. 660 impacts were made (66 average R values) on outcrops and block samples in a laboratory environment.

3.2 Permeability

Air-permeability (K_{air}) was obtained using a last-generation portable permeameter in sample blocks. Measurements were performed in perpendicular and parallel directions to the sedimentary layering (S_0) using 180 seconds as the maximum time for pressure decline. The median values were plotted in the sedimentary logs.

3.3 Dry Density

Dry density was calculated following the Method A (Water Displacement) according to ASTM D7263 (2009). Previously, paraffin density was calculated as 0.87 g/cm^3 . Dry density was calculated using the following formula:

$$\rho_d = \frac{Md}{\frac{(Mc - M_{sub})}{\rho_w} - \frac{(Mc - Mt)}{\rho_p}}$$

where: M_d = mass of dry specimen; M_c = mass of wax-coated specimen; M_{sub} = mass of submerged paraffin-coated specimen; ρ_p = density of paraffin; ρ_w = density of water at test temperature; ρ_d = dry density.

A total of $n=57$ samples were analyzed, and we used the average dry density of every block sample.

3.4 Unconfined Compressive Strength (UCS)

For UCS values, core plugs were prepared according to ASTM D4543 (2001). A total of 9 core plugs of homogeneous rock with a diameter of 32 mm and slenderness ratio $L/D = 2$ and tested following ASTM D7012 (2014). The UCS considered the average between both tests for block samples with more than one core plug.

4 RESULTS/DISCUSSION

In the CB locality, regarding the mechanical resistance values, the highest values were found in the CBS3 sample (fine-grained sandstones well cemented) belonging to channel lithofacies with values of $R_N = 58$ and $R_L = 56$. In contrast, the lowest values were detected in the poorly cemented CBS2 sample (medium to coarse-grained sandstone) belonging to channel lithofacies with $R_N = 26,5$ and $R_L = 28$. Concerning dry densities, the maximum value was found in the CBS5 sample (Marker Bed) with a value of 2.28 g/cm^3 , while the lowest value was seen in the CBS1 sample (coarse-grained sandstone with conglomerate base) with a value of 1.98 g/cm^3 . The highest estimated UCS is that of the CBS3 sample (fine-grained sandstone) with a value of 25.5 MPa, and the lowest is that of the CBS2 sample (medium to coarse-grained sandstone poorly cemented) with a value of 3.4 MPa. Regarding air permeability, the highest permeability was measured in the CBS1 sample (coarse-grained sandstone with conglomerate base) of the channel lithofacies with a median of 2000 mD for the measurements made perpendicular to S_0 and 3200 mD for the measurements made parallel to the S_0 . The lowest value was measured in CBS4 sample with a median of 44 mD (parallel to S_0) and 3 mD (perpendicular to S_0) (Fig. 3).

In the CG location, in terms of mechanical resistance values, the highest values were found in the CGS2 sample (massive tuff) with values of $R_N= 47$ and $R_L= 45.5$, which responds to a tuffaceous bed associated with paleosoils lithofacies. On the other hand, the lowest values were found in the CGS3 sample (very friable coarse-grained sandstone with poorly cemented) belonging to the channel lithofacies with $R_N= 14$ and $R_L=15.5$, respectively. Regarding the dry densities, the maximum value was found in the CGS7 sample (medium-grained greenish sandstone) belonging to the top of a channel with an average value of 1.9 g/cm^3 . In comparison, the lowest dry density value was found in the CGS2 sample (massive tuff), with a value of 1.53 g/cm^3 . The highest estimated UCS corresponds to the CGS2 sample (massive tuff) with a value of 7.9 MPa and the lowest to the CGS3 sample belonging to a very friable whitish channel sandstone with a very abundant tuffaceous matrix with a value of 1.5 MPa . Regarding air permeability, the highest was measured in the CGS5 sample (greenish sandstone with cross-stratification poorly cemented) with a median of 1100 mD for measurements parallel to the foresets and 374 mD for measurements made perpendicular to them. The lowest value was measured in CGS2 sample (massive tuff) with a median of 45 mD (parallel to S_0) and 22 mD (perpendicular to S_0) (Fig. 3)

A trend of the Rock Strength and Dry Density of the rocks concerning the stratigraphic position is not observed, nor is there a clear relationship between them. The lithology controls the Rock Strength and Dry Density.

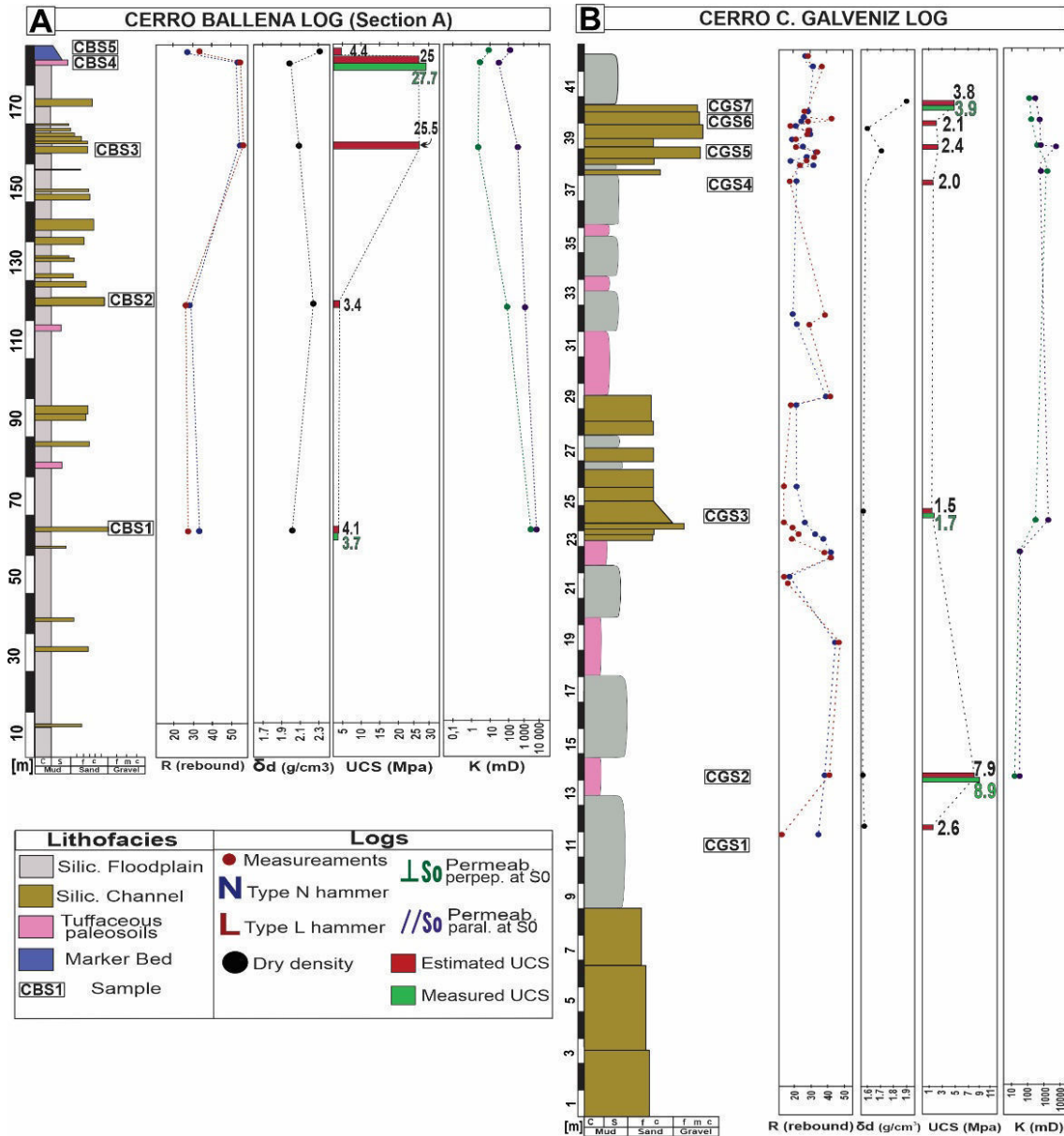


Figure 3: Stratigraphic sections with rebound number, dry density, UCS and permeability logs. A) Cerro Ballena (CB) stratigraphic section and B) Cerro Colorado de Galveniz (CG) stratigraphic section.

Generally, dry densities in rocks from the CB locality are at least 0.5 g/cm³ higher than those from the CG locality (Fig. 4A). CB values show more variability than CG. The Schmidt hammer rebound index in the CB locality shows higher values than CG, with a difference of approximately 12R among the median and mean values of both localities (Fig. 4B).

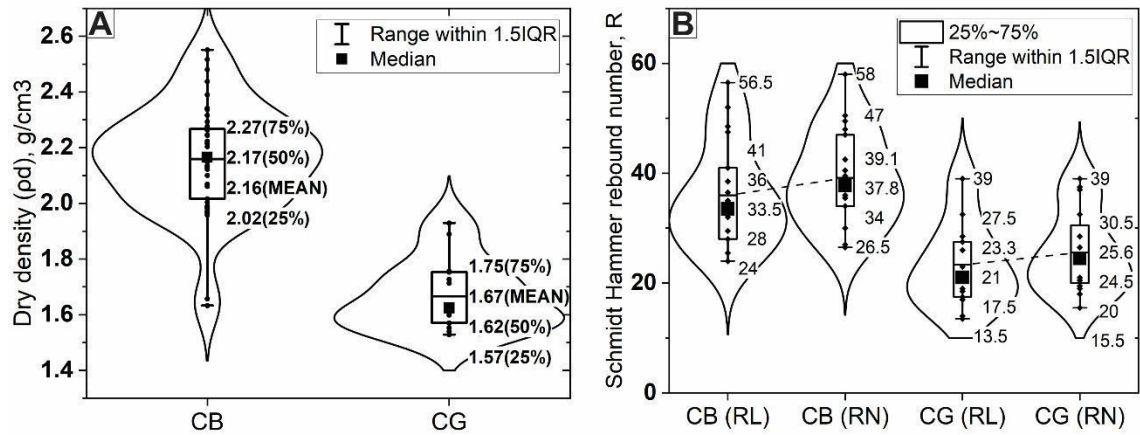


Figure 4: Violin and boxplot graphics of Bajo Barreal Formation samples: A) Dry Density; B) Schmidt hammer rebound number.

In the stress-strain curves, we can observe that the samples belonging to tuffaceous beds of lithofacies paleosoils show a plastic behaviour at the beginning of the test and then a brittle behaviour until the specimen breaks (Figs. 5A, B). The curves belonging to the medium to coarse-grained sandstones (lithofacies of the channel) (Figs. 5C, D) show a brittle behaviour from the beginning of the test until failure.

In the case of the samples CGS3U1 and CGS3U2 (very friable whitish channel sandstone with very abundant tuffaceous matrix), they show a small development of plastic behaviour at the beginning of the test.

This variability in the behaviour of the samples could correlate to the genesis of the deposit and their tuffaceous content, with tuffs having a plastic behaviour: CGS2U1, CGS2U2, CBS4U1 (tuffaceous paleosoils) and to a lesser extent, CGS3U1 and CGS3U2 measurements (sandstone with tuffaceous matrix). It is hypothesized that this behaviour at the beginning of the test can be caused by the micro-crack closure and due to the nature of the pyroclasts exposed to stress. To corroborate this hypothesis, it is necessary to make thin sections of the samples previous to the compression and after the compression to evaluate, for instance, pumice and shards collapse in the samples tested.

Regarding UCS and R, it can be seen that rock strength is not correlated to the stratigraphic position of the samples. In floodplain lithofacies, tuffaceous content increases de rock strength values, having the greatest strength in the column and with the highest Young's moduli (Table 1). This behaviour is not observed in channel lithofacies, probably due to the poor cementation or alteration of the tuffaceous matrix by fluid circulation.

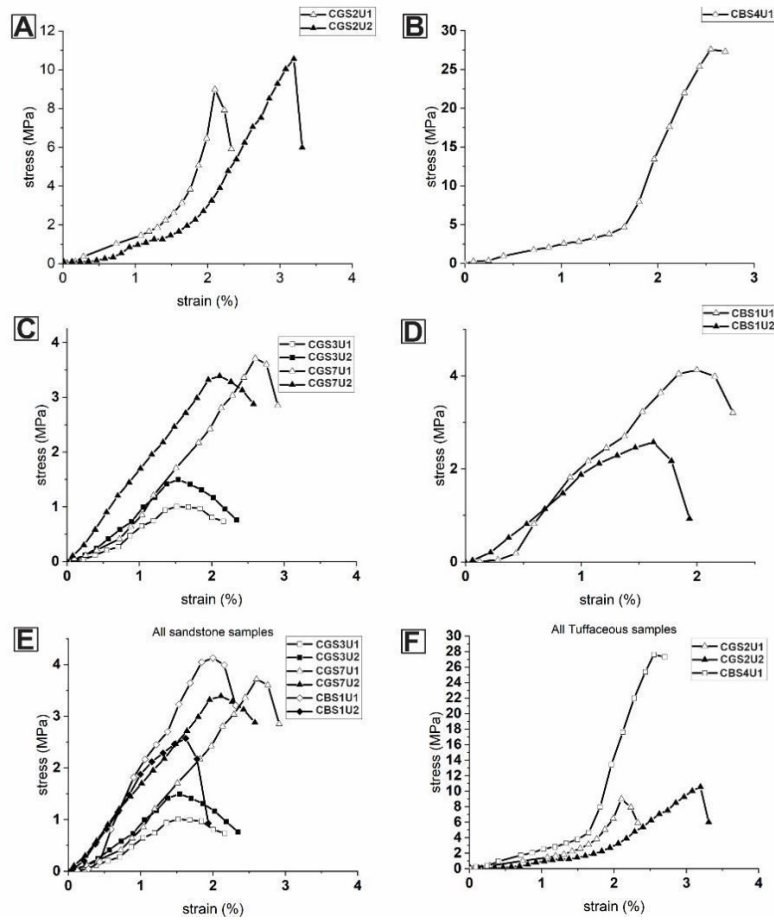


Figure 5: Strain-Stress curves of Bajo Barreal Formation samples. A) Tuffaceous paleosoils samples (Cerro Galveniz). B) Tuffaceous paleosoils samples (Cerro Ballena). C) Channel sandstone samples (Cerro Galveniz) CGS3 in the middle of the stratigraphic column and CGS7 in the top, both separated 15 m. D) Channel sandstone samples (Cerro Ballena) at the beginning of the stratigraphic column. E) All Channel sandstone samples. F) All tuffaceous paleosoils samples.

Table 1. Young modulus calculated in the analyzed samples.

Samples	Lithofacies	Grain Size	E (MPa)
CGS2U1	Tuffaceous Paleosoil		27
CGS2U2	Tuffaceous Paleosoil		11
CGS3U1	Channel Sandstone	coarse	2
CGS3U2	Channel Sandstone	coarse	2.8
CGS7U1	Channel Sandstone	medium to coarse	4.2
CGS7U2	Channel Sandstone	medium to coarse	3.5
CBS4U1	Tuffaceous Paleosoil		46.8
CBS1U1	Channel sandstone	coarse	5.3
CBS1U2	Channel sandstone	coarse	3.6

CB locality has higher values on dry density and R index. This spatial variability in the parameters correlates with the degree of exhumation and the sedimentary overload of each locality: the more exhumation and the less overload, the lower values.

A trend of the Rock Strength and Dry Density of the rocks concerning the stratigraphic position is not observed, nor is there a clear relationship between them. The lithology controls the Rock Strength and Dry Density.

5 CONCLUSIONS

The quantitative analysis carried out shows that the CB outcrops present, on average, the highest R index and the highest dry densities, while for CG the R index and dry densities are the lowest of the two studied locations.

The preliminary results show that the highest R values are found in rocks with the highest tuffaceous content in the sandstone matrix and, in turn, impact the permeability, conferring the lowest permeabilities of the entire column. Tuffaceous content generally increases rock strength and decreases permeability in floodplain rocks. It is observed that the highest densities do not necessarily coincide with the highest UCS. The two rocks with the highest UCS have intermediate or low densities.

This study demonstrates the potential of testing with portable tools for rapid and non-destructive geomechanical and petrophysical characterization. The results contribute to the comprehensive understanding of outcrop analogues to improve subsurface interpretations obtained from conventional well-logs, which control the static and dynamic models. In particular, the data obtained could contribute to calibrating rock types defined from the combination of well profiles that evaluate mechanical resistance, permeability and tuffaceous content. Future characterizations will increase the UCS data and the outcrop measurements in the main fluvial deposits to calibrate the trends recognized in this study.

6 REFERENCES

- ASTM D4543. 2019. Standard Practices for Preparing Rock Core as Cylindrical Test Specimens and Verifying Conformance to Dimensional and Shape Tolerances. ASTM International, West Conshohocken, PA. www.astm.org.
- ASTM D5873. 2014. Standard Test Method for Determination of Rock Hardness by Rebound Hammer Method. ASTM International, West Conshohocken, PA. www.astm.org.
- ASTM D7263. 2009. Standard Test Methods for Laboratory Determination of Density (Unit Weight) of Soil Specimens. ASTM International, West Conshohocken, PA. www.astm.org.
- ISRM (1979) Suggested methods for determining the uniaxial compressive strength and deformability of rock materials. *Int J Rock Mech Min Sci* 16(2):135–140

Evaluation of physio-mechanical properties of Gyeongju bentonite using X-ray CT

M. Diaz, S.S. Kim, G.W. Lee, S. Yun, K.Y. Kim
Korea Maritime and Ocean University, Busan, Republic of Korea

C. Lee, J.S. Kim, M. Kim
Korea Atomic Energy Research Institute, Daejeon, Republic of Korea

ABSTRACT:

This study presents measurements of the physical and mechanical properties of Gyeongju bentonite, a candidate sealing material for radioactive waste disposal in South Korea. Cylindrical samples were prepared with different dry densities and water contents. The samples were used to measure the Uniaxial Compression Strength and P-wave velocity and also used for X-ray CT inspection. Afterward, the physical and mechanical properties were contrasted with the CT observations. The results showed that the Uniaxial Compression Strength and the P-wave velocity have a linear and increasing relationship with the dry density. Also, higher water content increased the values of the measured parameters, especially for the P-wave velocity. The X-ray CT analysis indicated a clear relation between the mean CT value and the dry density, Uniaxial Compression Strength, and P-wave velocity. The effect of the higher water content was also captured with the mean CT values, where higher values were recorded for samples of the same dry density but higher water content. These relationships between the mean CT value and other properties are a handy non-destructive tool to characterize local internal variations and predict physical properties using images only.

1 INTRODUCTION

Engineered Barrier Systems (EBS) are key elements of deep geological disposal of high-level radioactive waste (Smith, 1990). EBS are composed of multiple disposal tunnels, from which smaller wells are drilled to allocate canisters that contain nuclear spent fuel. Other components of EBS, are the buffer, and backfill materials (Booker et al., 2004). The buffer material serves to cover the interior of the wells and isolate the canister from the host rock. Finally, once all the wells of a disposal tunnel are full, the tunnel is sealed with the backfill material.

Since the early development of the concept of EBS, it was recognized that the properties of the host rock strongly affect its performance, and therefore a careful selection of the site should be carried out (Pigford, 1992). Moreover, the buffer material is meant to protect the canister from the deformation of the surrounding rock and isolate it physically, chemically, hydraulically and biologically to block the outflow of radionuclides. On the other hand, the backfill is placed to hydraulically isolate the well, maintaining the cushioning material intact, and mechanically stabilize the shaft's entrance.

South Korea is working on the design and development of radioactive waste repositories, and testing the performance of local materials. Most domestic studies in Korea have been carried out with Ca bentonite made in Gyeongju by CLIRIANT KOREA, which has produced mainly two types named KJ-I and KJ-II fabricated before and after 2015 respectively (Yoon et al., 2018). The thermal conductivity of KJ-II has been said to be higher due to a higher concentration of high thermal conductivity minerals such as Quartz, Cristobalite, and Calcite. Similarly, Yoo et al. (2016) evaluated the physical and chemical properties of KJ-II bentonite, and reported a water content of 10.96% and a moisture content of 12.31%. These values are in line with the requirements of average water content of $\leq 13\%$ with a max. of 15%, set for Ca bentonite as a buffer material (Kiviranta et al., 2011). On the other hand, the swelling index of KJ-II bentonite

was 6.5 mL/2g, a value lower than the minimum of 10 mL/2g suggested by Kiviranta et al. (2011). In order for cushioning materials to function properly as barriers, they must have a high swelling capacity. However, the swelling pressure must be maintained properly so as not to impose an excessive load on the canister and surrounding rock. In this regard, Lee et al. (2011) observed the effect of the temperature on the swelling pressure of Gyeongju bentonite. At room temperature, the swelling pressure was 5.3 MPa, and it tended to decrease with increasing temperature. These results were consistent with the studies of Towhata et al. (1993) and Suzuki & Fujita (1999), which also reported that heating induced volume contraction under loading. More recently, Yoon et al. (2020) studied the unsaturated behavior of Gyeongju bentonite, and drew soil-water characteristic curves considering temperature variations. These examples show how the complex thermal-hydrological-mechanical-chemical conditions, in which the engineered barrier is placed, induce constant changes on its physical and mechanical properties. Moreover, the usage of pre-fabricated bentonite blocks was proposed recently to speed up the construction process (Tan et al., 2021), an alternative that South Korea has also considered.

In this work we evaluated the basic physico-mechanical properties of Gyeongju bentonite as a candidate buffer material under the assumption that it will be pre-fabricated and installed in the form of blocks. The samples were fabricated with varying water content and dry density, and properties such as elastic wave velocity, and uniaxial compressive strength were measured. These properties were later compared with X-ray CT analysis to derive relations that are meant to be used as non-destructive tools for detailed material characterization.

2 MATERIALS AND METHODS

The cylindrical samples used in this study were prepared with Gyeongju bentonite. Basic mechanical, hydraulic and thermal properties of this bentonite have been studied (Lee et al. 2010), and it has been reported that upon hydration, it can yield swelling pressures of 5.3 MPa. Additionally, the swelling pressure of Gyeongju bentonite decreased with increasing temperature. Moreover, bentonite blocks used as buffer material generally should have a dry density of at least 1.6 g/cm³ to secure stability. In this study, cylindrical samples of 3 and 5 cm in diameter and height were prepared with Gyeongju bentonite. The samples had three dry densities of 1.4, 1.6 and 1.8 g/cm³, and three water contents of 10, 20, and 30%. In the end, three sets of six samples were prepared. Each set consisted of three samples of 10% of water content and different dry density, two samples of 20% of water content and dry densities of 1.4 and 1.6 g/cm³, and one sample of 30% of water content and 1.4 g/cm³ of dry density. The first two sets were used for UCS, and P-wave velocity measurements, while the third was taken for X-ray CT inspection.

During the sample preparation process, the amount of dry bentonite powder and water were determined to achieve each dry density, using as a reference the size of the compression cell. First, the dry bentonite powder (Fig. 1a) and the specified amount of water were mixed using a stirrer to achieve a uniform consistency. Then, the mixture were put into the compression cell, and loaded until each specified dry density was reached (Fig. 1b). However, for certain conditions such as 30% of water content, it was impossible to fabricate samples at 1.6 and 1.8 g/cm³ of dry density because that would mean increasing the maximum load beyond the cell's allowable strength. Finally, figure 1 shows the Uniaxial Compressive Strength equipment (c), the P-wave velocity device (d), and the X-ray CT equipment (e) used in this study.

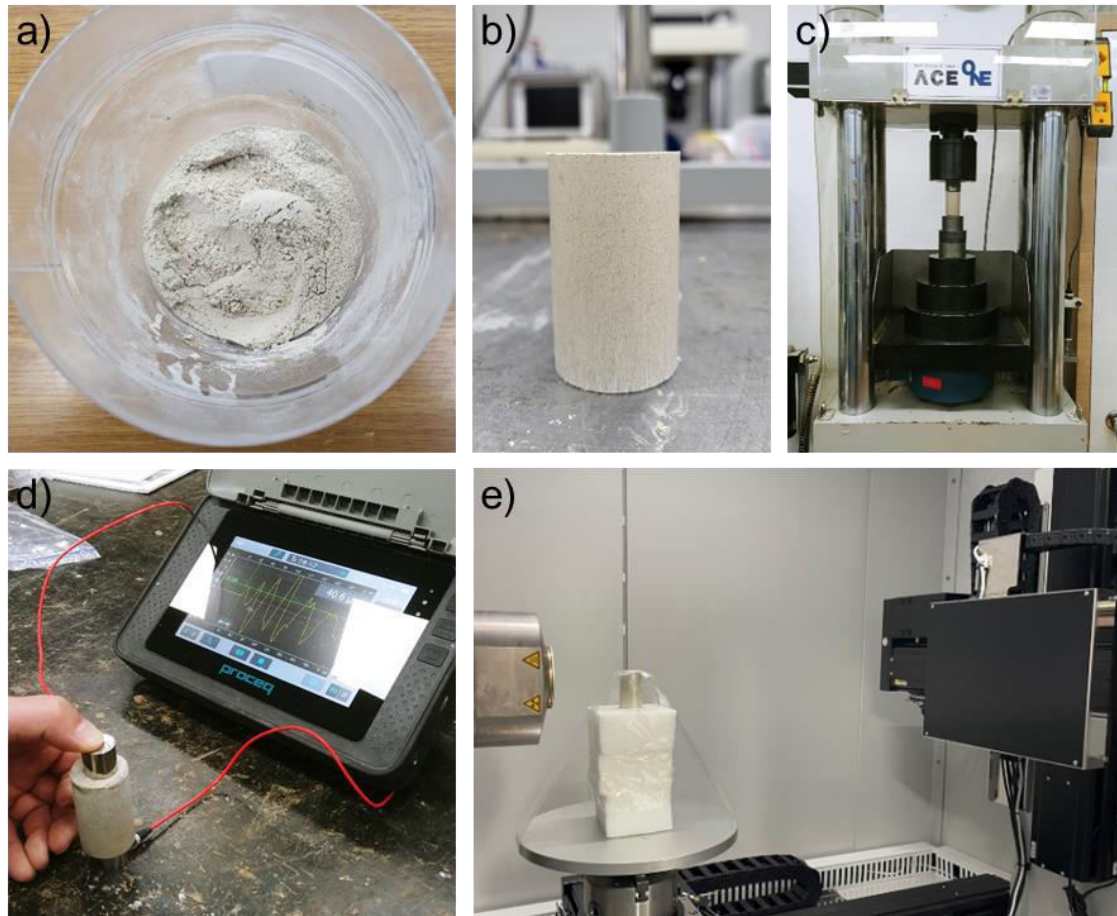


Figure 1. Bentonite sample and testing equipment. Bentonite powder before adding water (a), final cylindrical sample (b), Uniaxial Compressive Strength (c), P-wave velocity (d) and X-ray CT equipment (e).

3 RESULTS

3.1 *Uniaxial compressive strength and P-wave velocity*

Results of the UCS and P-wave velocity tests for the first two sets of bentonite samples are presented in Figure 2, which shows relationships among dry density, UCS, and P-wave velocity. The results of UCS and P-wave velocity tests shown here represent the mean values of sets 1 and 2 of samples prepared under the same dry density and water content. The UCS value increased with increasing dry density (Fig. 2a), and the water content had a small effect on the UCS. Similarly, the P-wave velocity also increased with increasing dry density. However, the effect of the water content was more evident to that observed for the UCS, with larger P-wave velocities for samples with the same dry density but higher water content (Fig. 2b). This resulted in a larger gradient for samples with a higher water content of 20%. The elastic wave velocity is affected by the individual characteristics of the constituting material. As the voids in samples decrease, especially in those with higher dry density, the elastic wave velocity increases. Lastly, the uniaxial compressive strength and the P-wave velocity also showed a linearly increasing relationship, with a smaller gradient for cases with a higher water content (Fig. 2c).

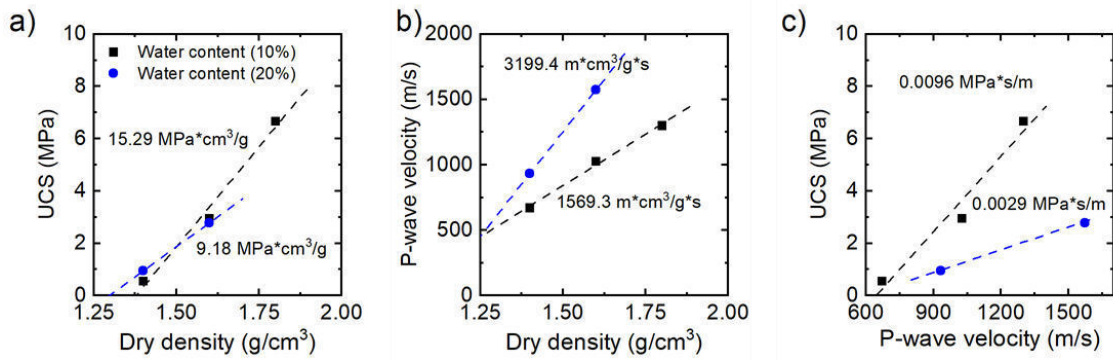


Figure 2. Results of Uniaxial Compressive Strength (a), and P-wave velocity (b) against dry density. Relationship between UCS and P-wave velocity (c).

X-ray CT values and physio-mechanical properties

The internal structure of bentonite samples was evaluated through X-ray CT scanning using the third set. As mentioned above, the bentonite samples are composed of a mixture of bentonite powder and water. Dry density variations within each sample can be expected due to localized changes resulting from the preparation process. These changes can be quantified at every pixel or voxel from the CT images. Figure 3 shows typical X-ray CT image of the cross sections of the Gyeongju bentonite samples, indicating the region of analysis, which had a diameter of 15 mm and it was located at the center of the cross section.

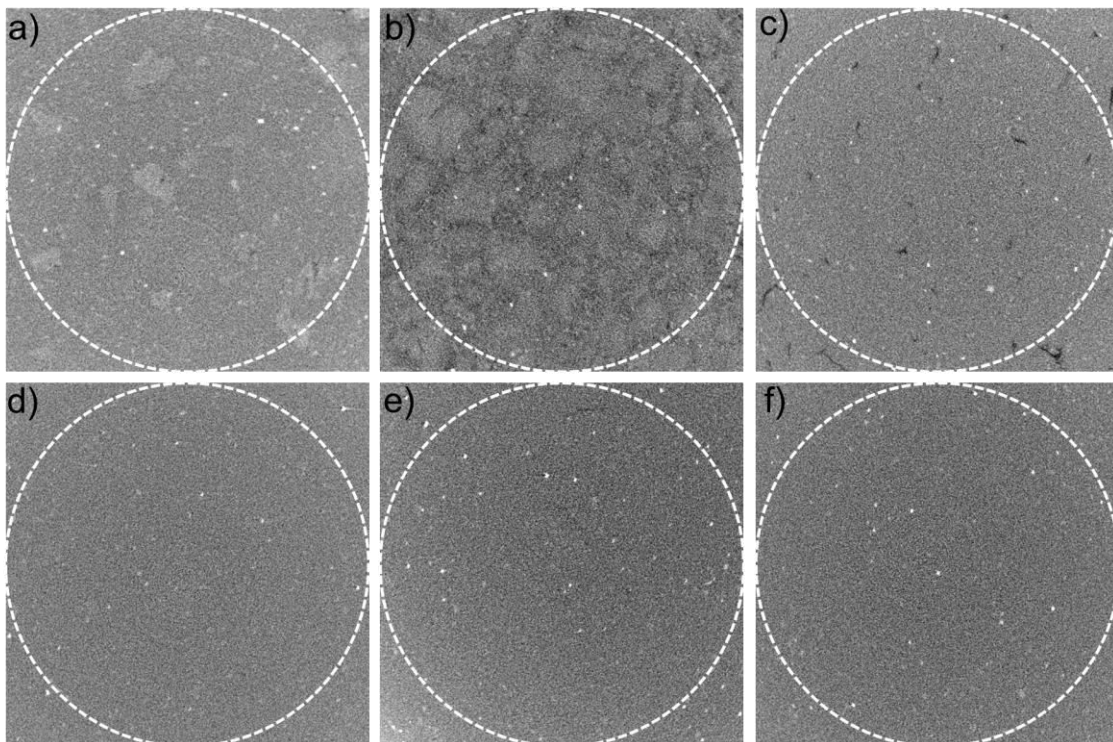


Figure 3. X-ray CT cross section used for the CT analysis. The cross section corresponds to samples prepared with dry density (g/cm³) and water content (%) of; 1.4(10%) (a), 1.4(20%) (b), 1.4(30%) (c), 1.6(10%) (d), 1.6(20%) (e), and 1.8(10%) (f).

Darker areas indicate zones of lower density, while lighter areas represent zones of higher density. Figures 5a – c correspond to bentonite samples with the same dry density of 1.4 g/cm^3 , but with 10, 20 and 30% of water content, respectively. Similarly, Figures 5d and e show cases with the same dry density of 1.6 g/cm^3 , but 10 and 20% of water content, respectively. Lastly, Figure 5f corresponds to a sample with a dry density of 1.8 g/cm^3 and a water content of 10%. In Figure 5, most samples exhibit a uniform internal structure composed of small particles. However, Figures 5a and b present areas with lighter CT values. These differences resulted from poor mixing of water and bentonite during sample preparation that ended up forming localized large particles.

The values of the pixels composing the X-ray CT images have a direct relation with the density of the material. Because of this, the correlation between the sample properties and the mean CT values were analyzed in Figure 4. The mean CT value tends to increase with the dry density of the material (Fig. 4a). Also, for samples with the same dry density, the mean CT values were higher when the water content increased (20%). This is because with a higher water content, the samples were able to reach higher densities. Similarly, the correlation between the mean CT and the UCS also shows a positive linear relationship. Although the measured mean CT values are higher for cases with a 20% water content, their gradient of mean CT values was lower. Finally, Figure 4c shows the mean CT value against the P-wave velocity, which also presents a linear relationship, and similar to the previous cases, the gradient of mean CT value was lower for the cases with higher water content (20%). In summary, a higher water content resulted in lower gradients for the relations between the mean CT value and the dry density and UCS. However, the mean CT values were generally higher for samples with a higher water content.

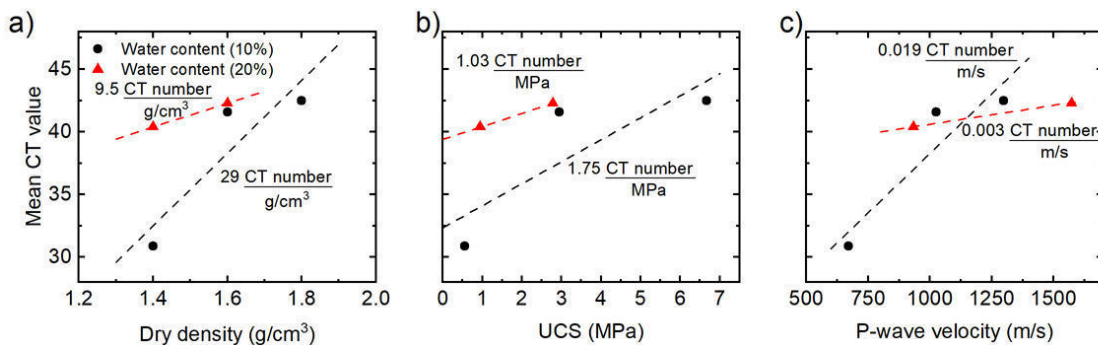


Figure 4. Results of mean X-ray CT values of each region of analysis against the dry density (a), Uniaxial Compressive Strength (b), and P-wave velocity (c).

The relationships between the CT values and the dry density and P-wave velocity are useful as they can be used to discriminate local variations within the sample by using CT images only. Moreover, these relationships can also be used to predict physical and mechanical properties from a new set of samples based on CT images of their internal structure. For example, in Figure 4a, the gradient for samples of 10% of water content is $29 \text{ CT units}/(\text{g/cm}^3)$. Then, this relation can be used to obtain the dry density based on CT values. Finally, X-ray CT inspection can also be used as a quality control step during bentonite block manufacturing.

4 CONCLUSIONS

A physico-mechanical characterization of Gyeongju bentonite as an engineering barrier for underground nuclear waste repositories has been carried out. Cylindrical bentonite samples were prepared under different dry densities and water content. Afterwards, the Uniaxial Compressive

Strength, the P-wave velocity were measured and correlated with CT values. The conclusions are as follows.

UCS and P-wave velocity increased with increasing dry density for samples with the same water content. P-wave velocity also increased for samples with increasing water content and equal dry density. Conversely, the effect of the water content on the UCS was less evident. Moreover, the UCS also showed an increasing trend with increasing P-wave velocity.

The X-ray CT analysis indicated that the mean CT value increased with increasing dry density, UCS, and P-wave velocity. The mean CT value also increased with increasing water content, for samples under the same dry density. Finally, the gradients between the mean CT value and the dry density were used to create density maps and therefore obtain physical properties based on CT images only.

Acknowledgment:

This work was supported by the Institute for Korea Spent Nuclear Fuel (iKSNF) and National Research Foundation of Korea (NRF) grant funded by the Korea government (Ministry of Science and ICT, MSIT) (No. 2021M2E1A1085197 & No. 2021R1A2C2011634).

5 REFERENCES

- Booker, J.R., Brachman, R., Quigley, R.M. and Rowe, R.K., 2004. Barrier systems for waste disposal facilities. Crc Press.
- Kiviranta, L. and Kumpulainen, S., 2011. Quality control and characterization of bentonite materials (No. POSIVA-WR--11-84). Posiva Oy.
- Lee, J.H., Lee, M.S., Choi, H.J. and Choi, J.W., 2010. Temperature effect on the swelling pressure of a domestic compacted bentonite buffer. *Journal of Nuclear Fuel Cycle and Waste Technology (JNFCWT)*, 8(3), pp.207-213. (In Korean).
- Pigford, T.H., 1992. The Engineered Barrier System: Performance Issues. MRS Online Proceedings Library (OPL), 294.
- Smith, M.J., 1980. Engineered barrier development for a nuclear waste repository in basalt: an integration of current knowledge (No. RHO-BWI-ST-7). Rockwell International Corp., Canoga Park, CA (USA). Energy Systems Group.
- Suzuki, H. and Fujita, T., 1999. Unsaturated hydraulic property of buffer material (No. JNC-TN--8430-99-010). Japan Nuclear Cycle Development Inst.
- Tan, Y., Zhang, H., Zhang, T., Zhang, G., He, D. and Ding, Z., 2021. Anisotropic hydro-mechanical behavior of full-scale compacted bentonite-sand blocks. *Engineering Geology*, 287, pp.106093.
- Towhata, I., Kuntiwattanaku, P., Seko, I. and Ohishi, K., 1993. Volume change of clays induced by heating as observed in consolidation tests. *soils and foundations*, 33(4), pp.170-183.
- Yoo, M., Choi, H.J., Lee, M.S. and Lee, S.Y., 2016. Measurement of Properties of Domestic Bentonite for a Buffer of an HLW Repository. *Journal of Nuclear Fuel Cycle and Waste Technology (JNFCWT)*, 14(2), pp.135-147. (In Korean).
- Yoon, S., Cho, W., Lee, C. and Kim, G., 2018. Thermal Conductivity Investigation of Korean Bentonite Buffer Materials. In *Proceedings of the Korean Radioactive Waste Society Conference* (pp. 131-132). Korean Radioactive Waste Society.
- Kiviranta, L. and Kumpulainen, S., 2011. Quality control and characterization of bentonite ma-

- terials (No. POSIVA-WR--11-84). Posiva Oy.
- Lee, J.H., Lee, M.S., Choi, H.J. and Choi, J.W., 2010. Temperature effect on the swelling pressure of a domestic compacted bentonite buffer. *Journal of Nuclear Fuel Cycle and Waste Technology (JNFCWT)*, 8(3), pp.207-213. (In Korean).
- Pigford, T.H., 1992. The Engineered Barrier System: Performance Issues. *MRS Online Proceedings Library (OPL)*, 294.
- Smith, M.J., 1980. Engineered barrier development for a nuclear waste repository in basalt: an integration of current knowledge (No. RHO-BWI-ST-7). Rockwell International Corp., Canoga Park, CA (USA). Energy Systems Group.
- Suzuki, H. and Fujita, T., 1999. Unsaturated hydraulic property of buffer material (No. JNC-TN--8430-99-010). Japan Nuclear Cycle Development Inst.
- Tan, Y., Zhang, H., Zhang, T., Zhang, G., He, D. and Ding, Z., 2021. Anisotropic hydro-mechanical behavior of full-scale compacted bentonite-sand blocks. *Engineering Geology*, 287, pp.106093.
- Towhata, I., Kuntiwattanaku, P., Seko, I. and Ohishi, K., 1993. Volume change of clays induced by heating as observed in consolidation tests. *soils and foundations*, 33(4), pp.170-183.
- Yoo, M., Choi, H.J., Lee, M.S. and Lee, S.Y., 2016. Measurement of Properties of Domestic Bentonite for a Buffer of an HLW Repository. *Journal of Nuclear Fuel Cycle and Waste Technology (JNFCWT)*, 14(2), pp.135-147. (In Korean).
- Yoon, S., Cho, W., Lee, C. and Kim, G., 2018. Thermal Conductivity Investigation of Korean Bentonite Buffer Materials. In *Proceedings of the Korean Radioactive Waste Society Conference* (pp. 131-132). Korean Radioactive Waste Society.
- Yoon, S., Jeon, J.S., Go, G.H. and Kim, G.Y., 2020. An Evaluation of Soil-Water Characteristic Curve Model for Compacted Bentonite Considering Temperature Variation. *Journal of the Korean Geotechnical Society*, 36(10), pp.33-39. (In Korean).

Fuzzy expert system for preliminary qualification of Carbon Capture and Storage projects.

J.H. Martínez-Meneses

Posgrado de Ingeniería - UNAM, Mexico City, Mexico

S.R. García-Benítez (Director thesis)

Instituto de Ingeniería - UNAM, Mexico City, Mexico

ABSTRACT:

Carbon capture and storage (CCS), as the process that separates CO₂ emitted by industry and energy-related sources, transports it to a storage site and isolates it from the atmosphere over the long term, is an alternative for stabilizing atmospheric concentrations of greenhouse gases. The selection of the capture-storage site is a complex and multiparametric task that requires handling a large number of variables on the natural environment, infrastructure and repercussions on the environment, among other parameters. Taking into account that the number of capture and storage sites from where could collect experiences for discarding or ratifying hypotheses, still minimal. In this research, a fuzzy expert system (FES) that helps in the qualification of the susceptibility of a geographical context for the development of a CSS project is presented, based on preliminary information on the state of the emission, the availability of infrastructure for transport, the tectonic environment, the specific qualities of the geological formations involved, the geothermal and pressure conditions, as well as the hydrodynamics of the system. The proposed FES extracts the experiences of experts on the subject who have rated environments and prioritized their effectiveness in CSS and translates it into clear rules that conclude on a rating for each site.

1 INTRODUCTION

The Intergovernmental Panel on Climate Change includes carbon dioxide capture and storage (CCS) in the set of measures to stabilize atmospheric concentrations of greenhouse gases (IPCC 2005). CCS is flexible (especially with respect to the social, financial and legislative changes required for its adoption) and defining a implementation method technologically affordable and sustainable could mean its establishment as the preferred option in the world, as long as the issues that make it expensive to implement are addressed (GCCSI 2020).

It is essential that the whole process must be taken into account when deciding on the qualities of a site for a CCS project (Bui and Mac-Dowell 2019). In this sense the number of variables involved in the decision on the project site is very large and their sources are diverse and their formats are different. For example, regarding storage, in general, sites with geological storage potential must show capacity, injectivity, confinement, geological stability and cannot be considered for other uses (Newell and Ilgen 2019), so the evaluation of a basin must consider aspects such as tectonic activity, sediment type, geothermal and hydrodynamic regimes, hydrogeochemical factors, among others. With the large number of variables and the parallel conditions in which they interrelate, making a decision on the most suitable site to develop a CCS project is an extremely complex task (Boot-Handford et al. 2014, GCCSI 2020).

In this research, a fuzzy expert system (FES) is proposed to preliminarily qualify sites for CCS projects through scenario simulations in a language familiar to most experts and managers involved in decision-making. The idea of a FES for CCS is to extract human experience and knowledge and transfer it to a computer that handles vagueness, uncertainty (natural in measurements and deductions) and reasoning in large dimensions to deliver a qualification (Hájek and Novák 2003).

The FES proposed in this research qualifies the susceptibility of a site (geographical context) for the development of a CCS project based on preliminary information about emission status, the availability of transport infrastructure, the tectonic environment, the specific qualities of the geological formations involved, geothermal, pressure, and hydrodynamic conditions. Experience and human intelligence are stored in the form of fuzzy sets and If-Then rules from which the FES gives users specific output advice in the form of an evaluation. For site qualification, the recommendations of Bachu (2000), CIEMAT (2007), Dávila-Serrano (2011) and NETL (2017) are mainly integrated.

This FES is flexible and robust enough to be applied to the qualification of various geo-situations and regions in the world. Accepting or rejecting a place requires specifying, refining and analyzing various ideas and ranking them according to the advantages they represent for a specific purpose, so this FES is proposed to be scaled up and, by integrating other subsystems, cover more aspects, go deeper, or consider other types of representations.

2 DESIGN OF THE FES TO QUALIFY CCS SITES

The following FES is designed according to the reasoning recommendations of Bachu (2000), CIEMAT (2007) and Dávila-Serrano (2011). The application is aimed at developments in sedimentary basins; however, the method is applicable to other geo-conditions. The input variables considered in this system are: (1) the level of anthropogenic CO₂ emissions, (2) the availability of infrastructure for CO₂ transportation from the capture site to the storage site, (3) the tectonic environment, (4) the qualities of the storage and seal formations, (5) the geothermal and pressure qualities of the sedimentary basin and (6) the governing hydrodynamic regime at the site. The output is a qualification of the susceptibility of the site to develop CCS projects (Fig. 1). In this qualification, which is preliminary in nature and requires minimum inputs to be issued, hydrogeochemical, social, economic and legal factors are not considered as they belong to a more complex argumentation process that requires inputs defined in acute exploration campaigns and structured rules based on successful projects (fully documented); information that is normally obtained when the sites with the best qualities for developing a project have been selected.

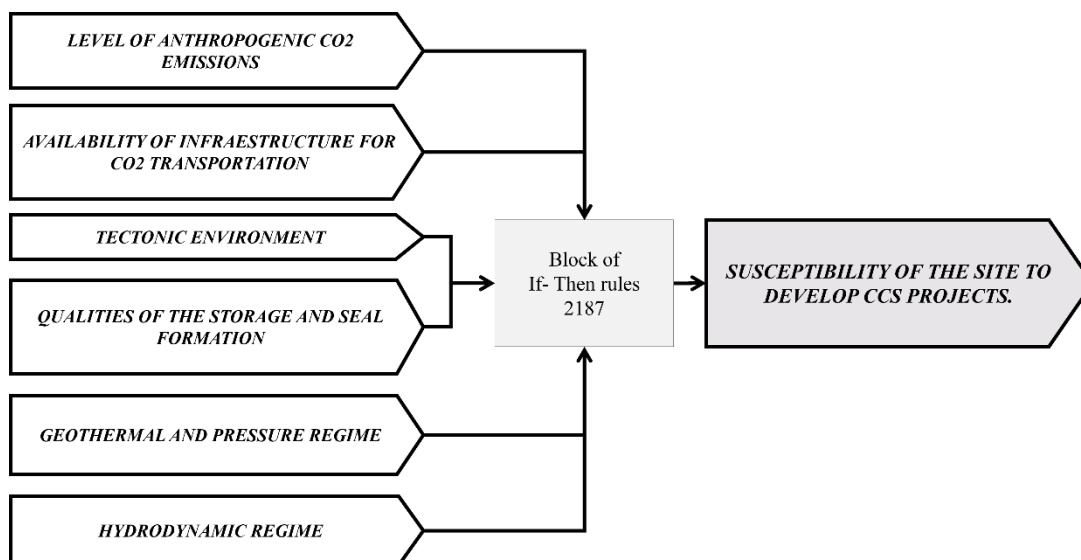


Figure 1. Fuzzy Expert System

Among the most important variables are those that rate the properties of the formations depending on their role as store or seal. In this case, a subsystem with three inputs is proposed: i) the qualification of the Quality of the storage formation, ii) the qualification of the Quality of the seal formation and iii) the qualification of the Geometric configuration of the formations. Formations, categorized with representative porosity and permeability and homogeneity, are labelled according to property values between the ranges considered optimal for adequate injection and storage, without risk of inducing fracturing and with large-scale capacities (CIEMAT 2007, Ruíz et al. 2008, NETL 2017).

The definition of the fuzzy sets of representative porosity and permeability variables is based on the classification by Levorsen for hydrocarbon-producing rocks (Lorenzo and Morato 2018) and is in line with the recommendations of Bachu (2000), CIEMAT (2007), Dávila-Serrano (2011) and NETL (2017) (Fig. 2). To integrate homogeneity, in terms of continuity of materials, the evaluation of the thicknesses of sandstone or limestone and shale strata (preferred for the store and seal formations, respectively) is proposed according to Equation 1.

$$H = \frac{h_t - \sum h_i}{h_t} \times 100\% \tag{1}$$

where H = homogeneity of the storage or seal formation (value expected to be as close to 100%); h_t = thickness of the analyzed strata; h_i = Thickness of the rock formation(s) without store/seal characteristics, the sum of thicknesses.

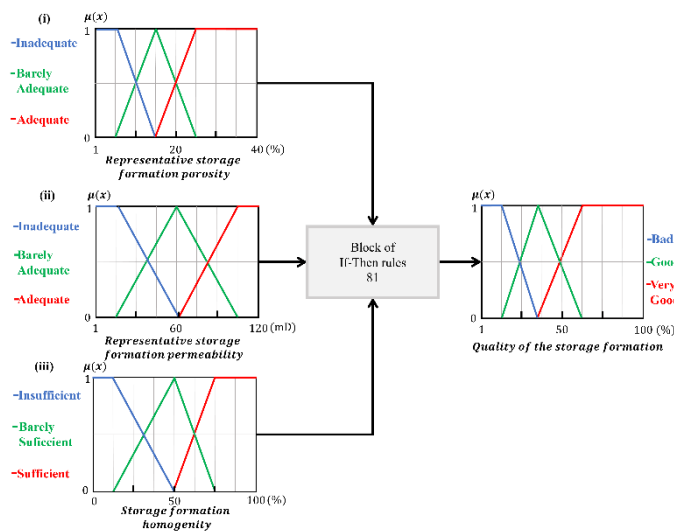


Figure 2. Fuzzy systems for the qualification of Quality of the storage formation

The structure of this subsystem is completed by the block of rules containing 81 logical expressions according to the experiences of CIEMAT (2007), Sánchez et al (2008) and GCCSI (2020).

Among the conditions that have the most significance on the final site qualification for CCS is the Geometric configuration of the formations (Fig. 3). With this subsystem, the degree to which the seal formation overlies (roof and wall) the reservoir formation is rated (IPCC 2005, Ruíz et al. 2008, NETL 2017) using a spatial metric that relies on experience and technique (stratigraphic correlations, geophysical logs, well cores, as well as seismic sections) to define the distribution and obtain comparable views between formations (Caja-Rojas 2017).

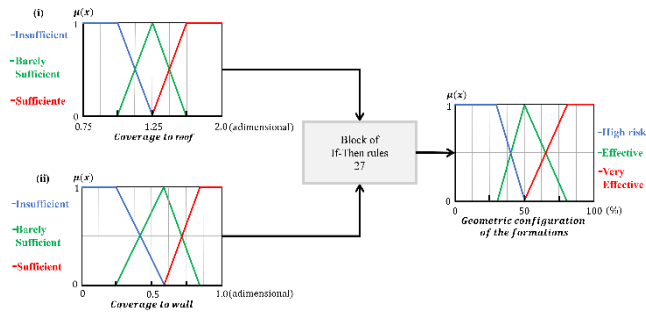


Figure 3. Fuzzy systems for the Geometric configuration of the formations

The idea behind this qualification is to relate the size of the two formations using a simple basic unit (cube) so that the fit to the required sizes for formation walls and roof can be measured (Fig.4). The areas and thicknesses of both formations must first be recognized and then discretized into minimum cubic units (details in Garcia and Martinez (2021)) so that the cube contacts between the store and seal are accounted for with the constraints being 1) that all units in the roof of the store formation are in the same area and 2) that all the units in the walls of the store formation are in contact with the seal formation units. The relative is obtained with the Equations 2 and 3.

$$Ct = \frac{U_{fs}}{U_{fa}} \tag{2}$$

where Ct = coverage to roof (the value that assures coverage is equal to 1); U_{fs} = Number of cube units, of the seal formation, which are in contact with the roof of the units of the storage formation.; U_{fa} = Number of cube units in the effective floor of the storage formation.

$$Cm = \frac{CU_r}{CU_t} \tag{3}$$

where Cm = coverage to wall (the value that ensures coverage is equal to 1).; CU_t = Number of cube units, of the seal formation, in lateral contact (wall) with units of the storage formation.; CU_r = Number of cube units in the effective thickness of the storage formation.

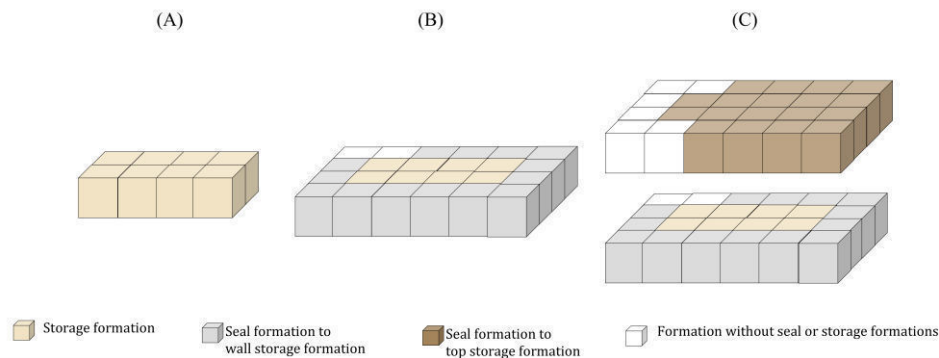


Figure 4. Discretization of formations

For this subsystem the inference engine is composed of 27 rules following the recommendations of CIEMAT (2007), Sánchez et al. (2008), Ruíz et al. (2008)

When the variables Quality of the storage formation, Quality of the seal formation and Geometric configuration of the formations are integrated, they become the variable that qualifies the Qualities of the storage and seal formations (Fig. 5). The composition of the remaining FES feed variables is shown in Figure 6.

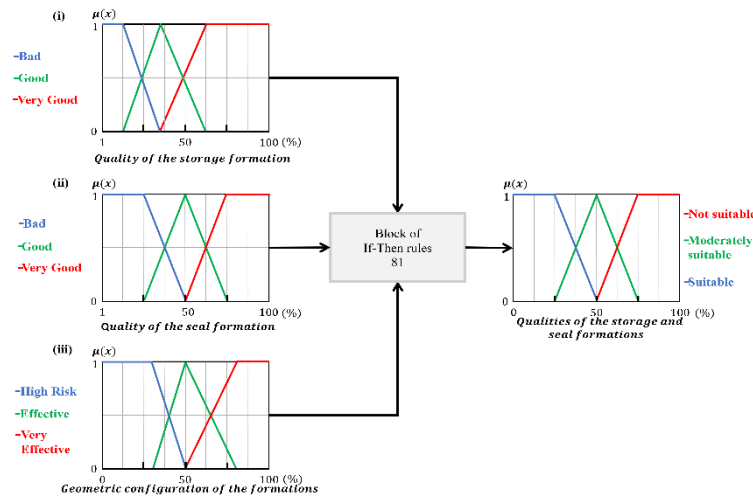


Figure 5. Fuzzy set for the qualification of Qualities of the storage and seal formations.

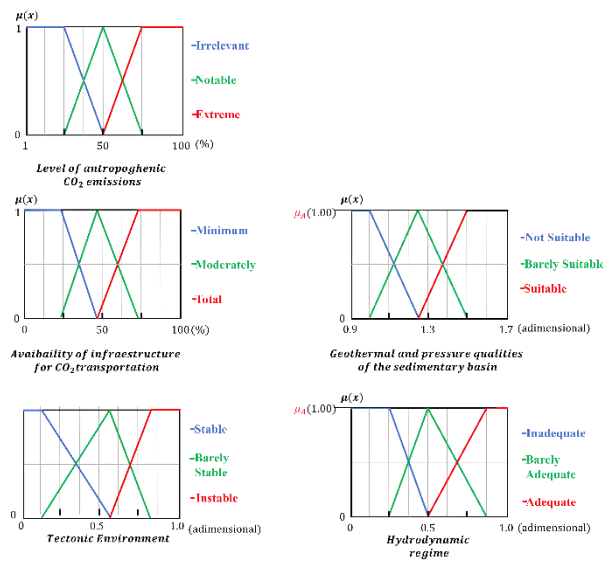


Figure 6. Fuzzy sets for the input variables.

The six input variables, i) level of anthropogenic CO₂ emissions, ii) availability of infrastructure for CO₂ transportation from the capture site to the storage site, iii) tectonic environment, iv) qualities of the storage and seal formations, vi) geothermal and pressure qualities of the sedimentary basin and v) dominant hydrodynamic regime at the site, allow for rating the Susceptibility of a site to develop a CCS Project. The fuzzy sets that make up the FES output variable, Susceptibility to develop a CCS Project, were labelled as Null, Moderate and High and the final inference engine is composed of 2187 If-Then rules. The universe of discourse for this variable ranges from 0.01 to 1.00, where a value of 1.00 indicates that the site has the best characteristics to develop

CCS projects, it has all the infrastructure for the transport of CO₂ from capture to storage without requiring major adjustments, being located in an aseismic zone and having a geological environment with characteristics that allow a large storage, easy injection and guarantee the tightness of the fluid; added to the fact that the geothermal and pressure conditions guarantee that the CO₂ is present in its supercritical phase. In addition, the hydrodynamic regime presents benefits to the fluid entrapment.

3 EXAMPLES OF THE USE OF FES FOR CCS

In order to use the fuzzy expert system, the first step is to define the geographic location where the analysis will be carried out, so that all the information necessary to feed the system is compiled for that site. The data considered for this hypothetical example, which states that a CCS project is to be carried out in some region of southeastern Mexico, and therefore it is necessary to determine its susceptibility. In the Annex A are the information for this exercise. Each property value, as input to the FES, is fuzzified as shown in Figure 7.

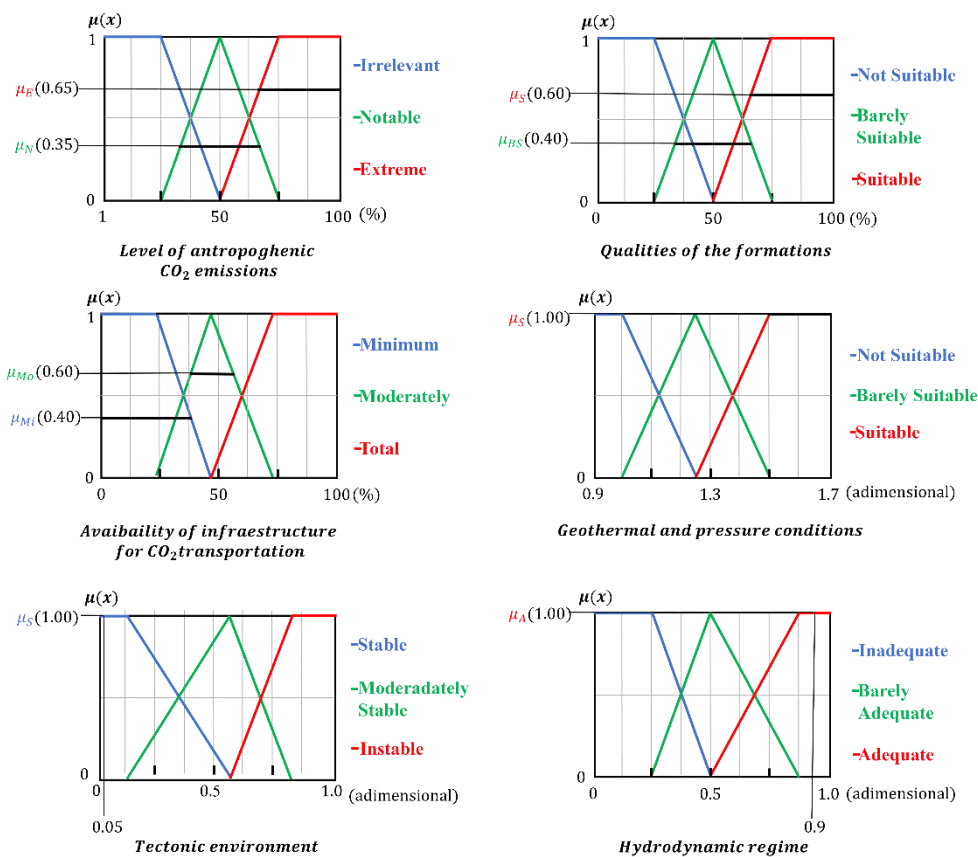


Figure 7. Fuzzification process.

Subsequently, the rules that are activated for the membership functions resulting from the fuzzification process are evaluated. As an example, the analysis of rule 519 is shown (Fig. 8): IF level of anthropogenic CO₂ emissions is Extreme AND Availability of infrastructure for transporting CO₂ from the capture site to the storage site is Minimum AND tectonic environment is Stable

AND qualities of the storage and seal formations are Barely Adequate AND geothermal and pressure qualities of the sedimentary basin are Suitable AND dominant hydrodynamic regime at the site Is Adequate THEN the Susceptibility of a site to develop a CCS Project is Moderate.

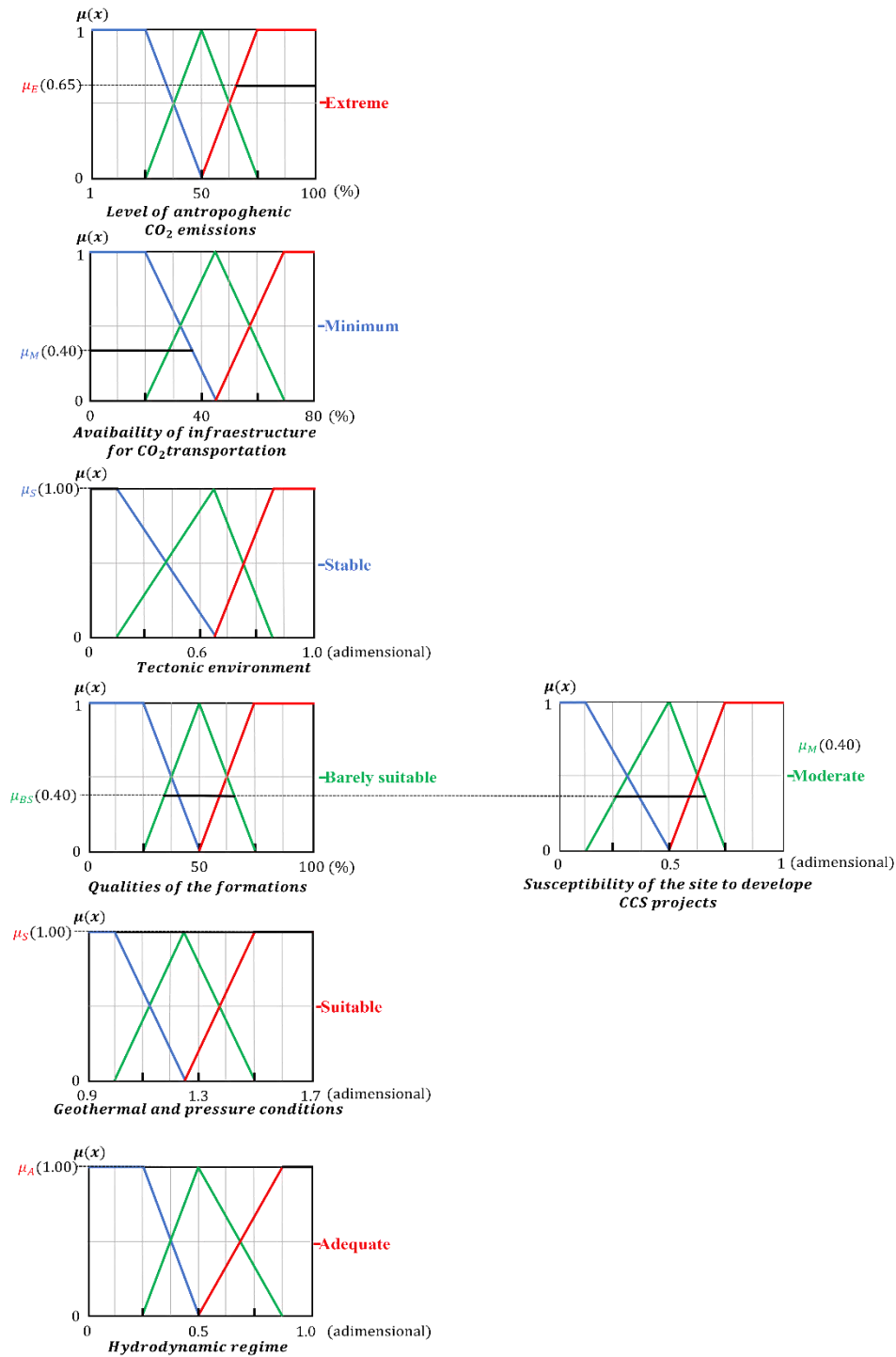


Figure 8. Inference process: Evaluation of If – Then rule number 519.

Aggregation (Fig. 9) and defuzzification (Fig. 10) allows to generate the numerical output on the susceptibility of the site to develop a CCS project.

The values of the six variables generate a Susceptibility qualification for the example site of 0.78 (the maximum qualification is 1.0 and the minimum is 0.01), i.e. the site conditions are suitable for the development of a CO₂ geological storage project. It is observed that the highest weight on the output is related to the infrastructure and the qualities of the storage formation (geometry-cover), these indications drive the following simulations, for example, by increasing the objects that allow the transport of gas or redefining the quality values on porosity, permeability and geometry.

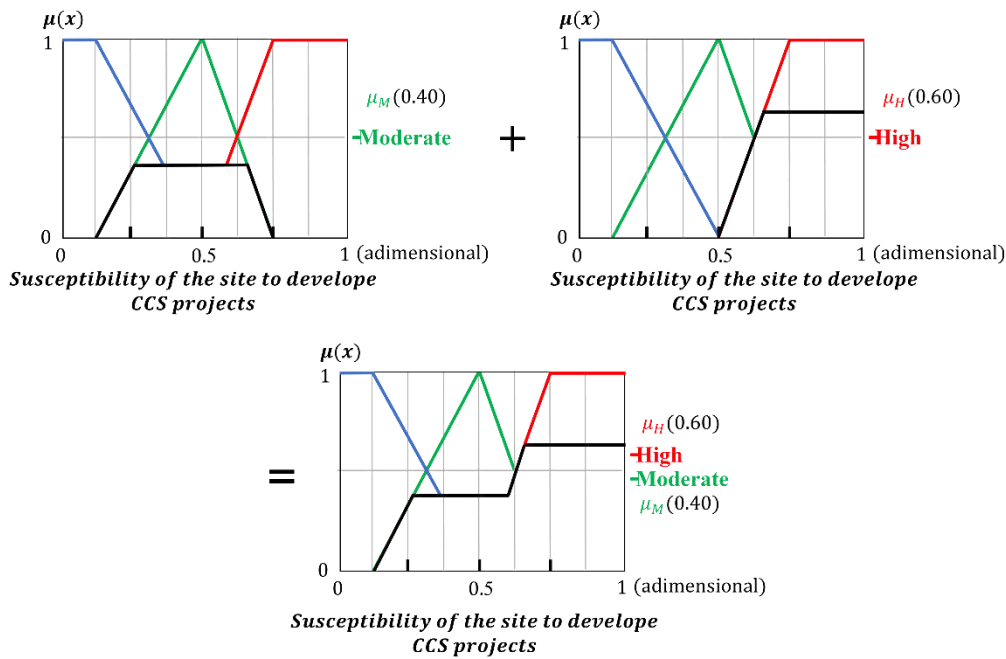


Figure 9. Inference process:Aggregation.

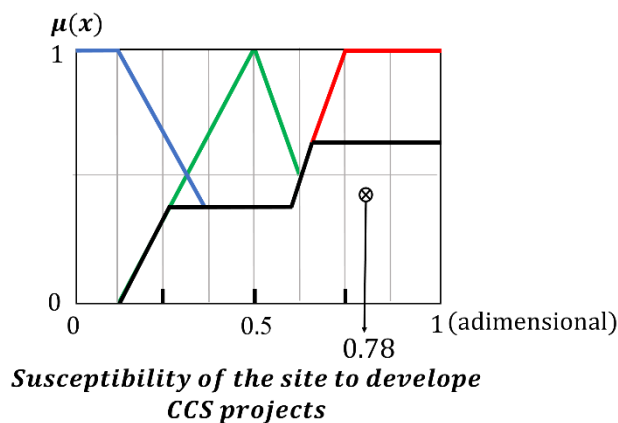


Figure 10. Defuzzification.

4 CONCLUSIONS

The challenges of the oil industry in the discovery, drilling, production and refining of oil are becoming ever greater, demanding the development of new technologies. Problems are becoming (or are recognized to be) complex and solutions are beyond the capabilities of conventional techniques. The use of intelligent computing (particularly fuzzy logic) for decision-making contributes significantly to overcoming obstacles and biases in understanding problems when groups of diverse professionals/managers must address them. The basic intention of the presented system is to have a simple and transparent method that contributes to find the best results for the assigned task in the shortest possible time and cost.

The FES allows for preliminary qualification of a site's susceptibility for CCS project development. The assessment, based on categorization and inferences from engineering reasoning and knowledge, can be used in the effective delineation of project exploration campaigns once the best candidates have been selected. It is recognized that the parameters involved in this system do not exhaust those necessary to study all aspects of a CCS project, but as a research premise, it was considered that the complementary ones (or even those presented, but in a more specific version) should be addressed at later stages where it is sufficiently useful to adjudicate more specific exploration campaigns.

REFERENCES

- Bachu, S. 2000. Sequestration of CO₂ in geological media: criteria and approach for site selection in response to climate change. *Energy Conversion and Management* 41: 953-970.
- Boot-Handford, M.E. Abanades, J.C. Anthony, E.J. Blunt, M.J. Brandi, S. Mac-Dowell, N. Fernández, J.R. Ferrari, M.C. Gross, R. Hallet, J.P. Haszeldine, R.S. Heptonstall, P. Lyngfelt, A. Makuch, Z. Mangano, E. Porter, R.T.J. Pourkashanian, M. Rochelle, G.T. Shah, N. Yao, J.G. and Fennell P.S. 2014. Carbon capture and storage update. *Energy & Environmental Science* 7(1): 130-189.
- Bui M and Mac-Dowell N. 2019. *Carbon Capture and Storage*. Royal Society of Chemistry, London, United Kingdom.
- Caja-Rojas N.C. 2017. *Correlación Litoestratigráfica de la Formación Yumagual comprendida en los sectores de Ronquillo, Puyllucana y la Encañada*. Facultad de Ingeniería, Universidad Nacional de Cajamarca. Cajamarca, Peru.
- CIEMAT. 2007. *Almacenamiento Geológico de CO₂. Criterios de Selección de Emplazamientos*. Madrid, Spain: Departamento de Medio Ambiente, Centro de Investigaciones Energéticas, Medioambientales y Tecnológicas..
- Dávila-Serrano M. 2011. *Viabilidad técnica y ambiental para el almacenamiento geológico de CO₂ en México*. Mexico City, Mexico: Centro Interdisciplinario de Investigaciones y Estudios sobre Medio Ambiente y Desarrollo, Instituto Politécnico Nacional.
- García S.R. and Martínez J.H. 2021. *Lógica Difusa en la calificación de sitios para captura y almacenamiento de CO₂*. Mexico: XXX Reunión Nacional de Ingenieros Geotecnistas.
- GCCSI. 2020. *Global Status of CCS 2020*. Melbourne, Australia: Global Carbon Capture and Storage Institute.
- Hájek P. and Novák V. 2003. The sorities paradox and fuzzy logic. *International Journal of General Systems* 32(4): 373-383.
- IPCC. 2005. *Carbon Dioxide Capture and Storage*. Cambridge, England: Intergovernmental Panel on Climate Change.
- Lorenzo E. and Morato A. 2008. *Geología del Petróleo*. Editorial UPSE, Santa Elena, Ecuador.
- Nava-Jiménez A. 2014. *Análisis de las condiciones del equipamiento e infraestructura urbano - industrial de los parques industriales en el Estado de México, 1980-2010*. Tenancingo, Mexico: Centro Universitario Universidad Autónoma del Estado de México Tenancingo, Universidad Autónoma del Estado de México.
- NETL. 2017. *Best Practices: Site Selection, and Site Characterization for Geologic Storage Projects*. USA: National Energy Technology Laboratory.
- Newell P. and Ilgen A.G. 2019. *Science of Carbon Storage in Deep Saline Formations*. Elsevier, London, United Kingdom.

Ruíz, C. Prado, A.J Campos, R. Hurtado, A. Pelayo, M. De la Losa, A. Martínez, R. Sastre, J. Pérez, L. Eguilior, S. Lomba, L. and Recreo, F. 2008. *Almacenamiento geológico de CO₂: Criterios de selección de emplazamientos*. Madrid, Spain: 9no Congreso Nacional del Medio Ambiente.

Sánchez J.M. González A., Navarrete B., Del Castillo G., Martín M. 2008. *Sostenibilidad de los recursos energéticos fósiles y minerales: uso racional en el abastecimiento y el consumo*. Madrid, Spain: 9no Congreso Nacional del Medio Ambiente.

ANNEX A

Variable 1. Level of anthropogenic CO2 emissions	
Parameter	Value
Size	64 (hectares)
Labor force	3700 (employees)
Industry turn	32: (% of contribution)
Variable 2. Availability of infrastructure for CO2 transportation	
Parameter	Value
Pipeline coverage	30 (%)
Another CCS infrastructure	10 (%)
Communication	60 (%)
Variable 3. Tectonic Environment	
Parameter	Value
Tectonic Environment	0.05 (adimensional)
Variable 4. Qualities of the storage and seal formations	
Parameter	Value
Representative porosity of the storageformation	21 (%)
Representative permeability of the storage formation	100 (mD)
Homogeneity of the storage formation	75 (%)
Representative porosity of the seal formation	0.1 (mD)
Representative permeability of the seal formation	0.1 (mD)
Homogeneity of the seal formation	80 (%)
Coverage to roof	1.25 (adimensional)
Coverage to wall	0.70 (adimensional)
Variable 5. Geothermal and Pressure regime	
Parameter	Value
Depth	1 (km)
Temperature	115 (°C)
Pressure	26.477 (MPa)
Variable 6. Hydrodynamic regime	
Parameter	Value
Hydrodynamic regime	0.9 (adimensional)

Mechanical and microstructural behavior of cement-rock interface for CO₂ geological storage

J.C. Barría

Facultad de Ingeniería, Universidad Nacional de la Patagonia (UNPSJB), Ciudad Universitaria, Comodoro Rivadavia, Chubut, Argentina

D.G. Manzanal

Mecánica de Medios Continuos y Teoría de Estructuras, Universidad Politécnica de Madrid Escuela Técnica Superior de Ingenieros de Caminos Canales y Puertos, Ciudad Universitaria, Madrid, Spain.

J.M. Pereira

Navier, Ecole des Ponts, Univ. Gustave Eiffel, CNRS, Marne-la-Vallée, France.

S. Ghabezloo

Navier, Ecole des Ponts, Univ. Gustave Eiffel, CNRS, Marne-la-Vallée, France.

ABSTRACT:

Carbon sequestration in abandoned oil fields and deep saline aquifers are being considered effective solutions for reducing CO₂ emissions to the atmosphere. These deposits permit the storage of large amounts of CO₂. The reservoir requires high porosity, which would allow good injectivity, and a caprock with very low permeability to prevent CO₂ leakage through it. While drilling, the zone near the well is damaged, and it could provide leakage paths of supercritical CO₂ to upper environments. Within the triple interface of the intervening materials (reservoir rock, caprock, and cement), the cement glass G used in the oil industry is chemically unstable against CO₂ and much less against scCO₂. This work presents the microstructural and mechanical behavior of G-cement under supercritical carbonation. Uniaxial tests (UCS), mercury intrusion porosimetry (MIP), and X-ray diffraction (XRD) characterized the cement carbonated for 28 days at 20 MPa pressure and 90°C temperature. The results indicate a decrease in its mechanical strength despite the reduction in its capillary porosity. These experimental studies were simulated using a coupled chemo-hydro-mechanical model. The model simulates the carbonation front advance in cement subjected to supercritical CO₂ and the changes generated by the chemical reactions, using the classic balance equations of porous continua based on conservation of mass and momentum.

1 INTRODUCTION

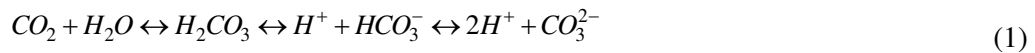
The concept of CO₂ storage is gaining importance worldwide and offers an important solution to reduce CO₂ emissions into the atmosphere (Gielen 2017). The amount of CO₂ storage can be increased by various methods (Herzog et al. 2004, Voormeij et al. 2004). One of these methods is based on the geological storage of CO₂ (Ringrose 2020), by which millions of m³ of CO₂ can be stored (Michael 2010, Bachu et al. 2007).

The reservoir requires sufficient capacity and high porosity to allow good injectivity and a cover rock with very low permeability to prevent CO₂ leakage through it. The way to inject CO₂ into a geological reservoir is to drill to the desired depth, and inject it under pressure. However, this task requires the injection well to be stable and safe. In practice, a steel pipe is placed centered in the well and then a cement slurry is injected to protect it from corrosion. The cement insulates the casing from damaging formation fluids and maintains the structural integrity of the well.

The cement will then be in contact with the rock formation, the geological formation fluids, and the injected gases. The rock-cement interface will be subjected throughout the injection process and to the accumulation of the injected gas in the reservoir at high temperature and high

pressure over its lifetime, so the integrity of the well must be maintained against the supercritical CO₂ (scCO₂) attack on the cement.

At temperatures and pressures above 32°C and 8 MPa, CO₂ is in a supercritical state, so it has the density of a liquid and the viscosity of a gas. These conditions enhance the chemical reactions in the carbonation process of cement. CO₂ dissolves first in the aqueous phase, generating carbonic acid and lowering the pH. This carbonic acid (H₂CO₃) can dissociate into carbonate (CO₃²⁻) and bicarbonate (HCO₃⁻) ions in the pore solution.



The advance of carbonic acid through the cement paste produces mainly the dissolution of portlandite (CH or calcium hydroxide) and C-S-H (hydrated calcium silicate) and the precipitation of calcium carbonate (CaCO₃). The first carbonation reaction in cement is the dissolution of CH:



The characteristic times of the chemical reactions are very small in relation to the slow diffusion of the ions in the fluid within the pore, so the reactions can be assumed to be instantaneous. These chemical reactions induce changes in the porosity and mineral composition of the solid phase. After the dissolution of the CH, the pH level is significantly reduced, allowing the second reaction describing C-S-H carbonation.



The formation of amorphous silica (AmSi) increases porosity and reduces structural integrity, while the formation of CaCO₃ increases cement impermeability and compressive strength. This is only temporary, as CaCO₃ in an acidified medium with water in the presence of CO₂ causes the dissolution of the minerals. This dissolution continues until thermodynamic equilibrium is reached [13]. The latter reaction causes CaCO₃ leaching, which increases porosity, permeability and reduces compressive strength. The end result of the cement matrix is a porous medium of very low strength, unable to maintain well integrity and sealing.

The effects of this type of carbonation on the physico-chemical properties of cement remain a subject of study. Therefore, the objective of this work is to study the variation of the mechanical and microstructural properties of cement once it is subjected to carbonation at a pressure of 20 MPa and 90°C of temperature. This is carried out through unconfined strength tests, mercury intrusion porosimetry, and x-ray diffraction tests. A numerical simulation of carbonation is also presented using the finite element method with a chemo-hydro-mechanical coupling. The reaction advance and its effects over time are determined.

2 MATERIALS AND METHODS

The cement used in this study was class G API Portland Cement. The clinker and calcium sulfate were dosed to satisfy the chemical requirements of the American Petroleum Institute (API) Standard 10A for cement (American Petroleum Institute 2010). Its Blaine specific surface is 367 m²/kg. Fresh deionized water was used at a temperature of 23 °C ± 1 °C. A high-speed mixer with a standard blade type was used (American Petroleum Institute 2010). The mixing procedure consisted of 15 s at a rotation speed of 4,000 ± 200 rpm, and then, 35 s at 12,000 ± 500 rpm. The cement was passed through an ASTM No. 20 sieve. Each slurry was prepared with 792 ± 0.5 g of cement and 349 ± 0.5 g of distilled water at a temperature of 23 ± 1 °C, obtaining water to cement (w/c) ratio of 0.44.

The cement slurry was poured into cylindrical molds of 38 mm x 100 mm. It was then compacted 27 times in two layers with a puddling rod. The molds were placed in the curing chamber at a temperature of 20 ± 1 °C, and after 24 h inside the molds, the specimens were removed and put under water saturated with limestone for 28 days until testing. After setting, the top and bottom

of the cylindrical specimen were cut with a diamond wire saw to geometry of 38 mm diameter and 76 mm height.

2.1 *Supercritical carbonation and mechanical tests*

The carbonation tests were carried out in a titanium vessel of 16 cm inner diameter and 20 cm high, under static conditions. The cement samples were carbonated under wet supercritical CO₂ at 20 MPa and 90 °C for 120 days. Before carbonation, the container with the specimens under water was placed inside a vacuum vessel for removing the air bubbles possibly trapped inside the specimens. Then, the saturated specimens were identified, measured, weighed, and placed on a container grid (Figure 1). A water layer was poured at the bottom of the vessel for maintaining humidity (500 ml).

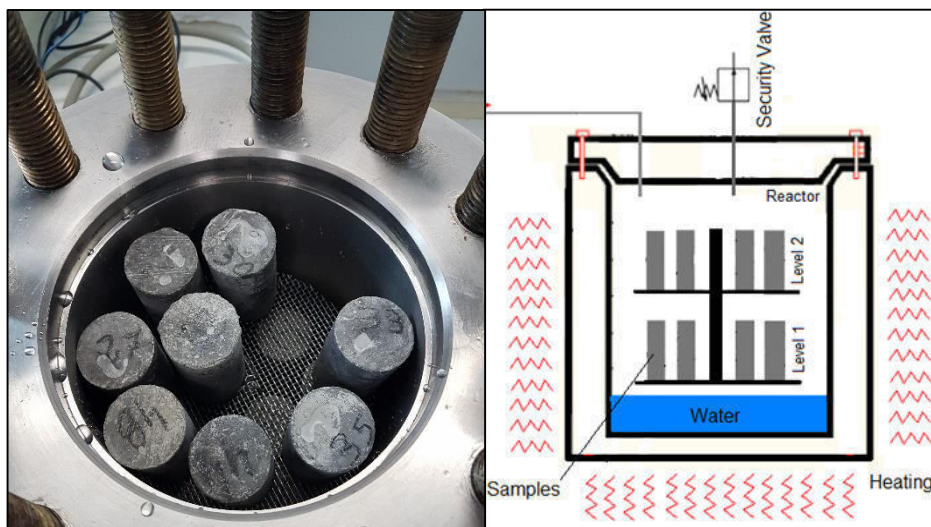


Figure 1. Cement samples and carbonation cell schematic.

The cell was then sealed and connected to the CO₂ pressure line, equipped with a manometer. CO₂ pressure was increased to 8 MPa. The heating system was turned on until 90 °C and the pressure regulated at 20 MPa with the leak valve, removing the remaining air at the top of the vessel. Once the desired pressure and temperature were reached, they were maintained throughout the entire test in static conditions. This process allowed the water to remain liquid. In contrast, the CO₂ went from a gaseous state, then liquid, and finally to a supercritical state when the pressure reached 7.4 MPa and the temperature 31.6 °C. These conditions allow the samples to remain saturated and CO₂ to penetrate by diffusion.

Unconfined compression tests were performed on a 100 kN testing machine with a loading rate of 0.5 mm/min. Vertical displacement and applied force were monitored during the compression tests. The compressive strength and Young's modulus were calculated for all specimens. The averages of strength values and Young's modulus were calculated from 3 specimens.

2.2 *Microstructural analysis*

The mercury intrusion porosimetry (MIP) allows the characterization the pore structure of a sample in terms of porosity and pore size distribution. Mercury is a non-wetting fluid that can enter the pore structure of the cement when external pressure is applied. The basic assumption to interpret MIP data is that pores are cylindrical and interconnected, thus allowing a simple calculation through the Jurin or Washburn Equation 4:

$$d = - \frac{4\gamma \cos(\theta)}{P} \tag{4}$$

where γ = mercury surface tension = 0.485 N/m, θ = mercury contact angle = 130°, P = mercury pressure, d = pore diameter. According to the amount of mercury that penetrates the sample, it is then possible to calculate the total capillary porosity and the pore size distribution. However, the technique does not allow the characterization of isolated pores and is limited by the ink-bottle effect that can occur in the micropores.

Before the MIP tests, the samples were dried by the freeze-drying method and kept sealed in containers with silica gel to prevent rehydration until the MIP test was performed. The equipment utilized was a Micromeritics AutoPore IV 9500 with a maximum pressure of 230 MPa.

XRD analysis was performed on a Philips 3020 diffractometer using CuK α radiation with a Ni-filter (35 kV, 40 mA). Scanning was performed between 3° and 70°, with a step of 0.04° and a count time of 2 s/step. No monochromator was used, and openings were 1° for divergence, 0.2° for the reception, and 1° for dispersion. The identification of the mineral phases in the material was performed using the X'Pert High Score program. For identification and quantification, the procedures described by Moore and Reynolds (Moore & Reynolds 1989) were followed, while quantification was based on the work of Biscaye (Biscaye 1965).

3 RESULTS

3.1 Effect of carbonation on mechanical performance

The samples tested are shown in Figure 2, and Table 1 shows the results after 120 days of carbonation. The cement lost 33% of its original strength. Young's modulus follows a similar trend to the compressive strength. It decreases by 37% after 120 days.



Figure 2. Uniaxial compression test on carbonated samples.

Table 1. Results of the unconfined compressive strength tests.

Mixture	Not carbonated [MPa]		120 days of carbonation [MPa]	
	Maximum strength	Young's modulus	Maximum strength	Young's modulus
Portland Cement	52	25.7	36	16.4

The density and Young's modulus are higher for CaCO₃ than for CH, i.e. CaCO₃ precipitation should increase mechanical performance. However, under extreme conditions, the compressive strength is adversely affected.

The C-S-H degradation can create a discontinuity that decreases the mechanical properties. Precipitated calcite may not fill the pores to bear the stress i.e., they can precipitate on the surface of the pores with no positive impact on UCS. This calcite can also have a weak form (aragonite or vaterite) with intrinsic porosity occurring within itself during the precipitation. Moreover, during the compressive strength tests, a small layer of material was observed to be the first part to be dislodged in different sectors of the sample when a small force was applied, suggesting that there is a thin layer on the external surface of the specimen that has a very low mechanical strength. This zone probably undergoes re-dissolution of the precipitated calcite. However, this cannot be determined with certainty from the tests performed, it requires more specific microstructural analysis such as computed tomography scans to determine the extent of the re-dissolution zone.

3.2 Effects of carbonation on microstructure

The degree of penetration of the sample is given by the diffusion of CO₂ into the sample. This diffusion also depends on the porosity and the connection between the pores. The pre-carbonated cement has 19% porosity (Figure 3), due to the long curing time. After carbonation, the porosity near the CO₂ contact surface of the sample is reduced to 6%, and in the inner zone, it is reduced to 14%. A larger quantity of calcite will precipitate where the ion concentration is higher, however, it also depends on other parameters such as pH. This generates a porosity profile in which the porosity in areas near to the exposed surface is reduced, except for the re-dissolution zone.

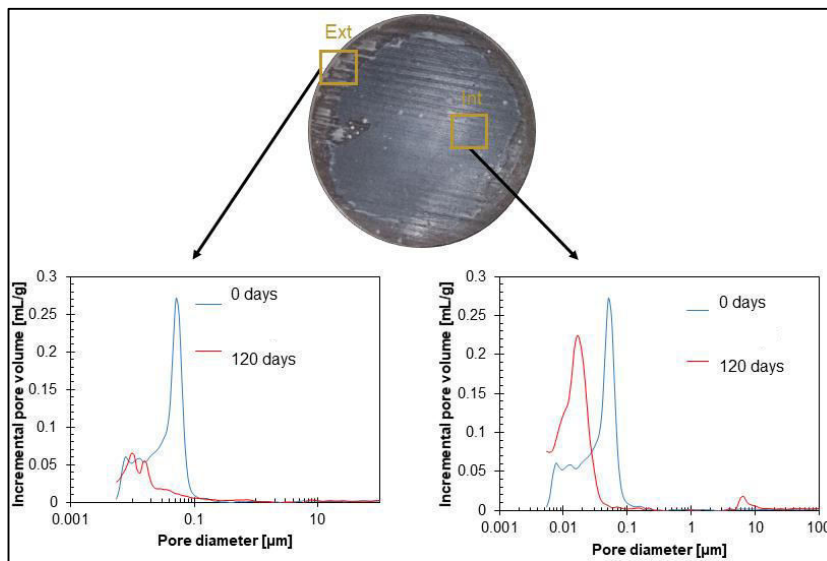


Figure 3. MIP tests results on carbonated samples.

Table 2. Relative quantities of crystalline elements.

Crystalline phase	Relative fractions (%) after and before carbonation
Portlandite	05 (50)
Katoite	- (16)
Brownmillerite	09 (16)
Okenite	- (05)
Calcite	12 (13)
Aragonite	73 (-)

The post-carbonation XRD results in Table 2 on the exposed surface indicate almost complete carbonation of the cement hydrates, as measured by the MIP results. A large amount of aragonite

in this zone denotes increased instability due to the high solubility of aragonite, which can lead to the dissolution of this phase and the reduction of solid material at the outer edge of the sample.

4 NUMERICAL MODELLING

4.1 Coupled chemo-hydro-mechanical model used to simulate progress of carbonation and changes in physico-chemical properties

Cement is considered a porous multi-phase material composed of a solid matrix and water-saturated pores. The skeleton is composed of different materials, such as calcium hydroxide (CH), calcium silicate hydrate (C-S-H), aluminates, and calcite (CC).

The experimental tests are simulated with a chemo-poromechanical coupled model (Vallin et al. 2013) implemented in a finite element code BIL 2.3.0 (Dangla & Bonnard 2017).

The model can simulate the carbonation advance in 1D or 2D materials. It contains the balance equations of equilibrium of the continuum mechanics based on mass conservation, momentum, and energy (Vallin 2014).

The pore structure of the materials is considered fully saturated and the CO₂ is a dissolved species within the fluid. As cement starts to carbonate, its porosity suffers several variations. The solid phases of CH and C-S-H are leached and CC precipitates in the pores.

A homogenization of the medium is carried out to determine the bulk properties of the specimen, including the fluid. The poroelastic parameters can then be simplified following the relations (Equation 7, 8, 9, 10) (Ulm et al. 2004)

$$K_d^{hom} = \sum_r f_r k_r A_r^v \quad (5)$$

$$G_d^{hom} = \sum_r f_r g_r A_r^d \quad (6)$$

$$b^{hom} = 1 - \sum_r f_r A_r^v \quad (7)$$

$$\frac{1}{N^{hom}} = \sum_r f_r \frac{1 - A_r^v}{k_r} \quad (8)$$

Where K_d^{hom} is the drained bulk modulus, G_d^{hom} is the drained shear modulus, b^{hom} is Biot's parameter, N^{hom} is the Biot skeleton modulus, f_r is the volumetric proportion of the phase r , k_r and g_r are the elastic parameters of the solids r and A_r^v and A_r^d are the volumetric and deviatoric strain localization coefficients.

The model considers an elastic isotropic porous material of an infinitesimal representative volume element. The poroelastic balance in isothermal conditions is the following:

$$\boldsymbol{\sigma} - \boldsymbol{\sigma}_0 = \left(K - \frac{2}{3} G \right) (\boldsymbol{\varepsilon} - \boldsymbol{\varepsilon}_0) \mathbf{1} + 2G(\boldsymbol{\varepsilon} - \boldsymbol{\varepsilon}_0) - \sum_{k=F,C} b_k (p_k - p_{k,0}) \quad (9)$$

$$\varphi_J - \varphi_{J,0} = b_J (\boldsymbol{\varepsilon} - \boldsymbol{\varepsilon}_0) + \sum_{k=F,C} b_k \left(\frac{p_k - p_{k,0}}{N_{J,K}} \right); J = F, C \quad (10)$$

Where $\boldsymbol{\sigma}$: Stress tensor, $\boldsymbol{\varepsilon}$: Infinitesimal strain tensor, $\boldsymbol{\varepsilon}$: Volumetric strain. ($\text{tr}(\boldsymbol{\varepsilon})$), K, G = Bulk and shear modulus in drained conditions, φ_J : Porous volume deformation occupied by the phase J (solid or fluid), b_J : Generalized Biot coefficient, N_{JK} : Generalized poroelastic coupling moduli (Coussy 2010).

The mass conservation is applied to the fluid and the molar amount of CO₂ in Equation 11 and Equation 12.

$$\left(\frac{\rho_f \phi_f}{K_f} + \frac{\rho_f}{N_{FF}} \right) \frac{\partial p_f}{\partial t} + \rho_f b \operatorname{div} \left(\frac{\partial \mathbf{u}}{\partial t} \right) + \rho_f \sum_{Ri} Y_{Ri} \frac{\partial \xi_{Ri}}{\partial t} - \operatorname{div} \left(\rho_f \frac{k}{\eta} \operatorname{grad} \rho_f \right) = 0 \quad (11)$$

$$\frac{\partial (\phi_f c_{CO_2})}{\partial t} + \sum_{Ri} a_{Ri} \frac{\partial \xi_{Ri}}{\partial t} - \operatorname{div} \left(d_{eff} \operatorname{grad} (c_{CO_2}) + c_{CO_2} \frac{k}{\eta} \operatorname{grad} \rho_f \right) = 0 \quad (12)$$

Where ρ_f is the density of the fluid, ϕ_f is the fluid porosity, K_f is the bulk modulus of the fluid, p_f is the fluid pressure, a_{Ri} is the stoichiometric coefficient of the reaction Ri, c_{CO_2} is the CO_2 concentration in fluid, η is the dynamic viscosity of the fluid phase, Y_{Ri} is a variable that depends on the molar volumes of reactive species, \mathbf{u} is the skeleton displacement vector, ξ_{Ri} is the reaction advance depending on κ and d_{eff} , which are the permeability and diffusion coefficients.

We use Shen's model (Equation 13), which simplifies the chemical equilibrium of calcite in one variable called sigma. This variable depends on the moles of calcite and portlandite, the constant equilibrium K and ions activity of CC.:

$$\varsigma_{Ca} = \frac{n_{C\bar{C}} + n_{CH}}{n_{Ca}^0} + \log \left(\frac{Q_{C\bar{C}}}{K_{C\bar{C}}} \right) \quad (13)$$

Where $n_{C\bar{C}}$, n_{CH} and n_{Ca}^0 are the numbers of moles of calcite and portlandite (current and initial). $Q_{C\bar{C}}$ and $K_{C\bar{C}}$ are the ions activity and chemical equilibrium constant, respectively.

Under our carbonation conditions, we can determine the constants of the carbonation process. Some equations relate these constants and leave the concentration of the carbonates as a function of CO_2 concentration. With this value, we can determine the unknown ions activity of carbonates and sigma, which considers the calcite dissolution if this parameter is lower than zero.

4.2 Isotropic damage and damage evolution

From a microscopic point of view, the damage corresponds to the creation of microcracks. In the theory of damage, effective stress, now called damaged stress, is based on a decrease in the effective area due to the appearance of micro-cavities (Kachanov 1971). Considering damage as isotropic, a simplification for calculating the damaging stress can be made (Equation 14):

$$\tilde{\sigma} = \frac{\sigma'}{1-d} \quad (14)$$

When $d = 0$, there is no damage. When damage is between 0 and 1, the material is in a damaged state. If $d = 1$, the material is broken.

The interior of the yield surface ($f_d < 0$) corresponds to the effective stress space for which no damage occurs, and the exterior ($f_d > 0$) is the space for which the effective stress state cannot be reached. Thus, as long as the stress state remains within the damaged surface, the damage will not evolve. Similarly, if the stress state reaches the loading surface, but the material point under study is subjected to unloading, there will be no evolution of the damage. On the other hand, if the stress state is on the yield surface and the loading increases, the damage will increase.

The model adopts a Drucker-Prager criterion, suitable for the behavior of high confinement geomaterials (Vallin 2014). The criterion takes the following form in Equation 15:

$$f_d = q + ff \sigma_m - cc \quad (15)$$

Where ff and cc are parameters depending on the friction angle of the material and its cohesion, while q and σ_m are the deviatoric stress and effective mean stress.

The mean and deviatoric stresses are evaluated from the imposed deformation and the homogenized modulus (Equation 16 and Equation 17):

$$\sigma_m = \sigma_{m0} + K_d^{hom} \Delta \varepsilon_v \quad (16)$$

$$q = q_0 + G_d^{hom} \Delta \varepsilon_s \quad (17)$$

Where $\varepsilon_v = Tr(\boldsymbol{\varepsilon})$ and $\varepsilon_s = \sqrt{\frac{2}{3} J_{2\varepsilon}}$. $\Delta \varepsilon_v$ and $\Delta \varepsilon_s$ are the increments of the volumetric and deviatoric strains.

Once the stress state reaches the Drucker-Prager criterion and f_d is greater than zero, the damage is calculated in function of an increment of deviatoric and volumetric deformations (Equation 18):

$$d_{n+1} = 1 - \frac{cc - q - ff \sigma_m}{3G_c^{hom} \Delta \varepsilon_s + ff K_c^{hom} \Delta \varepsilon_v} \quad (18)$$

Where K_c^{hom} and G_c^{hom} are the compressibility and shear modulus of the homogenized medium right before reaching the criterion.

And the new damaged stress state will be (Equation 19):

$$\boldsymbol{\sigma}' = \boldsymbol{\sigma}_0 + (1 - d_{n+1}) \left(2G_c^{hom} (\boldsymbol{\varepsilon} - \boldsymbol{\varepsilon}_0) + \left(K_c^{hom} - \frac{2}{3} G_c^{hom} \right) (tr(\boldsymbol{\varepsilon}) - tr(\boldsymbol{\varepsilon}_0)) \mathbf{1} \right) \quad (19)$$

Finally, in a simplified way, the mechanical modulus is affected as Equation 20 describes:

$$K = (1 - d) K_d^{hom} \quad (20)$$

4.3 Chosen geometry and boundary conditions

A 2D rectangular shape was used to simulate the carbonation advance in these specimens. The rectangular shape consisted of one-quarter of a sample (19 mm-radius by 38 mm-height) using a mesh of 22x11 elements (Figure 4). The bottom horizontal contour has restricted movements in the X direction, while the left vertical contour has restricted movements in the Y direction. The top and right-hand contours are subjected to the carbonation of the cell and with liquid pressure as a boundary condition.

The pressure is that which was used in the experiment, and the fluid and gas conditions are set for a temperature of 90°C. The material is first carbonated with a molarity of 1.2. After 120 days of carbonation, the pressure is released and later tested to failure with axial loading.

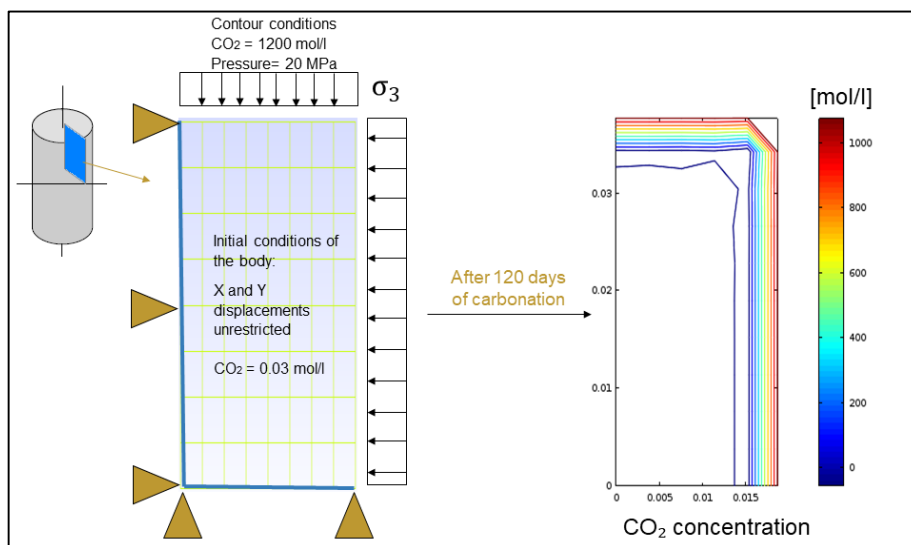


Figure 4. Geometry considered and CO₂ concentration in the specimen after 120 days of carbonation.

4.4 Results

The volumetric fractions depend on this concentration, and they can also be calculated as the advance of the chemical reaction. We can observe that we have a calcite dissolution layer similar to the one observed in the experiments near the outer rim (Figure 5). Deeper in, we find the carbonation front (calcite accumulation), a CH dissolution zone, and the unaltered cement core.

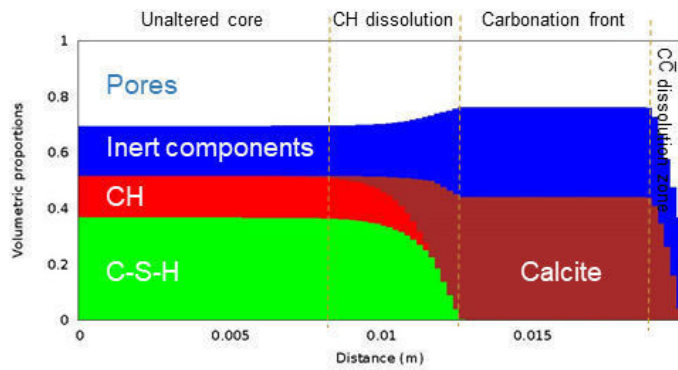


Figure 5. Cement volume fractions after supercritical carbonation.

We performed the compressive strength test before and after carbonation to compare them with the experimental results. The only entry parameter was the final strength measure in the experiments. The elastic moduli and strains are predictions of the model. Figure 6 shows that strength and stiffness are also affected due to carbonation. It is also observed that the results agree reasonably well with the experimental data.

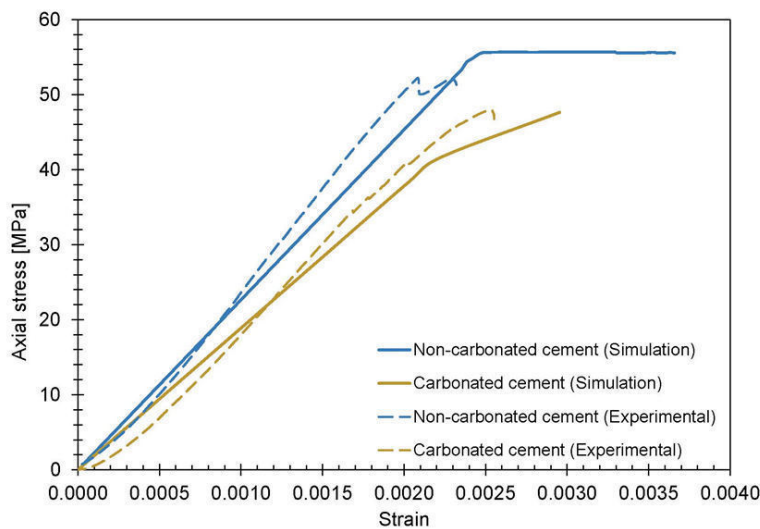


Figure 6. Variation of modulus of elasticity in cement after supercritical carbonation.

The validation of this model provides insight into the effects on cement under supercritical carbonation and can also be extended to study the effects at the reservoir scale.

5 CONCLUSIONS

The result of the process of immersing the samples in supercritical CO₂ at a pressure of 20 MPa and a temperature of 90 °C for 120 days is intended to emulate the conditions to which the cement sheath is subjected in depleted oil wells used in the geological storage of CO₂.

The mechanical behavior of cement is characterized before and after carbonation by uniaxial compression tests. Furthermore, the microstructural changes are studied by means of mercury intrusion porosimetry and X-ray diffraction tests.

The results showed that the strength and Young's modulus of the cement matrix were reduced, although CC precipitation was observed in the cement matrix. The authors believe that this is due to the high degradation of C-S-H and the intrinsic amorphous property of calcite. The precipitation of calcite reduces the pore size distribution but it is not strong enough to improve the mechanical properties of the cement matrix.

A chemo-hydro-mechanical coupled model was used to simulate the carbonation test and the uniaxial tests. The numerical results reasonably match the experimental data. The numerical results in this study confirm the formation of four main zones in the cement matrix due to exposure to supercritical CO₂: a calcite dissolution zone (or degraded zone), a calcite precipitation zone, a Portlandite dissolution zone, and an unaltered zone.

REFERENCES

- American Petroleum Institute. 2019. Specification for Cements and Materials for Well Cementing 10A.
- Bachu, S. *et al.* 2007. "CO₂ storage capacity estimation: Methodology and gaps", *International Journal of Greenhouse Gas Control*, vol. 1, no. 4, , pp. 430–443.
- Biscaye P. E. 1965. Geological Society of America Bulletin Mineralogy and Sedimentation of Recent Deep-Sea Clay in the Atlantic Ocean and Adjacent Seas and Oceans. *Geological Society American Bulletin* 76.7.
- Coussy O. 2010. Mechanics and Physics of Porous Solids.
- Dangla P. and Bonnard A. 2017. *Ifsttar/bil: first version in github (Version v2.4)*. Zenodo.
- Gielen, D. 2003. The Future Role of CO₂ Capture and Storage Results of the IEA-ETP Model.
- Herzog, H. & Golomb D. 2004. "Carbon Capture and Storage from Fossil Fuel Use", *Encyclopedia of Energy*, vol. 1.
- Kachanov L. 1971. Introduction to Continuum Damage Mechanics.
- Michael, K. *et al.* 2010. "Geological storage of CO₂ in saline aquifers — A review of the experience from existing storage operations", *International Journal of Greenhouse Gas Control*, vol. 4, no. 4, pp. 659–667.
- Moore D. & Reynolds R. 1989. X-Ray Diffraction and the Identification and Analysis of Clay Minerals.
- Ringrose P. 2020. How to Store CO₂ Underground: Insights from early-mover CCS Projects. Springer.
- Ulm F. J., Constantinides G. & Heukamp F. H. 2004. Is concrete a poromechanics material? A multiscale investigation of poroelastic properties. *Materials and Structures/Materiaux et Constructions*.
- Vallin V., Pereira J. M., Fabbri A., & Wong H. 2013. Numerical modelling of the hydro-chemo-mechanical behaviour of geomaterials in the context of CO₂ injection.
- Vallin V. 2014. Modélisation chimio poromécanique du comportement des géomatériaux dans le contexte du stockage géologique du dioxyde de carbone: Application au puits d'injection. *PhD thesis. Université Paris-Est*.
- Voormeij, D. A. & Simandl G. J. 2004 "Geological, ocean, and mineral CO₂ sequestration options: A technical review", *Geoscience Canada*, vol. 31, no. 1.

Wellbore Closure in Salt Section with Consideration of Primary Creep.

D. D. E. F. Melo

GTEP PUC-Rio, Rio de Janeiro, Brazil

S.A.B. Fontoura

GTEP PUC-Rio, Rio de Janeiro, Brazil

ABSTRACT:

Oil reservoirs underneath salt rocks are very common due to the sealing capabilities of these rocks. Drilling across salt layers requires a careful consideration of the rock behavior. Due to its inability to sustain deviatoric stresses, the time-dependent deformations close the wellbore and may jeopardize the drilling plan. Many creep laws try to describe the creep deformations of the salt, but applicability in the wellbore drilling usually neglect the transient creep. Therefore, this work focuses on quantifying the differences in the short-term creep when primary creep is added to the steady state creep response. Based on a Multimechanism Deformation creep law, two salts from U.S. Gulf Coast were considered: i) Big Hill, and ii) Bryan Mound. Results indicate that in the short term, the addition of primary creep results in wellbore displacements 3-6 times faster for mud weights lower than 80% of the overburden stress. However, stress relaxation is also faster, and the differences reduce to 1.5 to 2 times after 10 days.

1 INTRODUCTION

The low porosity and low permeability of salt rocks result in a great environment for hydrocarbon trapping. To reach these reservoirs, the well plan must carefully consider the salt rock behavior. Wellbore closure can be a challenge during drilling operations and may lead to drill string sticking, inability to run the casing strings or the necessity of an unplanned redrilling. To avoid non-productive time and an increase in well cost, in-situ stresses, geothermal temperature and creep law must be accounted for prior well execution in order to obtain the drilling mud requirements and adequate the drilling time frame.

Salt rocks are unable to sustain a deviatoric stress state, leading to inelastic deformation associated with a stress relaxation toward an isotropic stress state. Figure 1 exhibits the typical time-dependent strain response of salt rocks. During the first stage (primary creep) salt undergoes a high deformation rate that gradually slows down until it reaches a steady state (secondary) creep. Finally, during tertiary creep the strain rate increases until rupture (Jaeger et al, 2007; Goodman, 1989). Mineralogical composition, temperature, confining stresses, deviatoric stresses and impurities are some of the factors that affect creep rate (Liu *et al.*, 2013, Fjaer *et al.*, 2008, Poiate, 2012). Therefore, creep data from surficial evaporite deposits must be carefully used in subsurface conditions (Gevantman *et al.*, 1981).

Many empirical creep laws have been proposed to describe primary and/or secondary creep stages such as Power law, Double-Power law, Multimechanism deformation law, Double Mechanism law and Enhanced Double Mechanism law. The multimechanism deformation law is one of the most sophisticated, covering both the transient and steady-state creep. It was developed based on an extensive laboratory test for the Waste Isolation Pilot Plant (WIPP), and further fitted to U.S. Gulf Coast salts (Munson & Dawson, 1979, Fredrich *et al.*, 2006).

The initial transient creep with high strain rates is usually ignored in the well design due to its short period. Therefore, the current work aims to quantify the magnitude of the displacement error

associated with the primary creep consideration in a short-term wellbore closure. The analyses considered Big Hill and Bryan Mound salts.

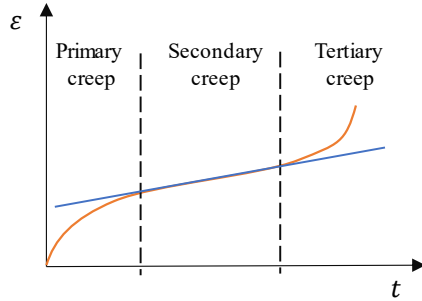


Figure 1. Creep strain stages.

2 SALT CONSTITUTIVE BEHAVIOR

Salt behaves as a visco-plastic material, and the time-dependent deformation is accompanied by a stress relaxation. In the Multimechanism Deformation creep law, the steady-state strain rate, $\dot{\epsilon}_{SS}$, accounts for three individual creep mechanisms according to Equation 1: i) Dislocation glide, $\dot{\epsilon}_{DG}$, ii) Dislocation climb, $\dot{\epsilon}_{DC}$, and iii) Undefined mechanism, $\dot{\epsilon}_{UM}$.

$$\begin{aligned}\dot{\epsilon}_{SS} &= \dot{\epsilon}_{DC} + \dot{\epsilon}_{UM} + \dot{\epsilon}_{DG} \\ \dot{\epsilon}_{DC} &= A_1 \exp\left(\frac{-Q_1}{RT}\right) \left(\frac{\tilde{q}}{G}\right)^{n_1} \\ \dot{\epsilon}_{UM} &= A_2 \exp\left(\frac{-Q_2}{RT}\right) \left(\frac{\tilde{q}}{G}\right)^{n_2} \\ \dot{\epsilon}_{DG} &= |H_{(\tilde{q}-\sigma_0)}| \left(B_1 \exp\left(-\frac{Q_1}{RT}\right) + B_2 \exp\left(-\frac{Q_2}{RT}\right) \right) \sinh\left(\mu \left(\frac{\tilde{q}-\sigma_0}{G}\right)\right)\end{aligned}\quad (1)$$

Where A_1 , A_2 , B_1 , and B_2 are constants, Q_1 and Q_2 are activation energies, T is absolute temperature, R is the universal gas constant, G is the shear modulus, n_1 and n_2 are the stress exponents, μ is the stress constant, H is the Heaviside function, \tilde{q} is the deviatoric stress, and σ_0 is the stress limit for the dislocation glide mechanism.

The transient creep response depends on an evolutionary hardening variable of the material, ζ , and on the transient strain limit of the material, ϵ_t^* . It is empirically described by the function F which comprises work-hardening, equilibrium, and recovery (Eq. 2). The transient strain limit correlates with temperature and deviatoric stress according to Equation 3.

$$F = \begin{cases} \exp\left[\Delta \left(1 - \frac{\zeta}{\epsilon_t^*}\right)^2\right] & , \zeta < \epsilon_t^* \\ 1 & , \zeta = \epsilon_t^* \\ \exp\left[-\delta \left(1 - \frac{\zeta}{\epsilon_t^*}\right)^2\right] & , \zeta > \epsilon_t^* \end{cases}\quad (2)$$

Where Δ is the work-hardening parameter (Eq. 3), and δ is the recovery parameter.

$$\epsilon_t^* = K_0 \exp(cT) \left(\frac{\tilde{q}}{G}\right)^m \quad (3)$$

Where K_0 , c and m are rock constants.

$$\Delta = \alpha_w + \beta_w \log\left(\frac{\dot{q}}{G}\right) \quad (3)$$

Where α_w and β_w are rock constants.

The evolution rate of the hardening variable, ζ , is governed by Equation 4, and approaches to zero in the steady state condition.

$$\dot{\zeta} = (F - 1)\dot{\epsilon}_{SS} \quad (4)$$

Based on the U.S. Gulf Coast, Big Hill and Bryan Mound salts represent the upper and lower limits for creep rate (Fredrich, 2006). Table 1 show each salt properties and creep parameters. A Fortran subroutine code was implemented, and the finite element model (FEM) validated by a triaxial test simulation with 10 MPa deviatoric stress and 66° C. The creep strain rate results showed good accuracy when compared to the literature (Fig. 2).

Table 1. Salt properties for Big Hill and Bryan Mound salts (Fredrich, 2006).

Creep parameter	Big Hill	Bryan Mound
G (GPa)	12.4	12.4
E (GPa)	31.0	31.0
A_1 (s-1)	13.75E22	0.2516E22
Q_1 (Kcal/mol)	25	25
n_1	5.5	5.5
B_1 (s-1)	9.981E6	0.1826E6
A_2 (s-1)	15.85E12	0.2609E12
Q_2 (Kcal/mol)	10	10
n_2	5.0	5.0
B_2 (s-1)	4.976E-2	0.0910E-2
σ_0 (MPa)	20.57	20.57
μ	5.335E3	5.335E3
R (cal/mol-deg)	1.987	1.987
m	3.0	3.0
K_0	8.512E5	1.335E5
c (T-1)	9.198E-3	
α_w	-13.73	-13.37
β_w	-7.738	-7.738
δ	0.58	0.58

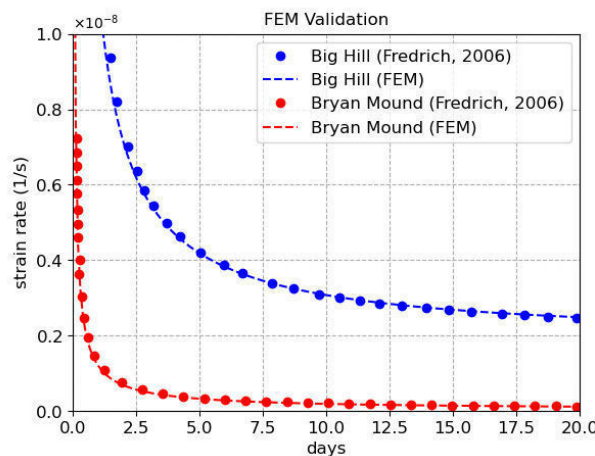


Figure 2. Validation of creep subroutine code for Bryan Mound and Big Hill salts.

3 NUMERICAL ANALYSIS

The finite element analysis (FEA) employs a plane strain model of the wellbore. The model uses Abaqus®, a well-known commercial software. The first step is the geostatic equilibrium, where the application of the undisturbed stresses state and the undisturbed rock temperature represent the in-situ condition. The maximum and minimum horizontal stresses equal to overburden stress. After drill bit excavates the rock, the wellbore is set unconstrained, and the drilling mud weight imposes a distributed pressure load on its surface. The thermomechanical drilling step also accounts for the mud temperature and its thermal effects on rock creep response.

The analyses consider a homogeneous layer of Halite from 3000m to 5000m. At the top of salt, overburden stress and rock temperature equal to 41.75 MPa and 27.75°C respectively. At salt base the initial stress is 95.7 MPa and the temperature is 65.25°C. Table 2 presents two drilling scenarios considered for the simulations. In a shallower section at 3200 m depth, wellbore has 17.5 in (0.4445 m) diameter. At 4550m, hole size is 12.25 in (0.311 m). In each depth of analysis, FEA considers Big Hill and Bryan Mound salts with full creep regime and with steady state regime only. The analyses compare underbalanced mud weight with pressures ranging from 60%, 70%, 80% and 90% of the overburden stress. The mud temperature is 45 °C at 3200m and 63 °C at 4550m.

Table 2: Drilling scenarios at 3200 m and 4550 m.

Depth (m)	Rock stress (MPa)	Rock temp. (°C)	Hole size (m)
3200	45.42	30.96	0.4445
4550	73.15	52.66	0.3112

Creep rate strongly depends on the deviatoric stress magnitude around the wellbore. The closer the mud pressure is to the overburden stress, the lower is the wellbore closure. Table 3 and Figure 3 present the 10 days (240 hours) closure results for 3200 m depth. The addition of primary creep (full creep law) presents small closure differences with high values of mud pressure. However, the reduction of mud pressure led to differences in closure deformation of 0.136 inches when compared to the steady state branch only for Big Hill salt.

Table 3: Wellbore closure in 10 days at 3200m.

Mud pressure (%)	Big Hill		Bryan Mound	
	Full creep law	Steady state only	Full creep law	Steady state only
90	0.011 in	0.006 in	0.006 in	0.005 in
80	0.041 in	0.016 in	0.017 in	0.011 in
70	0.103 in	0.036 in	0.034 in	0.017 in
60	0.203 in	0.068 in	0.059 in	0.026 in

Table 4 shows the closure results at 4550 m, and Figure 4 shows the evolution of wellbore size for mud pressures representing 60%, 70%, 80% and 90% of the overburden. The higher stresses at deeper salt increase the differences between the full creep regime and the steady state creep regime branch only. The lower mobile Bryan Mound shows a difference in hole size reduction of 0.084 inches with mud pressure of 60% of the overburden. With the same mud to overburden ratio, the difference for Big Hill salt is 0.39 inches.

Table 4: Wellbore closure in 10 days at 4550m.

Mud pressure (%)	Big Hill		Bryan Mound	
	Full creep law	Steady state only	Full creep law	Steady state only
90	0.020 in	0.009 in	0.009 in	0.006 in
80	0.102 in	0.039 in	0.031 in	0.015 in
70	0.290 in	0.110 in	0.071 in	0.030 in
60	0.640 in	0.249 in	0.138 in	0.054 in

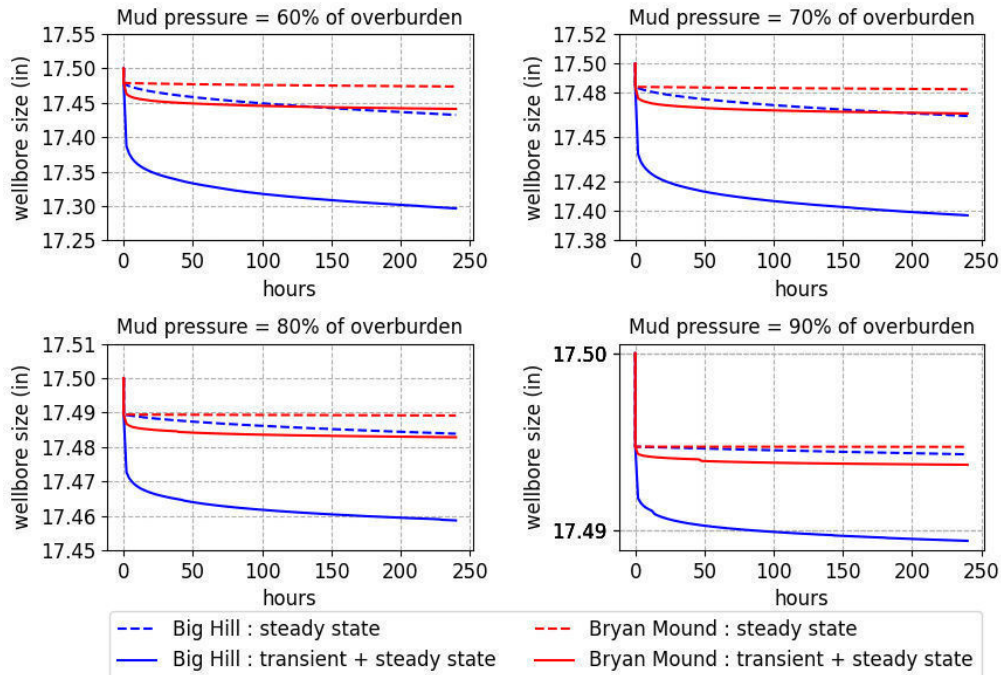


Figure 3. Evolution of wellbore diameter for different mud pressures at 3200 m considering Big Hill and Bryan Mound salts.

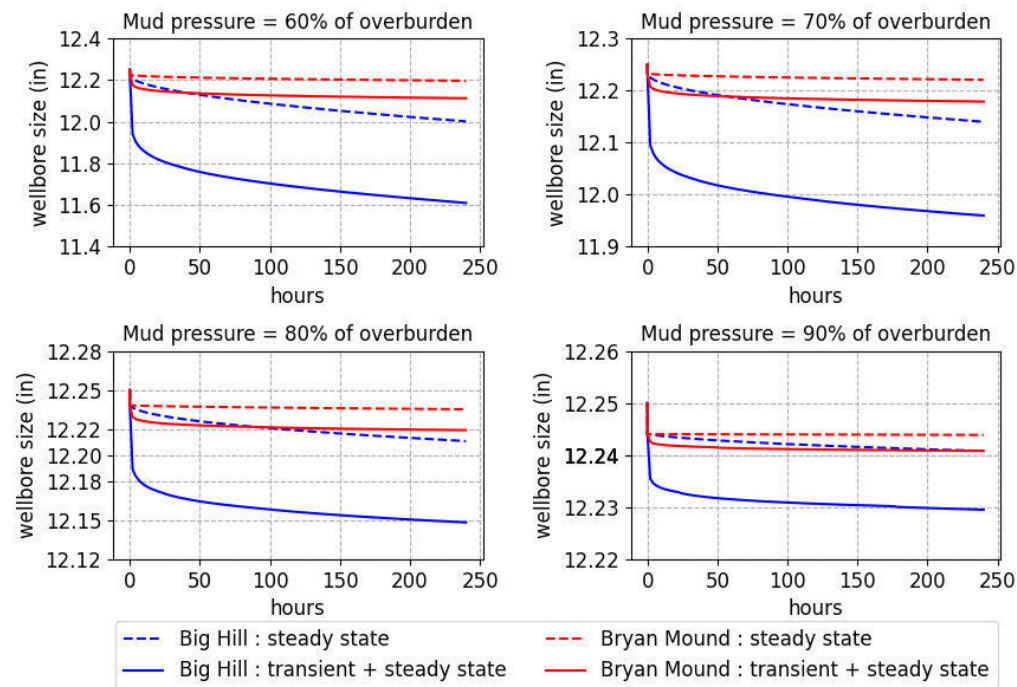


Figure 4. Evolution of wellbore diameter for different mud pressures at 4550 m considering Big Hill and Bryan Mound salts.

Figure 5 shows the associated error when creep law considers primary creep, i.e., the ratio between displacements with and without the transient creep. In the early stages, the wellbore displacement is significantly higher. For a mud pressure equivalent to 60% of the overburden,

closure is 6 times higher when primary creep is accounted for. After salt reaches steady state, the error reduces to 180%. This reduction is associated with the faster relaxation of stresses.

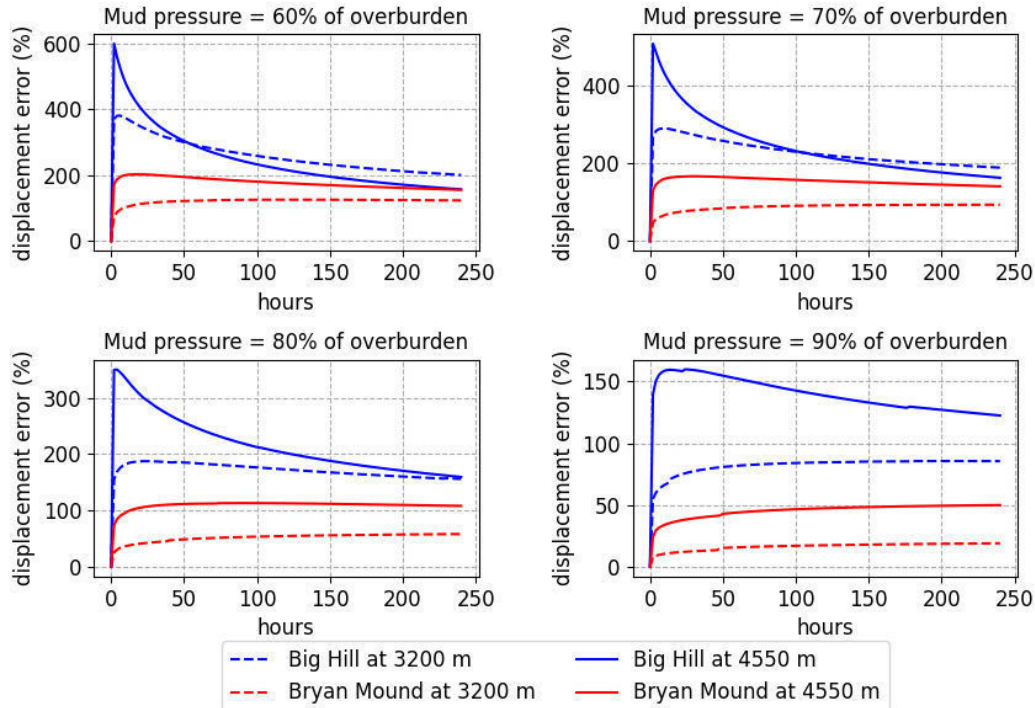


Figure 5. Evolution of wellbore diameter for different mud pressures at 4550 m considering Big Hill and Bryan Mound salts.

4 CONCLUSIONS

Accurately prediction of the salt creep behavior is important to avoid drilling problems. Neglecting the primary creep branch requires care. In the short term, the differences between wellbore displacement are high and depend on the magnitude of deviatoric stresses. In the FEA for mud pressures of 80% to 60% of the rock stress, the addition of primary creep in the Multimechanism Deformation creep law led to displacements 3 to 6 times higher in the short term. As salt creeps and stresses relax, the differences in wellbore closure reduce. Therefore, for high temperature and high-pressure wells expecting a small annulus clearance between bottom hole assembly equipment and the hole size, or in case of mud depressurization, the primary creep should not be neglected.

5 REFERENCES

Fjaer, E., Holt, R.M., Horsrud, P., Raaen, A.M., Risnes, R. (2008). *Petroleum Related Rock Mechanics*. Elsevier Science Publishers B.V, 2008.

Goodman, R.E. (1989). *Introduction to Rock Mechanics*. 202-217. New York, U.S.A.: John Wiley & Sons.

Jaeger, J.C., Cook, N.G.W., and Zimmerman, R.W. (2007). *Fundamentals of Rock Mechanics*. 4th Ed. Blackwell Publishing: Malden.

Liu Wei, Li Jinping, Yang Chunhe, Heng Shuai, Wang Bingwu. (2013). Analysis of physical and mechanical properties of impure salt rock. In Proc. 47th US Rock Mechanics/ Geomechanics Symposium, San Francisco, CA. American Rock Mechanics Association.

- Munson DE, Dawson PR (1979). Constitutive model for the low temperature creep of salt (with application to WIPP), SAND79-1853. Sandia National Laboratories, Albuquerque
- Poiate Jr E (2012) Rock mechanics and computational mechanics for the design of oil wells in salt zones. DSc. thesis, Department of Civil Engineering—Pontifical Catholic University of Rio de Janeiro
- Fredrich J.T., Fossum, A.T. and Hickman, R.J. (2007). Mineralogy of deepwater Gulf of Mexico salt formations and implications for constitutive behavior. *Journal of Petroleum Science and Engineering* 57 (2007) 354–374
- Gevantman, L.H. *et. al.* (1981). Physical Properties Data for Rock Salt. U.S. Departments of Commerce / National Bureau of Standards, Monograph 167.

Laboratory 3D rock joint roughness evaluation with basic, uncomplicated close-range photogrammetry

José Muralha

LNEC, Lisbon, Portugal

André Paixão

LNEC, Lisbon, Portugal

CONSTRUCT - University of Porto, Faculty of Engineering, Porto, Portugal

Ricardo Resende

ISCTE-Instituto Universitário de Lisboa, Lisbon, Portugal

Eduardo Fortunato

LNEC, Lisbon, Portugal

ABSTRACT:

Photogrammetry-based methods using everyday, easily available photographic equipment and free software have gained relevance for roughness measurement of rock joints. However, the influence of some aspects, such as the number and orientation of camera poses, the parameters of the Structure-from-Motion (SfM), Multi-View Stereo (MVS) and meshing algorithms, which influence the resolution and accuracy of the reconstructed models, require proper appraisal. To assess the surface roughness of a granite rock joint specimen using such photogrammetry methods, 3D models generated using different settings (i.e., camera sensors, camera poses, open/free software and workflows), were compared with a reference model obtained by contact digitization. The results suggest that comparable results can be achieved if the photos adequately cover the specimen and, at least, equivalent vertex densities are attained. Percentiles p5 and p95 of surface deviations of the tested models to the reference mesh were, in general, lower than ± 0.1 mm. Results also showed that this methodology is far more accessible, easier to use, faster to implement, and less expensive than most currently available equipment and approaches.

1 INTRODUCTION

Discontinuities – a collective term encompassing all geological features resulting in physical fractures of the intact rock with zero or very low tensile strength, e.g., joints, faults, foliation, bedding, or cleavage planes (ISRM, 1978) – are commonly regarded as two-dimensional planar entities, since the size of the out-of-plane dimension – the roughness of the surface related to the rock grains size, which generally does not exceed a few centimetres – is much smaller than the in-plane dimensions. They determine the mechanical and hydraulic behaviour of most rock masses in common rock engineering projects located within a few hundred meters from the surface, such as large bridges, concrete dams, excavated or natural slopes, underground caverns, tunnels, or mines.

The surface roughness of rock joints has long been recognized as a prominent characteristic influencing the mechanical behaviour of rock discontinuities and hence affecting the structural design in the rock engineering. Patton (1966) carried out shear tests on "sawtooth" specimens and disclosed the direct increase of the shear strength of the surface as shear displacement can only take place if the surface moves up the inclined faces causing dilation. This approach had the advantage of demonstrating the relevance of roughness and dilation, but it has to be considered too simplistic. At higher normal stresses, the strength of the rock at the tips of the roughness teeth will be exceeded, and the shear strength derives from the strength of the intact rock material. Commonly, rock joint shear strength results from the combination of these two effects, and it is

reasonable to accept that rock joint shear strength increases nonlinearly with the normal stress. Based on energy principles, Ladanyi & Archambault (1970) extended Patton's joint model to account for the sliding and shearing mechanisms found in rock joints. However, their model involves several parameters that are not easily estimated, and thus it is seldom used. More widely used, Barton's model addressed joint roughness explicitly in terms of a Joint Roughness Coefficient (JRC) that can be determined either by tilt or pull tests of rock joint samples, or by visual comparison with a set of roughness profiles ISRM (1978).

Subsequently, joint roughness measurement has developed into an unavoidable topic in rock mechanics. Nowadays, several different methods can be used to measure rock fracture surface roughness (Ge *et al.*, 2014). In recent years the increasing capabilities of digital photography technology along with the substantial cost reduction of photographic equipment have allowed for new developments in joint surface measurement, both in situ and in laboratory-controlled conditions (Gaich & Pötsch, 2015; Wernecke & Marsch, 2015; Gaich *et al.*, 2019; Uotinen *et al.*, 2019; An *et al.*, 2021). These factors allowed the development of more flexible photogrammetric methods with softcopy photogrammetry for rock joint surface reconstruction, now widely used by the geoscience community in several fields. A set of images can be used to reconstruct 3D scene geometry where the extrinsic (rock surface) and intrinsic (photographic camera) calibration parameters are unknown (Fraser & Stamatopoulos, 2014). This approach can produce digital models of equivalent or higher quality than previous methods, allowing advanced and automated rock joint roughness analyses from a 3D perspective.

A preliminary investigation on the application of close-range photogrammetry for the three-dimensional reconstruction of rock joints and roughness assessment is presented herein. A reference photogrammetry scanning workflow is presented, and the impact of key aspects of the photogrammetry are also analyzed and tested: camera poses; number of required image captures; 3D reconstruction software/algorithms; Digital Single-Lens Reflex (DSLR) vs smartphone camera. The triangulated meshes obtained by photogrammetry are aligned and compared with a 3D model obtained from contact digitalization of the rock joint specimen.

This work evaluates the application of a digital scanning approach that makes use of open and free software/algorithms and inexpensive equipment to form dense cloud points and construct very detailed 3D models of rock joints, with sufficient detail of the topography, retaining the texture, and compatible with a wide range of rock mass sizes. The adoption of rock joint digital reconstruction approaches by close-range photogrammetry, such as the method presented herein, may constitute a valuable tool to be used routinely in the laboratory and in the field that is far easier and faster to implement and less expensive than the currently available approaches.

2 DIGITAL 3D JOINT SURFACE ROUGHNESS RECONSTRUCTION

A granite rock joint encapsulated with cement mortar was used for the digital three-dimensional reconstruction and subsequent surface roughness evaluation (Ramos, 2013; Resende *et al.*, 2015). The rock is a medium grain-sized granite with two micas and feldspar phenocrystals of yellowish to greyish colour displaying reddish oxide deposition and a very thin film of iron oxide.

The contact digitization used as reference was performed with a Roland MDX-20 milling/scanner, a 3D needle-tip contact scanner which allows the three-dimensional scan of solids with a resolution of 0.05 mm over the horizontal plane (x and y directions) and of 0.025 mm in the vertical direction (z). After some preliminary tests, planned to assure reproducibility of results, a horizontal resolution of 0.5 mm was adopted, allowing scanning the surface of a rock joint sample in six to ten hours. The detail level was considered appropriate considering that the grain size in the granite samples under study is approximately 2 mm. The initial tests showed that a higher resolution would not significantly improve data quality while considerably increasing data acquisition duration and encumbering the data handling and processing. The dedicated software from the scanner manufacturer - *Dr. PICZA* (Roland, 1999) - controls the scanning process, checks its quality, allows for a rough visualization of the scanned surface, and exports

the data in various formats. Posterior processing and analysis were performed with specific routines developed in *MATLAB*.

To some extent, the close-range photogrammetry digitization process follows, with some modifications, a workflow used with rail ballast (Paixão *et al.*, 2018; Paixão & Fortunato, 2021). Compared to other three-dimensional contactless scanning methods, it is relatively fast and significantly less expensive (Ge *et al.*, 2021). The equipment that was used is as follows (approximate costs of the equipment are included to show the limited expenses required):

- Digital camera and lens: Canon 600D, 18-MPixel (APS-C format CMOS sensor: 22.3×14.9 mm) DSLR camera (<300 USD), equipped with a fixed focal length macro lens, the Sigma 50 mm f/2.8 EX DG Macro (<300 USD);
- Camera Tripod (100 USD);
- Turntable to support the specimen (10 USD);
- Matte white background cardboard (negligible);
- Uniform and diffuse lighting are achieved with ceiling lights, complemented by two additional lamps, one on each side of the camera, covered by translucent white covers (40 USD).

The generation of triangulated meshes from image captures involved three steps. Although several free or affordable commercial software packages perform these three steps automatically in a straightforward workflow, namely *Meshroom* (Jancosek & Pajdla, 2011) or *3DF Zephyr* (3DFlow), among others (Nikolov & Madsen, 2016; Ortiz-Sanz *et al.*, 2021), previous experience and preliminary tests revealed that using different codes for each step was preferable as shorter computation effort and greater control over the process was achieved. The following software were used for each step:

- Relative pose (i.e., camera position) estimation between images is performed with the Structure-from-Motion (SfM) technique: *VisualSfM*, Win 64-bit Version 0.5.26 for nVidia CUDA (available at <http://ccwu.me/vsfm>) (Wu *et al.*, 2011; Wu, 2013);
- Estimation of cloud points by dense reconstruction: Clustering Views from Multi-view Stereo (*CMVS*) algorithms (available at <https://www.di.ens.fr/cmvs>) (Furukawa *et al.*, 2010);
- Cloud point cleaning and mesh construction: *MeshLab*, Win 64-bit Version 2020.07 (available at <http://www.meshlab.net>) (Cignoni *et al.*, 2008).

The first two software packages, *VisualSfM* and *CMVS*, work together and can be run automatically in sequence. For the last step, *MeshLab* was chosen because it is an open-source software, has an efficient cloud-point handling graphic user interface, includes state-of-the-art meshing functions, its algorithms are open and auditable and provides to most parameters. Moreover, it contains features for automatic alignment and distance calculation between meshes that simplify their handling, making it a particularly useful tool. All three codes can run in batch mode from a command line, thus reducing human intervention and promoting the automation of most tasks.

The following items describe the main operation sequence, from sample preparation to final mesh analysis (Figure 1):

- Sample placement: every part of the joint surface must be accessible to be photographed in detail with a large overlap between photographs. Instead of moving the camera to capture sequential images around the sample, it is faster and more convenient to place the camera in a fixed position and rotate the sample using a turntable. A neutral background and diffuse illumination are essential to "trick" the photogrammetry algorithm into considering that the camera moves around the object.
- Photography session (Figure 1.a): sequential images are captured around the joint by turning the table in 10° increments up to 360°; this process is repeated for each of two camera positions - an inferior and a superior pose. Thus, $2 \times 36 = 72$ images, with 18 MPixel resolution (5184 x 3456 pixel), are captured to render an overall coverage of the joint. Camera settings were as follows: f/22 aperture, 0.6 s exposure time and ISO 200, white

balance custom calibrated against the background, focal length of about 55 mm, depending on the vertical position of the camera (Figure 1.a), thus obtaining a depth of field of roughly 9 cm to cover a large portion of the sample surface.

- Point cloud generation using *VisualSfM* and *CMVS* algorithms (Figure 1.b and c):
 - Feature detection and full pairwise image matching: SfM → Pairwise Matching → Compute Missing Match function;
 - Sparse reconstruction: SfM → Reconstruct Sparse function;
 - Dense reconstruction using *CMVS* package: SfM → Reconstruct Dense function;
- Mesh generation using *MeshLab* (Figure 1.d):
 - Cleaning of undesired points in the dense point cloud, i.e., points in the background and base;
 - Scaling by performing distance measures between know positions in the specimen and applying a scaling factor to the coordinates of the point cloud;
 - Poisson Surface Reconstruction: Filters → Remeshing, Simplification and Reconstruction → Screened Poisson Surface Reconstruction function to generate a 3D triangular mesh.

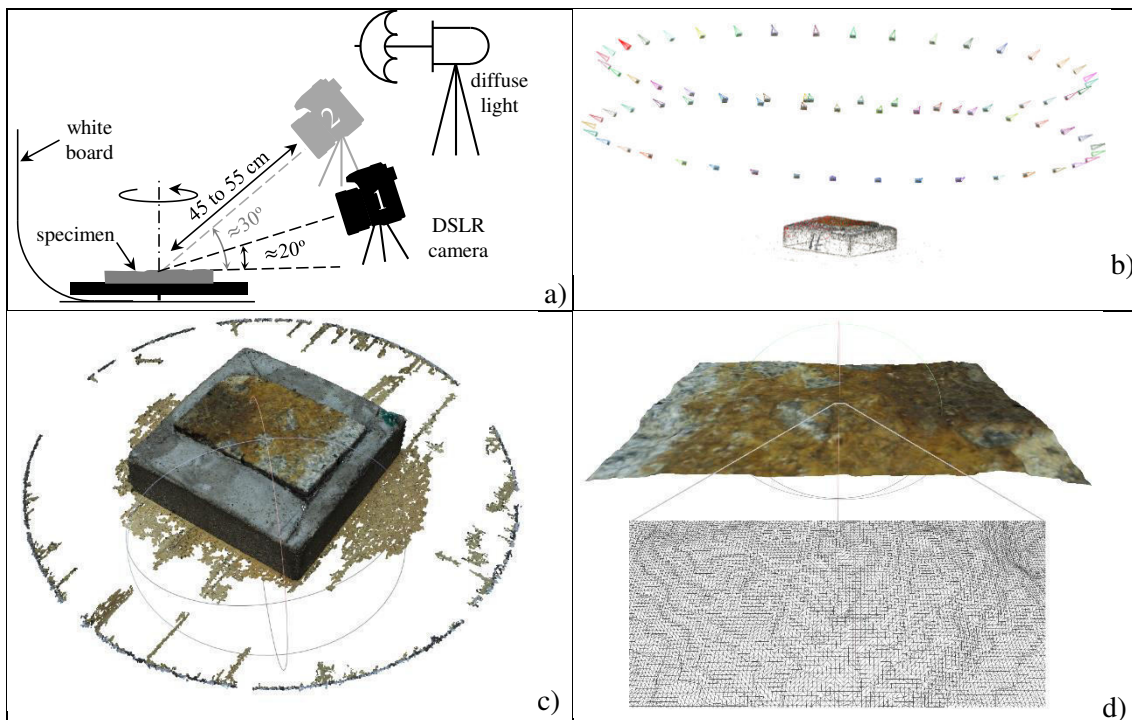


Figure 1. Workflow: a) setup of the photography session; b) camera pose calculation, image matching and sparse reconstruction; c) dense reconstruction (the base is also captured); d) generated mesh (after Paixão *et al.*, 2018).

The initial total cost of the setup was roughly €1300, and the largest parcels were, clearly, the DSLR camera and the 50 mm prime lens, which might already be available in many laboratories, offices, or households. Although the quality of the cloud point reconstruction depends on the settings of the photo session, optical quality and pixel density, a prime lens and a high pixel count are not essential, and acceptable results can be achieved with cheaper cameras, even with a smartphone. The setup can be assembled in a few minutes by an experienced operator. A room with diffuse or no exterior light is preferred; white light lamps must be placed and oriented to guarantee an even, diffuse illumination without shadows and reflections over the sample. The

digital 3D reconstruction of the rock sample takes approximately 1 hour for an experienced operator, including the time required for the photo session, the point cloud generation, cleaning, and scaling, followed by the mesh generation and alignment.

Tests with slight variations of the above-presented workflow were performed to assess the impact of different factors, aiming at providing more information about the best conditions, settings, and tools. The following factors were considered: camera poses and number of captures of the same specimen, reconstruction software, and photographic camera (smartphone instead of a DSLR photographic camera).

Firstly, to assess the influence of the camera poses and the number of captures on the mesh reconstruction, different sub-sets of the total captured images of the same rock joint (nr 71) by the DSLR camera were used to generate different meshes, which were analyzed in *MATLAB*. These sub-sets included the following images and respective designations:

- 71 dslr 2x18 – 18 images from both camera levels;
- 71 dslr 1x18L – 18 images from the lower camera level;
- 71 dslr 1x18H – 18 images from the higher camera level;
- 71 dslr 2x36 – 36 images from both camera levels;
- 71 dslr 1x36L – 36 images from the lower camera level;
- 71 dslr 1x36H – 36 images from the higher camera level.

The second group of tests considered different photogrammetry reconstruction software and algorithms, in particular *Meshroom*, a free, open-source software based on the *AliceVision* framework, and *3DF Zephyr* (3DFlow), a commercial photogrammetry and 3D modelling software (the trial version of the program was used, limiting to 50 the number of images considered by the algorithm). Two additional models were generated in this test:

- 71 dslr 2x36M – 36 images from both camera levels with Meshroom software;
- 71 dslr 2x18Z – 18 images from both camera levels with Meshroom software;

The third group of tests consisted of using a smartphone (abbreviated as "sphn") to capture images around the specimen, using similar camera poses. The smartphone OnePlus 8 pro (model IN2023) was used for this task due to its photographic capabilities: a Sony IMX689 sensor with 48 megapixels and a 25 mm lens. The following photographic settings were considered: f/1.8 aperture, 1/15 s exposure time and ISO 100. Captures with image resolution of 12MP and 48MP were tested (designations 71 sphn 12MP 2x36 and 71 sphn 48MP 2x36, respectively), and a final model was also constructed using *3DF Zephyr's* feature of generating 3D meshes from videos – 50 frames of a 4k UHD resolution video (3840 × 2160 pixel) – obtained with the same smartphone (71 sphn 4k).

3 RESULTS AND DISCUSSION

Figure 2 shows 3D top views of the reference mesh "71.ply", obtained with the Roland MDX-20 scanner, and the meshes obtained by photogrammetry using the above-mentioned sets of images. The 3D visualization of the reference mesh is slightly sharper than that of the other meshes, which seems to be a consequence of the constant spacing of the quadrangular mesh imposed by the scanning equipment.

The mesh generation algorithm of the photogrammetry models is more flexible in adapting the shape and orientation of the mesh triangles to the point cloud representing the surface of the specimen, which somewhat explains the smoother visual aspect of those meshes. Even though the models were generated using a different number of captures (18, 36 or 72), the reconstruction algorithms generated triangular meshes with a very similar number of vertices/faces, with a density of about 20 vertices per mm². Regarding the influence of the reconstruction algorithm, note that *Meshroom* used twice the number captures than *3DF Zephyr*. However, the mesh density was roughly the same: 15 vertices per mm² for the *Meshroom* reconstruction and 17 vertices per mm² for the *3DF Zephyr*. This does not necessarily mean that one mesh and software is more

accurate than the others. In fact, in this case, it appears to be a consequence of the different triangulation algorithms, as *Meshroom* seems to generate a more isotropic and dynamic (i.e., adapted to the geometry) mesh with improved triangle aspect ratio and topological regularity.

The mesh from the smartphone model 71 sphn 4k has the softest appearance, and model 71 sphn 12MP 2x36 looks quite like model 71 dslr 2x36, while model 71 sphn 48MP 2x36 appears to be as sharp as the reference model.

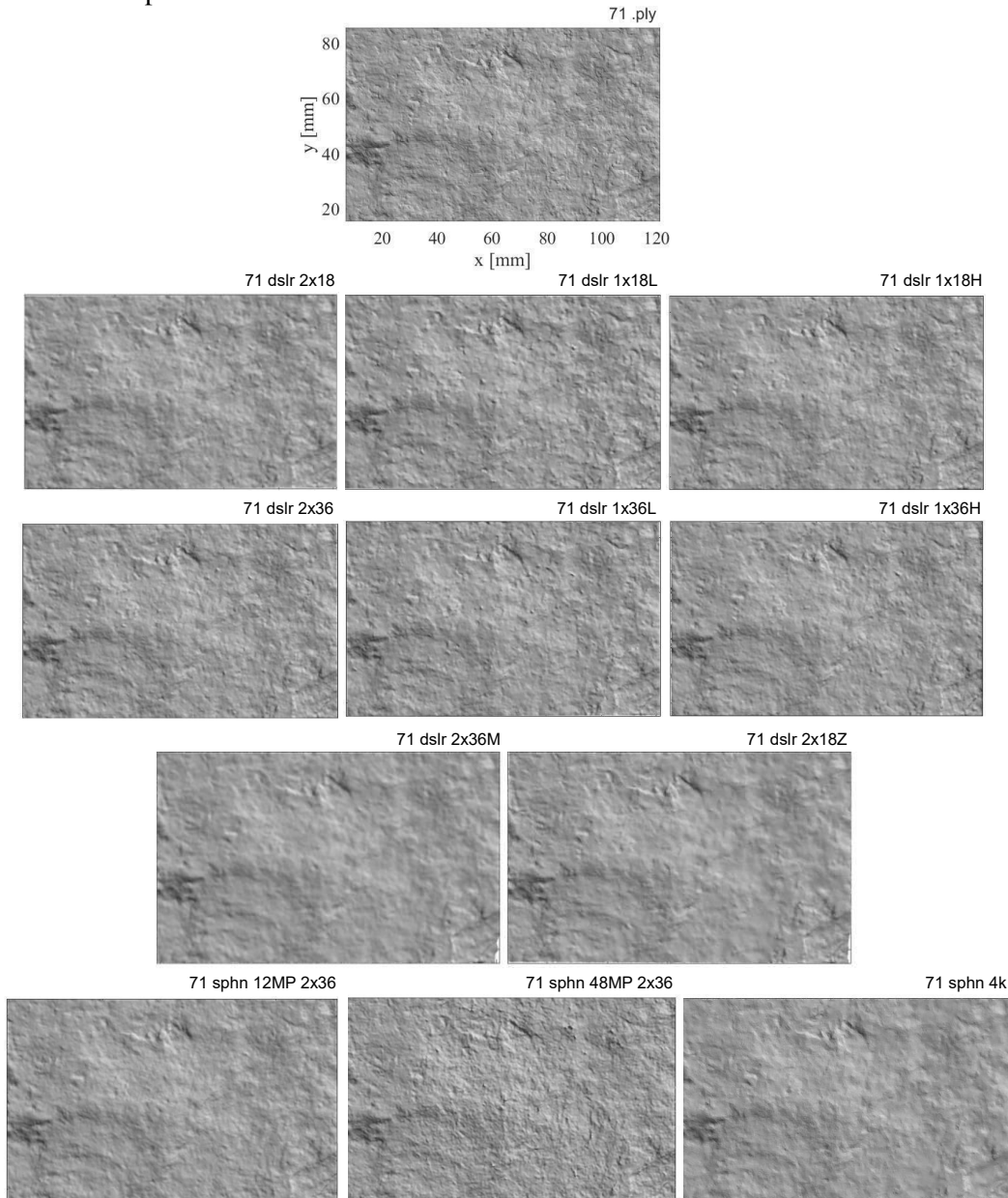


Figure 2. Digitalisations from different sub-sets of camera poses.

Figure 3 displays colour maps of the deviations in the vertical coordinate, z , between the reference mesh and the photogrammetry meshes. The colour amplitudes are truncated between -0.5 mm and 0.5 mm without loss of relevant information for a more straightforward interpretation of the results. Some yellow spots located around the position $x=75$ mm, $y=65$ mm are clearly identified in the colormaps, which appear to have been caused by localized material loss from the specimen due to handling between the reference scan and the photography sessions. Dark blue regions

correspond to rapid changes in geometry, where the meshes generated by photogrammetry show higher divergence from the reference mesh. Except for these regions, an excellent reproduction of the surface of the specimen is achieved, denoted by the general greenish-blue colours indicating deviations quite close to 0 mm.

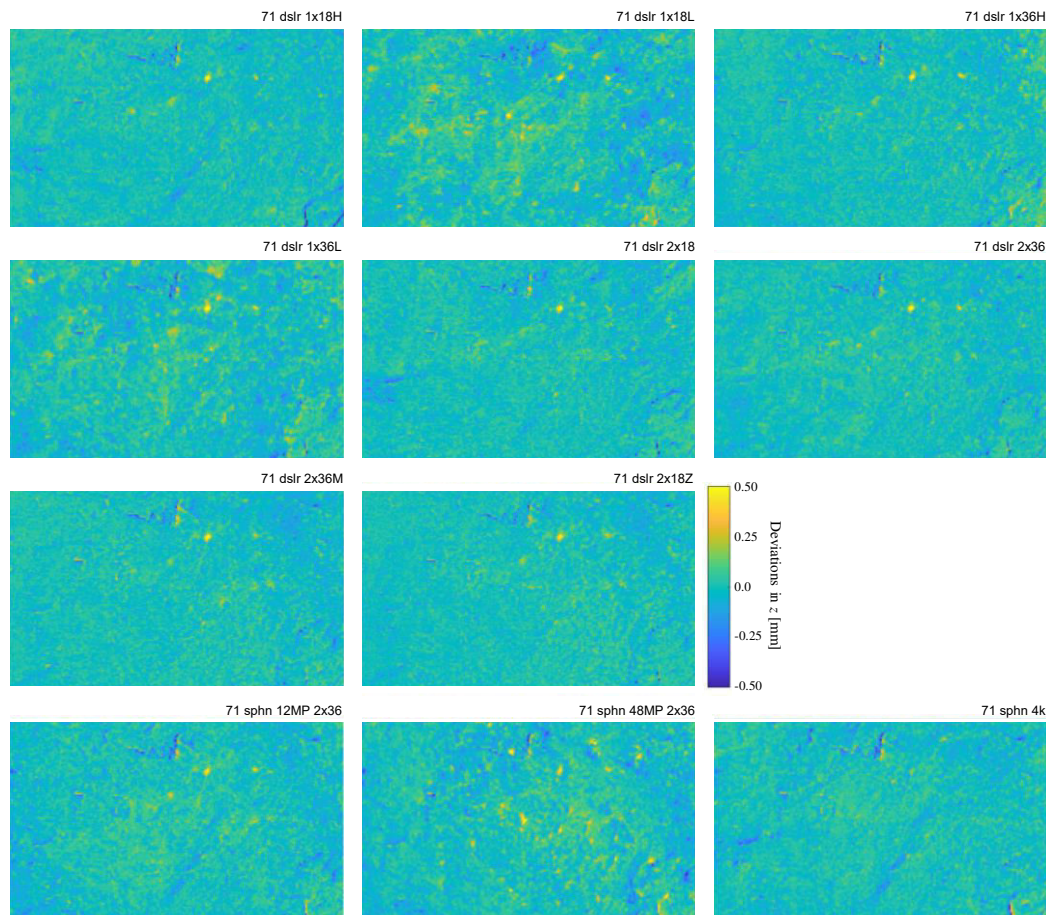


Figure 3. Deviations in z coordinates with respect to the reference mesh in mm.

A statistical analysis was performed to analyze the deviation distribution. Figure 4 depicts the histogram plots of the deviations in z coordinates of all tests. It is important to note that, to enable a direct comparison between the curves, the position of the photogrammetry meshes was adjusted in the z direction so that the median value of the deviations is equal to zero.

The main conclusion is that 95% of the calculated deviations are in the range ± 0.17 mm, which can be considered a very good reproduction of the specimen, considering the application that is intended with this method. The two meshes generated using only sub-sets of captures from the lower level (71 dslr 1x18L and 71 dslr 1x36L), yielded higher deviation amplitudes, denoted by the wider histogram curve. This was probably due to the larger portion of the specimen being out of focus in each of the captures when the camera was positioned in the lower level, increasing the dispersion of the point cloud obtained with the reconstruction algorithm, thus reducing the mesh accuracy. These results highlight the importance of adjusting the adequate photography settings. The remaining four models of the first group of tests yielded very similar results, in terms of variability of the obtained deviations, which suggests that the consideration of only 18 photos (spaced at 20° degree intervals), from an angle of about 30° with the shear plane, might be sufficient to achieve good results if optimal photographic conditions are met. Though not presented here, it is worth mentioning that tests using other sub-sets of captures displayed

comparable results. For instance, considering sub-sets of 18 images spaced 20° from the same level, very similar results were obtained using either the sub-set of 18 images starting at 0° ($0^\circ, 20^\circ, 40^\circ, \dots, 340^\circ$) or the sub-set starting at 10° ($10^\circ, 30^\circ, 50^\circ, \dots, 350^\circ$).

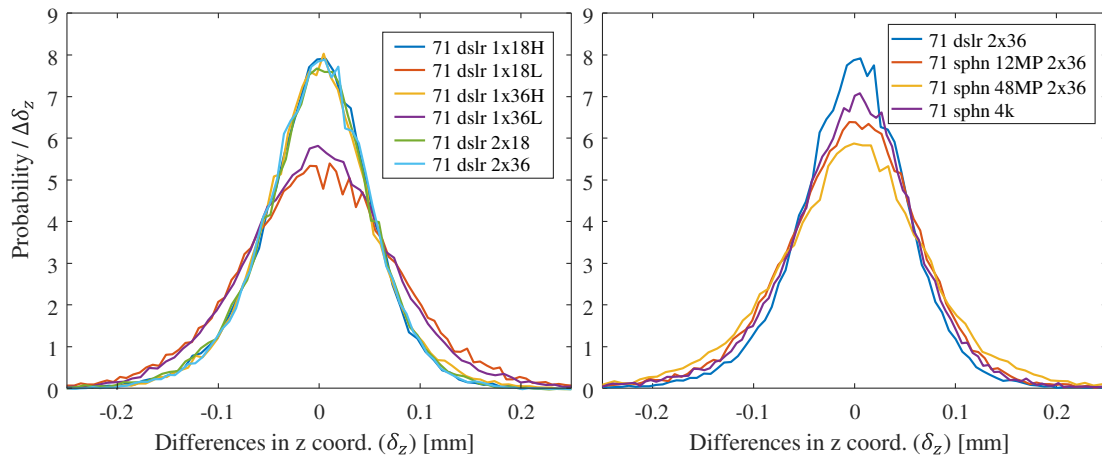


Figure 4. Distribution functions of the deviations in z coordinates with respect to the reference mesh.

Despite the variation in the number of images included in the photogrammetry reconstruction, in mesh generation algorithms, in vertices density and in the visual aspect of the models, the two mesh generating software (*Messhroom* and *3DF Zephyr*) did not provide any reduction of the deviations. Thus their distributions are not displayed to improve readability.

The model from the video frames (71 sphn 4k) showed a surprisingly good result, as the deviations of the generated mesh to the reference mesh were the lowest of the smartphone captures. This is especially relevant considering that the video frames were captured with the turntable in motion, which would lead to expect the frames to be blurred. Despite this potential issue, *3DF Zephyr* reconstruction algorithm renders a relatively good result.

Figure 5 compares the box plots of the deviations in z with respect to the reference mesh. On each box, the central mark indicates the median, and the bottom and top edges of the box indicate the 25th ($q1$) and 75th ($q3$) percentiles. Differences within the range specified as 1.5 times the interquartile range are represented by the dashed black lines whiskers. As the percentage of outliers is relatively small in absolute terms, they were not represented in the figure. This figure emphasizes previous conclusions: the majority of deviations are relatively small; all meshes show similar results, except those from DSLR captures from the lower level (71 dslr 1x18L.ply and 71 dslr 1x36L.ply) and the mesh generated using higher resolution captures with the smartphone (71 sphn 48MP 2x36).

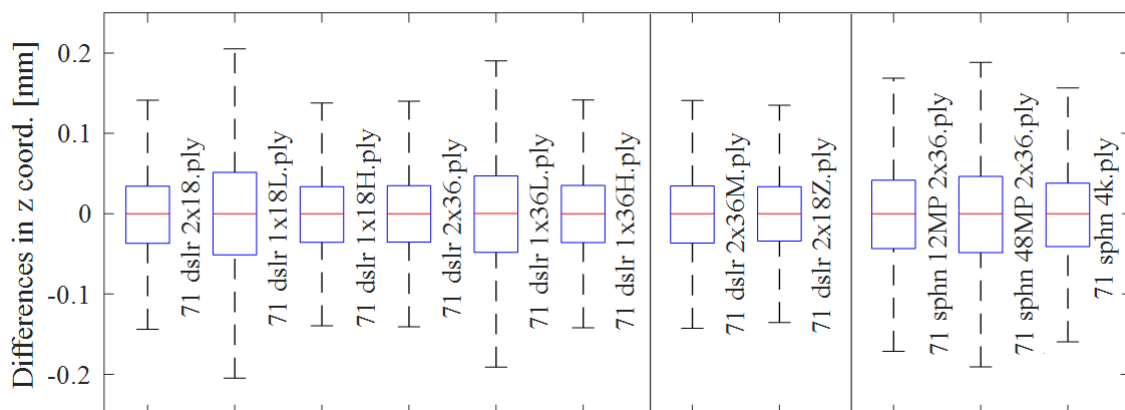


Figure 5. Box plots of the deviations in z coordinates to the reference mesh.

4 CONCLUSIONS

This study tests methods to produce accurate 3D representations of joint roughness surfaces using affordable photographic equipment and open-source software (namely, VisualSFM and MeshLab) in a tolerable lapse of time (a couple of hours for the whole procedure).

The main conclusion is that the comparison between joint surfaces reconstructed with different techniques and the reference contact digitization shows minor differences. If the photos adequately cover the joint surface, equivalent results can be achieved as long as the meshes generated by the reconstruction workflows have similar vertex densities. It can be stated that 18 photos spaced at 20° intervals taken at 30° dip angle relative to the joint mean plane render satisfactory results, given sufficient photographic conditions regarding camera distance and lighting.

The test of two other software – *Meshroom* and *3DF Zephyr* – concluded that the mesh generation is influenced by different built-in triangulation algorithms and their respective governing parameters. Though the reconstructed joint surfaces show specific differences, namely regarding the sharpness of the contour, they do not have a significant impact upon comparison with the reference mesh.

It must be acknowledged that since all methodologies were applied to the same rock joint, the results only allow conclusions regarding the abilities of the methodologies to fulfil this objective. However, some of the methods, namely those that produced better outcomes, were also tested with several other rock joint surfaces allowing us to gain experience concerning several issues of the procedures.

The main objective of this research was to verify the hypothesis of joint roughness photogrammetric evaluation with accessible means, both in terms of photographic equipment, laboratory settings, software for surface reconstruction, and know-how. The experiments and analysis allowed us to recognize that, after some training with the reconstruction software, it is possible to measure rock joint roughness, from camera photographs to the outcome, within one hour, which seems quite reasonable.

An additional objective was to build experience and knowledge to extend the use of close-range photogrammetry to measure the roughness of joints *in situ*. Comparing the results from the conventional camera and the smartphone camera showed that it is a serious and advantageous possibility to reach this goal. Moreover, the use of frames of video from the smartphone camera is a path that dully explored can provide interesting outcomes for field applications.

ACKNOWLEDGMENTS

Part of this work was financially supported by: Base Funding–UIDB/04708/2020 of the CONSTRUCT – Instituto de I&D em Estruturas e Construções – funded by national funds through the FCT/MCTES (PIDDAC), and Base Funding FCT UIDB/04466/2020 of ISTAR - Instituto Universitário de Lisboa. The valuable help of Mr. Rui Coelho with the photographic sessions and mesh processing is also acknowledged.

REFERENCES

- 3DFlow 2019. 3DF Zephyr Free v. 5.013. (accessed November 2020): <http://www.3dflow.net/>
- An, P., Fang, K., Jiang, Q., Zhang, H. & Zhang, Y. 2021. Measurement of Rock Joint Surfaces by Using Smartphone Structure from Motion (SfM) Photogrammetry. *Sensors* 21(3): 922.
- Cignoni, P., Callieri, M., Corsini, M., Dellepiane, M., Ganovelli, F. & Ranzuglia, G. 2008. MeshLab: an Open-Source Mesh Processing Tool. In: Scarano, V., et al. (Eds.), *2008 Eurographics Italian Chapter Conference, Salerno, Italy, 2-4 Jul. 2018*. p. 129-136;

- Fraser, C.S. & Stamatopoulos, C. 2014. Automated Target-free Camera Calibration. In: *ASPRS 2014 Annual Conference, Louisville, Kentucky USA, March 23-28, 2014*.
- Furukawa, Y., Curless, B., Seitz, S.M. & Szeliski, R. 2010. Towards Internet-scale multi-view stereo. In: *2010 IEEE Computer Society Conference on Computer Vision and Pattern Recognition (CVPR), San Francisco, CA, USA, 13-18 Jun. 2010*. p. 1434-1441;
- Gaich, A. & Pötsch, M. 2015. 3D images for data collection in tunnelling – applications and latest developments. *Geomechanics and Tunnelling* 8(6): 581-588.
- Gaich, A., Pötsch, M., Rieder, B. & Schubert, W. 2019. Drone imagery for the acquisition and assessment of rock fall areas. In: Fontoura, S. D., et al. (Eds.), *14th International Congress on Rock Mechanics and Rock Engineering (ISRM 2019), Foz do Iguaçu, Brazil, 13-18 Sep*. Paper 15036.
- Ge, Y., Kulatilake, P.H.S.W., Tang, H. & Xiong, C. 2014. Investigation of natural rock joint roughness. *Computers and Geotechnics* 55: 290-305.
- Ge, Y., Lin, Z., Tang, H. & Zhao, B. 2021. Estimation of the appropriate sampling interval for rock joints roughness using laser scanning. *Bulletin of Engineering Geology and the Environment* 80: 3569–3588.
- ISRM 1978. Suggested methods for the quantitative description of discontinuities in rock masses. *International Journal of Rock Mechanics and Mining Sciences & Geomechanics Abstracts* 15(6): 319-368.
- Jancosek, M. & Pajdla, T. 2011. Multi-view reconstruction preserving weakly-supported surfaces. In: *CVPR 2011, 20-25 June 2011*. p. 3121-3128, ISBN: 1063-6919.
- Ladanyi, B. & Archambault, G. 1970. Simulation of shear behaviour of a jointed rock mass. In: Somerton, W. H. (ed.) *11th Symposium on Rock Mechanics: Theory and Practice, Berkeley, California, June 16-19*. p. 105-125,
- Nikolov, I. & Madsen, C. 2016. Benchmarking Close-range Structure from Motion 3D Reconstruction Software Under Varying Capturing Conditions. In: *EuroMed 2016: Digital Heritage. Progress in Cultural Heritage: Documentation, Preservation, and Protection, Nicosia, Cyprus, Oct. 31 - Nov. 05*. p. 15-26, ISBN: 978-3-319-48496-9.
- Ortiz-Sanz, J., Gil-Docampo, M., Rego-Sanmartín, T., Arza-García, M. & Tucci, G. 2021. A PBeL for training non-experts in mobile-based photogrammetry and accurate 3-D recording of small-size/non-complex objects. *Measurement* 178: 109338.
- Paixão, A. & Fortunato, E. 2021. Abrasion evolution of steel furnace slag aggregate for railway ballast: 3D morphology analysis of scanned particles by close-range photogrammetry. *Construction and Building Materials* 267: 121225.
- Paixão, A., Resende, R. & Fortunato, E. 2018. Photogrammetry for digital reconstruction of railway ballast particles – A cost-efficient method. *Construction and Building Materials* 191: 963-976.
- Patton, F.D. 1966. Multiple Modes of Shear Failure In Rock. In: *1st ISRM Congress, Lisbon, Portugal, Sep. 25–Oct. 01*. Paper 87.
- Ramos, A.L. 2013. Characterization and modelling of the roughness of rock discontinuities (in Portuguese). M.Sc. Thesis, Porto: Faculdade de Engenharia da Universidade do Porto.
- Resende, R., Muralha, J., Ramos, A.L. & Fortunato, E. 2015. Rock joint topography: three-dimensional scanning and numerical analysis. *Géotechnique Letters* 5(4): 318-323.
- Roland 1999. Dr. PICZA. Roland DG Corporation.
- Uotinen, L., Janiszewski, M., Baghbanan, A., Caballero, E., Oraskari, J., Munukka, H., Szydłowska, M. & Rinne, M. 2019. Photogrammetry for recording rock surface geometry and fracture characterization. In: Fontoura, S. D., et al. (Eds.), *14th International Congress on Rock Mechanics and Rock Engineering (ISRM 2019), Foz do Iguaçu, Brazil, 13-18 Sep*. Paper 14698.
- Wernecke, C. & Marsch, K. 2015. Mapping Rock Surface Roughness with Photogrammetry. In: Schubert, W. & Kluckner, A. (Eds.), *ISRM Regional Symposium EUROCK 2015 - Future Development of Rock Mechanics, Salzburg, Austria*, p. 1175-1180; Paper 192.
- Wu, C. 2013. Towards Linear-Time Incremental Structure from Motion. In: *2013 International Conference on 3D Vision (3DV 2013), Seattle, Washington, USA*, p. 127-134;
- Wu, C., Agarwal, S., Curless, B. & Seitz, S.M. 2011. Multicore bundle adjustment. In: *2011 IEEE Conference on Computer Vision and Pattern Recognition, Colorado Springs, Colorado, 20-25 Jun. 2011*. p. 3057-3064;

Toward a new definition of terms in the rock geomechanical classification and its relation to the numerical analysis of tunnels

W. Naime

Central University of Venezuela, Caracas, Venezuela

R. García

Andrés Bello Catholic University, Caracas, Venezuela

ABSTRACT:

It is proposed that terms such as persistence and discontinuity should be eliminated from the rock mass geomechanical classification, since these include the formational planes of the classification of rocks according to their origin, highlighting the continuous planes of the layers in sedimentary rocks and the foliation planes in metamorphic rocks. The term joint, widely known as non-moving fractures, should be redefined for its proper use in geomechanical classification, as non-moving fractures where the extension and frequency depend on the stress state of the rock mass. In a tunnel analysis, the existing empirical classifications consider various parameters related to the joints, analyzed as constant patterns, with valuations up to 75% of the total, without considering the effect of the development and frequencies of joints, according to the change of the stress state. This has repercussions in the tunnels numerical analyzes, where the development and frequencies of joints depend on the state of stress and the stress release by the excavation, so that the geomechanical conditions of the rock mass are the most affected in the vicinity of the excavation and the less affected at a greater distance from the excavation. According to observations in physical models, the deformations around a tunnel tend to form resistance ovals, which can be represented in numerical models in a similar way. The results of the analyzes that consider the variation of the resistance, show a decrease in the stress and deformation towards the cavity. In this research, various practical examples are presented that support the hypothesis that joints develop as a function of the change in the stress state. Through examples by applying numerical methods, it is shown that the deformations of a rock with constant parameters is greater than those obtained with a zoned mass model by changes in the geomechanical characteristics as a function of the distance from the tunnel excavation. The results have an impact on the design and on the costs.

1 INTRODUCTION

According to the International Society for Rock Mechanics and Rock Engineering (ISRM), Discontinuity is a general term denoting any separation in a rock mass having zero or low tensile strength. It is the collective term for most types of joints, weak bedding planes, weak schistosity planes, weakness zones, and faults (Brown, 1981). The previous definition involves a mixture of terms, covering the formational planes, no displacement fractures or joints, and moving fractures, in general with different mechanical behaviors. This diversity hinders the correct application of terms in the rock mass engineering classification and also affect the numerical analysis on rock mechanics (Naime & García, 2022).

The bedding planes and foliation planes are terms associated with the rock classification according to their origin, sedimentary and metamorphic respectively, constituted by continuous planes that control the mechanical behavior according to the requirements against the rock mass. These planes present fixed patterns related to their origin, additionally these patterns are not modified by the change in the stress state.

Joint formation and extension depend on the stress state of the rock mass. The change in the confinement state determines the evolution and size of the cracks. With greater confinement, smaller joint size and vice versa.

It's a common error to consider joints with predefined patterns and uniform characteristics in the rock mass, since these can vary with changes in the stress state. Joints form a very significant component of the criteria for the engineering classification of rock mass which were mainly developed for empirical tunnel analysis.

Then, in the rock engineering characterization, it's important to separate the planes of origin, such as bedding planes and foliation planes, from the joints, which are formed due to mechanical effects.

Both for the geomechanical rock mass classifications and for the numerical modeling, the terms *discontinuity* and *persistence* should allow to differentiate between the formational structural planes, not related to the stress state, and the joints, that depend on the regionally and local stresses (Naime & García, 2022).

It is proposed that terms such as persistence and discontinuity should be eliminated from the rock mass geomechanical classification, since these include the formational planes of the classification of rocks according to their origin, highlighting the continuous planes of the layers in sedimentary rocks and the foliation planes in metamorphic rocks.

2 JOINT FORMATION STAGES

The presence of microcracks is detected by the microscope, which will control the joint patterns in outcrops. Figure 1 shows, schematically, the transition from microcracks at the microscope level to microfractures that can be visually identified with a magnifying glass, then, at the outcrop, the joints are on full display.

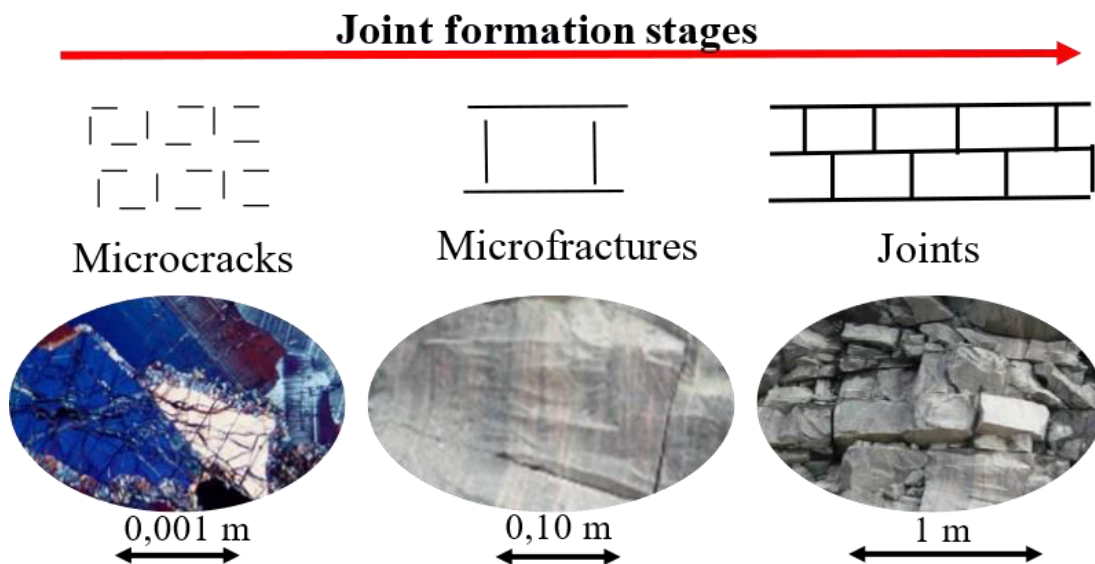


Figure 1. Transformation from microcracks to joints due stress changes.

The joint growth is related to the stress state and the rock shear strength. Mohr-Coulomb, Hoek & Brown and Drucker & Prager and several other criteria, like the Griffith fracture criterion (Griffith, 1921), could be applied to the joint growth analysis. This criterion could be applied to explain joint formations due to the microcracks in the rock mass, making it compatible

with the crack generation criterion.

Previous studies have shown that shear fractures generated from microcracks in the rock mass are mainly tensile cracks, (e.g. Hadley, 1976; Howarth, 1987; Kranz, 1979; Tapponnier & Brace, 1976; Wong, 1982). When the rock mass is deforming, the crack density increases significantly, microcrack densities are consistently higher on the dilatation side of the cut with respect to the compression side, and at first, joints are mainly tensile cracks which will later rotate relative to the applied stress tensor (Moore & Lockner, 1995).

According Freire (2016), in strong granite rock, the decompression generated by the lithostatic load reduction generates microcracks perpendicular to the direction of the unloaded stress. Generally, the orientation of the microcracks is horizontal at significant depths and concentric at shallow depths. In high confined triaxial tests, four successive stages can be distinguished in regard to the crack growth: first, rock behaves like an elastic solid, and microcracks do not grow, second, microcracks start to grow so that inelastic volumetric strain appear, then, microcracking is considerably accelerated with the inelastic strain, and finally, the crack density, as well as the dilatancy, increases rapidly in conjunction with the growth of the failure zone (Takemura & Oda, 2005).

3 JOINT PATTERNS AND JOINT EXTENSION

3.1 *The effects on the microcracks formation and microfractures growth according to the scale of the rock mass*

The effects on the microcracks formation and microfractures growth, must be analyzed according to the scale of the rock mass. The mechanical behavior is usually related to an intact rock core, which subjected to compression tests, shows elastic properties and the first microcracks appear with the plastic deformations. But the mechanical behavior of the jointed rock mass, is controlled at a larger scale, according to the stress state changes, like schematized in figure 2 (Naime & García, 2022):

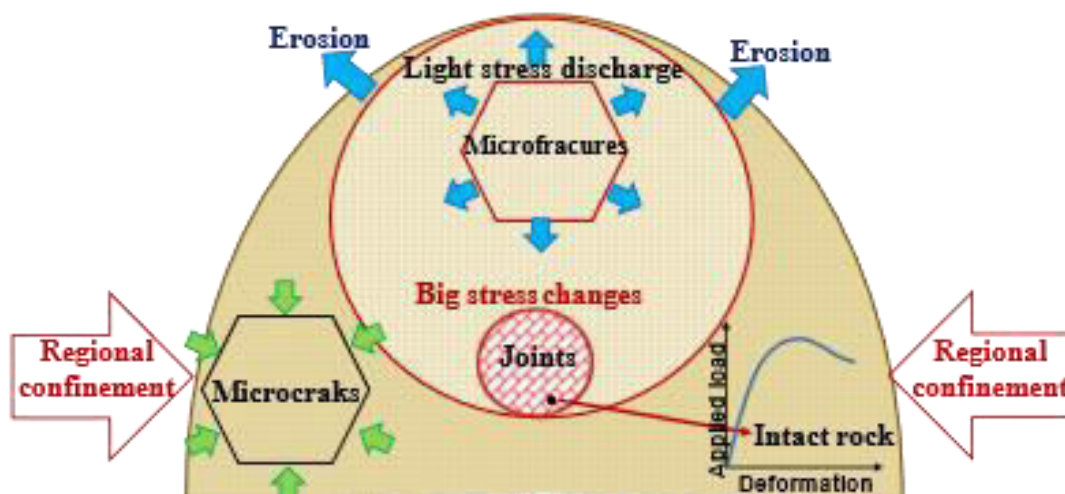


Figure 2. The scale of the rock mass and its mechanical behavior (Naime & García, 2022).

Both, the geostatic loads and the tectonic forces exert an effect on the regional lithological masses. Erosion processes cause changes in the stress state, transforming some microcracks into microfractures. The final orientation of the microfractures will depend on the original orientation of the microcracks and the change in stress state in the rock mass. Subsequently, with fur-

ther decreases in confinement pressure, some microfractures, with pre-established orientation patterns, evolve to form a joint system.

3.2 Joint patterns and the rock origin

Joint patterns are related to the rock origin: Igneous, Sedimentary and Metamorphic. The continuous planes as the bedding planes and foliation planes, control joint patterns that generally remain perpendicular to these planes, maintaining orthogonal systems. Joint patterns in sedimentary and metamorphic rocks are related to the position of the principal bedding or foliation planes, respectively. In general, there are three joint patterns: one parallel and another perpendicular to the main plane, and lastly, an oblique to plane strike, commonly sub-vertical.

Figure 3 shows outcrops of sedimentary rocks (a) and (b), in a metamorphic rock (c), and the Salto Angel (d), the highest waterfall in the world, where the escarpment is controlled by a sequence of thick silicified sandstone layers, affected by sub-vertical joints that are controlled by the sheer wall. In these cases it's clearly observed that the orthogonal joints are limited to the layers thickness, showing the joints formation in layers.

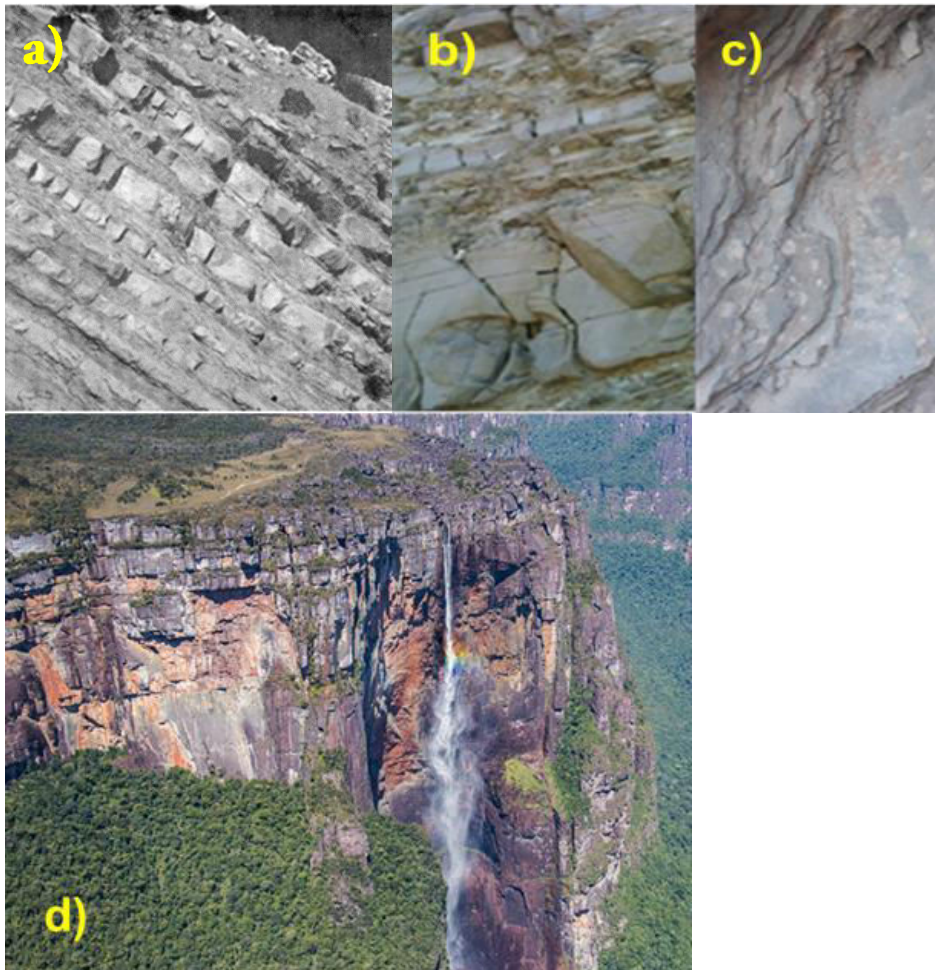


Figure 3. Joint formation in layers (Naime & García, 2022)

In igneous rocks, joint patterns present systems related to the geological history of regional stresses, with similar inclination among each other and a variation in the size of the joint planes, usually forming orthogonal systems.

3.3 Joint extension

The term persistence should be eliminated from the rock mass geomechanical classification, since include very large formational planes as planes of the layers in sedimentary rocks and the foliation planes in metamorphic rocks. It's proposed to change it to the term *Joint Extension*, as the area of the non-moving fracture, which will depend on the change in the stress state in the rock mass (see Figure 4). The terms frequency, roughness, and fill will continue to apply to joints.

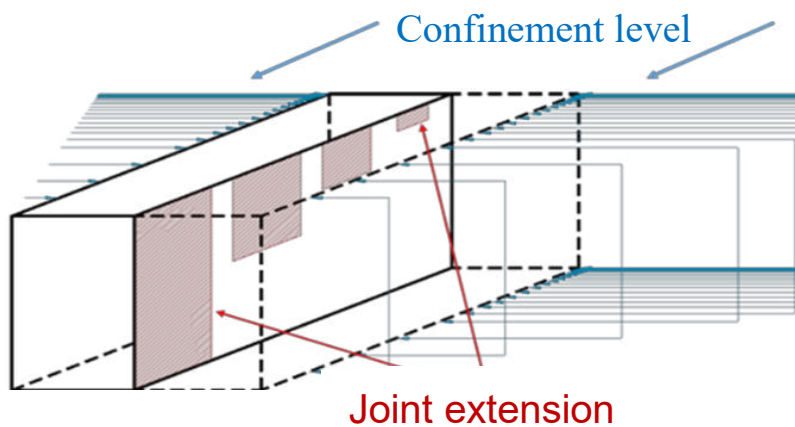


Figure 4. Joint extension in layers (Naime & García, 2022)

4 ZONIFIED MODEL ON THE TUNNEL NUMERICAL ANALYSIS

Both for the geomechanical rock mass classifications and for the numerical modeling, the term discontinuity should allow to differentiate between the formational structural planes, no related with the stress state, and the joints, that depend on the regionally and local stresses. With planes of infinite extension, such as bedding planes and foliation planes, the deformation effect towards the tunnel, generates open fractures orthogonal to these planes, although blocks are formed, the deformation is controlled by the main planes. Naime & García (2022) show through physical models and numerical analysis that the tunnel excavation on stratified rocks generates a bending effect in the layers and orthogonal opened joints. The lateral deformations of the layers are limited, generating an oval shape in the deformation zone. The layer thickness/tunnel diameter ratio (D/ϕ) has a great influence on the deformations. If $(D/\phi) \geq 1$, the bending effect is minimal, but if (D/ϕ) is small, then large deformations will occur. The blocks formed in the vicinity of the excavation will be larger than those formed further away.

In igneous rocks, a tunnel excavation generates joint patterns with high density or frequency at the edge of the excavation, but due to the confinement at a certain distance, the joint density is significantly reduced. At great depths, the joints will form with sub-horizontal patterns on the tunnel vault and sub-vertical patterns towards the gables. Explosive rocks can appear produced by the sub-horizontal joints, forming layers, which, when subjected to sudden stress changes, produce abrupt failures.

Generally, a tunnel excavation will develop joints whose density will be reduced with the distance from the excavation. Figure 5 outlines the zoning of the rock mass, to model changes in

joint density and strength variation in numerical tunnel analysis, based on stress changes and also according to some well-known elasto-plastic models.

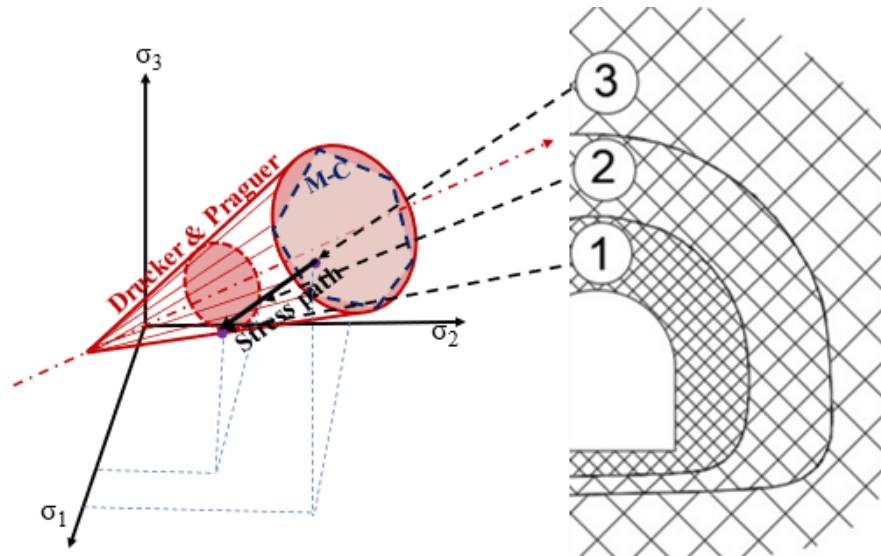


Figure 5. Zoning of the rock mass to model changes in joint density and strength variation in numerical tunnel analysis. (Naime & García, 2022)

It's a common error to consider joints with predefined patterns and uniform characteristics in the rock mass, since these can vary with changes in the stress state. Joints form a very significant component of the criteria for the engineering classification of rock mass which were mainly developed for empirical tunnel analysis. The initial stress state and the size of the tunnel excavation, are factors that determine the change in stress of the rock mass, and consequently, also determine the formation, density and the extension of the joints. The resulting decompressed zone, near the excavation border, is related to the joint patterns larger size and high density, compared to the zones with small stress changes, occurring beyond the decompressed zone.

Figure 7 shows the cut slope in the discharge channel of the Tocoma dam in Venezuela, which was built on granitic rocks. Is observed the sub-horizontal joint planes limiting the vertical joints. Despite the aperture in the observed joints system, the rock mass is totally impermeable, which shows that the joints pattern in the outcrop is formed due to the total and rapid stress discharge, but in the nearby areas, with a higher level of stress, joints are not fully formed or open, confirming the relationship between the joint formation and the stress state.

Table 1 presents the measured seismic velocities after construction was completed, in three tunnels in Venezuela: i) the Yacambú hydraulic tunnel, with 4 m of diameter and 500 m of coverage (on the measurement zone), ii) the Aguaviva hydraulic tunnel, with 6 m of equivalent diameter and 80 m of coverage, and iii) the Estanques vehicle tunnel, with 9 m of equivalent diameter and 300 m of coverage. In each case, the area adjacent to the excavation border presented low seismic velocities, associated with a higher density of the joints due to the decompression effects. The size of the decompressed zone was 0.25 to 0.9 times the excavation diameter. Beyond this zone, there are clearly distinguished areas less affected by the stress discharge, which maintained the original seismic velocities. In these three cases, it was observed that the decompressed zone loses between 35 and 70% of the seismic velocity with respect to the unaffected zone.

Figure 7 present a schematic model defining decompressed zone (DZ) and joints density during tunnel excavation according to the micro-seismic velocities (V_p , V_s) and the distance from the excavation /tunnel diameter ratio (d/ϕ) (Naime & García, 2022).



Figure 6. Cut slope in the discharge channel of the Tocoma dam in Venezuela.

Table 1. Seismic velocities measured after tunnel completion in three cases (Naime & García, 2022).

Tunnel		DZ Size m	V_p	V_s	NDZ ⁺	
					V_p	V_s
Yacambú (4 m)	Maximun	3,5	2.750	1.330	4.000	2.200
	Mnimum	0,3	400	180	1.400	750
	Mean	0,9	1.569	699	2.593	1.406
Aguaviva (6 m)	Maximun	4,0	3.000	350	5.500	3.400
	Mnimum	0,5	670	1.710	1580	960
	Mean	1,1	1.764	981	3.437	2.057
Estanques(9 m)	Maximun	1,5	1.500	1.100	3.200	1.700
	Mnimum	0,5	860	400	1.600	900
	Mean	0,7	1.135	714	2.330	1.226

* Non decompressed zone

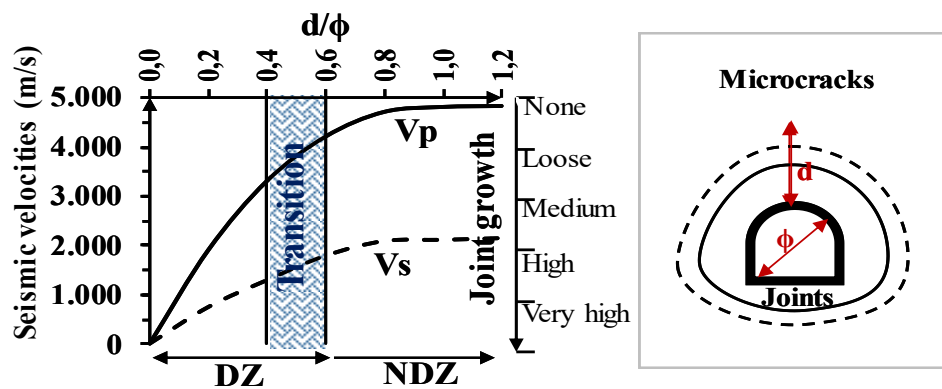


Figure 7. Schematic model defining decompressed zone (DZ) and joints growth during tunnel excavation according to the micro-seismic velocities (V_p , V_s) and the distance from the excavation /tunnel diameter ratio (d/ϕ) (Naime & García, 2022).

5 RESULTS OF THE NUMERICAL ANALYSIS

Significant differences are obtained in the results of the numerical analysis, if the rock mass is modeled with a homogeneous material, equivalent to those observed directly in the excavation, when compared with the results of the analysis against the rock mass zoning model, as shown in figure 5.

In the finite element numerical analysis for the Estanques tunnel (9m) and for the Aguaviva tunnel (6m), both in Venezuela, the maximum deformations obtained with the rock zoning models are approximately half than those obtained by the rock mass without zoning models, the results fit the observed behavior more closely (Naime & García, 2022).

According to figure 7, we analyzed several tunnels with different equivalent diameters (ϕ). In all cases, the decompressed zone (DZ) was $0,75\phi$ (zone 1) and the transition zone $0,25\phi$ (zone 2). The primary seismic velocities considered were: zone 1 (550 m/s), zone 2 (726 m/s) and beyond the decompressed zone (1190 m/s). Figure 8 presents the displacements obtained by numerical modeling for the $\phi = 9$ m tunnel, with and without zoning model. In the homogeneous rock model it was considered that the material is the same as that of zone 1.

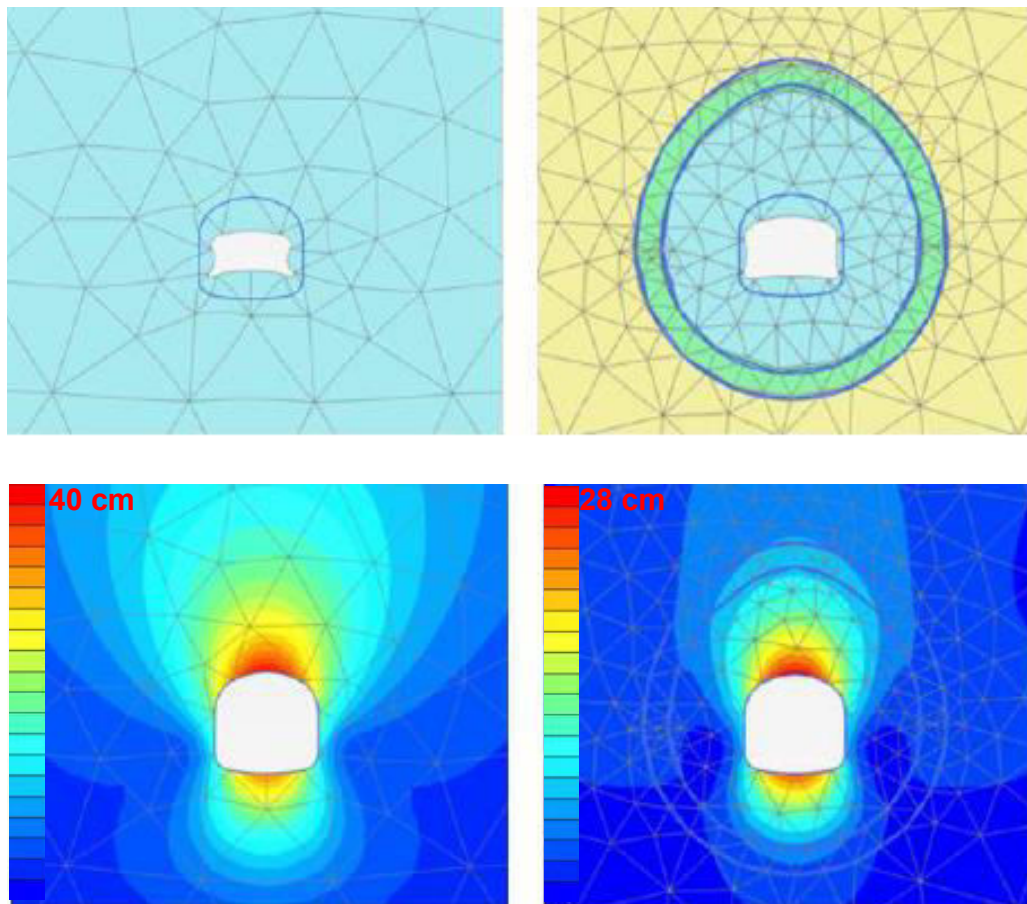


Figure 8. Displacements and total deformation results obtained by numerical modeling for the tunnel with $\phi = 9$ m. In the left side is present de homogeneous model and in the right side is present the zoning rock model.

Figure 9 show the mean displacement on the tunnel contour with different excavation sizes and for rock mass with and without zoning model. Mean displacements were estimated at six different points on the tunnel contour.

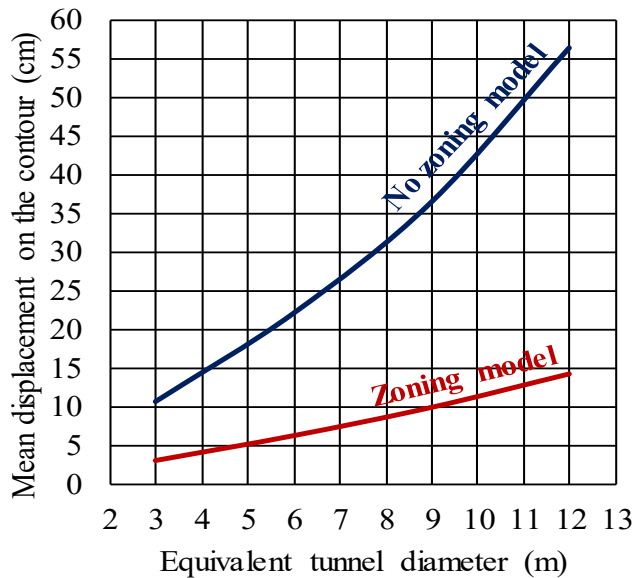


Figure 9. the mean displacement on the tunnel contour with different excavation sizes and for rock mass with and without zoning model.

Zoning the homogeneous rock mass to model changes in joint density and strength variation in numerically tunnel analysis, present significant differences from only homogeneous material model. The mean displacement on the tunnel contour obtained with the rock zoning models present reductions between 65 and 75% with respect to those obtained with the homogeneous rock models.

6 CONCLUSIONS

The term joint, should be redefined for its proper use in geomechanical classification, as non-moving fractures where the extension and frequency depend on the changes of the stress state of the rock mass.

For the geomechanical rock mass classifications, the term discontinuity should allow to differentiate between the formational structural planes, no related with the stress state, and the joints, that depend on the regionally and local stresses.

The term persistence should be eliminated from the rock mass geomechanical classification, since include very large formational planes as planes of the layers in sedimentary rocks and the foliation planes in metamorphic rocks. It's proposed to change it to the term *Joint Extension*, as the area of the non-moving fracture, which will depend on the change in the stress state in the rock mass.

Tunnel excavation will develop joints whose density and extension will be reduced with the distance from the excavation. The resulting decompressed zone, near the excavation border, is related to the joint patterns larger size and high density, compared to the zones with small stress changes, occurring beyond the decompressed zone.

Significant differences are obtained in the results of the numerical analysis, if the rock mass is modeled with a homogeneous material, equivalent to those observed directly in the excava-

tion, when compared with the results of the analysis against the rock mass zoning model, that consider the joint density and extension reduction with the distance from the excavation. Based on the analyzed of several tunnels with different equivalent diameters (ϕ), assuming that the decompressed zone is $0,75\phi$ and the transition zone $0,25\phi$, the mean displacement on the tunnel contour obtained with the rock zoning models present reductions between 65 and 75% with respect to those obtained with the homogeneous rock models.

REFERENCES

- Brown, E. T. (1981). Rock characterization testing and monitoring. ISRM suggested methods. *Rock Characterization Testing and Monitoring. ISRM Suggested Methods*. [https://doi.org/10.1016/0148-9062\(81\)90524-6](https://doi.org/10.1016/0148-9062(81)90524-6)
- Freire, D. M. (2016). Deterioro de granito utilizado en construcción tradicional. *Naturaleza Aragonesa*, 33, 27–31. <http://hdl.handle.net/10261/184702>
- Griffith, A. A. (1921). The Phenomena of Rupture and Flow in Solids. *Philosophical Transactions of the Royal Society of London. Series A, Containing Papers of a Mathematical or Physical Character*, 221, 163–198. <http://www.jstor.org/stable/91192>
- Hadley, K. (1976). Comparison of calculated and observed crack densities and seismic velocities in Westerly granite. *Journal of Geophysical Research*, 81(20), 3484–3494. <https://doi.org/10.1029/JB081i020p03484>
- Howarth, D. F. (1987). The effect of pre-existing microcavities on mechanical rock performance in sedimentary and crystalline rocks. *International Journal of Rock Mechanics and Mining Sciences & Geomechanics Abstracts*, 24(4), 223–233. [https://doi.org/https://doi.org/10.1016/0148-9062\(87\)90177-X](https://doi.org/https://doi.org/10.1016/0148-9062(87)90177-X)
- Kranz, R. L. (1979). Crack growth and development during creep of Barre granite. *International Journal of Rock Mechanics and Mining Sciences & Geomechanics Abstracts*, 16(1), 23–35. [https://doi.org/https://doi.org/10.1016/0148-9062\(79\)90772-1](https://doi.org/https://doi.org/10.1016/0148-9062(79)90772-1)
- Moore, D. E., & Lockner, D. A. (1995). The role of microcracking in shear-fracture propagation in granite. *Journal of Structural Geology*, 17(1), 95–114. <http://pubs.er.usgs.gov/publication/70019720>
- Naime, W., & García, R. (2022). The rock mass and the development of joints during the tunnel excavation. *Eurock 2022*, in press.
- Takemura, T., & Oda, M. (2005). Changes in crack density and wave velocity in association with crack growth in triaxial tests of Inada granite. *Journal of Geophysical Research: Solid Earth*, 110(B5), 13–16. <https://doi.org/https://doi.org/10.1029/2004JB003395>
- Tapponnier, P., & Brace, W. F. (1976). Development of stress-induced microcracks in Westerly Granite. *International Journal of Rock Mechanics and Mining Sciences & Geomechanics Abstracts*, 13(4), 103–112. [https://doi.org/10.1016/0148-9062\(76\)91937-9](https://doi.org/10.1016/0148-9062(76)91937-9)
- Wong, T.-F. (1982). Micromechanics of faulting in westerly granite. *International Journal of Rock Mechanics and Mining Sciences & Geomechanics Abstracts*, 19(2), 49–64. [https://doi.org/https://doi.org/10.1016/0148-9062\(82\)91631-X](https://doi.org/https://doi.org/10.1016/0148-9062(82)91631-X)

Effect of artificial joints on the mechanical response of a granitic rock

J. Arzúa

Department of Metallurgical and Mining Engineering, Universidad Católica del Norte

L. Cuevas-Ugalde

Department of Metallurgical and Mining Engineering, Universidad Católica del Norte

H. Ledesma-Osorio

Department of Metallurgical and Mining Engineering, Universidad Católica del Norte

M. Cánovas

Department of Metallurgical and Mining Engineering, Universidad Católica del Norte

M. Maleki

Department of Metallurgical and Mining Engineering, Universidad Católica del Norte

ABSTRACT:

The scale effect is still an unsolved problem on rock mechanics discipline, there are some empirical approaches that work reasonably well, but lack of knowledge of the affecting parameters. For instance, Hoek-Brown generalized failure criterion is a good and practical way to estimate rock mass strength. It considers the quality of the rock mass and, indeed, the characteristics of the discontinuities as a whole, by means of GSI, but it is not known how the different parameters of the discontinuities affect the rock mass strength. Trying to bring some light into the topic, some authors have argued about the necessity to split scale effect into size effect and structure effect. Size effect has been reasonably solved by means of classic or novel approaches, although there are some issues about the range of applicability of each approach. Structure effect has been addressed mainly by means of synthetic non-rock material specimens, and only a few authors have tried to prepare and test actual-rock jointed specimens. The current study revisits the issue of the presence of artificial joints in laboratory rock specimens, although it is mainly focused on testing the equipment capabilities of the Rock Mechanics Laboratory of the Catholic University of the North in northern Chile. Two series of specimens of a local granitic rock (Loa's granite) are tested. First series includes five intact specimens tested under unconfined conditions, and second series includes eleven jointed specimens featuring two sets of discontinuities tested under triaxial conditions. Tests results show a clear dependence of strength on jointing, and that the strain localization occurs mainly on the artificial discontinuities.

1 INTRODUCTION

The scale effect term stands for the observed difference between the strength and deformability observed on laboratory scale testing and actual scale excavations. It has been recognized as one of the key topics on rock mechanics since it allows to correctly predict the behavior of the surroundings of an excavation and, for instance, optimize the amount of required support.

The scale effect has been solved by means of experimental approaches, for instance, GSI approach (Hoek, 1994, Hoek et al., 1995, Hoek & Brown, 1998). This kind of approaches performs reasonably well in most cases, but still there isn't a complete understanding of the phenomena behind this effect.

Main difficulty on understanding these phenomena lays on the fact that "scale effect" is a general term that includes two origins for the same effect. First one is that related to the effect of

the size of the sample (size effect), and second one relates to the structure (or macro-discontinuities) existing into the sample (structure effect).

Size effect has been traditionally solved by means of the approach proposed by Hoek and Brown (1980) where strength decreases as size increases up to reaching the REV size. Some authors (Shuren et al., 2020, Masoumi, 2016, Quiñones et al., 2017), have been postulating that the Hoek and Brown approach is not universal and that there are some rocks that does not follow such behavior. Instead, some strength test results show a reverse size effect, where strength increases and then decreases as the sample size increases.

Structure effect considers the effect of the presence of discontinuities on the sample. Traditionally, this effect was studied at laboratory scale using rock-like materials (concrete, plaster of paris...), but a group of researchers recently began to test rock materials (Alejanot et al., 2017, Arzua et al., 2014, Arzua, 2015) attaining relevant results.

This paper describes the first steps of a new rock mechanics laboratory to perform strength tests on artificially jointed specimens, as well as the first obtained results.

2 METHODOLOGY

The studied rock is a granite coming from an old ornamental quarry located at Cerro Las Papas, (21°54'16.53" S, 68°36'3.61" W), in Alto Loa Province, some 80 km to the north away from Calama, in Northern Chile. Some irregular samples were collected and carried to the Rock Mechanics Laboratory of the Universidad Católica del Norte, in Antofagasta, Chile.

Two series of specimens were prepared. First series was a regular series of five intact specimens. Second series included eleven jointed specimens, featuring two sets of discontinuities, one sub vertical discontinuity and 2 sub horizontal parallel joints.

The irregular field samples were reduced to parallelepiped shaped blocks using a circular saw with a 1 m diameter cutting disc (Norton Clipper Jumbo 1000), to be able to easily handle them and to perform the consecutive cuts required to obtain the specimens.

For the first series of specimens, rock cores were extracted from the parallelepiped shaped blocks using a BAIER 8325 drilling machine. The cores were cut transversely to their axis up to the nominal length of a cylindrical specimen using a Controls 45-D0536 circular saw machine, and, finally, their flat faces were ground using a surface grinder KENT KGS1224AH up to meet requirements of the Suggested Methods of the ISRM (2007).

Second series of specimens (jointed ones) used the same equipment as the first series, but, in this case, the procedure is a little bit different (Arzua et al., 2014). The parallelepiped shaped block was cut in two parts forming the subvertical joint (85° dip) using the Controls 45-D0536 circular saw. These two parts were then firmly rejoined using clamps, and the core was carefully cut using the BAIER drilling machine, in such a way that the subvertical joint crossed the full length of the rock core. This procedure avoids the loss in section that would occur if the subvertical joint is cut after the core is extracted (Figure 1).

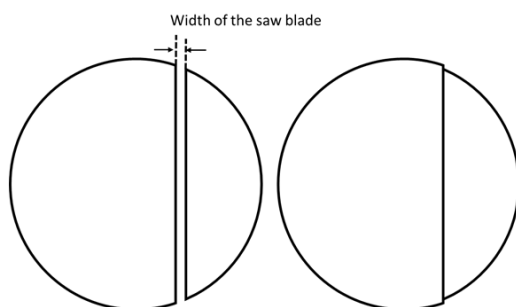


Figure 1. Problem arising if the subvertical joint is cut after the core is extracted.

Once the core with the subvertical joint is extracted from the sample using the drilling machine, the two subhorizontal joints (23° dip) and the flat faces are cut, and thus obtaining the jointed specimen (Figure 2).

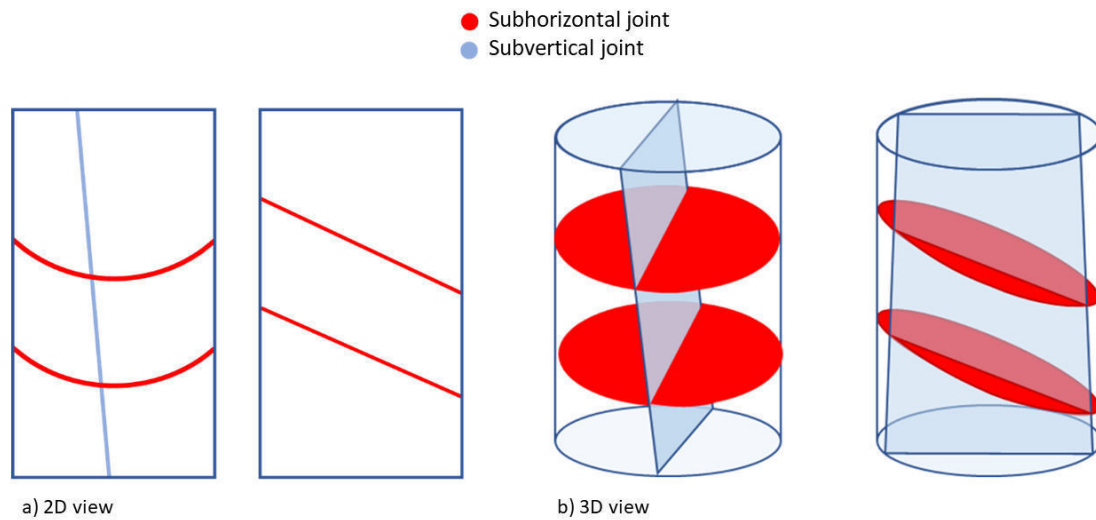


Figure 2. Schematic view of the jointed specimen in 2d and 3D and front and lateral view.

3 TESTING EQUIPMENT

The Rock Mechanics Laboratory of the Department of Metallurgical and Mining Engineering of the Universidad Católica del Norte has available a rock strength testing machine CONTROLS MCC8 50-C8422/M (Figure 3) with a load capacity of 3000 kN. The load in the frame is controlled by a computer which allows to fix the load velocity by means of a servo-controlled hydraulic pump. The computer also allows to connect up to four strain gauges in order to measure strains during strength tests.

For the regular specimens, the strain gauges were stuck to the specimen at mid height, two of them longitudinally and the other two transversely (Figure 4.a) to have available two measures of each strain. In the case of the jointed specimens, the strain gauges were stuck to the four upper pieces, in order to measure the longitudinal or transversal strain of these pieces.

The regular specimens were tested under uniaxial conditions, but the jointed specimens were tested under triaxial conditions because these specimens will only reach very low values of load under uniaxial load. The triaxial conditions were attained by means of a Hoek's cell and confining stress was pumped by the Controls Sercomp 7 50-C7022/S (Figure 3). The equipment records the stress and strain of the strength test up to the failure of the specimen.



Figure 3. Rock strength testing machine, Controls MCC8 50-8422/M and triaxial module Controls SERCOMP 7 50-C7022/S available on the Rock Mechanics Laboratory of the Department of Metallurgical and Mining Engineering of the Universidad Católica del Norte

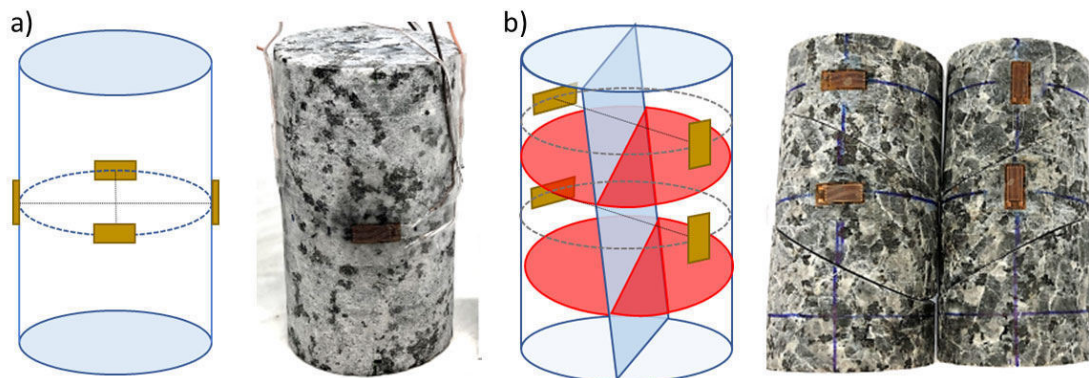


Figure 4. Location and orientation of the strain gauges in the case of a) regular specimens, b) jointed specimens.

4 RESULTS

The comma separated values file recorded by the testing equipment allows to obtain stress-strain curves, as well as elastic parameters and peak strength of each test. As previously commented, intact specimens were tested under uniaxial conditions, while jointed specimens were tested under triaxial conditions. To be able to compare results, an estimation of the Hoek & Brown criterion (Hoek et al., 2022) for intact rock was obtained based on bibliographical data (Rocscience, 2019).

4.1 Intact specimens

Five intact and regular specimens were tested under unconfined conditions. Table 1 shows the main results of these tests as well as the dimensions of each specimen. Regrettably, the strain results of specimen G/RI-1 were out of range, so they were discarded.

Table 1. Strength test results of the intact specimens under uniaxial conditions.

Specimen	Length (mm)	Diameter (mm)	σ_3 (MPa)	σ_{peak} (MPa)	E (GPa)	ν (-)
G/RI-1	99.5	54.6	0	72.0	-	-
G/RI-2	98.1	54.6	0	164.0	64.0	0.16
G/RI-3	99.6	54.6	0	137.4	65.7	0.27
G/RI-4	100.0	54.6	0	130.0	59.9	0.35
G/RI-5	100.0	54.6	0	73.0	59.4	0.28
Mean	99.4	54.6	-	115.3	76.4	0.26
St. Dev.	-	-	-	41.0	3.1	0.08

The results for these intact specimens are in accordance with the expected results for a granite (Stagg & Zienkiewicz, 1968, Hoek, 2007, Arzua, 2015). Figure 5 shows an example of a stress-strain curve of intact specimens, in this case it is the stress-strain curve of the G/RI-3 specimen, please take into account that this specimen is attaining values of axial strain of 2200-2300 $\mu\text{str.}$ at peak strength.

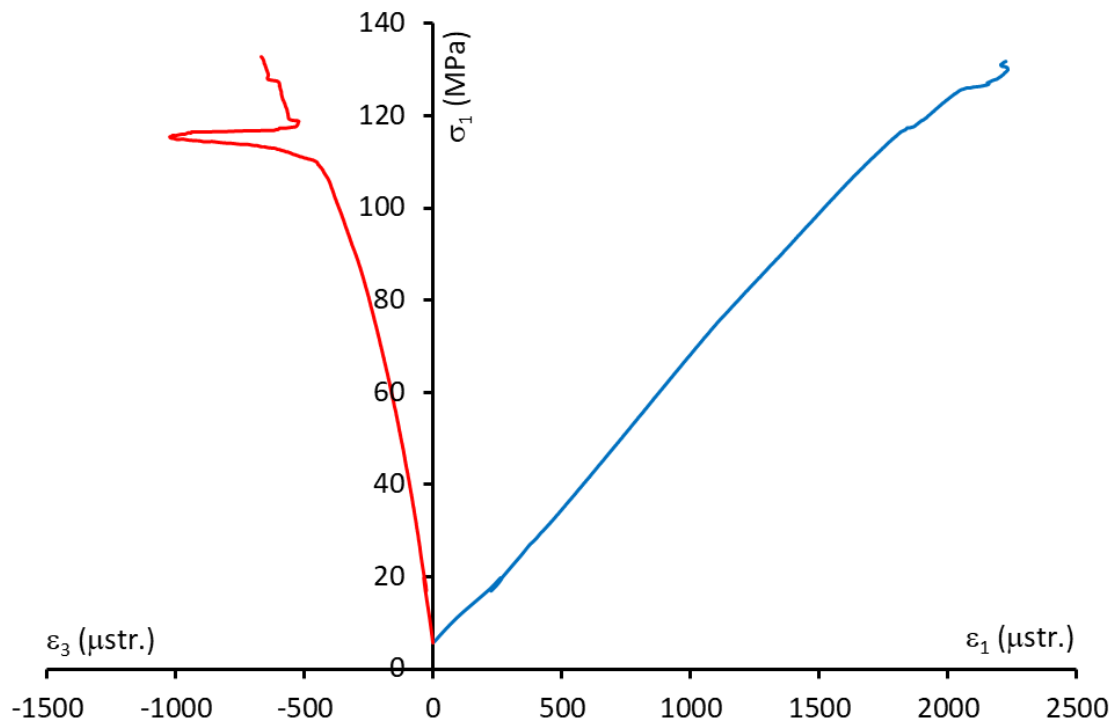


Figure 5. Stress-strain curve for the G/RI-3 intact specimen

4.2 Jointed specimens

Eleven specimens of these small-scale rock masses were tested under triaxial conditions, with a constant confining pressure of 5 MPa. The results of these tests are shown on Table 2. The dimensions of the specimens were the same as in the case of intact specimens, 54.6 mm in diameter and about 100 mm in length, but it was difficult to precisely measure them because of the different pieces of the specimens.

It is remarkable that, during testing of the GD.TR-8 specimen, the confinement fell abruptly, and the specimen failed under uniaxial conditions, therefore no data were recorded. Moreover,

the wires used to connect the strain gauges were too much thin, and, in many cases, they failed mechanically when submitted to the confining pressure and by effect of the sharp borders of the pieces of the specimens. Anyway, we could recover the data for enough specimens and the trend was fairly revealed.

Table 2. Strength test results of the jointed specimens under triaxial conditions.

Specimen	σ_3 (MPa)	σ_{peak} (MPa)	E (GPa)
GD.TR-1	5	151.8	2381.0
GD.TR-2	5	155.4	2625.3
GD.TR-3	5	153.2	2050.4
GD.TR-4	5	98.1	-
GD.TR-5	5	126.1	-
GD.TR-6	5	144.4	-
GD.TR-7	5	140.2	-
GD.TR-8	-	-	-
GD.TR-9	5	123.4	1755.0
GD.TR-10	5	86.7	2025.8
GD.TR-11	5	138.6	-
Mean	-	131.8	2167.5
St. Dev.	-	23.5	338.8

A first sight at Table 2 reveals an extremely high value of Young's modulus (2167 GPa), but it is to remark that this value is associated with the strain of the different pieces of the jointed specimen instead of the deformation of the specimen as a whole. Therefore, this extremely high value of Young's modulus is showing the localization of the strain on the already existing joints instead of the strain of the rock. Figure 6 shows an example of a stress-strain curve of a jointed specimen using the same procedure as for the intact specimens. Please consider that the intact specimen attained an axial strain of about 2000-2500 $\mu\text{str.}$, while the recorded strains on the jointed specimens using the strain gauges are in the order of around 80-150 $\mu\text{str.}$

Another interesting observation can be performed on Figure 6, the axial and radial strain are on the same values range, so the Poisson's ratio would give values near 1, which is not possible according to elastic theory (Ortiz-Berrocal, 1998). Both the extremely high value of Young's modulus and the out-of-range values of Poisson's ratio, make clear that the deformation of the specimen at this lab scale does occur on the discontinuities, while the strain of the pieces of intact rock is negligible.

In order to compare strength results of intact and jointed specimens, Hoek-Brown failure criterion for intact rock (Hoek et al., 2002) was estimated according to UCS test results and recommended values of m_i parameter for a granite (Rocscience, 2015), and the corresponding strength value under a minimum principal stress of 5 MPa was obtained.

180 MPa is the estimated strength value of the intact specimens under a confinement of 5 MPa, which, compared to the 132 MPa of the jointed specimens, means a reduction in strength of about 27% for the jointed specimens. This is in accordance with other studies of the authors in the topic (Arzua, 2015) where the reduction in strength obtained for another granite and the same confinement was about 29%. Therefore, as expected, the presence of discontinuities has a relevant effect on the peak strength of rocks.

That same study (Arzua, 2015) also reported Young's modulus of jointed specimens, but, in that case, the strains were recorded using LVDT's and measuring the strain of the specimen as a whole. Therefore, the reported Young's modulus of the granite jointed specimens (17.5 GPa) is not comparable to the obtained Young's modulus on the current study. For this study we did not have available any other device for measuring strains of the jointed specimens during testing, so

we are working now on implementing LVDT's on the equipment in order to record the strain of the whole specimen.

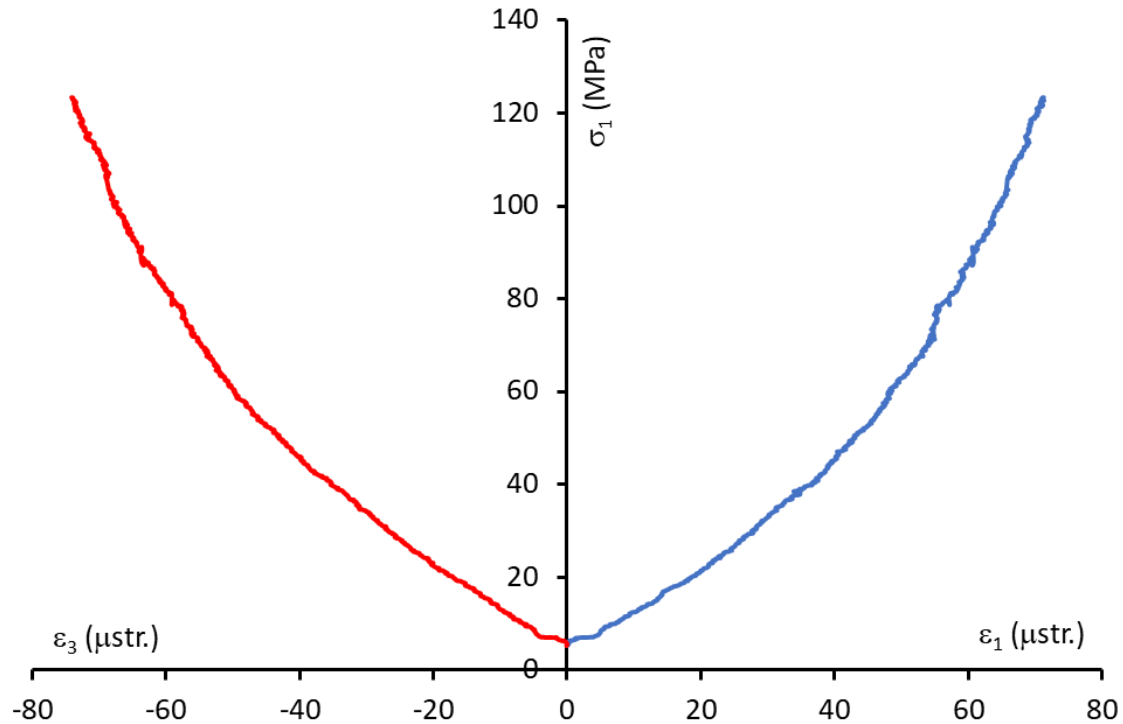


Figure 6. Stress-strain curve for the GD.TR-9 jointed specimen

5 CONCLUSIONS

This study was intended to test equipment capabilities of the Laboratory of Rock Mechanics of the Department of Metallurgical and Mining Engineering of the Universidad Católica del Norte, in Antofagasta, Chile. Despite the evident limitations, such as the inability to attain post-peak stage, or the limited strain measurement capabilities, we were able to create “small scale rock masses” and test their strength and deformability up to failure.

The results show that the strain of the jointed specimens localize on pre-existing discontinuities, and that the pieces of rock does not seem to attain any significant deformation. It was also obtained the notable reduction of strength when there are discontinuities on the specimen, as obtained in other studies. If these results are confirmed at larger scales, the discrete modelling of discontinuous rock masses considering rigid blocks may be valid.

6 ACKNOWLEDGEMENTS

The authors would like to thank Universidad Católica del Norte and ANID for partially funding this study by means of project VRIDT-UCN19101 and Fondecyt Iniciación n° 11190065.

7 REFERENCES

Alejano, L.R., Arzua, J., Bozorgzadeh, N., Harrison, J.P. 2017. Triaxial strength and deformability of in-

- tact and increasingly jointed granite samples. *International Journal of Rock Mechanics and Mining Sciences* 95, 87-103.
- Arzua, J., Alejano, L.R., Walton, G. 2014. Strength and dilation of jointed granite specimens in servo-controlled triaxial tests. *International Journal of Rock Mechanics and Mining Sciences* 69, 93-104.
- Arzua, J. 2015. *Study of the mechanical behavior of intact and jointed rocks in laboratory with particular emphasis on dilatancy*. Ph.D. Thesis, Universidade de Vigo, España.
- Cai, M., Kaiser, P. K., Uno, H., Tasaka, Y., & Minami, M. 2004. Estimation of rock mass deformation modulus and strength of jointed hard rock masses using the GSI system. *International Journal of Rock Mechanics and Mining Sciences* 41(1): 3-19.
- Hoek, E. 1994. Strength of rock and rock masses. *ISRM News Journal* 2:4-16.
- Hoek, E., Kaiser, P.K., Bawden, W.F. 1995. *Support of underground excavations in hard rock*. Balkema, Rotterdam.
- Hoek, E., Brown, E.T. 1980 *Underground excavations in rock*. Institution of Mining and Metallurgy, London.
- Hoek, E., Brown, E.T. 199). Practical estimates of rock mass strength. *International Journal of Rock Mechanics and Mining Sciences* 34:1165-11186.
- Hoek, E., Carranza-Torres, C., & Corkum, B. 2002. Hoek-Brown failure criterion-2002 edition. *Proceedings of NARMS-Tac*, 1(1): 267-273.
- Hoek, E. 2007. *Practical rock engineering*. Available at <https://bit.ly/3OMaCPW>. Accessed on June 27th 2022.
- ISRM. 2007. *The complete ISRM suggested methods for rock characterization, testing and monitoring: 1974–2006*. Prepared by the commission on testing methods, ISRM. Ankara, Turkey: Ulusay R, Hudson JA.
- Masoumi, H., Saydam, S., Hagan, P.C. 2016. Unified size-effect law for intact rock. *International Journal of Geomechanics* 16(2), 04015059
- Ortiz-Berrocal, L. 1998. *Elasticidad, 3rd Ed.* McGraw-Hill/Interamericana de España, Madrid.
- Quiñones, J., Arzua, J., Alejano, L.R., Garcia-Bastante, F., Mas Ivars, D., Walton, G. 2017. Analysis of size effects on the geomechanical parameters of intact granite samples under unconfined conditions. *Acta Geotechnica* 12(6), 1229-1242.
- Rocscience. 2015. *RocLab User's Guide*. Rocscience Inc. Toronto, Canada
- Stagg, K.G., Zienkiewicz, O.C. 1968. *Rock mechanics in engineering practice*. Wiley, London
- Wang, S., Oh, J., Masoumi, H., Zhang, S. 2020. *Scale-size and structural effects on rock materials*. Elsevier, Duxford UK

Assessment of Effect of Anisotropy On Failure Mode and Shear Parameters of Chamoli Rock Using Triaxial System

Dinesh Jaganiya

P.G. Student, Dept. of Applied Mechanics, L D College of Engineering, dineshjaganiya0707@gmail.com

Dr. Manish Shah

Asst. Prof, Dept. of Applied Mechanics, L D College of Engineering, drmvshah@ldce.ac.in

ABSTRACT:

The Chamoli district of Uttarakhand (India) due to its spiritual significance attracts more and more people every year which demands rapid development of infrastructure in terms of highways, railways, tunnels, hydropower, and tourism facilities. Chamoli region has been witnessing heavy landslides/rockslides for the last many years and the frequency of such disasters is rapidly increasing drawing major loss of human lives and the economy. The objective of this research paper is to examine the effect of natural foliation and the anisotropic behavior of metamorphic rock (Chamoli, Uttarakhand) on shear characteristics and failure patterns through different orientation angles of natural schistosity using an automated triaxial system. Further, the effect on dynamic properties of the natural foliation of rock using ultrasonic pulses velocity test based on longitudinal and shear wave velocity is estimated using co-relations. A cylindrical specimen of diameter 50mm and length of 100mm is cored from collected chunk at different orientation angles of natural schistosity (0°, 15°, 30°, 45°, 60°, 75° and 90°). The strength of the different anisotropic rocks was estimated using the Mohr-Coulomb strength theory (1900) and modified Hoek-Brown strength theory (2016). Simulation of foliation at different degrees reveals how the failure planes propagate under natural formations and the effect of bonding under confining pressures.

Keyword: - Chamoli rock · Metamorphic rocks · Anisotropic rocks · Modulus Anisotropy · Shear fracture · Triaxial system

1 INTRODUCTION

Himalaya, the youngest and tallest mountain ranges, forming the extra-peninsular and Indo-Gangetic part of the Indian subcontinent, has attracted people since times immemorial and has spiritual significance. The Chamoli, Uttarakhand area under investigation is one such part of the Lesser Himalaya which still evidences a number of natural landslide/rockslide records and had undergone many unsolved problems. Then some researchers worked on, (Oldham 1883, 1888; Middlemiss 1885, 1887) mapping of the Kumaun-Garhwal Lesser Himalaya and described its geology. The rocks of the Kumaun and Garhwal Lesser Himalaya have been subjected to repeated phases of tectonic movements (Auden 1937; Gairola 1975; Kumar and Agarwal 1975; Gairola and Srivastava 1982) which has resulted in a very complex geology. The rocks type (D. H. Shugar et al. 2021) of the Chamoli region which is high to medium metamorphic rock (gneiss & schist) contain abundant of soft, platy, oriented minerals and weathering will further weaken these rocks. So the rocks have anisotropic behaviour due to these factors.

In spite of many attempts made in the past to describe the engineering performance of transversely anisotropic rocks still their nature is not adequately understood. The oriented structures within the rock matrix such as schistosity, foliation, lamination and/or cleavage are responsible for anisotropic behaviour of rocks (Goodman 1989; Singh et al. 1989; Ramamurthy 1993; Nasser et al. 2003; Esamaldeen et al. 2014). For rocks with an anisotropic structure, their properties change and vary with different directions of loading (Agliardi et al. 2014) like mechanical,

hydraulic and/or seismic properties. The mechanical behaviour of anisotropic rocks including the strength and deformation properties, as well as failure patterns of the rocks, has been studied by many researchers (Ramamurthy 1993; Nasseri et al. 2003; Ghazvinian et al. 2012; Basu et al. 2013; Esamaldeen et al. 2014; Plinninger and Alber 2015; Singh et al. 2015; Usol'tseva et al. 2017; Yin and Yang 2018). The natural foliation knowledge is must required. Because the stability of the slope can be reduced in case of the unfavorable orientation of the planes of weakness compared to the attitude of the slope.

The anisotropic strength behaviour of the rocks can be characterized according to the classification suggested by Ramamurthy (1993). He classified three different curves of strength anisotropy based on strength [MPa] and the anisotropy angle α [°], called “shoulder shaped”, “U-shaped” and “wavy shaped” anisotropy as illustrated in figure 1. Also, The Young’s modulus, i.e. the modulus of elasticity E [GPa] is one of the most important parameters that characterize the elastic deformability of rocks. The anisotropic deformation behaviour of rocks can be characterized according to Nasseri et al. (2003). They specified and named two different types of curves of modulus anisotropy to reflect the relationship between the values of Young’s modulus E [GPa] and the anisotropy angle α [°]: “U-shaped” and “decreasing order-shaped” curves.

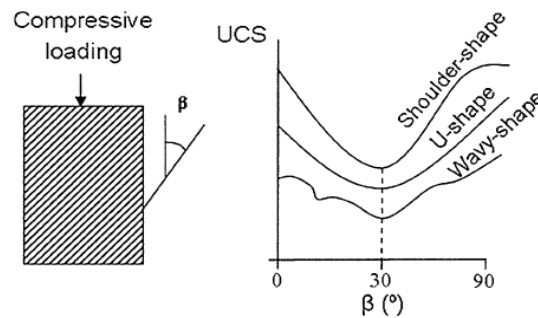


Figure 1. Curves of strength anisotropy according to Ramamurthy (1993)

Due to the restricted knowledge of the deformational and strength of the rock in the Chamoli region, the prime focus of this research paper is (i) To study the anisotropic behaviour of Chamoli rock in terms of compressive strength and deformational responses in triaxial compression at various confining pressures. (ii) To evaluate the failure mechanisms of Chamoli rock with foliation and discuss the importance of the effect that the orientation of the planes of weakness has on the failure of the tested rock using a triaxial system. (iii) To compare the experimental and predicted strength using modified Hoek-Brown theory.

2 ROCK MATERIAL AND EXPERIMENTAL TECHNIQUE

2.1 Sampling Location and Lithology

Keeping the objective in view large block samples of rock were collected from the recently rock sliding place of Chamoli, Uttarakhand (India) for laboratory investigation. Macroscopically, the rocks exhibit a distinct planar systematic-metamorphic fabric that characterized with near perfect metamorphic layering and mineral elongation (schistosity) and stretching lineation. The foliation band varies in thickness ranging from 1 to 3 mm.

2.2 Sampling Location and Lithology

The collected rock blocks were trimmed with their sides perpendicular to each other to facilitate coring at different angles. The schematic of coring direction in relation to weakness plane is shown in Figure 2. For the current study, forty-two cylindrical specimens as per conformation IS: 9179 (1979) of length to diameter ratio equal to 2 at different orientation of anisotropy planes β ($0^\circ, 15^\circ, 30^\circ, 45^\circ, 60^\circ, 75^\circ$ and 90°) were cored for dynamic and triaxial compressive tests as shown in Figure 3. The vertical deviation was <0.001 radian (3.5 minutes) or 0.05 mm in 45 mm diameter specimen. The Triaxial tests were conducted on different orientation specimen of rock angle at confining pressures (σ_3) of 1, 2, and 3 MPa as per the IS 13047 (1991) testing outlined. The first subjected to hydraulic stress to be applied then the axial stress was increased until the specimen failed. This test gives a stress-strain curve based on that calculates young's modulus E [MPa].

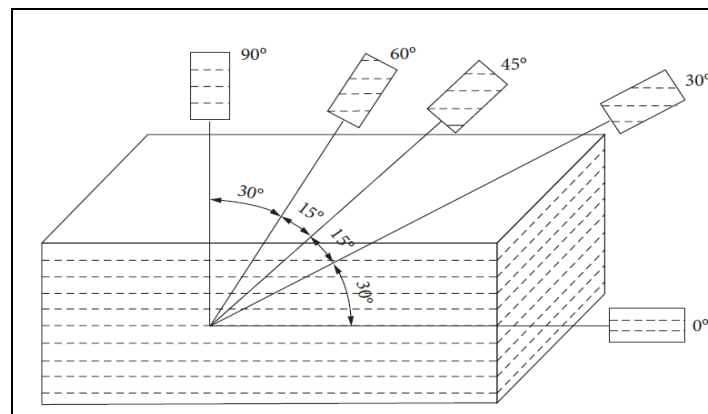


Figure 2. Schematic illustration of rock sample preparation

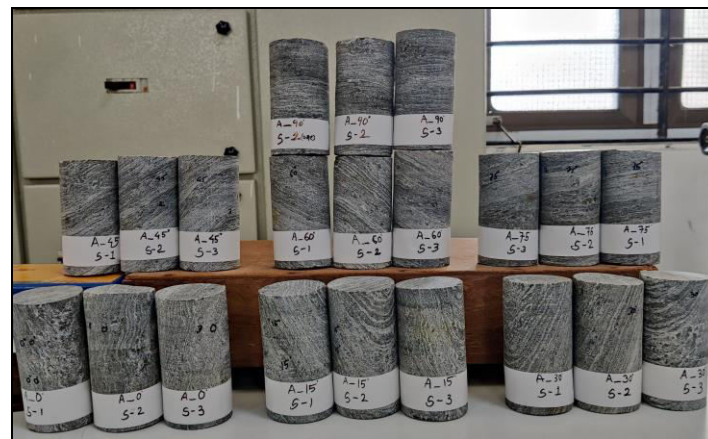


Figure 3. Specimens prepared at various anisotropic angles(β°)

2.3 Petrographic Description of Rocks

The main step towards obtaining a good relationship is to carry out an effective study of the petrographic(chemical) features of the rocks. Thus, to evaluate the Petro-fabric of the studied rocks, thin sections across and along the schistosity were prepared and observed under a high-power polarized microscope. The mineral composition verities of subtype samples of collected rock were determined by the X-ray diffraction method (XRD) as shown in Figure 4. The XRD analysis of selected rock samples was performed based on the microscopic textural variation of Chamoli rocks. The predominant mineralogical composition is almost calcite, quartz, and

Si₁₄O₂₈. The main microstructure of these rocks is well-developed alternative layers of calcite and quartz characterized by a higher degree of texture anisotropy.

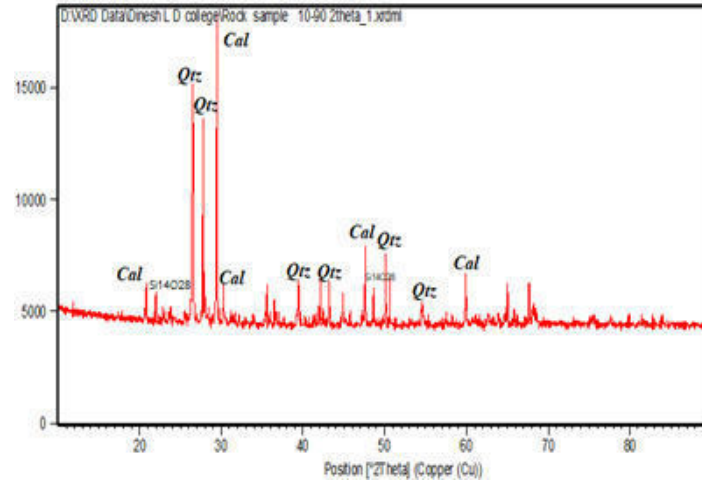


Figure 4. XRD Analysis of Chamoli Rock

2.4 Physical, Mechanical, and Dynamic Properties

Physical properties are determined/identification of the rock as per conformed IS 13030 (1991). Physical properties like density, water content, and porosity are given in Table 1. as per the standard range of physical properties tested rock fall in metamorphic type rock.

The velocities of ultrasonic waves (compression waves) V_p (km/h) were measured along the core axes for each core sample with reference to the foliation angle. P-waves were determined as per the IS 13311-1 (1992) standard. Table 1. Summarizes the ultrasonic waves velocity measurements on the core samples where an average of 3 sample results was determined.

Table 1. Physical, mechanical, and dynamic properties of the rock.

PROPERTIES	GROUP 0°	GROUP 15°	GROUP 30°	GROUP 45°	GROUP 60°	GROUP 75°	GROUP 90°
γ [Kg/m ³]	2883.41	2853.28	2837.58	2835.19	2803.04	2941.92	2824.04
Porosity[%]	0.54	0.32	0.34	0.24	0.44	0.43	0.29
V_p [m/s]	5365.67	5254	4976	4809	4005.33	3656.33	4856.33
V_s [m/s]	2958.14	2844.16	2775.69	2446.18	2303.09	2795.09	2958.14
UCS[MPa]	39.745	41.783	38.783	35.159	40.764	43.822	46.879
E_{stat} [GPa]	29.29	28.20	23.36	24.97	24.56	28.29	30.38
E_{dyn} [GPa]	66.18	63.32	57.73	54.62	40.34	36.55	55.26
μ_{dyn}	0.272	0.268	0.257	0.250	0.203	0.171	0.252
G_{dyn} [GPa]	26.02	24.97	22.96	21.84	16.77	15.60	22.06
K_{dyn} [GPa]	48.32	45.47	39.66	36.44	22.60	18.52	37.18

3 THEORY

3.1 Mohr-Coulomb Strength Criterion (1900)

The linear M-C failure criterion was proposed by Coulomb in 1773. He suggested that developed shear stress is related to the angle of internal friction, cohesion and the applied normal stress (Eq. 1). Mohr proposed that shear failure takes place across a plane where shear stress is a function of normal stress.

$$\tau = C + \sigma_n \tan \Phi \quad (1)$$

Where, τ = Shear stress, c = Cohesion, σ_n = Normal stress, and a positive value is considered to be compressive, Φ = Angle of internal friction.

In terms of major and minor principal stresses, the above (Eq. 2) can be written as

$$\sigma_1 = \sigma_3 + \sigma_c \tan^2 \left(45 + \frac{\Phi}{2} \right) \quad (2)$$

Equations 1 and 2 are both straight lines in the $\tau - \sigma_n$ and $\sigma_1 - \sigma_3$ planes. One of the limitations of the Mohr-Coulomb failure criterion is that it cannot predict the nonlinear response of rock mass. And this criterion may produce incorrect results if the failure mechanism is not shear.

3.2 Modified Hoek-Brown Failure Criteria (2016)

In the present study, the variation of uniaxial compressive strength of intact anisotropic rocks is taken into account. And the parameter α_β (Eq. 3) represents the effect of strength anisotropy is considered in the modified failure criterion.

$$\sigma_1 = \sigma_3 + \sigma_{c\beta} \left(m_i \frac{\sigma_3}{\sigma_{ci}} + 1 \right)^{\alpha_\beta} \quad (3)$$

Where, α_β is the anisotropic index that determines the curvature of the failure envelope, m_i is material constant.

4 EXPERIMENTAL RESULTS AND ANALYSIS

4.1 Velocity Anisotropy

The wave velocities with the angle between the wave propagation direction and the foliation plane relationship are shown in Figure 5. The influence of dynamic properties is summarized in Table 1. The velocities parallel to foliation range from 5217-5517 m/s with a mean of 5365.67 m/s, while 4724-5000 m/s with a mean value of 4856.33 m/s was recorded in a perpendicular direction. The anisotropy degree, the ratio of the maximum to the minimum wave velocity, is equal to 1.47 for the longitudinal wave velocity and 1.30 for the shear wave velocity.

Measuring the longitudinal and shear wave velocities, the dynamic elastic material parameters for anisotropic rock with the help of the following (Eq. 4), (Eq. 5), and (Eq. 6) (Martinez-Martinez et al. 2012) and variation of the following properties with respect to the natural foliation are presented in Table 1.

$$E_{Dyn}(GPa) = \frac{\rho V_S^2 (3V_P^2 - 4V_S^2)}{V_P^2 - V_S^2} \quad (4)$$

$$\mu_{Dyn}(GPa) = \frac{(V_P^2 - 2V_S^2)}{2(V_P^2 - V_S^2)} \quad (5)$$

$$G_{Dyn}(GPa) = \frac{E_{Dyn}}{2(1 + \mu_{Dyn})} \quad (6)$$

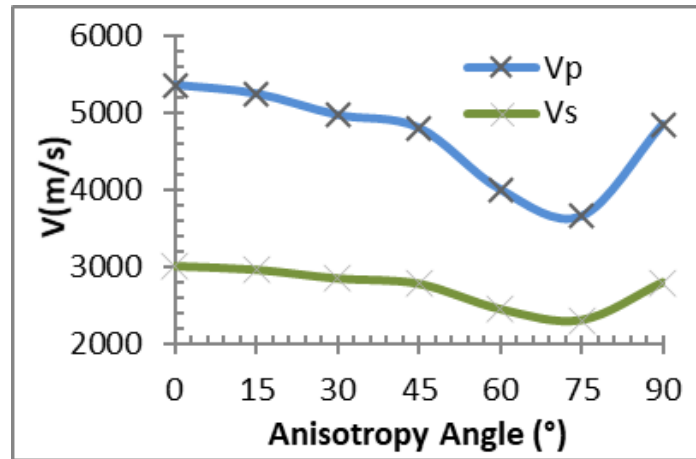


Figure 5. P-wave S-wave velocities with the orientation of the foliation plane

4.2 Strength Anisotropy

Triaxial compressive strength tests were performed at seven anisotropic angles (β) and different confining pressure (σ_3) as suggested by ISRM (2007). The maximum principal stress (σ_1) and axial strain of specimens were recorded during the test of each specimen. The variations of σ_1 with β for tested rock are plotted in Figure 6. In studied rock, with increasing σ_3 , the value of σ_1 is increased. Variation rates of σ_1 at $\beta = 90^\circ$ are greatest in all anisotropy angles. These results are comparable to the results presented by Saroglou et al. (2004a, b) Akai et al. (1970), Goshtasbi et al. (2006), Ramamurthy et al. (1993), and Nasser et al. (2003).

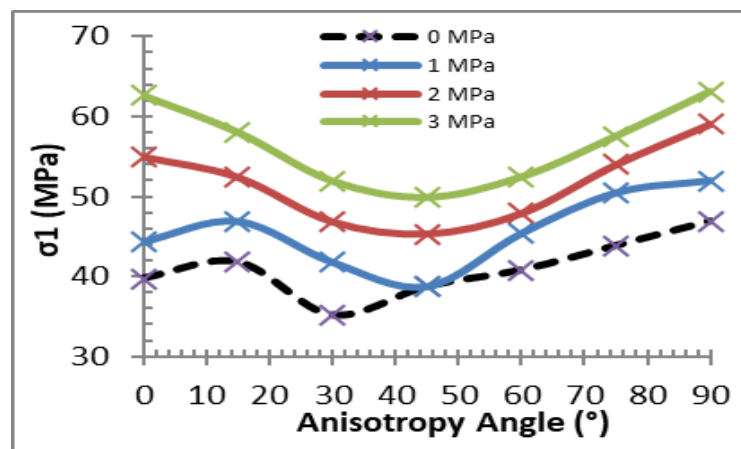


Figure 6. variation of σ_1 and σ_3 with angle β

In unconfined condition ($\sigma_3 = 0$), the minimum values of compressive strength of studied rocks were obtained at $\beta = 90^\circ$. In confined conditions ($\sigma_3 > 0$), the minimum values of compressive strength were obtained at higher anisotropy angles. In other words, by increasing confining pressure, the anisotropy angle corresponding to minimum strength is increased as shown in Figure 6. For example, in the Chamoli rocks, the minimum values of unconfined compressive strength were obtained at $\beta = 30$, whereas the minimum value of confined compressive strength at $\sigma_3 = 3\text{MPa}$ was obtained at $\beta = 45$.

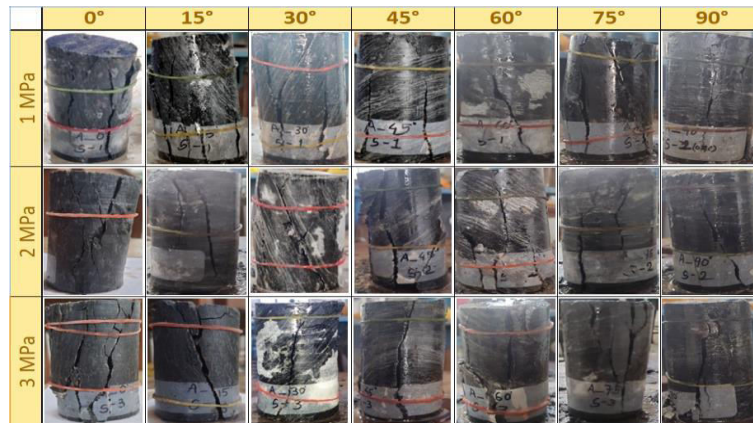


Figure 7. Failure pattern with the orientation of foliation plane

Figure 7 shows the failure patterns of the sample of studied rock after performing the triaxial compressive strength tests at different σ_3 and β as a representative sample. After performing the tests, failure planes in specimens are matched to anisotropy planes at $\beta = 0^\circ, 15^\circ$ and 30° . At $\beta = 60^\circ$ failure planes propagate parallel to anisotropy planes. This failure pattern led to a crushed rock specimen.

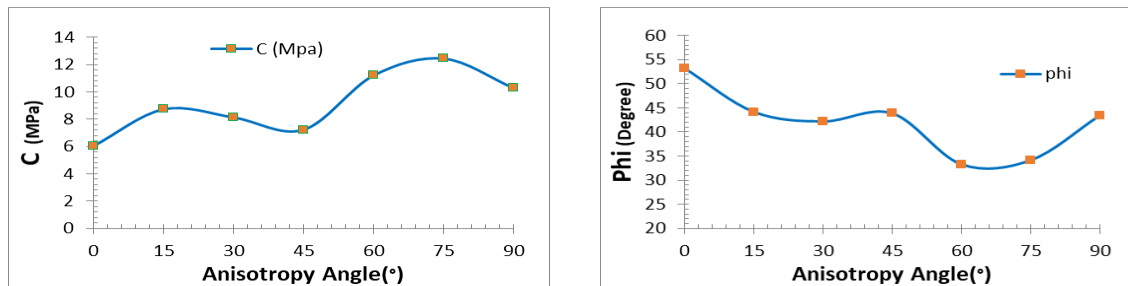


Figure 8. Comparison (c and Φ) and anisotropy angles (β) for samples

In this research, in most tested specimens the ratio of σ_1/σ_3 is higher than one. Thus, at the anisotropy angles of less than 30° , the shear failure pattern of tested rock specimens is affected by anisotropy planes, whereas at the anisotropy angles of more than 45° , the failure pattern of tested rock specimens is usually controlled by the shear failure mechanism in intact rock.

Correlation curves between shear strength parameters (C and Φ) and anisotropy angles (β) are presented in Figure 8. For tested rocks, the maximum values of cohesion and friction angles were obtained at $\beta = 75^\circ$ and $\beta = 0^\circ$, respectively, whereas the minimum values of cohesion and friction angle were obtained at $\beta = 0^\circ$ and $\beta = 60^\circ$, respectively.

4.3 Analysis using modified Hoek-Brown criterion

The natural foliations and their degree of orientation are compared with intact rock and jointed rock samples. The experimental results were compared with the modified Hoek-Brown (2016)

criterion. In this criterion, the effect of anisotropic behavior is considered. The variation of experimental and theoretical major Principal stress is given in Figure 9.

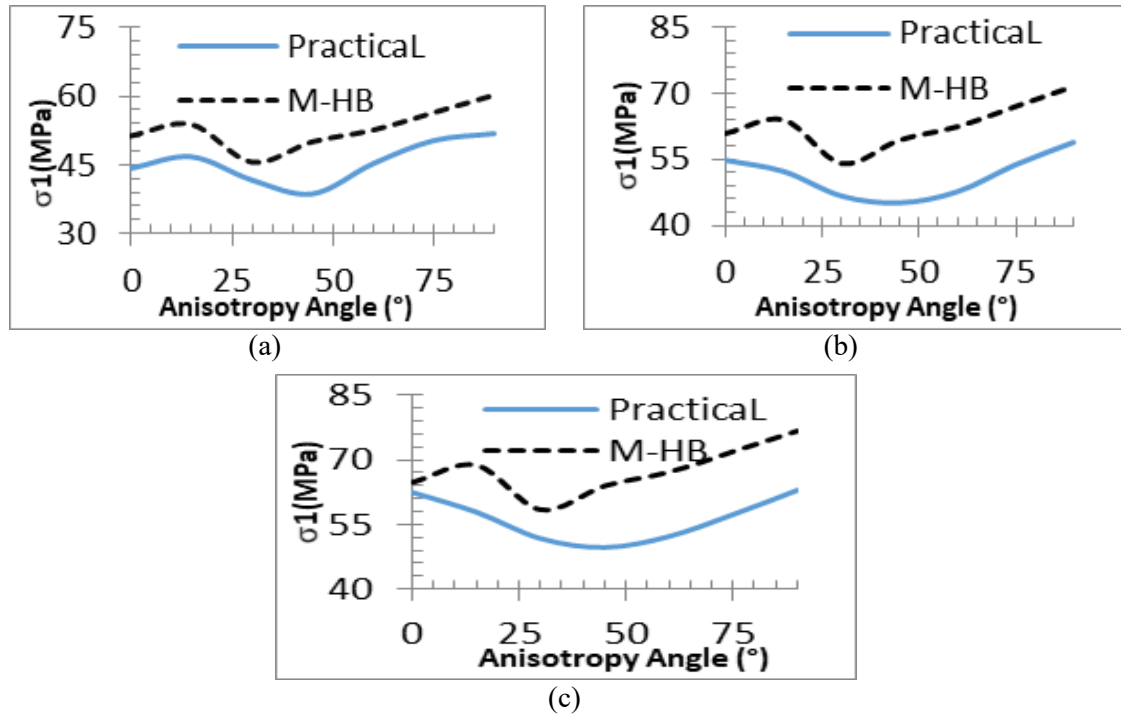


Figure 9. Comparison of experimental and theoretical (σ_1) (a) $\sigma_3 = 1$ MPa (b) $\sigma_3 = 2$ MPa (c) $\sigma_3 = 3$ MPa

5 CONCLUSION

The research study was set out to identify the strength anisotropic and deformation responses of Chamoli rock, Uttarakhand, India, and the following conclusions were drawn:

- For Chamoli rock, when natural foliation plane is increased from 0° to 90° the percentage increment in cohesion (C) with respect to 0° (6.05 MPa) is 44.31%, 34.56%, 19.63%, 85.16%, 105.65% and 70.02% while the percentage decrement in angle of internal friction (Φ) with respect to 0° (53.22°) is 17.03%, 20.79%, 17.62%, 37.59%, 35.95% and 18.39%.
- The Ultrasonic pulse velocity test data indicate the P-wave and S-wave getting high velocity for wave propagating parallel to foliation and significantly lower velocities 75° to it.
- Triaxial test data reveals, the value of Young modulus (E) for confining pressure of 1 MPa varies from 20.26 – 27.34 GPa, for 2 MPa varies from 23.58 – 30.43 GPa and for 3 MPa it varies from 25.39 – 33.86 GPa for different anisotropic angle.
- For Chamoli rock, the dynamic young modulus evaluate from the Ultrasonic pulse velocity test data is 2.26 time higher than static young modulus evaluate from triaxial data.
- The percentage error in experimental and theoretical (MHB) value of major principle stress at 1 MPa varies from 8.08 – 22.50%, at 2 MPa varies from 9.67 – 23.68% and at 3 MPa varies from 3.18 – 21.92%. The percentage error shows that the theoretical value of major principle stress which is calculated by the Modified Hoek-Brown theory is overestimated.
- Failure patterns in tested specimens under confined conditions are matched to anisotropy planes at all anisotropy angles from 0° to 30° . At anisotropy angles from 45° to 90° , failure planes are not matched to the anisotropy planes.

This study confirms that the tested rock shows mechanical anisotropy and the orientation of the foliation that was distinguished inside the rock influences fracture processes in the rock and such type of simulation studies using a rock triaxial system gives a better understanding of rock mass behavior under a range of confining stress both under static and dynamic condition.

ACKNOWLEDGEMENTS

The authors are thankful to Prof. Dr. R. K. Gajjar, Principal, L.D. College of Engineering, Ahmedabad and Dr. C S Sanghvi, Head of Applied Mechanics Department, L.D. College of Engineering for providing all necessary testing facilities for the fulfillment of this research work.

REFERENCES

- Agliardi F, Zanchetta S, Crosta GB (2014) Fabric controls on the brittle failure of folded gneiss and schists. *Tectonophysics* 637:150–162.
- Al-Harathi AA (1998) Effect of planar structures on the anisotropy of Ranyah sandstone, Saudi Arabia. *Eng Geol* 50: 49–57
- Allirote D, Boehler JP (1970) Evaluation of mechanical properties of a stratified rock under confining pressure. *Proceedings of the fourth congress on. I.S.R.M., Montreux, vol 1, pp 15–22*
- Auden., J.B., 1937. Structure of the Himalaya in Garhwal., *Rec. Geol. Surv. India.*, 71, v. 4, pp. 407-433.
- Barla G (1974) Rock Anisotropy, Theory and laboratory Testing. In: Muller L (ed) *Rock mechanics*. Springer, New York, pp 131–169
- Basu A, Mishra DA, Roy Chowdhury K (2013) Rock failure modes under uniaxial compression, Brazilian and point load tests. *Bull Eng Geol Environ* 72:457–475.
- Chen CS, Hsu SC (2001) Measurement of indirect tensile strength of anisotropic rocks by the ring test. *Rock Mech Rock Eng* 34(4):293–321
- Colak K, Unlu T (2004) Effect of transverse anisotropy on the Hoek–Brown strength parameter ‘mi’ for intact rocks. *Int J Rock Mech Min Sci* 41:1045–1052
- Cvetkovic SM (1993) Static and dynamic properties of gneiss as a function of foliation. In: Anagnostopoulos et al. (eds) *Geotechnical engineering of hard soils–soft rocks, vol 1, pp 63–67*
- Esamaldeen A, Wu G, Zhao Z, Jiang W (2014) Assessments of strength anisotropy and deformation behaviour of banded amphibolites rocks. *Geotech Geol Eng* 32:429–438.
- Gairola, V.K., 1975. On the petrology and structure of the Central Crystallines of the Garhwal Himalaya. *Him. Geol.*, v. 5, pp.455-468.
- Gairola, V.K., and Srivastava, H.B., 1982. Structure and deformation history of a part of Dudhatoli Synform around Srinagar, District Pauri Garhwal, U.P. *Mitt. Geol. Ist. ETH Zurich, Neue Folge*, 239a, pp. 106-108.
- Ghazvinian A, Geranmayeh Vaneghi R, Hadei MR (2012) Behavior and failure mechanism of angoran schists under uniaxial compression loading. In: *Rock Engineering and technology for sustainable underground construction. EUROCK 2012—ISRM International Symposium*.
- Goshtasbi K, Ahmadi M, Seydi J (2006) Anisotropic strength behavior of slates in the Sirjan-Sanandaj Zone. *J S Afr Inst Min Metall* 106(1):71–76
- Goodman RE (1989) *Introduction to rock mechanics*, 2nd an. Wiley, Hoboken, pp 179–220
- Horino FG, Ellickson ML (1970) A method of estimating strength of rock containing planes of weakness. *USBM Rep. Inv. 7449*, 26 pp
- Karakul H, Ulusay R, Isik NS (2010) Empirical models and numerical analysis for assessing strength anisotropy based on block punch index and uniaxial compression tests. *Int J Rock Mech Min Sci* 47(4):657–665
- Kern H, Popp T, Gorbatshevich F, Zharikov A, Lobanov KV, Smirnov YuP (2001) Pressure and temperature dependence of V_p and V_s in rocks from the superdeep well and from surface analogues at Kola and the nature of velocity anisotropy. *Tectonophysics* 338:113–134
- Kumar, G., and Agarwal, N.C., 1975. Geology of the Srinagar- Rudraprayag area (Alaknanda Valley), Chamoli, Garhwal and Tehri-Garhwal District, Kumaun Himalaya, U.P., *Him. Geol.*, v. 5, pp. 29-59.

- Middlemess, C.S., 1885. A fossiliferous series in the Lower Himalaya in Garhwal. *Rec. Geol. Surv. India*. v. 18, pp. 73-77.
- Middlemess, C.S., 1887. Crystallines and metamorphic rocks of the Lower Himalaya, Garhwal and Kumaun., *Rec. Geol. Surv. Indian*, v. 20(3), pp. 134-143.
- Nasseri MHB, Rao KS, Ramamurthy T (2003) Anisotropic strength and deformational behaviour of Himalayan schists. *Int J Rock Mech Min Sci* 40:3–23.
- Oldham, R.D., 1883. Note on geology of Jaunsar and the Lower Himalaya. *Rec. Geol. Surv. India*, v. 16(4), pp. 193-198
- Oldham, R.D., 1888. Some notes on the geology of northwest Himalayas. *Rec. G.S.I.*, v. 12, pp. 149-167.
- Omid S, Rashid GV, Vamegh R, Raouf G (2013) A modified empirical criterion for strength of transversely anisotropic rocks with metamorphic origin. *Bull Eng Geol Environ*.
- Plinninger RJ, Alber M (2015) Assessment of intact rock strength in anisotropic rock—Theory, experiences, and implications on-site investigations. In: Schubert W (ed) *Proceedings of the ISRM*
- Ramamurthy T (1993) Strength modulus response of anisotropic rocks. In: Hudson JA (ed) *Compressive rock engineering 1*. Pergamon, Oxford, pp 313–329
- Singh M, Samadhiya NK, Kumar A, Kumar V, Singh B (2015) A nonlinear criterion for triaxial strength of inherently anisotropic rocks. *Rock Mech Rock Eng* 48:1387–1405.
- Singh J, Ramamurthy T, Venkatappa RG (1989) Strength anisotropies in rocks. *Ind Geotech J* 19:147–166
- Srivastava, H.B., Thomas, T., and Tripathi, R.N., 2003. A petrographically approach to strain estimation in deformed rocks; example from granitic gneisses of a part of Almora Synform Garhwal Lesser Himalaya. *Mem. Geol. Soc. India*, v. 52, pp. 427-446.
- Usol'tseva O, Tsoi P, Semenov V (2017) The influence of anisotropy angle on the strength and deformation properties of artificial geomaterials and rocks. *Procedia Eng* 191:512–519.
- Yin P-F, Yang S-Q (2018) Experimental investigation of the strength and failure behaviour of layered sandstone under uniaxial compression and Brazilian testing. *Acta Geophysics* 66:585–605.

Investigation of desiccation cracking of clay-rock by Heaviside-based digital image correlation

S. Hedan, S. Tormos, R. Giot & Ph. Cosenza

University of Poitiers (ENSI Poitiers), CNRS, UMR 7285 IC2MP- HydrASA, Poitiers, France

ABSTRACT:

The Heaviside-based digital image correlation (H-DIC) method, a new technique capable of accurately investigating the kinematics of cracks (displacement, opening/closure, sliding) was used on a cubic sample of clay rock taken from the Meuse/Haute-Marne Underground Research Laboratory (URL) at Bure (France). This sample was subjected to a controlled thermal loading (25°C-90°C) and a controlled hygrometry (62% relative humidity).

The results obtained confirmed that (a) the dominant mode of opening of desiccation cracks is type I (i.e., opening/closing is dominant over sliding) and (b) that desiccation cracking occurs parallel to bedding. Our results also illustrate two antagonistic effects from a thermo-hydro-mechanical point of view. On the one hand, the water loss associated with heating contributes to shrink the sample but on the other hand, the heating of the rock contributes to thermally expand the sample.

1 INTRODUCTION

The disposal of nuclear waste in clay rocks is a topic of interest in many industrialized countries. Among the critical issues related to the long-term safety assessment of such geological repositories, the study of the excavation-damaged zone (EDZ) surrounding the galleries is particularly important. The initiation and extension of the EDZ are partly controlled by the hydric state existing in the galleries. As a matter of fact, fractures associated with the desaturation of the argillaceous medium have been observed on gallery fronts in several underground research laboratories.

An experimental investigation has been carried out to provide fundamental insight in deformation mechanisms involved in the desiccation cracking process of clay-rocks. A clay-rock sample taken from the Meuse/Haute-Marne Underground Research Laboratory (URL) at Bure (France) has been submitted to a transient desiccation sequence (drying at fast heating up to 90°C, at constant relative humidity) and the resulting strains and desiccation cracks have been monitored by a new and improved Digital Image Correlation (DIC) procedure (i.e., the Heaviside-based digital image correlation, H-DIC, e.g., Hedan et al., 2018; 2020).

This communication is divided in three parts. After briefly describing the geological setting and sampling, the experimental device and procedure of this study are given in a second part. The results are presented and discussed in the third part of this communication.

2 GEOLOGICAL SETTING AND SAMPLING

The Callovo-Oxfordian (COx) mudstone involved in this study is a clayey formation at the site of the French Meuse/Haute-Marne Underground Research Laboratory (MHM-URL) excavated by the French National Radioactive Waste Management Agency (ANDRA). The thickness of this formation is 130 m and its age 150–160 My, the formation is located 420–550 m below the surface, in the eastern part of the Paris Basin (Andra, 2005). The Callovo-Oxfordian formation contains mainly 25–65 wt.% clay minerals, with 20–42 wt.% carbonates (calcite, dolomite, ankerite) and 15–31 wt.% quartz and feldspars. The most abundant clay minerals include R0-type interstratified illites/smectites (piles of unorderly flakes, 50–70% smectite) in the upper part of the formation (down to a depth of 490m).

The cylindrical core used to make the sample under study was taken at a depth of 24.5 m, from borehole EST60808 (far from the EDZ), and measured 8 cm in diameter and 35 cm in length.

Immediately after the completion of drilling, in order to prevent loss of water and damage, it was stored in confining and sealing cells named T1 cells (the confining effect in a T1 cell is ensured by (a) an axial load of about 0.6MPa obtained by a an axial spring and (b) a radial pressure achieved by an expansive mortar).

3 EXPERIMENTAL PROCEDURE

3.1 *Thermo-hydric loading procedure and experimental set-up*

A cubic centimetric sample (5x5x5 cm³) was prepared by a dry cutting from the cylindrical sample with respect to the transverse isotropy of CO_x formation: its top and bottom faces were parallel to bedding planes. This sample was used to measure local displacements induced by an increase in temperature (from 25 °C to 90 °C) with a thermal slope of 65° C.h⁻¹ at a constant relative humidity value of 62%. This thermo-hydric loading was achieved with an atmospheric test chamber which allowed to record actual values of relative humidity and temperature every 30 seconds. This atmospheric chamber was equipped with a transparent window to monitor, at the same time, a sample surface by an external CMOS camera. The sample surface which displayed bedding planes was monitored each fifteen minutes, with a camera of 1.31 megapixels (1280x1024 pixels) (magnification $\gamma= 0.07 \text{ mm}\cdot\text{pixel}^{-1}$) controlled by an in-house software. A 150 W tungsten lamp spotlight was oriented to illuminate the studied surface.

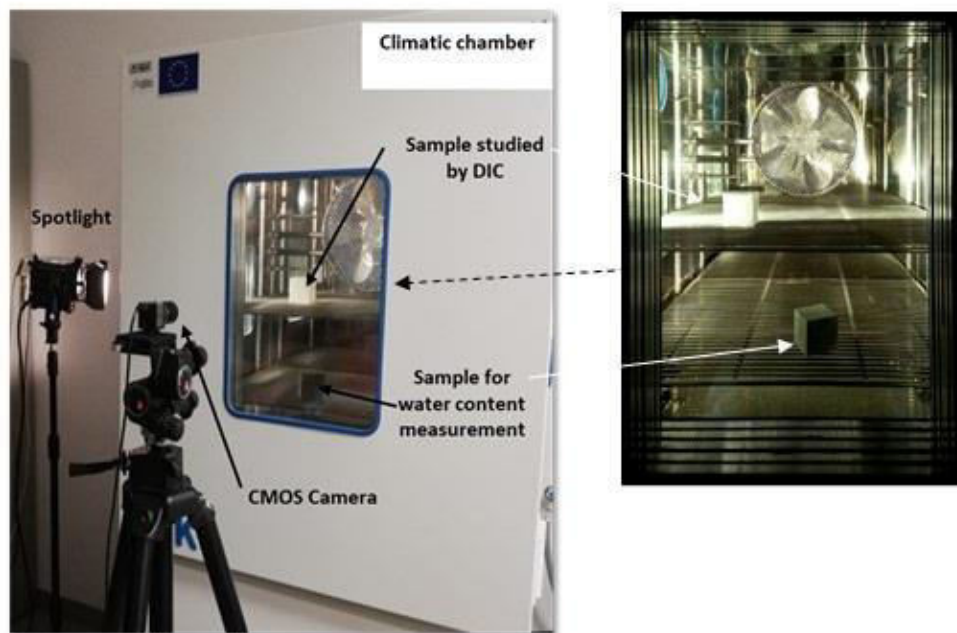


Figure 1. Experimental set-up.

3.2 *Heaviside-based digital image correlation*

Heaviside-based digital image correlation (H-DIC) method (Valle et al., 2014) is an adapted technique based on a local DIC approach to be able to extract cracks using an enrichment of the kinematical transformation used in classical DIC process:

$$\underline{X}^* = \underline{X} + \underline{U} + \frac{\partial \underline{U}}{\partial \underline{X}} \cdot \underline{X} - \underline{U}' \cdot H(\underline{X}) \quad (1)$$

where \underline{X} is the location of the subset in the reference image, \underline{X}^* is the location of the subset in the current state and \underline{U} is an in-plane translation describing the kinematic transformation. The Heaviside function H often called the jump/step function defines the magnitude of the kinematic discontinuity in both the horizontal and the vertical directions associated with the jump vector \underline{U} .

To get displacement and strain fields, H-DIC method similarly to conventional DIC method studies the positional changes of a speckle pattern on the sample surface. The speckle pattern used in this study was an artificial speckle patterns formed of different sizes of sand particles: 125-200 μm and 400-500 μm glued by a spray on the sample surface.

3.3 *Water content measurement*

In addition, measuring the mass of H-DIC sample by an external balance was impossible because the sample position must be fixed in the chamber for using H-DIC method. Therefore, another procedure described in a previous study (Hedan et al., 2012) was used. Another cubic sample, called “mass sample”, taken from the same geological formation and made with similar dimensions was submitted to the same thermo-hydric loading in the chamber (Figure 1). During the test, this second sample was used as a control sample and its water content changes were assumed to be representative of those of the sample studied by H-DIC method. Following this procedure, the door of the climatic chamber was opened which did not modify significantly the measured temperature (T) and relative humidity (RH) in the chamber (see small peaks in figures 4a and 4b). At the end of the test, the “mass sample” has been placed one day at 105°C to measure its dry mass. No modification of the thermo-hydromechanical response of the H-DIC sample was observed during the openings of the chamber door.

4 RESULTS AND DISCUSSION

4.1 *Desiccation crack and aperture mode*

Images taken each 15 minutes were compared to the first initial image (reference image at time t_0). Results were analyzed by using H-DIC algorithm. A minimum of 0.05 pixels was chosen as a threshold to detect local crack opening, with an image magnification of 0.07 mm. pixel⁻¹.

Figures 2a, 2b, 2c and 2d display respectively horizontal displacement, vertical displacement, crack opening displacement (Mode I) and crack sliding displacement (Mode II) obtained after the thermo-hydric loading (drying). These figures show two main features. First, horizontal displacement (figure 2a) and vertical displacement (figure 2b) evidence a clear discontinuity which is associated with a desiccation crack induced by the thermo-hydric loading. This desiccation crack was parallel to the direction of bedding, which is consistent to the results obtained in literature (e.g., Fauchille et al., 2016).

Second, regarding crack opening displacement called hereafter o-component and crack sliding displacement called hereafter s-component (figure 2c and 2d), the white color indicates the solid phase of the sample, while the colored sub-horizontal line delimits the crack location. Color levels give the values of both components i.e., o-component and s-component expressed in millimeter. The small values of s-component in most parts of the crack shows that aperture mode in our case is mainly an opening mode (mode I). This feature is not surprising since the sample was submitted to a free deformation thermo-hydric loading (no embedding condition submitted to the sample).

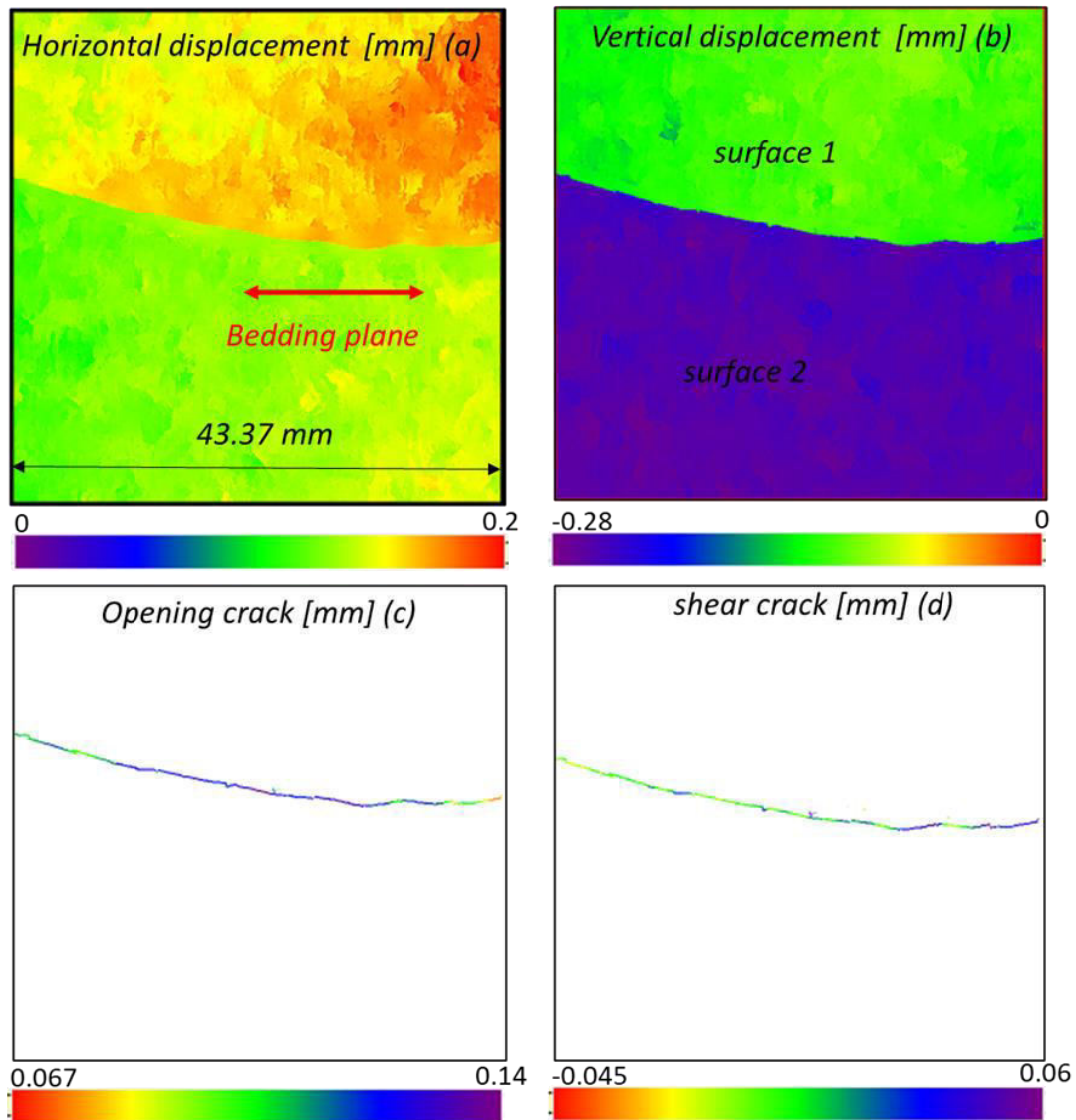


Figure 2. a: horizontal displacement; b: vertical displacement; c: crack opening displacement (o-component) and crack sliding displacement (s-component).

4.2 Calculation of porosity crack and robustness of the H-DIC method

Our results allowed to calculate the following parameters:

- The crack porosity ϕ_{crack} which corresponds to the deformation due to the opening/closure of desiccation cracks:

$$\phi_{crack} = \frac{CA(t)}{area_{ROI}(t_0)} \times 100 \quad (2)$$

with the crack aperture CA(t) given by

$$CA(t) = \sum_{i=0}^N o_i(x, y, t) \cdot \gamma \times l_f(x, y, t) \cdot \gamma$$

where γ is the magnification ($0.07 \text{ mm} \cdot \text{pixel}^{-1}$), $l_f(x, y) = 1 \text{ pixel}$, N is the number of cracked pixels at each deformed state (t) with an aperture of desiccation cracks o_i greater than 0.14 pixels (Hedan et al., 2020). Parameter $area_{ROI}(t_0)$ is the area of the region of interest (ROI) before the thermo-hydric loading (drying) at t_0 and equal to $43.37 \times 43.37 \text{ mm}^2$.

- The bulk strain $\epsilon_{ROI}(t)$ is calculated for each state t , from the locations of the four corners of the region of interest (ROI). This parameter is thus obtained using the equation of the parallelogram forming these four corners.

$$\epsilon_{ROI}(t)[\%] = \frac{area_{ROI}(t) - area_{ROI}(t_0)}{area_{ROI}(t_0)} \times 100 \quad (3)$$

where parameter $area_{ROI}(t)$ is the area of the region of interest at the deformed state (t).

- The parameter ϵ_s , called solid surface strain is the mean strain measured from the derivation (i.e. following a finite differences procedure) of the local displacements measured by H-DIC method. This calculation does not account for the displacements close to the desiccation cracks.

Figure 3 shows that crack porosity correlates well with the difference, $\epsilon_{ROI} - \epsilon_s$, where it is recalled that ϵ_{ROI} is the bulk deformation of the sample measured by four markers present at the four corners of the sample. This bulk deformation ϵ_{ROI} results from the deformation of the solid matrix and the global opening/closing of the desiccation crack. The good agreement obtained between the two parameters crack porosity ϕ_{crack} and difference $\epsilon_{ROI} - \epsilon_s$, both calculated independently, validates the robustness of the analysis method used in this work i.e., the H-DIC approach.

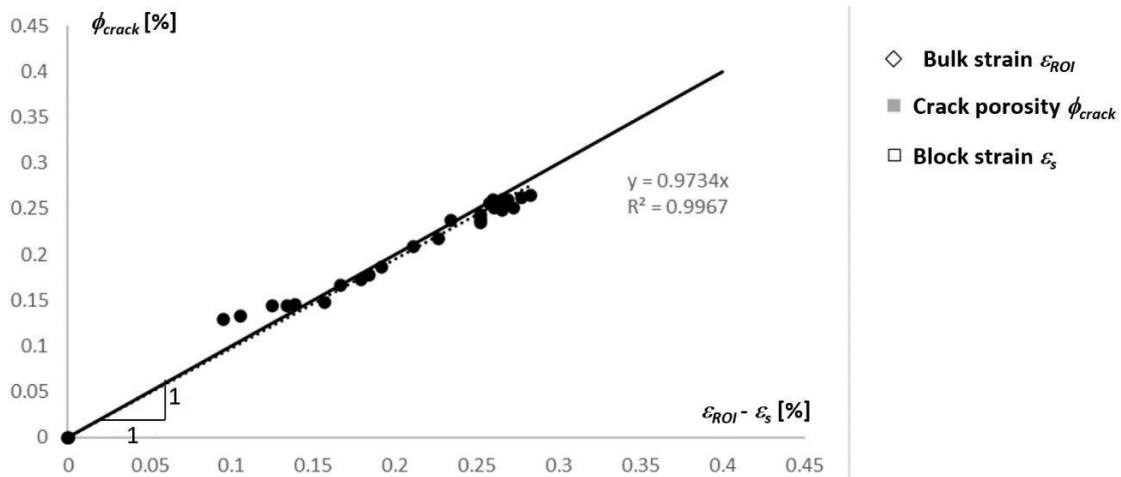


Figure 3. Comparison between ϕ_{crack} and difference $\epsilon_{ROI} - \epsilon_s$.

4.3 Kinematics of the desiccation cracking and thermo-hydric behavior of the sample

Figures 4a, 4b and 4c display the transient evolution of crack porosity, bulk strain ϵ_{ROI} and solid surface strain ϵ_s , respectively.

In the first phase, between the beginning of the test and the time 0.17 days, the sample was subjected to a relative humidity value of 62% and a temperature value of 25°C. During the setting of this equilibrium, the sample lost some water (its water content decreased from 3.2 to 2.7%) and showed small negative deformations of 0.011% (close to the accuracy of the measurement) associated with a contraction (shrinkage) of the sample (Figure 4c).

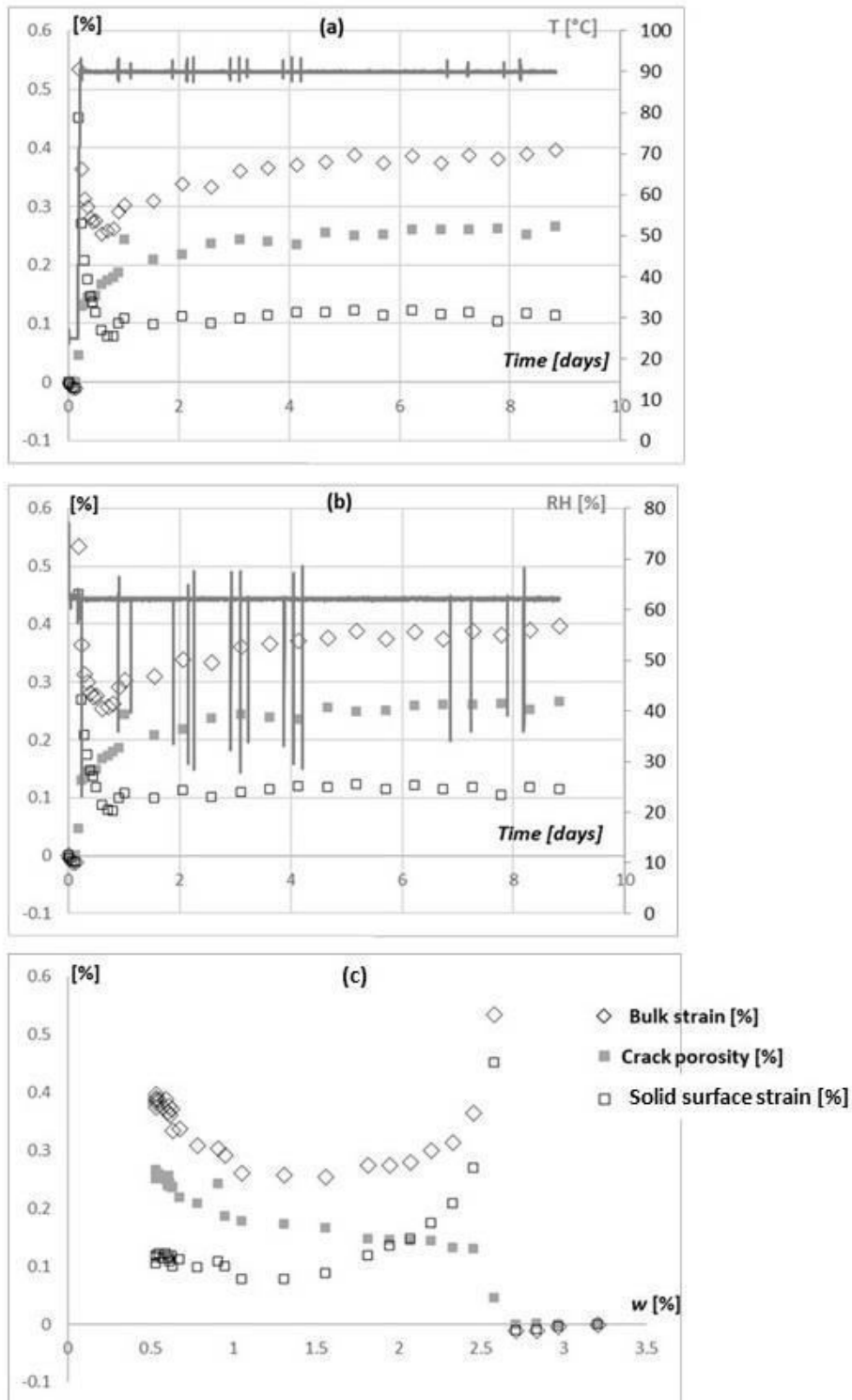


Figure 4. (a) Temperature, bulk strain, solid surface strain and crack porosity as a function of time. (b) Relative humidity, bulk strain, solid surface strain and crack porosity as a function of time. (c) Bulk strain, solid surface strain and crack porosity as a function of water content.

In a second phase, between 0.17 and 0.2 days, after an increase of the chamber temperature from 25°C to 90°C (slope of 65 °C.h⁻¹), the ε_{ROI} and ε_s strains increased rapidly due to the thermal expansion of the material (mineral phases and interstitial water) to reach their maximum value of 0.53 and 0.43 % respectively. Then, ε_{ROI} and ε_s strains started to decrease until the time 0.2 days and in parallel the crack porosity ϕ_{crack} *a contrario* increased. These last two evolutions, i.e., shrinkage of the sample and opening of the desiccation crack, resulted from the sudden loss of water caused by heating at 90°C. After a few dozens of minutes from the beginning of the thermal loading, desiccation cracks were observed parallel to bedding planes.

In a third phase, after 0.2 days and up to 6 days, the bulk strain ε_{ROI} started to increase significantly while the solid surface strain ε_s stabilized in time and the crack porosity continued to increase more slowly. This reversal of the bulk strain evolution results from the competition of two antagonistic effects. On the one hand, the water loss associated with heating contributes to shrink the sample but on the other hand, the heating of the rock contributes to thermally expand the sample. From our experimental results, over the period 0.2-6 days, the thermal expansion of sample dominated over the shrinkage effect associated with water loss.

After about 6 days of test, the sample reached an equilibrium for which the water content, bulk strain, solid surface strain and crack porosity stabilized at the values of 0.6%, 0.4%, 0.11%, 0.25% respectively.

5 CONCLUSION

A new experimental procedure based on the Heaviside-based digital image correlation (H-DIC) method and a climatic chamber specially dimensioned to control a large range of thermo-hydric loadings were used to study the kinematics of a desiccation crack (displacement, opening/closure, sliding) of a cubic sample of clay rock taken from the site of the French Meuse/ Haute-Marne Underground Research Laboratory (MHMURL). This sample was subjected to a controlled thermal loading (25°C-90°C) and a controlled hygrometry (relative humidity of 62%).

After about ten minutes from the beginning of the thermos-hydric loading, desiccation cracks parallel to bedding were generated. Our device allowed to highlight that the deformations were concentrated in two zones around the desiccation crack under study. The results also confirmed that the opening mode is indeed type I (i.e., opening/closing is dominant over sliding). Our results illustrated two antagonistic effects from a thermo-hydro-mechanical point of view. On the one hand, the loss of water associated with heating contributes to shrink the sample but on the other hand, the heating of the rock contributes to thermally expand the sample.

References

- Andra 2005, Dossier 2005 Argile: Synthesis. Evaluation of the feasibility of a geological repository in an argillaceous formation. Andra, France.
- Fauchille AL, Hedan, S, Valle V, Prêt D, Cabrera J. & Cosenza P. 2019. Effect of microstructure on hydric strain in clay rock: A quantitative comparison. *Applied Clay* 182:105244.
- Hedan S, Cosenza P, Valle V, Dudoignon P, Fauchille AL, Cabrera J. 2012. Investigation of the damage induced by desiccation and heating of Tournemire argillite using digital image correlation. *International Journal of Rock Mechanics and Mining Sciences* 51: 64-75.
- Hedan, S., Valle, V., Cabrera, J., & Cosenza, P. 2018. A new approach to quantify the anisotropy of hydro-mechanical strains in clay-rock at the gallery scale. *International Journal of Rock Mechanics and Mining Sciences*, 111, 45-53.
- Hedan S, Valle V, Cosenza P. 2020. Subpixel precision of crack lip movements by Heaviside-based digital image correlation for a mixed-mode fracture. *Strain*. 56 (6):e12346.
- Valle, V, Hedan S, Cosenza P, Fauchille AL, Berdjane M 2014. Digital image correlation development for the study of materials including multiple crossing cracks. *Experimental Mechanics* 55(2):379–391.

Characterization of three potentially high expansive layers belonging to Chenque and Sarmiento geological formations

S. Orlandi

Universidad Nacional de la Patagonia San Juan Bosco (UNPSJB), Argentina

C. B. Laskowski

Universidad Politécnica de Madrid (UPM), España

D. Manzanal

Universidad Politécnica de Madrid (UPM), España

ABSTRACT:

Geological formations containing expansive clay layers have been reported by many authors all around the world. Identifying these layers during geotechnical prospection is important, as a slight change in their moisture content can produce changes in their behavior. Using simple tests such as free swell ratio, free swell index, free swelling, contraction index, superficial area, Atterberg's limits, mineralogy, granulometry using Mastersizer 3000 and DRX, it is possible to characterize and identify the swelling potential of expansive soils. Three potentially high expansive contiguous layers have been associated with numerous pathologies in Comodoro Rivadavia city. These layers, which have been widely studied and characterized, belong to two different geological formations: Sarmiento and Chenque. Sarmiento geological formation belongs to the Paleogene period, and it is formed by tuffs deposited on low slope alluvial plains. Chenque geological formation belongs to the Paleogene and Neogene periods, which are formed by sandstones and claystones with marine fossils. In this paper, properties of the three expansive clay layers, and methods employed to identify their swelling potential are presented.

1 INTRODUCTION

Geological formations constituted by layers of expansive clays are a local problem for Comodoro Rivadavia city, with a high impact on civil constructions. This group of clays has been mentioned in several articles and by several authors. In these articles, the clay's behavior, the study of their properties, and the pathologies caused by them were included (Manzanal et al., 2019).

The first step to adequately design the buildings is to identify these soils in the geotechnical exploration stage. Depending on the type and the magnitude of the civil construction will be the studies carried out in the geotechnical exploration stage. Civil works that discharge lower pressures than those developed by expansive soils may suffer damage if they are not properly designed or if the properties of the soil are not modified.

In the coastal Patagonian city Comodoro Rivadavia, three closes to each other strata, belonging to two different formations, Sarmiento (Spalletti & Mazoni, 1979) and Chenque (Bellosi, 1990) have been identified for having a high to very high expansion potential (Manzanal et al., 2019). The clays of these three strata will be named as CRclay, GAclay and FRclay from now on.

The Sarmiento Formation, the oldest among the studied, is mainly composed of pyroclastic rocks, with lava flows and dikes of basaltic origin within the rock sequence in some places of San Jorge Gulf Basin (Bellosi, 1995). Among these rocks there are chonites, tuffs, and bentonites, with fossils (Bellosi, 1995). The Chenque or Patagonia formation, which origin is marine, is over the Sarmiento formation that is Eocene-Oligocene. This formation is composed by coquinas, a local typical greenish grey sandstone, and tuffaceous sandstones.

The expansive clays belonging to the San Jorge Gulf Basin were deposited in a marine environment, characterized for being sodic alkaline and having a high content of sulphate. The pre-

sented clays in this article are mostly composed by montmorillonite. These soils will be analyzed using easy-to-determine properties such as free swell ratio, free swell index, swelling pressure, contraction index, superficial area, Atterberg's limits, mineralogy, granulometry using Mastersizer 3000 and DRX to characterize and identify their swelling potential.

2 MATERIALS AND METHODS

2.1 *Materials: CRclay, FRclay, and GAclay Paper page limit and Page size and margins*

Samples taken from strata of two different formations (Spalletti & Mazoni, 1979, Bellosi, 1990) were sampled using open pits. The rock samples were hand-crushed in a mortar, and the different fractions to be used were determined according to the specifications of each test. The test was selected to identify the expansion potential of the clay fraction. The particle size and pH results are included in Table 1.

Table 1. Properties of the three selected Patagonian rocks

Sample N°	FRclay	GAclay	CRclay
Textural class	clay	clay	clay
pH 1:2,5	7.53	7.18	8.51
CE [dS/m]	5.83	5.09	10.81
% MO W & B	0.7	0.4	0.6
% CO W y B	0.4	0.2	0.3
P disp [mg/kg]	23	23	11
SO ₄ ⁻ [mg/kg]	12460	11721	3608
Mg [meq/100g]	12.5	11.0	1.5
K [meq/100g]	4.2	5.3	7.8
Na [meq/100g]	23.3	24.8	28.5
CEC	49	54	55

2.2 *Methods*

Non-traditional methods used to assess the expansion potential of CRclay, GAclay, and FRclay allow simple identification of expansive behavior and qualitative classification. In this article some of them are presented.

Free swell ratio and free swell index

The free swell ratio (FSR) and the free swell index (FSI) (IS:1498, Bureau of Indian Standards, Shridharan & Prakash, 2000) are two of these non-traditional methods. The procedure consists of placing two 10g samples of oven-dried material at 110°C passing sieve N°10 in separate 50ml test tubes. One test tube is filled with kerosene (non-polar fluid) and the other one with demineralized water (Fig.1). The ratio between the readings of the material immersed in demineralized water and the material immersed in kerosene is the FSR (Equation 1).

The FSI is calculated as the variation in the volumes taking as a reference the volume obtained for the material immersed in demineralized water (Equation 2). Once these indices are obtained, using Table 2 (FSR) and Table 3 (FSI) it is possible to identify the swelling potential of the material. These two indexes are qualitative.

$$\text{FSR [\%]} = (\text{reading in distilled water}) / (\text{reading in kerosene}) \quad (1)$$

$$\text{FSI} = (\text{Volumen en agua destilada} - \text{Volumen en kerosene}) / (\text{Volumen en kerosene}) \quad (2)$$



Fig.1- FSR and FSI test with FR-clay

Table 2. Swelling potential as function of free swell index (FSR)

FSR	Group of clay	swelling potential	Dominant type of clay mineral
≤1.0	non expansive	insignificant	kaolinite
1.0-1.5	mixture of clays	low	kaolinite and montmorillonite
1.5-2.0	expansive	moderate	montmorillonite
2.0-4.0	expansive	high	montmorillonite
>4.0	expansive	very high	montmorillonite

Table 3. Swelling potential as function of free swell ratio (FSI)

Swelling potential	FSI [%] IS:1498 (1970)
low	<50
medium	50-100
high	100-200
very high	>200



Fig.2. Linear shrinkage limit (LS) test as parameter to identify swelling potential

Linear shrinkage limit

The linear shrinkage limit (LS) is an index property which is less operator-dependent according to the results presented by Cerato and Lutenegeger (2006). It has the same limitation as the contraction limit (LC) determined using mercury: in both methods during the air-drying of the specimens, if cracks are developed, the determinations lose accuracy. In the case of volume measurement with mercury, the high surface tension of mercury prevents it from entering the cracks, overestimating the measured volume (ASTM D427-98). In the case of the linear shrinkage limit, the cracks do not usually go completely through the specimen, so an estimation of the average final length can be made. LS is calculated as the percentage of variation of the length of the sample. Samples are molded according IS:1498, with a liquid limit moisture (ASTM D4318-05).

Table 4- Swelling potential according to the linear shrinkage limit

Swelling potential	LS [%]
	IS:1498 (1970)
Low	<15
Medium	15-30
High	30-60
Very high	>60

Specific surface area

The specific surface area (SE) (Santamarina et al., 2002) determination allows classifying the particles according to their mineralogy. Different clays have different particle shapes, from spherical (kaolinite) to lamellar (montmorillonite) and depending on the particle shape will be the corresponding specific surface area (Table 6). The methods employed to obtain SE are the nitrogen adsorption method (BET), atomic force microscopy (AFM), ethylene glycol monoethyl ether (EGME), and methylene blue end-point method (MBM).

Table 5- Swelling potential according to the liquid limit (Chen, 1956; Snethan et al., 1977; IS:1498, 1970) From Sridharan & Prakash (2016).

Swelling potential	LL [%]		
	Chen (1965)	Snethan et al. (1977)	IS:1498 (1970)
low	<30	<50	20-35
medium	30-40	50-60	35-50
high	40-60	>60	50-70
very high	>60	-	70-90

One of the simplest, cheapest, and fastest methods is the methylene blue end-point method (MBM) described by Santamarina et al. (2002). The specific surface area is calculated by computing the amount of methylene blue cations absorbed by the negative charges distributed on the surface of the clay particles. SE is calculated by determining the number of adsorbed cations because each cation occupies a specific surface area. The way to identify the moment when the methylene ions stop being adsorbed on the surface is when a dispersed halo around a drop placed on a filter paper develops. The droplet is composed of a solution of methylene blue incorporated n times into a solution of distilled water-soil particles. The n is used to determine the

concentration of blue methylene in the solution. In this paper MBM was used to determine primary specific surface.

Consistency limits

The consistency limits were traditionally employed to classify soils, but they can be also used to identify the expansion potential of a soil (Holtz & Gibbs, 1956, Atterberg, 1911, Chen, 1988). Their advantages are that they are widely spread, they require a small sample quantity, and they are easily determined. The method used to determine the liquid limit (LL) is crucial, and the human factor is their main disadvantage (Ballard & Weeks, 1936). The first and most widespread method used to obtain the LL is the Casagrande's apparatus, followed by the penetration cone in all its variants. Several authors have published results comparing the discrepancies obtained using the penetration cone and the Casagrande breaker (Casagrande, 1958, Di Matteo, 2012). In this paper Casagrande's apparatus was employed.

Activity

Skempton (1953) introduced the concept of activity. It is necessary to prepare soil samples with different percentages of particles smaller than 200 μm to estimate the activity. A distribution of the plastic index is plotted in terms of the weight percentage of particles smaller than 200 μm . In this graph, the line's slope is the true activity for most inorganic soils (Mitchell, 1976). The average activity for various clay minerals is presented in Table 7.

Three methods can be employed to determine the particle percentage smaller than 200 μm : hydrometer or Bouyoucos, pipette method, and Mastersizer 3000. The hydrometer or Bouyoucos method assumes some hypothesis that limit the result accuracy, especially in expansive soils. The most important assumption is that the particles are spherical, necessary to apply Stokes' law. A deflocculant is used in this method to break up the clay flocs (ASTM D422-63). Deflocculation is obtained chemically (Calgon, Na hexametaphosphate, HONa, Co_3Na_2 , etc.) and mechanically (by stirring and shaking). As a part of the test preparation, neither organic material nor calcium carbonate is removed. In this paper two methods were used: Bouyoucos and Mastersizer 3000. Once the particle percentage smaller than 200 μm is obtained, the activity can be calculated (Equation 3).

$$A_s = IP / (\text{percentage particle size} < 200 \mu\text{m}) \quad (3)$$

Free swelling

The determination of free swelling using the oedometer method (ASTM D4546-14) can be considered a direct method for evaluating the expansion potential of soil (Holtz & Gibbs, 1956, Sivapullaiah, 1987) (Table 7). The procedure consists of a free expansion test of a specimen diametrically constrained, with strain versus time measurements. The sample is submerged, water has access to both ends, and an initial load of 1kPa is applied. The initial time corresponds to the time in which the cell flooded. The test ends when the axial strain recordings stabilize. Plotting the free expansion curve allows identifying the different stages (Soltani, 2017). These stages are visible in a semi-logarithmic graphic in which the deformation is in the arithmetic axis, and in the logarithmic axis is the time. The three stages are an initial explosive deformation (ES), a second primary deformation (PS), and at the end, a third secondary deformation (SS) (Delage, 2007). The free expansion oedometer results are expressed as a percentage of deformation. This result allows us to classify the tested soil according to its expansion potential (Table 7).

The three selected natural rocks are strongly cracked, so the oedometer test couldn't be performed with original state samples. As a consequence, the tested samples were remolded at dry density and optimum moisture, determined by using the Proctor III test. The diameter-height ratio was 6, compared to the 2,5 recommended by the normative.

Table 7- Swelling potential according to the free swelling

Swelling potential	Free swelling [%]	Swelling potential [-]
	Holtz & Gibbs (1956)	Seed et al. (1964)
low	<10	0 - 1.5
medium	10 - 20	1.5 - 5
high	20 - 30	5 - 25
very high	>30	>25

3 RESULTS AND DISCUSSIONS

The results of LL, plastic limit (LP), clay fraction, SE (Mitchel & Toga, 1986), AS (Skempton, 1953), FSI and FSR (Asuri & Keshavamurthy, 2016, IS:2720), LS (ASTM D427), for each material are in Table 8.

A sequence of photographs of the linear shrinkage test can be seen in Fig. 2. The specimen with the highest linear shrinkage was FRclay with a value of 30%, followed by GAclay with 18% and CRclay with 16%. As it is shown these soils present high to a very high expansion potential characteristics, corresponding to the same order in their liquid limits.

Table 8. Parameters obtained for CRclay, FRclay, and GAclay

Clay	LL [%]	LP [%]	FSI [%]	FSR []	SE []	LS [%]
FRclay	76	40	150	2.5	563	30.1
GAclay	105	40	100	2.0	549	17.7
CRclay	160	46.5	70	1.7	648	15.6

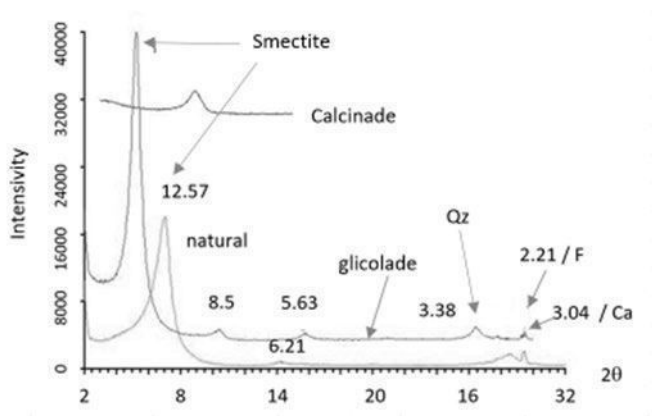


Fig.3- DRX of FRclay

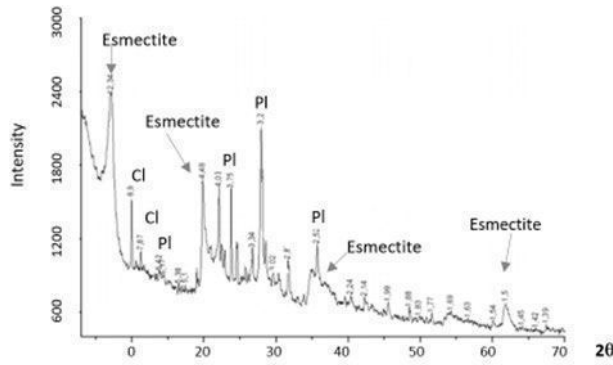


Fig.4- DRX of GAclay

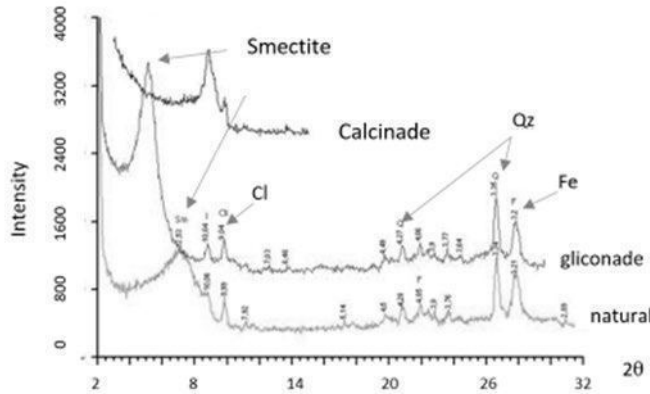


Fig.5- DRX of CRclay

Table 9. Swelling potential for the three clays

Author	property	material		
		CRclay	GAclay	FRclay
Chen (1965)	LL	Very high SP	Very high SP	Very high SP
Snethan et al. (1977)	LL	Very high SP	High SP	Very high SP
IS:1498 (1997)	LL	Very high SP	Very high SP	Very high SP
Holtz & Gibbs (1956)	IP	Very high SP	Very high SP	Very high SP
Chen (1988)	PI	Very high SP	Very high SP	Very high SP
IS:1498 (1970)	PI	Very high SP	Very high SP	Very high SP
Holtz & Gibbs (1956)	LC	Low SP	Very low SP	Low SP
Altmeyer	LC	Noncritical volume change	Marginal volume change	Noncritical volume change
IS:1498 (1977)	IC	Low SP	Low SP	Low SP
Chen (1965)	Clay fraction	Medium SP	High SP	High SP
IS:1498 (1977)	activity	Inactive	Medium SP	Active
Holtz & Gibbs (1956)	Oedometer	Very high SP	Very high SP	Very high SP
Seed (1962)	Oedometer	Very high SP	Very high SP	Very high SP
IS:1498 (1977)	FSI (over 24hs)	Medium SP	Very high SP	Medium SP
IS:1498 (1977)	FSR	Medium SP Dominant clay: montmorillonite	Medium-high SP Dominant clay: montmorillonite	Medium-high SP Dominant clay: montmorillonite

For FRclay, deformation and breakage of the specimen can be observed due to factors such as heterogeneity of the material including the possible concentration of sand or silt particles, differential moisture reduction, and strong shrinkage of the specimen, among others.

By applying different methods in the classification of expansive materials, it is possible to difference the clays according to the qualitative swelling potential (SP). Table 9 shows the classification of the three soils analyzed using the systems proposed by some authors.

Salts, cation exchange capacity and pH correspond to strata of marine origin (Table 1). The Atterberg limits show that the three materials are highly plastic, the surface areas show that the clay fraction is composed by montmorillonite, and the DRX results are coincident with the classification. The three clays are considered to have a high to very high expansion potential according to most of the selected parameters, except for LC (Table 9).

Free swelling tests performed with molded samples show that the three clays have a very high swelling potential, despite them having been molded with a density lower than its natural density (Fig.6).

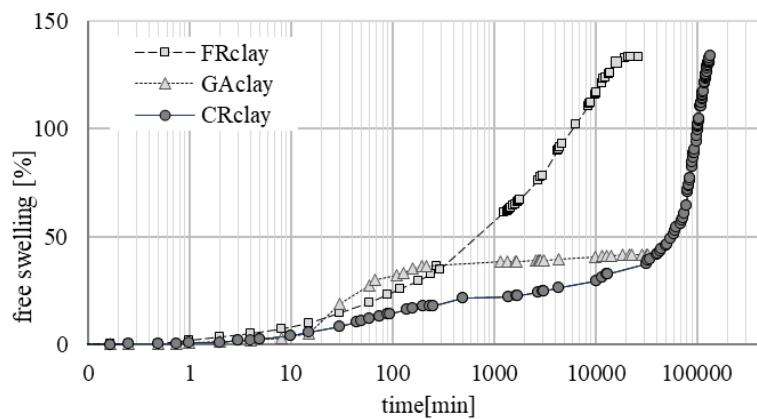


Fig.6- Free swell test

4 CONCLUSIONS

When studying rock materials, it is necessary to identify the presence of expansive clays at the exploration stage. The simple laboratory tests which allow determining clay's expansive potential, also contribute to the decision of including structures compatible with their behavior (Duncan, 1992). Their identification permits the design of drainage systems and foundations that prevent moisture change in the stress bulb or loading affected area.

Several authors developed simple methods that allow a qualitative classification of expansive materials according to the variation of the moisture content. In all of the cases, the mineralogy of the soil dominates its behavior, and the recognition of the clay group by means of the specific surface area (SE) surpasses the DRX test because of its simplicity and low cost. Using simple and low-cost tests, it is possible to prevent damages produced by the action of expansive clays.

The simple and low-cost tests previously mentioned are liquid limit, plastic limit, plastic indexes, superficial area, activity, free swell ratio, free swell index, and free swell test. In this paper they were used to determine the swelling potential in three different rocks composed mostly by clay mineral, over 80% montmorillonite. Linear shrinkage and contraction limit results were opposite to the general tendency, their results classified the volume change as non-critical, and the swelling pressure as low. The other tests showed that the three rocks have expansive properties, and that the swelling potential was very high. The simple tests employed to qualify the swelling potential of these three rocks were useful, simple and coincident in their results.

ACKNOWLEDGEMENT

The authors acknowledge “Consejo Nacional de Investigaciones Científicas y Técnicas (CONICET)”. The authors also acknowledged the financials support of Universidad Nacional de la Patagonia San Juan Bosco (Project UNPSJB SYT PI 1508) and “Secretaría de Políticas Universitarias” (MEYD-SPU) (Project “Agregando Valor 2017 – Fundaciones Sustentables” RESOL-2017-5157-APN-SECPU#ME), and the personal of LISHA (Laboratorio de investigación de Suelos, Hormigones y Asfaltos).

5 REFERENCES

- ASTM D427-98 (2008) Standard test method for shrinkage factors of soils by the mercury method. Book of ASTM Standards, Philadelphia, PA, USA (2008).
- ASTM D4318-05 (2005) Standard Test Method for Liquid Limit, Plastic Limit, and Plasticity Index of Soils.
- ASTM D4546 – 08 (2008) Standard Test Methods for One-Dimensional Swell or Settlement Potential of Cohesive Soils, American Society for Testing and Materials
- Asuri, S., Keshavamurthy, P. (2016) Expansive Soil Characterisation: An Appraisal. *INAEL* 1, 29–33 (2016). <https://doi.org/10.1007/s41403-016-0001-9>.
- Atterberg, A. (1911) Die Plastizität der Tone Internationale Mitteilungen fuer Bodenkunde, pp. 10-43. Atterberg, A. (1911). On the investigation of the physical properties of soil and on the plasticity of clays. *Int. Mitt. für Bodenkunde*, 1, 10–43. https://library.wur.nl/isric/fulltext/isricu_t4eb158d9_001.pdf
- Ballard, G.E.H. & Weeks, W.F. (1963) The human factor in determining the plastic limit of cohesive soil. *Material Research and Standard*, ASTM, Vol 3, pp. 726-729.
- Belloso, E.S. (1990) Formación Chenque: registro de la transgresión patagónica de la Cuenca del Golfo San Jorge. 11° Congreso Geológico Argentino, Actas 2: 57-60. San Juan.
- Belloso, E.S. (1995) Paleogeografía y cambios ambientales de la Patagonia central durante el Terciario medio. *Boletín de Informaciones Petroleras*, 44: 50-83.
- Casagrande, A. (1958) Notes on the Design of the Liquid Limit Device. *Geotechnique*, vol. 8, pp. 84-91
- Cerato, A. & Lutenecker, A. (2002) Determination of Surface Area of Fine-Grained Soils by the Ethylene Glycol Monoethyl Ether (EGME) Method. *Geotechnical Testing Journal* 25, no. 3 (2002): 315-321. <https://doi.org/10.1520/GTJ11087J>
- Chen, F. H. (1965) The use of piers to prevent the uplifting of lightly loaded structure founded on expansive soil. In: *Concluding proceedings engineering effects of moisture change in soils, International Research and Engineering Conference on Expansive Clay Soils*. A&M, Texas, pp 152–171.
- Chen, F. H., (1988) *Foundations on Expansive Soils*, 2nd ed. Elsevier Science Publishers, Amsterdam, the Netherlands, pp 464. ISBN 044460166X, 9780444601667. 295 pp
- Delage, P. (2007) Microstructure Features in the Behaviour of Engineered Barriers for Nuclear Waste Disposal. In: Schanz T. (eds) *Experimental Unsaturated Soil Mechanics*. Springer Proceedings in Physics, vol 112. Springer, Berlin, Heidelberg. https://doi.org/10.1007/3-540-69873-6_2 https://www.researchgate.net/publication/226881442_Microstructure_Features_in_the_Behaviour_of_Engineered_Barriers_for_Nuclear_Waste_Disposal January 2007.
- Di Matteo, L. (2012) Liquid Limit of Low- to Medium-Plasticity Soils: Comparison between Casagrande Cup and Cone Penetrometer Test. *Bulletin of Engineering Geology and Environment*, Vol. 71, pp. 79-85. (2012). DOI: 10.1007/s10064-011-0412-5
- Duncan, C. I. (1992) *Expansive Clay*. In: *Soils and Foundations for Architects and Engineers*. Springer, Boston, MA. https://doi.org/10.1007/978-1-4757-6545-8_11.
- Holtz W., Gibbs H. (1956) Engineering Properties of Expansive Clays. *Journal Article*. *Transactions of the American Society of Civil Engineers*. 641-663. V 121. N 1R doi: 10.1061/TACEAT.0007325. <https://ascelibrary.org/doi/abs/10.1061/TACEAT.0007325>.
- Holtz W., Gibbs H. (1956) Engineering Properties of Expansive Clays. *Journal Article*. *Transactions of the American Society of Civil Engineers*. 641-663. V 121. N 1R doi: 10.1061/TACEAT.0007325. <https://ascelibrary.org/doi/abs/10.1061/TACEAT.0007325>.
- IS: 1498 (1970) (reaffirmed 1987) Indian standard classification and identification of soils for general engineering purposes. BIS, New Delhi.
- IS: 2720 (1977) Part 40, Indian standard methods of test for soils: determination of free swell index of soils. BIS, New Delhi.
- Manzanal, D., Orlandi, S., Barria, J. C. (2019) Swell characterization of expansive clays from Comodoro

- Rivadavia - Argentina. XVI Pan-American Conference on Soil Mechanics and Geotechnical Engineering. Geotechnical Engineering in the XXI Century: Lessons learned and future challenges N. P. López Acosta et al. (Eds.). IOS Press Publisher. 17-20 November 2019. Cancun, México. doi:10.3233/STAL190107.
- Mitchell J. K. & Soga K. (2005) Fundamentals of soil behavior. Wiley, New York, 3rd Edition ISBN: 978-0-471-46302-3 May 2005 592 Pages
- Santamarina, J. C., Klein, K. A., Wang, Y. H., & Prencke, E. (2002) Specific surface: determination and relevance. Canadian Geotechnical Journal, 39(1), 233–241. doi:10.1139/t01-077
- Seed, H. B. , Woodward, R. J. & Lundgren, R. (1964) Fundamental aspects of Atterberg limits. Journal of SMFE Div., ASCE, Nov., pp 75-105
- Sivapullaiah, P., Sitharam, T., Subba Rao, K. (1987) Modified Free Swell Index for Clays. Geotechnical Testing Journal 10, no. 2 (1987): 80-85. <https://doi.org/10.1520/GTJ10936J>
- Skempton, D. (1953) Reprinted from Proc. 3rd Int. Conf. Soil Mech., Zurich, 1953, 1, 57-61 The Colloidal "Activity" of Clays L'Activite colloïdale des argiles by A.W.SKEMPTON, D.SC, A.M.I.C.E., F.G.S., University Reader in Soil Mechanics and Assistant Professor at Imperial College, University of London, England
- Snethan, D.R., Johnson, L.D., Patrick, D.M. (1977) An evaluation of expedient of methodology for identification of potentially expansive soils. In: Soils and Pavements Lab, US Army Eng. Water Way Exp. Station, Vicksburg, MS, Report No. FHWARE-77-94, NTIS PB-289-164. ASCE 88(SM3):53–87
- Soltani, A., Taheri, A., Khatibi, M. et al. (2017) Swelling Potential of a Stabilized Expansive Soil: A Comparative Experimental Study. Geotech Geol Eng 35, 1717–1744. <https://doi.org/10.1007/s10706-017-0204-1>
- Spalletti, L. & Mazzoni, M. (1979) Estratigrafía de la Formación Sarmiento en la Barranca Sur del Lago Colhué Huapi. Asociación Geológica Argentina, Revista XXXIV (4): 271-281
- Sridharan, A., Prakash, K. (2000) Classification procedures for expansive soils. Geotech Eng 143:235–240. Proceedings of the Institution of Civil Engineers - Geotechnical Engineering. ISSN 1353-2618 | E-ISSN 1751-8563. Volume 143 Issue 4, October 2000, pp. 235-240 <https://doi.org/10.1680/geng.2000.143.4.235>
https://www.researchgate.net/publication/344218452_Swelling_Stress_and_Suction_Correlation_of_Compacted_Heaving_Soils

Estimation of Geological Strength Index in stratified rock mass based on fractal theory

E.E. Palmezano

Integral S.A. Medellín, Colombia

Universidad EAFIT, Medellín, Colombia

J. Ramos

Universidad EAFIT, Medellín, Colombia

ABSTRACT:

The geological strength index system (GSI), widely used for the design and practice of underground numerical process, is a rock mass classification system that considers to the rock mass strength and deformation parameters based on the generalized Hoek-Brown and Mohr-Coulomb failure criteria. The GSI can be estimated using standard chart and field observations of rock mass block size and discontinuity surface conditions. The GSI value gives a numerical representation of the overall geotechnical quality of the rock mass. This study proposes a method to determine the GSI quantitatively using photographic images of in situ stratified heterogeneous rock masses with image processing technology, fractal theory and the geomechanic analysis for joints. Using the GSI system to characterize the jointed rock mass around the Guillermo Gaviria Echeverri or El Toyo Road tunnel, Antioquia, Colombia.

1 INTRODUCTION

1.1 *General information*

The Guillermo Gaviria Echeverri Tunnel and its access roads described above “Túnel del Toyo”, is one of the 4G (Fourth Generation) road projects that will allow the most efficient connection of the main production centers in the interior of Colombia with the Caribbean and Pacific coasts. Particularly in the department of Antioquia, these works seek to improve the connectivity between Medellín and the port projects that are planned to be built in the Urabá sub-zone.

For the classification of rock masses, different methodologies or systems have been proposed that seek to establish zones with homogeneous behaviors. As well as to provide the basis for understanding the characteristics that define each zone and finally, to quantitatively evaluate the rock mass to establish the most appropriate type of support to meet the stresses of the terrain in the underground excavations.

Currently, the most widely used geomechanics rock mass classification systems are: the Q Index proposed by Barton N., Lien R. and Lunde J. (1974), and the Rock Mass Rating (RMR) developed by Bieniawski (1976). In addition, the implementation of the Geological Strength Index (GSI), presented by Hoek (1994) to define the geotechnical quality of the rock mass, has taken relevance due to its use in the design and construction of underground spaces and it is already seen as a widely accepted classification system in the trade.

This paper presents a conceptual review of the classification of stratified rock masses using GSI, as well as the rationale of fractal theory and its potential use in geotechnical engineering. In addition, it summarizes the geological-geotechnical characterization in each of the development stages of the Guillermo Gaviria Echeverri Tunnel Road Project and its access roads, such as design and construction, in order to expose the conditions for the estimation of the quality of the rock masses by means of the Geological Strength Index (GSI).

1.2 The Geological Strength Index (GSI)

The evaluation of the shear strength of a fractured rock mass will depend on the assessment of the properties of the intact rock and of the walls of the joints, framed in the behavior of these two features under stress.

To estimate the above effect as a response of the rock mass to underground excavations, Hoek et al. (1995) provides a system to calculate the decrease in strength that a rock mass would present under different geological conditions by means of a geological strength index (GSI).

Hoek presented the GSI in order to calculate the s and m_b parameters in his generalized rock failure criterion. This index has been updated several times for use in weak rock masses, 1998, 2000 and 2001, Marinos et al. (2007). The evaluation of the GSI index is made by comparison of the actual conditions with the typical characteristics of the typical GSI chart proposed by Hoek et al. in 1995, this index can vary from 0 to 100, which allows defining 5 classes of rock masses (Karzulovic, 2006):

- Very Poor (00 < GSI < 20)
- Poor (20 < GSI < 40)
- Fair (40 < GSI < 60)
- Good (60 < GSI < 80)
- Very Good (80 < GSI < 100)

In some cases, it may be necessary to implement a special version of the GSI estimation chart, as is the case for stratified heterogeneous rock masses. For example, Figure 1 presents a chart developed by Hoek & Marinos in 2000 to determine the quality of stratified heterogeneous rock masses (Flysch).

The flysch term to geologist B. Studer and comes from the German word "fliessen" meaning flow, probably denoting the frequent landslides in areas consisting of these formations (Hoek & Marinos, 2000). In general, it is a sedimentary deposit consisting of thin layers of shales or marls alternating with thicker strata such as sandstones or conglomerates.

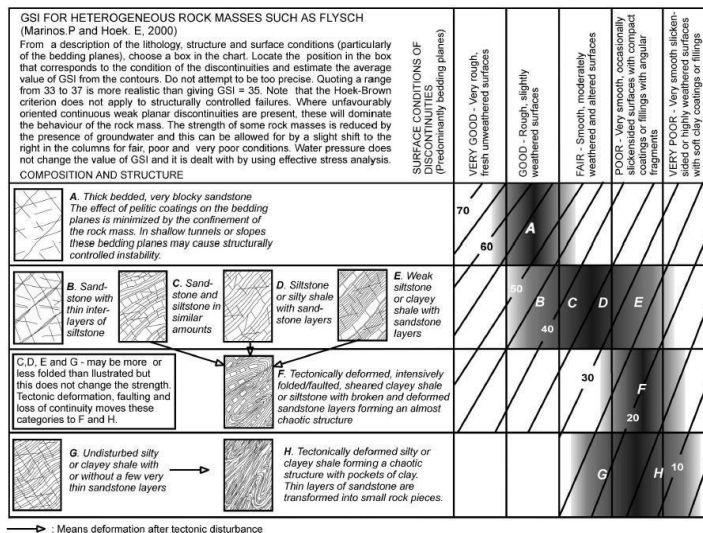


Figure 1. GSI estimation for heterogeneous rock masses such as Flysch, (Hoek & Marinos, 2000).

1.3 Fractals theory and fractal dimension

Fractal geometry allows a mathematical description of irregular shapes such as those found in nature, i.e. mountains, coastal strips, hydrographic systems, clouds, leaves, trees and other bod-

ies that cannot be easily described through traditional geometry. These shapes have been termed fractals (Barnsley, 1990).

According to Magaña et al. (2011), in mathematics a measure is a function (or mapping or operator) that assigns a number to subsets of a given set, for example, to a "volume" or "probability". To define a fractal, the following characteristics must take into account:

- Self-similarity: At different scales, a fractal retains the same appearance; there is always a clear similarity between very distant parts of the same fractal figure.
- Infinite detail: Related to the previous characteristic, as a fractal enlarged.
- Non-integer dimension: A fractal can develop in a non-integer dimension. This dimension is deduced from the Hausdorff measure.

2 METHODOLOGY

For the development of this work, the qualitative approach for the methodological design proposed by (Hernández et al., 2014) taken into account. This approach has nine phases, starting with the literature search and ending with the presentation of the research results.

Focused on the idea of presenting a methodology for the estimation of GSI under the implementation of fractal theory and the geotechnical characterization of the walls of joints in stratified heterogeneous rock masses, a compilation of information made to provide a conceptual approach to the development of the project.

The information gathered in the study area during the design and construction stages provided the basis for the analysis of the data to obtain the results for estimating and quantifying the quality of the rock mass with specific geomechanical characteristics (Figure 2). Following the findings, recommendations and lessons learned by Hong et al. (2017) and Moná (2019) applying this method to rock masses and extracting the Geological Strength Index (GSI). According to Palmezano (2022), a parallel methodology was proposed to estimate GSI from image processing to anisotropic rock masses as sedimentary rocks, to finally present the comments and recommendations for its use.

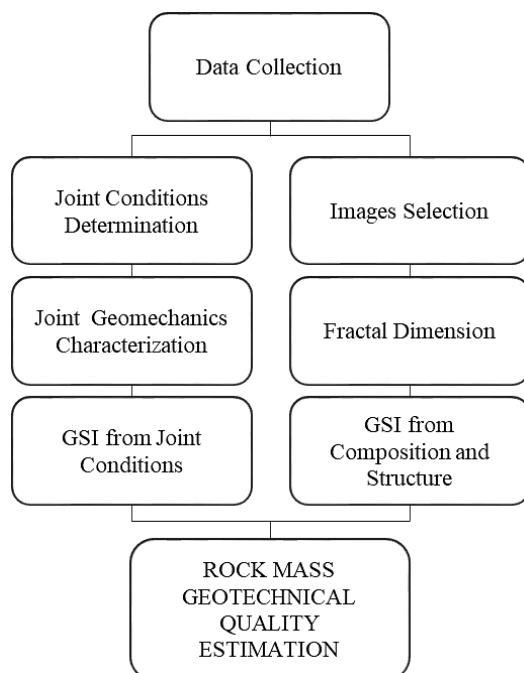


Figure 2. GSI estimation methodology.

3 STUDY ZONE

This paper takes as study area the route of the Guillermo Gaviria Echeverri Tunnel, initially called Tunnel 17 -El Toyo- hereinafter referred to as GGE Tunnel. The GGE tunnel layout is located in the department of Antioquia, Colombia, with a total length of 9370 m, starting at km 27+125 (Entrance Portal - Giraldo) and ending at km 36+855 (Exit Portal - Cañasgordas). The main tunnel has a horseshoe-shaped section with an average area of 110 m². Due to its arched nature, the selected geometry allows adequate stress redistribution around the cavity, minimizing the concentration of compressive stresses and the generation of tensile stresses.

3.1 Geological model of the GGE Tunnel

The geological model of the GGE tunnel divided into two large homogeneous zones, which in turn subdivided into 42 homogeneous sections defined by lithology, geotechnical behavior and/or vertical cover. Figure 3 shows the geological design model in plan and profile. The volcanic domain representing the Barroso Formation shown in pink and the sedimentary domain of the Penderisco Formation in yellow.

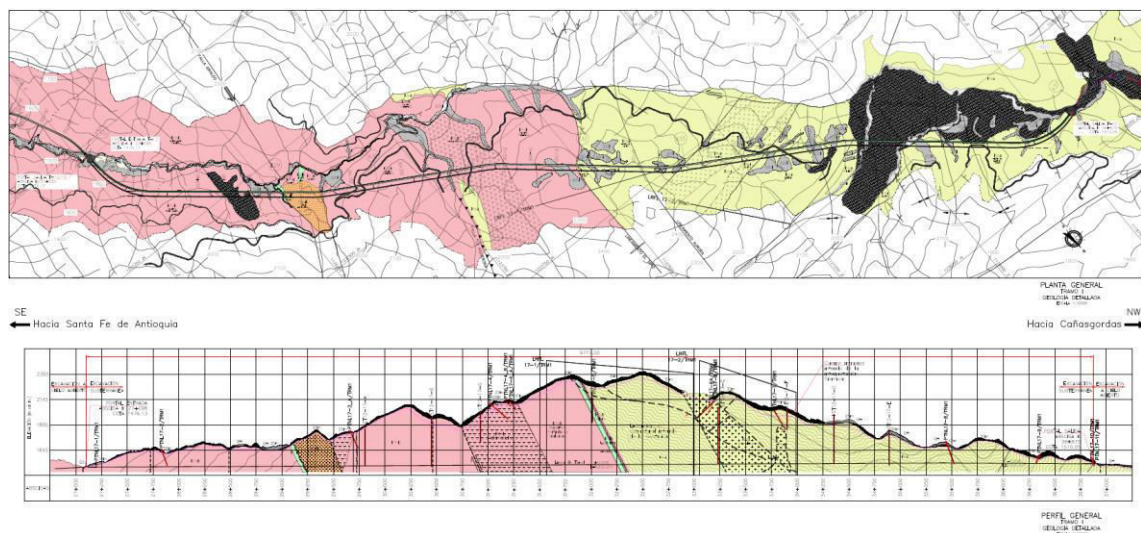


Figure 3. Geological model of the GGE Tunnel, (Consorcio Antioquia al Mar 2017).

4 GEOMECHANICAL CHARACTERIZATION DURING GGE TUNNEL CONSTRUCTION

During construction stage, the tunnel had an advance close to one kilometer, a section where 182 MRLs carried out between km 35+211.00 and km 34+214.25, excavation carried out against the increase of the abscissae of the road. With the information contained in the logs of the advance fronts, it was possible to establish the strength of the rock matrix, the degree of fracturing represented by the RQD index and the separation of the discontinuities, the surface condition of the joint walls and the hydrogeological conditions.

It found a rock of very low-to-low resistance to uniaxial compression (5 - 50 MPa). According to the RQD index, the geotechnical quality classified as poor to very poor, predominantly less than 50%. This is associated with a separation of discontinuities of predominantly less than 60 mm, generating a very high degree of fracturing of the rock mass, allowing decimetric or centimetric rock blocks to be found, controlled by a thin stratification of the sedimentary rocks present in the section (Figure 4).

Water infiltrations along the GGE Tunnel excavation through the outlet portal, and particularly in the study section, had an irregular behavior, in some sectors they found as wet zones or slight drips between the stratification planes.

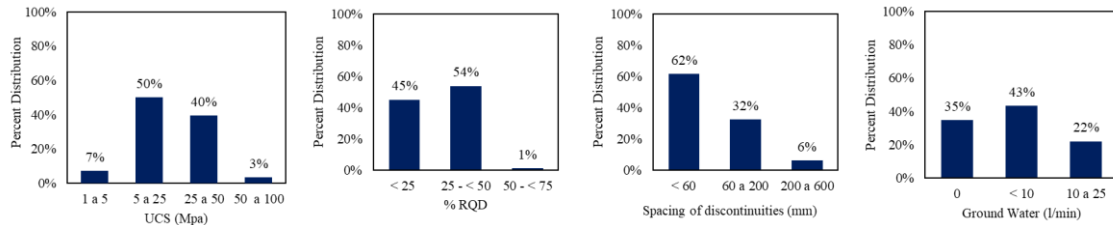


Figure 4. Rock mass classification parameters in the GGE Tunnel, km 35+211.00 - km 34+214.25.

4.1 Joint Geomechanical Characterization

This characterization consisted of taking structural data and its geomechanical characteristics, considering mainly parameters such as persistence, aperture, roughness, and weathering, defined by Bieniawski in 1989 for the classification of the rock mass under the implementation of the RMR system. The results show that persistence is mainly moderate (3 to 10 m), discontinuities with open (1 to 5 mm) to wide (>5 mm) walls are commonly encountered, wall surfaces are usually smooth to slightly rough, due to the openness of the walls fills of mainly soft consistency are encountered, and, they are moderately altered usually (Figure 5).

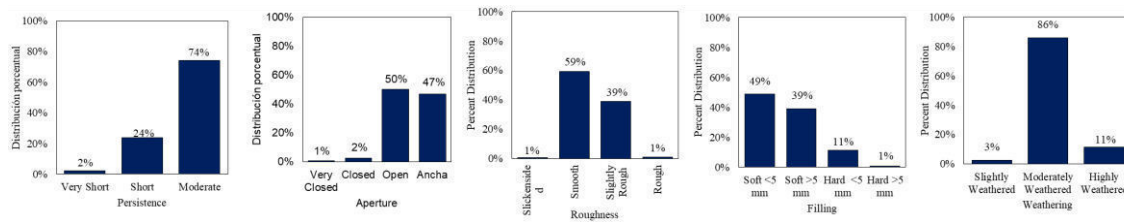


Figure 5. Main geomechanical joint conditions in the GGE Tunnel, km 35+211.00 - km 34+214.25.

4.2 Structural trends

Statistical analysis of the orientations of the rock mass discontinuities in the GGE Tunnel between km 35+211.00 and km 34+214.25 (direction of travel), identified a predominant trend in the stratification of the sedimentary rocks excavated, three families of major joints and two to three shear fracture trends, as shown in Table 1.

Table 1. Predominant structural trends in the GGE tunnel, km 35+211.00 - km 34+214.25.

Nº	ID	Structure type	Dip/Dip Dir
1	E1	Stratification	75°/285°
	Cz1	Shear fracture	
	E2	Stratification	75°/110°
2	D1	Joint	
3	D2	Joint	65°/145°
	D3	Joint	
4	Cz2	Shear fracture	25°/250°

5 PRE-POST IMAGE PROCESSING

The image processing for the development of this work was done following stages a, b, c, d and e of the methodology proposed by Basirat et al. (2019), which can be seen in Figure 6. In that

sense, with the Rock Mass Surveys executed in the different advance fronts of the GGE Tunnel in the study section, abscissae km 35+211.00 to km 34+214.25 (direction of advance), an equal number of photographs were taken to analyze, 182 images in total.

Thus, the original photographs were converted to grayscale, an area representative of the dominant fracture degree in the tunnel pediment was taken, the edge points were detected with the Canny algorithm. Finally, the fractures were detected by means of the Hough transform, which was developed using the numerical computation system that offers an integrated development environment with its own programming language, MATLAB in its online version.

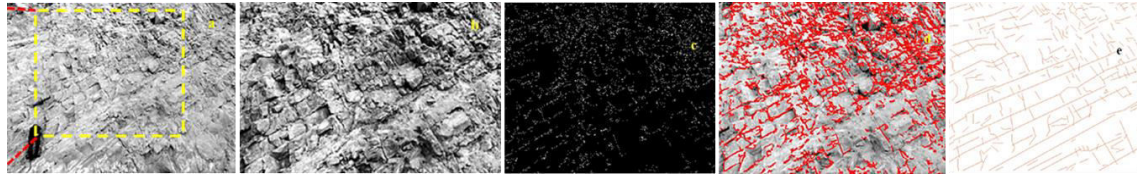


Figure 6. Stages for fractal dimension (FD) determination using image-processing technique, (modified from Basirat et al., 2019).

5.1 Fractal Dimension

At the date of structuring this work, several publications were found that have been carried out to estimate the degree of fracturing of rock masses by means of fractal theory, based on the typical GSI chart for fractured rock masses, without a marked tectonic affectation and without the inclusion of the conditions of discontinuities, a topic that this research tries to address.

From these publications, the work of Hong et al. (2017) stands out for introducing for the first time the application of fractals to GSI in sedimentary rocks through image processing and its application to neural networks. Later, Moná (2019) for presenting the first proposal of GSI in homogeneous massifs using fractal theory in La Queibra tunnel, Colombia, taking into account the degree of fracturing and establishing some initial ranges of fractal dimension for each of the divisions of the classification system.

In order to obtain the fractal dimension from previously processed images, different ways have been proposed that involve the use of programming languages under free or licensed codes and/or software. In this work, the Harmonic and Fractal Image Analyser software was used (HarFA - Zmeskal et al (2001)), because of the good results obtained by Moná (2019) in its implementation in rock masses.

Focusing on the sedimentary rocks of the study area, DF was calculated from the composition and structure cases A. to F. of the GSI chart proposed by Hoek & Marinos (2000) for heterogeneous stratified rock masses under the procedure described above. The results for the boxes that determine the fracturing and tectonic involvement in each case are shown in Table 2.

Table 2. Fractal dimension (DF) and GSI ranges based on Hoek & Marinos (2000).

GSI Type	DF	GSI Range	Ranking
A	<1.52	>52	Fair to Good
B	1.52 – 1.65	44 – 52	
C	1.65 – 1.75	36 – 44	
D	1.75 – 1.80	28 – 36	Poor to Fair
E	1.80 – 1.84	20 – 28	
F	>1.84	<20	Very Poor to Poor

6 CASE STUDY: GUILLERMO GAVIRIA ECHEVERRI TUNNEL GAVIRIA ECHEVERRI TUNNEL - TÚNEL DEL TOYO

The information gathered in each rock mass survey of the study section provides the basis for the calculation of the fractal dimension from the photographs of the Guillermo Gaviria Echeverri Tunnel (GGE Tunnel) advance pediments, as well as the rock mass parameters for the validation of the model.

6.1 Fractal Dimension use in the Guillermo Gaviria Echeverri Tunnel

Figure 7 shows an example of the calculation of the fractal dimension from the digitization of the photograph taken with the tunnel at the abscissa km 35+047.00 as a result rounded to two (2) decimal places, $FD=1.82$ was obtained.



Figure 7. Fractal Dimension analysis of GGE Tunnel, Abscissa km 35+055.25

The mobilization of DF along the study section is shown in Figure 8 (a). Where it can be seen that the lowest values of the fractal dimension are concentrated between the abscissae km 34+620 and km 34+550 approximately, with DF values below 1.70, implying that, in that section of the tunnel, the rock mass can be classified as Fair to Good, as far as fracturing or tectonic affectation is concerned.

Likewise, it is clear that the lowest values of the fractal dimension are established at the limits of the study section, as well as between the abscissae km 34+800 and km 35+000, which may be above 1.80 points. Indicating, a greater degree of fracturing and possibly greater mechanical alteration of the rock due to the tectonic affectation by the presence of weakness structures such as faults or shear fractures. Figure 8 (b) shows that, the dominant rock mass quality in the study section, as established in Table 2 is "Poor" with GSI types D and E outstanding, i.e. with DF values between 1.75 and 1.84.

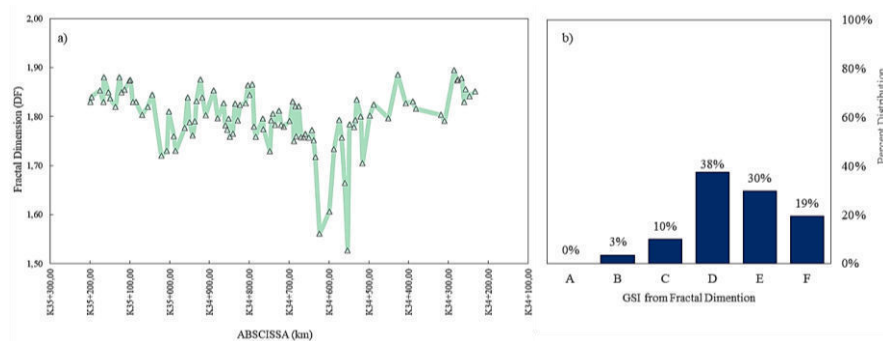


Figure 8. FD distribution a) and Occurrence percentage by GSI type b) of GGE Tunnel, between km 35+211.00 and km 34+214.25.

6.2 Joint conditions

With the data from the MRLs carried out between the abscissae km 35+211.00 and km 34+214.25 of the GGE tunnel in the Cañasgordas sector, we obtained the sum of the joint conditions (JC) -persistence, openness, roughness, fill and weathering-. The above, in order to be able to estimate the GSI according to equation proposed by Hoek et al (2013). The distribution of the calculated JC values in the study reach are presented in Figure 9.

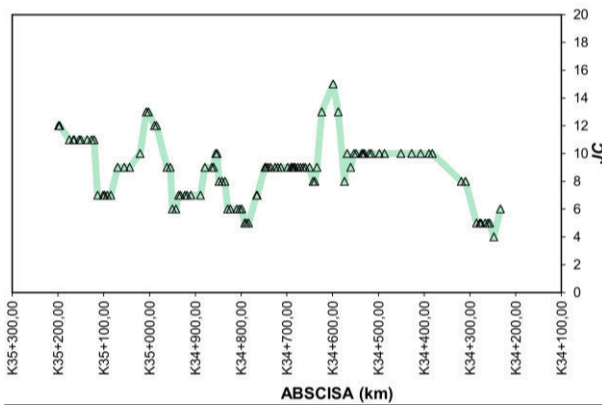


Figure 9. JC distribution of GGE Tunnel, between the abscissae km 35+211.00 and km 34+214.25.

6.3 GSI estimation and Fractal value calibration

Having the degree of fracturing estimated by means of the fractal dimension for the photographs of the advancing faces, and the joint conditions established in each MRL, we proceeded to look for the relationship that would allow obtaining an equation for the quantification of the GSI by means of the methodology proposed in this work. For this, the starting point was the expression shown in equation proposed by Hoek et al (2013), replacing the estimate of the rock mass blockiness (RQD/2), by the GSI value obtained through the fractal dimension (DF).

Equation 1 shows the expression found to relate the discontinuity wall conditions to the degree of fracturing established by the fractal dimension, corresponding to a linear regression model.

In relation to the previous two paragraphs, it can be seen in Figure 10 that the lowest GSI values are found towards the end of the study section and near the abscissa km 34+800. Reciprocally, the highest values were found around the abscissae km 34+600 and km 35+000. Notwithstanding the above, it should be noted that in all cases the estimated GSI values are below 60, and are even mostly concentrated between GSI values 20 and 40, this situation allows establishing rock masses of predominantly low geomechanical quality.

$$GSI = 2.5 JC_{89} + GSI_{DF}/3.5 \tag{1}$$

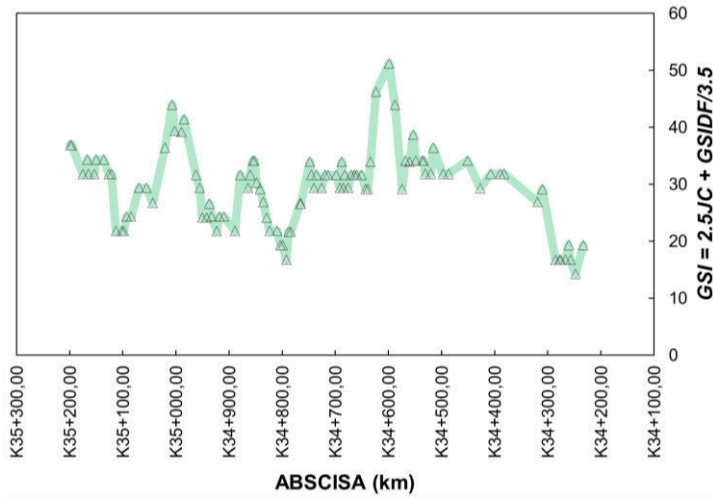


Figure 10. Estimated GSI distribution for GGE Tunnel, between km 35+211.00 and km 34+214.25.

To verify whether or not the proposed GSI quantification works, GSI values estimated using Equation 1 were confronted against GSI values estimated from field-mapped discontinuity and fracture wall conditions.

Therefore, the GSI values calculated from JC and RQD using equation proposed by Hoek et al (2013) (Field GSI) were plotted against the GSI values estimated under the methodology proposed in this work and the results can be seen in Figure 11.

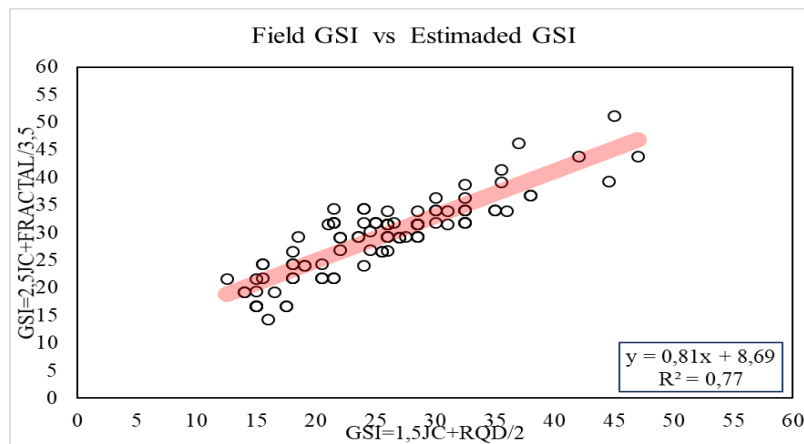


Figure 11. Comparison between Field GSI and Estimated GSI based on JC and DF.

This figure shows a correlation between calculated and mapped GSI values is reasonably good, even though it is a little far from the ideal 1:1 ratio that refers to a perfect fit. This suggests that, once additional field data are obtained for heterogeneous and stratified rock masses, the application of the proposed methodology for GSI estimation could be recommended for future works.

7 CONCLUSIONS

Considering the main objective of this work, which seeks to provide the industry with a method to quantitatively determine the GSI with the implementation of fractal theory and prior characterization of joint conditions to estimate the quality of stratified heterogeneous rock masses, the following conclusions are presented:

- The area where the Guillermo Gaviria Echeverri Tunnel - GGE Tunnel - initially called Toyo Tunnel - is located, especially towards the Cañasgordas sector presents the geological-structural conditions for the application of this methodology.
- The GSI chart for heterogeneous stratified Flysch-type stratified rock masses allows quantification by fractal dimension to obtain the GSI ranges that correspond to the compositional and structural characteristics.
- The GSI estimation carried out in this work allowed establishing the geomechanical quality of the rock masses excavated in the section of the GGE Tunnel between km 35+211.00 and km 34+214.25, direction of the advance of the excavation, in predominantly Mala. of the excavation, in predominantly Mala.
- The application of the methodology proposed in this work could be recommended for the classification of heterogeneous stratified rock masses by estimating GSI in other areas provided that reliable field data of discontinuity wall conditions are obtained and representative photographs of the dominant fracturing degree in the available outcrops are available.

8 REFERENCES

- Barnsley, M. F. 1990. *Fractals Everywhere*. New York: Academic Press.
- Barton et al. 1974. Engineering classification of rock masses for design of tunnel support. *Rock Mechanics*, 6(4), 189-236.
- Basirat et al. 2019. Determination of the Fractal Dimension of the Fracture Network System Using Image Processing Technique. *Fractal and Fractional*.
- Bieniawski, Z. T. 1976. Rock mass classification in rock engineering. En Z. T. Bieniawski, *Proceedings of the symposium on exploration for rockengineering exploration.*, (págs. 97-106). A.A. Balkema.
- Bieniawski, Z. T. (1989). *Engineering Rock Mass Classifications*. New York: Wiley.
- Consortio Antioquia al Mar. (2017). Volumen IX. Estudios y Diseños de Túneles Capítulo 4. Estudio de Geología y Geotecnia Túnel 17 Toyo.
- Correa Villa, E. (2014). Resistencia de las Discontinuidades Rocosas al Esfuerzo Cortante. Medellín: Proyecto de Grado, Universidad EAFIT.
- Hernández et al. (2014). *Metodología de la investigación* (6ª ed.). McGraw-Hill.
- Hoek et al. (1995). *Support of Underground Excavations in Hard Rock*. Rotterdam: Balkema.
- Hoek et al. (2013). Quantification of the Geological Strength Index chart. *47th US Rock Mechanics / Geomechanics Symposium*, 23 - 26.
- Hoek, E. (1994). Strength of rock and rock masses. *ISRM News Journal*, 2(2):4-16.
- Hoek, E. & Marinos, P. 2000. Predicting Tunnel Squeezing. *Tunnels and Tunnelling International*.
- Hong et al. 2017. Determination of geological strength index of jointed rock mass based on image processing. *Journal of Rock Mechanics and Geotechnical Engineering*.
- Karzulovic, A. 2006. Métodos de calificación geotécnica de macizos rocosos.
- Magaña et al. 2011. Análisis con elemento finito y remalleo fractal en geotecnia. *Ingeniería Investigación y Tecnología*, 103-118.
- Marinos et al. 2007. Geological Strength Index (GSI). A characterization tool for assessing engineering properties for rock masses. *Underground works under special conditions*, eds. Romana, Peruchio Olalla, 13-21.
- Moná, J. E. 2019. Aplicación de la Teoría Fractal para la Estimación de la Distribución Geométrica de Fallas en Macizos Rocosos. Medellín: Trabajo de Grado, Universidad Nacional de Colombia.
- Palmezano, E. E. 2022. Estimación del Índice de Resistencia Geológica en macizos rocosos estratificados basado en la teoría fractal. Medellín: Trabajo de Grado, Universidad EAFIT.

Use of statistical techniques for improving rock mass characterization

K. Suzuki Morales
University of Chile, Santiago, Chile

ABSTRACT:

Most of the empirical approaches used today were proposed 40 years ago, and their updates do not include most of the new understanding of mining geomechanics acquired since then. Even though numerical modeling is used today for designing purposes, rock mass characterization is still based on the input parameters required by traditional rock mass classification methods without considering their limitations. In recent years, data acquisition methods have improved the quality of geotechnical data and machine learning algorithms have become widely used. However, it is important to note that geomechanics is a data limited problem and that empirical methods are still widely used, which indicates that the relation between the amount of data and decision support has not changed due to limitations in geotechnical methodologies. This paper discusses the limitations related to the identification of critical parameters influencing the rock mass behavior, alternatives to characterize the geology and the options to define weightings for critical parameters. Additionally, a regression that reduces the multidimensionality of a problem is presented to have a better visualization of the problem. The use of traditional statistical techniques showed to be useful to highlight which parameters have a more significant effect on the final response and, therefore, where the efforts in rock mass characterization should be directed.

1 INTRODUCTION

Logical conclusions that improve the understanding of rock mass behavior have been drawn mainly after the occurrence of geotechnical disasters. There have been catastrophic events that have been used for back analysis, but an enhanced understanding of the problem could have helped prevent these events. Unfortunately, approaches such as caveability prediction methods suggest that the future of cave mining requires the development and implementation of new geotechnical methodologies to evaluate challenging conditions. Despite technological trends, most of the empirical approaches used for designing caving mines were proposed 40 years ago, and their updates do not include most of the new understanding of mining geomechanics acquired since then. In fact, most of the empirical methods used today were developed when geoscientists did not have easy access to computers and when the experience of operating caving mines was completely different. Today, a lot of data is obtained through sensors and data collection devices in this era of digital transformation. However, the connection between the amount of data and decision support has remained the same for decades (Phoon et al. 2022).

In this context, it is important to note that most geomechanical problems are data and understanding limited (Starfield and Cundall, 1988) and that empirical methods are valuable because of the databases used to calibrate them (Milne and Hadjigeorgiou, 2000). Geomechanics is a data limited problem because relevant data is generally unavailable or cannot be easily obtained to characterize rock mass behavior adequately. For instance, the quality of the data in underground mines is scarce due to mapping difficulties such as limited access and coverage of wall exposures with shotcrete or wire mesh. For this reason, in rock mechanics, any model should be simple and targeted at gaining understanding of the possible failure mechanisms to improve design and decision-making rather than to make absolute predictions (Starfield and Cundall, 1988). Many studies using sophisticated artificial intelligence techniques in rock mechanics range from insufficient data to non-availability, which gives researchers the option to use advanced numerical modeling methods to simulate and generate enough data (Lawal and Kwon, 2021).

On the other hand, the current use of empirical methods reflects the challenge to modify well-established classification methods, which are valuable because of the databases used to calibrate them (Milne and Hadjigeorgiou, 2000). Empirical methods reflect the observed performance of design rules or structures that consider the overall complexity of the problem without explicitly considering the physics of the problem. These methods are convenient to evaluate the problem, and to validate and calibrate numerical models since they are closer to the true behavior of engineering structures in natural materials (Franklin, 1993). The components of rock mass classification systems are three elements that simplify rock mass complexity in an overall index: a combination of critical parameters influencing the rock mass behavior for a specific engineering application, the characterization of the geology, and the weighting of critical parameters. This paper discusses the current limitations related to each element and presents an application of a statistical regression that reduces the multidimensionality of a problem to have a better visualization of the problem. The use of statistical techniques can highlight where the focus of rock mass characterization should be in problems characterized by small data sets.

2 CRITICAL FACTORS INFLUENCING THE ROCK MASS BEHAVIOR

The identification of critical parameters influencing the rock mass behavior for a specific engineering application is required before starting a project. An alternative for selecting critical parameters is using a Rock Engineering System (RES) (Hudson, 1992). The twelve terms considered by Hudson (1992) for underground excavations are: excavation dimensions, rock support, depth of excavations, excavation methods, rock mass quality, discontinuity geometry, rock mass structure, in situ rock stress, intact rock quality, rock behavior, discontinuity aperture, and hydraulic conditions. The interaction matrix coding is based on the experiences and judgments of tunneling experts, which can be highly subjective because people tend to be overconfident and predictions are based on their experiences on a small number of observations (Baecher and Christian, 2005).

Another alternative is the development of a rock mass classification system. In this case, these empirical approaches must include the rock mass properties considered critical for a specific purpose and must be calibrated against case histories representing the field application (Einstein et al., 1979). For example, the Q-system incorporates critical parameters that are relevant to recommend support and reinforcement for the arch and walls of underground excavations. Barton et al., (1974) suggest that the Q-system should be used with full awareness of its limitations in mining, and the chosen parameters should be re-evaluated for assessing other problems. It is then highlighted that no approach can be correctly applied beyond the limits established by the database that was used to define them.

However, there are some engineering problems where there is still uncertainty and unknowns about the rock mass behavior under certain conditions, making challenging the determination of which parameters affect the final response and how. An example is caveability prediction. Some authors have discussed the relevance of critical factors (Kendorski, 1978; Laubscher, 2000; Brown, 2002; Mawdesley, 2002; Rafiee et al., 2016, Suzuki Morales & Suorineni, 2017). More specifically, there is evidence that the presence of veins having less than 1/3 of hard minerals of infilling and thickness greater than or equal to 2 mm are more likely to define blocks during caving in El Teniente mine (Brzovic and Villaescusa, 2007). Bewick et al. 2022 suggest that porphyry rock mass characterization should consider the definition of intact rock strength, vein tensile strengths, and shear strengths in domains based on the spatial intensity distribution of weak veins, small-scale faults, and joints. Despite evidence suggest veins control caving, there are no clear guidelines on how veins should be characterized to make better predictions in empirical and numerical models, mainly because of the limited understanding of caving mechanisms. The most accepted model of caving was proposed by Duplancic (2001), but there is evidence that this might be a specific model that does not represent all the factors that could influence caving mechanisms (Cumming-Potvin et al. 2018).

3 CHARACTERIZATION OF GEOLOGY

Geological features are characterized qualitatively or quantitatively, using different criteria, to evaluate empirical or numerical methods. For example, roughness is typically described using descriptive and subjective terms for two scales of observation, small scale (several centimeters) and intermediate scale (several meters). Another example is joint persistence, parameter that is almost impossible to measure in practice and that is often estimated from trace lengths observed in rock exposures that are small compared to the real length of persistent. In fact, classification systems do not explicitly incorporate this parameter, but they assume that joints are fully persistent and continuous. Currently, the relative value of different procedures to determine different geological parameters are not established or recognized.

In the last decades, significant research has been conducted for acquiring discontinuity characteristics exposed on the surface of the rock mass using laser scanning or photogrammetry. Approaches for rock mass discontinuity characterization from 3D models with strengths and limitations are presented in Battulwar et al. (2021). An interesting example is the use of autonomous drones in underground mining, which has provided data in previously inaccessible areas, improving safety, efficiency, and productivity (Jones et al. 2019). However, as previously mentioned, the connection between the amount of data and decision support has remained the same for decades. On the one hand, the resolution of these approaches varies from thousandths to singular points per square meter, while Barton's Q-system considers the joint set with the lowest shear strength and Laubscher's MRMR considers a weighted average of all joint sets to establish the joint condition in a rock mass with a maximum of three joint sets. On the other hand, full-scale modeling of processes such as caving remains one of the greatest challenges in caving geomechanics, despite increased modeling ability, and simple models are preferred over complex models. In this case, data acquisition methods can be useful in improving the understanding of rock mass behavior and failure mechanisms but are still limited to providing information to empirical or numerical models.

Another challenge faced in rock mechanics is making a reliable estimation of the mechanical properties of a rock mass. Given that the mechanical properties of a rock mass cannot be measured directly, it is a common practice to use empirical correlations with rock mass classification systems to estimate the rock mass strength. A promising alternative for estimating rock mass properties is the use of numerical methods, but they still require further validation. In particular, post-failure behavior plays a relevant role in caving methods and the estimation of plastic zones around underground excavation. However, in general, empirical and numerical methods are used to avoid failure, and because of that, they are based on the elastic and peak mechanical behavior of rocks. In this context, a complete characterization of the stress-strain curve should be required as input data in numerical models.

4 WEIGHTING OF KEY PARAMETERS

The term rock mass describes an assemblage of intact rock blocks separated by geological discontinuities, which vary in size from hardly visible fissures to a regional fault zone, including veins as a special category. As a result, the behavior of a rock mass and its failure process combine deformations and failure in the intact rock and deformations and sliding along discontinuities. This definition describes a very complex natural material that is used for engineering purposes, and because of this, assumptions and simplifications need to be made to estimate rock mass behavior. In this context, the weighting of critical parameters affecting the rock mass behavior for a specific engineering application should account for the loading conditions, scale effects and potential failure modes, which is not always the case.

One of the limitations in understanding rock mass behavior is related to the complexity of rock mass as an engineering material. Even though laboratory tests and field mapping can indicate the rock mass quality, they represent a small volume compared to the entire rock mass, which is the input data required. For this reason, empirical methods usually only incorporate the uniaxial

compressive strength of the intact rock and a qualitative description of single discontinuities without considering other information that can be obtained from laboratory tests or from the field. Another limitation refers to the estimation of the mechanical properties describing rock masses, which is limited because experimental models at mine scale are not feasible. As an alternative empirical and numerical methods have been used to estimate properties at large scales. Finally, one critical limitation is related to the identification of rock mass failure mechanisms. In this context, rock mass characterization is relevant since it gives the input parameters to empirical and numerical methods that aim to represent the rock mass behavior, estimate its mechanical properties, and represent possible failure mechanisms.

It is then required to have an adequate and standardized rock mass characterization to define reliable input parameters to estimate a rock mass response. The impact of typical errors in core logging for design in caving mines was measured recently by Russo et al. (2022). Some of the errors identified were associated with a mistaken distinction among natural and mechanical discontinuities, erroneous joint counts, wrong assessment of the RQD, and errors in the assessment of the joint condition. One of the examples resulted in an estimation of the hydraulic radius required to undercut to start the caving that needed to be increased up to 5,600 m² once the errors were fixed in one of the geotechnical units analyzed. Other examples result in classification systems that increase up to 20 points in the final rating.

As mentioned before, the effect of each factor can be quantified by using an interaction matrix based on expert experience or calibrating a classification system or empirical method for a given application. Unfortunately, as most of these approaches have not been updated with time, it is not possible to adjust the weighting of key parameters. In recent years, machine learning algorithms have become widely used in different disciplines, which has set a modern trend in geomechanics. Some applications found in the literature are evidence of the transformations that are being faced in recent years, but also indicate that operating mines collect more instrumentation data than ever before. These techniques need to be used with care and understanding of their assumptions since they might be inappropriate for a full statistical analysis given their qualitative to semi-quantitative scales of measurements (Elmo et al. 2020).

Another option is the use of traditional statistical techniques. The main differences between traditional and statistical (or machine) learning techniques are their interpretability and flexibility (James et al., 2013). Statistical methods based on inference are more restrictive than statistical learning methods, but they allow easier interpretation. For example, a multiple regression analysis directly incorporates weights that indicate the relationship between the independent variables and the dependent variable. In cases when the interest is the predictive ability of the model and the interpretability is not relevant, usually, a statistical learning approach fits better. In fact, these techniques work well when many variables can be measured on a specific entity, for example, in industrial processes where there is a simultaneously record of a condition that needs to be forecasted, such as machine failure or the mineral and geometallurgical properties of rock, or the output of a process (McGaughey, 2019). Unfortunately, this is not the case of most geomechanical problems that still require conceptual validation since data and understanding limit quantitative validations.

4.1 *Use of statistical techniques for weighting key parameters in caveability prediction*

The following example shows how statistical techniques can be used to estimate the weighting of critical parameters affecting caveability. For this purpose, the numerical model presented in Suzuki Morales et al. (2020) is used to represent a basic system in which blocks can deform and fail (Figure 1). The study modeled 102 combinations of seven factors at two levels: factor A is joint orientation, factor B is joint persistence, factor C is joint intensity, factor D is intact rock properties, factor E is joint condition category, factor F is in-situ stresses magnitude and factor G is the undercut area. The two levels are low and high levels, where the low level of each factor is the less favorable case for caveability and the high level the most favorable case for caveability. The measured response is the volume at which displacements in the z-direction are higher than 1 cm, which is used as an indicator for caveability prediction. In this case, a numerical experiment is

useful to elucidate information about why and how the system works and has the advantage over the observation since it allows variables of interest to be changed intentionally and their effect measured. Given the limited number of caving mines, observations do not give enough information and control over the variables.

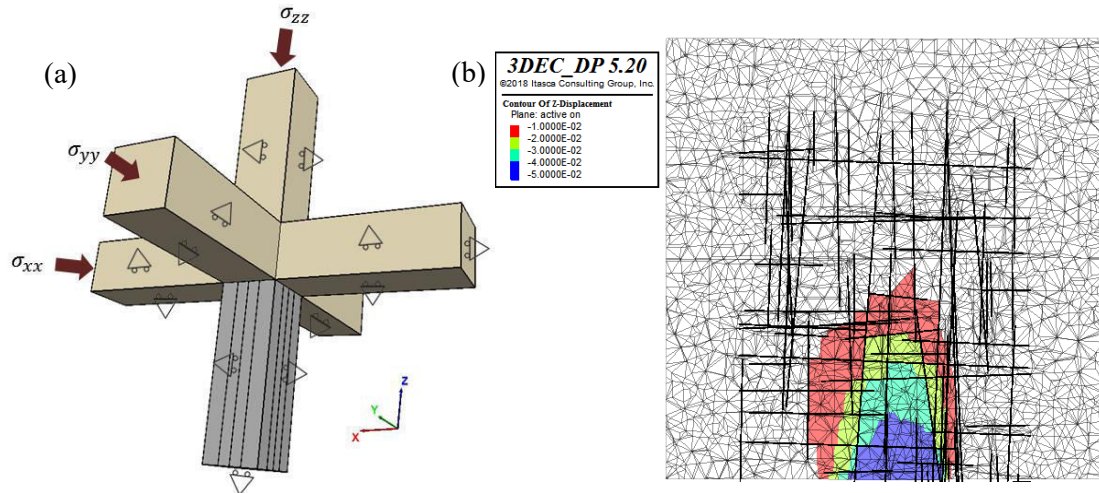


Figure 1. (a) Boundary conditions applied to the model, and (b) displacements at the final stage for the combinations of factors more favorable for caveability (Suzuki Morales et al., 2020).

Results from observations or experiments can be used to adjust a model using different techniques, such as a generalized linear model (GLM) to predict the responses or a partial least squares (PLS) regression to reduce the dimensionality of the problem. Results from a PLS are presented in this work, which is based on the algorithm implemented for R in the pls package (Mevik et al. 2018).

The main purpose of reducing the dimensionality of a problem is to have a better visualization of the parameters affecting the main response. A correlation loading plot can reveal important design factors that model the variations in Y when the original multidimensionality is reduced (Martens et al., 1986). Caveability prediction charts are presented in 2D using the rock mass quality on one axis and the hydraulic radius on the other axis. The available 2D caveability charts may not be optimized to show on a proper scale how the factors affect the variations in the final response. Additionally, the procedure used to construct a caveability chart makes it difficult to include interactions between rock mass quality variables and the undercut area.

The model adjusted using PLS considers main and interaction effects. The main effect of a factor is calculated as the change in response between levels of the factor, whereas the interaction effect between factors is the difference in response between the levels of one factor at different levels of other factors. Both effects are relevant because a significant interaction effect may hide significant main effects. The model evaluated using PLS considers all main factors and incorporates interactions between factors but deletes all non-significant factors at $\alpha = 0.25$. Given the nature of results, data is transformed to a logarithmic scale, which means that responses are replaced by the natural logarithm of the original response, $Y' = \ln(Y)$.

Results presented in Figure 2 show the estimated regression coefficients for the PLS model with their individual estimated uncertainties, where x is the coded variable for factor i: factor A is joint orientation, factor B is joint persistence, factor C is joint intensity, factor D is intact rock properties, factor E is joint condition category, factor F is in-situ stresses magnitude, factor G is the undercut area and E:F is the two-factor interaction between E and F. The model considers two components that account for 86% of the variance in $\ln(Y')$ from X. A model with one component only explains 79% of the variance, while a model containing seven components can explain 93% of the variance.

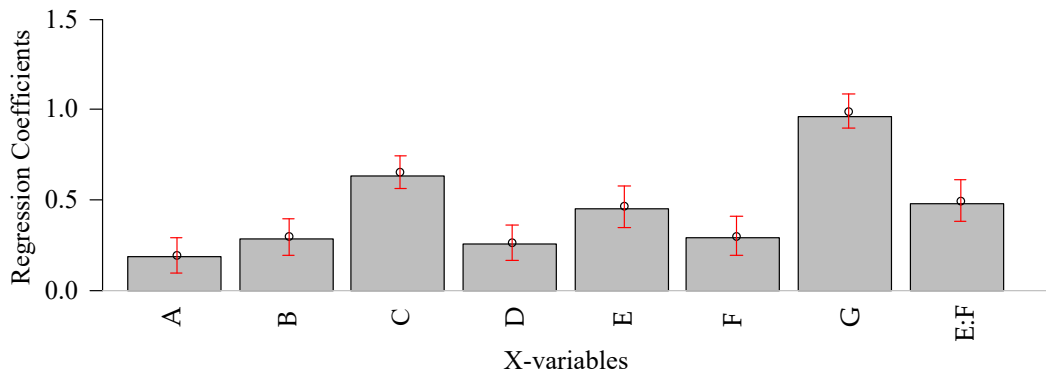


Figure 2. PLS regression coefficients (The bars indicate 95% confidence intervals).

The fitted versus the measured values are presented in Figure 3. The transformation of the data to a logarithmic scale and the incorporation of one two-factor interaction resulted in a plot that does not visually show anomalies. The variance explained by the model resulted in $R\text{-sq} = 0.86$. The variance that could not be explained by the model could have been generated by the complex model run in 3DEC, which incorporates blocks as discrete elements.

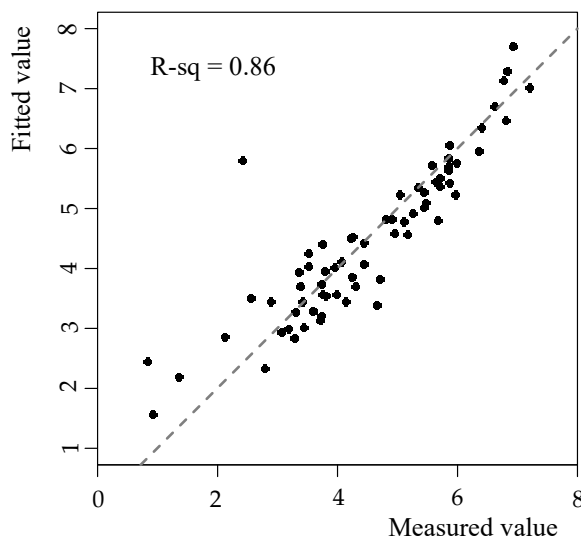


Figure 3. Cross-validated predictions for the response for the simplified model with two components.

The relationship between the X-variables is presented in Figure 4 in terms of the correlation loading. Two components are used to represent the problem: 1 and 2. The loadings (P') represent the coefficients of each variable for each component. The correlation loadings are plotted with concentric circles that correspond to 50% and 100% of the explained variance. The squared distance between the point defining one variable and the origin is equivalent to the variance fraction of the variable explained. Results indicate that the first component mostly represents the two-factor interaction E:F and factors A, B, E and G. The only factor that is not represented by the first component is C, which is mostly represented by the second component. In general, the variance of the system is mostly explained by factors C, E, E:F and G because they are close to the circle explaining 50% of the variance. The 2D visualization groups the factors representing the rock mass structure, A, B and C, in two different components, and C is the most significant factor of the second component. These results indicate that the interaction effect E:F is even higher than the effect of main factors.

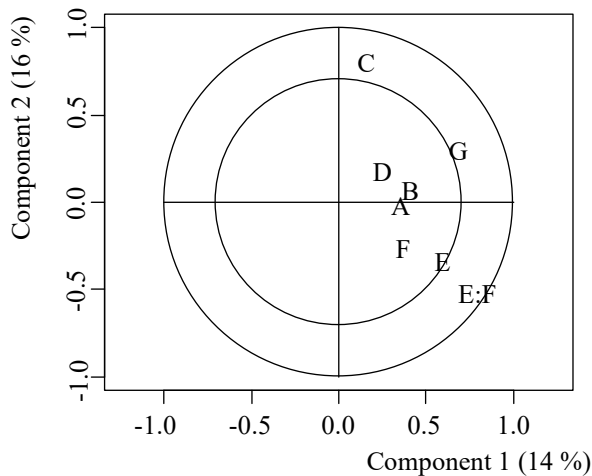


Figure 4. Correlation loading plot for the first two components.

In summary, the practical relevance of applying the PLS regression is that the responses can be predicted and compared using the coefficients presented in Equation 1.

$$\ln(Y) = 4.08 + 0.19X_A + 0.29X_B + 0.64X_C + 0.26X_D + 0.45X_E + 0.29X_F + 0.96X_G + 0.48X_{E:F} \quad (1)$$

where x_i is the coded variable for factor i : factor A is joint orientation, factor B is joint persistence, factor C is joint intensity, factor D is intact rock properties, factor E is joint condition category, factor F is in-situ stresses magnitude and factor G is the undercut area. Y is the volume at which displacements in the z-direction are higher than 1 cm, which is used as an indicator for caveability prediction.

5 CONCLUSIONS

This paper presented a PLS regression that reduced the multidimensionality of a problem from seven factors to two components to have a better visualization of the problem. This model was adjusted with results obtained from a numerical model and coefficients could be easily updated if more simulations need to be included. These results indicate that undercut area is critical for caveability and that joint intensity and the interaction between joint condition and in-situ stresses are significant in the final response. In other words, it means that joint intensity is relevant for caveability, as reported by some authors, and efforts should be directed in improving its characterization, but it is also important to evaluate the relationship between joint and stress condition. All these factors are related to the geology and cannot be changed. However, these factors need to be evaluated in a context defined by the mine design and the operation, which can be controlled and monitored. The use of traditional statistical techniques showed to be useful to highlight which parameters have a more significant effect on the final response and, therefore, where the efforts in rock mass characterization should be directed.

REFERENCES

- Baecher, G. B. & Christian, J. T. 2005. *Reliability and Statistics in Geotechnical Engineering*. John Wiley & Sons.
- Barton, N., Lien, R., & Lunde, J. 1974. Engineering classification of rock masses for the design of tunnel support. *Rock Mechanics*, 6(4), 189-236.
- Battulwar, R., Zare-Naghadehi, M., Emami, E., & Sattarvand, J. (2021). A state-of-the-art review of automated extraction of rock mass discontinuity characteristics using three-dimensional surface models. *Journal of Rock Mechanics and Geotechnical Engineering*, 13(4), 920-936.

- Bewick, R., Brzovic, A., Rogers, S., Griffiths, C. & Otto, S.A. 2022. Benchmarking framework for porphyry copper-gold rock masses for caveability and fragmentation decision-making. In Potvin (ed.); *Caving 2022: Fifth International Conference on Block and Sublevel Caving*, Perth, pp. 1303-1318.
- Brown, E. T. 2002. *Block Caving Geomechanics*. Brisbane: Julius Kruttschnitt Mineral Research Centre, The University of Queensland.
- Brzovic, A., & Villaescusa, E. 2007. Rock mass characterization and assessment of block-forming geological discontinuities during caving of primary copper ore at the El Teniente mine, Chile. *International journal of rock mechanics and mining sciences*, 44(4), 565-583.
- Duplancic, P. 2001. Characterization of caving mechanism through analysis of stress and seismicity. PhD Thesis, University of Western Australia.
- Einstein, H. H., Steiner, W. & Baecher, G. B. 1979. Assessment of empirical design methods for tunnels in rock. In Maevis & William (eds.); *Proceedings of the 4th Rapid Excavation and Tunneling Conference*, Atlanta: pp. 683-706.
- Cumming-Potvin, D., Wesseloo, J., Jacobsz, S.W. & Kearsley, E. 2018. A re-evaluation of the conceptual model of caving mechanics. In Potvin & Jakubec (eds.); *Caving 2018: Proceedings of the Fourth International Symposium on Block and Sublevel Caving*, Perth, pp. 179-190.
- Elmo, D. & Stead, D. 2020. Disrupting rock engineering concepts: is there such a thing as a rock mass digital twin and are machines capable of learning rock mechanics? In: Dight (ed.), *Proceedings of the 2020 International Symposium on Slope Stability in Open Pit Mining and Civil Engineering*, Perth, pp. 565-576.
- Franklin, J. A. 1993. Empirical design and rock mass characterization. In: Hudson (ed.) *Comprehensive Rock Engineering: Principles, Practice and Projects*. Pergamon Press.
- Hudson, J. A. 1992. *Rock engineering systems — Theory and practice*. Chichester: Horwood Ltd.
- James, G., Witten, D., Hastie, T. & Tibshirani, R. 2013. *An Introduction to Statistical Learning*. Springer.
- Jones, E., Sofonia, J., Canales, C., Hrabar, S & Kendoul, F 2019, Advances and applications for automated drones in underground mining operations; in Joughin (ed.), *Deep Mining 2019: Proceedings of the Ninth International Conference on Deep and High Stress Mining*, Johannesburg, pp. 323-334,
- Kendorski, F. S. 1978. The cavability of ore deposits. *Mining Engineering* 30(6): 628-631.
- Laubscher, D. H. 2000. *A Practical Manual on Block Caving*. Brisbane: Julius Kruttschnitt Mineral Research Centre, The University of Queensland.
- Lawal, A. I., & Kwon, S. (2021). Application of artificial intelligence to rock mechanics: an overview. *Journal of Rock Mechanics and Geotechnical Engineering*, 13(1), 248-266.
- Martens, H., Izquierdo, L., Thomassen, M. & Martens, M. 1986. Partial least-squares regression on design variables as an alternative to analysis of variance. *Analytica Chimica Acta*, 191: 133-148.
- Mawdesley, C. A. 2002. Predicting rock mass cavability in block caving mines. PhD Thesis, University of Queensland.
- McGaughey, J. 2019. *Artificial intelligence and big data analytics in mining geomechanics*. In Joughin (ed.); *Proceedings of the Ninth International Conference on Deep and High Stress Mining*, Johannesburg, pp. 45-54.
- Mevik, B.-H., Wehrens, R. & Liland, K. H. 2018. *Package 'pls': Partial Least Squares and Principal Component Regression* [Online].
- Milne, D. & Hadjigeorgiou, J. 2000. Practical considerations in the use of rock mass classification in mining; *Proceedings of the GeoEng2000 Conference*, Melbourne.
- Phoon, K. K., Ching, J., & Cao, Z. 2022. Unpacking data-centric geotechnics. *Underground Space* 7, 1-24.
- Rafiee, R., Ataei, M., Khalokakaie, R., Jalali, S. M. E. & Sereshki, F. 2016. A fuzzy rock engineering system to assess rock mass cavability in block caving mines. *Neural Computing and Applications*, 27(7): 2083–2094.
- Russo, A, Montiel, E & Hormazabal, E. 2022. Impact of the typical errors in geotechnical core logging for geomechanical design in large caving mines. In Potvin (ed.); *Caving 2022: Fifth International Conference on Block and Sublevel Caving*, Perth, pp. 1319-1334.
- Starfield, A. M., & Cundall, P. A. 1988. Towards a methodology for rock mechanics modelling. *International Journal of Rock Mechanics and Mining Sciences & Geomechanics Abstracts*, 25(3), 99-106.
- Suzuki Morales, K. & Suorineni, F.T. 2017. Using numerical modelling to represent parameters affecting cave mining. In Hudyma & Potvin (eds); *UMT 2017: Proceedings of the First International Conference on Underground Mining Technology*, Sudbury, pp. 295-307.
- Suzuki Morales, K., Suorineni, F.T., Hebblewhite B & Oh J. 2020. Investigation of the effect of critical parameters affecting caveability using numerical modelling. In Billaux, Hazzard, Nelson & Schöpfer (eds); *Proceedings of the 5th International Itasca Symposium*, Vienna, paper 11-03.

Geomechanical characterization of the rock mass in tunnels

J. Chable

JC Estudios Geotécnicos, Jalisco, Mexico

J. Lopez

Comision Federal de Electricidad, Ciudad de Mexico, Mexico

ABSTRACT:

This article shows the results of the geomechanical characterization of the rock mass, to demonstrate the importance of generating field information on its geotechnical characteristics, according to the results of the geological and geotechnical conditions of the study site, since the intact rock does not represent the entire rock mass. According to the results of the geological-geotechnical condition of the site, it is divided into two study zones, a rock zone and a breccia zone, in which the procedure to define the geomechanical properties of heterogeneous materials is described, based on information of field and laboratory, data that will be of great importance to be able to evaluate the stability and the necessary treatments in the excavations of the later works.

1 OBJETIVE

The main objective of this article is to present the geomechanical characterization in rock and breccia areas, as well as its analysis together with the results obtained from field work and laboratory tests.

2 METHODOLOGY

In order to synthesize the geomechanical characterization methodology of the rock mass, a process diagram was made specifying the activities to be developed in each work area.

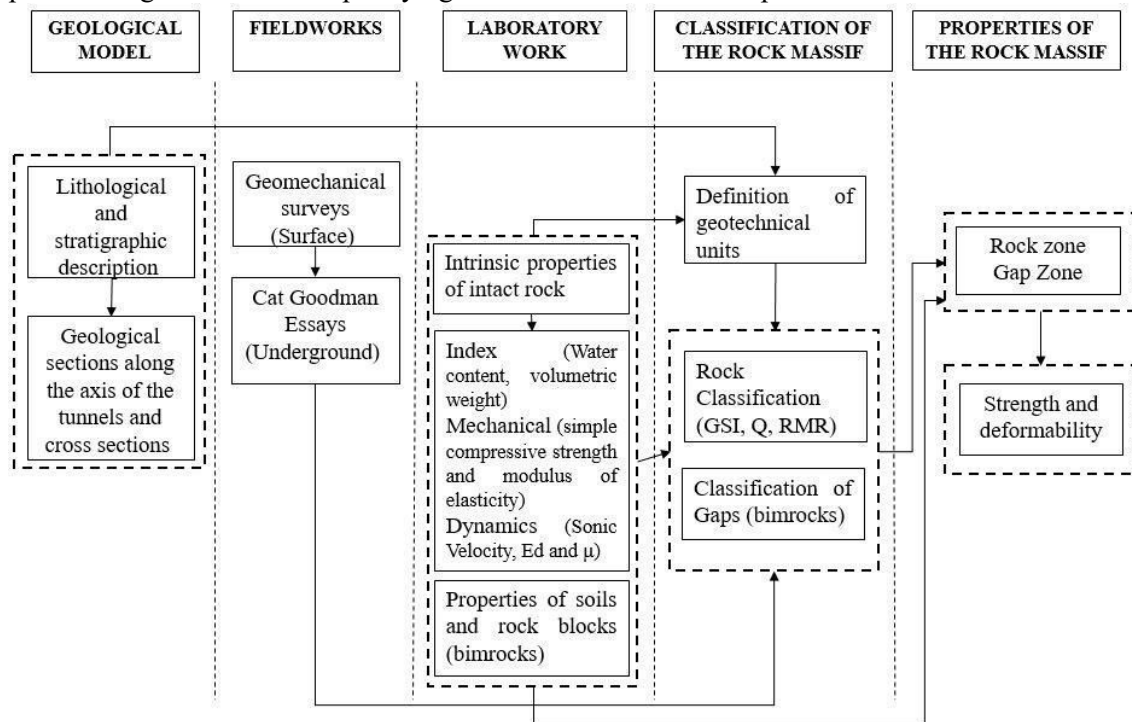


Figure 1. Geotechnical characterization process.

3 STRUCTURAL GEOLOGY

With the data obtained from the geological surveys carried out in the area, the stereogram of figure 4 was elaborated, these fault and fracture systems of the site also coincide with the orientations of the dominant systems at the regional level.

First, it began by identifying the orientations of the main fault and fracture systems in the study area.

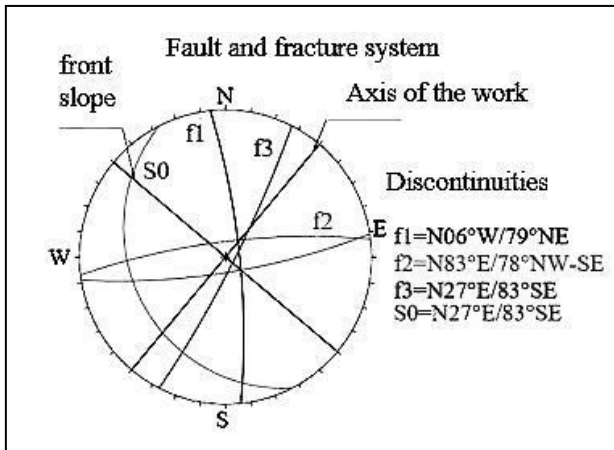


Figure 2. Stereogram with the orientations of the main fault and fracture systems.

4 LABORATORY WORK

In the laboratory work, healthy samples without alteration and without fractures are chosen to carry out simple compressive strength tests on them and thereby obtain the modulus of elasticity, as well as its dynamic properties (E_d and μ).

4.1 Index properties

The table 1 presents the average values corresponding to the water content and the volumetric weight of the tests carried out in the laboratory.

Table 1. Average values of index properties of the intact rock.

Description	Properties	UG-3a	UG-3b	UG-3c
		(Andesite)	(Oxidized andesite)	(Andesite Breccia)
Index Properties	Water content (%)	2.51	4.91	6.41
	Volumetric ambient weight (kN/m ³)	24.53	21.98	20.59

4.2 Mechanical properties

To evaluate the stress-strain behavior of the intact rock, simple compressive strength tests were performed to obtain the modulus of elasticity, as well as indirect and triaxial stress tests. The average results by rock type are shown in Table 2.

Table 2. Average values of mechanical properties of the intact rock.

Lithology	Description	σ_{ci}	E_{i50}	σ_t	m_i	Relation of Poisson
		(MPa)	(MPa)	(MPa)		
Ug-3a	Andesite	74	14,675	6.41	12	0.12
Ug-3b	Oxidized andesite	23	7,350	4.15	12	0.13
Ug-3c	Andesite Breccia	7.5	5,566	3.49	9	0.11

4.3 Classification of geotechnical units

In the rock mass classification, the geological information was taken as a reference, together with the results of the laboratory tests, the geotechnical units were defined.

Based on the above, the classification of (Deere and Miller, 1966) was used, which takes into account the simple compressive strength and the E_{t50} modulus of the intact rock.

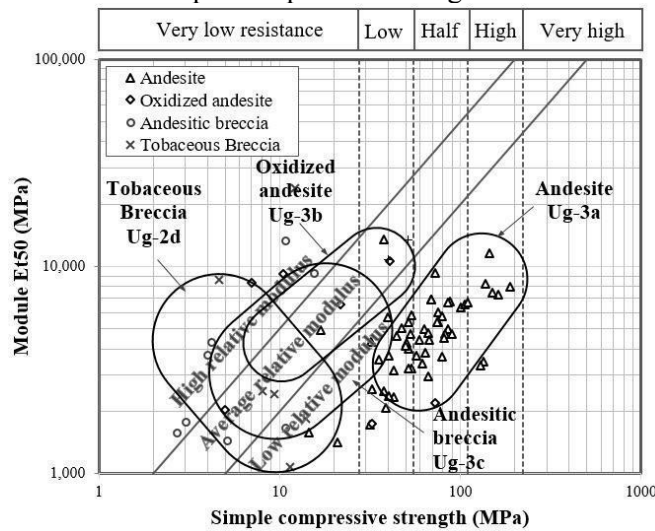


Figure 3. Classification of geotechnical units, Deere-Miller 1966 [1].

5 FIELD WORK

5.1 Geomechanical surveys

In the geotechnical characterization, during the field work, geomechanical surveys were carried out in the study area, in which an area of rocks and another of gaps were identified.

In the rock zone, geomechanical surveys were carried out with the methodology proposed by Bieniawski RMR 1989[2], Barton Q 2002 [3], Hoek GSI 2002 [4] and Morelli, 2017 [5].

In the breccia zone, the surveys were carried out with the methodology proposed by (Kalender et al. 2013) [6] for bimrocks.

Within these surveys, the degree of weathering of the rock is described, according to the method suggested by (ISRM, 1978) [7].

6 GEOMECHANICAL CLASSIFICATION

6.1 Rock Zone

For the geomechanical survey of the discontinuities in the rock zone, the following criteria were considered.

6.1.1 Compressive strength of discontinuities, JCS

To calculate the JCS value, the average rebound values are obtained with the Schmidt hammer for the different rock-rock contacts, to later calculate the resistance with the abacus of (Miller, 1965) [8], (Figure 4) or by means of the following equation:

$$\log_{10} JCS = 0.00088 \gamma r + 1.01 \tag{1}$$

Where, r is the average rebound value; γ is the volumetric weight of the rock in kN/m³; and JCS in MN/m²;

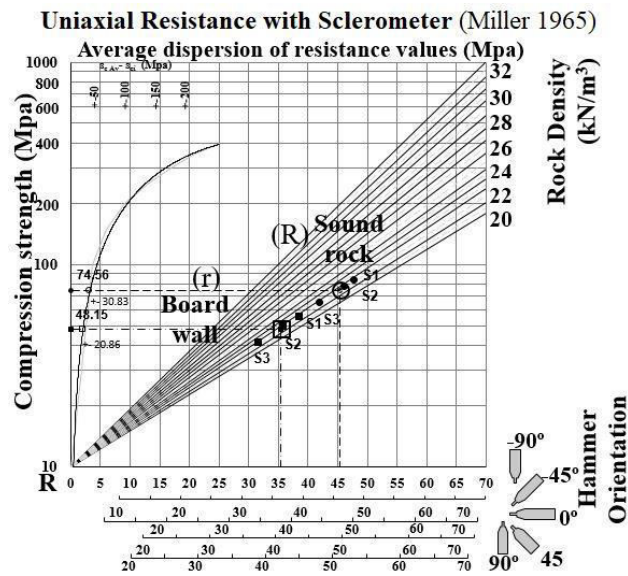


Figure 4. Abacus for calculating the JCS with the sclerometer in the field, from Miller 1965 [8].

6.1.2 Roughness, JRC

The roughness coefficient of the discontinuity (Joint Roughness Coefficient) was determined in the field on a small scale with the criterion (Barton-Choubey, 1977) [9], and on a large scale with that of (Barton, 1982) [10]. (Figure 5).

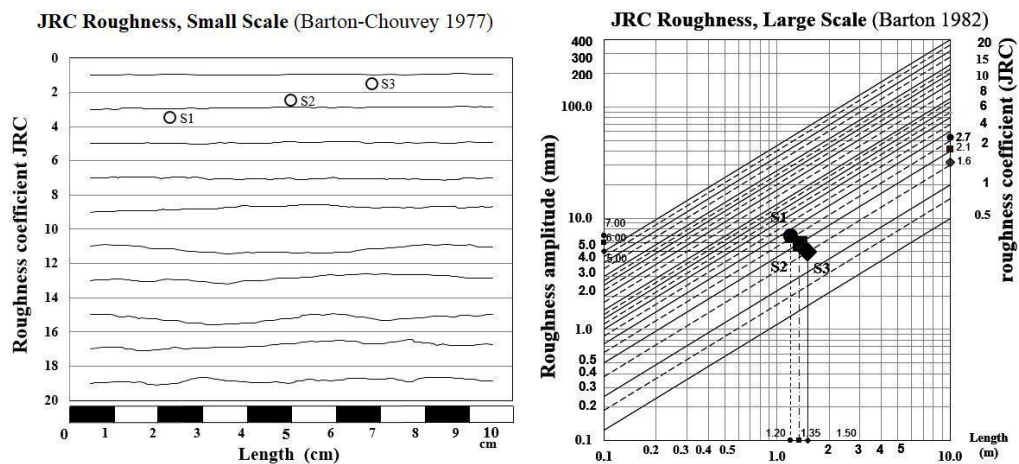


Figure 5. Abacus for calculating the JCS with the sclerometer in the field, from Miller 1965 [8].

6.1.3 Shear strength of discontinuities

To determine the shear strength of discontinuities in rock-rock contact, the Barton-Choubey criterion [9] was used:

$$\tau = \sigma_n \tan \left[JRC_n + \log_{10} \left(\frac{JRC_n}{\sigma_n} \right) \right] + \phi_r \quad (2)$$

Where, τ and σ_n are the tangential and normal stresses on the plane of discontinuity ϕ_r , is the angle of residual friction; JRC_n is the Joint Roughness Coefficient of the discontinuity; and JCS_n is the compressive strength of the walls of the discontinuity.

To calculate the residual friction angle ϕ_r , the following equation was used:

$$\phi_r = (\phi_b - 20) + 20 \left(\frac{r}{R} \right) \quad (3)$$

Where ϕ_b is the basic or sound rock angle, R and r are the rebounds of the sclerometer on sound rock and the joint wall, respectively, (figure 4).

The maximum friction angle is a function of the residual angle and the components of roughness and resistance of the discontinuities, given by the following equation:

$$\phi_{max} = JRC_n \left[\log_{10} \left(\frac{JRC_n}{\sigma_n} \right) \right] + \phi_r \quad (4)$$

$$\text{If } \left(\frac{JCS}{\sigma_n} \right) > 50, \quad \phi_{max} = \phi_r + 1.7(JRC) \quad (5)$$

The JRC and JCS values were normalized for the large-scale massif, according to the length of the discontinuities, by means of the equations:

$$JRC_n = JRC_0 \left(\frac{L_n}{L_0} \right)^{-0.02JRC_0} \quad (6)$$

$$JCS_n = JCS_0 \left(\frac{L_n}{L_0} \right)^{-0.03JCS_0} \quad (7)$$

The table 4 presents the estimation of the basic, residual and maximum friction angles in the discontinuities (rock-rock contact), for 3 fracturing systems in different geotechnical units.

Table 3. Basic, residual and maximum friction angle of discontinuities, Barton-Choubey criterion.

System	Friction angle	(Ug-3a)	(Ug-3a)
S1	ϕ (básico)	39	35
	ϕ_r (residual)	32	29
	ϕ (máximo)	41	40
S2	ϕ (básico)	35	35
	ϕ_r (residual)	31	30
	ϕ (máximo)	41	40
S3	ϕ (básico)	35	35
	ϕ_r (residual)	31	29
	ϕ (máximo)	41	40

6.1.4 Geological Strength Index, GSI

The GSI value (Geological Strength Index) was determined with the criteria of (Hoek et al. 2013) [11] using the equation:

$$GSI = 2J_{Cond76} + \left(\frac{RQD}{2}\right) \quad (8)$$

Where, J_{Cond76} = Condition of the joint (Bieniawski 1976) [12], RQD = Rock Quality Designation.

Additionally, the criterion of (Morelli, 2017) [5] was used to estimate the GSI value (Figure 6), which results from plotting the SR (Structure Rating) as a function of the SCR (Surface Condition Rating), which are described next.

$$SR = 1.75 \ln(J_v) + 79.8 \quad (9)$$

$$SCR = R_r + R_w + R_f \quad (10)$$

Where, J_v = joint volumetric index; R_r , R_w , and R_f are parameters from (RMR 1989) for joint roughness, fill, and alteration, respectively.

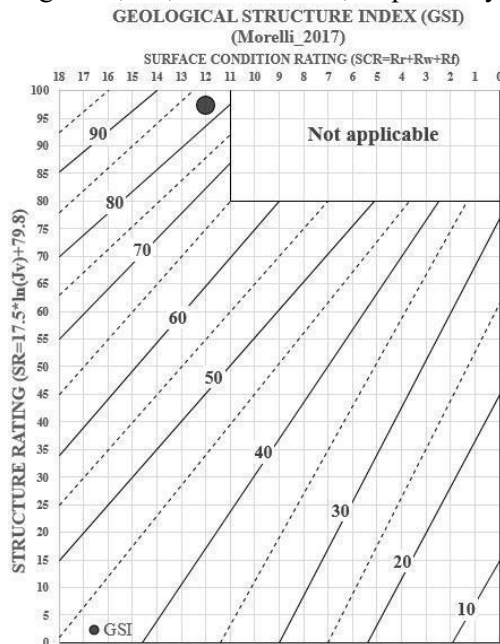


Figure 6. Calculation of GSI (Morelli, 2017) [5].

6.1.5 Strength and deformability

To calculate the resistance parameters of the Mohr-Coulomb criterion (c y ϕ) in the rock zone, the quality constants (m_b , s , a) representative of the rock mass in the area studied were calculated through the criterion of (Hoek-Brown 2002) [8], together with the GSI (Geological Strength Index) values. The approximation of the resistance parameters was obtained using the following equations:

$$\phi' = \sin^{-1} \left[\frac{6am_b(s+m_b\sigma'_{3n})^{a-1}}{2(1+a)(2+a)+6am_b(s+m_b\sigma'_{3n})^{a-1}} \right] \quad (11)$$

$$c' = \frac{\sigma_{ci} [(1+2a)s+(1-a)m_b\sigma'_{3n}](s+m_b\sigma'_{3n})^{a-1}}{(1+a)(2+a)\sqrt{(1+(6am_b(s+m_b\sigma'_{3n})^{a-1}))((1+a)(2+a))}} \quad (12)$$

Where, $\sigma_{3n} = \sigma_{3max} / \sigma_{ci}$

The deformability parameters were defined from the results of the laboratory mechanical tests and application of the empirical formula proposed by (Hoek and Diederichs 2006) [13]:

$$E_m = E_i \left(0,02 + \frac{1-D/2}{1+e^{((60+15D-GSI)/11)}} \right) \quad (13)$$

Where: E_i is the modulus of the intact rock, equivalent to Et50 and D is the disturbance factor, (values from 0 for unaltered rock masses and up to 1 for highly altered massifs).

6.2 Breccia Zone

As indicated in reference [6], the characterization of the breccia or mixed materials was carried out based on the methodology proposed by (Kalender et al., 2013), to evaluate the mechanical properties of materials formed by geotechnically significant blocks within a finer textured matrix (bimrocks). The mechanical parameters of these materials are estimated from the following equations:

$$\phi_{br} = \phi_m \left[1 + \frac{1000[(\alpha/\phi_m)-1]}{1000+5[(100-VBP)/15]} \right] \left(\frac{VBP}{VBP+1} \right) \quad (14)$$

$$RCS_{br} = \frac{\left(A-A \left(\frac{VBP}{100} \right) \right)}{(A-1)} (RCS_m) \quad (15)$$

$$c_{br} = \frac{(RCS_{br})(1-\sin(\phi_{br}))}{2\cos(\phi_{br})} \quad (16)$$

The RCS_m parameter (simple compressive strength of the matrix) was determined using several methodologies: with a Schmidt hammer (figure 7), to define the upper limit of resistance in areas where the cemented matrix was found, through laboratory tests on recovered cores and from empirical considerations according to the appearance of the matrix (ISRM, 1978) [7], figure 10.

The parameter ϕ_m (internal friction angle of the matrix), was determined from the results of the field tests (classification of the material and phicometer); as well as from laboratory triaxial tests.

The parameters VBP (volumetric proportion of blocks) and α (Angle of repose of the blocks) were determined from the number and shape of the blocks present in the characterized units. This information was primarily defined on representative excavation outcrops (figure 10).

According to (Sonmez et al. 2009) [14], the parameter A (figure 10) quantifies the contribution of the matrix and the blocks in the shear strength of the bimrock and can present values from 0 to 500. The value of A it increases when the adhesion between the blocks and the matrix increases, as well as when the angularity of the blocks increases (Table 4).

Based on the criteria described above, Table 4 presents the parameters identified in each geotechnical unit.

The deformability of the breaches was obtained in the field through pressure meter tests:

Table 4. Variation of parameter A (Sonmez et al., 2009) [13].

Test	Parameter A
No adhesion (cohesion) between blocks and matrix with rounded blocks.	0
Weak adhesion (cohesion) between blocks and matrix with half rounded blocks.	10
Moderate adhesion (cohesion) between blocks and matrix with half angular blocks.	50
Strong adhesion (but less than matrix cohesion) between blocks and matrix with angular blocks.	500

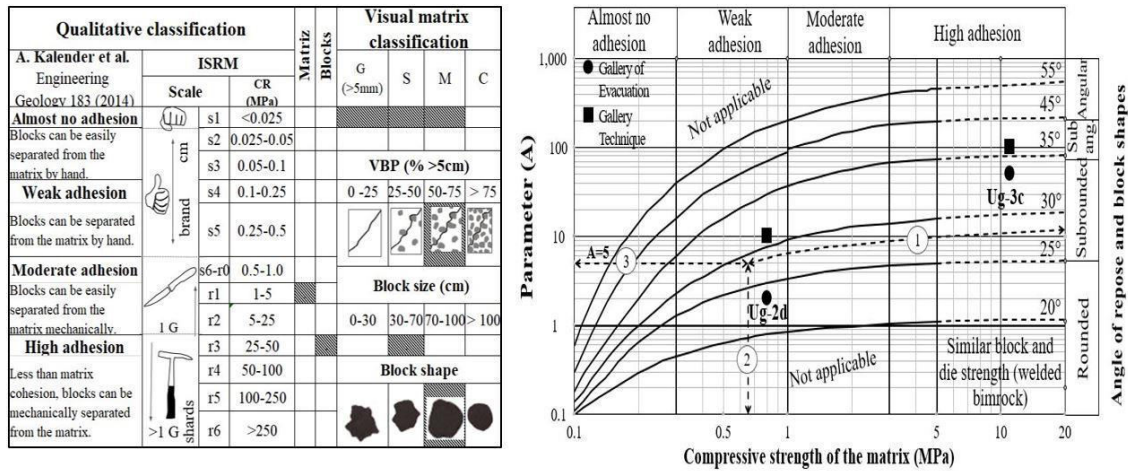


Figure 7. Bimrock qualitative, visual and “A” parameter classification (matrix and block size), (A. Kalender et al. Engineering Geology 183, 2014) [5].

Table 5. Characterization parameters of the gaps.

Geotechnical Unit	Block Size (m)	V.B.P (%)	Angle of repose	Parameter A
Ug-2d	0.15-0.25	25-50	22-32	2-10
Ug-3c	0.20-0.30	50-75	30-40	50-100

7 PROPERTIES OF MATERIALS IN ROCK AND BRECCIA ZONES

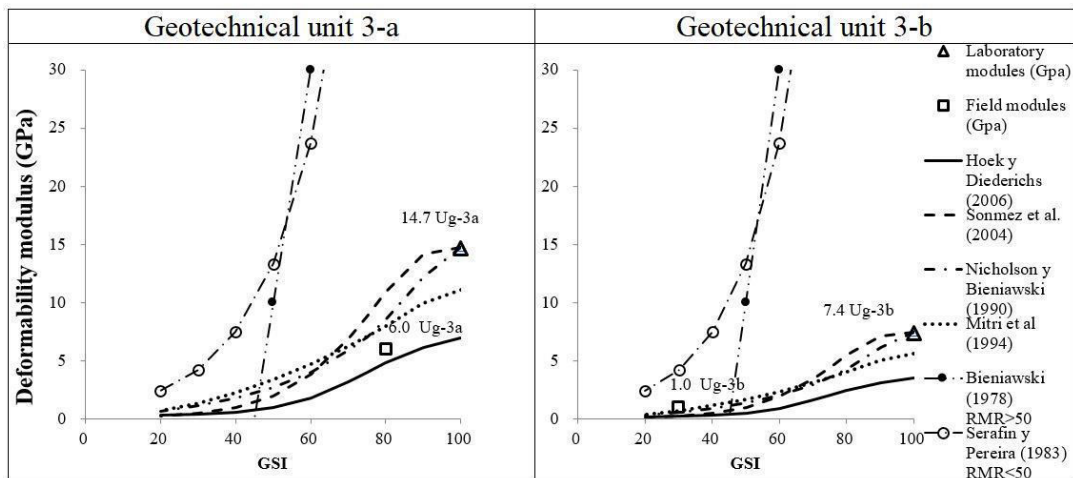
7.1.1 Strength and deformability

According to the criteria indicated in section 6, Table 6 presents the parameters determined for each geotechnical unit, being the equation of (Hoek and Diederichs, 2006) [13], the one that most closely approximates the parameters of the rock mass, (figure 11).

Table 6. Characterization parameters of the gaps.

Geotechnical Unit	RMR	Q	GSI	Rock Mass constant m_i	Cohesion c (MPa)	Friction angle ($^\circ$)	Deformability modulus E_m (GPa)
Ug-3a (Andesita)	87	32	84	12	1	47	6
Ug-3b (Andesita Oxidada)	22	11	22	12	0.28	40	1
Ug-2d (Brechas Tobácea)	NA	NA	NA	9	0.15	30	0.1
Ug-3c (Brecha Andesítica)	NA	NA	NA	9	0.2	37	0.7

NA, Does not apply



.Figure 8. Rock mass deformability with empirical equations, Hoek and Diederichs 2006 [13].

8 CONCLUSIONS

Derived from the geomechanical surveys that were carried out in the excavation area of the technical and evacuation galleries of the bitunnel, as well as the field and laboratory tests carried out, it was possible to zone the materials and determine the most appropriate methodologies to determine quality parameters, resistance, deformability and treatments of the rock mass.

In relation to the andesite lithological unit, two conditions were presented in the rock mass, one with average RMR values of 80 and the other with 22, as well as simple compressive strength of the intact rock of 74 and 23 MPa, respectively. Treatments ranged from selective anchoring for the most favorable condition, to metal frames and shotcrete for the most critical condition.

In the zone of andesitic and tuffaceous breccias, there is an average V.B.P. of 25-50% and a matrix of low resistance, which corresponds to a treatment of metal frames every meter and shotcrete with a thickness of 0.10 m.

REFERENCIAS

- [1] Deere, D. U., & Miller, R. P. 1966. Engineering classification and index properties for intact rock. Illinois Univ. At Urbana Dept. Of Civil Engineering.
- [2] Bieniawski, Z. T. 1989. Engineering rock mass classifications: a complete manual for engineers and geologists in mining, civil, and petroleum engineering. John Wiley & Sons.
- [3] Barton N. 2002. Some new Q-value correlations to assist in site characterisation and tunnel design. International journal of rock mechanics and mining sciences.
- [4] Hoek, E., Carranza-Torres, C.T., and Corkum, B. (2002): 2002. Hoek-Brown failure criterion, edition. Proc. North American Rock Mechanics Society.
- [5] Morelli, G. L. 2017. Alternative Quantification of the Geological Strength Index Chart for Jointed Rocks, Springer International Publishing AG.
- [6] Kalender, A.; Sonmez, H.; Medley, E.; Tunusluoglu, C.; Kasapoglu, K.E. 2014. An approach to predicting the overall strengths of unwelded bimrocks and bimsoil, Hacettepe University, Department of Geological Engineering, Applied Geology, Division, Oakland, CA, USA.
- [7] ISRM. 1978. Suggested Methods for the Quantitative Description of Discontinuities in Rock Masses. International Journal of Rock Mechanics and Mining Sciences & Geomechanics Abstracts, 15, 319-368.

- [8] Miller, R.P. 1965. Engineering classification and index properties for intact rock. Tesis de Doctorado, University of Illinois.
- [9] Barton, N., & Choubey, V. 1977. The shear strength of rock joints in theory and practice. *Rock Mechanics* 1/2:1-54.
- [10] Barton, N. 1982. Modelling rock joint behaviour from in situ block tests: implications form nuclear waste repository design. Office of Nuclear Waste Isolation, Columbus, Ohio, ONWI-260.
- [11] Hoek, E., Carter, T.G., Diederichs. 2013. Quantification of the Geological Strength Index Chart. 47th US Rock Mechanics / Geomechanics Symposium, San Francisco, CA, USA.
- [12] Bieniawski Z. T. 1976. Rock mass classification in rock engineering applications. *Proceedings of a Symposium on Exploration for Rock Engineering*, Vol. 12, pp. 97-106.
- [13] Hoek, E., Diederichs, MS. 2006. Empirical estimation of rock mass modulus”, *International Journal of Rock Mechanics and Mining Sciences*, 43(2), 203-215.
- [14] Sonmez, H., Kasapoglu K.E, COSKUN A, Tunusluoglu, C., Medley, EW., Zimmerman, RW. 2009. A conceptual empirical approach for the overall strength of unwelded bimrocks. *ISRM Regional Symp. Rock Engineering in Difficult Ground Conditions, Soft Rocks and Karst*, (pp. 357-360).

Effect of water content on the physico-mechanical properties of mudstone of Shimajiri Formation and its water absorption and desorption characteristics

T. Ito, Ö. Aydan and N. Tokashiki,
University of the Ryukyus, Okinawa, Japan

ABSTRACT:

The authors have been involved with the evaluation of physico-mechanical properties of mudstone as a function of water content. Furthermore, they have attempted to evaluate groundwater diffusion characteristics of mudstone and related volumetric changes. In experiments, some samples failed along some existing structural weakness planes and the experiments also revealed physico-mechanical characteristics of these weakness planes related to faulting in Shimajiri formation during their tectonic past. The authors present the outcomes of various experiments and discuss their implications in practice.

1 INTRODUCTION

Ryukyu Islands constitute the south-west part of the Japanese archipelago. The age of the basement is pre-Cenozoic and the basement rocks are chert and schists. Cenozoic sandstone, shale and limestone overlay the basement rocks. These rock units are followed by Tertiary Shimajiri formation and all formations are covered by Quaternary Ryukyu limestone and Holocene deposits (Figure 1). The geo-engineering issues are mainly associated with the Shimajiri formation and Ryukyu Limestone. Landslides in Shimajiri formation are major geo-engineering problems. In recent years, many twin shallow tunnels are constructed in Shimajiri formation. In addition, some underground shelters remaining from the Second World War exist and cause some sinkhole issues from time to time.

It is well known that they are subjected to degradation due to cyclic wetting and drying in relation to the water content variation. They also have time-dependent characteristics. The intact mudstone has uniaxial compressive strength (UCS) ranging between 0.6-3.6 MPa under natural water content conditions. Particularly, younger mudstone belonging to Shinzato Formation has lower UCS while older mudstone belonging to Yonabaru Formation has higher UCS. When mudstone layers are exposed to atmospheric conditions they absorb or desorb water and they exhibit volumetric swelling or shrinkage. This interaction with water causes their degradation and their physico-mechanical properties become a function of water content.

The authors have been involved with a project where the mudstone layers belonging to Shinzato Formation and having some small normal faults caused some instability problems during a construction of a deep waste storage facility as a result of groundwater level changes during a heavy rainy period. New horizontal borings were done and cores from these borings utilized for tests on uniaxial compressive strength and Brazilian tests under different water content. The experimental studies involved the evaluation of physico-mechanical properties as a function of water content. Furthermore, groundwater diffusion characteristics of mudstone and related volumetric changes are experimentally investigated. During experiments, it is observed that some samples failed along some existing structural weakness planes. As landslides in Shimajiri formation generally involve existing discontinuities such as faults and bedding planes, these experiments also revealed physico-mechanical characteristics of these weakness planes related to faulting in Shimajiri formation during their tectonic past. The outcomes of various experiments are presented and their implications on their degradation characteristics are discussed.

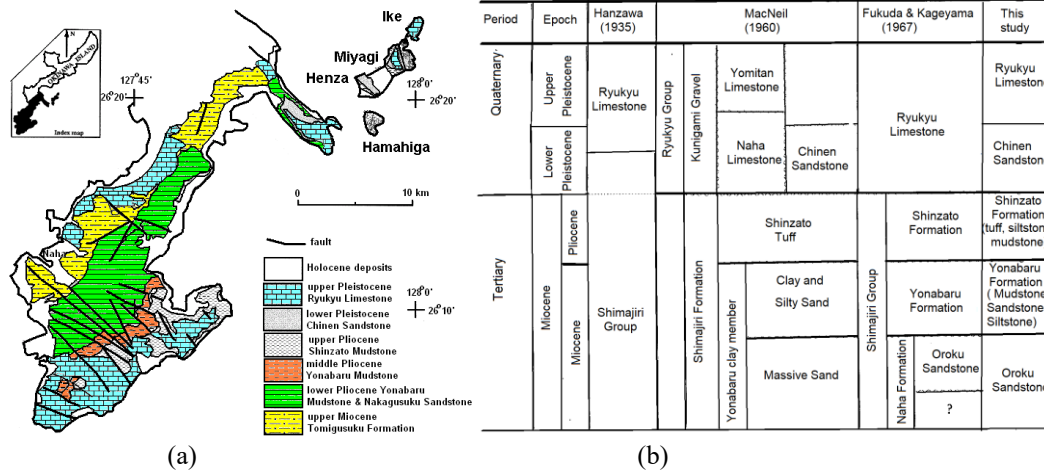


Figure 1. (a) Regional geology and (b) interrelations of geologic units and their interpretation.

2 A SUMMARY OF PREVIOUS STUDIES ON ROCKS OF SHIMAJIRI FORMATION

Shimajiri formation broadly classified into Shinzato, Yonabaru and Naha Formations. Experimental results on mudstone and sandstone samples of Shinzato and Yonabaru formations were summarized by Tokashiki and Aydan (2010). Table 1 give some mechanical properties of sandstone and mudstone. The sandstone of Shimajiri Formation has a very low strength ranging between 300-340kPa and it is very porous. The intact mudstone has uniaxial compressive strength (UCS) ranging between 0.6-3.6 MPa under natural water content conditions. Particularly, younger mudstone belonging to Shinzato Formation has lower UCS while older mudstone belonging to Yonabaru Formation has higher UCS.

Table 2: Properties of Shimajiri Formation

Type	γ (kN/m ³)	σ_c (MPa)	c (MPa)	ϕ_i
Sandstone	17.6-22.6	0.34	0.1	34-38
Mudstone	14.7-18.5	0.6-3.6	0.4-1.1	24-28

In-situ tilting tests on bedding planes of dry samples of Shimajiri formation indicated that the friction angle ranges between 34-38 degrees. Tilting tests on saw-cut surfaces in laboratory ranged between 24-28 degrees. The friction angle of saw-cut surfaces of Ryukyu limestone ranges between 24-28 degrees. The natural surfaces of Ryukyu limestone are generally rough and the friction angle is more than 36 degrees. Table 2 summarizes the frictional properties of interfaces.

Table 2. Frictional properties of discontinuities

Interface	Friction angle
Sandstone to sandstone (sawcut)	34-38
Mudstone to mudstone	24-28
Sandstone to mudstone	32-36
Mudstone natural	28

The authors carried out visual observations and investigations on Shimajiri formation. The characterization of the Shimajiri formation was done at Kita-Uebaru landslide, Shikina tunnel in Okinawa island and Shimajiri area of Miyakojima Island. When Shimajiri formation is exposed to atmosphere, it easily disintegrates by slaking and it becomes like a soil. Except such zones, it

may be called soft sedimentary rocks. The characterization of Shimajiri formation according to rock classification systems such as RMR, Q-system and RMQR are given in Table 3.

Table 3: Rock classifications of Shimajiri Formation.

Rock Type	BASIC RMR	Q-Value	RMQR
Mudstone(Kitauebaru)	32 - 38	0.8-2.1	22-28
Mudstone (Shikina)	39 - 44	2.7-5.5	28-35
Sandstone(Kitauebaru)	32 - 42	0.8-2.1	29-32

3 EXPERIMENTS ON MUDSTONE BELONGING TO SHINZATO FORMATION

As mentioned previously, the geology of the project site is designated to be belonging to Shinzato formation and it is located in the southern part of Okinawa Main Island (see Figure 1a). As this formation contains tuff layers and cliffs up to 30 m are observed in this formation, it is believed that any deep excavation in this formation would be stable. However, a 14 m deep excavation caused some structural instability problems after a heavy rainy period and the authors were consulted about the possible causes. The authors present some experimental data in this section in relation to the causes of instability.

3.1 Sample Preparations

Samples of mudstone for uniaxial compression and Brazilian tests were prepared from the cores of three horizontal borings at selected depth. At least, three experiments on mudstone with their original natural water content were carried out. In addition, samples were wrapped with wet towels in order to increase their water content and to determine their maximum water content absorption capacity. Figure 2 shows several stages of sampling, sample preparation and samples. Some of samples were naturally dried to perform uniaxial compression and Brazilian tests under different water contents.



Figure 2. Views of stages of sampling, samples and sampling preparations

Table 4. Unit weight and water content of samples.

Parameter	Range	Average
Saturated unit weight	19.97-20.35	20.22
Dry unit weight	15.11-16.08	15.76
Maximum water content	27.3-33.0	29.10

3.2 Mechanical Tests

Strain-stress relations for uniaxial compression and Brazilian tests of samples with different water content are shown in Figure 3. Although the specific values of water content for each curve are not shown in the respective figures, the curves show the possible range of relations from dry to fully saturated conditions. The results are re-plotted and discussed in the next section. Nevertheless, the most important implication is that strain-stress responses of rocks, which absorb or desorb water, would be quite different.

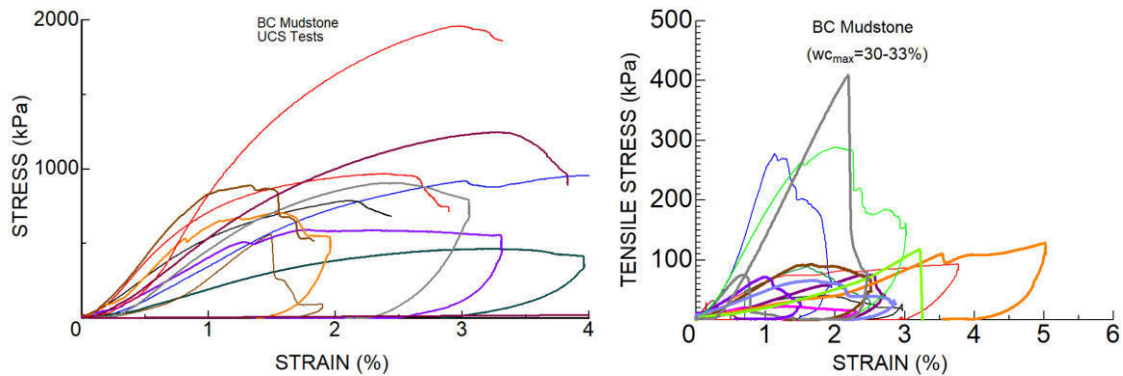


Figure 3. Strain-stress responses of mudstone under uniaxial compression and Brazilian tests.

Figure 4 shows the several relations of experimental results shown in Figure 3 and compares the similar results of mudstone belonging Shimajiri Formation. Figure 4(a) shows the relation between UCS and elastic modulus together with the empirical relation proposed by Aydan et al. (1993) for squeezing rocks. As noted from the figure, the experimental results follow almost the same trend of the estimation from the empirical relation.

The elastic, peak and flow strain limits are quite important for the assessment of the stability of structures such as tunnels during excavation. Figure 4(b,c,d) show the elastic, peak and flow strain limits as a function of uniaxial compressive strength. In the respective figures, some empirical relations are also shown. The overall experimental results follow previously established empirical relations by Aydan et al. (1993, 1996) and Aydan and Tokashiki (2017).

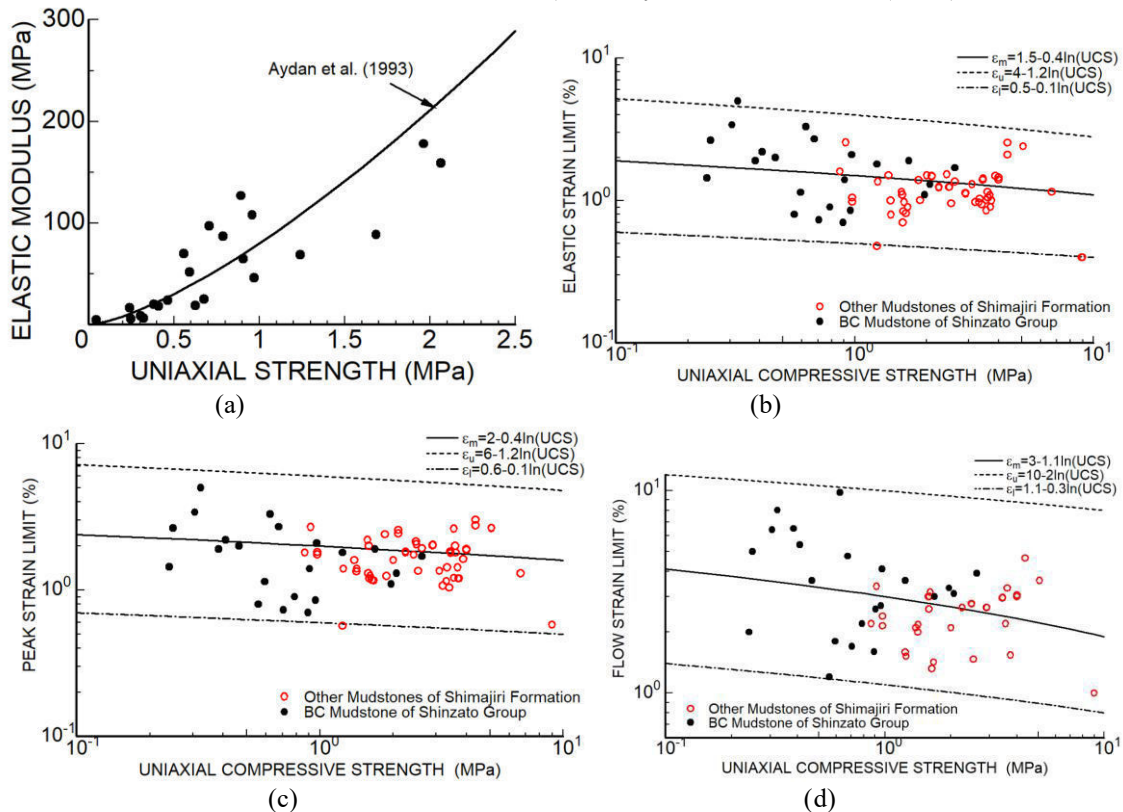


Figure 4. Relations among several parameters of mudstone and comparisons with the available data of mudstone belonging to Shimajiri Formation.

3.3 Water Diffusion Characteristics and Volumetric Strain Changes

Water absorption and desorption processes of rocks involve volumetric changes as discussed previously by Aydan et al. (2006) and Aydan (2016). These volumetric changes may induce expansion upon water absorption and shrinkage upon water desorption. Aydan (2003, 2016) described some experimental set-ups to measure volumetric strain changes in relation to the water content variations. One of the easiest ways is to allow rock specimen to dry out under natural room condition. Figure 5 shows an example for water content and saturation variations of a mudstone sample during absorption and desorption processes. As noted from the figure, water absorption occurs almost in 17.08 hours while the water desorption takes place for duration of about 130 hours. In other words, the time required for drying process is almost 7.6 times that required for absorption process. In practice, the water impregnation into rock would occur in a very short period of time. If the mechanical properties of rocks and discontinuities are vulnerable to water content increase, the instability problems would take place soon after heavy rain-falls. This was the actual case studied in this paper.

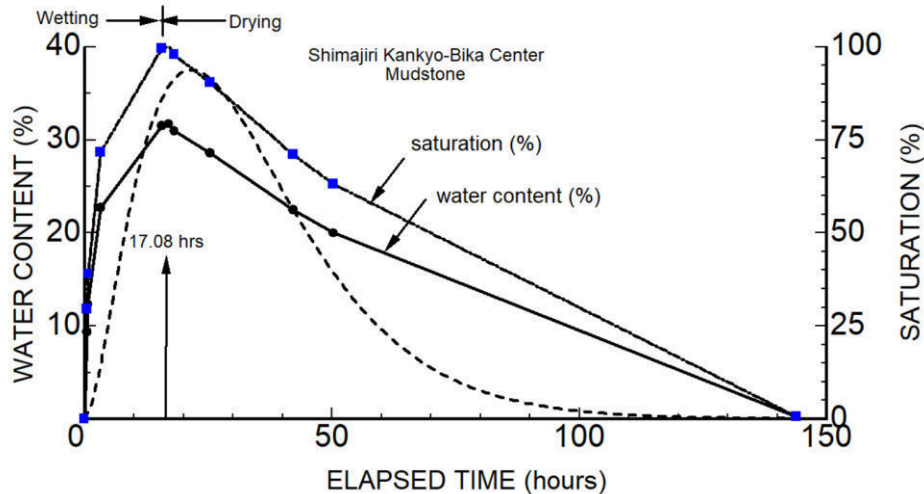


Figure 5. Water content and saturation variations during absorption and desorption processes.

As an ultimate situation, the mudstone was powdered and it was made to be in a slurry state, initially. The slurry mudstone powder was put in a container with a size of 98.6x98.6x80 mm. Figure 6 shows the views of the sample during drying process. As noted from the figure, cracking took place and the clay-cake shrunk in plan and vertically. The vertical shrinkage was about 20%. Regarding the cracking area, an image analysis was carried out using the image in the center of Figure 6. Figure 7 shows the digitized image and its converted black and white image for image processing. The image analysis indicated that the area of cracks was 1874 mm² and the ratio of the crack area over the total area (9722 mm²) was obtained as 19.3%. This value is very close to the vertical shrinkage strain obtained from the side-view images.

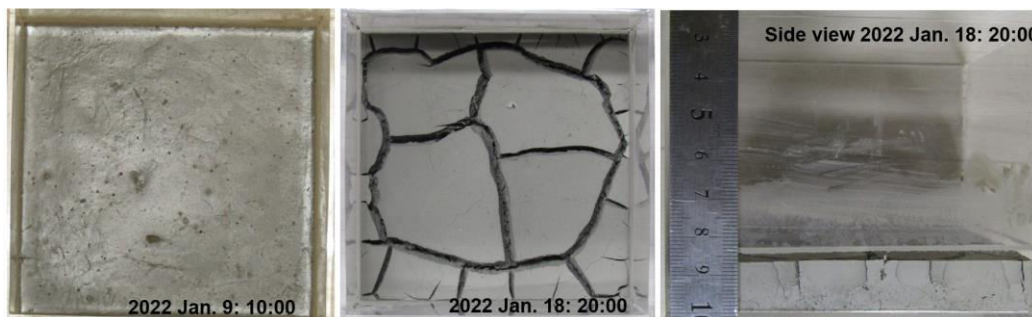


Figure 6. Top and side views of clay-cake at different times

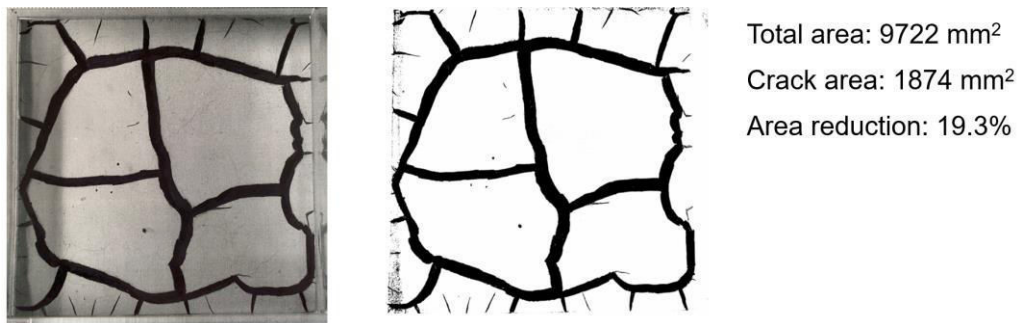


Figure 7. Results of the image processing.

The same experiment was repeated while measuring both the water content variation and shrinkage simultaneously. Figure 8 shows the water content variation and shrinkage strain, which was computed from the vertical settlement of the sample surface. The state of sample changed from slurry state to solid state approximately after 460 hrs and cracks started to appear at the surface of the sample. The shrinkage strain increases almost linearly with time up to 760 hours and the shrinkage strain tended to become asymptotic to 20% shrinkage value. This value was also quite similar to the previous experiment. It should be noted that the top surface of the sample is in touch with air. The experimental results presented herein can be used to assess the volumetric straining using some procedures for evaluating material properties relate to coupled finite element analyses done previously by Aydan et al. (1994, 2006) and Aydan (2016).

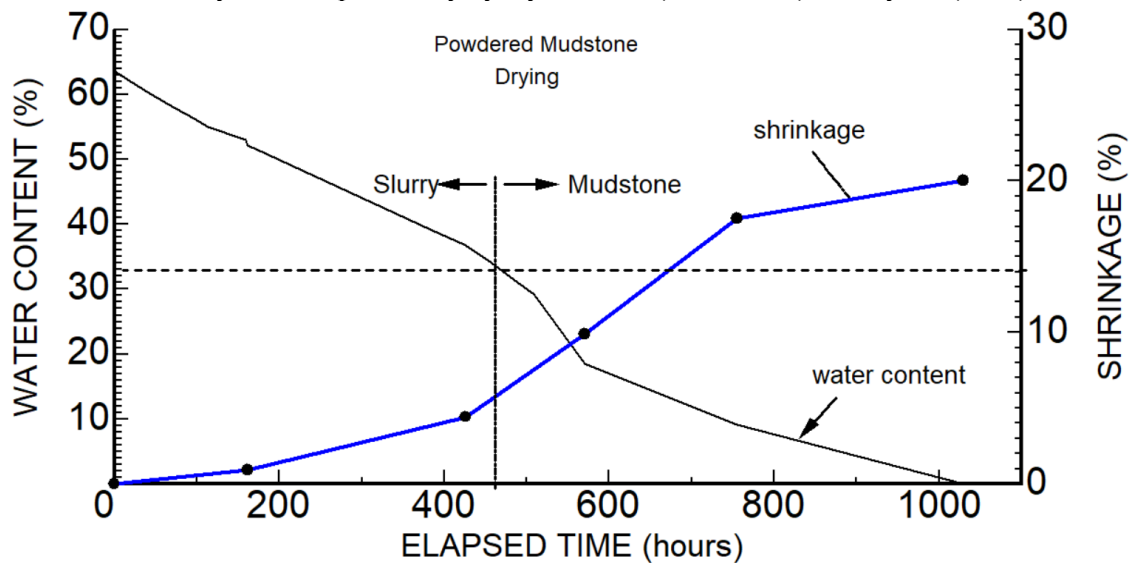


Figure 8. The water content variation together with shrinkage for powdered mudstone.

4 EFFECT OF WATER-CONTENT ON PHYSICO-MECHANICAL PROPERTIES

In this section, the effect of water content on physico-mechanical properties of mudstone belonging to Shinzato Formation is discussed. Figure 9 shows the variation of uniaxial compressive strength (UCS) and Brazilian tensile strength (BTS) as a function of water content. As noted from the figures, the UCS and BTS decrease with increase of water content variation. The yield function incorporating the effect of water content may be given as a convolution of classical yield criterion and water content influence function as given below (Aydan et al. 2014, Aydan 2022).

$$f^* = f \cdot g(\theta) \tag{1}$$

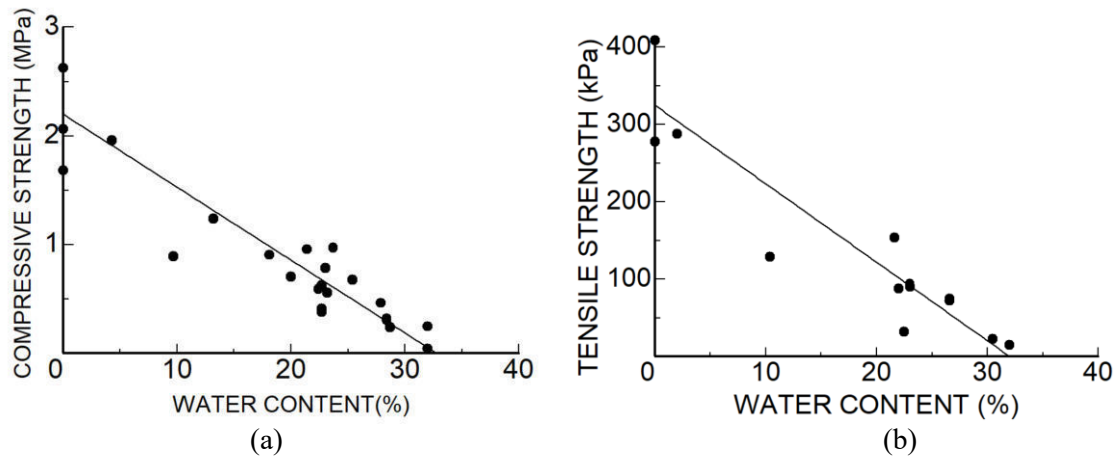


Figure 9. the variation of (a) UCS and (b) Brazilian tensile strength (BTS) as a function of water content.

The water content influence function may be specifically given as

$$g(\theta) = 1 - a \frac{\theta}{\theta + \beta(100 - \theta)} \quad (2)$$

Where θ , a and β are water content (%) and empirical coefficients. Considering the experimental results shown in Figure 8, the specific form of Eq. (2) takes the following form:

$$g(\theta) = 1 - 3\theta \quad (3)$$

If Mohr-Coulomb yield criterion is used and is applied to the experimental results, one can easily get the results shown in Figure 10. As noted from this figure, the friction angle remains almost constant while the cohesion decreases with the increase of water content. This experimental fact clearly illustrates why structures fail when they are excavated in rocks prone to the effect of water absorption and desorption processes.

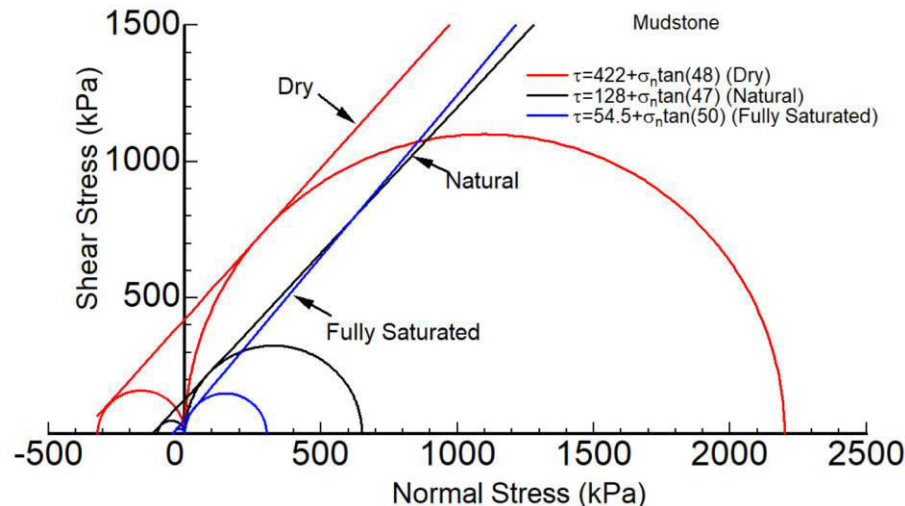


Figure 10. Illustration of the effect of water content on yield criterion for mudstone.

The instability of the deep excavation was associated with pre-existing minor normal faults as seen in Figure 11(a). The strikes of these minor faults were parallel to the longitudinal and transverse side of the excavation pit. The horizontal borings at three levels on the longitudinal side of the excavation were implemented. As the dip angle of these minor faults was about 45 degrees. There was a high possibility that cores may contain some minor weakness planes. During both UCS and BTS experiments some samples failed along the weakness planes as expected.

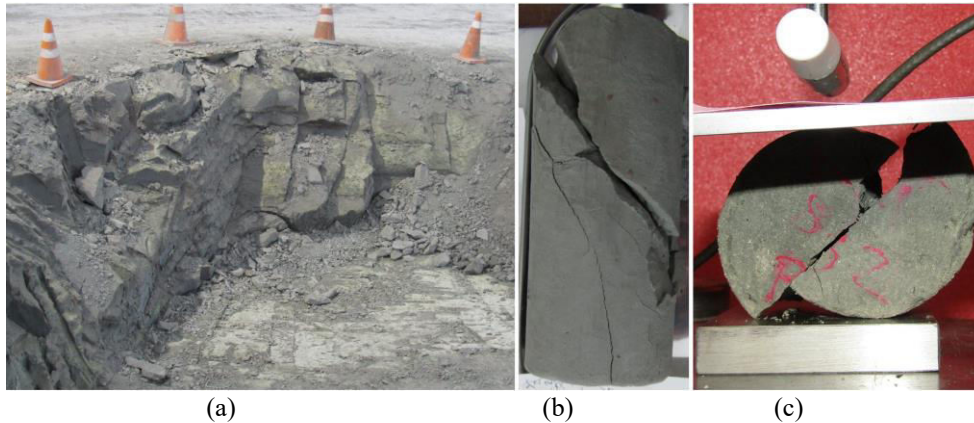


Figure 11. (a) Views of minor faults, failure along weakness planes in (b) UCS and (c) BTS tests.

Some friction experiments on mudstone weakness planes and minor faults were performed. Experiments indicated that the friction angle ranged between 30.4 and 34.0 degrees with an average value of 31.64 degrees. Assuming that the friction angle of weakness plane is equal to the average value of friction angle, the cohesion would be obtained as 14.4 kPa and 8.83 kPa for natural water content and fully saturated states, respectively. These results are illustrated in Figure 12 using Mohr-Coulomb type yield criterion. As noted from the figure, the overall strength of rock mass would be drastically reduced by the existence of weakness planes. This experimental finding also confirms why the instability took place in the deep excavation.

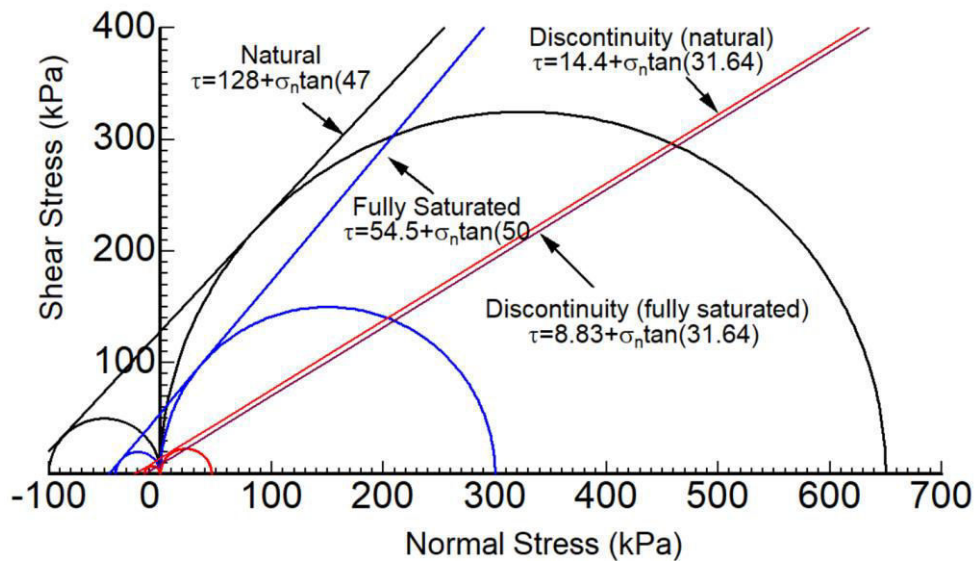


Figure 12. Illustration of the effect of weakness plane and water content on yield criterion for mudstone.

Needle penetration index is particularly useful for evaluating properties of rocks belonging to Shinzato and Yonabaru Formations (Aydan and Tokashiki 2017). Aydan et al. 2014 proposed some empirical relations and it was shown that they can be used to assess the mechanical properties of soft rocks in Okinawa Prefecture, Japan. Figure 13 shows a view of testing and experimental responses of penetration vs. applied force. As noted from this figure, the overall needle penetration index (NPI) decreases in relation to the increase of the water content. One of the interesting observations is that the pull-out resistance of the needle also increases as the water content decreases. This feature can be also utilized to infer additional mechanical properties from this index testing technique.

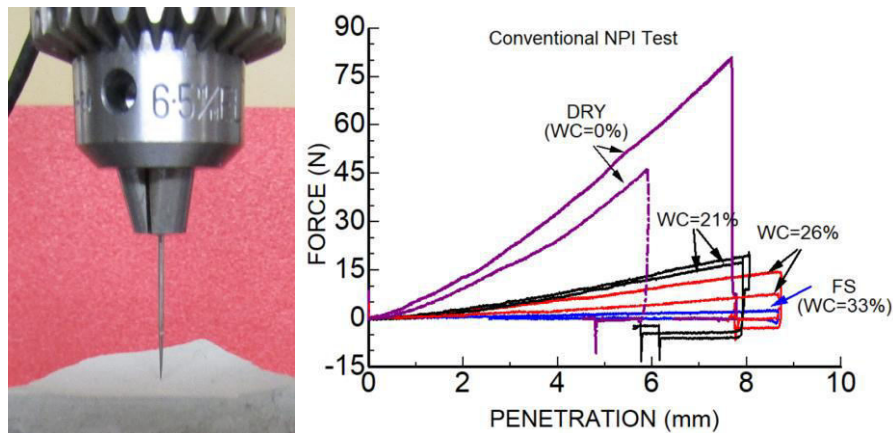


Figure 13. A view of testing and experimental responses of penetration vs. applied force for various water content.

Aydan et al. (2008) developed another needle penetration index device using a needle with a circular flat tip. The diameter of the needle can be various. However, Aydan et al. (2008) suggests the utilization of needle with a diameter of 3 mm. Figure 14 shows the nominal penetration strain versus nominal tip pressure. As shown by Aydan et al. (2008), one can evaluate the mechanical properties of rocks from a single response of nominal penetration strain versus nominal tip pressure. Therefore, one will be also able to infer the mechanical properties of soft rocks from this testing technique with different water content.

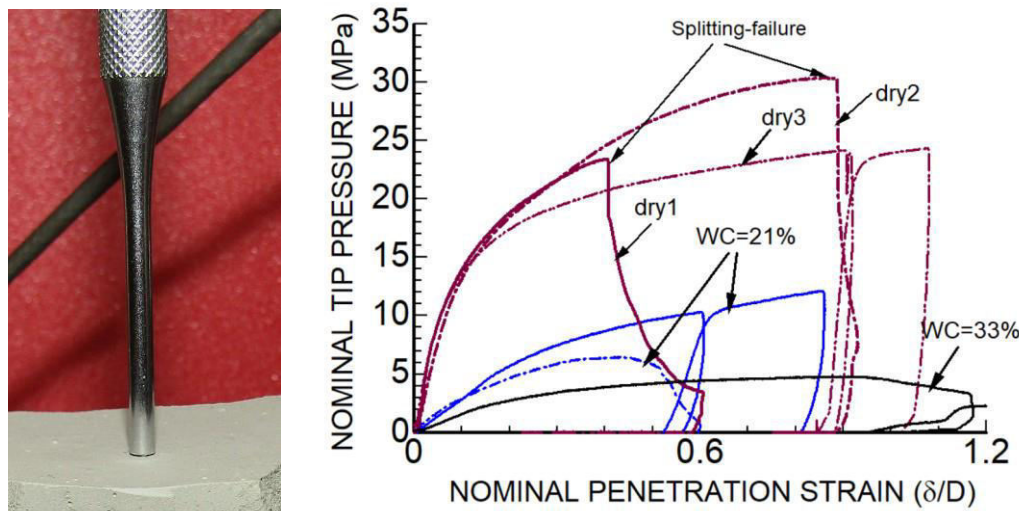


Figure 14. A view of testing and experimental responses of the nominal penetration strain versus nominal tip pressure for various water contents.

5 CONCLUSIONS

The authors attempted to evaluate the physico-mechanical properties of mudstone belonging to Shinzato Formation with different water contents. The physico-mechanical properties of this mudstone are lower than those of the mudstone of Yonabaru Formation as its geological age is younger and natural water content is higher. Unfortunately, many engineers wrongly interpret this mudstone as weathered on the basis of unsuitable index parameter SPT, which may be only valid for soils not even soft rocks.

The procedures presented or mentioned in this study could be effectively used to assess the physico-mechanical properties as a function of water content.

It is also shown that the mudstone cores can be utilized for studying their physico-mechanical properties as the wet-towel wrapping technique on dried cores provides another chance for such a purpose.

Pre-existing weakness planes due to geological past events affect the shear behavior of mudstone layers and they can have a drastic negative effect on their mechanical strength. The experimental results as well as its evaluation could be quite useful for engineers when they assess the stability of geotechnical structures.

REFERENCES

- Aydan, Ö. 2003: The moisture migration characteristics of clay-bearing geo-materials and the variations of their physical and mechanical properties with water content. 2nd Asian Conference on Saturated Soils, *UNSAT-ASIA 2003*, 383-388.
- Aydan, Ö. 2016. *Time-dependency in Rock Mechanics and Rock Engineering*, CRC Press – Taylor and Francis Group., ISRM Book Series, No. 2, 246p.
- Aydan Ö. (2022). A comparative study on the determination of tensile strength of rocks by different testing methods and its utilization in failure criteria. *13th Regional Rock Mechanics Symposium, Isparta , Turkey*, 3-11 (invited keynote paper).
- Aydan, Ö. and Tokashiki, N. (2017). Geotechnical issues in Ryukyu Archipelago and some solutions. *KISOKO*, Vol. 45, No.5, 21-25 (in Japanese).
- Aydan, Ö. and Ulusay, R. 2003. Geotechnical and geo-environmental characteristics of man-made underground structures in Cappadocia, Turkey. *Engineering Geology*, Vol. 69, 245-272.
- Aydan, T. Akagi and T. Kawamoto (1993). Squeezing potential of rocks around tunnels; theory and prediction. *Rock Mechanics and Rock Engineering*, **26**(2), 137-163.
- Aydan, Ö., T. Ito, T. Akagi and T. Kawamoto (1994). Theoretical and numerical modelling of swelling phenomenon of rocks in rock excavations. *Int Conf. on Computer Methods and Advances in Geomechanics, IACMAG*, Morgantown, **3**, 2215-2220.
- Aydan, Ö., T. Akagi, T. Kawamoto (1996). The squeezing potential of rock around tunnels: theory and prediction with examples taken from Japan. *Rock Mechanics and Rock Engineering*, **29**(3), 125-143.
- Aydan, Ö., Daido, M., Tano, H., Nakama, S. and Matsui, H. 2006. The failure mechanism of around horizontal boreholes excavated in sedimentary rock. *50th US Rock Mech. Symp.*, Paper No. 06-130.
- Aydan, Ö., Watanabe, S., Tokashiki, N. (2008). The inference of mechanical properties of rocks from penetration tests. *5th Asian Rock Mechanics Symposium (ARMS5)*, Tehran, 213-220.
- Aydan, Ö., Sato A., Yagi. M. 2014: The Inference of Geo-Mechanical Properties of Soft Rocks and their Degradation from Needle Penetration Tests. *Rock Mechanics and Rock Engineering*, **47**, pp.1867–1890, 2014.
- Barton, N., Lien, R. and Lunde, I.: Engineering classification of rock masses for the design of tunnel supports. *Rock Mechanics*, Vol. 6, No. 4, pp. 189-239, 1974.
- Bieniawski, Z.T.: Geomechanics classification of rock masses and its application in tunnelling. Third Int. Congress on Rock Mechanics, ISRM, Denver, IIA, pp. 27-32, 1974.
- Fukuda, O., Motojima, K., Ijima, S., Oyama, K., Fujii, N., Sato, Y., Ueda, Y., Suzuki, Y., Kageyama, K., Natori, H., Takagi, S., Tanaka, S., Ogawa, K., Suda, Y., Oka, S., Ishibashi, K., Kato, K., Fujinuki, T., Kawano, M., Nagata, S., Hirukawa, T., Ito, S., Murakami, T., Ishida, M. and Murase, T., 1970. Natural gas resources of the Ryukyu Islands. Preliminary Report of 5th Phase Survey Team of GSJ. *Bull. Geol. Surv. Japan*, **21**, 627–672
- Hanzawa, S. (1935) Topography and geology of the Riukiu Islands. *Sci. Rep. Tohoku Imp. Univ.*, 2nd Ser. (Geol.), **17**, p. 1-61. H
- Kizaki, K. (1986): Geology and tectonics of the Ryukyu Islands. *Tectonophysics*, **125**, 193-207.
- MacNeil, F. S. (1960) Tertiary and Quaternary Gastropoda of Okinawa. *Geol. Surv. Prof. Pap.* **339**, 148p.
- Tokashiki, N. and Aydan, Ö. (2010): Kita-Ubaru Natural Rock Slope Failure and Its Back-analysis. *Environmental Earth Sciences*, Vol.62, No.1, 25-31.

Shales and Slates of El Sillar (Bolivia). Description of degradation processes.

V. Ugarte
Consultora Connal, Bolivia

D. Rodriguez
Grupo Estabiliza, Bolivia

ABSTRACT:

“El Sillar” is a stretch of main Bolivia’s highway, where landslides problems are frequent. Geological factors and environment conditions (with variations in humidity and high rainfall) are the main factors for degradation progressive of rocks. In fact, chemical and physical weathering are also responsible for a time-dependent weakening of the rock, which combined with other phenomena can cause slope failure. At the present time, there is few research on the behavior of these rocks.

Based on laboratory data, tests at microscopic level, and field observations, this paper examines causes and processes of deterioration of El Sillar’s clay shales. Additionally, describes parameters calibration of C-CASM model by triaxial tests.

1 INTRODUCTION

One of the main highways of Bolivia is the way 4, which connects La Paz with Cochabamba and Santa Cruz. As well, this route is a part of the Bioceanic Corridor that connects Brazil, Bolivia and Chile (Fig. 1). El Sillar's zone is a stretch of this highway, where landslide problems are frequent. These problems are not recent, but rather are of decades ago. At present, this highway is being reconstructed, and presents at least 13 critical sectors that require special works of stabilization.



Figure 1. Location of "El Sillar" zone. Highway Cochabamba – Santa Cruz, Bolivia. (Google Earth).

1.1 *Particular characteristics*

This zone is characterized by having a humid subtropical weather, with relative humidity that oscillates between 55 % and 95 %, and rainfalls that happen almost every day (260 days on average). Pluvial precipitations are higher than 4000 mm a year.

Orography is complex, topography is mountainous. This tranche begins at Km 100 of the road to 1935 masl, and ends in at Km 130 to 565 masl.

weather changes suddenly of sunny to covered with clouds (generally with fog and lack of visibility). In this environment, with high and changing temperatures, with variations in the relative humidity and with abundant rainfalls, weathering of the materials is very intense (Fig 7).

1.2 *Geological description*

El Sillar is in Sub-Andean zone of Eastern Range of the Andes. Rocks pertain mainly to "Kiru-sillas" Formation of Paleozoic. Rocks are principally dark- gray color Shales with organic carbon contents. These rocks got formed for sedimentation of an ancient sea.

Due to subduction of the Nazca plate beneath South America, rock mass has been deformed and compressed. At present, it can observe structures folded of Slates with intercalations of Orthoquartzite rocks, with faults and folding in stratigraphic series. Tunnels constructed in this zone show sectors with folded structures, quartz veins and pyrite veins (in smaller proportion) between its discontinuities (Fig. 2).

Tectonic movements continue deforming to rock mass. Brooks et al. (2011) recorded superficial motions of 5mm a year. In fact, El Sillar is part of the Boomerang Chapare Transfer Zone (with Orogenic-wedge deformation).

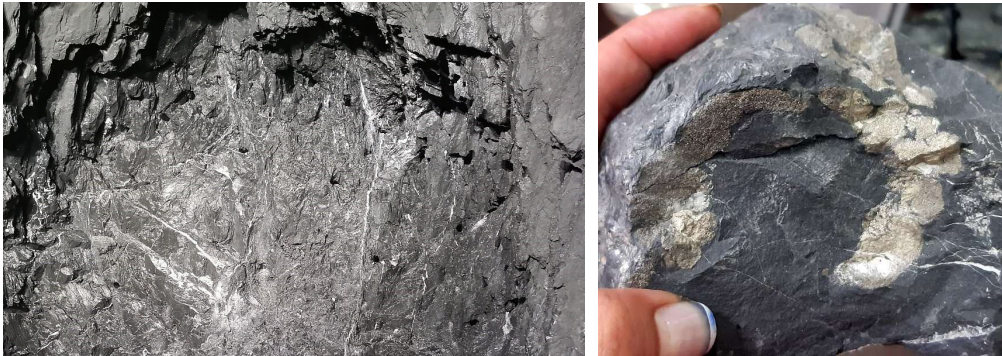


Figure 2. Left: Quartz veins in the rock mass. San José Tunnel. Right: Pyrite veins in Slate.

2 BEHAVIOR OF SOFT ROCKS

2.1 *Weathering Processes*

Weathering is a combination of progressive processes in which physical and chemical changes act continuously so that the rock becomes increasingly weathered with time, and to a greater depth, Duncan C, (2018). A recurrent observation in these materials is its evolutive nature that happens when are excavated and exposed to weathering processes (Fig. 7).

In the first instance, processes of degradation that happen in soft rocks are irreversible changes in their mechanical properties, that can be caused by weathering processes and by mechanical actions, Pineda et al. (2013). According to Alonso and Pineda (2006), environmental variations lead to wetting and drying cycles by changes in relative humidity (i.e. suction), this pattern of degradation is associated principally with generation of microfissures (physical weathering).

Additionally, chemical weathering involves chemical reactions between water and the minerals in the rock resulting in either dissolution of the minerals or the formation of new compounds. This type of weathering is the greatest cause of rock degradation, Duncan C. (2018).

2.2 Weathering and bonding

Mechanical behavior of soft rocks is very related to its geological history, reflected in its structure, that it is a combination of fabric and bonding, where bonding refers to the interconnection of solid particles product of geological processes. Generally, residual soils are also frequently bonded as a relic of the rock structure still present to some degree within the weathered soil, Gens, (2010). In this sense, it can be stated that weathering is essentially the opposite of development of bonding.

At microscopic level, weathering causes progressive destruction of the cementing particles (modifications in their structure and porosity), Pineda et al. (2013). At macroscopic level it causes loss of strength and stiffness, irreversible volume change (expansion), and loss of mass continuity (fissuration), Alonso & Alcoverro, (2004). The most relevant consequence is progressive reduction of the yield surface, that is, reduction of the elastic domain (Fig. 3), Castellanza et al. (2002).

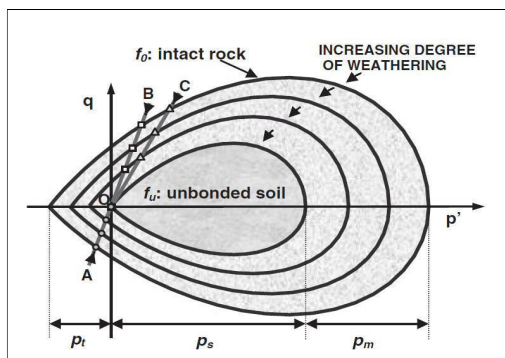


Figure 3. Yield surfaces of a rock with different degrees of weathering. (Castellanza et al. 2002).

To model the effect of the weathering (physical and chemical) in the behavior of the materials is not an easy task, (Castellanza et al. 2003, Nova et al. 2003, Pinyol et al. 2007). For instance, it would be necessary to quantify degree of damage that takes place for chemical weathering in time. At present, it is possible to reproduce the behavior of soft rocks with advanced constitutive models focused in the behavior of the structure and bonding, one of them is the constitutive Model C CASM, that can be used in the program Plaxis.

3 ANALYSIS

3.1 Tests at a microscopic level

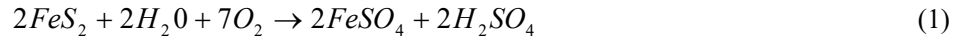
In order to study weathering processes of El Sillar's rocks, tests were realized in samples of Slates with different degrees of weathering. These samples have been identified like: M26m fresh rock, M2 weathered rock and M1 residual soil. In these samples were realized Petrographic analysis, X-Ray Diffraction (XRD), X-ray fluorescence (XRF) and Scanning Electronic Microscope (SEM).

Table 1 shows results of petrography tests carried on different rocks. It can be observed that Pyrite reduces from 5 % (fresh rock) to 2 % (weathered rock). X-Ray Diffraction tests have detected Quartz, Muscovite, Pyrite, Clinocllore, Gypsum and Cordierite in fresh rock. However, in weathered rocks did not detect Pyrite and Cordierite (Table 2).

Additionally, fresh rock was submitted to wetting and drying cycles, simulating the effect of environmental variations. Figure 4 shows the generation of microfissures of this rock by means of Electronic Microscope (SEM), Rodriguez, (2021).

According to Littke et al. (1991) and Tuttle & Breit (2009), in humid subtropical weathers the first reaction that takes place in weathering processes of Shales-Slates is oxidation of Pyrite. In fact, reaction of Pyrite exposed to water and oxygen generates ferrous sulfate and the sulfuric

acid, as shown in the following equation:



Pyrite + Water + Oxygen → Ferrous sulfate + Sulfuric acid

Oxidation of Pyrite generates secondary reactions in minerals, like the PH increment of water. Iron and SO₄ get free of Pyrite, Ca of Calcite and along with other elements they form sulfate salts efflorescent, like Gypsum. Iron sends round in secondary phases forming iron oxides. Once finished oxidation of Pyrite, O₂ attacks the organic matter, beginning also process of oxidation of organic Coal (CH₂O + O₂ → CO₂ + H₂O), Wildman et al. (2004). At the end, iron oxides and the efflorescent salts, Quartz, Illite and others minerals, remain in the ground, accumulating for illuvial processes, Tuttle and Breit, (2009).

Figure 5 shows results of SEM and diffractogram tests of fresh rock and weathered rock. Comparing both diffractograms can be observed a reduction of the Coal in weathered rock, what suggests the oxidation of organic Coal. Also, diffractograms shows that Iron finds as much in fresh rock as in the weathered rock. And Figure 6 shows SEM results of sample M1 (residual soil).

Table 1. Petrographic description. Summary of results.

Mineral	Slate Fresh Rock	Slate Weathered	Mudstone Weathered	Quartz Greywacke
Quartz	7	18	16	62
Muscovite	10	3	3	15
Clayey matrix*	58	77	76	20
Epidote	20	-	-	-
Pyrite	5	2	2	< 1
Biotite	-	-	3	1
Chlorite	-	-	< 1	2
Apatite	-	-	< 1	-
Turmaline	-	< 1	< 1	< 1

* Clay minerals, Quartz, Sericite. Source: Study TESA (2018).

According to Hawkins (2014) microfissures (of chemical and mechanical origin) facilitate motion of the water with components of sulfuric acid inside the particles, increasing in this way the effective index of pores and the permeability.

A characteristic of this zone is that the residual grounds are largely brown color for the oxidation of iron, also gray dark color where the organic matter prevails, presenting in some cases values of Liquid Limit bigger to 50 % (Fig. 7).

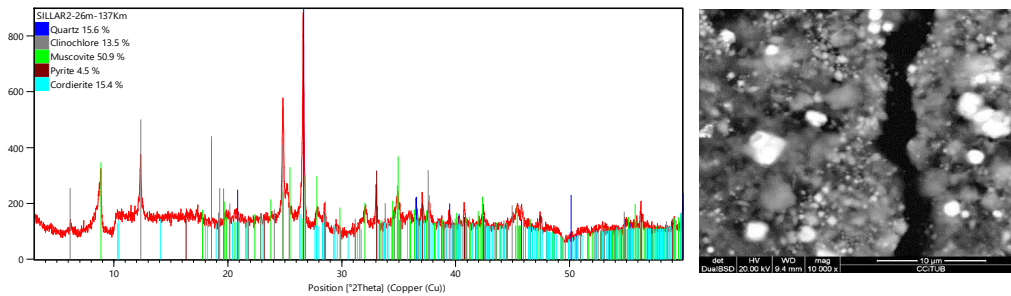
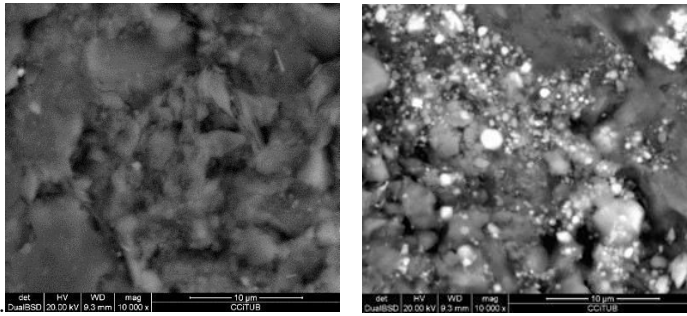
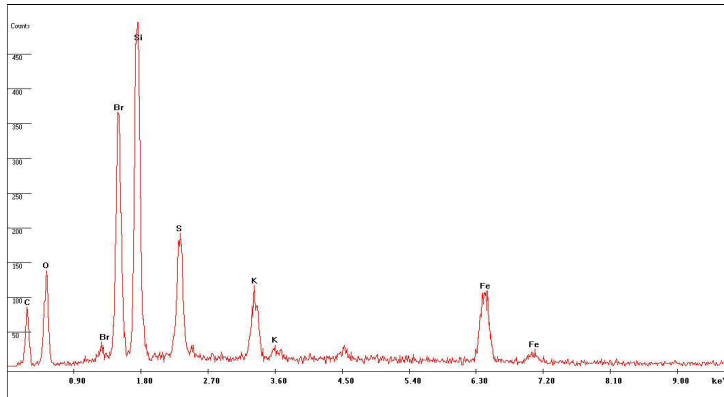


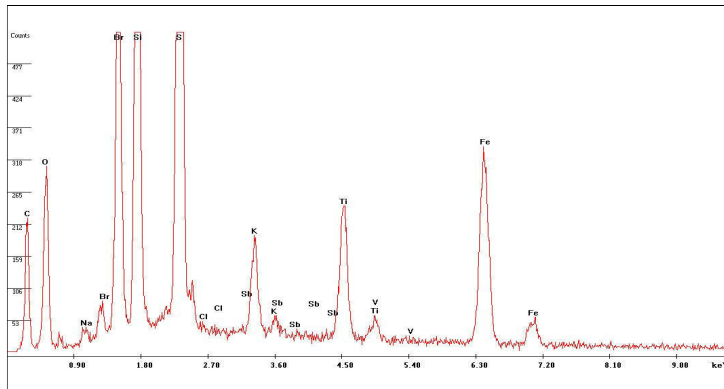
Figure 4. Diffractogram M26m fresh rock (Slate). Image of SEM, shows generation of microfissures.



a) Image of SEM. Weathered rock (M2).



b) Diffractogram Weathered rock (M2). Coal, Oxygen, Bromine, Silicon, Sulphur, Potassium, Iron.



c) Diffractogram fresh rock. Carbon, Oxygen, Silicon, Sulphur, Titanium, Iron, Quartz.

Figure 5. Results of SEM Tests. Comparison between fresh rock and weathered rock.

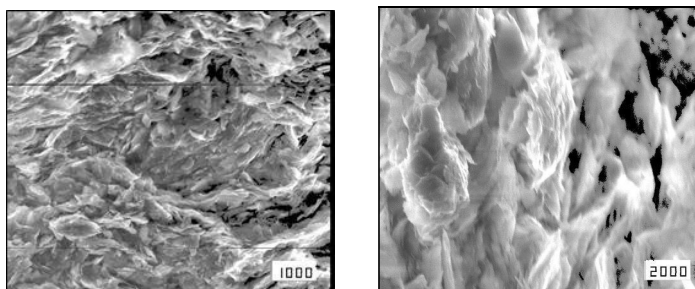


Figure 6. Results of SEM, residual soil M1. Identification of clay minerals Illite and Caolinite.

Table 2. Quantitative determination of the minerals.

Mineral	Slate Fresh rock	Slate Weathered	Residual Soil
Quartz	15,6	46	56,4
Muscovite	50,9	26,7	34,1
Clinocllore	13,5	27,2	9,5
Gypsum	-	0,1	-
Pyrite	4,5	-	-
Cordierite	15	-	-

Source: Rodriguez (2021).



Figure 7. a) Cut of slope, grey color weathered rock, brown color residual soil. b) Cracks in slope and weathered rock. c) Residual soil. d) Oxidations and efflorescences of salts of shales and Slates.

3.2 Mechanical Tests

It has been compiled a data base of projects realized in El Sillar, this data are a reference of properties and behavior of the rocks. Table 3 presents main results of test carried on Shales-Slates. It was observed that uniaxial compression of weathered rock is between 1 and 5 MPa (from Point Load Tests).

Additionally, for the purpose of applying the Model C-CASM on the rocks of El Sillar, were realized Triaxial Tests on M26m fresh rock, M2 weathered rock and M1 residual soil. Furthermore, were realized Consolidation Tests and Shear direct tests on the samples M2 and M1. Samples were extracted from the ground in molds of 20x20x15 cm, however, Tests were realized in samples remolded due to maximum size of their particles. Table 4 and figures 8 and 9 present summaries of results.

Table 3. Compilation of Tests. Physical and mechanical properties in Shales-Slates.

Parameter	Unit	Mean	Standard deviation	Minimum	Maximum	Number of tests
Dry unit weight, γ_d	kN/m^3	26	1	21	27	75
Specific gravity, G_s	-	2,77	-	2,7	2,8	5
Porosity, n	-	0,04	-	0,02	0,06	5
Absorption, α	%	1,1	-	0,1	2,4	5
Uniaxial compression, σ_c	MPa	15	8	1	35	84
Young's modulus, E	GPa	5	3	1	8	8
Internal friction angle*	(°)	27	-	18	32	4

* Direct shear tests on predetermined fissure

Table 4. Summary of results. One-Dimensional Consolidation Tests

Parameter	Unitad	Residual Soil	Slate Weathered
Plasticity index	%	12	10
Water content	%	17	12
Voids ratio	-	0,5	0,4
Initial effective stress	KPa	240	40
Overconsolidation ratio	-	4	5
Compression Index	-	0,22	0,13
Swelling Index	-	0,04	0,02

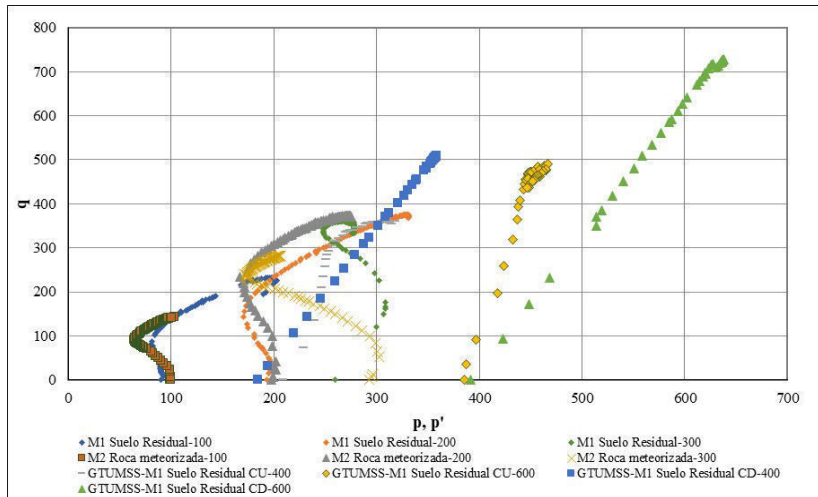


Figure 8. Stress paths of triaxial Tests (CU and CD). Samples M2 and M1. Tests were realized in Laboratory of Geotechnics San Simon University.

3.3 Calibration of the Model C-CASM

Cemented-CASM model is based on the formulation for cemented soils proposed by Gens & Nova (1993), this model takes into account effects of bonding in yield surfaces and his degeneration during the processes of load. The constitutive equations and examples of use of the model are in González, (2011) and Rios et al. (2016).

Basically, parameters that describe the mechanical degradation of bonding, are: b_0 that represents the degree of initial bonding, h_1 y h_2 parameters that define the rate of degradation (for plastic volumetric strains and plastic shear strains), P_s is the equivalent pre-consolidation pressure of the ground and P_c that controls yield surfaces of bonding (Fig. 10).

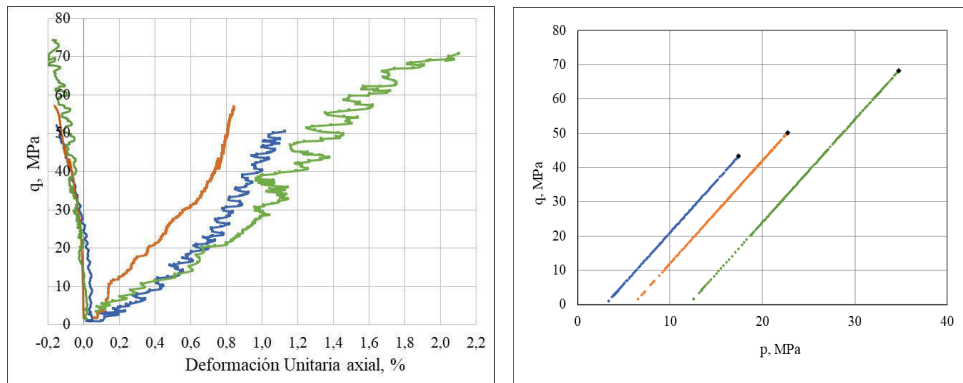


Figure 9. Stress paths. Rock Triaxial tests. Sample M26m.

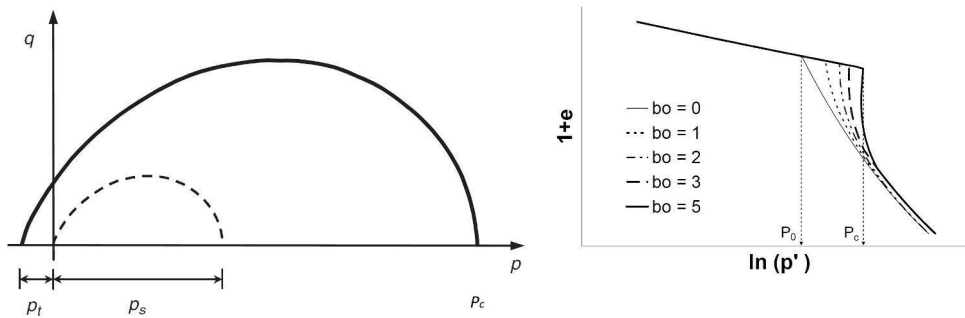


Figure 10. Left: Yield surfaces for both unbonded and bonded materials. Right: Influence of b_0 in the compression curve. Rios et al. (2016).

Table 5 and Figure 11 present results of calibration of the model. Evidently, using of a model more advanced requires more parameters and more tests. Concerning the tests, the main inconvenience was working with re-molded samples, due to size of particles. As well, it is necessary to know post-failure behavior of rocks to get more accurate values of h_1 and h_2 .

The model C-CASM, being an isotropic model, can reproduce the answer fragile - dilating of soft rocks, that is the key to success. Logically, this cannot be achieved with Mohr Coulomb, Ciantia et al. (2021).

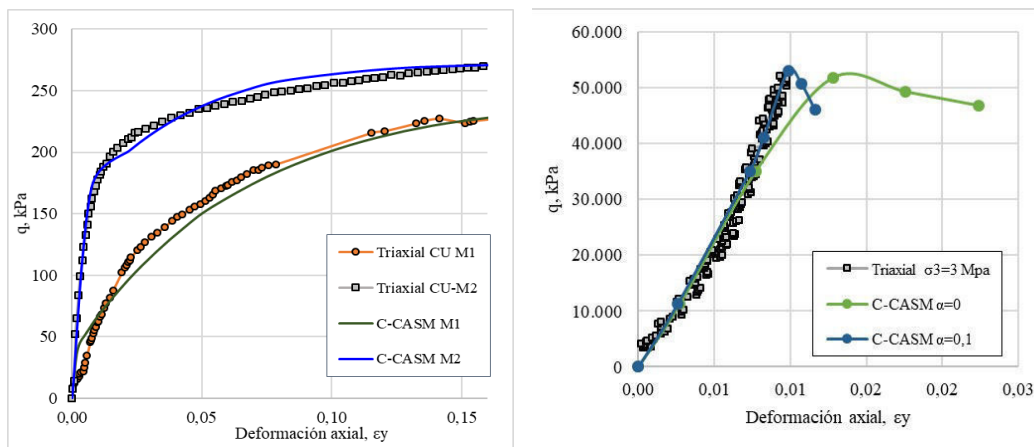


Figure 11. Results of the calibration of the Model C-CASM with Triaxial tests.

Table 5. Results of calibration. Parameters of the Model C CASM for the samples M1, M2 and M26m.

Parameter	Unit	Residual Soil (M1) $\sigma'_3 = 125$ kPa	Slate Weathered (M2) $\sigma'_3 = 115$ kPa	Slate fresh Rock M26m $\sigma'_3 = 3$ MPa
v	%	0,3	0,3	0,3
k	-	0,02	0,01	0,01
λ	-	0,09	0,065	0,65
M	-	1,2	1,35	2
ϕ_c	(°)	30	33	48
r	-	2	0,13	2
n	-	1,5	0,02	1,5
e_0	-	0,5	0,4	0,04
P'_{so}	KPa	55 - 75	130 - 150	1500
b	-	0 - 1	0 - 2	38
h_1	-	0	0	0
h_2	-	0	0	0
a	-	0	0	0,1

Initial state: e_0 : Initial Voids ratio, K_0 : Coefficient of earth pressure at rest, OCR : Overconsolidation ratio.

Critical state: v : Poisson's ratio, k : Slope of the isotropic swelling line, λ : Slope of the isotropic compression line, M : Critical state stress ratio, ϕ_c : Angle of shear strength at critical state.

Yield function shape: r : Spacing ratio, n : Shape parameter, P'_{so} : equivalent pre-consolidation pressure.

Variables of the model: b : Bonding, h_0 : Initial degradation, h_1 : Degradation rate for compression, h_2 : Degradation rate for shear, a : Parameter to control tensile strength, w : Contribution of plastic deviatoric strain to the hardening parameter.

4 CONCLUSIONS

Weather conditions of El Sillar's zone, with variations in humidity and high precipitations, constitute one of the main factors for the progressive deterioration of the rocks.

According to the field observations, in some slopes that were cut or excavated appeared tensile cracks. These cracks were growing progressively until slope failure. In effect, these slopes were exposed to weather conditions (since vegetation was removed and tensional states were modified), increasing weathering processes and degradation in time (Fig. 7). It can be indicated that most of landslides happened in season of rains, being pluvial precipitation the trigger factor.

Wetting and drying cycles tests, along with X-ray diffraction (XRD) and scanning electronic microscope (SEM) showed the generation of microfissures in the sample of fresh rock (Fig. 4). With the increase of range of relative humidity cycles, it was observed that deterioration of the rock is significant. These results agree with Alonso & Pineda (2006) realized on soft rocks with high clayey-silty content.

At the same time, chemical weathering takes place, incrementing degradation with time and to greater depth. It has realized a series of test a microscopic level in samples of fresh rock, weathered rock and residual soil. Results confirm the oxidation of Pyrite (Table 2). In fact, in a humid, subtropical climate, the first reaction in the weathering process of grey Shale-Slate is oxidation of pyrite. According to Hawkins and John (2013), this oxidation produces expansions for alteration of microcrystals and liberation of sulfuric acid. Microfissures facilitate the motion of the water with sulfuric acid, increasing in this way the effective porosity and permeability. Tuttle & Breit (2009). Other chemical reactions like oxidation of the organic coal, liberation of Calcite, alteration of the clinocllore and the pinitization of the Cordierite also take place in shales and slates.

With the intention of reproducing behavior of these rocks in an advanced Constitutive Model, it has studied the model C-CASM. For calibration of the model, it was realized Triaxial tests in samples of fresh rock, weathered rock and residual soil, obtaining good correlations (Fig. 11).

At present, it is continuing with investigations of El Sillar's rocks. Understanding his behavior will help to give comprehensive solutions, principally to problems of slope stability.

4.1 References

- Alonso, E.E. & Alcoverro, J. 2004. Swelling and degradation of agillaceous rocks. Keynote lecture, Proc 3rd Int. Conf. Unsat. Soils, Recife, Balkema: 951-969.
- Alonso, E.E. & Pineda, J.A. 2006. Weathering and degradation of shales: experimental observations and models of degradation. VI Congreso Suramericano de Mecánica de Rocas. Cartagena: Sociedad Colombiana de Geotecnia.
- Brooks, B. Bevis, M. Whipple K. Arrowsmith, J. Foster, J. Zapata, T. Kendrick, Minaya, E. Echalar, A. Blanco, M. Euillades, Sandoval, M. & Smalley, R.J. 2011. Orogenic-wedge deformation and potential for great earthquakes in the central Andean backarc. *Nature Geoscience*. 4(6): 380–383.
- Castellanza, R. Nova, & R. Tamagnini, C. 2002. Mechanical effects of chemical degradation of bonded geomaterials in boundary value problems. *Numerical Modelling in Geomechanics*. 1169 -1192.
- Ciantia, M. O. Arroyo, M. & Kaiser, P. (2021). Application of a bonded critical state model to design tunnel support for rockmass bulking. *Mechanics and Rock Engineering, from Theory to Practice*. IOP Conf. Series: Earth and Environmental Science 833 (2021) 012162.
- Duncan, C. W. 2018. *Rock Slope Engineering*. Taylor & Francis Group. Vancouver, Canada.
- Estudio TESA. 2018. Construcción del tramo central Doble vía “El Sillar”. Administradora Boliviana de Carreteras.
- Gens, A. & Nova, R. (1993). Conceptual bases for a constitutive model for bonded soils and weak rocks. In *Geotechnical engineering of hard soils–soft rocks* (eds A. Anagnostopoulos et al.). Vol. 1, pp. 485–494.
- Gens, A. 2010. Soil-environment interactions in geotechnical engineering. *Géotechnique* 60. No. 1: 3–74.
- González NA. 2011. Development of a family of constitutive models for geotechnical applications. PhD Thesis. Technical University of Catalonia, UPC.
- Hawkins, A. 2014. Implications of Pyrite Oxidation for Engineering Works. Springer International Publishing Switzerland. pp. 1-99.
- Kanji, M. He, M. & E Souza, L.R. 2020. *Soft rock mechanics and engineering*. Switzerland. Springer Nature Switzerland AG 2020.
- Littke, R. Klusmann, U. Krooss, B. & Leythaeuser, D. 1991b. Quantification of loss of calcite, pyrite, and organic matter due to weathering of Toarcian black shales and effects on kerogen and bitumen characteristics. *Geochimica et Cosmochimica Acta* 55 (11).
- Nova, R. Castellanza, R. & Tamagnini, C. 2003. A constitutive model for bonded geomaterials subject to mechanical and/or chemical degradation. *International Journal for Numerical and Analytical Methods in Geomechanics* 27: 705–732.
- Pineda, J. A. Alonso E.E. & Romero, E. 2013. Environmental degradation of claystones. *Géotechnique* 64 (1): 64–82.
- Pinyol, N. Vaunat, J. & Alonso, E. E. (2007). A constitutive model for soft clayey rocks that includes weathering effects. *Géotechnique* 57. No. 2: 137–151.
- Rios, S. Ciantia, M. Gonzalez, N. Arroyo, M. & Viana da Fonseca, A. 2016. Simplifying calibration of bonded elasto-plastic models. *Computers and Geotechnics* 73: 100 – 108.
- Rodriguez, D. 2021. Caracterización química y geomecánica de las rocas de El Sillar (Bolivia). Master Thesis. Departamento de Ingeniería Civil y Ambiental UPC.
- Tuttle, M. & Breit, G.N. 2009. Weathering of the New Albany Shale, Kentucky, USA: I. weathering zones defined by mineralogy and major-element composition. *Applied Geochemistry* 24. 1549–1564.
- Wildman, R.A. Berner, R. Petsch, S.T. Bolton, E. Eckert, J. Mok, U. & Evans, J.V. 2004. The weathering of sedimentary organic matter as a control on atmospheric O₂: I. Analysis of black shale. *American Journal of Science*. 304: 234–249.

Rock Load Estimation for Underground Structures

C.A. Stone
HNTB, New York, USA

ABSTRACT:

Two equations are proposed for the estimation of rock loads on underground structures. The first equation is an equation for the equivalent rock load on shallow underground caverns based on the rock tunneling quality index and the scaled crown span at the given cavern location. The second equation proposes a method for estimating the horizontal stress ratio in the rock zone for cut and cover subway stations based on the jointing patterns of the rock at the site. The actual rock loads on both types of structures can range from zero to very high based on the localized geotechnical conditions. Good practice in the design of underground structures requires that equations for rock loads can effectively determine a close estimate of the rock load based on the limited geotechnical data often available.

1 EQUATIONS FOR ROCK LOADS ON SHALLOW CAVERNS AND CUT AND COVER STRUCTURES

1.1 *Good practice in rock engineering*

During concept engineering for underground structure projects design engineers are frequently required to estimate rock loads that will be imparted to those structures by the surrounding rock mass with a relatively small amount of geotechnical data available for consideration. Rock loads are highly dependent on localized geotechnical conditions which may be unknown until the geotechnical investigation program is complete. The range of values for rock loads on underground structures can range from zero to very high based on the geotechnical conditions at the project site.

Design of underground structures requires that reasonably conservative estimates of rock loads be developed. Good practice in the design of underground structures requires the following:

- sufficient geotechnical data of high quality be obtained during the investigation period
- equations used to estimate equivalent rock loads are effectively used to develop reasonably conservative estimates of the insitu geotechnical conditions
- a crown pillar of adequate thickness is provided around cavern structures

This paper presents two equations that have been proposed for the estimation of rock loads on underground structures. The first equation is an equation for the equivalent rock load on shallow underground caverns based on the rock tunneling quality index and the scaled crown span at the given cavern location. The second equation proposes a method for estimating the horizontal stress ratio in the rock zone for cut and cover subway stations based on the jointing patterns of the rock encountered at the site.

1.2 *Vertical rock loads on shallow caverns*

An equation for estimating geotechnical rock loads in shallow mined caverns was presented by Charles Stone and Changsoo Moon at the Rapid Excavation and Tunneling Conference (RETC) in 2019. (Stone and Moon, 2019). The method is based on previously measured rock loading data from final lining instrumentation and empirical geotechnical data from previously constructed mined subway station caverns in Washington, D.C. and New York, correlated with geological data and cavern geometry using the Q tunneling index value and scaled crown span equation.

That publication provided the background for development of the new equation for the estimation of rock loads that would likely be imparted on shallow mined cavern final linings permanently supporting underground cavern excavations. The development of the equation from the following published methods was explained: Karl Terzaghi, (1946); Deere, (1970); Rose (1982); Cording, (1972); Bieniawski, (1973); Barton, (1974); and Carter, (1992).

1.3 *Horizontal rock loads on cut and cover structures*

An equation for estimating the horizontal stress ratio for the rock zone in shallow cut and cover subway stations was presented by Charles Stone and Eric Wang at the North American Tunneling (NAT) conference in 2022. (Stone and Wang, 2022). Following a literature study on equations for the insitu horizontal stress, the authors developed an equation for estimating horizontal in situ stress ratios in rock resulting from rock blocks formed by intersecting joint sets sliding along the intersections of joint planes into the excavation.

2 SHALLOW CAVERN DESIGN

2.1 *Crown pillar stability analysis*

A crown pillar is the zone of rock directly above the limits of a mining, tunnel, or cavern excavation. The stability of a crown pillar can be analyzed by various empirical and numerical methods. The crown pillar thickness is the rock cover, excluding the soil zone over the cavern, that forms the crown pillar to the outside edge of the cavern excavation. This information can generally be obtained only from borehole data. The unsupported rock mass in a crown pillar can be either stable, subject to failure over time when unsupported, or subject to immediate collapse upon excavation. This crown pillar condition is determined by four factors: rock mass quality, excavation width, excavation method, and proximity to the surface.

The rock mass quality can be expressed by the numerical indices RMR and/or Q. With respect to both of these systems, as well as other rock mechanics systems, the stability of the excavation decreases as the rock quality decreases. If less rock cover is provided than the critical span, ultimate failure of the crown span is likely, and the resulting rock loads will necessarily need to be accommodated by initial lining support and final lining structure. Likewise, an equivalent thickness of rock should be provided in each rib on the two sides of the cavern. If one of the ribs has been removed for some reason, such as excavation for a nearby building foundation, instability of the crown pillar becomes a definite construction risk.

The proximity of the excavation to the ground surface adversely affects the cavern stability. This is because as the cavern approaches the surface, the ability to employ arching action diminishes, and the support is required to develop beam action. Effects of this phenomena are considered by the scaled crown span equation. There are two basic cavern configurations available, which are suited to construction under shallow rock cover. An arched cavern configuration is typically constructed where there is sufficient crown pillar thickness to allow for the development of arching action in the rock mass. Alternatively, a binocular cavern configuration should be used where the cavern excavation would otherwise preclude development of a stable crown pillar.

The method of excavation is also a factor affecting stability of the crown pillar during excavation. Blasting will tend to loosen up rock blocks around and cause blast damage to the periphery of the excavation to a greater extent as compared to excavation by roadheaders. Drill and blast excavations will tend to be less stable and require more support for a given cavern width, rock quality and proximity to the surface. This effect is accounted for in some systems used in rock mechanics today. However, it is not currently accounted for in a practical system for evaluating the crown pillar stability.

The basis for the design acceptability of new cavern excavations for civil engineering structures is achieving a very low degree of risk. In particular, subway station caverns typically fea-

ture public access over the structure and buildings directly over near-surface underground excavations. Tolerance to risk in such cases is limited and the acceptable degree of risk must be essentially zero. To the extent possible, and where economically feasible, the crown pillar geometry and rock quality should provide for a cavern crown pillar probability of failure for an unsupported cavern excavation of less than 5%. To the extent that any probability exists, the crown pillar requires rock reinforcement and structural support.

2.2 Historical rock load data for Washington, D.C. subway station caverns

Ed Cording and others at the University of Illinois carried out a geotechnical study during construction of nine shallow mined station caverns in Washington D.C. in the 1970's which included observations and measurements of geotechnical data as related to site geologic conditions. (Cording, et. al., Vol 1 1983) This study included field observations, displacement measurements, and cavern lining load estimations that increase over a wide range with respect to varying geotechnical conditions.

These caverns were driven with rock reinforcement and steel set-shotcrete structural linings as initial support and experienced an equivalent rock load on the structural lining of 12 to 49 feet after a heavy rock bolting program. Since the initial support served as the final structural lining in these cases, these caverns are very well suited to provide an indication of mined cavern lining loads. Rock loads were lowest, and correlated with elastic theory, where there was an absence of shear zones. Rock loads and rock displacements were highest where the geotechnical conditions included shear zones.

With these caverns serving as a basis for providing actual measured rock loadings on shallow mined cavern linings, and the use of the Q and scaled crown span classification systems for correlating the geotechnical conditions of the crown pillar with the lining loads for shallow caverns, an effective rock load prediction methodology for shallow caverns was developed.

The descriptions of geotechnical conditions for Washington D. C. subway station caverns have been condensed from the information provided in the reference study report. (Cording, et. al., Vol 1 1983), (Cording, et. al., Vol 1, p. 235 1983), (Cording, et. al., Vol 1, p. 27 1983) Equivalent rock loads on the station caverns linings back calculated from strain gage measurements have been estimated by Cording et. al. to be as provided in Table 1 below. (Cording, et. al., Vol 3, p. 126 1983) (Cording, et. al., Vol 1, p. 235 1983) It was necessary to assume Q value parameters based on the study report, which are also shown in the table.

Table 1. Assumed parameters for Washington D. C. subway caverns.

Station Cavern	Actual Cavern Span (feet)	Estimated Scaled Crown Span (feet)	RQD	Assumed Q Parameters					Q	Actual Rock Load (feet)
				Jn	Jr	Ja	Jw	SRF		
Medical Center	62	30	75	9	5	3	0.5	2.5	2.78	12
Rosslyn	80	36	85	12	1	4	.66	5	0.23	16
Bethesda	62	44	75	12	1	5	0.5	5	0.1	20
Cleveland Park	58	55	75	12	3	2	1	7.5	1.25	23
Van Ness	58	31	75	15	2	3	.66	5	0.44	23
Zoological Park	58	24	75	12	3	3	.66	5	0.83	30
Dupont Circle	76	45	75	15	1.5	5	.66	7.5	0.13	30
Tenley Circle	60	22	75	15	2.5	2	.66	7.5	0.55	28
Tenley Circle*	60	22	75	45	2.5	2	.66	7.5	0.18	41
Friendship Heights	67	29	75	15	1.5	6	.66	10	0.08	42
Friendship Heights*	67	29	75	45	1.5	6	.66	10	0.03	49

*For cavern intersection

3 PROPOSED EQUATION FOR ESTIMATING ROCK LOADS ON SHALLOW CAVERNS

Based on the geotechnical conditions for the subway station caverns in Washington, D. C., as discussed above the rock loads are plotted with respect to the estimated Q and C_s parameters for the subway station caverns in Figure 1. The slopes of the rock load lines in the figure are adapted from the scaled crown span probabilities of failure. (Carter 2014) The resulting chart of rock loads has the rock tunneling quality index, Q, plotted on the x-axis and the estimated scaled crown span in meters plotted on the y-axis. The locations for the various station caverns are plotted with visual symbols of decreasing intensity as shown on the figure. What is important to note is that the caverns with the largest measured rock loads are concentrated at the lower end of the rock quality scale (Q).

The measured data from the Washington Caverns plots loosely with the rock tunneling quality index as explained above. The trend of data is for low rock loads at the higher quality end of the scale to progress to heavy rock loads at the lower end of the quality scale. Note that the station with the highest rock quality, $Q=3$, for Medical Center Station has the lowest measured rock load at 12 feet. On the other end, the station with the lowest rock quality, $Q=.03$, for Friendship Heights station has the highest measured rock loading at 49 feet. The progression of measured data supports an increasing trend of rock loads with decreasing rock quality. Also note that the dispersion of rock data is very wide. The trend in the data is not smooth due to the widely varying nature of geotechnical conditions and variable excavation sequences employed.

As a predictive method, therefore, this method is not adequate to predict the actual values of measured rock loads. However, this method can be used to provide a good estimate of design loads for future caverns if the estimated loads are set at the high end of the variance in data. To do this, the rock load for the 100% probability of failure can be set at 40 feet of rock, which corresponds with the data for Friendship Heights and Tenley Circle Station at 41 to 42 feet. The line corresponding to a 0.5% probability of failure is then set at 2 feet corresponding to periphery control rock loads. This allows an equation for estimated rock load in feet to be established as shown in Equation 1 below (Stone and Moon, 2019):

$$P(C_s, Q) = 3.297758 \times C_s^{0.969} \times Q^{-0.3926} \quad (1)$$

where $P(C_s, Q)$ = estimated rock load (feet); C_s = scaled crown span (meters); and Q = rock tunneling quality index.

This equation was established by assuming an equation of the form $P = A C_s^B Q^C$. Solution of the following three equations; $P(0.8, 0.001) = 40$ feet (12.192 meters), $P(100, 150) = 40$ feet (12.192 meters), $P(9.8, 1000) = 2$ feet (0.6096 meters), leads to the establishment of the constants as follows; $A = 3.297758099$, $B = 0.969083869$, $C = -0.39259$. The precision of these constants is to best fit the risk rating divisions used in the scaled crown span method publications.

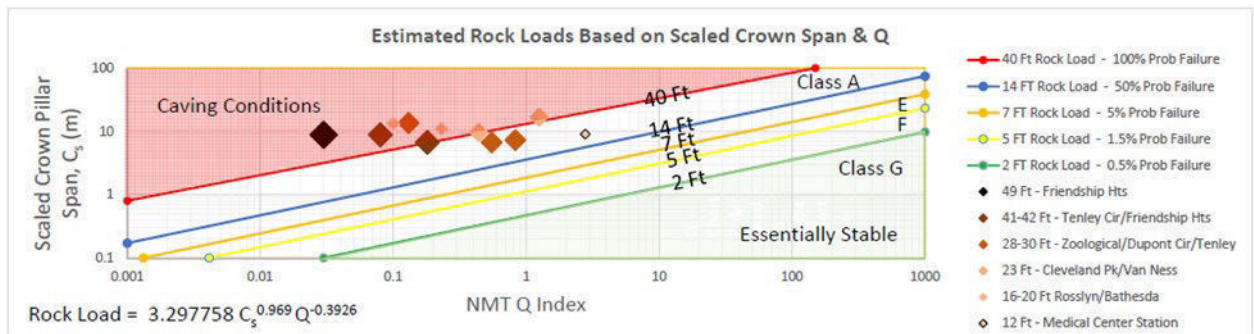


Figure 1. Estimated rock loads for shallow caverns based on Q and Cs.

4 PROPOSED EQUATION FOR ESTIMATING HORIZONTAL STRESS RATIO ON CUT AND COVER STRUCTURES

4.1 Rock wedge calculations

The authors have noted that the methods of determining horizontal loads in soil zones were originally developed based on first principles. These methods trace back to Coulomb's original consideration of what kinds of soil wedges would form in different soil types, particle sizes and physical parameters. Similarly, the authors have considered the question, apart from the horizontal stresses in the rock mass due to tectonic stresses, what kinds of horizontal loads would develop in rock due to rock blocks formed by intersecting joint sets sliding along the intersections of joint planes into the excavation?

The authors have carried out numerical calculations for rock wedge loading imparted to horizontal trenches 20 to 100 feet deep (6 to 30 meters). This analysis is based on the following example. The trench is aligned in the north-south direction. There are two joint sets which form a rock block sliding into the horizontal trench. The block is formed with an apex at the bottom depth of the trench and three corners at the top of rock surface. There is a soil zone of clay at the surface, and a soil zone of sand between the rock and the clay. The initial input parameters for the analysis are as follows:

- Joint Set #1 Dip Angle = 45 Degrees, Dip Azimuth = 225 Degrees, Friction Angle = 30 Degrees
- Joint Set #2 Dip Angle = 45 Degrees, Dip Azimuth = 315 Degrees, Friction Angle = 30 Degrees
- Unit weight of Rock = 155 Pounds per cubic foot (2.5 T/m³)
- Unit weight of Clay = 110 Pounds per cubic foot (1.7 T/m³)
- Unit weight of Sand = 120 Pounds per cubic foot (1.9 T/m³)
- Trench depths range from 20 Feet to 100 Feet (6 to 30 meters)
- Percentage of rock in the bottom of the trench, RR, ranges from 10% to 90%
- Dip angle ranges from 5 degrees to 85 degrees
- Friction angle ranges from 20 degrees to 50 degrees

The model considered for this analysis is a clay layer and sand layer overlaying a tetrahedral block of rock formed such that it can slide along two joint planes into the trench wall. The subject model is shown in Figure 2. This analysis is based on the following example. The trench is aligned in the north-south direction. There are two joint sets which form a rock block sliding into the horizontal trench. There are 20 feet of rock in a 60-foot trench, resulting in a rock ratio of 33 percent. The rock ratio, RR, is the percentage of rock in the bottom of the trench. This can also be expressed as the distance from top of rock to the trench invert level divided by the distance from the ground surface to the trench invert level.

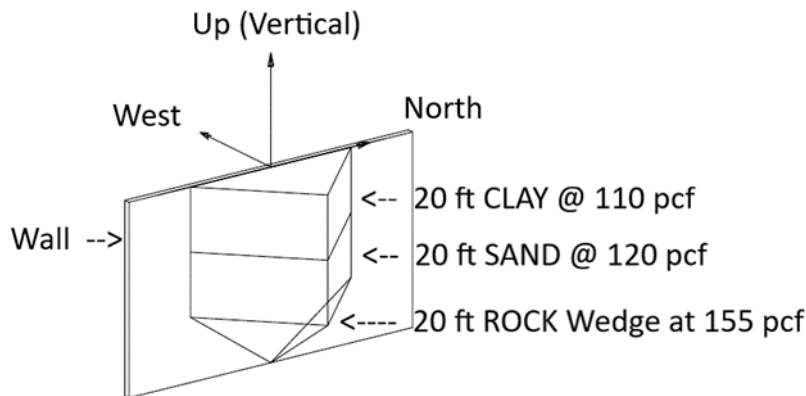


Figure 2. Model of tetrahedral rock wedges formed in rock by two joint sets used for numerical analysis

4.2 Results of wedge analysis

A graph of the results of this analysis, including over 50 cases, is provided in Figure 3. These results indicate the following six identifiable trends.

First - Horizontal stresses do not develop until the dip angle exceeds the friction angle by greater than 12 degrees.

Second – The horizontal stresses are essentially unrestrained by friction if the dip angle exceeds the friction angle by greater than 55 degrees.

Third – The horizontal stress ratio, K_0 , of the blocks ignoring the effect of friction is based on the percentage of rock in the bottom of the trench, RR. The value of K_0 can be approximated by Equation 2 as indicated below (Stone and Wang, 2022):

$$K_0 = 0.949472 - 0.653618 \times RR \quad (2)$$

where RR = percentage of rock in the bottom of the trench.

Fourth – The reduction in the horizontal stress ratio due to the effect of friction on the blocks can be approximated in terms of the dip angle in degrees, DA, and friction angle in degrees, FA, by the following term developed by the authors:

$$\text{Reduction due to friction} = [((75 - DA + FA)^{2.5} / 75^{2.5}) \times (0.5 / RR)^{0.5}] \quad (3)$$

where DA = dip angle of relevant joint set; FA = friction angle of relevant joint set; RR = percentage of rock in the bottom of the trench.

Fifth – The resulting equation for the horizontal stress ratio can therefore be expressed by the following equation developed by the authors:

$$K_0 = 0.949472 - 0.653618 \times RR - [((75 - DA + FA)^{2.5} / 75^{2.5}) \times (0.5 / RR)^{0.5}] \quad (4)$$

where DA = dip angle of relevant joint set; FA = friction angle of relevant joint set; RR = percentage of rock in the bottom of the trench.

For example, if one third of the trench contains rock below the soil zone, and the dip angle is 70 degrees and the friction angle is 40 degrees, the horizontal stress ratio in the rock zone can be approximated as $K_0 = 0.3901$. Likewise, if two thirds of the trench contain rock below the soil

zone, and the dip angle is 80 degrees and the friction angle is 20 degrees, the horizontal stress ratio in the rock zone can be approximated as $K_0 = 0.4982$.

Sixth – The code requirement of 30 to 65 pounds per cubic feet (4 to 10 kN/m^3) expressed as a range of ratios, $k_0 = 0.19$ to 0.42 (for rock unit weight of 155 pounds/cubic foot (24 kN/m^3)) is shown in the graph plotted along with the results of the analysis. As can be seen in Figure 3 the code requirement is conservative for results up to a point where the dip angle exceeds the friction angle by 30 degrees. Above 30 degrees, the code requirement is less than the horizontal loads that may be imparted to the structure. Therefore, designers should be aware of this relationship and increase horizontal rock loading in the rock zone above the code requirements when rock wedge loads are likely to be formed.

Note that the negative loads shown at the bottom left side of Figure 3 represent cases where keyblocks are found to be mechanically stable.

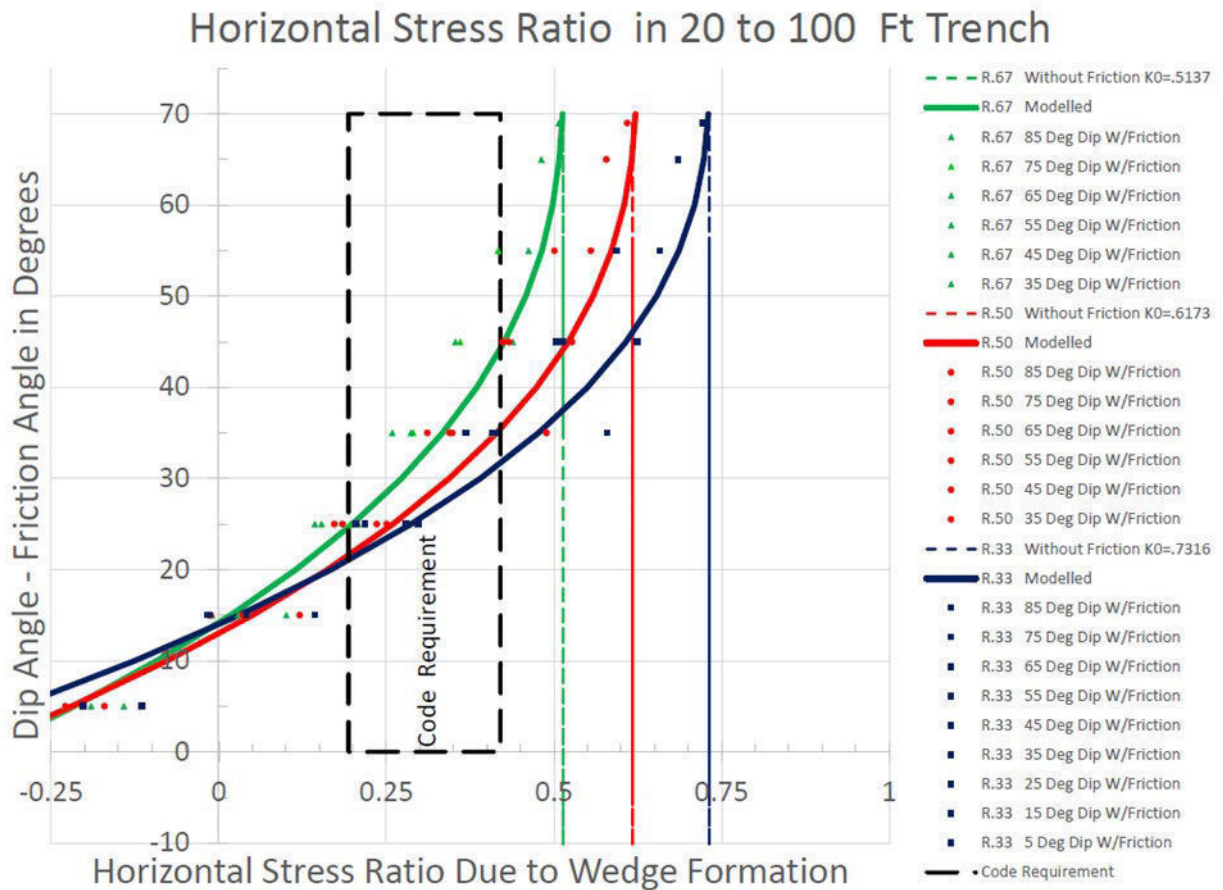


Figure 3. Graph of results of numerical analysis of tetrahedral rock wedges formed in rock, where RR is the percentage of rock in the bottom portion of the trench

5 CONCLUSION

Geotechnical conditions remain hidden underground and difficult to determine with sparse geotechnical borings. Nevertheless, principles and methods for estimating insitu stresses and rock loads on underground structures have been developed over a period of eight decades. Two recent equations for estimating rock loads on underground structures are proposed in this paper.

The first equation is a method for estimating rock loads on shallow underground caverns based on previously measured rock loading data from final lining instrumentation and empirical geotechnical data from previously constructed mined subway station caverns in Washington, D.C. and New York, correlated with geological data and cavern geometry using the Q index value and scaled crown span equation.

The actual horizontal stress ratio in rock at a project site can range from near zero to an upper end of 29 based on Sheorey theory. The high end of this range is generally not observed on cut and cover excavations. However, if present some degree of high stresses must be accounted for during design. Depending on the local geotechnical conditions, tectonic stresses can lead to tensile horizontal stresses or very high compressive stresses which tend to be unknown. The state of the industry can therefore be advanced by providing additional expenditure for measurement of horizontal in-situ stresses during the geotechnical investigation. Horizontal rock stresses may also result from Hooke's law due to horizontal restraint of the adjacent rock mass, or a plethora of other local geotechnical conditions. More typically for cut and cover transportation structures, rock wedge loadings may generate horizontal rock stress ratios that range from zero to 0.95 if the joint set dip angle is sufficiently greater than the joint set friction angle. All of these issues must be accounted for during the appropriate phase of design to ensure safe construction of structures in cut and cover rock excavations.

6 REFERENCES

- AASHTO, American Association of State Highway and Transportation Officials. 2020. *LRFD Bridge design specifications, Ninth Edition*.
- AASHTO, American Association of State Highway and Transportation Officials. 2017. *LRFD Road tunnel design and construction guide specifications, First Edition*.
- AASHTO, American Association of State Highway and Transportation Officials. 1973. *Standard specifications for highway bridges, Eleventh Edition*.
- AASHTO, American Association of State Highway and Transportation Officials. 2002. *Standard specifications for highway bridges, Seventeenth Edition*.
- ASTM, American Society for Testing Materials Standard D4623-16. 2016. *Standard test method for determination of in situ stress in rock mass by overcoring method—three component borehole deformation gauge*.
- Barton, Nick. 2002. Some new Q-values correlations to assist in site characterization and tunnel design. *International Journal of Rock Mechanics*, 39, Pergamon Press, pp. 185-216, February 5, 2002.
- Barton, Nick, & Grimstad, Eystein. 2014. *Forty years with the Q system in Norway and abroad*.
- Barton, Nick, Lien, R., & Lunde, J. 1974. Engineering classification of rock masses for the design of tunnel support. *Rock Mechanics* 6, Springer Verlag, p. 13, August 31, 1974.
- Bieniawski, Z. T. 1989. *Engineering rock mass classifications*. John Wiley and Sons.
- Bock, Carl, G. 1974. Rosslyn station, Virginia: geology, excavation, and support of a large, near surface, hard rock chamber. *RETC*, pp. 1373-1391.
- Brady, B.H.G. & Brown, E.T. 1985. *Rock mechanics for underground mining*. London, Allen and Unwin.
- Brown, E. T. & Hoek, E. 1978. Trends in relationships between measured in-situ stresses and depth. *Int. J. Rock. Mech. Min. Sci. & Geomech.* Abstr. Vol. 15, pp. 211-215.
- Caltrans, California State Transportation Agency. 2018. *Standard Specifications*.
- Caltrans, California Amendments to AASHTO. 2019. *LRFD Bridge design specifications – 8th Edition*.
- Carter, T. G. 1992. A New approach to surface crown pillar design. *Proc. 16th Canadian Rock Mechanics Symposium*, Sudbury, pp. 75-83.
- Carter, T. G. 2000. An Update on the scaled crown span concept for dimensioning surface crown pillars for new or abandoned mine workings. *Proc. 4th North American Rock Mechanics Conference*, Seattle, pp.465-47.
- Carter, T. G. 2014. *Guidelines for use of the scaled span method for surface crown pillar stability assessment*.
- Carter, T. G. & Miller, R. I. 1995. Crown-pillar risk assessment-planning aid for cost-effective mine closure remediation. *Trans. Inst. Min. Metl*, Vol 104, pp. A41-A57.
- Cording, E. J. & Mahar, J.W. 1974. The Effect of natural geologic discontinuities on behavior of rock in

- tunnels, *Rapid Excavation and Tunneling Conference Proceedings*.
- Cording, E. J., Van Sint Jan, M., Rodriguez, C., Mahar, J. W., Fernandez, G., & Ghaboussi, J. 1983. *Ground and lining behavior of station chambers in rock for the Washington, D. C. metro, Volume 1, observations during construction*. University of Illinois at Urbana-Champaign, U. S. Dept. of Transportation, Federal Highway Administration, October 1983.
- Cording, E. J., Van Sint Jan, M., Rodriguez, C., Mahar, J. W., Fernandez, G., & Ghaboussi, J. 1983. *Ground and lining behavior of station chambers in rock for the Washington, D. C. metro, Volume 3, analysis of rock displacements and lining performance*. University of Illinois at Urbana-Champaign, U. S. Dept. of Transportation, Federal Highway Administration, November 1983.
- Deere, D. U., Peck, R. B., Parker, H. W., Monsees, J. E., & Schmidt, B. 1970. Design of tunnel support systems, *High Res Rec* no 339, pp. 26 – 33.
- Desai, Drupad, Naik, Madan, Rossler, Karel, & Stone, Charles. 2005. New York subway caverns and crossovers. *Rapid Excavation and Tunneling Conference Proceedings*, Seattle, Washington, pp. 1303-1314.
- Desai, Drupad, Lagger, Hannes, & Stone, Charles. 2007. New York subway stations and crossover caverns - update on initial support design. *Rapid Excavation and Tunneling Conference Proceedings*, pp. 32-43.
- Enercon Services, Inc. 2013. *Lateral pressure calculation sheets, Comanche peak combined operation license application*, Calculation Number TXUT-001-FSAR-2.5-CALC 10, September 16, 2013.
- Grimstad, E. 2007. The Norwegian method of tunnelling – a challenge for support design. *XIV European Conference on Soil Mechanics and Geotechnical Engineering*, Madrid.
- Grimstad, Eystein, Bhasin, Rajinder, Wold Hagen, Anette, Kaynia, Amir, & Kankes, Kalpana. 2003. Q-system advance for sprayed lining, *Tunnels and Tunneling International*, pp. 44-48, January, 2003.
- Hanssen, Tor Harald. 1997. Investigations of some rock stress measuring techniques and the stress field in Norway. Doctor of Engineering Thesis, Department of Geology and Mineral Resources Engineering, Norwegian University of Science and Technology.
- Hoek, Evert. 2021. *Practical Rock Engineering*, On-line version. Rocscience.com, December 2021.
- Hoek, E., Kaiser, P.K., & Bawden, W. F. 1995. *Support of underground excavations in hard rock*. Balkema, Rotterdam.
- Hoek, Evert. 2000. Big tunnels in bad rock. *ASCE Civil Engineering Conference and Exposition*, Seattle, October 18–21, 2000.
- Mahar, J. W., Gau, F. L., & Cording, E. J. 1972. Observations during the construction of rock tunnels for the Washington, D. C. Subway. *Rapid Excavation and Tunneling Conference Proceedings*.
- Martin, C. D., Kaiser, P.K., & Christiansson, R. 2003. Stress, instability, and design of underground excavations. *International Journal of Rock Mechanics and Mining Sciences*, June 30, 2003.
- McCutchen, W. R. 1982. Some elements of a theory for in-situ stress. technical note, *Int. J. Rock Mech. Min. Sci. & Geomech. Abstr.*, Vol. 19. pp. 201–203.
- Muir Wood, A. M. 1975. The Circular tunnel in elastic ground. *Geotechnique*, 1, p115-127.
- Nemcik, Jan, Aziz, Naj, & Ren, Ting. 2012. Large excavations and their effect on displacement of land boundaries. *Proceedings of the 2012 Coal Operators' Conference*. Mining Engineering, University of Wollongong, February 18-20, 2012.
- Proctor, R. V., White, T. L., with introduction by Terzaghi, Karl. 1946. *Rock tunneling with steel supports with an introduction to tunnel geology*. Commercial Shearing and Stamping Company, Youngstown, Ohio.
- Quigley, R. M., Thompson, C.D., & Fedorkiw, J. P. 1978. A Pictorial case history of lateral rock creep in an open cut into the Niagara escarpment rocks at Hamilton, Ontario. *Canadian Geotechnical Journal*, Volume 15, pp. 128-133.
- Reinecker, J., Stephansson, O, & Zang, A. 2021. Stress analysis from overcoring data, World Stress Map project guidelines: overcoring, On-line version, December 2021.
- Rose, Don. 1982. Revising Terzaghi's tunnel rock load coefficients. *Proceedings of the 23rd U. S. Symposium on Rock Mechanics*, AIME, New York, pp. 953-960.
- Rossler, Karel & Stone, Charles. 2007. New York second avenue subway – initial support design of shallow rock caverns. *ITA-AITES World Tunneling Congress*, Prague, Czech Republic.
- Sheorey, P. R. 1994. A Theory for in-situ stresses in isotropic and transversely isotropic rock. *Int. J. Rock Mech Min. Sci. & Geomech. Abstr.* Vol. 31, No. 1, pp. 23-34.
- Stone, Charles, Kusznau, Joel, Boontun, Amarin, & Young, Dae. 1996. Comparison of a theoretical and numerical approach to probabilistic keyblock analysis. *North American Rock Mechanics Symposium 96*, Montreal, Canada, June 1996.

- Stone, Charles & Moon, Changsoo. (2019). Rock load estimation for shallow rock caverns. *Rapid Excavation and Tunneling Conference*, Society for Mining, Metallurgy and Exploration, Chicago, June 16-19, 2019.
- Stone, Charles & Wang, Eric. (2022). Lateral rock load estimation for cut and cover structures. *North American Tunneling 2022 Proceedings*. Society for Mining, Metallurgy and Exploration, Underground Construction Association, Philadelphia, June 19-22, 2022.
- Terzaghi, Karl & Richart, Jr., F. E. 1952. Stresses in rock about cavities. *Géotechnique*, Volume 3, Issue 2, pp. 57-90, June 1952.
- World Stress Map. 2021. <http://www.world-stress-map.org>, On-line version, August 17, 2021.

Analysis of the monitored behaviour of a hydraulic tunnel using structural and statistical models

R. Pereira

LNEC – Portuguese National Laboratory for Civil Engineering, Lisbon, Portugal

M. Espada

LNEC – Portuguese National Laboratory for Civil Engineering, Lisbon, Portugal

L. Lamas

LNEC – Portuguese National Laboratory for Civil Engineering, Lisbon, Portugal

N. Reis

EPAL - Empresa Portuguesa de Águas Livres, Lisbon, Portugal

ABSTRACT:

The Castelo do Bode hydraulic tunnel is part of the Lisbon water supply system. During its construction a monitoring system was implemented, aiming at monitoring the behaviour of the concrete tunnel lining and of the surrounding rock mass, and including visual inspections.

This work presents the monitoring system and introduces the relevant aspects of the analysis of the tunnel lining behaviour, based on the observed structural response to the imposed actions, namely the hydrostatic internal and external pressures, thermal variations, contact pressures and time effects. Two types of models are used: i) a structural model, based on axisymmetric analytical solutions of concentric permeable rings allows setting a reference situation from which it is possible, by comparison, to assess the tunnel's structural response; ii) a quantitative interpretation model, based on semi-empirical assumptions and error minimization statistical techniques, allows the quantification of the effect of each action on the observed structural response.

It is shown that the tunnel's behaviour observed during its service life can be effectively reproduced using these two approaches. Some considerations are made about the deterioration of the tunnel and the follow-up of its structural response.

1 INTRODUCTION

The concrete lined Castelo do Bode hydraulic tunnel is part of the Lisbon water supply system. The assessment of the safety conditions of hydraulic tunnels is of great importance, especially when they are part of the water supply system of large cities. A monitoring system was implemented to provide *in situ* information regarding its behaviour. The analysis and interpretation of the observed behavior are the main tasks that LNEC have been providing to the owner EPAL.

Tunnel linings must satisfy performance requirements related to the stability of the surrounding rock mass, the limitation of water losses and hydraulic jacking potential, and friction head losses (Lamas *et al.* 2014). Hydraulic tunnels are under loadings with seasonal fluctuations due to water pressure and thermal variations. The tunnel excavation causes a stress relief, changing the stress field of the ground. Water flowing under pressure inside the tunnel causes an internal water pressure in the concrete lining, while the groundwater in the rock mass causes an external pressure. Concrete linings are not impermeable, due to fissures that allow water seepage, and this must be considered in the analysis of the tunnel behaviour (Lamas 1993). Time effects due to the viscoelastic behaviour of concrete and possible swelling reactions are to be accounted for. All these loading sources, as well as the tunnels response to them, should then be properly monitored to allow the correct interpretation of the structural behaviour and its safety assessment.

The resort to structural models, when the necessary simplifications are acceptable, can be attempted. When structural models cannot reproduce the loading conditions and the structural re-

response, other assessing methods must be sought and quantitative interpretation models, based on statistical techniques, can be used for that purpose.

2 DESCRIPTION OF THE TUNNEL AND OF THE MONITORING SYSTEM

The Castelo do Bode dam is a 115 m high arch concrete built in 1957 in the Zêzere river, in the centre of Portugal (Figure 1a). The reservoir has a total capacity of 1095 hm³ of water which is mostly used for energy production and water supply to the Lisbon district (more than 2 million people) with a maximum production of 0.625 hm³ per day. Figure 1b illustrates the Lisbon water supply system. The hydraulic tunnel, inaugurated in 1987, is the first element of the Lisbon water supply system, starting at the outlet tower at the dam's reservoir.



Figure 1a. Castelo do Bode dam.

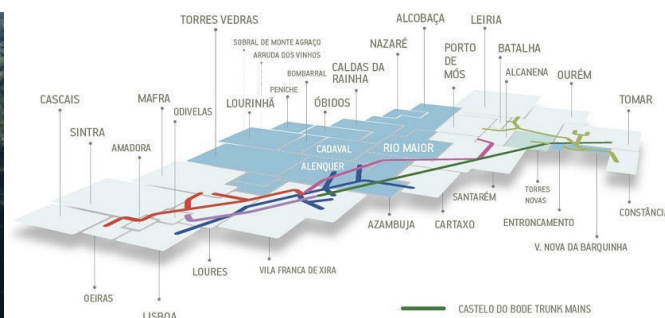


Figure 1b. Scheme of the Lisbon water supply system.

The hydraulic tunnel is 1088 m long, with floor elevation between 50,00 m at the beginning and 41,59 m at the end. Figure 2 shows its plant and longitudinal profile. The tunnel has a 0,35 m thick concrete lining with 3,00 m of interior diameter. Given its key role for supplying water to the Portuguese largest city, a monitoring system was implemented (LNEC, 1985), based on visual inspections and on the observed structural response to imposed actions, through:

- a set of six boreholes (SCB₁₂ to SCB₁₇) located along the tunnel's alignment, from the surface downwards, to monitor the evolution of the underground water level;
- two rod extensometers (SEB₁ and SEB₂) located approximately at the beginning and the end of the tunnel's alignment to monitor the ground movement, with two anchored points;
- a manometer at the end of the tunnel to measure the internal hydrostatic pressure and to estimate pressure losses by comparison with the reservoir water level; and
- an instrumented section (S₁), located 156 m from the end of the tunnel, with four active (A1 to A4) and two corrective (C1 and C2) Carlson extensometers, disposed as shown in Figure 3, connected to a reading unit at the surface, to measure strains in the concrete lining.

By disposing the extensometers this way one can measure strains at the tunnel ceiling (A2) and on the internal (A3) and external (A4) faces and in mid-thickness (A1) of tunnel walls. Corrective extensometers allow to correct measured strains, by removing the effects due to concrete volume variations.

The ageing of the monitoring equipment, whose consequences can already be felt, is now a cause of concern, 35 years after the tunnel begun operating. The corrective extensometer C1 has not produced coherent results since 1993 and was considered lost. Fortunately, the monitoring system has a second corrective extensometer (C2), which is used to correct the measured strains in active extensometers. Finally, extensometer A4 has also not produced coherent results since 2016, being the measured values, according to the manufacturer, outside the range of acceptable values, so it has been considered lost. The analysis of the structural response of the external face of the concrete ring is now limited, admitting that measured strains until 2016 can be extrapolated. It is believed that any serious event regarding the tunnel's safety can still be identified using other active extensometers as long as the corrective extensometer C2 remains functioning.

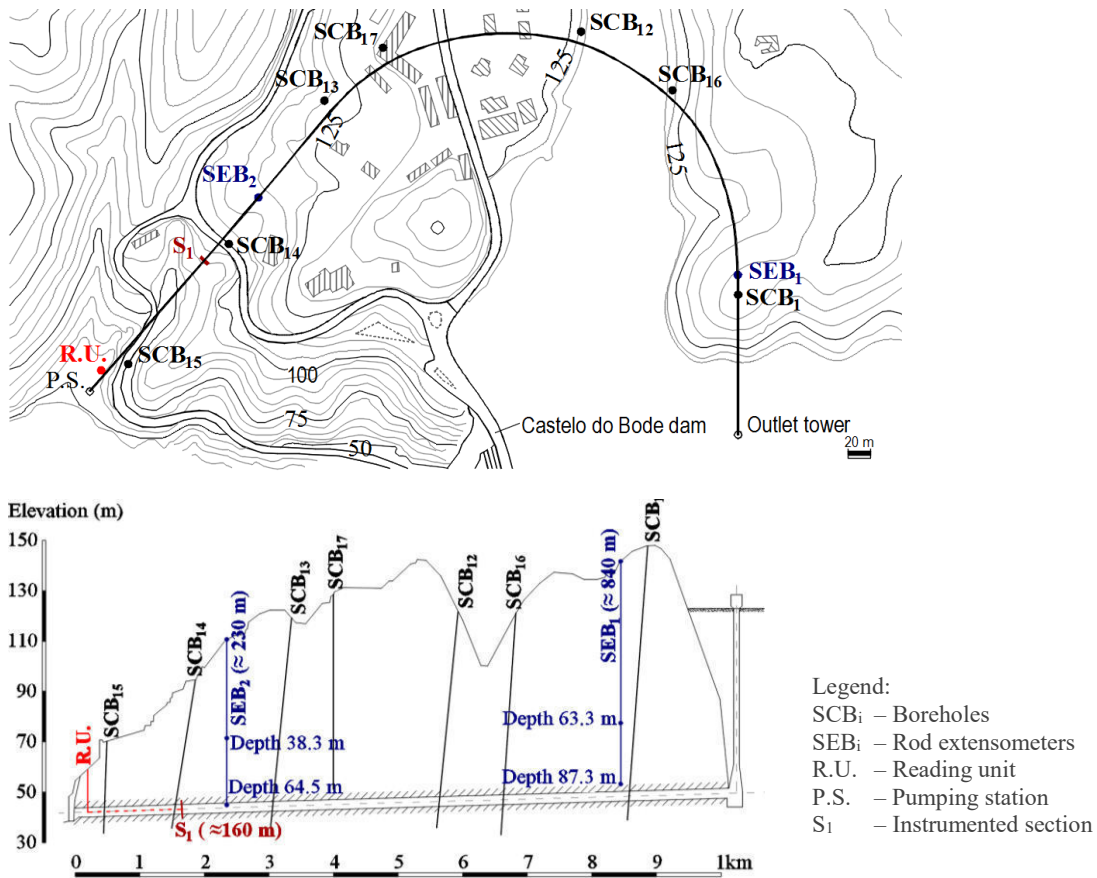


Figure 2. Plant (above) and longitudinal profile (below) of the hydraulic tunnel.

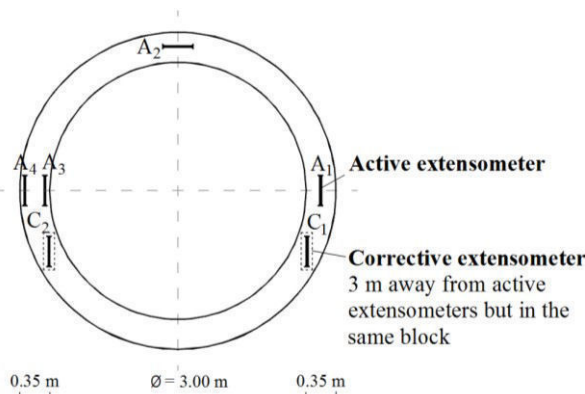


Figure 3. Disposal of Carlson extensometers into the concrete lining, in the instrumented section.

3 STRUCTURAL AND STATISTICAL MODELING

The analysis and interpretation of the observed strains at the instrumented section are a continuous task that has been performed since the beginning of the tunnel operation. During the initial operation period, while time effects were negligible, a structural model based on axisymmetric analytical solutions of concentric permeable rings was developed (LNEC 1999) and successfully used for this purpose (LNEC 2000, 2004). The analytical solution that characterizes the struc-

tural response requires the exact integration of the differential equations that govern the equilibrium, compatibility and constitutive laws of continuous media which can only be achieved considering simplistic idealizations of the geometry, material mechanical properties and loads. The idealized structural model (Figure 4) contemplates a concrete ring (1), corresponding to the lining, a fractured rock ring (2), which surrounds the support, and compact rock (3).

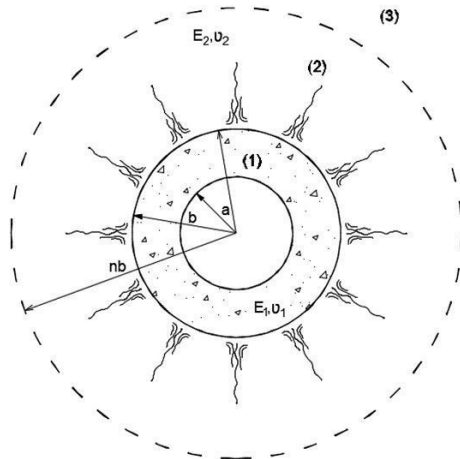


Figure 4. Structural model of the concrete lining confined by the surrounded rock mass.

The material and geometrical properties adopted were such that a better fit between computed and observed strains was achieved (LNEC 1999), disregarding time effects. Around the concrete lining, three zones with different properties were distinguished: a grouted zone considered by means of an increment of 0.75 m of the external radius of the lining ($r_1 = 2.6$ m); a zone of fractured rock which extends until three times the external radius of the lining ($r_2 = 5.55$ m); and a zone of compact rock taken as an infinite external media. The concrete and rock mass properties are summarized in Table 1.

Table 1. Concrete and rock mass properties.

Material	Young's Modulus (GPa)	Poisson's ratio	Thermal dilatation coefficient ($^{\circ}\text{C}^{-1}$)
Concrete	30	0.20	$10.80 \cdot 10^{-6}$
Rock mass	13	0.15	$4.32 \cdot 10^{-6}$

Loads acting on the concrete lining are: the pressure applied onto the internal and external faces; the thermal variations of the water in contact with the internal face; the stress relief of the surrounded rock mass caused by the excavation of the tunnel. Additionally, time effects due to the viscoelastic behaviour and swelling reactions of the concrete must also be accounted for.

Due to water flowing under pressure, the concrete lining is loaded internally by the corresponding hydrostatic pressure. Not only the groundwater applies pressures on its external face but also a reaction due to the constrained deformation caused by the surrounded rock mass. These actions are uniform hydrostatic pressures applied on the faces of the concrete ring (Figure 5a), which are known from the records of the internal and external water levels. Strains in the concrete lining due to thermal variations (Figure 5b) must also be compatibilized with the rock mass. From the temperature recorded in active extensometers A3 and A4, it is possible to estimate the temperature at any distance assuming a stationary state. There are analytical solutions for all these loading situations (Timoshenko and Goodier, 1970). Finally, the stress relief due to excavation originates external loads on the concrete lining. Assuming that the decompressed zone formed above the excavation has the form of a parabolic or elliptical load and that there is perfect lateral confinement (Figure 5c), an analytical solution (Einstein and Schwarz, 1979) was adopted assuming that the rock mass does not transmit shear stresses to the concrete lining.

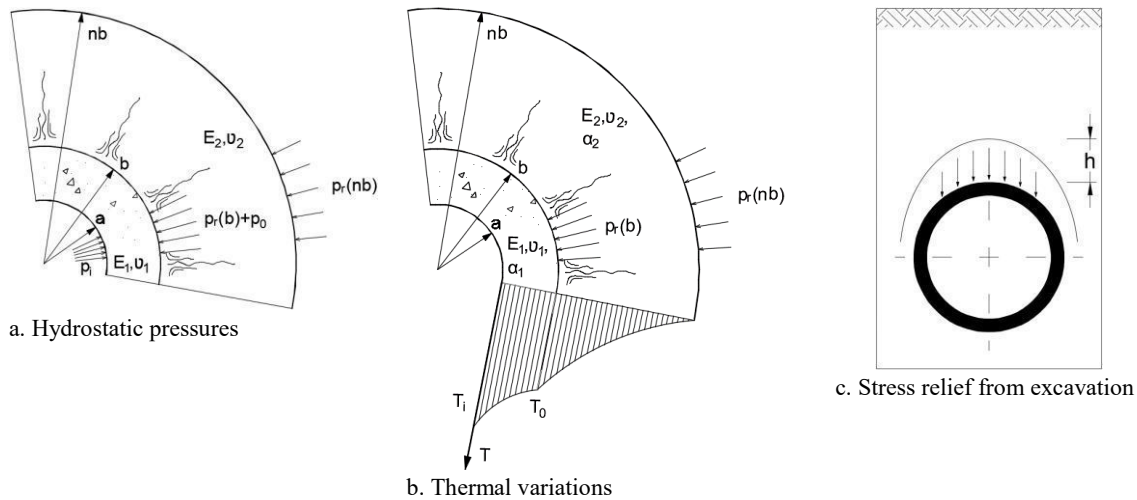


Figure 5. Load models.

The way it was build, this structural model is unable to account for the time effects, which became relevant as concrete creep and swelling reactions developed, having therefore difficulties in reproducing the observed behaviour. Consequently, an alternative approach, based on semi-empirical assumptions and error minimization statistical techniques (Rocha et al; 1958), *i.e* a quantitative interpretation model, was adopted (LNEC 2010, 2014, 2018, 2020), allowing the separation of the effects of each load source that mostly contribute to the global structural response. In this approach, it is assumed that the tunnels behaviour reflects a combination of the effects of thermal variations (ε_T), of the hydraulic gradient installed (ε_p) and of time (ε_t). Thus, the strains observed since the beginning of the operation were adjusted by a linear model, combining empirical laws accounting for the evolution of each effect with time, separately:

$$\varepsilon(t) = \varepsilon_T(t) + \varepsilon_p(t) + \varepsilon_t(t) + b_0 \quad (1)$$

where b_0 is the model error due to other effects not considered.

Having no other evidence than the observed data, it was assumed that:

- the part associated with the thermal variation varies linearly with the difference between the temperature at each time and the initial recorded temperature:

$$\varepsilon_T(t) = b_1 \cdot [T(t) - T_0] \quad (2)$$

- the part associated with the hydrostatic pressure varies linearly with the pressure gradient between the internal and external faces:

$$\varepsilon_p(t) = b_2 \cdot [p_i(t) - p_e(t)] \quad (3)$$

- the part associated with time effects is given by a logarithmic function which ensures a monotonic evolution with decreasing ratio:

$$\varepsilon_t(t) = b_3 \cdot \log(1+t/t_a) \quad (4)$$

where t and t_a , which is the first date with recordings (01/08/1986), are counted in days in relation to an average date assumed for the concreting works (01/01/1985).

The coefficients b_i are regression parameters, estimated through the weighted least square method, in such a way that the varying data monitoring frequency does not influence the results.

A mixed approach has also been tested (LNEC 2010, 2020), having the structural model been retaken to set a reference situation from which it is possible, by comparison, to assess the evolution of time effects, which are still quantitatively interpreted using statistical techniques. Both approaches were followed here and the results are presented below.

4 RESULTS

4.1 Quantitative interpretation model

For the quantitative interpretation model, values of the regression parameters b_i were estimated from the observed strains at each extensometer separately, using the weighted least square method. Observed strains were first obtained from the measured ones by subtracting the strains due to volumetric variations, measured in corrective extensometer C2. Time effects, for the case of the active extensometer A2, were corrected by adding a linear part ($b_4 \cdot [t-t_a]$) to the logarithmic model (Eq. 4). Figures 6 to 9 show the adjustment obtained using the quantitative interpretation model. The regression errors may characterize minor effects not explicitly considered.

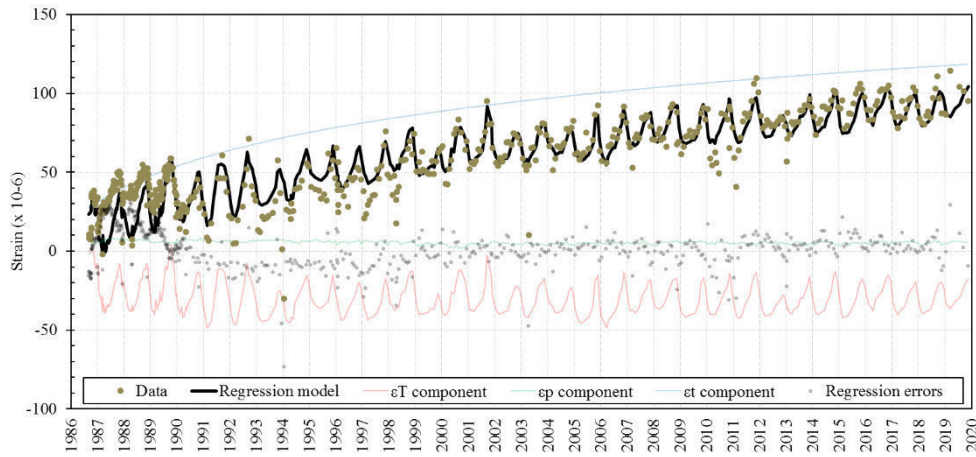


Figure 6. Quantitative interpretation model applied to data gathered in extensometer A1

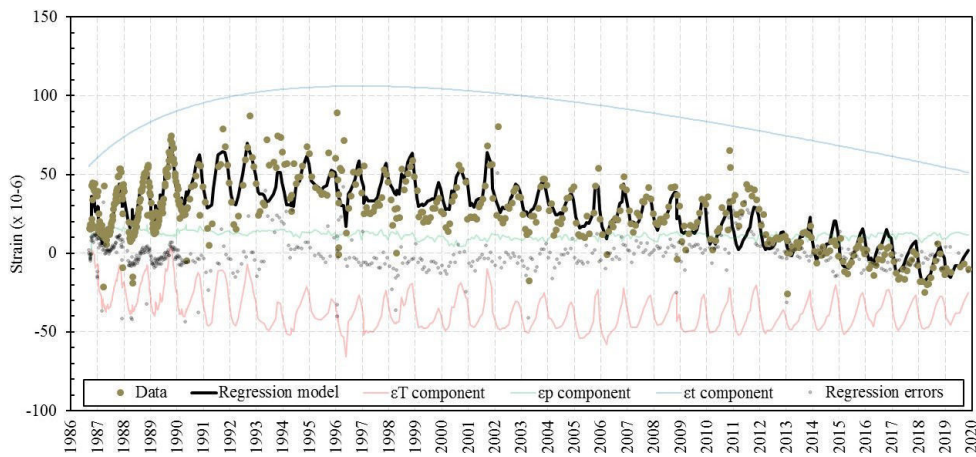


Figure 7. Quantitative interpretation model applied to data gathered in extensometer A2

A good agreement could be achieved using this model, as it will be evident afterwards, when the regression information is presented. The punctual strains that cannot be caught using the quantitative interpretation model are more likely to be outliers, since in most cases strains immediately before and after are well explained by this model. In fact, the tunnel was emptied in specific moments, generally before visual inspections carried out in its interior, and a steady state takes time to recover after refilling.

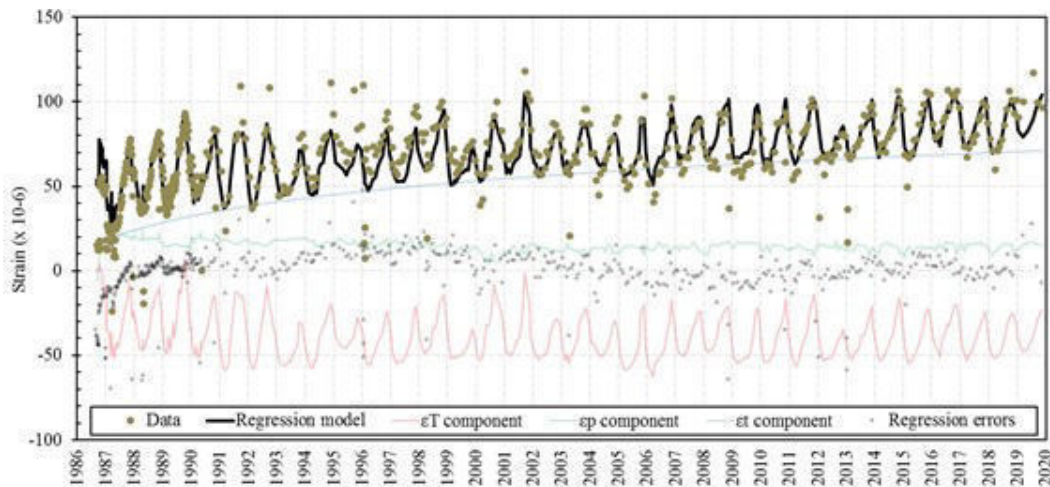


Figure 8. Quantitative interpretation model applied to data gathered in extensometer A3

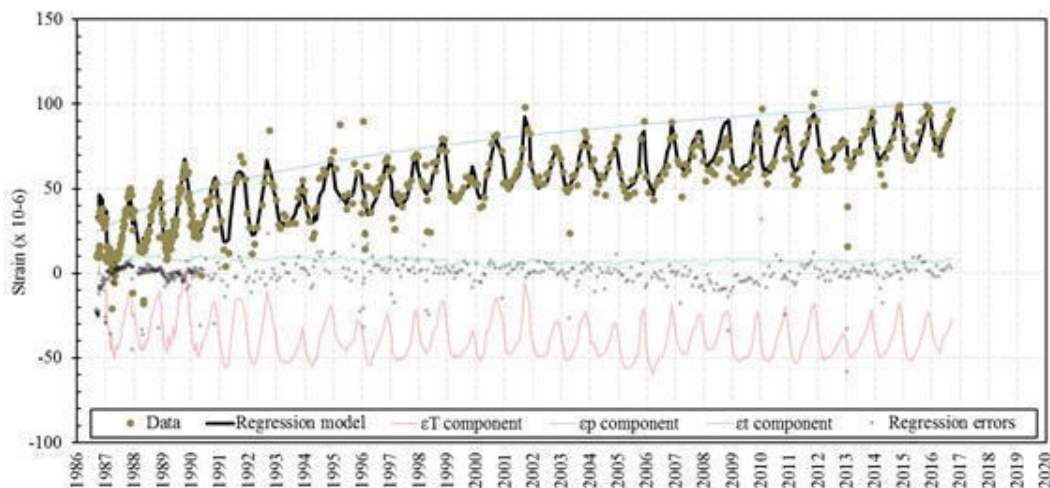


Figure 9. Quantitative interpretation model applied to data gathered in extensometer A4

4.2 Structural model

For the structural model, the same linear laws concerning the components associated with thermal variations and hydrostatic pressure (Eq. 2 and Eq. 3) were adjusted, by regression, to the computed strains at the location of each extensometer. The difference between observed and computed strains were then assumed to characterize the time effects to which Eq.4 (plus a linear part for extensometer A2) was also adjusted. Figures 10 to 13 show the adjustment obtained following this approach. Here, residuals (not represented) include minimization errors caused by two sources: the first regression procedure for the computed strains; and the second regression procedure for the difference between observed and computed strains.

A good agreement could also be obtained with the structural model. The known limitation of the structural model of not being able to account for time effects can this way be surpassed by using this mixed approach that split the procedure in two steps: firstly, the computed strains are interpreted and, then the time effects are analysed taking the difference between observed and computed strains. A comparison between the two approaches are made below.

4.3 Synthesis and analysis

The regression information, namely coefficient parameters, residual standard errors, and goodness-of-fit measurements (coefficients of determination) are displayed in Table 2, allowing the comparison between both approaches.

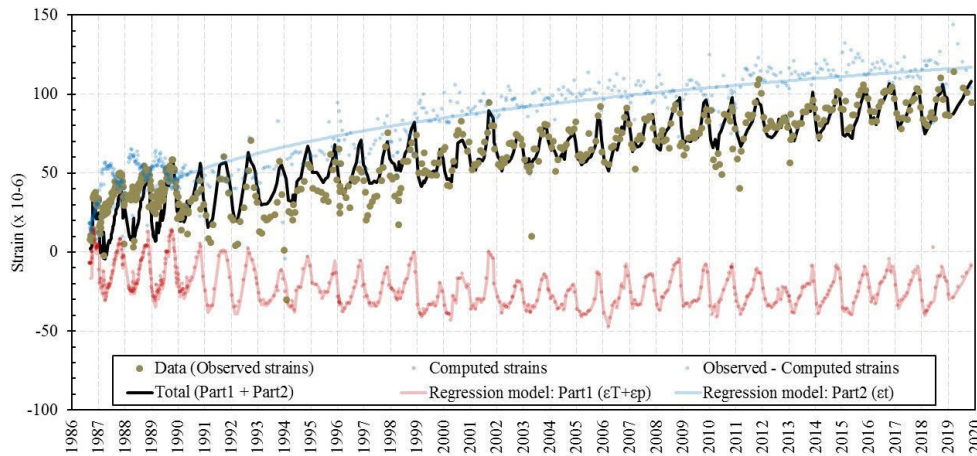


Figure 10. Structural model considering the location of extensometer A1 (mid-thickness)

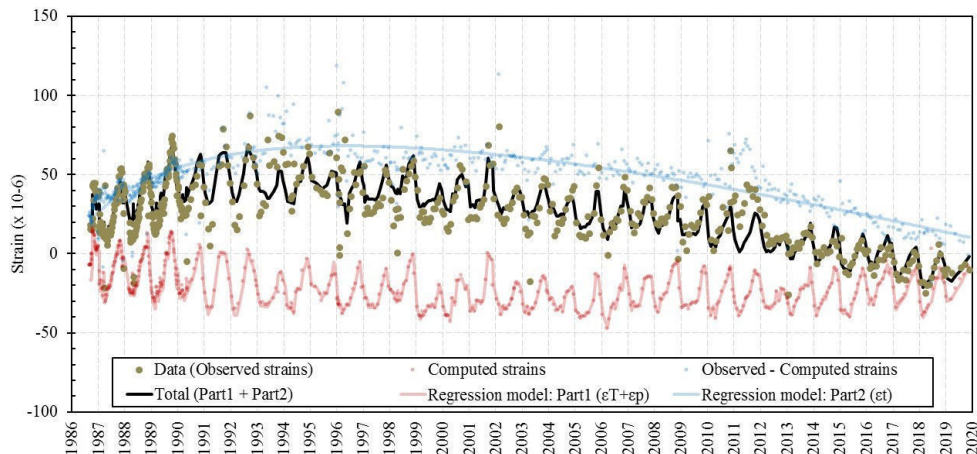


Figure 11. Structural model considering the location of extensometer A2 (ceiling/mid-thickness)

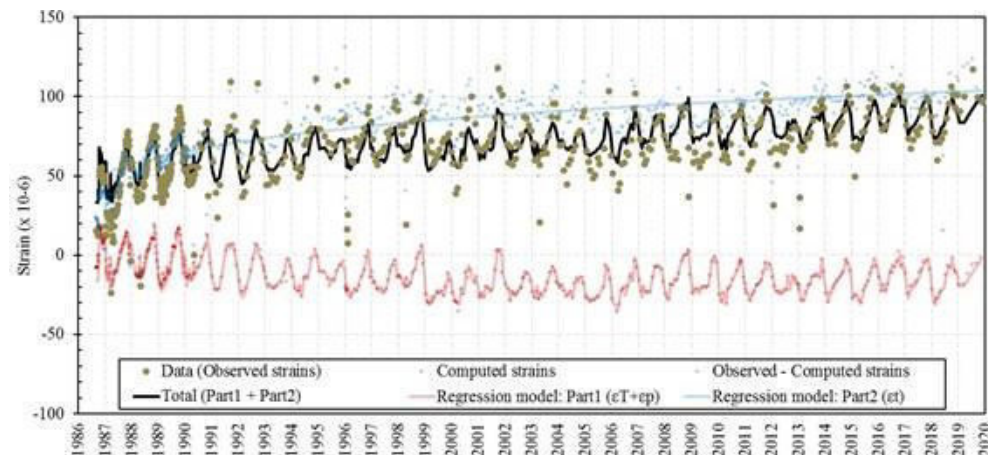


Figure 12. Structural model considering the location of extensometer A3 (internal face)

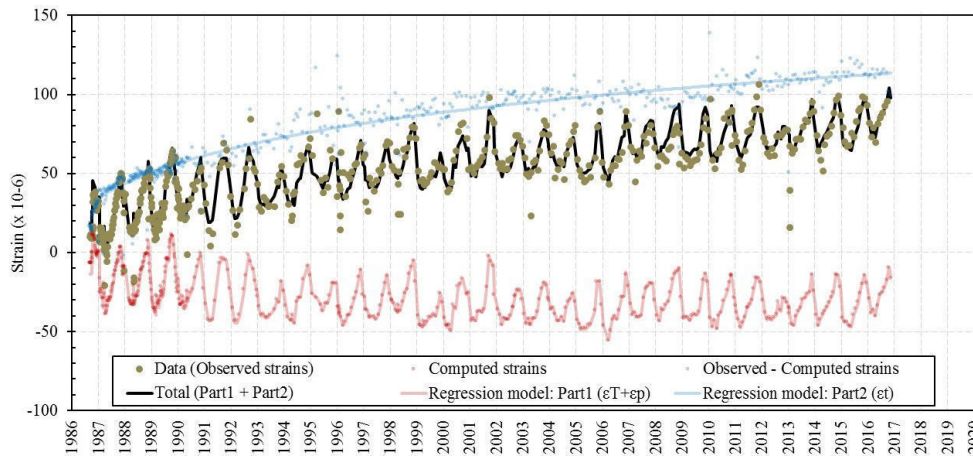


Figure 13. Structural model considering the location of extensometer A4 (External face)

Table 2. Coefficients b_i ($\times 10^{-6}$), standard deviation (σ) of residuals (ϵ) and coefficient of determination (R^2) obtained in the regression procedures followed.

Regression values	Quantitative interpretation model				Structural model			
	A1	A2	A3	A4	A1	A2	A3	A4
b_1	5.75	6.11	7.31	7.23	6.31	5.67	5.13	7.40
b_2	1.33	34.04	43.99	22.33	0.05	38.50	66.84	50.47
b_3	86.90	177.31	52.00	76.34	93.71	170.61	51.47	80.87
(b_4)		-0.02				-0.02		
σ (ϵ)	12.11	10.65	14.35	8.96	12.32	10.89	14.53	8.94
R^2	0.83	0.78	0.66	0.85	0.83	0.73	0.55	0.88

Regression coefficients b_i obtained using both approaches do not differ considerably. The small contribution of the effect of the hydraulic gradient installed, such as seen in Figures 7 to 9 (light green line), justifies the larger difference obtained for coefficient b_2 . For the quantitative interpretation and the structural model, the regression coefficient b_1 is smaller than the thermal dilatation coefficient ($10.80 \times 10^{-6} \text{ } ^\circ\text{C}^{-1}$) of the concrete. This is due to the presence of the surrounding rock mass that constrains the free deformation of the concrete ring, reducing the strains measured in the external face (extensometer A4), caused by thermal variations, to about two thirds of that value. Another aspect that both approaches could reproduce is that extensometer A2 (tunnel ceiling) presents less sensitivity to the hydraulic gradient and the thermal variations, given the smaller regression coefficients b_1 and b_2 . This is due to the external loads on the concrete ring caused by the stress relief of the excavation process, which are more relevant in the ceiling than in the walls (LNEC, 1982). Finally, the time effects proved to be predominant in the structural response, given its larger regression coefficients b_3 (and b_4 for extensometer A2). The difference between observed and computed strains has grown gradually with at a monotonic and descending rate. This effect, also relevant for the corrective extensometer C2 (not displayed here), may be mostly due to swelling reactions of the concrete, also having a minor contribution from concrete creep. The strange values measured in extensometer A2, that required a linear part to be added to the logarithmic law describing the time effects, are more likely to be due to its malfunction than to any structural effect.

5 CONCLUSIONS

In this paper, the analysis and interpretation of the behaviour of Castelo do Bode hydraulic tunnel is presented. For that, a structural model, adapted to take the time effects into account, based

on axisymmetric analytical solutions of concentric permeable rings, is compared to a quantitative interpretation model, based on semi-empirical hypotheses and error minimization statistical techniques. The main input of data comes from the Carlson extensometers installed in a specific instrumented section of the concrete lining.

Overall, measured strains in the concrete lining reflect the expected structural behaviour, which were caught by both the structural model and the quantitative interpretation model. Measured strains coherently reproduce the hydraulic pressure and thermal variations. Time effects, mostly due to swelling reactions of the concrete, are the component that contributes most to the structural response. These internal loads show a monotonic evolution at a descending rate, not yet stabilized.

At this moment, two extensometers are considered lost: corrective extensometer C1 (even though this does not jeopardize the interpretation of the tunnels behaviour since another corrective extensometer is still functional), and the active extensometer A4 (monitoring the structural response in of the external face concrete lining).

ACKNOWLEDGEMENTS

The authors thank EPAL – *Empresa Portuguesa de Águas Livres* for allowing the publication of the results of these studies.

REFERENCES

- Einstein HH & Schwartz CW 1979. Simplified analysis for tunnel supports. Journal of Geotechnical Engineering Division, ASCE, Vol. 105, No. GT4, pp. 499-518.
- Lamas L 1993. Contributions to understanding the hydromechanical behaviour of pressure tunnels. PhD Thesis, Imperial College, London, UK.
- Lamas L, Leitão NS, Esteves C & Plasencia N 2014. First infilling of the Venda Nova II Unlined High-Pressure Tunnel: Observed behaviour and numerical modelling. Rock Mechanics and Rock Engineering, Vol. 47, pp. 885-904.
- LNEC 1982. Problemática das estruturas subterrâneas em rocha. Seminário 285.
- LNEC 1985. Plano de observação do túnel do Castelo do Bode. Relatório 5/1985 – DBB/NOS.
- LNEC 1999. Observação do túnel de Castelo do Bode: Interpretação do comportamento observado. Relatório 17/99 – DBB/NOS.
- LNEC 2000. Observação do túnel de Castelo do Bode: Relatório final correspondente ao plano de trabalhos 1994-1998. Relatório 63/00 – DBB/NOS.
- LNEC 2004. Observação do túnel de Castelo do Bode: Relatório final correspondente ao plano de trabalhos 1999-2013. Relatório 156/04 – DBB/NFOS.
- LNEC 2010. Observação do túnel de Castelo do Bode: Relatório final correspondente ao plano de trabalhos 2004-2008. Relatório 297/2010 – DBB/NFOS.
- LNEC 2014. Observação do túnel de Castelo do Bode: Relatório final correspondente ao plano de trabalhos 2009-2013. Relatório 4/2014 – DBB/NMMR.
- LNEC 2018. Observação do túnel de Castelo do Bode: Relatório final correspondente ao plano de trabalhos 2014-2017 e revisão do plano de observação. Relatório 202/2018 – DBB/NMMR.
- LNEC 2020. Observação do túnel de Castelo do Bode: Relatório final correspondente ao plano de trabalhos 2018-2019. Relatório 194/2020 – DBB/NMMR.
- Rocha M, Serafim L & Silveira A 1958. A method of quantitative interpretation of the results obtained in the observation of dams. 6th Congress on Large Dams, R.83 Question 21. ICOLD, New York.
- Timoshenko SP & Goodier JN 1970. Theory of elasticity. McGraw-Hill Book Company, USA.

Influence of geotechnical parameters, in-situ stresses, and tunnel advance rate on rockburst's strain energy

C. Segura & A. Delonca

Departamento de Ingeniería Metalúrgica y de Materiales (DIMM), Universidad Técnica Federico Santa María, Santiago, Chile

Y. Gunzburger

GeoResources, UMR 7359, Université de Lorraine – CNRS, Ecole des Mines de Nancy, Nancy, France

ABSTRACT:

Rockburst in tunnels is a threat for both workers and equipment. Therefore, their assessment is of major importance. However, these events are difficult to predict, due to their complexity. Additionally, there is an uncertainty regarding the characteristics of the environment in which the rockburst can occur, and the influence that they can have on the intensity of the event. This work proposes to study the influence of (1) the Young modulus, (2) the Poisson coefficient, (3) the in-situ stresses, and (4) the stress-ratio K , on the strain energy of a potential rockburst. To do so, 3D numerical modelling have been conducted using the FLAC3D code, considering an elastic constitutive model. To characterize the rockburst, the following parameters are assessed: maximum strain energy around and in the front of the tunnel. To validate the results, they are compared to analytical ones obtained considering Lamé's solution. The results between the analytical and numerical approaches were consistent, which allow us to confirm the numerical procedure. Results show that the maximum strain energy is always located around the tunnel and never in the front of the tunnel. Moreover, the in – situ stress is the parameter with the highest impact on the maximum strain energy. The young's modulus and the stress ratio k present the second highest impact. The Poisson ratio has zero to low impact. Finally, the maximum strain energy is not located at the front of the tunnel but at the countour of the start of the excavation.

1 INTRODUCTION

The present study is related to the understanding and analysis of violent rock release events, known as rockbursts, that can occur in deep underground mining. Rockbursts can be classified into three large groups depending on the possible source of the event (Blake and Hedley, 2003): (1) strain burst, (2) pillar burst, and (3) fault slip. Strain bursting is the most common type of unstable rock failure in underground openings (Diederichs, 2018), where the intensity and scale are usually less than the other two types of phenomena, but their repercussions are still as significant. Triggering mechanisms for strain burst can range from high stress concentration at the edge of the excavation to buckling of discontinuities that are parallel to the axial direction of underground openings (Wang and Kaunda, 2019). This type of failure can generate as consequences the ejection of fragments of surface rock at high speeds or gravitational detachment of sheets of rock, which strongly compromise the health of personnel and the correct functioning of equipment at different levels. mine site operations.

There are several rockburst evaluation methods, including empirical methods (Askaripour et al., 2022; Wu et al., 2022), numerical modeling and theoretical or mathematical approaches (Zhou et al., 2018). Currently, the theoretical approach that has been commonly adopted to study and prevent the occurrence of these types of phenomena has focused on the mechanical energy balance developed by Salamon (1984), which allows each of the energy components that are part of the thermodynamic balance of the rock mass during the construction of a mining development to be calculated.

Chen and Guo (2020) state that the main energy to be considered during the rock failure phenomenon corresponds to the elastic strain energy. This parameter has been cataloged as the pre-

cursor variable of all energy processes associated with rockfall events, and therefore, its generation, propagation and dissipation is of great interest in the mining industry.

Despite the great advances and numerous investigations on the subject (Zhou et al., 2018), at present it is still not possible to obtain a complete understanding of the physical phenomenon of rock bursts or how they affect each of the multiple factors. to the frequency of occurrence and the magnitude of these events.

The main purpose of this article is to identify, through 24 numerical models considering the FLAC3D software, the factors that have a more significant influence on the amount of strain energy stored in a rock that is prone to experiencing a rockburst. In all the models, the excavation process of a cylindrical underground opening in a finite elastic rocky medium subjected to pre-defined forces is simulated. The analysis considers the calculation of the total strain energy of the models, together with the determination of the magnitude and spatial distribution of the maximum strain energy of the simulations. The numerical models consider the variation of different geomechanical parameters of the rock mass: (1) Young's modulus (E); (2) Poisson's ratio (ν); (3) magnitude of in-situ stresses ($\sigma_x, \sigma_y, \sigma_z$); (4) horizontal and vertical stress ratio (k_x, k_z); as of operational parameters: (5) excavation step of the underground opening.

In the first part of the investigation, a simple exemplification of the energy balance in the excavation of an underground opening and the analytical derivation of the elastic strain energy is presented. The second section details the numerical modeling procedure carried out in the FLAC3D software for the different simulations together with the analytical validation methodology corresponding to each model. Finally, in the third section, the results and conclusions of the sensitivity analysis built with the different numerical models are presented.

2 MECHANICAL ENERGY BALANCE

2.1 General considerations

The balance of energy stored in a rock volume provides the energy that can be dissipated when a geometric or tensional change occurs in the rock mass. To understand the origin of the energy released in a strain burst, the energy balance is evaluated in a simplified scenario composed of two stages. In stage (I), the natural state of the rock mass at a certain depth from the earth's surface is considered. In a later stage (II), a circular excavation of an underground opening is carried out on the study rock. From the configured system, the energy changes that occur between stages (I) and (II) on the volume of non-excavated in-situ rock are analyzed (figure 1).

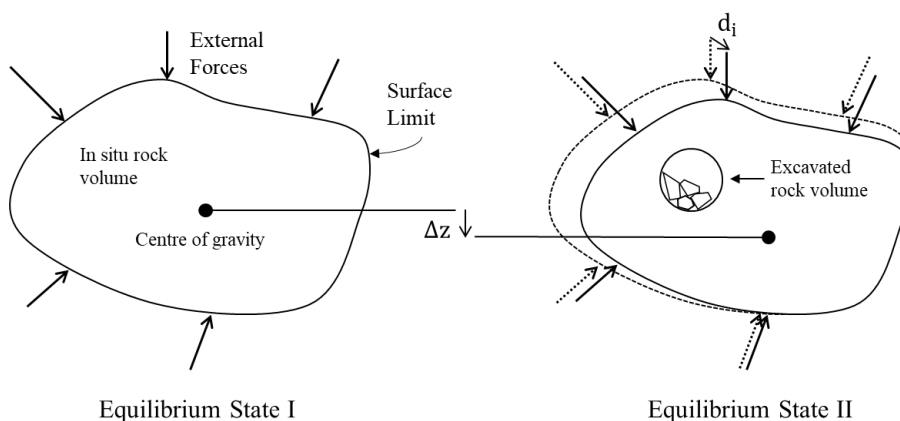


Figure 1. Energy changes experienced by a rock mass as a result of the creation of an underground excavation.

In the initial stage (I), before carrying out the excavation, the considered isolated rock mass is in equilibrium under a set of limit forces that act on the surface of the system, and that represent the in-situ forces of the rock. Consequently, the rock mass has an internal stress state, and there-

fore a certain amount of elastic strain energy U_c . Likewise, due to the spatial location of its center of gravity, the rock mass also has a gravitational potential energy, E_{av} .

In the final stage (II), in response to the completion of the underground opening, the external forces acting on the boundary of the system perform work W_{ext} . In the remaining rock volume, there is an increase in elastic strain energy ΔU_c compared to the initial state, due to stress redistribution in the model. Likewise, the gravitational potential energy of the system also has a variation in relation to its initial value, in an amount ΔE_{av} , since there is a displacement of the center of gravity of the rock mass in the direction of the excavation product of the mined or extracted rock. According to the first law of thermodynamics, the energy balance in the closed system between the two equilibrium states is expressed through the following equation:

$$U_{c_i} + E_{gp_i} = U_{c_f} + E_{gp_f} - W_{ext} \quad (1)$$

$$W_{ext} = \Delta U_c + \Delta E_{gp} \quad (2)$$

Salamon (1984) demonstrated through various analytical examples that: $W_{ext} > \Delta U_c + \Delta E_{av}$. According to equation (2), the consequence of this inequality is due to the fact that a percentage of energy dissipation W_{diss} must be involved in the system, so that it recovers equilibrium after the excavation. The nature of this dissipated energy can be broken down into two main components. Firstly, the energy released by the rock that fails, that is, that presents plastification W_{plas} . And secondly, an energy component, corresponding to kinetic energy W_k , which manifests itself as a seismic wave that travels through the rock mass and can lead to the expulsion of rock fragments at high speed.

$$W_{diss} = W_k + W_{plas} \quad (3)$$

In this way, the energy released by a rockburst phenomenon is formulated from the following expression (Hauquin et al., 2018):

$$W_k + W_{plas} = W_{ext} - (\Delta U_c + \Delta E_{gp}) \quad (4)$$

If the analysis of an ideal elastic medium is considered, where there is no energy dissipation due to fracturing or inelastic deformation of the rock ($W_{plas} = 0$), and additionally, the system is evaluated in a deep reservoir where the magnitude of the stresses in – situ are considerably greater than the gravitational forces ($\Delta U_c \gg \Delta E_{av}$ y $W_{ext} \gg \Delta E_{av}$), the final expression of the energy released will exhibit a unique dependence on the W_{ext} and ΔU_c components.

$$W_k = W_{ext} - \Delta U_c \quad (5)$$

From equation (5) it is observed that the energy released in a deformation rockburst event can be directly associated with the difference between the value of the work of the external forces and the deformation energy between two equilibrium states of the rock system.

2.2 Elastic strain energy

When an elastic body is deformed, the forces that cause the deformation work on the body as they deform it. According to the principle of conservation of energy, this work is stored in the deformed body as elastic strain energy.

For isotropic rocks, the stored strain energy can be written in many different ways. Equation (6) defines the elastic strain energy for an equilibrium state as a function of the principal stresses (Jaeger et al., 2007):

$$U_c = \frac{v}{2E} [\sigma_1^2 + \sigma_2^2 + \sigma_3^2 - 2v(\sigma_1\sigma_2 + \sigma_1\sigma_3 + \sigma_2\sigma_3)] \quad (6)$$

where E corresponds to Young's modulus, v to Poisson's ratio, v to the volume of rock analyzed, and $\sigma_1, \sigma_2, \sigma_3$ to the maximum, intermediate, and minor principal stresses, respectively.

2.3 Analytical determination of strain energy

In 1852, Lamé published a 2D closed form solution to determine the stresses and displacements induced in a hollow elastic cylinder subjected to radial loads on its outer and inner surfaces. This mathematical method was one of the pioneering scientific methodologies to represent a circular opening with a uniform internal pressure, located in an elastic rock mass subjected to an in – situ hydrostatic stress field.

Equations (7), (8) and (9) correspond to the expressions derived from the Lamé solution to determine the radial (σ_r), tangential (σ_t), and axial (σ_a) induced stresses around a circular excavation in an semi-infinite elastic medium, subject to an initial far-field principal stress under plane strain conditions (figure 2).

$$\sigma_r = \frac{p \cdot r_e^2}{r_e^2 - r_i^2} \left(1 - \frac{r_i^2}{r^2} \right) \quad (7)$$

$$\sigma_t = \frac{p \cdot r_e^2}{r_e^2 - r_i^2} \left(1 + \frac{r_i^2}{r^2} \right) \quad (8)$$

$$\sigma_a = (\sigma_r + \sigma_t)v \quad (9)$$

where: p corresponds to the external hydrostatic stress, r_i the excavation radius of the underground opening, r_e the radius of the outer limit of the cylinder, r the radius where the stresses are to be determined, and v the Poisson's ratio of the rock medium.

In the analysis scenario studied by Lamé, the axial, tangential, and radial stresses correspond to the major, intermediate, and minor principal stresses, respectively (this condition is not unrestrictedly fulfilled in the total spatiality of the case to be analyzed). In this way, using expressions (7), (8), and (9) in equation (6), it is possible to determine the analytical value of the total deformation energy of a model composed of the excavation of a circular opening.

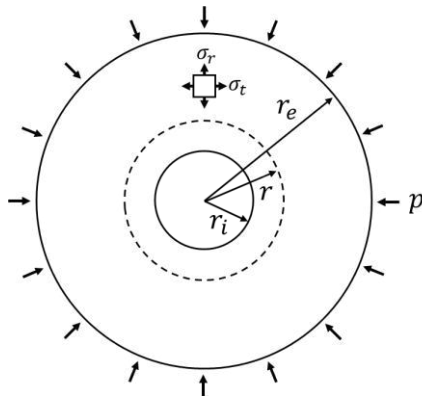


Figure 2. Thick-walled cylinder without internal pressure proposed by Lamé.

3 METHODOLOGY

For the analysis of this study, the following methodological steps were adopted:

1. Construction of the numerical analysis base model for the study of strain energy.
2. Definition of the analysis scenarios based on the variation of mechanical, tensional and operational parameters.
3. Analytical validation of the different numerical models built through the calculation of the deformation energy through the Lamé equations.

3.1 Strain energy modeling

For the simulation of the different numerical models, the FLAC3D software (v7.0) of the ITASCA company was used. This finite difference code, together with the internal programming language FISH, allowed the calculation of the elastic deformation energy of the predefined

models, based on the elastic parameters of the rock and the distribution of stresses induced by the excavation. Additionally, the implementation and creation of external functions through the FISH code allowed: (1) to determine the total and maximum values of the deformation energy, both in the full extension of the models, and in the volume ahead of the advance front ; (2) spatially identify the areas of the models that presented a greater magnitude of ΔU_c ; and (3) estimate the radius of influence around the excavation, where the magnitudes of ΔU_c represented a significant percentage of the maximum strain energy of the model. 24 analysis scenarios were performed, where the excavation process of a circular opening in a cylindrical continuous elastic medium (without failures or fractures) was simulated. The different models were discretized into approximately 70,000 quadrilateral elements of different sizes (figure 3). The initial geometry of all the simulated models was identical, and corresponded to a quarter of the cylindrical symmetry, in order to obtain greater savings in computational resources. In dimensional terms, the models were made up of an excavation radius of 1 (m), an external analysis radius of 10 (m), a length of the model in the axial direction to the z-x plane of 50 (m) and an excavation step of variable dimension, depending on the analysis scenario (detailed in the next item).

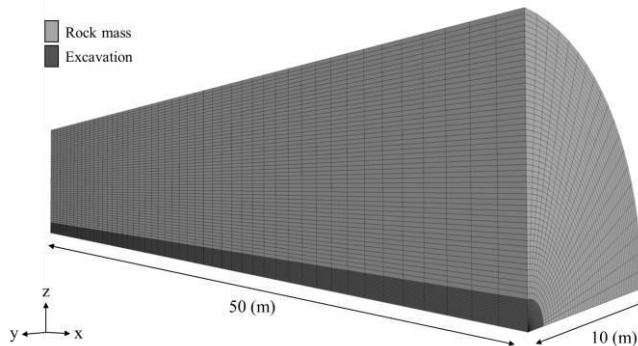


Figure 3. 3D geometry of the initial phase of the simulated models.

The boundary conditions assigned to the different models are detailed in figure (4), where the displacement restriction is established in the normal direction of the different faces (the horizontal displacement is fixed to the vertical faces and the vertical displacement to the horizontal faces), with the exception of the lateral circular surface of the cylindrical opening. This area is free in relation to the displacements and presents as a limiting condition the application of in-situ stresses ($\sigma_x, \sigma_y, \sigma_z$) in a direction normal to the different cartesian orientations (x, y, z).

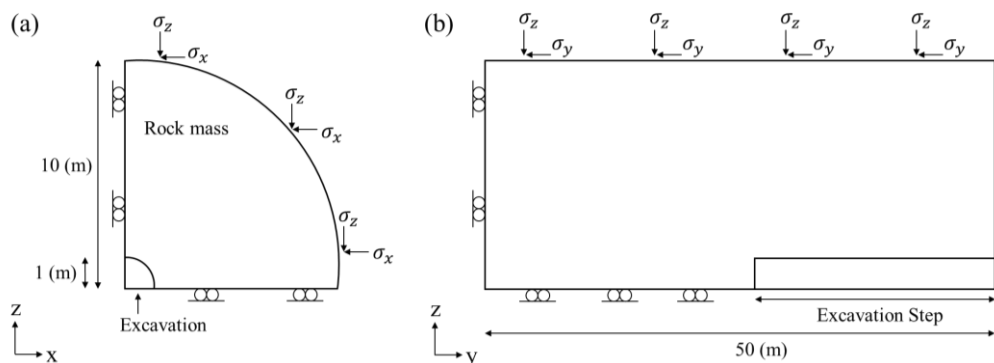


Figure 4. Dimensions and boundary conditions of the 3D models in the planes: (a) z - x and (b) z - y.

The construction stages of all the models are made up of an initial phase of assignment of the elastic constitutive model, establishment of the boundary conditions, and initialization of the stresses in-situ; and a secondary phase, where the excavation of the underground opening is simulated, that is, the instantaneous removal of the volume of rock predefined by the excavation radius and by the excavation step of the model in the axial direction to the z-x plane.

3.2 Sensitivity analysis

The reference model corresponds to an analysis scenario found at an operating depth of 1000 (m), in a state of geostatic stress, where the effects and stresses generated by the gravitational field are neglected. The mechanical properties detailed in table 1 are identical both for the rock that makes up the excavation opening and for the surrounding rock mass. Young's modulus and Poisson's coefficient were defined in relation to a granitic lithology (Weng (2017) studies a real case of rockburst with very similar elastic parameters) and the initial stress field ($\sigma_x, \sigma_v, \sigma_z$) is fixed based on detailed operating depth.

Table 1. Base parameters of the different numerical models.

Parameter	Value
Density (kg/m ³)	2750
Young' Modulus (GPa)	50,0
Poisson Ratio	0,30
$\sigma_x, \sigma_v, \sigma_z$ (MPa)	27,0
k_x, k_z	1,0

Feng (2017) establishes that four main parameters control the occurrence of rockburst events: the properties of the rock, the depth of the gallery, the extension of the mining area, and the extraction rate of the deposit. Based on what was mentioned by the author, the influence of the elastic, tensional and operational parameters on the value of the deformation energy when an underground opening is created was analyzed. The variables considered were: (1) Young's modulus; (2) Poisson's ratio; (3) normal stresses ($\sigma_x, \sigma_v, \sigma_z$); (4) horizontal and vertical stress ratio (k_x, k_z); and (5) length of the excavation step. The geometric and mechanical properties were fixed and each parameter was modified by a specific magnitude independently, creating 24 different analysis scenarios. Table 2 summarizes all the simulated configurations. For models #6 - #24, the excavation step used corresponded to 10 (m). This value was chosen in correspondence between the analytical results and the numerical results of models #1 - #5 (where a low percentage error was obtained), and additionally considering the average rate of advance in a competent rock mass at great depth. in real operations (Morrison et al., 2014).

Table 2. Variation parameter of each model.

Model	Variation parameter	Value	Change (%)	Model	Variation parameter	Value	Change (%)
#1	Excavation Step (m)	1	-	#13	Poisson Ratio	0,21	-30,0
#2	Excavation Step (m)	2	-	#14	Poisson Ratio	0,17	-43,3
#3	Excavation Step (m)	5	-	#15	Poisson Ratio	0,35	+16,7
#4	Excavation Step (m)	10	-	#16	$\sigma_x, \sigma_v, \sigma_z$ (MPa)	13,5	-50,0
#5	Excavation Step (m)	20	-	#17	$\sigma_x, \sigma_v, \sigma_z$ (MPa)	35,1	+30,0
#6	Young' Modulus (GPa)	62,5	+25,0	#18	$\sigma_x, \sigma_v, \sigma_z$ (MPa)	48,6	+80,0
#7	Young' Modulus (GPa)	25,0	-50,0	#19	$\sigma_x, \sigma_v, \sigma_z$ (MPa)	21,6	-20,0
#8	Young' Modulus (GPa)	40,0	-20,0	#20	$\sigma_x, \sigma_v, \sigma_z$ (MPa)	40,5	+50,0
#9	Young' Modulus (GPa)	15,0	-70,0	#21	$\sigma_x, \sigma_v, \sigma_z$ (MPa)	54,0	+100,0
#10	Young' Modulus (GPa)	75,0	+50,0	#22	k_x, k_z	0,5	+25,0
#11	Young' Modulus (GPa)	100,0	+100,0	#23	k_x, k_z	1,5	-50,0
#12	Poisson Ratio	0,26	-13,3	#24	k_x, k_z	2,0	-20,0

3.3 Analytical validation of numerical models

From equations (7), (8), and (9) the calculation of the tensional field was made between the initial equilibrium state (intact rock mass) and the final equilibrium state (rock mass with excavation) of each one of the models. Using the results obtained from each of the two construction phases in equation (6), the analytical value of the stored elastic strain energy variation for each

analysis scenario was determined. The calculated theoretical solution was used for its verification and validation with the recently detailed numerical methods.

4 RESULTS

4.1 Verification of analytical - numerical results

Figure 5 presents the numerical results of the total variation of the strain energy against the analytical calculation through the Lamé equations for each simulated model.

The percentage difference between the numerical and analytical results is exclusively influenced by the size of the excavation step. For an extraction length of 1 (m) there is a maximum error of 28.3%, which potentially decreases to a minimum value of 2.61% when considering an excavation step of 20 (m). The changes in the other characteristic parameters generate very low magnitude variations in the percentage values. Models #6 - #21 represented by an excavation step of 10 (m) present a mean percentage error of 4.3%.

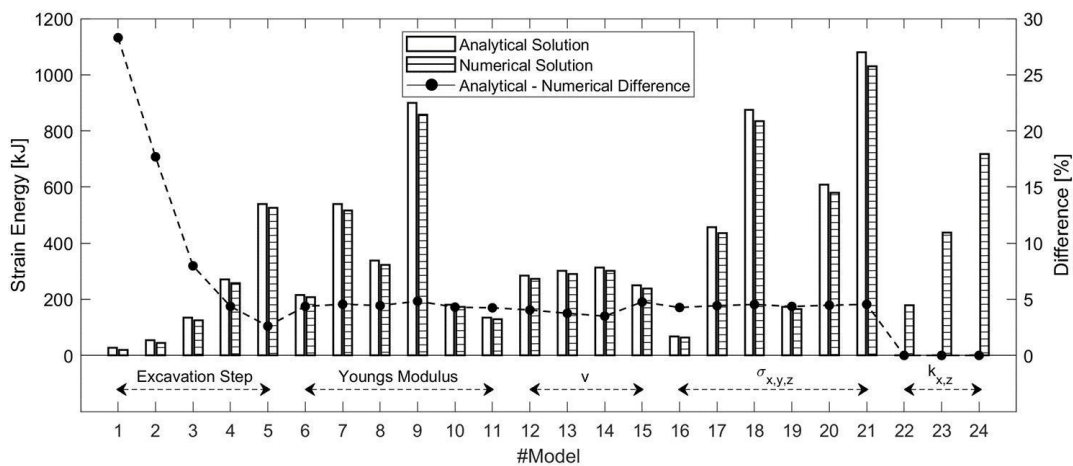


Figure 5. Analytical and numerical solution of the total strain energy of the different simulated models.

It was found that the analytical results overestimate the value of the strain energy, since as it is a solution for 2D problems, the equations only determine a stress distribution profile in the plane perpendicular to the axis of the excavation (y axis). In this way, the variability of the stress generated in the axial direction of the tunnel is not included in the calculation, nor is the influence caused by the advancing front on the radial and tangential stresses associated with the areas surrounding the excavation. As there is a smaller excavation step, the estimated strain energy in the vicinity of the advance front corresponds to a higher proportion in relation to the total energy of the model and consequently the numerical-analytical difference increases. In the models where the stress ratio was varied percentagewise, the analytical validation was not carried out (models #22 - 24), because the Lamé equations only allow a stress state in hydrostatic condition as input.

4.2 Most influential factors

Figure 6 presents the influence of the different parameters studied in the value of the strain energy in the simulated models. Here the results of the maximum values of ΔU_c , differentiated by the spatial sector of analysis, are observed either in the area surrounding the excavation or in the area behind the advance front. The results of the different simulations are grouped according to the corresponding sensitization parameter.

In order for the results associated with the strain energy to be independent of the discretization size of the model, the numerical values normalized by the respective analysis volume were adopted for analysis. From here on, strain energy is referred to as a parameter expressed in units of strain energy density (J/m^3 o kJ/m^3).

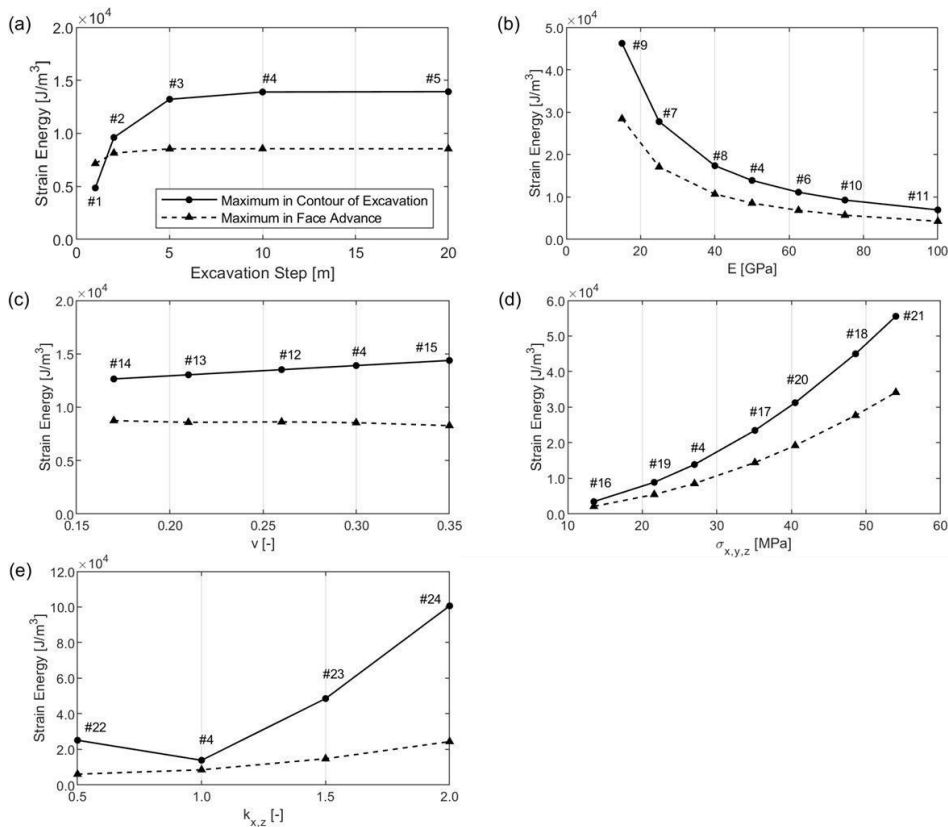


Figure 6. Maximum strain energies associated with sensitization of: (a) excavation step; (b) Young's modulus; (c) Poisson's ratio; (d) in-situ stresses; (e) stress ratio.

In figure (6.a) it is observed that the values of the maximum energies both in the advance front and in the contour of the opening present an asymptotic tendency for the strain energy as the excavation step is varied, which stabilizes when the latter is greater than or equal to 5 (m). That is, for extractive lengths greater than this value, the maximum strain energy density in the model remains constant. For an excavation step of 1 (m), independent of the other parameters of the model, the maximum strain energy density is greater at the excavation front than at the edge of the opening. In figures (6.b) and (6.d) the percentage variation of Young's modulus and in-situ stresses in the different models generates an exponential trend in the values of the maximum strain energy similar to the trajectory obtained for the total ΔU_C values. Decreasingly for the increase in E , and incrementally for the overall increase in σ_x , σ_v , y σ_z . Figure (6.c) shows that a percentage increase in ν generates very low linear variations in the value of the maximum strain energy, both at the front of the excavation and around its contour. However, there is an increasing linear trend for the first scenario and a decreasing linear trend for the latter.

Finally, for the variation of the stress ratio, a parabolic behavior is produced in the magnitudes related to the strain energy in the contour of the excavation, presenting a minimum value for $k=1$. While the maximum strain energy at the front presents an incremental linear relationship. These two tendencies generate that for values of $k \neq 1$, the strain energy in the opening contour represents a much larger percentage of the total energy in the model compared to the other simulations carried out. To directly visualize the influence of the parameters analyzed in the variation of the total strain energy, figure 7 is presented. Among the modified mechanical and tensile parameters, it is found that the modulus of elasticity, the in-situ stresses and the stress ratio have a similar and considerable effect on the amount of elastic strain energy. An increase of 100% in the value of the in-situ stresses generates an increase of 299.5% in the value of the total strain energy. Producing a variation of similar magnitude is the parameter associated with the elastic stiffness of the rock. When the elasticity module varies its magnitude between -70% and

100%, it generates a variation of total ΔU_c between 232.3% and 50.0%, respectively. The stress ratio parameter has an inversely proportional influence very similar to the variation of E. Finally, the sensitization of ν , which generates a lesser impact on the energy index. Here a linear trend is observed between the modification of ν and the change in the total strain energy density. A variation of this parameter by 43.3% only generates a change of 4.0% in the value of ΔU_c .

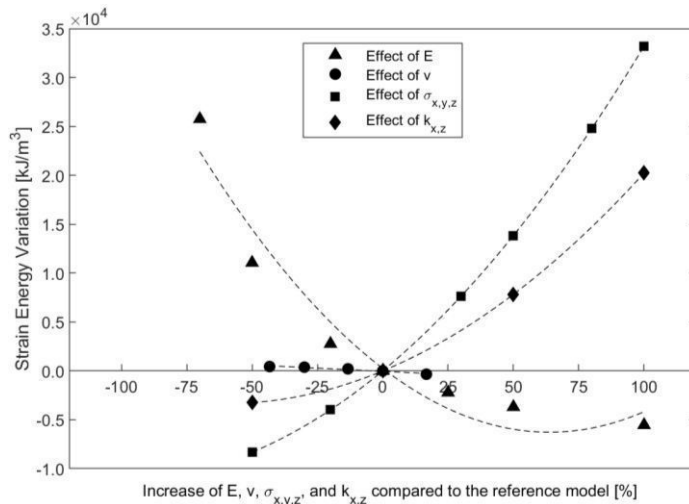


Figure 7. Influence the different parameters analyzed in the total value of the strain energy.

5 DISCUSSION

A rockburst occurs when a volume of rock leaks beyond the elastic limit, and the accompanying failure is of such a nature that the stored energy is instantly released. For a violent collapse to occur, the rock mass in the contour of the excavation must be of low stiffness, strong, and brittle. First, for the same amount of applied stress, a low-stiffness rock will accumulate more strain energy. Second, a more brittle rock, once failure occurs, will tend to release the strain energy it had accumulated more quickly and to a greater extent. Third, the high strength that generally accompanies high brittleness increases the level of elastic strain energy accumulated in the material before failure. This, in turn, increases the energy that can potentially be released in the event of a failure. Thus, an increase in Young's modulus decreases both the total strain energy and the maximum strain energy.

As it is well known, the greater the extraction depth, the greater the stress state in-situ. The high in-situ stress gradients added to the stresses induced by the excavation of an underground opening are conditions that favor the accumulation of a greater amount of strain energy in the rock mass surrounding the excavation. As long as this condition exists, there will be a greater risk of a sudden release of much of the energy stored in the rock. This point is added to the conditions generated by a stress ratio value $k \neq 1$, where stress concentrations at certain points surrounding the excavation generate local zones with very high maximum strain energy values. In view of the study of the operational parameters, it is known that as the advancing front of an underground gallery develops in a highly stressed terrain, a zone of stress rearrangement extends in front of and around this face. While most of this zone occurs within a few hours after the advancing face is excavated, the tension-affected zone continues to migrate for about 24 hours. Too fast a facial advance does not allow this self-stressed zone to occur gradually and the balance of efforts in the rock to be reached. If stress equilibrium cannot be reached, rockburst is likely. Likewise, an excavation length of the gallery that is too large will increase the volume of rock affected by the transfer of tensile stresses and will also increase the maximum strain energy accumulated in the advance front and in the area surrounding the tunnel, raising the potential risk of rockburst.

The present study took into account the analysis of various factors to evaluate the distribution of strain energy in the excavation process of an underground gallery, with the aim of increasing the field of study and the prediction of these phenomena. However, the models carried out present a series of simplifications (elastic constitutive model, rejection of the gravitational force) that are not necessarily representative of the real phenomena that operate in discontinuous conditions. Simulations with elasto-plastic models are recommended to more accurately determine the conditions that can lead to sudden energy release events in underground mines.

CONCLUSIONS

Numerical simulations of simplified and 3D underground tunnels have been performed for different mechanical, stress and operational configurations in order to understand their effect on the distribution and magnitude of the elastic strain energy variation when a circular excavation is suddenly created. It has been shown that three parameters have a considerable influence on the variation of the total strain energy of the overstressed rock: the modulus of elasticity, the magnitude of the pre-existing in-situ stresses and the ratio of the horizontal and vertical stresses typical of the lithological environment. When the value of one of these parameters is high, the order of magnitude of the energy stored in the rock can grow considerably, creating a potentially dangerous environment for the instantaneous release of energy. Additionally, it has been numerically demonstrated that the relationship of tensional stresses in the rock mass can create local zones of high de-formation energy in the contour of the excavation, which can lead to the generation of a rockburst event. Considering that strain energy is used as an indicator of the magnitude or violence of rock failure and, therefore, of the rock's rupture potential, this study highlights the importance of expanding the field of knowledge of the different factors and variables that affect this concept and therefore deepen the understanding of the rockburst phenomena.

REFERENCES

- Askaripour, M., Saeidi, A., Rouleau, A., Mercier-Langevin, P., 2022. Rockburst in underground excavations: A review of mechanism, classification, and prediction methods. *Underground Space*.
- Blake, W., Hedley, D.G.F., 2003. *Rockbursts: case studies from North American hard-rock mines*. Society for Mining, Metallurgy, and Exploration, Littleton, Colo.
- Chen, L., Guo, L., 2020. Discussions on the Complete Strain Energy Characteristics of Deep Granite and Assessment of Rockburst Tendency. *Shock and Vibration* 2020, Article ID 8825505, 9 pages.
- Diederichs, M.S., 2018. Early assessment of dynamic rupture hazard for rockburst risk management in deep tunnel projects. *Journal of the Southern African Institute of Mining and Metallurgy* 118.
- Feng, X.-T., 2017. *Rockburst: Mechanisms, Monitoring, Warning, and Mitigation*. Oxford, England ;
- Hauquin, T., Gunzburger, Y., Deck, O., 2018. Predicting pillar burst by an explicit modelling of kinetic energy. *International Journal of Rock Mechanics and Mining Sciences* 107, 159–171.
- Jaeger, J.C., Cook, N.G.W., Zimmerman, R., 2007. *Fundamentals of Rock Mechanics*. Wiley.
- Morrison, D., Akerman, A., Parsons, H., Hudyma, M., Potvin, Y., 2014. Development in deep, hard rock mines – beyond 10 m/day. Presented at the Deep Mining 2014: Seventh International Conference on Deep and High Stress Mining, 2014 16-18 September, Sudbury, Australian Centre for Geomechanics.
- Salamon, M.D.G., 1984. Energy considerations in rock mechanics : fundamental results. *Journal of the Southern African Institute of Mining and Metallurgy* 84, 233–246.
- Wang, F., Kaunda, R., 2019. Assessment of rockburst hazard by quantifying the consequence with plastic strain work and released energy in numerical models. *International Journal of Mining Science and Technology, Special issue on ground control in mining in 2018* 29, 93–97.
- Weng, L., Huang, L., Taheri, A., Li, X., 2017. Rockburst characteristics and numerical simulation based on a strain energy density index: A case study of a roadway in Linglong gold mine, China. *Tunnelling and Underground Space Technology* 69, 223–232.
- Wu, M., Ye, Y., Wang, Q., Hu, N., 2022. Development of Rockburst Research: A Comprehensive Review. *Applied Sciences* 12, 974.
- Zhou, J., Li, X., Mitri, H.S., 2018. Evaluation method of rockburst: State-of-the-art literature review. *Tunnelling and Underground Space Technology* 81, 632–659.

Possible causes of unexpected cracks in a large-span railway tunnel after ring closure

S. Karahan, O. Yilmaz

Directorate General of Turkish Railway System, Ankara, Turkey

C. Gokceoglu

Hacettepe University, Ankara, Turkey

ABSTRACT:

The T4 tunnel constructed within the scope of the Ankara - İzmir High-Speed Train Project (Western Part of Turkey), is 2350 m long. While the excavation works in the tunnel were continuing, cracks occurred in the sections where the ring was closed, and invert concrete was completed. The aim of this study is to explain the possible causes of these unexpected cracks. T4 Tunnel is located in the northern horst of the Gediz Graben. This horst-graben system is controlled by normal active faults. For this reason, the causes of cracks cannot be explained only by the quality of the rock mass and the support inadequacy. Although the supports were increased after the occurrences of the cracks, the deformations continued. As an additional measure, consolidation injections were performed, and deformations were stopped in the section where cracks occurred. To understand the possible causes of cracking, besides the deformation measurements in the tunnel, the deformations in the rock mass and support system were measured by 3 sets of extensometers. According to the results obtained from the extra measurements, it has been determined that the highest stresses occur in the shoulder region close to the active normal fault and the deformations reach up to 15 m from the tunnel wall. In other words, it was understood that the plastic zone formed around the tunnel reached up to 15 m and was not symmetrical. Considering this finding, a consolidation injection application was performed, and the tunnel was successfully completed.

1 INTRODUCTION

Depending on the increase in population, technological developments, fast, safe, and comfortable transportation demands, many high-speed train projects have been initiated in Turkey. Due to serious geometrical limitations, when constructing a high-speed railway, several infrastructures such as tunnels and viaducts must be necessary if the topography is rugged. A high-speed railway construction was started between Ankara (capital city of Turkey) and Izmir (the third most populous city of Turkey). During this project, several tunnels were constructed successfully. The problems encountered when constructing tunnels were the subject of some scientific studies because complex geological and geotechnical structures are problematic but challenging for the international tunneling community. The studies of Aksoy et al. (2012, 2014 and 2016), Komu et al. (2020), Aygar and Gokceoglu (2020, 2021a and b), and Gokceoglu (2022) can be given as examples of the railway tunnels constructed in complex geological and geotechnical conditions. One of these interesting cases is the T4 tunnel constructed within the scope of the Ankara - Izmir High-Speed Train Project (Western Part of Turkey). While the excavations were continuing, cracks occurred in the sections where the ring was closed, and invert concrete was completed. The purpose of the present study is to explain the possible causes of these unexpected cracks by employing the data obtained from extensometers and deformation measurements. The case is interesting because the causes of the unexpected cracks cannot be explained only by the quality of the rock mass and the support inadequacy. Consequently, the study presents the results of the measurements, interpretations of these results, and extra engineering measures to prevent a catastrophic tunnel failure.

2 PROJECT DESCRIPTION

The T4 tunnel is located in the Western part of Turkey (Figure 1a) and the northern part of the Gediz Graben (Figure 1b). When the project is completed, Ankara and Izmir will be connected with a high-speed railway with a speed of 250 km/h. The project region has an extremely complex geology and high seismicity because the normal faults forming the horst-graben system are active and the region has experienced large earthquakes in the last century. During the T4 tunnel excavations, gneisses and schists of the Menderes massif were encountered. The tunnel was constructed with NATM principles, and the NATM classes along the tunnel were C2 and C3.

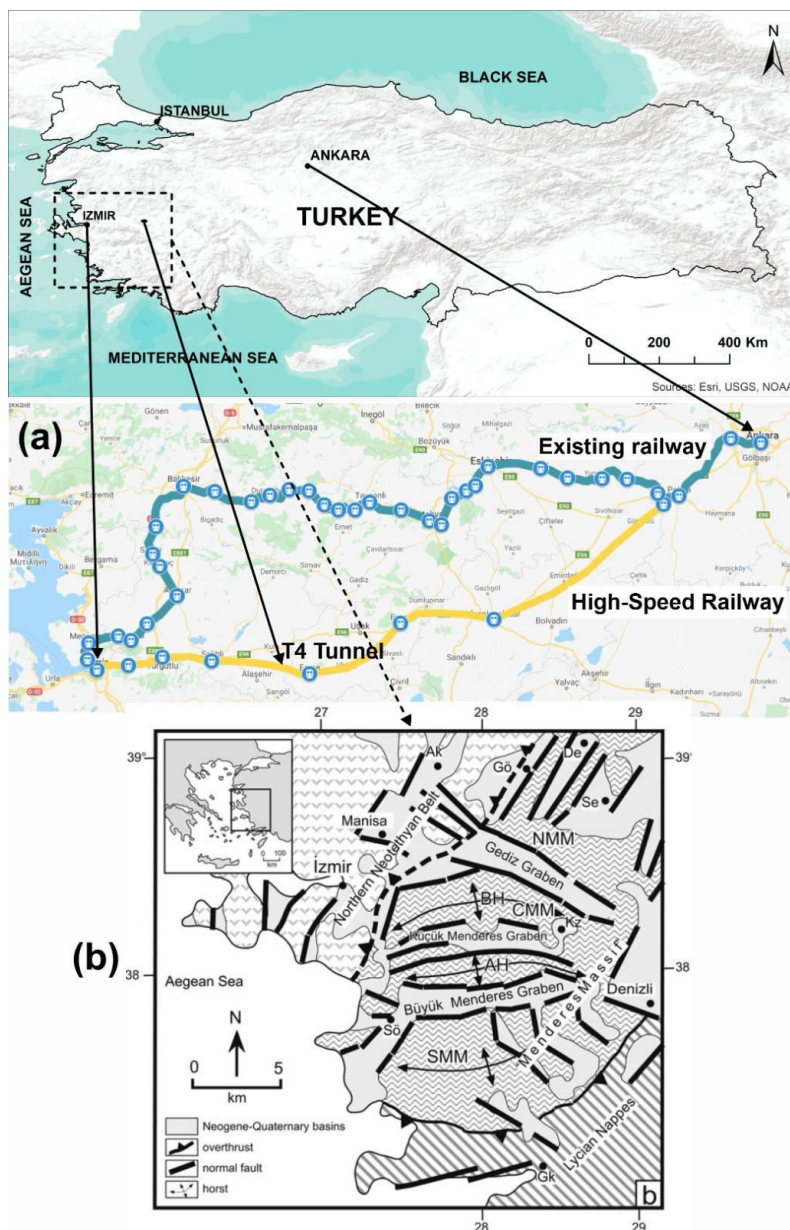


Figure 1. Location map of the T4 tunnel (a); and the general geological characteristics of the region (b) (Bozkurt and Rojay, 2005).

3 DESCRIPTION OF THE PROBLEM

While the excavation face was at Km: 383+030, 25 days after the face excavation, cracks due to excessive deformation occurred between Km: 382 + 815 – 382 + 121 (Figure 2) on the part where the upper half, bench, and invert productions were completed, in other words, ring was closed. In the section where cracks occurred, the bolt lengths were increased from 6 m to 9 m, and additional bolts were inserted. After the additional measures, the deformations were stopped, and the excavation continued. Although the ring was closed a year ago, new cracks occurred in the tunnel axis again. In order to prevent a complete failure, a consolidation injection was performed. After the consolidation injection application, the supports were increased, and excavation was started in C3E NATM class. In the C3E class, the excavations continued in the form of 0.60 m and 6 rising steel arches, the self-drilling bolts were increased from 1.5” to 2”. 6 m long self-drilling bolts were inserted for injection from the top of the axis. Deformations continued during this construction stage. The class was changed again to overcome the ongoing deformations, and excavations continued in C3F class. Progress in the C3F NATM class continued in the form of 0.75m and 4 rising steel arches. However, the deformations continued.



Figure 2. Some views from the cracks occurred after ring closure.

4 IN-SITU MEASUREMENTS

While the tunnel excavation continues, the cracks that follow the tunnel excavation from behind and the axis descending to the shoulders and down from the shoulders from time to time revealed that an eccentric loading was encountered in the tunnel. To understand the mechanisms of crack occurrence, extensometers were installed in addition to convergence measurements, and the measurements were performed (Figure 3). Rod extensometers were placed on the shoulders and axis in 3 different sections (Km:383+595, Km:383+632, Km:383+710). Each extensometer was designed to obtain deformations at the 5th, 10th, 15th and 20th meters, considering the crack map (Figure 4).

The extensometer measurements in each region are given in Figures 5, 6 and 7 in comparison with the convergence measurements at the same points.

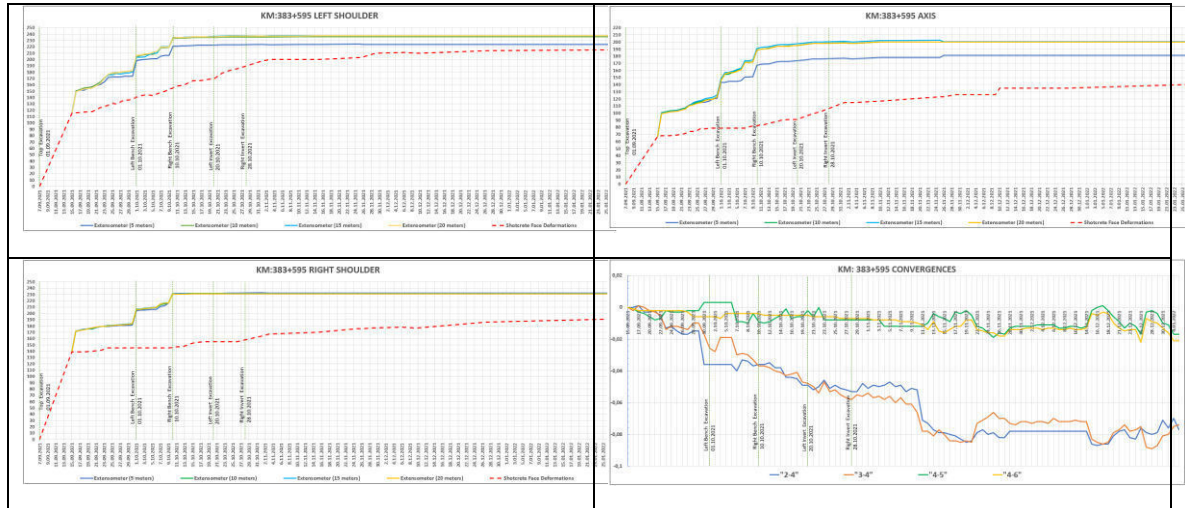


Figure 5. Measurement results at Km: 383+595

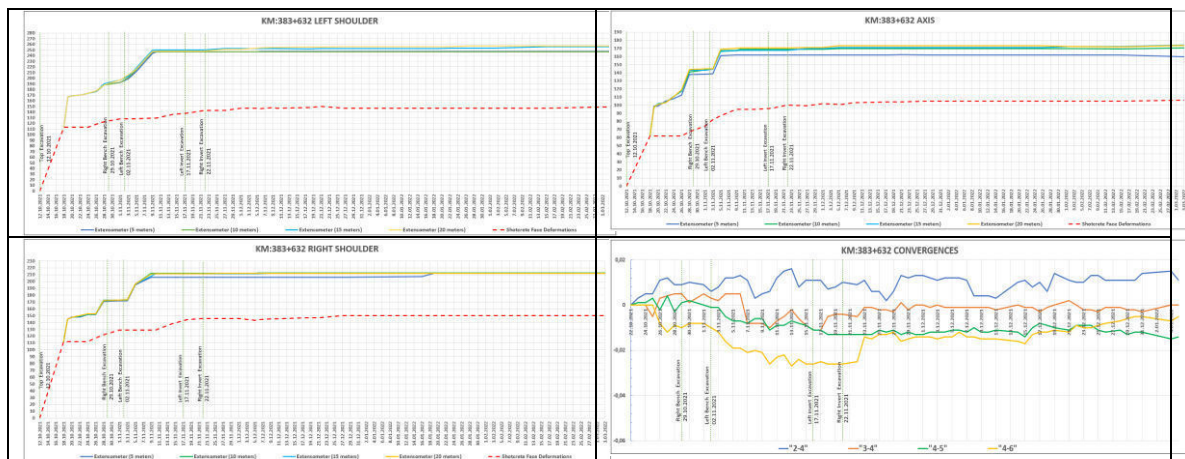


Figure 6. Measurement results at Km: 383+632

Total deformations of 21 cm on the left shoulder, 15 cm on the axis, and 18 cm on the right shoulder occurred (Figure 5) at Km: 383+595. The extensometer measurements showed that it is between 5-10 m on the right shoulder, between 5-10 m on the axis, and between 0-5 m on the left shoulder (Figure 5). It is seen from the convergence graph (Figure 5) that the left side of the tunnel ("2-4", "3-4" convergences) is closed more than the right side ("4-5", "4-6" convergences). It is observed that the cracks develop in this region from the axis to the left shoulder on the crack map (Figure 4).

Total deformations of 13 cm in the left shoulder, 10 cm in the axis, and 13 cm in the right shoulder occurred (Figure 6) at Km: 383+632. The extensometer measurements showed that it is between 0-5 m on the right shoulder, between 5-10 m on the axis, and between 0-5 m on the left shoulder (Figure 6). Considering the convergence graph, it is seen that the left side of the tunnel (convergences "2-4", "3-4") and the right side of the tunnel (convergences "4-5", "4-6") are similarly closed minimum.

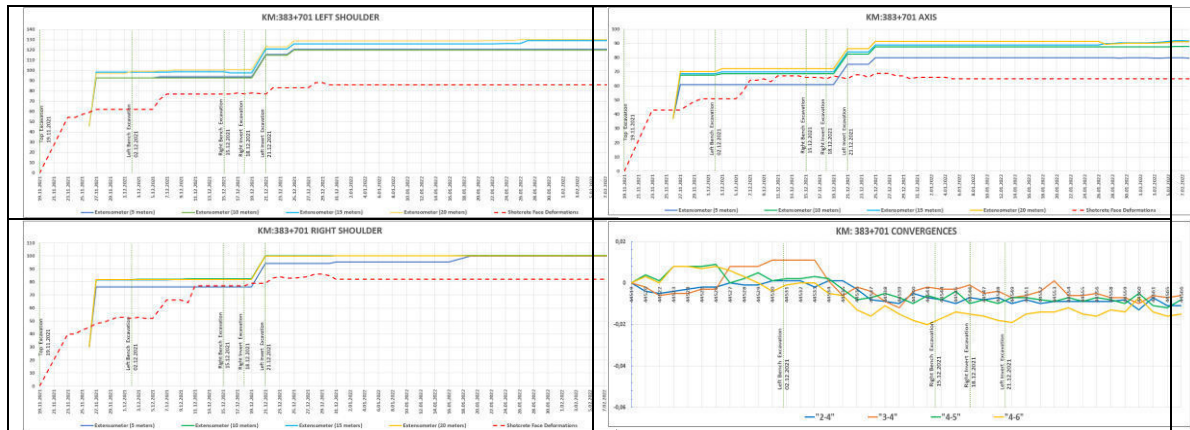


Figure 7. Measurement results at Km: 383+701

Total deformations of 12 cm in the left shoulder, 9 cm in the axis, and 10 cm in the right shoulder occurred (Figure 7) at Km: 383+701. The extensometer measurements showed that it is between 0-5 m on the right shoulder, between 0-5 m on the axis, and between 0-5 m on the left shoulder. It is seen that the left side of the tunnel (convergences "2-4", "3-4") and the right side of the tunnel (convergences "4-5", "4-6") are similarly closed minimum (Figure 7).

Consequently, extensometer measurements, convergence measurements, and crack development revealed that the tunnel was subjected to eccentric loading in this section. To prevent the eccentric load effect, consolidation injection was applied (Figure 8), and the excessive deformations and crack developments were prevented completely, and the tunnel was completed successfully.

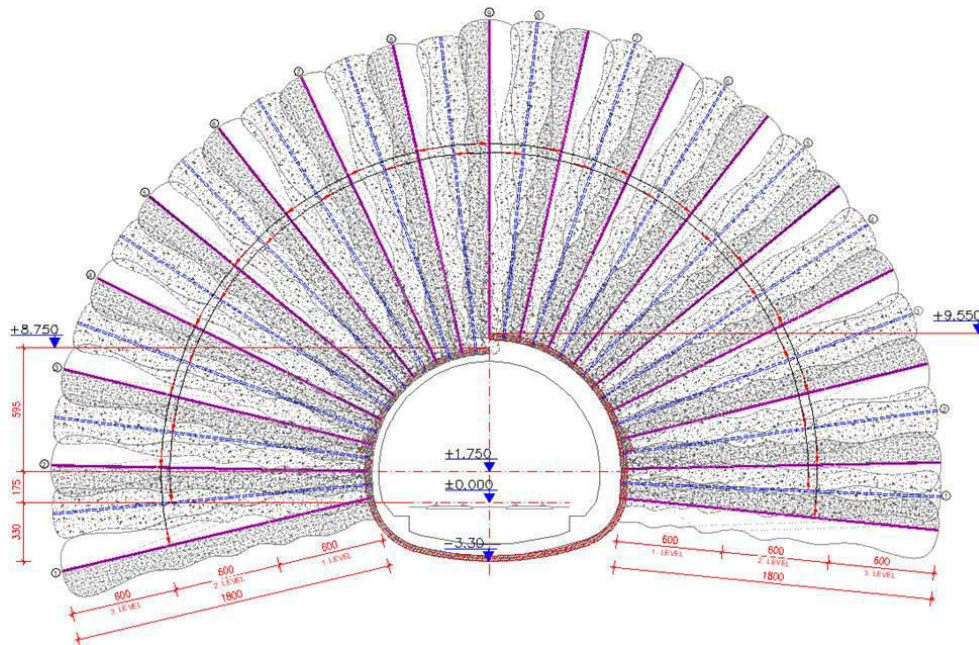


Figure 8. Schematic representation of consolidation injection

5 RESULTS AND CONCLUSIONS

The T4 tunnel was constructed in a highly complex geological region. In addition, the region has a high seismicity. During the construction stage, after ring closure, some unexpected cracks were developed. To prevent crack development, extra support systems were installed but the crack development was not prevented. For this reason, to understand the possible causes of cracks, besides the convergence measurements in the tunnel, the deformations in the rock mass and support system were measured by 3 sets of extensometers. According to the results obtained from the rod extensometer measurements, it was determined that the highest stresses occur in the shoulder region close to the active normal fault and the deformations reach up to 15 m from the tunnel wall. In other words, it was understood that the plastic zone formed around the tunnel reached up to 15 m and was eccentric. Considering this finding, a consolidation injection application was performed, and the tunnel was successfully completed. Consequently, if a tunnel is constructed in an active fault zone, the eccentric loads should be taken into consideration.

ACKNOWLEDGMENT

The authors thank Kolin Construction for its support, and Yasin Karsli for his technical support during this study.

REFERENCES

Aksoy, C.O., Ogul, K., Topal, I., Ozer, S.C., Ozacar, V., Posluk, E., 2012. Numerical modeling of non-deformable support in swelling and squeezing rock. *International Journal of Rock Mechanics and Mining Sciences*, 52, 61-70, DOI: 10.1016/j.ijrmms.2012.02.008

Aksoy, C.O., Ogul, K., Topal, I., Posluk, E., Gicir, A., Kucuk, K., Aldas, G.U., 2014. Reducing deformation effect of tunnel with Non-Deformable Support System by Jointed Rock Mass Model. *Tunnelling and Underground Space Technology*, 40, 218-227, DOI: 10.1016/j.tust.2013.10.016

Aksoy, C.O., Uyar, G.G., Posluk, E., Ogul, K., Topal, I., Kucuk, K., 2016. Non-deformable support system application at tunnel-34 of Ankara-Istanbul high speed railway project. *Structural Engineering and Mechanics*, 58, 869-886, DOI:10.12989/sem.2016.58.5.869

Aygar EB, Gokceoglu C., 2020. Problems Encountered during a Railway Tunnel Excavation in Squeezing and Swelling Materials and Possible Engineering Measures: A Case Study from Turkey. *Sustainability*, 2020; 12(3), 1166. <https://doi.org/10.3390/su12031166>

Aygar, E.B., Gokceoglu, C., 2021a. Analytical solutions and 3D numerical analyses of a shallow tunnel excavated in weak ground: a case from Turkey. *Geo-Engineering* 12, 9 (2021). <https://doi.org/10.1186/s40703-021-00142-7>

Aygar, E.B., Gokceoglu, C., 2021b. A special support design for a large-span tunnel crossing an active fault (T9 Tunnel, Ankara-Sivas High-Speed Railway Project, Turkey). *Environmental Earth Sciences*, 80 (1), 37, DOI:10.1007/s12665-020-09328-1

Bozkurt, E., Rojay, B., 2005. Episodic, two-stage Neogene extension and short-term intervening compression in western Anatolia: field evidence from the Kiraz basin and Bozda... *Horst. Geodinamica Acta*, 18, 295-312.

Gokceoglu, C., 2022. Assessment of rate of penetration of a tunnel boring machine in the longest railway tunnel of Turkey. *SN Applied Sciences*, 4, 19, <https://doi.org/10.1007/s42452-021-04903-y>

Komu, M.P., Guney, U., Kilickaya, T.E., Gokceoglu, C., 2020. Using 3D Numerical Analysis for the Assessment of Tunnel-Landslide Relationship: Bahce-Nurdag Tunnel (South of Turkey). *Geotechnical and Geological Engineering*, 38 (2), 1237-1254, DOI10.1007/s10706-019-01084-9

Technical aspects of tunnel construction in anhydrite containing rocks

V. Jovičić

IRGO, Institute for Mining, Geotechnology and Environment, 1000 Ljubljana, Slovenia

B. Hekić

Euroasfalt d.o.o., Sarajevo, Bosnia and Herzegovina

M. Mujkić

Euroasfalt d.o.o., Sarajevo, Bosnia and Herzegovina

A. Husić

JP Autoceste BiH, Mostar, Bosnia and Herzegovina

ABSTRACT:

Chemical reaction between anhydrite and water results in the formation of gypsum followed by a significant increase in the volume of the rock mass. Tunnel excavation enables increase of water conductivity around the underground opening which, superimposed to the impact of unloading on rock mass, forms sufficient conditions for the transition of anhydrite to gypsum. Suppression of the volume change caused by the primary support results in the build-up of swelling pressure in the rock mass causing damage to the tunnel lining. In the long-term anhydrite reacts to a slow change of moisture of the rock mass, which can affect functionality of the tunnel both due to swelling and sulphate aggression on concrete. Caverns filled with gypsum concentrated solutions can be encountered during tunnel excavations at transgressions between anhydrite rock mass and different geological strata due to abrupt change in rock mass transmissivity and consequent water retention. Experience gained from the construction of tunnel Ivan is presented in the paper to demonstrate the key technical aspects of tunnel construction in anhydrite containing rocks.

1 INTRODUCTION

The problems related to geotechnical works in anhydrite and gypsum containing rock are recognized in tunnel industry as a major obstacle. Before the second World War structures built on anhydrite are known to have suffered major damages (Yuzer, 1982). The Vobarno tunnel in Italy, excavated through anhydrite and gypsum formations was successfully completed in 1931 but in 1940 suddenly began to crack, fracture and progressively heave, following the complete disintegration of the concrete lining into rubble (Redfield, 1963). Following experience gained in several subsequent projects in previous century much more attention and detailed research was granted to tunneling in anhydrite contain rocks e.g. (Butscher et al., 2016) and (Alonso et al., 2013). However, due to complexity and severity of the problem several issues are still poorly recognized. The experience gained during the construction of tunnel Ivan is presented with an aim to summarize good practice and develop technical recommendations to deal with similar challenging conditions.

1.1 Gypsum-anhydrite-gypsum cycle

The name anhydrite is used for a mineral with the chemical formula CaSO_4 , of typical density ranging from 2.9 to 3.0 g/cm^3 and hardness of 3.0 up to 3.5 on Mohr's scale (Freye, 1981). In its pure form it occurs within the orthorhombic crystal system, with three directions of perfect cleavage parallel to the planes of symmetry.

A subaqueous environment forms circumstances for the accumulation of thick evaporite deposits that consist of nearly monomineralic beds. Evaporation of water in a shallow-water or deep-water basin, which is separated from the open ocean by a shelf, would produce brines of increasing concentration. Where the salinity of such a brine reaches about five times that of normal seawater, calcium sulfate would begin to precipitate forming gypsum/anhydrite rock mass (Murray, 1964). Anhydrite containing rocks are fairly common, typically being the product of re-crystallization of gypsum rocks during diagenesis. Under high overburden this process leads to formation of metamorphic anhydrite, which in turn resolves back to gypsum if the anhydrite rock is exposed to the surface or is subject to excavation. Once exposed and under humid conditions the anhydrite slowly alters to gypsum, which in turn can significantly increase in volume. A schematic diagram illustrating gypsum-anhydrite-gypsum cycle (Rauh, et al, 2006) based on the work of Murrey is presented in Figure 1.

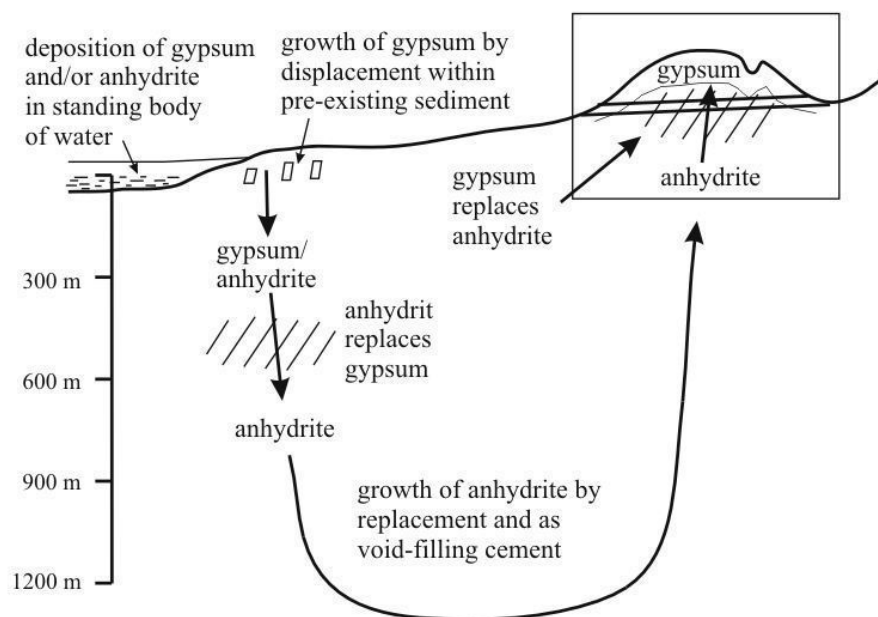


Figure 1. Schematic diagram illustrating gypsum-anhydrite-gypsum cycle (after Rauh et al, 2006). The rectangle on the upper right side shows a typical layout of the tunnel within the anhydrite rock mass, which is characteristic for tunnel Ivan.

Normally there is no water conductivity in the intact and dry anhydrite body and the anhydrite containing rock mass typically acts as an aquitard. If the tunnel is constructed within it, the natural inflows of ground water are getting developed and new water channels are formed so that anhydrite containing rock mass gets exposed to the new humidity conditions and direct contact with water. The presence of water is a condition for transition of anhydrite to gypsum so that swelling can only appear if there is a contact between the two. The chemical reaction (Eq. 1) is typically developed as a two-stage process, in which the first step presents solution of anhydrite to gypsum and the second step is the crystallization of gypsum resulting in the increase in volume. The volume change due to the hydration of anhydrite is +62.6% for open systems, whereas it is -9.0% for closed systems. Similarly, the volume change due to dehydration of gypsum is -38.5% for open systems and +9.9% for closed systems (Zanbak and Arthur, 1986). A closed system is defined as an environment where water is trapped with calcium sulphate minerals before and after the transition and an open system as an environment where free water may enter into the hydration process or be released during dehydration and leave the system. Actual volume changes are controlled by the porosities before and after the transitions (Zanbak and Arthur, 1986). Theoretically the maximum increase in volume can be up to 60%, but the com-

plexity of conditions for crystallization are rarely present in natural environments. Both stages are caused by different saturation concentrations of anhydrite and gypsum and are not necessarily fully accomplished, as their value is dependent on temperature, pressure, and external ions within the closed system (Rauh et al., 2006). In ideal conditions, the calcium or sulphate ions are not lost and the required amount of water is always available. However, in nature the substances can move freely within the open system so that the amount of solution and subsequent swelling can vary significantly along seemingly same geological and hydrogeological conditions.



Anhydrite rocks were seldom deposited directly from water. Instead, most of the anhydrite rocks were re-crystallized from gypsum rocks through diagenesis in which increasing overburden forms conditions to development of metamorphic anhydrite (Rauh et al., 2006). The same authors argue that the swelling potential of anhydrite containing rock can differ significantly relative to their origin so that the swelling potential depends mostly on the crystallinity and thus on the former rock cover, which is reflected in the size of the single crystals and the specific surface of minerals. The gypsum-anhydrite-gypsum cycle is concluded when the anhydrite rock returns to the surface or it is subjected to exposure due to tunnel excavation, as indicated by schematic given in Figure 1.

2 CASE EXAMPLE

2.1 Geological and hydrogeological conditions of tunnel excavation

The technical aspects of tunnel construction in anhydrite containing rocks will be shown on the case example of a construction of 1.75 km long tunnel Ivan. This is a twin motorway tunnel situated at European transit Corridor Vc in Bosnia and Herzegovina at the section Tarčin – Mostar. Excavation of the tunnel cross section of approximately 100 m² was excavated following the principles of NATM (Rabcevicz, 1964). The tunnel was located within the geological sequence of the tectonic unit of Central Bosnian shale highlands underlaid by Bosnian Flysch, which is some 500km long belt of Late Jurassic to Cretaceous rock mass. The microlocation of the tunnel on the map showing the major structural units of Dinarides is shown in Figure 2.

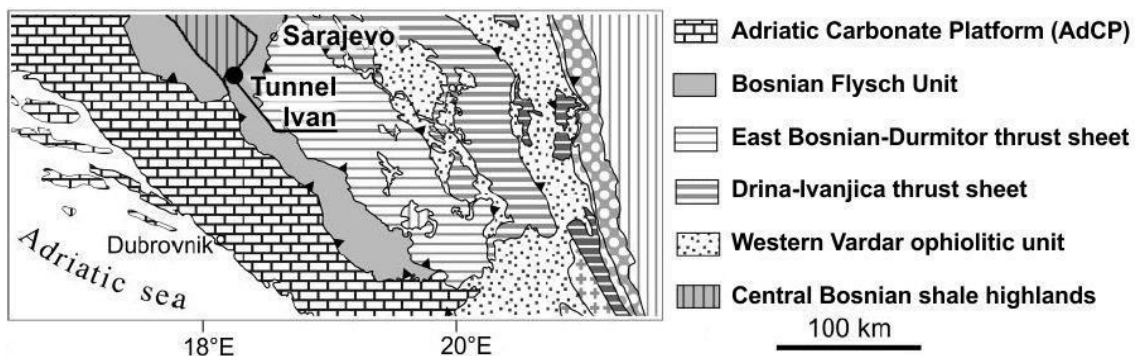


Figure 2. The approximate micro-location of tunnel Ivan on the map showing the major structural units of Dinarides (intercept adapted from Schmid et al, 2008)

The Bosnian Flysch unit is formed by a complex geological sequence composed of carbonate-dominated, thin-bedded marly to micritic limestones and red or grey shales. These formations are often inserted with calcareous turbidites and coarse catastrophic carbonate mass flow deposits, which can be several tens of meters thick. On the contact with older Triassic and Paleozoic

tectonic unit of Central Bosnian shale highlands there were conditions for the formation of Permian evaporites, which progressed to the surface during orogenesis. The longitudinal geological section of tunnel Ivan is presented in Figure 3, showing a large body of anhydrite rock which was embedded within weathered sandstone and breccia dominated rock.

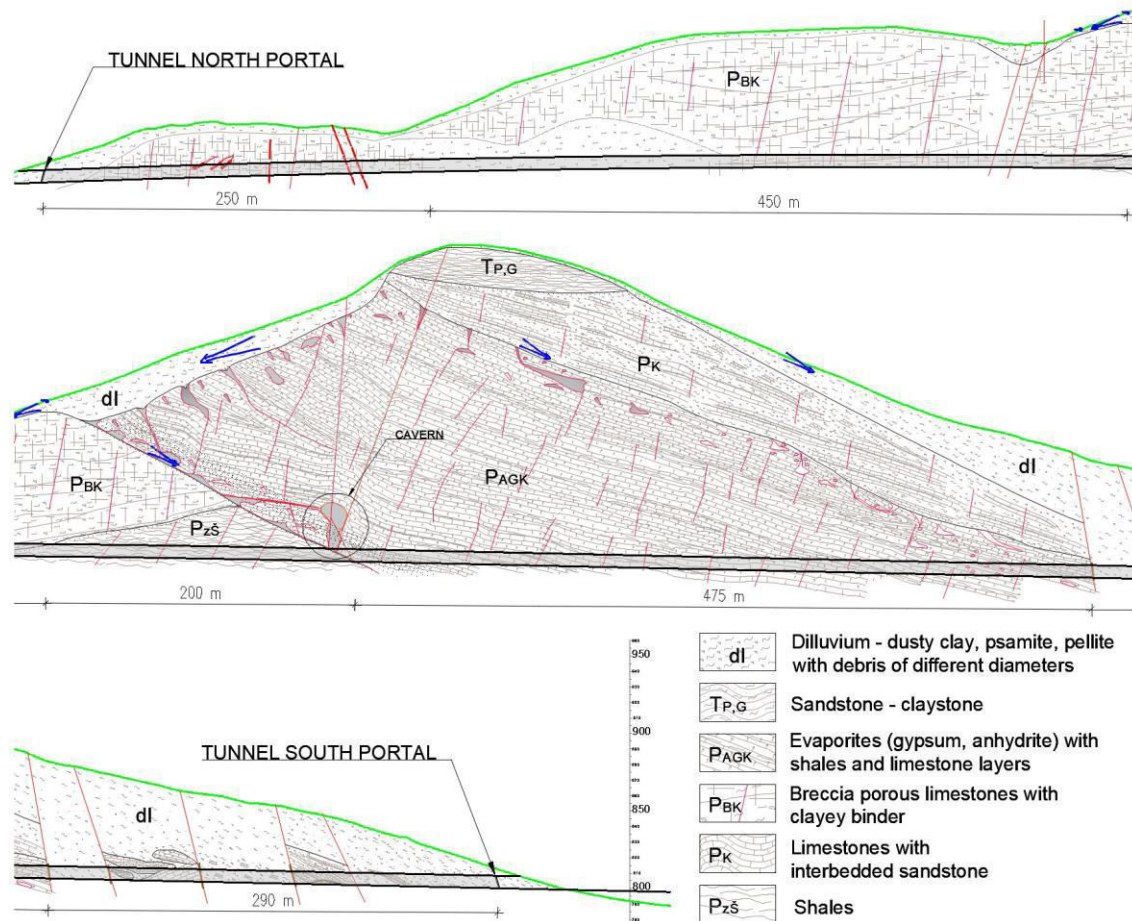


Figure 3. The longitudinal geological section of tunnel Ivan

The first lithological section in north to south direction comprised some 250 meters of highly weathered rock featuring clayey-dusty material (dusty clays, psammities, carbonate pelites) with sole fragments of different size, practically without any cohesive binder. Semi solid clay (weak claystone) was characterized by the presence of fragment material, the percentage of which varied abruptly in the structure of this lithological environment. The presence of water further weakened the characteristics of the ground and caused frequent local collapses of the material at the head of the excavation.

As the excavation progressed from north to south, a change in the lithological environment in the next 450 meters occurred in the form of brecciated hollow limestones with clay binder. Due to the active exposure to tectonic processes, there was a chaotic and unclear appearance of evaporite interlayers - gypsum and anhydrite. Caverns without or with clay filling were commonly encountered but there were of meters scale, so it did not significantly hamper the progress of the excavation.

The transition zone of approximate length of 200 m occurred between evaporite and shale at the area of contact of two lithological environments was represented by an erosive-tectonic boundary. Paleozoic clastic rocks here suffered many endogenous processes, due to which the

degree of their decay was different. The increased weathering of the slate material was one of the reasons for the local instability at the head of the excavation. Due to the dense structure and compactness of the layer surfaces, the process of seepage and the appearance of water was reduced. The slate material mostly retained the same mechanical characteristics along the entire transition zone. The appearance of water along the tunnel was, as a rule, present at the contacts between the two lithological sections. Evaporite and shale contact zone was extremely unstable geological environment in which large-diameter caverns with muddy fillings were found resulting in major collapse event, which will be explained in detail later.

Along the following 475 meters the rock mass consisted purely of Permian evaporites represented by gypsum and anhydrite. The texture within the rock mass was layered while the structure was crystalline. The colour was dark grey and white, with dark grey anhydrite dominating. The anhydrite rock, the fragment of which is presented in Figure 4, was subject to mineral and petrographic examination. The results for two samples, shown in Table 1, confirmed the dominant presence of anhydrite to some 66% of the total mass with the rest of the minerals dominated by calcium and magnesium carbonates.

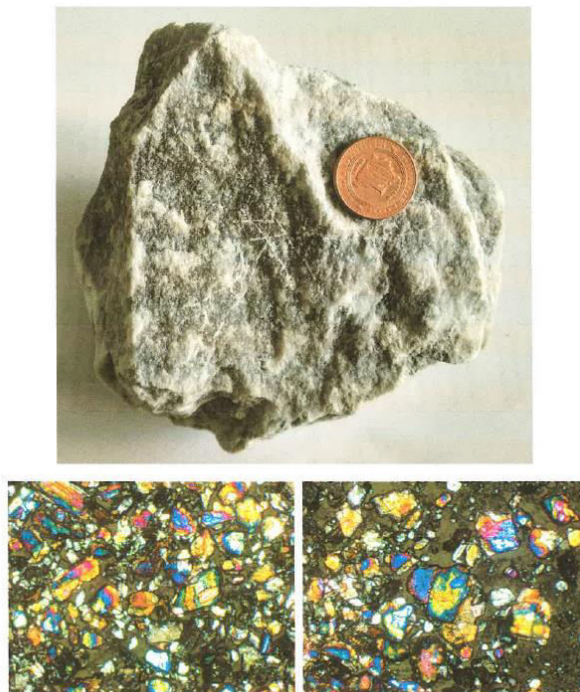


Figure 4. The anhydrite rock and microscopic cross-section showing crystals of minerals of anhydrite and sporadically gypsum in live colours (Hadžić, 2020).

Table 1. Results of mineral and petrographic analyses of anhydrite containing rock in tunnel Ivan.

Mineral %	Sample	
	LTC-SP	DTC-JP
CaSO ₄	66.64	65.31
CaCO ₃	7.03	13.35
MgCO ₃	1.99	3.11
SiO ₂	0.9	1.49

Interlayers of clastic fine-grained sedimentary shale textures were identified in some places while non-systemic cracks were present in the zone of wedge folds, which were mostly filled with carbonate filling. The excavation in this section, dominated with anhydrite, was carried out by blasting.

The final lithological section through which the excavation was carried out in the south direction to some 290 meters was represented by clayey-dusty material (dusty clays, psammites, carbonate pelites) with sole fragments of different size. Semi-solid plastic clay was dominant in places and characterized by the presence of fragmented material of different origins. The material has poor physical and mechanical characteristics, while the presence of water further weakened the material characteristics and caused local collapses and flows of the material at the head of the excavation. A couple of major collapses at the top heading stopped the excavation in the left tunnel tube several times.

3 TECHNICAL ASPECTS OF TUNNEL CONSTRUCTION IN ANHYDRITE CONTAINING ROCKS

3.1 *Overcoming of caverns and remedial measures*

Erosive-tectonic boundary at the transition from shale rock to evaporites was encumbered by a constant inflow of water, which was followed by the appearance of gypsum and anhydrite decayed material with extremely poor physical and mechanical characteristics. Such processes within the massif constantly affected the change of stress state and degree of disintegration of the rock mass itself. With the further presence of water, there was a further dissolution of anhydrite or gypsum forming caverns filled with (oversaturated) heavy liquid of gypsum solution.



Figure 5. Loss of stability at the occurrence of cavern in the roof of the right tube of tunnel Ivan

During the excavation of the right tunnel tube, the stability of the material in the roof of the top heading was suddenly lost due to the presence of the cavern. Loss of stability shown in Figure 5 was manifested by the abrupt release of heterogeneous material in heavy fluid state (gypsum solution with lone blocks of anhydrite) at the top of excavation. The cavern was emptied in several minutes. After measuring using a digital laser rangefinder, it was found that the cavern was approximately 30 m high, with variable width in both horizontal directions (6-18 m) comprising the total volume of approximately 5500 m³. The cavern edge occupied about a third of the ceiling of the right tunnel tube. The layout of the cavern and the tunnel tubes is shown in Figure 6.

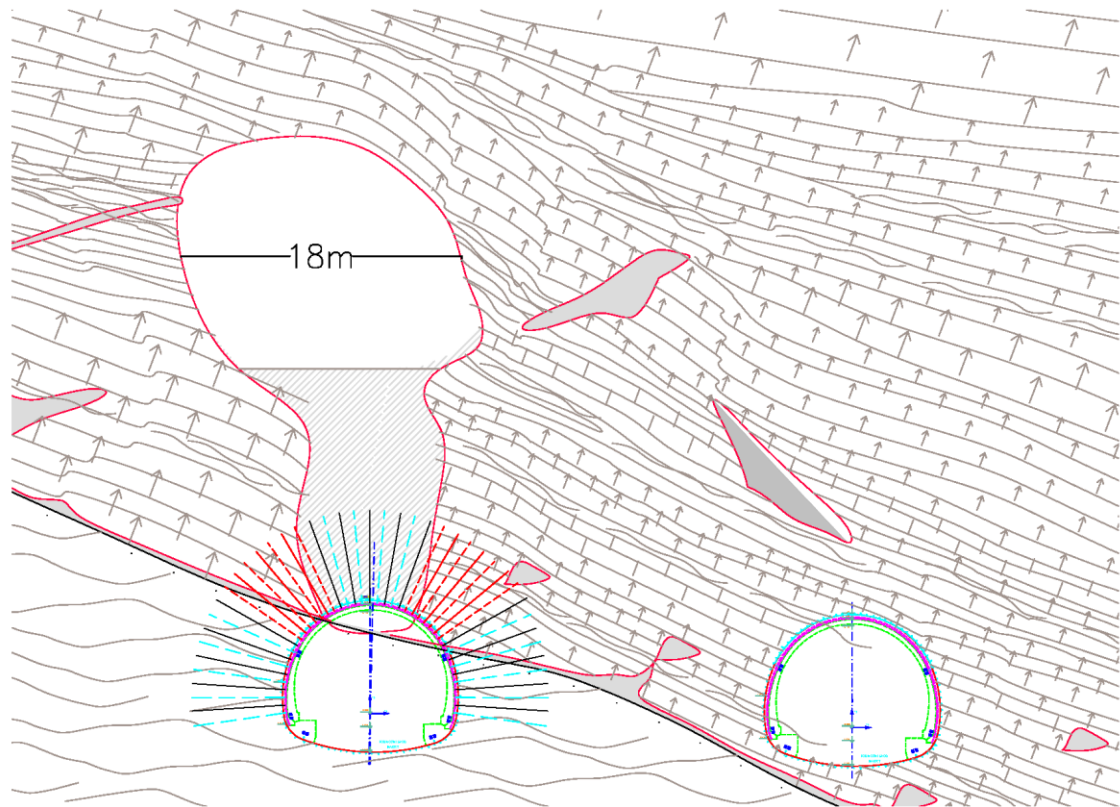


Figure 6. A schematic showing the layout of the tunnel tubes and the cavern encountered during the excavation of tunnel Ivan (location of the cavern is indicated in Fig. 3).

Rehabilitation works, which ensured global stability of the tunnel excavation, included the use of a heavy support (lattice girder PS 180/10/30 with a horizontal spacing of 50 cm) and the installation of the primary support which comprised of 30 cm thick reinforced shotcrete lining and 9 to 12 meters long IBO anchors at 1.5 m radial spacings. Remediation measures relied heavily on the efficiency of the pipe roof, which was installed prior to the advance beneath the cavern. Pipe roof was also subject to collapse on two occasions as, despite the use of consolidation grouting, there was no firm ground on the opposite side of the cavern to provide the required fixity. After the second failure of the pipe roof, it has been observed that the grouted body above the tunnel was mixed with heavy liquid of gypsum solution and didn't have integrity.

In the third attempt of consolidation grouting, it was decided not to close the cavern completely, but to leave an open part to ensure that the gypsum solution have the possibility to drain into the tunnel. After the installation of the grouting pipes, it was possible to inspect their position in the cavern. Prior to the grouting, once the bottom of the cavern was drained and cleaned of gypsum solution, the cavern was closed. In the next twelve hours, the cavern was filled up to 6-8m high with lightweight concrete, the level of which was confirmed using inspection pipes. Once the lightweight concrete had hardened, the additional drainage pipes were installed to drain percolating gypsum solution and water from the cavern.

After construction of the primary lining the cavern was further filled up to 18 meters high with lightweight concrete, which was an upper limit for the lining capacity. The remaining empty space of the cavern was about 12 m high and some 12m to 18 m wide. It was expected that the empty space of the cavern would be soon naturally filled with water, and further on as the chemical process continues, with gypsum solution, which had been the content of the cavern in pre-disturbed state. Before the construction of the secondary lining, the contact injection around the

tunnel was carried out to minimize the water inflow into the tunnel.

A final remediation measure that should ensure the long-term stability of the tunnel was the construction of the heavily reinforced secondary lining along the full length of the collapse section (some 12 m long). The amount of reinforcement was determined based on the capacity and integrity calculations for the secondary lining. Also, the foundations and the invert were reinforced to improve the durability of the structure.

3.2 *Swelling pressures and remedial works*

At the areas of transitions between lithological units decomposed anhydrite in contact with water increased the volume and loaded the primary lining by swelling pressure. This subsequent swelling was mainly present in the sections bordering the anhydrite gypsum section due to contact percolation of the ground water. The swelling pressures caused the need for the installation of additional radial anchors as well as reprofiling of the tunnel cross-section. The reprofiling and reconstruction of the tunnel lining was mainly accomplished within the period of 12 months following the excavation of the tunnel. After this period no further displacement or stresses were detected acting on the lining and reinforced secondary lining was installed with the capacity to counteract some possible long-term swelling pressures.

The section in which pure anhydrite containing rock dominated the tunnel was practically dry. Under these conditions, caused by the absence of water, no swelling pressures or subsequent damage of the primary lining were detected. Nevertheless, due to long term risk of increase in volume the secondary lining was reinforced along this section too.

3.3 *Influence of aggressiveness and use of sulphate-resistant concrete*

Mineralogical-petrographic analysis of the sample, shown in Section 2.1 confirmed the presence of gypsum solution. The natural processes of gypsum dissolution in the presences of water, represent a chemically very aggressive environment for concrete. According to the test data, chemical aggressiveness was classified as protection category XA3 and XA2 (according to EN 206-1). In this regard, the primary support had to be adapted to the aggressive conditions in both tunnel tubes.

The use of micro-reinforced shotcrete with sulphate-resistant cement has been proposed as a replacement for a conventional shotcrete liner reinforced using wire mesh. Also, sulphate-resistant cement was made mandatory for the foundations and footing at this section of the tunnel while sulphate resistant cement grout is used for grouting of the rock anchors.

After the mentioned activities, the frequency of chemical testing of water aggressiveness during the construction of the tunnel was increased. At certain locations, according to the results of testing the chemical aggressiveness of water, it was determined that it is necessary to install sulphate-resistant cement in the foundations and the invert. Finally, the decision was taken to construct secondary lining with the use of sulphate resistant cement along the full length of the tunnel.

4 DISCUSSION AND CONCLUSIONS

4.1 *Discussion*

Typically, tunneling in anhydrite containing rock is related to high risks associated with the excavation works. Once exposed at the surface the anhydrite containing rock is usually in heavily weathered state, so the portal tunnel areas are bound to be in poor geological conditions following the appearance of gypsum and anhydrite decayed material with extremely poor physical and mechanical characteristics. The presence of lenses filled with soil like materials and instabilities

associated with flow of this material from the top heading of the tunnel excavation were quite common.

The swelling potential of anhydrite rock is not always fully realized since the conditions for two stage process of transition of anhydrite and gypsum and are not necessarily fully accomplished in natural environment. The reason for this is that the required conditions for temperature, pressure, and external ions within the closed system in which the calcium or sulphate ions are not always present, and the required amount of water is not always available in right amounts. The experience shows that the swelling process and subsequent additional pressures on tunnel lining are encountered mainly at the contacts of different lithological units, in which ground water freely percolates. Normally the intact and dry anhydrite body is impermeable to water. In the anhydrite dominated rocks, which are typically of very low permeability, the conditions for swelling are typically not formed since the swelling potential of anhydrite without the groundwater presence cannot be realized and there would be no or little additional swelling stresses acting on tunnel lining. However, even in these favorable conditions there could be some localized areas that will be prone to swelling in the long term. This is typically caused by the change of moisture content of the rock mass initiated by the re-direction of the underground water flow by the tunnel drainage system.

4.2 Conclusions

Based on the experience gained from the construction of Tunnel Ivan, the key technical aspects of tunnel construction in anhydrite contain rocks can be summarized as follows:

1. Caverns filled with gypsum concentrated solutions can be encountered during tunnel excavations and should be regarded as major hazards for tunneling works. Additional site investigation works should be carried out during the construction of the tunnel (e.g. pre-drilling with the use of geophysical testing such as reflection and cross-hole methods) to locate the caverns in front of the excavation and so mitigate the risks and prevent failures.
2. Swelling potential of anhydrite rock is realized at the most at the transgressions between anhydrite and different geological strata due to abrupt change in rock mass transmissivity and consequent water retention. In that case the additional swelling pressures will cause the damage of the tunnel lining and a necessity for remedial works. The use of deformation elements can be instrumental to mitigate the extent of damage, but this measure should be applied with caution, since the swelling can be of irregular nature due to heterogeneity of the transitional rock mass.
3. In the intact and dry anhydrite there would be a small potential for swelling in short term, that is during the construction of the tunnel. In the long term, there is high probability that some swelling can occur due to impact of tunnel excavation and drainage on the hydrogeological conditions for groundwater flow. In that case, the reinforcement of the secondary lining should be used to enable the long-term functionality of the tunnel.
4. Gypsum solution in the presence of water represent in anhydrite containing rocks an aggressive chemical environment which would cause sulphate corrosion of concrete. Sulphate resistant cement should be used for both primary support (shotcrete lining, micro-fibre shotcrete, cement for anchor injection etc.) and for the cast in place concrete for the secondary lining.

5 REFERENCES

- Alonso, E. E., Rerdugo, I. R., & Ramon, A. (2013). Extreme expansive phenomena in anhydritic-gypsiferous claystone: the case of Lilla tunnel. *Géotechnique*, 63(7), 584–612. <https://doi.org/10.1680/geot.12.P.143>
- Butscher, C., Mutschler, T., & Blum, P. (2016). Swelling of Clay-Sulfate Rocks: A Review of Processes

- and Controls. *Rock Mechanics and Rock Engineering*, 49(4), 1533–1549.
<https://doi.org/10.1007/s00603-015-0827-6>
- Freye., K. (1981). *The encyclopedia of mineralogy. Encyclopedia of earth sciences. Vol. IVB*. Hutchinson Ross.
- Hadžić. H. (2020). *Mineralno petrografska analiza i ispitivanje hemijskih osobina i kiselosti stijenskih materijala iz iskopa tunela Ivan (in Bosnian)*.
- Murray, R. . (1964). Origin and diagenesis of gypsum and anhydrite. *Journal of Sedimentary Geology*, 34(3), 512–523.
- Rabcevicz, L. V. (1964). The new Austrian Tunelling Method (Part 1 and Part 2). *Water Power, November 1*, 511-515 and pp. 19-24.
- Rauh, F., Thuro, K., Spaun ., G. (2006). Assessment of the swelling potential of anhydrite in tunnelling projects. *10th IAEG Congress, Paper No. 473*.
- Redfield., R. C. (1963). *Report on attendance at the 1st International Conference on Public Works in Gypsiferous Terrain*.
- Schmid, S. M., Bernoulli, D., Fügenschuh, B., Mañenco, L., Schefer, S., S., & R., Tischler, M. & Ustaszewski, K. (2008). The Alpine-Carpathian-Dinaridic orogenic system: correlation and evolution of tectonic units. *Swiss Journal of Geosciences*, 101, 139–183.
- Yuzer., E. (1982). Engineering properties of evaporites and evaporitic formations of Turkey. *Bull IAEG*, 107–110.
- Zanbak., C, and Arthur. R., C. (1986). Geochemical and engineering aspects of anhydrite/gypsum phase transition. *Bull Assoc Eng Geol*, 133(4), 419–433.

Modeling of the damage in the contour of tunnels caused by the use of blasting using the Discrete Element Method

H.F. González

Instituto de Ingeniería, Universidad Nacional Autónoma de México, México

J. Sánchez

Facultad de Estudios Superiores Aragón, Universidad Nacional Autónoma de México, México

G. Auvinet

Instituto de Ingeniería-Universidad Nacional Autónoma de México, México

ABSTRACT:

The explosives used for rock excavations induce compression and tension waves, these agents cause the rupture of the medium. To estimate fracturing, an analysis based on the discrete element method (DEM) is presented. Using a set of spheres that are bonded together by a cemented contact model, a rocky environment is represented. In the simulation, the blasting is applied by particle expansion algorithm.

A type of simulation considers a detonation point with different stress states in situ. The second type uses drilling patterns under three different condition of contour boreholes. The contact rupture patterns between particles show the fracturing of the rock mass, which allowed identifying the areas damaged by the blasting. The results of drilling patterns simulations with different arrangements in the contour blastholes allow determining which conditions favor the perimeter of an underground excavation. In the case of the modeled rock, a better contour was obtained with the arrangement of more blastholes.

1 INTRODUCTION

1.1 Introduction

Tunnel engineering is faced with the need to carry out constructions or various works on competent materials. Because of this, excavation methods that employ blasting are used. These techniques take advantage of the energy released during the detonation of explosives, which fractures and fragments the rock.

Blasting invariably causes damage to the surrounding rock mass of the excavation, threatening the stability, designed perimeter and functionality of the constructions (Kumar *et al.*, 2014). Therefore, the damage caused by detonation in the rock must be controlled and quantified, mainly in the excavation contour (López, 2015).

To simulate the blast-induced damage of rock materials, computational codes based on the theory of the continuous medium have been used, which describe the phenomenon from the constitutive model suitable for the material and a generalized law of elasticity. These models only give estimates of the region damaged by the detonation. However, they are not able to represent the fracturing of the rock, the movement of the blocks and the fragmentation of the material caused by blasting (Potyondy & Cundall, 1996). On the other hand, codes based on the theory of discontinuous medium, the damage to the rock from blasting is estimated directly, through the formation and monitoring of microcracks.

This paper describes a methodology to simulate the process of a blast and the fracturing mechanism that causes detonation of a borehole or of a drilling pattern in rock. In simulations with a blasthole, the area of damage is analyzed under different stress state conditions. The influence of the wave reflection phenomenon on the use of explosives is also discussed. In the simulations with a drilling pattern, the fracturing and detachment of the excavated material is analyzed, depending on the contour blastholes arrangement. Likewise, the damage to the excavation contour is discussed. For this, a discontinuous description is used, by Discrete Element Method (DEM). The rock is represented by a set of circular particles (two-dimensional models) that are bonded together, with the PFC software

(Itasca, 2016). The properties of explosive agents are modeled with a particle expansion algorithm that simulates the explosion. This study focuses on the effects of shock wave.

1.2 Objectives

- Generate a two-dimensional rocky medium by discrete elements method, through a set of particles joined by bonded contacts. Calibrated by mechanical and physical properties obtained from compression and indirect tension tests on rock cores.
- Simulate the explosion in a blasthole and in a drilling pattern in two-dimensional models of rock masses using the Discrete Element Method, verifying that the representation is consistent with the physical phenomenon.
- Analyze the propagation of waves in the medium made up of discrete elements.
- Analyze the effects of different contour blastholes arrangements in a drilling pattern.
- Explain the mechanical response of the rock mass to the detonation of the explosive at different stress ratio conditions.

1.3 Limitations

Blasting and its damage to rocks are analyzed from the perspective of discontinuous media, as well as the effects caused by stresses that are due to the wave propagation in them. The models of this work are conducted simulating blasting in intact rock, without the interaction with the discontinuities that are part of the structure of a rock massif. The damages in the rock discussed in this work, are due to the use of high explosive, that is, by shock wave.

2 FOUNDATIONS OF BLASTING DESIGN AND FRACTURING ROCKS THEORY

2.1 Principles of explosives

Explosives are chemical substances, manufactured by a mixture of solids and liquids with a certain degree of instability. When excited, they release stress waves with a large volume of high-pressure gases, in a brief period, which causes the fracturing of the rock (González I., 2012).

Konya (1990) mentions that the energy released during detonation by the chemical reaction of the explosive is classified into two main types, shock energy and gas energy. The shock energy propagates with greater speed, also has a larger magnitude, which is why it is mainly responsible for the cracking of the rock during a blast and results from the detonation pressure.

According to Bernalao *et al.*, (2013) the properties of explosives that influence their efficiency as a generator of rupture and fragmentation are as follows:

- Detonation velocity (D). It refers to the speed at which the detonation propagates in the explosive column, expressed in m/s.
- Density (ρ_e). It refers to the weight per unit volume of an explosive, usually manufacturers express it in g/cm^3 , this property helps to define the quantity and distribution of the explosive in its design of the drilling patterns.
- Breaking power. It is the energy of the explosive used to generate fractures in the medium, it is related to the shock energy.

2.2 Theory of rock response to detonation in a blasthole.

The response of the rock to the detonation of explosives is dictated by its physical and mechanical properties. In this work, only the parameters of the intact rock are mentioned since the models are made in a rock matrix.

Compressive strength, σ_c , and tension, σ_t , are mechanical properties that dictate the intensity of the shock wave required to cause cracking, while larger, required more energy shock, which can be correlated with the compressive strength of the rock. The static resistance of the rock can be used as

an indicative parameter to calculate the necessary breaking force; however, it is better to consider the dynamic resistance, which is usually above the static one (Oyanguren & Monge, 2004).

Impedance refers to the resistance that opposes a medium for the propagation of waves through it. If the explosive reaches an impedance equal to that of the rock, it will perform better. This property is related to the modulus of elasticity, the Poisson ratio, the porosity, and the density of the rock.

2.3 *Detonation mechanism and fracturing of the rock*

At the instant of detonation, high-pressure gases impact the walls of the borehole and generate an intense pressure wave. The energy is transmitted to the rock forming waves of compression and tangential tension. The stresses can exceed the resistance of the material, which causes breakage and fragmentation of the rock (Hoek and Brown, 1986).

The compressive stresses pulverize the rock around the blasthole, in a space 3 to 7 times the radius of the blasthole. The wave generates tangential tension stresses, creating radial fractures. These ruptures will continue to propagate if the tangential stress exceeds the resistance of the rock, 7 to 12 times the radius of the blasthole. According to the pressure wave moves away from the detonation point, its energy decays (Oyanguren and Monge, 2004; Hoek and Brown, 1986).

When the shock wave reaches a free face, it becomes a reflected wave that moves in the opposite direction to the one that reached the free face, if the rock resistance is exceeded again, greater fracturing will occur. In the tunnels there is no free front, therefore, a wedge is produced, made up of unloaded boreholes and blastholes that are detonated first, to create a free face (Hoek and Brown, 1986).

Depending on the time in which the magnitude of the pressure exerted by the detonation reaches its maximum point, it will be the extent of damage zones. For explosives with detonation speeds of less than 3000 (*m/s*), a crush zone greater than the crack zone is expected. The area of influence is smaller than that of explosives with detonation speeds greater than 3600 (*m/s*), in which the crack zone is greater than that of crushing.

2.4 *Blasting design and influence of the stress condition of the material*

Blasting in underground excavations consists of generating a pattern of boreholes, the direction of which is perpendicular to the excavation. The boreholes have different objectives, different explosive charges, different detonation sequence and may or may not even have a charge.

A wedge has uncharged boreholes (larger diameter) and charged blastholes (smaller diameter). Wedge blastholes are the first to detonate in the detonation sequence. From them, the other blastholes are detonated as they move away from the wedge (López, 2015).

Finally, the contour blastholes are detonated, in them is where the damage to the perimeter of the excavation is controlled, they are regularly made with a greater spacing, less explosive charge and only with the use of high explosive (López, 2015; Hoek and Brown, 1986).

The post-cutting technique is the most widely used in underground blasting to detonate contour blastholes, as it benefits from the stress field generated at the perimeter of the excavation. Hudson and Harrison (1997) explain that the directions of the main stresses at the excavation boundary are radial and tangents to it. Radial stresses are zero and tangential stresses become the major principal stress. The stress state of the rock influences its breakage. That is, the cracking generated in massive rock by the detonation of explosives is greater in the direction of the least main effort (Pernía *et al.*, 1987).

3 MODELING METHODOLOGY

Numerical methods have been used to simulate the generation of fractures (damage to the material) using explosives can be continuous and discontinuous medium. The former implement elasticity laws dependent on the deformation caused by the wave, to predict the generation and distribution of fractures. To do this, they use constitutive models for the rock, a limitation is that they cannot simulate the fracture and movement of the rock.

The discontinuous medium models, compose the medium by individual particles, which can be rigid or deformable, these interact with each other in contact zones, they allow to represent large displacements and the separation between them (Cundall and Strack, 1979). The general behavior of the simulation is given by stiffness laws, cohesion, and friction between the particles. In these methods, the formulation to represent contacts between particles allows them to separate and have large slides. Therefore, the simulations carried out using these methodologies can represent the mechanism of rock fracture induced by the use of explosives (Potyondy & Cundall, 1996).

In this paper, the rock mechanical behavior subjected to stresses caused by blasting is simulated using the Discrete Element Method.

3.1 Modeling an intact rock by DEM

The described methodology simulates the behavior of rock medium with a collection of particles (disks) bonded by cement with flat contact surfaces. The mechanical response of the system is determined by each particle and the effects of forces and moments on each contact. The contact model to simulate the rock is the “Flat-Joint” (FJ).

The bonds can broke completely or partially broken, when the first case occurs, remain as linear contacts, where only frictional and compressive forces act between particles. In the second case, the cemented model acts only on the part that is still bonded.

The contacts are simulated with an interface between two planar ideal surfaces of finite length, each connected to a particle, rather than a single surface between the two particles. The interface coincides with the middle surface that is centered on the contact plane. This is how the effective surface of each grain is defined by the disc diameter, as well as by the “ideal surfaces” adhered to particle, which interact at each junction with the ideal surface of another particle. Finally, it should be noted that these formed surfaces do not disappear after the breakage of the contact.

The FJ contact model is defined by micro-parameters that dictate the interaction between the particles, for the simulation of a rock material the micro-parameters must be calibrated with parameters of the intact rock. In this article, the model was calibrated according to the properties of uniaxial compression test, Brazilian test and triaxial compression test of an andesitic rock.

The calibration is carried out by proposing values of the micro parameters until obtaining in the simulations the same macroscopic response as the laboratory tests. The two-dimensional models used for the simulation of the Brazilian tests are circular of 0.06m in diameter, have 2309 particles, the models of the uniaxial and triaxial compression tests are rectangular of 0.06m × 0.14m, contain 6598 particles. For all models, the size of the grains is due to a uniform distribution of radii between 7.6×10^{-4} y 4.58×10^{-4} m. Figure 1 shows the rock models and the simulations of the different tests.

The model was calibrated according to the algorithm described by Potyondy (2017), after this procedure the micro-parameter values calibrate were:

- Particle/ Linear contact: grain density = 2,340 kg/m³; effective modulus = 20.5 GPa; friction coefficient = 0.4; and stiffness ratio = 2.3
- Cement/ Flat-Joint contact: bond effective modulus = 20.5 GPa; bond stiffness ratio = 2.3; bond tensile strength = 8.8 MPa; bond cohesion = 59.98 MPa; and bond friction angle = 40°.

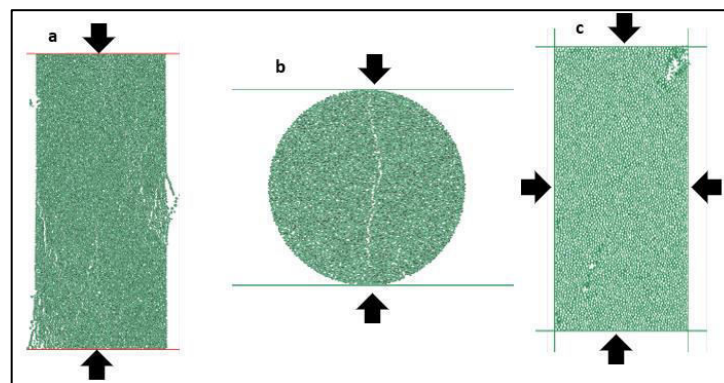


Figure 1. DEM simulation tests: a) uniaxial compression test; b) Brazilian test; c) triaxial compression test

The average rock strength parameters obtained by the simulations and laboratory tests are as follows:

- Laboratory: $E = 18.7 \times 10^9$ [Pa]; $\nu = 0.24$; $\sigma_{usc} = 87.6 \times 10^6$ [Pa]; $\sigma_t = 6.7 \times 10^6$ [Pa]
- Simulation: $E = 18.7 \times 10^9$ [Pa]; $\nu = 0.24$; $\sigma_{usc} = 87.6 \times 10^6$ [Pa]; $\sigma_t = 6.7 \times 10^6$ [Pa]

In the values it is observed that they have very little difference, that is, the modeled material adequately represents the rock mechanical behavior.

3.2 Boundary conditions and wave propagation.

Models made with Discrete Elements can transmit waves and represent the reflection phenomenon. However, when you have sources that cause large pulses, such as explosive detonations, you need a medium that is too wide for the energy to dissipate completely and ensure that unwanted reflection phenomena do not occur.

In this paper, the theory of viscous limit is used, at the model boundary, so that the influence of reflected waves on contours is eliminated. For this, Lysmer and Kuhlemeyer (1969) proposed Equation 1, which is used to generate absorbing boundaries, which cancel out the waves that impinge on them.

Let F_{vis} the viscous force, C the wave velocity, ρ_r the density of the rock, v_n the n -particle velocity, r_n the n -particle radius, L the length of the boundary of the model y N_n the number of particles of the boundary.

$$F_{vis} = -\rho_r C v_n \left(\frac{L r_n}{\sum_i^{N_n} r_i} \right) \quad (1)$$

To apply the viscous forces on the particles of the model, a dynamic condition is applied, since it will vary according to the speed acquired by the particles that are at the boundaries.

If you want to impose static stress states (σ_s) on the boundary of the DEM model, these must be translated into forces that are applied to the centers of the boundary particles. In the models made for this article, the boundary conditions were imposed with a mixed force (F_n) (Equation 2) on each particle, which considers the viscous limit and the static stress state (Li *et al.*, 2015). Figure 2 shows the model with the particles that impose the boundary conditions.

$$F_n = (\sigma_n - \rho_r C v_n) \left(\frac{L r_n}{\sum_i^{N_n} r_i} \right) \quad (2)$$

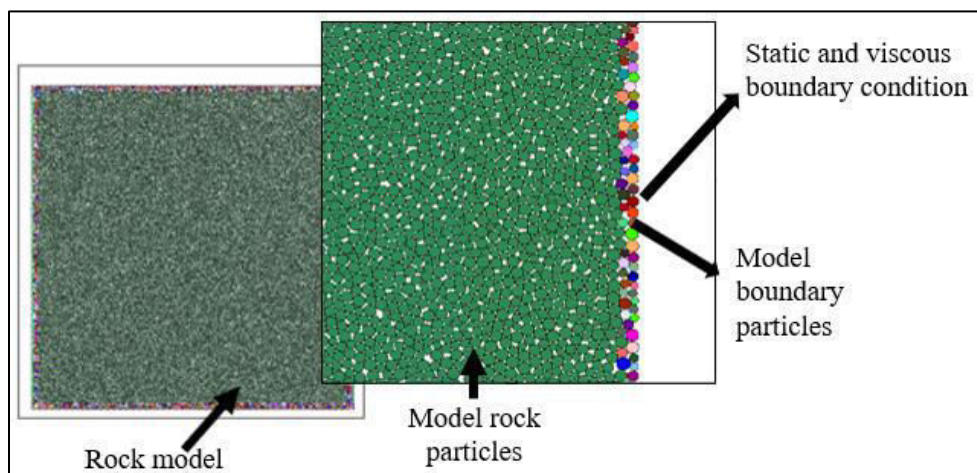


Figure 2. Schematic diagram of the two-dimensional numerical analysis.

On the other hand, it was also verified that the model performs an adequate simulation of wave propagation, also, the phenomenon of wave reflection. To do this, in the model of larger dimensions used in this work (10 m×10 m), and consisting of 156,587 particles, a sinusoidal impulse was applied on the left side, while on the right side two conditions were applied, for two simulations. In the first, no force was imposed, so that it could be observed if the wave reflection phenomenon is generated properly. In the second, the absorbing limit was set to eliminate the reflected wave phenomenon.

Likewise, 9 wave velocity measurement points were placed, three at the beginning, three in the middle and three at the end; with three different depths in the model (Figure 3).

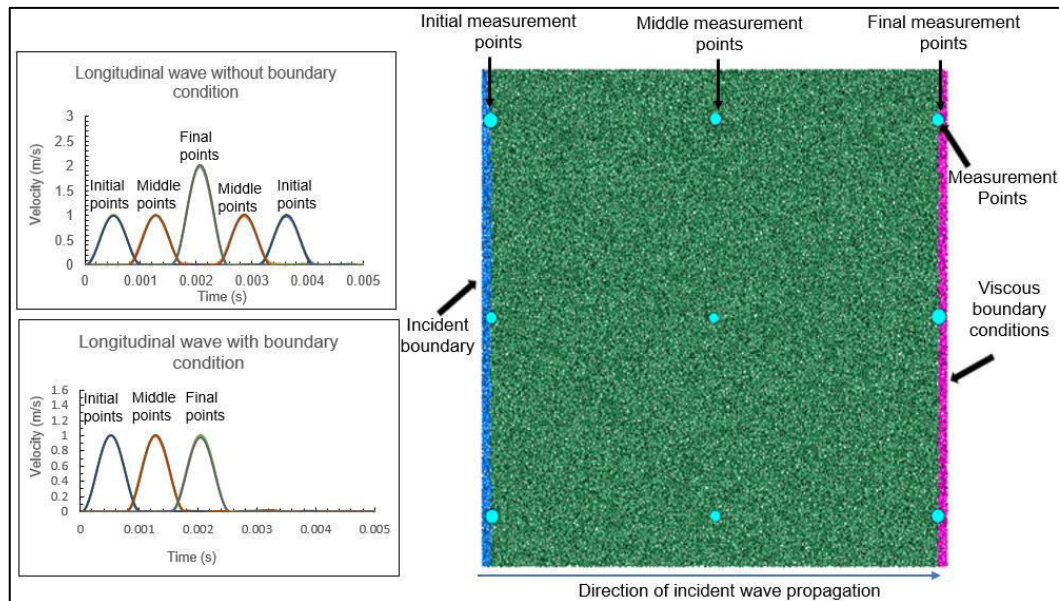


Figure 3. Wave propagation test

To verify that the speed of wave in the model were representative of the material, this parameter was calculated in the simulations with the range of times between ridges and the distances between the measuring points of the same depth, obtaining a value of 3,210 m/s, this is compared with the speed of propagation of wave measurement in the laboratory that was 3,423 m/s and the calculated theoretically, which was 3,033 m/s. Observing the wave propagation velocities obtained, it can be concluded that the model is reliable and has a reasonable medium representativeness.

In the graphs shown in Figure 3, the behavior of the frequency of the wave according to time is the same in the three depths. The upper graph shows the results of wave speed when there is no boundary condition, he appreciates that the model adequately simulates the phenomenon of wave reflection, since after the speed record on the end point, is recorded speed at the mid-point. In the case of the graph below that shows the results when imposes boundary condition viscose, it is observed that there is no reflection, because the speed reading ends with the record speed at the end point, as well as, the amplitude of this point is equal to that of the other, as if it react with more of the medium, even if it is not there, that is to say, the boundary condition works properly, representing an infinite medium.

3.3 Application and model of the explosive charge

In the simulation of the explosion effect in cemented particle models, there are two ways. In the first, the stress of the shock wave is applied indirectly through the velocities to the particles of the borehole contour. The pressure of the detonation gas is applied on the fractures caused by the shock wave (Yuan *et al.*, 2019). another way is through an explosive particle, which expands its diameter instantly. After the expansion of the explosive particle, an overlap will be generated between the explosive particle and the surrounding particles. As the particles and contacts are considered rigid, forces or moments would be generated, pushing the surrounding particles in the adverse direction from the point of explosion (Zehua *et al.*, 2020). The latter was used in this article.

To simulate this phenomenon, the pressure in the walls of the hole, the product of the detonation of an explosive, was first obtained by Equation 3 (for coupled conditions). The same one that Dai (2002) determined through controlled detonation experiments where pressure measurements were made, considers the adiabatic phenomenon to calculate the pressure on the walls of the hole.

Let P_b be the detonation pressure on the walls of the borehole (Pa) and r is the ratio to the specific heat of the system, for the detonation pressure of explosives it is taken equal to 3.

$$P_b = \frac{(\rho_e)(D^2)}{2(1+r)} \quad (3)$$

To simulate detonation, the explosive particle must have the physical properties of the explosive (Figure 4). According to the force generated by the contact, we assume a particle with initial radius (r_0), which will expand until it reaches the walls of the hole, this will cause pressure on the particles that the contour of the hole (P_b). To calculate Zehua *et al.* (2020) proposes Equation 4 and Equation 5 to determine the stiffness (k_{ne}) of the explosive particle. The density of the explosive used is 1,250 kg/m³ and the detonation speed is 5,200 m/s, these values are kept constants for all simulations. Let r_{max} and r_{min} be the maximum and minimum radius that the particle will have.

$$d_r = \frac{P_b * 2 * r_0 * \pi}{k_n} \quad (4)$$

$$k_{ne} = \frac{2 * P_b * (r_{max} + r_{min}) * \pi}{(r_{max} - r_{min})} \quad (5)$$

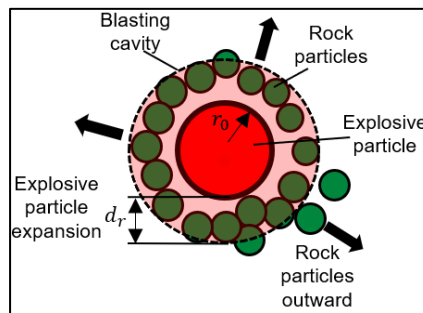


Figure 4. Schematic diagram of the charge explosion (modified from Zehua *et al.*, 2020)

The shock wave propagates outward spherically, with a rise time (t_r) until it reaches a peak pressure. In this work it is simplified by representing it with an exponential function as a function of time, a t_r of 2 ms was used (Wenzhuo *et al.*, 2016).

3.4 Verification of the explosive model

The application of gas pressure is a common obstacle when using the discrete element method for blasting simulation, in the particle expansion algorithm the effect of the explosion stress wave and the detonation gas cannot be re-strapping separately. Therefore, to examine the reliability of the method, a verification model with a dimension of 10 m×5 m was established (Figure 5). In which the attenuation of the stress caused by the explosion with distance was measured and compared with the theoretical one. As can be seen in Figure 5, the maximum stresses derived from the model were relatively close to those theoretically derived, demonstrating the feasibility of simulating rock blasting through the particle expansion algorithm.

It should be emphasized that the theoretical calculations do not take the discontinuous of the medium, nor all the properties of the rock, unlike the DEM, so it is considered that the measurement made in the simulations, are more representative of reality.

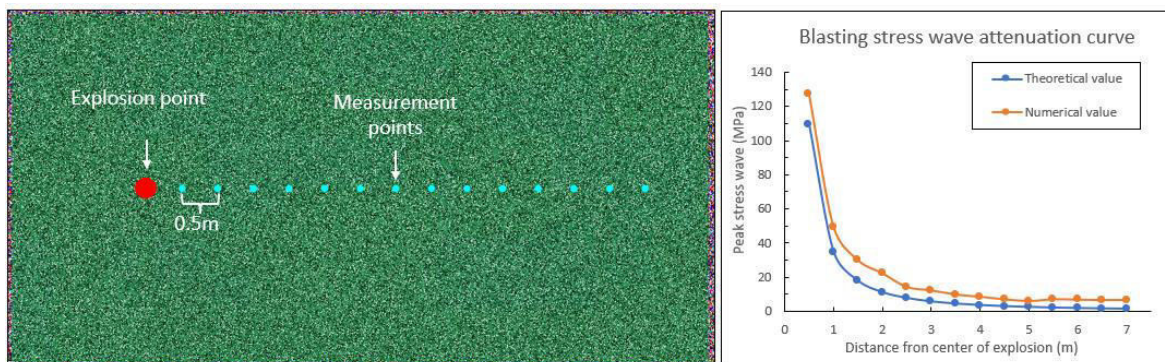


Figure 5. Blasting stress wave attenuation curve

4 RESULTS OF THE SIMULATIONS

The methodology described above was applied in two types of blasting simulations. In the first type, the detonation of a hole with different states of forces in the middle was simulated. In the second type, blasting was simulated on a template of loaded boreholes, in each model different arrangements of unloaded boreholes were assigned. The same explosive and rock properties previously described were used in all simulations.

4.1 Simulation of blasting with different stress states

The two-dimensional model used for the analysis of the detonation of a hole with different stress states contains 38,547 particles of 1.16×10^{-2} m to 1.71×10^{-2} m radius in normal distribution. The explosive particle has an initial radius of 3.0×10^{-2} m. The model is a square with a length per side of 100 times the average diameter of the particles. A vertical effort of 10 MPa was imposed for all simulations, only one was performed with different values of lateral pressure coefficient ($k = \sigma_h / \sigma_v = 0.25, 0.5, 1, 1.5, 2$).

The explosive particle was placed in the center, after detonation the geometry of the fractures that occurred and the number of these were reviewed. The number of fragments generated by the explosion was also obtained, as well as the scope of the crushed and fractured areas. The crushed area, which does not vary considerably in the different simulations, is preserved with a crushed area of 6 times the radius of the hole.

In the simulation with k of 0.25 (Figure 6-a) a total of 1,361 cracks were recorded. These extend with a maximum of 26 times the radius of the hole in the vertical direction and 8 times in the horizontal direction. The ratio of the horizontal and vertical length of the cracks is 0.33.

On the other hand, with a lateral pressure coefficient of 0.5, 905 fractures were generated. Which extended up to 21 times the radius of the bore vertically and 11 times horizontally. So, the ratio between the horizontal and vertical length of the cracks is 0.54.

When the rock is subjected to a coefficient k of 1 (Figure 6-b). The number of fractures generated is 733. The cracks had a maximum length of 13 times the radius of the hole in the vertical direction and 11 times in the horizontal direction. With this, the ratio of the length of the fractures is 0.89. In the simulation it has a k of 1.5. A total of 684 fractures were recorded. These extend with a maximum of 9 times the radius of the hole in the vertical direction and 15 times in the horizontal direction. Therefore, they are more persistent in the direction of the major main effort, up to 1.6 times more with respect to the minor main effort.

Finally, Figure 6-c belongs to the simulation with a lateral pressure coefficient of 2; and 671 fractures were recorded. The cracks in the vertical direction have a maximum length of 9 times the radius of the hole and in the horizontal direction of 17 times. Therefore, the ratio between the horizontal and vertical length of the cracks is 2.

The five previous simulations had a lower number of fractures as the lateral pressure coefficient increased, also, the cracks had greater persistence in the sense of greater applied main stress. The ruptures generated were mostly concentrated in the area surrounding the explosion. This is due to the low detonation speed of the simulated explosive, which generates a greater crushing with shorter fracture lengths.

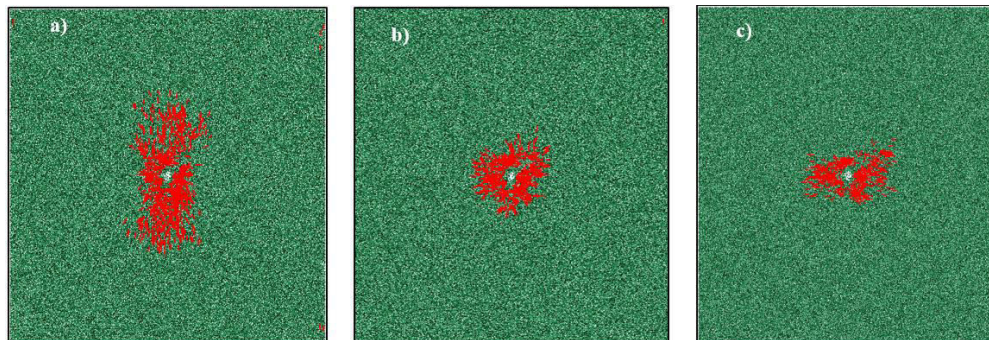


Figure 6. Crack distribution in the surrounding blasthole for various lateral pressure coefficients.

4.2 Blasting simulation on drilling patterns with different contour hole arrangements

The simulation of the detonation in a drilling pattern with three different conditions of contour blastholes was made with a $5\text{ m} \times 5\text{ m}$ model, formed by 58 drills. The explosive charge of all the blastholes has the same characteristics as the one used in the previous tests. Figure 7 shows the base drilling pattern, it shows the detonation sequence, which is governed by the numbering, the separation between each detonation is 25 ms . Also, three arrangements of contour sweeps are presented. The first case is designed according to the empirical formulas of Konya (1990); in the second case, no-load boreholes are added between the load-two boreholes, in the walls and the floor; in the third case, the no-load blastholes of the previous case are loaded with explosive.

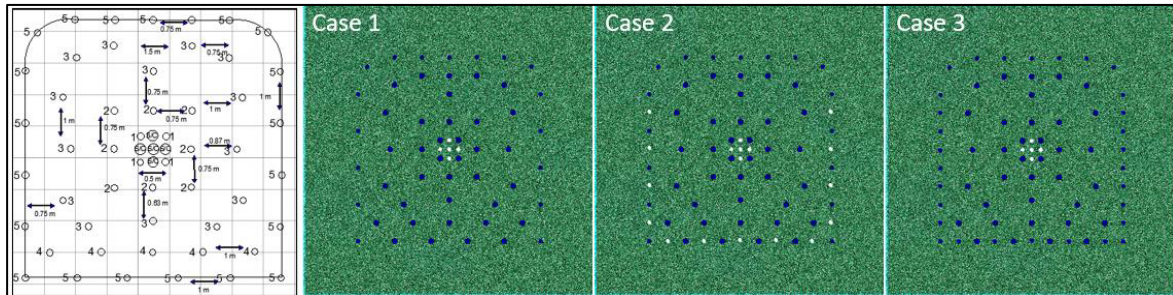


Figure 7. Drilling pattern and tree different condition of contour boreholes

Figure 8 shows the three models after detonating without fragments or elements that were completely separated from the rock modeling. In the first model (case 1) a non-uniform contour can be seen, where a regular section of the excavation is not preserved. In addition, large edges are observed without detaching from the perimeter of the section. Fragmentation and fracturing were only conserved in the contour of the trunks, with a higher density of fissures outside the contour of the section.

In case 2, there are no large blocks in the excavation contour. However, a uniform contour is not achieved, mainly, on the floor of the section compared to the previous one. The fracturing and fragmentation had a higher density in the direction of the free face, this is due to the wave reflection phenomenon.

In the third, like the second model, there are no large blocks in the excavation contour, nevertheless, a uniform perimeter is appreciated (on the walls and the floor of the section), and even half of the blasthole is observed, which indicates a good blasting. The fragmentation and fracturing had no noticeable changes.

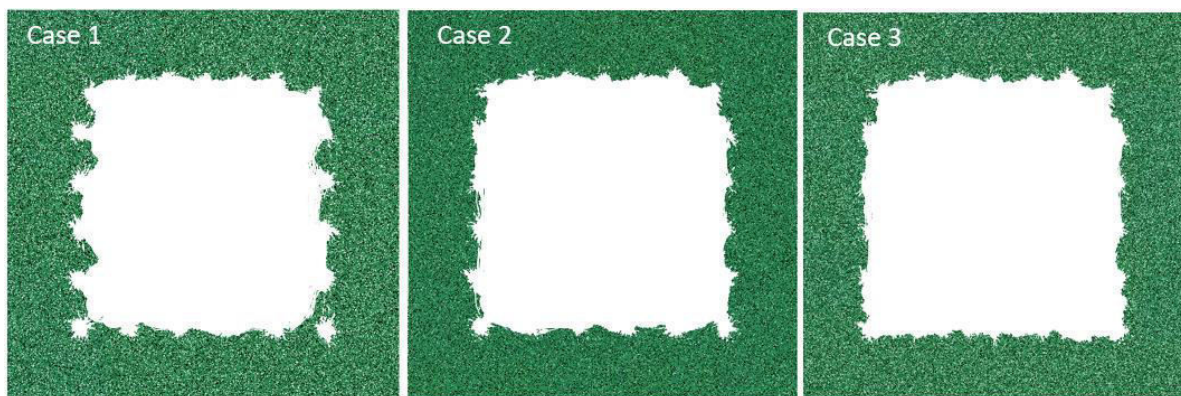


Figure 8. Drilling pattern models after of detonation.

5 CONCLUSIONS

- The simulations of the rock tests using the Flat Joint contact model, present behaviors, and representative parameters of the physicists. The calibration method proposed for simulations with

laboratory results is applied satisfactorily. The DEM can represent the breaking mechanisms in a rock; therefore, it favors the study of fracturing caused by explosives.

- The phenomenon of wave reflection was represented satisfactorily by the discrete element method. The boundary condition used worked correctly since it removed wave reflection in the model contour.
- The effects of the shock wave can be observed in the breakdown of contacts between particles and the formation of fractures. These show the area of influence of the hole and even the geometry and type of propagation that the fractures will have in the rock.
- In the analysis of explosions with initial stress conditions, congruent behaviors were observed. It is advisable to use an algorithm that imposes radial efforts or in all directions, to obtain results that are closer to reality.
- Fractures generated by explosives have a greater length in the direction of the greater main stress, this behavior is consistent with the physical phenomenon and with fracturing rocks theory
- The relationship between the length of the fractures in the horizontal and vertical direction is like the horizontal pressure coefficient to which the material is subjected.
- The implementation of a free face in a blast generates a greater fracturing and fragmentation in the direction of this, due to the phenomenon of wave reflection. On the other hand, in the different conditions of contour blastholes, sections with different uniformity in the perimeter were obtained, congruent with reality, with which the use of the DEM for the design of drilling pattern can be proposed.
- Workovers in case 2 and 3 contour boreholes proved to have better results. Case 3 was the one in which the most uniform contour was obtained, however, it requires greater use of explosives, unlike case 2, in which a complete excavation with an acceptable perimeter was obtained. Finally, in case 1, the drills did not generate enough rock breakage to obtain a complete section of the tunnel.
- The simulation of the blasting in a drilling pattern shows that it is possible to represent the effect of the explosions of several boreholes by DEM. As well as perform analysis of different drilling patterns.
- Through the blast simulations of a blasthole and a drilling pattern, we can conclude that the discrete element method with the blast simulation methodology shown is a tool for the analysis and design of blasts, which allows studying phenomena that are not possible to analyze by empirical criteria or continuous descriptions.

6 REFERENCIAS

- Bernalao, J., Castilla, J., & Herrera, J. (2009). *Perforación y voladura de rocas en minería*. Madrid, España: Universidad Politécnica de Madrid.
- Cundall, P., & Strack, O. (1979). A Discrete Numerical Model for Granular Assemblies. *Géotechnique*, 29, 47-65.
- Dai, J. (2002). *Rock Dynamics and blasting theory*. China: Metallurgical Industry Press.
- González, I. (2012). *Introducción al diseño de voladuras*. Ciudad de México, México: Austin Powder Company.
- Konya. (1990). *Manual de Voladuras*. EUA: ESING.
- Kumar, H., Kumar, N., Singh, M., & Venkat, V. (2014). Blast induced damage to surrounding rock mass underground excavation. *Journal of Geological Resource and Engineering*, 13-19.
- Li, B., Liu, X., Chen, W., & Li, L. (2015). Discret element simulation of attenuation law of blasting stress wave. *International Conference on Chemical, Material and Food Engineering*.
- López, V. (2015). *Fundamentos de explotación de minas*. Ciudad de México, México: UNAM.
- Oyanguren, P. R., & Monge, L. A. (2004). *Mecánica de Rocas: Fundamentos e Ingeniería de Taludes*. Madris, España: Universidad Politécnica de Madrid.
- Potyondy, D. (2017). *Material-Modeling Support in PFC [fistPkg25]*. Minneapolis, Minnesota, EUA: Itasca Consulting Group, Inc., Technical Memorandum ICG77.
- Potyondy, D., & Cundall, P. (1996). *Modeling of shock and gas driven fractures induced by a blast using bonded assemblies of spherical particles*. Minneapolis, EUA: Itasca colsutling group.

- Yuan, W., Wang, W., Su, X., Li, J., Li, Z., Wen, L., & Chang, J. (2018). Numerical study of the impact mechanism of decoupling charge on blasting-enhanced permeability in low-permeability sandstones. *International Journal of Rock Mechanics and Mining Sciences*, Vol. 106, 300-310.
- Zehua, Z., Wenle, G., Kunpeng, L., & Baojie, L. (2020). Numerical simulation of rock mass blasting using particle flow code and particle expansion loading algorithm. *Simulation modelling practice and theory* , 102-119.

The book "Proceedings from the IX Latin American Rock Mechanics Symposium" contains the summary of all the articles presented at the IX Latin American Symposium on Rock Mechanics, which took place in Asunción, between October 16 and 19, 2022.

The main topics included in this book are related to rock mechanics testing, case studies, mining engineering, numerical methods and models applied to rock mechanics, geothermal engineering, soft rocks and tunneling.

ISBN: 978-99925-3-874-6



ORGANIZED BY :



HOST: